

LEVEL

AGARD-CP-247

AGARD-CP-247

ADA067323

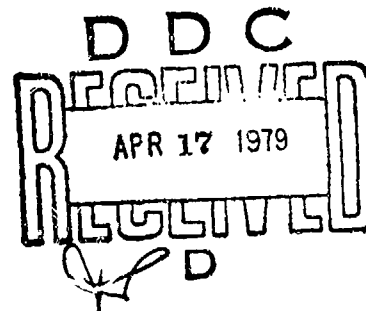
AGARD

ADVISORY GROUP FOR AEROSPACE RESEARCH & DEVELOPMENT

7 RUE ANGELLE 92200 NEUILLY SUR SEINE FRANCE

AGARD CONFERENCE PROCEEDINGS No. 247

High Angle of Attack Aerodynamics



NORTH ATLANTIC TREATY ORGANIZATION



DISTRIBUTION AND AVAILABILITY
ON BACK COVER

DISTRIBUTION STATEMENT A

Approved for public release;
Distribution Unlimited

79 04 17 145

NORTH ATLANTIC TREATY ORGANIZATION
ADVISORY GROUP FOR AEROSPACE RESEARCH AND DEVELOPMENT
(ORGANISATION DU TRAITE DE L'ATLANTIQUE NORD)

AGARD Conference Proceedings, No. 247

HIGH ANGLE OF ATTACK AERODYNAMICS

(11) Jan 71

(12) 548p.

ACCESSION for	
WTS	Write Section <input checked="" type="checkbox"/>
CND	Diff Section <input type="checkbox"/>
UNANNOUNCED	<input type="checkbox"/>
JUSTIFICATION	
BY	
DISTRIBUTION/AVAILABILITY CODES	
Dist.	AVAIL. RDG/ or SPECIAL
A	

DISTRIBUTION STATEMENT A

Approved for public release;
Distribution Unlimited

DDC
RECEIVED
APR 17 1979
D

Papers presented and discussions from the Fluid Dynamics Panel Symposium held at the Park Hotel, Sandefjord, Norway, 4-6 October, 1978.

400 043

LB

THE MISSION OF AGARD

The mission of AGARD is to bring together the leading personalities of the NATO nations in the fields of science and technology relating to aerospace for the following purposes:

- Exchanging of scientific and technical information;
- Continuously stimulating advances in the aerospace sciences relevant to strengthening the common defence posture;
- Improving the co-operation among member nations in aerospace research and development;
- Providing scientific and technical advice and assistance to the North Atlantic Military Committee in the field of aerospace research and development;
- Rendering scientific and technical assistance, as requested, to other NATO bodies and to member nations in connection with research and development problems in the aerospace field;
- Providing assistance to member nations for the purpose of increasing their scientific and technical potential;
- Recommending effective ways for the member nations to use their research and development capabilities for the common benefit of the NATO community.

The highest authority within AGARD is the National Delegates Board consisting of officially appointed senior representatives from each member nation. The mission of AGARD is carried out through the Panels which are composed of experts appointed by the National Delegates, the Consultant and Exchange Programme and the Aerospace Applications Studies Programme. The results of AGARD work are reported to the member nations and the NATO Authorities through the AGARD series of publications of which this is one.

Participation in AGARD activities is by invitation only and is normally limited to citizens of the NATO nations.

The content of this publication has been reproduced directly from material supplied by AGARD or the authors.

Published January 1979

Copyright © AGARD 1979
All Rights Reserved

ISBN 92-835-0230-2



*Printed by Technical Editing and Reproduction Ltd
Harford House, 7-9 Charlotte St, London, W1P 1HD*

FOREWORD

The Symposium was organised at this time because of the continuing need for design data and principles relevant to the flight of aircraft and missiles at high angles of attack and because of the substantial effort that had been devoted over recent years to the development of aircraft and missiles capable of controlled flight at high angles of attack.

Aerodynamics spans the behaviour of air vehicles and the behaviour of fluids. At high angles of attack, we need dynamic stability parameters to describe the behaviour of air vehicles and we need an understanding of separated flow, usually highly 3-dimensional and often unsteady, to describe the behaviour of the air. The Symposium made it clear that the present state of knowledge in the area of high angle-of-attack aerodynamics is descriptive of the dynamics of the vehicle and of the fluid, despite the needs of the designer for rational methods of prediction.

The Round Table Discussion included pleas for attention to a large number of problems and principles, some of which are mentioned below.

- (a) Well-designed experiments, in which theoretical ideas are taken into account; and a willingness to repeat them.
- (b) Further development of methods, leading in particular to the prediction of maximum lift coefficient and the occurrence of vortex breakdown.
- (c) Closer collaboration between practical aerodynamicists and experts in fundamental fluid mechanics.
- (d) Attention to controllability, rather than stability; this to include attention to the aerodynamics of control surfaces.
- (e) Acceptance, by the designer, of the largest available measurements of out-of-plane forces where asymmetric separation is possible on configurations at high angle of attack.
- (f) Avoiding prejudicing the low incidence behaviour of military aircraft in the pursuit of carefree manoeuvring.
- (g) Attention to the end product, which is an air vehicle to be designed and manufactured in a limited time scale.

The diversity and difficulty of the problems addressed prevented the emergence of well-defined technical conclusions; but it is clear that many of the topics discussed will continue to present challenges to designers and research workers for many years to come, and will reappear in future Symposia of the FDP.

AGARD FLUID DYNAMICS PANEL

CHAIRMAN: Mr J.L.Jones – MS 200-10
NASA Ames Research Center
Moffett Field, California 94035
USA

DEPUTY CHAIRMAN: Dr K.J.Orlik-Rückemann
National Aeronautical Establishment
National Research Council
Montreal Road, Ottawa K1A 0R6
Canada

PROGRAM COMMITTEE MEMBERS

Dr W.J.McCroskey (Chairman)
US Army Air Mobility Research and
Development Laboratory
Ames Research Center, N215-1
Moffett Field, Calif. 94035, USA

M. l'Ing. General A.Auriol
Directeur Scientifique Central
ONERA
29 Avenue de la Division Leclerc
92320 Châtillon, France

Dr J.E.Green
Head of Aerodynamics Department
RAE
Farnborough
Hants. GU14 6TD, UK

Prof. Dr J.L. van Ingen
Department of Aerospace Engineering
Delft University of Technology
Kluyverweg 1
2629 HS Delft – Netherlands

Prof. Dr F.J.Hindelang
Fachbereich Luft-und Raumfahrttechnik
Hochschule der Bundeswehr München
8014 Neubiberg
Germany

Dr K.J.Orlik-Rückemann
National Aeronautical Establishment
National Research Council
Montreal Road, Ottawa-Ontario K1A 0R6
Canada

Dr G.G.Pope
Head of Group A
RAE
Farnborough
Hants. GU14 6TD, UK

M. Ph.Poisson-Quinton
Adjoint au Directeur Scientifique Central
ONERA
29 Avenue de la Division Leclerc
92320 Chatillon – France

PANEL EXECUTIVE

Robert H.Rollins II
AGARD
7 rue Ancelle
92200 Neuilly sur Seine
France

CONTENTS

	Page
FOREWORD	iii
PROGRAM AND MEETING OFFICIALS	iv
	Reference
 <u>SESSION I – STUDIES OF CONFIGURATIONS OF PRACTICAL APPLICATION</u>	
EFFECT OF HIGH ANGLES OF ATTACK ON DYNAMIC STABILITY PARAMETERS by K.J.Orlik-Rückemann	1
HIGH ANGLE OF ATTACK CHARACTERISTICS OF DIFFERENT FIGHTER CONFIGURATIONS by H.John and W.Kraus	2
HIGH ANGLE OF ATTACK BEHAVIOUR: INCIDENCE LIMITS AND MEANS FOR IMPROVEMENTS* by D.Booker	3
SOME UK RESEARCH STUDIES OF THE USE OF WING-BODY STRAKES ON COMBAT AIRCRAFT CONFIGURATIONS AT HIGH ANGLES OF ATTACK by G.Moss	4
DESIGN GUIDELINES FOR THE APPLICATION OF FOREBODY AND NOSE STRAKES TO A FIGHTER AIRCRAFT BASED ON F-16 WINDTUNNEL TESTING EXPERIENCE by C.W.Smith and C.A.Anderson	5
FOREBODY-WING VORTEX INTERACTIONS AND THEIR INFLUENCE ON DEPARTURE AND SPIN RESISTANCE by A.M.Skow, A.Titiriga, Jr and W.A.Moore	6
STRAKE-INDUCED SEPARATION FROM THE LEADING EDGES OF WINGS OF MODERATE SWEEP by S.P.Fiddes and J.H.B.Smith	7
AERODYNAMIC CHARACTERISTICS OF A FIGHTER TYPE CONFIGURATION DURING AND BEYOND STALL by W.Staudacher, B.Laschka, Ph.Poisson-Quinton and J.P.Ledy	8
THE APPLICATION OF SPANWISE BLOWING FOR HIGH ANGLE OF ATTACK SPIN RECOVERY by J.J.Cornish III and M.W.M.Jenkins	9
COMPORTEMENT A HAUTE INCIDENCE D'UN AVION DE TRANSPORT A AILE A GRANDE ELANCEMENT par D.Collard	10
AERODYNAMIC DESIGN OF THE SPACE SHUTTLE ORBITER by W.E.Bornemann and T.E.Surber	11
 <u>SESSION II – MATHEMATICAL MODELLING AND SUPPORTING INVESTIGATIONS</u>	
SYSTEME TOURBILLONNAIRE PRESENT A L'EXTRADOS D'UNE AILE EN FLECHE A GRANDE INCIDENCE par J.Mirande, V.Schmitt et H.Werlé	12
STABLE AND UNSTABLE VORTEX SEPARATION by E.H.Wedemeyer	13

* Not to be published.

CALCUL INSTATIONNAIRE DE NAPPES TOURBILLONNAIRES EMISES PAR DES SURFACES PORTANTES FORTEMENT INCLINEES par C.Rehbach	14
ON THE VORTEX FORMATION OVER A SLENDER WING AT LARGE ANGLES OF INCIDENCE by D.Hummel	15
SYMMETRICAL AND ASYMMETRICAL SEPARATIONS ABOUT A YAWED CONE by D.J.Peake, F.K.Owen and H.Higuchi	16
PRESSURES ON A SLENDER BODY AT HIGH ANGLE OF ATTACK IN A VERY LOW TURBULENCE LEVEL AIR STREAM by B.L.Hunt and P.C.Dexter	17
WIND AND WATER TUNNEL INVESTIGATIONS OF THE INTERACTION OF BODY VORTICES AND THE WING PANELS OF A MISSILE CONFIGURATION by J.R.Deane	18
CARACTERISTIQUES AERODYNAMIQUES DES CORPS DE REVOLUTION MUNIS D'AILES D'ALLONGEMENTS DIVERS par L.Mifsud	19
AERODYNAMIC CHARACTERISTICS OF A MISSILE FEATURING WING WITH STRAKES AT HIGH ANGLES OF ATTACK by M.Akcay, B.E.Richards, W.Stahl and A.Zarghami	20
ON THE LEE SIDE FLOW OVER DELTA WINGS AT HIGH ANGLE OF ATTACK by J.Szodruch and U.Ganzer	21
MEASUREMENTS OF THE SUPERSONIC FLOW FIELD PAST A SLENDER CONE AT HIGH ANGLES OF ATTACK by W.J.Bannink and C.Nebbeling	22
NUMERICAL SIMULATION OF SUPERSONIC CONE FLOW AT HIGH ANGLE OF ATTACK by D.C.McRae and M.Y.Hussaini	23
<u>SESSION III – DESIGN METHODS</u>	
RECENT THEORETICAL DEVELOPMENTS AND EXPERIMENTAL STUDIES PERTINENT TO VORTEX FLOW AERODYNAMICS – WITH A VIEW TOWARDS DESIGN (REVIEW PAPER) by J.E.Lamir and J.M.Luckring	24
A COMPUTATIONAL MODEL FOR THE CALCULATION OF THE FLOW ABOUT WINGS WITH LEADING-EDGE VORTICES by H.W.M.Hoeijmakers and B.Bennekers	25
SUBCRITICAL DRAG MINIMIZATION FOR HIGHLY SWEPT WINGS WITH LEADING EDGE VORTICES by E.N.Tinoco and H.Yoshihara	26
NORMAL FORCE AND PITCHING MOMENT OF WING-BODY-COMBINATIONS IN THE NON-LINEAR ANGLE-OF-ATTACK RANGE AT SUBSONIC SPEEDS by C.P.Schneider and D.Nikolitsch	27
PREDICTION OF AERODYNAMIC CHARACTERISTICS FOR SLENDER BODIES ALONE AND WITH LIFTING SURFACES TO HIGH ANGLES OF ATTACK by L.H.Jorgensen	28
PREDICTION OF LATERAL AERODYNAMIC LOADS ON AIRCRAFT AT HIGH ANGLES OF ATTACK by S.B.Spangler, S.C.Perkins, Jr and M.R.Mendenhall	29

PREDICTION AND MEASUREMENT OF THE AERODYNAMIC FORCES AND PRESSURE DISTRIBUTIONS OF WING-TAIL CONFIGURATIONS AT VERY HIGH ANGLES OF ATTACK

by R.P.White, Jr

30

SESSION IV – AIR INTAKES

HIGH ANGLE OF INCIDENCE IMPLICATIONS UPON AIR INTAKE DESIGN AND LOCATION FOR SUPERSONIC CRUISE AIRCRAFT AND HIGHLY MANEUVERABLE TRANSONIC AIRCRAFT

by L.L.Presley

31

INTAKE DESIGN AND INTAKE/AIRFRAME INTEGRATION FOR A POST-STALL FIGHTER AIRCRAFT CONCEPT

by K.W.Lotter and J.Malefakis

32

OPEN DISCUSSION SESSION

COMPRESSIBILITY EFFECTS ON THE SYMMETRIC BODY VORTEX WAKE OF AN OGIVE NOSE CYLINDER

by W.L.Oberkampf and T.J.Bartel

OD1

HIGH ANGLE OF ATTACK INLET TEXT*

by G.K.Richey

OD2

WIND TUNNEL TEST AT LOW SPEEDS OF A DORSAL AIR INTAKE ON A FIGHTER CONFIGURATION

by S.O.Ridder

OD3

VISUALISATIONS AND CALCULATIONS OF AIR INTAKES AT HIGH ANGLES OF ATTACK AND LOW REYNOLDS NUMBERS

by P.C.Perrier and J.Periaux

OD4

STATE OF ART OF NONLINEAR DISCRETE-VORTEX METHODS FOR STEADY AND UNSTEADY HIGH ANGLE OF ATTACK AERODYNAMICS

by O.A.Kandil

OD5

ON SLENDER WINGS WITH LEADING EDGE CAMBER

by R.K.Nangia

OD6

AN EXPERIMENTAL INVESTIGATION OF THE ENTRAINMENT OF A LEADING-EDGE VORTEX

by N.G.Verhaagen and L. van der Snoek

OD7

A SURVEY OF RECENT HIGH ANGLE OF ATTACK WIND TUNNEL TESTING AT AERITALIA

by G.Bucciantini, R. De Silvestro and L.Fornasier

OD8

ROUND TABLE DISCUSSION

RTD

* Not to be published.

by

K.J. Orlik-Rückemann
 Unsteady Aerodynamics Laboratory,
 National Aeronautical Establishment,
 National Research Council of Canada,
 Ottawa, Ontario, K1A 0R6,
 Canada

SUMMARY

A review is presented of the effects of flight at high angles of attack on dynamic stability parameters and their significance for the analysis of aircraft motion at those flight conditions. The review is based primarily, but not exclusively, on the material presented at the Spring 1978 FDP Symposium on Dynamic Stability Parameters. The topics discussed include (a) the strong non-linear variations of many stability parameters with angle of attack, (b) the emergence of new categories of parameters such as cross-coupling derivatives that are only of interest for high angle-of-attack or other asymmetrical flight conditions, (c) the significance of time-dependent parameters, such as represented by derivatives due to time rates of change of angles of attack and sideslip, (d) the strong configuration dependence of aerodynamic characteristics, as illustrated by large effects of strakes and of various shapes of aircraft forebody, and (e) the need for establishing and verifying a mathematical model that would satisfactorily describe the motion of an aircraft in the presence of all these high angle-of-attack effects.

0. INTRODUCTION

As is certainly well-known to this audience, there has been in recent years a considerable revival in our interest in dynamic stability of aircraft. The most important reason for this revival is the fact that flight at high angles of attack has been found to have dramatic effects on the various dynamic stability parameters and this, in turn, often has significant influence on the flight history of the aircraft. In recognition of this renewed interest, the Fluid Dynamics Panel of AGARD has recently held a well attended and very successful symposium on Dynamic Stability Parameters (Ref. 1). Since high angle of attack is obviously a key element in that field, I have been asked to review some of the material presented at that meeting with particular emphasis, of course, on the problems involving high angle-of-attack aerodynamics.

The fact that this presentation has been selected as the opening paper of the present symposium does not necessarily indicate that dynamic stability provides the most important manifestation of high- α effects. It is rather the result of an obvious effort on the part of the Programme Committee to provide a continuity and a direct link between two consecutive meetings of the Panel. There is, however, an additional and probably unintended meaning to this honorable first-place location. And this has to do with the fact that, although dynamic stability problems probably are not among the most important worries of an aircraft designer, high- α aerodynamics is likely to have much more pronounced effects on *dynamic* or *unsteady* parameters than on their *static* counterparts. So from this point of view, maybe that first location is, after all, not entirely undeserved.

What are now the aerodynamic phenomena that cause that kind of effects in oscillatory flight at high angles of attack? Some of the more important ones are listed in Figure 1. As the angle of attack goes from small to moderate, we observe flow separation over various components of the aircraft, such as wings, forebody and tail surfaces. As the angle of attack increases further, the cross flow around the fuselage becomes more and more important and begins to sweep the boundary layer to the leeward side of the body, gradually rolling it up into a pair of vortices. As the angle of attack increases even more, these vortices become asymmetric. At about the same time wing leading-edge vortices are formed (especially on delta wings), become unstable and finally break down. This vortex burst arrives over the wing at the trailing edge and moves forward with increasing angle of attack. Furthermore, the body vortices and the flow over the leeward side of the wing may sometimes strongly interact with each other.

The phenomena listed so far are, of course, not necessarily associated with dynamic flight conditions but occur in both steady and oscillatory flows. What makes the oscillatory flows particularly involved is the introduction of the time element into this already rather complex picture. The various vortices change their lateral positions as functions of angle of attack, which itself is a function of time. So does the longitudinal location of "fully developed" vortex bursts. The various components of the aircraft, such as the fin and the horizontal stabilizer, move in and out of local flow regions in which they are embedded. To make matters even more complex, all these motions take place not in a manner simultaneous with the motion of the aircraft, but with a certain delay, mainly due to the convective time lag, which in turn is a function of the distance

of the station under consideration from the station at which a particular flow phenomenon, such as a vortex, leaves the surface of the aircraft. Thus aerodynamic reactions that are both in-phase and out-of-phase with the motion of the aircraft can be expected to materialize.

It should be noted, that although for an aircraft flying at high angle of attack asymmetric flow may occur even at zero nominal sideslip (as discussed above), such an asymmetric flow will also occur, of course, at lower angles of attack when the aircraft is exposed to finite angles of sideslip. Since such a flight condition is encountered quite frequently, the remarks in this paper that deal with the effects of flow asymmetries have a rather general application. It should also be mentioned, that the phenomenon of vortex burst is quite sensitive to the sweep angle of the wing and therefore is also strongly dependent on the angle of sideslip. For instance, even if an aircraft flies at an angle of attack below vortex burst, an oscillatory variation in the instantaneous angle of sideslip may, under some circumstances, cause periodic vortex bursts on the wings. High angle of attack, therefore, is to some extent equivalent to a combination of a somewhat lower angle of attack and a finite angle of sideslip, and these two flight conditions will be considered together in the remaining part of this paper.

1. NON-LINEARITIES

Let us examine the effects that the aforementioned aerodynamic phenomena have on dynamic stability parameters. The most important such effects are (Figure 2): (a) very large non-linear variations of stability parameters with the angle of attack, (b) significant static and dynamic aerodynamic cross-coupling between the lateral and the longitudinal degrees of freedom, (c) various time-dependent and hysteresis effects, (d) strong configuration dependence of some stability parameters, and (e) need for more sophisticated mathematical modelling, which now has to include all the above effects and may even introduce additional stability parameters.

Some examples of the non-linear variations of dynamic stability derivatives with angle of attack and the rate of spin are given in the next two figures. In Figure 3 the subsonic pitch damping and yaw damping of a wing-body configuration is shown as measured at NAE (Ref. 2). The curves amply illustrate both the magnitude and the suddenness of the variations with angle of attack. It can be appreciated that if the angle of attack about which the oscillation takes place happens to be in the region where a sudden change in a derivative occurs, large effects of the amplitude of oscillation may be expected. In cases like this the derivative concept can only give an equivalent linearized description of the dependence of the aerodynamic reaction on the variable of motion and a better mathematical formulation is definitely needed.

Similar non-linearities in damping derivatives were measured at NASA Langley (Ref. 3) for a fighter aircraft at low subsonic speeds and are shown at the top of Figure 4. The yaw damping derivative exhibits a very sudden and very large unstable peak at angles of attack around 60° . This is usually the result of the vortex pattern that is associated with long, pointed forebodies. The roll damping derivative shows marked irregularities and a large dependence on the amplitude of oscillation at angles of attack between 25° and 45° . The smaller the amplitude of oscillation, the more pronounced is the local instability in roll. It has also been observed (although not shown here) that a decreasing oscillation frequency has a similar destabilizing effect, indicating that the governing factor for this phenomenon is the maximum angular velocity in roll experienced by the aircraft. This effect, which is usually the result of flow separation and loss of lift on the downward wing, is often responsible for the occurrence of wing rock. Finally at the top right of Figure 4, the non-linear variation of the yawing moment with the rate of rotation in a right spin is shown. Positive values of C_n contribute to the driving moment in the spin and correspond to positive (destabilizing) values of the yaw damping derivative. It is this type of dependence of the stability derivatives on the spin rate that may necessitate the introduction of more sophisticated mathematical models, to be discussed later.

Equally dramatic non-linearities with angle of attack occur also in other dynamic derivatives, such as the familiar cross derivatives between the rolling and yawing degrees of freedom shown at the bottom of Figure 4. It is interesting to note from Ref. 4 that the angle of attack at which these peaks occur is largely independent of both the wing sweep angle and the presence of vertical tails. [The height of the peak, however, is decreased when the vertical tails are off and when the reduced frequency is increased.] This suggests that the primary mechanism for these effects is associated with the existence and motion of the forebody vortices.

A set of yawing and rolling moment derivatives obtained from rotary-balance experiments for a current combat aircraft (Ref. 5) is shown in Figure 5. The measured roll damping compares favourably with flight test data (up to 20°), but shows a non-linear behaviour at higher angles of attack which is different from estimates based on static wing pressure measurements. The measured yawing moment derivative, on the other hand, shows a much smoother variation with angle of attack than the predicted one, but exhibits a well pronounced peak totally absent in the estimates. In both cases the non-linearities are significant and, on the whole, not satisfactorily predicted.

2. AERODYNAMIC CROSS-COUPLING

The second important effect of high angle of attack on dynamic stability considerations is the presence of aerodynamic cross-coupling (Figure 6) caused by asymmetric flow conditions. As already mentioned, asymmetric flow occurs not only when an aircraft flies at non-zero sideslip but also when it flies at zero sideslip but at high angles of attack, as the result of the asymmetric shedding of forebody vortices. In both cases we may expect the occurrence of secondary *lateral* aerodynamic forces and moments in response to a primary *pitching* maneuver and vice-versa, the onset of secondary *longitudinal* reactions in response to a primary *lateral* maneuver. Due to various *time lags*, these secondary reactions will consist of components that are both in-phase and out-of-phase with the primary motion, and will give rise, therefore, to both static and dynamic cross-coupling effects. In the first approximation such effects can be described by introducing the concept of static and dynamic *cross-coupling derivatives*. These quantities, which at the present time may be difficult to determine theoretically or from flight tests, can now be obtained from special dynamic experiments in a wind tunnel. It should be mentioned also, that in the presence of significant cross-coupling it becomes necessary to consider the lateral and the longitudinal equations of motion of an aircraft *simultaneously*, and not in two separate groups as often done in the past.

To gain some understanding of the fluid dynamics phenomena that may be responsible for aerodynamic cross-coupling, oil visualization of the surface flow is often found very helpful. In Figure 7 (from Ref. 2) such surface flow is shown for an aircraft-like configuration at an angle of sideslip of 10° and at a Mach number of 0.7. One can see one of the primary separation lines moving from one side of the model to the other as the angle of attack increases from 12.5° to 14° and then to 17.5° . This, of course, indicates a corresponding movement of one of the forebody vortices, which is located just above and a little to the side of the separation line. It can easily be appreciated that, if the same model were performing an oscillation in pitch around a mean angle of attack of 15° and with an amplitude of $\pm 2.5^\circ$, the vortex would be oscillating laterally to and fro, thereby causing lateral aerodynamic reactions as functions of the angle of attack. Due to convective time lags involved, these lateral reactions are both in phase and out of phase with the model motion, giving rise to both static and dynamic derivatives of the yawing and rolling moments and the side force, with respect to pitching. An additional, and at least as important, contribution to these derivatives is provided by the highly dissimilar flow over the two wings (and highly dissimilar changes in this flow with angle of attack) as also shown in Fig. 7. And, of course, once the flow becomes basically asymmetric, there is no longer any reason why significant derivatives should not also exist in the opposite direction, i.e., derivatives of the longitudinal forces and moments due to a lateral motion, such as static and dynamic pitching moment derivatives due to yawing. All such derivatives provide aerodynamic cross-coupling between the lateral and the longitudinal degrees of freedom of an aircraft and are called therefore *cross-coupling derivatives* (reserving the name of *cross derivatives* for the traditional derivatives relating the two *lateral* degrees of freedom, such as the rolling moment derivative due to yawing or vice versa).

In most cases, the determination of cross-coupling derivatives requires access to special-purpose experimental equipment. Since the interest in this type of derivatives is of a relatively recent date, the necessary equipment is not yet generally available and, therefore, very little experimental data have so far been accumulated. One set of data, on the same aircraft-like configuration as shown on the flow-visualization pictures, has been obtained at NAE (Ref. 6), and some examples are presented in Figure 8. At the top, the dynamic yawing and rolling moment derivatives due to pitching are shown, and at the bottom, the pitching moment derivative due to yawing. In all cases the derivatives are relatively small for low angles of attack but attain large values and display sudden variations at angles of attack of 16° to 19° , which coincides quite well with the angle of attack at which, according to the flow visualization studies, one of the separated forebody vortices moves over the fin. Another series of rapid and large variations occur for angle of attack of 31° to 34° . In all cases both the level attained and the suddenness of variations is much larger for the derivatives of the lateral moments due to pitching than for the pitching moment derivative due to yawing.

The inclusion of dynamic cross-coupling terms in the equations of motion may have large effects on the predicted motion time history as shown in Figure 9, where the angular rates following a sudden perturbation in α of 0.05 rad. are presented for a hypothetical military aircraft in a turning flight (Ref. 7). Had the dynamic cross-coupling terms not been included, the rates p , r and $\dot{\delta}$ would have remained essentially constant. It was shown in the sensitivity study of Ref. 7 that among the dynamic cross-derivatives considered, the derivatives of the lateral moments due to pitching were particularly significant and in some cases could have an effect on the predicted motion as large as that of some of the well-known damping and cross derivatives. Similar results were independently obtained in Ref. 8.

3. TIME-DEPENDENT AND HYSTERESIS EFFECTS

In addition to *quasi-steady* effects, such as represented by derivatives of various aerodynamic reactions due to angular velocities, we have to consider the existence of purely *unsteady* effects, such as those represented by derivatives due to the time rate of change of angular deflections, $\dot{\alpha}$ or $\dot{\beta}$ (Fig. 10). These derivatives have been known for many years, since they constitute part of the dynamic results obtained with standard

wind-tunnel techniques of oscillation around a fixed axis, which always give composite derivative expressions such as $(C_{mq} + C_{m\dot{\alpha}})$. Up to now, however, it was standard practice to ignore the $\dot{\alpha}$ and $\dot{\beta}$ effects (or to introduce a simple correction for them) and to use the composite derivatives in place of the purely rotary ones. At low angles of attack the error introduced by such a procedure was often small and the simplification large enough to be justifiable.

At higher angles of attack, however, the $\dot{\alpha}$ and $\dot{\beta}$ effects unfortunately become quite substantial and can no longer be ignored or corrected for in a simple fashion. This is illustrated in Figure 11, where the composite derivatives obtained from oscillatory experiments around a fixed axis are compared with purely rotary derivatives obtained from experiments in a curved or rotating flow for two fighter aircraft (Refs. 9 and 10). The difference between each set of results represents the unsteady effects due to the time rate of change of the angular deflection (in this case the angle of sideslip) and becomes quite significant for higher angles of attack.

Derivatives due to the time rate of change of angular deflections are aerodynamically equivalent (in the first approximation) to derivatives due to translational acceleration in the same plane of motion. This fact renders them of high interest for aircraft designs using direct-lift or direct-sideforce controls and also makes it possible to determine them experimentally using a translational oscillatory motion in the vertical or lateral direction (Ref. 11).

High angle-of-attack flow phenomena such as asymmetric vortex shedding and vortex breakdown (burst) are very sensitive to small variations in both α and β . This is frequently responsible for aerodynamic hysteresis effects. Figure 12 shows an α -hysteresis in the variation of location of the vortex burst on a delta wing (Ref. 12) and an example of β -hysteresis in the variation of lateral aerodynamic coefficients for an aircraft configuration (Ref. 10). In the presence of such hysteresis effects the dynamic characteristics of an aircraft can be expected to be strongly dependent on both the amplitude and the frequency of oscillation. When conducting experiments in the critical range of, say, $25^\circ < \alpha < 40^\circ$, it is advisable to obtain data (both static and dynamic) in very small increments of angle of attack.

4. CONFIGURATION DEPENDENCE

The vortex pattern that exists around an aircraft configuration at high angles of attack is very sensitive to even small changes in aircraft geometry. A particularly critical part of the aircraft is the forebody, and especially the nose itself, which is the area where the body vortices are formed. An example is presented in Fig. 13, where the effect of a flat, broad nose (called the "Shark Nose") developed by Northrop (Ref. 10), on the variation with angle of attack of the dynamic directional stability parameter, $C_{n\beta_{DYN}}$, is shown. The Shark Nose geometry attenuates the unfavourable local reduction in that parameter and at the same time extends this favourable influence on stability to somewhat lower angles of attack. It has also been demonstrated in Reference 10 (but is not shown here) that the presence of Shark Nose enhances greatly the directional stability at small non-zero angles of sideslip ($|\beta| < 5^\circ$).

The most common method of ensuring a symmetrical shedding of forebody vortices at zero sideslip is, of course, the use of forebody strakes. Although, when used alone, these strakes often prevent the formation of a unique vortex pattern at non-zero sideslip, thereby seriously reducing the directional stability of the configuration, they can be amazingly effective when used in combination with a suitable nose geometry. Figure 13 presents the effect of the Shark Nose used together with a particular leading edge extension (LEX), which can be considered to be a form of strake. It can be seen that the negative peak in $C_{n\beta_{DYN}}$ is almost totally eliminated and that the favourable influence on stability now extends to both lower and higher values of angle of attack.

The effect of strakes (or leading edge extensions) on various dynamic stability derivatives is presented in Figure 14. In all cases the addition of strakes reduces the magnitude of derivatives, practically eliminates non-linearities with angle of attack in the range investigated (except for pitch damping derivative), and makes the derivatives independent of reduced frequency (Ref. 13). The dynamic yawing derivative due to rolling becomes essentially zero. The negative damping in roll (for $\alpha > 13^\circ$), in pitch (for $12^\circ < \alpha < 23^\circ$) and in yaw (for $\alpha > 11^\circ$) completely disappear.

As is well-known, however, strakes do have certain disadvantages. Their successful development for a particular application may require much trial and error. They often adversely affect the directional stability. If mounted near the tip of the nose radome, they may disturb the radar operations. The strake vortices may adversely interact with aircraft components further downstream, such as air intakes or control surfaces. Therefore, alternative approaches continue to be of high interest.

One such recent approach makes use of "helical trips" on the forebody, as illustrated in Fig. 15. According to Ref. 14, the concept of such a device is based on the idea of distributing the shed vorticity along the forebody, thereby preventing its concentration into discrete vortices. The trip must be located relative to the boundary layer flow in such a way as to maximize the chances of flow separation at angles of attack of interest

(that is at angles of attack at and above the value where the onset of flow asymmetry would otherwise occur on the basic configuration). It can be seen from Figure 15 that the helical trip is quite successful in alleviating the onset of asymmetry on both body alone and wing-body configurations; in addition, it maintains lateral stability of a wing-body-tail configuration in the entire range of angle of attack investigated (while the basic configuration displays a sudden decline in lateral stability for $\alpha > 30^\circ$).

It should be noted that both strakes and helical trips, if used in single pairs, rapidly lose efficiency as the banking angle increases; such devices would therefore be of little use on bodies which have to rotate in roll at high angles of attack, such as certain missiles and projectiles.

5. MATHEMATICAL MODELLING

The mathematical modelling used in most countries at the present time to describe the aircraft flight history applies strictly to flight at small to moderate angles of attack, where non-linearities are small, time-dependent effects insignificant and aerodynamic cross-coupling non-existent. A much more sophisticated modelling, which would include all the above effects, is obviously required for a satisfactory description of flight at high angles of attack. In addition, at very high angles of attack, a satisfactory representation of spinning or coning is also required.

Substantial progress has already been made in some of these areas. A generalized formulation which includes the non-linear pitch-yaw-roll coupling and non-linear coning rates is now available (Ref. 15). Time-history effects have recently been included in that formulation (Ref. 16). Among things still to be done is an adequate modelling of sudden variations of aerodynamic reactions with angle of attack and other variables, and a satisfactory verification of some of the more advanced mathematical models. The verification should be conducted by determining a complete set of stability parameters for a particular configuration, by predicting a series of rather extreme maneuvers, and by comparing them with the actual flight histories. Although the verification should be sought at the lowest necessary level of sophistication of the mathematical model, it is almost certain that at high angles of attack such a model must include non-linear and time-dependent terms. One of the principal difficulties in conducting such a verification at the present time is the lack of complete static and dynamic aerodynamic data for the required test cases.

For low to moderate angles of attack stability criteria in general use include parameters such as $C_{n\beta}$ and LCDP (Lateral Control Departure Parameter). Recently these criteria have been extended (Ref. 17) to include non-linear aerodynamics and non-zero moments at zero sideslip. However, only static aerodynamic cross-coupling has so far been considered, although plans exist to expand the analysis to also include the dynamic cross-coupling.

6. SOME IMPORTANT DIRECTIONS FOR FUTURE WORK

Although the manifestations of the high-angle-of-attack or asymmetrical flows in terms of their effects on dynamic stability parameters are slowly becoming known, the nature of these flows - especially in oscillatory or unsteady situations - is still largely undefined. A satisfactory understanding of the one-to-one relation between the causative fluid dynamics phenomenon and the resulting effect on dynamic stability parameters is in most cases lacking. More research into the basic fluid dynamics aspects of dynamic stability problems, especially at high angles of attack, is therefore needed.

Much of such research will have to be based on experimental work in wind tunnels. Our understanding of the wind-tunnel and support interference effects on oscillatory experiments is sadly inadequate and at high angles of attack is simply non-existent. Much work is needed in this area and there should be very good possibilities for cooperative programmes involving several organizations or countries.

Sets of aerodynamic data, as complete as possible, on stability parameters at high angles of attack are urgently needed to provide input for verification of some of the existing mathematical models as well as sufficient material for development of more advanced models, if required.

Pending satisfactory development and verification of these models, preference should be given in dynamic stability testing at high angles of attack to *direct* methods. In such methods the measurement is based on an assumed relation (which may be non-linear or of higher order) between the aerodynamic reaction to be determined and the causative primary motion and is totally independent on the remaining parts of the equations of motion. The results of such measurements may be expected to be valid for any formulation of these equations as long, of course, as the principle of superposition is still applicable, that is as long as the concept of stability derivatives can be used.

7. REFERENCES

1. Dynamic Stability Parameters, AGARD Conference Proceedings 235, 1978.
2. Orlik-Rückemann, K.J. Aerodynamic Coupling Between Lateral and Longitudinal Degrees of Freedom. AIAA J. Vol. 15, No. 12, Dec. 1977, pp 1792-1799.
3. Chambers, J.R.
Gilbert, W.P.
Nguyen, L.T. Results of Piloted Simulator Studies of Fighter Aircraft at High Angles of Attack. Paper 33 in Ref. 1.
4. Grafton, S.B.
Anglin, E.L. Dynamic Stability Derivatives at Angles of Attack from -5° to 90° for a Variable-Sweep Fighter Configuration with Twin Vertical Tails. NASA TN D-6909, 1972.
5. Matthews, A.W. Experimental Determination of Dynamic Derivatives due to Roll at British Aerospace, Warton Division. Paper 4 in Ref. 1.
6. Orlik-Rückemann, K.J.
Hanff, E.S. Experiments on Cross-Coupling and Translational Acceleration Derivatives. Paper 8 in Ref. 1.
7. Curry, W.H.
Orlik-Rückemann, K.J. Sensitivity of Aircraft Motion to Aerodynamic Cross-Coupling at High Angles of Attack. Paper 34 in Ref. 1.
8. Butler, R.W.
Langham, T.F. Aircraft Motion Sensitivity to Variations in Dynamic Stability Parameters. Paper 35 in Ref. 1.
9. Coe, P.L., Jr.
Newson, W.A., Jr. Wind-Tunnel Investigation to Determine the Low-Speed Yawing Stability Derivatives of a Twin-Jet Fighter Model at High Angles of Attack. NASA TN D-7721, 1974.
10. Skow, A.M.
Titiriga, A., Jr. A Survey of Analytical and Experimental Techniques to Predict Aircraft Dynamic Characteristics at High Angles of Attack. Paper 19 in Ref. 1.
11. Orlik-Rückemann, K.J. Techniques for Dynamic Stability Testing in Wind Tunnels. Paper 1 in Ref. 1.
12. Ericsson, L.E. A Summary of AGARD FDP Meeting on Dynamic Stability Parameters. AGARD FMP Symposium on Stability and Control, September 1978, Paper 2.
13. Staudacher, W.
Laschka, B.
Schulze, B.
Poisson-Quinton, P.
Canu, M. Some Factors Affecting the Dynamic Stability Derivatives of a Fighter-Type Model. Paper 11 in Ref. 1.
14. Rao, D.M. Side-Force Alleviation on Slender, Pointed Forebodies at High Angles of Attack. AIAA Atmospheric Flight Mechanics Conference, Paper 78-1339, August 1978.
15. Tobak, M.
Schiff, L.B. On the Formulation of the Aerodynamic Characteristics in Aircraft Dynamics. NASA TR R-456, 1976.
16. Tobak, M.
Schiff, L.B. The Role of Time-History Effects in the Formulation of the Aerodynamics of Aircraft Dynamics. Paper 26 in Ref. 1.
17. Kalviste, J. Aircraft Stability Characteristics at High Angles of Attack. Paper 29 in Ref. 1.

SOME AERODYNAMIC PHENOMENA ASSOCIATED WITH OSCILLATORY FLIGHT AT HIGH ANGLES OF ATTACK

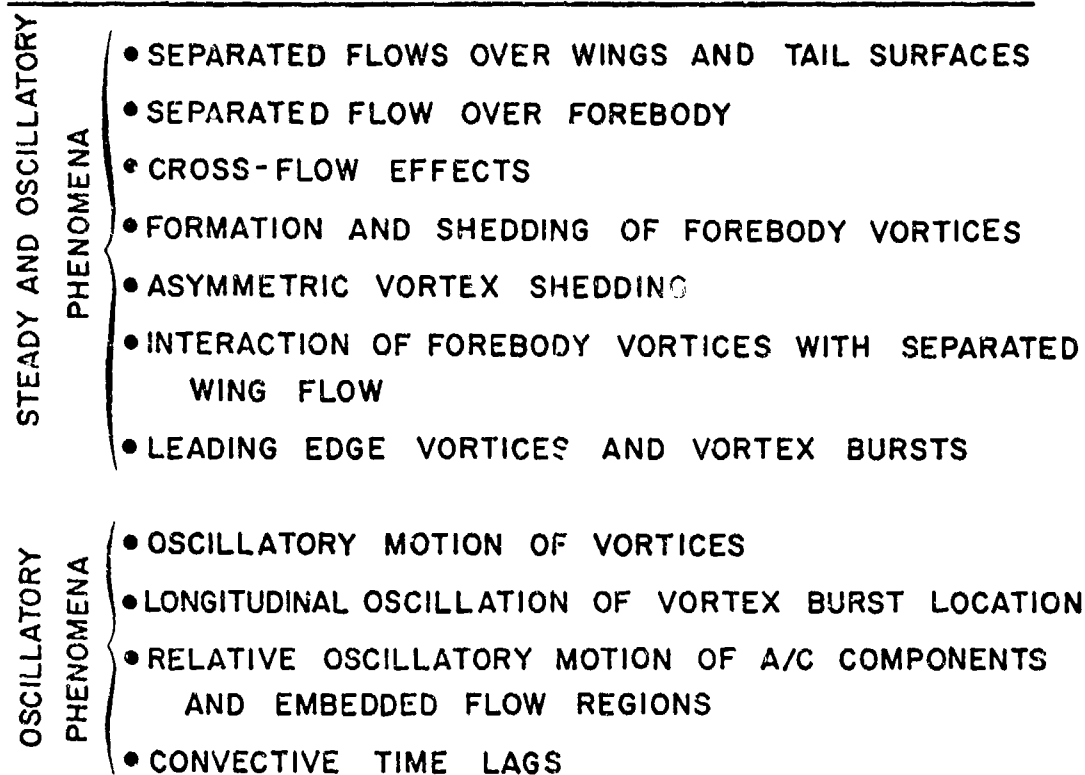


FIG. 1

EFFECTS OF HIGH ANGLES OF ATTACK ON DYNAMIC STABILITY PARAMETERS

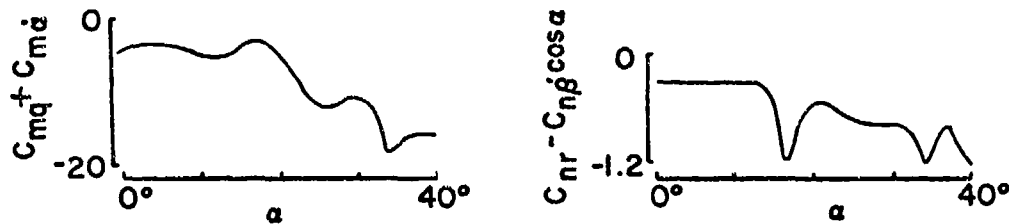
- NON-LINEARITIES
- AERODYNAMIC CROSS COUPLING
- TIME-DEPENDENT AND HYSTERESIS EFFECTS
- STRONG CONFIGURATION DEPENDENCE
- NEED FOR ADVANCED MATHEMATICAL MODELS

FIG. 2

NON-LINEARITIES

- DYNAMIC STABILITY PARAMETERS ARE FUNCTIONS OF α , β , Ω
- AMPLITUDE EFFECTS MAY BE IMPORTANT
- DERIVATIVE CONCEPT MAY BE INADEQUATE

EXAMPLES

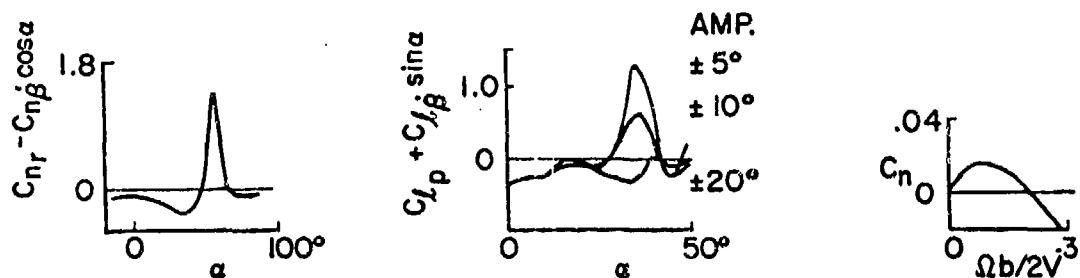


SUBSONIC DAMPING DERIVATIVES FOR A WING-BODY
CONFIGURATION; $M=0.7$
NAE (REF. 2)

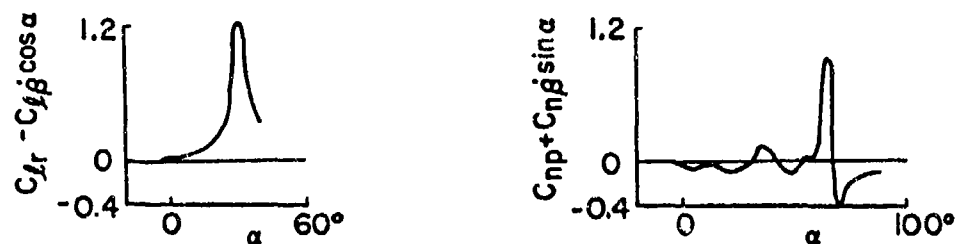
FIG. 3

NON-LINEARITIES

EXAMPLES (CONT.)



LOW-SUBSONIC DAMPING DERIVATIVES AND YAWING MOMENT
FOR A FIGHTER AIRCRAFT
NASA LANGLEY (REF 3)

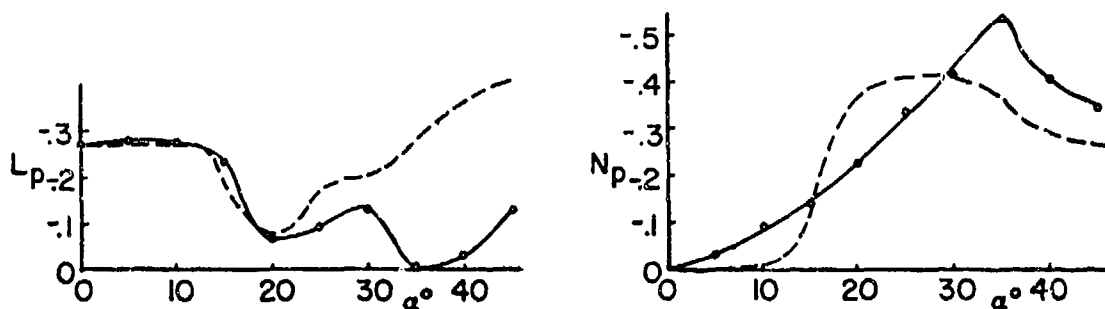


LOW-SUBSONIC CROSS DERIVATIVES FOR A SWEEP-WING FIGHTER
AIRCRAFT. NASA LANGLEY (REF. 4)

FIG. 4

NON-LINEARITIES

EXAMPLES (CONCL.)



—●— ROTARY DERIVATIVE RIG DATA
AERODYNAMIC DEPT. ESTIMATES
---- (0 < α < 20° FLIGHT TEST DATA, $M \leq 0.5$
 $\alpha > 20^\circ$ WING PRESSURE DATA)

ROLLING AND YAWING MOMENT DERIVATIVES DUE TO ROLLING
FOR A CURRENT COMBAT AIRCRAFT (ALL DERIVATIVES IN
WIND AXES) - BAC (REF. 5)

FIG. 5

AERODYNAMIC CROSS-COUPLING

- ASYMMETRIC FLOW CAN RESULT FROM :
 - FLIGHT AT NON ZERO SIDESLIP
 - FLIGHT AT ZERO SIDESLIP BUT HIGH ANGLE OF ATTACK
- IN ASYMMETRIC FLOW LATERAL AERODYNAMIC REACTIONS MAY MATERIALIZE AS RESULT OF A PITCHING MANEUVER AND VICE VERSA, LONGITUDINAL REACTIONS AS RESULT OF A LATERAL MANEUVER
- DUE TO VARIOUS PHASE LAGS, REACTIONS BOTH IN-PHASE AND OUT-OF-PHASE WITH THE PRIMARY MOTION CAN BE EXPECTED. THIS CAUSES STATIC AND DYNAMIC CROSS-COUPLING EFFECTS.
- IN THE PRESENCE OF CROSS-COUPLING, THE LATERAL AND LONGITUDINAL GROUPS OF EQUATIONS OF MOTION HAVE TO BE CONSIDERED SIMULTANEOUSLY

FIG. 6

AERODYNAMIC CROSS-COUPLING



$\alpha = 12.5^\circ, \beta = 10^\circ$

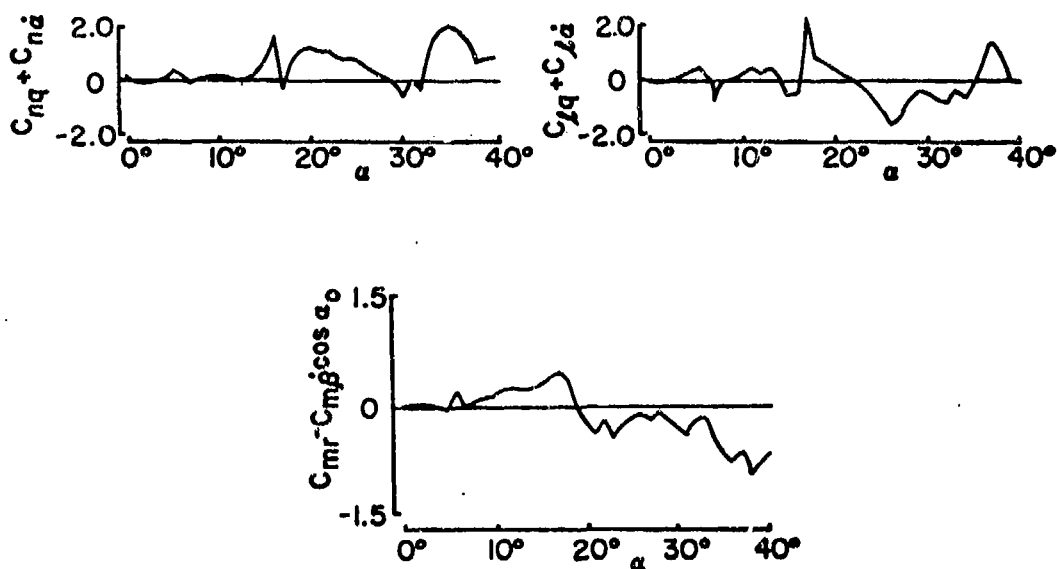
$\alpha = 14^\circ, \beta = 10^\circ$

$\alpha = 17.5^\circ, \beta = 10^\circ$

SURFACE FLOW ON A SCHEMATIC AIRCRAFT CONFIGURATION. $M=0.7$
NAE (REF 2)

FIG. 7

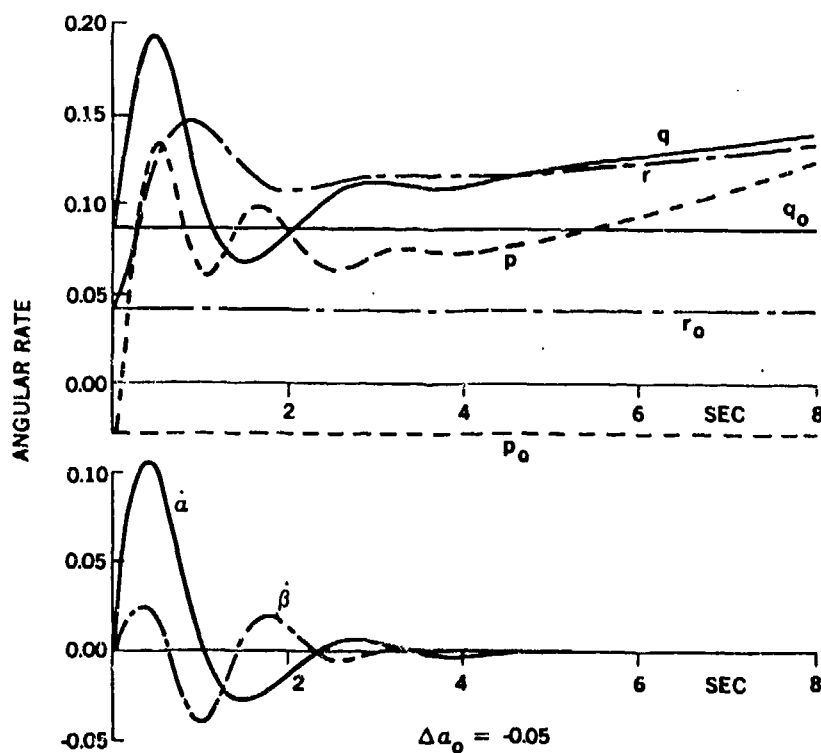
AERODYNAMIC CROSS-COUPLING



DYNAMIC CROSS-COUPLING MOMENT DERIVATIVES DUE TO PITCHING
AND YAWING FOR AN AIRCRAFT-LIKE CONFIGURATION. $M=0.7; \beta=5^\circ$
NAE (REF. 6)

FIG. 8

AERODYNAMIC CROSS-COUPLING



NOTE 1: ANGULAR RATES FOR THE UNPERTURBED CASE REMAIN CONSTANT
AND ARE DENOTED BY p_0 , q_0 , r_0 .

NOTE 2: WITH ALL AERODYNAMIC CROSS COUPLING DERIVATIVES EQUAL
TO ZERO, THE RATES p , r , AND $\dot{\beta}$ REMAIN ESSENTIALLY CONSTANT WHEN
PERTURBED IN α

EFFECT OF DYNAMIC CROSS-COUPLING TERMS
FOR A MILITARY AIRCRAFT IN $2g$ TURNING FLIGHT;
LOCALLY LINEARIZED COEFFICIENTS; $\alpha_0 = 33^\circ$
SANDIA/NAE (REF. 7)

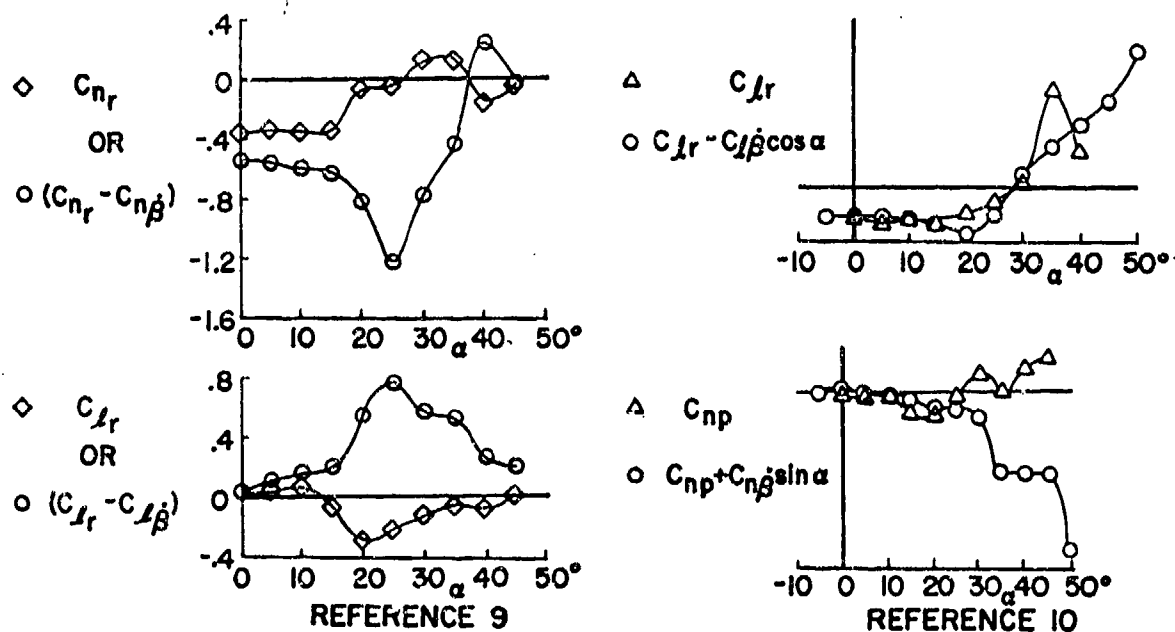
FIG. 9

TIME-DEPENDENT DERIVATIVES

- NEEDED TO SEPARATE EFFECTS DUE TO PURE ROTATION (such as q) AND TIME RATE OF CHANGE OF ANGULAR DEFLECTION (such as $\dot{\alpha}$) IN THE SAME PLANE OF MOTION, WHICH IN STANDARD OSCILLATORY EXPERIMENTS APPEAR TOGETHER
- TIME RATE OF CHANGE OF ANGULAR DEFLECTION IS AERO-DYNAMICALLY EQUIVALENT TO TRANSLATIONAL ACCELERATION IN THE SAME PLANE OF MOTION ($\dot{\alpha} = \dot{w}/V$)
- TRANSLATIONAL ACCELERATION DERIVATIVES OF INTEREST FOR AIRCRAFT USING DIRECT-LIFT OR DIRECT-SIDEFORCE CONTROLS

FIG. 10

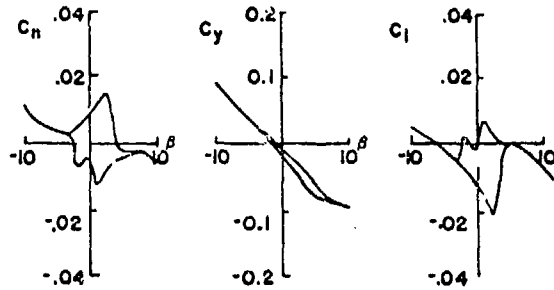
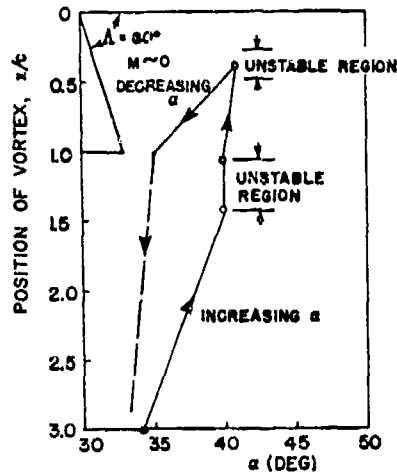
β -DERIVATIVES



DIFFERENCE BETWEEN PURELY ROTARY AND OSCILLATORY DERIVATIVES REPRESENTING DERIVATIVES DUE TO TIME RATE OF CHANGE OF ANGLE OF ATTACK OR SIDESLIP.

FIG. 11

HYSTERESIS EFFECTS



LATERAL AERODYNAMIC COEFFICIENTS AS FUNCTION OF ANGLE OF SIDESLIP (REF. 10)

VORTEX BURST LOCATION ON A DELTA WING (REF. 12)

AERODYNAMIC HYSTERESIS IN A REGION OF VORTEX BREAKDOWN

FIG. 12

CONFIGURATION DEPENDENCE

SHARK NOSE AND LEADING EDGE EXTENSION (LEX) NORTHROP (REF. 10)

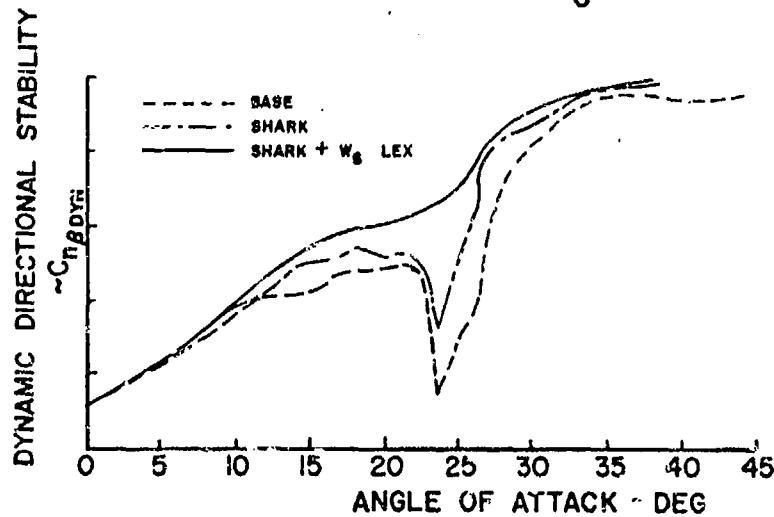
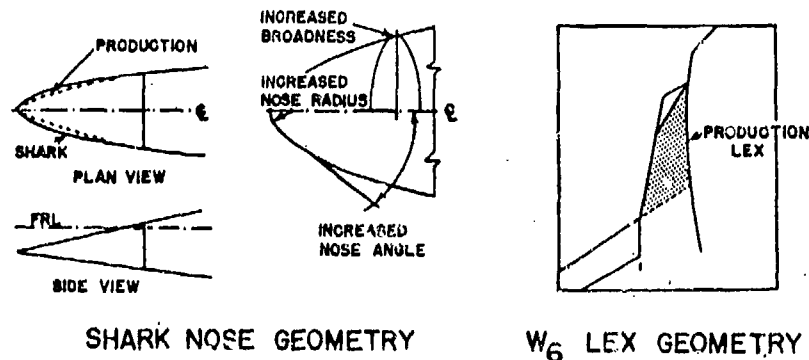
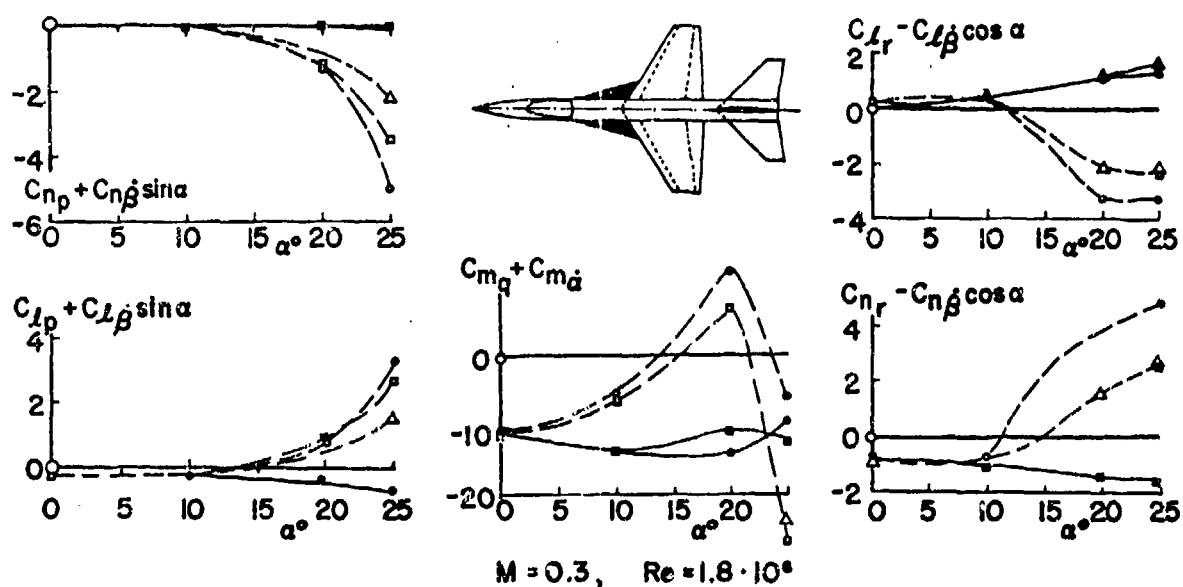


FIG. 13

CONFIGURATION DEPENDENCE

EFFECT OF STRAKES (MBB/ONERA - REF 13)



$\frac{p \cdot b}{2V}$	STRAKE OFF	STRAKE ON	$\frac{q \cdot c}{V}$	STRAKE OFF	STRAKE ON	$\frac{r \cdot b}{2V}$	STRAKE OFF	STRAKE ON
0.047	---	---	0.03	---	---	0.05	---	---
0.057	---	---	0.038	---	---	0.062	---	---
0.07	---	---	0.047	---	---	0.068	---	---

ROLLING

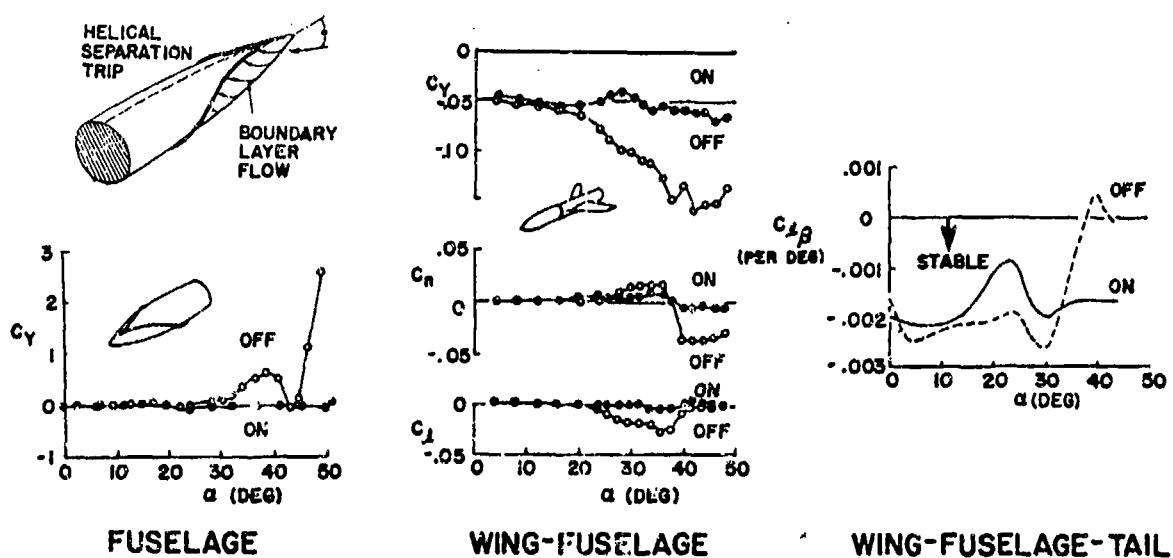
PITCHING

YAWING

FIG. 14

CONFIGURATION DEPENDENCE

HELICAL TRIPS (OLD DOMINION UNIV., VIRGINIA - REF. 14)



FUSELAGE

WING-FUSELAGE

WING-FUSELAGE-TAIL

FIG. 15

HIGH ANGLE OF ATTACK CHARACTERISTICS OF DIFFERENT FIGHTER CONFIGURATIONS

by

H. John and W. Kraus

Messerschmitt-Bölkow-Blohm GmbH, Munich, Germany

SUMMARY

Increased manoeuvrability at the lower end of the flight envelope offers new and attractive possibilities for fighter aircraft. To extend the flight regime at low speeds up to high angles of attack beyond maximum lift requires the ability to trim and control the aircraft and by this avoid departure and spin susceptibility at those conditions.

The paper reviews basic aerodynamic characteristics of different fighter configurations at separated flow beyond maximum lift where the resultant derivatives are completely different from those associated with attached flow. The change in trim conditions is primarily dependant on wing planform and overall aircraft configuration. Results are shown about the aerodynamic development of aircraft configuration which meet these requirements and, at the same time, minimize the resulting drag penalties in the conventional angle of attack regime.

Furthermore problem areas and deficiencies must be identified to allow the definition of concepts for stabilizing such configurations artificially by aid of the flight control system. It will be shown that an auxiliary momentum generating system will be necessary for controlling the aircraft at flight conditions where aerodynamic control power is not sufficient.

NOTATION

b	span
\bar{c}	mean aerodyn. chord
c_L	lift coefficient
c_l	rolling moment coefficient
$c_{l\beta}$	roll stability
$c_{l\zeta}$	coupled rolling moment due to rudder deflection
$c_{l\delta}$	roll control power due to aileron deflection
c_n	yawing moment coefficient
$c_{n\beta}$	directional stability
$c_{n\zeta}$	yaw control power due to rudder deflection
$c_{n\delta}$	coupled yawing moment due to aileron deflection
g	gravitational constant
n_z	load factor
q	dynamic pressure
x, y, z	coordinates
M	Mach number
R_n	Reynolds number
α	angle of attack
β	side slip angle
ϵ_E	upwash angle at canard position
ϵ_H	downwash angle at tail position
ζ	rudder deflection
η_E	canard deflection
η_H	tail deflection
η_W	wingeron deflection
v	dihedral angle
ξ	aileron deflection
$\omega_{x,y,z}$	angular velocities
$\dot{\omega}_{x,y,z}$	angular acceleration

Indices

L.E. leading edge
T.E. trailing edge

Abbreviations

ACT Active Control Technic
CCV Configuration Controlled Vehicle
FCS Flight Control System
PST Poststall
LCDP Lateral Control Departure Parameter
 $c_{n\beta Dyn}$ Directional Departure Parameter

All derivatives shown are given in the body axis system.

1. INTRODUCTION

1.1 Design goal

During the last few years new fighter airplanes have been introduced into service and have been extensively flight tested at high angles of attack and low speeds. Pilots have found, that by flying above $\alpha = 30^\circ$, they effectively convert the aircraft into a flying speed brake. This effect permitted pilots to quickly discover the advantages of high α flight in the dog fight arena.

Consequently it will be highly desirable for the next generation of fighter airplanes to abandon any angle of attack limitation at low speeds. The design goal will be not only to fly the aircraft beyond the conventional stall limits, but also to provide a fully manoeuvrable aircraft in the "Poststall" region. This new capability will be called PST-capability in the following context.

Figure 1 shows the PST area in an altitude-Machnumber diagram. At the high Machnumber end the PST boundary is given by the 9g structural limit corresponding to c_{Lmax} . At the lower Machnumber end, the limit shown is set up by manoeuvre boundaries, which result from the requirements for coordinated flight at PST. Outside this area the aircraft can still be flown but at reduced control rates only.

The control requirements, in terms of angular accelerations about all three axes, have been defined as follows:

- o pitch acceleration

$$\dot{\omega}_y = 1.5 \frac{\text{rad}}{\text{sec}^2}$$
 - o yaw acceleration

$$\dot{\omega}_z = 0.5 \frac{\text{rad}}{\text{sec}^2}$$
 - o roll acceleration varies with angle of attack, dependent on control law designed into flight control system, $\dot{\omega}_x = \dot{\omega}_z \cdot \text{ctg } \alpha$, which allows coordinated turns at high angles of attack.
- } constant for all
} angles of attack

The requirements for pitch and yaw control acceleration are of such magnitude, that for low dynamic pressures an additional momentum system will be needed. Trade studies have shown that a gimbaled nozzle, which provides vectored thrust control about all 3 axes, is the best solution to the problem. There will be no detailed discussion about the vectored nozzle design in this context.

At medium and higher dynamic pressures, aerodynamic forces and moments have a large contribution to the overall six degree of freedom behavior at Poststall. All requirements for the controllability are always set up out of a trimmed condition. Therefore an additional requirement for the aerodynamic design is, that the aircraft must be trimmable aerodynamically up to $\alpha = 70^\circ$ angle of attack.

Requirements in terms of stability about all three axes do not exist; but stability would be helpful about the roll and yaw axes.

Due to the application of "Active Control Technic" (ACT/CCV) by use of the "Flight Control System" (FCS) artificial stability can be provided as long as sufficient controllability is available.

1.2 Selection criteria

Since it can be expected, that different configurations will have advantages and disadvantages with respect to different problem areas, a priority list of criteria has to be defined to assist in the final decision process. The following ranking was set up:

1. Optimum conventional performance.
This means the configuration has to have the most favorable drag standard by applying optimum instability margin to obtain best induced drag polars and minimum surface distribution.
2. Controllability.
The configuration must be trimmable and controllable up to $\alpha = 70^\circ$. The additional momentum system shall be used for control purposes only.
3. Stability.
Deficiencies in roll and yaw stability shall be as small as possible. To assist in judging the lateral stability, criteria developed by R. Weissmann (1), the so-called "Directional Departure Parameter" ($c_{n\beta Dyn}$) and the "Lateral Control Departure Parameter" (LCDP) have been used.

1.3 Approach for Solution.

Since a theoretical prediction of derivatives in the range between $30^\circ < \alpha < 90^\circ$ is nearly impossible, a selection of a suitable configuration according to the above given criteria can only be done on the basis of windtunnel test results. For this purpose in 1977 an experimental program has been defined by use of a modular windtunnel model (compare figure 2). For the definition of model parameters, literature studies and results of pilot models (2, 3, 4) have been used.

Those results lead to a delta wing with $\varphi_{LE} = 59^\circ$ leading edge sweep and a trapezoidal wing with $\varphi_{LE} = 32^\circ$ sweep angle. Further configuration elements are:

For the delta wing: see figure 2 and 3 top.

- o Nose- and trailing edge flaps
- o Canard, all movable from $+30^\circ$ to -90°
differential deflection possible
2 z-positions, variable dihedral angle
4 planforms
- o wingerons (part of wing movable; see figure 3 top)
- o underwing fins with rudder,
at the same time end plats
and fixing device for wingeron } can be used
combined only

For the trapezoidal wing: see figure 2 and 3 bottom

- o Nose- and trailing edge flaps
- o taileron, all movable from $+30^\circ$ to -90°
2 z-positions, 3 dihedral angles
3 planforms
differential deflection possible
- o Different strakes
- o vented fins (see figure 3 bottom)
mounted on a strut, which connects wing and taileron

Elements for both wings:

- o Fin variation
Single fin mounted on fuselage center line
double fins mounted on fuselage edges
ventral fins mounted on fuselage edges
and appropriate variation in x-position
and dihedral angle.
- o Spoilers on and below wing
- o Cockpit variation
- o Intake modifications

Most of the additional model parts were selected and defined for improvement of controllability at high angles of attack.

These model parts allow establishment of 5 basic configurations:

- o a delta wing see also Foto 1
- o a delta wing with wingers and fins below the wing Foto 2
- o a delta wing with canard Foto 3
- o a trapezoidal wing with tail Foto 4
- o a trapezoidal wing with tail and vented fins Foto 5

Due to the additional model parts a wide variation of interesting parameters could be investigated to provide a complete survey about the aerodynamic characteristics at high angles of attack. Tests were performed in the 5 m x 7 m Low Speed Windtunnel in Emmen Switzerland at $R_n = 3.0 \cdot 10^6$ for the delta wing and $R_n = 1.6 \cdot 10^6$ for the trapezoidal wing respectively. Derivatives are given in the body axis system.

2. LONGITUDINAL CHARACTERISTICS

2.1 Tail Configuration

Of basic influence in the total α -regime on the trim and control power at various stability margins is the downwash angle ϵ_H versus α as shown in top of figure 4. Up to α_{max} the characteristic is as expected. Right at c_{Lmax} the downwash angle drops according to the loss in circulation. But after this drop a second smaller rise can be seen, which is due to the displacement effect of the separated flow running off the wing. This displacement of the wake of the wing produces a downwash angle at the position of a short coupled tail.

The maximum respectively minimum usable tailangle η_H by use of the downwash angle ϵ_H , can be written

$$\eta_{Hmax} = -(\alpha - \epsilon_H) + \alpha_{eff max}$$

$$\eta_{Hmin} = -(\alpha - \epsilon_H) - \alpha_{eff max}'$$

wherein $\alpha_{eff max}$ is defined as the planform dependent maximum angle of attack at free flow conditions. Outside of $\eta_{Hmin} \leq \eta_H \leq \eta_{Hmax}$ no trim or control power in pitch is available for the respective configuration.

Starting from the $c_{M\alpha}$ -characteristic of the trapezoidal wing, the trim and control power margin can be seen, after plotting the η_{Hmin} and η_{Hmax} boundaries on top of it. Comparing the pitching characteristic of a 5 % stable and a 5 % unstable center of gravity location, as shown in figure 4, it can be seen, that at medium angles of attack there exists a gap for the unstable configuration, where no trim condition can be obtained and no control power will be available. For the stable configuration there is no problem area in terms of trim and control power.

Unfortunately establishment of a minimum induced drag polar requires a 5 % unstable configuration. This means that for the trapezoidal wing configuration as tested criterion 1 and 2 are contradicting; in other words: when high angles of attack have to be trimmed an optimum induced polar cannot be reached for this configuration.

2.2 Canard Configuration

For a canard configuration the corresponding problem area is the wing upwash at the canard position as shown in top of figure 5. The upwash ϵ_E increases up to α_{max} of the wing and remains constant for the rest of the α -regime. Transforming this information into a trimchart, as can be seen from the bottom of figure 5, there is for the stable canard configuration, comparable to the unstable tail configuration, no trim and control power available from medium angles of attack on. The unstable configuration has good trim and control power margins throughout the total angle of attack range.

Furthermore there is an advantage for a canard configuration, when using a trailing edge flaps. Because there is no tail behind the wing, which is collecting the total downwash change and wake effects when flaps are utilized, trailing edge flaps can also be used for trim and control purposes. Combined effects of trailing edge flaps and canard allow establishment of an optimum polar throughout the conventional angle of attack range. This

means that criterion 1 and 2 are not contradicting, which results in a big advantage for the unstable canard configuration. A complete trim diagram including flaps for an unstable delta canard configuration can be seen from figure 6. The dark, full line gives a possible trim-schedule, where the first part up to $\alpha \approx 17^\circ$ would represent an optimum (L/D) flap schedule. From there on, an optimum control schedule has to be defined, which allows to trim and control the aircraft up to $\alpha = 70^\circ$.

3. YAW CONTROL POWER AND DIRECTIONAL STABILITY

3.1 General Remarks

The classical instrument of producing directional stability and yaw control power is a central fin combined with a rudder, double fins and rudders or all moving fins.

When flow separation occurs a conventionally arranged fin and rudder combination gets with increasing angle of attack continuously more and more merged in separated flow running off the wing fuselage combination. This results in a loss of dynamic pressure at the position of the fin and thus means a loss in effectiveness.

One of the main targets of the windtunnel tests was to find means, which allow extension of fin and rudder effectiveness up to high angles of attack, or to find new devices which provide effectiveness, when conventional one's end.

3.2 Conventional Arrangement of Fins and Rudders

All movable fins have been investigated, but they are triggering an early vortex bursting when deflected, and by this effect cause large asymmetries. Therefore they have been abandoned from further testing.

Tests with variation in x-position, dihedral angle, central and double fins and rudders did not produce a remarkable extension of the yaw control power, as can be seen from figure 7 nor in directional stability, as can be seen from figure 8, versus angle of attack.

3.3 Underwing Location of Fin and Rudder

A very effective location of a fin and rudder for a delta wing is below the wing at about half span. In this position a nearly constant dynamic pressure can be achieved, which results in good yaw control power, see figure 9, and a provers rolling moment due to a rudder deflection. The contribution to directional stability can be taken from figure 8. The difference in effectiveness compared to a conventional fin at low angles of attack is due to differences in fin and rudder volume. The problem which arises with such a configuration lies in the realization of a feasible design taking into account take off and landing ground clearances.

3.4 Vented Fin and Rudder

For the trapezoidal wing a vented fin and rudder mounted on a strut, see figure 3 + 10, connecting wing and horizontal tail was tested. At the same time the fin was acting as an end plate for the tail. Since the tail is rotated downwards at high angles of attack to obtain trim conditions, fin and rudder are always exposed to attached flow with no reduction of dynamic pressure. A loss of effectiveness with increasing α occurs due to the increasing sweep angle of rudder hinge line with increasing angle of attack. Therefore a second rudder was installed on top of the fin, which started to work at angles of attack above $\alpha \approx 30^\circ$. The effect of each rudder and the combined effectiveness can be seen from figure 11. The contribution of the vented fin to the directional stability is shown in figure 12. The comparison gives a fin off curve, a conventional fin, a vented fin with trailing edge flaps not extended and a configuration where trailing edge flaps are extended into a manoeuvre position.

In terms of stability and control power this configuration is the most promising one, which is capable to fly in the PST region without problems.

3.5 Differential Canard Deflection and Variable Canard Dihedral

A further possibility to obtain good yaw control power for a delta wing is the differential deflection of the canard. This produces induced pressures at the canopy side wall, but the attainable values are small. A promising configuration was found for a positive dihedral angle of attack of $\nu = 45^\circ$ for the canard. By rotating the total nose cone out of a trim condition, relatively large side forces and yawing moments can be generated above an angle of attack of $\alpha \approx 35^\circ$. Combined with a conventional rudder, as shown in figure 13, a very good effectiveness throughout the total angle of attack range can be achieved. The problem for this arrangement is a viable design solution.

3.6 Influence of Leading Edge Flap on Directional Stability

Figure 14 gives the effect of leading edge flap on directional stability for a central fin arrangement. There is an improvement of $\Delta\alpha = 10^\circ$, which is an increment higher than could be expected.

The effect on yaw control power is very small.

4. ROLL CONTROL POWER AND ROLL STABILITY

4.1 Roll Control Power

For a conventional design roll control is either provided by ailerons or by a rolling tail.

4.1.1 Ailerons

Results are shown for a full span flap deflection on the delta wing.

Ailerons lose their effectiveness as soon as the wing starts to stall and the induced effect of the ailerons on the main wing is lost, as can be seen from figure 15. Beyond stall roll effectiveness drops to about 30 % of that value attained for attached flow. Roll effectiveness beyond stall is produced by the upgoing aileron only and is proportional to aileron volume times drag coefficient.

By deflecting the effective aileron part only the adverse yawing moment can be avoided, as is shown in figure 15 also.

In total it can be stated, that the roll power from ailerons in the PST region is small.

4.1.2 Differential Tail Deflection

The effectiveness of a differential tail is very good throughout the total angle of attack range, as can be seen from figure 16, because for trim conditions, out of which roll input is commanded, the tail has to be always at tail angles, such that well attached flow is attained. At the same time a proverse yawing moment is obtained, when a roll input is generated.

4.1.3 Differential Canard Deflection

A differential canard deflection has no usable contribution for roll control, because due to the downwash change in the main wing behind the canard will cancel any rolling moment produced by the canard alone.

4.1.4 Differential Wingeron Deflection

A differential deflection of wingerons produces large rolling moments throughout the total angle of attack range. This can be a very powerful mean for roll control, if it is possible to adjust the longitudinal trim conditions. Roll control power and coupled yawing moment are shown in figure 17.

4.2 Roll Stability

4.2.1 General Remarks

In the conventional angle of attack range roll stability can be obtained classically by two means

- o positive wing dihedral angle
- o high wing arrangement

At sideslip angles in both cases additional lift is generated on the wing part going to the wind, while a loss in lift is produced on the other side.

Evidently such linear properties are lost at angles of attack during stall and beyond stall. For highly swept wings and strake-wing combinations, both of which produce strong leading edge vortices, roll stability largely depends on vortex break down characteristics. Since vortex bursting depends on leading edge sweep angle, both categories of wings experience, at and slightly beyond maximum lift a gap where roll instability occurs, as is schematically shown in figure 18.

Proper means to avoid this gap are all kinds of devices which either produce an early symmetrical vortex bursting, a simultaneous vortex bursting, delay vortex bursting on the foregoing wing part or rotate part of the wing back into attached flow with increasing

angle of attack.

4.2.2 Means for an Early Vortex Bursting

A forced early vortex bursting can be generated by use of spoilers in front of the trailing edge flap. Close to α_{max} both spoilers can be rotated to an angle of 70° .

As can be seen from figure 19 an improvement in roll stability can be obtained. From this angle of attack onwards a distinct drag increment is spoiling the drag to lift characteristic. A similar effect can be obtained by rotating trailing edge flaps up. In this case a distinct lift loss has to be taken into account.

4.2.3. Nose Flaps

A mean to delay vortex bursting is to rotate nose flaps down to about 40° degrees.

As can be seen from figure 20 roll stability is attained throughout the total angle of attack range. But nose flaps are not curing the problem completely, because as soon as trailing edge flaps are used at the same time, due to the increase in circulation, part of the effect of nose flaps is neutralized.

4.2.4. Wingerons

A further possibility to attain roll stability for the delta wing was, to rotate part of the wing, which was possible for the wingeron concept, back into attached flow with increasing angle of attack. As can be seen from figure 21, a wingeron deflection of $\eta_W = -20^\circ$ provides roll stability up to an angle of attack $\alpha = 50^\circ$.

4.2.5 Vented Fin Arrangement

As could be seen from figure 12 already, the vented fin arrangement has also a very good roll stability behavior throughout the angle of attack range.

5. CONCLUSIONS

The main results for 5 different configurations, which were obtained from windtunnel tests, have been illustrated in previous chapters. The characteristics at high angles of attack and low speeds together with the selection criteria listed in chapter 1.2 lead to the following final judgement:

5.1 A pure delta wing is not trimmable and controllable throughout the complete angle of attack range.

5.2 A delta wing with wingerons has a relatively poor pitch control power at PST-conditions. Lateral control power versus angle of attack is good. In spite of a very small directional stability a positive $c_{n\beta Dyn}$ -value can be obtained throughout the total angle of attack range which allows penetration into PST.

The problem for this configuration is to be seen in the realization of a feasible design, where fins below the wing, acting as end plates for the wingeron, will not provide sufficient ground clearance for take off and landing. Furthermore the housing of the wingeron pivot bearing in a relatively thin delta wing is a big problem.

5.3 The trapezoidal wing has problems in achieving an optimum instability margin for minimum induced drag polars when at the same time adequate trim and control power is a requirement for high angles of attack. Thus in terms of conventional performance the trapezoidal wing is inferior to a delta wing with canard. Furthermore this configuration has problems at high angles of attack for directional stability and for yaw control power.

5.4 The trapezoidal wing with vented fins has a positive $c_{n\beta Dyn}$ throughout the total angle of attack range and good yaw and roll control power is available at PST. In total this configuration has superior PST-properties.

For the conventional angle of attack regime relatively high interference drag coefficients have been measured and for transonic speeds even higher values can be expected.

The area distribution shows relatively high rear end gradients, which indicates rather high wave drag increments. Furthermore the optimum instability margin with adequate trim and control power, comparable to the pure trapezoidal wing (see paragraph 5.3) can also not be verified. Therefore it can be concluded, that this configuration does not meet the first selection criterion, because poor conventional performance characteristics are to be expected throughout the Machnumber range.

5.5 The best compromise between good conventional performance and good behavior at high angles of attack can be stated for the delta-canard configuration. The selection of

this configuration can be justified due to the following reasons:

1. Drag standard at conventional angles of attack throughout the total Machnumber range is superior to all configurations tested.

The optimum instability margin for minimum induced drag polars can be obtained without any difficulty. This requirement is also not contradicting to trim and control requirements at high angles of attack.
2. Pitch-, Roll- and Yaw control power is available up to high angles of attack and still can be increased by further development work, if required.
3. The problem area of a weak $c_{n\beta Dyn}$ behavior at medium angles of attack can be overcome by further development work as discussed in paragraph 4.2. Sufficient yaw and roll control power will allow to apply "Active Control Technic" by use of the Flight Control System and artificially stabilize the configuration.

6. REFERENCES

1. Weissmann, R. Status of Design Criteria for Predicting Departure Characteristics and Spin Susceptibility

AIAA-Paper No. 74-791
2. John, H. Die Eignung von Delta-Flügeln für hohe Anstellwinkel

MBB-Bericht Nr. UFE 1375
Kapitel 3, März 1978
3. Kraus, W. Analyse der Göttinger Windkanalversuche und Vergleich der Konfigurationen 1 bis 4 des AFT 80.

MBB interner Bericht
Aero. MT. 280, Januar 1977
4. Staudacher, W. Flügel mit und ohne Strakes im Poststallbereich

Teil 2: Analyse der Ergebnisse
MBB-Bericht Nr. UFE 1300, Januar 1977

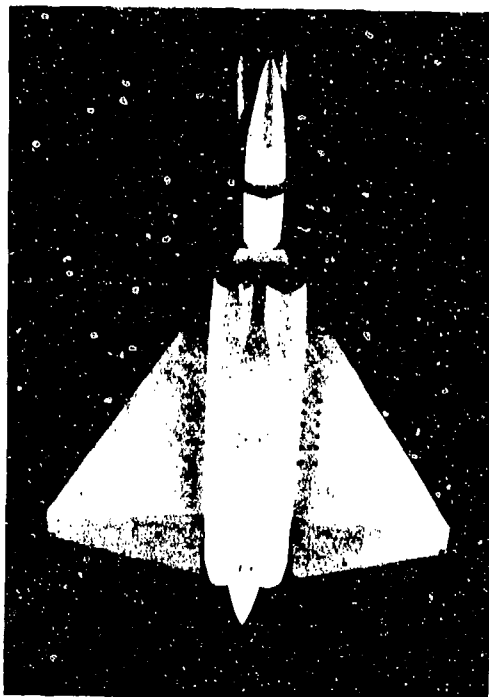


Foto 1

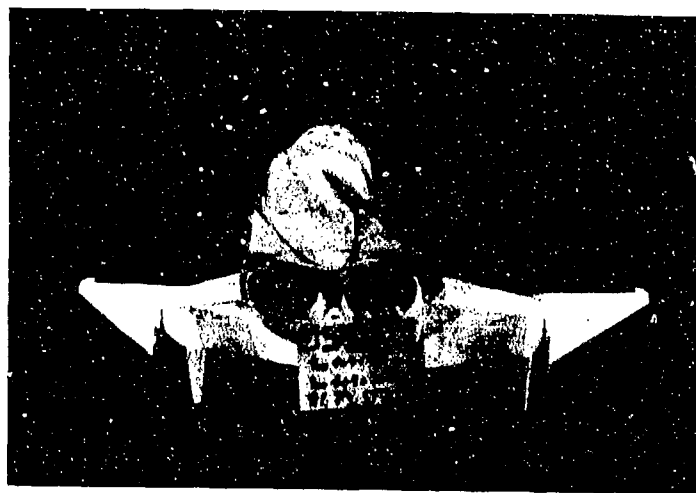


Foto 2

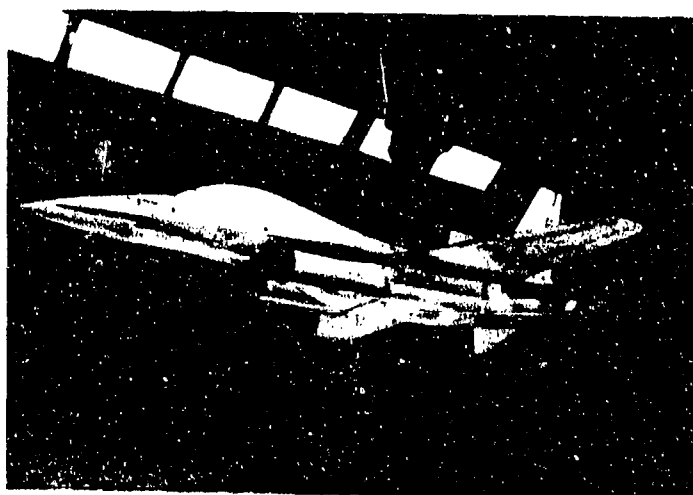


Foto 4

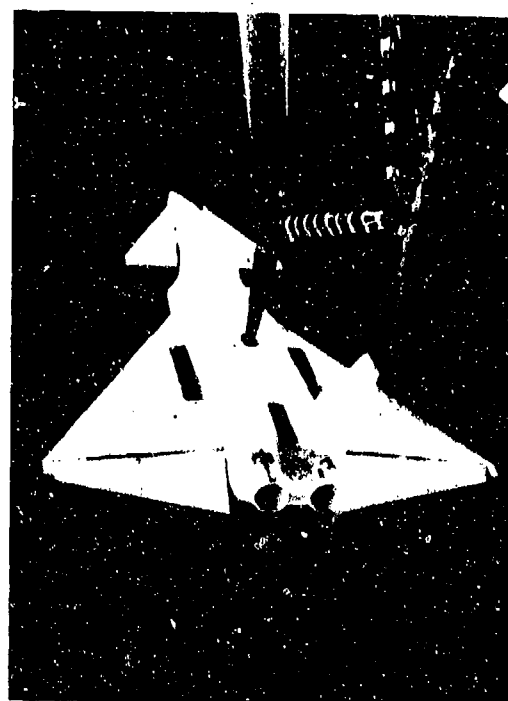


Foto 3

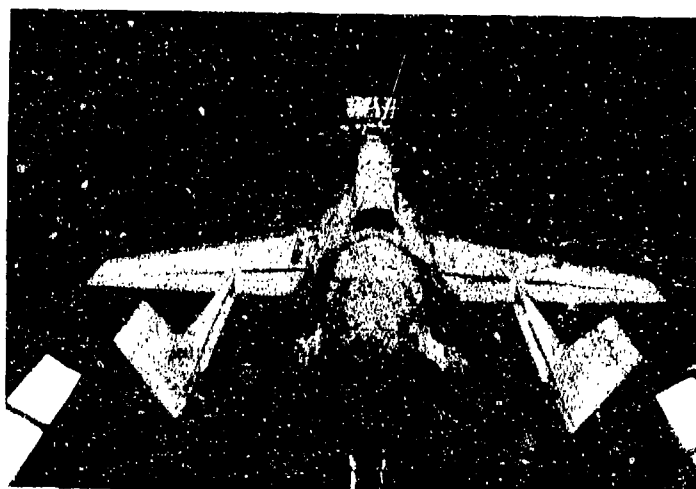
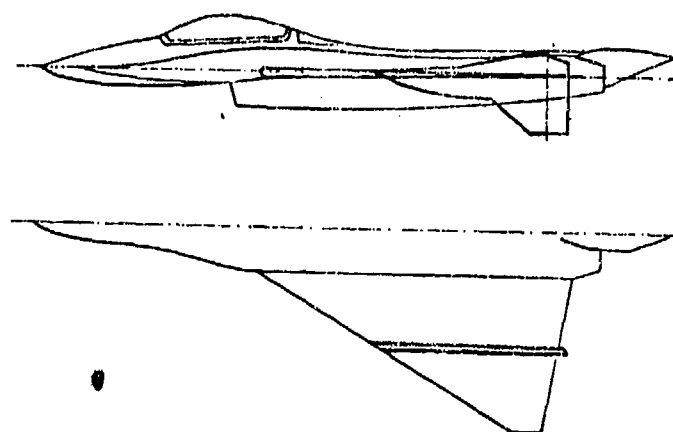
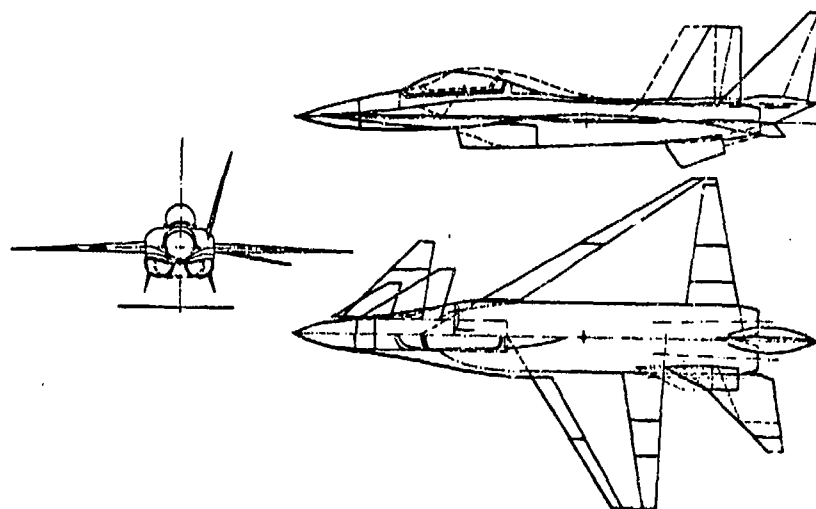
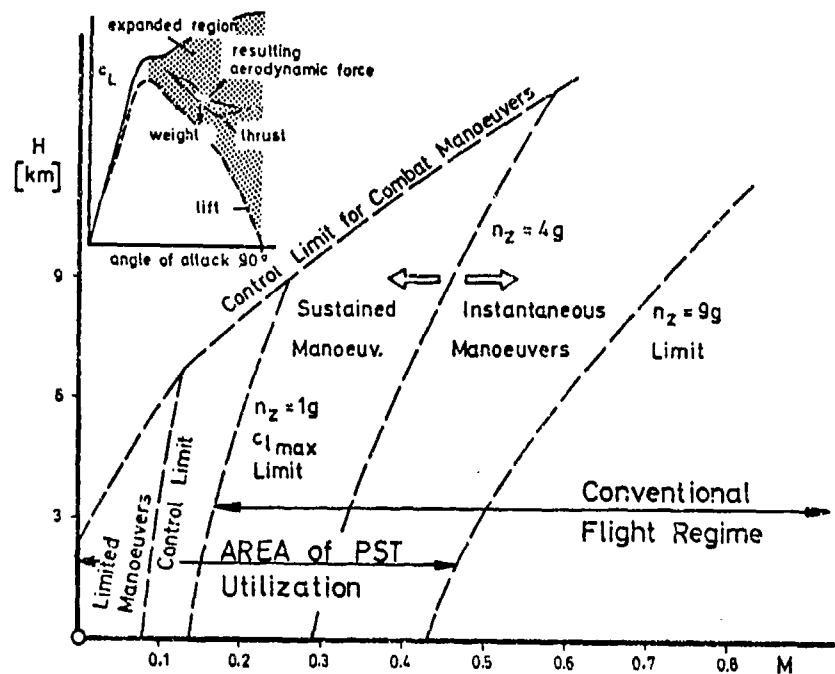


Foto 5



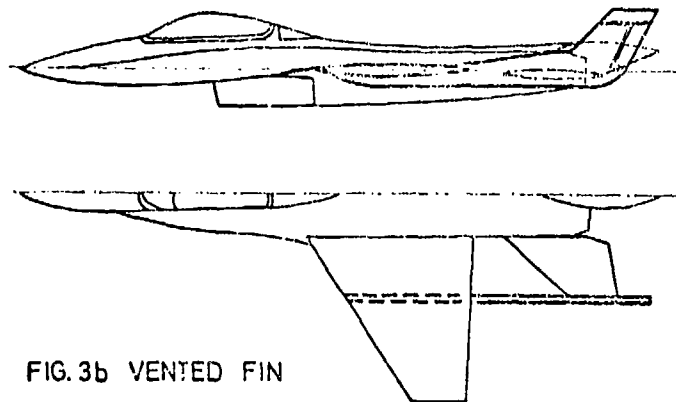
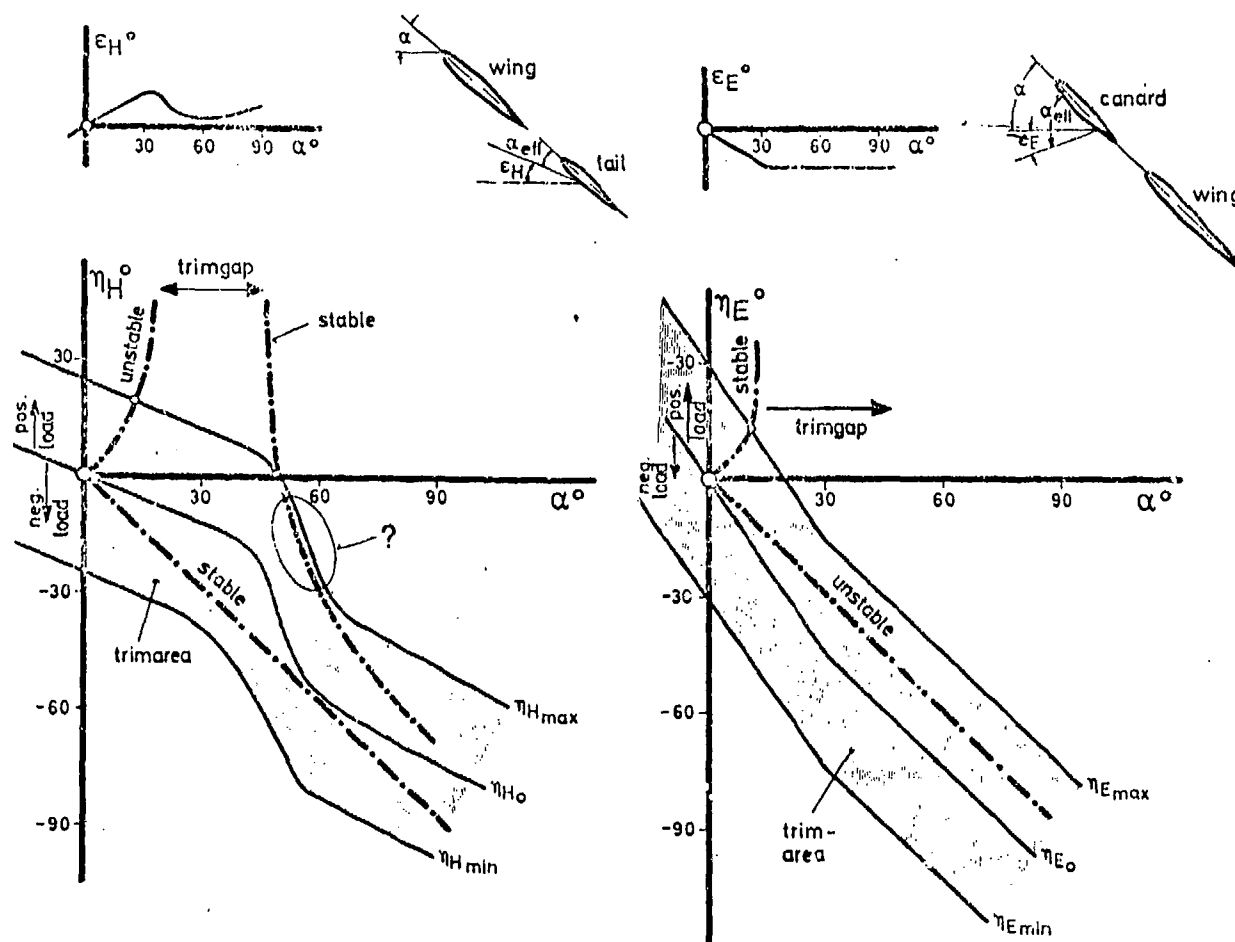


FIG. 3b VENTED FIN

FIG. 4 TAIL-CONFIGURATION
Longitudinal CharacteristicFIG. 5 CANARD-CONFIGURATION
Longitudinal Characteristic

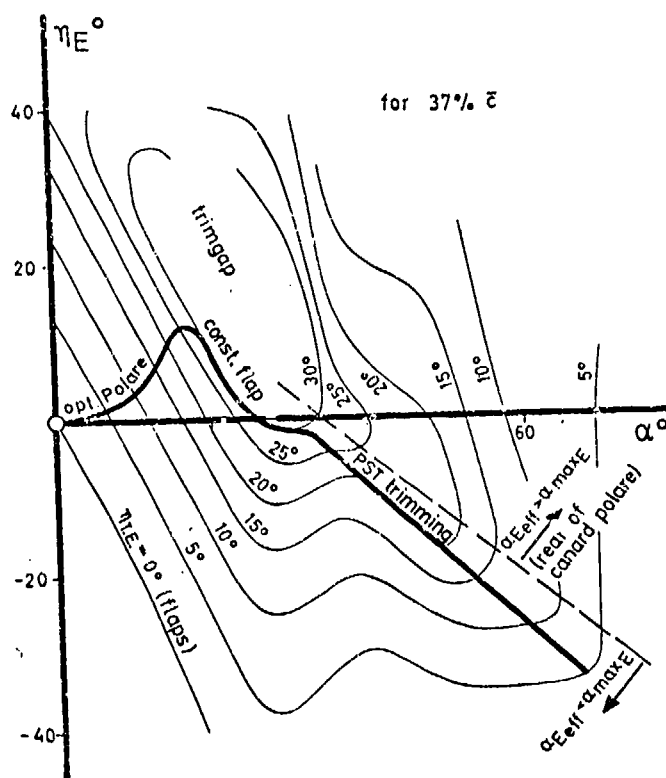


FIG. 6 CANARD - CONFIGURATION
Trimdiagram

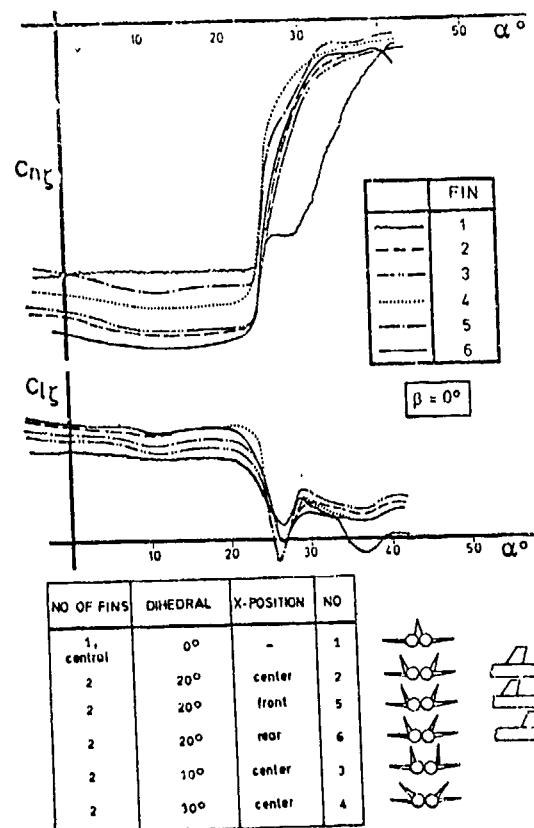


FIG. 7 FIN VARIATIONS FOR YAW CONTROL

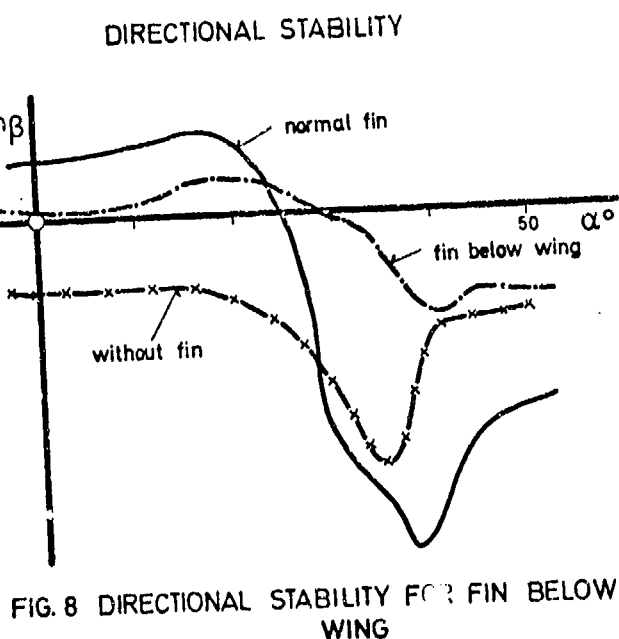
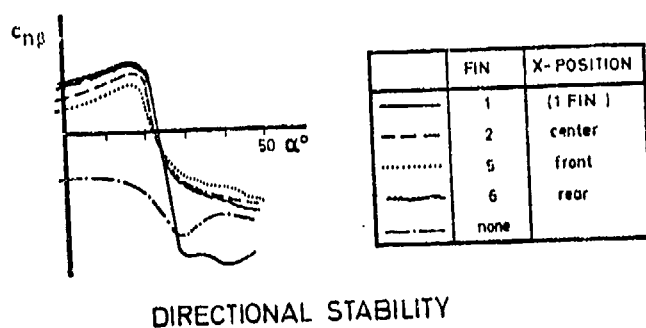


FIG. 8 DIRECTIONAL STABILITY FOR FIN BELOW WING

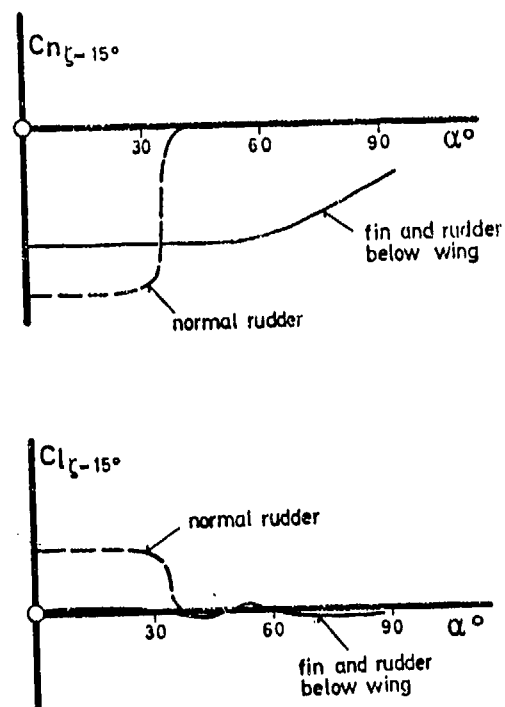


FIG. 9 FIN AND RUDDER BELOW WING
YAW CONTROL POWER

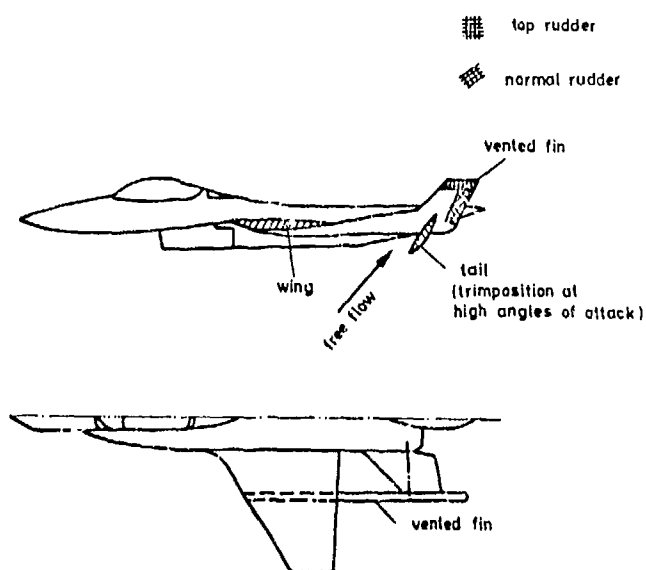


FIG. 10 VENTED FIN ARRANGEMENT

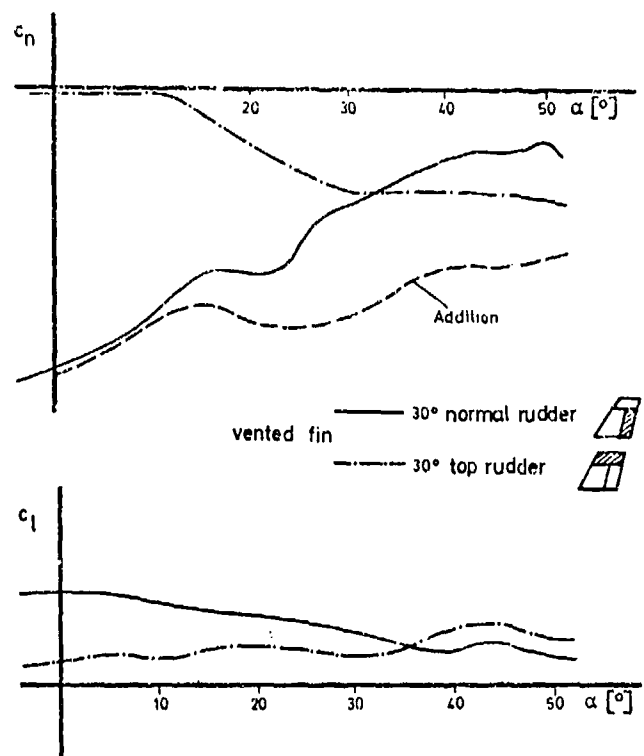


FIG. 11 VENTED FIN FOR YAW CONTROL

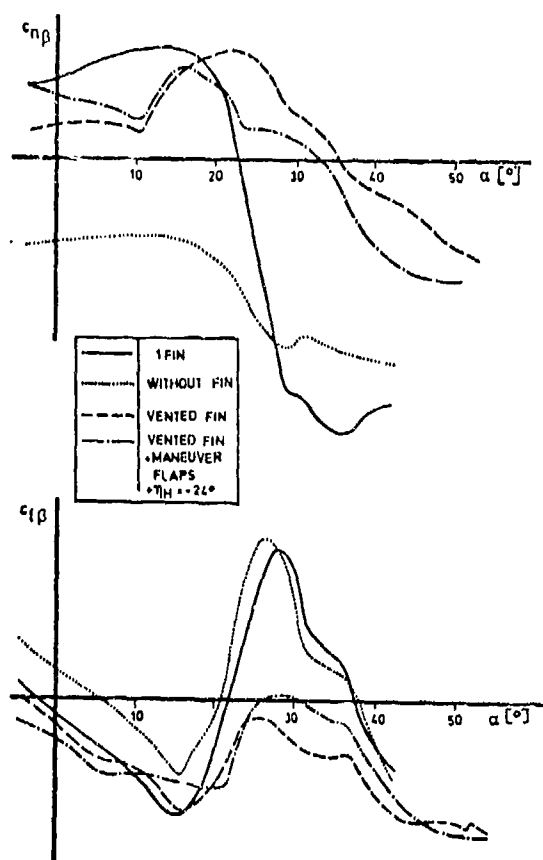


FIG. 12 DIRECTIONAL- AND ROLL STABILITY FOR VENTED FIN

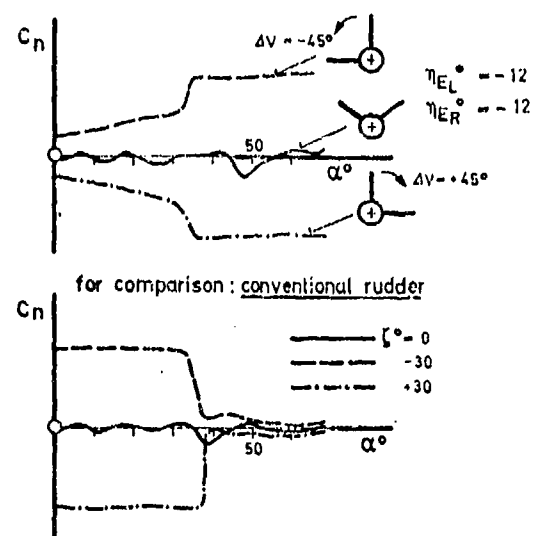


FIG. 13 CANARD FOR YAW CONTROL

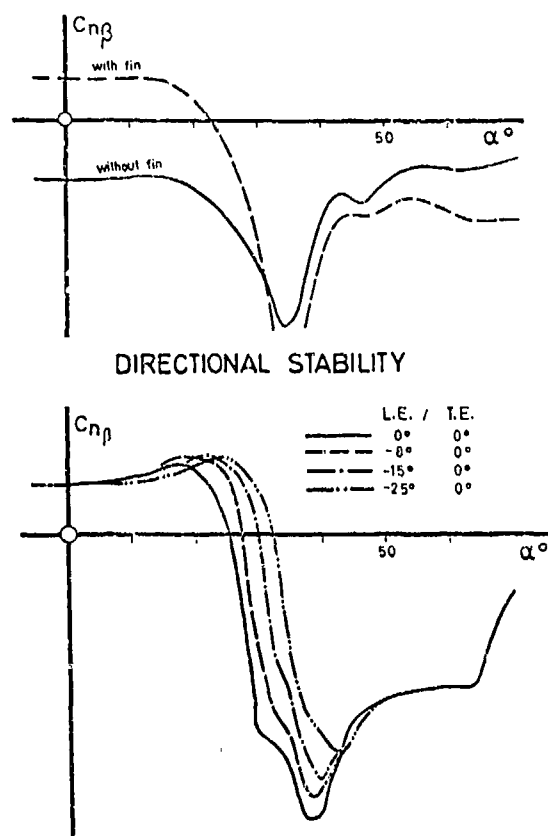


FIG. 14 IMPROVEMENT OF DIRECTIONAL STABILITY DUE TO LEADING EDGE FLAPS

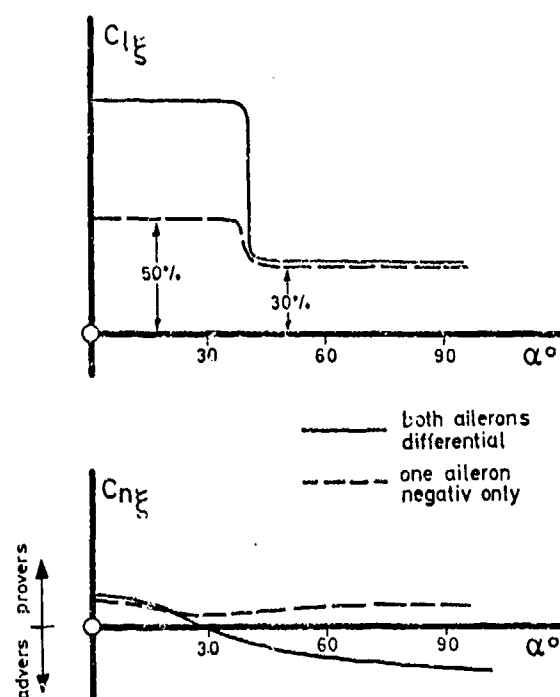


FIG. 15AILERONS FOR ROLL CONTROL

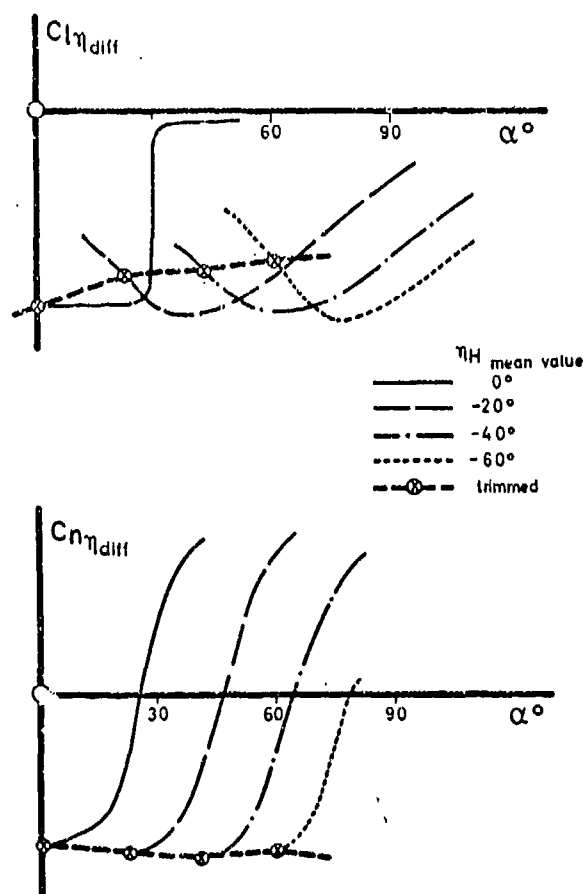


FIG. 16 ROLLING TAIL FOR ROLL CONTROL

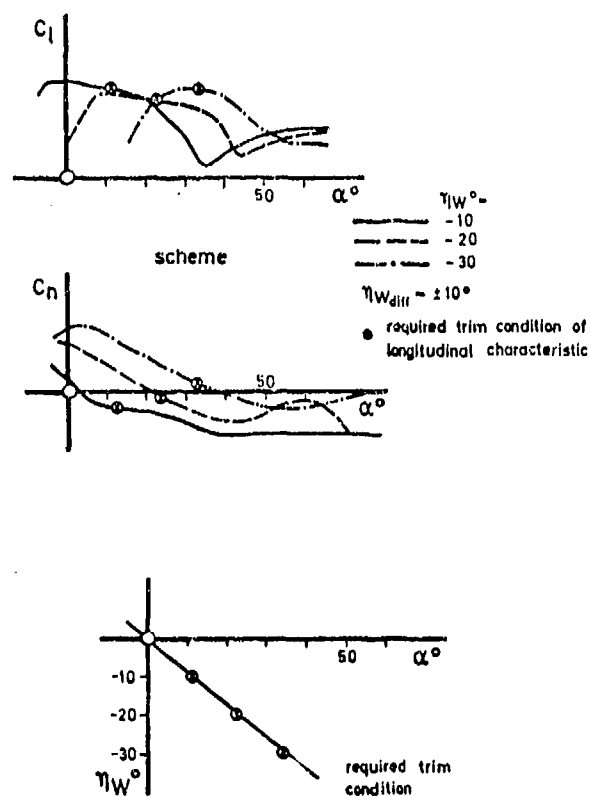


FIG. 17 WINGERON FOR ROLL CONTROL

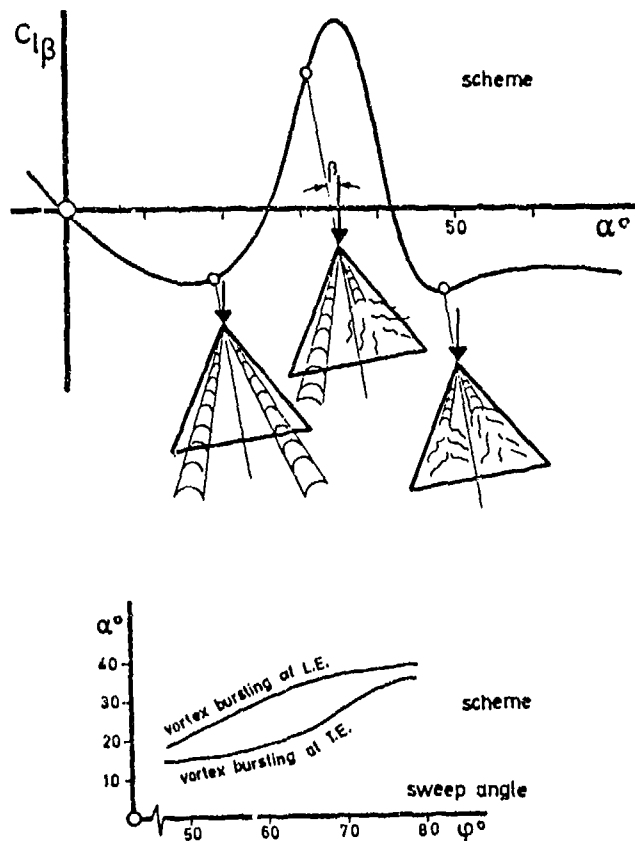


FIG. 18 ROLL STABILITY VERSUS ANGLE OF ATTACK FOR A PURE DELTA WING

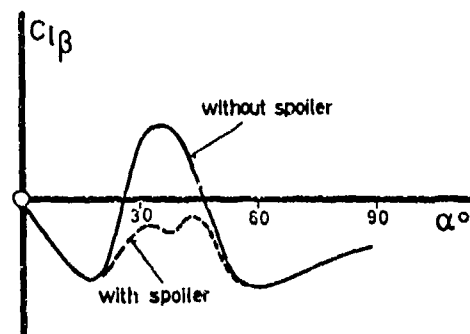


FIG. 19 ROLL STABILITY UTILIZING SPOILERS

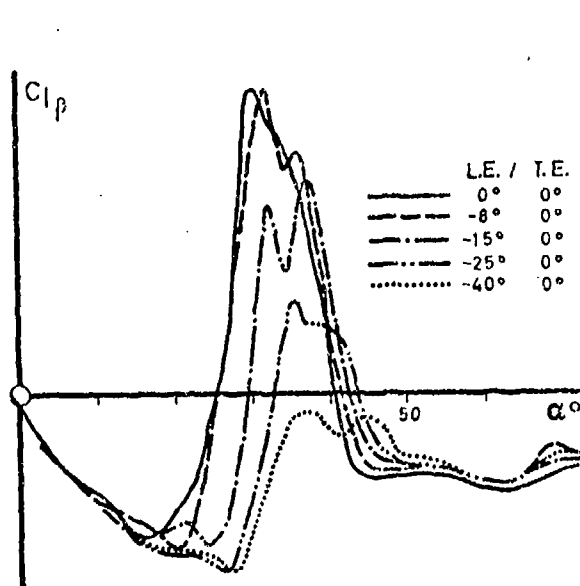


FIG. 20 ROLL STABILITY DUE TO LEADING EDGE FLAPS

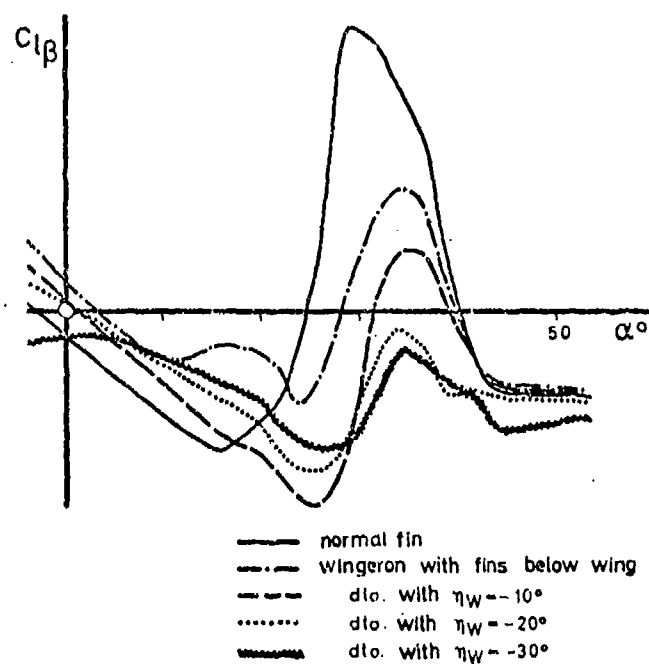


FIG. 21 ROLL STABILITY DUE TO WINGERONS

PAGES Session 1 3-1
ARE
MISSING
IN
ORIGINAL
DOCUMENT

SOME UK RESEARCH STUDIES OF THE USE OF WING-BODY
STRAKES ON COMBAT AIRCRAFT CONFIGURATIONS AT
HIGH ANGLES OF ATTACK

by

G F Moss

Royal Aircraft Establishment
Farnborough Hants UK

SUMMARY

This paper quotes from selected items of experimental research of interest to design engineers incorporating strakes in combat-aircraft configurations. It is likely to be many years before a satisfactory mathematical model is achieved for the detailed flow about such configurations and there is thus an urgent need to explore the various aerodynamic features of these devices experimentally both to obtain satisfactory solutions to current problems and to guide theoretical work which will form the basis of future design methods.

NOMENCLATURE

α	angle of incidence or attack	C_l	rolling-moment coefficient
β	angle of sideslip	C_B	wing-root bending moment coefficient
M	Mach number	q	dynamic head ($\frac{1}{2} \rho V^2$)
V, U	wind speed	$\frac{H-H_0}{\frac{1}{2} \rho U_0^2}$	total head deficit
η_T	tail setting angle	$\frac{\Gamma}{U_0}$	streamwise vorticity
\bar{c}	geometric mean chord	n_v	yawing moment due to sideslip derivative
b	wing span	l_v	rolling moment " " " "
l	see Fig 2	n_r	yawing moment due to rate of yaw (r) derivative
C_p	static-pressure coefficient	l_r	rolling moment " " " " roll (p) derivative
C_N	normal-force coefficient		
C_L	lift coefficient		
C_m	pitching-moment coefficient		
C_D	drag coefficient		

1 INTRODUCTION

Over the last few years, the potential of sharp-edged strakes in the junction of the body with the leading-edge of the wing on combat aircraft configurations has been investigated in the United Kingdom, as in many places elsewhere. Previous acquaintance with the vortex flows over slender wings¹ has been of value, including the considerable in-house work which first led to several research aircraft (including the HP115² and BA1 221³) and then to Concorde, but the combination of such flows inboard with classic, attached flows outboard into one interactive flow field has raised many new matters of importance, particularly at high incidences at high subsonic speeds. This paper seeks to high-light some of these matters, drawing on the more recent experimental evidence which has been accumulated during research and project studies. To make the presentation of more use to those interested in the detail, the data quoted is limited, apart from one exception, to that so far not released in outside publications. The variety of the work referred to emphasizes the range of new problems raised by the use of strakes for the design engineer. Since it is likely to be many years before satisfactory mathematical models can be formulated and used to derive reliable design methods, it is important to carry out experimental studies such as those quoted in this paper to cover all aspects of importance.

2 EFFECT ON LIFT AND DRAG

The general pattern of behaviour as regards lift coefficient at high incidence when strakes are added to a configuration is by now very familiar to most people. At low speed, as in the curves shown in Fig 1 for RAE Model 494*, there is usually a dramatic extension of the lift curve through the stall, and indeed often the wind-tunnel engineer runs out of incidence-angle range before any sign of a turn-over appears. There is little change in lift-curve slope up to the incidence for the stall, no strakes, but normally some change in linearity occurs above this. Thus the effect overall is not that obtained by simply adding the non-linear lift from the additional 'slender wing' of the strake surface: there is obviously considerable interaction taking place between the two lifting surfaces.

*The planforms of Models 494 and 589/1 are very similar. A sketch of the former is given in Fig 12 and a photograph in Fig 11.

At higher speeds, but before strong shocks appear in the flow, the effect is generally less marked but very similar in character as shown for the data from Model 589/1 at $M = 0.6$, but at still higher speeds when the performance of the main swept wing becomes completely dominated by compressibility effects, a quite different and often disappointing effect occurs. As may be seen from the curves for $M = 0.8$, the addition of the strake can reduce the non-linear lift generated over the main wing surface before the main lift break (at A) and also give a poorer lift increment at higher incidences as stalled conditions are penetrated. Overall, however, the lift curve is somewhat smoother, encouraging the hope for a higher value of usable-lift in flight. The other type of somewhat disappointing performance at high speeds is demonstrated in Fig 1 at $M = 0.9$. Here there is no change to the first lift break, eg at point B, and virtually no relief at all at the crucial kink at a higher incidence, at point C. It is thus very doubtful whether the benefits in lift at incidences beyond this point, which still occur as at lower speeds, could ever actually be enjoyed in flight. An understanding of these typical effects is obviously essential if progress is to be made in the future with the use of strakes. It must be emphasized that the basic wing-body configuration of this Model 589/1 was a fairly successful one, as "mildly-advanced" wing designs go, and of course the use of strakes was not taken into account during the design procedure of the wing since there was no means of doing so.

One of the earliest experiences we had in the UK arose during the design of the inboard fairing or 'nib' over the wing pivot mechanism of the Tornado aircraft. The original shape of this nib was rather bluff and caused unwanted penalties to the lift-drag performance of the wing. To reduce this bluntness the leading-edge was extended forward at one stage in some RAE research investigations⁴ to see whether an improvement could be obtained (Fig 2). By accident it was discovered that a dramatic improvement could indeed be obtained if the extended leading-edge of the nib was increased in sweep and sharpened as shown at B. This change apparently had a direct beneficial interference effect on the inward spanwise progression of the leading-edge separation on the main wing, as may be seen in Fig 2, and significantly improved the lift and lift-drag performance. However other engineering considerations intervened and in fact the idea was never put into practice. This was our first insight into the aerodynamic benefits which can occur when a vortex is generated locally over the wing root in this manner.

3 STRAKE PROFILE

That the benefits in lift performance need to be balanced with disadvantages from any increases in drag will be self-evident. The high lift-dependent drag of slender wings and other configurations with similar energetic vortex flows is well known and strakes are no exception. Thus the planform, camber, sharpness and other local details of the strake surface are important. What is required is a vigorous and tidy vortex shed across the upper surface of the wing root and this must grow with increasing angle of attack to be strong enough to do some good by the time it is needed, ie at the point at which the flow on the main swept-wing is starting to break down. From this point onwards at higher incidences the lift benefit should outweigh the drag penalty, but up to this point positive harm can be done to performance. Fig 3 shows plots of lift-drag ratio at high subsonic speeds for a number of strake designs. In each case the full line refers to the configuration before the strake is added. At the top, the effect of sharpening a 75° swept strake (ie one swept enough to be effectively sharp even with a round leading-edge) is shown to increase drag at low and moderate lift coefficients by strengthening the shed vortex (eg at point A) and yet to have no beneficial effect on performance at high incidence (point B). This can obviously sometimes be the wrong thing to do. The next sketch shows the effect of camber on the same 75° swept strake planform for a Mach number of 0.7 and clearly demonstrates an exchange between the drag at low and moderate lift coefficients and the usable-lift achieved at high incidence. Lastly, the lowest sketch shows a good-compromise design for a 'Gothic' planform of strake (strake 8) compared with the poorer performance for a similar type of planform with 20% less span (strake 6). The nose-up camber included in the latter design has only been marginally beneficial at high incidence and has certainly contributed to the marked reduction in lift/drag ratio at lower angles of attack.

4 WING DESIGN

The intersection point of the leading-edge of the strake with that of the main wing is important because this fixes the spanwise position of the flow field of the strake with respect of that of the wing. The sweep of the strake leading-edge locally at this point and the detail of how the two leading-edges are faired together geometrically are also important factors. At high subsonic speeds an intersecting shock system occurs on the wing upper surface at high incidences which is crucial as regards the onset and subsequent development of flow separation on which the value of maximum usable lift ultimately depends. Fig 5 shows (full lines) how the comparatively weak, swept forward shock and the almost unswept rear shock intersect at some point (A) to form a strong shock further outboard (double line) which often is the trigger point for flow separation to begin (shaded area). In many cases this strong shock can sweep forward and intersect the leading edge at the tip and cause a major collapse of the flow (not shown here). With the strake added, the point from which the forward shock springs is moved outboard and the position and strength of the rear shock can be modified. As a result the shock intersection point moves outward from A to B and the severity of the induced onset of flow separation can be affected. Nominally the extent and strength of the shock outboard will be reduced, to the benefit of the value of usable lift, but this will not always be the case: unfortunately it is quite possible to trigger a more violent tip stall and thus make things worse rather than better at some point in the high subsonic range.

The stalling characteristics of the basic wing design can thus be a factor in the successful use of strakes at high incidence, but this is only one facet of the more general problem associated with the standard of aerodynamic performance of the original design. From our experience it is evident that usually a poorer design of wing is easier to improve with the addition of strakes than a wing of better design. One problem for the wing designer, equipped as he is now with now sophisticated wing-body design methods, is to know what allowances to make for the important influence of the separated flow field of the strake on the attached flows over the inner wing. At present there are no satisfactory methods of mathematically modelling this. In Fig 6 the effect is shown of adding strakes of very similar shape to two quite different designs of swept wing, each conceived without the effects of strakes. A photograph of a model of one of these is shown in Fig 4. The 589/3A wing, some sample results for which are shown

in the top two sketches of Fig 5, was designed as a research project to carry a larger proportion than usual of the lift at high incidence over the inner half of the span. The design had shortcomings in other ways however, and did not perform well. In the event the addition of even a modest size of strake (strake 4) improved the lift break and the lift/drag ratio over the whole incidence range even at moderate angles of attack. This is compared in the figure with the addition of a similar design of strake (strake 6) to the 589/2 wing which had a much better basic performance to start with. Only marginal improvements to the lift curve are apparent in this latter case and certainly there is a large reduction in lift/drag at moderate incidence.

The most important single problem in wing design is perhaps the improvement of maximum usable-lift at high speeds. Unfortunately, at such limiting conditions the flows are always complex and much of the wind-tunnel evidence as regards the use of strakes can be confusing and inconsistent. We are now dealing with flight conditions well beyond the separation-onset boundary when a large area of the wing surface is carrying unsteady separated flows under the influence of strong shock waves. Fig 6 shows a comparison of the upper surface flow patterns for an advanced condition with and without strakes present as drawn from visualization studies. The remains of the basic intersecting shock system which triggered the separation of the flow initially is visible in both cases and one important effect of the addition of the strake is to reduce the area subject to high suction ahead of this shock system. The loss of lift from this effect is more than offset, however, by the increase of area under attached flow elsewhere, and of course the vortex shed from the strake across the inner wing intensifies the suction locally under its path. Generally the important effects to note are the overall reduction of area subject to flow separation and the beneficial effect on the aft shock inboard. The length of wing trailing-edge subject to separation is very much less, although the extreme tip region of the wing seems to be completely separated to the leading-edge as much with as without the strake. Hopefully it will not be too long before we can model mathematically such complex situations as this, because there is no doubt that this way real progress lies.

5. USE OF WING CONTROLS

It will not have gone unnoticed from the sketches in Fig 6 that the addition of strakes regularizes and improves the upper surface flows inboard, particularly at and near the trailing edge. This is important because of the use of trailing-edge controls to improve manoeuvre performance. Some data for a wing which had a drooped variable-camber leading-edge control used in conjunction with a simple flap at the trailing-edge is given in Fig 7. The wing in its 'clean' condition (left-hand sketch) had a penalty in lift-drag ratio at low and moderate lift coefficients due to the addition of strakes and a benefit at high values, both as expected. Included in this sketch are the drag polars* for reference. However, with the controls deflected for a "manoeuvre configuration" (right-hand sketch) suitable for a Mach number of 0.6, there was a much broader, but lower, peak in the L/D plot for the wing without strakes and much higher values were achieved at high lift coefficient. Adding the strakes had the result of improving L/D at lift coefficient up to $C_L = 0.5$ by a substantial amount and above this C_L there was a penalty followed by a marked improvement at very high lift.

Unfortunately, no flow visualization studies are available for this particular case, but at the bottom of Fig 7 some oil-flow studies are shown for the same manoeuvre wing configuration at the higher speed of $M = 0.8$, and these give a clue as to the reason for these effects. The addition of strakes moves the outboard strong shock, and the flow separation behind it, further out towards the tip as shown previously in Fig 5, thus improving the flow over the trailing-edge flap in this region. Also the flow is improved over the flap at its extreme inboard end which lies under the path of the strake vortex. Between these two regions at mid-span the initial tendency for the flow to separate over the flap is apparently made worse by the addition of the strake, although the precise reason for this is not clear. However, the total result of adding the strake is clearly the sum of a number of separate effects, some good and some bad. At $M = 0.6$, as comparison between the two sets of curves in Fig 7 shows, although the use of manoeuvre flaps is almost as effective on L/D at high lift coefficients with strakes present as without, the penalty in drag incurred at lower lift coefficients is very much less.

If we turn our attention now to the use of slotted devices at low speeds the sample results for the RAE Model 494 quoted in Fig 8 are of interest. The fully developed slats and 40° double-slotted flaps were separately or together very effective on this wing design and particular care was taken to avoid gross interference on the upper-surface flows from the brackets used to hold these devices in place. The left-hand sketch at the top of Fig 8 shows that the addition of strakes** was equally effective in broad terms for the wing 'clean' or with the trailing-edge flaps deployed. The plot of lift increment due to flaps, ΔC_L , with and without strakes present shows the beneficial interaction of these with the flaps at high incidences, the flaps giving apparently up to 30% more lift with the strakes present at some high incidence. The reasons for this are not clear, apart from the rather obvious one that, as we have seen in Fig 6 for a wing at high subsonic speed, the strake generally improves the flow over the inner wing right back to the trailing edge. The flow above the deployed flaps is thus more energetic and regular and the increased suction under the strake vortex could be making the flap slots more effective. The photographs at the bottom of Fig 8 demonstrate this at an incidence angle of 22° (point 'A' on the plot of ΔC_L), although there is no visible change in the flow over the two flap surfaces themselves.

*Actually for convenience $C_D - C_L^2/\pi A$ has been plotted. This allows small changes at high lift to be seen more clearly.

**These are shown in the sketch of Fig 12 and the photograph of Fig 11.

The right-hand diagram at the top of Figure 8 has been included to demonstrate that complex interactions between the high-lift system of a wing and strakes can occur when efficient leading-edge devices such as slats are involved. This particular wing develops better lift at high incidences with full span slats than when both slats and strakes are used. In this latter case the span of the slat had to be reduced in order to fit the strake, and the benefits of adding the strake did not offset this loss of span.

6

EFFECTS AT THE TAILPLANE

The vortices shed by the strakes as they convect downstream can have a marked effect at the position of the tailplane as might be expected and Fig 9 shows the change in mean downwash for the typical configuration shown in Fig 6, the tailplane being arranged below the plane of the wing, which itself was mounted in a high position on the body (see Fig 4). The mean downwash is shown to be greater over the whole incidence range, but, which is important, rather more so at the higher incidences. The tailplane angle to trim, η_T , can thus be contrived to be less variable with incidence and this effect can be used to advantage in project designs, enabling control power to be maintained up to high incidences. From the lift/drag ratio for this tail-on configuration, plotted for trimmed conditions, the effect of adding the strakes is shown to be rather different from the tail-off (untrimmed) case. There is apparently a penalty at low incidences and the maximum value achieved is reduced, although, happily there seems to be little effect at high incidence.

Some pitot-static measurements made just aft of the tailplane of a straked configuration in a high speed manoeuvre condition are shown in Fig 10. The incidence was high (21°) for the Mach number of 0.84, so this may be regarded as an extreme flight case at high altitude for the range of wing loading currently in fashion for combat air craft configurations. Three cases are shown to demonstrate the effect of 4° sideslip and of including the fin, and the plots take the form of contours of apparent q or $2PV^2$. The probes used could not be lined up along the local streamlines so it is doubtful what the absolute numbers mean, but it is interesting to see the way the field becomes distorted with sideslip and the effect the fin has on the symmetry of the flow above the tailplane. The shaded area in each case has nominally zero 'q', which is perhaps a little surprising in a position as far aft of the trailing edge of the wing (two wing mean-chords).

In a more elegant experiment, some data from which are shown in Fig 12, a detailed survey with a five-tube yawmeter was carried out, this time at low speed, in a plane through the quarter-chord line of the tailplane position of a research model. The traverse equipment is seen behind the model in the photograph of Fig 11 and was part of a sophisticated computer-controlled system with a comprehensive on-line data processing capability. The probe normally would be automatically kept in line with the local stream, but in this case only the pitch motion of the probe could be kept active because of the proximity of the body and fin.

However, the downwash angles quoted here are not compromised in any way and are plotted for four heights with respect to the nominal tailplane position, with and without the strakes present. The core of the vortex from the strake evidently passes not very far above the tailplane position, somewhere very near point P on traverse B. The mesh of the measurement grid was fine enough to enable downwash angles up to about $\pm 50^\circ$ near the vortex centre to be established and significant changes in downwash over a diameter of about half the tailplane semi-span are apparent. It is an open question whether this vortex has 'burst' by the time it has reached this position so far aft of the wing. The wing incidence for this particular survey was 14° , ie just beyond the point at which the flow over the main wing has started to break down (see flap 0° case in the lift curve of Fig 8). Certainly the data in both Figs 10 and 12 demonstrate how careful the design and positioning of the tailplane need to be when strakes are included in a configuration. Very similar remarks could be made about the fin, particularly at very high incidences, although there is somewhat less freedom here unless twin fins are used, when the spacing and cant angle of these provide some options.

It is also of some interest to consider the flow field further forward just behind the wing with the strake at this same incidence of 14° . This time the measurements were made with the fully active self-aligning probe system so it is possible to plot contours of true total-head deficit and local vorticity. These are shown in the top two sketches in Fig 13. The model had strut supports on the lower surface of the wing and the wake of these may be seen at about $Y = 520$ mm but fortunately the main features of the flow field are not unduly affected. The core of the strake vortex is clearly seen, and at this forward position this seems to be a little further inboard than as shown in Fig 12 at the tailplane position, as might be expected. The total head defect at the centre of the much larger wing-wake 'vortex' outboard is $1.2q$. The plot of local vorticity, given in the second sketch clearly shows the strong primary vortex shed from the strake and the weaker wing-wake 'vortex' outboard, both of positive sign. The secondary vortex from the strake at this position just downstream from the wing trailing edge appears as an elongated tongue of negative vorticity partially wrapped around the outside of the primary and is joined to a thin layer of negative vorticity lying across the whole span beneath these two centres of positive vorticity. This layer has a comparatively strong local region beneath the strake primary vortex, presumably caused by the confluence of the boundary layers from the two wing surfaces which must have very different spanwise components of velocity at this point. As may be seen in the diagram of Fig 12, there is little or no sign of this subsidiary negative vortex at the position of the tailplane further aft.

At a higher incidence of 25° , as the lowest diagram in Fig 13 shows, the strake vortex must have previously 'burst' at some point ahead over the wing and the diffuse core has virtually become amalgamated with the equally diffuse 'vortex' shed from the wing leading edge to form an unexpectedly thick combined area of positive vorticity over the whole span of the exposed wing. Underneath this large area of positive vorticity there is the thinner layer of negative vorticity across the whole semi-span of the exposed wing arising from the wing boundary layers which by now is more uniform and comparatively strong. This will be of special interest to fluid dynamicists, particularly since the gradients through this layer are so steep. The one general comment that can safely be made about the data from this experiment, is that, the complexities of the flow field being what they are due in part to viscous effects, the development of adequate design methods for wings with strakes is going to be a difficult task. It must be stressed

that by 'adequate' methods it is implied that the mathematical modelling of the real flow fields must be reasonably representative.

7 UNSTEADY STRUCTURAL RESPONSE

It is a matter of fairly common experience that the addition of strakes to a wind-tunnel model apparently reduces buffet amplitudes at high incidence. Models with wings of advanced aerodynamic design without strakes have often been found to be unusually violent in the way unsteadiness develops, particularly immediately after the stall at high subsonic speeds, and in some cases this has made meaningful measurements of any kind impossible at this important point in the incidence angle range (even when it is safe to attempt these). Often at higher incidences calmer conditions of buffeting are regained. To read across to the buffet behaviour of the corresponding aircraft in flight from such wind-tunnel tests raises difficulties, although new techniques are now available for this purpose⁵. Some test results are quoted in Fig 14 for a model fitted with a special flexible wing⁶, aeroelastically more representative of full-scale than a 'rigid' metal model in some respects, in which the effect of adding strakes to the wing buffet response was investigated. A commonly used criterion in model tests for the onset of buffeting in flight is the break in the lift/axial-force curve, and if one accepts as fair the points marked 'A' and 'B' on the curves for this model shown at the top of Fig 14a, the strakes can be seen to be adverse at the Mach number in question, $M = 0.8$. However, a plot of such 'break' points over the speed range as given in the centre sketch of Fig 14a shows that this adverse effect only occurs for a limited range of Mach number near $M = 0.8/0.85$. There are plausible fluid-dynamics reasons for behaviour such as this in this particular limited speed range, but these considerations are somewhat academic in view of the more important problem of the limitation of usable-lift at incidences well beyond this 'onset' point. At the bottom of Fig 14a some frequency spectra for the RMS pressure at a critical upper-surface point P_1 are shown at three incidences which straddle the onset points A and B at $M = 0.8$. At $\alpha = 6.3^\circ$, ie before any signs of flow separation on the wing, the strakes appear to reduce the level of unsteadiness in the local pressure at P_1 , but by $\alpha = 8.7^\circ$ the reverse is true and this trend continues up to $\alpha = 10.6^\circ$ at which angle the flow has separated from the leading edge over most of the wing span.

The response of the model can be seen in Fig 14b in the corresponding spectra from an accelerometer at a point A, which was close to the pressure point P_1 . Paradoxically the addition of the strake appears to increase the response in both the primary bending mode (at 40 Hz) and the primary torsion mode (at 275 Hz) at the first incidence of $\alpha = 6.3^\circ$. However at $\alpha = 8.7^\circ$ the tendency for the primary torsion mode to be excited is reduced with the strake, but at $\alpha = 10.6^\circ$ the reverse is true, the presence of the strake inducing a high response in this mode. Reference back to the spectra for the pressure at the point P_1 given in Fig 14a suggests that there could be some small degree of coupling between the excitation and response in this mode both for the basic wing at $\alpha = 6.7^\circ$ and the configuration with strake at $\alpha = 10.6^\circ$. The plot of total apparent damping in this torsion mode (as a percentage of critical) is given in the lower sketch in Fig 14b and shows that in both these instances the total damping is low, lower in fact than the structural damping alone, and thus it is evident that the addition of the strake can change significantly the aerodynamic damping of a wing. The increase caused in the aerodynamic damping immediately post stall, in this case between $7\frac{1}{2}^\circ$ and 10° of incidence, is fairly typical and is consistent with observations made of model buffeting in many other tunnel experiments.

8 STABILITY CHARACTERISTICS

Fig 16 shows the effect of adding strakes to a model of the Harrier aircraft at two Mach numbers, $M = 0.5$ and 0.8 . The model carried external stores, as indicated in the sketch of the aircraft at the bottom of the figure, this particular configuration having been found to be an unusually unsteady one in flight at high incidence. The strakes were designed to be compatible with the aircraft structure and basic stability requirements in flight so that full-scale trials could be made at a later date. The tunnel data shown in the figure demonstrate a dramatic improvement to lift, to rolling-moment at zero sideslip and to the steadiness of the wing-root bending-moment at high incidence, all of which is in line with experience from research models such as those referred to in previous sections. However, particular note should be taken of the rolling-moment plots. In these diagrams the plotted points are shown in addition to lines which give the upper and lower bounds of the instantaneous signal observed during the incidence sweep. A useful correlation of this 'scatter' in rolling-moment at zero sideslip in wind-tunnel experiments has previously been found with 'wing rock' characteristics in flight for this particular aircraft: also the occurrence of large static values of rolling-moment in the tunnel has been found to correlate fairly well with wing-drooping in flight. Thus the considerable improvement found in the tunnel tests in these rolling-moment characteristics when the strakes were added promises well for the flight tests. At the time of writing the test aircraft had just made its first flight. A photograph taken from the airfield control tower is shown in Fig 15.

Some oscillatory derivative measurements carried out as a research investigation with another aircraft configuration with and without strakes are shown in Fig 17. The wind tunnel technique, which is a sophisticated one, is adequately described elsewhere⁸. The model was oscillated at high subsonic wind speeds over small ranges of yaw, roll and sideslip in turn, the mean pitching moment being kept zero by a remotely controlled tailplane. The samples of the data quoted in this figure demonstrate the beneficial effect of strakes at high incidence on directional and lateral stability (derivatives n_y and l_y respectively) at high subsonic speeds, and it should be noted that without strakes present the model on this flexible rig became too unsteady to test safely at a comparatively early incidence, but that with strakes present no such limitation occurred. The yaw damping derivative ($n_r - n_y \cos \alpha$) was reduced by the strakes at low incidence but was apparently not affected at high incidence. The roll damping derivative ($l_r + l_y \sin \alpha$) on the other hand was falling-off sharply at the point at which the test had to be curtailed without strakes present, and the addition of strakes had an important beneficial effect in this case as may be seen in the lowest sketch of this figure.

Some continuous-rolling values of the roll-damping derivatives, l_p , are shown in Fig 18 for yet another aircraft model configuration, tested at low speed this time, both in a high-speed manoeuvre configuration and with slats and flaps deployed as for landing purposes. The results speak for themselves;

the addition of strakes to both wing configurations gives a significant improvement in l_p at high incidence and at no point in the range does the derivative ever drop below acceptable levels.

9 VARIABLE GEOMETRY

To end this presentation a brief mention may perhaps be made of the potential of variable-geometry strakes. As discussed earlier in this paper any fixed geometry of strake has to balance the benefits in usable-lift at high incidence with the drag-due-to-lift penalties at lower angles. A strake with variable incidence or camber could be used to reduce the need for such a compromise, either by means of flaps along the leading edge of the strake or by a direct control on the incidence of the whole device. In Fig 19 some data at low speeds is shown for a research model which used the deflection of a wing leading-edge flap in a schedule to keep the drag as low as possible over the incidence range. The model had strakes which could themselves also be deflected, so pitching-moment could in effect be controlled by both these means. The total range of pitching-moment available is shown in the diagram between the upper and lower broken lines and the range from 10° deflection of the strakes alone is shown by the full lines for a low-drag schedule of the wing flaps. As may be seen the result can be a smooth contribution to pitch control within a total system that could be used in a variety of ways.

Fig 20 shows two configurations of another model which has a remotely controlled variable-camber flexible strake to investigate possible pitch-control functions as well as the optimisation of drag. Such studies could well lead to somewhat different ideas on the use of strakes on future aircraft.

10 CONCLUDING REMARKS

The complexity caused in the flow field by the use of strakes on wing-body configurations adds considerably to the difficulties in mathematical modelling techniques which are used as a basis of engineering design methods. The design engineer, therefore, is likely to have to rely on empirical rules from experimental studies for many years yet until adequate theoretical methods are available. This paper highlights some of the experimental research in the UK which is generally investigating various aspects of the use of strakes, but it must be stressed that, in the UK as elsewhere, no logical and totally consistent technical framework has yet emerged which can be used with confidence, for example at the 'drawing-board' stage of a new design. For every trend emerging from a set of experimental data, credible inconsistencies can usually be quoted with the use of strakes in some particular way or other, and such is the incomplete nature of our understanding of the overall flow mechanisms involved these inconsistencies simply cannot be ignored. This is particularly so as regards aerodynamic effects at high speeds when flow separations have started to occur on the wing and the achievement of high values of usable lift is at a premium, limited by such phenomena as structural buffeting, wing rock, pitch-up or other symptoms of 'departure'. There continues to be an urgent need to explore all the various aerodynamic features of strakes experimentally in order to enlarge our understanding and to guide the theoretical work which will form the basis of future design methods. This is in addition to the routine work on an 'ad hoc' basis to obtain satisfactory solutions to current design problems.

11 ACKNOWLEDGEMENT

The help received from colleagues within British Aerospace and the Royal Aircraft Establishment in assembling the material for this paper is gratefully acknowledged.

REFERENCES

- 1 D Kuchemann The aerodynamic design of aircraft. Chapters 6 and 7: The properties and design of slender aircraft. Pergamon Press (1978)
- 2 P L Bisgood Results of flight tests on a slender wing low-speed research aircraft (HP 115) AGARD Report 535 (1966)
- 3 C S Barnes and R Rose Some flight and wind tunnel longitudinal stability measurements on the BAC 221 slender-wing aircraft. RAE TR 71077, ARC R & M 3692 (1977)
- 4 W E Lamar (et al) The effects of buffeting and other transonic phenomena on manoeuvring combat aircraft. AGARD AR 82 (1975) Chapter 12: Improvement of aircraft buffet characteristics.
- 5 W E Lamar (et al) As above. Chapter 4: Dynamic response of aircraft structure.
- 6 G F Moss and D Pierce Some aeroelastic distortion effects on aircraft and wind tunnel models. AGARD FMP 46th Meeting, Valloire, June 1975.
- 7 G F Moss and D Pierce The dynamic response of wings in torsion at high subsonic speeds. AGARD CMP 44th Meeting, Lisbon, April 1977
- 8 J S Thompson and R A Ffai Oscillatory derivative measurements on sting-mounted wind-tunnel models at RAE Bedford RAE TR 66197 (1966) AGARD OP 17

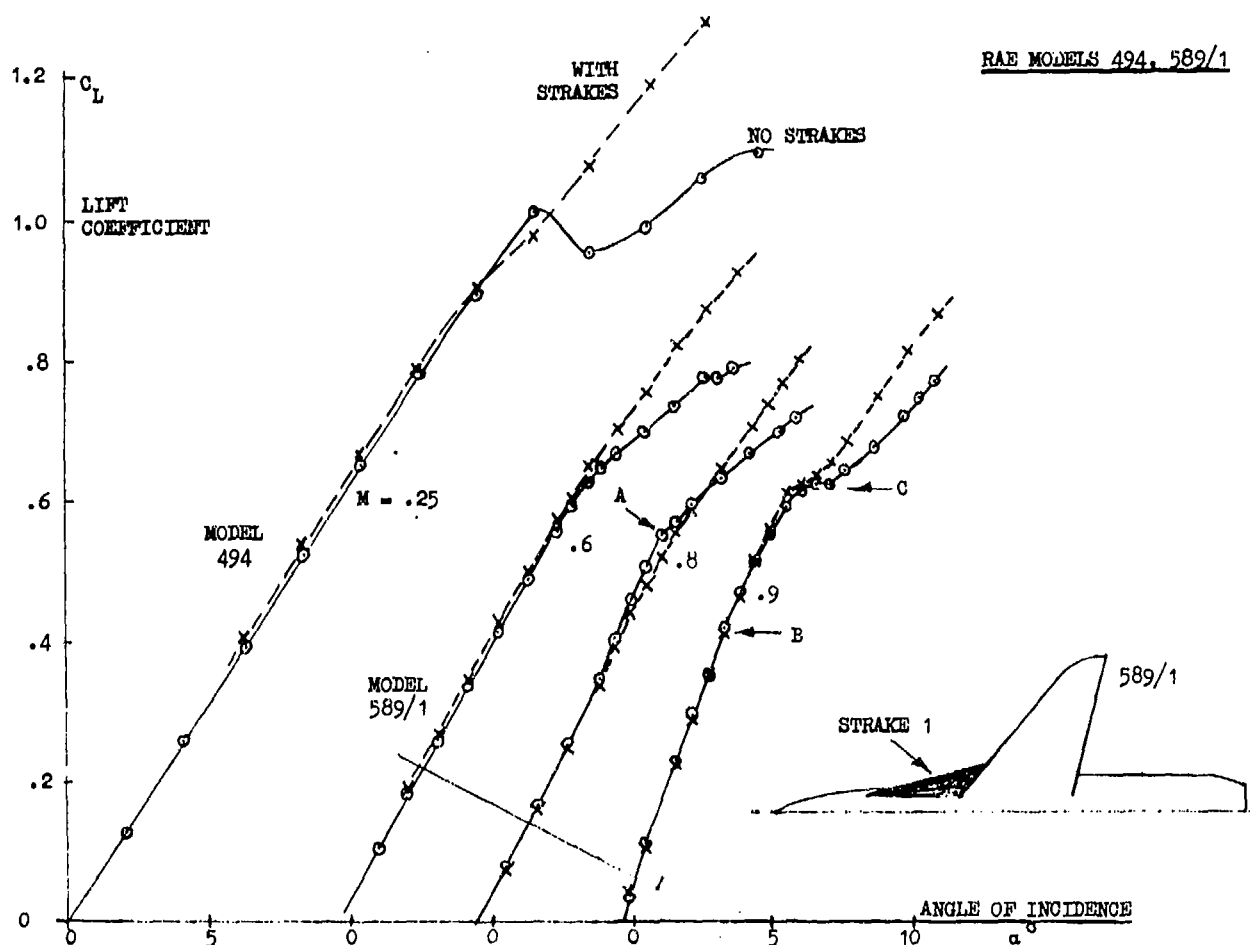


Fig 1 Typical effect of wing-body strakes on lift coefficient

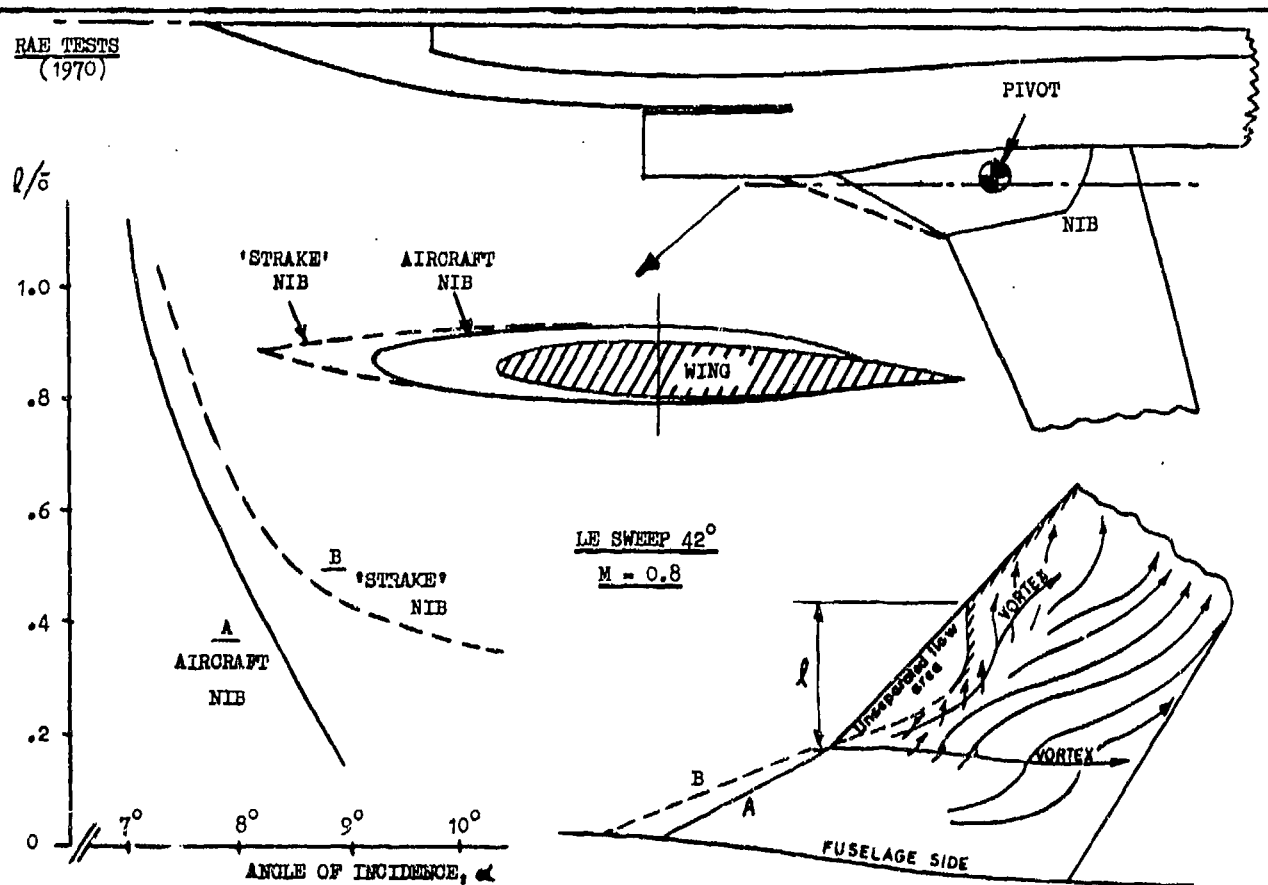
RAE TESTS
(1970)

Fig 2 The use of a 'strake' nib on a variable-sweep design

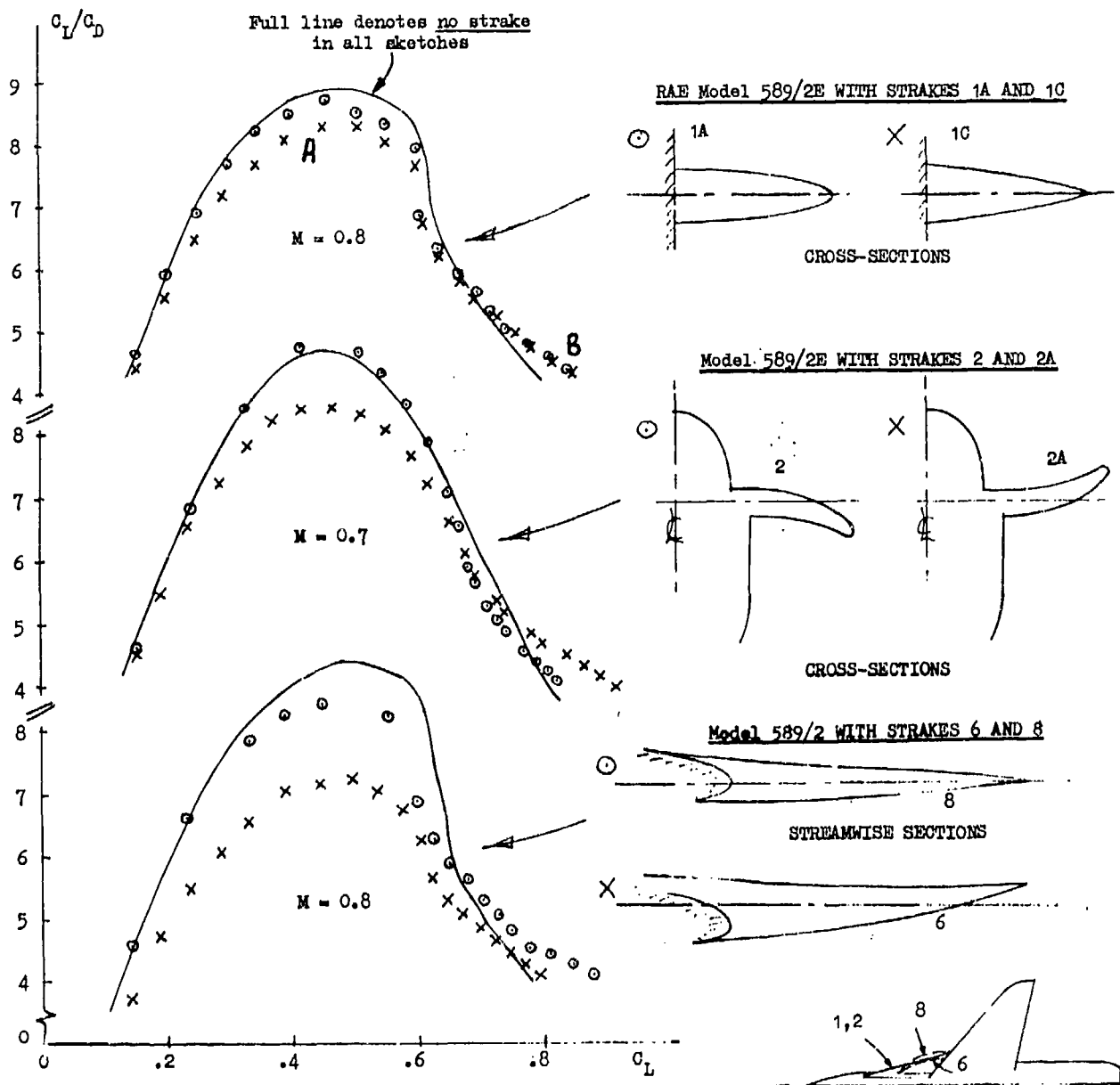


Fig 3 Effect of strake bluntness and camber on overall lift/drag

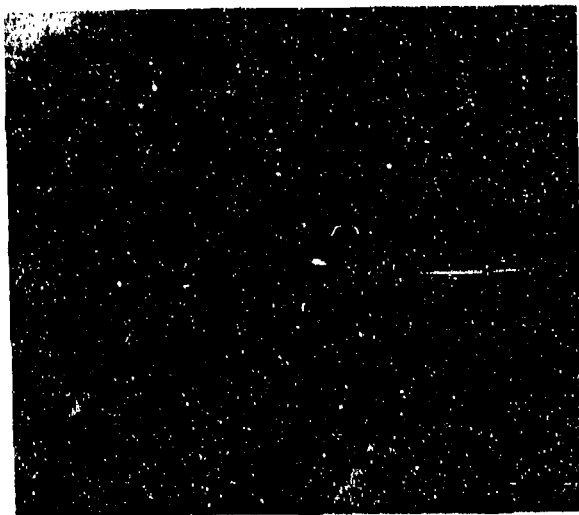


Fig 4 Photograph of RAE model 589/3A

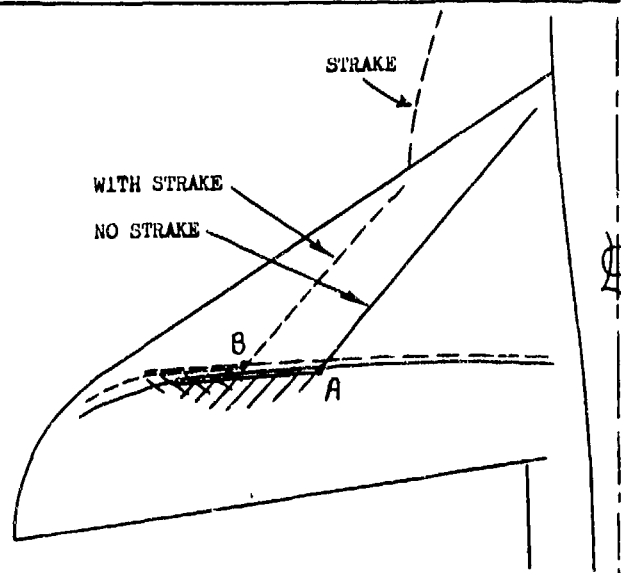


Fig 5 Typical shock positions at high speeds

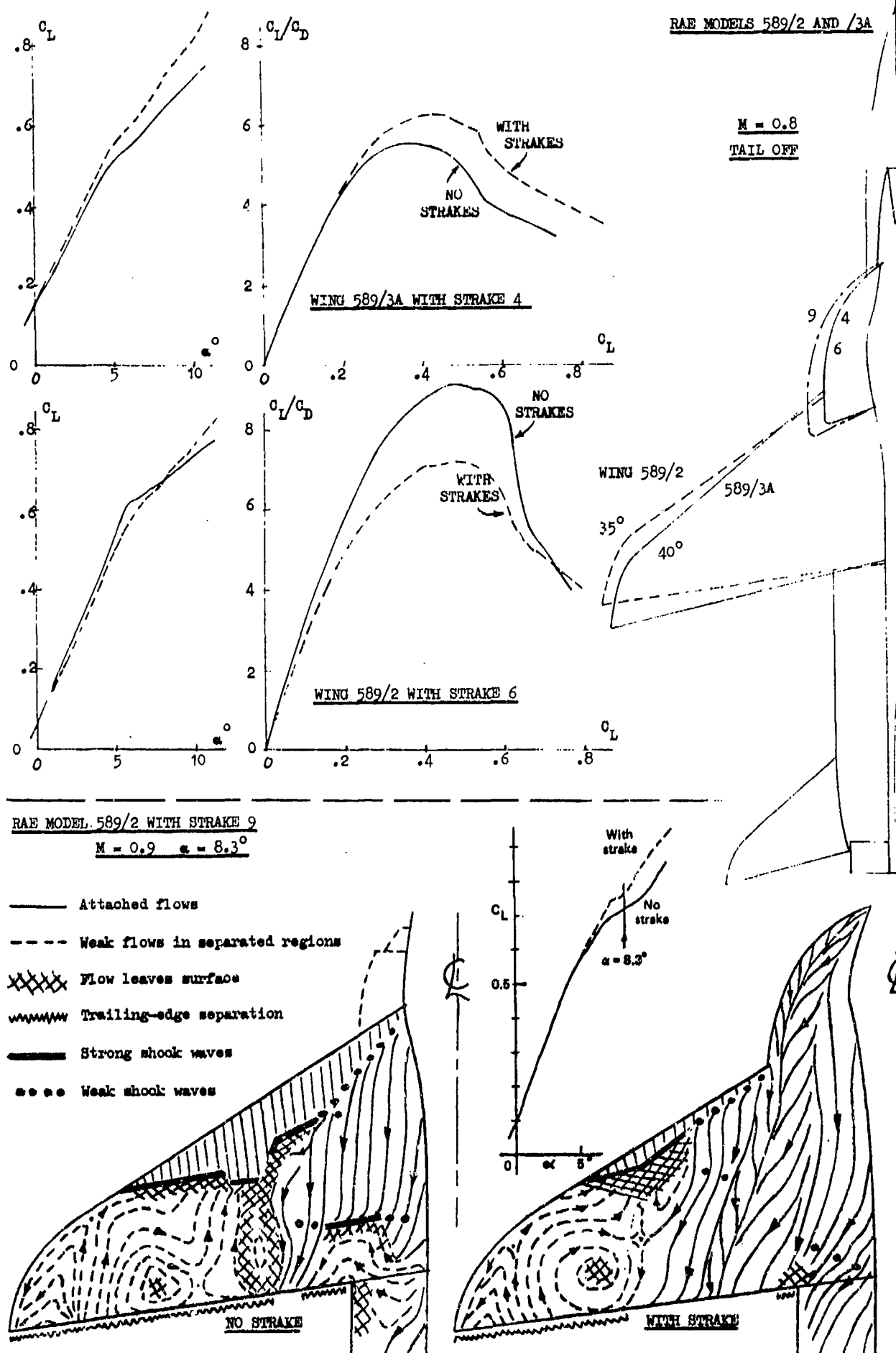
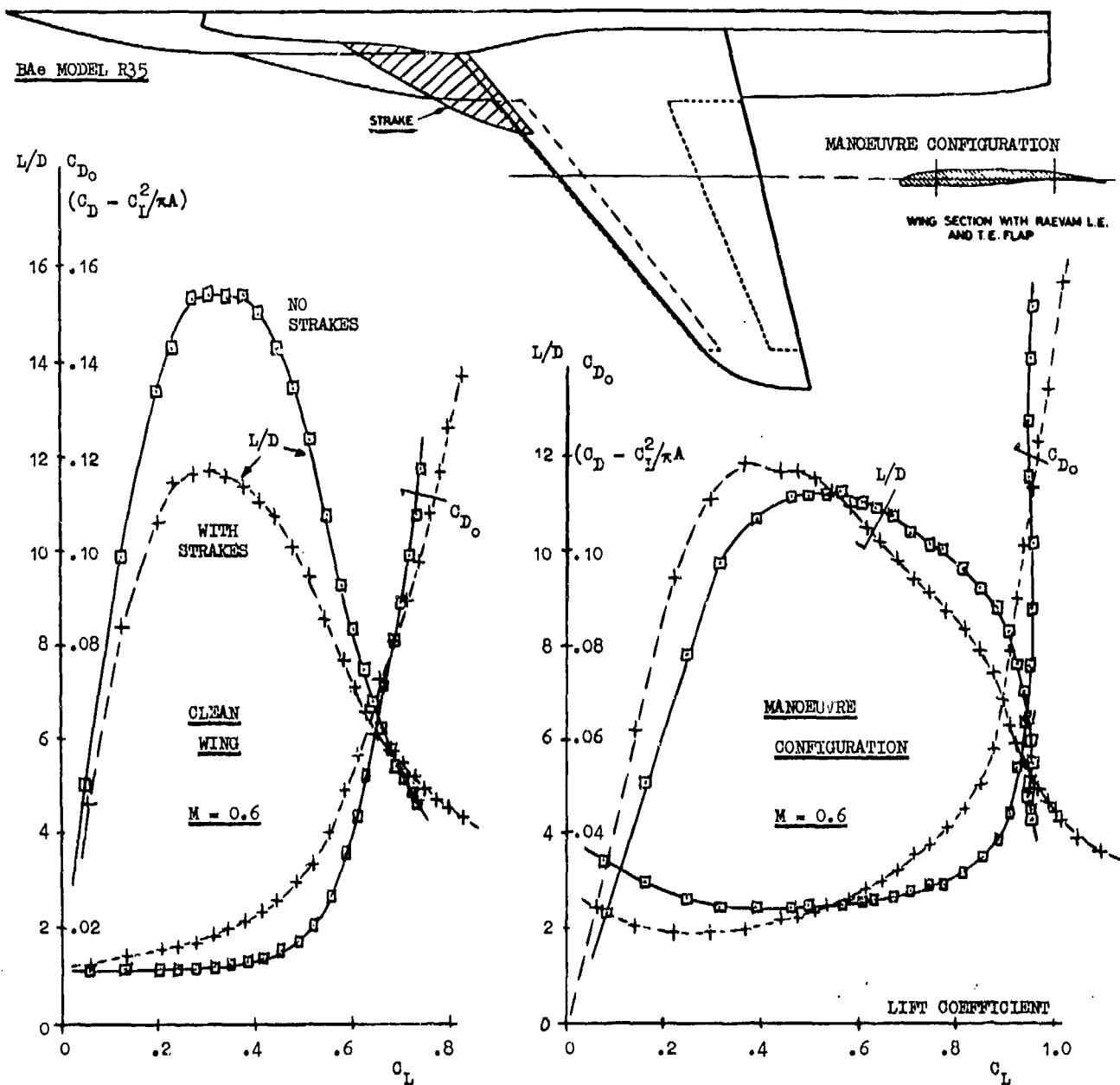


Fig 6 Effect of strakes on wing performance at high speeds



OIL FLOW
STUDIES
AT
 $M = 0.8$
FOR
MANOEUVRE
CONFIGURATION
 $\alpha = 5.6^\circ$

NO
STRAKES

WITH
STRAKES

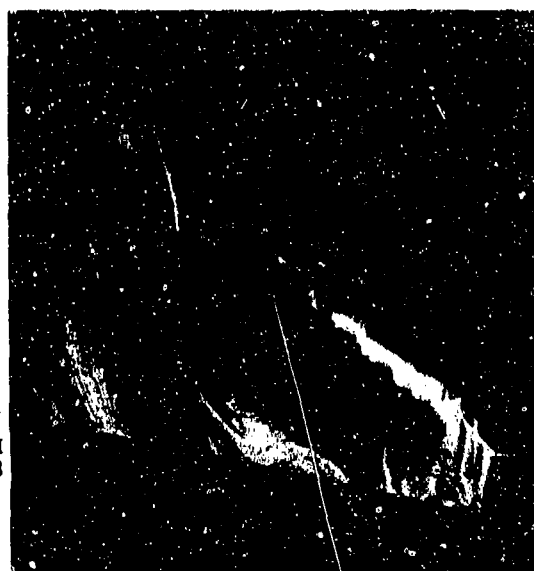


Fig 7 Effect of strakes with high-speed manoeuvre devices

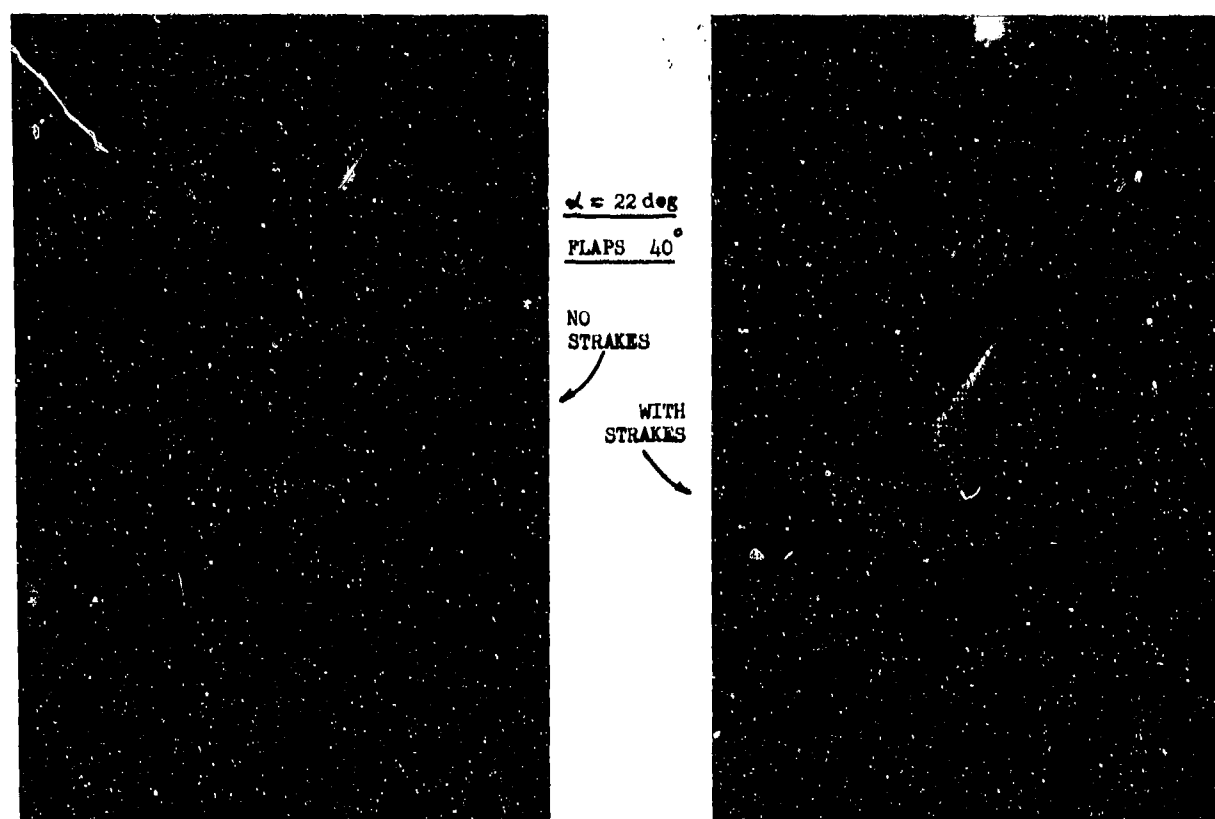
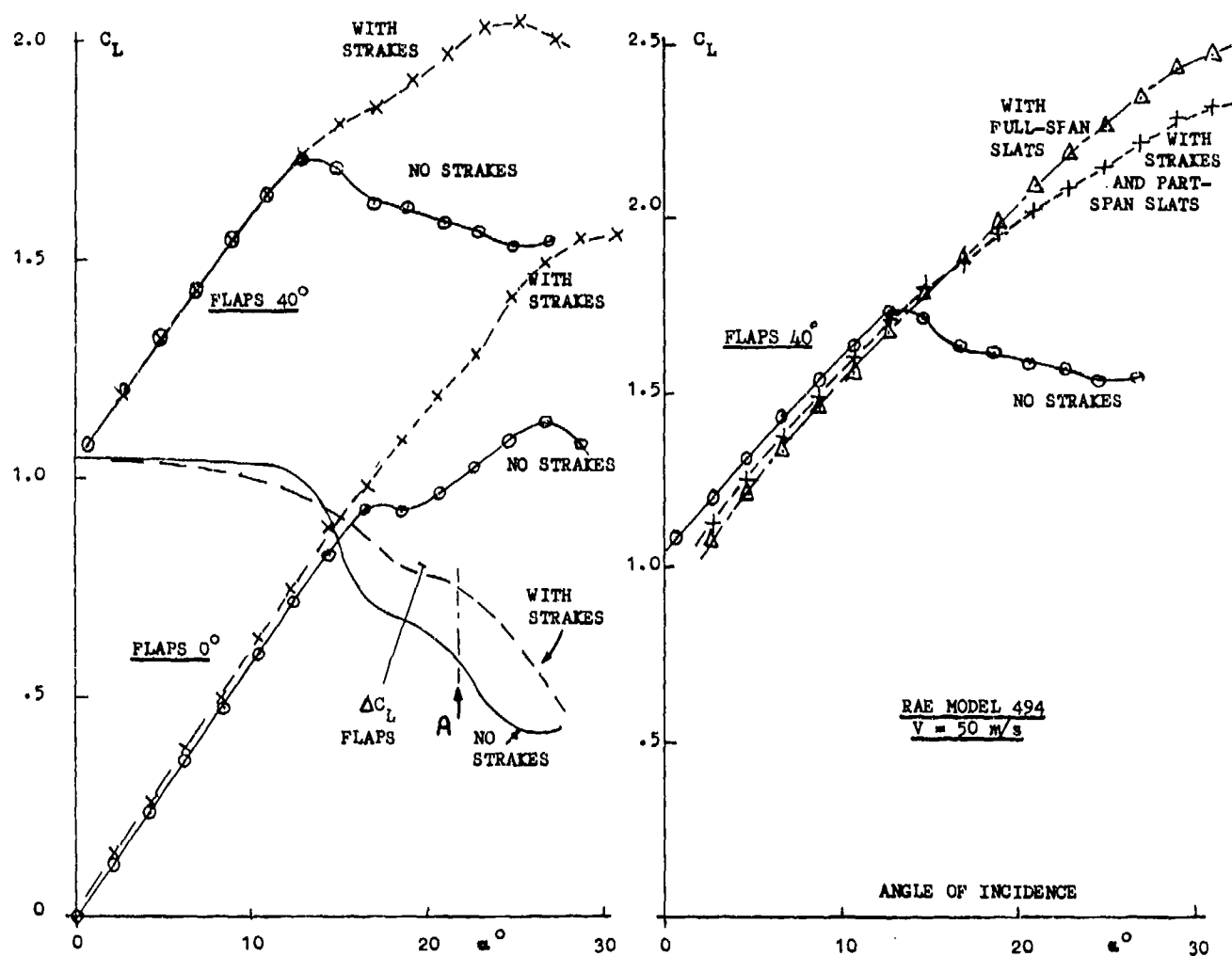


Fig 8 Effect of strakes with double-slotted flaps

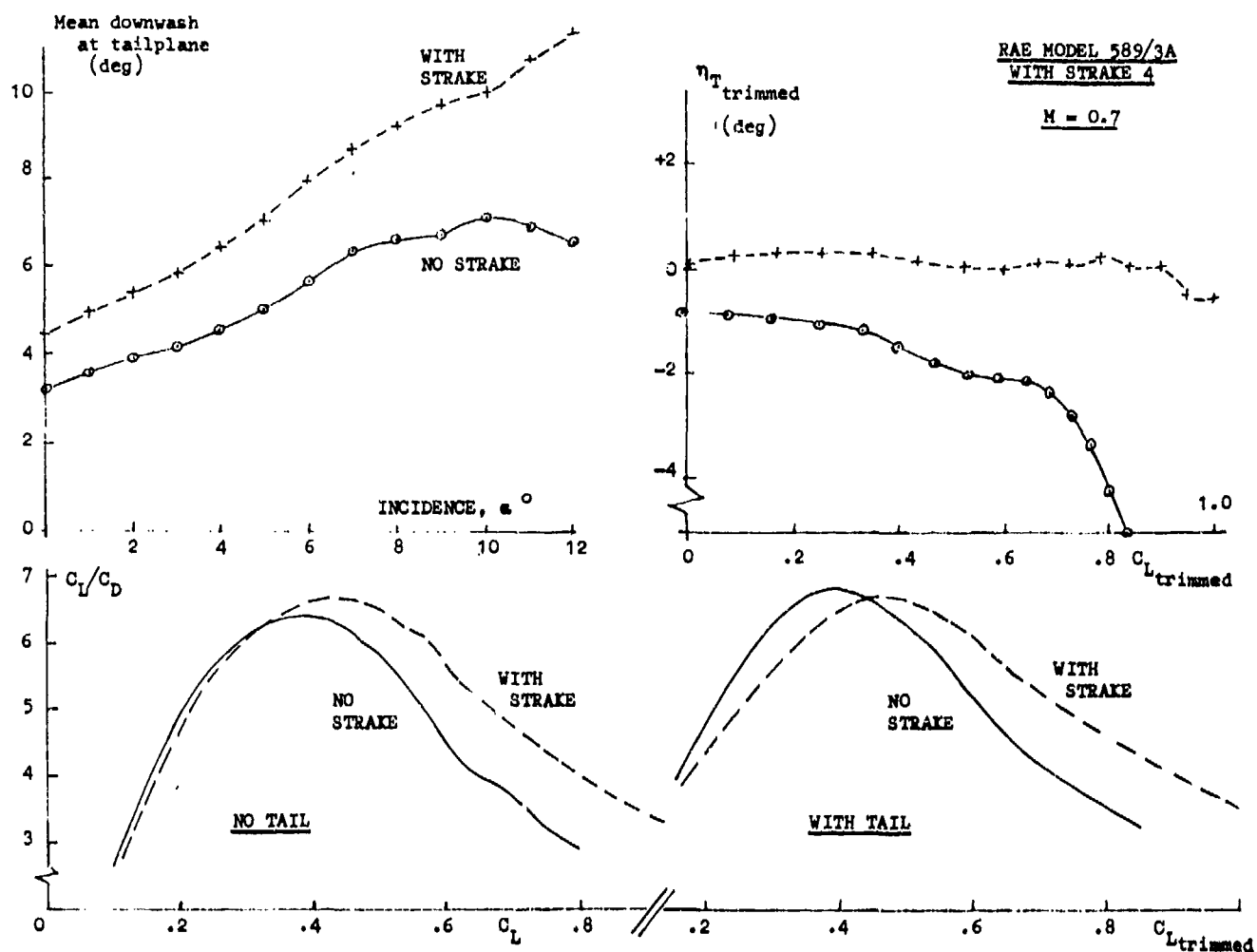


Fig 9 Effect of strakes on tailplane contribution

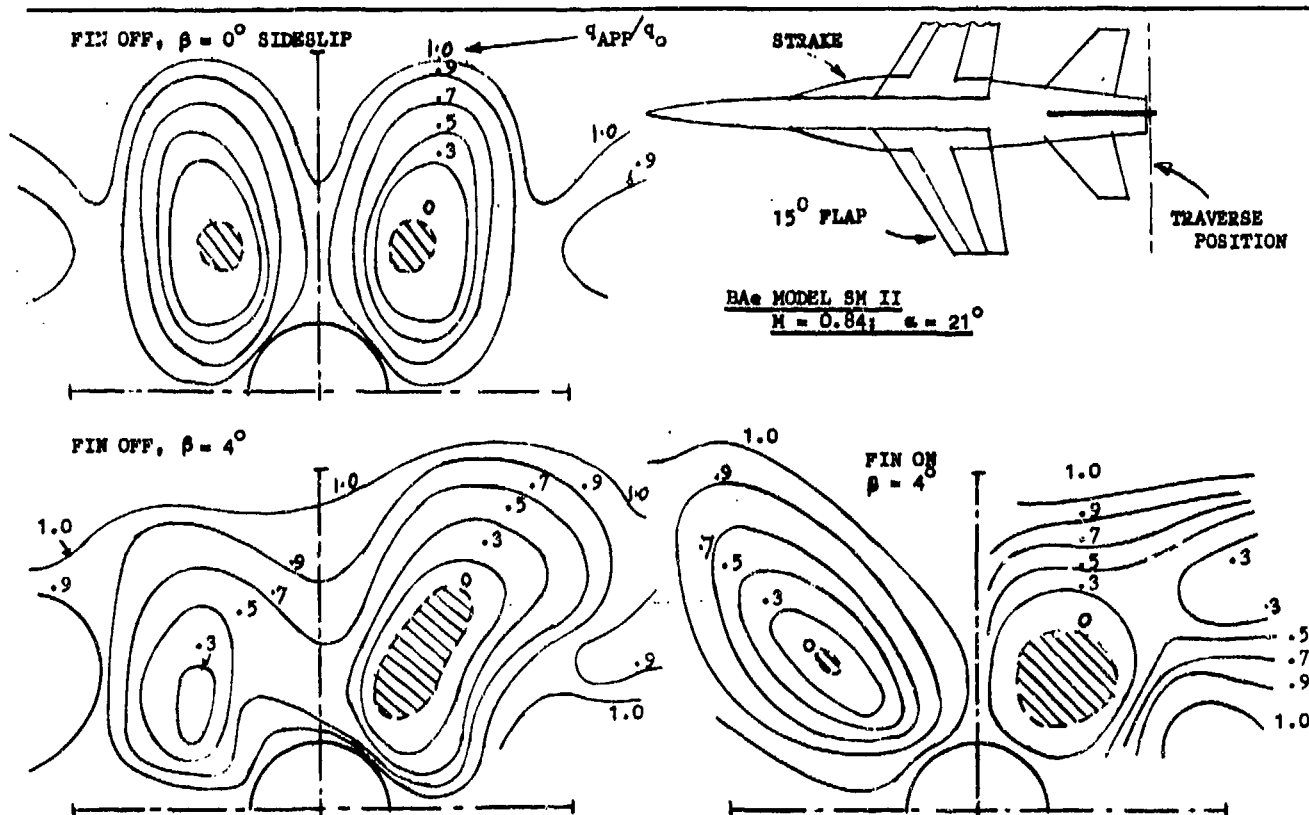


Fig 10 Pitot-static surveys at position of tail unit

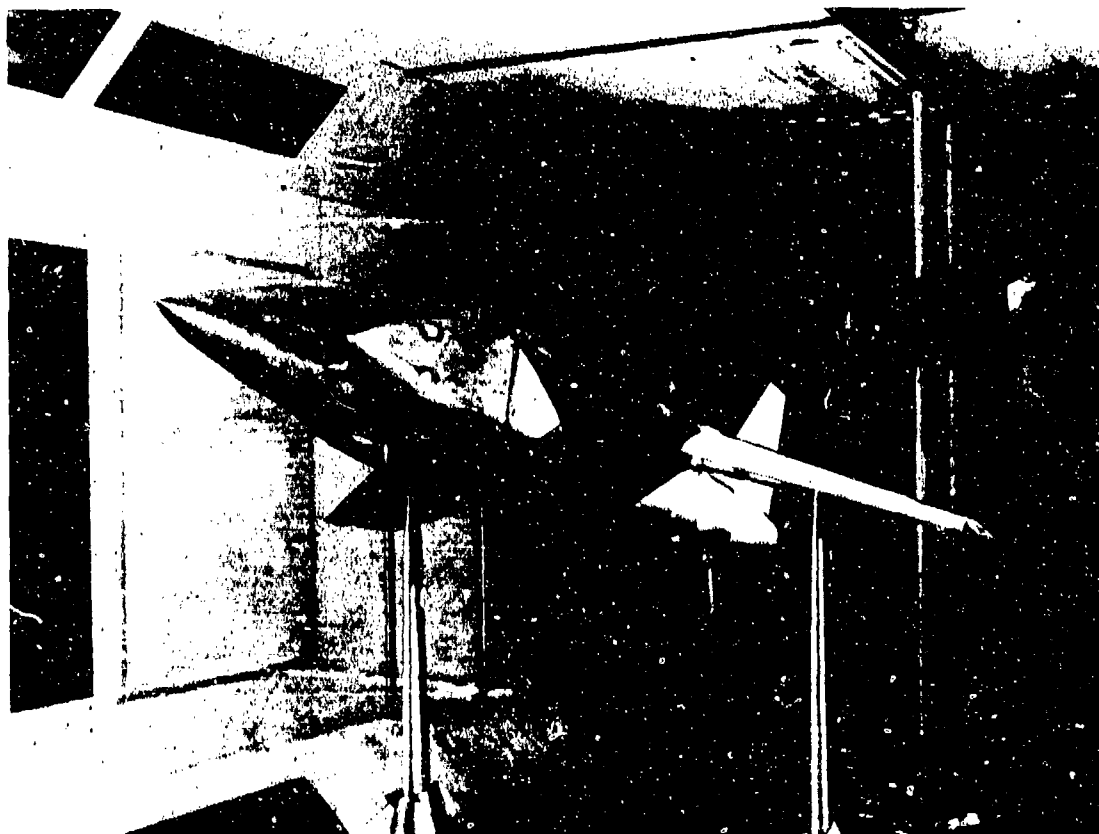


Fig 11 Probe traverse equipment in RAE No.2 11½ ft tunnel

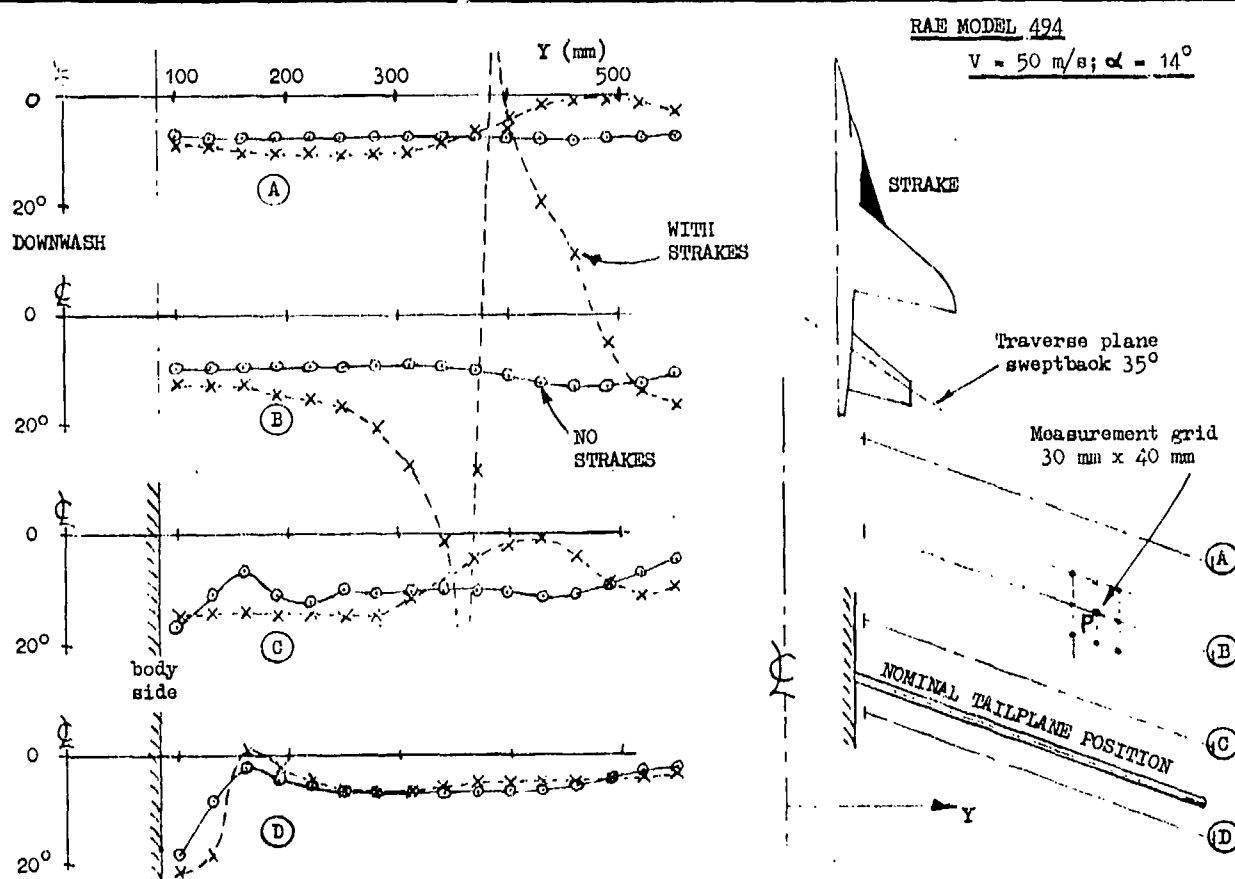


Fig 12 Effect of strakes on downwash at tailplane position

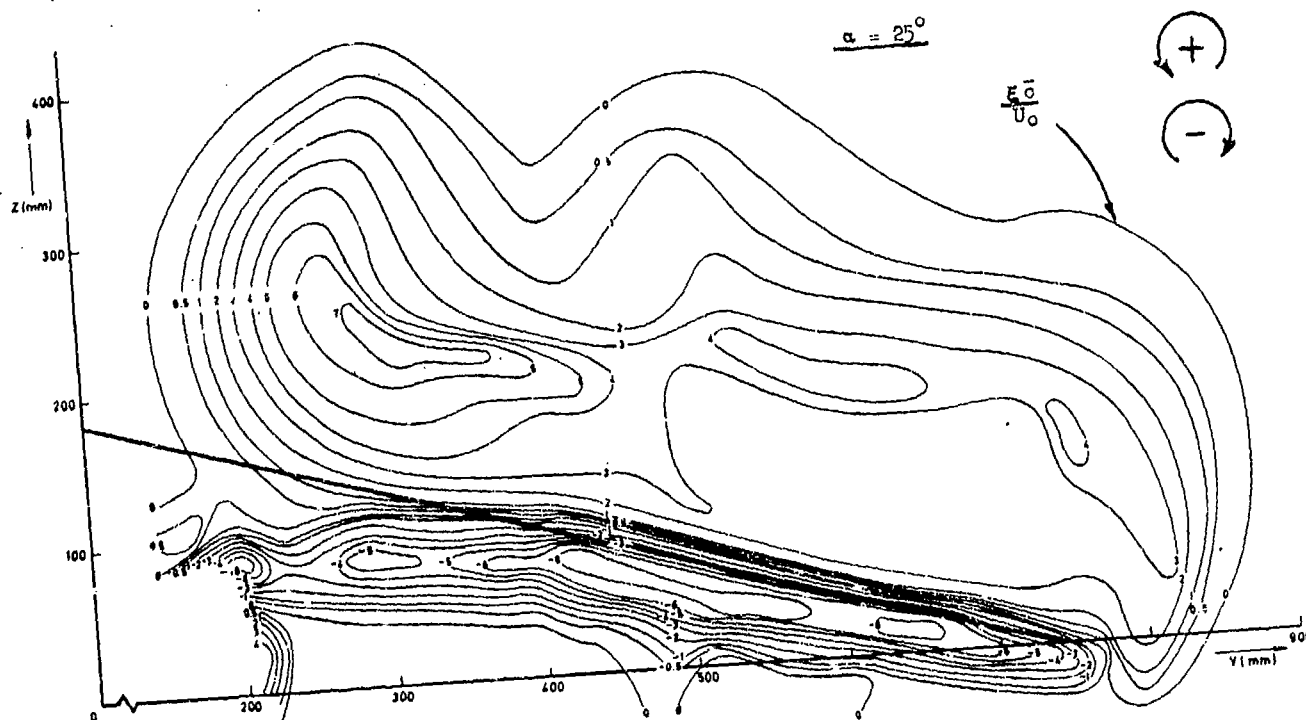
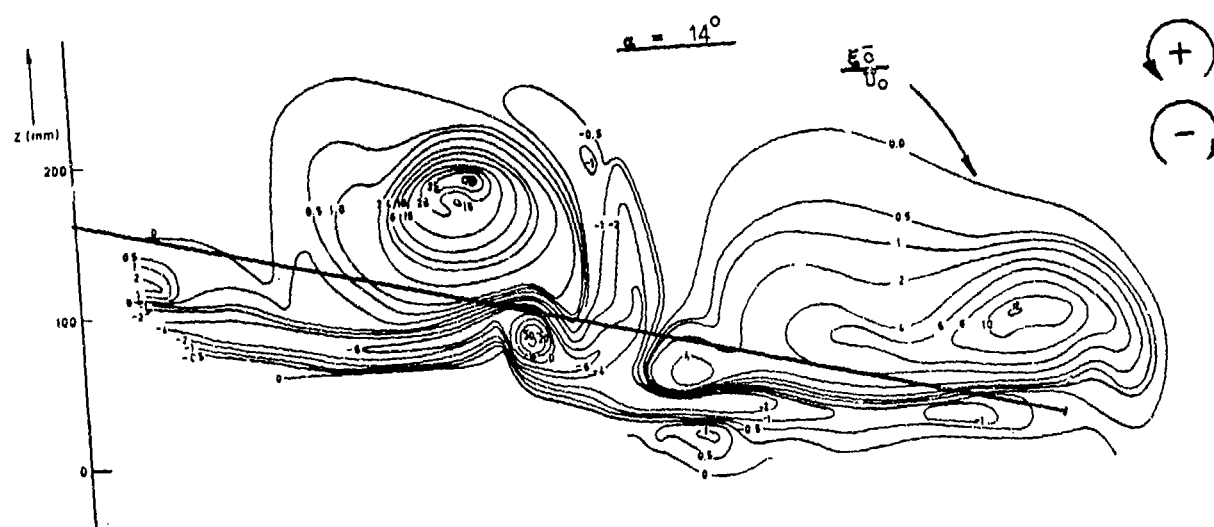
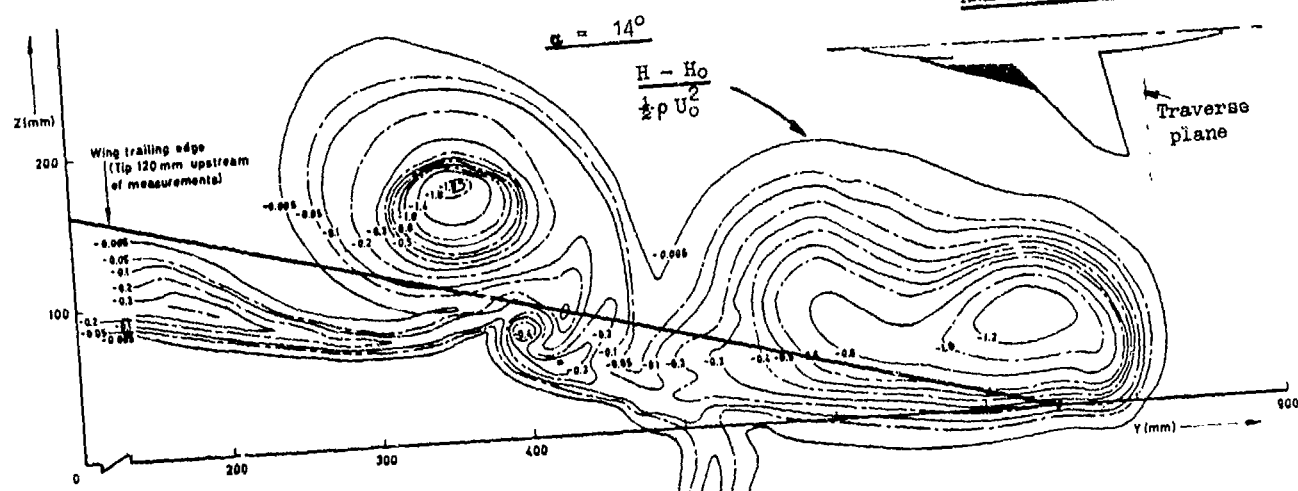


Fig 13 Flow field behind a straked configuration at high incidence

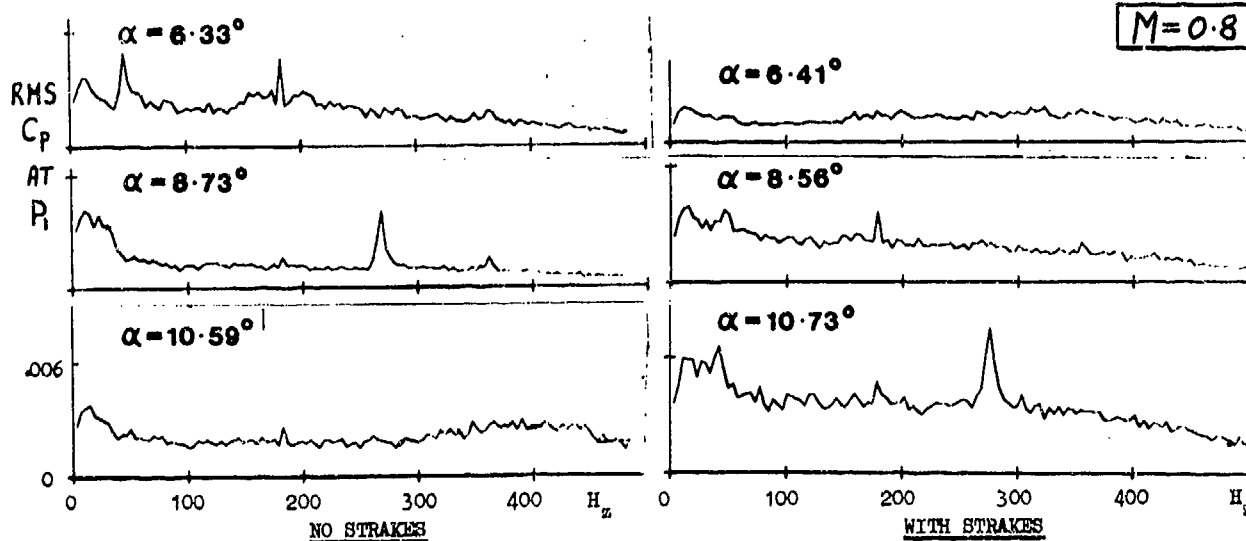
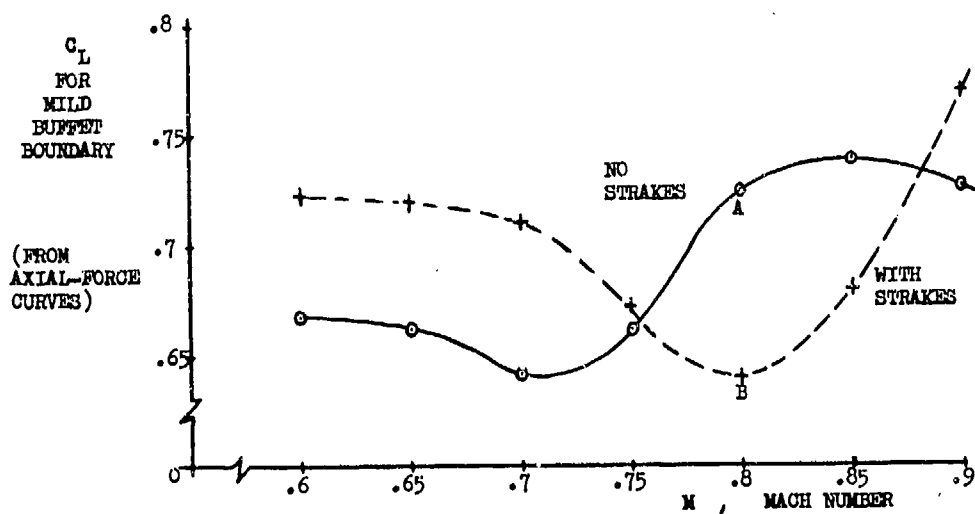
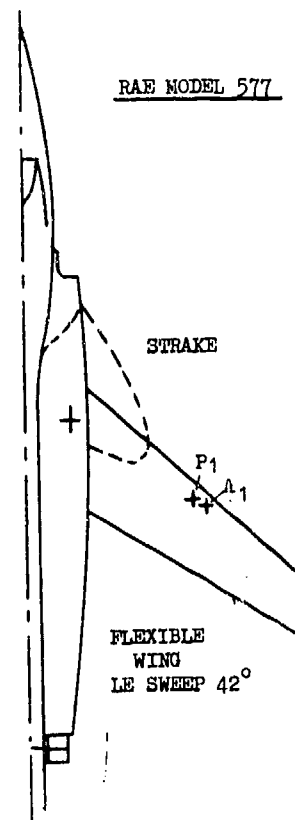
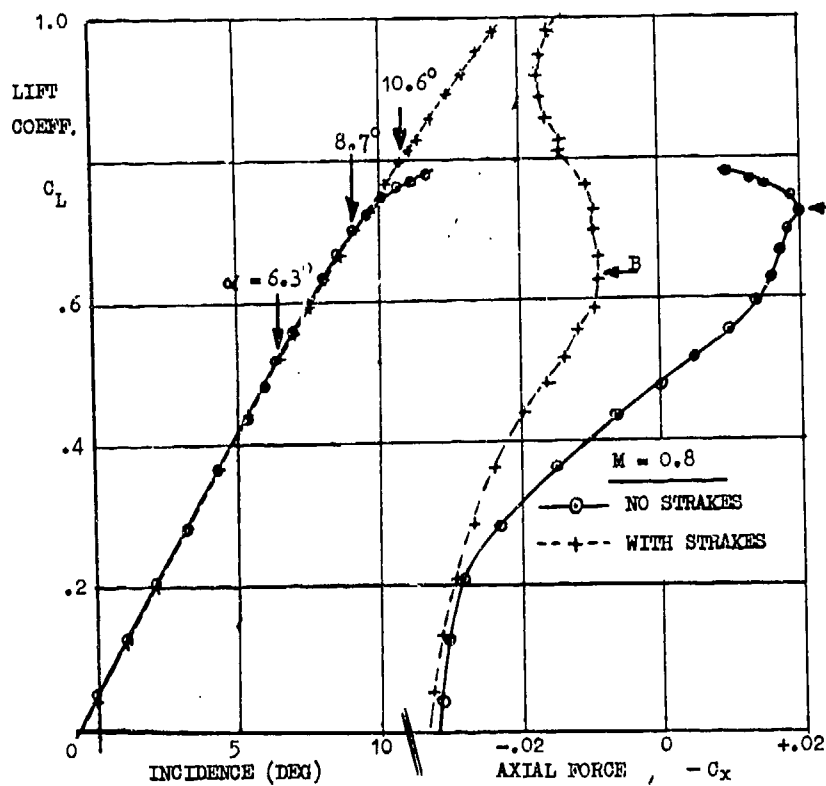


Fig 14a Effect of strakes on buffeting: RAE model 577

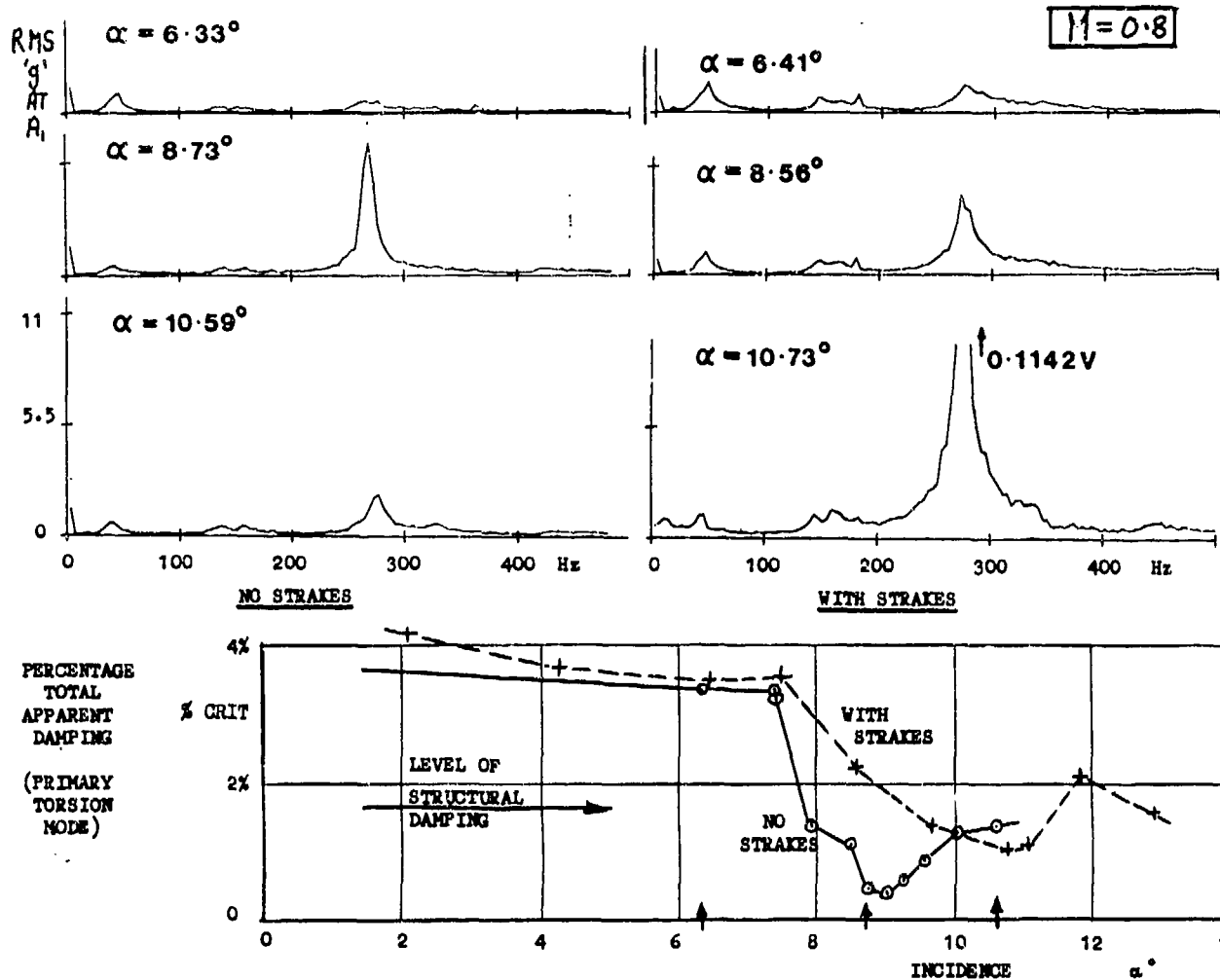


Fig 14b Effect of strakes on buffeting: RAE model 577



Fig 15 Harrier test aircraft in flight

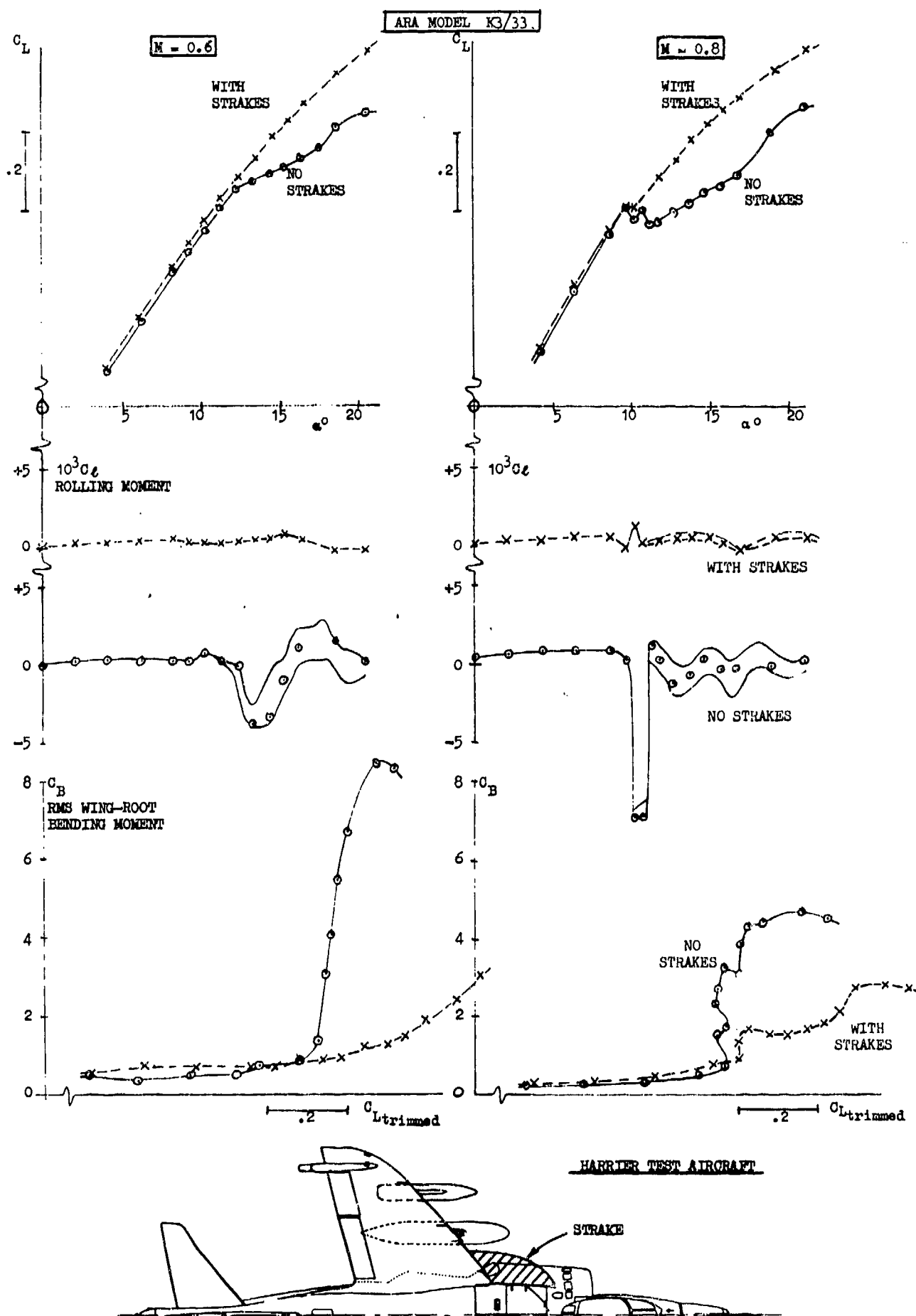


Fig 16 Effect of strakes on wing buffeting and unsteady rolling

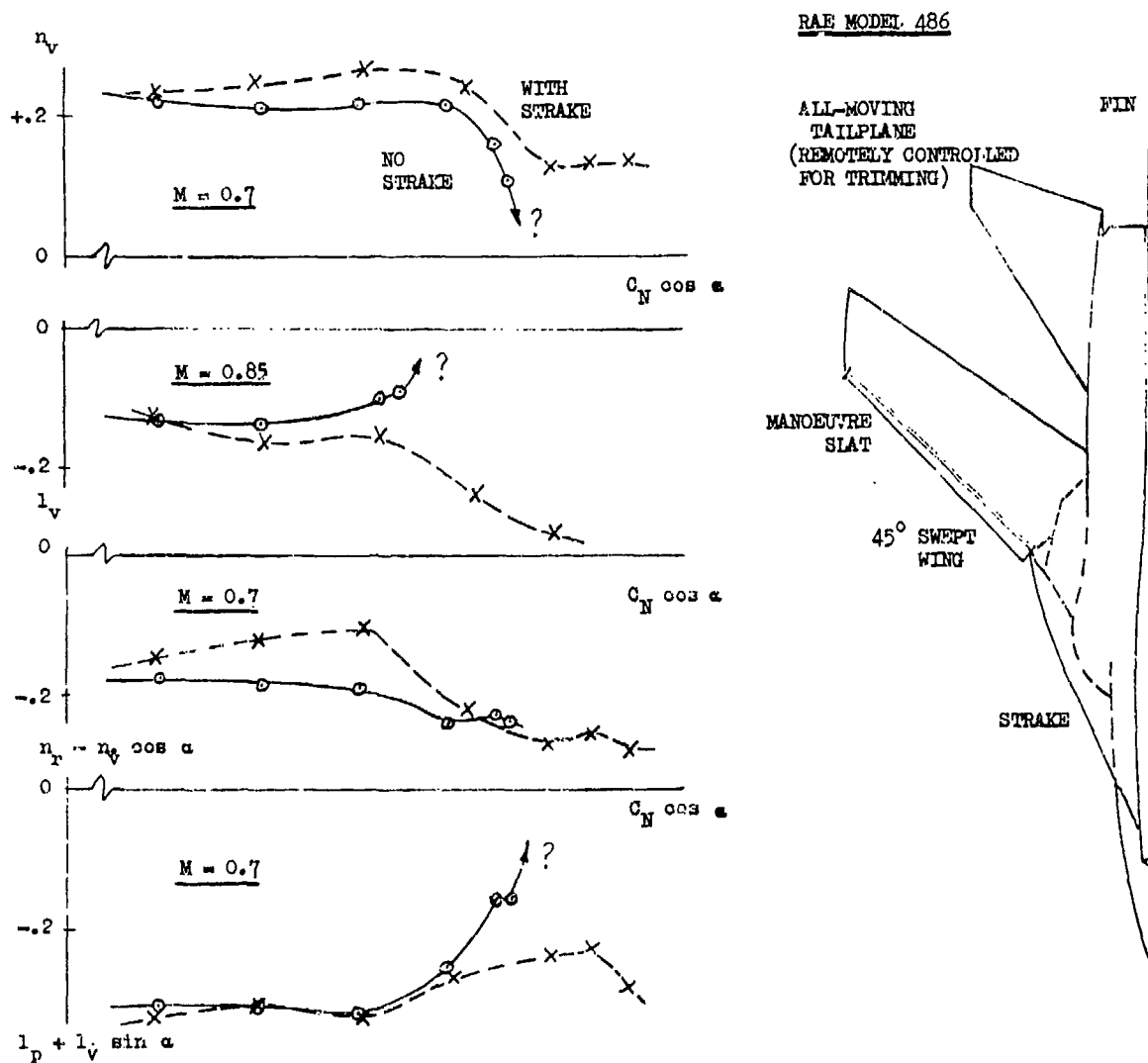


Fig 17 Oscillatory derivative data with and without strakes

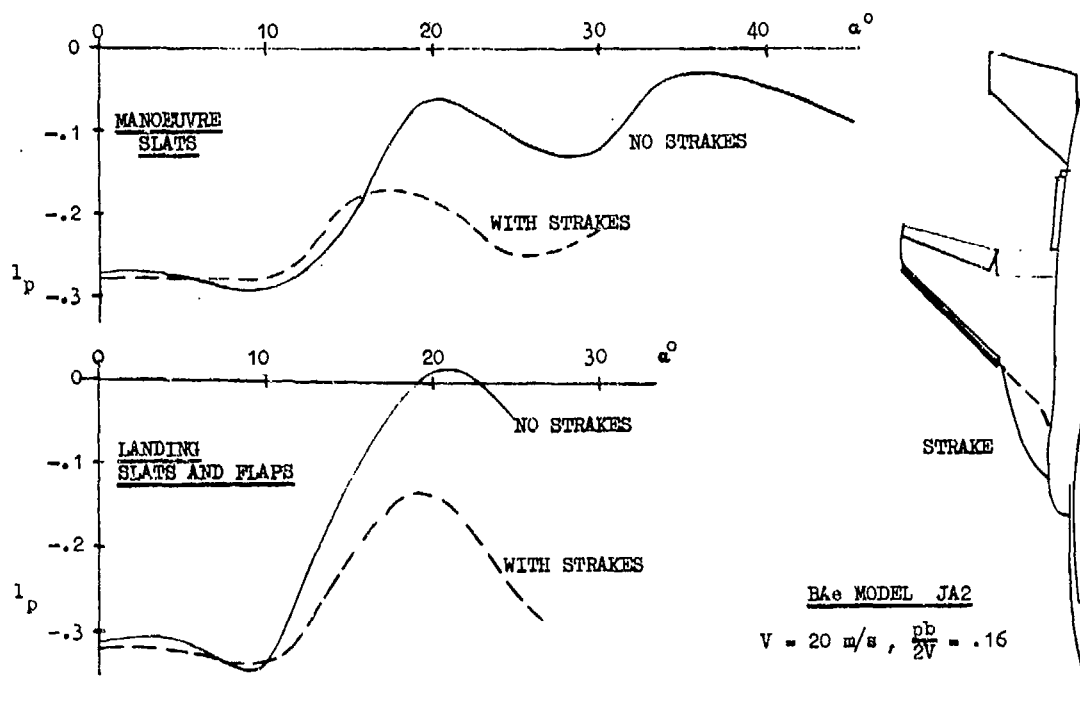


Fig 18 Effect of strakes on roll damping (continuous rolling)

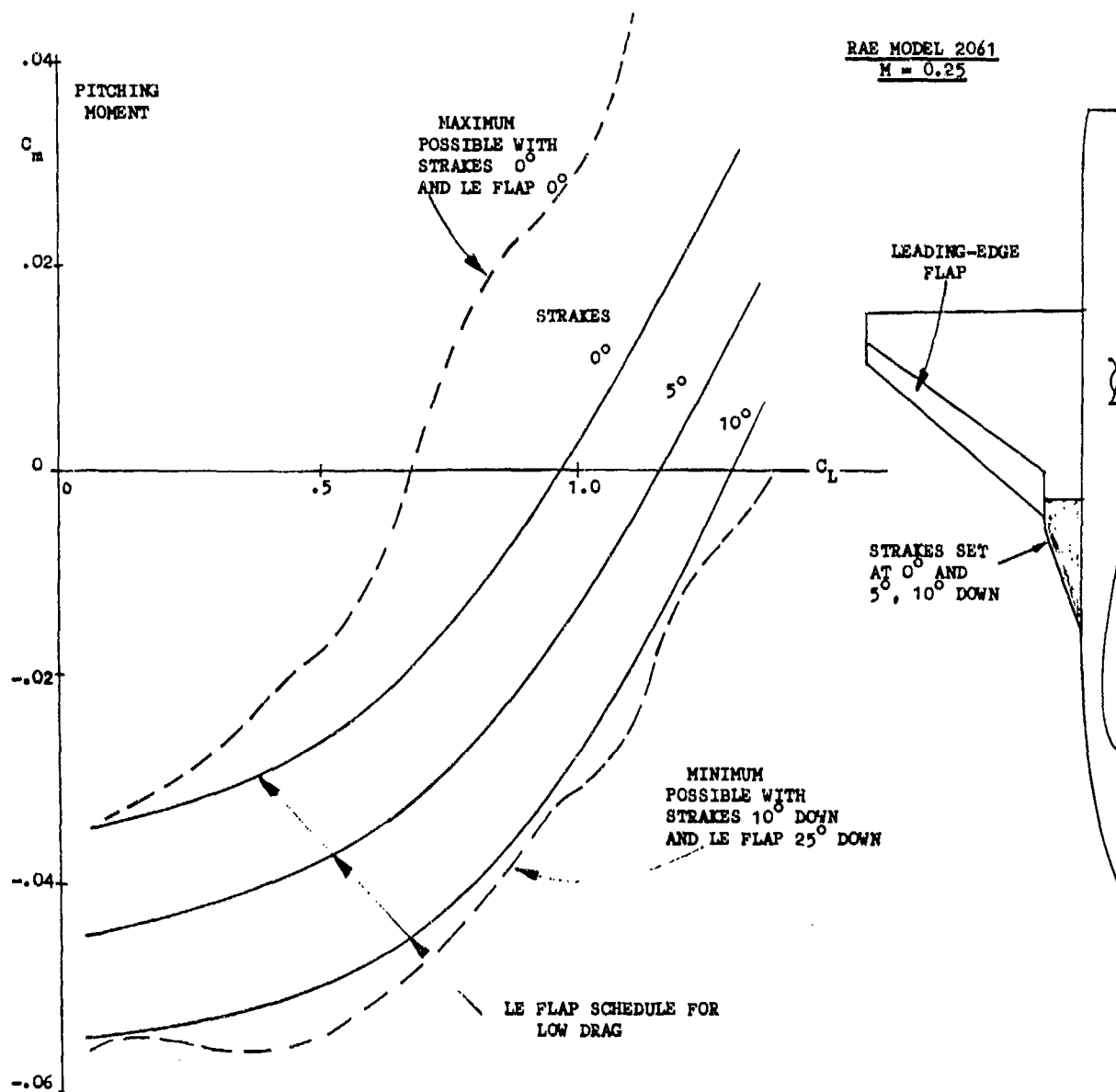


Fig 19 Possible use of strake droop as a pitch control

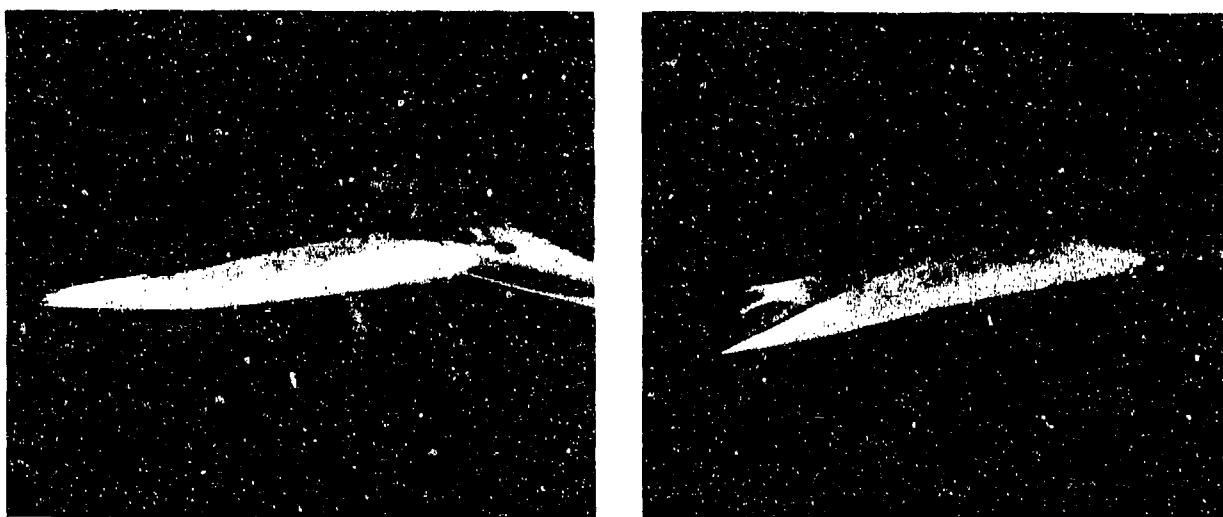


Fig 20 Variable camber strakes on RAE model 2091

DESIGN GUIDELINES FOR THE APPLICATION OF
FOREBODY AND NOSE STRAKES TO A FIGHTER
AIRCRAFT BASED ON F-16 WIND
TUNNEL TESTING EXPERIENCE¹

by

C. W. Smith² and C. A. Anderson³
General Dynamics Fort Worth Division
P. O. Box 748
Fort Worth, Texas 76101, U.S.A.

SUMMARY

During the YF-16 and F-16 developmental wind tunnel test program, numerous variations in nose and forebody strakes were investigated. These data have been reviewed, and the strake aerodynamic characteristics coalesced into design guidelines for the application of strakes to fighter aircraft. The design guides take the form of general equations governing the modification of forebody strakes to obtain a linear pitching moment curve and the calculation of the resulting lift and drag increments. Additionally, qualitative comments are made concerning the effects of strake geometry on lateral/directional stability.

It is concluded that the generation of incremental strake lift is primarily dependent upon the area affected by the strake-induced vortex and that strake planform is of secondary importance. Forebody strakes have small beneficial effects on lateral/directional stability if properly designed; however, significant gains are easily attained with nose strakes.

NOTATION

A_{EFF}	Area affected by strake-induced vortex
ΔAC_1	Aerodynamic center increment due to the strake in the linear region
ΔAC_2	Aerodynamic center increment due to the strake in the non-linear region
C_D	Drag coefficient, D/qS_{REF}
ΔC_D	Strake incremental drag coefficient
C_L	Lift coefficient, L/qS_{REF}
ΔC_L	Strake incremental lift coefficient
$C_{L_{\alpha_s}}$	Lift curve slope of the inboard panel
C_l	Rolling moment coefficient
C_m	Pitching moment coefficient relative to $.25 \bar{c}$
C_n	Yawing moment coefficient relative to $.25 \bar{c}$, unless noted
$C_{n\beta}$	Yawing moment slope with sideslip
\bar{c}	Mean aerodynamic chord of the theoretical wing planform
HT	Horizontal-tail deflection angle
i	Strake incidence relative to the wing chord plane
LEF	Leading-edge-flap deflection angle
l_s	Length from the aerodynamic center of the effective strake area to the wing-alone aerodynamic center

¹ This work was sponsored by the National Aeronautics and Space Administration, Langley Research Center under Contract No. NAS1-15006

² Engineering Specialist

³ Director, Aerospace Technology

M	Mach number
S_{REF}	Reference area for aerodynamic coefficients, $26m^2$ ($280 ft^2$), unless noted
TEF	Trailing-edge-flap deflection angle
α	Angle of attack of the wing chord plane
β	Angle of sideslip

1. INTRODUCTION

The vortex lift generated by delta planform wings at moderate-to-high angles of attack has been utilized in aircraft design for many years. Recently, designs have taken advantage of this vortex-lift characteristic by employing auxiliary surfaces, e.g., canards and forebody strakes, to generate vortices in conjunction with moderately swept primary wing planforms. In this manner it is possible to couple the desirable subsonic and transonic characteristics of the moderate-sweep wing with the good high-angle-of-attack vortex characteristics of the high-sweep surface.

The latest generation of American fighter aircraft, the F-16 and F-18, are prime examples of the utilization of forebody and nose strakes to provide significant increases in usable maneuver lift. These aircraft are the culmination of long design evolutions, which relied extensively on wind tunnel testing. As a consequence, an extensive body of experimental aerodynamic data exists. An experimental approach was required because no reliable aerodynamic prediction methods are available that address the highly complex flow field present at the moderate-to-high angles of attack under consideration.

In particular, during the course of configuration development of the YF-16 Lightweight Fighter Prototype and the F-16 Air Combat Fighter, General Dynamics wind-tunnel-tested many strake variations at low and/or transonic speeds. Both conventional and highly blended configurations were investigated early in the YF-16 development program. The effects of variations in strake size, strake planform, strake location relative to the span of the wing, and leading-edge-flap deflection received considerable interest. Several types of strakes were investigated. These consisted of strakes that extended from the forebody to the wing leading edge (forebody strakes), strakes that started at the nose and extended only a short way back on the forebody (nose strakes), and relatively short strakes that were placed aft of the nose but did not extend to the wing leading edge (canard strakes). The findings are summarized from an extensive review of these data and the initial efforts presented toward the development of design guidelines for the application of forebody strakes to future aircraft.

A few comments concerning the aerodynamic characteristics of forebody and nose strakes are helpful. The primary benefit attributed to forebody strakes is a significant increase in usable lift at transonic speeds compared to that from a conventional wing configuration. However, significant interactions occur between the vortex flows generated by strakes, the wing flow field, and the empennage flow field, and these interactions can be favorable or unfavorable. While it is relatively simple to achieve a high maneuvering lift capability with forebody strakes, it is necessary to tailor the strake-wing-empennage combination to enhance the moderate-to-high-angle-of-attack lateral/directional stability characteristics and thus make the additional lift usable. Some strake-wing configurations create an adverse stall situation at angles of attack in the range from 35 to 60 degrees; therefore, it is also necessary to evaluate low-speed pitch-control effectiveness in this angle-of-attack range.

Finally, forebody nose shape plays an important role in the high-angle-of-attack lateral/directional stability characteristics. The effects of nose shape can be minimized by employing nose strakes but, again, it is necessary to limit the nose-strake size to prevent adverse effects in pitch at high angles of attack.

2. CONFIGURATION EVOLUTION

The F-16 design evolution is briefly discussed here to lay the groundwork for evaluation of the impact of strake-effects comparisons from the multitude of configurations tested. A study of the YF-16 aerodynamic features began in 1968. After intensified analysis in 1970-71, detailed designs were finalized in 1972-73. Configuration refinement and growth modifications continued through wind-tunnel testing until the full-scale development aircraft, F-16A and F-16B, were finalized in 1975.

Early design studies set the basic features of two very different design approaches. One was a simple wing-body-empennage design with a single vertical tail (Configuration 785, shown in Figure 1). The other approach was a highly blended wing-body with a wide lifting forebody and twin tails mounted on booms extending aft on either side of the engine exhaust nozzle (early configurations in the 401F series). The best features of the two separate initial models were combined into one model, and the resulting configuration refined through several tunnel entries to produce the final design. Significant intermediate steps included the combination of the Configuration 785 afterbody with the early 401F configuration forebody to obtain Configuration 401F-5, Figure 2, and the addition of afterbody shelves to which the horizontal tails were mated, Configuration 401F-10A, Figure 3. Minor modifications continued leading to the YF-16 prototype lines.

After Configuration 401F-10A it became apparent to the design team that a forebody strake would be part of the final configuration. As a consequence, forebody strake-off configurations were no longer tested; however, variations in the size and shape of strakes on the blended configuration continued.

3. LIFT AND DRAG

The effects of nose strakes on lift and drag are negligible for the size of strakes tested during the F-16 program. However, the addition of forebody strakes significantly increases high-angle-of-attack lift and decreases high-angle-of-attack drag. General observations as to the character and extent of these effects with respect to the strake geometry are presented, and empirical correlations of the strake lift and drag increments with appropriate geometrical parameters are made. These correlations lead to the development of design guides that relate these aerodynamic effects to strake geometry.

Of primary importance is the effect of forebody strake size and shape on lift and drag and the associated interaction of the strake and leading-edge flap. Typical examples of the lift and drag benefits attributed to forebody strakes are shown in Figures 4a and 4b. The data of Figure 4 are for a family of delta planform strakes, shown in Figure 5, tested on the simple wing-body configuration, 785 (Figure 1). Lift and drag benefits are apparent beginning at approximately a 10-degree angle of attack. The most significant geometric parameter appears to be the area: the bigger the strake, the more the lift.

The data of Figure 4 show significant beneficial effects of forebody strakes on the lift and drag of a wing with no leading-edge flap. Deflection of the wing leading-edge flap has a most significant effect on the magnitude of the strake increments. It improves the aerodynamics of the strake-off configurations more than it improves the strake-on configurations. The result is that the effects of forebody strakes on the envelope lift and drag curves representative of aircraft, such as the F-16, that have scheduled leading-edge-flap deflections are significantly reduced from the no-leading-edge-flap case. Envelope curves, shown in Figures 6a and 6b, that result from a minimum-drag leading-edge-flap schedule illustrate this point. This effect is logical when the effect on the wing upper surface flow is considered. Without a leading-edge flap or a strake, the flow over the F-16 wing, which is rather thin ($t/c = .04$), begins to separate at approximately a 10-degree angle-of-attack (Figure 4a). A leading-edge flap delays this separation considerably and thus improves the lift and drag characteristics. A forebody strake accomplishes much the same effect at high angles of attack by passing high-energy vortex flow over the region of the wing that has separated airflow. These effects are not entirely additive, thus the strake benefit in the presence of leading-edge flaps is reduced from the no-flap case.

The comparisons of Figures 6a and 6b are with a zero horizontal-tail deflection, i.e., untrimmed. Trim effects are generally favorable to the forebody strake configurations because of the linearization of the pitching moment curves, as discussed in Section 4.

Initial observations noted above indicate a strong effect of strake area on the incremental lift. It is helpful, therefore, to remove this effect from the data so that effects that are perhaps secondary can be identified. A first attempt at this consisted of referencing the strake incremental lift to the exposed area of the strake, thereby obtaining a pure strake lift coefficient. Results showed that the exposed area was much too small to collapse the data.

At this point it was hypothesized that the strake incremental lift would be a direct function of the total area affected, or energized, by the strake vortex. This is similar in concept to the augmented vortex method employed by Lamar at NASA/Langley, Reference 1. Due to the lack of diagnostic data to determine the area being influenced by the strakes, a geometrical definition of an area considered to be representative was necessary. The definition of such an area is illustrated in Figures 7 and 8. For a conventional strake-wing-body-combination, the definition is simply the exposed strake area plus the wing planform area that falls within the projected strake exposed area, as shown in Figure 7. For a highly blended configuration, which does not have a well-defined strake planform, the

definition was not as straightforward. For these configurations, the blended area between the strake and body was included with the strake exposed area as illustrated in Figure 8. This definition yields a much improved correlation between strakes within a family, as the subsequent comparisons will show.

Three families of strakes were tested for which a definite strake-off baseline exists. Strake geometry is shown in Figures 5, 9, and 10. The lift increments referenced to the strake-wing effective area, as defined in Figures 7 and 8, are shown in Figures 11 through 14. The strake lift increments by family tend to collapse to a single curve for a fixed value of wing leading-edge-flap deflection.

This is an important fact. It says that for a given configuration the overriding factor in determining the strake lift is the area affected by the strake-generated vortex. An exception is the ogee family of data, Figure 13, at angles of attack greater than 18 degrees. Strakes Z16, Z18, and Z17 intersect the wing at increasing butt lines. It is probable that for the larger span strakes (Z17 for example) the effective area needs to be redefined to include less of the inboard part of the wing, as shown in Figure 15. This would tend to further collapse the data of Z16, Z17, and Z18 in Figure 13 at high angles of attack. Strake Z14 is the least effective of those shown in Figure 13, which indicates that it is too narrow to generate as strong a vortex as, say, Z18 (which has the same span).

Average fairings representing the collapsed data of Figures 11 through 14 are shown in Figure 16 for each family. Variations in strake shape are of only secondary importance in the generation of lift, as shown by the 10-degree flap data on Configuration 401F-5 for delta (Z4), ogee (Z14, Z16-Z18), and gothic (Z5) planforms. Also, incremental lift decreases for the more highly blended configuration; Configuration 401F-10A is the most highly blended configuration shown in Figure 16 and has the lowest incremental strake lift. Configurations 785 (simple wing body) and 401F-5 (blended) show approximately the same level of strake lift. This is fortuitous, however, because the strakes of Configuration 785 have a nominal negative 2 degrees of incidence at the leading edge relative to those of Configuration 401F-5. The strakes on the simple wing body would be more effective at high angle of attack if they had the same incidence as those of Configuration 401F-5. The dependence of the lift increments on wing leading-edge-flap deflection is also apparent in Figure 16.

Since forebody strakes are generally of high sweep with sharp leading edges, it is expected that the drag, ΔC_D , due to the strake lift, ΔC_L , would be close to the no-suction value, $\Delta C_L \tan \alpha$. This concept is evaluated in Figure 17 for several strakes with zero leading-edge-flap deflection. Since strakes Z7 through Z10 have leading-edge incidences, i , of nominally 2 degrees, the angle of attack has been appropriately modified. The data are reasonably approximated by an adaptation of the Reference 2 methodology for double delta wings:

$$\Delta C_D = .95 \Delta C_L \tan (\alpha + i) \quad (1)$$

The incremental lift effects of forebody strakes have been shown to be primarily a function of the affected area, as defined in Figures 7 and 8. Thus, given a particular strake, leading-edge flap, and body configuration, the lift increments that can be obtained by modifying the strake (e.g., to the strake area required for a linear pitching moment curve) are easily estimated:

$$\left(\Delta C_{L \text{ STRAKE}} \right)_2 = \left(\Delta C_{L \text{ STRAKE}} \right)_1 \frac{(A_{\text{EFF}})_2}{(A_{\text{EFF}})_1} \quad (2)$$

Furthermore, incremental lift due to adding a strake to a simple wing-body configuration or a blended configuration can be estimated to the first order with the curves of Figure 16 by simply selecting a similar configuration. The incremental drag resulting from the strake lift can also be obtained by use of the relation given in Eq. (1).

4. LONGITUDINAL STABILITY

Proper strake design and location can result in a beneficial influence on directional stability and/or longitudinal stability as well as maneuver lift at high angles of attack. In the longitudinal case, strakes can yield improved linearity of pitching moment characteristics, particularly in the transonic regime where wing stall usually results in a large stable break of the pitching moment curve. Although nose strakes tested during the F-16 program have little effect on the longitudinal characteristics (presumably because of their relatively small exposed area with respect to wing area), forebody strakes affect longitudinal characteristics and, in some cases, introduce nonlinearities.

It is apparent that the major influences on the forward shift of aerodynamic center due to the strake are the strake's exposed area and its location ahead of the wing. The family of ogee-shaped strakes of Figure 18 provide information as to trends due to certain geometrical variations. Strakes Z63 and Z64, which have similar planforms, except that Z64 extends approximately 102 centimeters further forward on the nose, have essentially the same aerodynamic center location at .20 Mach number (Figure 19). Strakes Z65 and Z66, both of which retain the extension forward and the basic shape of Z64 but increase area in the region in front of the wing, yield proportional decreases in pitch stability. These data indicate that either the more powerful vortex produced by the larger area in front of the wing or the effect of the basic wing upwash, or both, tend to make this portion of the strake highly effective in influencing the overall aerodynamic center location in the linear region of lift.

The region above the linear C_L is crucial from a strake design standpoint, primarily because of the effect of the strake on the airplane stall. The addition of a strake of the type of Figure 18 enables the wing-strake combination to continue lifting to angles of attack of 30 to 40 degrees, whereupon the combination stalls. The pitching moment curve, linear up to stall in most cases, tends to break erratically stable or unstable after stall, depending on the configuration (see Figure 19). As in the lower-angle-of-attack region, strake area has a major influence, the larger strakes (Z66) being more susceptible to an unstable break. Stall characteristics are also degraded by a forward extension of the strake and forward extension of the forebody (fuselage stretch). Similarly, the control effectiveness of the horizontal tail beyond stall is degraded with increasing strake size, strake forward extension, and forebody lengthening.

Transonically, the aerodynamic center shift has been correlated with pertinent strake parameters. On the basis of the results of the lift increment analysis described in Section 3, the strake is assumed to be a low-aspect-ratio-wing, spanning from the body/strake juncture to the wing-leading-edge/strake intersection and inclusive of the portion of the wing directly aft of the strake (the shaded areas in Figures 7 and 8). The strake lift curve slope, $C_{L\alpha_s}$, and the distance from the aerodynamic center of the constructed strake area to the aerodynamic center of the basic wing alone, l_s/c , are predicted by the methods of References 3 and 4, respectively. The change in the aerodynamic center in the linear C_L region due to the strake (ΔAC_1) is plotted as a function of the parameter $l_s A_{EFF} C_{L\alpha_s} / \bar{c} S_{REF}$ for the various strake families in Figure 20. For all of the strakes investigated, regardless of shape, flap deflection, or fuselage configuration (785 and 401F-5), a linear relationship of aerodynamic center with $l_s A_{EFF} C_{L\alpha_s} / \bar{c} S_{REF}$ is essentially obtained. Only strake Z17 falls considerably off the correlating line. This is believed to be a result of the affected-area definition for large span strakes, as discussed in Section 3. A similar linear relationship is shown in Figure 21 for the strakes tested at Mach 1.2.

The relationship of aerodynamic center with $l_s A_{EFF} C_{L\alpha_s} / \bar{c} S_{REF}$ indicates that the stability change in the linear lift region due to the addition of the forebody strake is a function of the lift produced by the strake and its influenced area on the wing. This relationship shows promise for the development of a semi-empirical prediction method for strakes similar to the Paniszczyn aerodynamic-center prediction method for cranked wings (Reference 2). At this time, estimation of the strake effect on aerodynamic center in the linear lift region can be estimated by use of the relationships established in Figures 20 and 21.

$$\Delta AC_1 = 0.483 \ l_s A_{EFF} C_{L\alpha_s} / \bar{c} S_{REF} \text{ at } 0.80 \text{ Mach number} \quad (3)$$

$$\Delta AC_1 = 0.296 \ l_s A_{EFF} C_{L\alpha_s} / \bar{c} S_{REF} \text{ at } 1.20 \text{ Mach number} \quad (4)$$

The change in aerodynamic center due to strakes in the nonlinear lift region beyond wing stall (ΔAC_2) is plotted as a function of the parameter $l_s A_{EFF} / \bar{c} S_{REF}$ in Figure 22. The lift-curve slope term is omitted because of the characteristic nonlinear lift variation of low-aspect-ratio wings (constructed strake "wing") at high angles of attack. All strake configurations exhibit essentially the same linear variation of aerodynamic center with the parameter $l_s A_{EFF} / \bar{c} S_{REF}$ for given leading-edge-flap deflections. Deflecting the leading-edge flap in the nonlinear lift region reduces the shift due to the strake (as expected, based on the reduced lift, Figure 16). For strake Z4 and a flap deflection of 25 degrees, there is a noticeable change in stability over the strake-off configuration, although for this flap deflection the increment in lift due to the strake is small. Thus, strakes can provide beneficial linearization of the pitching moment even when the flap effects reduce the increment in lift due to the strakes.

A translation between Configurations 785 and 401F-5 is shown in Figure 22. This is due to the fuselage blending of 401F-5, which results in a further forward strake-off aerodynamic center location and a smaller overall shift in aerodynamic center due to the strake.

Since all configuration leading-edge-flap combinations have the same slope for ΔAC_2 versus L_{sEFF}/CS_{REF} the effects of variations in strake size can easily be estimated for a particular configuration. Thus, Figure 22 in conjunction with Figure 20, can be used to size a forebody strake to provide a linear pitching moment curve at .80 Mach number.

5. LATERAL/DIRECTIONAL STABILITY

Maintaining directional stability to maximum usable lift is of major importance in the design of high-performance maneuvering aircraft. Generally progressive deterioration in static directional stability begins at moderate-to-high angles of attack for most conventional configurations and, consequently, limits the maximum usable lift. Strakes, both nose and forebody, have proven effective in extending the usable lift range.

The nature of the strake's effectiveness, its vortex generation, and effects on the wing and forebody is highly dependent on the general configuration of the aircraft. Isolation and correlation of these effects (particularly in regard to lateral/directional stability characteristics) are difficult considering that in the F-16 program most families of strakes were tested on different forebody configurations. However, there are sufficient variations within the families of strakes tested on given forebodies to allow several comments to be made concerning the relative importance of several strake geometric parameters.

Especially at low speed and high- and very high-angle-of-attack ranges, nose strakes have a pronounced effect on lateral/directional stability characteristics. Improvement in lateral/directional stability is influenced by the size (length and width) of the nose strake. All nose strakes were tested on configurations that have an integrated forebody strake. In all cases, the improvement in lateral/directional stability due to the nose strake over the baseline forebody strake is significant. Typical results are displayed in Figure 23 for representative nose strake Z124 at .20 Mach number. The strake width and extension aft are the most significant design parameters. A typical example of the effect of nose-strake extension is shown in Figure 24. The wider nose strakes also result in better lateral/directional characteristics (Z112 vs Z114 in Figure 25). Strake leading-edge shape is of little consequence; however, truncation of the strake (e.g., Z112 and Z114) improves stability, especially laterally, over the same strakes faired back into the fuselage (Z110 and Z113 in Figure 25).

The significant difference in effectiveness between the nose and forebody strakes emphasizes the importance of the nose flow characteristics on lateral/directional stability. Without nose strakes, the shed vortices from the forebody emanate from variable locations along the nose depending on the angle of attack, sideslip, configuration, etc. With nose strakes applied, especially the truncated nose strakes, the location of vortex initiation is fixed, and the vortex is directed along the fuselage in a symmetrical manner resulting in improved lateral/directional behavior. In the case of the forebody strakes, their effects on directional stability are not as significant as the nose strakes since most are located behind the actual initiation of forebody vortices, plus the probability that their vortices are affected by the flow field surrounding the wing.

Examination of the forebody-strake transonic data (mostly .80 Mach number) supports several general conclusions. Although the impact of forebody strakes on lateral/directional stability is significantly less than that of nose strakes, proper design can result in stability improvements. Adjustment of the forebody-strake shape has definite effects on the performance of the strake, both with and without leading-edge-flap deflection. The most obvious area of influence is the extension of the strake forward on the nose and the width of the strake at this point.

This conclusion is supported by the relative stability within the family of strakes shown in Figure 10. The forebody strake that extends all the way to the nose (Z25) shows the greatest improvement over the strake-off case (Figure 26). The least effective strake (Z27) has most of its area aft on the nose. It does, however, produce a relatively small improvement in stability. This is the result of the formation of a vortex along the strake. This strake vortex, when sufficiently strong, provides a stabilizing influence on the wing flow field and in the afterbody region. The strength of this vortex is dependent on strake shape and the interaction with the wing flow field. Improvements associated with leading-edge deflection suggest the importance of the wing flow field on stability. With no flap deflection, the separated flow over the wing interferes with the vortex effects on the fuselage afterbody. As flap deflection increases, the improved flow yields a reduction in interference and results in an improvement in lateral/directional stability.

6. CONCLUDING REMARKS

Nose strakes offer significantly improved lateral/directional performance with a minimum increase in wetted area and little effect on longitudinal characteristics. Forebody strakes provide beneficial linearization of the pitching moment curve and improved maneuver lift. Although application of the strakes is highly configuration-dependent and optimization undoubtedly requires tunnel testing, initial design guidelines have been developed and several recommendations can be forwarded.

Design guidelines have been developed that allow forebody strakes to be sized to obtain a linear pitching moment curve and the resulting lift and drag increments to be estimated. The incremental lift effects have been shown to be primarily a function of the area affected by the strake-induced vortex. Forebody-strake-planform shape is of secondary importance to lift generation but has a significant effect on lateral/directional characteristics.

The nose strake leading-edge shape is of minor importance for lateral/directional stability. The major positive influences are found to be the width and length of the strake and the truncation of the surface. The nose strakes tested have little effect on longitudinal stability; however, increasing surface widths or lengths, and consequently area, may lead to possible adverse effects in the subsonic high-angle-of-attack region.

Forebody strakes have (relative to nose strakes) limited effectiveness laterally-directionally unless the strake is extended quite far forward on the nose. The extension forward on the nose, however, can become undesirable from the point of view of longitudinal stability at high subsonic angles of attack.

A need has been identified for further well-structured testing designed to isolate the effects of strake geometry on, in particular, the lateral/directional-stability and low-speed-stall characteristics. It is recommended that systematic families of forebody strakes be designed for a simple wing-body configuration and these definitive tests conducted. These data will also serve to verify and/or expand the initial design guidelines that have been developed for longitudinal effects.

REFERENCES

1. Lamar, J.E., "Some Recent Applications of the Suction Analogy to Vortex-Lift Estimates," NASA TM X-72785, 1976.
2. Benape, David B., Kouri, Bobby G., and Webb, J. Bert, et al, "Aerodynamic Characteristics of Non-Straight-Taper Wings," AFFDL-TR-66-73, October 1966.
3. Stancil, R.T., "Theoretical Lift and Drag Due to Lift of Trapezoidal Wings at Subsonic and Supersonic Speeds," General Dynamics' Fort Worth Division Report MR-A-1044, 18 March 1955.
4. "USAF Stability and Control DATCOM", Air Force Flight Dynamics Laboratory, October 1960 (Revised August 1968).

ACKNOWLEDGEMENTS

The authors wish to express their appreciation to J.N. Ralston for his contributions to the stability sections of this paper and to I.C. Bhatelley for the development of the automated data plotting routines used in this study.

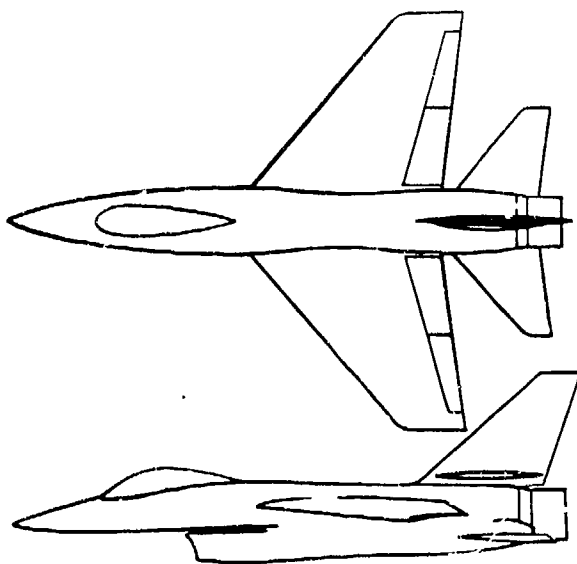


Figure 1 Sketch of Configuration 785

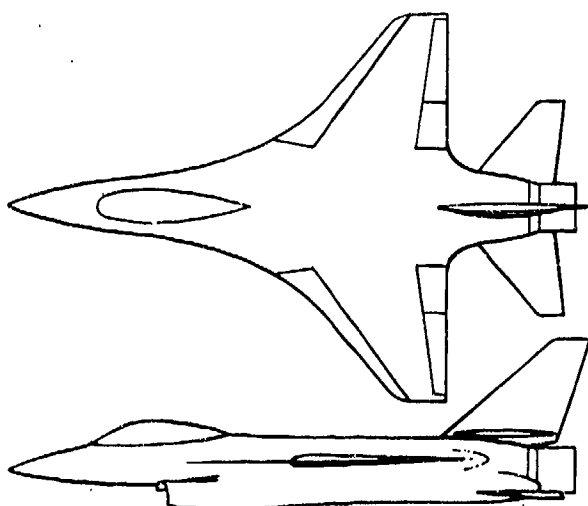


Figure 2 Sketch of Configuration 401F-5

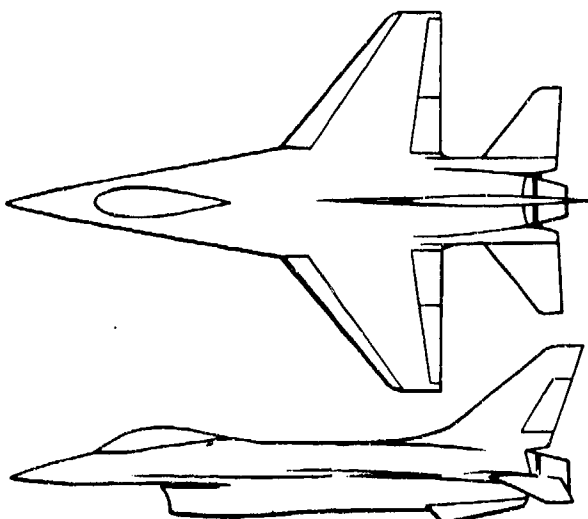


Figure 3 Sketch of Configuration 401F-18A

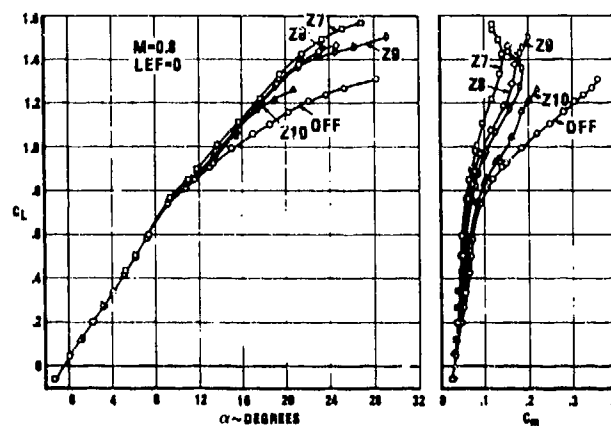


Figure 4a Lift Effects of a Family of Delta Planform Forebody Strakes on Configuration 785

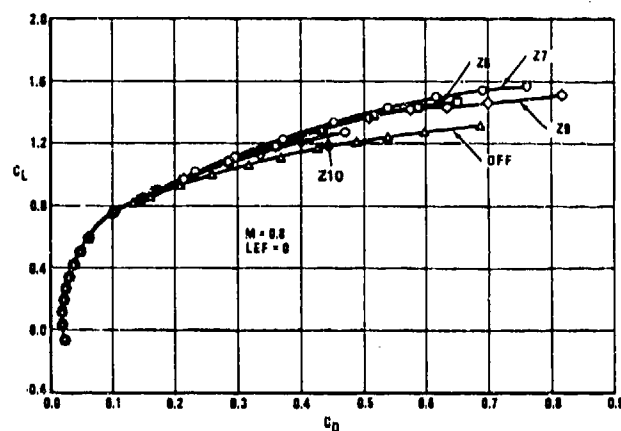


Figure 4b Drag Effects of a Family of Delta Planform Forebody Strakes on Configuration 785

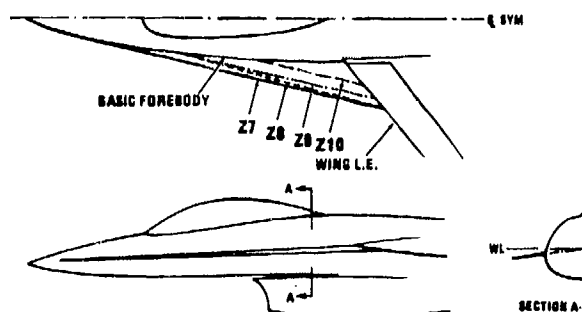


Figure 5 Delta Planform Strakes on Configuration 785

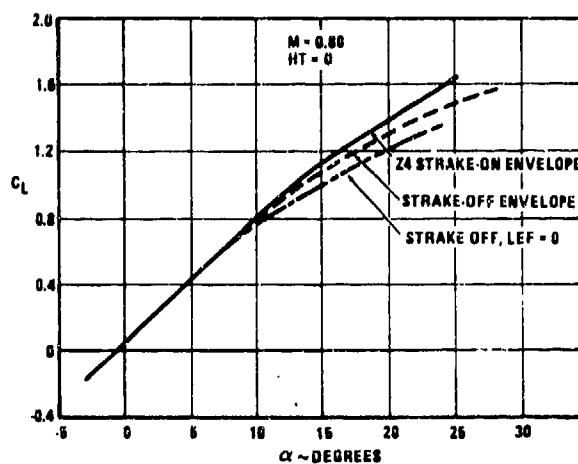


Figure 6a Effect of Forebody Strake on the Envelope Lift Curve

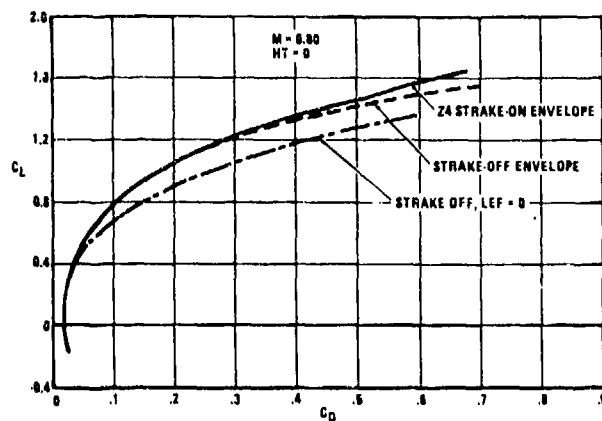


Figure 6b Effect of a Forebody Strake on the Envelope Drag Polar

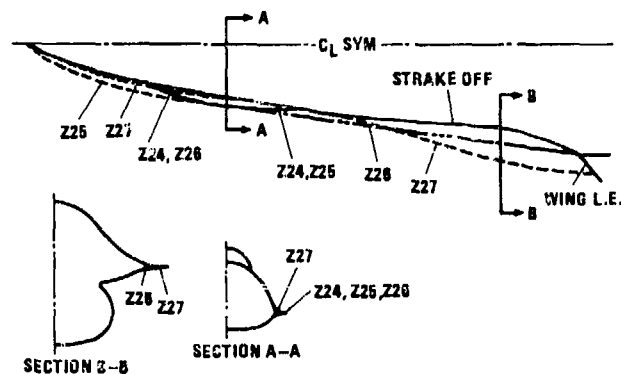


Figure 10 Forebody Strakes on Configuration 401F-10A

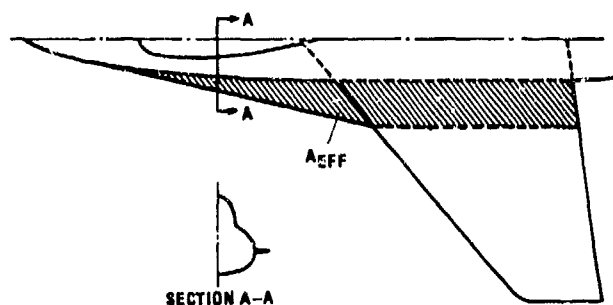


Figure 7 Definition of Effective Strake Area for a Simple Wing Body Configuration

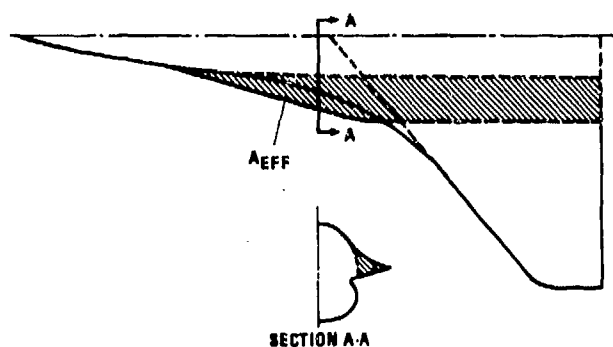


Figure 8 Definition of Effective Strake Area for a Blended Configuration

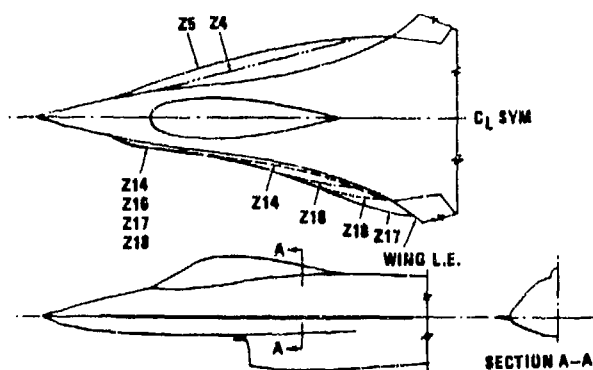


Figure 9 Forebody Strakes on Configuration 401F-5

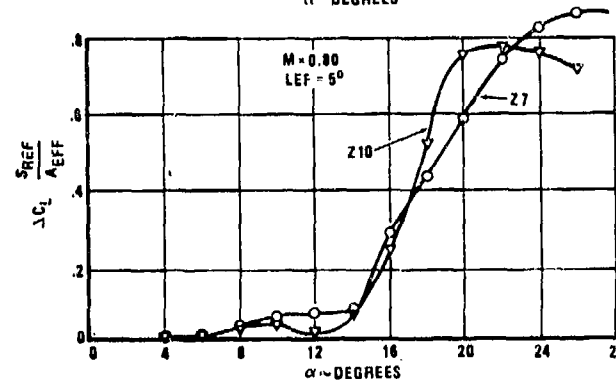
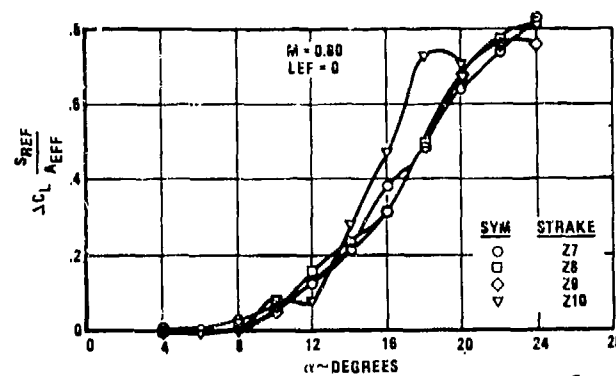


Figure 11 Incremental Strake Lift for a Family of Delta Planform Strakes on Configuration 785

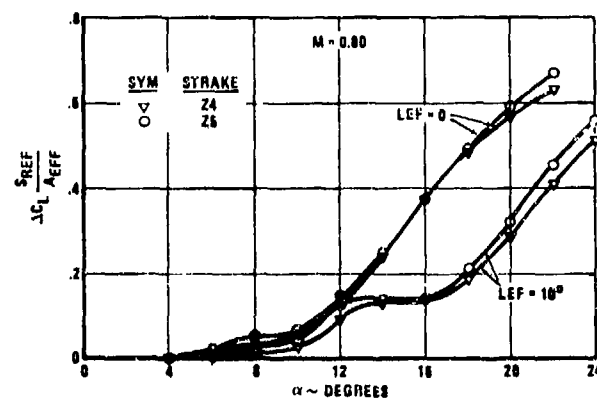


Figure 12 Incremental Strake Lift for Delta and Gothic Planform Strakes on Configuration 401F-5

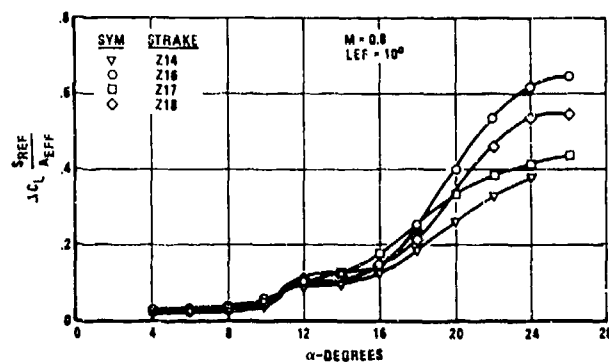


Figure 13 Incremental Stroke Lift for a Family of Ogee Planform Strakes on Configuration 401F-5

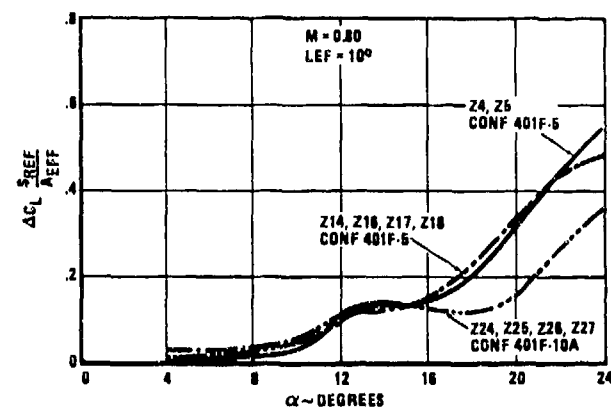
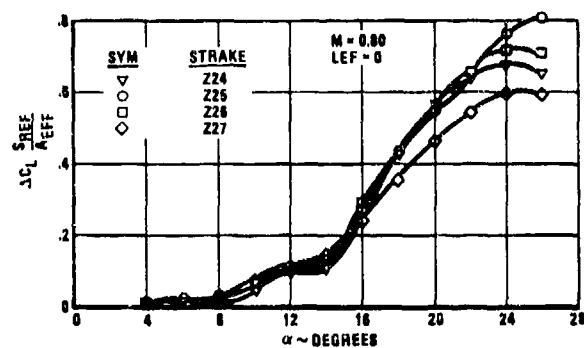
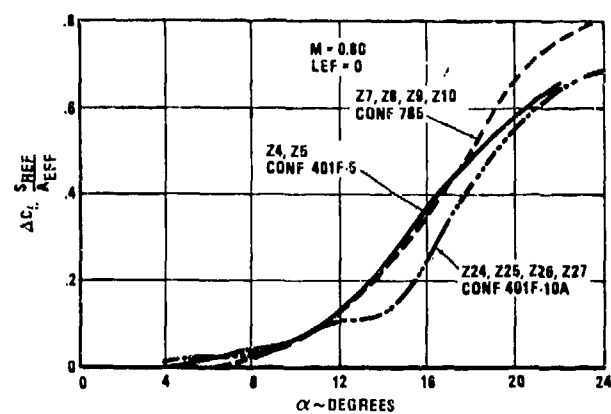


Figure 16 Effects of Configuration and Strake Geometry on Incremental Lift

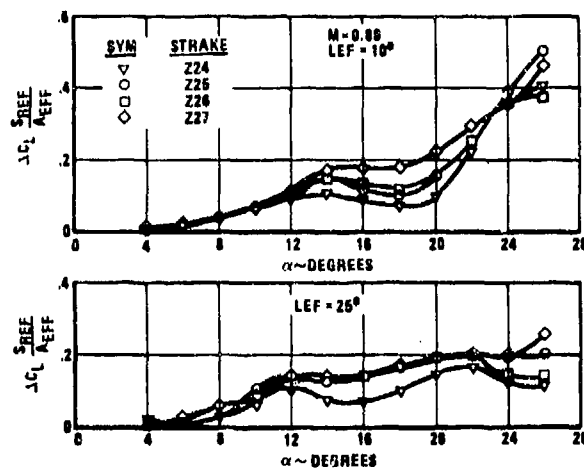


Figure 14 Incremental Stroke Lift for a Family of Ogee Planform Strakes on Configuration 401F-10A

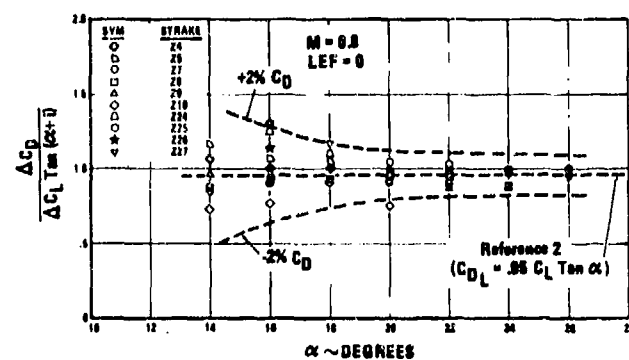


Figure 17 Incremental Drag Correlation for Forebody Strakes

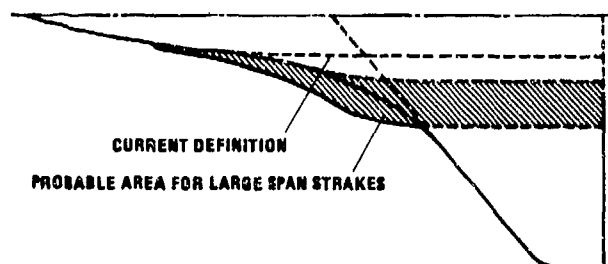


Figure 15 Definition of Effective Strake Area for Large Span Strakes

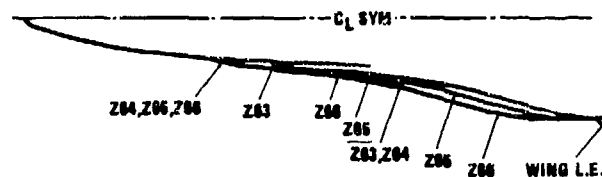


Figure 18 Ogee Planform Strakes on a Stretched YF-16

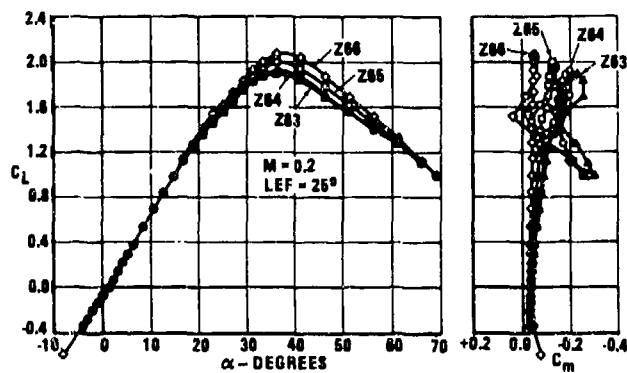


Figure 19 Pitch Effects of a Family of Ogee Planform Forebody Strakes on a Stretched YF-16

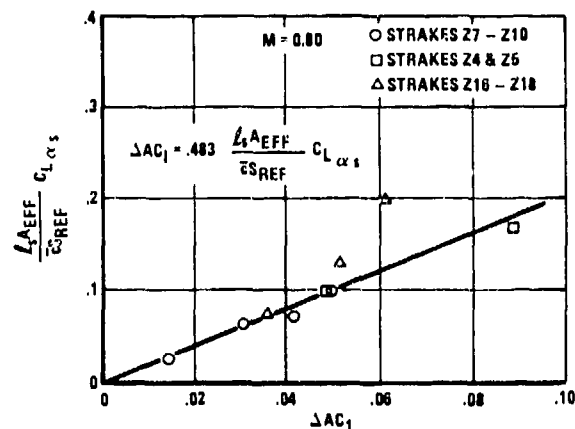


Figure 20 Linear Region Stability Shift Due to Forebody Strakes, M=0.80

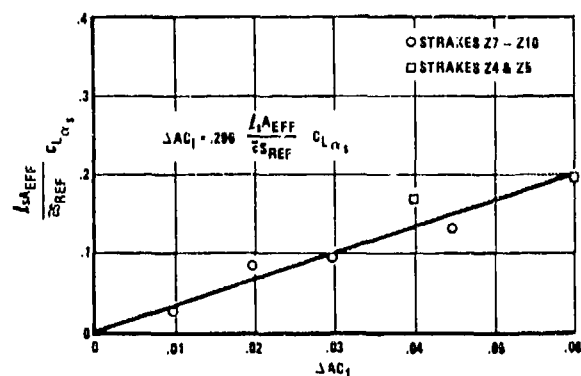


Figure 21 Linear Region Stability Shift Due to Forebody Strakes, M=1.20

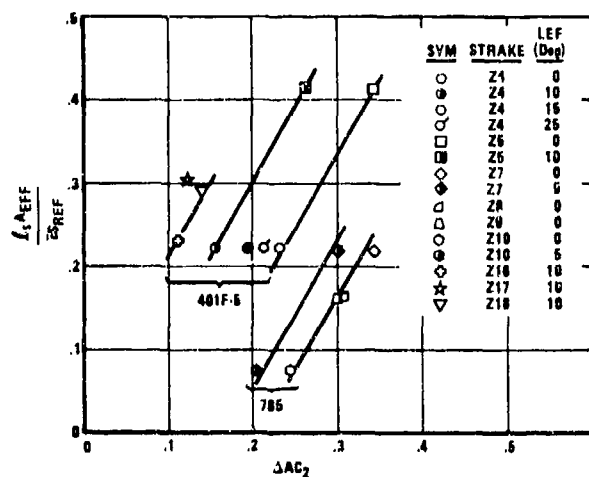


Figure 22 High Angle of Attack Stability Shift Due to Forebody Strakes, M=0.80

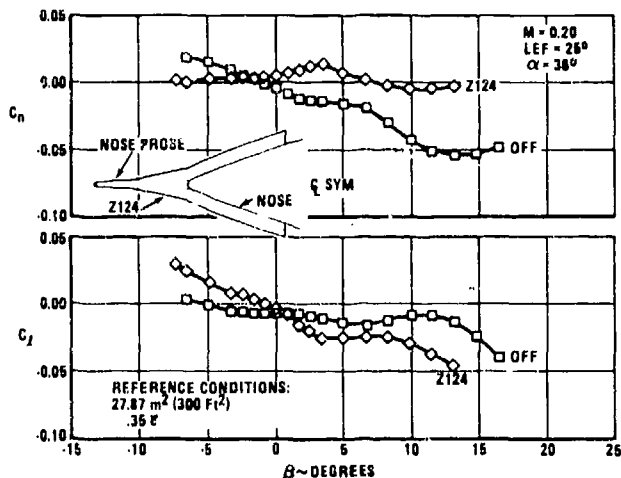


Figure 23 Sideslip Characteristics of Nose Strake Z124 on the F-16

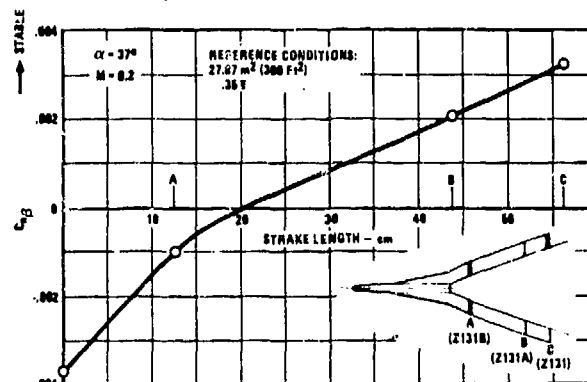


Figure 24 Effect of Nose Strake Length on Directional Stability

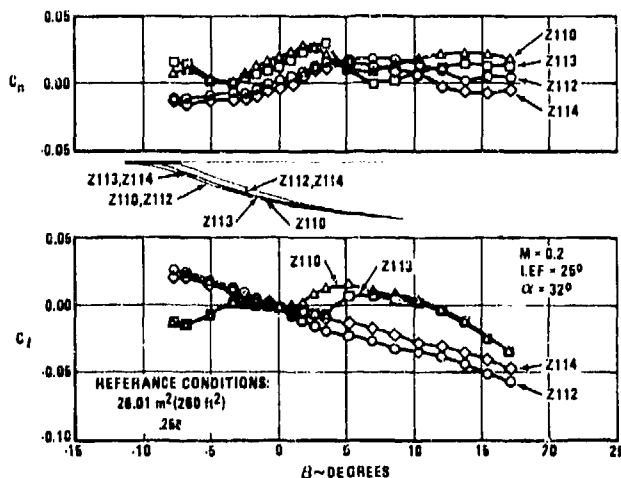


Figure 25 Effect of Nose Strake Shape on the F-16 Sideslip Characteristics

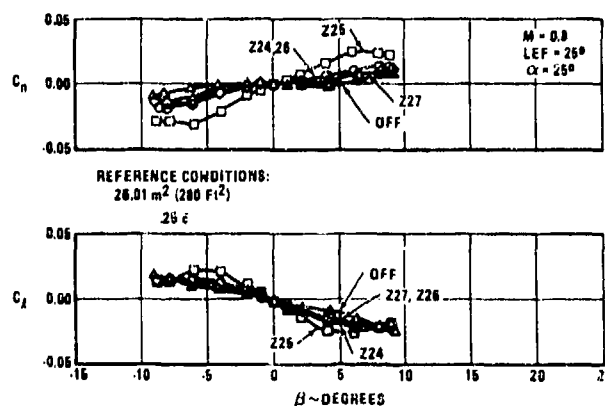


Figure 26 Sideslip Characteristics of a Family of Ogee Planform Forebody Strakes on Configuration 401F-10A

FOREBODY/WING VORTEX INTERACTIONS AND THEIR INFLUENCE ON DEPARTURE AND SPIN RESISTANCE

by

A. M. Skow, Manager, Aerodynamics Research Department
Northrop Corporation, Aircraft Division
3901 West Broadway, Hawthorne, California 90250

A. Titiriga, Jr., Manager, F-S Aerosciences and Propulsion Analysis Department
Northrop Corporation, Aircraft Division
3901 West Broadway, Hawthorne, California 90250

W. A. Moore, Engineer, Aerodynamics Research Department
Northrop Corporation, Aircraft Division
3901 West Broadway, Hawthorne, California 90250

CONTENTS

I. Introduction	1	IV. Forebody/Wing Vortex Interactions	17
II. Forebody Effects	3	V. Conclusion	26
III. Wing/LEX Vortex Characteristics	21	References	26

SUMMARY

In recent years it has been shown that vortical flows emanating from the forebody and from hybrid wings can have a strong influence on the high angle-of-attack handling qualities and the departure and spin resistance of fighter aircraft. Depending on the strengths, orientation, and breakdown characteristics of these vortices, an aircraft may be departure prone or departure resistant.

Northrop has conducted in-depth studies to determine the effects of these shed vortices and to isolate parameters which strongly influence them. Arising from these studies, methodologies were developed which can be used as general guidelines in the design of both aircraft forebody shapes and hybrid-wing planform shapes such that the interactions between these vortex systems will enhance aircraft stability.

I. INTRODUCTION

Aerodynamic effects associated with aircraft forebodies can have a dominating effect on stability at post-stall angles of attack. In this angle-of-attack region, the vertical tail effectiveness is usually severely degraded as the tail is immersed in the low energy wing wake. The vortices which emanate from the forebody can be very strong and depending on their orientation, can produce large yawing moments at zero sideslip. These vortices can also determine the degree of directional stability which the configuration will exhibit. Several geometric parameters influence the formation of the forebody vortices. These include nose fineness ratio, bluntness, and cross-sectional shape.

Vortices generated by a hybrid-wing planform contribute significantly to the lift capability of the aircraft at high angles of attack. These vortices also contribute strongly to the stability characteristics, especially in the vicinity of the stall angle of attack. When the aircraft is sideslipped, these vortices can burst asymmetrically over the main wing panels, degrading the lateral-directional stability. Studies have been conducted at Northrop to determine methods whereby the lift increment generated by these vortices could be maintained while minimizing the adverse lateral-directional effect. Results from the studies show the location of the vortex burst points over the wing panels are a strong function of the LEX (wing leading-edge extension) planform shape, wing leading-edge sweep angle, and deflection of the inboard trailing-edge flap. Delaying the vortex breakdown to higher angles of attack is found to delay wing stall and improve the adverse effect on lateral-directional stability.

For some configurations, there can be a significant interaction between the forebody and wing vortices. These interactions appear to be highly configuration dependent. However, for configurations which have hybrid wings with leading-edge extensions in close proximity to the forebody, there is a higher degree of vortex interaction. Due to the high degree of configuration dependence, a uniform methodology can not be developed from the existing data base which will predict the effect of these vortex interactions. Designers must, however, be aware of the potential magnitude of the interactions and their effect on aircraft stability.

This paper will discuss the methodologies developed to predict forebody and wing/LEX vortex effects on aircraft stability. Examples will be presented of configurations that exhibit strong forebody and wing/LEX vortex interactions and also configurations which have minimal interactions. The paper will conclude by presenting details of the development of a new forebody shape and LEX planform for the F-5 configuration which were designed using the methodologies presented.

II. FOREBODY EFFECTS

AERODYNAMIC ASYMMETRIES

A significant interest has developed in recent years in the study of aerodynamic asymmetries at high angles of attack. Historically the phenomenon has been primarily concentrated in missile aerodynamics, due to the characteristically long and slender bodies of most missiles. Reference 1 presents a good survey and bibliography of the missile problem. Recent trends, however, in fighter aircraft design have led to aircraft fuselages which have forebody fineness ratios in the same range as some missiles, thus forcing aircraft designers to deal with the problem of asymmetries. Figure 1 illustrates the forebody lengths of three Northrop aircraft nondimensionalized to the mean aerodynamic chord of the wing in each case.

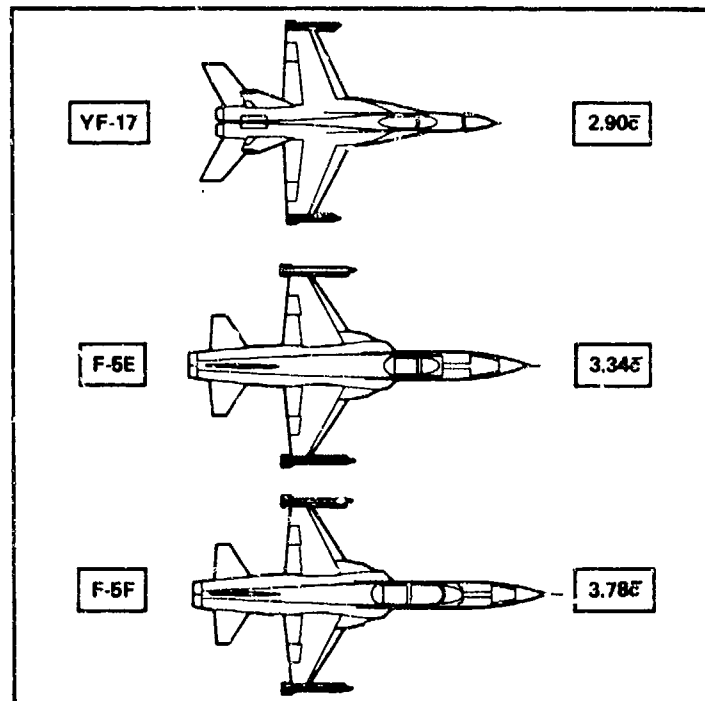


FIGURE 1. TYPICAL FIGHTER FOREBODY LENGTHS

It has been convincingly shown in small-scale wind tunnel and water tunnel experiments that the aerodynamic phenomenon which is responsible for these asymmetric forces and moments is the growth of a strong vortex system from the aircraft forebody. For sufficiently slender forebodies, this vortex system becomes asymmetric at high angles of attack and can exert a significant effect on the other components of the airframe. Figure 2 illustrates these vortices. Figure 3 shows dye patterns emanating from an aircraft forebody at a high angle of attack taken during a water tunnel test. An asymmetric vortex pattern is clearly shown.

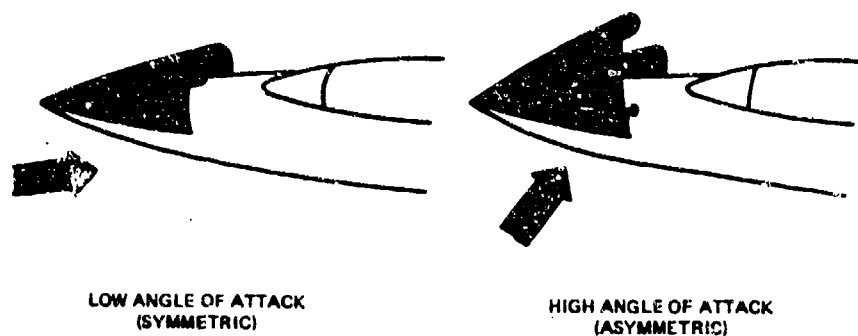


FIGURE 2. FOREBODY VORTEX PATTERNS

An understanding of details of the vortex systems generated by forebodies at high angles-of-attack can be developed from results of tests made in the water tunnel. Numerous water tunnel investigations on several forebodies have shown the existence of similar vortex patterns which characteristically include a pair of apex vortices emanating from the tip of the nose, plus a secondary vortex pair arising from the separated flow along the fuselage side. A typical example of a forebody vortex system is shown in Figure 4.

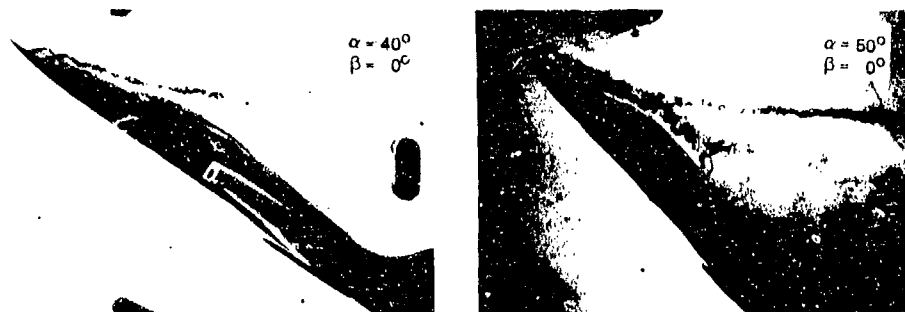


FIGURE 3. ASYMMETRIC FOREBODY VORTEX PATTERNS AT HIGH ANGLES OF ATTACK

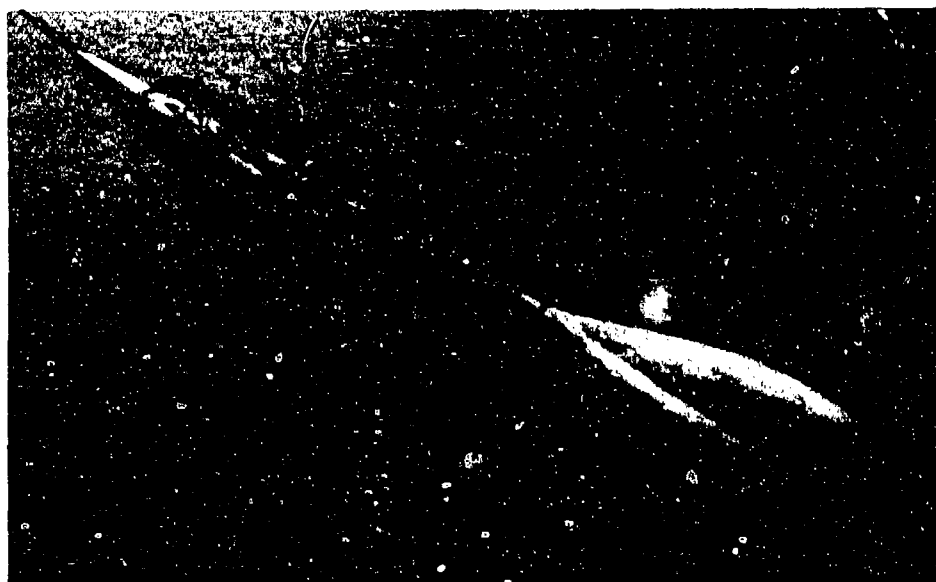


FIGURE 4. FOREBODY VORTEX SYSTEM

The vortex arrangement on the forebody can be represented by a simplified cross-sectional view of the nose, as shown in Figure 5. This figure illustrates the effects of both a symmetric and an asymmetric vortex pattern around the nose at zero angle of sideslip. The asymmetric vortex pattern generates a resultant forebody force which has a large component in the side-force direction. This side force, acting on the forebody and coupled with a long moment arm to the aircraft center of gravity, can produce large yawing moments at zero sideslip at high angles of attack.

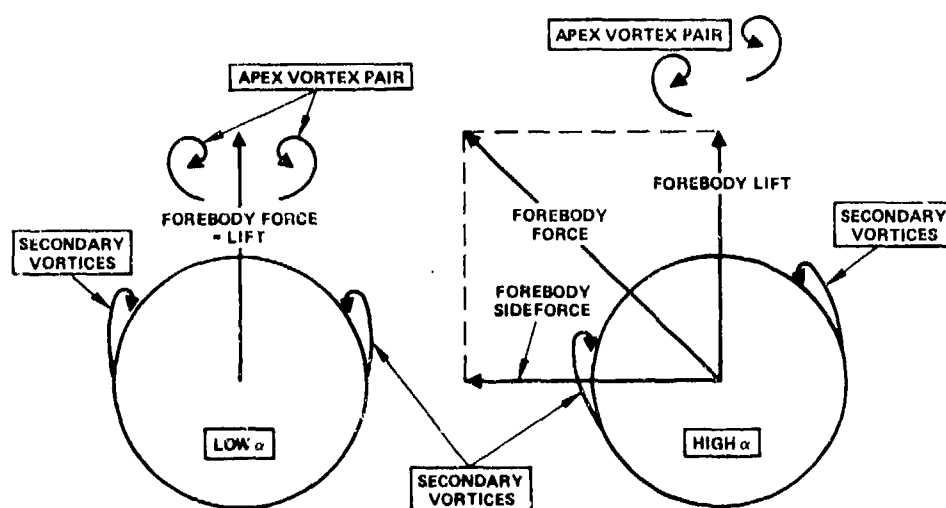


FIGURE 5. FOREBODY VORTEX PATTERNS

Until recently, it had not been convincingly shown that asymmetric vortex shedding and the resulting asymmetric forces which have been measured on wind tunnel models and observed in water tunnels actually exist on the full scale aircraft at flight Reynolds numbers. Figure 6 shows a comparison of yawing moment coefficient at zero

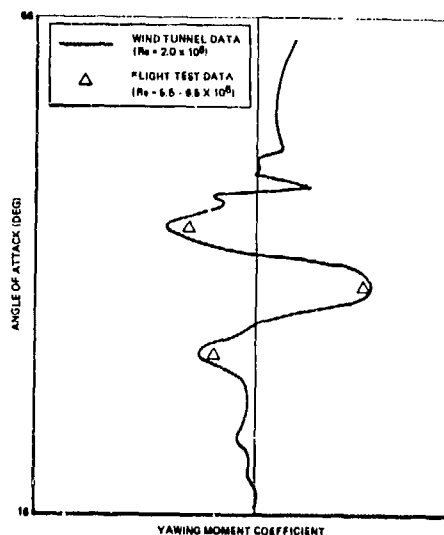


FIGURE 6. WIND TUNNEL/FLIGHT TEST CORRELATION

sideslip for a small-scale wind tunnel model and full-scale aircraft. The wind tunnel data were gathered at Reynolds numbers of 2.0×10^6 and the flight-test data were extracted at Reynolds numbers of between 5.5 and 6.5×10^6 . The asymmetric vortex shedding can greatly impact the departure and spin resistance of fighter aircraft. Figure 7 presents the effect of the aerodynamic asymmetries on the analytical spin-entry boundary. When the asymmetries are ignored, the calculated boundary is symmetric and indicates a false level of spin resistance. When the asymmetries are included, a strong bias is evidenced. Flight test results of two spins are shown, indicating an agreement with the asymmetric spin boundary, thus further substantiating the existence of the aerodynamic asymmetries.

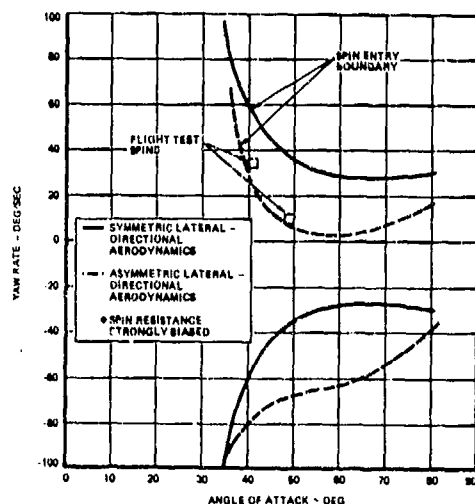


FIGURE 7. EFFECT OF AERODYNAMIC ASYMMETRIES

Any analysis, therefore, conducted on the departure and spin characteristics of a fighter aircraft must consider aerodynamic asymmetries and the forebody contribution to stability.

EFFECT OF FOREBODY FINENESS RATIO

One of the primary geometric parameters which influences forebody aerodynamics is the forebody fineness ratio (examples shown in Figure 1).

The definition of forebody length used in the calculation of fineness ratio depends on the aircraft geometry. For aircraft with fairly long forebodies, a reference line is drawn four body diameters forward of the wing trailing-edge. The forebody length is defined as the length forward of that reference line. This convention is taken from Reference 2 and is illustrated in Figure 8(a). For aircraft with large wing-body strakes (LEX's) or large inlets which extend fairly far forward, a modified definition for forebody length is used as shown in Figure 8(b).

Figure 9 shows the variation in absolute magnitude of yawing moment coefficient at zero sideslip developed from the analysis of data on several aircraft whose fineness ratios varied from approximately 3.5 to 6.0. Also shown is the variation of onset angle of attack with fineness ratio taken from Reference 3. As can be seen, increasing the forebody fineness ratio tends to produce large asymmetric yawing moments and lower the onset angle-of-attack at which the asymmetries occur.

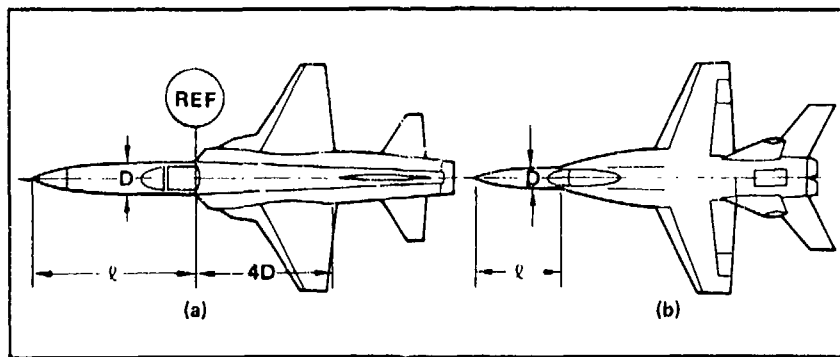


FIGURE 8. DEFINITION OF FINENESS RATIO

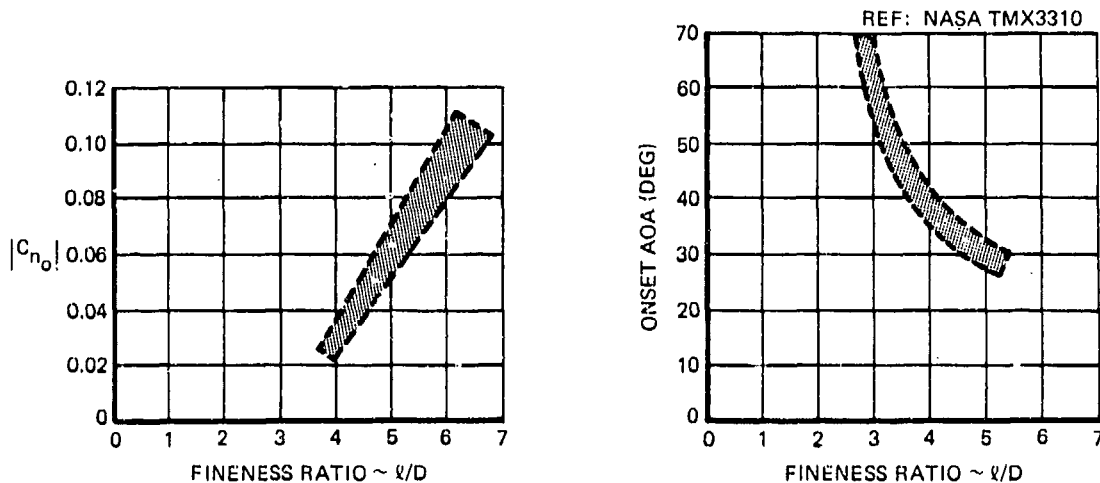


FIGURE 9. EFFECT OF FINENESS RATIO

NOSE EFFECT ON STABILITY

In addition to the effect of the forebody vortices on aerodynamic asymmetries, properly shaped aircraft forebodies can provide a favorable contribution to aircraft stability at high angles of attack. Researchers at NASA investigated the F-5A nose shape and found it to be the major contributor to the directional stability of the aircraft above the stall angle of attack as shown in Figure 10. The primary cause of this stabilizing effect was found to be the unique orientation which the forebody vortex system assumes when the aircraft is sideslipped.

EFFECT OF NOSE CROSS-SECTIONAL SHAPE

Nose cross-sectional shape has a dominant effect on directional stability at high angles-of-attack. Figure 11, taken from Reference 4, shows the effect of nose cross-sectional shape on directional stability for vertical tail-off configurations of the F-5E/F, P530, YF-17, and P630 for an angle-of-attack range up to 60° . These configurations represent a full range of nose cross-sectional shapes including an ellipse with the major axis vertical to an ellipse with the major axis horizontal. As expected, all configurations are unstable at low angles-of-attack, and remain unstable until approximately 25° angle of attack. Above 25° angle of attack, cross-sectional effects are evident; the horizontal ellipse cross-sectional shape becomes stable while the vertical ellipse shape becomes even more unstable.

To further illustrate the effects of nose cross-section on directional stability in the post-stall angle-of-attack range, Figure 12, extracted from Reference 4, is presented. The directional stability is shown as a function of nose ellipticity ratio at 35° angle-of-attack. Although some scatter is present, a reasonable correlation is shown which conforms to the previous conclusion that a flat elliptic nose section is required to produce positive directional stability at high angles-of-attack.

The directional stability obtained at high angles-of-attack with the flat elliptic nose shapes is influenced by Mach number, and eventually is eliminated when the Mach number exceeds a certain value. This effect is illustrated in Figure 13 which presents directional stability data for both low and transonic Mach number cases.

Any geometric changes to the aircraft forebody which affect lateral-directional stability would also be expected to affect the aircraft longitudinal stability, particularly since the forces on the forebody act at a considerable distance from the moment center. Figure 14 shows pitching moment due to sideslip for two different types of elliptic nose

shapes. Data indicate that nose shapes which have a stabilizing directional stability force component also have an unstable, nose up pitching moment contribution ($+C_{m|\beta|}$).

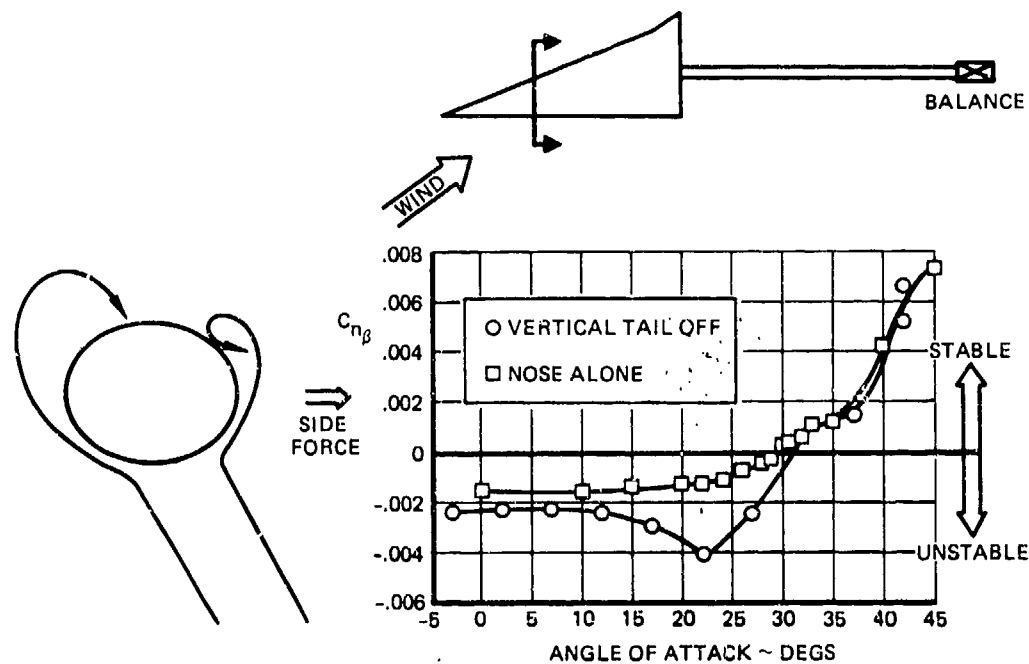


FIGURE 10. NOSE EFFECT ON STABILITY

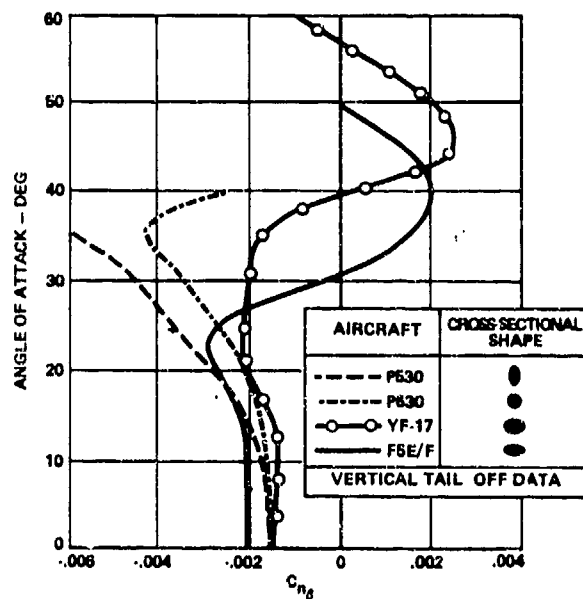


FIGURE 11. EFFECT OF NOSE SHAPE ON STABILITY

The converse is true for noses that have a destabilizing directional force component. To further substantiate this trend, Figure 15 presents data for an F-5F at 40° angle-of-attack. As shown, the stabilizing nose effect in yaw is accompanied by a nose up pitching moment.

EFFECT OF STRAKES

The most common means of ensuring that the forebody vortices will shed symmetrically at zero sideslip has been the use of thin strakes placed on the maximum half-breadth of the forebody. Unfortunately, however, in many cases these nose strakes prevent the formation of the unique forebody vortex orientation at nonzero sideslip, which is responsible for the positive directional stability contribution of the forebody at high angles-of-attack. This is illustrated on the F-5E/F configurations in Figures 16 and 17.

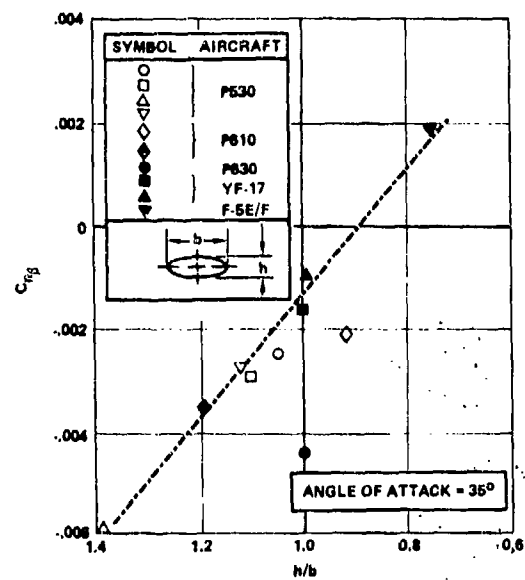


FIGURE 12. EFFECT OF NOSE ELLIPTICITY ON $C_{n\beta}$

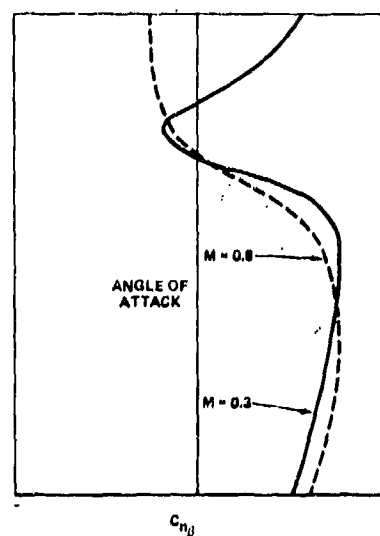


FIGURE 13. TRENDS IN DIRECTIONAL STABILITY

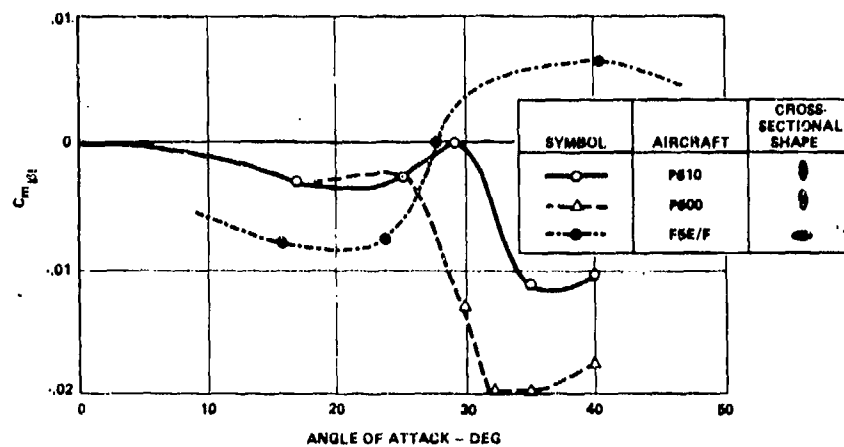


FIGURE 14. PITCHING MOMENT DUE TO SIDESLIP

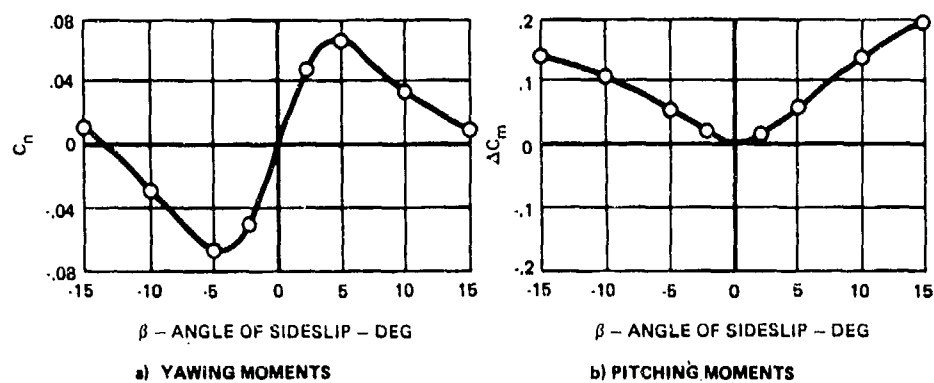


FIGURE 15. F-5F NOSE EFFECTS AT 40° ANGLE OF ATTACK

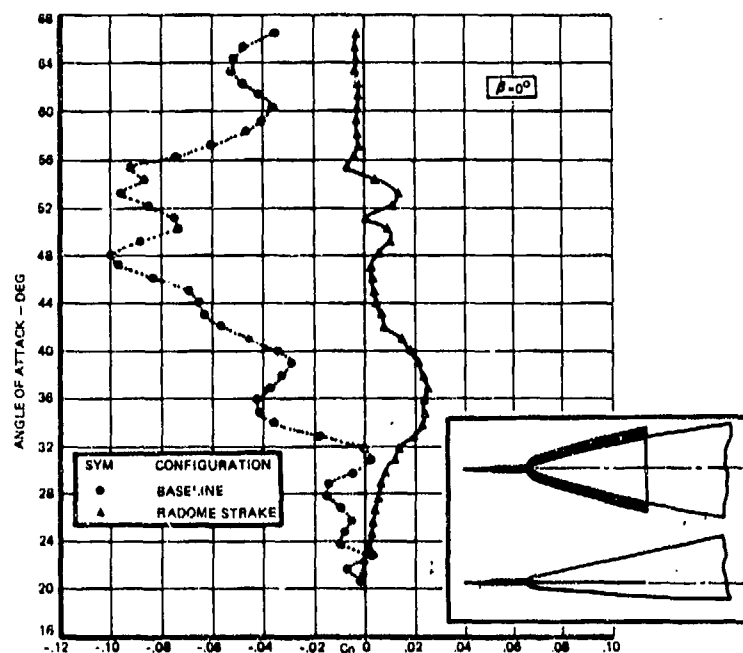


FIGURE 16. STRAKE EFFECT ON ASYMMETRIES AT ZERO SIDESLIP

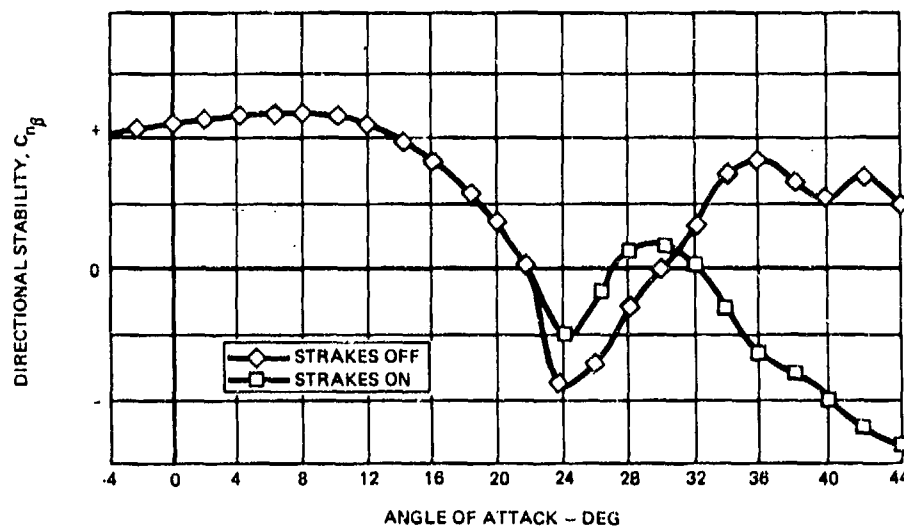


FIGURE 17. STRAKE EFFECT AT NONZERO SIDESLIP

An example of an aircraft where directional stability was improved by the addition of nose strakes is the YF-17. The addition of a flight-test nose boom destabilized the aircraft in yaw. Nose strakes were added to the configuration, seen in Figure 18, and directional stability was improved as shown in Figure 19.

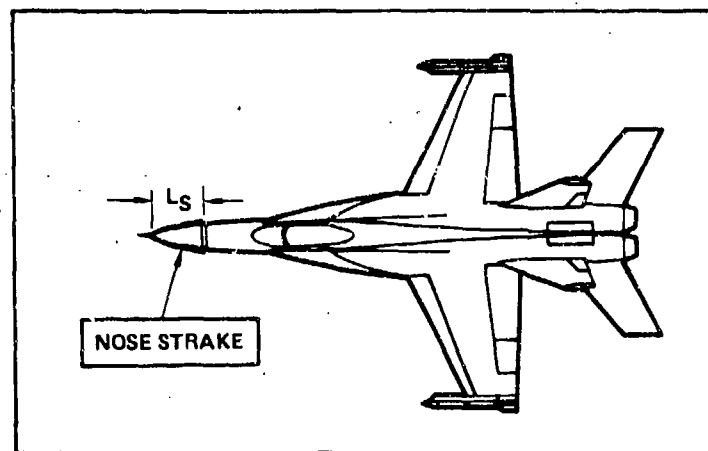


FIGURE 18. YF-17 STRAKE GEOMETRY

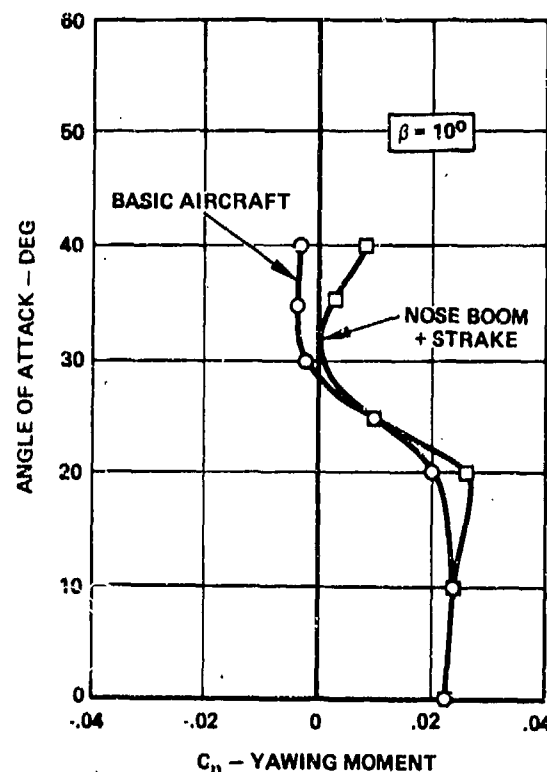


FIGURE 19. EFFECT OF NOSE BOOM AND STRAKE

The difference in the strake effectiveness illustrated here between the F-5E/F and YF-17 configurations indicates the effect of strakes on directional stability at nonzero sideslip is configuration dependent while the application of strakes to reduce nonzero yawing moments at zero sideslip is not.

EFFECT OF BLUNTNESS

Studies performed at Northrop have shown the forebody nose radius has an effect on high angle-of-attack aerodynamics and the results of these studies agree with the trends found by researchers at NASA. The data of Figures 20 and 21 are extracted from data presented in Reference 5 and show that nose bluntness affects both the magnitude and the onset angle-of-attack at which directional asymmetries at zero sideslip occur. As the nose bluntness angle is increased, the onset angle-of-attack is delayed and for increased nose bluntness, the magnitude of the aerodynamic asymmetry is reduced. Northrop results, Figures 22 and 23, also show that nose bluntness raises the onset angle-of-attack and also has an important effect on the peak asymmetric yawing moment at zero sideslip.

EFFECT OF FLIGHT TEST NOSE BOOMS

Flight testing requirements often result in the addition of a large instrumentation boom to the nose of the aircraft to mount an angle-of-attack and sideslip vane and pitot-static system. Figure 24 shows a typical configuration. This boom, over seven feet long and with a four-inch base diameter, modifies both the nose shape

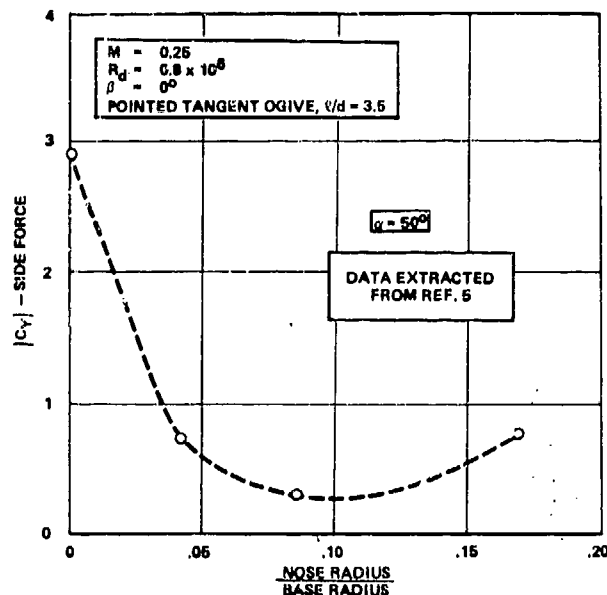


FIGURE 20. EFFECT OF NOSE BLUNTNES OF SIDE FORCE

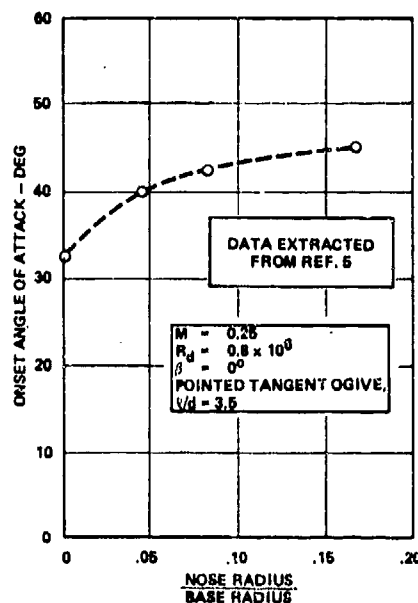


FIGURE 21. EFFECT OF NOSE RADIUS ON ONSET ANGLE OF ATTACK

and the effective fineness ratio, altering the nose vortex system. In addition, a vortex pattern is shed by the boom itself. This modification to a test aircraft can significantly affect the lateral-directional stability of the configuration at high angles-of-attack and could, potentially, alter the departure susceptibility and recover characteristics which would be determined.

Figure 25 illustrates an example of the variation in lateral-directional stability which can be caused by the installation of a large (4-inch diameter) flight-test nose boom on a fighter aircraft. A significant change to the forebody vortex system is produced by the nose boom.

III. WING/LEX VORTEX CHARACTERISTICS

Many fighter aircraft configurations have been designed such that a fully attached flow would be maintained over the lifting surfaces in order to maximize both the performance and the maneuvering capability of the design. Experimental studies and flight tests on a variety of configurations have shown that significant increases in maximum lift coefficient and reductions in drag at high lift can also be obtained by careful generation and control of concentrated vortices which favorably interact with the flow over a low aspect ratio main wing surface. These vortices have been generated by such devices as close-coupled canards, wing leading-edge discontinuities or sawteeth and wing-body strakes or leading-edge extensions (LEX's). The discussions of wing flow field effects in the present paper will be

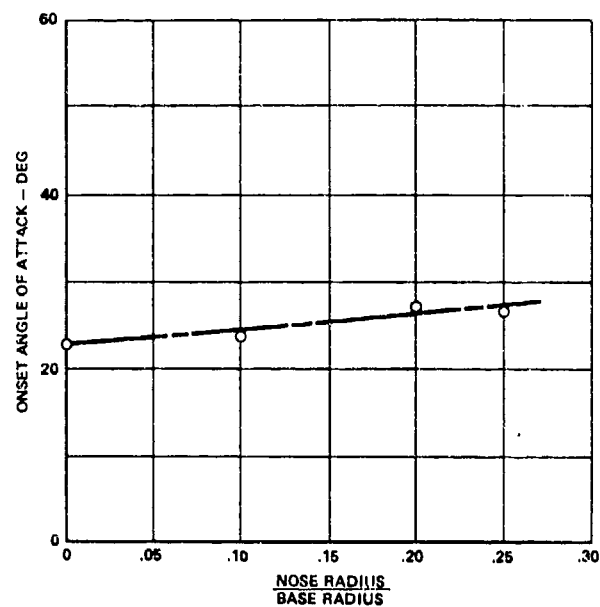


FIGURE 22. EFFECT OF NOSE RADIUS INCREASES ON ONSET ANGLE OF ATTACK

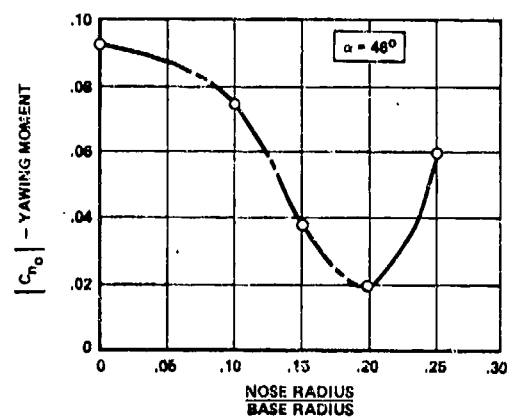


FIGURE 23. EFFECT OF NOSE RADIUS ON PEAK ASYMMETRIC YAWING MOMENTS



FIGURE 24. F-5F WITH FLIGHT TEST NOSE BOOM INSTALLED

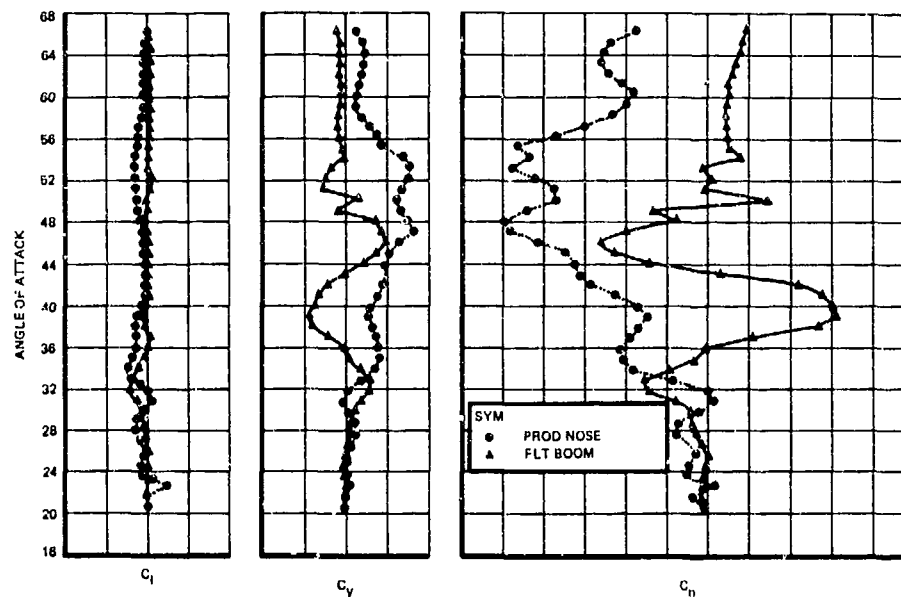


FIGURE 25. EFFECT OF FLIGHT TEST NOSE BOOM

limited to hybrid wing geometries designed to maximize vortex induced lift. These geometries will be highly swept delta wings or wing/LEX or wing/strake combinations. Figure 26 illustrates an example of the induced lift increments which can be generated by LEX vortices.

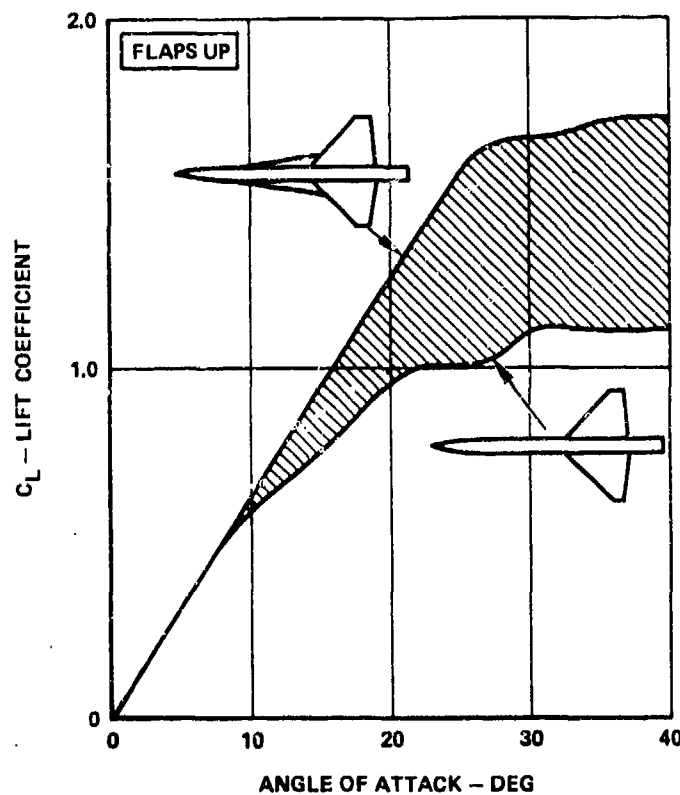


FIGURE 26. LEX EFFECT ON LIFT

WING/LEX VORTEX BREAKDOWN

Several factors can singly, or in combination, limit the amount of maneuver performance improvement which can be obtained with a wing/LEX combination. Such factors as an unstable break in the pitching moment curve or an abrupt loss of directional stability at the stall angle-of-attack, or a loss of lateral stability at high sideslip angles can impose a limit to the geometry of a wing/LEX configuration. For each of these flight mechanics problems, the cause can be attributed to the same fluid mechanic phenomenon: a breakdown of the LEX vortex system. This breakdown can occur in either a symmetric or an asymmetric manner, depending on the sideslip angle.

For a basic discussion of the geometric factors which affect vortex breakdown, reference is made to Figure 27, taken from Reference 6, which illustrates the forward progression of the vortex burst point on a sharp-edged delta wing with increased angle-of-attack. Planforms with leading-edge sweep angles of from 55° to 82° are presented. Two main points can be made from a review of these data. First, for a given leading-edge sweep angle, vortex burst point progresses forward with increasing angle-of-attack. The progression is more rapid when the burst point is in the region of the trailing edge (large adverse pressure gradients) and less rapid near the apex of the wing. Secondly, for vortex burst at a constant value of x/c_o , a higher breakdown angle of attack is observed with increasing leading-edge sweep angle.

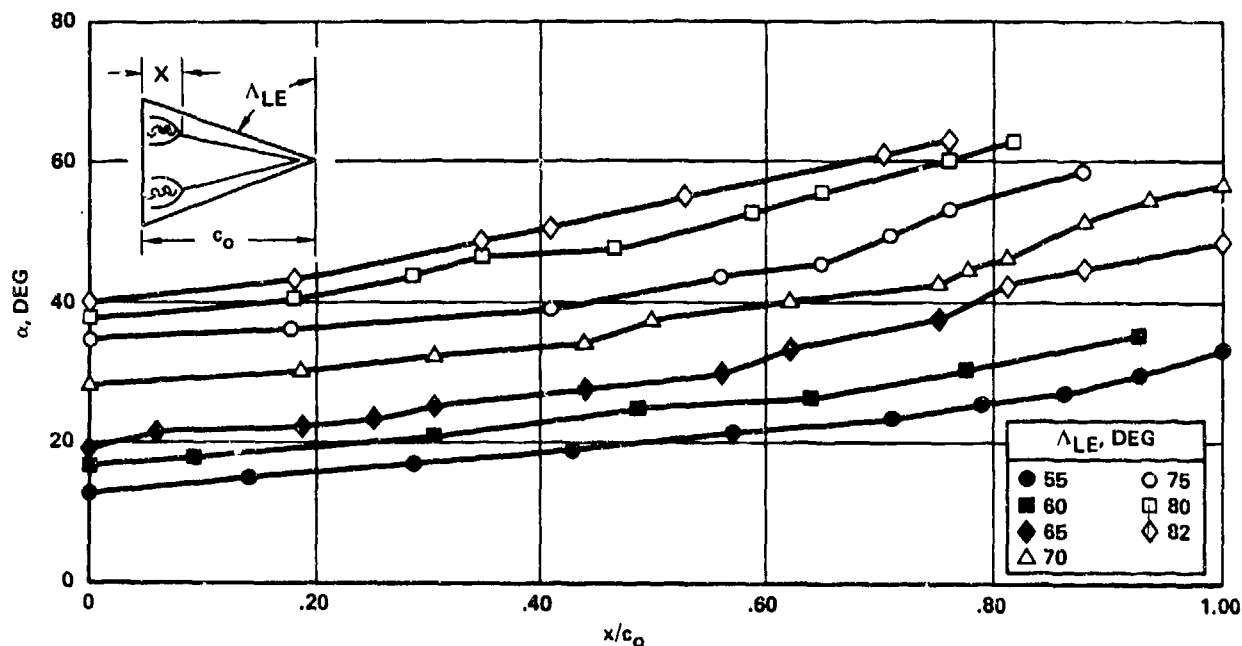


FIGURE 27. EFFECT OF ANGLE OF ATTACK AND SWEEP ANGLE ON VORTEX BREAKDOWN LOCATION

Similar effects are present on hybrid wings (wing/LEX combinations). When the vortex burst point begins to move forward of the trailing edge of the wing, a reduction in induced lift is observed. Also at a constant value of sideslip, vortex bursting becomes asymmetric due to an effective increase in the sweep angles of the leeward LEX and wing and a similar reduction in the windward LEX and wing sweep angles as illustrated in Figure 28. This can lead to lateral instabilities and when the vortex burst points are in close proximity to the vertical or horizontal tails, abrupt loss of directional or longitudinal stability is often experienced. An example of abrupt lateral-directional stability loss due to asymmetric LEX vortex breakdown is presented in Figure 29.

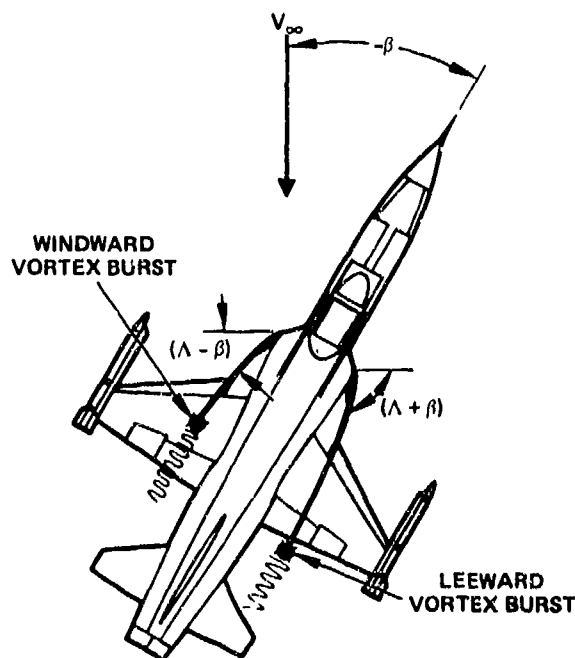


FIGURE 28. SCHEMATIC OF LEX EFFECT IN SIDESLIP

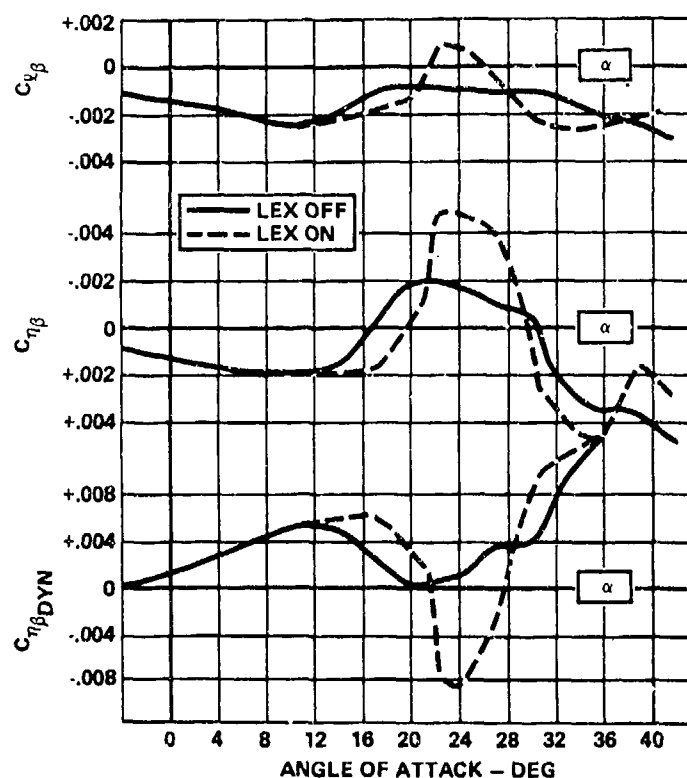


FIGURE 29. EFFECT OF ASYMMETRIC LEX
VORTEX BREAKDOWN

The data presented in the previous two figures are for triangular wings or for triangular LEX's on trapezoidal wings. Careful shaping of the wing or LEX planform can greatly alter the vortex breakdown characteristics observed. For instance, Figures 30 and 31 illustrate the effect of planform geometry variations on vortex breakdown characteristics for constant aspect ratio delta wings. A high degree of sensitivity is noted.

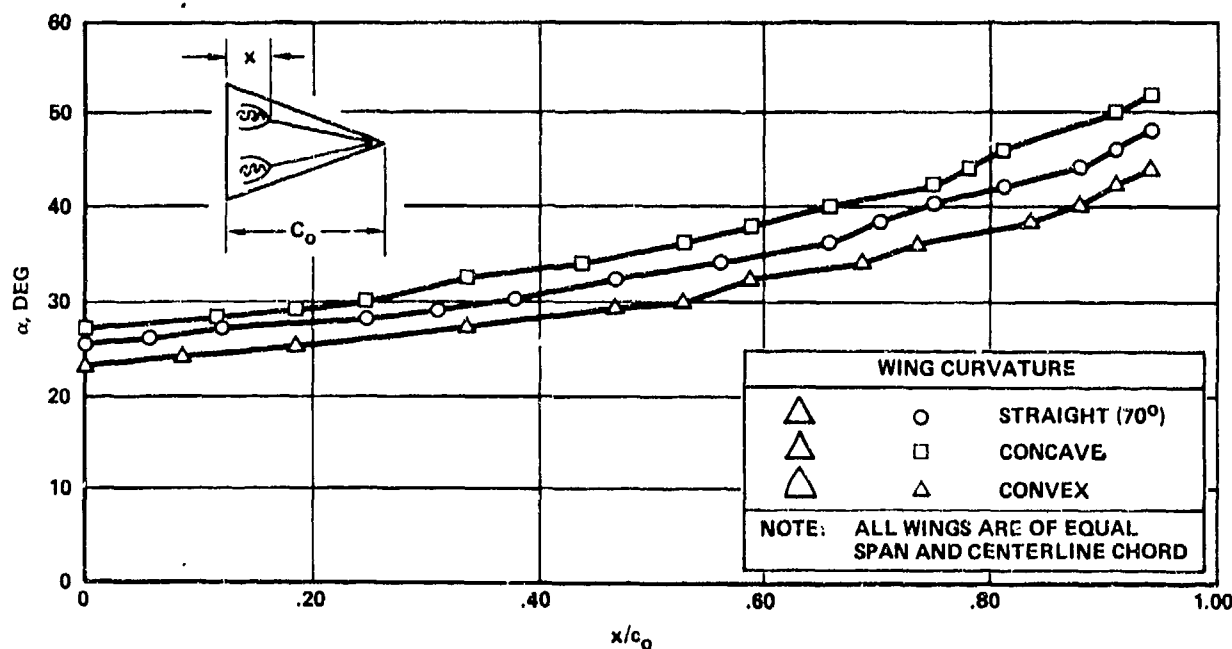


FIGURE 30. EFFECT OF LEADING-EDGE CURVATURE ON VORTEX BREAKDOWN LOCATION

WING LEADING-EDGE DISCONTINUITIES

For a given wing/LEX geometry, an additional improvement in induced lift or lateral-directional stability may be achieved by the incorporation into the design of certain features. One such feature, wing leading-edge discontinuities, or sawteeth, has the effect of promoting an earlier breakdown of the primary wing leading-edge vortex, as shown in Figures 32 and 33. The sawtooth creates two vortices which rotate in opposite sense. The vortex which

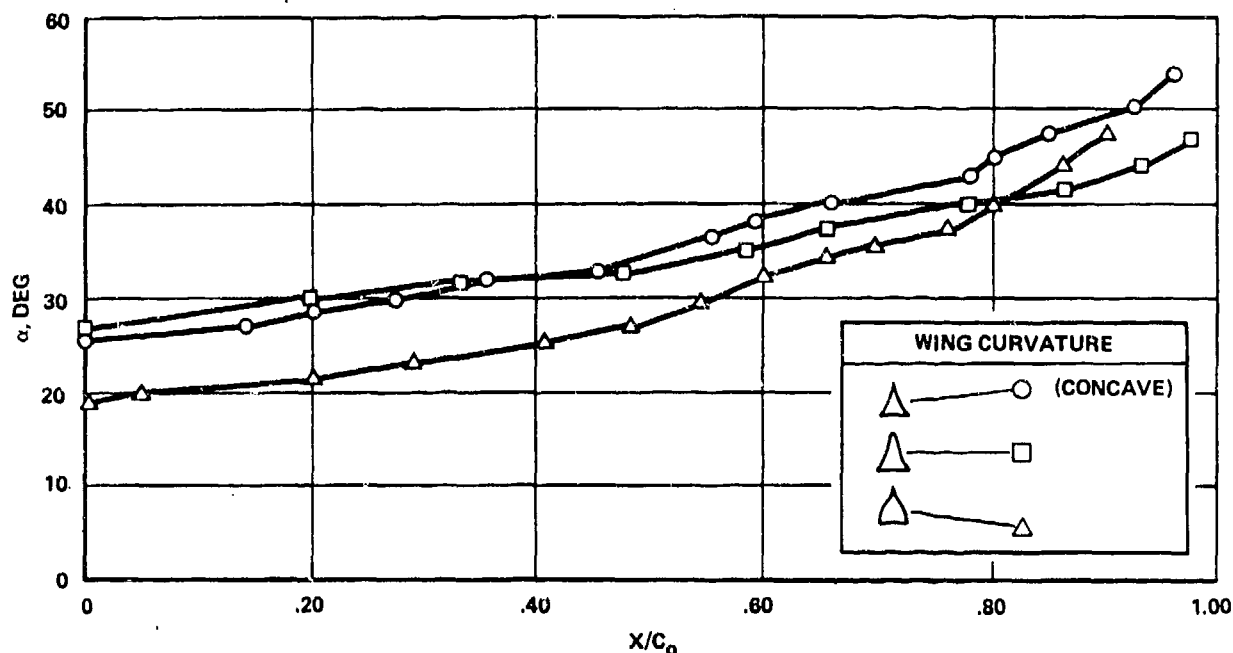


FIGURE 31. EFFECT OF LEADING-EDGE CURVATURE ON VORTEX BREAKDOWN CHARACTERISTICS

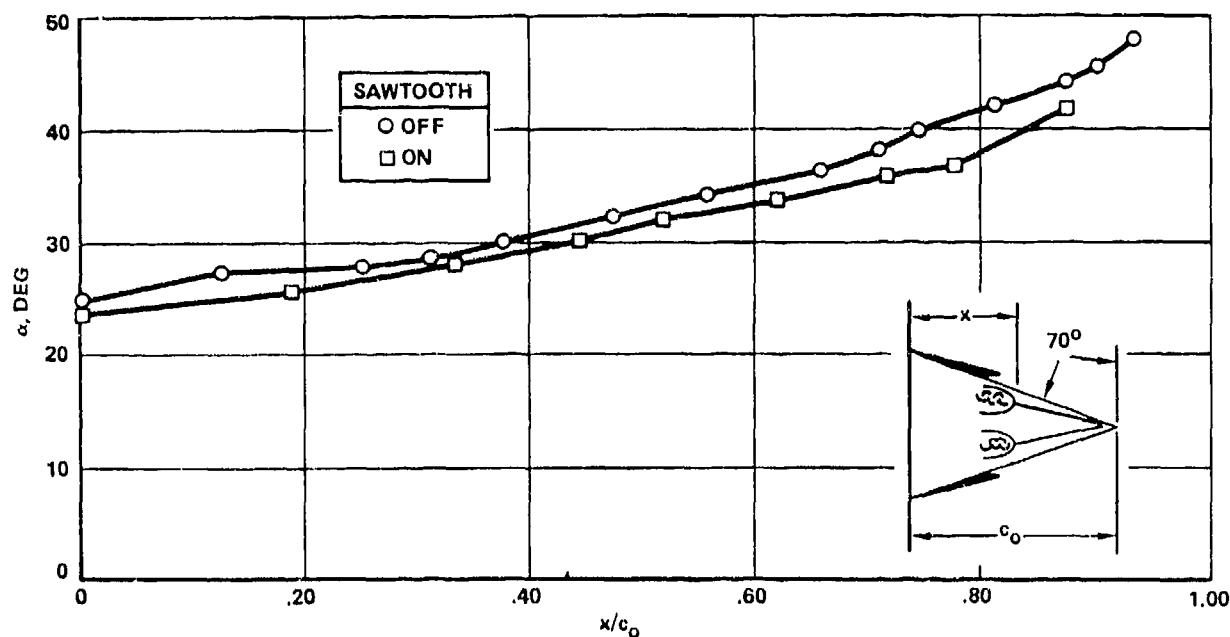


FIGURE 32. EFFECT OF SAWTOOTH ON VORTEX BREAKDOWN CHARACTERISTICS OF 70° DELTA WING

forms at the notch has a sense of rotation which tends to inhibit outboard spanwise flow, causing a premature breakdown on the wing leading-edge vortex. The second vortex forms from the leading edge and is in the same sense as the primary wing vortex and the LEX vortex. This secondary leading-edge vortex improves the flow over the outboard wing panel and can provide an improvement to the induced lift and the lateral stability contribution ($C_{l\beta}$) of the wing. Figure 34, taken from Reference 7, illustrates the effect of a sawtooth on a fighter with a hybrid wing/LEX geometry.

WING FENCES

Wing upper-surface fences produce an aerodynamic effect very similar to wing leading-edge discontinuities. Like the notch vortex, the fence inhibits outboard spanwise flow and promotes an early wing leading-edge vortex breakdown. This effect is illustrated in Figure 35. The fence promotes a more symmetric vortex breakdown when the wing is at a non-zero value of sideslip, thereby resulting in an improvement in lateral stability as shown in Figure 36. In contrast to the sawtooth, however, which creates a secondary wing leading-edge vortex, the fence causes a reduction in vortex induced lift on the wing. This effect is illustrated in Figure 37. Above the stall angle-of-attack, the effect of the fence becomes diminished as it is immersed in the separated flow over the wing.

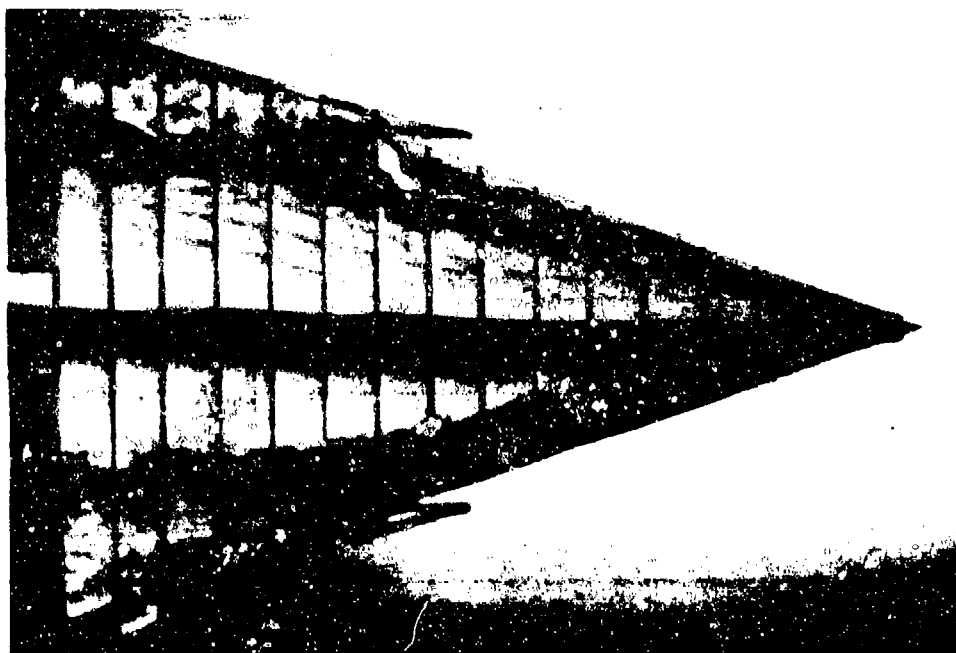


FIGURE 33. EXAMPLE OF SAWTOOTH EFFECT ON VORTEX BREAKDOWN

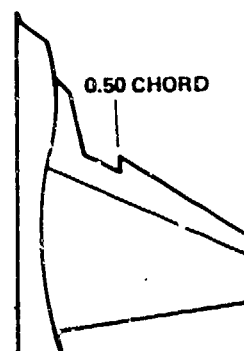
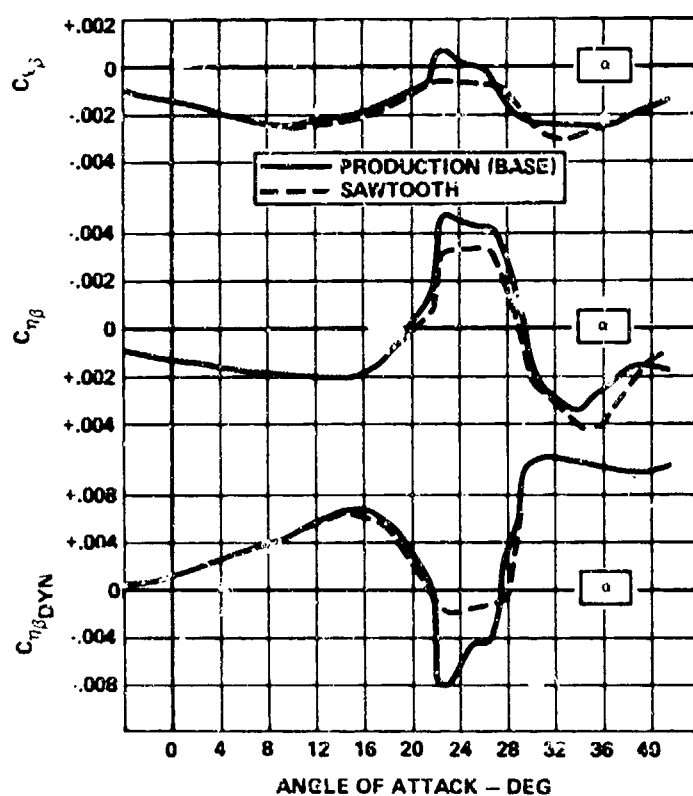


FIGURE 34. EFFECT OF SAWTOOTH

WING TRAILING-EDGE FLAPS

The effect of deflecting plain flaps located at the wing trailing-edge is to increase the aft camber of the wing resulting in some improvement in CL_{MAX} . When trailing-edge flaps are deflected at high angles of attack in the presence of a strong wing or LEX vortex, a detrimental effect on vortex breakdown is produced as shown in Figures 38 and 39 for a 65° delta wing. This premature vortex breakdown can cause a reduction in directional stability, as shown in Figure 40. These data are for the YF-17 configuration, which has a plain, unslopped, hinged trailing-edge flap. For this geometry, the flow field above the flap at an angle of attack of 20 degrees or greater has been observed to be totally separated, producing a strong adverse pressure gradient on the wing upper surface. This

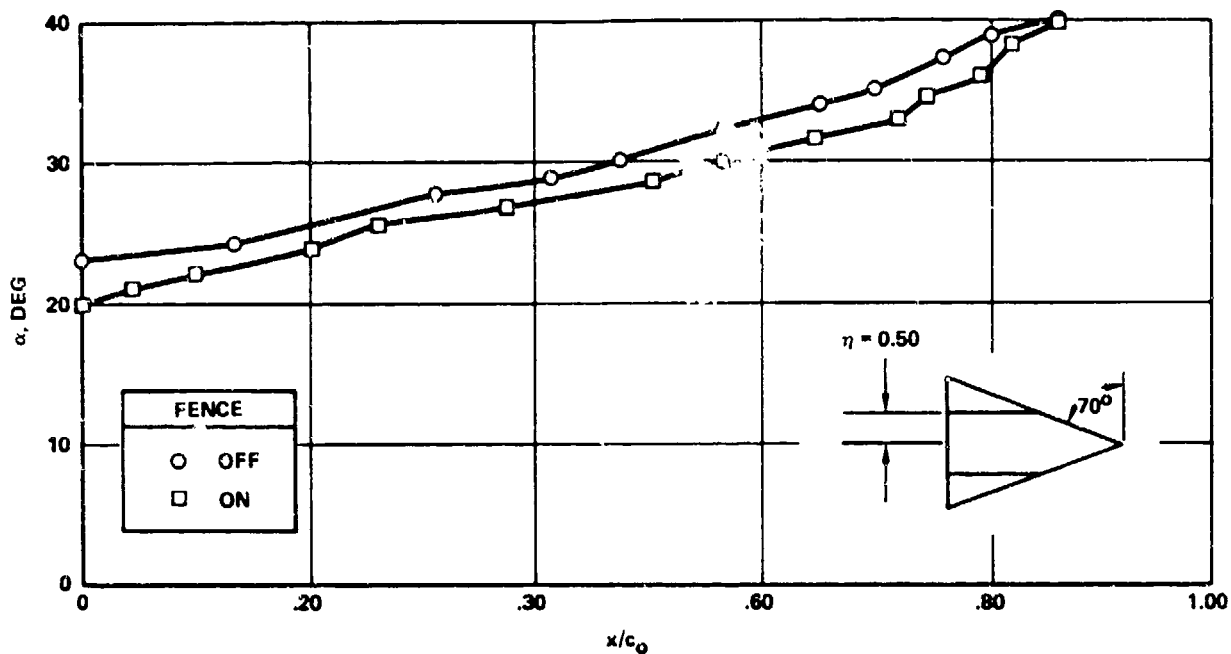


FIGURE 35. EFFECT OF FENCES ON VORTEX BREAKDOWN

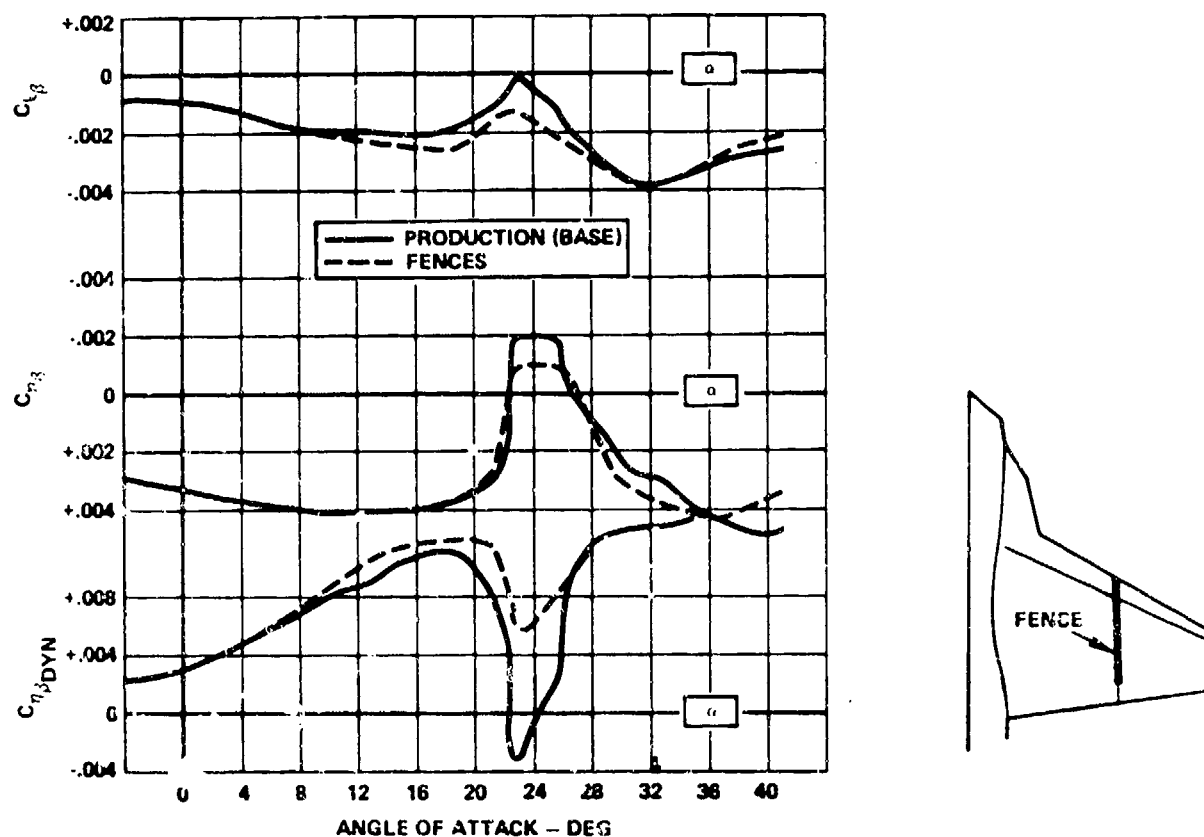


FIGURE 36. EFFECT OF WING FENCES ON STABILITY

adverse pressure gradient acts to induce a premature bursting of the LEX vortex, adversely affecting the flow field around the twin vertical tails. For configurations with single vertical tails and/or smaller LEX's which produce weaker vortex systems, typified by the F-5 series, this adverse interaction has been observed to be less pronounced.

IV. FOREBODY/WING VORTEX INTERACTIONS

Having discussed the fundamentals of forebody and wing vortex formation and breakdown, the more subtle, but sometimes more pronounced, effects of forebody and wing vortex interactions will be addressed. Examples can be

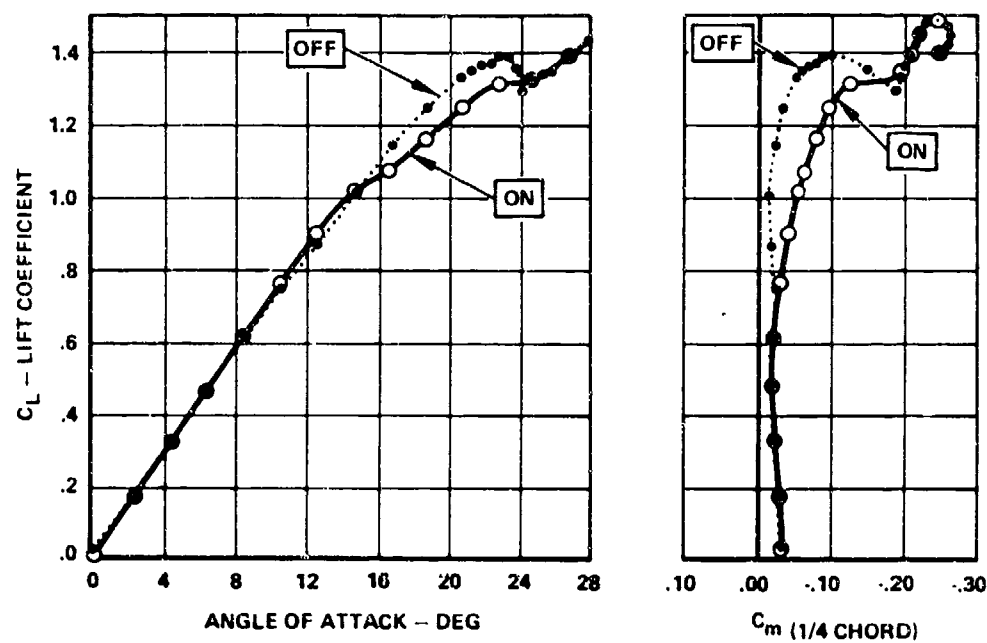


FIGURE 37. EFFECT OF WING FENCES IN PITCH

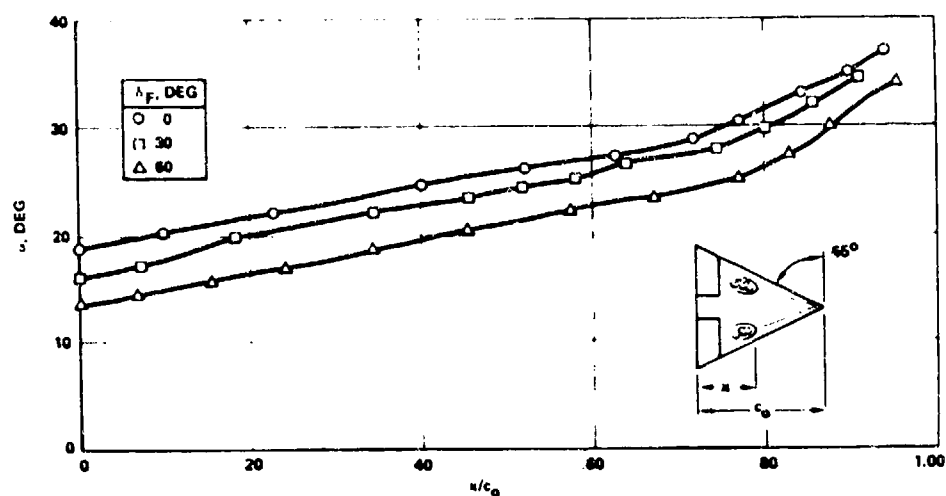


FIGURE 38. EFFECT OF DEFLECTED TRAILING-EDGE FLAP ON VORTEX BREAKDOWN

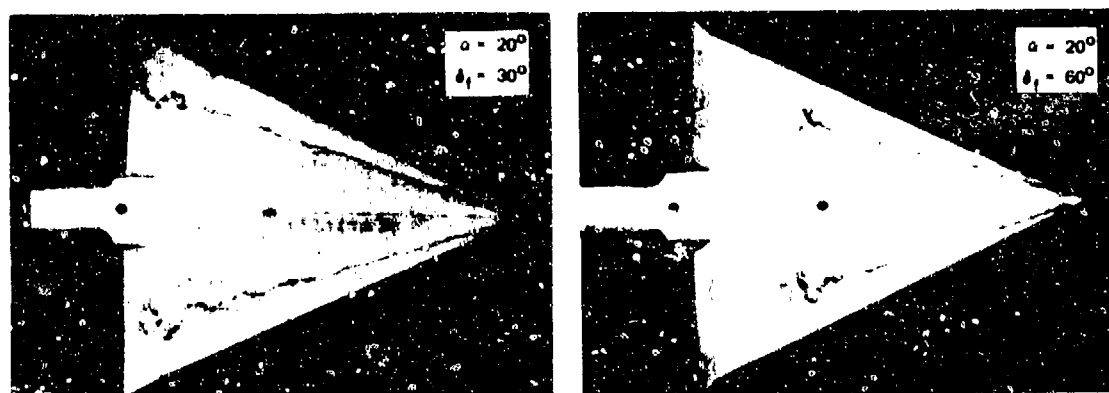


FIGURE 39. EXAMPLE OF FLAP EFFECT ON VORTEX BREAKDOWN

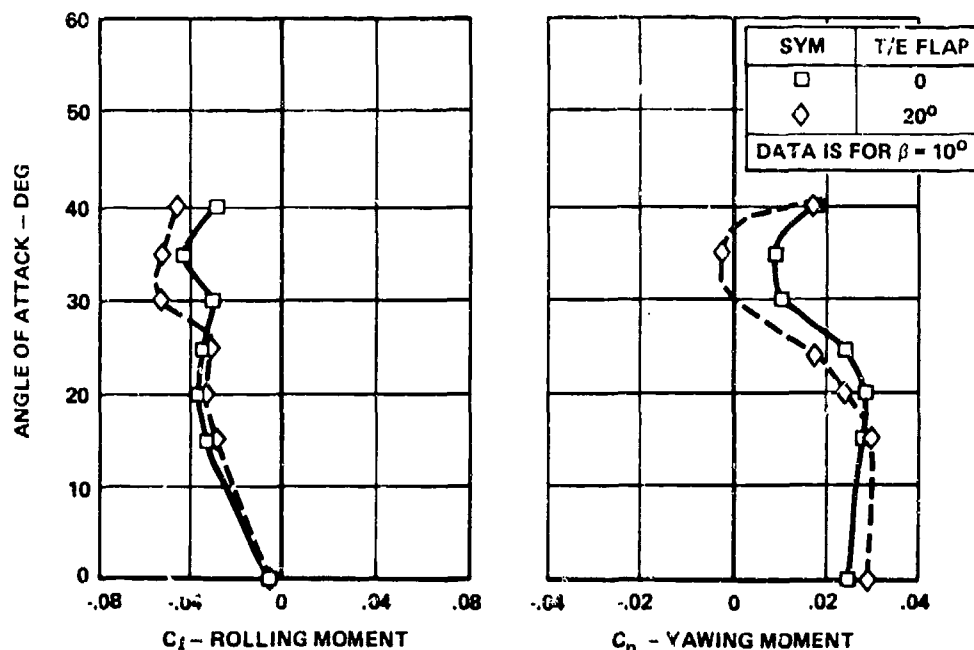


FIGURE 40. EFFECT OF TRAILING-EDGE FLAP DEFLECTION

cited of aircraft configurations which have minimal forebody influences. The high angle-of-attack behavior of these aircraft tends to be dominated by the wing vortex system. The F-4 is such an aircraft. Fairly extensive changes to the forebody geometry of the F-4 have been shown to have a very small effect on its stall and post-stall characteristics, whereas changes to the wing geometry, such as with the addition of wing leading-edge slats, have produced large changes. Examples can also be cited of aircraft configurations which have strong forebody and wing influences which do not interact and can, therefore, be separated. The F-5A is an example of such an aircraft. At angles of attack below approximately 30 degrees, the wing contribution to lateral-directional stability is pronounced and the influence of the forebody is quite small. Above this angle-of-attack, the wing influence diminishes rapidly and the forebody provides essentially all of the directional stability to the aircraft.

Current generation, highly maneuverable aircraft with hybrid wing planforms and slender forebodies are characterized by strong interactions between the forebody and the wing/LEX vortex systems. As an example of these strong interactions, Figure 41 is presented. This figure illustrates the vortex pattern for a configuration which was developed to maximize the favorable interactions between the forebody and upper LEX vortices and between the upper and lower LEX vortices. At the conditions illustrated ($\alpha = 24^\circ$, $\beta = 10^\circ$), the leeward secondary vortex formed by the long forebody coalesces completely with the upper LEX vortex, greatly improving the breakdown characteristics when compared to those in the presence of the non-optimum forebody shape. The upper LEX vortex, in turn, acts to improve the lower LEX vortex breakdown characteristics, thus enhancing the induced vortex lift on the wing. The upper and lower LEX modifications illustrated represent a total increase in wing area of 9.6% but produce an increment in trimmed lift coefficient of 64%. The lateral-directional stability of this configuration was significantly enhanced by the favorable vortex interactions, as well.

The design methodology utilized to develop these enhancements to maneuver performance and high angle-of-attack flying qualities is illustrated in Figures 42, 43 and 44. These figures present a typical variation of directional stability with angle-of-attack. The characteristic loss of directional stability is due to the progressive forward movement of the LEX vortex breakdown point as angle-of-attack is increased. This effect was discussed in detail in Section III of this paper. The objective of the design methodology is to maximize the LEX vortex strength to produce large induced lift increments while at the same time delaying the breakdown of the vortex to as high an angle-of-attack as possible.

As was discussed in Section II of this paper, at angles-of-attack beyond the stall, the forebody of an aircraft can strongly influence the directional stability characteristics which are present. Figure 43 illustrates a typical improvement in high angle-of-attack directional stability which can be achieved by proper shaping of the forebody.

An otherwise unstable aircraft can be made stable or a stable configuration can be enhanced by this shaping. When a forebody and wing/LEX geometry are optimized, as illustrated in Figures 42 and 43, and are then combined on the same configuration, it is possible for a favorable interaction to be generated. This synergistic effect is illustrated, conceptually, in Figure 44.

As a part of Northrop's ongoing research into forebody/wing vortex interactions, an optimum forebody geometry and LEX planform shape were developed using the methodologies discussed in the preceding paragraphs. The nose planform and cross-sectional shape were designed to attenuate the asymmetric vortex formations which are characteristic of forebodies of this high fineness ratio ($L/d = 6.0$) while enhancing the favorable directional stability effects at non-zero sideslip. The LEX geometry was developed to delay vortex breakdown in the region of the stall angle-of-attack. The forebody geometry is referred to as the "Shark Nose" due to its flat, broad nose, resembling the nose of a shark. The LEX planform is denoted by its wind tunnel model part number "W₆." The Shark Nose geometry is

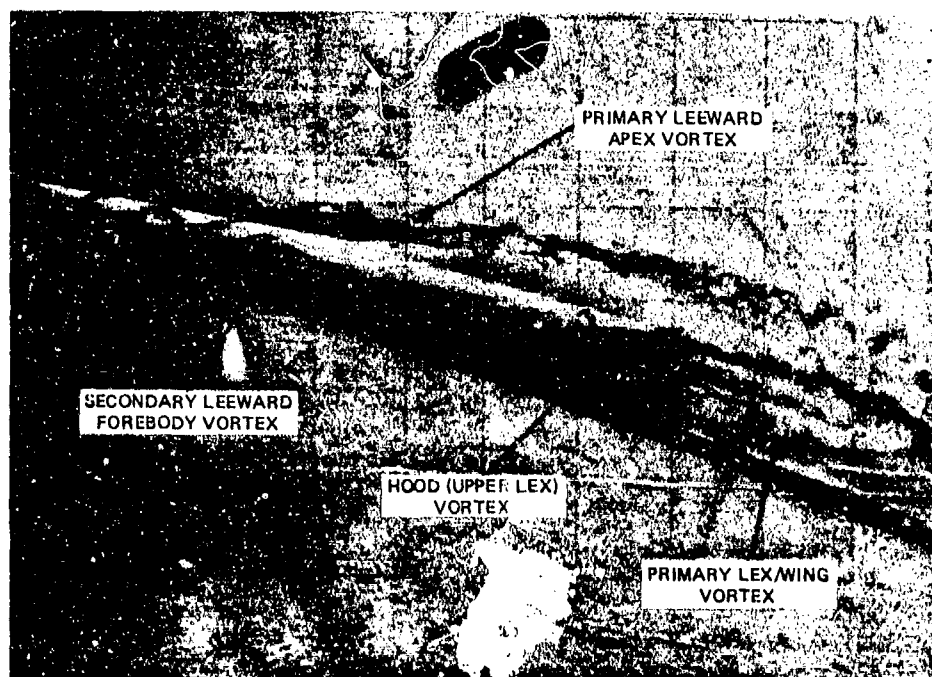


FIGURE 41. STRONG VORTEX INTERACTIONS

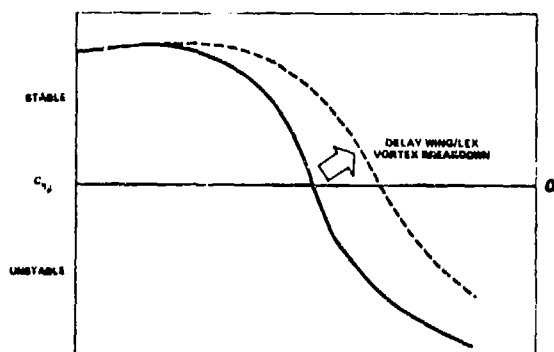


FIGURE 42. WING/LEX DESIGN OPTIMIZATION

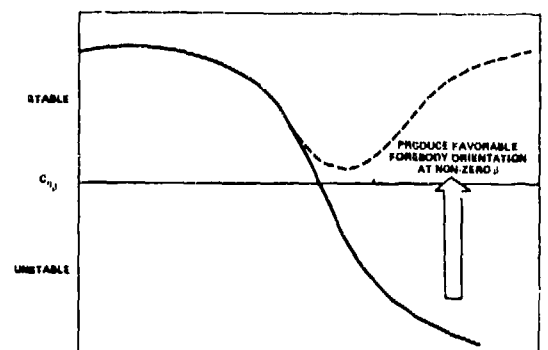


FIGURE 43. FOREBODY SHAPE OPTIMIZATION

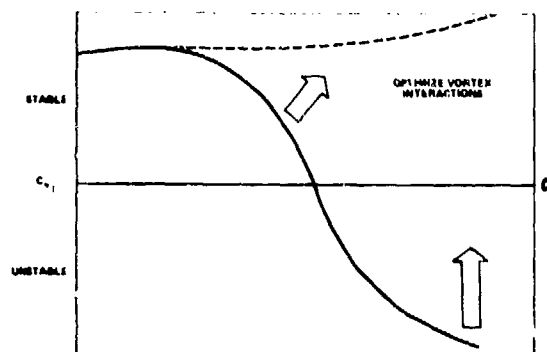


FIGURE 44. VORTEX INTERACTIONS/DESIGN OPTIMIZATION

depicted in Figure 45. The Shark Nose is shown alongside of the basic unmodified nose in Figure 46. The W_6 LEX geometry is shown in Figure 47.

Figure 48 illustrates the effect of the Shark Nose on the magnitude of yawing moment at zero sideslip at high angles-of-attack. An order-of-magnitude reduction is obtained. Figure 49 presents the effect of the Shark Nose on directional stability at $\alpha = 46^\circ$. Figure 50 presents the effect of the Shark Nose on directional stability as a function of angle-of-attack.

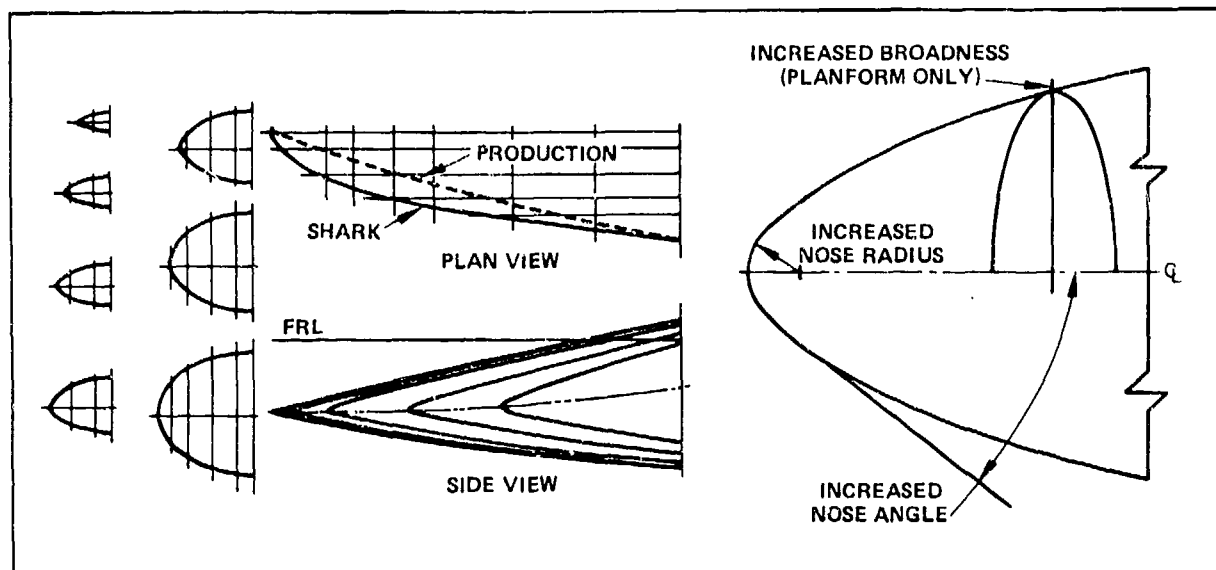
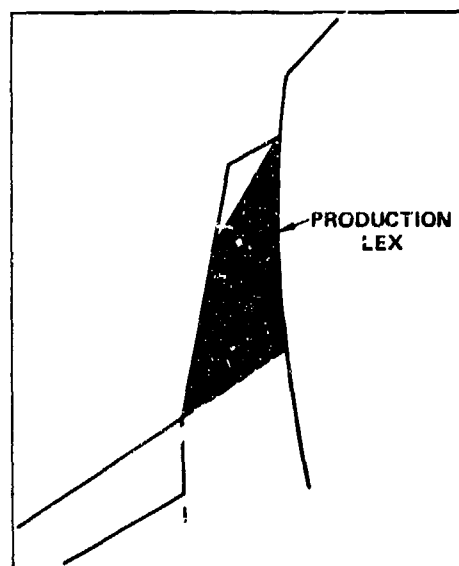


FIGURE 45. SHARK NOSE GEOMETRY



FIGURE 46. COMPARISON OF SHARK NOSE AND BASELINE NOSE

FIGURE 47. w_6 LEX GEOMETRY

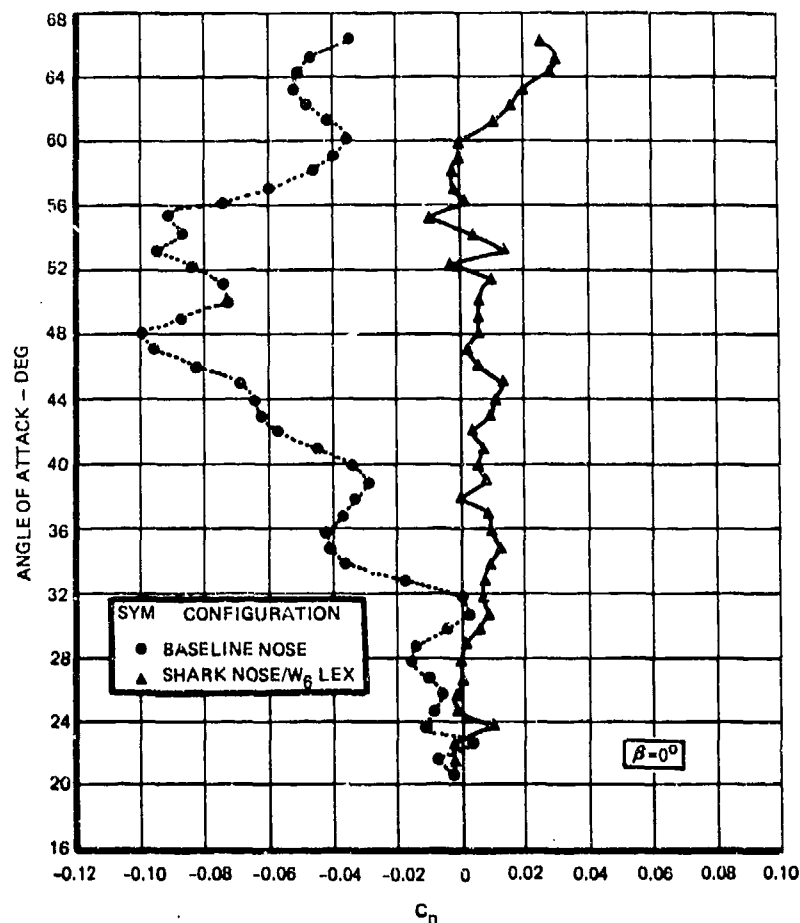


FIGURE 48. SHARK NOSE EFFECT ON AERODYNAMIC ASYMMETRIES

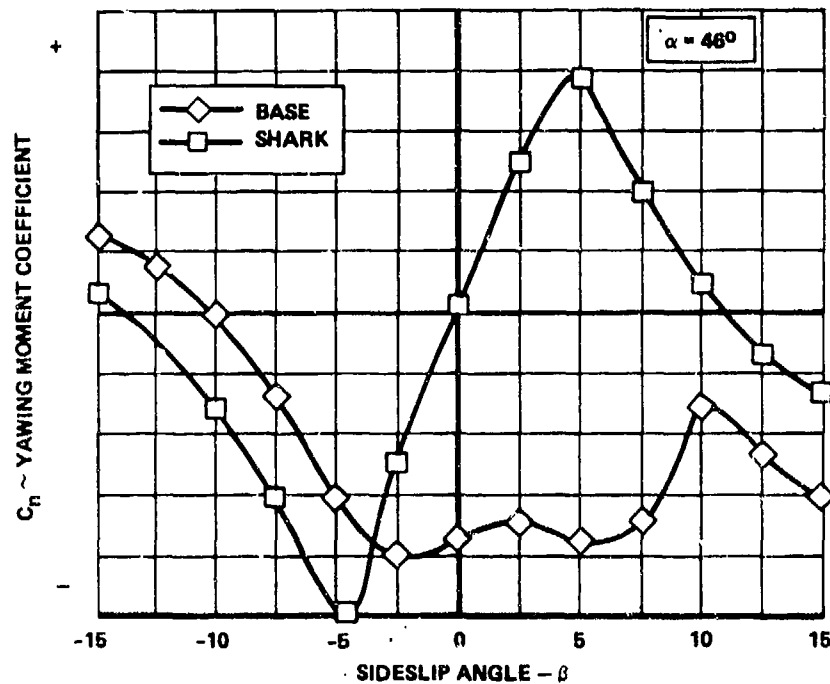


FIGURE 49. SHARK NOSE EFFECT ON STABILITY

Figure 51 illustrates the effect of the W_6 LEX planform on vortex breakdown as observed in the Northrop water tunnel. The forward progression of the vortex burst with increasing angle-of-attack is delayed when compared to the production LEX.

Figure 52 presents the effect of the W_6 LEX on the directional stability of the configuration. The characteristic loss of stability associated with vortex breakdown is seen to be delayed in the stall angle-of-attack region.

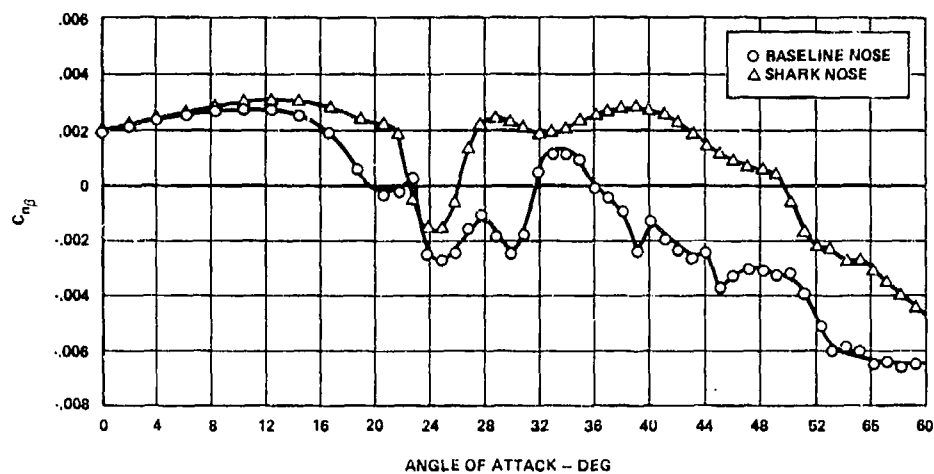


FIGURE 50. EFFECT OF SHARK NOSE ON STABILITY

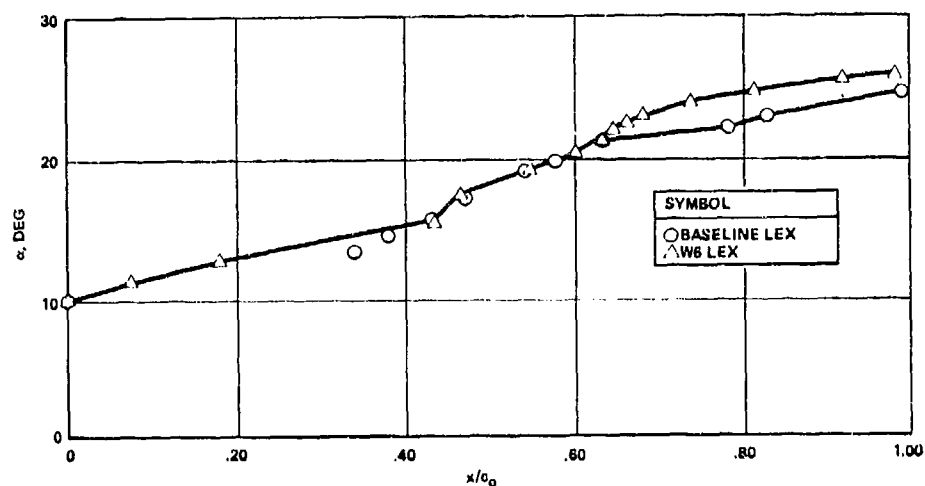
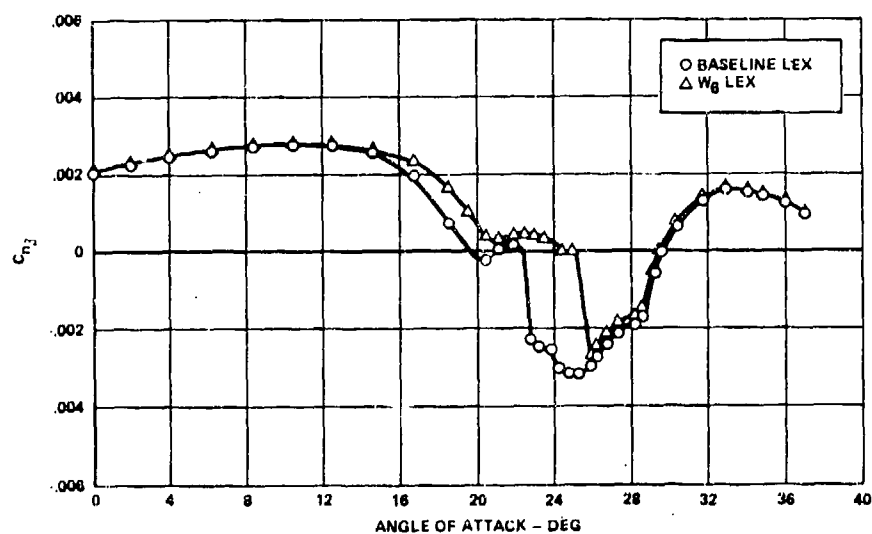
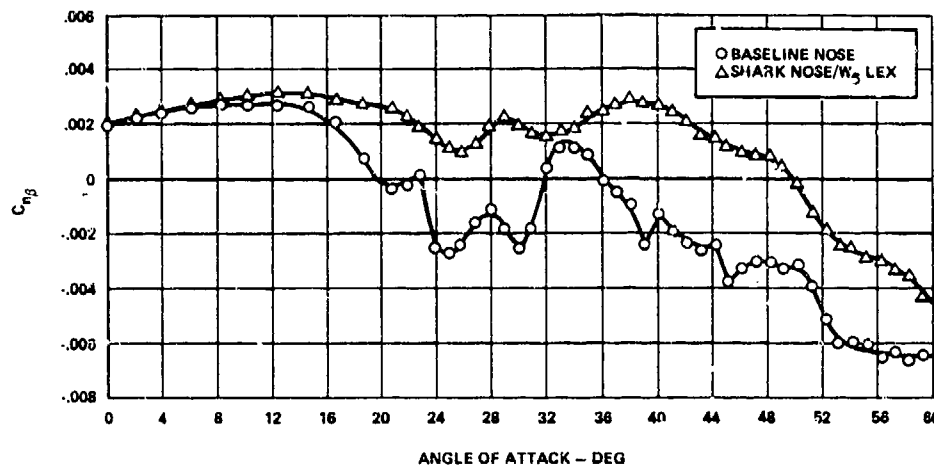
FIGURE 51. EFFECT OF W_6 LEX ON VORTEX BREAKDOWNFIGURE 52. EFFECT OF W_6 LEX ON STABILITY

Figure 53 presents the effect of the Shark Nose in combination with the W_6 LEX on directional stability. The loss in stability near the stall angle-of-attack is completely eliminated. This represents a very significant improvement in directional stability and was achieved through very minor, but important, modifications to the forebody and LEX geometries.

FIGURE 53. EFFECT OF SHARK NOSE/ W_6 LEX ON STABILITY

As an example of the predicted improvement in departure resistance which results from Shark Nose/ W_6 LEX combination, Figure 54 is presented. This figure presents one selected time history from an extensive open-loop 6 DOF analysis of the Shark Nose/ W_6 LEX. The maneuver simulated was the abrupt application of full nose-up horizontal stabilizer at time $t = 0$ from a trim condition at 150 knots at 35,000 feet altitude. No lateral-directional control inputs were applied. Full-up stabilizer was maintained throughout the maneuver. Only yaw rate and angle of attack are presented here. The aerodynamic data package for this simulation consisted of small scale, low speed, static wind tunnel data with estimated rotary derivatives (strip theory method). As can be clearly seen in the figure, the base configuration experiences a large, uncommanded increase in yaw rate at $t = 2.3$ seconds as an angle-of-attack of approximately 45 degrees is attained. This yaw rate couples inertially with roll rate (not shown) to produce a further increase in angle-of-attack, producing a spin condition. The same control inputs to the Shark Nose/ W_6 LEX configuration produces a higher initial angle-of-attack, but no uncommanded yaw departure, and the angle-of-attack begins to converge to a full-aft-stick trim value of approximately 30 degrees. The results of this maneuver and many others indicated a dramatic increase in departure resistance could be expected from the Shark Nose/ W_6 LEX configuration when compared to the baseline.

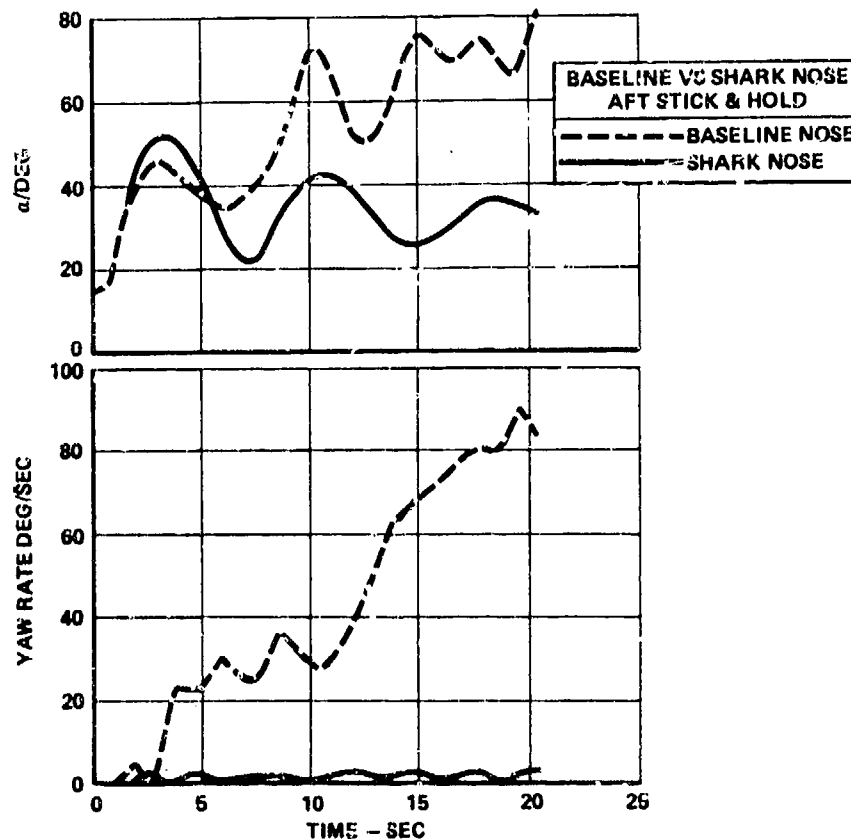


FIGURE 54. DIGITAL 6 DOF SIMULATED MANEUVER - EFFECT OF SHARK NOSE

Based on the small scale experimental tests and analytical predictions, a full scale Shark Nose and W_6 LEX were constructed and a flight test investigation of their effects was made using a specially modified spin test aircraft. Figure 55 presents a photograph of the test aircraft. The results of this flight program verified the analytical predictions and confirmed that the nose vortex system had been stabilized and the asymmetric yawing moments previously experienced were eliminated.

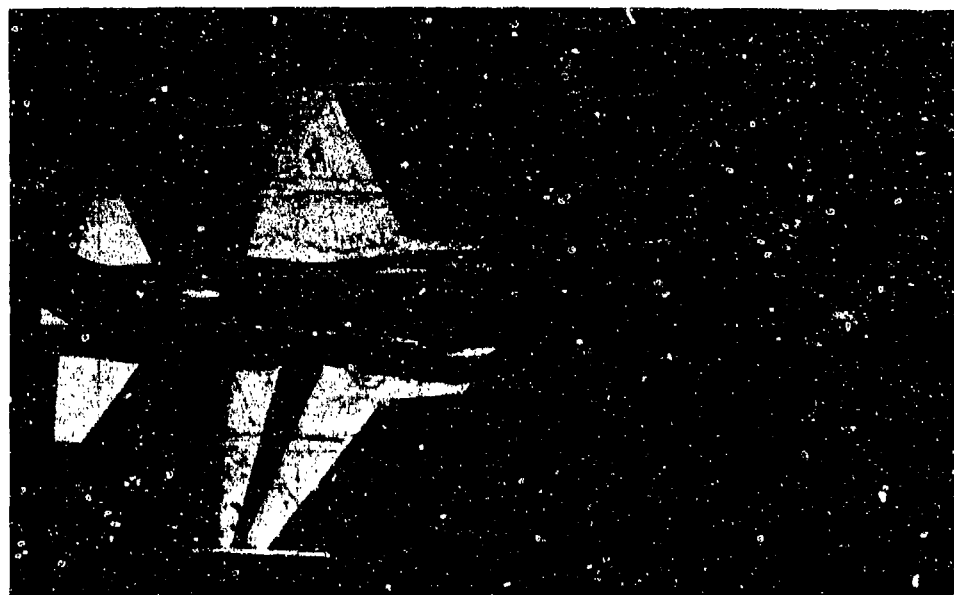


FIGURE 55. FLIGHT TEST VEHICLE WITH SHARK NOSE AND W_6 LEX INSTALLED

Figures 56 and 57 present a comparison of full scale flight test results with 6 DOF simulation for two maneuvers. Figure 56 shows a longitudinal stick snap similar to that described in Figure 54 but with slightly different initial conditions. The exact flight test control inputs and initial condition were used in the digital simulation. The agreement shown is excellent. Figure 57 shows a one-g stall, and again, except for a slight phase discrepancy in roll angle, the agreement is excellent.

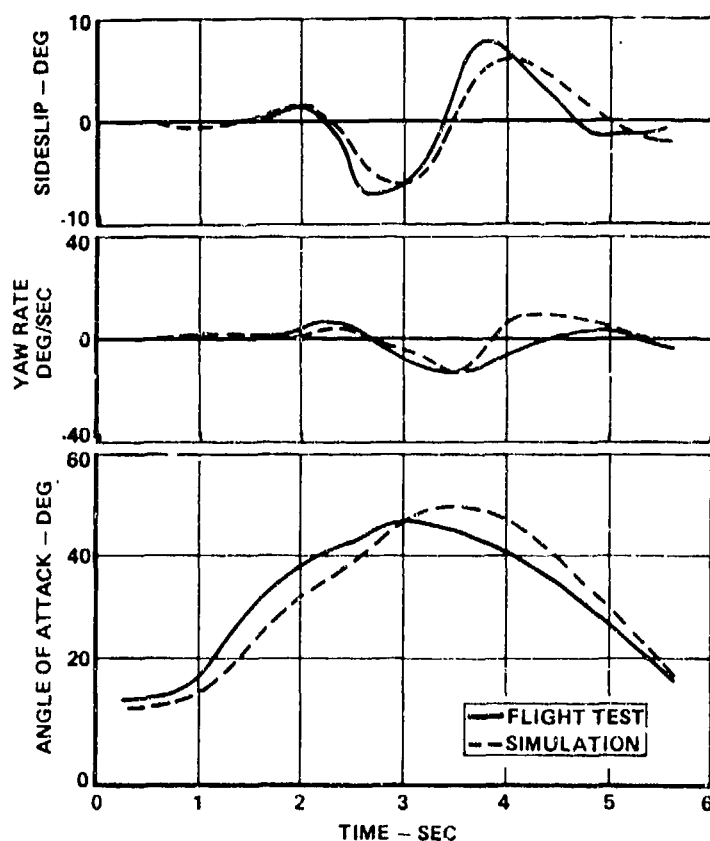


FIGURE 56. DIGITAL/FLIGHT TEST CORRELATION STICK SNAP MANEUVER

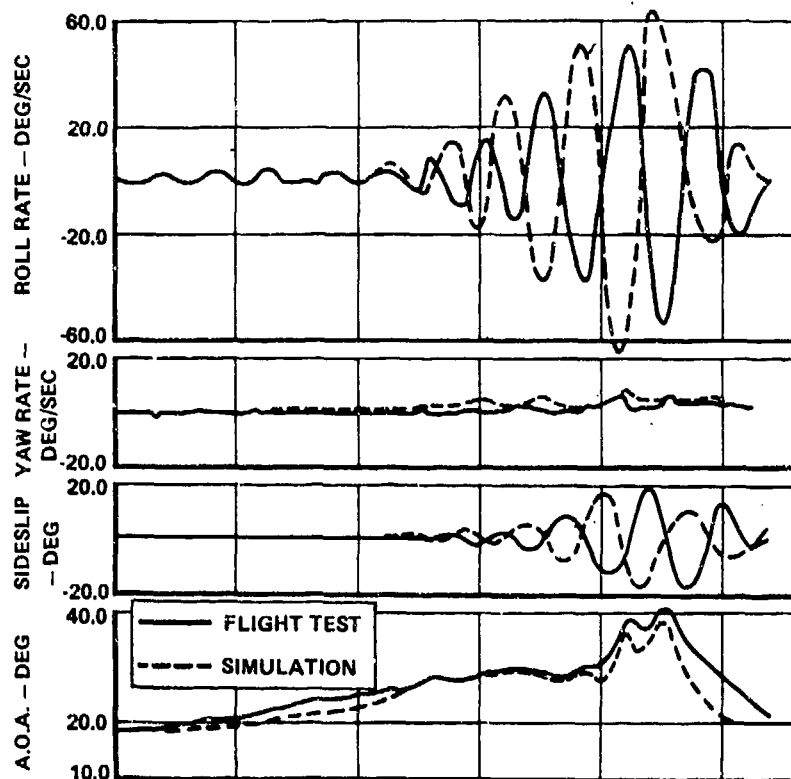


FIGURE 57. DIGITAL/FLIGHT TEST CORRELATION 1.0g STALL MANEUVER

V. CONCLUSION

Vortical flows shed from the forebody and wings can have a dominant influence on the stability of fighter aircraft at high angles of attack. Through careful configuration design, the induced effects of these vortices can be made to enhance stability. Methodologies have been developed to provide guidelines for the design of forebody and hybrid wing geometries which will improve stability at high angles of attack. Proper forebody shaping can attenuate asymmetric vortex shedding and reduce the magnitude of yawing moments at zero sideslip while enhancing lateral-directional stability. Selection of hybrid wing planform shapes which delay the breakdown of the wing/LEX vortices can increase both the stall angle of attack and aircraft lateral stability in the stall region. For some configurations, especially those having hybrid wings which are in close proximity to the forebody, there can be interactions between the forebody and wing/LEX vortices which can either improve or degrade stability. These interactions are highly configuration dependent; however, the aircraft designer can make use of these interactions to maximize departure and spin resistance of a specific configuration.

REFERENCES

1. Nielsen, J.N.; Nonlinearities in Missile Aerodynamics, AIAA Paper 78-20, January 1978.
2. Jorgensen, Leland H.; Nelson, Edgar R.; Experimental Aerodynamic Characteristics for Slender Bodies with Thin Wings and Tail at Angles of Attack from 0° to 58° and Mach Numbers from 0.6 to 2.0, NASA TM X-3310.
3. Titiriga, A., Jr.; Ackerman, J.S.; Skow, A.M.; Design Technology for Departure Resistance of Fighter Aircraft, AGARD CP-199, June 1976.
4. Headley, J.W.; Analysis of Wind Tunnel Data Pertaining to High Angle-of-Attack Aerodynamics, AFFDL-TR-78.
5. Chapman, G.T.; Keener, E.R.; Malcolm, G.N.; Asymmetric Aerodynamic Forces on Aircraft Forebodies at High Angles of Attack - Some Design Guides, AGARD CP-199, June 1976.
6. Erickson, G.E.; Water Tunnel Measurements of Vortex Breakdown Characteristics of Delta Wings Having Leading Edge Sweep of 55° to 85°, Northrop AR-78-1.
7. Skow, A.M.; F-5E/F Yaw Departure Analysis, Northrop AR 75-5.

STRAKE-INDUCED SEPARATION FROM THE LEADING EDGES OF WINGS OF MODERATE SWEEP

by

S. P. Fiddes
J. H. B. SmithRoyal Aircraft Establishment
Farnborough, Hampshire, EnglandSUMMARY

Mechanisms are proposed to account for the observation that, on a wing of moderate sweep and aspect ratio, leading-edge separation occurs at a lower incidence when strakes (*ie* highly swept, forward extensions to the wing root) are attached ahead of it. The effect on the main wing of the vortices resulting from the leading-edge separation on the strake is considered, and a simplified approach to modelling the flow over strake-wing combinations is introduced.

LIST OF SYMBOLS

a,b,c,d	coefficients, equation (3)
c(y)	local chord
G(y)	coefficient of leading-edge singularity, equation (1)
h(x)	camber
K	tangent of semi-apex-angle
$l(x,y)$	loading ($= \Delta C_p$)
L	see equation (A-3)
n	coordinate measured normal to leading edge
N	see equation (A1)
s	semi-span of main wing
s(x)	local semi-span
U	free-stream speed
v	sidewash due to vortex pair
w	upwash due to vortex pair
W(x)	cross-flow speed
x	chordwise coordinate
y	spanwise coordinate
z	coordinate normal to planform
α	incidence
γ	semi-apex-angle; distributed bound circulation (spanwise)
Γ	circulation
ξ	chordwise coordinate, see equation (A-1)
ϕ	angular chordwise coordinate, see equation (A-5)
Φ	velocity potential
Subscript	
s	spanwise

1 INTRODUCTION

In 1971, Küchemann¹ proposed combining vortex and classical aerofoil flows by placing a slender wing in front of a wing of high aspect ratio and moderate sweep. The resulting wing, when at incidence, produces the slender-wing type of separated flow over the highly swept inner part, and was envisaged as having attached flow over the outboard sections, except perhaps at the tips. The combination was intended to remove the central kink effect in the loading of the basic, moderately swept wing; in particular, to avoid the formation of a forward leg to the shock system at transonic speeds. At about the same time, research was in progress in the USA for the light-weight fighter programme. The two aircraft that reached prototype stage, the General Dynamics YF-16 and the Northrop YF-17 (see Refs 2 and 3), both featured highly-swept leading-edge extensions at the wing root, or 'strakes'. These strakes appear to have been first introduced to fix the unsteady or asymmetrical forebody separations on the aircraft, which could have caused problems of stability and control at high incidence. Further research (see, *eg* Staudacher⁴) has shown that the strakes may have beneficial effects at low speeds in delaying the conventional stall and reducing drag at high lift, at transonic speeds in reducing buffet intensity, and at supersonic speeds in reducing wave drag.

These prospects have encouraged further investigation of wing-strake combinations, and, in the course of a series of wind-tunnel tests at RAE, surface oil-flow photographs have been obtained. Fig 1 shows a comparison between the flow patterns at low speed on a wing of 40° leading-edge sweep and aspect ratio 3,

at 14° incidence, with and without a strake of 75° leading-edge sweep. It can be seen that, even for this moderate sweep of the outboard section, a separation near the leading edge is induced by the strake, at an incidence for which the flow over the same wing without the strake is attached. This Paper is concerned with possible mechanisms for this premature separation.

For a wing of given planform and thickness distribution, it is likely that the tendency of the flow to separate at the leading edge is dependent upon the magnitude of the leading-edge suction force, which is related to the coefficient of the inverse square-root singularity in the loading there, as given by the linearised theory of attached flow⁵. If, for instance, it is intended to avoid leading-edge separation on a sharp-edged wing, the mean surface of the wing is warped so that this coefficient vanishes. It might therefore be hoped that an indication of the effect of the strake could be obtained by calculating the attached flow over the planform, with and without the strake, and comparing values of this coefficient on the main wing outboard of its intersection with the strake leading edge. From the results of such a calculation it appears that the increase in leading-edge suction produced by the strake in wholly attached flow would probably be insufficient to explain the early separation on the outboard section of the wing.

In any case, it is clear that the vortex shed from the highly swept leading edge of the strake will modify the distribution of leading-edge suction, reducing it to zero along the strake itself. Accordingly, a simple representation of the flow with separation from the strake was devised, and the corresponding distribution of leading-edge suction over the main wing was calculated. This showed, as expected, that the suction near the kink in the leading edge is very small, though further outboard the increased upwash induced by the strake vortices produces an increase in leading-edge suction. It also emerged that the vortices induce a large sidewash in the neighbourhood of the kink in the leading edge. This outward component of velocity changes the direction of the flow approaching the leading edge of the main wing, increasing its effective angle of sweep and so encouraging separation there.

The appearance of leading-edge separation on the straked wing at a lower angle of incidence than on the basic wing is therefore attributed to:

- (a) an increase in the effective sweep of the leading edge of the main wing near the kink section, and
- (b) an increase in the effective incidence of the outboard sections of the main wing.

Both of these effects are caused by the strake vortices. It also seems likely that

- (c) a leading-edge vortex, formed on the outer wing near the kink, itself induces an outboard flow which tends to sustain the separation.

2 CALCULATION METHODS

2.1 Attached flow

Two methods, both lifting-surface treatments based on the linearised theory of subsonic flow, were used for the attached-flow calculations. One, due to Hewitt and Kellaway⁶, uses a global mode representation of the loading, with modes specially chosen to reflect the singular behaviour of the loading at the apex of the wing^{7,8}. The computer program was modified to calculate the coefficient of the singularity in the loading at the leading edge. This coefficient is defined as

$$G(y) = \lim_{n \rightarrow 0} n^{1/2} \ell(y, n), \quad (1)$$

where ℓ is the loading, y is a spanwise coordinate and n is the distance from the leading edge, measured normal to it. As $G(y)$ is dimensional, the convention is introduced that all lengths are scaled on the semi-span of the planform. The second method used is an iterative technique based on vortex lattice theory, developed by Sells at RAE and briefly described in the Appendix. In this program a term closely related to $G(y)$ is calculated as part of the standard output.

The planform selected for this study is one for which a lifting-surface theory calculation had already been performed by Kellaway⁹, using the method of Ref 6. It is shown as A in Fig 2, with an outline of the planform of the wind-tunnel model (which included a fuselage and a faired intake) shown as B for comparison. The basic wing, without strake, is obtained by extending the leading edge of the outboard section to the root in each case. Despite the differences between the planforms A and B, the qualitative results of the study are expected to be applicable to the experimental situation.

The two calculation methods were applied to the basic wing as a check of consistency: they predicted the same distribution of $G(y)$, except for a small discrepancy at the wing tip, introduced by rounding the planform corner in the method of Ref 6. It was concluded that the two methods could be used interchangeably on wings of this type.

When the strake is added ahead of the basic wing, a kink is introduced in the leading edge of the planform. It can be shown, from exact local solutions^{7,8} to the linearised, thin-wing problem in subsonic flow, that $G(y)$ should become infinite at such a concave corner in the leading edge. This singularity will not appear, unless specially incorporated, in results obtained by numerical methods. However, by selecting a vortex lattice that concentrated elements in the vicinity of the kink, the failure could apparently be localized to its immediate neighbourhood. The use of global modes in the method of Hewitt and Kellaway⁶ produced a much smoother variation of $G(y)$, which appeared unlikely to represent the effects of the change in sweep correctly. For this reason, the iterative method based on the vortex lattice and described in the Appendix was preferred for the determination of $G(y)$ on the straked planform.

2.2 Strake separation

The only methods available for calculating the flow over the strake with leading-edge separation rely on slender-body assumptions. In particular, they do not allow for the upstream influence of the main wing. This means that, for a plane strake of delta planform, they predict a conical flow in which the loading on the strake is uniform along conical rays through the apex. Calculations by Kellaway⁹ using the method of

Ref 6 on planform A of Fig 2 show that the attached flow is far from conical over the strake. The curves labelled LST (lifting surface theory) in Fig 3 show the variation in the attached flow loading along the conical rays on the strake. The abscissa, x/s , is the downstream distance measured in terms of the overall semi-span, so that the kink in the leading edge occurs at $x/s \doteq 0.94$. It is apparent that the loading approximately doubles over the length of the strake. A straightforward use of slender-body methods would therefore be inadequate and some adaptation is needed.

The increase in loading shown in Fig 3 must be due to the upwash induced by the bound vortices of the main wing. It is plausible that:

- (a) although this upwash falls off rapidly ahead of the wing, it varies little across the span of the strake; and
- (b) the induced upwash in the real flow is close to that calculated for the same geometric incidence by lifting surface theory for attached flow. This suggests that the lifting surface theory can be used to generate an 'equivalent lengthwise camber' of the strake, the amount of this camber being proportional to the geometric incidence of the wing. The limitation to purely lengthwise camber, in which cross-sections of the strake are plane, is necessary because this is the only case for which a general calculation method¹⁰ for leading-edge separation is available. The equivalent lengthwise camber is constructed by matching the loadings on the strake calculated for attached flow,

- (a) by lifting surface theory^{6,9} for the actual plane wing, and
- (b) by slender-body theory for the strake with equivalent lengthwise camber.

The loading according to slender-body theory can be obtained readily from the well-known expression for the velocity potential on a plane slit of semi-span $s(x)$ in an upward cross-flow $W(x)$:

$$\phi = \pm W(x)(s^2(x) - y^2)^{1/2}$$

where the upper and lower signs refer to the upper and lower surfaces of the slit. The loading $l(x,y)$ is then given by:

$$l = \Delta C_p = -\frac{2}{U} \Delta \frac{\partial \phi}{\partial x} = \frac{4}{U} \frac{\partial}{\partial x} \left(W(x)(s^2(x) - y^2)^{1/2} \right),$$

where U is the free-stream speed. For a delta wing of apex angle 2γ , $s(x) = Kx$, where $K = \tan \gamma$. For a lengthwise camber $h(x)$, measured downwards, superposed on a uniform incidence α :

$$W(x) = U(\alpha + h'(x)).$$

Hence

$$l(x,\eta) = 4K \left(\frac{\alpha + h'(x)}{(1 - \eta^2)^{1/2}} + xh''(x)(1 - \eta^2)^{1/2} \right), \quad (2)$$

where $\eta = y/Kx$ is a conical coordinate running from zero at the centre line to 1 at the leading edge. The problem is now to choose a function $h(x)$ so that the loading given by (2) matches the loading from the lifting surface theory shown in Fig 3.

A very simple approach was found to give adequate result. The camber was represented by a quartic polynomial

$$h(x) = h_0 + ax + bx^2 + cx^3 + dx^4, \quad (3)$$

where h_0 is a vertical displacement which does not affect the loading (2). The loading as given by (2) and (3) was then equated to the loading given by the lifting surface theory⁹ at four points along the conical ray $\eta = 0.7$. This yields four linear equations for the four constants a, b, c, d . The fitted, slender-body theory, loading which results is shown by the broken curves in Fig 3. The discrepancies are mainly due to the variation in the induced upwash across the strake semi-span; they are not large enough to discredit the approach adopted.

We note that the coefficients a, b, c, d are proportional to the incidence, α , of the wing. The camber line obtained is shown in the lower part of Fig 4. The camber is reflex, the local incidence falling from its value at the apex over the first part of the chord, though this is not obvious in the figure.

It is now assumed that the development of the leading-edge separation on the strake of the actual wing is approximated by the development of the leading-edge separation, as calculated by slender-body theory, on the strake with the equivalent lengthwise camber. The separated flow on the strake with lengthwise camber was calculated first using the method of Clark¹⁰, which uses a vortex-sheet representation of the leading-edge vortex. Convergence difficulties were experienced at low angles of incidence, probably because the local incidence initially decreases downstream of the apex. Further calculations at low angles of incidence were made using the isolated vortex representation of the leading-edge vortex, by an extension of Smith's technique¹¹. The two methods gave similar results for the overall circulation of the vortex, as shown in Fig 4 for an incidence of 0.15 radians. It is well known that the isolated vortex model predicts a vortex position too far outboard. This is relatively unimportant in the present context, since an error significant on the scale of the strake span is much less so on the scale of the overall wing span. The use of the inferior model therefore seems acceptable.

Each calculation method needs a conical starting solution: for the vortex sheet model this is taken from the solutions of Smith¹², for the isolated vortex model it comes from the solutions of Brown and Michael¹³. The conical starting solution must approximate to the exact solution for the non-conical wing at an initial station which is a small distance downstream of the apex. The conical solution chosen is the one determined by the local incidence and local leading-edge sweep at this initial station. The calculations then proceed by integration of ordinary differential equations in the downstream direction. An example of

the results obtained from Clark's method is shown in Fig 5, for $\alpha = 0.25$ radians. The departure from conicality is indicated in Fig 5 by the departure of the circles, which represent the positions of the vortex core in successive cross-sectional planes, from the crosses, which lie where the straight line drawn through the apex and the first of the circles meets the cross-sectional planes. Fig 4 shows the corresponding effects on the overall circulation. For a conical flow this grows linearly with distance downstream; the non-linear growth is particularly marked near the rear of the strake, where the influence of the main wing is strongest.

2.3 Overall flow

The calculation of the development of the strake vortex as far back as the kink in the leading edge has been described. It is assumed that this vortex is no longer fed by separation from the wing aft of this point, so that its overall circulation remains constant. This assumption is based on the interpretation of oil-flow patterns like that in Fig 1. It would not be appropriate if the outboard panel of the wing were highly swept and the kink in the leading edge were less pronounced. When Clark's method¹⁰ is used, the position of the vortex in the cross-flow plane through the kink is defined as the centroid of the circulation in the sheet and the core in that plane, as though an instantaneous rolling-up process occurred there. Finally, in order to calculate the upwash field induced over the wing by the pair of vortices shed from the strake leading edges as simply as possible, these vortices are replaced by a pair of infinite line vortices of this constant strength, parallel to the free-stream direction (and consequently parallel to the plane on which the wing boundary condition is satisfied), passing through the calculated position in the cross-flow plane containing the kink.

This pair of infinite line vortices induces an upwash which is equivalent to a simple twist of the wing. This twist was evaluated for an incidence of 0.25 radians, and the coefficient $G(y)$ of the leading-edge suction on this twisted wing was evaluated using the lifting-surface method of the Appendix. We note that in order to evaluate the loading over the wing we should have needed to consider the contribution to the Bernoulli relation made by the product of the mean sidewash induced by the line vortices and the jump in sidewash across the wing. We note also that the wake in this simple model is no longer force-free, because of the sidewash induced by the line vortices. We do not expect this to invalidate the conclusions drawn in the next section.

The distribution across the wing span of the downwash and sidewash induced by the pair of line vortices was also calculated for other angles of incidence, since these distributions depend on incidence in a highly nonlinear fashion; but no further lifting-surface theory calculations were made.

3 DISCUSSION

3.1 Results and their interpretation

As explained in the Introduction, the magnitude of the leading-edge suction, or the coefficient $G(y)$ of the singularity in the loading at the leading edge, provides a measure of the tendency of the flow to separate on a wing of given planform and thickness. Fig 6 shows the variation of $G(y)$ across the span for three cases. For the basic wing without a strake, the plain curve shows a fairly uniform level across most of the span, falling to zero at the centre section and the tip, as would be expected from the local solutions^{7,8} for convex leading-edge corners. Adding the strake, but still assuming the flow remains attached everywhere, gives the curve labelled with circles. As would be expected, this lies close to the previous curve outboard. It rises above the previous curve as the kink is approached, but remains within 10% of the basic wing value. The exact local behaviour involves an infinite peak at the kink which the numerical method does not reproduce. Inboard of the kink the level is much lower, because the sweep is higher; this portion of the curve is not of present interest. Under the assumption of attached flow, therefore, adding the strake produces some increase in leading-edge suction just outboard of the kink, though the increase looks to be too small to be responsible for the earlier separation there.

The third, broken, curve in Fig 6 is based on the more realistic model described in the previous section, in which the strake vortices are represented for an incidence of 0.25 radians. Over almost all of the strake, the values of $G(y)$ are negative, because the infinite vortex introduced to represent the effect of the strake vortex drives the flow downwards round the leading edge of the strake. The real flow separates at the leading edge of the strake and the suction vanishes there. Near the kink $G(y)$ does vanish, indicating that the vortex is in the right place and has the right strength at that streamwise station. Just outboard of the kink $G(y)$ lies below the curve for the basic wing, so that in this vital area this mechanism is not the cause of the early separation. Further outboard the level of $G(y)$ is raised by some 20%.

Fig 7 shows the upwash, w , induced in the plane of the wing by the pair of infinite vortices introduced to represent the strake vortices at $\alpha = 0.25$ radians. Immediately outboard of the kink this exceeds the level due to the basic geometric incidence, αU , and even at the tip is about 20% of αU . This explains the increased level of leading-edge suction on the outboard part of the main wing which appears in Fig 6. The variation of the induced upwash field with incidence is illustrated in Fig 8. We see that the induced upwash is nearly proportional to the geometric incidence on the centre line and near the tip, but varies little with incidence near the kink section.

Fig 7 also shows the sidewash, v , induced in the plane of the wing by the same vortex pair. This falls off very rapidly towards the tip, but under the starboard vortex, near the kink in the leading edge, it is very large, of the order of the free-stream speed. This sidewash represents a significant outboard deflection of the flow approaching the main wing immediately outboard of the kink, that is to say, a significant increase in the effective angle of sweep of the main wing in this region. Fig 9 shows that this increase in effective sweep persists at lower angles of incidence, though its lateral extent shrinks. The maintenance of the large sidewash at the lower incidences is due to the decrease in height of the vortex pair above the wing compensating for the reduction in circulation.

This increase in the effective sweep of the leading edge of the main wing immediately outboard of the kink is a mechanism by which leading-edge separation on the outboard wing is encouraged by the presence of a strake. Not only is separation provoked at a lower angle of incidence, but the separation which occurs

can be expected to be of the steady type associated with vortex formation at highly swept leading edges. The rapid reduction in the induced sidewash further outboard limits the spanwise extent over which this mechanism can operate. A second mechanism brought out by the present calculations is the increase in leading-edge suction over the outboard part of the main wing. This is expected to encourage leading-edge separation further outboard. Finally, we expect that a leading-edge vortex initiated immediately outboard of the kink generates an outflow beneath itself, spreading the reduction in effective sweep further outboard, so that the leading-edge separation is, in a sense, self-sustaining.

Whether, at a given incidence, the vortex initiated at the kink in the leading edge extends along the leading edge to the tip, giving a unified flow pattern, or whether it streams back across the wing as a part-span vortex, leaving a variable extent of quasi-two-dimensional flow at the tip, clearly depends on:

- (a) the strength of the strake vortex and its height above the wing;
- (b) the lateral position of the strake vortex in relation to the overall semi-span;
- (c) the geometric sweep of the leading edge of the outboard wing, including the tip shape; and, to a lesser extent,
- (d) the leading-edge profile, the thickness, and the warp of the outer wing.

3.2 Further remarks

The present study was aimed at explaining early separation at low speeds and at an incidence well below the stall of the straked wing, since these conditions lay within the scope of existing modelling techniques. However, it is worth speculating how far the large predicted outflows may go towards explaining more relevant features of the behaviour of straked wings. First let us consider the behaviour of the flow at low speeds and larger angles of incidence. If a unified flow pattern is set up with a separation of vortex type along the whole of the leading edge, then, on the analogy of the slender wing, we can expect this to persist in a steady and stable form up to large angles of incidence. Even without the achievement of a unified flow, the outflow is likely to reduce the unsteadiness associated with separations of the two-dimensional, bubble type and to delay the stall over as much of the wing as it affects, its action resembling that of lateral jet blowing. At higher speeds, any explanation of reduced buffet intensity is necessarily more speculative. However, the strake separation will take the same form at transonic speeds, so large local outflows will still arise. If we consider the strength of the outboard shock wave on a swept wing to be governed by the Mach number of the flow component normal to wing sweep, then it is clear that the superposition of an outboard lateral velocity reduces the shock strength through a reduction in the velocity component normal to the sweep direction. Moreover, if we associate buffet with flow separations of a basically two-dimensional character, then we can expect a reduction in buffet intensity from an outflow which introduces, or augments, an element of three-dimensionality in the separated flow.

4 CONCLUSIONS

The influence of a strake in reducing the angle of incidence at which leading-edge separation occurs on a swept wing is attributed to:

- (a) an increase in the effective angle of sweep of the leading edge of the main wing near the kink section, and
- (b) an increase in the effective incidence of the outboard sections of the main wing.

Both of these effects are caused by the velocity field induced by the strake vortices. It also seems likely that

- (c) a leading-edge vortex formed on the outer wing near the kink will itself induce an outboard flow which tends to sustain the separation.

It is suggested that the outflows induced by the strake vortices may be instrumental in delaying the low-speed stall of the wing and in reducing the intensity of buffet at high subsonic speeds.

Appendix

THE VORTEX LATTICE ITERATIVE METHOD

For a wing with given camber and twist, at a given incidence, the method is designed to produce a load distribution which varies smoothly over the planform, with appropriate behaviour at the edges, such that the downwash induced by the load distribution at a set of collocation points satisfies the boundary condition of zero velocity normal to the camber surface, this velocity being calculated in the mean plane of the wing. It exploits the flexibility and speed of the classical vortex-lattice method, and the accuracy of an existing method due to Sells¹⁴ for the calculation of the downwash field due to a wing with a given load distribution. The vortex-lattice method used was developed at RAE by G.A. Carr-Hill. Using these two methods in conjunction, the loading on the given wing can be determined by iteration. The present method was developed by C.C.L. Sells.

The vortex lattice method follows a standard pattern. The spanwise extent of the planform is divided into a series of chordwise strips, the distribution of which is governed by the limitations that no strip should cover the planform centreline, and that the farthest on-board strip should not extend to the tip, its distance from the tip being one quarter of its width. A further constraint, imposed by the downwash calculation and discussed later, is that any planform kink (excluding the apex) must lie on the centreline of a chordwise strip. At each strip, the loading system is represented by a set of N swept horseshoe vortices, whose pivotal points (the centres of the bound portions of the vortices) lie on the centreline of the strip at proportions of the local chord which follow a Multhopp distribution:

$$\xi_j = \frac{1}{2} \left[1 - \cos \left(\frac{(2j-1)\pi}{2N+1} \right) \right] ; \quad j = 1, \dots, N \quad (A-1)$$

The bound segments of the vortices lie along lines of local sweep and extend over the width of the strip. The trailing segments are continued rearwards in the mean plane of the wing, parallel to the centreline. An associated set of N downwash sensing stations is placed along the centreline of each strip with a distribution given by

$$x_j = \frac{1}{2} \left[1 - \cos \left(\frac{2j\pi}{2N+1} \right) \right] ; \quad j = 1, \dots, N \quad (A-2)$$

Each horseshoe vortex is regarded as a discretised representation of the continuously distributed bound vorticity over a section of the chordwise strip. A Multhopp distribution of the vortex pivotal points and downwash sensing stations is chosen because this concentrates points near the leading and trailing edges of the planform, where most detail is required in the representation of the load distribution, while avoiding the edges themselves. With the planform and vortex geometry so defined, the velocity induced at each sensing station by the three segments of each horseshoe vortex is calculated from the Biot-Savart law. As this calculation is linear in the vortex circulations, an influence matrix relating the induced velocities at the sensing stations to the strengths of the bound vortices can be set up. This matrix is then inverted and stored. Given the wing twist and camber distribution, and its incidence, the inverted matrix is used to determine the vortex strengths required to satisfy the normal velocity condition at the downwash sensing stations. It is here that a conventional vortex-lattice method would stop. Sells' modification proceeds to improve this solution, first calculating the downwash which the vortex-lattice load distribution induces in the mean plane of the wing at another set of points.

For the downwash calculation, it is first necessary to recover the values of the bound vorticity, $\gamma(x,y)$, from the pointwise concentrated circulations of the horseshoe vortices, $\Gamma(\xi_j, y)$, at the $L+1$ points on the centreline of each strip corresponding to the Weber distribution:

$$x'_j = \frac{1}{2} \left[1 - \cos \left(\frac{(j-1)\pi}{L} \right) \right] ; \quad j = 1, \dots, L+1 \quad (A-3)$$

This is carried out in two stages. First, the value of γ at a vortex pivotal point is found by equating two forms for the circulation:

$$\Gamma_s(\xi_j, y) \doteq \gamma(\xi_j, y) \delta x ,$$

where Γ_s is the spanwise component of the circulation of the bound vortex at the pivotal point and δx is the length over which the bound vorticity is distributed. Then

$$\delta x = c(y) \delta \xi \doteq c(y) \frac{d\xi}{d\phi} \delta \phi ,$$

where $c(y)$ is the local chord, and the non-dimensional chordwise coordinate ξ is related to the parameter ϕ by:

$$\xi = \frac{1}{2} (1 - \cos \phi) , \quad 0 \leq \phi \leq \pi . \quad (A-4)$$

Then, by (A-1), $\delta \phi = 2\pi/(2N+1)$, so that

$$\gamma(\xi_j, y) = \frac{(2N+1) \Gamma_s(\xi_j, y)}{\pi c(y) \sin \phi_j} \quad (A-5)$$

where ϕ_j corresponds to ξ_j through (A-4). This expression is exact in the case of a Multhopp distributed vortex lattice system on a two-dimensional flat plate¹⁵, when values of γ as calculated by linear theory are compared at the pivotal points. The corresponding values at the Weber points are then obtained by a chordwise cubic-spline interpolation method. The loading, $l(x,y)$, is simply related to γ by:

$$l(x,y) = \frac{2\gamma(x,y)}{U} . \quad (A-6)$$

The downwash calculation also requires that the chordwise lines on which the loading is defined (strip centrelines) must include planform cranks. This imposes the condition on the panelling system mentioned earlier. With the loading now defined at suitable stations, the integration technique of Ref 14 is followed. The downwash is calculated at the Weber points along each strip centreline, and these values are compared with those required by the wing twist, camber and incidence to satisfy the normal velocity condition at those points. The residual errors are evaluated and then interpolated back to the vortex lattice sensing stations, x_j . These error values are then inserted into the influence matrix equation, and a set of corrections to the circulations of the vortex-lattice system is calculated. The corrections are added to the previous circulation values for re-submission to the downwash calculation routine, so continuing the iteration cycle. The sequence is terminated when sufficiently small error levels have been achieved, or the variables of interest (here the coefficient of the leading-edge singularity) have ceased to change significantly. Convergence difficulties have been experienced in two circumstances: the attempt to calculate the properties of very highly swept wings and the use of vortex-lattice panels of very low aspect ratio. No difficulties were encountered in the applications reported here.

REFERENCES

1. D. Küchemann The aerodynamic design of aircraft, *to be published*, p 254, Pergamon Press (1978)
2. J.K. Buckner and P.W. Hill Aerodynamic design evolution of the YF-16. AIAA Paper 74-935 (1974)
3. J. Patierno YF-17 design concepts. AIAA Paper 74-936 (1974)
4. W. Staudacher Verbesserung der Manoevertimeen im hohen Unterschall in DLR-Mitt. 73-04, given at DGLR Symp. Göttingen, Paper 72-129 (1972) also NASA TT-F-15406 (1974)
5. A. Robinson and J.A. Laurmann Wing theory. p 172, Cambridge University Press (1956)
6. B.L. Hewitt and W. Kellaway A lifting surface theory method for treating swept or slender wings in attached subsonic flow. BAC(MAD) Report Ae 351 (1973)
7. Patricia J. Davies The load near the apex of a lifting swept wing in linearised subsonic flow. RAE Technical Report 72031 (ARC R&M 3716) (1972)
8. R.T. Medan Aerodynamic loads near cranks, apexes and tips of thin lifting wings in incompressible flow. Paper 18 of AGARD-CP-204 (1977)
9. W. Kellaway Private communication.
10. R.W. Clark Non-conical flow past slender wings with leading-edge vortex sheets. RAE Technical Report 76039 (ARC R&M 3814) (1976)
11. J.H.B. Smith A theory of the separated flow from the leading edge of a slender wing. RAE Technical Note Aero 2535 (ARC R&M 1316) (1957)
12. J.H.B. Smith Improved calculations of leading-edge separation from slender delta wings. Proc. R. Soc. Lond. A 306, pp 67-90 (1968) RAE Technical Report 66070 (1966)
13. C.E. Brown and W.H. Michael On slender delta wings with leading-edge separation. Journ. Aeron. Sci. 21, pp 690-4 and 706, (1954) NACA TN 3430 (1955)
14. C.C.L. Sells Calculation of the induced velocity on and off the wing plane for a swept wing with given load distribution. RAE Technical Report 69231 (ARC R&M 3725) (1969)
15. R.H. Doe The vortex lattice method applied to thin aerofoil theory with general lattice spacing. BAC(CAD) AERO/TN/RHD/LJF/342 (1972)

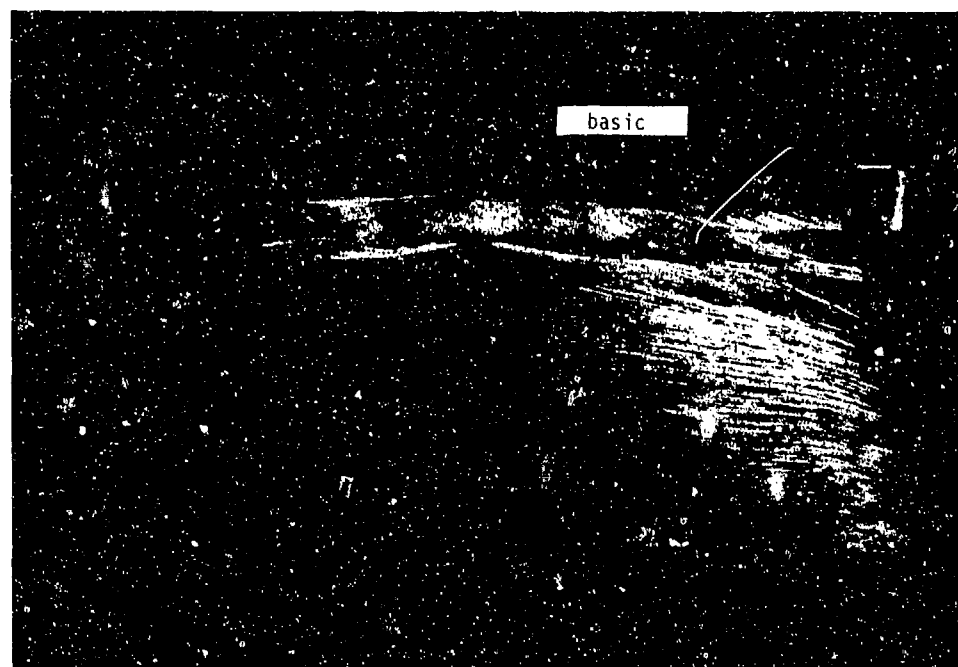
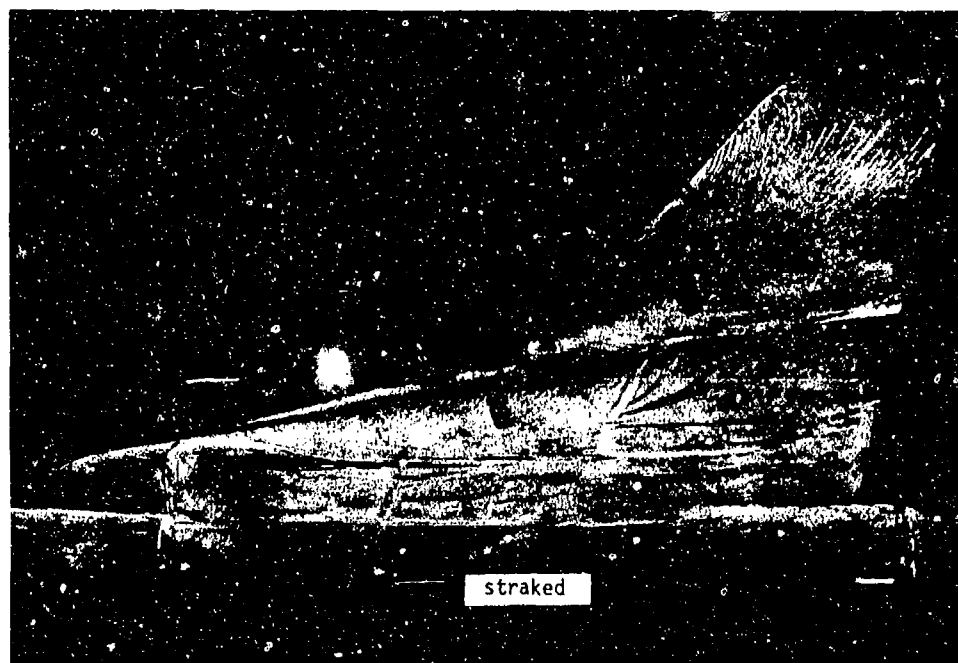


Fig 1 Surface oil-flow on swept wing, low speed, 14° incidence, with and without strake

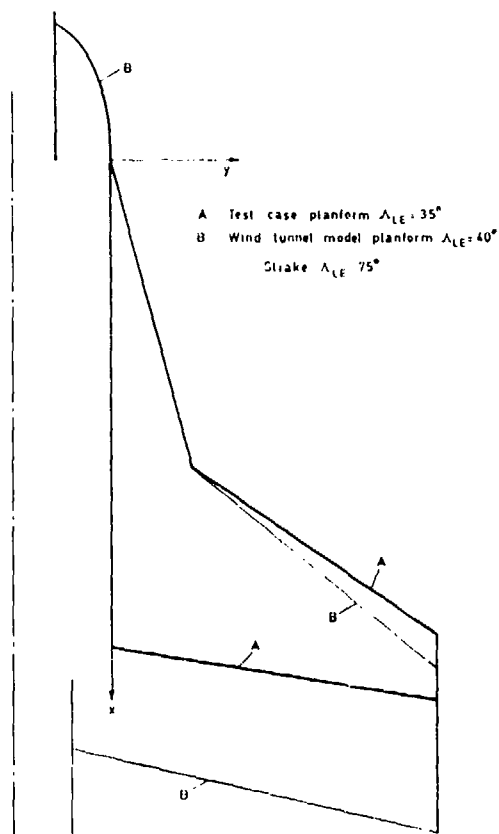


Fig 2 Planform of calculations compared with wind-tunnel model

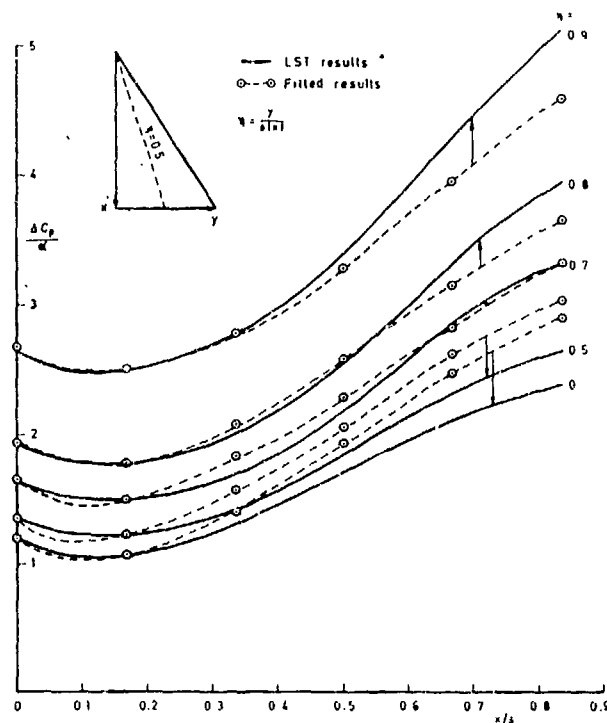


Fig 3 Results of camber fit - loading match

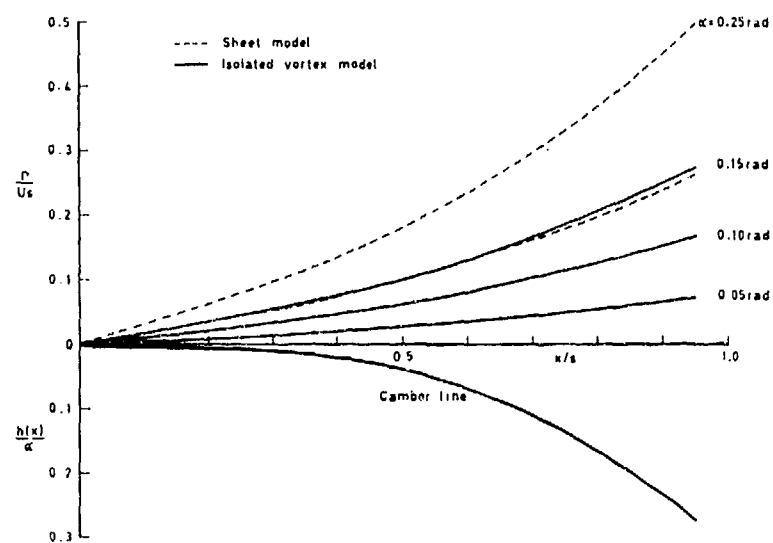


Fig 4 Fitted camber line and vortex circulation results

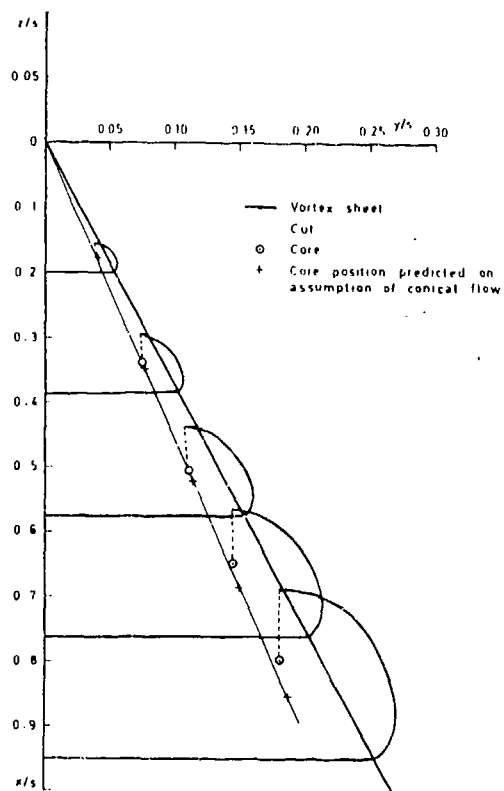


Fig 5 Cross-sections (at constant x/s) of calculated vortex system on strake

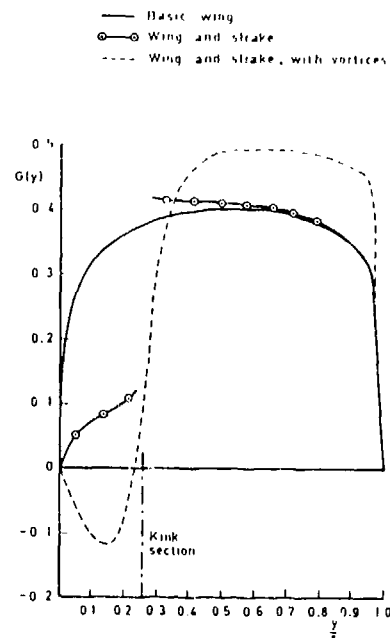


Fig 6 Coefficient of singularity in loading at leading edge

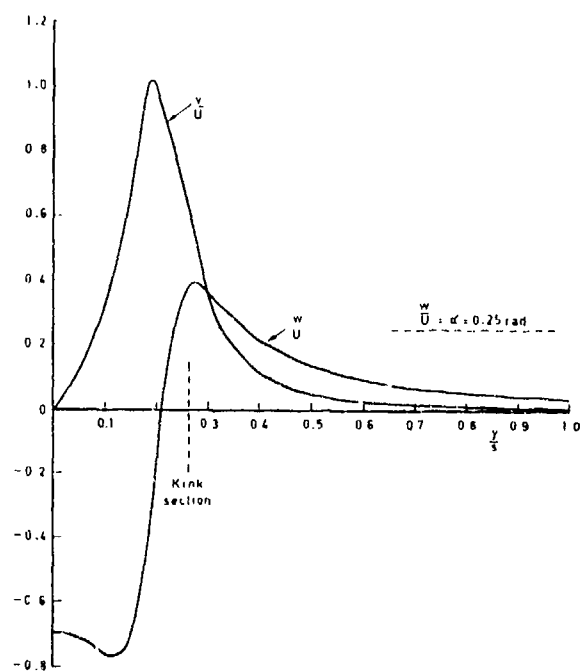


Fig 7 Velocities induced in wing plane by vortex pair

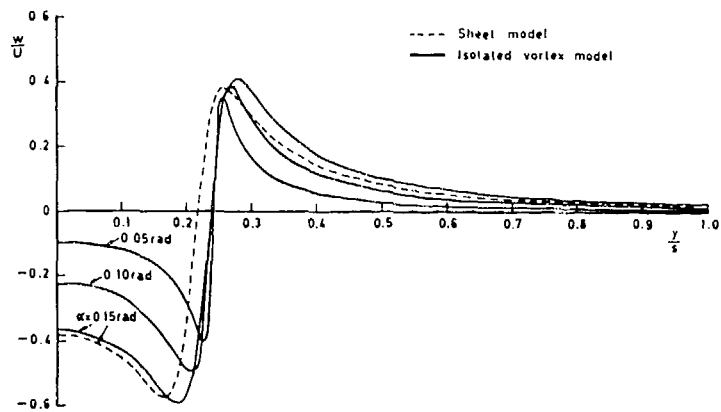


Fig 8 Variation of strake vortex downwash field with incidence

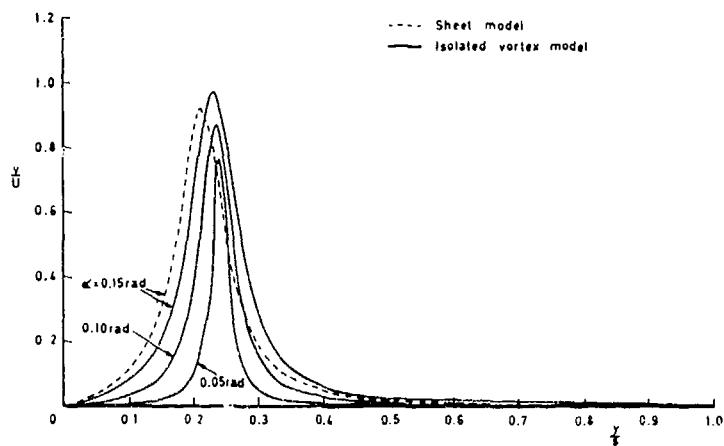


Fig 9 Variation of strake vortex sidewash field with incidence

AERODYNAMIC CHARACTERISTICS OF A FIGHTER-TYPE
CONFIGURATION DURING AND BEYOND STALL

by

W. STAUDACHER

PH. POISSON-QUINTON

B. LASCHKA

J.P. LEDY

MBB, W.-Germany

O.N.E.R.A., France

S U M M A R Y

In a German/French cooperation between MBB and ONERA an experimental investigation was conducted in order to study stability and control characteristics of a fighter-type configuration at extreme incidences.

Low speed wind tunnel tests were conducted with a MBB pilot model in the tunnel S1/ONERA Modane (ϕ 8m). Angle of attack regime investigated comprised $\alpha = 0 + 90^\circ$. Emphasis of the study was directed towards the stability and/or control contributions of configurational items such as strakes, canards, tails, rudders and controls and maneuver flap systems as well as the technique of "concentrated, spanwise blowing".

Isolated and combined effects of those devices and systems are demonstrated, some unconventional control devices are introduced.

1. INTRODUCTION

Since 1969 MBB is conducting an experimental investigation which is concerned with the development of "wings with controlled separation", i.e. hybrid wing planforms and strake wings. The scope of this programme, sponsored by the German Ministry of Defence within the so-called ZTL-Programm, is sketched in Fig. 1.

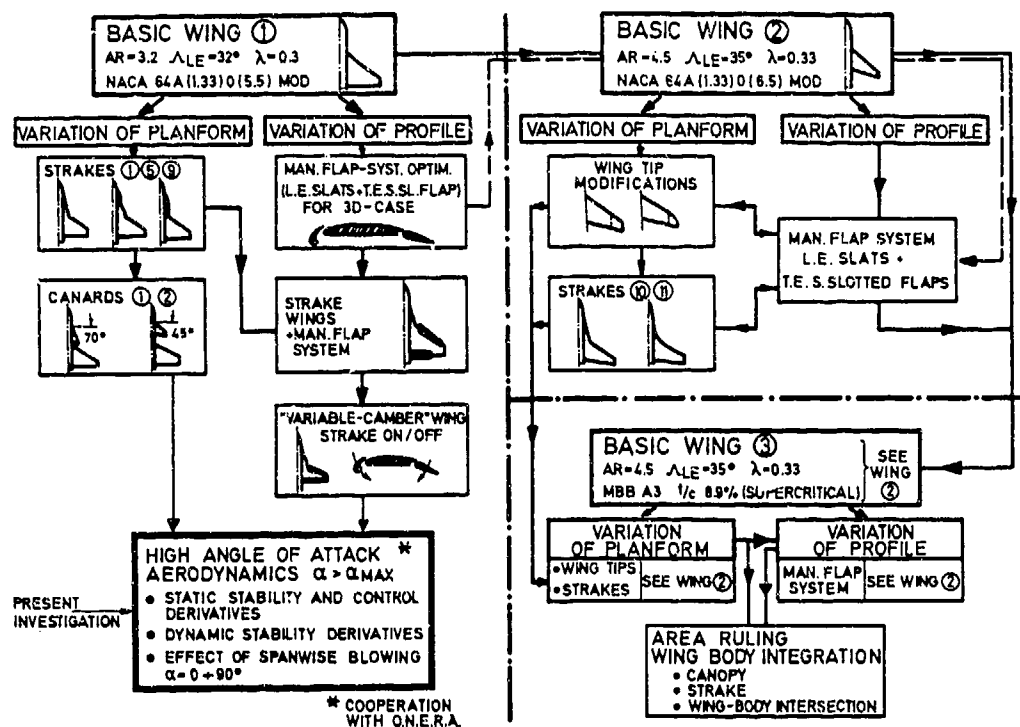


FIG.1 SCOPE OF EXPERIMENTAL PROGRAMME AND PRESENT INVESTIGATIONS

Part of these investigations was carried out in a working group named after the above mentioned objective "Wings with Controlled Separation", with members from research institutes (DFVLR) and industry (MBB, VFW-F). Based on different wing shapes (see Fig. 1, basic wings ① + ③) effects of planform modifications and profile variations were systematically investigated in the M-number regime $0.1 \leq M \leq 2.0$ in such a way, that from any status of the programme effects could be traced back and compared to the basic data in incremental form (this means that from step to step only one parameter was changed for sake of clarity). So all the modifications were done in strict analogy for the different planforms (strakes, canards, maneuver flap systems etc.).

Basic wing ① came out to have outstanding maneuver performances in combination with a slender strake (9 strake planforms were investigated), which extended the conventional maneuver boundaries to highly increased angles of attack. Hence it was decided to find out the performances of this configuration in the complete a.o.a. regime $\alpha = 0 + 90^\circ$.

This latter investigation was performed in the course of a French/German cooperation between O.N.E.R.A. and MBB, starting in 1976 and being concerned with the themes denoted in Fig. 1 as "Present Investigation".

2. MODELS AND APPARATUS

The investigation reported herein is based on static and dynamic tests with analogous models in various wind tunnels. Previous data were derived from extensive tests in the 3 x 3m Low Speed and 1 x 1m Transonic Wind Tunnel of DFVLR-AVA Göttingen. The models used are the MBB low speed or high speed pilot model respectively.

The configuration dealt with in the present investigation up to extreme a.o.a. is shown in Fig. 2. The original configuration with basic wing ① ($AR = 3.2 / \Lambda_{LE} = 32^\circ / \lambda = 0.3$) is modified by detachable strakes (here: strake ① with a straight L.E. 75° swept back) the exposed area of which is 11% of the reference area of the basic wing.

The strakes can be replaced by canards of the same area. The wing itself is equipped with a maneuver/high lift system, consisting of L.E. slats and single slotted T.E. flaps of Fowler-type, extending over 2/3 of the exposed span. Roll control is provided by tip ailerons and the all moving horizontal tail (taileron). Directional control is achieved by a conventional full span rudder. Forebody fins (some times denoted as "nose strakes" or "planning fins") are used to trigger symmetric vortex shedding from the pointed nose. All controls and rudders have an extended range of deflection up to $\pm 90^\circ$ (see Fig. 2).

The model further incorporates a system for spanwise blowing from a position 10% behind the strake L.E., blowing parallel to it.

Convergent, usually supercritical driven nozzles were used. The blowing system itself was sting fixed thus providing reaction-force free, mere aerodynamic effects. All low speed static tests in the a.o.a. regime $\alpha = 0 + 90^\circ$ were run in the tunnel S1 of O.N.E.R.A. Modane. Fig. 3 gives a photo of the model at $\alpha = 90^\circ$ mounted on a special rear sting support system in the 8m ϕ test section of S1.

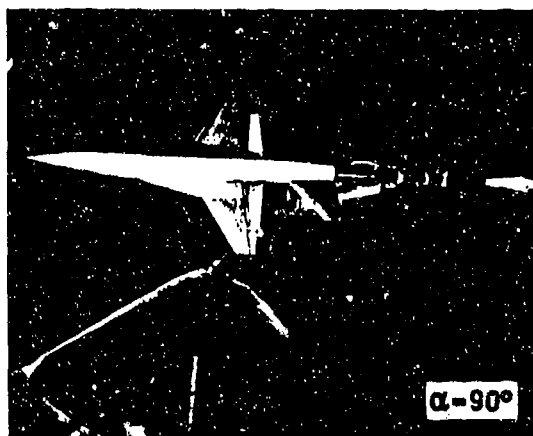


FIG. 3 PILOT MODEL IN TUNNEL S1,
ONERA, MODANE
(TEST SECTION 8m ϕ)

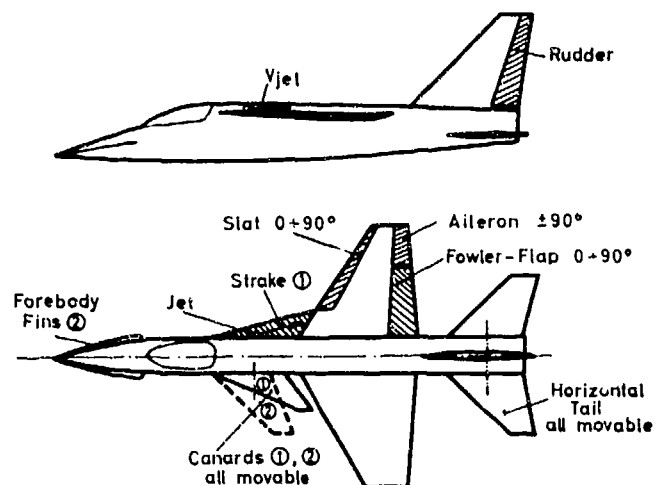


FIG. 2 PILOT MODEL

Dynamic tests were carried out using forced oscillation techniques up to $\alpha = 50^\circ$ with the weight reduced (50%) high speed pilot model in S2 Modane and later in the very new FAUGA F1 tunnel, Toulouse.

3. RESULTS

3.1 Previous Investigations

From extensive preceding tests the positive effects of an additional strake on performances and flying qualities are well known and will be summarized briefly here, as they are documented elsewhere (References [1] + [15]).

Proper combination of a slender strake with a moderately swept basic wing will result in drastic improvements. The most important ones are found for subsonic/transonic performances as increased maximum usable lift and reduced lift dependent drag at high incidences. Buffet characteristics are strongly affected in a positive sense for lift level and buffet intensity (penetration) as well. In the supersonic speed regime reductions of wave drag and trimmed induced drag are found simultaneously.

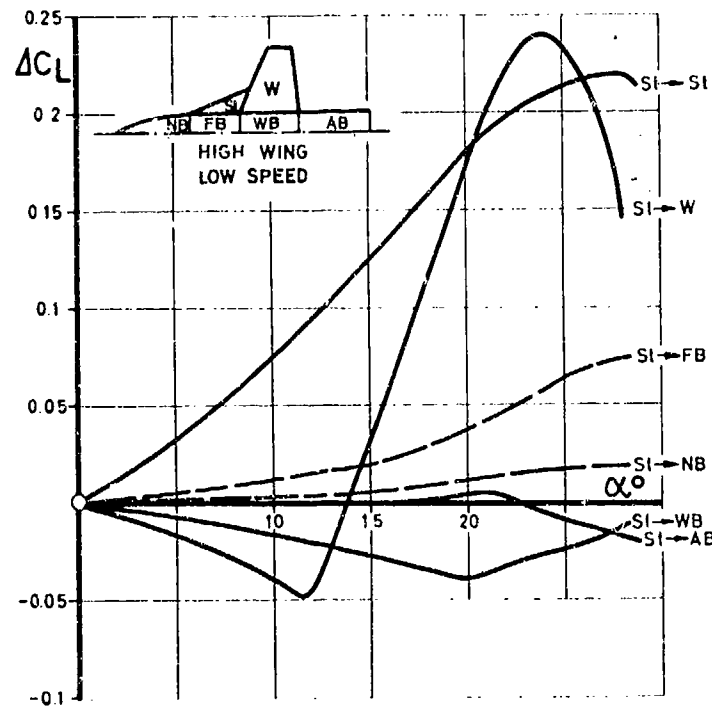


FIG. 4 INTERFERENCE LIFT OF THE STRAKE

These overall effects being well understood, Fig. 4 wants to give a measure for the degree and location of positive interaction between the strake and the rest of the configuration. Interference lift increments ΔC_L due to the strake are compared for different parts of the configuration. Data were derived with the VFW sectional load technique (Ref.[6]), subdividing the wing-body combination in segments as denoted in Fig. 4 by nose-, fore-, wing- and afterbody and by segments of the exposed wing (strake and basic wing), each equipped with its own balance. Results obtained with this technique were found to be in good agreement with pressure distribution data (Ref.[7]) taken from an analogous model.

Lift carry-over due to the strake is positive for the nose-body (NB) and fore-body section (FB), but is negative for the part designated wing-body (WB), lift of afterbody remains nearly unchanged. Interference of strake on wing is negative for low to moderate a.o.a., but when maximum angle of attack of the basic wing is approached positive interference lift is developing rapidly (St \rightarrow W), reaching a peak value near maximum lift of the strake configuration. To give some figures, about 40% of the additional maximum lift are acting on the strake itself, the same is true for the interference of the strake on the basic wing.

The leaving 20% of incremental lift are positioned on the body besides and in front of the strake, i.e. forebody and nose body.

3.2 Present Investigation

The present investigation may be divided in three major points of interest, concerning the characteristics of the configuration at extreme angles of attack in respect of

- static stability and control including
- effect of spanwise blowing
- dynamic stability derivatives

3.2.1 Longitudinal static data

Analysis is concentrated here on the effects of planform modifications such as strake or canards and the influence of spanwise blowing on the strake wing. It shall be pointed out again that all these modifications used here are devices to generate or stabilize and control concentrated stable vortex systems.

In Fig. 5a the effect of strake and/or spanwise blowing on lift and pitching moment is given and is compared to the data of the unmodified basic wing. There is an increase of about 60% in maximum lift due to the additional strake ($\Delta C_{Lstr} \textcircled{1}$), simultaneously applying spanwise blowing gives a further increment $\Delta C_{Lc_{\mu}} = 0.1$ of about the same magnitude for a blowing coefficient $c_{\mu} = 0.1$.

There is a "quasi-camber effect" induced by spanwise blowing at low lift coefficients, shifting the lift curves with increasing c_{μ} like positive flap deflections tend to do. This effect is not found for the pitching moment characteristics. Spanwise blowing neither altering zero pitching moment nor basic stability, center of pressure and neutral point locations remain roughly constant. But the pitch-up tendency of the unblown strake configuration is favorably reduced linearizing the pitching moment curves up to extended range of incidences.

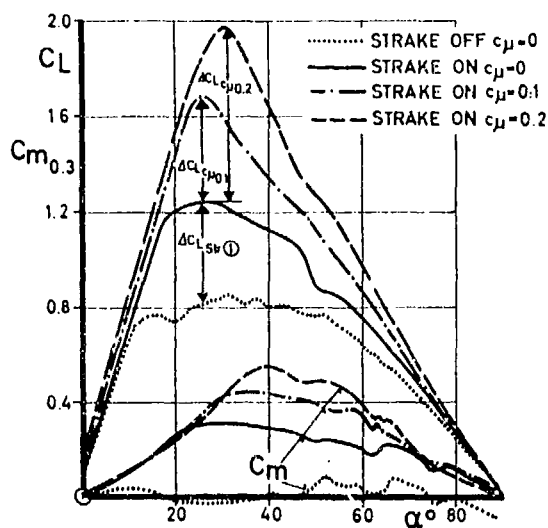


FIG. 5a EFFECT OF STRAKE AND/OR SPANWISE BLOWING ON LIFT AND PITCHING MOMENT (TAIL OFF)

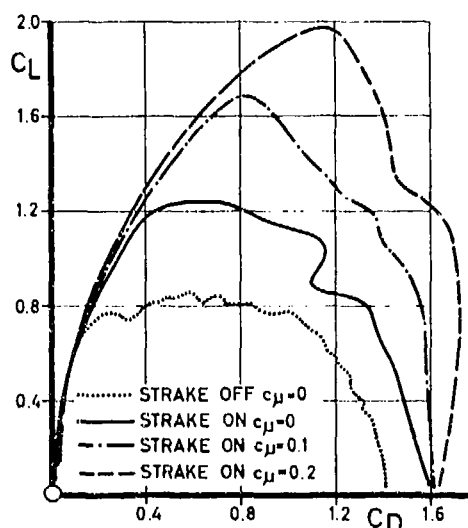


FIG. 5b EFFECT OF STRAKE AND/OR SPANWISE BLOWING ON DRAG-DATA (TAIL OFF)

Fig. 5b compares the drag characteristics, induced either by the strake and/or spanwise blowing. A more detailed analysis at low incidences would again show the above mentioned camber effect due to spanwise blowing, manifested in a cross-over of the drag polars and a shift of minimum drag to increased lift coefficients with increasing blowing intensity c_{μ} (see References [19], [23]). The reduction of lift dependent drag at high angles of attack is directly related to the development of additional non-linear lift either by the strake and/or spanwise blowing, not restoring L.E. suction but reducing a.o.a. for a given lift coefficient.

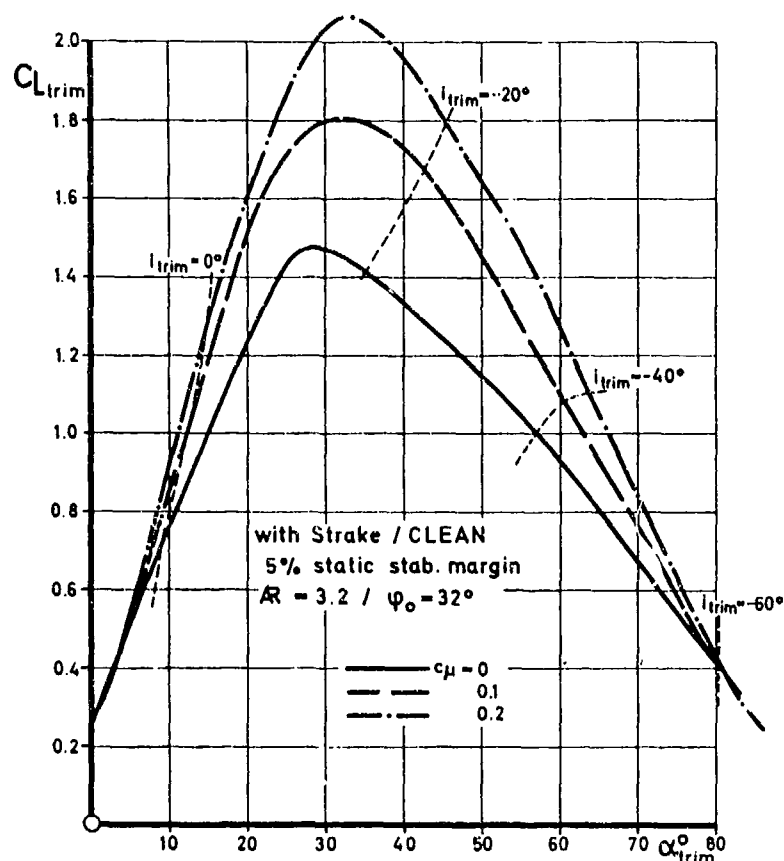


FIG. 6 TRIMMED LIFT POLARS FOR DIFFERENT BLOWING INTENSITIES c_μ

Trimmed lift data are given in Fig. 6, again demonstrating the excess lift produced by spanwise blowing up to angles of attack $\alpha \approx 80^\circ$. The all moving low horizontal tail provides sufficient trim power for all incidences, see Fig. 7. For an assumed static stability margin of 5% the horizontal tail trim settings i_{trim} are plotted versus the trimmed angle of attack for the unblown configuration and with spanwise blowing ($c_\mu = 0.1/0.2$). Trim characteristics are almost linear, spanwise blowing alleviating trimming as indicated by the reduced elevator deflections for constant angle of attack.

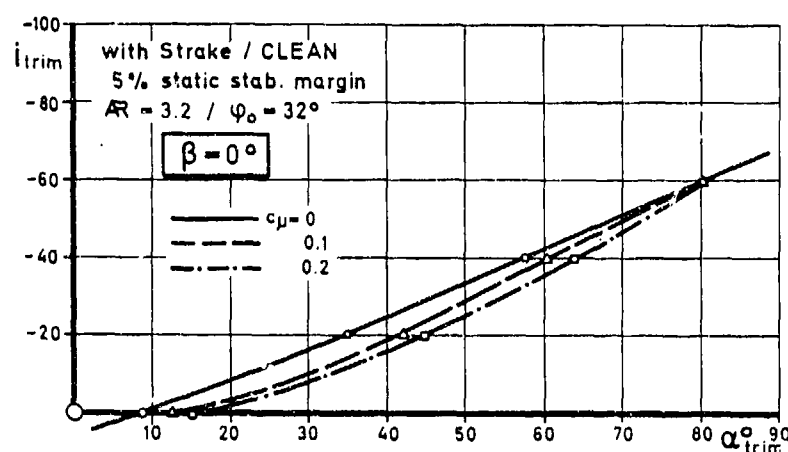


FIG. 7 HORIZONTAL TAIL TRIM ANGLES AS AFFECTED BY ANGLE OF ATTACK AND SPANWISE BLOWING

The strake can be replaced either by the slender canard (C1) ($\Lambda_{LE} = 70^\circ$) or the moderately swept canard (C2) ($\Lambda_{LE} = 45^\circ$) of identical wetted area (11% of the basic wing reference area). Comparison of the lift produced by the different configurations is given in Fig. 8a, demonstrating the superiority of the strake design.

This is further high-lighted by the corresponding drag curves plotted in Fig. 8b. Nevertheless the canards are helpful as trim and control devices for longitudinal and lateral/directional motions and can be favorably used for CCV-modes like direct lift control, sideforce control and maneuver enhancement etc, thus introducing a certain amount of flexibility for the design process.

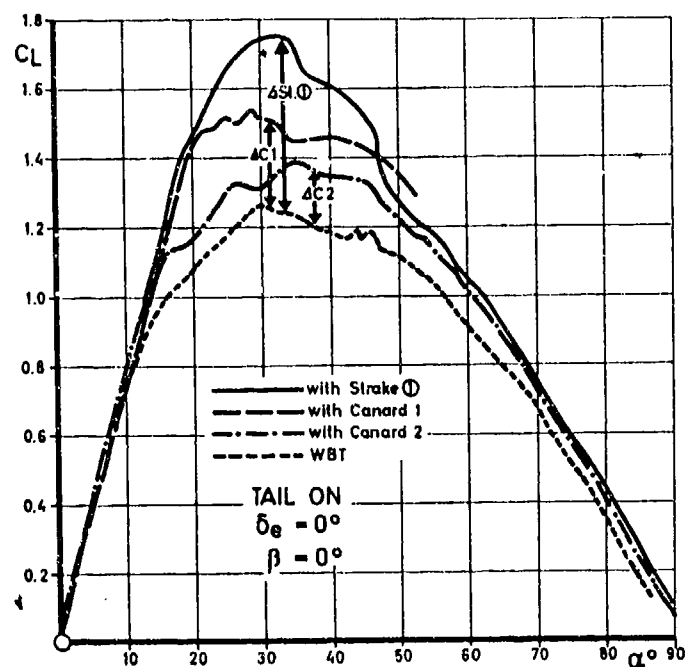


FIG. 8a EFFECT OF STRAKE OR CANARDS ON LIFT

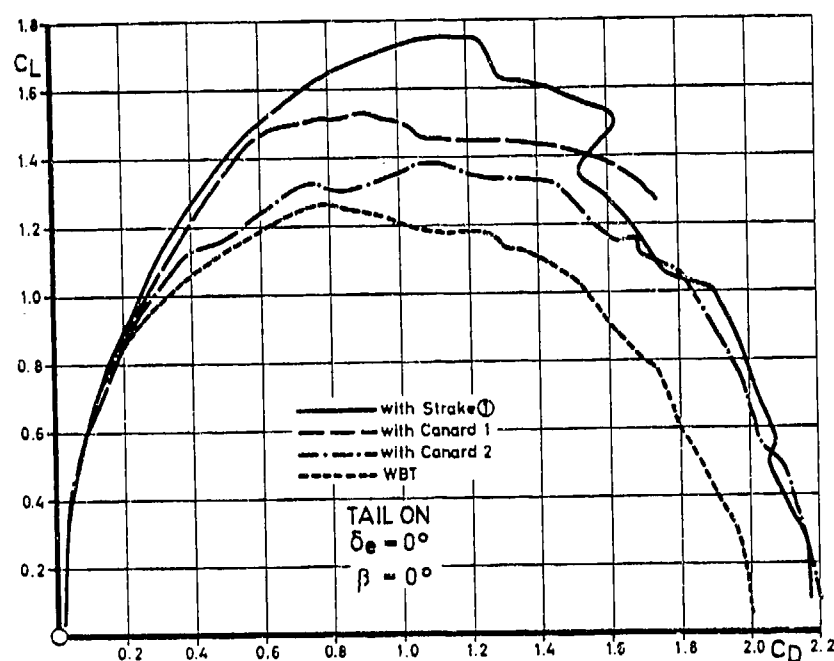


FIG. 8b EFFECT OF STRAKE OR CANARDS ON DRAG

3.2.2 Buffet tracking

Buffet characteristics were traced with strain gauges to determine the RMS data of wing root bending and torsional moments. Additional information was supplied by two tip accelerometers positioned at 25% and 65% tip chord. Results obtained with the different sensors all give the same message presented in Fig. 9 for the wing root bending moment RMS data.

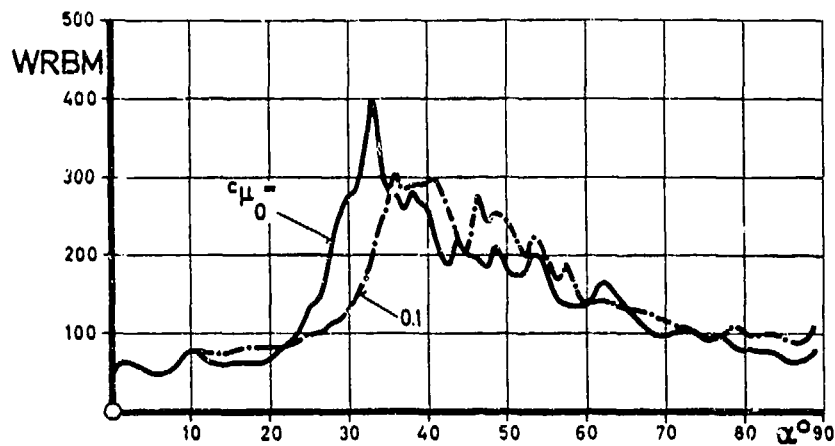


FIG. 9 EFFECT OF SPANWISE BLOWING ON
BUFFET INTENSITY
(RMS-DATA OF WING ROOT BENDING
MOMENT OSCILLATION)

Comparison of the strake wing with/without spanwise blowing indicates:

- some additional slight disturbances are induced by spanwise blowing at low incidences
- divergence a.o.a. is shifted to higher values thus an increase of buffet onset lift ($CL_{c\mu=0} = 1.2 / CL_{c\mu=0.1} = 1.68$) of 40% is found for $c\mu = 0.1$
- peak loads develop at angles of attack slightly above maximum lift
- peak intensities are reduced by spanwise blowing, despite of the higher static max. lift of the blown wing
- with further increased incidences buffet intensities vary approximately with the corresponding static lift and tend to level out at the niveau of the basic low angle of attack data.

3.2.3 Lateral/directional static data

Longitudinal motion came out to be the less problematic case for the poststall a.o.a. regime from an aerodynamic point of view. Stability and control was simply achieved by conventional devices with extended range of deflection (elevator, canards, flaps etc.). Main problems to be solved arose from lateral/directional stability for this configuration.

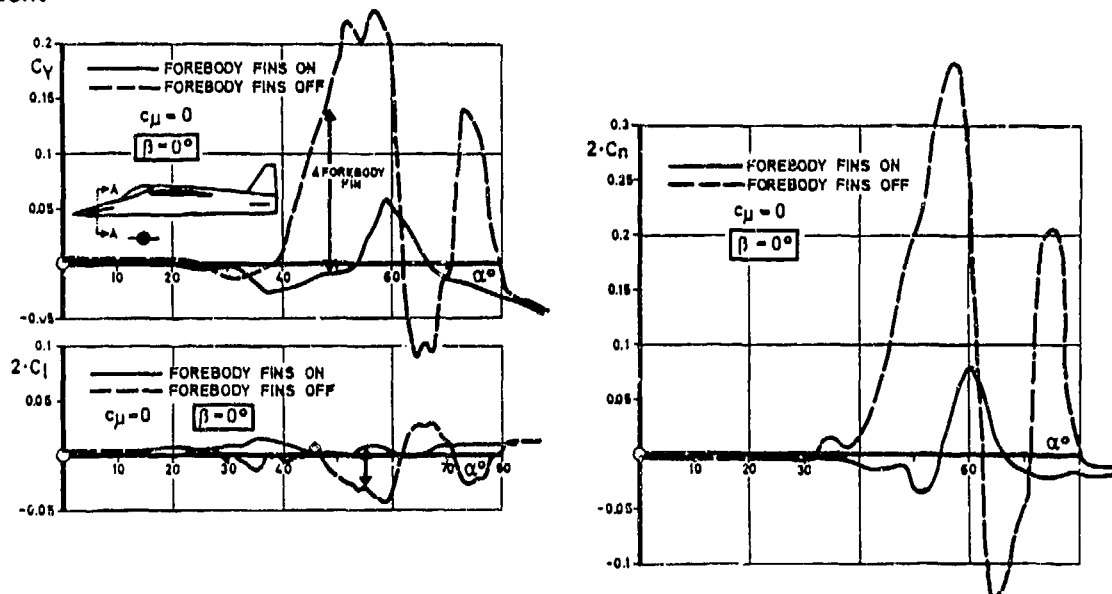


FIG. 10 EFFECTS OF ASYMMETRIC VORTEX SHEDDING ON
LATERAL / DIRECTIONAL CHARACTERISTICS FOR
ZERO-SIDESLIP, INFLUENCE OF FOREBODY FINs.

Even for symmetric flow ($\beta = 0^\circ$) large excursions were found for sideforce and yawing moment, Fig. 10, which are traced back on asymmetric vortex shedding from the pointed nose of the body at angles of attack near 50° (positive sideforces inducing positive yawing moments). Slender forebody fins were placed in the nose region of the configuration, immediately curing this deficiency. Fig. 11 is showing the answer on where the "nose strakes" should be placed longitudinally. Dividing the resulting moment by the acting force is giving the position of the resultant force. It is evident that

- the disturbances have their origin in the nose/forebody region of the configuration
- the "nose strakes" should extend longitudinally roughly up to the cockpit, thus triggering symmetric vortex shedding in a most efficient way.

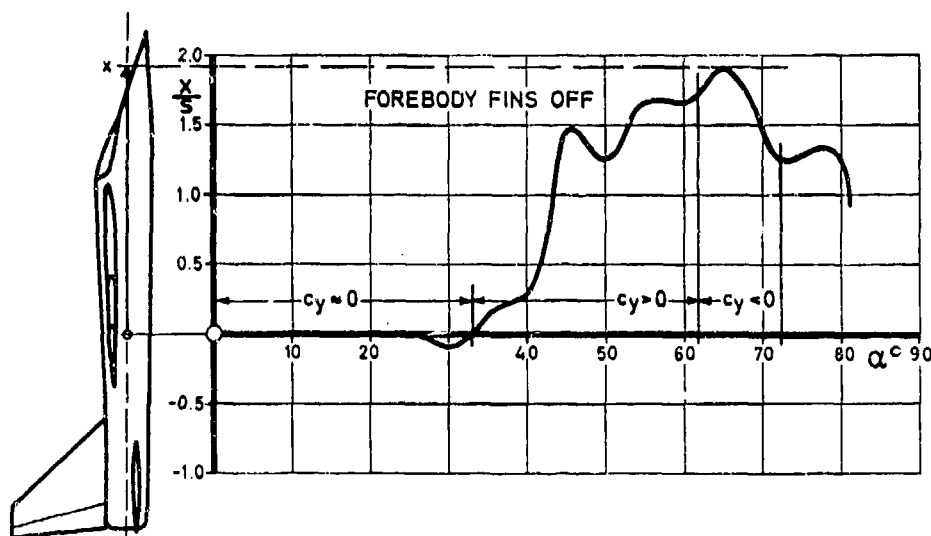


FIG. 11 LONGITUDINAL LOCATION OF RESULTANT SIDEFORCE, INDUCING YAW DIVERGENCE FOR ZERO SIDESLIP ($\beta = 0^\circ$)

From the simultaneous oscillations of sideforce and yawing moment data (depicted in Fig. 10) Fig. 11 can be divided in regions of zero sideforce ($0^\circ \leq \alpha \leq 33^\circ$), positive sideforce ($33^\circ \leq \alpha \leq 62^\circ$), negative sideforce ($62^\circ \leq \alpha \leq 72^\circ$) and so on, demonstrating that there is a certain amount of instability in the formation of those body vortices with increasing angle of attack, producing abrupt changes within about 2 degrees of incidence.

Another problem now related to asymmetric flow conditions ($\beta \neq 0$) at high a.o.a. is the loss and divergence of effective dihedral $C_{l\beta}$, which is regarded to be a vital problem for any high maneuverable fighter configuration. When establishing the stability parameter $C_{n\beta}$ dynamic, which is accepted as a criterion for lateral/directional divergence, $C_{l\beta}$ is multiplied by the inertia ratio I_z/I_x , thus growing in importance for slender (fighter-type) aircraft.

The next two Figs. 12a, 12b serve as a visual aid to explain how the divergence of $C_{l\beta}$ is developing for this specific configuration with the straight strake ①.

In Fig. 12a flow patterns on the windward and leeward half of the configuration are presented for an angle of attack of $\alpha = 20^\circ$, just near the point of lateral divergence as shown in the lower part of the figure. As can be seen from the oilflow graphs flow patterns of both wing halves are characterized by the presence of a strong strake vortex. Beginning disorientation is indicated on the windward wing tips ($\beta = +5^\circ$).

Now turning over to Fig. 12b it is evident that at $\alpha = 30^\circ$ the strake vortex has burst over the windward wing half and separation has progressed inboard from the tip. On the leeward wing there is still a stable strake vortex, interfering much further outboard. It is obvious from this comparison that there must be a lateral instability, which is indicated by the development of the rolling moment C_l on the bottom of Fig. 12b.

This is directly caused by the reduction of effective sweep on the protruding strake L.E. and is more pronounced for straight leading edges. This deficiency can be cured

by different means like tailoring the strake (planform and curvature of L.E., L.E. flaps on the strake), use of L.E. slats on the basic wing and wing-body modifications. This is shown in the paper by H. JOHN and W. KRAUS, the primary task of the present investigations was to define the problems when encountering extreme angles of attack.

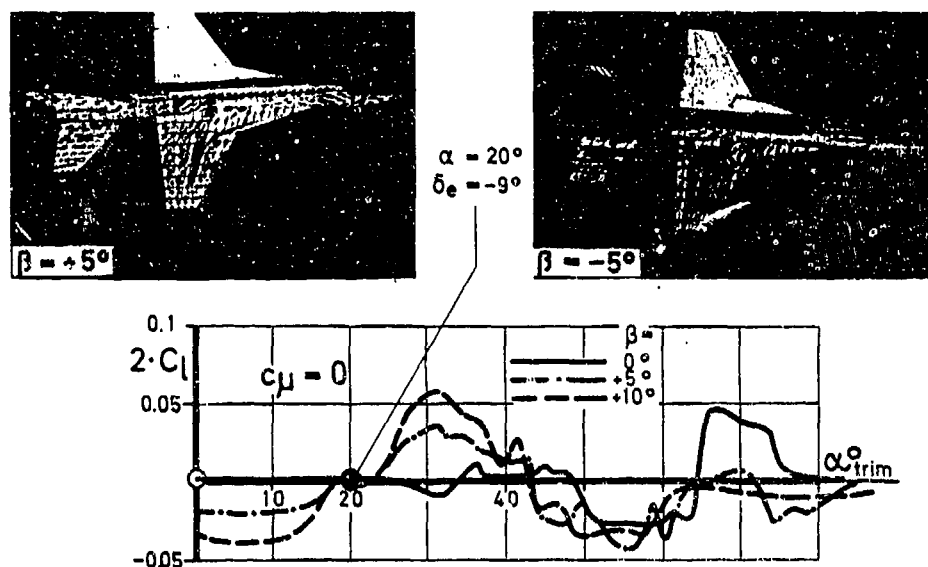


FIG. 12a DIVERGENCE OF EFFECTIVE DIHEDRAL $C_{l\beta}$ FOR STRAKE-WING CONFIGURATION, $\alpha = 20^\circ$

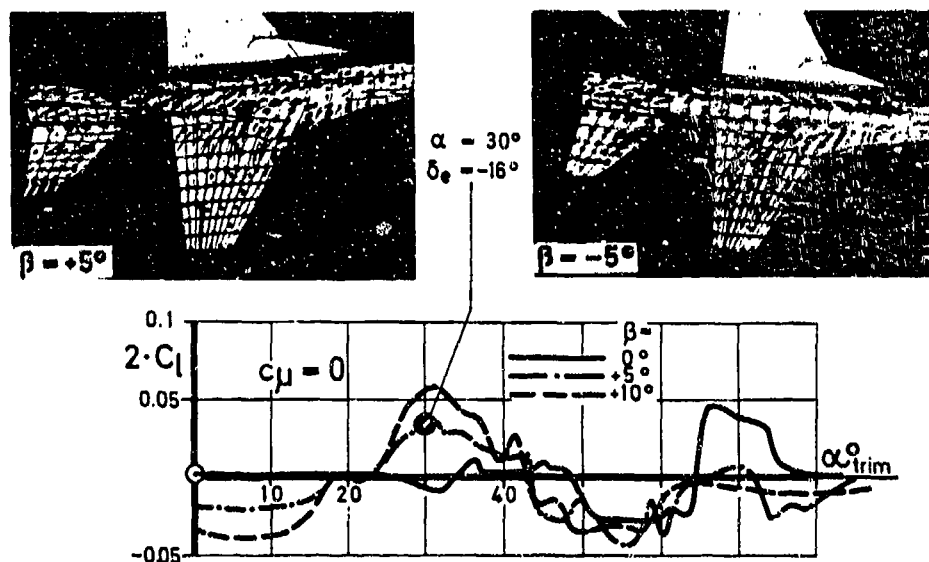


FIG. 12b DIVERGENCE OF EFFECTIVE DIHEDRAL $C_{l\beta}$ FOR STRAKE-WING CONFIGURATION, $\alpha = 30^\circ$

An additional possibility to stabilize $C_{l\beta}$ at near stall incidences is shown in Fig. 13. Use of symmetric spanwise blowing is stabilizing the vortex system restoring controlled separation and is increasing maximum lift and angle of attack of max. lift.

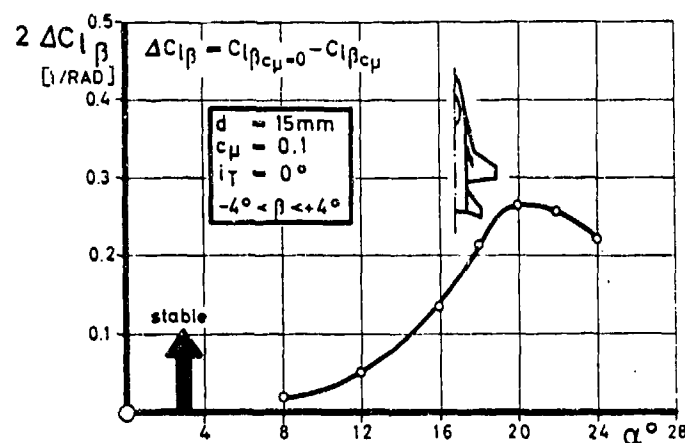
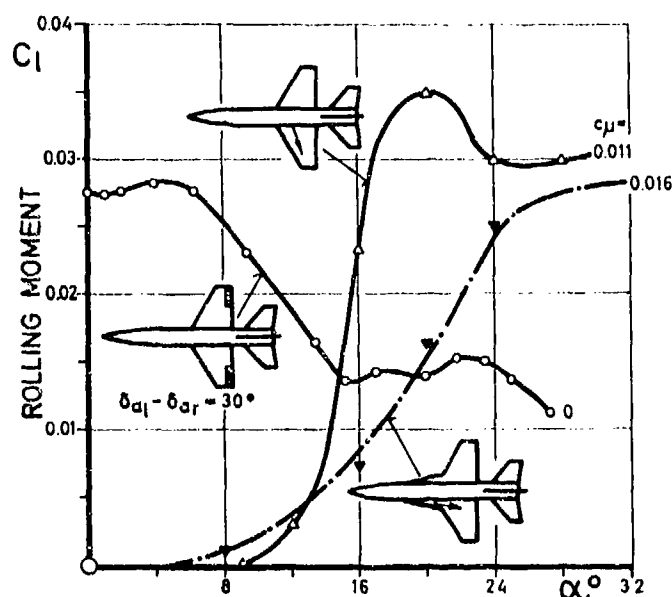


FIG. 13 EFFECT OF SPANWISE BLOWING ON EFFECTIVE DIHEDRAL (STRAKE ON, BLOWING ON STRAKE)

On the other hand application of nonsymmetric blowing (either on the strake wing or on the basic wing) is a means of roll control as presented in Fig. 14.

The effect is compared with the power of the conventional tip ailerons in an unblown case. A small amount of concentrated blowing on one wing-half induces considerable, non-linear increasing rolling moments especially in that a.o.a. regime, where conventional ailerons or spoilers have reduced efficiencies. On the bottom of Fig. 14 it is demonstrated that this technique has an efficiency factor of 6 for the basic wing, or 3.5 for the strake wing, when compared to the roll-efficiency of 1 for a hovering jet on the wing tip. This technique will become highly valuable, when the induced adverse yawing moments are avoided.





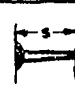
Blowing			
$\frac{C_l \cdot b}{c_{\mu} \cdot s}$	~ 6.0	~ 3.5	1.0

FIG. 14 ASYMMETRIC BLOWING FOR ROLL CONTROL AS COMPARED TO AILERON EFFECTS AND VECTORED THRUST

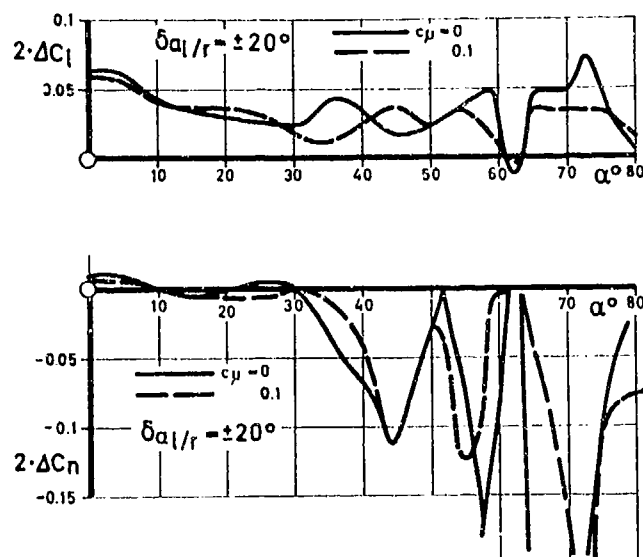


FIG.15 AILERON-EFFECTIVITY WITH/ WITHOUT SPANWISE BLOWING

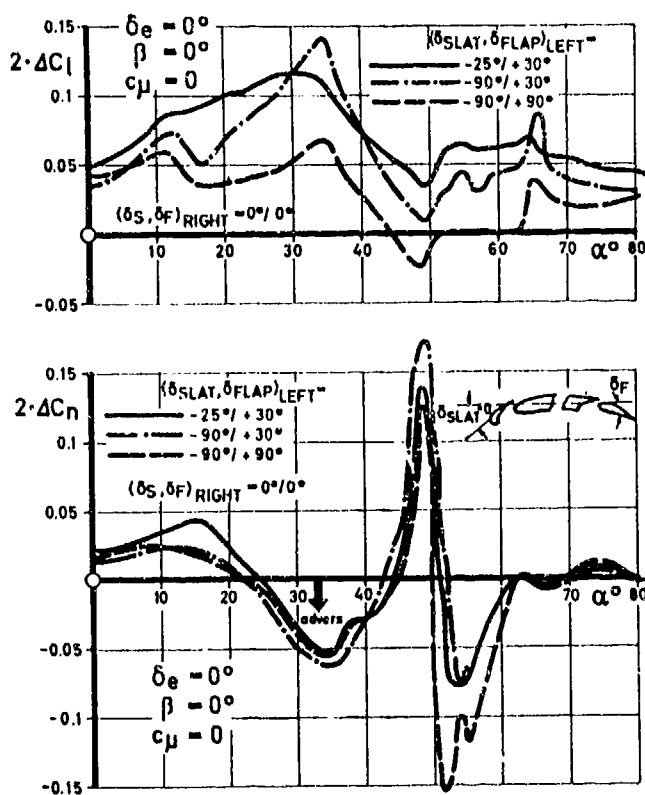


FIG.16 EFFECT OF ASYMMETRIC DEFLECTED HIGH LIFT FLAP SYSTEM ON ROLLING- AND YAWING MOMENT

The effect of the conventional roll controls aileron, asymmetric flap setting and rolling tail (taileron) is sketched in Figs. 15, 16, and 17 respectively.

Conventional ailerons (Fig. 15) are losing roll power near $\alpha = 10^\circ$ then stabilizing up to $\alpha = 60^\circ$ at about half the basic efficiency. Adverse yawing moments are found when exceeding maximum lift ($\alpha \approx 30^\circ$). This should be cured up to a certain extent by use of other combinations of differential deflections.

Asymmetric deflected high lift flaps (slat + T.E. flaps) produce a considerable increment of rolling moment all over the a.o.a. regime investigated (Fig. 16). Extreme flap deflections should be avoided, the defined (and optimized) high lift configurations ($\delta_s = -25^\circ$, $\delta_f = 30^\circ$) came out to be the overall optimum. Again adverse yawing moments are found near maximum lift conditions. The best conventional device investigated for roll control is the taileron (Fig. 17). Differential deflections of the all moving tail resulted in constant efficiency for all trim conditions. In Fig. 17 only two are shown for sake of clarity, including the negligible effects of spanwise blowing. Proverse yaw is favorably induced on the vertical tail, additionally qualifying the taileron as the most effective control surface. But care must be taken not to overload the tail running into conditions on the "back" of its polar. Hence its applicability is also depending on the chosen stability margin.

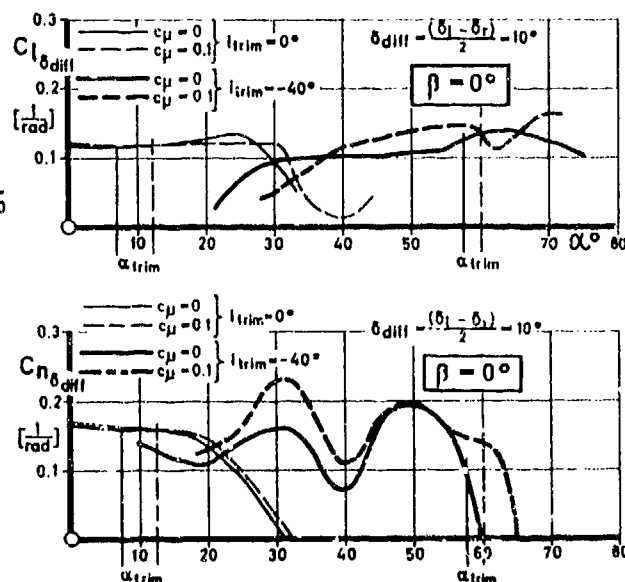


FIG.17 EFFECT OF ROLLING TAIL (TAILERON) AS ROLL- AND YAW CONTROL

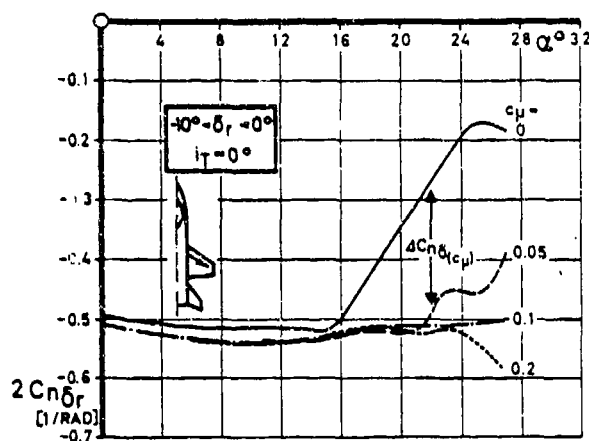


FIG. 18 EFFECT OF SPANWISE BLOWING
ON RUDDER EFFICIENCY
(BASIC WING, STRAKE OFF)

A fall-out effect of spanwise blowing is presented in Fig. 18 for the configuration without strake. Rudder efficiency $Cn\delta_r$ is breaking for the unblown configuration early, whilst for blowing cases the dynamic pressure is restored on the vertical tail via an improvement of the flow around the wing at high incidences, generating a stable, separated vortex system, similar to the conditions on the strake wing without blowing.

3.2.4 Dynamic results

Forced oscillation tests were carried out in two test periods in two different wind tunnels. Basic data were derived in tunnel S2 of O.N.E.R.A., Modane for the conventional a.o.a. regime $0^\circ \leq \alpha \leq 25^\circ$, reported in [22]. A second test period was performed in the new FAUGA F1 tunnel, O.N.E.R.A., Toulouse with extended range of incidences $0^\circ \leq \alpha \leq 50^\circ$. Test data are just going to be analyzed, so only some preliminary results for pitching motion are presented in Fig. 19, to demonstrate some effects of the strake. It should be pointed out, that part of the loss of derivatives $CN\dot{\alpha}$ and $Cm\dot{\alpha}$ is associated with the fact, that horizontal tail deflection was kept constant ($\rightarrow i_t = 0$) so that the tail contribution is vanishing when α_{max} of the H.T. is exceeded. Negative settings, as required for trim conditions, will help here.

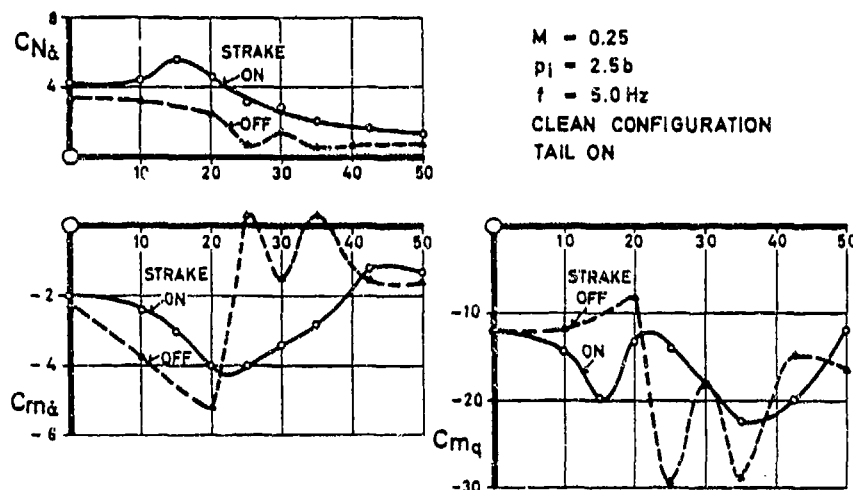


FIG. 19 PITCHING MOTION DYNAMIC DERIVATIVES

4. CONCLUSIONS

From the pilot tests it was learned, that when approaching and exceeding the conventional angle-of-attack limits, key problems are lateral/directional stability and control. Effective dihedral $C_{l\beta}$ is regarded to be the most delicate stability derivative, playing a dominant role in departure characteristics

$$(C_{n\beta_{dyn}} \text{ and L.C.D.P.} = C_{n\beta} - C_{l\beta} \left[\frac{C_{n\delta_a} - K_1 C_{n\delta_{...}}}{C_{l\delta_a} - K_1 C_{l\delta_{...}}} \right] =$$

= Lateral Control Departure Parameter, $K_1 = \frac{\delta}{\delta_a}$)

On the other side control problems are found to be decisive for the yaw axis.

Further it is felt, that small configurational modifications can trigger rather dramatic aerodynamic effects for stall and post stall conditions.

5. REFERENCES

- [1] STAUDACHER W.
Verbesserung der Manöverleistungen im hohen Unterschall
MBB-UFE 896-72 (DGLR-72-126) 1972
- [2] STAUDACHER W. / ZECH A.
Transsonische Profil- und Flügelformen (Hochauftriebsmittel für
den Luftkampf, $Ma = 0.5 + 0.9$)
MBB-UFE 908-72 ZTL 1972
- [3] ZECH A. / STAUDACHER W. / BRETTHAUER N.
Untersuchungen im Unterschall an Flügeln mit Strakes für
Kampfflugzeuge
MBB-UFE 1019-73 1973
- [4] STAUDACHER W.
Zum Einfluß von Flügelgrundriß-Modifikationen auf die aerodyna-
mischen Leistungen von Kampfflugzeugen
MBB-UFE 1033-73 (DGLR 73-71) 1973
- [5] STAUDACHER W.
Flügel mit Strakes (Transsonik, experimentell)
MBB-UFE 1059-73 ZTL 1973
- [6] KRAHL H.
Untersuchung der Interferenz und der Lastverteilung bei Kampf-
flugzeug-Konfigurationen mit Strakes
VFW-F 4.01/74 ZTL 1974
- [7] BAUMERT W.
Messungen am Prinzipmodell Flügel mit Strakes bei symmetri-
scher Anblasung
DFVLR IB 157-75A13 ZTL 1974
- [8] SCHRÖDER W.
Untersuchungen über die Umströmung von Tragflügeln mit ge-
knickten Vorderkanten und gepfeilten Außenflügeln bei
mäßiger Unterschallgeschwindigkeit
DFVLR IB 151-74/71 ZTL 1974
- [9] STAUDACHER W.
Flügel mit Strakes (experimentell)
MBB UFE 1154 ZTL 1974
- [10] BÖDDENER W.
Kraftmessungen an einem Flugzeugmodell mit Strakes, Bestimmung
der Ruderwirksamkeiten sowie Einfluß von Spoilern und Brems-
klappen
DFVLR IB 157-75C12 ZTL 1975
- [11] BAUMERT W.
Druckverteilungsmessungen am Prinzipmodell Flügel mit Strakes
bei unsymmetrischer Anblasung
DFVLR IB 157-75A17 ZTL 1975
- [12] STAUDACHER W.
Flügel mit Strakes (experimentell)
MBB-UFE 1223 ZTL 1975
- [13] KRAHL H. / STEUER F.
Klärung realisierbarer Möglichkeiten des Hochauftriebs
(Flügel mit Strakes)
VFW 4.01-75 ZTL 1975

- [14] HÜNECKE K. / KRAHL H.
Grundsatzuntersuchungen über spannweitiges Ausblasen
VFW-F KB Ef-626 1976
- [15] EBERLE A. / STAUDACHER W. / ZECH A.
Advanced Aerodynamics for Transonic Flight
ICAS Paper No. 76-12 1976
- [16] STAUDACHER W. / HÜNECKE K.
Flügel mit und ohne Strakes im Post-Stall-Bereich
Gemeinschaftsbericht MBB-UFE1300 / VF Ef-652 ZTL 1976
- [17] STAUDACHER W.
The Effects of Jets, Wakes and Vortices on Lifting Surfaces
AGARD FDP RTD / MBB-UFE122-AERO-MT-263 1976
- [18] LEDY J.P. / TURBIL R.
Essai d'une maquette complète d'un avion de combat MBB,
à l'échelle 1/5.5, avec jets transversaux, dans la veine
d'expérience n°1 de la soufflerie S1MA
Procès-verbal n° 2/3302 SNG 1977
- [19] STAUDACHER W. / BÖDDENER W. / WULF R.
Grundsätzliche Untersuchungen über spannweitiges Ausblasen
und stabilisierten Wirbelauftrieb
Gemeinschaftsbericht MBB-UFE1320 / DFVLR IB 157-77 A25 1977
- [20] STAUDACHER W.
Flügel mit kontrollierter Ablösung
MBB-UFE1343(Ö) / DGLR Nr. 77-028 1977
- [21] POISSON-QUINTON Ph.
Slender Wings for Civil and Military Aircraft
8th Theodore v. Karman Lecture 1978
- [22] STAUDACHER W. / LASCHKA B. / SCHULZE B. / POISSON-QUINTON Ph. /
CANU M.
Some Factors Affecting the Dynamic Stability Derivatives of
a Fighter-Type Model
AGARD FDP Athens, May 1978, Paper 11 1978
- [23] STAUDACHER W. / LASCHKA B. / POISSON-QUINTON Ph. / LEDY J.P.
Effect of Spanwise Blowing in the Angle-of-Attack Regime
 $\alpha = 0 \div 90^\circ$
ICAS A1-02 Lisbon 1978

THE APPLICATION OF SPANWISE BLOWING FOR HIGH ANGLE OF ATTACK SPIN RECOVERY

Dr. J. J. Cornish, III[†] and M. W. M. Jenkins[‡]
Lockheed-Georgia Company

SUMMARY

A unique autorotation tunnel test has been performed on a 1/30th scaled model of an F-4 fighter configuration. During this test, air was blown spanwise over the wing from various nozzle locations and the influence of this blowing on the spinning mode was recorded. Over 50 test conditions were evaluated for both flat ($\alpha = 45^\circ$) and steep ($\alpha = 80^\circ$) spin modes. The wing blowing was very effective in arresting the spin for the steep spin mode and not very effective in stopping the flat spin. Nose blowing was also evaluated with only marginal success. By using 2.25 turns to stop as a criteria, an optimum wing nozzle location and blowing level was identified. These data, when scaled to full-scale values showed that the required nozzle diameter was 1.92", located close to the wing root 1/4-chord point and 18 lb/sec. of air was required to affect recovery. More efficient and effective recovery is possible in the tunnel with an additional degree of freedom and with empennage blowing. Further, larger scale testing is urged.

NOTATION

b	wing span	α	angle of attack - degrees
C.G.	center of gravity	Δ	incremental change
C_μ	blowing coefficient	L	left
C_L	lift coefficient	R	right
C_D	drag coefficient	S_w	wing area
C_l	roll moment coefficient due to spanwise blowing	TTS	turns to stop
C_r	root chord	g	acceleration due to gravity
F	fuselage length	M_j	jet exit Mach number
q	dynamic pressure - pounds per square foot, psf, PSF	T_{TOT}	total temperature of jet
RPM	revolutions per minute	T	ambient temperature
psi	pressure, pounds per square inch	<u>Subscripts</u>	
V/STOL	vertical or short takeoff and landing	o	freestream - or - initial average
\dot{m}	mass flow	D	"down-going" wing in spin or stall
		U	"up-moving" wing in spin or stall

1. INTRODUCTION

One of the most promising applications of spanwise blowing is in the area of stall and spin prevention and recovery. Conceptual tests performed at Lockheed in 1976 showed that symmetric spanwise blowing on an unswept wing could stop its autorotation in the angle-of-attack range of 30 to 60 degrees. Subsequent testing on a 1/48th scale model of an F-4 aircraft showed that spanwise blowing will also stop spinning on swept wings in the angle-of-attack region of 30°. These simple concept demonstration tests led to the test reported on herein.

The mechanism of autorotation and spin entry has been known for many years. Spin entry conditions are usually set by the "near-wing-stall" flight regimes; and wing drop, caused by local separation, induces rolling moments, which precipitate autorotation. The aerodynamic forces occurring during this event are depicted in Figure 1. On approaching stall, point A, slight atmospheric disturbances can cause one wing to drop. This drop induces an increased angle of attack on that wing-side causing it to stall and to experience reduced lift, C_{L_D} , and increased drag. The up-going wing is subjected to a reduction in angle of attack, which induces a smaller lift-loss (C_{L_U}) than that of the downgoing wing with the net result that the up-going wing has a higher lift than the down-going wing and a destabilizing rolling moment develops. Because the up-going wing also experiences a drag reduction, a yawing moment is also induced. The rolling moment causes autorotation, and coupled with the yawing moment a spin develops.

Spanwise blowing the wing causes the lift curve slope to change (Figure 2). Because of this characteristic, a spin can be prevented, or a fully developed autorotation without spanwise blowing can be arrested, when spanwise blowing is activated. In a flat spin, the air flow impinging on the front fuselage separates behind it, causing a resulting force in the direction of the spin (Figure 3). The force is "self-feeding" and will cause rotation to continue unless some corrective action is taken. Nose blowing in a streamwise direction is intended to reattach this flow and thereby stop the spin.

[†]Director of Engineering, Lockheed-Georgia Co.

[‡]Research and Development Engineer - Staff. Flight Sciences Division, Lockheed-Georgia Co.

The purpose of the present test was therefore to establish, in measurable terms, the effectiveness of spanwise blowing as a spin inhibitor, or spin-recovery device. To do this, it was necessary to measure spin rate, blowing levels, turns-to-stop and then to reduce and analyze this data for optimum nozzle location. Optimum, in this instance, means the use of the minimum amount of blowing to effectively arrest the spinning motion in a given time. Therefore, several nozzle locations were chosen for evaluation on an F-4 model. This model was a 1/30th scale spin-tunnel model obtained on loan from NASA-Langley. The model exhibited, in NASA's spin tunnel, the two characteristic spin modes of the F-4; the flat spin $\alpha = 80^\circ$, and the steep spin $\alpha = 45^\circ$, and was therefore ideally suited to our needs.

2. EXPERIMENTAL EQUIPMENT

2.1 Test facility

Testing was conducted at the Lockheed-Georgia Low Speed Wind Tunnel (LSWT) facility. This tunnel is a horizontal, atmospheric static pressure, single return, closed throat system. It incorporates tandem test sections that provide for testing of V/STOL configurations in the upstream section and testing of low-speed models in the downstream section. The low-speed test section, which was used for this test, is 23.25 feet wide, 16.25 feet high, and 1/3 feet long with observation windows installed to permit filming and supervision of the test.

2.2 Model

The test model was a 1/30th aerodynamically and inertially scaled model of an F-4 fighter. This particular model has been used in numerous NASA-Langley spinning tests, and a three view of the model is presented in Figure 4 (see also Table I). It was modified to accept blowing on the nose and on the wing (Figure 5), and although only the left wing nozzles are shown in this figure, provisions were made for blowing both wings. (Nozzle details are given in Table I.)

2.3 Model mount system

A model mount system was fabricated to allow the model to spin freely and to accept pressurized air. This system was bolted to the wall of the wind tunnel, Figure 6, at a height of approximately seven feet above the tunnel floor, with a model wing-tip clearance of approximately $1\frac{1}{2}$ semispans from the tunnel wall. The plenum also served as a sting support and as the housing for the spin rate measuring device. The hollow sting which allowed the passage of high pressure air (approximately 60 psi) was attached to the model C.G. through the top of the fuselage. A two-position bracket permitted the selection of the appropriate angle for either a steep ($\alpha = 45^\circ$) or flat ($\alpha = 80^\circ$) spin. Compressed air is fed to the plenum and is transferred via the sting to the preselected nozzle on the model. A deflector plate was installed to prevent air leakage at the bearing from impinging on the model.

3. TEST PROCEDURES AND RESULTS

3.1 Procedures

Test conditions were determined by scaling the spin conditions for the steep and flat spin modes of the full-scale F-4 aircraft. The full-scale steep spin mode α range is from 45 to 50 degrees and the flat spin range is from 80 to 85 degrees. The full-scale aircraft descent velocities in a spin are 450 feet per second (fps) in a steep spin, and 300 feet per second in a flat spin. These, for a 1/30th scale model, correspond to 82.2 and 54.8 fps, respectively. However, with the model at $\alpha = 45^\circ$, a tunnel velocity of 82.2 fps produced flow separation and excessive vibration on both the model and mount. At 66.8 fps this vibration was not present and this was therefore chosen as the maximum test velocity ($q = 5.3$ psf). In the flat spin mode, similar vibration problems limited the test velocity to a maximum of 41 feet per second ($q = 2.0$ psf).

In most conditions tested, tunnel start-up was sufficient to cause the model to autorotate. In those few instances when this did not occur, rotation was initiated by hand. In all cases, autorotation was allowed to develop and to settle into a steady state condition before the spanwise blowing was activated. For this test, nozzles on the "downward" going wing in the spin were activated since it was found that these locations were more effective in arresting the spin.

A complete run log for the test (Table II) shows that 53 test conditions were examined, 47 of which were run for the steep spin. The first runs (1-27) were in the steep spin mode using nozzles 2 and 3. The flat spin testing consisted of runs 28 through 33 where nozzles 1 and 2 were tested and where spinning ceased on runs 30 and 31 only. The last portion of the test, runs 34 through 53, was conducted with the model in the steep spin mode using nozzles 3, 4, and 5. In all instances, C_u was varied by changing both the tunnel q and plenum pressure. In addition to the data shown in Table II, a spin time history was recorded during each run.

3.2 Results - steep spin

Typical tunnel measured time histories, in terms of rate of rotation versus time, are shown in Figures 7 (nozzle 2), 8 (nozzle 3), and 9 (nozzle 4), where time $t = 0$ corresponds to the time that spanwise blowing was activated. These data exhibit a characteristic oscillatory component that persists even over the period where the RPM decays to zero (Figure 10). In most cases tested, the nominal spin rate of the model showed an immediate reduction with the application of spanwise blowing. This immediate decay is indicative of the effectiveness of wing spanwise blowing because the mechanization of this particular test did not permit full C_u effectiveness to occur until about 1 second (t_m on Figure 10) after the initiation of the blowing. Should t_m approach t_0 in a practical application then it is clear that a significant improvement will occur in the effectiveness of spanwise blowing as applied here.

As anticipated, increasing C_u at a given nozzle location, reduces the time required to stop. This is shown by comparing Figures 11 and 12 with 7. At this nozzle location (nozzle #2), it is seen that the

time required to stop rotation decreases from 9 seconds, at a $C_u = 0.0275$, to about 3 seconds at a $C_u = 0.0392$.

One universal problem in spin model testing is repeatability of results and therefore particular attention was paid to this during the testing. Most test conditions were repeated at least once and an overall assessment of the excellent repeatability achieved can be seen by comparing the successive runs shown on Figures 7, 8, 9, and 12. Even when t_0 occurred at a different part of the cycle (Figure 8), the stopping time difference was only of the order of 0.5 seconds. For nozzle 2 (Figure 7) a difference in stopping time of 1.0 second results in only 0.15 of a revolution difference in turns-to-stop.

Blowing from nozzle 5 did not cause a cessation of spin even at the highest obtainable C_u . A typical time history for nozzle 5 is shown in Figure 13 where a reduction in spin velocity is apparent for the first seven seconds, but after this the rotation stabilized at a finite value. Clearly, the wing area being influenced by this spanwise-directed jet is insufficient to produce a large enough anti-spin moment to cause the spinning motion to stop.

A comparison of "nozzle location" effects is shown in figure 14 for the three most effective nozzle positions (10, 25 and 50% of the root chord). As the nozzle moves forward, the wing area influenced by the expanding spanwise jet is increasing and therefore its effectiveness in stopping the spin is increased. Spanwise blowing from the 10% or 25% root chord nozzle location causes the spin to stop in about 3 to 3.5 seconds, whereas with a nozzle at 50% and blowing at a slightly higher level, the time to stop is about 3.5 seconds longer.

Flat spin

A typical time history of the flat spin mode is given in Figure 15. In this case, nose blowing is used to attempt recovery but as can be seen the spin rate increased following the application of blowing. (This result was not anticipated since the sustaining moment in the flat spin mode of the F-4 appears to be the empennage.) However, the flat spin was stopped with blowing from nozzle 2 (Figure 16), but a very high blowing level of 0.2 was required. Even at this level, almost 20 seconds were required to stop rotation - a time which clearly indicates the ineffectiveness of this nozzle to affect a flat spin recovery.

Optimum nozzle location

One objective of this research was to establish the optimum nozzle location for spin recovery. A measure of the nozzle effectiveness, in this instance, is the number of turns to stop from a given rotation in terms of the expended momentum (C_u). Using 2.25 turns-to-stop as a criterion, the C_u required to meet this as a function of nozzle position was derived from the test data and is shown in Figure 17 for the steep spin only. At the lower tunnel speed of 54.8 fps ($q = 3.5$ psf), the optimum location of 25% requires a C_u of 0.0455. At the higher tunnel speed of 66.8 fps, a C_u of 0.032 is required at the most forward location tested. It is evident from this data that for this configuration the optimum nozzle location should be at or forward of 25% chord location.

4. ANALYSIS - INDUCED ANTI-SPIN ROLLING MOMENTS

In assessing the effectiveness of spanwise blowing as a means of arresting the spin, knowledge of the applied anti-spin moment is important from both an aerodynamic and structural viewpoint. Although structural analyses based on these data were considered outside the scope of this initial investigation, a determination of the anti-spin moments was considered necessary from an aerodynamic viewpoint. A comparison could then be made of the effectiveness of spanwise blowing in a dynamic environment (wing spinning) with that of a static environment (conventional tunnel test). Therefore, a single degree of freedom roll analysis was performed on some of the time history data to extract implied values of spanwise-blowing-induced rolling moment. Only those data gathered during the steep spin mode testing were evaluated since it was in this mode that the greater success in the application of spanwise blowing was achieved. The results are shown in Figure 18 as model scale rolling moments in lb. ft. plotted against turns-to-stop (TTS) as a function of initial rate of rotation R_0 . The ratio TTS/R_0 is used because for a given level of applied anti-spin rolling moment, TTS will increase with higher values of R_0 . Figure 18 clearly shows that at the lower values of applied anti-spin rolling moment, more turns are required to stop for a given rotational rate. A similar analysis parameter is the rate of change of RPM with time $d(RPM)/dt$ as a function of applied anti-spin rolling moment coefficient C_l (Figure 19). It is reasonable to assume that high values of C_l will result in increased values of $d(RPM)/dt$, and hence shorter stopping times for a given level of initial spin rate. Figure 19 demonstrates this quite clearly and shows that for an applied value of C_l of 0.08, the model RPM will reduce at the rate of about 10 RPM per second. This means that if the initial rotational rate is 40 RPM, the model rotation will stop in about 4 seconds after a C_l of 0.08 has been applied. The rolling moment coefficients deduced from the single degree of freedom analysis were compared with measured static data. It was found that NASA had performed static tests on a similar wing planform to that used in the current tests and a comparison with these data are shown in Figure 20. It can be seen that the mean values derived from the single degree of freedom analysis compare favorably, in magnitude of C_l , with reasonable extrapolation of the NASA data.

5. PRACTICAL CONSIDERATIONS

5.1 Spanwise blowing for steep spin recovery

This application of spanwise blowing for spin recovery is unique in that the spanwise blowing air would be used infrequently (only in emergency conditions) and only for limited periods. Based on these study results, the air supply for anti-spin should have the following characteristics:

- (1) Sufficient pressure to provide the nozzles with an operating pressure in the 2 to 4 atmosphere range.
- (2) A combination of pressure and flow rate sufficient to provide blowing momentum coefficients on the order of 0.035 to 0.045.
- (3) An air supply to allow operation of the blowing sufficiently long to effect recovery from the spin.
- (4) Rapid application of the blowing when demanded.

There are several means of obtaining the air on current aircraft, these are:

- (1) Engine bleed air (jet aircraft).
- (2) Diversion of primary or fan exhaust (jet aircraft).
- (3) Engine-driven compressor charging an accumulator.
- (4) Auxiliary-powered compressors charging an accumulator.
- (5) "Bottled" gas.

The type of aircraft would govern the most practical installation.

Based on these tunnel test results, a tentative assessment of the most optimum application to the F-4 can be made. The following were derived by using the appropriate scaling laws and are applicable to the full-scale aircraft:

Nozzle Diameter	1.92 inches
Nozzle Location	0.25 Root Chord (C_r)
Nozzle Centerline Orientation	61° Sweep Back
Operation Pressure	35 psi
Flow Rate, at about 40,000 ft.	18 lb/sec.

The above information shows the requirements well within the bounds of practical design concepts and enforces the desirability for developing the application. The results from the recommended larger-scale tunnel tests may well significantly reduce the optimum air quantity required as similar trends have been shown in other spanwise blowing tests.

Further reductions in the demanded air quantity are likely when multi-degree of freedom tunnel testing can be accomplished. The present test restricted the model degrees of freedom to the roll mode, a condition which was necessary for the effective initial evaluation of this new control method. However, it is clear that with the additional degree of freedom in pitch (and probably yaw) a significant improvement in the effectiveness of anti-spin spanwise blowing is possible since this additional mode is an accepted desirable spin recovery motion.

5.2 Spanwise blowing to promote recovery from the flat spin

Rear fuselage blowing is considered an ideal technique to recover from a flat spin on the F-4 vehicle. In this instance, rear fuselage blowing includes single or combinations of the potential locations shown in Figure 21. These include symmetric blowing up the fin, and symmetric upper surface blowing on the horizontal tail. It is anticipated that horizontal tail blowing will be the more effective recovery device since it has been shown that horizontal tail separation on the F-4 is the prime factor in permitting the flat spin to persist (Figure 22).

Figure 23(a) interprets Figure 22 into streamline patterns. Figure 23(b) shows the anticipated effect on these separated flows when symmetric spanwise blowing is applied to the horizontal tail. In this instance, tail reattachment occurs, vertical tail pro-spin force is removed, and the flat spin should cease. Significantly reduced blowing air requirements are anticipated for these locations compared to the wing values shown earlier. It is proposed that these locations be explored in future tunnel testing.

It is reemphasized that the demonstrated effectiveness of spanwise blowing in halting the spin rotation was achieved without deployment of any other control. Recognizing that the effect of spanwise blowing is primarily to unstall the down-going wing, it would be expected to also restore a measure of aileron effectivity which could also be used to arrest the roll/spin rate. Hence, the herein presented "turns-to-stop" the spin rate are undoubtedly quite conservative. Evaluation of the effectivity of ailerons for spin control in the presence of spanwise blowing could well be the subject of future investigations.

6. CONCLUSIONS AND RECOMMENDATIONS

6.1 Conclusions

Wing root spanwise blowing will arrest a steep spin on the 1/30th scale model F-4 configuration. The optimum nozzle location (i.e. for minimum C_{μ}) is close to the 1/4 wing-root chord station, and at this location a $C_{\mu} = 0.045$ will terminate rotation in 2.25 turns. At present there is every reason to assume that a similar anti-spin potential exists when these results are scaled to a full-scale F-4. At full-scale

a nozzle of 1.92" diameter delivering 18 lb/sec. of air will cause rotation to cease. Wing spanwise blowing was not conclusively effective in reducing the flat spin ($\alpha = 80^\circ$) rotation rate. Nose streamwise blowing seemed similarly ineffective. However, selective empennage blowing is considered appropriate to cause recovery from the flat spin mode for the F-4.

Because these results were constrained to a single rotational mode (i.e. rotation about the sting), then it is concluded that in free-air recovery will be more positive. In this instance where a pitching degree of freedom is permitted, then recovery at the above C_{μ} will be quicker; or a lower value of C_{μ} will be required to recover in the same time (i.e. 2.25 turns to stop).

A limited theoretical analysis performed on the test results showed that the implied values of C_l are comparable with statically derived data on a similar configuration. The trend of implied C_l with selected spin data, and with C_{μ} values is also correct.

It is also concluded that any advanced configuration that exhibits an unacceptable spin mode can be improved through the specific application of spanwise blowing.

6.2 Recommendations

The positive results obtained clearly demonstrate the effectiveness of spanwise blowing as a spin inhibitor and as a spin recovery device. Therefore, further testing on a small-scale model is not recommended. However, it is very appropriate to pursue larger-scale testing on an F-4 (say, 1/5th) if a pitching degree of freedom can be added to the model mount system. Such an additional degree of freedom will significantly reduce the magnitude of C_{μ} required to stop the spin. With this larger scale model, empennage blowing is also recommended as this will demonstrate a most effective means of arresting the flat spin motion. Such testing is strongly urged.

Table I Model Data

Model Geometry

Wing Area, S_w 0.589 sq. ft.
 Wing Span, b 1.29 ft.
 Aspect Ratio 2.82
 Centerline Chord 0.783 ft.
 Tip Chord 0.131 ft.
 Break Station Chord 0.32 ft.
 Fuselage Length, F 1.925 ft.
 Model Weight 3.06 lbs.

Nozzle Geometry

Inner Wing
 Locations 10, 25, 50% Root Chord, C_r
 Diameter 0.07 in.
 Exit Area 0.00385 sq. in.

Outer Wing
 Locations 10, 25% Break Station Chord
 Diameter 0.04 in.
 Exit Area 0.00126 sq. in.

Fuselage
 Location 0.10 F
 Diameter 0.04 in.
 Exit Area 0.00126 sq. in.

Table II Run Log

Run Number	Angle of Attack - Deg.	Nozzle Number	Tunnel q - psf	\dot{W} - lbs/sec.	C_u	Turns to Stop	Comments
1	45	2	6.0	.00235	.0201	--	No Stop
2	(steep spin)		5.3	.00235	.0241	--	
3				.00333	.0392	1.45	
4				.00333	.0392	1.69	No Stop
5				.00287	.0313	2.31	
6				.00287	.0313	2.46	
7				.00265	.0276	--	No Stop
8				.00265	.0276	4.45	
9			3.5	.00265	.0417	1.88	
10				.00265	.0417	3.80	No Stop
11				.00242	.0358	3.96	
12				.00232	.0335	--	
13				.00242	.0358	6.17	No Stop
14				.00320	.0563	1.94	
15				.00320	.0563	2.08	
16		3	3.5	.00320	.0563	2.53	No Stop
17				.00320	.0563	1.30	
18				.00289	.0482	2.15	
19				.00289	.0482	2.03	No Stop
20				.00252	.0387	3.03	
21			5.3	.00252	.0387	1.72	
22				.00252	.0255	2.97	No Stop
23				.00252	.0255	1.35	
24				.00286	.0313	3.27	
25				.00286	.0313	2.40	No Stop
26				.00331	.0392	1.74	
27				.00331	.0392	2.03	
28	80	1	1.0	--	--	--	No Blowing
29	(flat spin)			.00099	.0595	--	No Stop
30		2		.00332	.2096	8.75	
31				.00297	.1769	2.42	
32				.00297	.1769	--	No Stop
33	80	2	2.0	.00330	.1039	--	No Stop
34	45	3	3.5	.00326	.0594	3.22	No Stop
35	(steep spin)			.00326	.0594	3.69	
36		5		.00131	.0259	--	
37				.00131	.0259	--	No Stop
38		4		.00304	.0534	3.00	No Stop
39				.00304	.0534	--	
40				.00304	.0534	8.60	
41				.00349	.0654	1.83	No Stop
42				.00349	.0654	3.50	
43				.00383	.0746	2.25	
44				.00383	.0746	2.00	No Stop
45			5.3	.00383	.0493	1.58	
46				.00383	.0493	2.42	No Stop
47				.00349	.0432	5.08	
48				.00349	.0432	2.33	
49				.00331	.0402	1.92	No Stop
50				.00331	.0402	1.83	
51				.00349	.0432	3.75	
52				.00349	.0432	3.50	No Stop
53				.00303	.0493	1.83	

$$\text{where, } C_u = \frac{49 W M_j \sqrt{T_{TOT} \cdot \left(\frac{T}{T_{TOT}}\right)}}{q S_w}$$

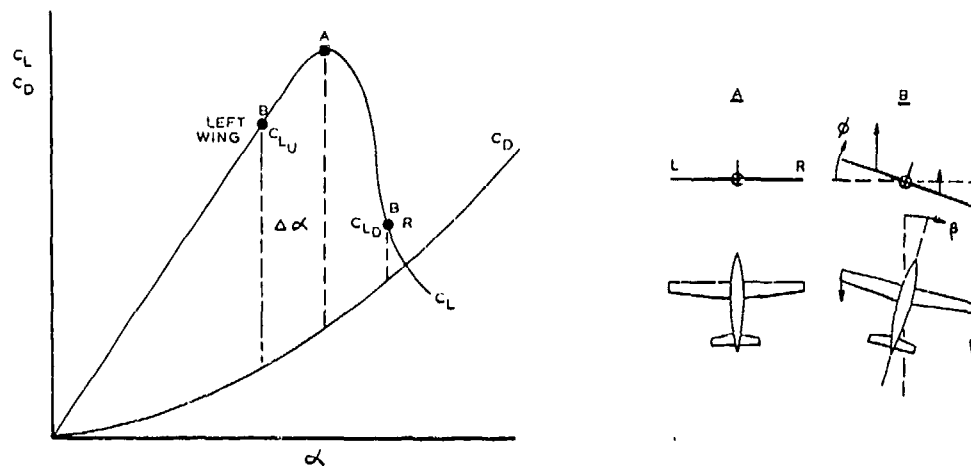


Figure 1 Mechanism of Auto-Rotation and Incipient Spin

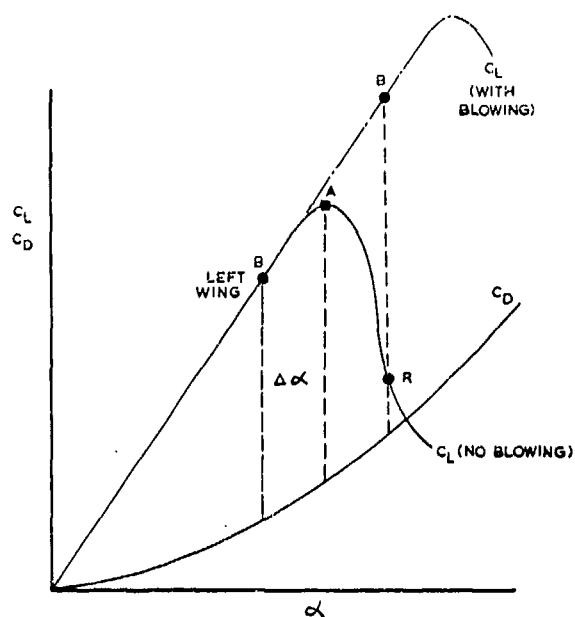


Figure 2 Effect of Spanwise Blowing of Lift Coefficient

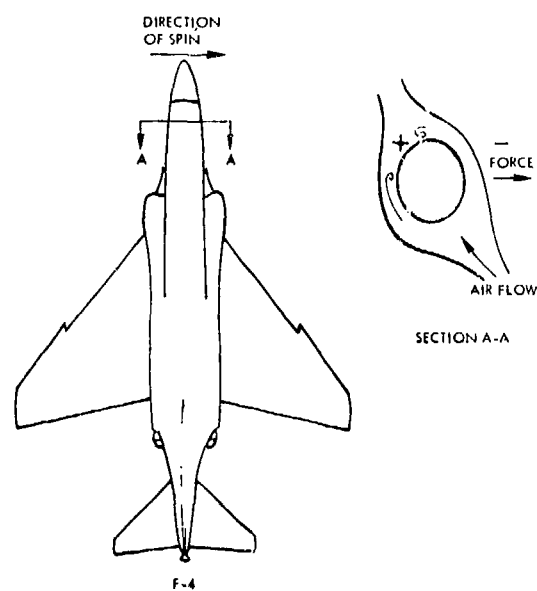


Figure 3 Fuselage Nose Contribution to the Flat Spin Equilibrium

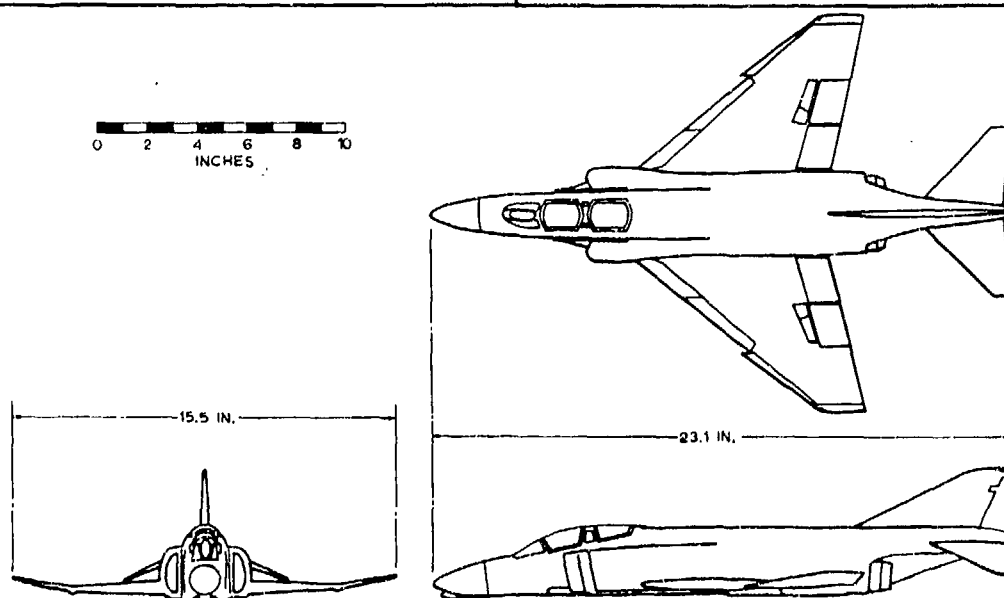


Figure 4 F-4 Model General Arrangement

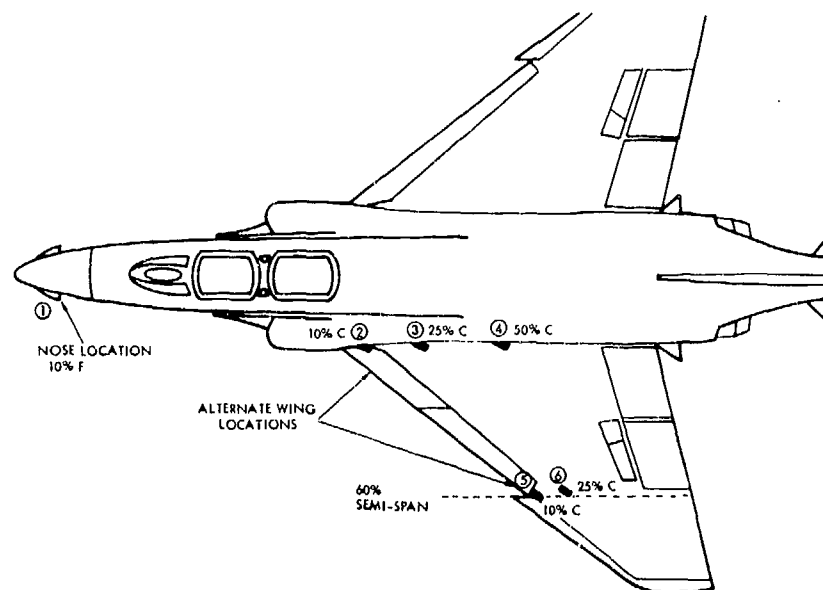


Figure 5 Nozzle Locations



Figure 6 Model Installed in Wind Tunnel

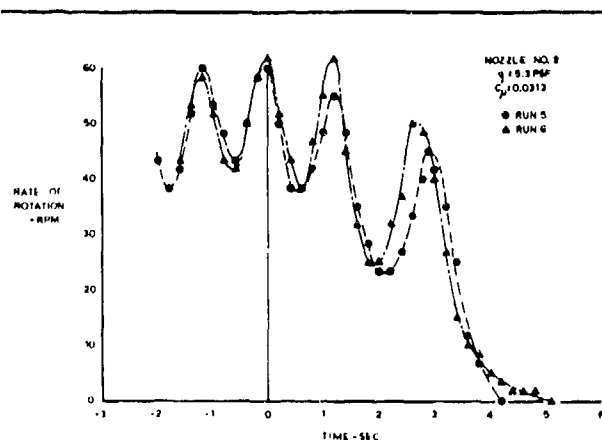


Figure 7 Time History - Steep Spin

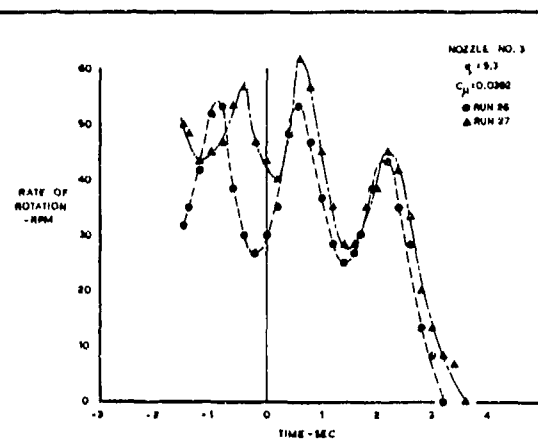


Figure 8 Time History - Steep Spin

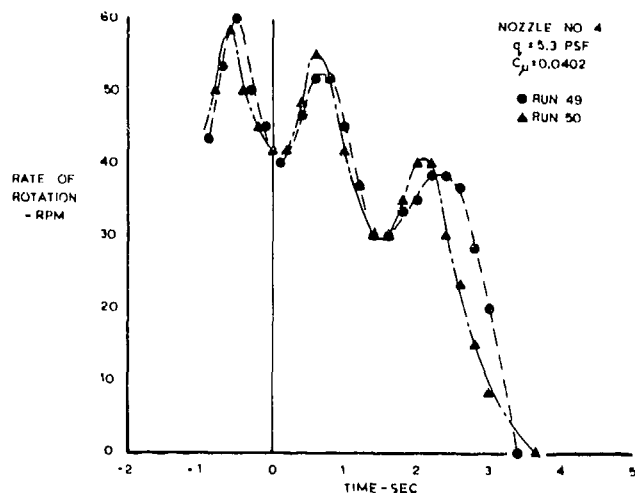


Figure 9 Time History - Steep Spin

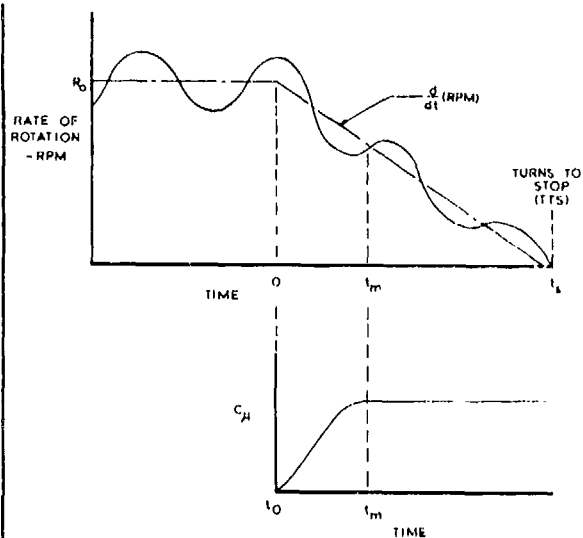


Figure 10 Characteristics of System Performance

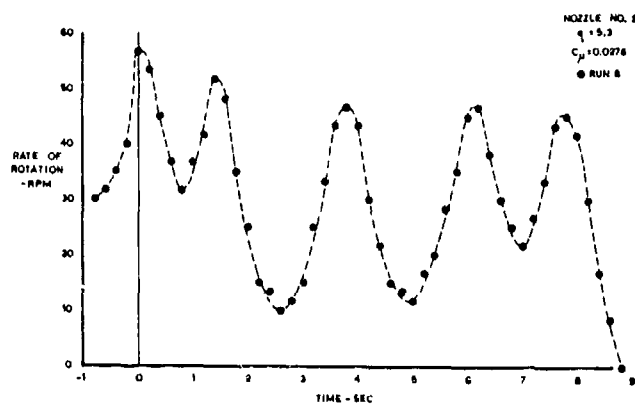


Figure 11 Time History - Steep Spin

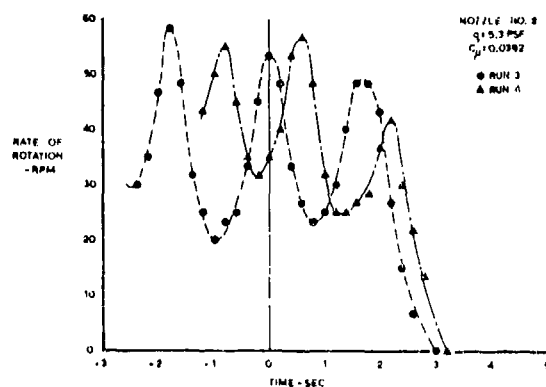


Figure 12 Time History - Steep Spin

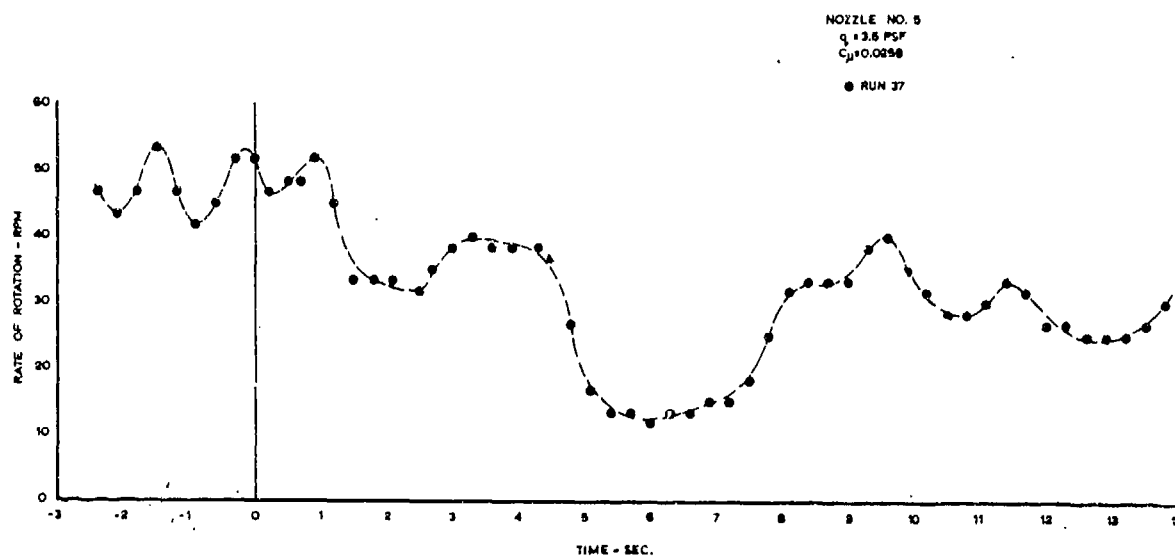
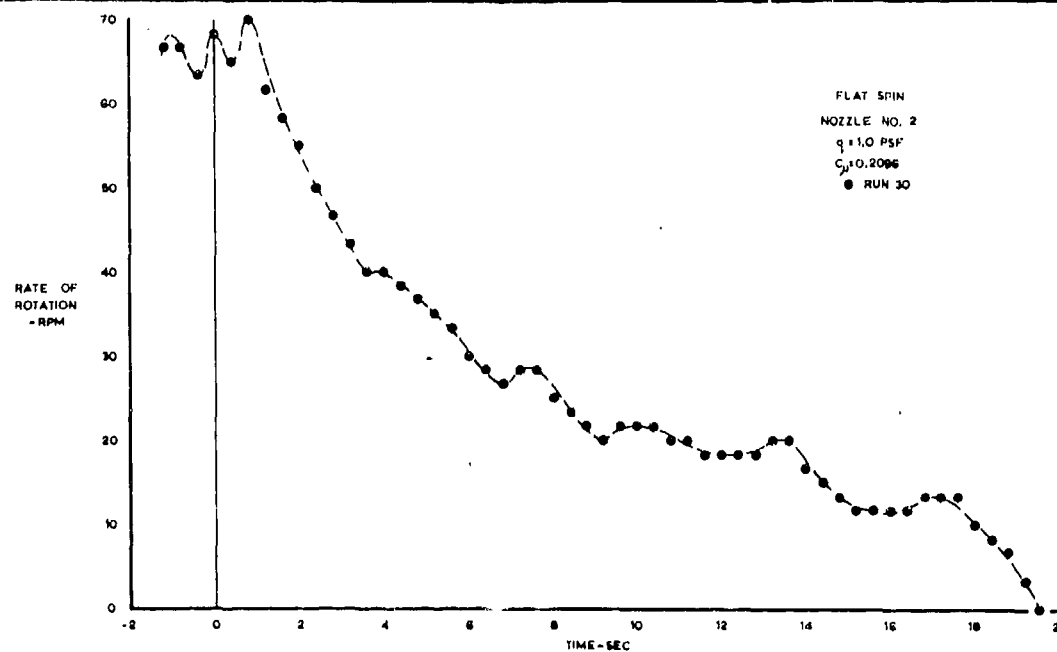
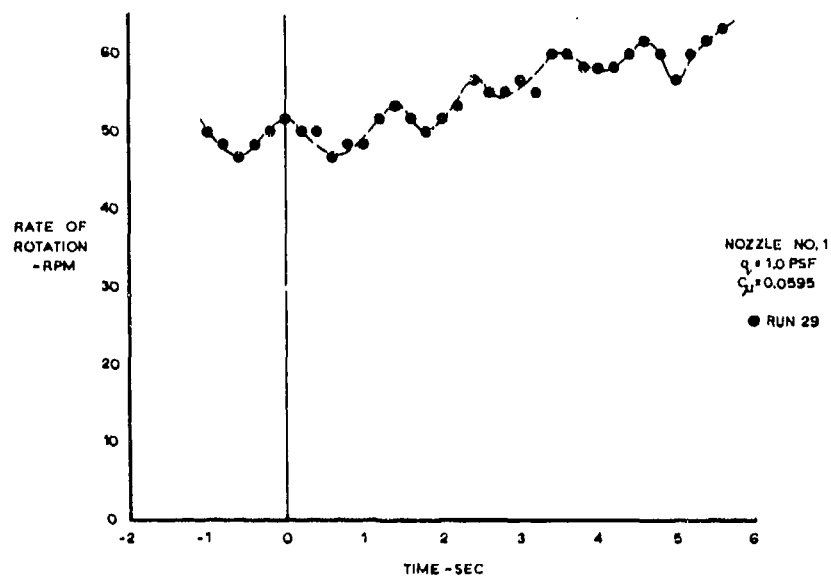
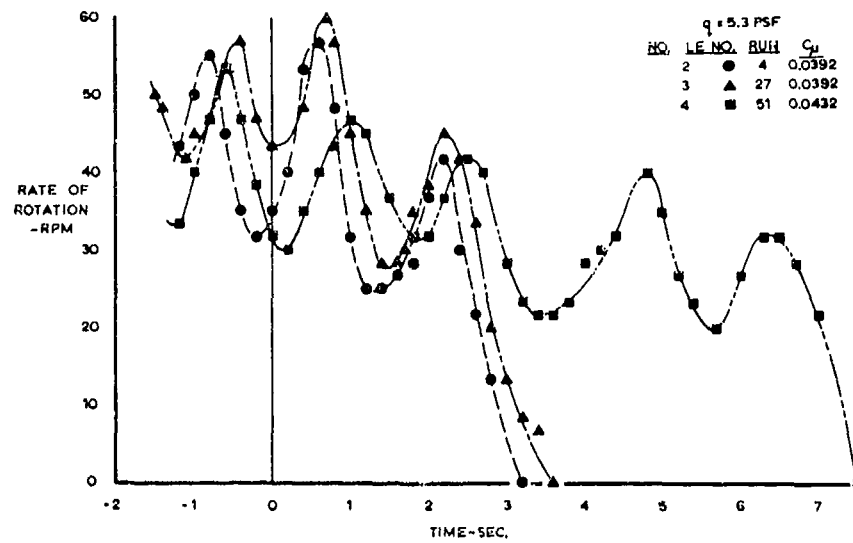


Figure 13 Time History - Steep Spin



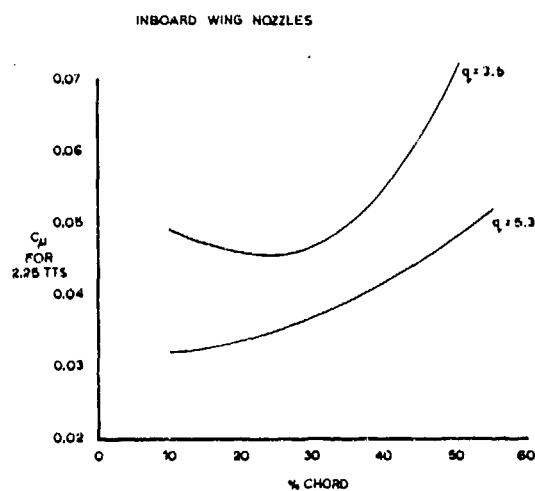


Figure 17 Comparison of Effectiveness of Nozzle Locations - Nozzles 2, 3, and 4

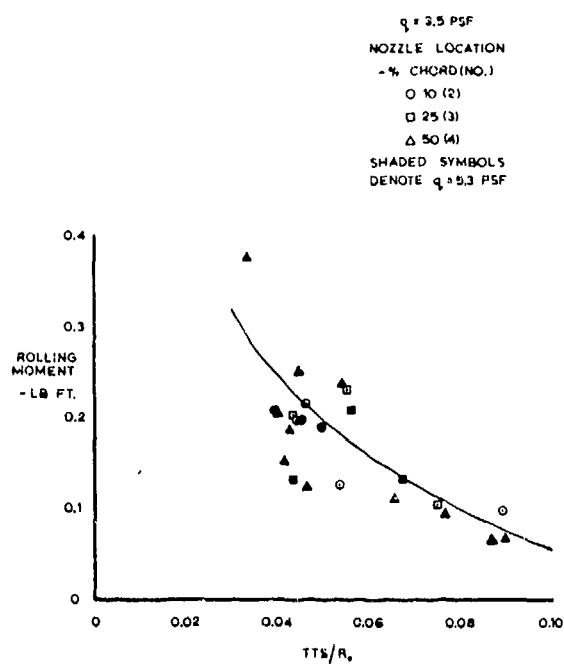


Figure 18 Rolling Moment Applied as a Function of TTS/R_0

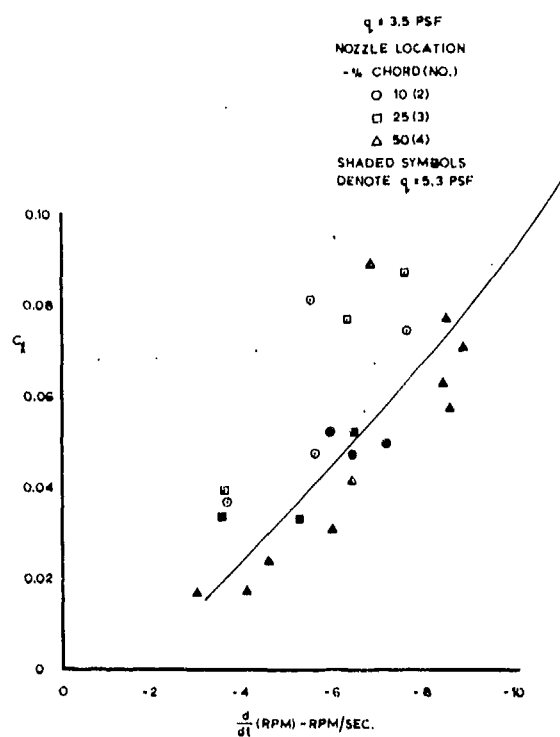


Figure 19 Applied Rolling Moment Coefficient as a Function of d RPM/dt

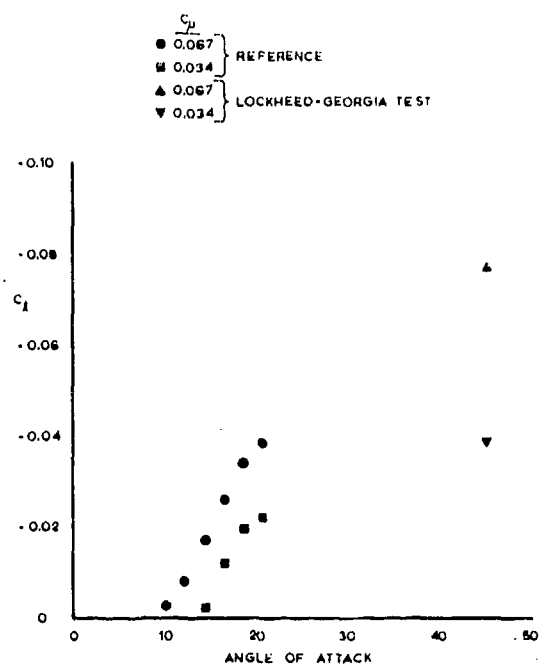


Figure 20 Comparison of Measured and Estimated Rolling Moment Coefficients

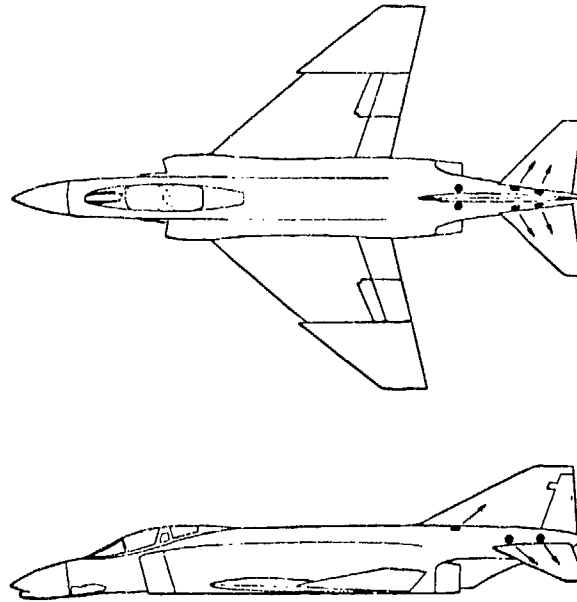


Figure 21 Rear Fuselage Blowing Locations for Flat Spin Recovery

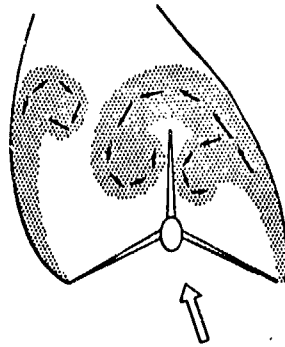
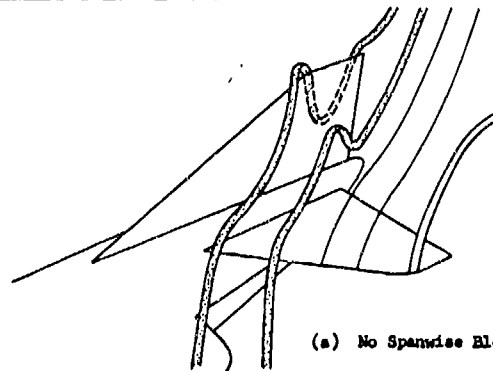
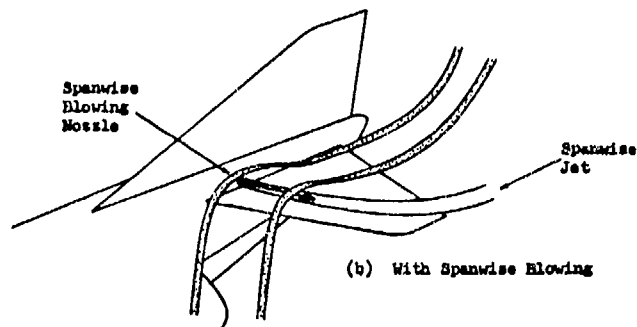


Figure 22 Tail Flow Conditions in Flat Spin



(a) No Spanwise Blowing



(b) With Spanwise Blowing

Figure 23 Influence of Spanwise Blowing on Separated Tail

COMPORTEMENT A HAUTE INCIDENCE D' UN AVION DE TRANSPORT A AILE A GRAND ELANCEMENT

par

D. COLLARD, Ingénieur,
Direction des Etudes Toulouse
AEROSPATIALE
316, route de Bayonne
31053 - TOULOUSE
FRANCE

SOMMAIRE

Sur l'avion de transport supersonique CONCORDE la portance continue à croître d'une façon à peu près uniforme jusqu'à une incidence de 35° . Cependant il existe, à une incidence d'environ $\alpha = 22^\circ$, un changement de la forme d'écoulement sur la voilure. Ce changement provoque un autocabrage et un avancement du foyer, et en dérapage un enfoncement de l'aile qui avance. En même temps il signale le début d'une dégradation progressive de l'efficacité des élevons et d'une diminution de la stabilité latérale.

La plupart des résultats présentés sont issus des essais en soufflerie sur des maquettes de l'avion de série. En particulier sont présentées des visualisations pariétales de l'écoulement à l'extrados de la voilure. A partir de ces visualisations et des mesures de pression il est possible de déduire approximativement l'évolution des différents tourbillons en fonction de l'incidence.

Plus loin sont données quelques remarques sur la différence de comportement à haute incidence de l'avion prototype par rapport à l'avion de série, ainsi qu'une comparaison partielle entre des résultats d'essais en soufflerie et en vol.

1. INTRODUCTION

L'utilisation de la portance tourbillonnaire à haute incidence fait partie de la conception aérodynamique de base de l'avion de transport supersonique CONCORDE. Sa voilure élancée, de forme en plan ogivale, planche 1, est cambrée et vrillée pour maximiser les performances globales de la mission.

Sa différence de configuration par rapport aux avions de transport subsoniques est telle qu'un travail particulier a été nécessaire pour s'assurer d'un comportement en qualités de vol au moins égal à ceux de ses prédécesseurs. Ses vitesses de référence au décollage et pendant l'approche sont liées à ses qualités de vol à haute incidence.

Son domaine en incidence et en dérapage, démontré en vol, est indiqué sur la planche 2. Dans ce domaine on n'accepte aucune anomalie de pilotage, et il est nécessaire de s'assurer que toutes les dérivées aérodynamiques restent continues en incidence et en dérapage.

2. AVION DE SERIE - RESULTATS DE SOUFFLERIE

A partir des mesures de la portance ($C_z(\alpha)$) et des moments de tangage ($C_m(C_z)$) de la planche 3 on remarque :

- une contribution de portance tourbillonnaire qui commence à $\alpha \approx 7^\circ$ mais qui ne modifie pas le foyer,
- un autocabrage à $\alpha = 22^\circ$ avec un changement du gradient de portance et une modification du foyer aux incidences plus élevées.

Des visualisations de l'écoulement pariétal à l'extrados de la voilure et des mesures de pression à la paroi sur sa partie arrière permettent une analyse du système tourbillonnaire.

Sur la planche 4 se trouve une série de croquis basés sur des visualisations à l'huile qui démontre comment varie l'écoulement en fonction de l'incidence.

A $\alpha = 8^\circ$ l'écoulement autour du bord d'attaque au voisinage du fuselage reste attaché, le bord d'attaque étant à la fois arrondi et cambré. En quittant le fuselage le rayon du bec diminue, l'écoulement se détache et un tourbillon se forme tout le long du bord d'attaque jusqu'à la jonction entre la partie centrale de la voilure et le bout d'aile, où la flèche diminue brusquement à 55° .

En ce point un tourbillon secondaire prend naissance mais les deux s'unissent pour quitter le bord de fuite entre le fuseau réacteur et l'extrémité de la voilure.

A côté du fuselage on note que la recompression en aval du bord d'attaque provoque un décollement et la formation d'un tourbillon d'intensité faible.

A $\alpha = 17^\circ$ l'écoulement autour du bord d'attaque est complètement décollé. Le tourbillon principal n'assimile plus le secondaire qui à cette incidence prend comme origine un point légèrement en amont de la jonction du bout d'aile.

Avec une augmentation d'incidence le tourbillon principal croît en intensité et en largeur aux dépens du secondaire de sorte qu'à $\alpha = 21^\circ$ ce dernier a pratiquement disparu. A l'incidence d'autocabrage l'écoulement est constitué d'un seul tourbillon d'intensité élevée relativement loin du bord d'attaque avec un deuxième tourbillon contra-rotatif entre le premier et l'extrémité.

L'analyse des répartitions de pressions présentée plus loin fait penser que l'intensité du tourbillon principal continue à croître même au-dessus de l'incidence d'autocabrage. Il semble qu'il s'éloigne de la voilure mais que l'autocabrage est associé à une réduction locale de la portance du tourbillon contrarotatif. A $\alpha = 23^\circ$, juste après autocabrage, les lignes de courant à l'extrados sous ce tourbillon deviennent pratiquement parallèles à l'axe de l'avion.

Au-dessus de $\alpha = 22^\circ$ l'écoulement se caractérise par un seul tourbillon qui se répand progressivement sur toute la voilure pour le couvrir complètement à $\alpha = 31^\circ$.

Ces visualisations nous amènent à penser :

- (1) Qu'à l'autocabrage, à la disparition du tourbillon secondaire et à la perte de portance locale à l'extrémité de voilure, l'efficacité des élevons est diminuée.

Cette diminution existe. Sur la planche 5 est présentée la variation de portance avec un braquage des élevons ($C_z(\delta)$) en fonction de l'incidence. Il semble qu'au voisinage de α autocabrage l'augmentation de portance due au braquage soit compensée en partie par une réduction locale de la portance tourbillonnaire. Cette diminution se manifeste également par une réduction de $C_m(\delta)$ et des moments de charnière des élevons. Un braquage positif des élevons semble diminuer légèrement la valeur de α autocabrage.

- (2) Qu'à partir de α autocabrage l'élargissement du tourbillon principal vers l'axe de l'avion entraîne une diminution de l'efficacité de la dérive. On remarque, en effet, planche 6, une diminution très importante des moments de lacet dus à la dérive ($\Delta C_n(\beta)$) entre $\alpha = 22^\circ$ et $\alpha = 26^\circ$.

- (3) Qu'aux incidences légèrement inférieures à autocabrage la mise en dérapage de l'avion provoque une augmentation de portance puis un autocabrage sur l'aile qui avance, de sorte que l'appareil subit brusquement un autocabrage, un moment de roulis et une légère perte de portance.

Cet effet est présenté sur la planche 7.

A $\alpha = 17^\circ$ on ne remarque pas de discontinuité des coefficients aérodynamiques en dérapage.

A $\alpha = 20^\circ$ la voilure qui avance perd brusquement à $\beta = 3^\circ$, de la portance près de l'extrémité, ce qui entraîne un moment cabreur et un moment de roulis qui provoque l'enfoncement de l'aile en question.

A une incidence au-dessus de α autocabrage le changement de l'écoulement est inversé.

A $\alpha = 23^\circ$, par exemple, l'aile sous le vent récupère de la portance pour donner un moment piqueur et un moment de roulis dans le même sens que dans le cas précédent.

Il est intéressant d'examiner la répartition en envergure des pressions statiques pariétales en amont du bord de fuite en fonction de l'incidence. Sur la planche 8 on présente de telles répartitions mesurées à l'axe de charnière des élevons avant et après l'autocabrage. Bien qu'elles soient données pour une version développée du CONCORDE d'envergure augmentée le mécanisme de l'écoulement reste semblable à celui de l'avion de série.

La variation en envergure des pressions, $K_p(\eta)$ entre le fuselage et l'axe du tourbillon principal a la même forme que celle provenant d'un tourbillon bidimensionnel ayant son axe parallèle à l'axe de l'avion.

Donc on peut penser que l'intensité du tourbillon principal et la hauteur de son axe au-dessus de la voilure sont définies par des équations semblables à celles d'un tourbillon bidimensionnel, c'est-à-dire

$$\Gamma = k_1 \int K_{p \max}^{1/2}$$

où Γ est l'intensité du tourbillon et \int la hauteur de son axe divisée par la demi envergure locale, et

$$\frac{K_p}{K_{p_{\max}}} = \left[1 + \left(\frac{\Delta\eta}{\eta} \right)^2 \right]^{-2}$$

de sorte que

$$\Gamma = R_2 \delta = R_2 \Delta\eta \frac{K_p}{K_{p_{\max}}} = 0,5 K_{p_{\max}}^{1/2}$$

On remarque planche 9 que δ croît plus ou moins linéairement avec α , et qu'il existe même une légère augmentation de δ au moment de l'autocabrage. Par contre, à α autocabrage δ augmente brusquement.

Il semble que sur la voilure du CONCORDE l'autocabrage soit le résultat d'une perte de portance associée à un éclatement ou à un changement de position du tourbillon contrarotatif.

3. RESULTATS DE SOUFFLERIE - COMPARAISON DES AVIONS PROTOTYPE ET DE SERIE

En ce qui concerne le vol à haute incidence la différence principale entre les avions prototype et de série réside dans la forme en plan du bout d'aile (planche 10). La différence de son angle de flèche du bord d'attaque, 60,3° et 55° pour les deux voilures, a un effet important sur les caractéristiques aérodynamiques.

Par rapport au prototype la modification du bout d'aile de l'avion de série a apporté un gain de performances dans toutes les différentes phases de la mission, au prix d'une certaine dégradation des qualités de vol à haute incidence.

Le foyer du prototype, sensiblement à la même position que celui de l'avion de série à faible incidence, avance progressivement avec le développement du système tourbillonnaire. Il en résulte que l'autocabrage, qui se trouve à $\alpha = 24^\circ$, est d'une intensité moins importante que sur l'avion de série.

Une comparaison à $\alpha = 19,5^\circ$ des répartitions en envergure des pressions sur la partie arrière de la voilure (planche 11) montre que la portance due au système de tourbillons secondaires est plus faible sur le prototype. Il est probable que son tourbillon principal est plus éloigné de l'extrados. Le système tourbillonnaire est semblable à celui de l'avion de série après l'autocabrage toutefois avec un tourbillon contrarotatif plus intense.

L'accident "autocabrage/enfoncement de la voilure" en dérapage sur le prototype est moins prononcé et arrive à un angle de dérapage plus élevé.

4. RESULTATS DES ESSAIS EN VOL

Les résultats des essais en vol obtenus sur l'avion de série recoupent ceux de la soufflerie. Cependant une comparaison quantitative est rendue difficile par des effets de souplesse de l'avion. L'incidence en vol est mesurée sur le nez de l'avion et des hypothèses sont nécessaires pour estimer l'incidence effective de la voilure.

Des mesures de la portance et des moments de tangage ont été obtenus par décélération en paller aux différents centrages. Pour effectuer une comparaison avec la soufflerie il est nécessaire de corriger les résultats en vol pour les différences de poussée brute et de débit des entrées d'air ainsi que pour l'effet de braquage des élevons.

Dans la comparaison présentée sur la planche 12 on note une bonne concordance à braquage nul des élevons ($\delta = 0$). Elle est moins satisfaisante avec les élevons braqués.

Une comparaison de la variation avec l'incidence de l'angle de dérapage où apparaissent les accidents d'autocabrage et de roulis est donnée sur la planche 13. Malgré la dispersion dans les mesures en vol le phénomène rencontré en soufflerie est bien reproduit en vol.

Sur le prototype, en vol comme en soufflerie, les possibilités de dérapage à haute incidence sont plus grandes que sur l'avion de série et l'autocabrage se trouve à une incidence plus élevée d'environ 2°.

5. CONCLUSIONS

D'après les résultats présentés il semble que sur des avions "semi élancés" de type similaire au CONCORDE, la portance continuerait à croître jusqu'aux incidences d'environ $\alpha = 35^\circ$.

Sur l'avion CONCORDE de série les interactions entre les tourbillons principal et secondaires sont telles que le foyer reste constant en incidence jusqu'à $\alpha = 22^\circ$, où une perte de portance à

l'extrémité du bout d'aile provoque un léger autocabrage, un avancement du foyer et une diminution progressive de l'efficacité des élévons.

L'intensité du tourbillon principal ne paraît pas diminuer à l'autocabrage. La perte de portance semble être liée plutôt à un changement brutal dans le système de tourbillons secondaires. Cet autocabrage, antisymétrique en dérapage, entraîne l'enfoncement de l'aile qui avance.

Au-dessus de α autocabrage le tourbillon principal se répand vers l'axe de l'avion de sorte qu'en dérapage des interactions avec la dérive entraînent une réduction très importante de stabilité latérale de l'appareil.

Une comparaison entre les avions prototype et de série montre la grande différence de comportement à haute incidence qui peut résulter d'un changement relativement mineur de la forme en plan de la voilure.

Les variations et les grandeurs des caractéristiques aérodynamiques à haute incidence déterminées en soufflerie sont retrouvées sur l'avion en vol.

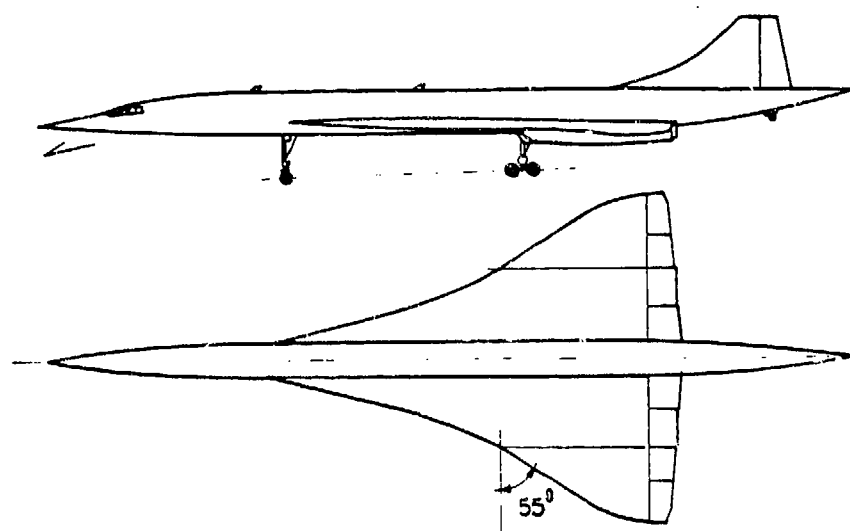


Planche 1 : Concorde - Avion de série.

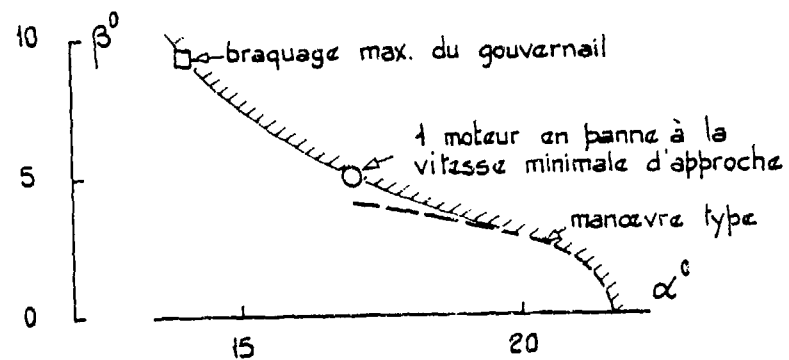


Planche 2 : Domaine de vol démontré en vol à faible vitesse.

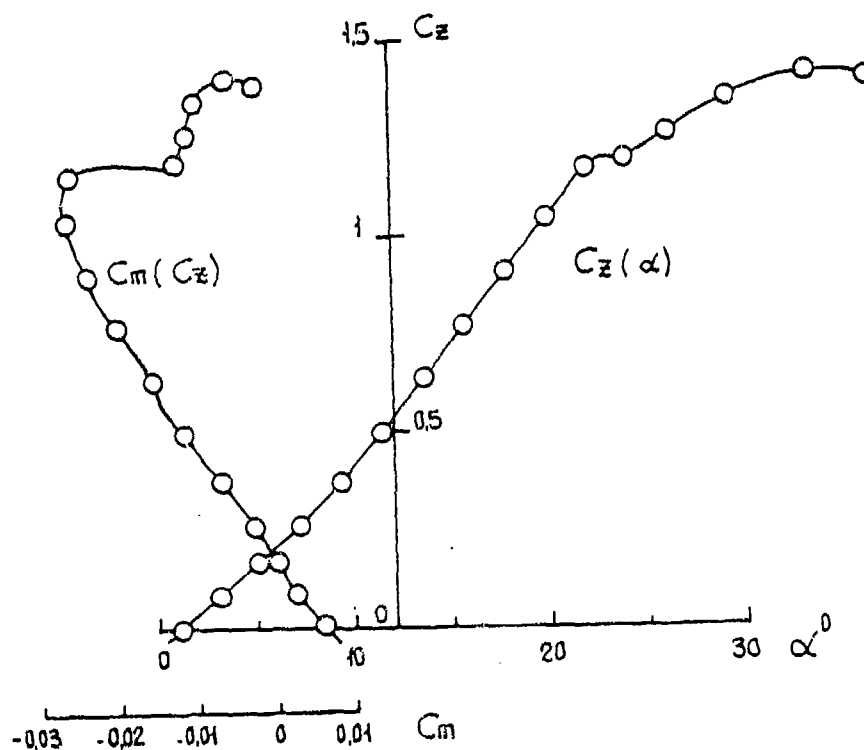


Planche 3 : Portance et moments de tangage à faible vitesse.
Avion de série - Essais en soufflerie

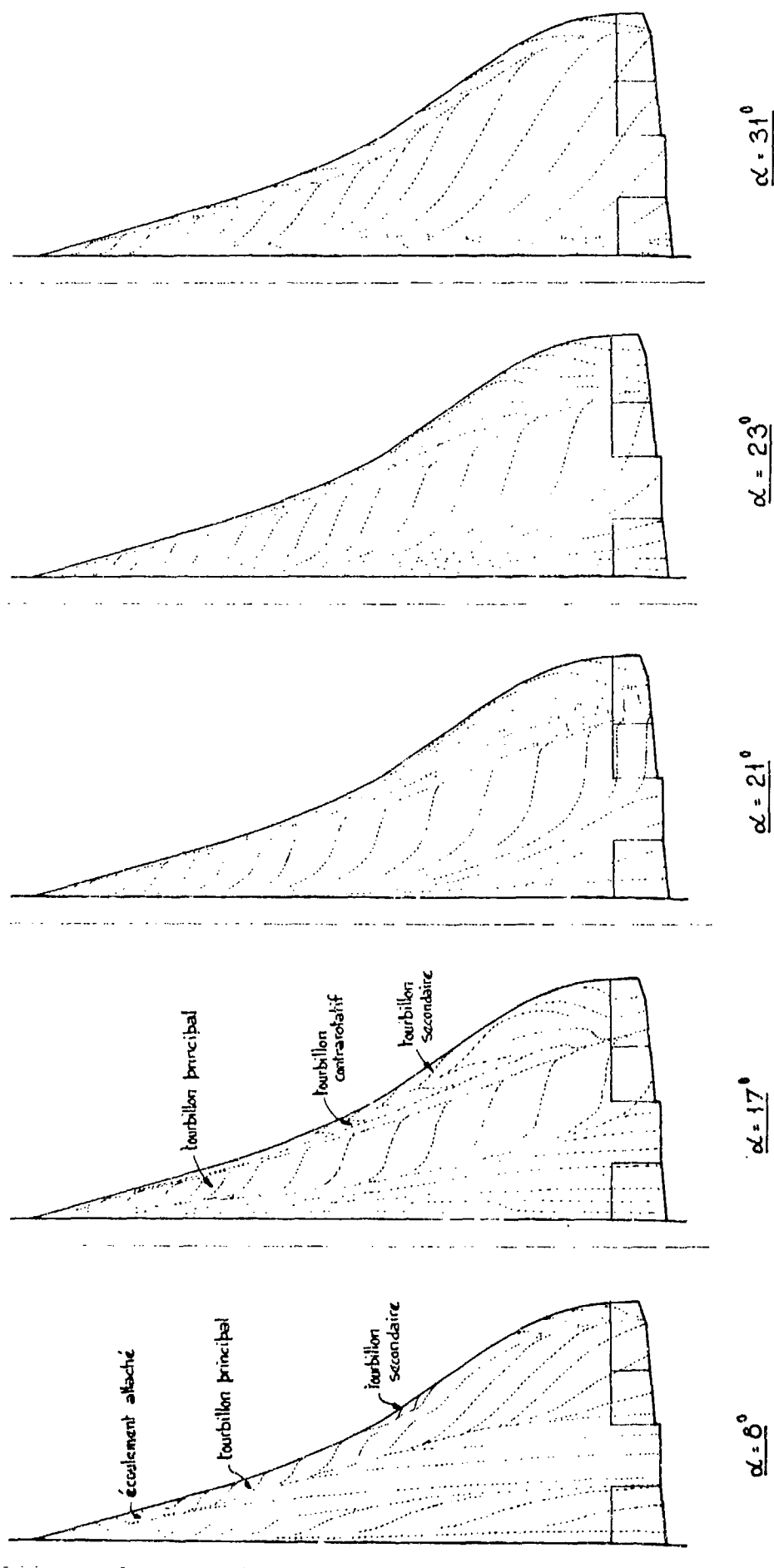


Planche 4 : Visualisation à l'huile de l'écoulement à l'extrados de la voilure en fonction de l'incidence.
Avion de série - Essais en soufflerie à faible vitesse.

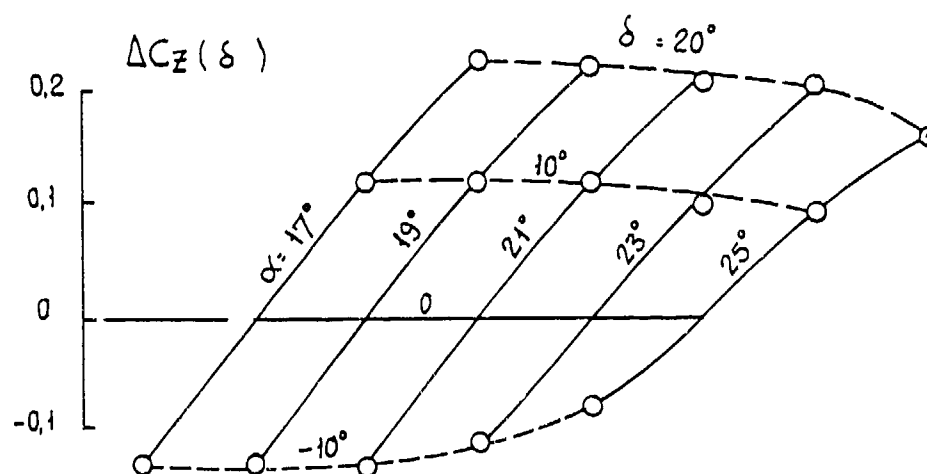


Planche 5 : Portance due au braquage des élevons en fonction de l'incidence.
Avion de série - Essais en soufflerie à faible vitesse.

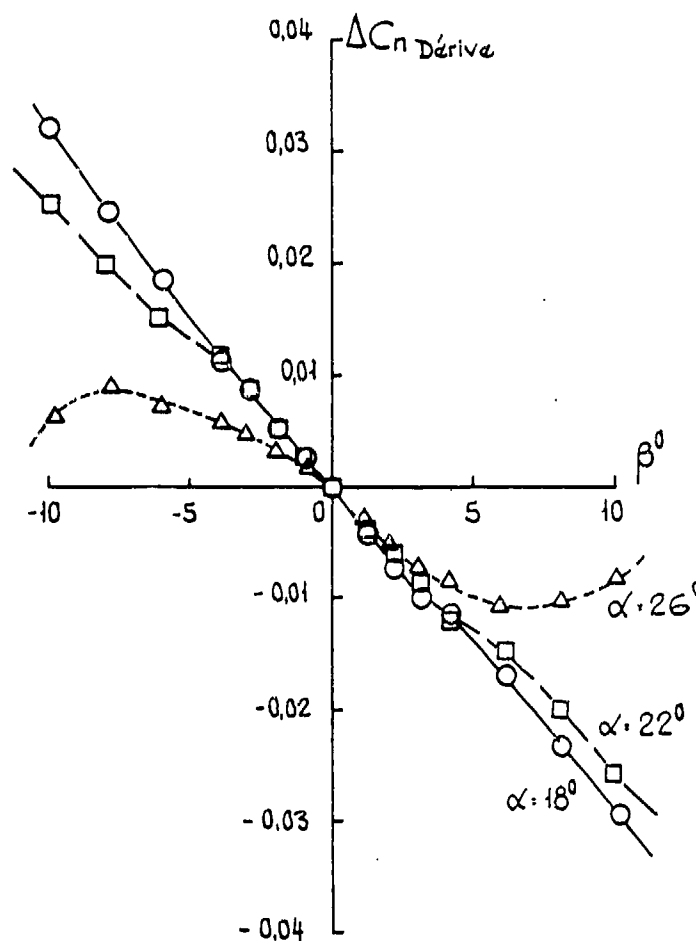


Planche 6 : Moment de lacet dû à la dérive en fonction de l'incidence et du dérapage.
Avion de série - Essais en soufflerie à faible vitesse.

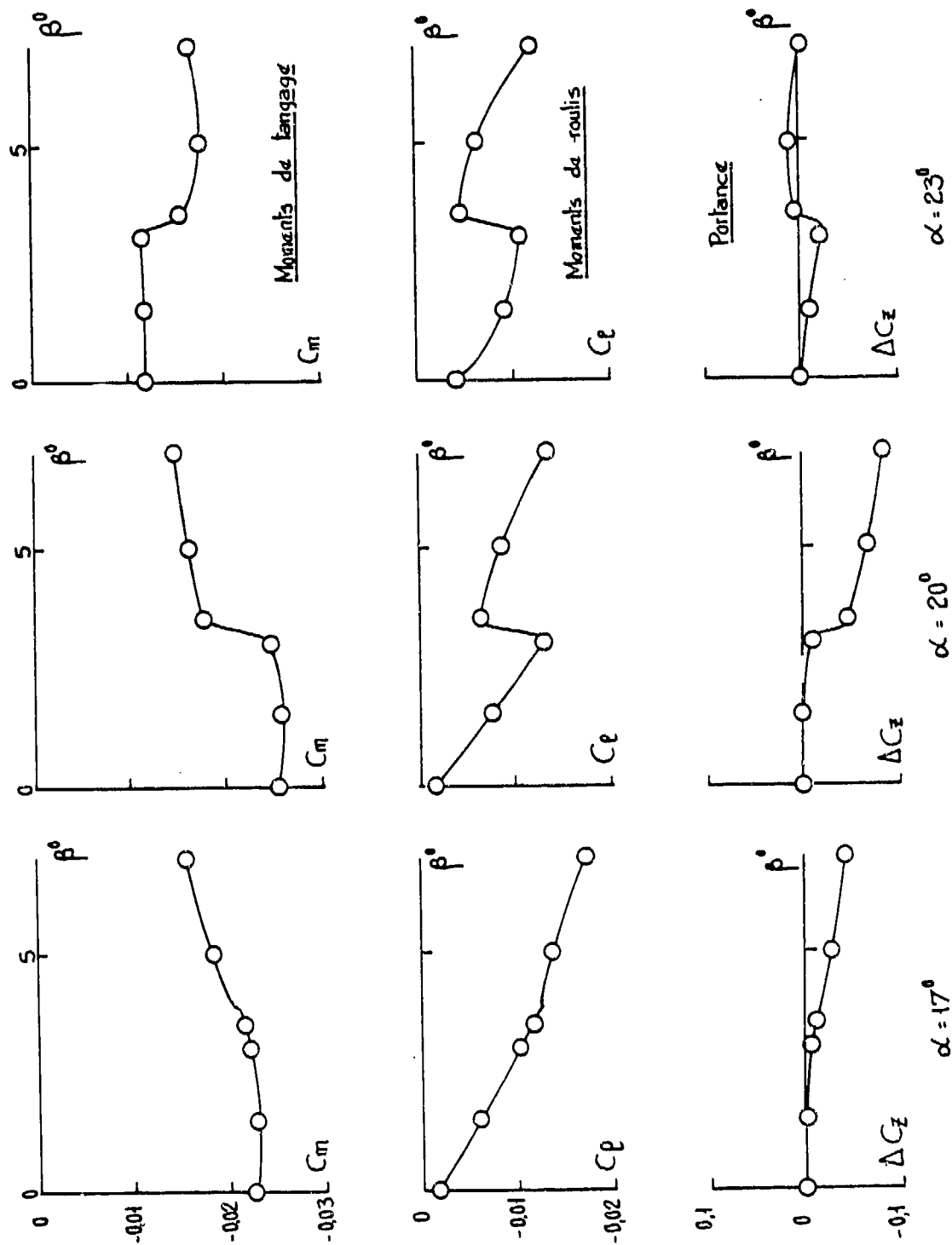
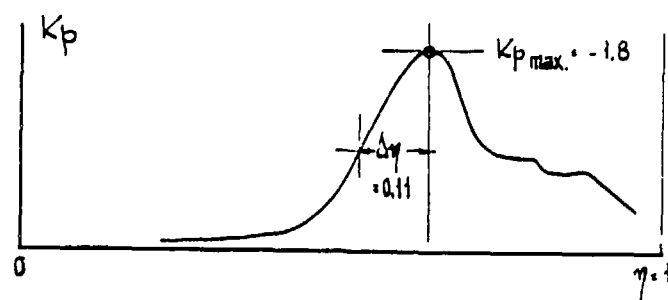
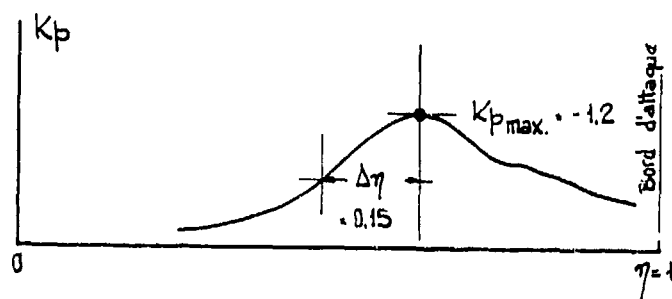


Planche 7 : Variation en dérapage à haute incidence des moments de tangage et de roulis et de la portance.
Avion de série - Essais en soufflerie à faible vitesse.



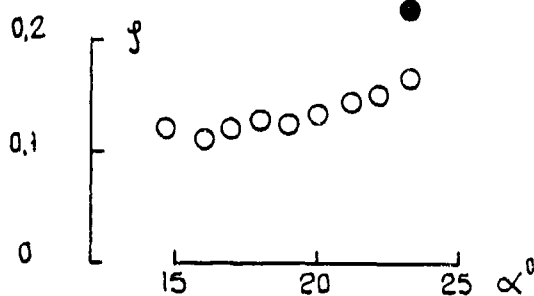
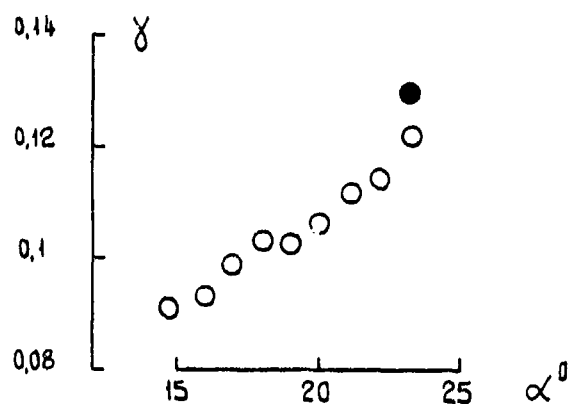
Avant autocabrage



Après autocabrage

Planche 8 : Répartition en envergure des pressions à l'extrados sur la partie arrière de la voilure à dérapage nul -

Avion développé - Essais en soufflerie à faible vitesse



○ avant "autocabrage"

● après "autocabrage"

Planche 9 : Variation en incidence de l'intensité et de la position au-dessus de l'extrados du tourbillon principal.

Avion développé - Essais en soufflerie à faible vitesse

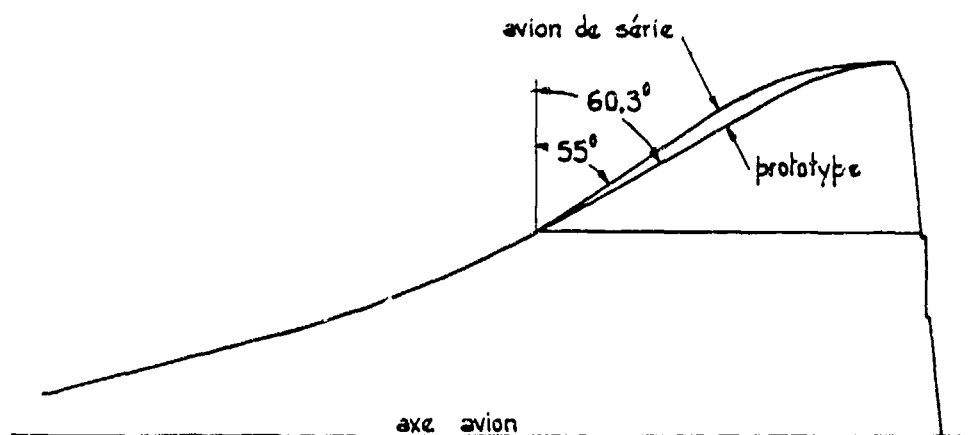


Planche 10 : Comparaison des formes en plan des avions prototype et de série.

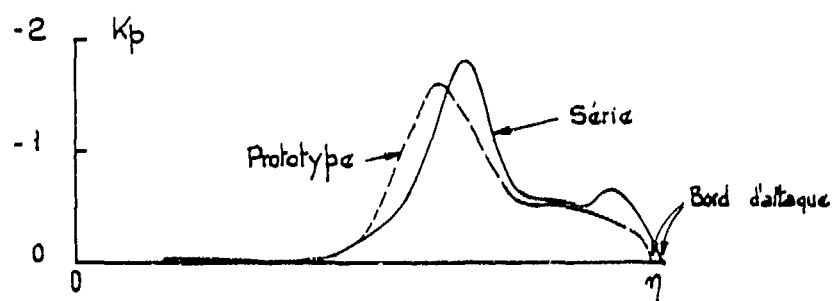


Planche 11 : Répartition en envergure des pressions à l'extrados sur la partie arrière de la voilure

Avions prototype et de série - Essais en soufflerie à faible vitesse.

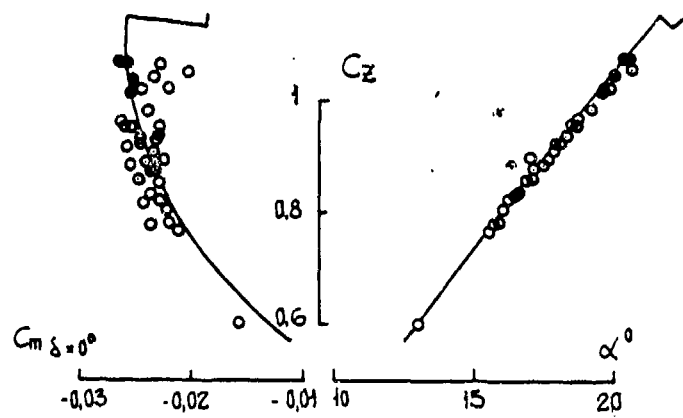


Planche 12 : Avion de série - Portance et moments de tangage à haute incidence.

Essais en soufflerie (faible vitesse) ———

Essais en vol : \circ ramenés à $\delta = 0$ - \bullet mesurés à $\delta = 0$

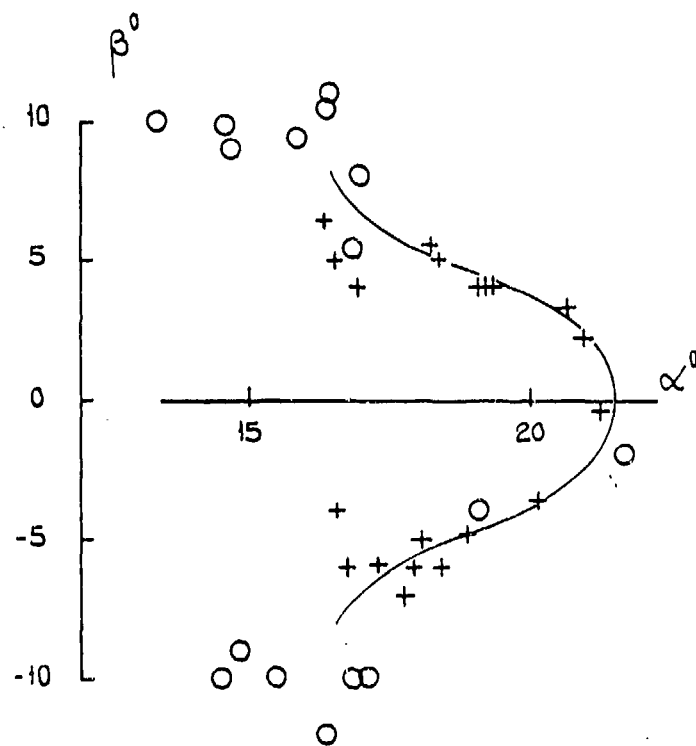


Planche 13 : Avion de série - Possibilités de dérapage à haute incidence.

Essais en soufflerie (faible vitesse) ——— accident en C_m , C_l et C_z

Essais en vol : \circ accident en C_m , C_l et C_z . + dérapage atteint sans accident

AERODYNAMIC DESIGN OF THE SPACE SHUTTLE ORBITER

by

W.E. Bornemann
Manager, Space Shuttle Aerodynamics
Rockwell International Corporation and
Space Systems Group
12214 Lakewood Boulevard
Downey, CA 90241

T.E. Surber
Supervisor, Orbiter Aerodynamics
Rockwell International Corporation
Space Systems Group
12214 Lakewood Boulevard
Downey, CA 90241

SUMMARY

The Space Shuttle Vehicle is being developed by the NASA to provide capability for lower cost space operations in the 1980's and beyond. This paper describes Shuttle Orbiter aerodynamic design conducted by Rockwell International under contract to NASA. Aerodynamic criteria key to establishing the external configuration are discussed together with evolution of the design including effects of wing-body blending on high angle of attack aerodynamics.

An overview of the wind tunnel program is given and aerodynamic characteristics of the final configuration are described. Aerodynamic parameters critical to definition of Orbiter entry control and performance are identified. During entry, the Orbiter flies over an angle of attack range from 50 to zero degrees. Trim capability and stability and control characteristics are discussed at critical regions in the entry trajectory. Methods are described to define reaction control rocket effectiveness and aerodynamic interactions during the initial portion of entry. At hypersonic speeds, wind tunnel results of viscous interaction effects at high angles of attack are discussed. In the supersonic region where transition from high to low angle of attack occurs, critical stability and control parameters and wind tunnel results are described. At subsonic speeds, comparisons are shown between predicted aerodynamic characteristics and data from the approach and landing flight test program.

NOMENCLATURE

Acronyms

AEDC	Arnold Engineering Development Center
ALT	Approach and Landing Test
ARC	NASA Ames Research Center
ATP	Authority to Proceed
CDR	Critical Design Review
EAFB	Edwards Air Force Base
ET	External Tank
ETR	Eastern Test Range
FCF	First Captive Flight
FMOF	First Manned Orbital Flight
JSC	NASA Johnson Space Center
KSC	NASA Kennedy Space Center
LaRC	NASA Langley Research Center (also LRC)
OMS	Orbital Maneuvering System
OV	Orbital Vehicle
PDR	Preliminary Design Review
PRR	Program Requirements Review
RCS	Reaction Control System
SRB	Solid Rocket Booster
SSME	Space Shuttle Main Engine
TAEM	Terminal Area Energy Management
WTR	Western Test Range

Symbols

b	Span
CA	Axial force coefficient
CD	Drag force coefficient
CL	Lift coefficient
CL	Rolling moment coefficient
CL β	Rolling moment coefficient due to sideslip (per degree)
CL δ_a	Rolling moment coefficient per degree aileron deflection
CL δ_r	Rolling moment coefficient per degree rudder deflection
Cm	Pitching moment coefficient
CN	Normal force coefficient
Cn	Yawing moment coefficient
Cn β	Yawing moment coefficient due to sideslip
Cn δ_a	Yawing moment coefficient per degree aileron deflection

Symbols (continued)

Cn δ_r	Yawing moment coefficient per degree rudder deflection
C ω	Factor of proportionality in linear viscosity-temperature relation, equation (5)
CG	Center of gravity
h	Altitude
L/D	Lift-to-drag ratio
M	Mach number
M.A.C.	Mean aerodynamic chord, also \bar{c}
\dot{m}_j	RCS jet mass flow ratio, equation (4)
\dot{m}_∞	
\bar{q}	Dynamic pressure = $1/2\rho V^2$
RE	Reynolds number, also Re
S	Reference area
Se	Standard error of estimate
V \bar{D}	Design touchdown speed
V ∞	Viscous parameter, equation (2)
\bar{x}_∞	Viscous interaction parameter, equation (1)
α	Angle of attack
β	Angle of sideslip (positive nose-up)
δ_a	aileron deflection (positive for positive rolling moment)
δ_{BF}	Body flap deflection (positive for nose-down pitching moment)
δ_e	Elevator deflection (positive for nose-left yawing moment)
σ	Standard deviation
ϕ_j	RCS jet momentum ratio, equation (3)
ϕ_∞	
Λ	Sweep angle
λ	Taper ratio
ρ	Mass density of air

Subscripts

LB	Body length
∞	Freestream

INTRODUCTION

The Space Shuttle Vehicle is being developed by the NASA to provide capability for lower cost space operations in the 1980's and beyond. The flight vehicle consists of a reusable orbiter, an expendable external propellant tank, and two reusable solid rocket boosters. Space Shuttle will be capable of launching a variety of payloads into earth-orbit from either the Eastern Test Range (ETR) at Kennedy Space Center or the Western Test Range (WTR) at Vandenberg Air Force Base. Maximum payload capabilities will be 29,480 kg for an easterly launch from ETR and 14,515 kg for launch into polar orbit from WTR.

The orbiter development contract, under the direction of NASA's Johnson Space Center, was awarded to Rockwell International in August 1972. Under this contract, two orbiter vehicles are being built—OV101 was delivered to the flight test center in February 1977, and approach and landing flight testing completed in October 1977. OV102, the first orbital flight vehicle, is in assembly and is scheduled for roll-out in late 1978. Orbital flight testing will begin in 1979.

Aerodynamic considerations have played a significant role in the vehicle design process. The Shuttle must fly satisfactorily with predicted aerodynamic characteristics; it is not feasible to approach flight testing by incremental expansion of the altitude and velocity envelope. Consequently, the NASA and Rockwell have given careful attention to the development of an extensive data base derived largely from wind tunnel tests, with detailed attention being given to defining uncertainties through statistical analysis of wind tunnel data and by comparisons of wind tunnel predictions with flight data from previous programs. In addition, the flight control system is being designed to minimize its sensitivity to uncertainties in aerodynamic parameters.

The objectives of this paper are to: (1) briefly describe the Shuttle mission in order to identify key aerodynamic design criteria; (2) summarize aerodynamic development of the orbiter; (3) describe the key aerodynamic parameters and their relationship to design and performance of the entry flight system; and (4) summarize recent flight results which verify the aerodynamic estimates for the approach and landing phase of the Shuttle mission.

VEHICLE/MISSION DESCRIPTION

The Shuttle Vehicle consists of four major elements: the orbiter; main engines (SSME); external tank (ET); and two solid rocket boosters (SRB). Overall vehicle configuration is illustrated in Figure 1. The external tank contains the liquid oxygen/liquid hydrogen propellants used by the main engines during ascent. Liquid oxygen is located in the forward tank to maintain an acceptable center of gravity for the combined vehicle. Nozzles on each booster are gimballed to augment control during ascent.

The orbiter, Figure 2, is a double-delta wing configuration comparable in size to a modern transport aircraft. Normally, the orbiter carries a crew of four—commander, pilot, mission specialist, and payload specialist—with provision for as many as seven persons. The orbiter can remain in orbit nominally for seven days (up to 30 with special payloads), return to earth with personnel and payload, land like an airplane, and be refurbished for a subsequent flight in 14 days. Three main rocket engines mounted in the aft section of the orbiter provide propulsive thrust during ascent. These two million Newton thrust liquid oxygen/liquid hydrogen engines are gimballed in pitch and yaw to provide thrust vector control. Smaller orbital maneuvering system (OMS) rocket engines are also located in the aft section to provide final impulse for orbit insertion, orbital maneuvers, and deorbit. Reaction control rockets (RCS) are located in both the forward and aft section of the orbiter to provide attitude control and three-axis translation during orbit insertion and on-orbit operations. The aft reaction control rockets are used in combination with aerodynamic surfaces for control during entry. Aerodynamic surface controls include split elevons along the wing trailing edge; a split rudder in the vertical fin which can also be flared open to serve as a speed brake during descent; and a hinged body flap located at the lower aft end of the fuselage to augment control during descent and landing approach. The body flap also shields the exposed main engine nozzles from aerodynamic heating during entry.

The entire external surface of the orbiter, except the windows, is protected by reusable insulation to maintain acceptable structural temperatures under entry heating environment. Figure 3 illustrates the application areas for the materials used in the thermal protection subsystem. Application is as follows:

1. Coated Nomex felt is used in areas where temperatures are less than 672°K for entry and 716°K for ascent; i.e., upper cargo bay door, mid- and aft-fuselage sides, upper wing, and OMS pod.
2. Low-temperature reusable surface insulation is used in those areas where temperatures are below 922°K and above 672°K under design heating conditions.
3. High-temperature reusable surface insulation is used in those areas exposed to temperatures below 1533°K and above 922°K under design heating conditions.
4. Reinforced carbon-carbon is used on areas such as wing leading edge and nose cap where predicted temperatures exceed 1533°K under design heating conditions.
5. Thermal window panes are used in the crew compartment and high temperature metal is used for forward reaction control system fairings and elevon upper surface rub seal panels.
6. Thermal barriers are installed around operable penetrations (main egress hatch, landing gear doors, etc.) to protect against aerothermal heating.

The thermal protection system is a passive system. It has been designed for ease of maintenance and for flexibility of ground and flight operations while satisfying its primary function of maintaining acceptable airframe outer skin temperatures.

Mission Profile

Mission performance capability is summarized in Table 1. A typical mission profile is shown in Figure 4. The Shuttle is launched with the main engines and solid rocket boosters burning in parallel. A maximum dynamic pressure of $31,100 \text{ N/m}^2$ is experienced approximately 62 seconds after launch at 11,280 meters altitude. Booster separation occurs at 122 seconds at an altitude of 43,280 meters, 46.3 kilometers downrange from the launch site. The solid rocket boosters descend on parachutes, are recovered after water impact, and are refurbished for subsequent reuse.

After booster separation, the orbiter continues to ascend with main engine cut-off and external tank separation occurring 479 seconds after lift-off when the orbiter has reached an altitude of 115,700 meters. The orbital maneuvering system engines, which provide the additional velocity needed for orbital insertion are cut-off approximately 600 seconds after launch.

After completion of the orbital operations phase, deorbit is accomplished by retro-fire of the orbital maneuvering engines, and the orbiter descends to the atmospheric entry interface (nominally, an altitude of 121,920 meters). A typical entry trajectory is shown in Figure 5. The initial entry phase extends to a dynamic pressure level of 957.6 N/m^2 (approximately 76,200 meters altitude) during which attitude control from two aft pods is blended with aerodynamic surface controls, the latter gaining in effectiveness as dynamic pressure increases. Entry, from a dynamic pressure level of 957.6 N/m^2 to a Mach number of less than five, is accomplished at a high angle of attack (initially 38 degrees) during which the blanketing effect of the wing essentially precludes any rudder control. Coordinated lateral-directional control is provided by combined yaw reaction control jets and aileron control. The terminal phase occurs as angle of attack is reduced below 18 degrees. As the orbiter descends to altitudes where winds can result in relatively large errors in inertially derived air data, probes are extended ($M=3.5$) to provide air data relative to the vehicle. During a typical normal entry, range control is achieved by bank angle while angle of attack follows a predetermined schedule to achieve (at approximately $M = 1.5$) an angle somewhat smaller than that corresponding to maximum L/D. A downrange capability of up to 7,960 kilometers with a cross range capability of 1,815 kilometers may be realized. Subsonic flight is achieved at an altitude of approximately 12,190 meters. Range control during the gliding descent is obtained by angle of attack modulation with velocity control maintained by the speed brake. The approach and landing interface occurs at 3,048 meters above ground level and a preflare is initiated at an appropriate altitude, followed by a deceleration float and touchdown. The initial approach target and flare altitude will be scheduled to provide a minimum of 25 seconds between flare initiate and touchdown. Touchdown occurs at an angle of attack of about 15 degrees. The nominal touchdown velocity is 88 meters/sec, and maximum landing speed with a 14,515-kilogram payload is about 106 meters/sec including dispersions for hot-day effects and tailwinds.

Orbiter Aerodynamic Criteria

Aerodynamic criteria, Reference 1, for the orbiter vehicle require the configuration to perform as both a spacecraft and an aircraft. Because of this, the external features must be carefully configured to provide the protection and versatility required for orbital and atmospheric flight, and the aerodynamic performance and control necessary for unpowered descent and landing. The aerodynamic lines must ensure performance that is acceptable over the hypersonic to subsonic speed range, and provide the required cross range capability and touchdown velocity. Aerodynamic requirements, Table 2, were developed from analysis of the entry phase of the mission. Landing requirements are shown in Figure 6. Static stability was not required since the design criteria allowed reliance on the flight control system to meet flying qualities criteria. Early simulations identified a flight control requirement for static longitudinal stability to be no more than two percent body length (5.45 percent mean aerodynamic chord) unstable so the pitching moment curve established the aft center of gravity limit at 67.5 percent of body length. Payload criteria established a center of gravity range of 2.5 percent, thus establishing the forward limit.

The selected configuration, Figure 2, evolved from a series of program and technical refinements directed to achieve the vehicle yielding the best combination of performance and cost. This evolution is discussed further in a later section. The double-delta planform combined with a moderately low fineness ratio (approximately five) body minimizes interference heating effects, provides the required cross range requirements, and possesses an acceptable trim and stability range, Figure 7, over the flight Mach number range.

The orbiter wing was sized to provide a 88 meters/second touchdown speed (V_D) at a 15-degree angle of attack (tail scrape attitude for main gear strut compressed, tire flat) with body flap retracted and the center of gravity at the forward limit. The leading edge sweep (45 degrees) and aspect ratio (2.265) were selected on the basis of aerothermodynamic trade studies to provide the design touchdown speed for a center of gravity at the forward limit with minimum wing size and to optimize the wing leading edge thermal protection system for a reuse cycle of 100 flights prior to major rework.

The fuselage was designed to accommodate a variety of payloads and house the crew and maneuvering control systems. Nose camber, cross section, and upward sloping forebody sides were selected to improve hypersonic pitch trim and directional stability and in conjunction with wind-body blending, to reduce entry heating on the body sides. Propulsion units for entry attitude control and orbital maneuvering have been incorporated in pods located in the aft body fairings. The body flap is used to protect the Shuttle main engine during entry and to provide trim capability to relieve elevator loads.

The vertical tail has been sized to provide a low-speed $C_{N\delta}$ of 0.0013 at an angle of attack of 13 degrees about a center of gravity located at the aft limit. It has a reference area of 38.39 m^2 including the rudder/speed brake. The rudder is split along the orbiter buttock plane to provide

directional stability augmentation in the hypersonic/supersonic flight regimes and to apply drag modulation for the subsonic flight phases, approach and landing. The section profile is a five-degree, half-angle, 60-40 double-wedge airfoil.

Aerodynamic and aerothermodynamic criteria, Reference 2, regarding surface discontinuities, thermal protection system tile steps and gaps, and waviness are shown in Figure 8. These criteria are based on aerodynamic efficiency requirements of lifting surfaces and the prevention of premature transition from laminar to turbulent boundary layers in the high heating portion of entry. Aerodynamic efficiency is affected to a much greater extent by surface conditions of the forward rather than aft regions of components. Hence, tolerance criteria are generally more restrictive for forward regions of the vehicle surfaces and somewhat relaxed at aft portions.

DEVELOPMENT APPROACH

Development Schedule

Major program milestones are illustrated in Figure 9, starting with authority to proceed (ATP) in 1972 and culminating with initial operational capability in 1980. The orbiter concept at ATP was a blended delta wing vehicle based on precontract studies and configured to meet initial Shuttle Program requirements. As a result of a continuing assessment of system requirements and technical refinements, early in the contract the orbiter concept was modified to reduce weight and decrease program and operating costs (Reference 3). As discussed in more detail later, refinements in the aerodynamic configuration led to a double-delta planform incorporating a more efficient lifting surface than the blended delta. The System Requirements Review in August 1973 finalized technical requirements for the Space Shuttle systems (i.e., the total vehicle, its elements, and their ground systems) and approved the design approach of the vehicle and associated support equipment. Preliminary Design Review (PDR) of the first orbiter (Orbiter 101) vehicle and subsystems for the approach and landing flight test program was completed in February 1974, followed by the Preliminary Design Review of the second orbiter (102) in March 1975. Orbiter 101 roll-out from final assembly in Palmdale, California, took place in September 1976. The vehicle was mated to the Boeing 747 carrier aircraft at the Dryden Flight Research Center, Edwards Air Force Base, and the first captive flight was completed in February 1977. The first airlaunch of Orbiter 101 for the approach and landing flight test (ALT) took place on August 12, 1977, and the final flight was completed on October 26, 1977. Delivery of OV101 to the Marshall Space Flight Center, Alabama, for ground vibration testing took place in March 1978. Fabrication and assembly of Orbiter 102, the first orbital vehicle, began in 1975. Rollout is scheduled for late 1978, followed by delivery to Kennedy Space Center, Florida, and first manned orbital flight in 1979. The first six orbital flights of the Shuttle are development test flights, and the seventh flight in 1980 is considered the initial operational capability flight.

Aerodynamic Design Approach

It is conventional in an aircraft program to approach flight demonstration by incremental expansion of the flight envelope. This is not feasible with the Shuttle vehicle. Once Shuttle is launched, it is committed to flight over the complete mission profile from ascent to orbiter insertion, deorbit, entry, and landing. Flight characteristics must be based on aerodynamic data derived from ground testing and analysis. Careful attention has been given to the interactions between flight control systems design and aerodynamic characteristics, and allowance has been made for uncertainties in basic aero data in flight control design. Predicted aerodynamic characteristics have been derived from extensive wind tunnel tests which have included a systematic investigation of data uncertainties, nonlinear effects, and effects of wind tunnel installation, blockage, and shock wave reflections. The Langley Research Center conducted detailed wind tunnel investigations of control surface characteristics and nonlinear aerodynamic effects, (i.e., Reference 4) to support development of the data base.

Wind Tunnel Program

Key to Space Shuttle development has been the acquisition of wind tunnel test data to support design and evaluation by providing a continuously maturing data base reflecting configuration and subsystem updates. By first orbital flight in 1979, approximately 40,100 total wind tunnel test hours will have been conducted for aerodynamics, heat transfer, and structural dynamics, consisting of approximately 20,200 for the orbiter vehicle, 16,100 for the mated launch configuration, and 3,800 for the carrier aircraft program, Table 3. A total of 94 models have been built—38 aerodynamic, 36 heat transfer, and 20 structural dynamic, Table 4. All wind tunnel testing is coordinated with and approved by NASA management at JSC.

In order to accurately simulate flight conditions in a wind tunnel, Reynolds number and Mach number must be matched. Problems in flow simulation (Reference 5, NASA CP-2009) occur when the geometric scaling of viscous flow is important, or when coupling between the viscous surface flow and the external flow field is strong. In the first case, the boundary layer can be considered separately from the inviscid flow field, and viscous effects can be scaled. This holds for Mach numbers up to about 10. It is well known, for example, that skin friction varies with Reynolds number in a predictable manner and can be scaled to flight conditions from suitable wind tunnel results.

For Mach numbers greater than about 10, a pressure interaction results from the outward streamline deflection induced by a thick boundary layer, and the viscous-inviscid interaction can no longer be neglected. For this case, there are two classical simulation parameters commonly considered:

- (1) \bar{x}_∞ , the viscous interaction parameter introduced by Hayes and Probstein (Reference 6)

$$\bar{x}_\infty = \frac{M_\infty^3 \sqrt{C'_\infty}}{\sqrt{Re_{\infty x}}} \quad (1)$$

- (2) V'_∞ , the viscous parameter introduced by Whitfield and Griffith (Reference 7)

$$V'_\infty = \frac{M_\infty \sqrt{C'_\infty}}{\sqrt{Re_{\infty x}}} \quad (2)$$

where M_∞ is the freestream Mach number, C'_∞ is the factor of proportionality in the linear viscosity-temperature relation (Reference 8), and $Re_{\infty x}$ is the freestream Reynolds number based on x . The parameter \bar{x}_∞ is the relevant parameter for the "pressure" in both the strong and weak interaction cases; whereas V'_∞ is the relevant parameter in terms of "pressure coefficient" (i.e., \bar{x}_∞/q_∞). For Shuttle, it has been observed that V'_∞ correlates total aerodynamic coefficients better than \bar{x}_∞ , and consequently, V'_∞ has been used as the hypersonic simulation parameter.

Figure 10 shows a comparison between flight Re and V'_∞ and the simulation capability of typical wind tunnels used to develop the Orbiter aerodynamic data base. It is seen that the tunnel capabilities closely match flight simulation requirements.

Orbiter aerodynamic test hours are summarized in Figure 11 which illustrates the phasing and relationship to program milestones, and the distribution by speed range. Approximately 38 percent of the hours were utilized in subsonic test, 44 percent in the transonic/supersonic range, and 18 percent in the hypersonic testing. Four test phases will be completed by first orbital flight. The first was a configuration definition phase to develop wing airfoil section and planform geometry in support of design trades to reduce orbiter weight which led to selection of the double-delta arrangement. This phase was completed by System Requirements Review in August 1973. The second phase extending essentially to OV102 Preliminary Design Review in March 1975 was dedicated to refinement of the orbiter vehicle and development of the ferry flight configuration. A tailcone configuration was developed to improve ferry performance and provide longer duration orbiter flights during the approach and landing test program. Orbiter tests were conducted to determine basic stability and control capability over the complete entry speed range. Control surface effectiveness and hinge moments were measured to support preliminary design and sizing of actuators. Initial RCS interaction tests were conducted to support entry control analysis. Tests were also performed to measure Reynolds number and viscous interaction effects and to identify wind tunnel sting tare corrections to test data. In addition, the Langley Research Center conducted testing to measure orbiter damping derivatives.

The third phase of the test program was implemented following OV102 Preliminary Design Review in March 1975 to provide more detailed OV102 design data and to verify the aerodynamic characteristics of OV101 prior to first captive flight in February 1977. The Langley Research Center program to investigate nonlinear aerodynamic and control surface interaction characteristics was continued during this phase. In addition, extensive testing was conducted to develop the orbiter air data system and provide sensor calibrations for both OV101 and 102. OV101 verification testing was also completed during this period utilizing a 0.36-scale model in the Ames Research Center 40x80-ft (12.2x24.4 m) wind tunnel. This model was an accurate replica of the actual OV101 flight vehicle and incorporated simulated thermal protection system tiles, outer moldline protuberances, and main engine and reaction control system exhaust nozzles.

The final phase, initiated in early 1978, is still in progress and is directed toward verification of OV102 characteristics prior to first orbital flight. Two models are employed (0.05 and 0.02 scale) to cover the speed range from Mach 16 to 0.2. Figure 12, illustrates the details of protuberances, cavities, and thermal seals simulated on the models.

Aerodynamic Uncertainties

Allowance has been made for uncertainties in basic aerodynamic data used in design of the Shuttle Vehicle, subsystems, and early mission profiles, Reference 9. Two categories of uncertainties have been defined: 1) Tolerances, which account for wind tunnel data accuracy and manufacturing tolerances; and 2) Variations, which account for unknowns in extrapolation of model data to free-flight. "Tolerances" are used in subsystem design, and were derived from a statistical analysis of wind tunnel data in which tests were conducted using the same models in several different wind tunnels and using different scale models in the same wind tunnel. "Variations" are used in establishing flight test plans and constraints, and were determined from comparisons between predicted aerodynamics and flight test results from lifting entry vehicles and selected high-speed aircraft. The flight data will allow reductions of the variations and removal of corresponding flight placards to achieve operational capability.

A multiple regression analysis computer program, Reference 10, was used to determine the "tolerances" on the derivatives C_L , C_D , C_m versus α ; C_H , C_g versus β , δ_a , and δ_r . Utilization of the program involved inputting available sets of wind tunnel data for a specified coefficient versus α , β , δ_a or δ_r at given conditions of Mach number, control surface setting, etc., with a proposed form of curve-fit; e.g., $C_L = K_0 + K_1\alpha + K_2\alpha^2 + \dots + K_5\alpha^5$. The regression program statistically determines which terms of the proposed

curve-fit equation are significant and eliminates those which are not significant by performing a least-square curve-fit of the test data. Subsequent to selecting a "best" curve-fit, the deviation of each test point from the curve is computed and the Standard Error of estimate, S_e , (which is a measure of the standard deviation, σ) is multiplied by three to estimate the three-sigma (3σ) tolerance of the aerodynamic coefficient, C , being analyzed. The three-sigma tolerance is an increment or band about a nominal value of the aerodynamic coefficient, C , for any given Mach number, body flap deflection, etc., where the probability that a measured coefficient at the specified condition lies within $C \pm 3\sigma$ is 99.73 percent. An example of the procedure for determining the tolerance on lift coefficient is shown in Figure 13. The regression program yields a polynomial expression for lift coefficient in terms of angle of attack:

$$C_L = -0.0546 + 0.0178 \alpha + 0.0003 \alpha^2 - 2 \times 10^{-9} \alpha^5$$

The standard error of estimate becomes $S_e = 0.0146$ and the corresponding three-sigma tolerance on lift coefficient at Mach 5.0 becomes 0.0438.

"Variations" were developed for three speed regimes from comparisons of flight and predicted values based on wind tunnel test data for representative vehicles, constructing the bounds of the data points and applying the larger bound as a plus or minus value. An example of the procedure used to develop variation uncertainties is displayed in Figure 14. The figure presents a comparison between predictions based on wind tunnel results and flight measured values of normal force for selected aircraft and space vehicles. The data bands were selected on the basis of engineering judgment and weighting "Shuttle-like" configurations more heavily than the lifting bodies. The speed regime groups were $M \leq 0.8$, $0.8 \leq M \leq 1.2$ and $M \geq 1.2$. The ratio of variation to tolerance at Mach 10.0 was assumed to apply throughout the viscous interaction speed region.

Later in this report where Orbiter flight data from the approach and landing test program are discussed, comparisons are shown between estimated tolerances and variations for several aerodynamic parameters. The measured flight test data points are seen to be distributed about the nominal value and to fall within the predicted tolerance band, and well within the estimated variations. It is anticipated that further correlation with flight data will permit reduction of the variations and removal of corresponding flight placards to achieve full operational capability.

CONFIGURATION EVOLUTION

Stability, control, and performance requirements for aerodynamic configuration design of the orbiter vehicle are, for the most part, established by the entry and recovery phases of flight. Consequently, it is these phases of flight which were key in determining aerodynamic requirements for the orbiter external arrangement. On the other hand, design airload conditions are primarily determined from the ascent phase.

Design issues key to achieving the proper aerodynamic balance to provide stability, control, and center of gravity range capability across the entry/recovery flight regime are wing design, wing-body integration, and integration of aerodynamic and flight control requirements. Wing design was key because of its influence on vehicle weight, thermal environment, aerodynamic stability, buffet characteristics, and gliding and landing performance capability. Wing-body integration was important in obtaining a balanced aerodynamic configuration capable of trim and control over the entire speed range, and in minimizing thermal environment due to interference flow effects. Fuselage dimensions were largely fixed by payload size and packaging efficiency while aerodynamic and aerothermodynamic considerations established forebody shape and local contours. Integration of aerodynamic control requirements was of major importance in meeting flying quality goals in all flight regimes, and minimizing vehicle weight as affected by control surface arrangement, size, and actuator requirements.

Prior to Shuttle Program go-ahead in August 1972, Rockwell International participated in extensive NASA-funded Shuttle System studies during which numerous trades (Reference 1) were conducted to determine Shuttle operational cost effectiveness, desired configuration and geometry, major subsystem definition, and identification of major design drivers for the orbiter configuration. Design requirements found to be key configuration drivers are landing speed; payload size, weight, and center of gravity envelope; entry cross range and aerodynamic heating; stability and control requirements; and flying qualities. From these studies emerged a basepoint configuration at Shuttle Program authority to proceed (ATP). Following ATP, further trade studies were conducted at NASA/JSC and Rockwell to refine the basepoint design. Essentially four aerodynamic basepoints were evaluated in arriving at the final selected design, as summarized in Figure 15.

ATP Configuration

For the ATP orbiter aerodynamic configuration, Rockwell selected a blended delta wing-body design to meet NASA mission requirements. Selection of the external arrangement was based on results of previous investigations at the NASA centers, and Rockwell design studies, supported by 4300 hours of wind tunnel testing. The orbiter aerodynamic shape incorporated a 50-degree swept delta wing planform sized to provide 77.2 m/sec touchdown speed with 18,100 kilograms return payload. Hypersonic L/D was 1.3 at 34-degree angle of attack, and maximum subsonic L/D was 5.7. Elevons were sized to provide trim at hypersonic speeds over an angle of attack range from 20 to 50 degrees with an operational center of gravity range of three percent body length. The cargo bay provided a 4.57 meter diameter by 18.2 meter long volume for a wide variety of payloads. Cargo deployment/retrieval manipulators were stowed in a dorsal fairing along the top of the payload bay doors. Provision was made for installing four airbreathing engines in the aft portion of the payload bay for early development flights. Three main propulsion system rocket engines were located at the base of the aft fuselage, and on-orbit propulsion engines were installed

in two removable pod modules alongside the aft fuselage. Reaction control rocket engines were located in the aft pods and in the forward fuselage compartment.

PRR - PDR Configuration

Upon initiation of Shuttle go-ahead, the development aerodynamic wind tunnel program was implemented, and further trade studies were conducted at NASA/JSC and Rockwell to refine the ATP basepoint. The ATP and PRR orbiters (Figure 15) were both blended delta wing configurations which were externally similar. The most obvious changes were: (1) a redesigned forebody to accommodate internal packaging revisions; (2) the movement of the OMS/RCS pod from the side of the aft fuselage to the shoulder location; and (3) deletion of airbreathing propulsion for landing assist following orbital flights.

A series of wind tunnel tests conducted over the Mach number range from 0.26 to 7.4, indicated revised wing twist, camber, and fuselage blending would improve low-speed lift capability. Results showed that reducing the wing-body fillet radius and changing from a faired to a straight fillet (wing-glove) increased the trim C_L significantly. In addition, significant system requirement changes were made by NASA to reduce vehicle weight and cost. Orbiter down payload weight was reduced from 18,100 to 11,300 kilograms, and the vehicle resized from a design dry weight of 77,100 kilograms to 68,000 kilograms. The minimum subsonic stability requirements were reduced from three percent to 0.5 percent body length static margin at the forward center of gravity. For the PDR configuration, Reference 3, direction was received from NASA to modify the wing planform to a double-delta design, and the wing was resized to meet the reduced dry weight and payload requirements. A 45/79 degree wing planform with reduced glove leading edge radius was incorporated for improved subsonic performance, Figures 16 and 17. Improved low-speed performance and the reduced static margin requirement permitted a reduction in wing size from 299 to 250 square meters and resulted in rebalancing the orbiter vehicle to meet stability and control requirements.

CDR Configuration

Wind tunnel investigations of the PDR configuration revealed a need for further configuration refinement. Aerodynamic tests showed a difficulty in providing trim capability at the forward center of gravity in the supersonic flight regime. Aeroheating tests indicated the blunt fuselage nose resulted in early transitional flow and high temperatures along the lower body surface. Also, wing incidence, camber, and thickness distributions designed for maximum subsonic performance led to local fairings on the lower wing and fuselage surfaces which caused high local heating.

Changes incorporated in the fuselage nose section are illustrated in Figure 18. The blunt nose shape was modified to a cross section which was basically parabolic in plan and side-view. Wing/fuselage fairings along the bottom of the orbiter were modified to provide a thermodynamically acceptable smooth lower surface with minimum reverse curvature, Figure 19. Leading edge sweep of the glove was slightly changed (from 78 to 81 degrees) as a result of refairing into the modified fuselage nose.

To achieve the best combination of performance and cost, further configuration refinements were made. The down payload requirement was increased to 14,500 kilograms and the design center of gravity range established at 2.5 percent body length. The OMS pod forebody fairing which extended onto the cargo bay door was shortened to reduce weight and simplify the door-to-fuselage seal design. In addition, the manipulator arm dorsal fairing along the top of the payload bay doors was deleted, and the manipulator was stowed inside the payload bay, Figure 20. Aerodynamic criteria for the final configuration are listed previously in Table 2.

ORBITER AERODYNAMIC CHARACTERISTICS

Aerodynamics characteristics of the final orbiter vehicle, Reference 2, are summarized in this section. These characteristics were derived from wind tunnel test results adjusted to account for scale effects or differences between model configurations and the final orbiter vehicle. Aeroelastic corrections have been estimated by standard methods. Wind tunnel skin friction drag and reaction control rocket plume interaction data have been corrected to free-flight conditions using Reynolds number scaling for skin friction, and jet-to-freestream-momentum ratio for plume effects.

Criteria for aerodynamic design of the Orbiter have been determined from analyses of the entry flight phase, considering requirements for vehicle trim, control, performance, and aerodynamic heating. A typical entry profile is illustrated in Figure 21. Trajectory guidance is accomplished by flying an angle of attack/velocity profile preselected to meet thermal design criteria, and using roll commands for range control. Flight control is accomplished in two modes termed spacecraft and aircraft. The spacecraft mode applies from initial through mid-entry phases where the Orbiter is at high angle of attack making the vertical fin and rudder ineffective. The aircraft mode includes mid-entry through approach and landing. Switching from spacecraft to aircraft modes is performed as a function of angle of attack and velocity. Transition begins at approximately Mach 5 and is completed at about Mach 1.5. In the spacecraft mode, control in all three axes is initially provided by the aft reaction control system jets mounted at the base of the Orbiter on either side of the vertical tail. As control authority of the aerodynamic surfaces becomes sufficient, the jets are deactivated. Utilization of the control surfaces and jets during entry is illustrated in Figure 22. At a dynamic pressure of 95.8 N/m², the elevons are used to supplement the jets in pitch and roll. The roll jets are turned off at a dynamic pressure of 478.8 N/m² at which point the yaw jets are used to initiate roll maneuvers (as well as yaw control) with the ailerons providing turn coordination until switchover to the aircraft mode. At a dynamic pressure of 957.6 N/m², the pitch jets are turned off and the elevons provide pitch control. Transition to the aircraft mode is initiated at approximately Mach 5 when the rudder is activated. The yaw jets are turned off at about Mach 1, and the

rudder provides control until landing. The speed brake is programmed to assist pitch trim and augment lateral stability during transition from spacecraft to aircraft control. During approach and landing, the speed brake setting is modulated for speed control. Additional pitch trim is provided by the body flap which is programmed as a function of velocity.

Significance of the aerodynamic parameters rests in their effects on vehicle performance, control, and airloads. Those parameters most sensitive to meeting entry mission requirements are listed in Table 5. Lift, drag, and pitching moment are the primary aerodynamic parameters governing the entry trajectory, range capability, and thermal system design requirements in terms of heat rate and load. Heating rate influences maximum surface temperature and affects material reuse capability. Heat load establishes material thickness to maintain structural temperatures and, therefore, affects thermal protection system weight. Pitching moment determines the elevon setting required for trim. Design areas sensitive to trim setting are elevon heating during initial entry, and control surface actuator stall limits at transonic speeds. In addition, there is an interaction between elevon setting and lateral-directional control capability because of the change in roll and yaw effectiveness of the ailerons with elevon position. Lateral-directional trim and control capability is governed by the aileron and rudder control derivatives. Above Mach 5 the aileron is used for both roll and yaw trim before the rudder become effective. Between Mach 5.0 and 1.5, the rudder provides both yaw and roll trim with the aileron providing turn coordination. Below Mach 1.5, roll trim is provided by the rudder. The derivatives $C_{n\beta}$, $C_{l\beta}$, $C_{n\delta_a}$, $C_{l\delta_a}$, $C_{n\delta_r}$, $C_{l\delta_r}$ are key to establishing control capability, reaction control system propellant usage, and the switch-over point from spacecraft to aircraft control modes.

High Altitude Aerodynamics

The entry interface, defined as the upper limit of the sensible atmosphere, begins at approximately 120,000 meters altitude. In this high altitude region, say 70,000 to 120,000 meters, rarefied gas flows are encountered by the orbiter as it enters the atmosphere. Aerodynamic design issues in this region involve determining the effectiveness of the control jets and their influence on the Orbiter flow field, in addition to defining viscous interaction effects associated with low Reynolds number/high Mach number flows.

Initial entry aerodynamic characteristics, Figure 23, are highly influenced by interactions between the reaction control system jet plumes and the local flow field over the Orbiter. The total jet effects are comprised of three factors:

- Jet thrust
- Surface impingement
- Flow field interaction

Impingement and interaction effects are inter-related and have been obtained from wind tunnel testing. Coupling is present between the plume effects and aero surfaces, and between the jets themselves.

A series of model nozzles with different expansion ratios were employed during the wind tunnel test program. General Dynamics/Convair, under contract to the NASA (NAS9-14095), Reference 11, developed a method whereby the experimentally measured induced plume effect (surface impingement plus flow field interaction) could be separated into two component parts and the impingement term extrapolated to flight conditions. To obtain a correct modeling of the reaction control system plume effects in the wind tunnel, it was necessary to observe certain scaling criteria. The primary factors for consideration, aside from dimensional scaling, are plume shape and jet-to-freestream momentum ratio, ϕ_j/ϕ_∞ . In some instances, namely, yaw thruster firings, mass flow rate ratio, \dot{m}_j/\dot{m}_∞ , scaling was found to be a slightly better modeling parameter than momentum ratio. The scaling parameters are defined as:

$$\frac{\phi_j}{\phi_\infty} = \frac{\dot{m}_j v_j}{2 \bar{q}_\infty S_{ref}} n = 7.3879 \frac{n}{\bar{q}_\infty} \quad (3)$$

and

$$\frac{\dot{m}_j}{\dot{m}_\infty} = \frac{\phi_j}{\phi_\infty} \frac{v_\infty}{v_j} \frac{1}{n} (\sin \theta_j)^{1/2} = 1.300 \times 10^{-3} \left(\frac{v_\infty}{\bar{q}_\infty} \right) \quad (4)$$

where

- \dot{m}_j = Jet mass flow rate
- \dot{m}_∞ = Freestream mass flow rate
- v_j = Exit velocity ~ meters/sec
- \bar{q}_∞ = Dynamic pressure ~ N/m²
- θ_j = Nozzle half-angle at exit

n = Number of thrusters

S_{ref} = Reference area (24.9 m²)

In scaling from wind tunnel to flight, certain adjustments to the data base are required to account for real exhaust plume effects since cold air was used as the jet media in the tunnel. Model plume impingement effects were theoretically extracted from the measured tunnel data and the remaining jet plume interaction effects correlated against ϕ_j/ϕ_∞ or \dot{m}_j/\dot{m}_∞ . Prototype impingement effects were then theoretically generated. Examples of the data correlation for pitching moment are presented in Figure 24.

The application of the reaction control system data to a typical entry flight condition of $\bar{q}_\infty = 478.8$ N/m² at an altitude of 79,250 meters are presented in Figure 25 for three aft left downfiring reaction control system thrusters. It is to be noted that adverse effects to control authority result from the impingement and flow interaction terms for roll and pitch; whereas, in yaw these terms tend to increase the jet moment.

Viscous interaction effects are scaled from wind tunnel test data to flight conditions by means of the hypersonic viscous parameter \bar{V}'_∞ discussed earlier:

$$\bar{V}'_\infty = M_\infty \sqrt{\frac{C'_\infty}{Re_\infty L_B}} \quad (2)$$

where

M_∞ = Freestream Mach number

$Re_\infty L_B$ = Freestream Reynolds number (based on body length, L_B)

C'_∞ = Proportionality factor for the linear viscosity-temperature relationship (Reference 8)

$$= \left[\frac{T'}{T_\infty} \right]^K \left[\frac{T_\infty + 122.1 \times 10^{-(5/T_\infty)}}{T' + 122.1 \times 10^{-(5/T')}} \right] \quad (5)$$

with Monahan's empirical relationship given by

$$\frac{T'}{T_\infty} = 0.468 + 0.532 \frac{T_w}{T_\infty} + 0.195 \frac{\gamma - 1}{2} M_\infty^2 \quad (6)$$

where

T' = Reference temperature, degrees Kelvin

T_∞ = Freestream static temperature, degrees Kelvin

T_w = Wall temperature, degrees Kelvin

γ = Specific heat ratio

K = Empirical constant = 0.5 for air

j = Empirical constant = 1.0 for air

NOTE: A constant wall temperature of 1367°K and specific heat ratio of 1.15 have been assumed for the flight conditions analyzed.

The primary viscous interaction effects are in shear forces with essentially no effect on normal force. Variation of \bar{V}'_∞ along the nominal entry trajectory is illustrated in Figure 26. High values of \bar{V}'_∞ correspond to low values of Reynolds number which is associated with the thickening of the hypersonic laminar boundary layer causing increased shear on the lower surface of the Orbiter. Evidence of this is seen as an increase in axial force coefficient with increasing \bar{V}'_∞ with no change in normal force, Figure 27. Pitching moment at zero degree control deflection, Figure 28, becomes slightly more negative with increasing \bar{V}'_∞ due to increased shear forces on the lower surface of the Orbiter. At negative (trailing edge-up) control deflections, the movement of the control surface has little effect on the boundary layer on the lower surface of the Orbiter, and consequently, the effect of \bar{V}'_∞ on pitching moment is similar to the zero degree deflection case. For positive (trailing edge-down) deflections, however, the pitching moment effectiveness of the control surface decreases with increasing \bar{V}'_∞ . At high \bar{V}'_∞ (corresponding to low Reynolds number) a thickening of the boundary layer results with a separation point which moves forward with increasing control deflection. This causes a net forward movement of the center of pressure, resulting in reduced pitching moment effectiveness with increasing \bar{V}'_∞ , Figure 28.

Effects of \bar{V}_0 on aerodynamic performance characteristics are indicated in Figures 29 and 30 for a nominal entry trajectory. The decrease in lift-to-drag ratio caused by the increase in axial force is accounted for in design of the entry trajectory. Reduced elevon effectiveness increases the control surface deflection required to trim, Figure 30.

Longitudinal Characteristics

Longitudinal stability and control characteristics for hypersonic to low speed Mach numbers are illustrated in Figures 31 and 32. These data have been determined as a result of extensive wind tunnel tests (representative data are shown on the curves) with hypersonic theory being used to bridge the gap between high supersonic data and the hypersonic wind tunnel data. Low-speed longitudinal characteristics shown in Figure 32 demonstrate stall-free characteristics over the operating angle of attack range. The predicted characteristics are compared with test data obtained with a 0.36-scale model in the Ames Research Center 40x80-ft (12.19x24.38 m) wind tunnel. The changes in stability evidenced in Figure 32 by the large changes in pitching moment at high angles of attack are due to leeside separation on the orbiter wing induced by vortices from the wing/fuselage junction.

The leeside flow separation influences the supersonic stability characteristics also. Referring to Figure 31, it can be seen that for $M = 10$ and 5, the variation of pitching moment with normal force coefficient for zero and positive elevon deflection follows the classical Newtonian "sine squared" relationship. This relationship between pitching moment and normal force coefficient does not follow the "sine-square" variation for negative elevon deflections. The change in characteristics is due to the change in flow pattern on the leeside of the Orbiter wing as influenced by negative elevon deflections.

The surface flow patterns on the leeside of the Orbiter wing consist of three distinct flows. At low angles of attack, the flow which is initially perpendicular to the leading edge is turned parallel to the freestream by the presence of the fuselage (Figure 33A). When the angle of attack is great enough to cause the wing leading edge shock to detach, the trailing edge shock will become strong enough to separate the boundary layer (Figure 33B). This separation is the result of subsonic flow aft of the detached shock expanding around the leading edge and reattaching at supersonic speeds. The flow must still be turned into the freestream direction as before. The turning is accomplished by a strong shock that causes the boundary layer to separate. The wake begins to affect the flow pattern at higher angles of attack causing a secondary type of separation (Figure 33C). Leeside flow boundaries for $M = 6.0$ are shown in Figure 34. The relationship between spanwise location of the shock induced separation b_s , and Mach number was obtained from a correlation of delta wing data. The shock detach boundary was obtained from oil flow photographs.

The effect of leeside separation on wing pitching moment is shown in Figure 35. The subsonic leading edge suction that occurs when the bow shock detaches results in a more stable pitching moment slope. The change to a more stable slope is the result of leading edge suction when the wing bow wave detaches and a reduction of lift over the wing area aft of separation line (Figure 35). The center of pressure is more aft for the lift gain (due to leading edge suction) than for the lift loss due to shock-induced pressure aft of the separation line. The wing pitching moment becomes more stable, thus accounting for the increased stability shown in Figure 31 for +10-degrees elevon deflection.

Elevon effectiveness is also influenced by leeside separation. Loss in elevon effectiveness at high negative (trailing edge up) deflection can be attributed to the effect of back-pressure on the leeside flow field. Flap type controls will often cause boundary layer separation, especially in hypersonic low-density flows. Such back-pressure effects are of practical concern since it is desirable to control the Orbiter with leeward control deflection (trailing edge up) in order to minimize control surface heating. Figure 36 shows elevon effectiveness data obtained from the AEDC Tunnel A at $M = 5$ for an elevon deflection -35 degrees. The measured elevon effectiveness is seen to be less than shown by shock expansion theory. This is probably due to shock-induced separation. The separation extent increases with angle of attack. After the angle of attack for shock detachment is reached, the back-pressure effect from the elevon will affect the wing flow. At high angles of attack, the positive lift produced by the wing vortices outweighs the negative lift generated by the elevon-induced flow separation over the inner wing surface. The result is a loss of elevon effectiveness below the shock expansion value. Adjusting the theory for leeside separation results in reasonable agreement between theory and experiment.

Static trim capability for the elevon and body flap positioned for trim to the forward and aft center of gravity positions is displayed in Figure 37. The control schedules presented on the figure are for determining maximum obtainable center of gravity trim limits. A reserve for maneuvering, trimming spanwise center of gravity offset, manufacturing misalignments, and aerodynamic uncertainties has been added to the limits of the elevon effectiveness data to establish the limits shown on the figure. The aft center of gravity limits are based on a positive elevon deflection of 15 degrees for Mach numbers less than or equal to ten. A positive elevon deflection of ten degrees was used for Mach numbers greater than ten due to thermal protection system design limits during maximum heating conditions. Forward center of gravity trim limits are based on an incremental pitching moment coefficient reserve of 0.015 for Mach numbers less than or equal to ten and 0.02 for Mach numbers greater than ten. Figure 37 indicates a slightly reduced forward center of gravity trim margin at Mach 5.0 in the angle of attack range from 20 to 45 degrees. This is attributed to the loss in elevon effectiveness due to leeside separation. Center of gravity trim limits for the entry angle of attack schedule have been shown earlier in Figure 7. Both Figures 7 and 37 indicate that a wide trim margin exists across the Mach number range.

Elevon control power in conjunction with the body flap and speed brake provide trim capability between the design center of gravity limits. The elevon schedule, shown in Figure 38, illustrates the nominal and the most positive and negative settings for trim at forward and aft center of gravity positions. The extreme settings account for control margin and uncertainties in aerodynamic characteristics. The speed brake is initially opened during entry at Mach 10, and is programmed as a function of velocity to

approximately Mach 1. Opening the speed brake at Mach 10 assists in longitudinal trim during the transition from high to low angle of attack. Below Mach 1, the speed brake setting is modulated to provide speed control during approach and landing. The body flap is used as a trim device to keep the elevons operating in an effective range, and, during the high heating portion of entry, to keep the elevons from overheating. Body flap deflection varies during entry. For entry at the forward center of gravity, the initial body flap position is normally full-up. For the aft center of gravity case, the initial position is approximately 16 degrees down.

Lateral-Directional Characteristics

Lateral-directional stability and control characteristics along the nominal entry trajectory are illustrated in Figures 39, 40, and 41. As shown in Figure 39, the Orbiter exhibits positive dihedral effect (negative $C_{l\beta}$) across the complete Mach range during both the spacecraft and aircraft control modes. During the spacecraft mode, and during transition to the aircraft mode, the directional stability derivative $C_{n\beta}$ is negative. $C_{n\beta}$ becomes positive indicating static stability in yaw at approximately Mach 1.7, and retains positive values throughout the aircraft mode (Mach numbers below approximately 1.5). Aileron and rudder control effectiveness characteristics are illustrated in Figures 40 and 41. Because the ailerons provide control authority across the complete Mach range, and the rudder is essentially ineffective above Mach 8, the ailerons are used in conjunction with the yaw jets to provide for roll control in the spacecraft control mode.

Early analytical studies predicted an elevon deflection interaction effect on the lateral-directional characteristics. Studies showed that the relatively large sized elevon in the presence of the deep, flat-sided fuselage could induce a change in the pressure distribution in the aft region of the fuselage. The resulting change in pressure distribution resulted in an incremental change in side force, yaw, and rolling moment when the vehicle was yawed. The effect of elevon interaction is illustrated for the yawing and rolling moment derivatives in Figures 42 and 43. The control derivatives $C_{l\delta_a}$ and $C_{n\delta_a}$ are also affected by elevon position. The influence of elevon position on the control derivatives is shown in Figures 44 and 45. The sensitivity of the derivatives to elevon position influences vehicle control boundaries.

The nature of the control derivatives define the Mach regions where aileron and/or rudder is used for lateral trim. Aileron-alone is used for YCG trim above Mach number 4.5 and rudder-alone is used for YCG trim below Mach number 3.5. A combination of aileron and rudder control is used for trim in the Mach number region between 4.5 and 3.5. The yaw reaction control system (RCS) jets are used to augment the aerodynamic controls where required.

The interrelation between the control derivatives and the method used to trim YCG offset during the spacecraft mode is best illustrated by examining the relations for aileron and rudder required to trim. Using aileron-alone:

$$\delta_{Atrim} = \frac{Y_{CG}}{b} \frac{C_N C_{n\beta} + C_A C_{l\beta}}{C_{l\beta} C_{n\delta_a} - C_{n\beta} C_{l\delta_a}} \quad (7)$$

and for rudder-alone:

$$\delta_{Rtrim} = \frac{Y_{CG}}{b} \frac{C_N C_{n\beta} + C_A C_{l\beta}}{C_{l\beta} C_{n\delta_r} - C_{n\beta} C_{l\delta_r}} \quad (8)$$

The critical boundary exists when the denominator goes to zero; i.e., the condition where aileron or rudder cannot produce a trim condition.

For aileron-alone, the boundary is defined by

$$C_{l\beta} C_{n\delta_a} - C_{n\beta} C_{l\delta_a} > 0, \frac{C_{n\beta}}{C_{l\beta}} > \frac{C_{n\delta_a}}{C_{l\delta_a}} \quad (9)$$

Using rudder-alone:

$$C_{l\beta} C_{n\delta_r} - C_{n\beta} C_{l\delta_r} > 0, \frac{C_{n\beta}}{C_{l\beta}} > \frac{C_{n\delta_r}}{C_{l\delta_r}} \quad (10)$$

Aileron and rudder cross coupling ratios are shown in Figure 46 for the nominal entry trajectory and nominal aerodynamics. For the spacecraft control mode, the boundary for YCG trim by aileron control is not violated for Mach numbers greater than about 1.9. Trim of a YCG offset by rudder-alone can be accomplished over the region from Mach 8 to approximately 1.1, resulting in an overlap from Mach 8 to 1.9 for nominal

aerodynamics. To allow for trajectory dispersions and uncertainties in aerodynamics, transition to the aircraft control mode; i.e., conventional aileron/rudder control, is initiated at approximately Mach 5 and is complete by Mach 1.5.

Low-speed directional stability characteristics exhibit a strong Reynolds number/angle of attack effect, Figure 47. The figure illustrates the importance of full-scale Reynolds number testing on high angle of attack aerodynamics. Test data obtained from models tested at low Reynolds numbers ($\leq 5 \times 10^6$ based on mean aerodynamic chord) show essentially no change of directional stability with angle of attack. The early work of Polhamus (Reference 12) and Jorgensen and Brownson (Reference 13) indicated that Reynolds number and body corner radius could have a significant effect on the high angle of attack characteristics of the Orbiter. These predictions were borne out when the Orbiter model was tested at near full-scale Reynolds number in the Ames Research Center 40x80-foot (12.2x24.4 m) wind tunnel. Referring to Figure 47, it can be seen that the high Reynolds number test data shows a decrease in directional stability with angle of attack which is in contrast to the low Reynolds number data which shows essentially no change in stability with angle of attack. At Mach numbers above 0.7, data representative of flight Reynolds numbers can be obtained in wind tunnel tests at low Reynolds numbers provided proper attention is paid to close matching of body corner rounding on the wind tunnel models and flight vehicles (Reference 13).

The early work of E.C. Polhamus (Reference 12) was used to predict the variation of directional stability with angle of attack. Based on Polhamus' work, it was determined that the low-speed/high angle of attack directional stability determined by wind tunnel tests would be erroneous unless the Reynolds number were sufficiently high to permit proper simulation of the cross flow on the forward fuselage. It was predicted that a close similarity in both magnitude and change with Reynolds number, existed between the cross flow drag coefficient for the Orbiter fuselage at high angles of attack (greater than 15 degrees) and a two-dimensional square cylinder at 90 degrees angle of attack. From this similarity, it was concluded that most of the low-speed Orbiter test data would be within the critical Reynolds number range, the range in which cross flow drag coefficient decreases from high to low values as the Reynolds number increases from subcritical to critical. Polhamus presented data from tests made on noncircular cylinders with the air flow directed normal to the cylinder axis. As illustrated in Figure 48 for a square-shaped cylinder with rounded corners, the air flow will separate on the leeward side at subcritical Reynolds number but will remain attached at supercritical Reynolds number, when the flow is directed at an angle not aligned with one of the major cross sectional axes. For the subcritical Reynolds number case, the resultant body axis side force, C_y , is positive while for the supercritical Reynolds number case, the side force is negative. Since the center of gravity is behind the nose, positive side force translates to positive yawing moment and negative side force translates to negative yawing moment. Consequently, the effect of going from subcritical to supercritical Reynolds number is to reduce the directional stability of the vehicle.

Presented in Figure 49 is the measured directional stability variation with cross flow Reynolds number from several wind tunnel tests at approximately 20 degrees angle of attack. As can be seen, there appears to be a trend for the Orbiter directional stability to decrease as the cross flow Reynolds number is increased. The reason for the reduction of directional stability with increased cross flow Reynolds number is the elimination of the flow separation at the nose with increased cross flow Reynolds number. At angles of attack of 15 degrees and below (Figure 47), there appears to be no change of directional stability for the different tests.

FLIGHT TEST RESULTS

The Approach and Landing Test (ALT) Program, Table 6, was conducted during the last half of 1977 as part of the Shuttle Development Program. The Orbiter Enterprise (OV101) was launched from the Boeing 747 Shuttle Carrier Aircraft over Edwards Air Force Base, California, and glided to either a landing on Rogers Dry Lake, or on the last flight, a landing on the Edwards Air Force Base runway. The program consisted of eight captive flights followed by three orbiter freeflights with the tailcone installed, and finally two freeflights in which the tailcone was removed, testing the orbital return configuration.

The captive flights verified the airworthiness of the mated configuration, accomplished Orbiter systems checkout and developed the separation procedures, and verified aerodynamic forces at separation. The separation of the Orbiter from the 747 was achieved through the aerodynamic forces on the vehicles, so one of the important objectives of the Captive Flight Program was to verify the predicted separation forces, and adjust the Orbiter elevon settings for separation, if required. Special load cells were installed on the Orbiter/747 struts in order to measure the separation forces to the required accuracy.

The orbiter lift and pitching moments in the presence of the 747 were the key parameters for safe separation. Figure 50 shows these coefficients as determined during the captive flights using load cell measurements, compared to estimates based on wind tunnel tests. The flight measured coefficients were well within the uncertainties in the prediction. Since dynamic analyses had shown acceptable separations if the key aero coefficients were within the uncertainty band, the flight measurements confirmed that separation would be acceptable, and the program proceeded to an Orbiter freeflight. The first separation occurred on August 12, 1977, and was as predicted.

The first three Orbiter freeflights were conducted with a tailcone installed to fair the Orbiter's blunt base. The tailcone provided increased glide range by increasing the Orbiter L/D from a maximum of 4.5 to 7.5. It also allowed increased launch altitude, from 6400 m to 7620 m. The tailcone also was intended to reduce buffet levels at the 747 empennage, since there was some concern that with the Orbiter tailcone-off, the Orbiter wake may induce excessive buffeting and reduce the 747 fatigue life. (Flight measurements of fluctuating structural loads in the 747 tail later relieved this concern.)

After three tailcone-on freeflights, the tailcone was removed and the test program completed with the orbital configuration simulated. Two Orbiter freeflights were accomplished with the tailcone removed. These flights obtained the data used to verify the subsonic aerodynamic characteristics of the Orbiter in its orbital return configuration. Separation of the orbiter/747 during the first tailcone-off freeflight is illustrated in Figure 50. In Figure 51, the orbiter is shown just prior to touchdown on the runway at Edwards Air Force Base during the final freeflight on October 26, 1977.

The significant Orbiter aerodynamic characteristics are compared with predictions based on wind tunnel tests, Figures 52 through 56. Key instrumentation used to derive these data were an "Aerodynamic Coefficient Identification Package" provided by the NASA/Dryden Flight Research Center, consisting of three accelerometers and three rate gyros, and a flight test noseboom which provided angles of attack and sideslip, and pitot and static pressures. A data extraction program was developed by the NASA to determine the flight-derived aerodynamic characteristics (Reference 14). The figures show that the flight measurements were in good agreement with wind tunnel predictions, with the lone exception of landing gear drag which was overpredicted by approximately 27 percent. Examination of the wind tunnel data revealed that the estimated Reynolds number correction to gear drag was inadequate. Thus, the aerodynamics objective of the Approach and Landing Test Program; to verify the low-speed aerodynamic characteristics, was achieved and provided increased confidence for the next phase of the Shuttle Program, the Orbital Flight Test.

CONCLUSIONS

Aerodynamic development of the Space Shuttle orbiter has been described. Extensive wind tunnel testing has provided a high confidence level in the estimated aerodynamic characteristics. Results from the approach and landing flight test program verify predicted aerodynamic characteristics in the subsonic speed regime. Accounting for uncertainties in aerodynamic data will allow incremental extension of flight envelopes to achieve predicted operational capability.

REFERENCES

1. Surber, T.E. and Olsen, D.C., "Space Shuttle Orbiter Aerodynamic Development," *Journal of Spacecraft and Rockets*, Vol. 15, No. 1, January-February 1978, pp 40-47
2. Rockwell International Space Division, "Aerodynamic Design Data Book, Volume 1, Orbiter Vehicle," November 1977, Report No. SD 72-SH-0060-1K
3. Smith, E.P., Rockwell International Space Division, "Space Shuttle Orbiter and Subsystems," June 1973, Report No. SD 72-SH-0144
4. Gamble, Joc D., Chrysler Corporation Space Division, "High Supersonic Stability and Control Characteristics of a 0.015-Scale (Remotely Controlled Elevon) Model 49-0 of the Space Shuttle Orbiter Tested in the NASA/LaRC 4-Foot UPWT (LA638)," May 1976, Report No. DMS DR-2279, NASA CR-144.606
5. NASA LaRC, "High Reynolds Number Research," October 1976, Report No. NASA CP-2009, pp 2-17
6. Hayes, Wallace D., and Probstein, Ronald F., "Hypersonic Flow Theory," New York and London, Academic Press, 1959, pp 333-345
7. Whitfield, Jack D., and Griffith, B.J., "Hypersonic Viscous Drag Effects on Blunt Slender Cones," *AIAA Journal*, Vol. 2, No. 10, October 1964, pp 1714-1722
8. Bertram, Mitchell H., NASA, "Hypersonic Laminar Viscous Interaction Effects on the Aerodynamics of Two-Dimensional Wedge and Triangular Planform Wings," August 1966, Report No. NASA TN D-3523
9. Rockwell International Space Division, "Aerodynamic Design Substantiation Report, Volume 1, Orbiter Vehicle," February 1978, Report No. SD 74-SH-0206-1K
10. Stein, Robert E., Jr., Lockheed Electronics Inc., "Project 3313, Multiple Regression Analysis Program for the Aerodynamic Coefficient Analysis System (NASA Contract NA9-122000)," January 1973
11. Rausch, J.R., General Dynamics Convair Division, "Space Shuttle Orbiter Rear Mounted Reaction Control System Jet Interaction Study," May 1977, Report No. CASD-NSC-77-003
12. Polhamus, E.C., "Effect of Flow Incidence and Reynolds Number on Low Speed Aerodynamic Characteristics of Several Noncircular Cylinders with Application to Directional Stability and Spinning," NASA Technical Report R-29, 1959
13. Jorgenson, Leland H. and Brownson, Jack J., "Effect of Reynolds Number and Body Corner Radius on Aerodynamic Characteristics for Space Shuttle-Type Vehicle at Subsonic Mach Numbers," NASA TN D-6615, January 1972
14. Romere, P.O., Eichblatt, D.L., Underwood, J.M., and Howes, D.B., "The Space Shuttle Orbiter Approach and Landing Tests—A Correlation of Flight and Predicted Performance Data," AIAA Paper 78-793, AIAA Tenth Aerodynamic Testing Conference, San Diego, CA, April 19-21, 1978

ACKNOWLEDGEMENTS

The aerodynamic design activities described in this report are being accomplished by the Space Division, Rockwell International, under NASA contract NAS9-14000. Overall technical management of orbiter development is accomplished by the Space Shuttle Program Office at the NASA Johnson Space Center (JSC). Aerodynamic development is directed by JSC through the Space Shuttle Flight Performance Technical Management area, Mr. Bass Redd, Technical Manager, supported by Mr. James C. Young, Aerodynamic Subsystem Manager. In addition to JSC, the other NASA Centers (Ames Research Center, Langley Research Center, and Marshall Space Flight Center) have provided extensive support to the Shuttle development in accomplishment of the Wind Tunnel Program and in analysis of test results. In addition, the Langley Research Center has provided additional program support through their independent investigations of nonlinear aerodynamics.

At Rockwell, significant contributions to this paper have been made by Messrs. D.C. Olsen, H.S. Dresser, W.R. Russell and L.M. Gaines.

Table 1 BASELINE REFERENCE MISSIONS

MISSION	LAUNCH SITE	OBJECTIVE	INCL. (DEG)	ORBIT		PAYLOAD (10 ³ kg)	
				ALTITUDE (10 ³ m)	DURATION (DAYS)	ASCENT	DESCENT
1	KSC	PAYLOAD DELIVERY	28.5	277.8	7	29.48	14.51
2	KSC	COMBINED REVISIT TO ORBITING ELEMENT & SPACELAB	55.0	500.0	7	---	---
3A	WTR	PAYLOAD DELIVERY	104.0	185.2	1 REVISIT	14.51	1.13
3B	WTR	PAYLOAD DELIVERY	104.0	185.2	1 REVISIT	1.13	11.33

Table 4 SPACE SHUTTLE WIND TUNNEL MODEL SUMMARY
AUGUST 1972 TO FIRST ORBITAL FLIGHT

	NUMBER OF MODELS			
	ORBITER VEHICLE	LAUNCHED LAUNCH VEHICLE	CARRIER AIRCRAFT	TOTAL
AERODYNAMICS	11	23	4	38
AERODYNAMIC HEATING	22	14	0	36
STRUCTURAL DYNAMICS	12	6	2	20
TOTAL	45	43	6	94

Table 2 AERODYNAMIC DESIGN REQUIREMENTS

PARAMETER	VALUE
ANGLE OF ATTACK	
HYPERSONIC	25 DEG TO 50 DEG
TRANSONIC	0 DEG TO 15 DEG
SUBSONIC	-5 DEG TO 20 DEG
CENTER OF GRAVITY RANGE	
MINIMUM TRAVEL	2% BODY LENGTH
DESIGN RANGE	0.65 L _B - 0.675 L _B
LANDING PERFORMANCE	
PAYLOAD	14,515 Kg
LANDING WEIGHT* (WITH PAYLOAD)	85,230 Kg
MINIMUM DESIGN TOUCHDOWN SPEED, V _D	88 m/sec
LONGITUDINAL STABILITY	
MINIMUM HYPERSONIC STATIC MARGIN	POSITIVE
MINIMUM SUBSONIC STATIC MARGIN (AFT CENTER OF GRAVITY)	-2% L _B (-5.45% MAC)
LIFT/DRAG MODULATION	
PEAK SUBSONIC VALUE (GEAR-UP, $\delta_{5B} = 0$)	NOT LESS THAN 4.4
PEAK SUBSONIC VALUE (GEAR-UP, $\delta_{5B} = 85$ DEG)	NOT LESS THAN 2.5

Table 5 SIGNIFICANT AERODYNAMIC PARAMETERS

AERODYNAMIC PARAMETERS	FLIGHT REGIME	WHY PARAMETERS ARE SIGNIFICANT	AERO CONCERN IN DEFINITION OF PARAMETERS
L/D	ALL	CROSS RANGE TERMINAL AREA ENERGY MANAGEMENT ELEVON TO TRIM XCS FUEL USAGE	VISCOSUS INTERACTION EFFECTS FLOW SEPARATION REAL GAS EFFECTS NOT DUPLICATED IN WIND TUNNEL
HINGE MOMENTS	TRANSONIC MACH 0.8 TO 1.5	DESIGN HINGE MOMENT CONDITIONS DEFINES CONTROL SURFACE STALL CONDITIONS	TRANSONIC WIND TUNNEL DATA ACCURACIES
	MACH 5 TO 6	AILENON USED FOR BOTH ROLL & YAW TRIM ABOVE MACH 5 BEFORE FLUDDER BECOME EFFECTIVE YAW JET FUEL USAGE (DUE TO CG OFFSET)	CONTROL SURFACE INTERACTION
	HIGH SUPERSONIC MACH 3 TO 5 SUPER/TRANS-SONIC MACH 2.5 TO 1.0	BETWEEN MACH 1.5 TO 5, RUDDER IS USED FOR BOTH YAW & ROLL TRIM, AILENON CO-ORDINATES TURN YAW JET NEEDED UNTIL RUDDER IS EFFECTIVE DEFINES SWITCH-OVER POINT	CONTROL SURFACE INTERACTIONS RUDDER EFFECTIVENESS AT HIGH MACH AERODYNAMIC EFFECTS TRANSONIC WIND TUNNEL DATA ACCURACIES

Table 3 SPACE SHUTTLE WIND TUNNEL TEST HOURS SUMMARY
AUGUST 1972 TO FIRST ORBITAL FLIGHT

	ORBITER VEHICLE	LAUNCHED LAUNCH VEHICLE	CARRIER AIRCRAFT	TOTAL HOURS
AERODYNAMICS	14,700	8,100	3,400	26,200
AERODYNAMIC HEATING	4,500	6,400	0	10,900
STRUCTURAL DYNAMICS	1,000	1,600	400	3,000
TOTAL	20,200	16,100	3,800	40,100

Table 6 APPROACH & LANDING TEST PROGRAM SUMMARY

	NO OF FLIGHTS	CONFIGURATION	OBJECTIVE
CARRIER ALONE	4	MODIFIED 747	FUNCTIONAL CHECK, FLUTTER, & STALL CHECKS
	7	MODIFIED 747 WITH ORBITER ATTACH STRUCTS & TIP FINS	FLUTTER CLEARANCE, PERFORMANCE, & STABILITY & CONTROL VERIFICATION
CAPTIVE FLIGHT	5	747 & ORBITER, TAILCONE-OFF, ORBITER UNMANNED & UNPOWERED	FLUTTER CLEARANCE, PERFORMANCE, & STABILITY & CONTROL VERIFICATION
CAPTIVE ACTIVE	3	747 & ORBITER, TAILCONE-OFF, ORBITER MANNED & POWERED-UP	ORBITER FUNCTIONAL CHECK, SEPARATION LOADS, & PROCEDURES VERIFICATION
ORBITER FREE-FLIGHT	3	TAILCONE-OFF	CRW FAMILIARIZATION, SYSTEMS CHECK, STABILITY & CONTROL, & PERFORMANCE VERIFICATION
	2	TAILCONE-OFF	VERIFICATION OF ORBITER APPROACH & LANDING CAPABILITY
CAPTIVE THURT	4	FERRY CONFIGURATION, TAILCONE-OFF	FERRY QUALIFICATION & PERFORMANCE VERIFICATION

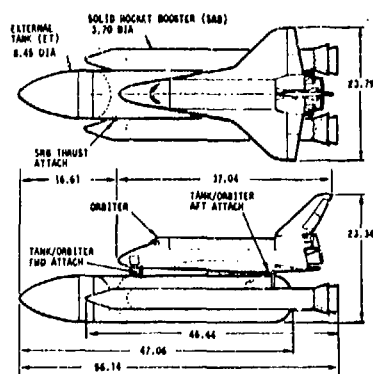


Fig. 1 SPACE SHUTTLE VEHICLE

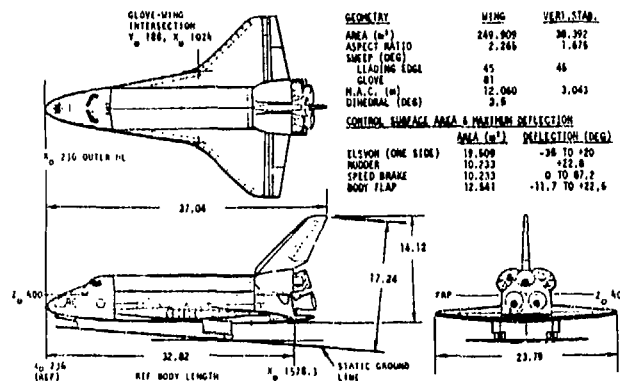


Fig. 2 ORBITER VEHICLE

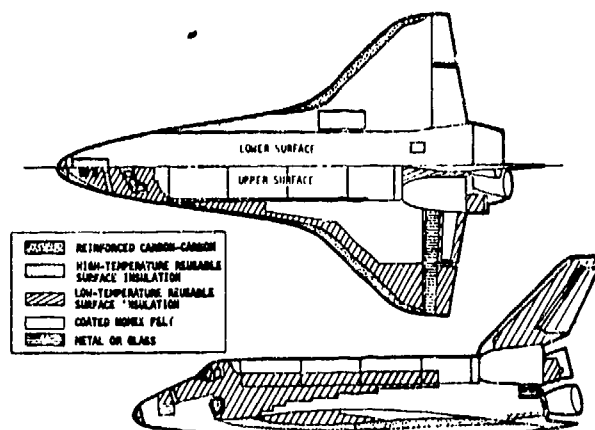


Fig. 3 THERMAL PROTECTION SUBSYSTEM

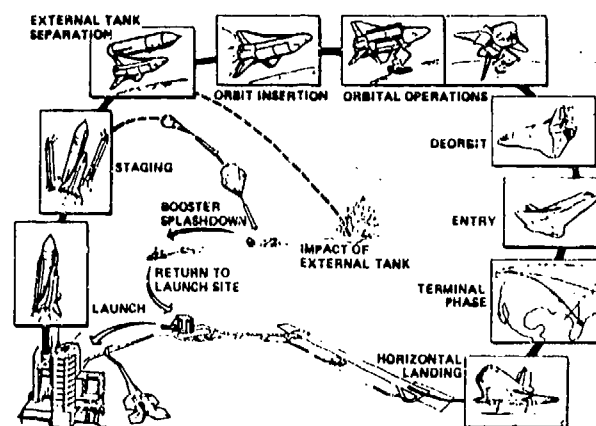


Fig. 4 SHUTTLE MISSION PROFILE

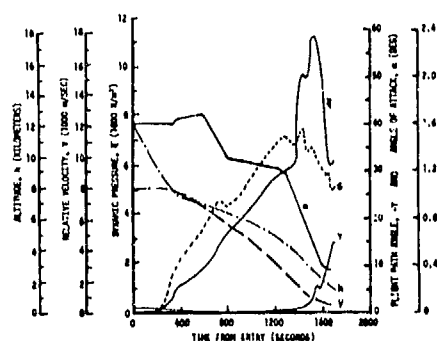


Fig. 5 ORBITER ENTRY TRAJECTORY

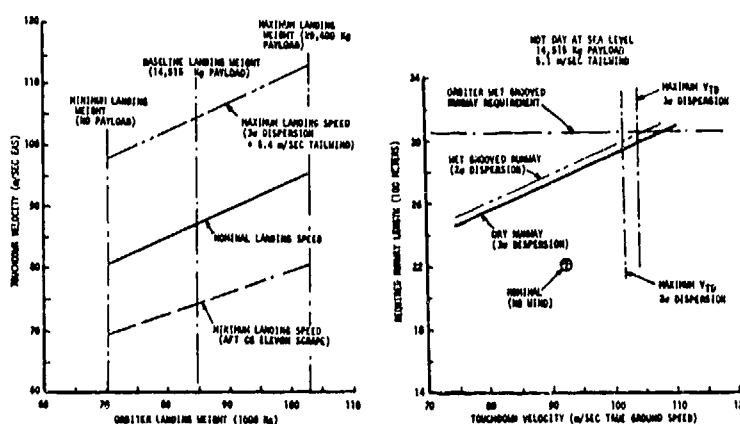


Fig. 6 LANDING REQUIREMENTS

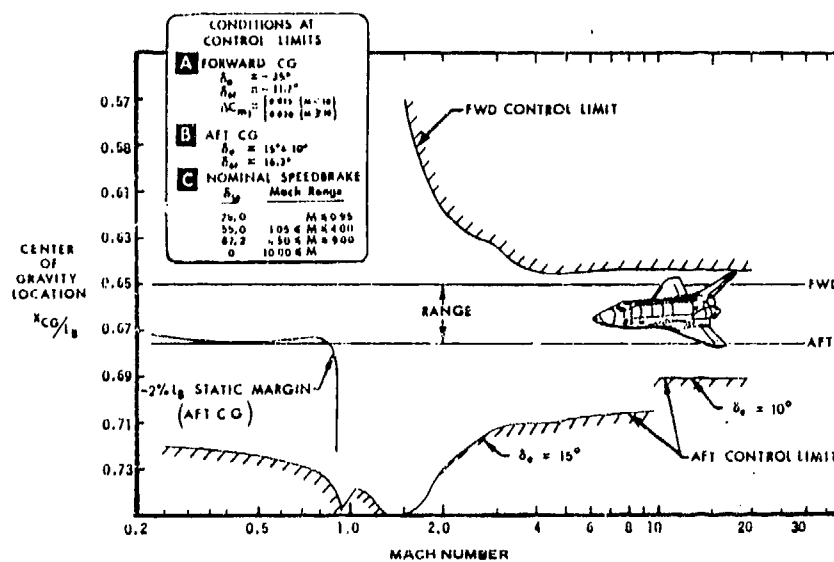


Fig. 7 ORBITER TRIM LIMITS

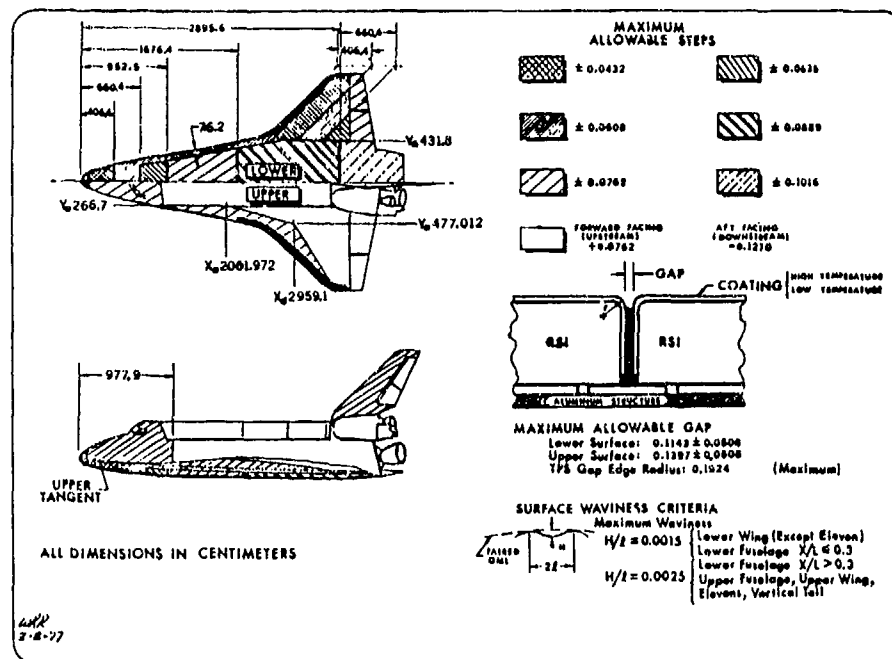


Fig. 8 ORBITER MOLD LINE/STEP CRITERIA

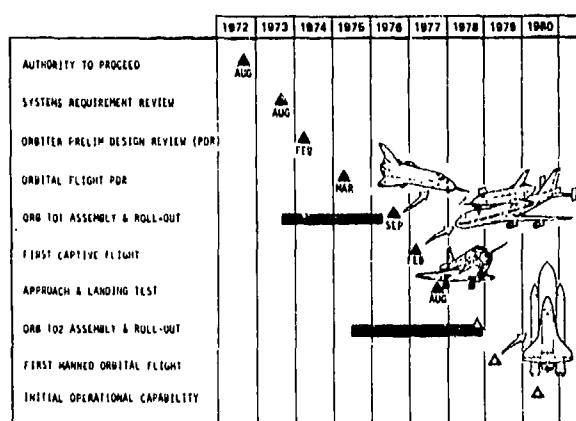


Fig. 9 SPACE SHUTTLE PROGRAM MILESTONES

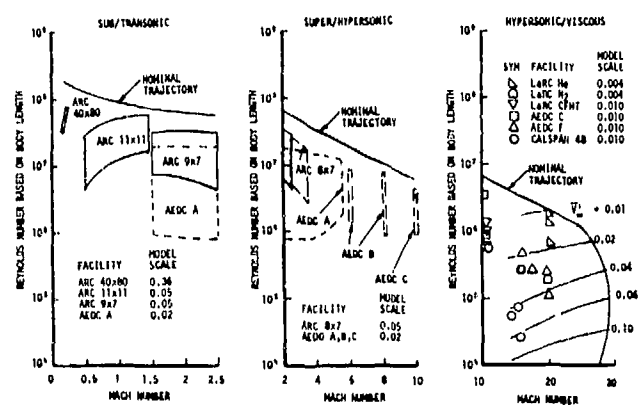


Fig. 10 ORBITER FLIGHT REYNOLDS NUMBER SIMULATION

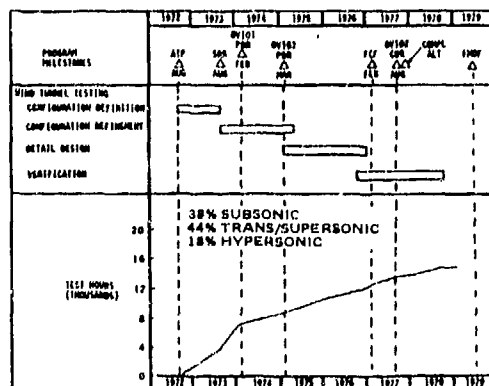


Fig. 11 ORBITER AERODYNAMIC WIND
TUNNEL PROGRAM

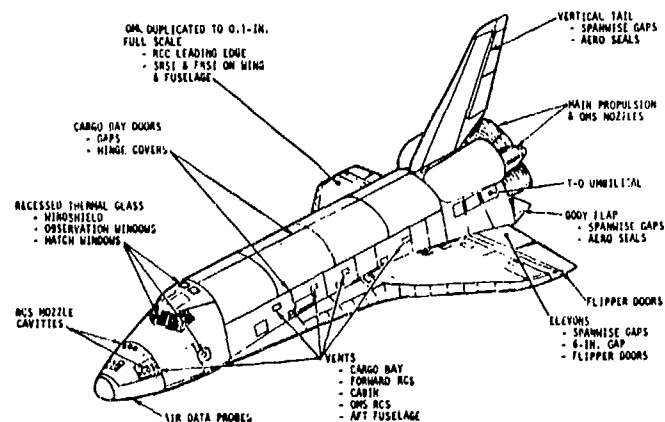


Fig. 12 OV102 MODEL FIDELITY

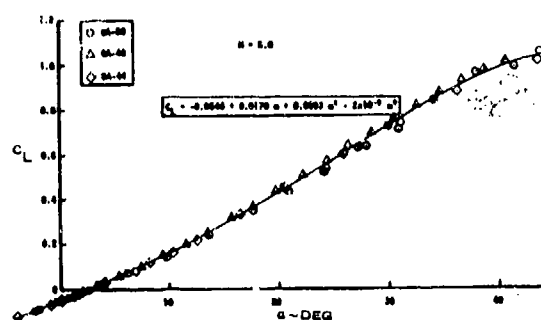


Fig. 13 LIFT COEFFICIENT TOLERANCES

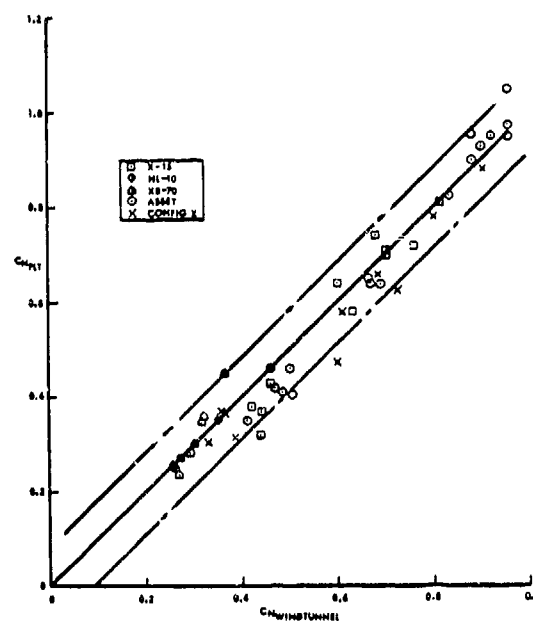


Fig. 14 NORMAL FORCE COEFFICIENT COMPARISON OF WIND TUNNEL TO FLIGHT DATA

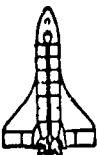
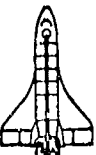

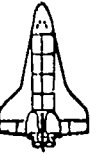
CONFIGURATION NUMBER	ATP	PRR	PDR	CDR
WING PLANFORM	50° BLENDED DELTA	50° BLENDED DELTA	45°/79° DBL DELTA	45°/81° DBL DELTA
PROFILE				
DRY WEIGHT (Kg)	77,110	77,110	68,039	68,039
PAYLOAD (Kg)	18,144	18,144	11,340	14,515
CG RANGE % Lb	65-68	65-68	65-67.5	65-67.5
WING AREA (m²)	299.15	299.15	249.91	249.91
WING SPAN (m)	25.60	25.60	23.80	23.80
OVERALL LENGTH (m)	37.79	38.10	38.10	37.28

Fig. 15 ORBITER EVOLUTION SUMMARY

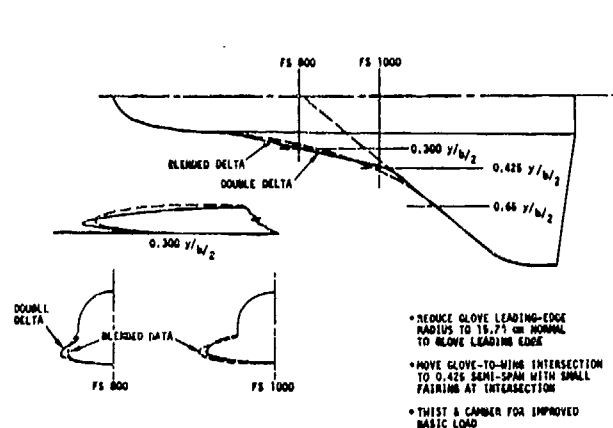


Fig. 16 BLENDED/DOUBLE-DELTA WING MODIFICATION

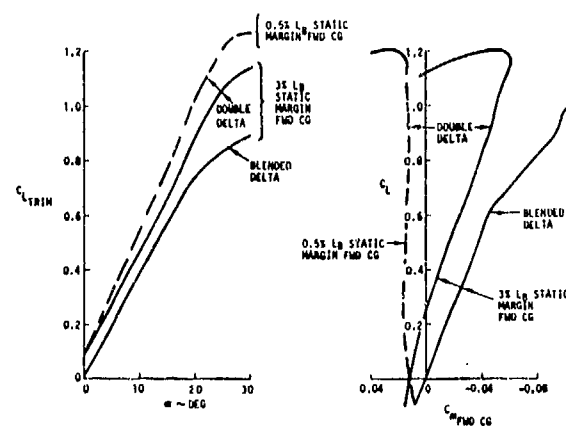


Fig. 17 BLENDED/DOUBLE-DELTA WING MODIFICATION EFFECT ON LONGITUDINAL CHARACTERISTICS

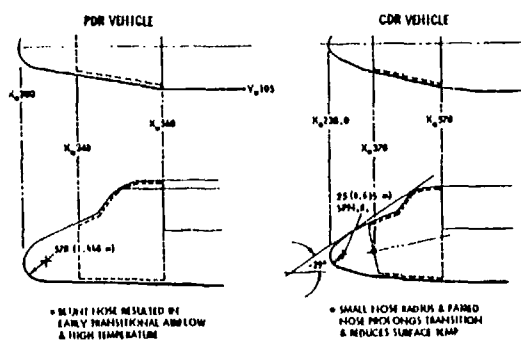


Fig. 18 REDUCED NOSE RADIUS, AND FAIRED NOSE SECTION

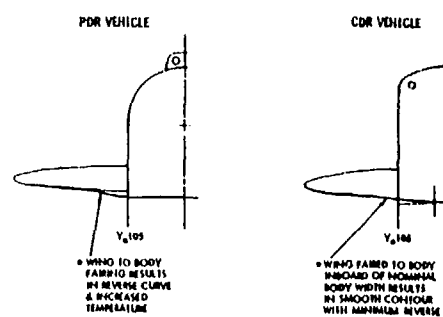


Fig. 19 LOWER WING/BODY FAIRING

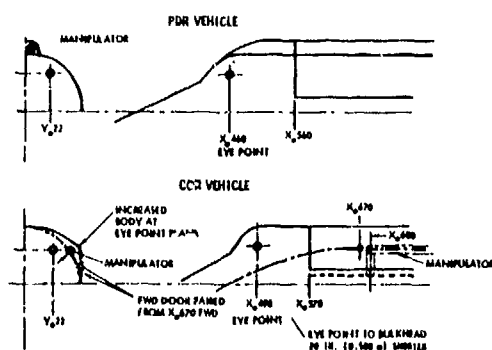


Fig. 20 UPPER BODY LINES

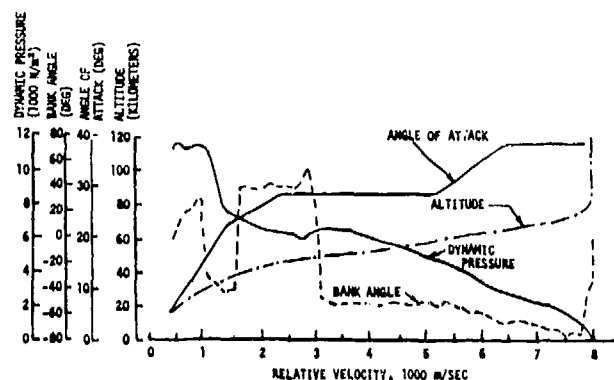


Fig. 21 TYPICAL ORBITER ENTRY PROFILE

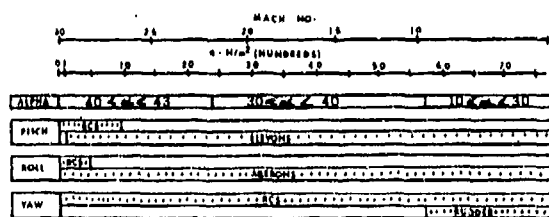


Fig. 22 RCS AND CONTROL SURFACE UTILIZATION DURING ENTRY

RCS EFFECTIVENESS COMPONENTS

- JET THRUST
- PLUME IMPINGEMENT
- FLOW FIELD INTERACTIONS

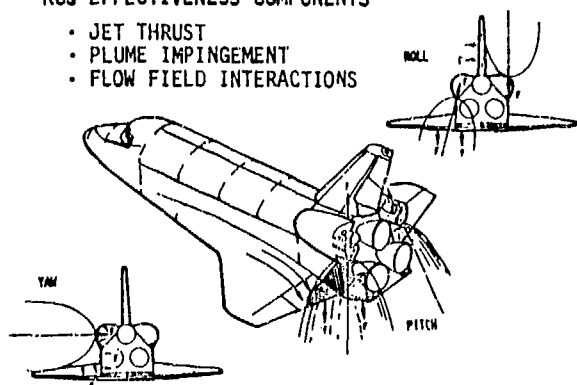


Fig. 23 REACTION CONTROL JET INTERACTIONS

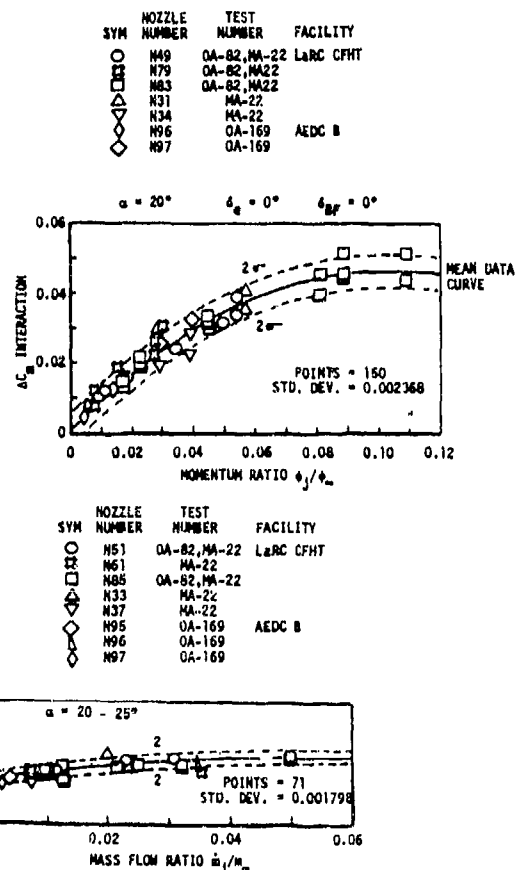


Fig. 24 REACTION CONTROL JET CORRELATION

$$\alpha = 20^\circ \quad \beta = 0^\circ \quad \delta_E = \delta_{BF} = 0^\circ \quad \bar{q}_\infty = 47.9 \text{ N/m}^2$$

CONTROL AXIS	3-JET MOMENT (N-m)	IMPINGEMENT MOMENT (N-m)	INTERACTION MOMENT (N-m)	HET MOMENT (N-m)
ROLL	+36,590	-8,030	-27,040	+1,520
PITCH	-126,600	+8,690	+43,775	-74,135
YAW	-38,300	-7,860	-4,860	-51,020

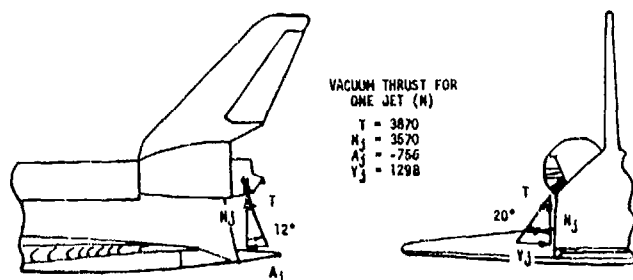


Fig. 25 REACTION CONTROL JET MOMENTS

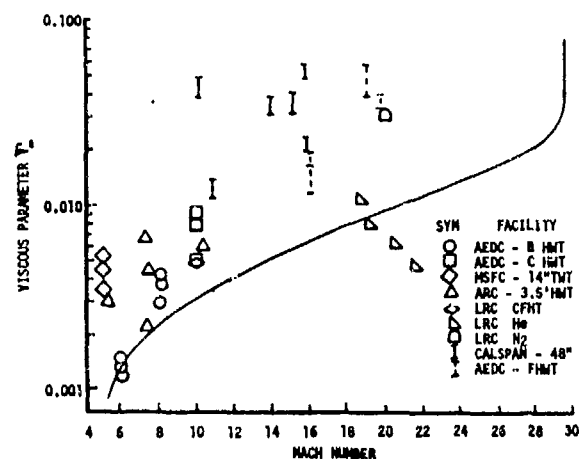


Fig. 26 VARIATION OF VISCOUS PARAMETER ALONG NOMINAL ENTRY TRAJECTORY

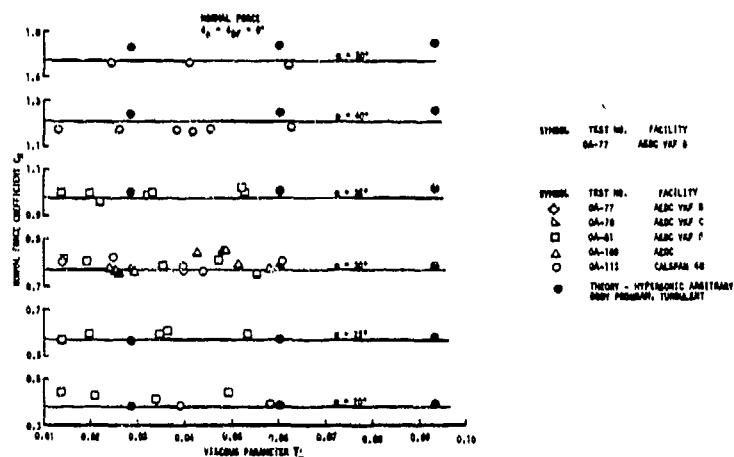


Fig. 27 EFFECTS OF VISCOUS INTERACTION ON NORMAL AND AXIAL FORCE

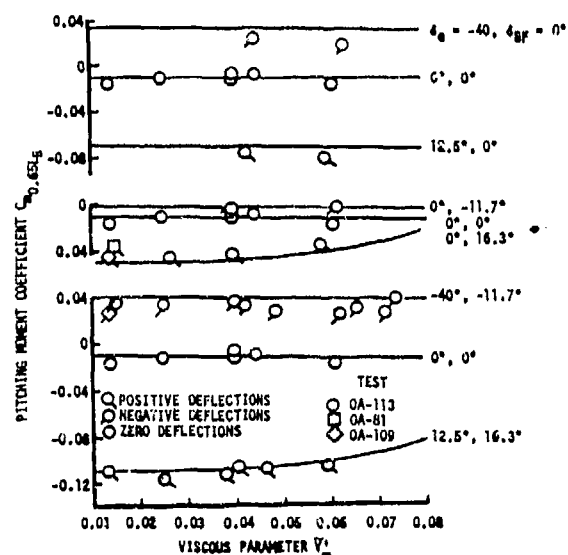


Fig. 28 EFFECTS OF VISCOUS INTERACTION ON PITCHING MOMENT

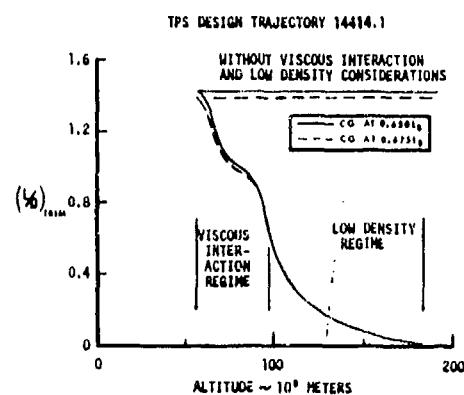
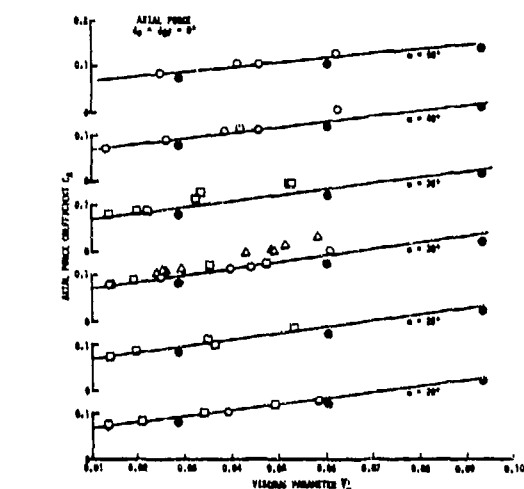
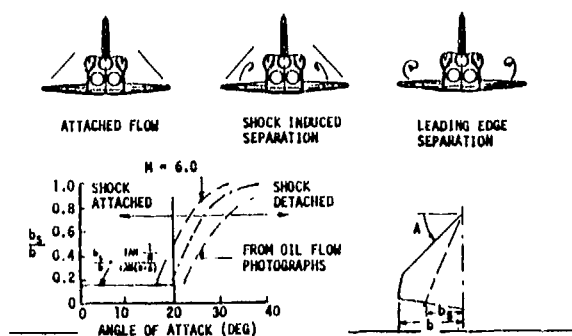
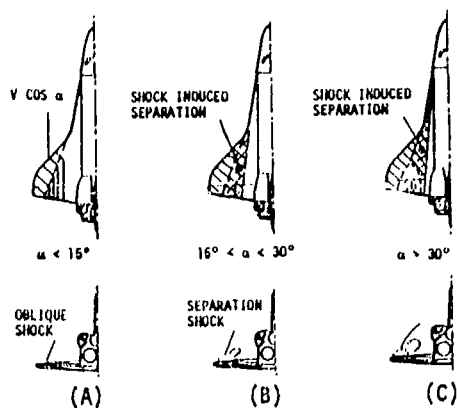
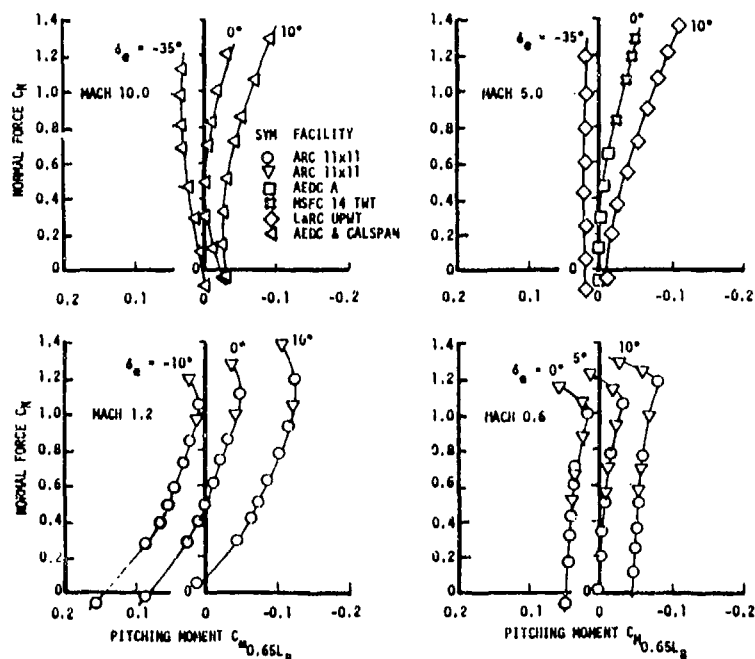
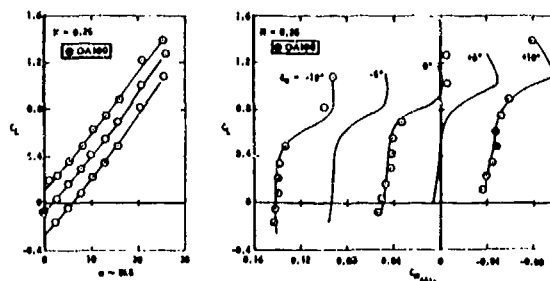
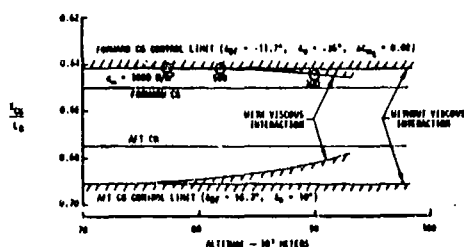


Fig. 29 VISCOUS INTERACTION EFFECT ON LIFT-TO-DRAG RATIO



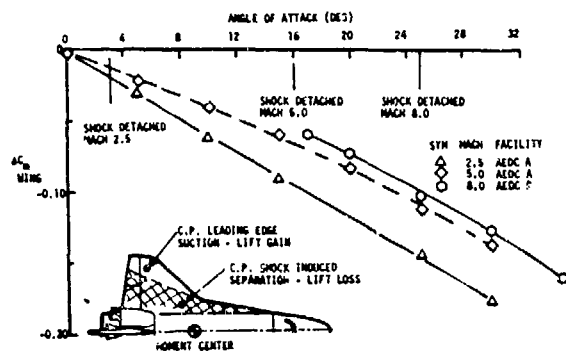


Fig. 35 LEESIDE FLOW SEPARATION EFFECT ON PITCH STABILITY

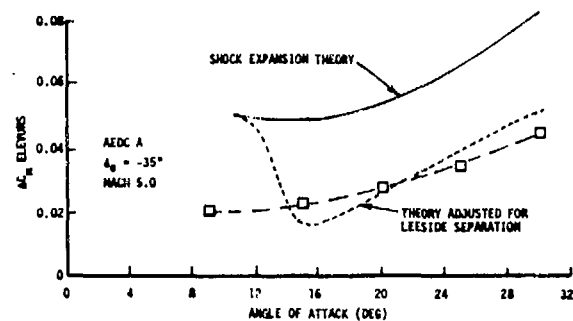


Fig. 36 HYPERSONIC CONTROL EFFECTIVENESS

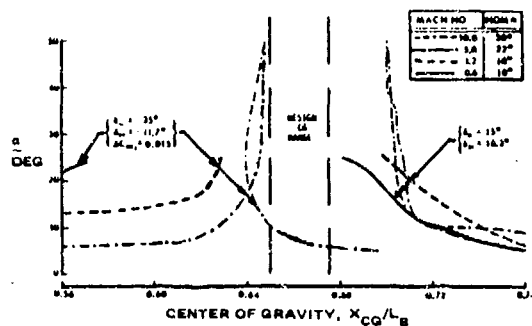


Fig. 37 TRIM CAPABILITY

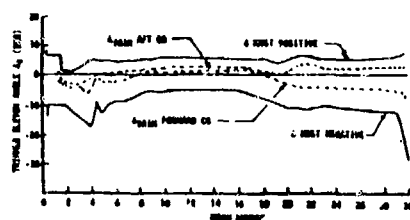


Fig. 38 ELEVON DEFLECTION SCHEDULE

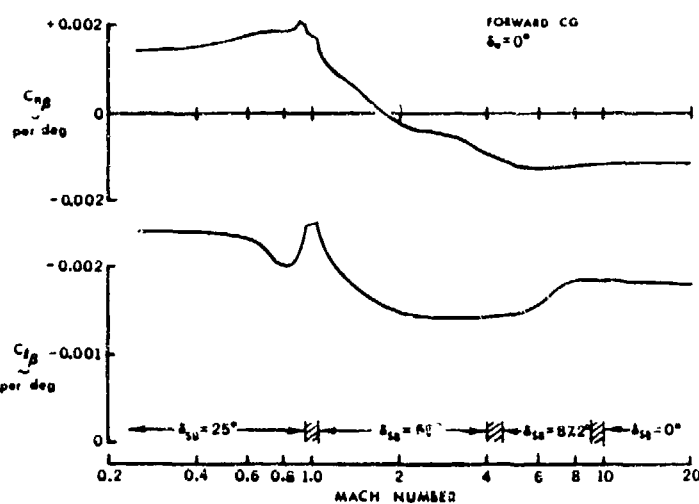


Fig. 39 LATERAL-DIRECTIONAL STABILITY DERIVATIVES

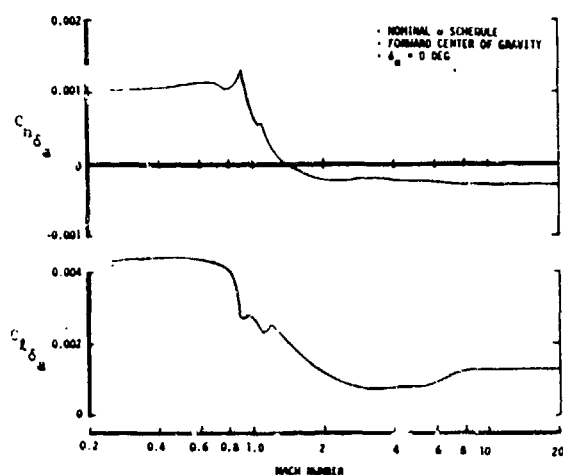


Fig. 40 AILERON EFFECTIVENESS

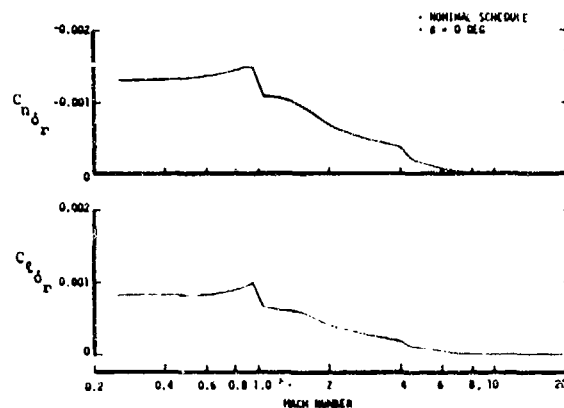


Fig. 41 RUDDER EFFECTIVENESS

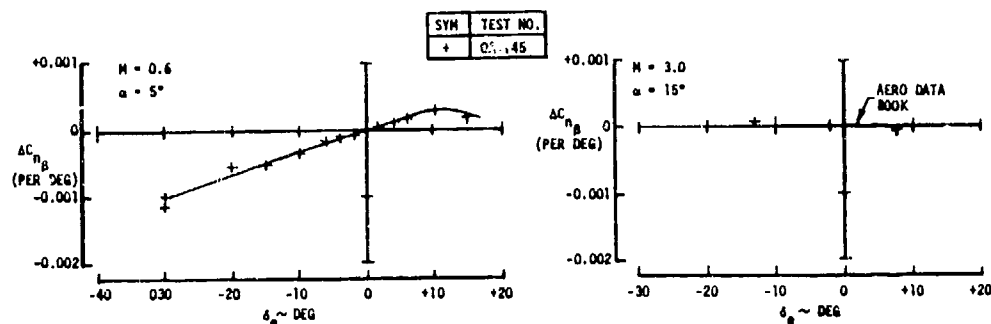


Fig. 42 EFFECT OF ELEVON DEFLECTION ON DIRECTIONAL STABILITY

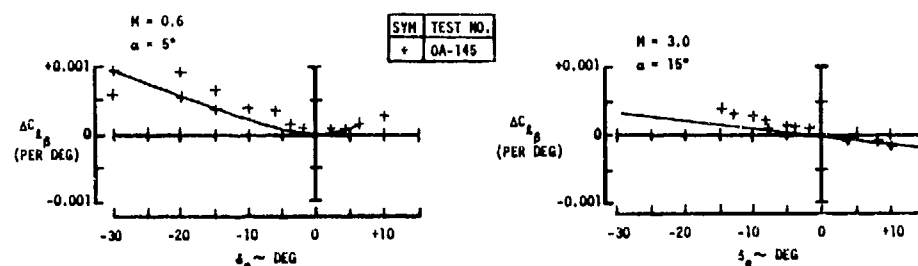


Fig. 43 EFFECT OF ELEVON DEFLECTION ON ROLL DUE TO SIDESLIP

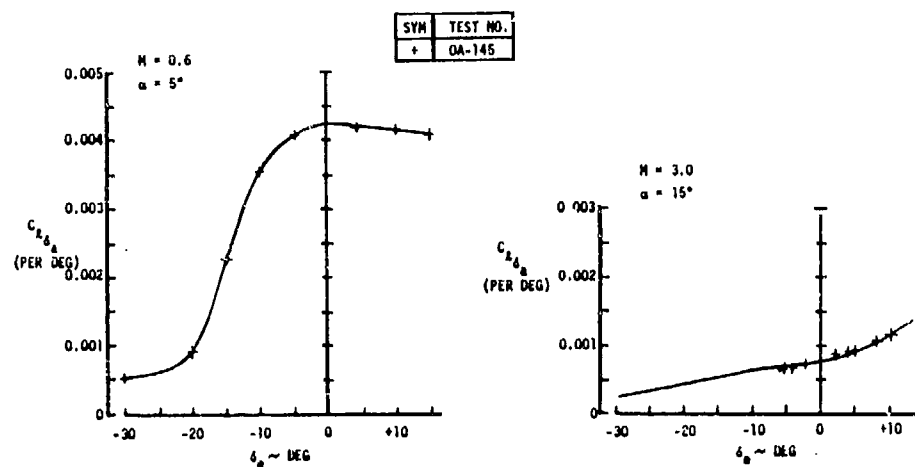


Fig. 44 EFFECT OF ELEVON DEFLECTION ON AILERON ROLL DERIVATIVE

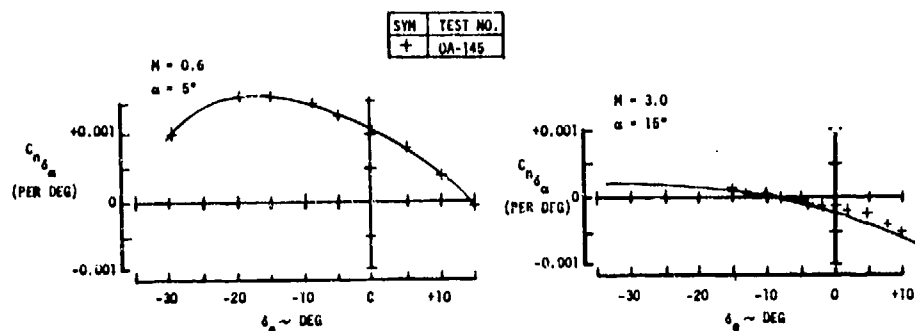


Fig. 45 EFFECT OF ELEVON DEFLECTION ON AILERON YAW DERIVATIVE

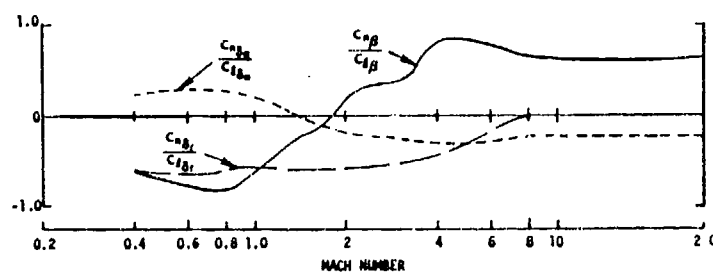


Fig. 46 CROSS COUPLING RATIOS

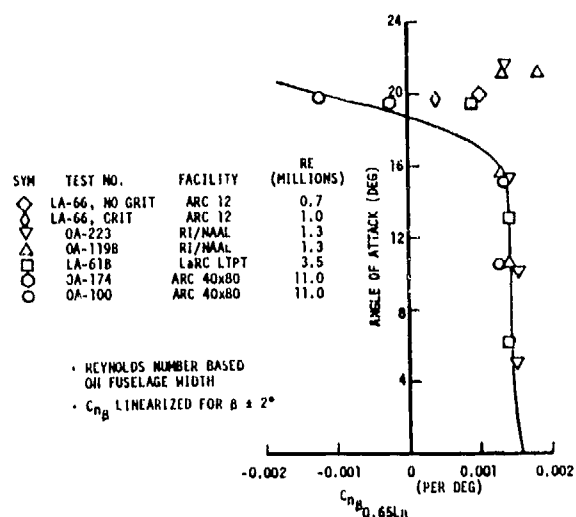


Fig. 47 EFFECT OF REYNOLDS NUMBER ON LOW-SPEED DIRECTIONAL STABILITY

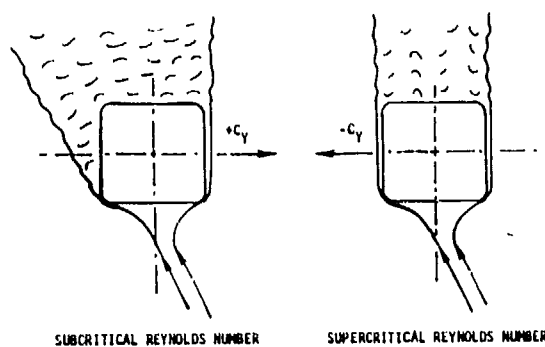


Fig. 48 ILLUSTRATION OF CROSS FLOW ON A SQUARE SHAPED CYLINDER

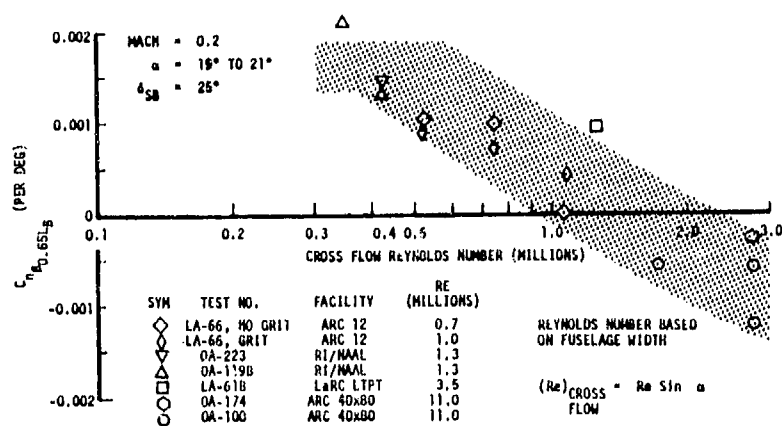


Fig. 49 VARIATION OF ORBITER DIRECTIONAL STABILITY AT HIGH ANGLE OF ATTACK WITH REYNOLDS NUMBER



Fig. 50 ORBITER/747 SEPARATION



Fig. 51 ORBITER 101 LANDING

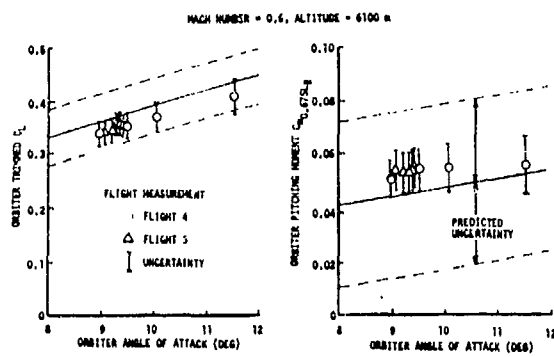


Fig. 52 COMPARISON OF FLIGHT VS. PREDICTED DATA FOR ORBITER MATED TO 747 CARRIER

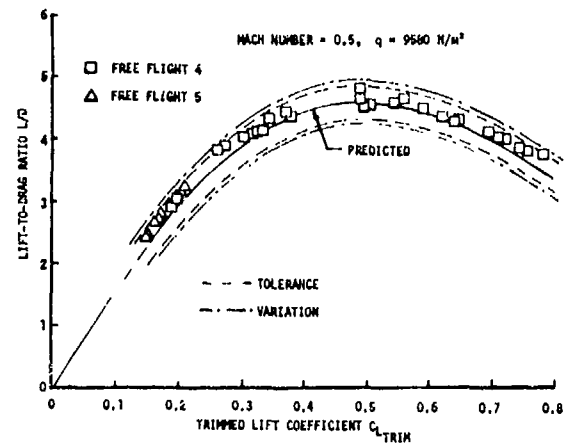


Fig. 53 COMPARISON OF FLIGHT VS. PREDICTED L/D

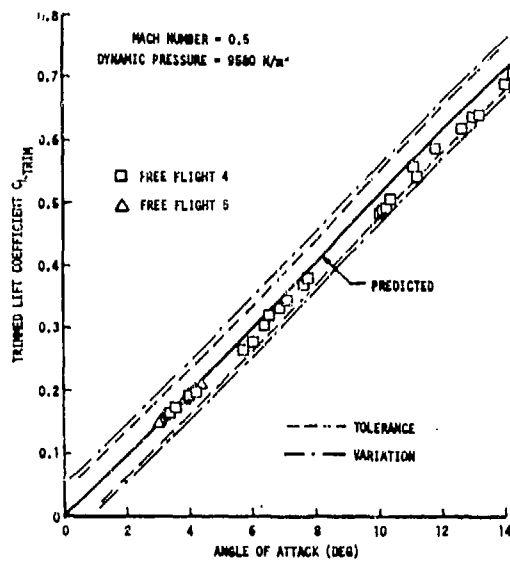


Fig. 54 COMPARISON OF FLIGHT VS. PREDICTED LIFT COEFFICIENT

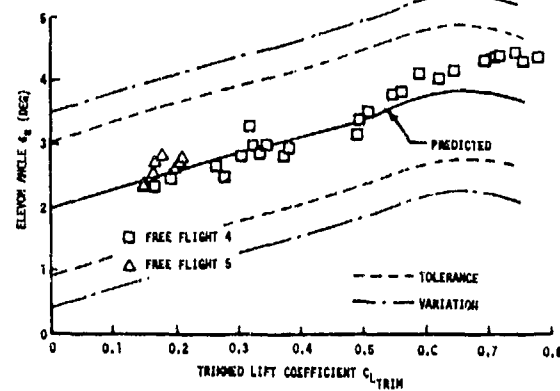


Fig. 55 COMPARISON OF FLIGHT VS. PREDICTED TRIMMED ELEVON DEFLECTION

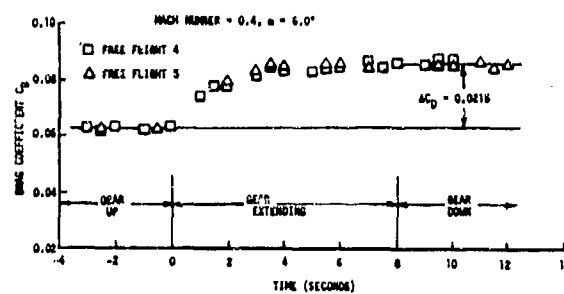


Fig. 56 COMPARISON OF FLIGHT VS. PREDICTED DRAG

SYSTÈME TOURBILLONNAIRE PRÉSENT A L'EXTRADOS D'UNE AILE EN FLÈCHE A GRANDE INCIDENCE

par Jean MIRANDE, Volker SCHMITT et Henri WERLÉ

Office National d'Etudes et de Recherches Aérospatiales (ONERA)
92320 Châtillon (France)

Résumé

Etant donné l'intérêt que suscite de plus en plus le vol à grande incidence, il importe d'approfondir les connaissances relatives aux écoulements décollés mais organisés en nappes tourbillonnaires stables qui conditionnent la qualité de vol et les performances des avions de combat. Une étude expérimentale ayant pour support une aile en flèche a donc été entreprise au tunnel hydrodynamique et en soufflerie aux basses vitesses ($V_0 < 90$ m/s) afin d'améliorer la compréhension des phénomènes mis en jeu et de faciliter leur modélisation.

Les effets de l'écoulement tourbillonnaire sur cette aile sont d'abord illustrés à partir des mesures des efforts globaux et des répartitions de pression statique. On en déduit le domaine d'existence de ce type d'écoulement en fonction de la flèche et de l'incidence. Par une étude phénoménologique au tunnel hydrodynamique on s'attache ensuite à décrire le schéma physique de l'écoulement tourbillonnaire depuis sa formation près de l'apex jusqu'à son éclatement près du bord de fuite. Enfin, on précise par des sondages effectués au moyen d'une sonde clinométrique, dans une configuration particulière, le champ d'écoulement autour de l'aile.

VORTEX PATTERN DEVELOPING ON THE UPPER SURFACE OF A SWEEP WING AT HIGH ANGLE OF ATTACK

Summary

In view of the ever greater interest shown for flying at high angle of attack, it seems necessary to further investigate the flows that, though separated from the wing, remain organized as stable vortex sheets, thus conditioning handling qualities and performance of combat aircraft. To this end, an experimental study, based on a swept wing, has been undertaken in the water tunnel and the wind tunnel at low speeds ($V_0 < 90$ m/s), with a view to improve our understanding of the intervening phenomena and to make easier their modelling.

The vortex flow effects on this wing are first illustrated from global effort measurements and static pressure distributions. We deduce the domain of vortex flow appearance, as a function of both sweep angle and angle of attack. By a phenomenological study in the water tunnel, we then attempt to describe the physical pattern of the vortex flow, from its formation near the apex to its breakdown at the trailing edge. Lastly, we determine, by means of a directional probe, the flow field over the wing.

1 - INTRODUCTION -

Les performances et les qualités de vol des avions de combat évoluant à grande incidence dépendent fortement du degré d'organisation des décollements apparaissant sur de telles configurations. Des visualisations réalisées au tunnel hydrodynamique sur la maquette d'un avion à géométrie variable (fig. 1) montrent, à titre d'exemples, un décollement inorganisé sur l'aile externe (fig. 1 a b b') ou un éclatement des tourbillons d'extrados (fig. 1 c d d') susceptibles de provoquer des effets indésirables au niveau des performances et des qualités de vol.

Il est donc essentiel de connaître la structure des écoulements décollés autour des ailes de ce type ainsi que les facteurs qui régissent les phénomènes de formation et de destruction des écoulements tourbillonnaires cohérents. Ce sont là les motivations et les objectifs de la présente étude à caractère fondamental menée à l'ONERA simultanément en soufflerie et au tunnel hydrodynamique. Elle a pour support l'aile à flèche variable AFV-D dont l'expérimentation s'inscrit dans le cadre plus général des recherches relatives aux écoulements tridimensionnels jusqu'aux vitesses transsoniques [1].

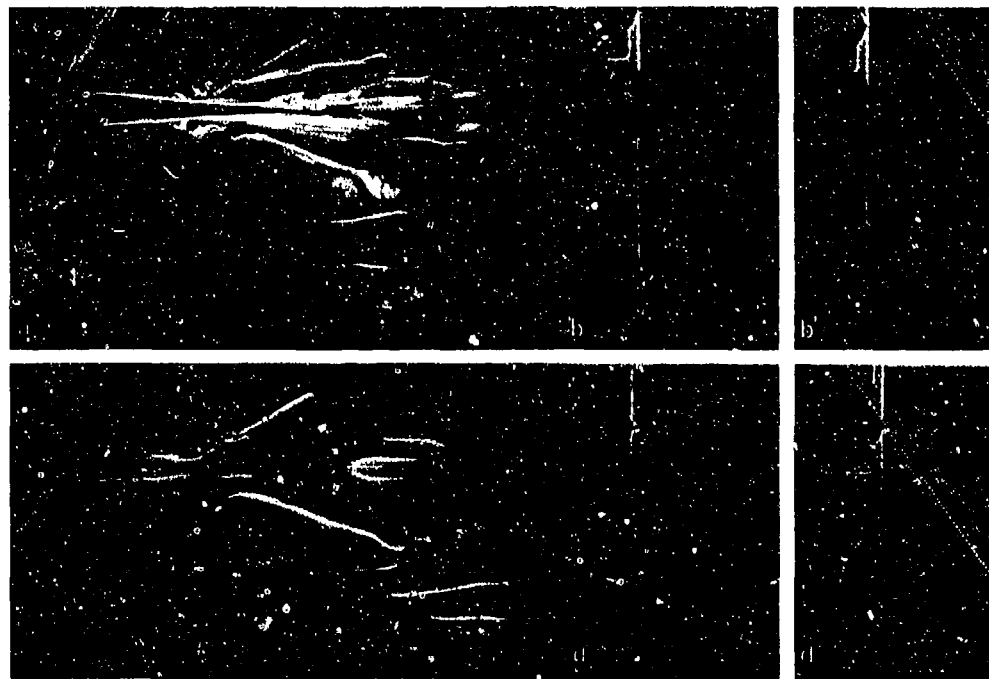


Fig. 1 - Ecoulement autour d'une maquette d'avion à flèche variable
(tunnel hydrodynamique $Re_l \approx 0,3.10^4$)

a, c : vues de l'extrados (visualisation par colorant)

b, b', d, d' : tranches transversales (visualisation par bulles d'air)

- en haut $\varphi = 25^\circ$ } Incidence $\alpha = 10^\circ$ (a, b, c, d) et 15° (b', d').
- en bas $\varphi = 60^\circ$

2 - ECOULEMENTS TOURBILLONNAIRES SUR L'AILLE A FLECHE VARIABLE -

2.1 - Conditions et techniques d'essai -

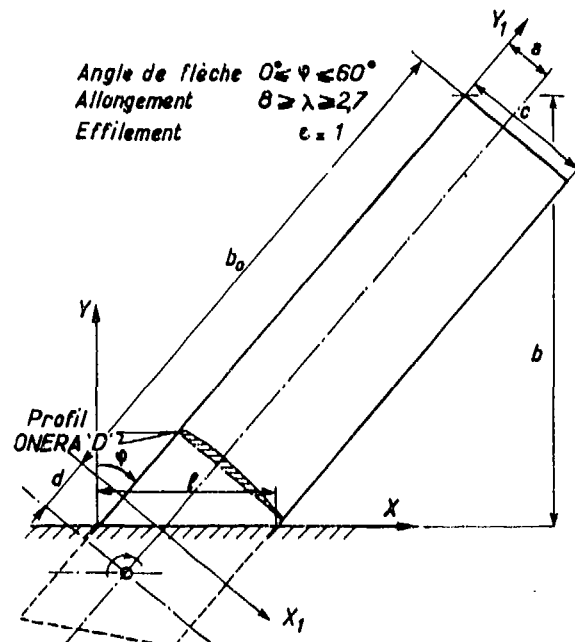


Fig. 2 - Schéma de l'aille à flèche variable AFV-D.

L'aille à flèche variable AFV-D est une aile rectangulaire équipée du profil symétrique ONERA 'D' ($e/c = 0,105$) à caractère "peaky" [2] dont la mise en flèche est obtenue par rotation autour d'un axe situé au voisinage de l'emplanture (fig.2). De par sa conception l'aille subit une variation importante d'allongement en fonction de la flèche qui peut atteindre $\varphi = 60^\circ$.

Les principales caractéristiques géométriques de la maquette utilisée lors des essais en soufflerie sont consignées dans le tableau 1 tandis que les coordonnées du profil 'D' sont précisées par le tableau 2.

Les essais ont été effectués dans la soufflerie S2Ch de l'ONERA. Il s'agit d'une soufflerie du type Eiffel à veine circulaire guidée (diamètre $\phi = 3m$) dont la vitesse maximale est de $V_0 = 110m/s$ et le taux de turbulence est modéré ($\tau = 0,003$). La soufflerie n'étant pas pressurisée, le domaine du nombre de Reynolds couvert par variation de la vitesse ($40 m/s \leq V_0 \leq 90m/s$) est relativement modeste $0,8 \times 10^6 \leq Re_c \leq 1,9 \times 10^6$, c représentant la corde de référence de l'aille.

La maquette est montée sur le plancher de la soufflerie par l'intermédiaire d'une tourelle assurant la mise en incidence. Une plaque de garde circulaire qui est solidaire de la tourelle soustrait l'aille aux effets de la couche limite présente sur la paroi de la soufflerie.

Les mesures effectuées concernent d'abord les efforts globaux déterminés au moyen d'une balance à la paroi à 6 composantes. L'équipement de mesure de la maquette comporte 341 prises de pression statique qui sont réparties en deux fois 11 sections. Par suite du principe de conception de cet équipement l'acquisition s'effectue au rythme de deux sections seulement par essai à l'aide de scanivalves.

La technique de visualisation des lignes de courant pariétales est basée sur l'emploi d'un enduit visqueux de fluidité quasi-permanente. Cet enduit est un mélange d'huile de paraffine et d'oxyde de titane. Très utiles pour compléter les informations issues des mesures effectuées et pour en faciliter l'analyse ces visualisations ne sont pas réversibles à cause de la viscosité de l'enduit ; il faut donc prendre des précau-

tions lors de leur interprétation.

En outre, un dispositif de sondage a été mis au point en vue d'une exploration de l'écoulement autour de l'aile, plus particulièrement au niveau des structures tourbillonnaires.

Tableau I - Caractéristiques géométriques de la maquette AFV-D ($a = 0,150$ m et $d = 0,060$ m - fig. 2)

φ : angle de flèche ; l : corde d'emplanture ;
 b : demi-envergure ; λ : allongement ;
 S_0 : surface mouillée.

φ°	l (m)	b (m)	λ	S_0 (m ²)
0	0,300	1,200	8,00	0,3600
30	0,346	1,107	6,86	0,3573
40	0,392	1,002	5,66	0,3546
50	0,467	0,865	4,28	0,3500
60	0,600	0,700	2,87	0,3420

Tableau II - Cotes du profil ONERA "D"

x_1/c	z_1/c	x_1/c	z_1/c
.000000	.000000	.072500	.035193
.000050	.001342	.077500	.035912
.000100	.002683	.082500	.036604
.000200	.004245	.087500	.037269
.000300	.006002	.092500	.037908
.000400	.007820	.095000	.039405
.000500	.009658	.100000	.041028
.000600	.011494	.105000	.042486
.000700	.013310	.110000	.042413
.000800	.015091	.115000	.042037
.000900	.016913	.120000	.041924
.001000	.018639	.125000	.041853
.001100	.020259	.130000	.041902
.001200	.021874	.135000	.042369
.001300	.023484	.140000	.042230
.001400	.025087	.145000	.041476
.001500	.026683	.150000	.040123
.001600	.028272	.155000	.038942
.001700	.029854	.160000	.037920
.001800	.031428	.165000	.037059
.001900	.032994	.170000	.036239
.002000	.034551	.175000	.035401
.002100	.036099	.180000	.034763
.002200	.037638	.185000	.034294
.002300	.039168	.190000	.033935
.002400	.040689	.195000	.033658
.002500	.042200	.200000	.033462
.002600	.043701	.205000	.033320
.002700	.045192	.210000	.033220
.002800	.046673	.215000	.033160
.002900	.048144	.220000	.033130
.003000	.049605	.225000	.033130
.003100	.051056	.230000	.033160
.003200	.052497	.235000	.033220
.003300	.053928	.240000	.033299
.003400	.055349	.245000	.033399
.003500	.056760	.250000	.033500
.003600	.058161	.255000	.033601
.003700	.059552	.260000	.033702
.003800	.060933	.265000	.033803
.003900	.062304	.270000	.033904
.004000	.063665	.275000	.034005
.004100	.065016	.280000	.034106
.004200	.066357	.285000	.034207
.004300	.067688	.290000	.034308
.004400	.069019	.295000	.034409
.004500	.070350	.300000	.034510
.004600	.071681	.305000	.034611
.004700	.073012	.310000	.034712
.004800	.074343	.315000	.034813
.004900	.075674	.320000	.034914
.005000	.077005	.325000	.035015
.005100	.078336	.330000	.035116
.005200	.079667	.335000	.035217
.005300	.081000	.340000	.035318
.005400	.082331	.345000	.035419
.005500	.083662	.350000	.035520
.005600	.085000	.355000	.035621
.005700	.086331	.360000	.035722
.005800	.087662	.365000	.035823
.005900	.089000	.370000	.035924
.006000	.090331	.375000	.036025
.006100	.091662	.380000	.036126
.006200	.093000	.385000	.036227
.006300	.094331	.390000	.036328
.006400	.095662	.395000	.036429
.006500	.097000	.400000	.036530
.006600	.098331	.405000	.036631
.006700	.099662	.410000	.036732
.006800	.101000	.415000	.036833
.006900	.102331	.420000	.036934
.007000	.103662	.425000	.037035
.007100	.105000	.430000	.037136
.007200	.106331	.435000	.037237
.007300	.107662	.440000	.037338
.007400	.109000	.445000	.037439
.007500	.110331	.450000	.037540
.007600	.111662	.455000	.037641
.007700	.113000	.460000	.037742
.007800	.114331	.465000	.037843
.007900	.115662	.470000	.037944
.008000	.117000	.475000	.038045
.008100	.118331	.480000	.038146
.008200	.119662	.485000	.038247
.008300	.121000	.490000	.038348
.008400	.122331	.495000	.038449
.008500	.123662	.500000	.038550
.008600	.125000	.505000	.038651
.008700	.126331	.510000	.038752
.008800	.127662	.515000	.038853
.008900	.129000	.520000	.038954
.009000	.130331	.525000	.039055
.009100	.131662	.530000	.039156
.009200	.133000	.535000	.039257
.009300	.134331	.540000	.039358
.009400	.135662	.545000	.039459
.009500	.137000	.550000	.039560
.009600	.138331	.555000	.039661
.009700	.139662	.560000	.039762
.009800	.141000	.565000	.039863
.009900	.142331	.570000	.039964
.010000	.143662	.575000	.040065
.010100	.145000	.580000	.040166
.010200	.146331	.585000	.040267
.010300	.147662	.590000	.040368
.010400	.149000	.595000	.040469
.010500	.150331	.600000	.040570
.010600	.151662	.605000	.040671
.010700	.153000	.610000	.040772
.010800	.154331	.615000	.040873
.010900	.155662	.620000	.040974
.011000	.157000	.625000	.041075
.011100	.158331	.630000	.041176
.011200	.159662	.635000	.041277
.011300	.161000	.640000	.041378
.011400	.162331	.645000	.041479
.011500	.163662	.650000	.041580
.011600	.165000	.655000	.041681
.011700	.166331	.660000	.041782
.011800	.167662	.665000	.041883
.011900	.169000	.670000	.041984
.012000	.170331	.675000	.042085
.012100	.171662	.680000	.042186
.012200	.173000	.685000	.042287
.012300	.174331	.690000	.042388
.012400	.175662	.695000	.042489
.012500	.177000	.700000	.042590
.012600	.178331	.705000	.042691
.012700	.179662	.710000	.042792
.012800	.181000	.715000	.042893
.012900	.182331	.720000	.042994
.013000	.183662	.725000	.043095
.013100	.185000	.730000	.043196
.013200	.186331	.735000	.043297
.013300	.187662	.740000	.043398
.013400	.189000	.745000	.043499
.013500	.190331	.750000	.043600
.013600	.191662	.755000	.043701
.013700	.193000	.760000	.043802
.013800	.194331	.765000	.043903
.013900	.195662	.770000	.044004
.014000	.197000	.775000	.044105
.014100	.198331	.780000	.044206
.014200	.199662	.785000	.044307
.014300	.201000	.790000	.044408
.014400	.202331	.795000	.044509
.014500	.203662	.800000	.044610
.014600	.205000	.805000	.044711
.014700	.206331	.810000	.044812
.014800	.207662	.815000	.044913
.014900	.209000	.820000	.045014
.015000	.210331	.825000	.045115
.015100	.211662	.830000	.045216
.015200	.213000	.835000	.045317
.015300	.214331	.840000	.045418
.015400	.215662	.845000	.045519
.015500	.217000	.850000	.045620
.015600	.218331	.855000	.045721
.015700	.219662	.860000	.045822
.015800	.221000	.865000	.045923
.015900	.222331	.870000	.046024
.016000	.223662	.875000	.046125
.016100	.225000	.880000	.046226
.016200	.226331	.885000	.046327
.016300	.227662	.890000	.046428
.016400	.229000	.895000	.046529
.016500	.230331	.900000	.046630
.016600	.231662	.905000	.046731
.016700	.233000	.910000	.046832
.016800	.234331	.915000	.046933
.016900	.235662	.920000	.047034
.017000	.237000	.925000	.047135
.017100	.238331	.930000	.047236
.017200	.239662	.935000	.047337
.017300	.241000	.940000	.047438
.017400	.242331	.945000	.047539
.017500	.243662	.950000	.047640
.017600	.245000	.955000	.047741
.017700	.246331	.960000	.047842
.017800	.247662	.965000	.047943
.017900	.249000	.970000	.048044
.018000	.250331	.975000	.048145
.018100	.251662	.980000	.048246
.018200	.253000	.985000	.048347
.018300	.254331	.990000	.048448
.018400	.255662	.995000	.048549
.018500	.257000	.1.000000	.048650

La figure 3 montre la maquette et le dispositif d'exploration permettant de déplacer une sonde dans des plans perpendiculaires à la corde d'emplanture. Il comporte un rail parallèle à la corde qui permet le positionnement en x et supporte une glissière verticale assurant le déplacement suivant y d'un coulisseau comportant une glissière horizontale définissant les déplacements d'axe z normaux au plan de l'aile.

La sonde, du type conique à 5 prises, permet la détermination du vecteur vitesse en module et direction avec une précision variant de 1,5 à 5 % dans une plage d'angle comprise entre 0° et 30° . Au-delà, jusqu'à environ 50° les indications sont encore exploitables qualitativement [3].

Outre les 5 pressions indiquées par la sonde, deux répartitions de pression pariétales (fig.3) ont été mesurées pendant les explorations pour contrôler la stabilité de la configuration et l'importance des effets d'interactions possibles du dispositif d'exploration.

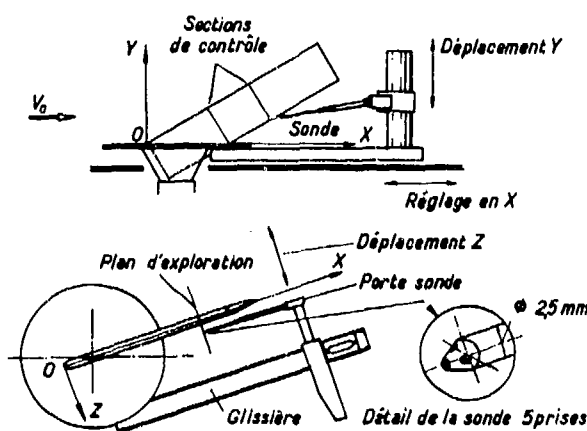


Fig. 3 - Ensemble du montage.

2.2 - Formation et effets des écoulements tourbillonnaires -

Lors des essais en soufflerie l'apparition des écoulements tourbillonnaires est observée dans un domaine d'incidence et de flèche bien délimité.

En effet, pour les angles de flèche supérieurs ou égaux à $\varphi = 40^\circ$ les courbes de portance indiquent une évolution non linéaire très caractéristique (voir fig.4).

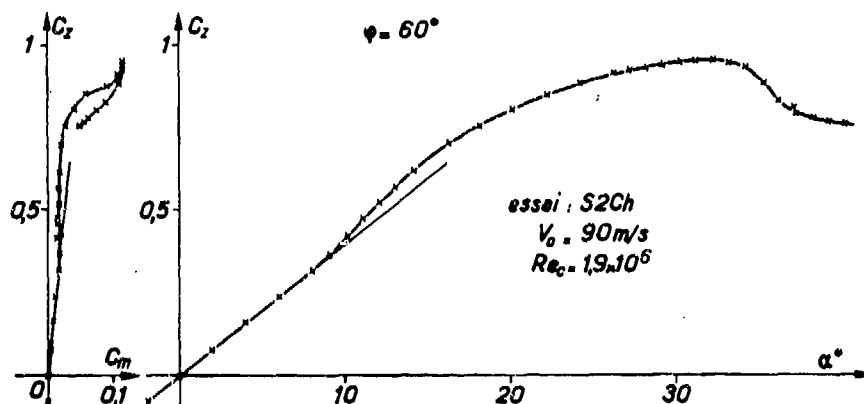
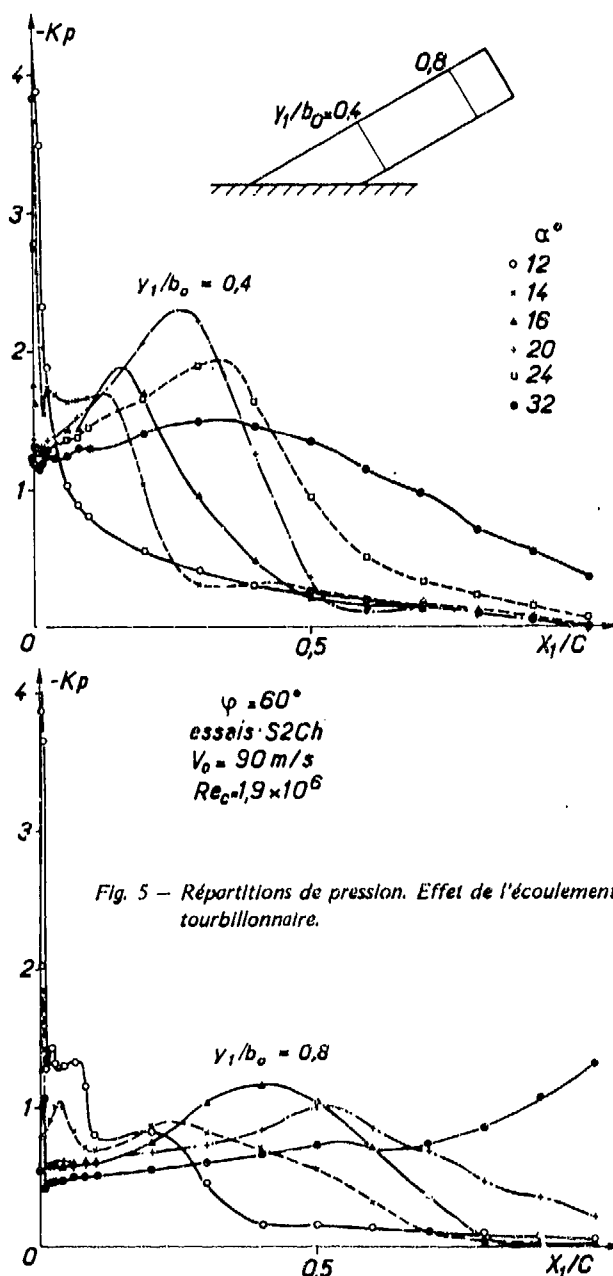


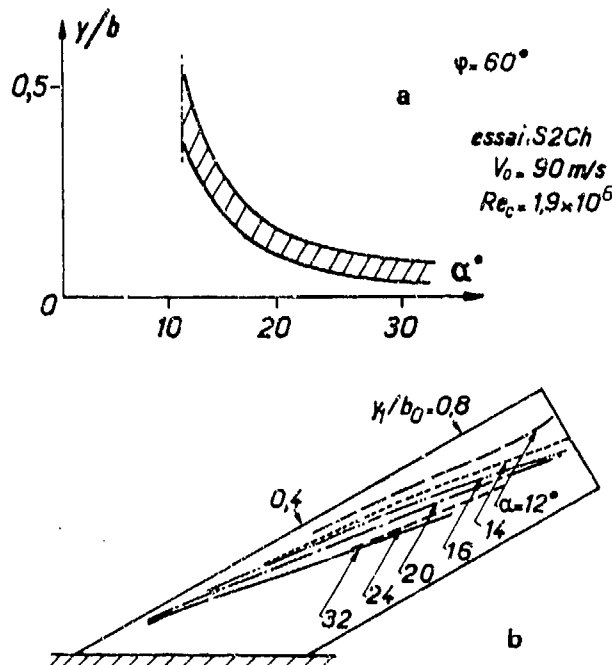
Fig. 4 - Portance et moment de tangage.

Ce comportement est la conséquence de la présence, à l'extrados de l'aile, d'un écoulement qui est décollé depuis le bord d'attaque, mais qui s'organise en formant un tourbillon en cornet générateur d'un gain appréciable en portance. L'étude fine de ce type d'écoulement soit au tunnel hydrodynamique soit en soufflerie au moyen des sondages a été effectuée à la flèche $\varphi = 60^\circ$ qui constitue un exemple typique.

Nous présentons donc quelques résultats caractéristiques relatifs à cette configuration de l'aile et en premier lieu nous analyserons les courbes de la portance et du moment de tangage (fig. 4) obtenues au nombre de Reynolds $Re_c = 1,9 \times 10^6$. Tandis que l'évolution de la portance présente bien les caractéristiques indiquées plus haut nous relevons, en examinant le moment de tangage, une tendance à piquer lors de l'apparition de l'écoulement tourbillonnaire ($\alpha \approx 9^\circ$) suivie d'un engagement à cabrer ; ceci traduit évidemment l'évolution du centre de poussée sous l'effet du tourbillon en cornet dont la position et l'intensité varient en fonction de l'incidence. Des polaires réalisées en incidence croissante puis décroissante conduisent généralement à des courbes exemptes d'un effet d'hystérésis.



Une étude plus détaillée est possible par l'analyse du champ de pression statique mesuré à l'extrados de l'aile. Afin de mettre en évidence l'évolution des phénomènes en fonction de l'incidence, nous examinons les répartitions de pression en 2 sections $y_1/b_0 = 0,4$ et $0,8$ (fig. 5). Le régime tourbillonnaire induit des répartitions en forme de cloche de façon plus prononcée dans la section interne que dans la section externe. Les dépressions maximales (K_{pmin} tourbillonnaire) situées au niveau de la projection de l'axe du tourbillon dans le plan de l'aile (voir aussi 4.1) se déplacent vers le bord de fuite lorsque l'incidence augmente. A $\alpha = 12^\circ$ la répartition de pression dans la section $y_1/b_0 = 0,4$ caractérisée par un pic de survitesse au bord d'attaque suivi d'une recompression continue jusqu'au bord de fuite, correspond à un écoulement encore non décollé ; l'origine du tourbillon qui, d'après la courbe de portance, existe pourtant, doit donc se situer à l'extérieur de la section $y_1/b_0 = 0,4$. L'aplatissement des courbes du coefficient de pression à forte incidence voire la disparition du K_{pmin} tourbillonnaire (par exemple $\alpha = 32^\circ$ à $y_1/b_0 = 0,8$) indique l'écèlement du tourbillon dont l'intensité se réduit de plus en plus à mesure que l'incidence augmente. L'examen conjoint des répartitions de pression dans toutes les sections et des visualisations pariétales discutées en détail plus loin permet alors de constater que la position de l'origine du tourbillon lors de son apparition est loin de se situer à l'apex de l'aile (fig. 6 a) mais elle y tend lorsque l'incidence croît. Toutefois, faute de moyens de mesure mieux adaptés cette origine ne peut être déterminée avec précision. Comme il a été déjà dit les relevés du coefficient de pression K_{pmin} tourbillonnaire conduisent à la détermination approximative de l'axe tourbillonnaire projeté dans le plan de l'aile. Ainsi est-il possible de décrire schématiquement l'évolution de cet axe qui pivote légèrement autour de l'origine du tourbillon vers l'emplanture (fig. 6 b) lorsque l'incidence augmente.



2.3 - Influence du nombre de Reynolds -

Ces essais ont également fourni quelques indications relatives à l'effet du nombre de Reynolds. Une augmentation du nombre de Reynolds obtenue par une variation de la vitesse se traduit par une réduction sensible du domaine d'existence des écoulements tourbillonnaires sur l'aile (fig.7). Leur apparition en fonction de l'incidence est déterminée sur cette figure par une valeur ΔC_z tourbillonnaire de $\approx 0,02$ compte tenu de la précision des mesures. Notons au passage que cette apparition tend aux fortes flèches vers une valeur déjà observée [4] pour les ailes élancées ($\alpha \approx 6^\circ$). La limite supérieure du domaine est définie par les valeurs $\alpha_{C_z \max}$ du décrochage qui correspond à l'écoulement prématuré du tourbillon. Enfin, la limite latérale du domaine indiquant la flèche minimale pour laquelle cette aile présente des écoulements tourbillonnaires n'est pas connue avec une grande précision car l'étude de la flèche a été effectuée par pas de 5° .

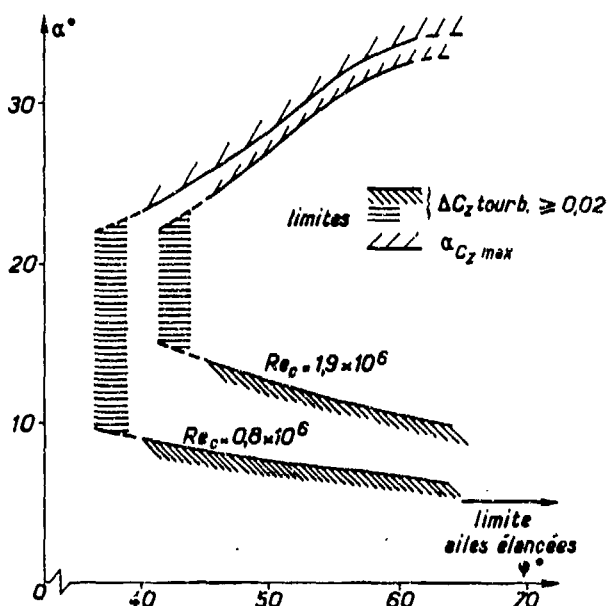


Fig. 7 -- Domaine d'existence des écoulements tourbillonnaires.

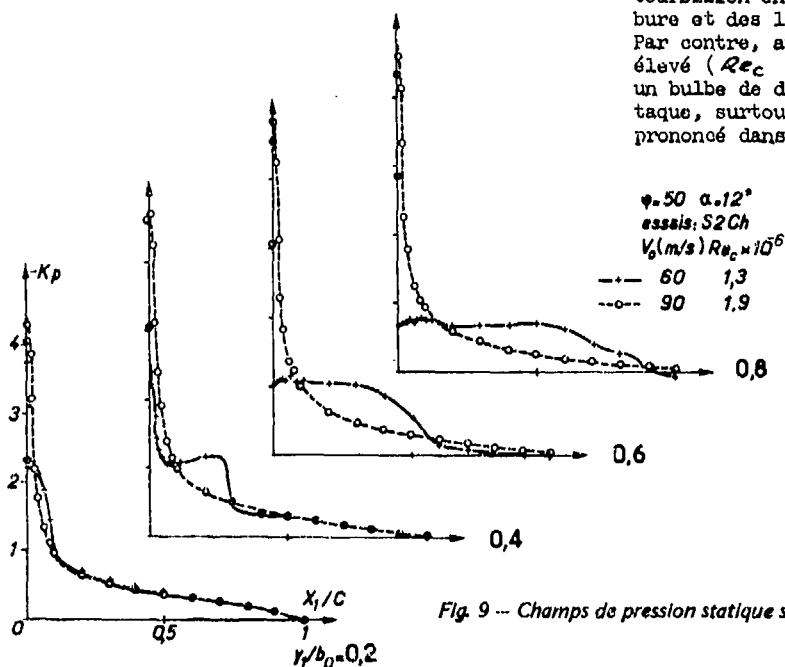


Fig. 9 -- Champs de pression statique sur l'extrados. Effet du nombre de Reynolds.

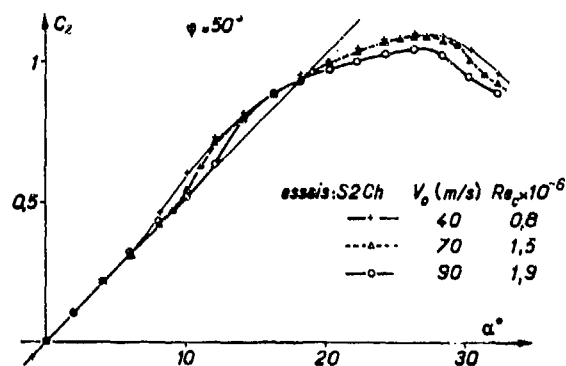


Fig. 8 -- Influence du nombre de Reynolds sur la portance.

L'influence du nombre de Reynolds est encore illustrée par les courbes de portance relatives à la flèche $\varphi = 50^\circ$ (fig.8). On remarque que l'incidence d'apparition de l'écoulement tourbillonnaire augmente sensiblement lorsque le nombre de Reynolds croît alors que la portance maximum $C_{z \max}$ et l'incidence correspondante $\alpha_{C_z \max}$ diminuent.

Pour mettre davantage en lumière la transformation profonde de l'écoulement à l'extrados de l'aile en fonction du nombre de Reynolds examinons en détail ce qui se passe à l'incidence $\alpha = 12^\circ$. D'après les courbes de portance l'écoulement tourbillonnaire est installé aux nombres de Reynolds $Re_c = 0,8 \times 10^6$ et $1,5 \times 10^6$, mais un effet tourbillonnaire n'est pas décelable à $Re_c = 1,9 \times 10^6$. Ceci est confirmé par les champs de pression de l'extrados (fig.9). En effet, les répartitions de pression correspondant au plus faible nombre de Reynolds ($Re_c = 1,3 \times 10^6$) montrent la présence d'un tourbillon qui est toutefois peu intense. En revanche, au nombre de Reynolds plus élevé, les répartitions de pression indiquent un écoulement essentiellement non décollé avec un fort pic de survitesse au bord d'attaque et une recompression continue jusqu'au bord de fuite. Les visualisations pariétales (fig.10) relatives à la même configuration de l'aile corroborent encore ce résultat. Au cas du faible nombre de Reynolds ($Re_c = 0,8 \times 10^6$) nous observons des lignes de courant pariétales révélatrices du tourbillon en cornet par une inversion de courbure et des lignes singulières caractéristiques. Par contre, au cas du nombre de Reynolds plus élevé ($Re_c = 1,9 \times 10^6$), on remarque, à part un bulbe de décollement laminaire au bord d'attaque, surtout un écoulement secondaire très prononcé dans la région du bord de fuite.

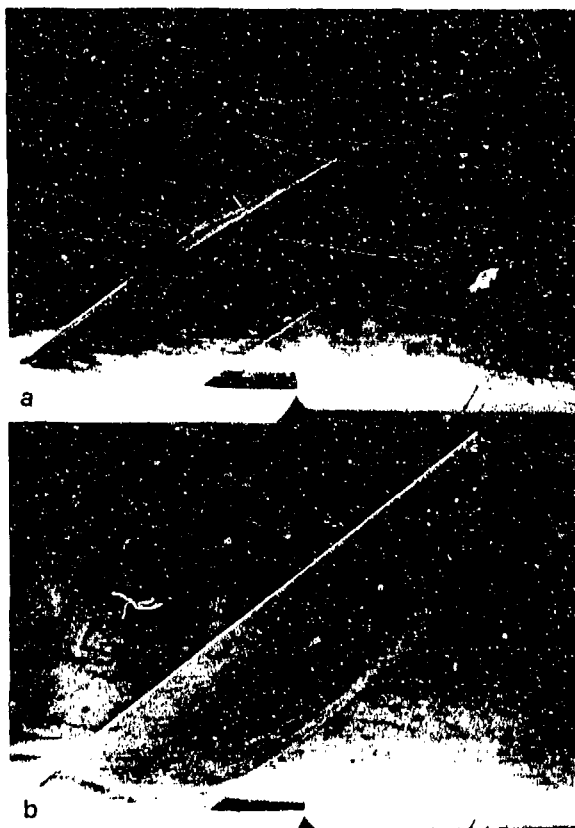


Fig. 10 - Visualisations des lignes de courant pariétales.
Effet du nombre de Reynolds - essai S2Ch, $\varphi = 50^\circ$,
 $\alpha = 12^\circ$;
a) $V_0 = 40 \text{ m/s}$; $Re_c = 0,8 \cdot 10^6$
b) $V_0 = 90 \text{ m/s}$; $Re_c = 1,9 \cdot 10^6$.

3 - ETUDE PHENOMENOLOGIQUE DE L'ÉCOULEMENT TOURBILLONNAIRE AU TUNNEL HYDRODYNAMIQUE A FAIBLE NOMBRE DE REYNOLDS -

3.1 - Conditions expérimentales -

Cette étude a eu pour cadre le tunnel vertical de l'ONERA [5] dont de nombreuses publications ont fait connaître les procédés de visualisation par traceurs liquides ou gazeux, et notamment leur application à de telles études d'écoulements décollés [6].

Le lecteur intéressé trouvera dans ces documents l'exposé complet de la technique expérimentale utilisée, dont on se contente ici de rappeler succinctement quelques détails nécessaires à la compréhension des résultats.

Les colorants de même densité que l'eau ont été émis à partir de la surface des modèles sous forme de filets isolés (par exemple fig. 1 a et c) ou de nappes pariétales (par exemple fig. 18 a-f) visualisant en régime stationnaire des lignes ou surfaces de courant plus ou moins extérieures ou pariétales suivant le réglage du débit du colorant. Dans les zones à caractère instationnaire ou turbulent, il se produit une répartition aléatoire et une diffusion rapide du colorant émis, qui ne révèle alors plus que l'allure moyenne des phénomènes.

Il en est de même pour les traceurs gazeux, minuscules bulles d'air obtenues au cours du remplissage du tunnel, dont on observe les trajectoires dans des plans transversaux (par exemple fig. 1 bb' dd') ou longitudinaux (fig. 17a).

Notons ici que ces coupes ne donnent que l'allure du pseudo-écoulement transversal révélée par les éléments de trajectoire des bulles d'air traversant la tranche éclairée dont l'épaisseur non négligeable ne peut et ne doit pas être trop réduite (lumière nécessaire à l'exposition des clichés, longueur des éléments de trajectoire). Mais cette allure dépend surtout de l'orientation de l'axe de visée (voir fig. 14). Il est donc toujours nécessaire d'interpréter soigneusement les différentes visualisations par bulles d'air en les recoupant notamment avec celles obtenues plus directement grâce aux colorants.

Pour effectuer une analyse aussi fine que possible de la structure tourbillonnaire du décollement d'extrados près de l'apex et examiner notamment les effets d'interaction susceptibles de se produire le long du panneau de garde qui sert de support à la voilure, nous avons fait appel à la technique du modèle agrandi qui représente à plus grande échelle le domaine dont on souhaite entreprendre une étude plus fine. Bien entendu, ce procédé exige une comparaison avec une maquette complète.

Tous les modèles essayés au tunnel sont représentés sur la figure 11, qui indique par ailleurs la position des tranches d'écoulement transversales visualisées par bulles d'air. Les caractéristiques géométriques des maquettes (flèche $\varphi = 60^\circ$, profil ONERA 'D') et le domaine de Reynolds simulé sont donnés sur le tableau 3.

Tableau III - Caractéristiques des modèles étudiés
au tunnel hydrodynamique.

Ref. fig.11	Modèle	c (mm)	b (mm)	λ	$Re_c \times 10^{-4}$
1	aile complète	50	109,5	2,7	0,25-1,0
2	aile agrandie	100	120	1,24	0,5-2,0
3	apex agrandi	100	100	1,33	0,5-5,0

3.2 - Structure de l'écoulement [12] -

Les visualisations obtenues avec le modèle complet (fig. 12) fournissent les indispensables vues d'ensemble de l'écoulement sur lesquelles on distingue la structure tourbillonnaire stable du décollement d'extrados et son évolution en fonction de l'incidence.

A 20° d'incidence (fig. 12 abb'), la nappe qui déferle le long du bord d'attaque en flèche s'enroule en "cornet" [7, 8] autour du tourbillon principal d'extrados issu près de l'apex. Ce tourbillon se place en diagonale au-dessus de cette aile non conique et tend à éclater côté aval devant le flux d'intrados qui contourne l'extrémité libre du modèle. Entre le bord d'attaque et ce tourbillon bien structuré se développe une zone marginale enfermée sous le cornet et qui se désorganise côté aval. Cette structure du décollement d'extrados est confirmée par l'allure du pseudo-écoulement transversal révélée par les bulles d'air (fig. 12b).

Quand l'incidence croît (fig. 12 acd), on observe la progression vers l'amont des remous marginaux, le développement du tourbillon principal et la nette remontée vers l'apex de son point d'éclatement, phénomène classique [9] affectant toutes les structures tourbillonnaires aux incidences élevées.

La fig. 12f précise la position de l'axe du tourbillon principal d'extrados sur le plan de la voilure pour différentes incidences. Cet axe, relevé sur les clichés obtenus au cours des essais ne concerne que la partie organisée du noyau comprise entre son origine approximative plus ou moins proche de l'apex et son point d'éclatement moyen situé côté aval. Dans les mêmes conditions, la fig. 12 g révèle d'autre part que la position en abscisse de l'éclatement dépend surtout de l'incidence.

Une variation du nombre de Reynolds, telle qu'elle peut être réalisée au tunnel (voir tableau 3), ne provoque aucun changement fondamental dans l'allure du pseudo-écoulement transversal (comparer fig. 12b et b'), ni dans celle de l'éclatement (comparer fig. 12 c et c'). Par contre, à égalité d'incidence, on enregistre des différences d'origine et de position du tourbillon principal avec celles observées en soufflerie à Reynolds élevé (comparer fig. 12f avec fig. 6b et 21b).

Enfin pour compléter cette description, notons la présence sur l'intrados (fig. 12 e) d'une ligne de partage qui sépare la partie du flux d'intrados qui se déverse sur l'extrados le long du bord d'attaque de celle qui rejoint le bord de fuite du modèle. La nappe tourbillonnaire qui se détache le long de ce bord en flèche accentuée s'enroule aussi en "cornet" pour venir former un tourbillon concentré dit de bord de fuite, mais fortement interactionné par le tourbillon principal d'extrados.

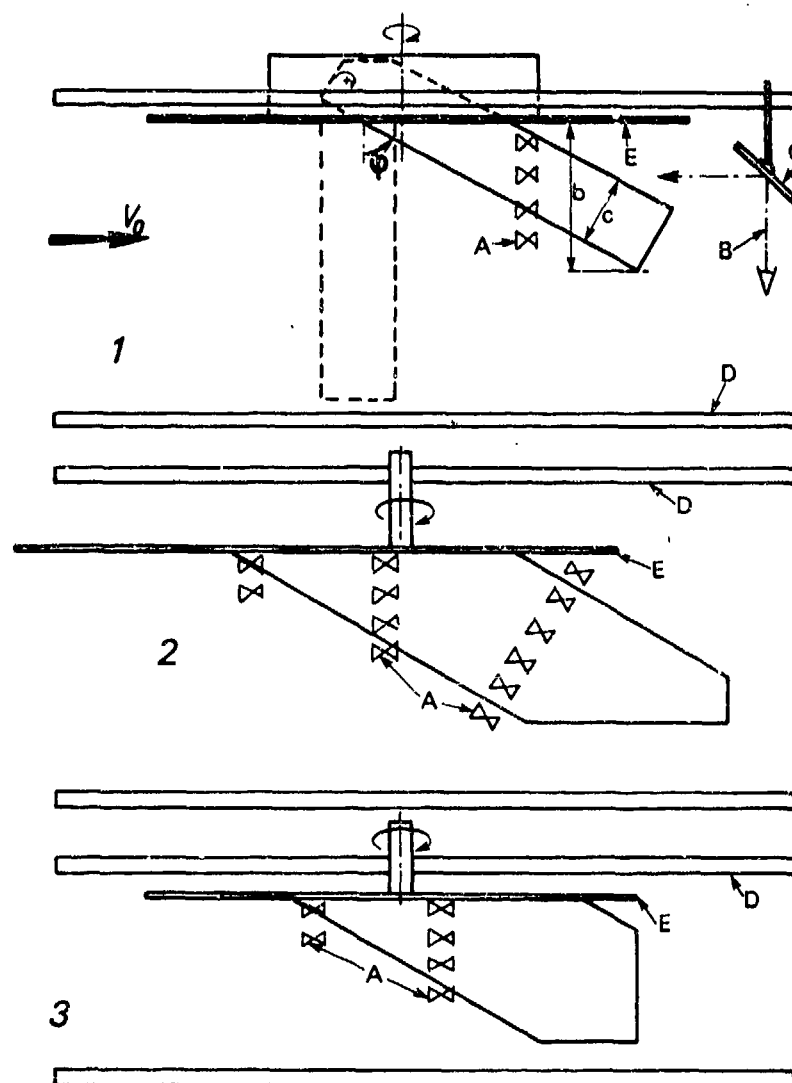


Fig. 11 — Schémas des modèles ($\varphi = 60^\circ$) essayés au tunnel hydrodynamique.

- A : tranches transversales visualisées par bulles d'air,
- B : axe de prise de vues correspondant,
- C : miroir à 45° ,
- D : paroi de la veine (normale ou réduite),
- E : panneau de garde du modèle.

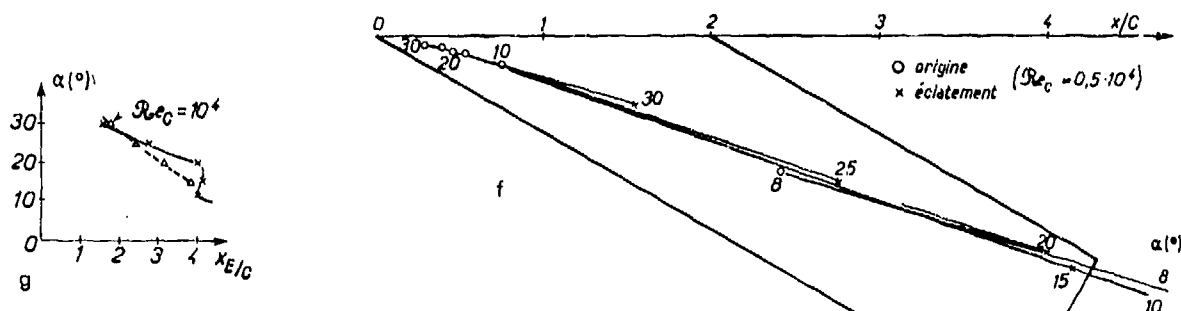
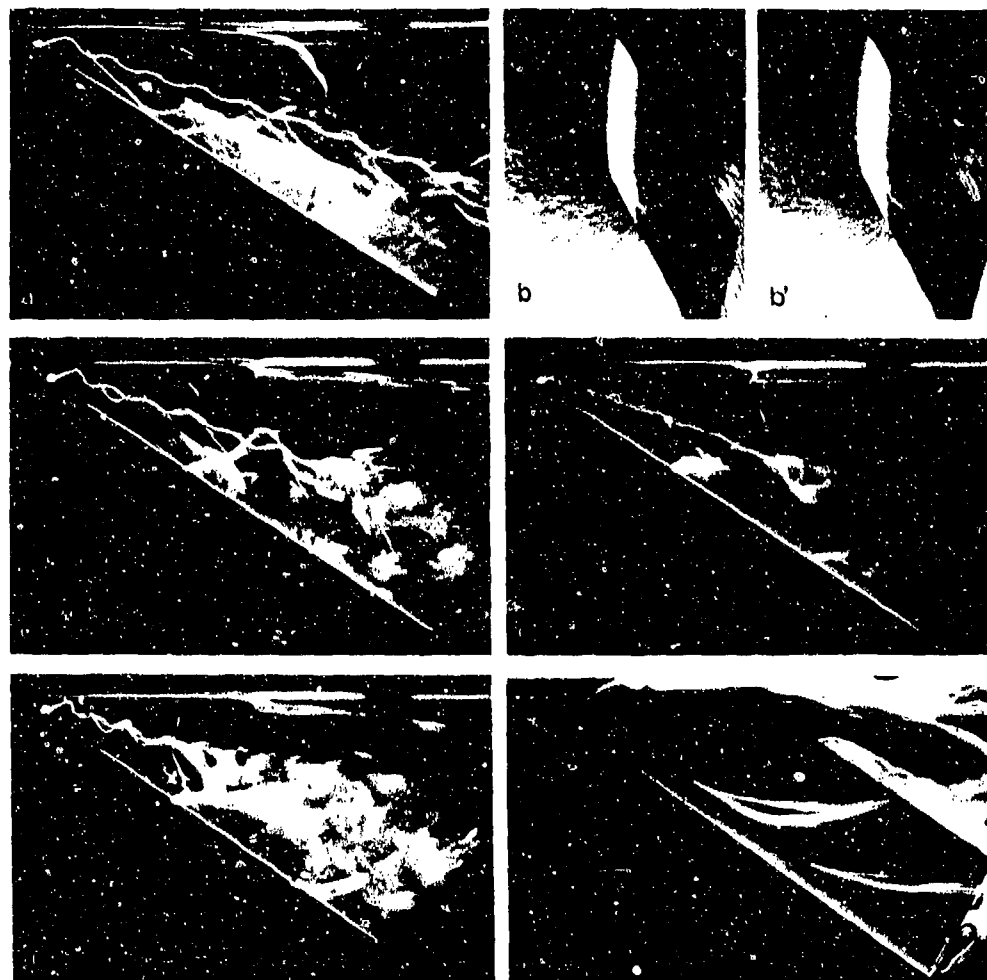


Fig. 12 — Ecoulement autour d'une maquette d'aile complète
(tunnel hydrodynamique - $Re_c \approx 0,5 \cdot 10^4$ sauf indication contraire)
Vues de l'extrados (a, c, c', d) et de l'intrados (e) tranches transversales (b, b')
— en haut $\alpha = 20^\circ$,
— au milieu $\alpha = 25^\circ$ ($Re_c \approx 10^4$ pour b' et c')
— en bas $\alpha = 30^\circ$.
— positions de l'axe du tourbillon principal (f)
— déplacement du point d'éclatement du tourbillon principal (g) } en fonction de l'incidence α

Les essais effectués à 20° et à 25° d'incidence avec l'aile agrandie ont permis d'approfondir le schéma physique de l'écoulement, notamment grâce aux nombreux émetteurs de colorant, qui équipent ce modèle (fig.13), ainsi qu'aux différentes coupes transversales visualisées par bulles d'air (fig.14), qu'il est possible de réaliser avec une telle maquette.

Dans ces conditions, le schéma d'écoulement qui peut être dégagé de ces essais à grande incidence et à faible Reynolds ($Re_c \approx 10^4$) est le suivant :

- la ligne de partage P d'intrados (fig.15 a) est issue d'un point d'arrêt unique non isotrope situé près de l'apex arrondi du

modèle. D'amont en aval, cette ligne frontière, d'abord orientée suivant la bissectrice de l'angle à l'apex, s'incurve ensuite pour devenir rapidement parallèle au bord d'attaque. Du point d'arrêt qui se présente comme un point de rebroussement se détache une deuxième ligne de partage incurvée dans le sens opposé et qui sépare le flux d'intrados qui rejoint le bord de fuite de celui qui se déverse sur le panneau de garde sous l'effet d'un tourbillon qui se forme le long de l'emplanture (fig. 13a et 17 b) ;

- la ligne de décollement S sur l'extrados (fig. 15c) se place aussi sur une génératrice du modèle, mais à proximité immédiate du bord

d'attaque, sauf au voisinage de l'apex où elle s'incurve vers l'emplanture (fig. 13d). Cette incurvation des lignes de partage et de décollement à l'apex indique une diminution de l'incidence locale accentuée par les effets de la couche limite du panneau de garde ;

- en effet, la couche limite qui se forme sur ce panneau décolle devant l'obstacle constitué par le modèle. Ce décollement tridimensionnel devient le siège de tourbillons en "fer à cheval", mais dans le cas dissymétrique constitué par un modèle en incidence [10, 11],

c'est surtout la branche intrados de ces tourbillons qui se développe (fig. 15b et A), et la ligne de décollement sur le panneau qui ne cesse de s'éloigner du modèle côté intrados, se rabat très vite vers l'emplanture côté extrados (fig. 17 c) ;

- enfin, comme cela a été maintes fois observé sur les ailes en flèche avec épaisseur la partie organisée côté amont du secteur marginal enfermé sous le cornet principal est le siège de deux tourbillons secondaires dont le premier (T_1)

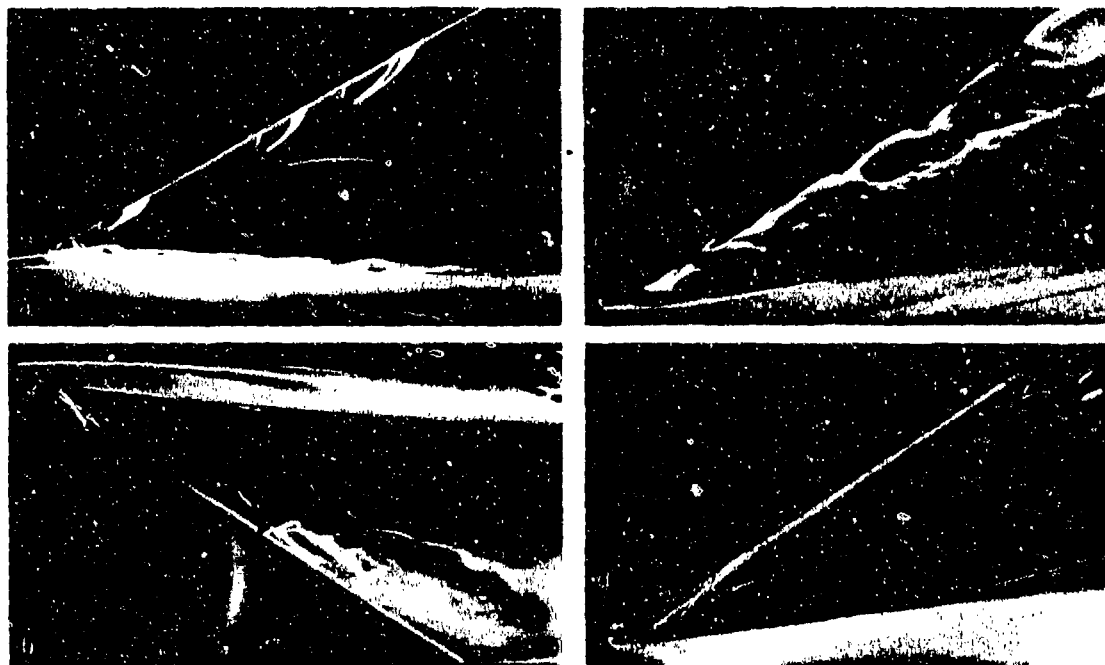


Fig. 13 - Ecoulement autour d'une maquette d'aile agrandie à 20° d'incidence (tunnel hydrodynamique - $Re_c \approx 10^4$). Vues de l'extrados (b, c, d) et de l'intrados (a).

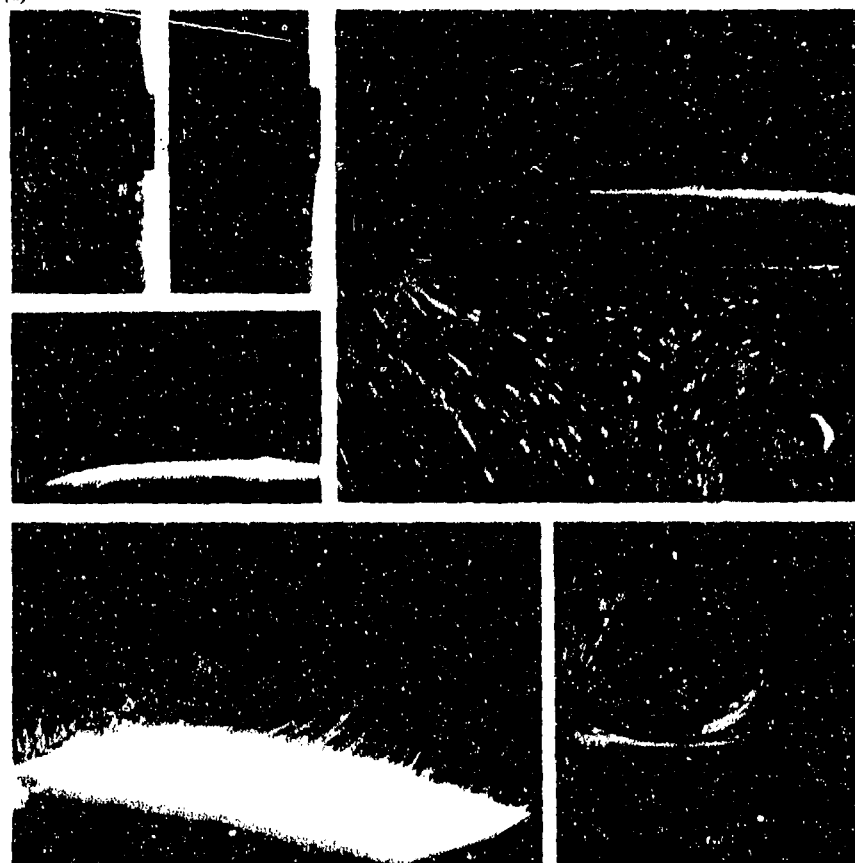


Fig. 14 - Ecoulement autour d'une maquette d'aile agrandie à 20° d'incidence (tunnel hydrodynamique - $Re_c \approx 10^4$) -

Tranches transversales situées près de l'apex (a, a'), au voisinage de la mi-corde (b, b') et en aval du bord de fuite (c, c') du profil d'emplanture selon figure 11-2 (pour c' voir nota) -

Visée suivant un axe parallèle à la tangente locale à l'intrados (a) ou à l'extrados (a'), à l'axe du tourbillon (b, c) ou au plan de la voilure (b', c')
Nota : la tranche c' est située en aval du point d'écèlement du tourbillon principal.

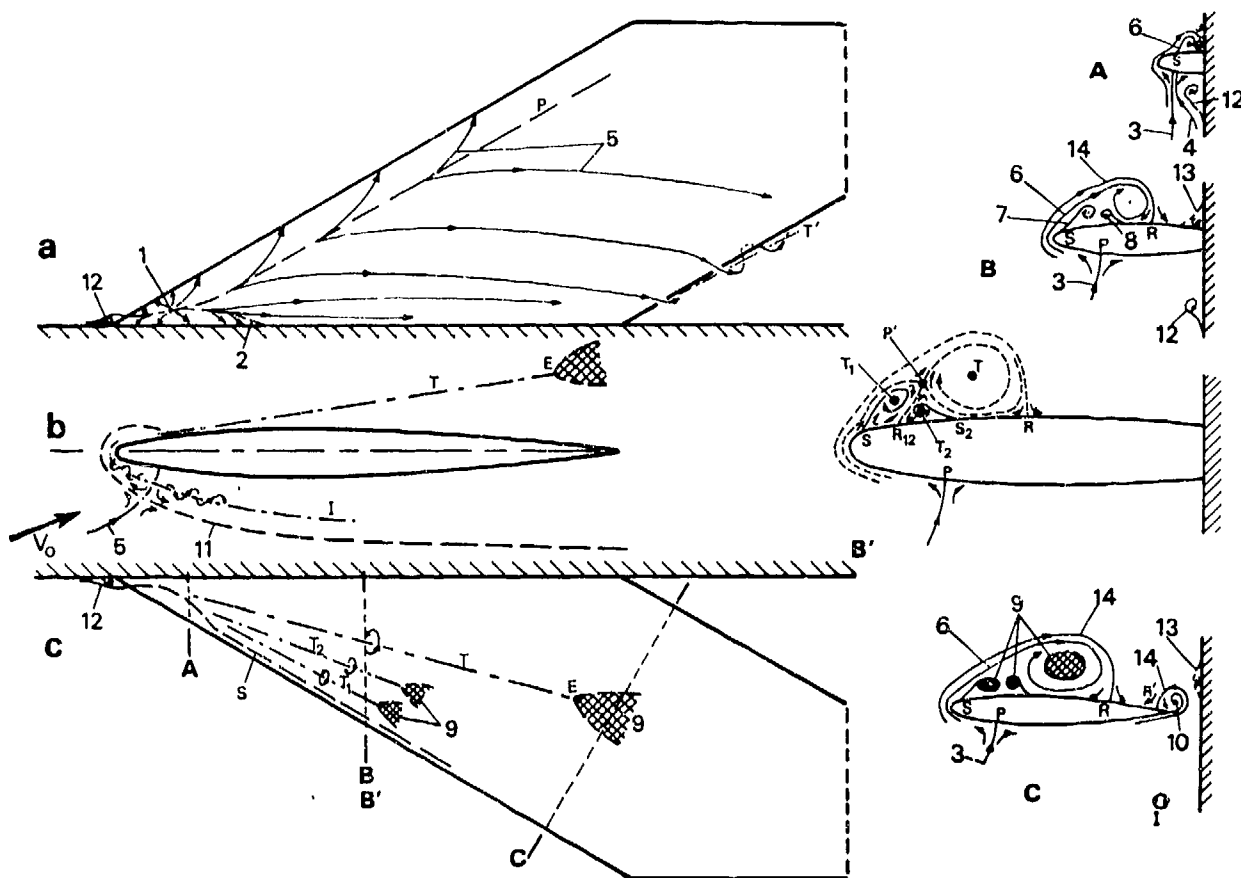


Fig. 15 - Schéma de l'écoulement autour d'une aile cylindrique en flèche accentuée placée à incidence élevée.

a, b, c, schémas relatifs à l'intrados, à l'emplanture et à l'extrados.

A, B-B', C, schémas du pseudo-écoulement transversal à la hauteur de l'apex, de la mi-corde et en aval du bord de fuite du profil d'emplanture.

Légende : 1 point d'arrêt unique non isotrope.

P) lignes de partage entre les flux { les bords d'attaque et de fuite

2) d'intrados qui se dirigent vers { le bord de fuite et le panneau de garde.

3 & 4 surfaces de courant qui aboutissent le long des lignes P et 2.

5 lignes de courant pariétales.

S ligne de décollement principale sur l'extrados.

6 nappe en cornet s'enroulant autour du tourbillon principal T qui éclate en E.

7 & 8 nappes secondaires s'enroulant autour des tourbillons T_1 de même sens et T_2 de sens opposé à T.

9 noyaux désorganisés des tourbillons T_1 , T_2 et T_3 .

10 nappe s'enroulant autour du tourbillon de bord de fuite T' .

11 ligne de décollement sur le panneau de garde incurvée de part et d'autre d'un point de partage.

12 nappe s'enroulant autour du tourbillon principal I incurvé en fer à cheval et caractérisant le décollement sur le panneau.

13 zones décollées de faible importance observées sur le panneau de garde.

14 surfaces de courant, frontières des couches de courant alimentant les différents tourbillons d'extrados et aboutissant le long des lignes de recollement R et R'.

P' ligne de partage au sein du fluide.

S_2 ligne de décollement secondaire.

R_{12} ligne de recollement secondaire.

se développe le long de la ligne de décollement près du bord d'attaque et tourne dans le même sens que le tourbillon principal T, tandis que le second (T_2) de sens opposé s'intercale entre ces deux tourbillons (fig. 15c, B et C). Dans ces conditions, la couche de courant qui déferle le long du bord d'attaque (fig. 13c), se scinde en deux sous-couches qui alimentent respectivement le tourbillon principal et le tourbillon secondaire de même sens.

Un schéma plus complet de l'écoulement observé à la mi-corde est donné par la fig. 15 B' tracée à plus grande échelle. Il précise notamment les surfaces de courant qui aboutissent le long de la ligne de partage P' située au sein du fluide, et d'où se détachent,

- d'une part, la surface qui se rattache à l'extrados le long de la ligne de recollement R_{12} séparant les tourbillons secondaires T_1 et T_2 ;

- d'autre part, la nappe qui s'enroule autour du tourbillon principal T.

3.3 - Influence de l'incidence -

Les différentes vues groupées sur la figure 16 permettent de suivre l'évolution de l'écoulement en fonction d'une incidence α croissante à $Re \approx 10^4$ constant. A faible incidence (fig. 16a') les lignes de courant pariétales côté extrados

dérangent dans la direction des génératrices de l'aile et ne décollent qu'au voisinage de l'extrémité libre du modèle.

A 15° d'incidence (fig. 16 b' b''), le décollement s'effectue le long d'une génératrice proche du bord d'attaque et il en résulte la formation de la structure tourbillonnaire décrite plus haut, avec un tourbillon principal bien organisé depuis l'arête au voisinage duquel se situe son origine jusqu'à l'extrémité du modèle.

A 20° (fig. 16 c') et a fortiori à 25° d'incidence (fig. 16 d' d''), la structure tourbillonnaire se développe, l'éclatement du tourbillon principal se produit côté aval et remonte vers l'amont, tandis que la désorganisation du secteur marginal progresse dans le même sens.

Lors que la ligne de décollement sur l'extrados tend à venir se placer de plus en plus près du bord d'attaque, la ligne de partage sur l'intrados s'en éloigne au fur et à mesure que croît l'incidence (fig. 16 a b c d).

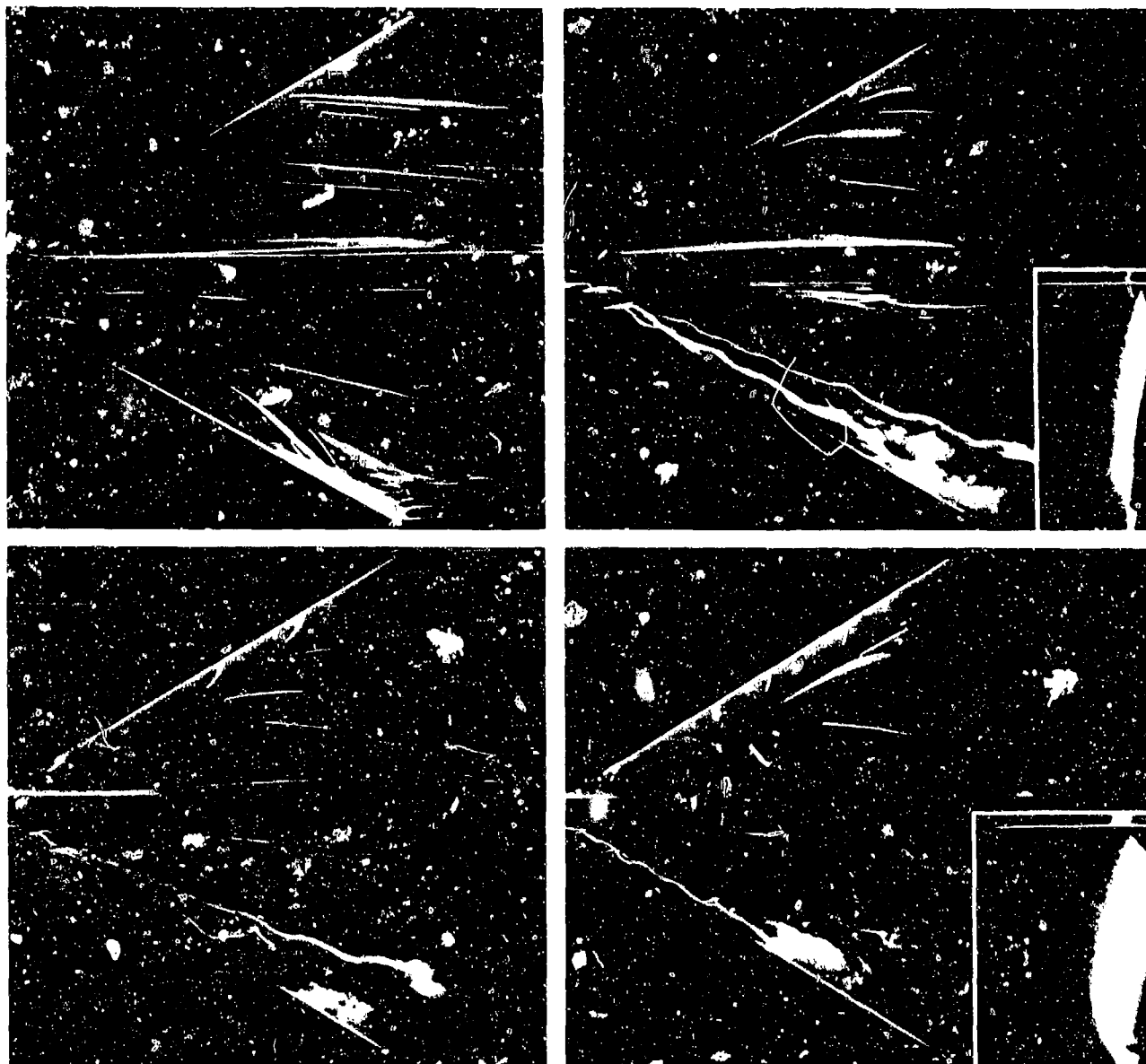


Fig. 16 -- Influence de l'incidence α sur l'écoulement autour d'une maquette d'aile agrandie (tunnel hydrodynamique - $Re_c \approx 10^6$) -

Vues de l'intrados (a, b, c, d) et de l'extrados (a', b', c', d').

Tranches transversales (b'', d'') en aval du bord de fuite du profil d'emplanture.

$\alpha = 5^\circ$ (a, a'), $\alpha = 15^\circ$ (b, b', b''), $\alpha = 20^\circ$ (c, c') et $\alpha = 25^\circ$ (d, d', d'').

A 25° d'incidence, tous ces phénomènes sont particulièrement bien développés : les visualisations révèlent alors la structure spirale de l'éclatement du tourbillon principal (fig. 17 d), et la forme incurvée en fer à cheval des tourbillons coiffant l'apex et caractérisant le décollement de la couche limite sur le panneau de garde (fig. 17a b c). Grâce à une fente disposée au bord d'attaque du modèle d'apex agrandi mis en jeu dans ces essais, il a été possible d'émettre un ruban de colorant qui visualise directement une tranche de la nappe tourbillonnaire qui s'enroule autour du tourbillon principal (fig. 17c d). De même, pour permettre une analyse plus fine du décollement tridimensionnel sur le panneau de garde et de son évolution en fonction de l'incidence (fig. 18), le colorant a été émis le long

de cette paroi plane à la fois sous la forme d'une nappe pariétale qui contourne la zone décollée et de filets isolés d'altitude variable, c'est-à-dire plus ou moins proches de cette paroi suivant le régime de leur débit, et qui alimentent les tourbillons en fer à cheval (fig. 17 b c) ou se déforment devant la plage décollée.

La figure 18 montre l'évolution en fonction d'une incidence croissante, de la forme de cette plage au voisinage de l'apex en régime laminaire (fig. 18 a - e) et confirme par ailleurs que l'allure des phénomènes ne change pas en régime turbulent, tel qu'il se déclenche à $Re_c \approx 0,5 \times 10^5$ (comparer fig. 18 e e' e'' et f f' f'').

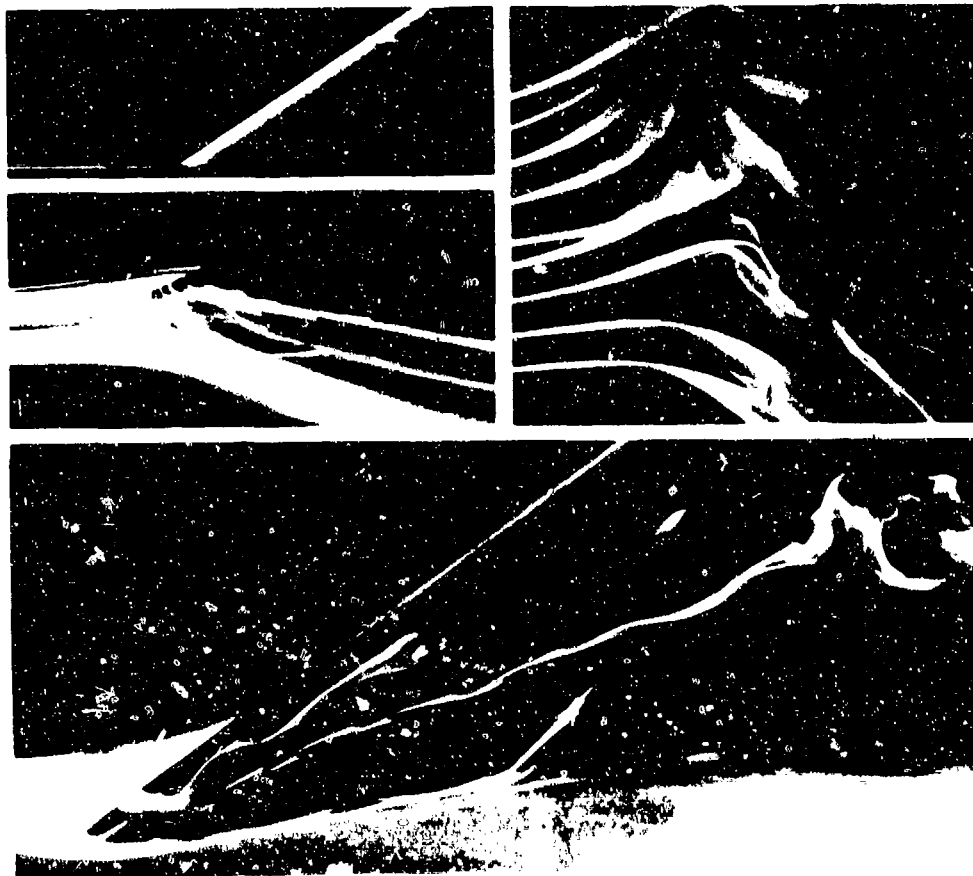


Fig. 17 - Ecoulement autour d'une maquette d'apex agrandi à 25° d'incidence (tunnel hydrodynamique $Re_c \approx 0,5 \cdot 10^6$).
Vues de l'extrados (d), de profil (c) et de l'intrados (b) tranche longitudinale passant par l'apex (a) visualisée par bulles d'air.

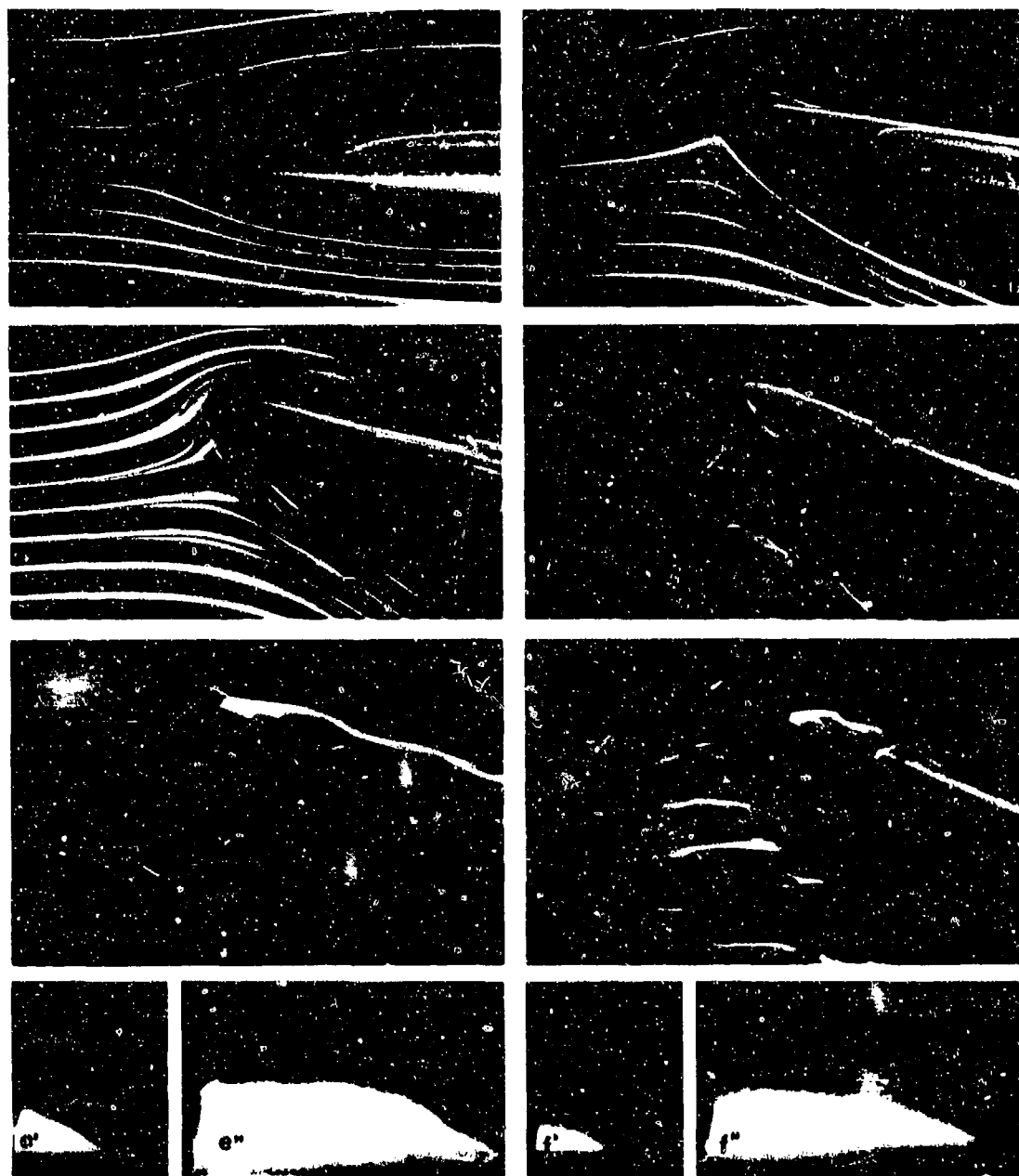


Fig. 18 - Influence de l'incidence α et du nombre de Reynolds Re_c sur l'écoulement le long du panneau de garde et autour d'une maquette d'apex agrandi (tunnel hydrodynamique - $Re_c \approx 0,5 \cdot 10^4$) sauf contre-indication.

$\alpha = 0^\circ$ (a) ; $\alpha = 10^\circ$ (b) ; $\alpha = 15^\circ$ (c) ; $\alpha = 20^\circ$ (d) ; $\alpha = 25^\circ$ (e, e', e'') ; $\alpha = 25^\circ$ avec $Re_c \approx 2 \cdot 10^4$ (f, f'') (régime turbulent).

Vues de profil (a, b, c, d, e, f) - tranches transversales situées près de l'apex (e', f') et de la mi-corde (e'', f'') du profil d'emplanture.

4 - ANALYSE EN SOUFFLERIE DU DÉCOLLEMENT TOURBILLONNAIRE -

Pour compléter les informations obtenues à des nombres de Reynolds faibles, une étude à caractère exploratoire du champ de l'écoulement à l'extrados de l'aile a été effectuée en soufflerie sur la configuration suivante : flèche $\varphi = 60^\circ$, incidence $\alpha = 19^\circ$ correspondant à un C_z égal à 80% du C_z max. Cette configuration présente un décollement tourbillonnaire intéressant la presque totalité de l'envergure de l'aile et structuré sur la majeure partie de son étendue transversale.

La vitesse d'essai retenue de 90 m/s ($Re_c = 1,9 \times 10^6$) a sure un déclenchement rapide de la transition notamment lorsque l'écou-

lement décolle.

4.1 - Caractéristiques générales de l'écoulement-

Les résultats des sondages effectués normalement à l'emplanture de la maquette dans 6 sections, définies par les valeurs de l'abscisse x/c , sont regroupés figure 19. Cette représentation de l'écoulement pseudo-transversal met en relief l'extension et l'évolution de l'écoulement tourbillonnaire à l'extrados de l'aile.

Près de l'apex ($x/c = 0,24$) la sonde ne peut atteindre que la partie extérieure du bulbe de décollement dont l'épaisseur est très faible. On notera par ailleurs l'effet de contournement marqué au voisinage du bord d'attaque.

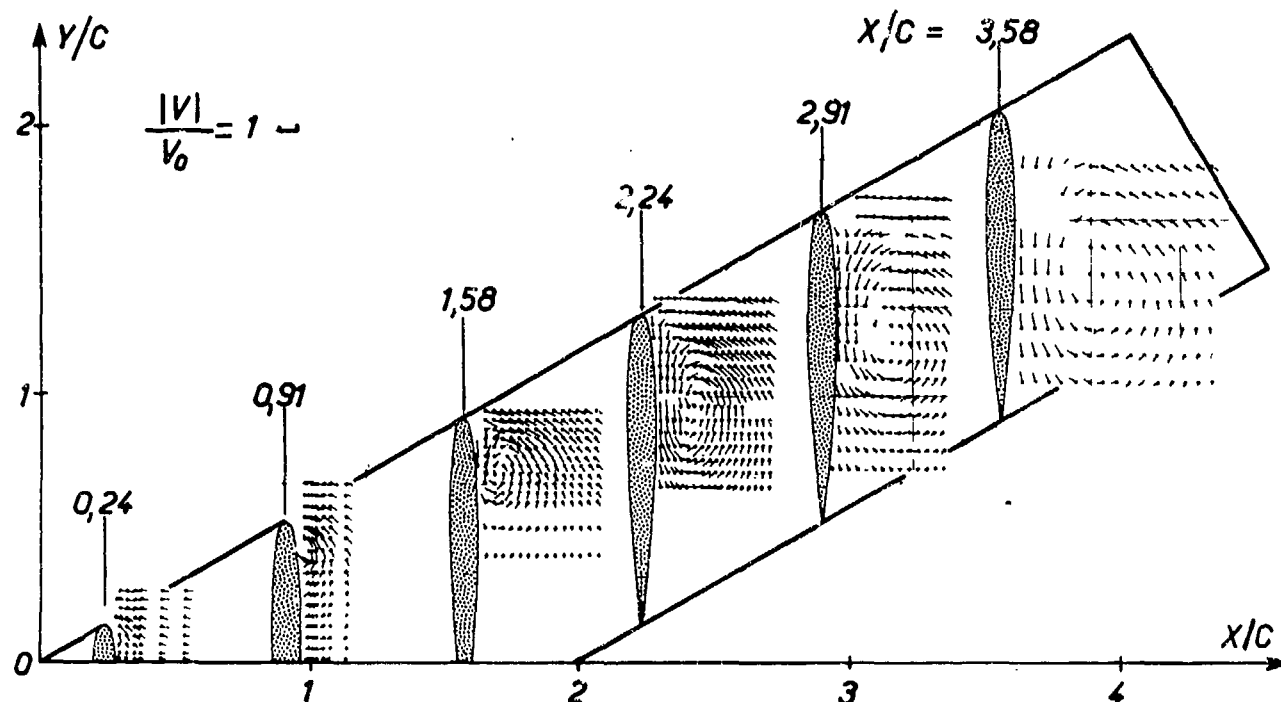


Fig. 19 — Projection du vecteur vitesse sur les plans d'exploration.



Fig. 20 — Visualisation de l'écoulement pariétal.

- a) Positions de l'axe de tourbillon par sondage (○)
b) Positions du minimum de pression pariétale (□)

Pour $x/c = 0,91$, une structure tourbillonnaire est mise en évidence. A la formation de cette structure est associé un redressement marqué de la direction de l'écoulement au niveau du bord d'attaque. Le domaine occupé par l'écoulement tourbillonnaire d'extrados, déjà important à partir de $x/c = 1,58$, croît ensuite rapidement en étendue lorsque x/c augmente en même temps que l'axe du tourbillon s'éloigne de la surface de l'aile. La position de cet axe déduite des sondages est donnée figure 21a en projection sur le plan d'emplanture Oxz et, figure 21b, en projection sur le plan des cordes Oxy . Ce dernier tracé est reporté figure 20 sur la photographie de la visualisation de l'écoulement pariétal ainsi que la position du minimum de la pression mesurée à la paroi dans différentes tranches de l'aile (voir 2.2).

La comparaison de ces résultats montre que le minimum de pression coïncide avec la projection sur le plan des cordes de l'axe du tourbillon principal et correspond sensiblement au point d'inflexion des lignes de courant pariétales.

L'évolution de la distance à la paroi de l'axe du tourbillon représentée figure 21a permet de distinguer nettement une zone initiale qui épaissit lentement et qui correspond à $x/c < 1$ d'une zone centrale où l'axe du tourbillon, sensiblement rectiligne, est beaucoup plus incliné sur la paroi ($\approx 5^\circ$).

On notera enfin que vers l'extrémité de l'aile ($x/c > 3,58$) l'axe du tourbillon s'écarte de plus en plus nettement de la paroi et s'incline vers l'emplanture (fig. 21 b) pour tendre vers une direction parallèle à celle de l'écoulement général.

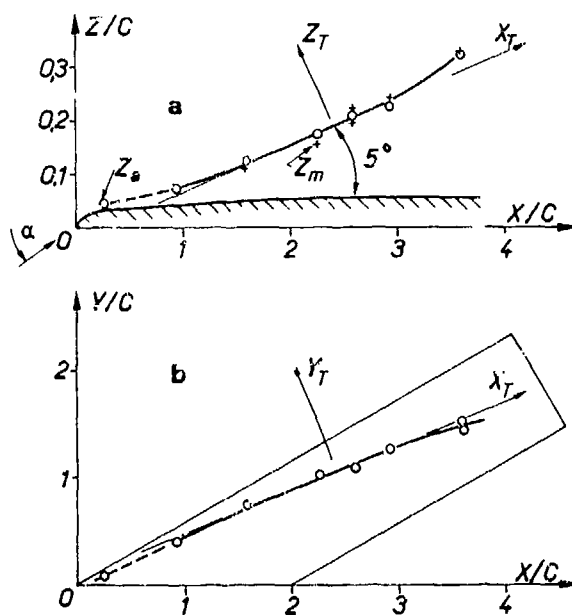
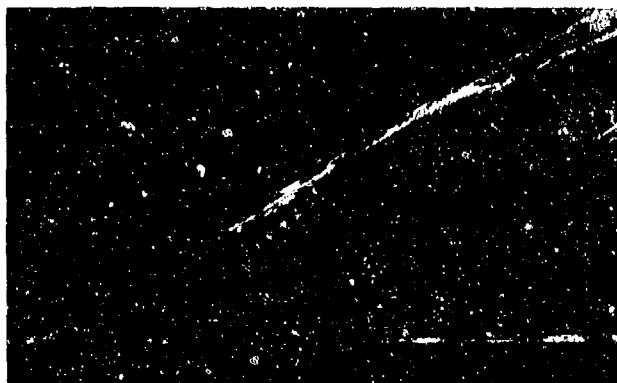
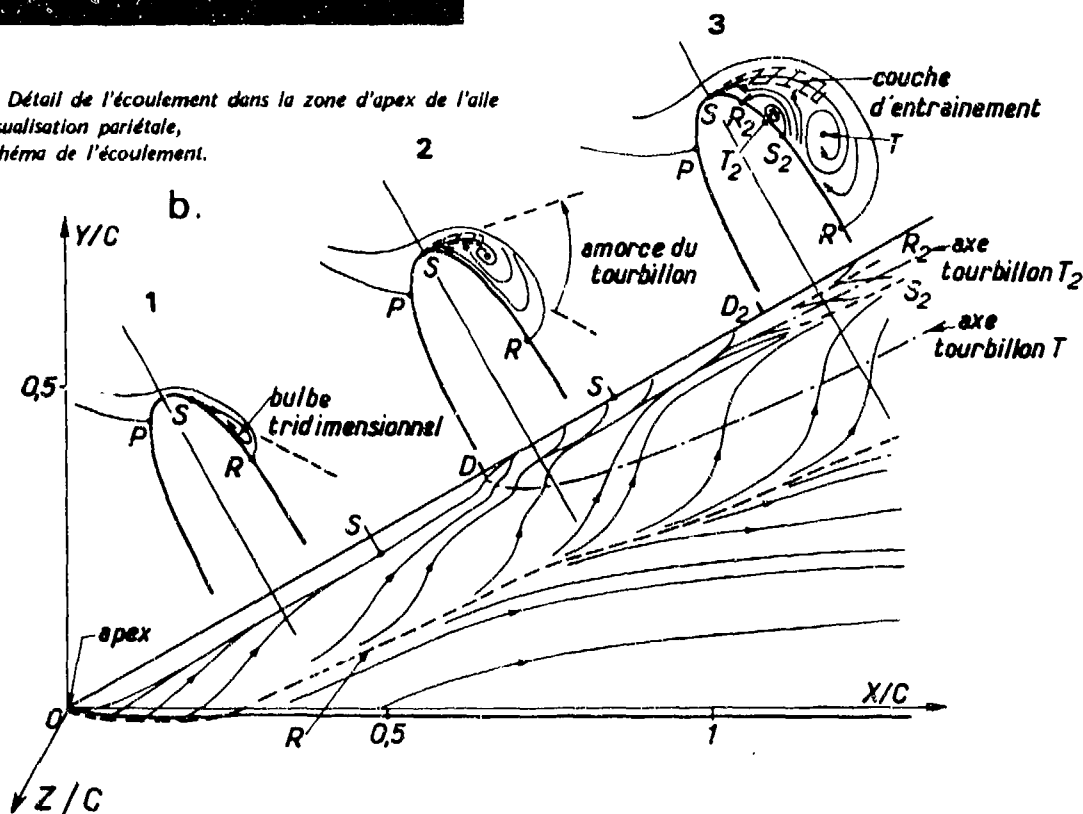


Fig. 21 - Position de l'axe du tourbillon par sondage
a) en projection sur le plan d'emplanture Oxz ,
b) en projection sur le plan de l'aile Oxy .



a.

Fig. 22 - Détail de l'écoulement dans la zone d'apex de l'aile
a) visualisation pariétale,
b) schéma de l'écoulement.



4.2 - Formation du tourbillon principal. Etude de la zone initiale -

Les sondages obtenus avec les moyens définies en 2.1 ne donnent qu'une information limitée dans les sections initiales ($X/C \leq 1$) où les couches dissipatives ont une épaisseur faible. Une étude détaillée des visualisations pariétales a donc été tentée pour préciser l'organisation de ce domaine de l'écoulement proche de l'apex. Malgré la part inévitable d'interprétation que comporte ce procédé, cette étude complète, pour une valeur du nombre de Reynolds nettement plus élevée, les observations détaillées obtenues au tunnel hydrodynamique (3.2).

Il convient tout d'abord de souligner que les effets dissipatifs plus marqués qui caractérisent les écoulements turbulents tendent à désagréger rapidement les structures tourbillonnaires de faibles dimensions ce qui peut entraîner une modification dans l'organisation des écoulements secondaires mis en évidence en régime laminaire. La figure 22 donne une vue détaillée de la visualisation pariétale obtenue sur l'extrados de l'aile au voisinage de l'apex et le schéma d'écoulement qu'elle représente dans lequel on peut distinguer trois domaines :

de 0 à D (schéma 1) l'écoulement venant de l'intrados contourne le bord d'attaque et décolle en 5 sous l'influence du gradient de pression défavorable qui nuit les survitesses de bord d'attaque. Dans ce processus, le décollement résulte d'une forte déstabilisation de la couche limite et la nappe décollée peu inclinée sur la paroi emprisonne une couche d'écoulement très ralenti. Le recollement s'effectue suivant une ligne Q sensiblement parallèle au bord d'attaque séparant le fluide qui reflue de celui qui s'écoule vers l'aval. L'écoulement dans le bulbe ainsi formé est aussi alimenté le long de l'emplanture par du fluide provenant de la plaque de garde, et s'écoule transversalement selon une direction d'abord évolutive qui tend ensuite à devenir parallèle au bord d'attaque.

- au point D, la visualisation montre une remontée rapide de la ligne de décollement vers le bord d'attaque (schéma 2, fig. 22).

Le phénomène de non contournement du bord d'attaque, dû principalement à l'accroissement progressif en envergure de la pseudo-incidence locale de l'écoulement jusqu'à une situation du type décrochage, entraîne un redressement brutal de la nappe fluide qui décolle créant ainsi une circonstance propice à l'amorçage de l'enroulement caractéristique d'un tourbillon en cornet.

Les lignes de courant pariétales comportent en aval immédiat du point D une inflexion très localisée qui s'étale ensuite en s'intégrant aux traces de l'écoulement provenant du bulbe initial pour former la trace pariétale caractéristique d'une structure tourbillonnaire en cornet (T).

On notera que la ligne de recollement R prend une direction plus inclinée vers l'aval, direction imposée par le développement du tourbillon (T). L'écoulement confiné entre le tourbillon T et le bord d'attaque est happé par la nappe fluide à vitesse accélérée qui décolle du bord d'attaque. Il s'écoule en suivant une direction qui devient sensiblement perpendiculaire à ce dernier. Cette configuration s'étend sur la partie du bord d'attaque comprise entre les points D et D₂.

- au-delà de D₂, l'accroissement des dimensions transversales du tourbillon T entraîne une modification de la zone confinée. Un décollement secondaire S₂ s'établit, il est suivi d'un recollement R₂ délimitant un petit contre-tourbillon T₂ (schéma 3, fig. 22), qui progresse le long du bord d'attaque avec le tourbillon T.

Cette description est conforme pour l'essentiel aux résultats obtenus au tunnel hydrodynamique. Elle permet toutefois de préciser, lorsque la transition laminaire-turbulent se produit très près du décollement, les conséquences que cette circonstance entraîne sur l'organisation de l'écoulement au voisinage de l'apex.

4.3 - Etude du tourbillon principal T -

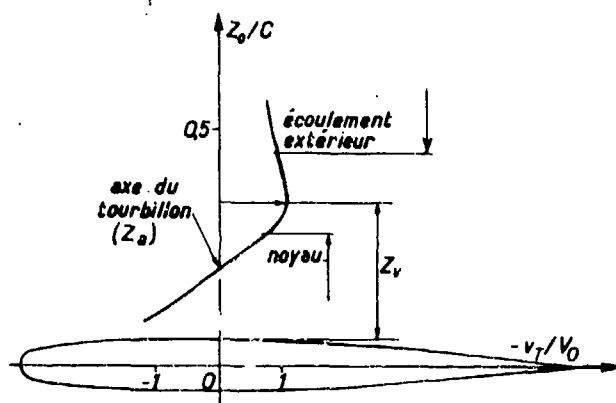


Fig. 23 - Profil de la composante de vitesse $v_T(z_0)$.

Pour caractériser l'évolution de l'écoulement tourbillonnaire à son passage dans chacun des plans d'exploration, il est commode d'examiner la variation de certaines grandeurs du champ dynamique suivant l'axe x_0 , perpendiculaire à l'aile et passant par le centre du tourbillon T. La figure 23 schématise l'évolution de la composante v_T de la vitesse de l'écoulement transversal définie dans un trièdre $Ox_T y_T z_T$ lié à l'axe du tourbillon (voir figure 21). Cette

représentation permet de distinguer le noyau du tourbillon constitué par un rouleau à rotationnel sensiblement constant de l'écoulement extérieur à rotationnel nul et de définir le centre du tourbillon ainsi qu'une dimension z_v caractéristique de son étendue transversale.

Cette structure du pseudo-écoulement transversal est très éloignée de celle d'un tourbillon au sens de la mécanique des fluides théorique. L'appellation "tourbillon", consacrée par l'usage, doit être prise dans un sens élargi.

La figure 24a donne l'évolution en envergure, pour sept plans de sondage, des profils de la composante v_T de la vitesse. On notera l'importance croissante du noyau avec l'abscisse x/c .

La figure 24b présente de la même façon les profils suivant z_0 du module de la vitesse V/V_0 qui mettent en évidence un creux caractéristique à la cote z_m coïncidant sensiblement avec l'axe du tourbillon (fig. 21a).

L'altitude z_m du maximum de vitesse permet également de caractériser l'étendue transversale du tourbillon. Elle est d'ailleurs peu différente de la valeur z_v définie précédemment (voir fig. 25a).

On notera en outre une dispersion importante des mesures dans certaines sections, dispersion qui ne peut être imputée entièrement à un fonctionnement incorrect de la sonde soumise à des angles d'attaque trop importants. L'instabilité de la structure tourbillonnaire, qui apparaît dès $x/c \approx 2,24$ et qui est particulièrement marquée pour $x/c = 2,58$, n'est pas à écarter. Elle coïncide d'ailleurs avec un changement de régime dans l'évolution de l'écoulement tourbillonnaire que nous allons examiner maintenant.

L'évolution longitudinale du tourbillon d'extrados est caractérisée, en première analyse, par les trois données typiques de son développement que sont la dimension transversale z_v ou z_m , l'intensité du rotationnel du noyau

$$ROT_a = \left(\frac{\partial w}{\partial y} - \frac{\partial v}{\partial x} \right) \frac{c}{V_0}$$

et la vitesse minimale V_{min} sur l'axe. L'évolution suivant x/c de ces diverses grandeurs est représentée figure 25. Deux domaines d'évolution distincts apparaissent :

- pour $x/c \leq 2,24$, une zone de développement où la vitesse minimale sur l'axe augmente pendant que la dimension transversale du tourbillon s'accroît d'une manière progressive avec une diminution corrélative modérée du rotationnel du noyau.

- en aval de $x/c = 2,24$, une zone où l'on note une brusque augmentation de la dimension transversale du tourbillon accompagnée d'une chute rapide du rotationnel et de la vitesse sur l'axe. L'origine de cette zone coïncide avec une instabilité marquée de la structure tourbillonnaire. Cette évolution rapide, provoquée par le ralentissement de l'écoulement général que traduit la diminution de la vitesse maximale V_{max} mesurée à la frontière du tourbillon, définit l'apparition du processus d'éclatement du tourbillon d'extrados qui semble atteint pour $x/c > 3$.

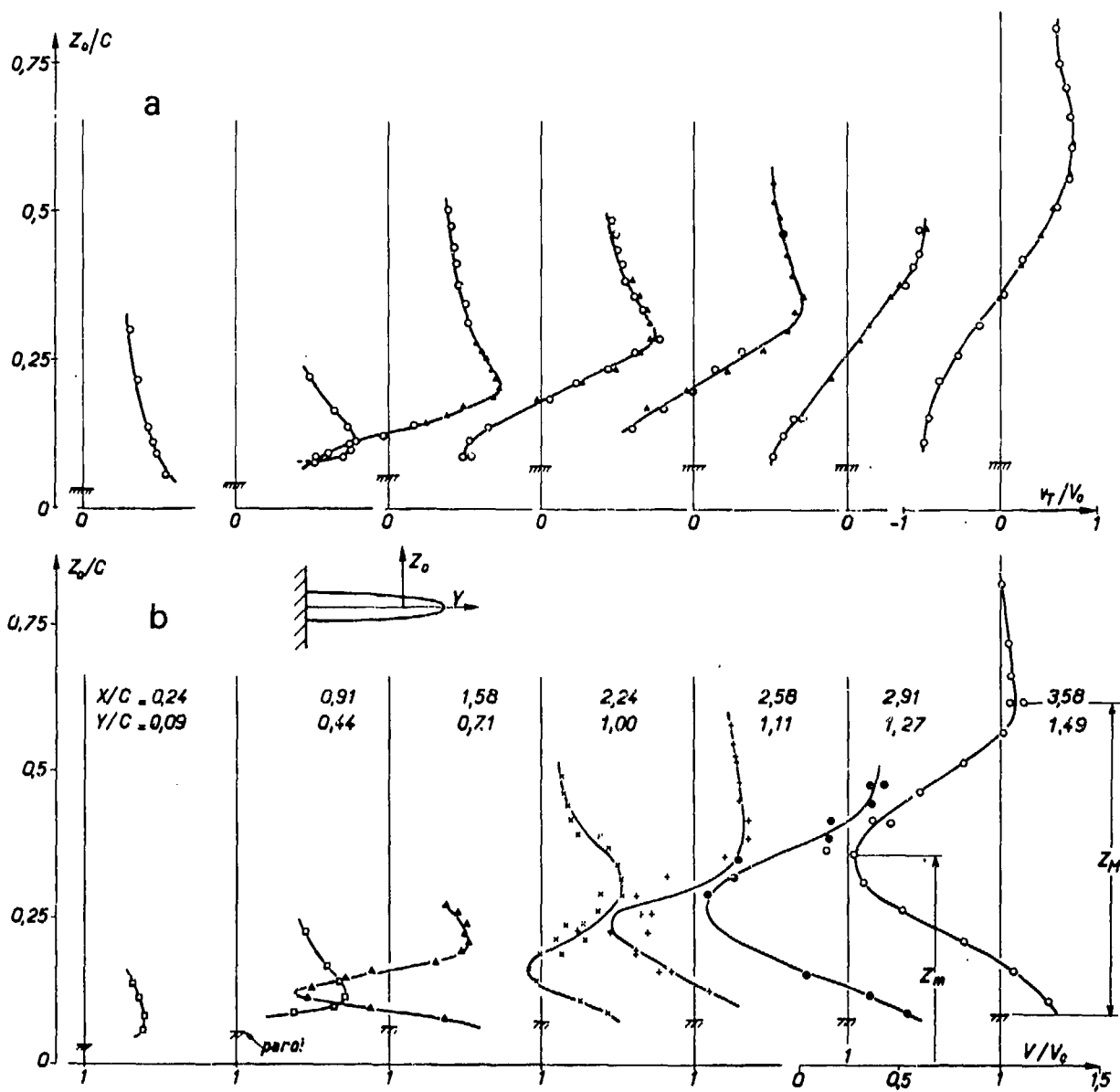


Fig. 24 - Evolution en envergure.
a) profil de la composante de vitesse $v_T(z_0)$
b) profil de la vitesse $V(z_0)$.

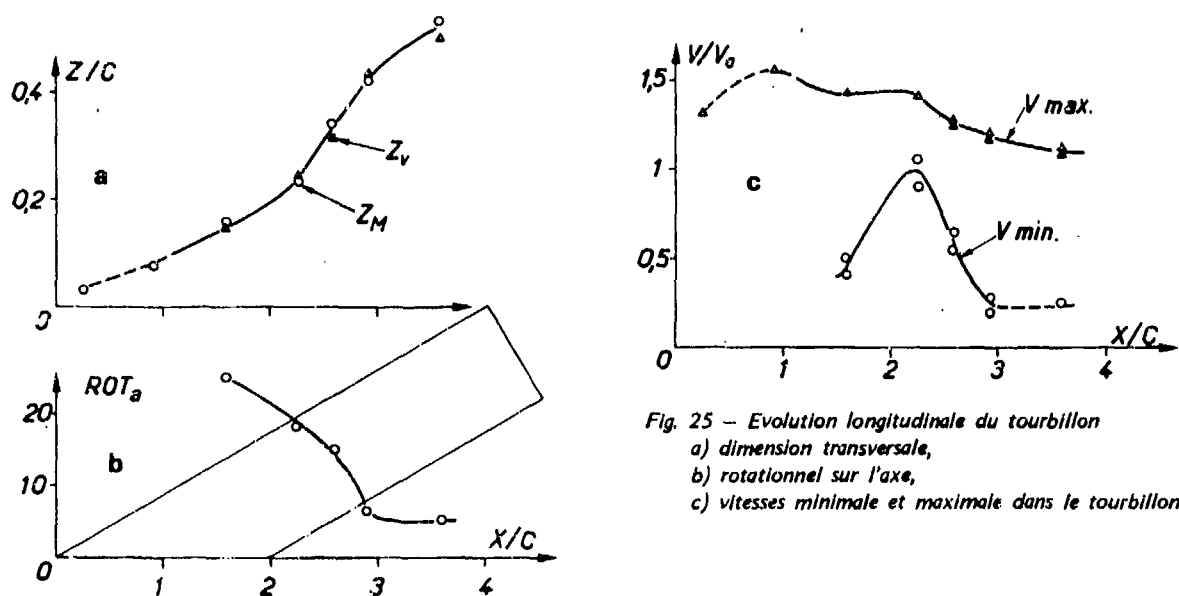


Fig. 25 - Evolution longitudinale du tourbillon
a) dimension transversale,
b) rotationnel sur l'axe,
c) vitesses minimale et maximale dans le tourbillon.

5 - CONCLUSIONS -

L'écoulement tourbillonnaire sur l'extrados d'une aile à flèche variable placée à forte incidence a fait l'objet d'une étude expérimentale approfondie en soufflerie et au tunnel hydrodynamique. Il a été possible, à partir des mesures d'efforts globaux, de déterminer, en fonction de l'incidence et de la flèche, un domaine d'existence de ce type d'écoulement qui a été analysé ensuite plus finement à l'aide du champ de pression statique et des visualisations pariétales. Un effet du nombre de Reynolds, en particulier sur l'incidence d'apparition de l'écoulement tourbillonnaire sur cette aile, a pu être observé.

L'examen au tunnel hydrodynamique à faible nombre de Reynolds de la structure même des décollements qui s'organisent autour d'un tourbillon en cornet conduit à la description d'un schéma très précis de l'écoulement tourbillonnaire incluant sa formation à proximité de l'apex et son éclatement dans la région du bord de fuite.

Ce schéma s'avère globalement assez proche de celui qui résulte d'une analyse effectuée en soufflerie à nombre de Reynolds beaucoup plus élevé, comportant l'exploration détaillée du champ de l'écoulement à l'extrados de l'aile ainsi que la visualisation pariétale pour une configuration particulière.

Ces explorations ont en outre permis une étude détaillée de l'évolution du tourbillon principal et constituent ainsi un élément très précieux en vue d'une modélisation de tels écoulements.

- REFERENCES -

- [1] MANIE F., REHBACH C., SCHMITT V.
Etude d'une aile à flèche variable en écoulement sub ou transsonique.
ICAS - Proceedings, Volume 2, Lisbonne (1978) (à paraître)
- [2] VINCENT DE PAUL M., DYMENT A.
Recherches sur les profils d'ailes en écoulement subsonique
l'Aéronautique et l'Astronautique, n° 19 (1970-3), p 15-30
- [3] EL-RAMLY Z.M., RAINBIRD W.S.
Computer controlled system for the investigation of the flows behind wings
Journal of Aircraft, Vol 14, n°7, p. 668-674 (1977)
- [4] REBUFFET F.
Aérodynamique expérimentale
Tome 2 - Dunod Paris (1966)
- [5] WERLE H.
Le tunnel hydrodynamique au service de la recherche aérospatiale
ONERA Publication n° 156 (1974)
- [6] WERLE H.
Ecoulements décollés
AGARD Conférence Proceedings n° 168 (1975)
Mémoire n° 39 p. 1-14
- [7] ROY M.
Caractères de l'écoulement autour d'une aile en flèche accentuée
CR Acad. Sc. 234 (1952) p. 2501-2503
- [8] LEGENDRE R.
Ecoulement au voisinage de la pointe avant d'une aile à forte flèche aux incidences moyennes
Recherche Aéronautique n° 30 (1952) & 31 (1953)
- [9] WERLE H.
Sur l'éclatement des tourbillons
ONERA Note Technique n° 175 (1971)
- [10] YOUNG A.
Some special boundary layer problems
Zeitschrift für
Flugwissenschaften und
Weltraumforschung 1 (1977)
Heft 6., p. 401 - 414
- [11] HUNT J., ABELL C., PETERKA J. & WOO H.
Kinematical studies of the flows around free or surface mounted obstacles ; applying topology to flow visualization
J. Fluid Mech. (1978) vol. 86 part 1
pp. 179 - 200
- [12] ONERA Film n° 932 (1978)
Tourbillons sur une aile en flèche à grande incidence (version provisoire mnette présentée au cours du Colloque AGARD à Sandefjord).

STABLE AND UNSTABLE VORTEX SEPARATION

by

Erich H. Wedemeyer
 Institut für Strömungsmechanik, DFVLR
 3400 Göttingen, Germany

SUMMARY

A theoretical study of the stability of leading edge separation on delta wings is presented. The theory explains the change from steady vortex type separation which is observed for highly swept wings to flow with unsteady "separation bubble" which is typical for wings of small sweepback. Calculations show, that solutions of the vortex-sheet model of leading edge separation can become unstable if the angle of attack is sufficiently high. The critical angle of attack beyond which no stable solutions exist, decreases with decreasing sweepback angle. The calculated stability boundary is in good agreement with the boundary for observed leading edge vortices. These findings suggest, that the change from "vortex type" to "bubble type" separation is due to the change from stable to unstable leading edge vortices. Finally, the theory explains the effect of a strake on a wing of moderate sweep and aspect ratio: The strong leading edge vortices generated by the strake induce an outboard flow on the main wing and thereby increase the effective sweep of the leading edge. The higher effective sweep stabilizes the leading edge separation on the main wing.

NOTATION

C	constant defined by equation (2)
C_1, C_2	constants defined by equation (1)
C_ϕ, C_z	non-dimensional velocity gradients defined by equation (8)
K	constant defined by equation (2)
l	midchord of delta wing
r	radial coordinate (figure 1)
r_0	radius of vortex core
s	semispan of delta wing
U, V, W	velocity components in axial, circumferential and radial directions
U_o, V_o	axial and circumferential velocity components at the outer edge of the vortex core
U_∞	free stream velocity
z	axial coordinate (figure 1)
α	angle of incidence
Γ	circulation of line vortex
Λ	aspect ratio of delta wing = $4s/l$
ϕ	circumferential coordinate (figure 1)
ξ	conical coordinate = r/z
ξ_0	= r_0/z
o	subscript denoting conditions at the outer edge of the vortex core

1. INTRODUCTION

On highly swept back wings at incidence the flow separates from the leading edge generally through formation of the well-known rolled-up vortex sheets over the wing. On the other hand, on wings with moderate sweep, leading edge separation takes the form of an unsteady "separation bubble". While the steady vortex separation on highly swept wings generates large nonlinear lift increments, the unsteady bubble type separation provides undesired effects such as lift decay and force fluctuations.

For the case of large or intermediate sweepback the type of leading edge separation may change with changing angle of incidence. Observations show that the initial leading edge vortex may suddenly break down and form - downstream of the breakdown point - a diffuse and turbulent structure resembling the separation bubble which is observed for wings of moderate sweep. The position at which the vortex breaks down moves upstream with increasing angle of incidence, until it finally - for a critical angle of incidence - reaches the apex of the wing. We can, thus, distinguish two regions: one in which leading edge vortices exist at least over part of the wing and a region in which separation is completely unsteady and takes the form of a separation bubble over the total wing.

In the following investigation it is supposed that the two distinct types of leading edge separation can be attributed to the existence or non-existence of a stable separated vortex. The theoretical study outlined in the following is an extension of a theory of vortex breakdown by Ludwig [1, 2]. In the course of investigations on the stability of helical flows Ludwig has shown, that a stable leading edge vortex, entering a region of increasing pressure, eventually transforms into a highly unstable vortex. This finding was offered by Ludwig as an explanation for the vortex breakdown phenomenon. At the same time other explanations were given [3, 4, 5] and so far no final decision is reached in favor of only one of the competing theories. One of the reasons, why a decision between the different theories of vortex breakdown is so difficult to obtain, is that none of the theories can predict the onset or even the location of breakdown. The present theory gives for delta wings a prediction of the stability boundary beyond which no stable vortex separation can exist. The theoretical stability boundary is not expected to coincide exactly with the boundary for observed leading edge vortices - since a slight instability does not lead at once to vortex breakdown - but the theoretical data are consistent with experimental findings. It is believed, therefore, that the present study gives additional support to the stability theory of vortex breakdown.

2. PROBLEM DEFINITION

As mentioned above, there are several explanations for the phenomenon of leading edge vortex breakdown. The different theories presume, that stable vortices are formed at the leading edges of the front part of the wing and that the vortices are suddenly transformed when they are subjected to the pressure rise at the rear part of the wing.

There is a strong interaction between the bursting vortex and the external flow - very similar to the interaction between a separating boundary layer and the external flow. It is, therefore, difficult to predict the location of vortex breakdown, and the various theories can hardly be compared on a basis of quantitative agreement with experimental data on breakdown locations.

The present study assumes a slightly different point of view: The question is not, what happens to an originally stable vortex when it enters a field of pressure rise, but under which conditions can a stable vortex exist near the apex of the wing. When a leading edge vortex is observed over sufficiently large part of the wing, one can assume that it is stable. When, on the other hand, the vortex disappears after reaching a critical angle of incidence, one can conclude that a stable leading edge vortex is no longer possible. It is, thus, reasonable, to investigate the conditions i.e. the angle of attack range, for which stable leading edge vortices can subsist near the apex of a delta wing.

3. THE STRUCTURE OF LEADING EDGE VORTICES

Figure 1 shows a sketch of the separated flow over a slender delta wing. A shear layer separates from each of the leading edges and forms a tightly rolled vortex core in which the velocity and pressure fields are nearly axially symmetric.

Whether a leading edge vortex is stable, depends on its internal structure, i.e. on the distribution of axial- and circumferential velocities in the vortex core. A theory for the core of a leading edge vortex was developed by Hall [6] and independently by Ludwig [2]. The theory is restricted to conical flow, i.e. to the leading edge vortices near the apex of slender delta wings. It is assumed that the flow field within the vortex core is axially symmetric and that the vorticity is continuously distributed, i.e. the shear layer is diffuse. Both these assumptions are very good approximations to a realistic vortex.

Assuming further, that the vortex core is slender i.e. its radius is small compared to the distance from the apex of the wing, the equations of motion (Euler equations) are approximately solved for conical flow. The following general solution for the velocity components in radial (W) circumferential (V) and axial (U) direction is found:

$$U = C_1 (C_2 - \ln \xi) \quad (1-a)$$

$$V = C_1 \sqrt{C_2 + \frac{1}{2} - \ln \xi} \quad (1-b)$$

$$W = -\frac{1}{2} C_1 \xi \quad (1-c)$$

ξ is the conical coordinate, $\xi = r/x$, and C_1, C_2 are two constants of integration. The solution is valid for $0 < \xi \leq \xi_0$ where $\xi_0 = r_0/x$ is a constant which is small against 1. The subscript o denotes quantities at the outer edge of the vortex core. Thus r_0 is the local core radius.

Using the normalized radius r/r_0 rather than ξ , the main components U, V can be written:

$$U = C (K - \ln r/r_0) \quad (2-a)$$

$$V = C \sqrt{K + \frac{1}{2} - \ln r/r_0} \quad (2-b)$$

with: $C = C_1$ and $K = C_2 - \ln \xi_0$.

The constant C gives the magnitude of the velocities while the constant K is a profile parameter. C and K can be chosen so that the velocity components assume prescribed values U_o, V_o at the outer edge of the core. It is:

$$U_o = C K \quad (3-a)$$

$$V_o = C \sqrt{K + \frac{1}{2}} \quad (3-b)$$

The ratio V_o/U_o , which is a measure of the helix angle of the streamlines at the outer edge of the core, is:

$$\frac{V_o}{U_o} = \frac{\sqrt{K + \frac{1}{2}}}{K} \quad (4)$$

The velocity profiles for U and V according to equations (2) are shown in figure 2 and figure 3 for various values of the profile parameter K . The profiles have a singularity at $r = 0$. Since the gradients of the velocity components are very large near the axis $r = 0$, viscous diffusion becomes appreciable and changes the velocity profiles within a small "sub-core" near the axis. For the case of laminar flow, Hall [6] has derived a "boundary layer" solution for the sub-core which is shown qualitatively by the dotted lines in figures 2 and 3. The solution for the sub-core will, however, not be needed in the following.

4. CONSTRUCTION OF THE OVERALL FLOW FIELD

A determination of the constants C and K of the velocity profiles (equations 2-a and 2-b) requires a knowledge of the flowfield outside of the vortex core. In the course of investigating the separated flow past slender delta wings as a whole, approximate solutions of the outer flow were obtained by Mangler & Smith [7] and to a much higher accuracy more recently by Smith [8].

In the calculations by Smith [8] an approximate model is used where one or several outer turns of the spiral vortex sheet are computed properly, while the inner part of the vortex is represented by a concentrated line vortex at the centre. The line vortex was introduced in order to avoid the difficulty of numerically handling an infinite number of turns.

The effect of the line vortex on the outer parts of the flow field is the same as that of an axially symmetric vortex core with distributed vorticity. A construction is made now, where the line vortex is replaced by Hall's solution for the vortex core i.e. by a vortex core with velocity components according to equations (2). The constants C and K must be adjusted so that the solution for the vortex core can be fitted continuously to the outer part of the flow field. Obviously, the circumferential velocity at the outer edge of the vortex core, V_o , must fulfill the following condition:

$$V_o = \Gamma / 2\pi r_0 \quad (5)$$

where Γ is the strength of the concentrated line vortex representing the vortex core. The radius r_0 of

the vortex core is equal to the distance from the vortex centre to the free end of the outer winding.

The axial velocity at the outer edge of the vortex core, U_o , is approximately equal to the free stream velocity:

$$U_o = U_\infty \quad (6)$$

Equation (6) is correct within the accuracy of slender body theory, where indeed the assumption is made that the axial velocity component deviates only very little from the free stream velocity. It should be noted that the requirement of nearly constant axial velocity is not fulfilled within the vortex core. It is for this reason that the application of slender body theory, which is correct for the outer part of the flowfield, can not be extended to the inner parts of the vortex core.

From equations (4), (5) and (6) it follows:

$$\frac{V_o}{U_o} = \frac{\sqrt{K + \frac{1}{2}}}{K} = \frac{\Gamma}{2\pi r_o U_\infty} \quad (7)$$

Equation (7) relates the profile parameter K to quantities Γ and r_o of Smith's outer solution. The value of the constant C (which will not be needed) follows from equations (3-a) and (6): $C = U_\infty/K$.

The evaluation of equation (7) contains a certain amount of arbitrariness since Γ/r_o depends on the arbitrary choice of the radius r_o , at which the cut is made between the outer winding and the inner core. It can be shown, however, that this dependence is very weak. Equation (2-b) and figure 3 show, that the value of $V (= \Gamma/2\pi r)$ varies only very little near the outer edge of the vortex core. Also from Smith's solution it is obvious that V is nearly constant within the outer part of the vortex. Table 1 shows the variation of the normalized values of Γ , r_o , and Γ/r_o with the number of turns of the outer winding, as obtained from Smith's calculations. The numbers show, that the constancy of Γ/r_o is better than expected from Hall's solution. This, certainly, is a consequence of the slender body approximation for the outer flow.

The above construction of the overall flow field, which joins the vortex core solution with the outer potential flow solution, has led to a simple relation between the profile parameter K and the value of Γ/r_o according to equation (7). The value of Γ/r_o , as obtained from Smith's calculation, depends on aspect ratio Λ and angle of incidence α of the wing. Table 2 shows some of the data from Smith's calculations. Thus, for any pair of values (Λ , α) the profile parameter K can uniquely be determined. It will be shown in the following sections, that the vortex core is unstable if the value of the profile parameter K is less than 1.16. Such profile parameters are found for high aspect ratio wings or for high angles of incidence.

5. THE STABILITY OF THE VORTEX CORE

There are several types of instability to which a leading edge vortex is subjected. One is the well-known shear layer instability, which makes an initially laminar shear layer wavy and finally turbulent. Figure 4 shows a shear layer instability on a leading edge vortex which was observed by Aupoix [9]. The vortex is visualized with the aid of smoke and illuminated by a thin plane beam of light perpendicular to the flow direction. The photograph shows clearly the wavy structure of the outer winding of the shear layer. This instability is relatively harmless and does not lead to the destruction of the vortex. Its effect on the vortex is, to smooth out the radial distribution of vorticity by making the shear layer turbulent and enhancing its diffusion.

Another mild instability is always present within the viscous sub-core. Figures 2 and 3 show, that the distributions of both the axial and the circumferential velocity have an inflection point within the sub-core region, which gives rise to a generalized inflection point instability according to a theory of Michalke and Timme [10]. The sub-core can also become unstable due to the helical instability of Ludwig which is discussed later in this section. In any case is an instability of the sub-core restricted to a relatively small part of the vortex. It has the effect of producing turbulence in the unstable zone near the axis and enhancing the diffusion of vorticity.

Much more serious is an instability of the outer parts of the vortex core which was proposed by Ludwig as an explanation for the vortex breakdown phenomenon.

Ludwig's stability theory [11] for helical flows is an extension of Rayleigh's well known stability criterion for rotating flows, to allow for an additional axial velocity component. It was shown by Ludwig, that a radial gradient of the axial velocity component has a destabilizing effect, so that an otherwise stable rotating flow can become highly unstable. Defining the non-dimensional velocity gradients:

$$C_\phi = \frac{r}{V} \frac{dV}{dr} \quad \text{and} \quad C_z = \frac{r}{V} \frac{dU}{dr} \quad (8)$$

Ludwig's stability criterion states, that a helical flow is locally unstable if:

$$(1 - C_\phi)(1 - C_\phi^2) - (5/3 - C_\phi)C_z^2 < 0 \quad (9)$$

In the limit $C_z = 0$ equation (9) reduces to Rayleigh's criterion for instability. A graphical representation of the stability criterion is given in figure 5, which shows the stable and unstable regions in a (C_ϕ, C_z) -plane.

It should be mentioned, that Ludwig's stability criterion was derived (and experimentally verified [12]) for helical flows in the small annular gap between two coaxial cylinders. The radial gradients (C_ϕ, C_z) are assumed to be constant throughout the gap. It was, however, conjectured by Ludwig, that his criterion is approximately valid as a local stability criterion for any helical flow, i.e. that a helical flow becomes locally unstable, if at any point in the flowfield the criterion for instability (equation 9) is fulfilled.

The stability theory of Ludwig was extended by Wedemeyer [13] to include more general velocity distributions. It was shown in [13] that the curvature of the velocity profiles has only little influence on the stability, so that Ludwig's criterion is a good approximation in most practical cases.

The stability criterion (equation 9) was applied by Ludwig [1, 2], to the vortex core, i.e. to a velocity field given by equations (2). The vortex core is not strictly cylindrical, it is assumed, however, that the gradients in axial direction are so small that - for the stability problem - the radius r_0 of the vortex core can be considered as constant. A simple calculation shows that the C_ϕ, C_z values encountered in the vortex core lie always on the lower half of the parabola $C_\phi = -C_z^2/2$ which is shown in figure 5. The inner endpoint ($C_\phi = C_z = 0$) corresponds to the vortex axis $r = 0$, the outer endpoint, which is a function of the profile parameter K , corresponds to the outer edge of the vortex core $r = r_0$. In figure 5 various endpoints are denoted by the corresponding value of K . The figure shows, that for profile parameters larger than a critical value of 1.16, all the points lie within the stable region, while for $K < 1.16$ the outer points fall into the unstable region. This means that for $K < 1.16$ the outer parts of the vortex core are unstable.

In [2] Ludwig has shown that a vortex core is transformed by an adverse pressure gradient so that the resulting vortex core belongs again to the same class of flows, given by equation (2), but with a decreased value of K . Thus, an originally stable vortex core can become unstable when subjected to an adverse pressure gradient. After the onset of instability, disturbance waves are amplified in such a way that the vortex becomes asymmetric. Ludwig conjectures, that the asymmetry leads finally to the breakdown of the vortex.

The present investigation is not concerned with the phenomenon of vortex breakdown but with the question, if a leading edge vortex is stable from the beginning. This question can now easily be answered: Any given values of the aspect ratio Λ and angle of incidence α determine uniquely a profile parameter K , as shown in the preceding section. If $K > 1.16$ the configuration is stable and vice versa it is unstable for $K < 1.16$. In figure 6 is shown the stability boundary $K = 1.16$, which divides stable and unstable regions in the (Λ, α) -plane. The diagram shows that the angle of incidence, above which no stable vortex exists, decreases with increasing aspect ratio. For aspect ratios larger than about 2 no stable vortices exist for any angle of incidence. Also shown in figure 6 is the boundary corresponding to $K = 0.8$. For this K -value, the part of the vortex core within 70 per cent of the radius or about 50 per cent of the cross section has become unstable.

6. COMPARISON WITH EXPERIMENTAL RESULTS

In the course of wind-tunnel experiments Earnshaw & Lawford [14] have observed the separated flow on a series of delta wings of varying aspect ratio. In particular, the positions of vortex breakdown on the wings were noted. The observed ranges of vortex breakdown are shown in the diagram of figure 6 as solid vertical lines. The lower endpoints of the lines correspond to breakdown positions at the trailing edge. The upper endpoints indicate the angles of incidence, at which vortex breakdown has reached the apex of the wing. For larger angles of incidence, no leading edge vortices were observed. The figure shows, that vortex breakdown is restricted to the unstable region and that the ranges of vortex breakdown follow in general the stability boundary except for large aspect ratios. For the wings of low aspect ratio, the observations are fully consistent with theoretical predictions: breakdown begins at the trailing edge when the initial vortex is just unstable. With increasing instability, the breakdown position moves towards the apex of the wing and reaches the apex, when about 50 per cent of the vortex have become unstable (corresponding to a value of $K = 0.8$). Naturally, the stability boundary does not coincide with the boundary for observed leading edge vortices, i.e. with the upper endpoints of the breakdown ranges. This is expected,

since a mildly unstable vortex can subsist for a short distance from the apex, before it is transformed by the growing disturbance waves sufficiently to burst.

With increasing aspect ratio, observations and theoretical predictions diverge. No explanation for this behavior can be given so far, but it should be noted that calculations of the separated vortex flow are based on slender body theory which becomes inadequate for higher aspect ratios. On the other hand, at the higher aspect ratios, the vortex core was less steady, as reported in [14], and the breakdown point could not be so clearly identified. Thus, theoretical and experimental results become increasingly unreliable for higher aspect ratios.

7. THE EFFECT OF STRAKES ON WINGS OF MODERATE SWEEP

The theoretical study described in the preceding sections was initiated by considerations regarding the effect of strakes on wings with moderate sweep. It is well known that the aerodynamic characteristics, especially the maximum lift and the buffeting behavior, of a moderately swept wing can be improved when a strake, i. e. a highly swept forward extension, is attached to the wing. Force measurements show that, while a strake has little effect in the regime of linear lift, it can shift the point of lift decay to much higher angles of incidence and thus increase the maximum lift. It was conjectured, that a strake is capable of stabilizing the leading edge separation but the underlying flow mechanism is not well understood. In the following a flow model is proposed, which accounts for the observation of a stable separated flow.

Figure 7 shows schematically the effect of the strake on the main wing. The strong leading edge vortices generated by the strake induce an outboard flow on the main wing, particularly near the kink of the leading edge. The induced flow velocity changes the initial flow direction and thereby increases the effective sweep of the leading edge. This effect of a strake was also noted by Fiddes & Smith [15].

If at large incidence the flow separates from the leading edge of the main wing, the separation on the inboard sections of the main wing is stabilized as a result of the higher effective sweep there. A stable separation now generates large lift increments while an unstable separation, which would occur on the wing without strake, leads to lift decay and force fluctuations.

As a partial check of the above flow model, experiments were performed to demonstrate the existence of a stable vortex over the main wing in a case where no stable separation would occur for the wing without strake. A test in the water towing tank of the AVA Göttingen was performed on a wing of 32° leading edge sweep with a strake of 75° leading edge sweep. Figure 8 shows a photograph of the flow over the wing at an angle of incidence $\alpha = 30^\circ$.

The separated flow on the main wing is visualized by means of the hydrogen bubble method. The photograph shows clearly a stable vortex originating at the kink of the leading edge. At the outboard sections of the wing, the cloud of hydrogen bubbles becomes diffuse indicating vortex breakdown.

Figure 9 shows a spanwise distribution of pressure measured in the AVA transonic wind tunnel on a wing with cylindrical fuselage and strake. The distribution has two suction peaks on a half wing, corresponding to separated vortices from the strake and the main wing. In Figure 10 the locations of measured suction peaks on the wing are plotted. The plot confirms, that separated vortices are formed on the leading edges of both the strake and the main wing. This is considered as a strong support for the assumed flow model, according to which the separation on the main wing is stabilized by an increase of the effective sweep of the leading edge.

REFERENCES

1. Ludwig, H. "Vortex breakdown", Deutsche Luft- und Raumfahrt FB 70-40, Deutsche Forschungs- und Versuchsanstalt für Luft- und Raumfahrt, Aerodynamische Versuchsanstalt Göttingen.
2. Ludwig, H. "Zur Erklärung der Instabilität der über angestellten Deltaflügeln auftretenden freien Wirbelkerne", Z. Flugwiss. 10 (1962), pp. 242-249.
"Erklärung des Wirbelaufplatzens mit Hilfe der Stabilitätstheorie für Strömungen mit schraubenlinienförmigen Stromlinien", Z. Flugwiss. 13 (1965), pp. 437-442.
3. Squire, H. B., "Analysis of the 'vortex breakdown' phenomenon. Part I", Imperial college of Science and Technology, University of London, Aeron. Dept. Rep. 102 (1960).
4. Brooke-Benjamin, T., "Theory of the vortex breakdown phenomenon", J. Fluid Mech. 14 (1962), p. 593.
5. Hall, M. G., "A new approach to vortex breakdown.", Proceedings of the 1967 Heat and Fluid Mechanics Institute, Stanford University Press. (1967).

6. Hall, M.G., "A theory for the core of a leading edge vortex", J. Fluid Mech. 11 (1961), p. 209
7. Mangler, K.W., Smith, J.H.B., "A theory of the flow past a slender delta wing with leading edge separation", Proc. Roy. Soc. A. 251, pp 260-217 (1959)
8. Smith, J.H.B., "Improved calculations of leading-edge separation from slender, thin, delta wings", Proc. Roy. Soc. A. 306, pp. 67-90 (1968)
9. Aupoix, B., "Experimental evidence of the presence of spiral disturbances in the vortex flow over a slender delta wing", Project Report, von Karman Institute Brussels, Belgium (1976)
10. Michalke, A., Timme, A., "On the inviscid instability of certain two-dimensional vortex-type flows", J. Fluid Mech. 29, (1967), pp. 647-666
11. Ludwig, H., "Stabilität der Strömung in einem zylindrischen Ringraum", Z. Flugwiss. 8 (1960), pp. 135-140.
Ergänzung zu der Arbeit: "Stabilität der Strömung in einem zylindrischen Ringraum", Z. Flugwiss. 9 (1961), pp. 359-361
12. Ludwig, H., "Experimentelle Nachprüfung der Stabilitätstheorien für reibungsfreie Strömungen mit schraubentlinienförmigen Stromlinien", Z. Flugwiss. 12 (1964), pp. 304-309
13. Wedemeyer, E., "Stabilität spiraler Strömungen in einem zylindrischen Ringraum", Mitteilungen aus dem Max-Planck-Institut für Strömungsforschung und der Aerodynamischen Versuchsanstalt Nr. 44, Göttingen (1969)
14. Earnshaw, P.B. and Lawford, J.A., "Low-Speed Wind Tunnel Experiments on a Series of Sharp-Edged Delta Wings", Aeronautical research council R.M. 3424 (1966)
15. Fiddes, S.P., Smith, J.H.B., "Strake induced separation at moderately swept leading edges", RAE TR 77128 (August 1977).

number of turns	$4\Gamma/s U_{\infty} \Lambda$	r_o/s	$4\Gamma/r_o U_{\infty} \Lambda$
0.5	3.25	0.185	17.57
1.5	2.14	0.124	17.26
2.5	1.69	0.094	17.98

Table 1: Variation of normalized values of Γ , r_o , and Γ/r_o with number of turns of outer winding ($4\alpha/\Lambda = 0.91$).

$4\alpha/\Lambda$	$4\Gamma/s U_{\infty} \Lambda$	r_o/s	$4\Gamma/r_o U_{\infty} \Lambda$
0.25	0.855	0.056	15.27
0.50	1.72	0.105	16.38
1.00	3.61	0.202	17.87
1.50	5.91	0.276	21.41

Table 2: Variation of normalized values of Γ , r_o , and Γ/r_o with α/Λ (number of turns = 0.5).

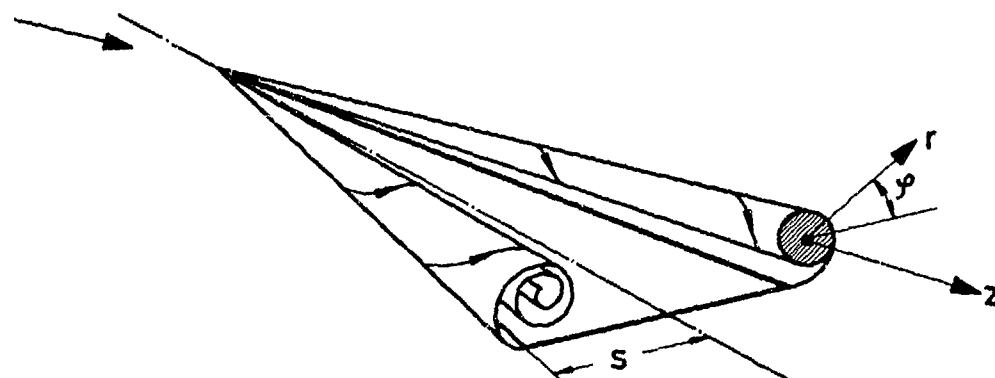


Fig. 1: Formation of a vortex core over a slender delta wing

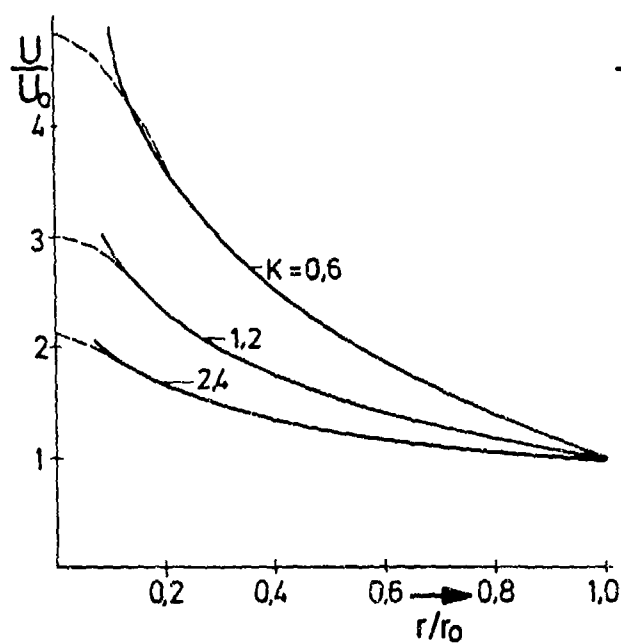


Fig. 2: Axial velocity profile of the core flow

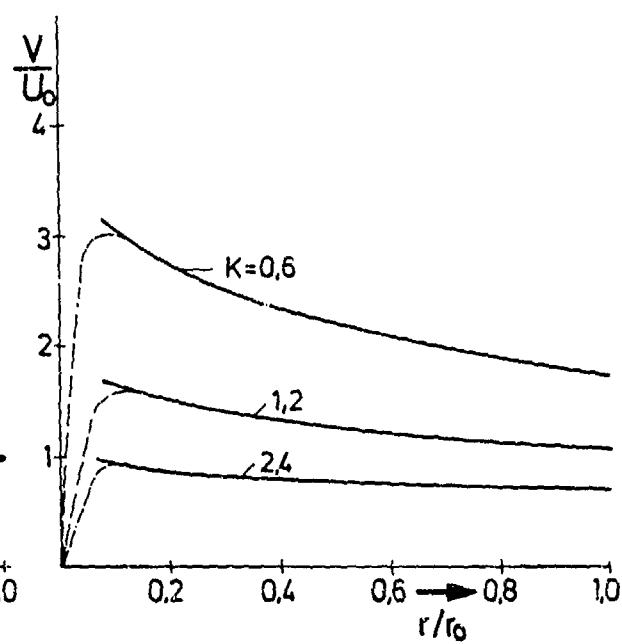


Fig. 3: Circumferential velocity profile of the core flow.

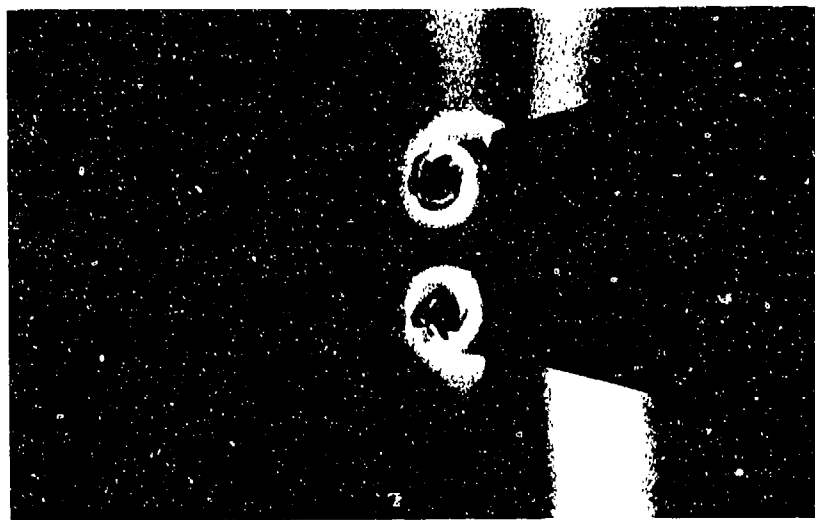


Fig. 4: Leading edge vortices showing shear layer instability

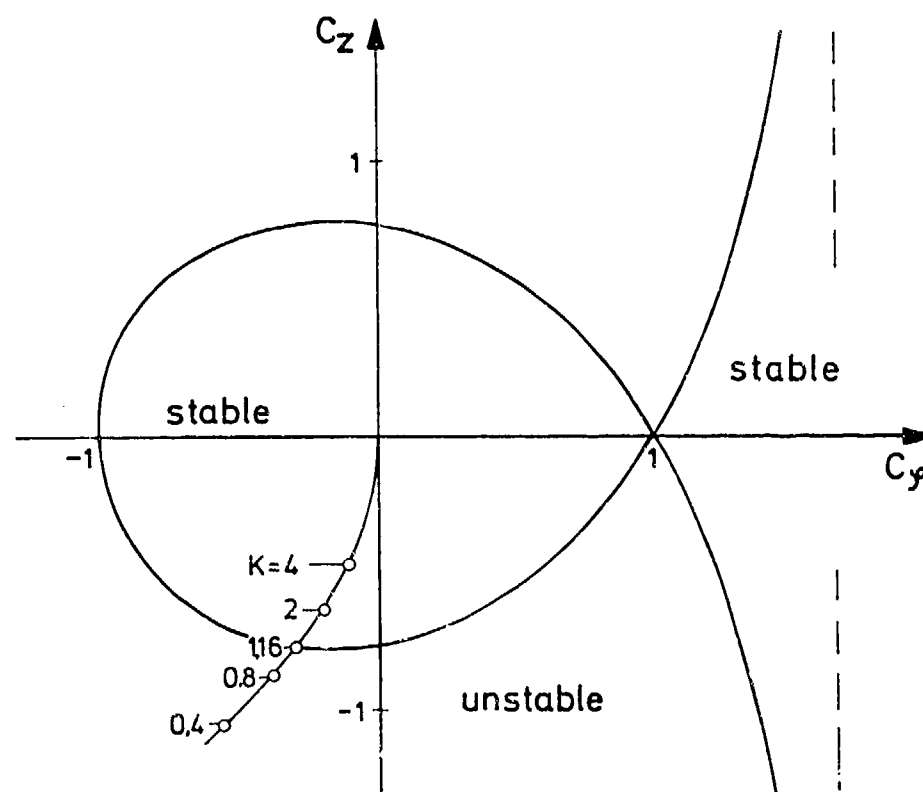


Fig. 5: Stability diagram for vortex flow.

$$C_{\phi} = \frac{r}{V} \frac{dV}{dr}, \quad C_z = \frac{r}{V} \frac{dU}{dr}, \quad K = \text{profile parameter}$$

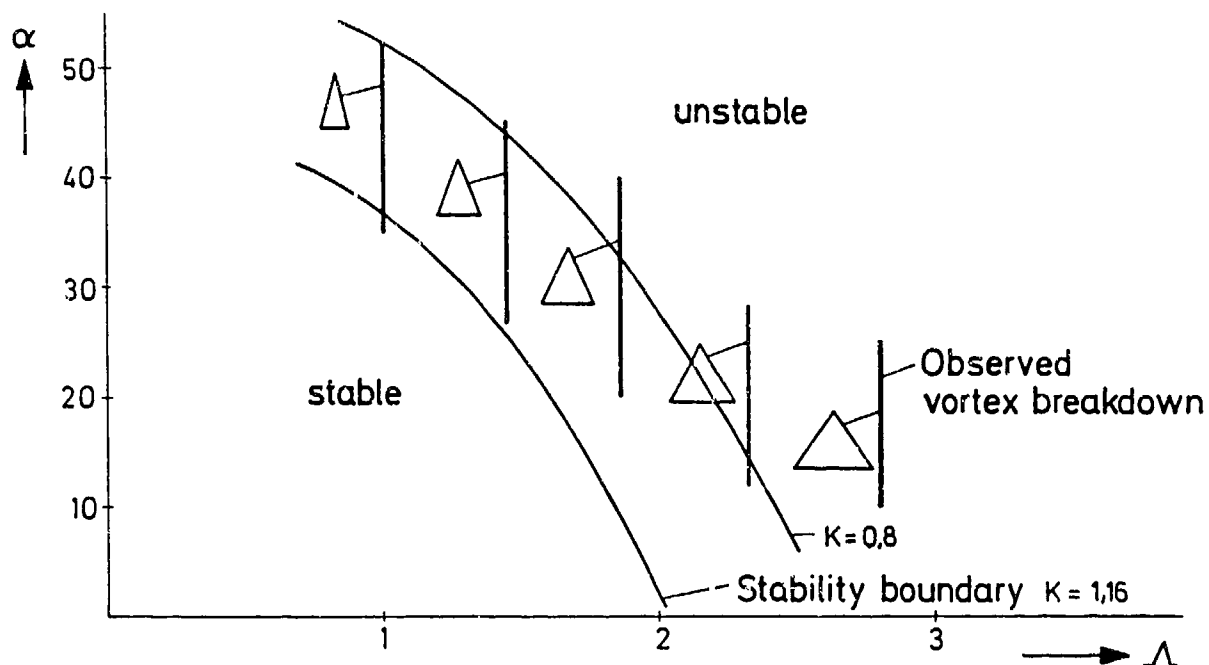


Fig. 6: Theoretical stability boundary and experimental ranges of vortex breakdown in the (Λ, α) -plane

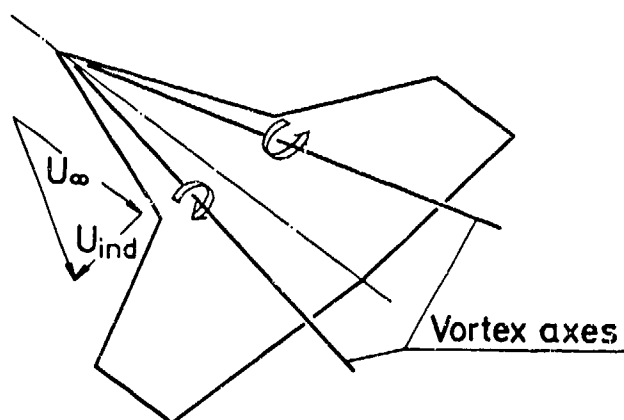


Fig. 7: Effect of the strake vortices on the main wing

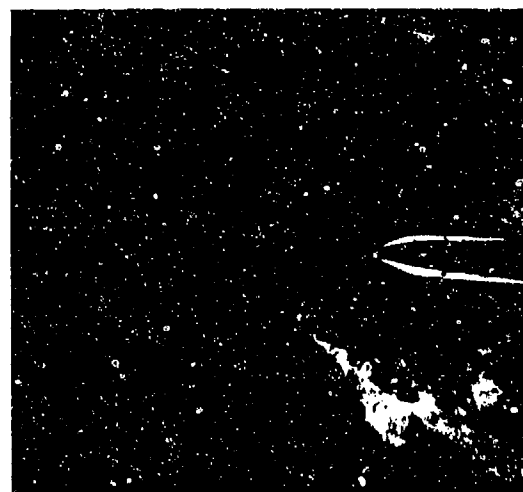


Fig. 8: Leading edge vortex visualized by hydrogen bubble technique

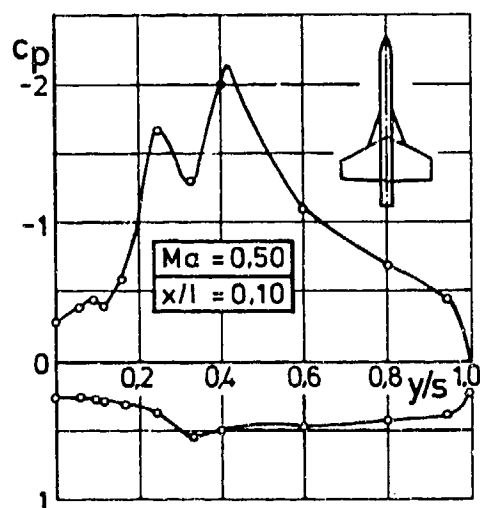


Fig. 9: Pressure distribution across semi-span of wing with strake. $\alpha = 15^\circ$

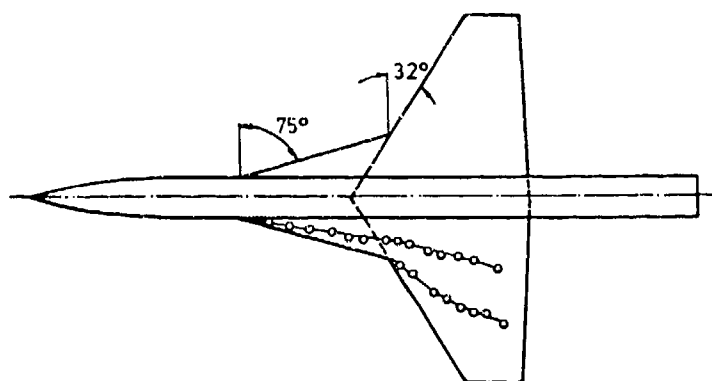


Fig. 10: —○— Measured locations of suction peaks on wing with strake. $\alpha = 15^\circ$

CALCUL INSTATIONNAIRE DE NAPPES TOURBILLONNAIRES ÉMISES PAR DES SURFACES PORTANTES FORTEMENT INCLINÉES

par Colmar REHBACH

*Office National d'Etudes et de Recherches Aérospatiales (ONERA)
92320 Châtillon (France)*

RÉSUMÉ

Les nappes tourbillonnaires qui se forment à partir du bord de fuite, des extrémités et, pour des incidences plus importantes, à partir du bord d'attaque de surfaces portantes inclinées ne tendent vers des formes bien organisées et stables que pour des configurations géométriques particulières (forte flèche par exemple) et dans des limites d'incidences bien déterminées. L'évaluation de leur forme par le calcul ne peut être abordée, avec une certaine généralité, que si l'on dispose d'une méthode de calcul instationnaire.

La méthode que nous utilisons ici est destinée aux écoulements tridimensionnels incompressibles. Elle est basée sur une application des variables de Lagrange au système intégral-différentiel constitué de l'identité de Green et de l'équation de Helmholtz que nous discrétisons sous forme de singularités tourbillonnaires ponctuelles.

Au cours de cette étude numérique de l'influence de la géométrie de l'obstacle et de son incidence sur l'évolution dans le temps et la stabilité de sa nappe tourbillonnaire, nous traitons la mise en mouvement subite de deux configurations géométriques simples : une aile rectangulaire et une aile delta planes, d'allongement 1. Nous nous intéressons tout particulièrement à deux problèmes, celui de la formation du noyau tourbillonnaire et celui soulevé par l'apparition progressive, et fortement influencée par la géométrie et par l'incidence, d'instabilités de nappe.

UNSTEADY CALCULATION OF VORTEX SHEETS EMITTED BY HIGHLY LOADED LIFTING SURFACES

SUMMARY

The vortex sheets that form at the trailing edge and tips and, for higher angles of attack, from the leading edge of lifting surfaces, tend towards well organized and stable shapes only for specific configurations (e.g. high sweep angles) and within a well-defined range of angles of attack. The evaluation of their shape can be undertaken with some degree of generality only if an unsteady method of calculation is used.

The method used here is intended for three-dimensional incompressible flows. It is based on an application of the Lagrangian variables to the integro-differential system made of the Green identity and the Helmholtz equation, discretized in the form of point vortex singularities.

During this numerical study of the influence of the obstacle geometry and incidence on the time evolution and stability of the vortex sheet, we deal with the sudden setting in motion of two simple configurations : a plane rectangular wing and a plane delta wing, both of unity aspect ratio. We deal especially with two problems : that of the vortex core formation and that of the gradual appearance, highly influenced by geometry and angle of attack, of the sheet instabilities.

1 - INTRODUCTION -

Les nappes tourbillonnaires qui se forment à partir du bord de fuite, des extrémités et, pour des incidences plus importantes, à partir du bord d'attaque de surfaces portantes ne tendent vers des formes géométriques bien organisées et stables que pour des configurations particulières de l'obstacle et dans des limites d'incidence bien déterminées. Le fait, confirmé par des nombreuses expériences en soufflerie et en tunnel hydrodynamique, que des nappes bien organisées pendant une période limitée suivant le démarrage de l'écoulement se désorganisent ensuite rapidement, montre à l'évidence que l'évaluation de leur forme par le calcul ne peut être abordée, avec une certaine généralité, que si l'on dispose d'une méthode de calcul instationnaire.

Les principales causes des instabilités de nappe sont, d'une part la tendance à l'amplification de la moindre perturbation (instabilité de Helmholtz) qui est inhérente à toute surface de discontinuité de vitesse et, d'autre part certains effets de la viscosité qui cependant, comme nos résultats, obtenus pour un écoulement non visqueux, semblent l'indiquer, joue dans la plus grande partie de l'écoulement, un rôle plus limité qu'on pourrait le penser au premier abord. Comme la forme des nappes, l'apparition des instabilités est fortement influencée par la géométrie de l'obstacle et par l'incidence.

2 - RAPPEL DES BASES THEORIQUES -

Les bases théoriques de la méthode de calcul que nous allons utiliser sont exposées en détail

dans les références [1] ou [2]. Pour situer le problème nous en reprenons ici l'essentiel.

Nous considérons l'écoulement d'un fluide incompressible non visqueux que nous décrivons à l'aide du champ des vecteurs tourbillon $\vec{\omega}$ définis par la relation :

$$\vec{\omega} = \text{rot } \vec{V}, \quad (1)$$

\vec{V} étant le vecteur vitesse.

L'écoulement considéré est instationnaire et nous suivons son évolution en fonction du temps à l'aide des variables de Lagrange. L'intérêt d'une telle description de l'écoulement vient du fait qu'un tourbillon ne peut être ni créé ni détruit à l'intérieur d'un fluide non visqueux homogène et est exclusivement produit sur les frontières. Pour le calcul de l'évolution du domaine tourbillonnaire, il suffit donc de suivre les particules tourbillonnaires émises sur la frontière, la variation dans le temps du vecteur $\vec{\omega}$ attaché à chacune d'elles étant gouvernée par l'équation de Helmholtz :

$$\frac{D\vec{\omega}}{Dt} = (\vec{\omega} \cdot \nabla) \vec{V}. \quad (2)$$

Le D majuscule désigne la dérivée particulière par rapport au temps t. Pour simplifier, nous ne considérons que le cas d'obstacles animés de mouvements de translation ; l'équation (2) peut alors être considérée comme écrite dans le repère relatif lié à l'obstacle, \vec{V} étant la vitesse dans ce repère.

La vitesse due au champ des vecteurs tourbillon $\vec{\omega}$ et à la présence d'un obstacle de surface S dans l'écoulement uniforme \vec{V}_∞ est :

$$\vec{V} = \vec{V}_\infty + \frac{1}{4\pi} \iint_S \text{grad} \left(\frac{1}{r} \right) \times \vec{\omega} dv + \frac{1}{4\pi} \iint_S \text{grad} \left(\frac{1}{r} \right) \times (\vec{n} \times \vec{V}) d\sigma, \quad (3)$$

avec \vec{n} , normale extérieure à S, et $r = |\vec{r}|$, valeur absolue du rayon vecteur séparant la particule du point de calcul, \vec{V}_∞ étant en général une fonction du temps. L'expression (3) peut être obtenue à partir de l'identité de Green.

La méthode de calcul consiste à suivre dans leur déplacement un nombre fini de particules fluides émises à intervalles de temps réguliers sur l'obstacle. Ces particules ont chacune un volume déterminé et peuvent être caractérisées, si nécessaire, par leur point d'émission. A chacune de ces particules est en outre attaché un vecteur tourbillon dont les valeurs initiales d'intensité et d'orientation sont déterminées par des conditions propres au type de décollement considéré. Comme déjà indiqué, l'évolution ultérieure des vecteurs $\vec{\omega}$ sera gouvernée par l'équation de Helmholtz (2), discrétisée ici sous forme d'un schéma aux différences. Dans les premières applications effectuées avec cette méthode [1], [2], nous avons utilisé un schéma précis au 1er ordre en temps. Nous montrons ici de nouveaux résultats obtenus avec un schéma de type prédicteur-correcteur précis au second ordre. Le théorème de Kelvin qui exige que la circulation autour de chaque ligne tourbillon reste indépendante du temps, théorème respecté explicitement dans les méthodes de réseau de tourbillons (par exemple [3]), est respecté ici implicitement grâce à la modification que cette équation fait subir à l'intensité et à l'orientation du vecteur $\vec{\omega}$ en fonction des distorsions du champ des vitesses, qui lui, est donné à chaque instant par l'expression (3) discrétisée sous forme d'une somme sur toutes les intensités vecto-

rielles discrètes $\vec{\omega}$ émises depuis l'instant initial sur l'obstacle.

Notons encore que toutes les particules émises par une même source sont à chaque instant situées sur une ligne d'émission qui, aussi longtemps que l'écoulement est instationnaire, ne doit pas être confondue avec une ligne tourbillon ou une ligne de courant. L'intérêt de la description d'un écoulement instationnaire sous forme de lignes d'émission réside dans son analogie étroite avec les méthodes courantes de visualisation par émission de traceurs.

La méthode de calcul utilisée ne nécessite aucune hypothèse sur le caractère des zones tourbillonnaires et le fait qu'il s'agit dans le cas des obstacles traités ici de surfaces tourbillonnaires constitue un résultat de calcul.

3 - ECOULEMENT INSTATIONNAIRE AUTOUR DE PLAQUES MINCES FORTEMENT INCLINEES -

Si nous nous bornons ici à l'étude de surfaces portantes minces, c'est que pour ce type d'obstacle, les lignes à partir desquelles une nappe tourbillonnaire se formera, sont connues. En effet, notre modèle de calcul non visqueux ne nous permet pas de déterminer la ligne de décollement dans le cas général. Dans le cas de l'obstacle infiniment mince traité ici, cette ligne est constituée par la totalité ou partie du bord de la surface portante.

3.1 - Aile rectangulaire plane sans décollement au bord d'attaque -

L'aile rectangulaire plane constitue une forme particulièrement simple de surface portante. Sa simplicité géométrique et le fait qu'en la choisissant de faible allongement (ici $\Lambda = 1$) il est possible de bien faire ressortir les effets tridimensionnels et non linéaires ainsi que d'accélérer [5] la convergence de certains calculs instationnaires (si par exemple l'état stationnaire est recherché en tant que limite d'un calcul instationnaire), l'ont fait choisir comme exemple par d'autres auteurs [4], [5], [6] et nous permettent ainsi de disposer de valeurs de référence.

Le mouvement de base de nos calculs instationnaires est la mise en mouvement instantanée de l'aile inclinée de l'incidence α par rapport au plan horizontal.

Comme déjà précisé plus haut, le modèle de calcul utilisé nécessite la connaissance de la ligne de décollement. Nous avons besoin aussi d'un procédé de création des vecteurs tourbillon le long de cette ligne. Dans un premier temps, nous allons, arbitrairement, limiter la formation de la nappe au bord de fuite et aux extrémités de la plaque. Il s'agit là d'un cas théorique à signification physique limitée, les expériences en soufflerie indiquant un décollement sur un bord d'attaque sans flèche même pour des incidences modérées. Ce schéma simplifié d'écoulement nous permet cependant de mieux préciser certains effets de l'incidence sur l'évolution dans le temps des nappes tourbillonnaires.

Pour la production des vecteurs tourbillon nous avons choisi la condition de Joukovskii : on crée des tourbillons dits libres, c'est-à-dire, pouvant se déplacer librement avec l'écoulement de façon à empêcher le contournement à vitesse infinie des bords infiniment minces de la plaque. Le déroulement satisfaisant des calculs

apportera une justification a posteriori de la validité de ce choix.

La nappe qui se forme à partir du bord de fuite et des extrémités de l'aile rectangulaire après une mise en mouvement subite tend pour des incidences petites et modérées vers une forme stationnaire bien organisée dans tout le domaine proche de l'aile. Nous montrons en bas de la figure 1, pour un tel type d'écoulement à l'incidence $\alpha = 14,5^\circ$, la projection dans un plan vertical de quelques lignes d'émission calculées, à l'instant $\tau = 2,8$ après la mise en mouvement où, près de l'aile, l'état stationnaire est pratiquement atteint. Une visualisation au tunnel hydrodynamique de l'ONERA du même phénomène est jointe. Les grandeurs de référence pour le temps adimensionné τ sont choisies telles que pour $\tau = 1$, l'aile a parcouru une distance égale à sa corde. On constate que, comme dans l'expérience, aucune instabilité n'affecte les lignes d'émission sur lesquelles les positions, à $\tau = 2,8$, des particules émises depuis l'instant initial sont matérialisées par des points. En donnant une même couleur aux particules émises par un même point d'émission et en variant la teinte d'un point d'émission à l'autre, on aurait l'image familière des émissions colorées obtenues au tunnel hydrodynamique.

Les expériences exécutées en soufflerie et au tunnel hydrodynamique, montrent que, au-delà d'une incidence limite dépendant du nombre de Reynolds, une nappe stationnaire et bien organisée n'existe plus. En effet, la nappe bien organisée pendant un bref délai suivant le démarrage se désorganise ensuite et le noyau tourbillonnaire constitué à partir des parties latérales fortement enroulées de la nappe "éclate" à la suite d'effets visqueux. Quelques lignes d'émission calculées correspondant à un tel cas d'écoulement (incidence $\alpha = 30^\circ$) sont représentées en haut de la figure 1 accompagnées, pour une comparaison ici purement qualitative, par une visualisation au tunnel hydrodynamique. Nous relevons sur le résultat de calcul une instabilité sur la ligne d'émission issue du bord de fuite et d'autres instabilités sur les lignes d'émission faisant partie des zones tourbillonnaires latérales de l'aile.

La précision du schéma aux différences utilisé pour la discrétisation de l'équation de Helmholtz peut avoir une influence sur l'apparition et la forme de ces instabilités. L'examen de cet effet est abordé sur la figure suivante (fig. 2). Il s'agit des lignes d'émission de la plaque à l'incidence $\alpha = 30^\circ$, à l'instant $\tau = 2,8$ après la mise en mouvement subite.

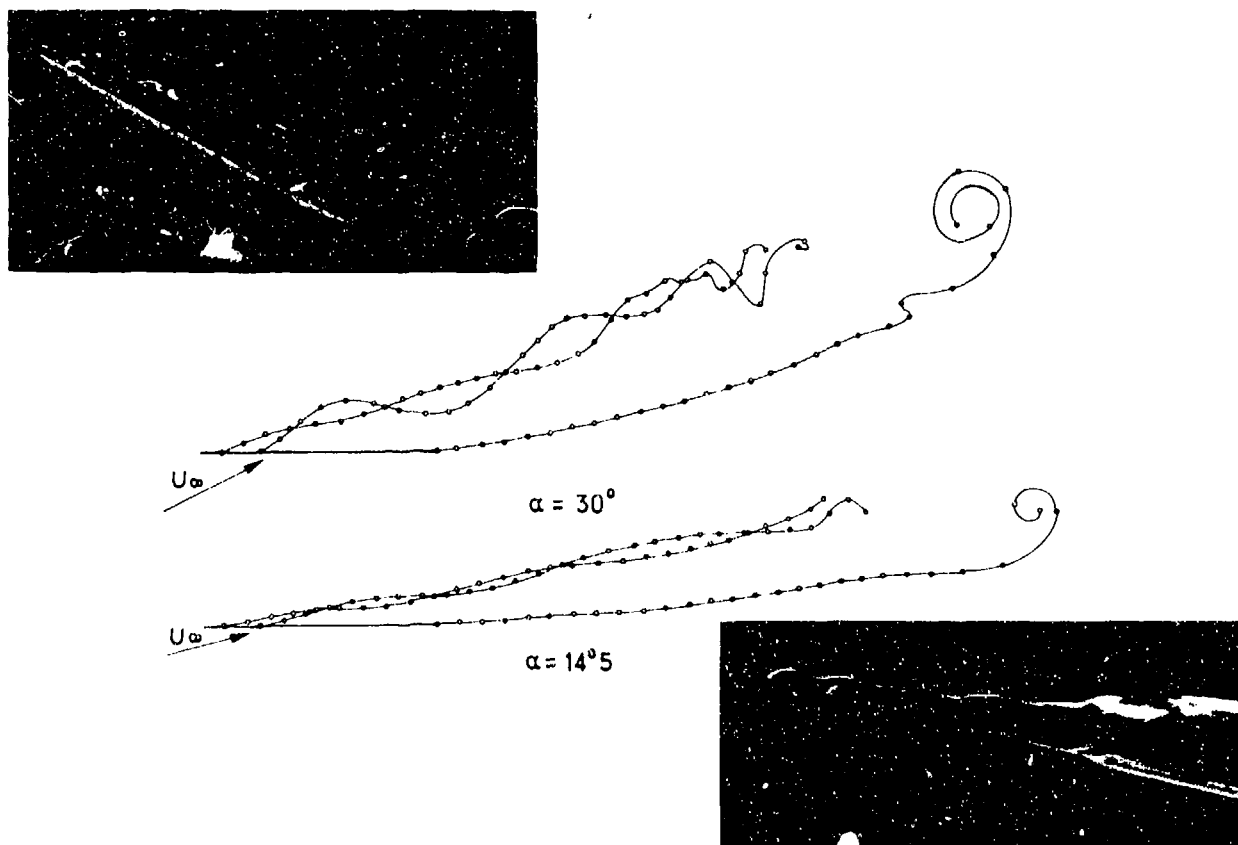


Fig. 1 - Aile rectangulaire plane d'allongement 1. Effet de l'incidence sur l'allure des lignes d'émission.

On observe que, pour un schéma précis à 0 ($\Delta\tau$) le taux d'enroulement de la deuxième ligne d'émission ainsi que celui de la partie aval (tourbillon de démarrage) de la ligne émise au bord de fuite sont faibles. L'allure de ces courbes ressemble aux résultats obtenus par les méthodes de réseau de tourbillons [3], [4]. L'utilisation d'un schéma précis à 0 ($\Delta\tau^2$) augmente considérablement le taux d'enroulement et on se rapproche avec ces résultats des images observées en tunnel hydrodynamique. Notons cependant que le passage d'un schéma numérique à l'autre n'a rien changé d'essentiel à l'écoulement calculé. On retrouve les mêmes instabilités apparaissant dans les mêmes domaines de l'écoulement. Dans le cas du schéma 0 ($\Delta\tau^2$), la désorganisation du domaine latéral se produit, sans signe annonciateur, subitement à environ une corde derrière l'aile. Dans le cas du schéma 0 ($\Delta\tau$), la désorganisation est progressive, surtout pour la ligne d'émission issue du voisinage du coin amont, mais dans la même zone que pour l'exemple précédent, l'écoulement est de nouveau totalement désorganisé. A noter également que même l'instabilité se produisant sur la ligne émise au bord de fuite apparaît, légèrement décalée dans l'espace, pour les deux schémas. On en conclut que l'influence de la

précision du schéma aux différences se limite aux détails géométriques des lignes d'émission mais n'affecte pas l'effet global de la forte incidence qui est la désorganisation de la nappe.

Quant au phénomène de la formation d'un noyau tourbillonnaire et de l'éclatement de celui-ci, dès que l'incidence atteint une certaine importance, nous l'aborderons sur la figure 3. On y observe l'évolution de la contraction de la zone tourbillonnaire latérale en fonction du temps ($\tau = 2,4$ et $\tau = 2,8$). Cette zone tourbillonnaire, loin encore de constituer un noyau tourbillonnaire compact avec prédominance des effets visqueux, se présente ici comme un domaine fluide à intensité tourbillonnaire forte mais bien organisée et donc parfaitement accessible à notre modèle de calcul non visqueux. L'analyse des visualisations de nappes obtenues à l'aide de traceurs particulièrement fins et donc peu soumis aux forces d'inertie, tels que des bulles d'hydrogène émises par une électrode noyée dans les bords d'attaque [7], [8], semble par les nombreux tours de spirale qu'elle permet de déceler, confirmer dans une large mesure ces résultats numériques.

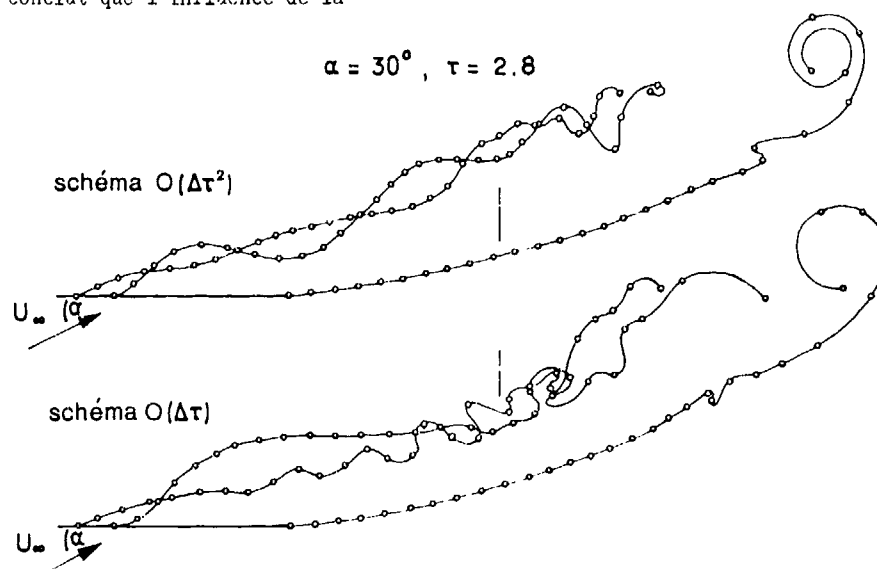


Fig. 2 - Aile rectangulaire plane d'allongement 1. Influence de la précision du schéma aux différences sur les lignes d'émission.

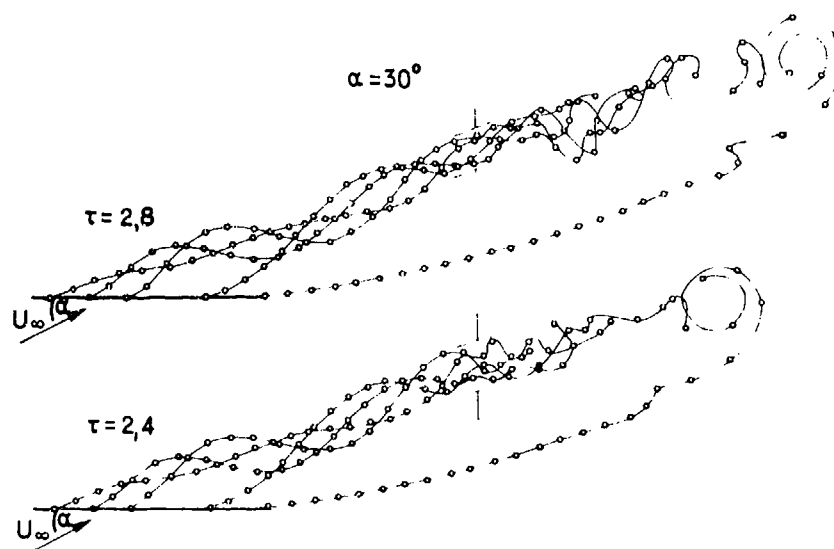


Fig. 3 - Aile rectangulaire plane d'allongement 1. Evolution de la zone tourbillonnaire latérale.

Nous constatons que si au départ le fort taux d'enroulement semble contribuer à la bonne organisation du domaine tourbillonnaire (voir figure précédente le schéma précis à 0 ($\Delta\tau$) où le taux d'enroulement est faible et où cette bonne organisation n'existe pas), une fois une certaine position aval atteinte, cet élément stabilisateur s'avère insuffisant et, presque sans transition, l'écoulement se désorganise. Il est intéressant d'observer que la contraction du domaine tourbillonnaire où la désorganisation se produit, augmente avec le temps.

Des résultats présentés pour l'aile rectangulaire sans décollement au bord d'attaque on peut déduire que les calculs, bien qu'obtenus à l'aide d'un modèle numérique non visqueux, semblent donner une indication au moins qualitative de la tendance à l'éclatement du "noyau" et à l'instabilité de la nappe se produisant aux fortes incidences en écoulement réel. Les raisons exactes de cette concordance entre écoulement réel et modèle numérique ne sont pas encore connues. Nous pouvons envisager de l'expliquer par un effet de viscosité numérique due à la discrétisation auquel peut s'ajouter l'effet des mouvements aléatoires des particules fluides chargées d'un vecteur tourbillon (interprétation donnée par A.J. CHORIN [9] en écoulement bidimensionnel). En effet, de petites perturbations aléatoires affectant les trajectoires des particules sont présentes dans tout calcul numérique en raison des erreurs de troncature.

L'évolution dans le temps du coefficient de force normale de l'aile rectangulaire plane d'allongement 1 à l'incidence $\alpha = 30^\circ$, après la mise en mouvement subite, est donnée sur la figure 4. En tant que référence nous indiquons en trait plein un résultat obtenu par S.M. Belotserkovskii et al., par une méthode de réseau de tourbillons [4].

Quant aux résultats obtenus par la présente méthode, nous indiquons d'une part ceux obtenus à l'aide du schéma précis à 0 ($\Delta\tau$) qui se caractérise par une concentration tourbillonnaire faible dans les régions latérales et d'autre part ceux obtenus avec le schéma précis à 0 ($\Delta\tau^2$).

Ce dernier présente une concentration tourbillonnaire beaucoup plus importante dans le domaine latéral. La valeur limite vers laquelle tend le coefficient de force normale est, à l'incidence élevée traitée ici, une valeur moyenne dans le temps et non une valeur stationnaire qui, une nappe stationnaire n'existant pas, n'aurait pas de signification physique. Les résultats du schéma de premier ordre tendent vers la valeur limite indiquée dans la référence [4], ceux du schéma du second ordre tendent vers une valeur limite environ 6 % plus petite. La raison de cette différence est à chercher dans l'influence de la modification de la zone tourbillonnaire latérale sur la valeur de la dépression située sur l'extrados de l'aile ainsi qu'il sur la position et l'étendue de cette zone dépressionnaire.

3.2 - Aile rectangulaire plane avec décollement au bord d'attaque -

Dans le cas de l'écoulement réel, la formation de la nappe ne reste pas, et ceci même pour des incidences modérées, limitée au bord de fuite et aux extrémités mais s'étend également au bord d'attaque sans flèche de l'aile rectangulaire. Une approche numérique de ce phénomène a déjà été faite à l'aide d'une méthode de réseau de tourbillons par S.M. Belotserkovskii et ses collaborateurs [4]. Dans ce qui suit, nous donnerons les résultats obtenus pour ce type d'écoulement à l'aide du schéma de tourbillons ponctuels décrit plus haut.

L'expérience en écoulement réel ainsi que les résultats de la référence [4] montrent que, plus encore que les parties de la nappe émises latéralement et au bord de fuite, la nappe qui se forme sur un bord d'attaque sans flèche n'a une existence sous forme bien organisée que pour une durée très limitée. Peu après le démarrage de l'écoulement cette partie de la nappe se décompose sur la plus grande partie de son étendue. Si l'incidence est élevée, cette décomposition a une grande influence sur l'évolution des valeurs aérodynamiques. L'étude numérique de ce type de décollement nécessite donc essentiellement une méthode de calcul instationnaire.

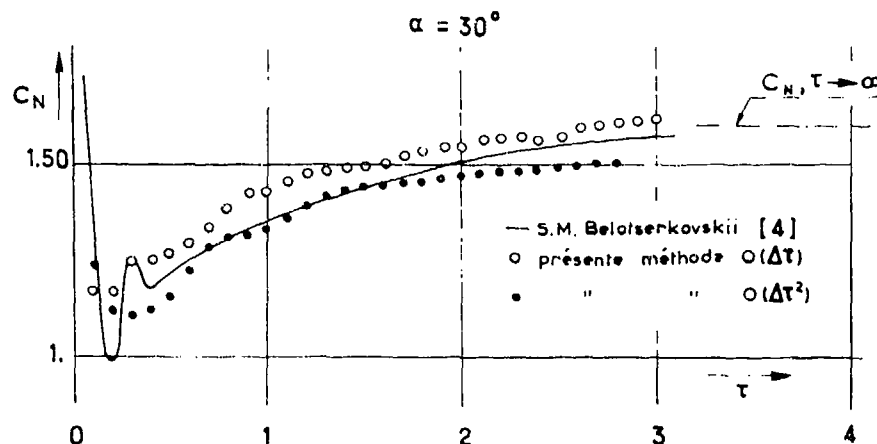


Fig. 4 - Aile rectangulaire plane d'allongement 1. Evolution de la force normale au cours d'une mise en mouvement subite.

Contrairement aux nappes émises au bord de fuite et aux extrémités d'ailes à faible flèche ou aux nappes émises au bord d'attaque d'ailes à forte flèche, les nappes qui se forment à partir d'un bord d'attaque à faible flèche semblent dues à des phénomènes visqueux dont l'effet ne peut plus être considéré comme local. Pour cette raison, la production des tourbillons est certainement mal approchée par une condition locale telle que la condition de Joukovskii que, à défaut d'un modèle numérique plus satisfaisant, nous continuons à utiliser. Une partie des difficultés et certaines anomalies dans les résultats (les lignes d'émission calculées se placent en moyenne plus près de la plaque que celles de l'écoulement réel) peuvent certainement être attribuées au caractère très particulier de cette condition qui concentre l'effet de viscosité sur une ligne là où, en fluide réel, son influence concerne tout un domaine de l'écoulement (formation d'un bulbe).

La figure 5 montre, projeté dans un plan vertical (en haut) et dans le plan de la plaque (en bas, on y indique également le découpage de la plaque en facettes) quelques lignes d'émission dans le cas de l'écoulement avec formation de nappe au bord d'attaque au moment $\tau = 0,5$ (schéma 0 ($\Delta\tau$)). La désorganisation du système tourbillonnaire se produit, pour ce calcul, vers $\tau = 1$. Ces résultats de calcul sont accompagnés, pour une comparaison qualitative, par deux

visualisations des lignes d'émission effectuées au tunnel hydrodynamique de l'ONERA, la première peu après le démarrage de l'écoulement (en bas à gauche), la seconde quelques instants plus tard (en haut à droite) à un moment où la nappe est déjà dans son ensemble désorganisée.

La désorganisation de la partie de la nappe issue du bord d'attaque a, aux grandes incidences, un effet très important sur ses parties se formant plus en aval et sur l'évolution des valeurs aérodynamiques. Alors que dans le cas des nappes se formant aux extrémités et au bord de fuite les perturbations apparaissent plus en aval et s'éloignent avec le courant influant ainsi peu le domaine amont, les perturbations liées au décollement de bord d'attaque déferlent tout le long de la surface portante pour perturber ensuite les parties de nappes formées en aval. Du fait du caractère aléatoire de la désorganisation, les résultats sont fortement marqués dans leur évolution par de faibles écarts des paramètres de calcul tels que pas en temps, position des points d'émission etc ... et aussi par des détails intéressant le débit tourbillonnaire. Nous en donnons comme exemple une comparaison entre un résultat relevé dans la référence [4] et un calcul effectué à l'aide de la présente méthode (schéma 0 ($\Delta\tau$)). Il s'agit de l'évolution du coefficient de force normale après mise en mouvement subite d'une aile rectangulaire d'allongement 1,5, inclinée de 30° .

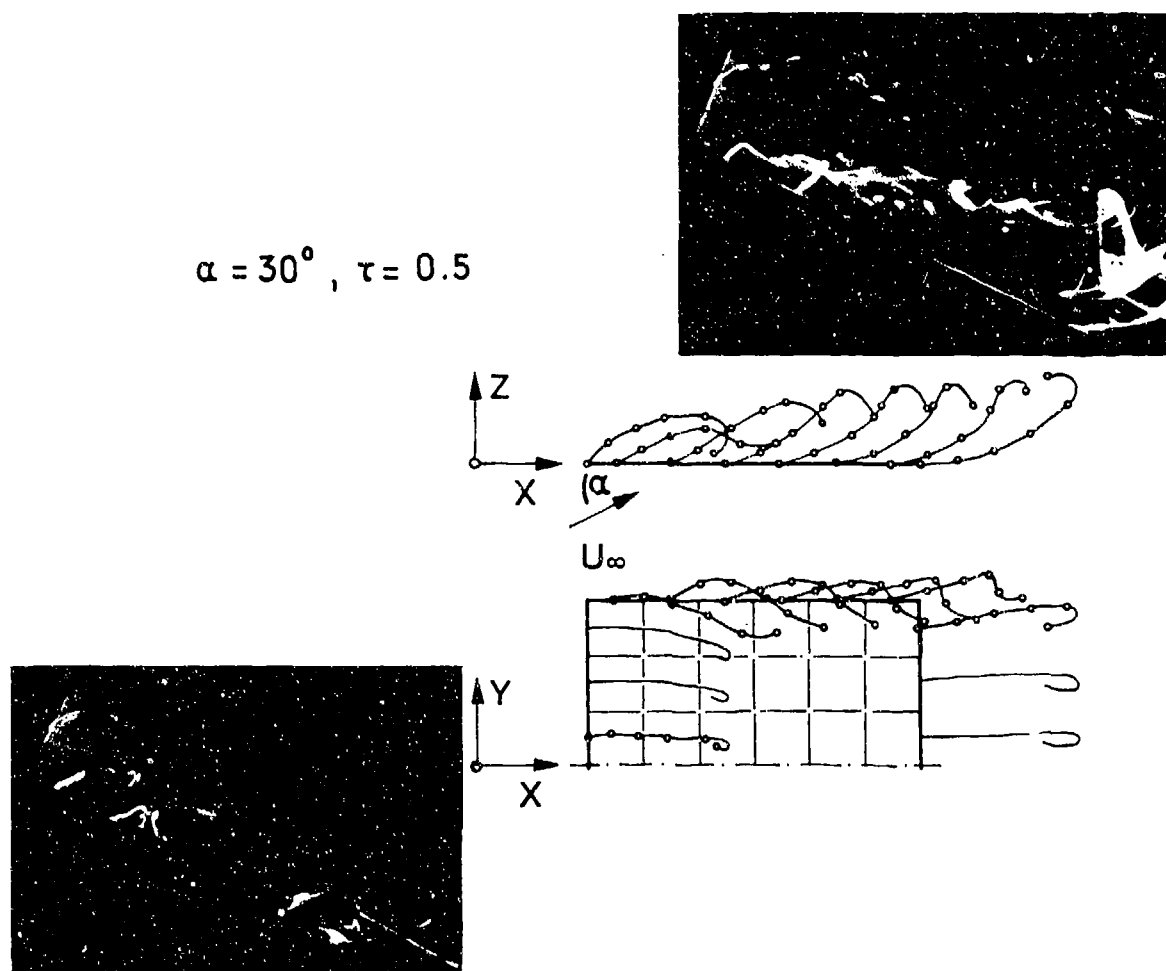


Fig. 5 - Aile rectangulaire plane d'allongement 1. Formation d'une nappe au bord d'attaque.

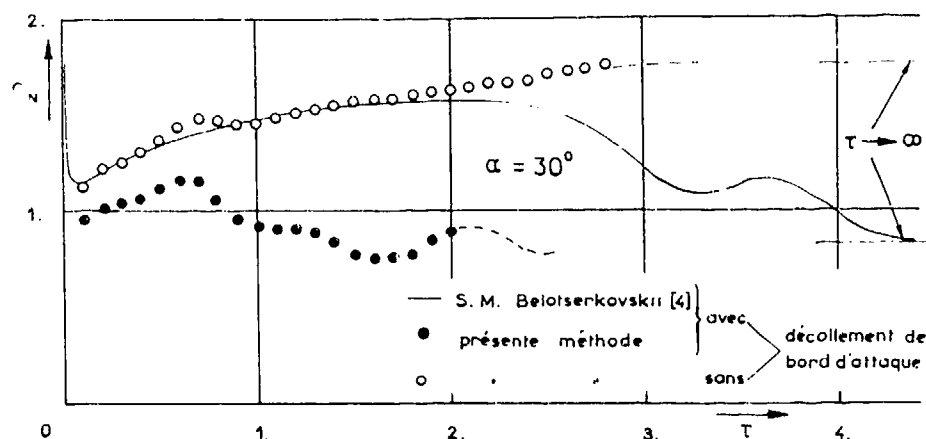


Fig. 6 – Aile rectangulaire plane d'allongement 1,5. Evolution de la force normale au cours d'une mise en mouvement subite.

A droite de la figure (fig. 6) sont indiquées les valeurs C_N de la plaque avec et sans décollement au bord d'attaque atteintes aux grandes valeurs de τ [4]. Dans le cas sans décollement au bord d'attaque, il s'agit d'une valeur calculée, dans le cas avec décollement d'une valeur expérimentale. On constate que l'apparition d'une nappe au bord d'attaque conduit à une importante diminution de la portance. Quant à la forme sous laquelle le C_N obtenu par les deux méthodes tend vers la valeur limite, elle est très différente d'une méthode à l'autre. La courbe des C_N donnée dans la référence [4] pour l'aile avec décollement au bord d'attaque suit d'abord, jusqu'à $\tau \approx 2$, l'évolution que nous obtenons pour l'écoulement sans décollement et est ensuite suivie d'une forte chute de portance suivie d'oscillations. L'examen de ce résultat donne l'impression que le décollement au bord d'attaque n'intervient qu'un certain temps après la mise en mouvement. La référence citée ne donne aucune précision à ce sujet.

Dans le cadre de la présente méthode nous imposons le décollement dès le moment initial, ce qui entraîne dès cet instant une baisse de portance. La courbe du C_N suit ensuite à peu près parallèlement la courbe du C_N sans décollement pour accusar dès $\tau \approx 0,8$ une chute suivie d'oscillations autour de la valeur limite pour grands τ .

Si cette comparaison de deux méthodes de calcul appliquées au même problème instationnaire montre bien le même caractère qualitatif du phénomène de déchirement de la nappe aux grandes incidences, son aspect quantitatif est moins satisfaisant et fait surtout ressortir que seule une connaissance précise de tous les paramètres de calcul permettrait éventuellement d'obtenir des résultats comparables.

3.3 – Aile delta plane d'allongement 1-

L'aile infiniment mince (surface portante) inclinée de 30° par rapport au plan horizontal subit à l'instant initial $\tau = 0$ une mise en mouvement instantanée. Ce cas a été traité à l'aide d'une méthode de réseau de tourbillons par S.M. Belotserkovskii [4], et à l'aide de la présente méthode, avec un schéma précis à $0(\Delta\tau)$ dans la référence [2]. Ici nous rapportons les résultats obtenus à l'aide du schéma amélioré précis à $0(\Delta\tau^2)$.

Pour respecter le caractère particulier de l'obstacle, c'est-à-dire sa conicité dans le domaine de l'apex, le découpage de sa surface (voir figure 7) a été effectué de façon à maintenir constant le rapport longueur/largeur des facettes doubles. L'endroit où ont lieu les émissions a été fixé en conséquence. Dans le cadre de la présente méthode cela est aisément réalisable en raison de l'indépendance du mécanisme de création des tourbillons (fonction de la discrétisation de l'obstacle) et de la propagation du domaine tourbillonnaire au sein du fluide.

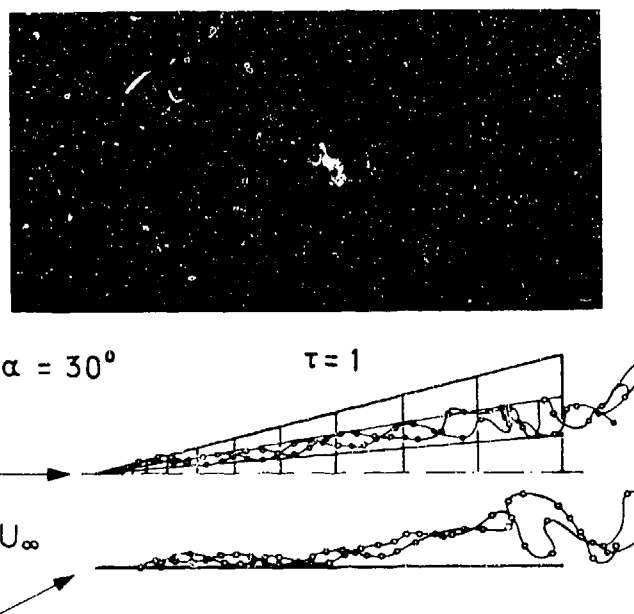


Fig. 7 – Aile delta plane d'allongement 1. Lignes d'émission.

La figure 7 montre, à l'instant $\tau = 1$, la projection dans le plan de l'aile de deux lignes d'émission, toutes les deux émises près de l'apex. Nous constatons que grâce au découpage particulier de la surface portante décrit plus haut et au schéma de discrétisation plus précis de l'équation de Helmholtz ($0(\Delta\tau^2)$) ces deux filets s'enroulent finement l'un autour de l'autre. On approche l'écoulement réel (visualisation effectuée au tunnel hydrodynamique de l'ONERA) que nous donnons à titre indicatif et qui montre, en outre, très nettement l'éclatement brutal du noyau qui se produit à l'incidence élevée de 30° .

que nous étudions. Comme pour l'aile rectangulaire, la tendance du noyau à l'éclatement semble indiquée par le calcul sous forme d'une rapide désorganisation des lignes d'émission. En amont de cette zone perturbée par contre, la nappe issue ici d'un bord d'attaque à flèche très importante, montre une remarquable stabilité et une grande insensibilité aux variations des paramètres de calcul indiquant par là que la condition de Joukovskii, utilisée pour le calcul du débit tourbillonnaire, constitue ici une approche correcte des phénomènes visqueux locaux.

L'évolution dans le temps du coefficient de force normale C_N donnée sur la figure suivante (fig. 8) montre d'une part que la réorganisation des nappes déferlant ensuite par dessus la surface portante de manière aléatoire, rend la comparaison quantitative avec d'autres méthodes de calcul (ici résultat de la référence [4] d'où nous avons également tiré la valeur expérimentale du C_N pour $\tau \rightarrow \infty$) toujours très délicate, et d'autre part que l'utilisation du schéma précis à 0 ($\Delta\tau^3$) nous éloigne des valeurs de la référence [4] et des valeurs que nous avons obtenues avec le schéma moins précis 0($\Delta\tau$) (voir référence [2]).

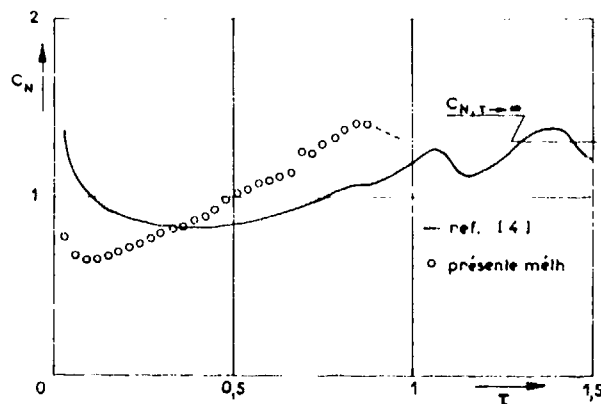


Fig. 8 - Aile delta plane d'allongement 1. Evolution de la force normale au cours d'une mise en mouvement subite.

4 - CONCLUSION -

L'étude de la mise en mouvement subite de deux configurations géométriques simples, une aile rectangulaire plane d'allongement 1 et une aile delta plane du même allongement, a permis de montrer que des nappes tourbillonnaires bien organisées et tendant vers une forme stationnaire n'existent que pour des incidences modérées et sont limitées à certaines formes géométriques de l'obstacle. Ce phénomène dû principalement à des effets visqueux est connu par les expériences en soufflerie et en tunnel hydrodynamique. Qu'il puisse être abordé à l'aide de modèles numériques non visqueux ([4] et la présente méthode), étonne, mais peut s'expliquer par un effet de viscosité numérique dû à la discrétisation et, dans une moindre mesure, aux petites perturbations aléatoires auxquelles sont soumises, en raison des erreurs de troncature, les trajectoires des particules fluides chargées d'un vecteur tourbillon.

Nous avons également pu remarquer que là où les nappes sont produites par des effets visqueux locaux bien pris en compte par la condition de Joukovskii (extrémités et bord de fuite de la plaque rectangulaire, bord d'attaque à forte flèche et bord de fuite de l'aile delta), la

qualité des résultats est supérieure et plus aisément reproductible par des méthodes de calcul différentes que là où les effets visqueux s'étalent sur tout un domaine fluide et sont, de ce fait, mal pris en compte par la condition de Joukovskii que, à défaut d'un meilleur modèle numérique, nous continuons d'utiliser (bord d'attaque sans flèche de la plaque rectangulaire).

L'utilisation d'un schéma précis à l'ordre $\Delta\tau^3$ pour la discrétisation de l'équation de Helmholtz, sans modifier l'essentiel des résultats, permet d'obtenir des enroulements de nappe très prononcés là où, dans l'écoulement réel, se forment les noyaux tourbillonnaires. Le taux de contraction calculé de ces domaines est important et donne lieu à des zones tourbillonnaires à forte intensité sans qu'il soit nécessaire de recourir à un modèle numérique simulant la viscosité. Celui-ci s'imposera à un stade ultérieur, qui n'est pas abordé ici, pour la constitution d'un noyau plus compact et peut être envisagé par un schéma d'amalgamation tel que celui proposé par D.W. Moore [10] en écoulement bidimensionnel. Cependant, la mise au point d'un tel schéma en écoulement tridimensionnel est beaucoup moins intuitive et pose un certain nombre de problèmes.

Toutes les visualisations d'écoulement figurant dans cette étude ont été obtenues au tunnel hydrodynamique de l'ONERA par H. WERLE et M. GALLON.

5 - REFERENCES -

- [1] - REHBACH C.
Calcul numérique d'écoulements tridimensionnels instationnaires avec nappes tourbillonnaires
Rech. Aérop., n° 1977-5, p. 289-298
- [2] - REHBACH C.
Numerical calculation of three dimensional unsteady flows with vortex sheets
AIAA Paper n° 78-111
- [3] - BELOTSERKOVSKII S.M.
Calculation of the flow about wings of arbitrary planform at a wide range of angles of attack
R.A.E. Library Translation 1433 (1970) de l'article original paru en Mekhanika Zhidkosti i Gaza 4 (1968) p. 32-44
- [4] - BELOTSERKOVSKII S.M. - NISHT M.I.
Non stationary non linear theory of a thin wing of arbitrary planform
Izv. Akad. Nauk SSSR, Mekh. Zhidk Gaza 4 : 100-3, Fluid Dyn. 9 (4) ; 533-39, 1974
- BELOTSERKOVSKII S.M.
Ecoulements décollés et caractéristiques non linéaires de surfaces portantes minces dans un fluide incompressible.
Non publié
- [5] - JONES R.T.
The unsteady lift of a finite wing
NACA T.N. n° 682 (1939)
- [6] - SCHOLZ N.
Kraft und Druckverteilungsmessungen an Tragflächen kleiner Streckung
Forschung Ing. Wes., Bd. 16, Heft 3 (1949-1950), p. 85-91

- [7] - THOMPSON D.H.
Visualization of separated flows in a water
tunnel
TM ARL/A.266, March 1971, ARL, Melbourne,
Australia
- [8] - Film ONERA n° 802,
Nappes en cornet issues d'ailes minces
élancées (1975)
- [9] - CHORIN A.J.
Numerical study of slightly viscous flow
J. Fluid Mech. (1973), vol. 57, part 4,
pp. 785-796
- [10] - MOORE D.W.
A numerical study of the roll-up of a
finite vortex sheet
J. Fluid Mech. (1974), vol. 63, part 2,
pp. 225-235.

ON THE VORTEX FORMATION OVER A SLENDER WING AT LARGE ANGLES OF INCIDENCE

by
 Prof. Dr.-Ing. Dietrich Hummel
 Institut für Strömungsmechanik
 Technische Universität Braunschweig
 Bienroder Weg 3
 D-3300 Braunschweig
 Federal Republic of Germany

SUMMARY

An experimental study of the flow field around an $A = 1$ delta wing at an angle of attack of $\alpha = 20.5^\circ$ is presented. The free vortex sheets generated at the wing leading-edges roll up into the well known leading-edge vortices which are accompanied by some secondary vortices at the wing surface as a result of boundary-layer separations. The effect of Reynoldsnumber on the formation of the secondary vortex is studied in detail. Boundary-layer measurements have been carried out for laminar and turbulent boundary layers and the bound vortex lines in the lifting surface have been determined for both cases. The free vortex sheet originating from the wing trailing-edge rolls up into a concentrated trailing vortex the rotation of which is opposite to that of the leading-edge vortex. The flow field has been measured in four planes perpendicular to the free stream direction and located in different positions downstream of the wing trailing-edge. The magnitude and the direction of the local velocity vector have been determined by means of a 5-holes-probe. The results are given for each plane by lines of constant total pressure, static pressure, dynamic pressure and by a presentation of the local flow directions. The interference between leading-edge vortex, secondary vortex and trailing-edge vortex is studied in detail. The positions of the vortex sheets and of all concentrated vortices in relation to the wing are given quantitatively. They are now available for comparisons with results of numerical calculations.

LIST OF SYMBOLSGeometric parameters

x, y, z	Rectangular wing-fixed coordinates, origin at wing apex according to Fig.2
$\bar{x}, \bar{y}, \bar{z}$	Rectangular aerodynamic coordinates, x - axis parallel to the free stream, origin at the wing trailing-edge according to Figs.12 to 15
ξ, η, ζ	Dimensionless aerodynamic coordinates ($\xi = \bar{x}/s$, $\eta = \bar{y}/s$, $\zeta = \bar{z}/s$) according to Figs.12 to 15
$A = b^2/S$	Aspect ratio of the wing
b	Wing span
$c(x)$	Local wing chord
\bar{c}	Mean aerodynamic chord
d	Maximum wing thickness
S	Wing area
$s = b/2$	Wing half span
$s_1(x)$	Local half span

Aerodynamic parameters

ρ	Density
ν	Kinematic viscosity
α	Angle of incidence (angle between the free stream direction and the plane $z = 0$)
$c_D = D/q_\infty S$	Drag coefficient
$c_L = L/q_\infty S$	Lift coefficient
$c_M = M/q_\infty S c$	Pitching moment coefficient, reference point N_{25} (see Fig.2), nose up positiv
g	Total pressure
$c_g = (g - p_\infty)/q_\infty$	Total pressure coefficient
q	Dynamic pressure
$c_q = q/q_\infty$	Dynamic pressure coefficient
p	Static pressure
$c_p = (p - p_\infty)/q_\infty$	Static pressure coefficient
$Re = V_\infty c_1/\nu$	Reynolds number
V_∞	Free stream velocity
\vec{v}	Local velocity vector

$v_{\bar{x}}, v_{\bar{y}}, v_{\bar{z}}$	Components of \vec{v} in the aerodynamic coordinate system
$v_{\bar{y}\bar{z}}$	Component of \vec{v} in planes $\bar{x} = \text{const.}$ ($v_{\bar{y}\bar{z}} = \sqrt{v_{\bar{y}}^2 + v_{\bar{z}}^2}$)
u, v, w	Components of \vec{v} in the wing-fixed coordinate system
\vec{k}	Vorticity vector in the lifting surface $z = 0$ according to equ.(3)

Subscripts

i	Inner section of the wing (at $y = 0$)
l	Lower surface of the wing
u	Upper surface of the wing
∞	Free stream conditions

1. INTRODUCTION

At moderate and large angles of incidence the flow separates from the sharp leading-edges of slender wings. These flow separations usually take the form of two free vortex layers joined to the leading-edges of the wing and rolling up to form spiral shaped primary vortices above the upper surface of the wing as sketched in Fig.1. The vortices over the wing induce additional velocities at the upper surface of the wing. The corresponding pressure distribution which is also drawn in Fig.1 shows distinctly marked minima beneath the vortex axes. Accordingly an additional lift force occurs which depends non-linearly on the angle of incidence. Due to the leading-edge vortices the flow at the wing surface is directed outwards. The steep pressure gradient between the minimum of pressure and the leading-edge causes flow separation which usually takes the form of a small secondary vortex. At the upper surface of the wing this secondary vortex induces additional velocities. The corresponding modification of the pressure distribution is indicated in Fig.1b by hatching.

This vortex formation is well known since a long time. The first experiments on slender wings are due to H. Winter [1]. The physics of the vortex formation have been studied mainly on delta wings. There exists a very large number of papers on this subject, for instance by P.T. Fink [2], D.J. Marsden, R.W. Simpson, W.J. Rainbird [3], N.C. Lambourne, D.W. Bryer [4], D.H. Peckham [5], P.B. Earnshaw, J.A. Lawford [6,7], D. Hummel and G. Redeker [8,9,10] and many others. The influence of Reynolds number on the vortex formation over a delta wing has been described by D. Hummel [8]. The various reviews published from time to time for instance by D. Küchemann [11,12], J.H.B. Smith [13] and D.J. Peake [14] show, that the basic flow over an inclined delta wing is regarded as well understood and that there was no need for further investigations in the last ten years.

From the very beginning of the exploration of the flow over slender wings at large angles of incidence the experimental work has been accompanied by theoretical investigations. The measurements of H. Winter [1] were followed by the very early nonlinear theory for rectangular wings of W. Bollay [15]. The basic idea that the free vortex lines leave the wing outside the wing plane has been taken up by K. Gersten [16] in his nonlinear theory for slender wings with arbitrary planform shape. Later the leading-edge suction analogy of E.C. Polhamus [17] and some extensions by J.E. Lamar [18] appeared for the calculation of the nonlinear aerodynamic characteristics of wings with pointed tips and side edges. By these methods [16,17,18] the overall characteristics of slender wings can be calculated with remarkable accuracy, but the details of the flow are not correct and the pressure distribution cannot be predicted.

More realistic representations of the physics of the vortex formation have been used in the single line vortex approaches of R. Legendre [19] and C.E. Brown, W.H. Michael [20] and in the vortex sheet method of K.W. Mangler, J.H.B. Smith [21] and in the improved calculations of J.H.B. Smith [22]. In all these methods the assumptions of slender body theory are used. This means that in the case of a slender delta wing the flow is conical. The vortex sheet model gives reasonably reliable predictions of the shape, position and strength of the leading-edge vortex over a flat plate delta wing. The lift on the forward part of the wing is also well predicted, but the pressure distributions in this part of the wing show some discrepancies between experiment and theory which are due to the fact that theory does not take into account any secondary separation, a defect shared by all theories so far.

The experimental investigations of the flow over delta wings, for instance by D.J. Marsden, R.W. Simpson, W.J. Rainbird [3] and D. Hummel [9,10], have shown that the flow is non-conical. Therefore conical flow theories cannot be applied to the rearward parts of slender wings as pointed out by D. Küchemann [23]. In the last years several attempts have been made to calculate the non-conical flow and to fulfil the Kutta-condition at the wing trailing-edge. Recently a review has been given by J.H.B. Smith [24]. Non-conical single line vortex methods are due to R.K. Nangia, G.J. Hancock [25] and T.K. Matoi, F.E. Covert, S.E. Widnall [26]. Multiple line vortex methods have been developed by G. Rehbach [27] and O.A. Kandil, D.T. Mook, A.H. Nayfeh [28]. Finally at Boeing P.E. Rubbert and collaborators [29,30,31] have applied a higher order panel method - which is actually a vortex sheet method - to calculate the non-conical flow field including the shape of the vortex sheet as well as the pressure distribution on the wing surface. During these calculations numerical difficulties appeared in the vicinity of the trailing-edge in the flow region between the trailing vortex sheet and the leading-edge vortex. The theoretical results for the shape of the vortex sheet in this

region seem to be doubtful but a comparison with experimental results is not possible since no measurements do exist.

It is the purpose of this paper to provide experimental data on the shape of the vortex sheet in the region close to the trailing-edge behind a slender delta wing. For comparisons with theoretical approaches all other interesting experimental data of the investigated flow are added as complete as they are available at the present time.

2. EXPERIMENTAL SET-UP AND PROGRAM

2.1 Wind-tunnel model

The measurements have been carried out on a sharp-edged delta wing of aspect ratio $A = 1$ the geometry of which is shown in Fig. 2. The wing has a flat surface and a narrow triangular cross section. The model is conical with respect to the wing apex as well as with respect to the wing tips. The maximum relative thickness is $d/c_1 = 0.021$ at $x/c_1 = 0.9$. On both sides of the model pressure tubes are embedded in the surface and the holes for the pressure measurements are drilled on lines $x = \text{const.}$ (see sections a to q in Fig. 2)

2.2 Description of the tests

All tests have been carried out in the 1,3 m wind-tunnel of the Institut für Strömungsmechanik at the Technische Universität Braunschweig.

2.2.1 Balance measurements

Comprehensive six-component balance measurements have been carried out on this model. The results have been published by D. Hummel [32], D. Hummel, P.S. Srinivasan [33] and D. Hummel, G. Redeker [34] in connexion with investigations on vortex breakdown. In these tests the flat surface has been used as the upper surface of the wing.

2.2.2 Pressure distributions

The pressure distribution has been measured for a large number of free stream conditions. The angle of incidence and the angle of sideslip have been varied at a fixed Reynolds number of $Re = 2 \cdot 10^6$. Some of these pressure distributions have been published in connexion with investigations on vortex breakdown in [8, 9, 32].

2.2.3 Surface oilflow patterns

The boundary layers on the upper and lower surface of the wing have been studied by means of oilflow patterns. For this purpose the wing surface was covered by a thin leaf of black synthetics which was painted by a mixture of aluminiumoxide-powder and petroleum and benzine (ratio of components: 1 g aluminium-oxide : 3 cm³ petroleum : 1 cm³ benzine) and exposed to the flow for about half a minute. Oilflow patterns of this kind have been published in connexion with boundary layer investigations for fixed angle of incidence and different Reynolds numbers in [8, 9, 10] and in relation to investigations on vortex breakdown for fixed angle of incidence and different angles of sideslip in [8].

2.2.4 Boundary layer measurements

Investigations of the boundary layers on the upper and lower surface of the wing have been carried out at an angle of incidence of $\alpha = 20.5^\circ$. This special value has been chosen since theoretical results after the method of J.H.B. Smith [22] are available for an $A = 1$ delta wing at this angle of incidence. The velocity distribution in the three-dimensional boundary-layer has been determined by measuring the surface pressure distribution through the pressure holes at the wall as well as by measuring the distribution of the total pressure and of the flow direction in planes parallel to the surface within the boundary layer at different distances from the wall by means of a 3-holes probe. In these boundary-layer measurements the flat surface of the model was used as upper side and as lower side. This means that the small camber of the wing has been neglected in these tests. The boundary layer measurements have been carried out for two flow conditions:

- i) Laminar boundary layers. The Reynolds number was chosen as $Re = 9 \cdot 10^5$. In this case the boundary layers were laminar on both sides of the wing. Some results of these boundary-layer measurements have been published by J.C. Cooke [35].
- ii) Turbulent boundary layers. The Reynolds number was again $Re = 9 \cdot 10^5$ but artificially turbulent boundary layers have been produced at the upper surface by means of turbulence generators. For this purpose wires, having a relative diameter of $D/s = 0.0053$, were fixed to the wing surface at $y/s_1(x) = \pm 0.5$. The boundary layer at the lower surface was still laminar.

In both cases the velocity vectors at the outer edge of the boundary layer on the upper and lower surface

$$\begin{aligned}\vec{v}_u &= u_u \vec{i} + v_u \vec{j} \\ \vec{v}_l &= u_l \vec{i} + v_l \vec{j}\end{aligned}\tag{1}$$

have been determined. The vector difference between upper and lower surface is

$$\begin{aligned}\Delta \vec{v} &= (u_u - u_l)\vec{i} + (v_u - v_l)\vec{j} \\ \Delta \vec{v} &= \Delta u \vec{i} + \Delta v \vec{j}\end{aligned}\quad (2)$$

and the vorticity vector in the lifting surface which is perpendicular to this vector difference turns out as

$$\begin{aligned}\vec{k} &= k_x \vec{i} + k_y \vec{j} \\ \vec{k} &= -\Delta v \vec{i} + \Delta u \vec{j}\end{aligned}\quad (3)$$

These vorticity vectors have been determined from the measurements and some experimental bound vortex lines have been evaluated by numerical integration [9,10]. In both cases for the outer edge of the boundary layer those points have been taken where the total pressure coefficient was $c_p = 0.99$. Near the leading-edge of the wing the secondary vortex has been regarded as a phenomenon belonging to the boundary layer. Therefore in this region the outer edge of the "boundary layer" was situated above the secondary vortex.

2.2.5 Flow field measurements

In these tests the wing was fixed at an angle of incidence of $\alpha = 20.5^\circ$, the flat surface of the model being used as upper side. The Reynolds number was $Re = 2.10^6$. In this case the boundary layers were mainly turbulent on the upper side [8] and mainly laminar on the lower side of the wing.

The flow field behind the trailing edge of the wing has been measured in four planes perpendicular to the free stream velocity at the stations

$$\xi = \bar{x}/s = 0.080/0.267/0.533/1.066.$$

In these planes the magnitude and the direction of the local velocity vector \vec{v} has been determined by means of a conical 5-holes-probe. The axis of the cone could be adjusted parallel to the local flow direction and in this position total pressure, static pressure and two flow angles have been measured. From these data lines of constant coefficients of total pressure, static pressure and dynamic pressure have been evaluated and the velocity vector has been split up into the component v_x perpendicular to the \bar{y}/\bar{z} -plane and into the component $v_{\bar{y}\bar{z}}$ in the \bar{y}/\bar{z} -plane.

3. RESULTS

3.1 Three-component measurements

The results of the three-component measurements are shown in Fig. 3. The nonlinear force and moment characteristics are well known. At high angles of incidence vortex breakdown occurs in the vortices. According to D. Hummel and P.S. Srinivasan [32,33] the breakdown point crosses the trailing-edge of the wing at $\alpha = 29^\circ$. At larger angles of incidence lift and nose-down pitching moment decrease and the slope of drag $dc_D/d\alpha$ becomes smaller. The reasons for this behaviour are discussed in [32] and [33].

The results plotted in Fig. 3 have been obtained for $Re = 2.10^6$. Similar tests have been carried out for other Reynolds numbers. In the whole region covered

$$0.6 \times 10^6 \leq Re \leq 2.0 \times 10^6$$

no influence of Reynolds number on the overall characteristics of the wing has been found. This does not mean that there are no Reynolds number effects in details but if one is interested only in forces and moments on a slender sharp-edged wing the Reynolds number is not an important parameter.

3.2 Vortex formation over the wing in the case of laminar boundary-layer separation

Detailed flow studies have been carried out at an angle of incidence of $\alpha = 20.5^\circ$ since for this special value the pressure distribution has been calculated by J.H.B. Smith [22]. The Reynolds number was $Re = 0.9 \times 10^6$. In this case the boundary layers at the lower surface as well as in the unseparated parts of the upper surface of the wing were laminar [9].

3.2.1 Pressure distribution

The pressure distribution measured at $\alpha = 20.5^\circ$ and $Re = 0.9 \times 10^6$ in four sections on both sides of the wing is shown in Fig. 4. It turns out that the flow is markedly non-conical on the upper and lower surface. The experimental results are compared with results of the conical flow theory of J.H.B. Smith [22]. Only in the forward part of the wing the real flow is nearly conical but reasonable values for the pressure coefficient are predicted by the conical flow theory only in the inner part of the wing. The value for the minimum pressure and the slope of the pressure distribution in the region between the suction peak and the leading-edge differ very much between theory and experiment. This is due to the fact that the secondary separation has not been taken into account in the theory. Slender body theory after R.T. Jones [36], which is also drawn for comparison, leads to unacceptable results even for the lower surface since the separation of the flow is not at all taken into account.

3.2.2 Oilflow patterns

The oilflow patterns taken for $\alpha = 20.5^\circ$ and $Re = 0.9 \times 10^6$ are shown in Fig. 3. The lower side boundary layer is completely laminar and this applies also for the upper surface in the region between the secondary separation lines. On the upper surface the flow separates at $y/s_1(x) = \pm 0.67$. This position is very close to the suction peak according to Fig. 4 corresponding to the point of inflexion of the wall streamlines in Fig. 5. In the case of the separation of a laminar boundary layer the secondary separation starts at great distance from the leading-edge and leads to a relatively large and strong secondary vortex. A detailed analysis [9] by comparing Figs. 4 and 5 led to the understanding that in this case also tertiary separations underneath the secondary vortex are present.

Finally it is remarkable that the flow at the wing surfaces turns out to be conical whereas the pressure distribution according to Fig. 4 is non-conical. This leads to the conclusion that the deviations from a conical flow are mainly due to a nonlinear slope of the height of the leading-edge vortices over the upper surface of the wing.

3.2.3 Bound vortex lines

Some results of the measurements of the three-dimensional laminar boundary-layers on the present wing at $\alpha = 20.5^\circ$ and $Re = 0.9 \times 10^6$ have been published by J.C. Cooke [35]. These results are not discussed in detail here but it must be mentioned that the velocity profiles of the three-dimensional laminar boundary layer are skewed up to 25° . This means that it is not possible to conclude from oilflow patterns - which show the local direction of the wall shear stress - to the flow direction at the outer edge of the boundary layer.

The velocity vectors at the outer edges of the upper and lower surface boundary layers have been determined from the boundary-layer measurements. The result has been published in [9]. From the vector difference between upper and lower surface the vorticity vectors have been evaluated according to equ. (3). The result is shown in Fig. 6. In the right-hand side of this figure the vorticity vectors determined from the measurements are drawn. In all sections $x = \text{const.}$ the vorticity increases from the wing center line outwards. In the region beneath the axis of the leading-edge vortex a maximum of vorticity is reached. The field of vorticity vectors characterizes the shape of the bound vortex lines since the vorticity vector is tangential to the bound vortex lines. Large vorticity at a certain station indicates that the bound vortex lines lie very close together there.

The bound vortex lines have been calculated for the present case by J.H.B. Smith [22]. Some of them are drawn on the right-hand side of Fig. 6. For a better comparison some bound vortex lines have been evaluated from the measurements by integration. The result is plotted in the left-hand side of Fig. 6. In the forward part of the wing there is a good agreement between theory and experiment apart from the deviations in the region of the secondary vortex. In the rearward parts of the wing large differences between conical flow theory and experiments occur which correspond to the results for the pressure distribution. The poor results according to slender body theory after R.T. Jones [36] are due to the fact that this attached flow theory leads to the wrong sign for the v-component at the upper surface of the wing.

From the slope of the bound vortex lines in the lifting surface some qualitative conclusions on the flow downstream of the trailing-edge of the wing can be drawn. The vorticity vectors close to the trailing-edge indicate that behind the wing trailing vortices should occur the rotation of which is opposite to that of the leading-edge vortex. This conclusion coincides with observations originally published by B.J. Elle, J.P. Jones [37].

3.3 Vortex formation over the wing in the case of turbulent boundary-layer separation

The flow studies at an angle of incidence of $\alpha = 20.5^\circ$ have been repeated using artificially turbulent boundary layers as described in section 2.2.4. The Reynolds number was again $Re = 0.9 \times 10^6$ but in this case the boundary layers on the suction side were turbulent in the regions $y/s_1(x) \gtrless \pm 0.5$ [10].

3.3.1 Pressure distribution

The pressure distribution measured in four sections on both sides of the wing is plotted in Fig. 7. The flow is again markedly non-conical. Compared with the pressure distribution for laminar boundary layers according to Fig. 4 much higher suction peaks are reached and the position of the minima is more outwards in the turbulent case. The relative pressure minima in the region of the secondary vortex are much lower than in the laminar case. The integral over the pressure distribution, however, is about the same for both pressure distributions. Therefore the overall characteristics of slender delta wings are independent of Reynolds number though marked differences in the pressure distribution may be present for different Reynolds numbers.

In the forward part of the wing the experimental results are in good agreement with the conical flow theory of J.H.B. Smith [22]. The position of the suction peak is well predicted by the theory. The measured magnitude of the suction peak is lower than predicted by the theory but if the additional low pressures measured in the region of the secondary vortex are taken into account the lift of the front part of the wing is again

well predicted by the theory.

3.3.2 Oilflow pattern

In the present case the oilflow pattern of the lower side of the wing is the same as shown in Fig.5a. The oilflow pattern of the upper side is given in Fig.8. In comparison with Fig.5b the artificially turbulent boundary layer is longer attached. The secondary separation occurs at $y/s_1(x) = \pm 0.8$. The distance between the secondary separation line and the leading-edge is small. In the case of a separating turbulent boundary layer the secondary vortex is small and weak.

From the present investigations the following conclusions on the effect of a secondary vortex on the flow field of the leading-edge vortex can be drawn. Starting point may be a potential flow theory of the leading-edge separation without any consideration of a secondary vortex, which leads to a pressure distribution with a suction peak on the upper surface as calculated for instance by J.H.B. Smith [22]. In real flow a secondary vortex occurs and its effect on the flow field is twofold:

- i) Displacement effect. The boundary layer displacement thickness is increased very much in the region of the secondary vortex if this vortex is regarded as belonging to the boundary layer. The displacement effect on the flow field is a dislocation of the axis of the leading-edge vortex upwards and inwards. For constant circulation of the leading-edge vortex the upward shift of its axis leads to a reduction of the suction peak on the upper surface of the wing.
- ii) Vorticity effect. The formation of a concentrated secondary vortex leads to additional velocities at the wing surface in its vicinity. Therefore in the neighbourhood of the secondary vortex suction is increased locally.

Both effects cancel with respect to the lift of a section $x = \text{const.}$. For smaller secondary vortices (separation of a turbulent boundary layer) the main effect is the reduction of the suction peak accompanied by a slight increase of suction in the secondary vortex region. For large secondary vortices (separation of a laminar boundary layer) these effects are enlarged and in addition the inward shift of the axis of the leading-edge vortex is more distinctly marked.

These results indicate that for comparisons with a potential flow theory without any secondary separations, experiments should be used in which the boundary layers were turbulent. In this case it can be expected that the positions of the suction peak coincide and only slight differences occur between theory and experiment with respect to the magnitude of the suction peak and the slope of the pressure distribution in the region of the secondary vortex.

3.3.3 Bound vortex lines

The vorticity vectors and the bound vortex lines have been determined from the measurements of the turbulent boundary layers too. The result is shown in Fig.9. It is very similar to that for laminar boundary layers in Fig.6. A detailed analysis [10] has shown that the experimental results for turbulent boundary layers are slightly closer to the nonlinear theory of J.H.B. Smith [22] than those for laminar boundary layers.

The vorticity vectors in the vicinity of the wing trailing-edge indicate that trailing vortices should occur the rotation of which is opposite to that of the leading-edge vortex. In the vicinity of the trailing-edge exist remarkable differences between the laminar and turbulent boundary layer results. In the case of laminar boundary layers according to Fig.6 the vorticity level at the trailing-edge is much higher than in the case of turbulent boundary layers. Therefore it must be expected that the rolling up of the trailing vortex sheet will also be different for both cases.

3.4 Vortex formation behind the wing in the case of turbulent boundary layers at the trailing-edge

3.4.1 Qualitative results

The slope of the bound vortex lines in the vicinity of the wing trailing-edge indicates that free vortices should occur the rotation of which is opposite to that of the leading-edge vortex. A schematic view of the flow field, based on water-tunnel investigations, has been given by B.J. Elle, J.P. Jones [37] and D. Hummel, G. Redeker [10]. It is shown in Fig.10a. Similar shapes of the free vortex sheet have been suggested by R.L. Maltby and published by D. Küchemann [12] and J.H.B. Smith [24].

Flow studies in a water-tunnel [10] have shown that a concentrated trailing vortex is formed downstream of the wing trailing-edge. Its origin at the wing lies in the region where the secondary vortex reaches the trailing-edge of the wing and its rotation has the same sense as that of the secondary vortex. However, it has been made sure by D. Hummel, G. Redeker [10] that the concentrated trailing vortex and the secondary vortex are two separate vortices. Their interference is still unknown.

The counter-rotating trailing vortex leads to a very heterogeneous downwash field behind the wing. D. Küchemann [23] has pointed out that this might be the reason for the relatively high induced drag of slender wings.

3.4.2 Status of the boundary layers on the wing

The investigations of the flow field behind the $A = 1$ delta wing at $\alpha = 20.5^\circ$ have been carried out at a Reynolds number of $Re = 2.0 \times 10^6$. The oilflow patterns of both sides of the wing for these conditions are shown in Fig. 11. The lower surface boundary layer is laminar up to the flat ridge near the trailing-edge of the wing. At the ridge transition takes place and at the trailing-edge an attached turbulent boundary layer is present. At the upper surface a natural transition from laminar to turbulent boundary layer flow takes place at $x_t/c_1 = 0.43$ corresponding to a transition Reynolds number of

$$Re_t = \frac{x_t V_\infty}{\nu} = 0.86 \times 10^6.$$

This value is in good agreement with the relation $Re_t(\alpha)$ given by D. Hummel [8]. The change of the structure of the boundary layer leads to the well known outwards shift of the secondary separation line which is distinctly marked in Fig. 11b. At the trailing-edge a turbulent boundary layer is present. The flow is attached in the inner region and secondary separation is observed at $y/s = \pm 0.83$.

These results mean that the investigations on the vortex formation behind the wing have been carried out for the case of a small and weak secondary vortex as well as for relatively weak counter-rotating trailing vorticity.

3.4.3 Formation of a concentrated trailing vortex

The total pressure contours in four planes downstream of the wing are shown in Fig. 12. As the starting point the corresponding results of boundary layer measurements at the trailing-edge ($\xi = 0$) are added. The attached boundary layers in the inner region of the trailing-edge as well as the secondary vortex marked by increased total pressure losses in the outer region on the upper surface of the wing are clearly indicated. The position of the secondary separation line at $y/s = 0.83$ coincides with the oilflow pattern according to Fig. 11b.

In all four planes behind the wing the vortex sheet is marked by a relative minimum and the center of the leading-edge vortex by the absolute minimum of total pressure. A short distance downstream of the trailing-edge ($\xi = 0.08$) the trailing vortex sheet is distinctly warped at about $\eta = 0.7$. In the next plane ($\xi = 0.267$) downstream this effect has increased. It is an open question whether or not a small concentrated vortex is already present at this station. In the two planes further downstream ($\xi = 0.533$ and $\xi = 1.066$) a concentrated trailing vortex has been found. The total pressure losses increase very much towards the center of this trailing vortex. The shape of the trailing vortex sheet which forms the concentrated trailing vortex and which is connected with the vortex sheet originating from the leading-edge is clearly indicated by relative minima of the total pressure.

The origin of the concentrated trailing vortex at the wing trailing-edge lies at about $\eta = 0.7$. In comparison with Fig. 9 this is exactly the region where the largest vorticity vectors in the lifting surface have been determined. Downstream of the wing the position of maximum warp of the vortex sheet and later of the center of the concentrated trailing vortex moves outwards and upwards. This motion is due to the fact, that the concentrated trailing vortex is embedded in the flow field of the dominant leading-edge vortex which induces velocities at the trailing vortex which lead to a helical path of the trailing vortex around the leading-edge vortex.

The dynamic pressure contours in the four planes downstream of the wing are shown in Fig. 13. The center of the leading-edge vortex is characterized by large values of the dynamic pressure and the vortex sheets are marked by a relative minimum of the dynamic pressure. In the region below the warped trailing vortex sheet relatively large values of the dynamic pressure have been obtained. This might be due to the fact that the counter-rotating trailing vorticity vectors are directed outwards in this region and thus induce positive perturbation velocities beneath the vortex sheet. During the process of the formation of the concentrated trailing vortex the regions of high dynamic pressure are always located between the rolling-up vortex sheet and the center of the concentrated vortex.

The static pressure contours in the four planes downstream of the wing are shown in Fig. 14. The axis of the leading-edge vortex is marked by an extremely high suction peak. Close to the wing the pressure field is symmetrical with respect to a rotation around the vortex center with the exception of a slight increase of suction towards the region where the trailing vortex sheet warps ($\xi = 0.08$). At the very beginning of a concentrated trailing vortex ($\xi = 0.267$) a relative pressure minimum is formed. This minimum marks the center of the concentrated trailing vortex. It moves outwards and upwards with increasing distance behind the trailing-edge of the wing ($\xi = 0.533$ and $\xi = 1.066$).

Finally the components of the local velocity vectors in the $\bar{y}\bar{z}$ -planes are shown in Fig. 15. The leading-edge vortex with increasing velocities towards its center as well as the concentrated trailing vortex, having the opposite sense of rotation, are clearly indicated. The vortex sheets have to be tangential with the local flow direction. The cross-flow components which appear in Fig. 15 at the vortex sheets are due to the fact that the vortex sheets are not perpendicular to the $\bar{y}\bar{z}$ -planes. In order to verify the tangential flow condition the component v_z/V_∞ has to be added perpendicular to the $\bar{y}\bar{z}$ -planes and the resulting local velocity vector \vec{v} is then tangential with the vortex sheet. Far away from the origin $\bar{y} = \bar{z} = 0$ the arrows tend to zero, since the free stream

velocity V_{∞} has no component in the $\bar{y}\bar{z}$ -planes. In all planes $\xi = \text{const.}$ the value zero is approached rapidly at low ξ and high η since in this region the perturbation velocities induced by the whole vortex system cancel largely.

3.4.4 Slope of the secondary vortex behind the wing

In the total pressure contours according to Fig.12 the secondary vortex is indicated by large total pressure losses on the upper surface in the outer region, $\bar{y}/s > 0.83$, of the trailing-edge ($\xi = 0$).

In the plane $\xi = 0.08$ the same total pressure losses are found in the corner between the leading-edge vortex sheet and the trailing-edge vortex sheet. This indicates that the secondary vortex is located far away from the origin of the trailing vortex. In the dynamic pressure contours of Fig.13 the secondary vortex is characterized by very low values of the dynamic pressure. In the static pressure contours according to Fig.14 no noteworthy pressure minimum is observed in the region of the secondary vortex. From Figs.13 and 14 it seems doubtful whether the secondary separation region has any longer a vortex type structure. It must be borne in mind that at the trailing-edge shedding of some vorticity into the secondary vortex has ceased and that this secondary vortex is now absorbed by viscous effects. A rotatory motion is not distinctly marked in the flow field at $\xi = 0.08$ in Fig.15.

Further downstream in the planes $\xi = 0.267, 0.533$ and 1.066 the total pressure contours in Fig.12 show that the total pressure losses originating from the secondary vortex run into the losses of the vortex sheet. The area of losses is no longer thickened at the upper surface of the vortex sheet. The vorticity of the secondary vortex seems to be absorbed by the vortex sheet, the only effect being large total pressure losses there. The sequence of planes in Fig.12 shows clearly that the remains of the secondary vortex roll into the trailing vortex. The same can be deduced from the movement of the dynamic pressure losses according to Fig.13.

3.4.5 Final remarks

From the present investigations the schematic view of the vortex formation behind a slender wing as shown in Fig.10a has to be corrected slightly. The result is drawn in Fig.10b. Compared with Fig.10a there are two differences. Firstly, the formation of the concentrated trailing vortex starts much more inboard than suggested so far. Secondly, the secondary vortex can be added. This vortex decays very rapidly and its remains roll up into the trailing vortex.

The present investigations have been carried out for turbulent boundary layers at the trailing-edge of the wing. This means that the formation of a weak trailing vortex and the decay of a small secondary vortex have been observed. In the case of laminar boundary layers at the trailing-edge the formation of a stronger trailing vortex and the decay of a larger secondary vortex should occur. For these conditions even larger effects must be expected. An experimental investigation of this kind is in progress.

4. CONCLUSIONS

A survey on experimental investigations on an $A = 1$ delta wing is given. The flow field has been studied in detail for an angle of incidence of $\alpha = 20.5^\circ$. The free vortex sheets generated at the leading-edges of the wing roll up into the well known leading-edge vortices which are accompanied by a pair of secondary vortices at the wing surface as a result of boundary layer separations.

The flow at the wing has been studied by means of pressure distribution measurements and by visualization of the flow at the surface of the wing using the oilflow technique. These experiments have been carried out for laminar and turbulent boundary layers. In both cases the flow field was non-conical. The presence of a secondary vortex has two main effects on the flow field: Firstly, there exists a displacement effect by which the center of the leading-edge vortex is shifted inwards and upwards, corresponding to an inward movement and a reduction of the suction peak of the pressure distribution. Secondly, there exists a vorticity effect, which increases suction in the region of the secondary vortex. The two effects are small for turbulent boundary layers and large for laminar boundary layers, since turbulent boundary layers stay longer attached and form a small secondary vortex whereas laminar boundary layers separate early and lead to a large secondary vortex.

For laminar and turbulent boundary layers the bound vortex lines in the lifting surface have been determined from the experiments. In both cases in the front part of the wing the agreement with the nonlinear conical flow theory of J.H.B. Smith [22] is good. In the rear part of the wing the flow is non-conical. At the trailing-edge of the wing free vortices are shed the rotation of which is opposite to that of the leading-edge vortex. For laminar boundary layers the vorticity of these trailing vortices is larger than in the case of turbulent boundary layers at the trailing-edge.

The flow downstream of the wing trailing-edge has been studied by measuring the flow field in four planes perpendicular to the free stream for the case of turbulent boundary layers at the trailing-edge. The formation of a concentrated trailing vortex is described the rotation of which is opposite to that of the leading edge vortex. The trailing vortex starts at about 70% of the semispan and moves downstream on a helical

path around the leading-edge vortex. At the center of the trailing vortex high velocities as well as minima of total pressure and static pressure have been found. The secondary vortex decays rapidly downstream of the wing trailing-edge. Its remains are found rolling up into the trailing vortex.

The positions of the vortex sheets and of all concentrated vortices in relation to the wing are given quantitatively. They are now available for comparison with theoretical results.

5. ACKNOWLEDGEMENTS

The author is very much indebted to the late Professor Dr.rer.nat. Dietrich Küchemann for his encouragement to carry out these investigations.

6. REFERENCES

- [1] H. Winter: Strömungsvorgänge an Platten und profilierten Körpern bei kleinen Spannweiten. *Forschg. Ing.-Wes.* 6 (1935), 67-71
- [2] P.T. Fink: Wind-tunnel tests on a slender delta wing at high incidence. *Z. Flugwiss.* 4 (1956), 247-249
- [3] D.J. Marsden, R.W. Simpson, W.J. Rainbird: The flow over delta wings at low speeds with leading-edge separation. College of Aeronautics, Cranfield, Rep. 114 (1958)
- [4] N.C. Lambourne, D.W. Bryer: Some measurements in the vortex flow generated by a sharp leading-edge having 65° sweep. *ARC CP* 477 (1959)
- [5] D.H. Peckham: Low speed wind-tunnel tests on a series of uncambered slender pointed wings with sharp edges. *RAE Rep. Aero* 2613 (1958), *ARC Rep. Mem.* 3186 (1961)
- [6] P.B. Earnshaw, J.A. Lawford: Low-speed wind-tunnel experiments on a series of sharp-edged delta wings. Part I: Forces, moments, normal force fluctuations and positions of vortex breakdown. *RAE TN Aero* 2780 (1961)
- [7] J.A. Lawford: Low-speed wind-tunnel experiments on a series of sharp-edged delta wings. Part II: Surface flow patterns and boundary layer transition measurements. *RAE TN Aero* 2954 (1964)
- [8] D. Hummel: Experimentelle Untersuchung der Strömung auf der Saugseite eines schlanken Deltaflügels. *Z. Flugwiss.* 13 (1965), 247-252
- [9] D. Hummel: Zur Umströmung scharfkantiger schlanker Deltaflügel bei großen Anstellwinkeln. *Z. Flugwiss.* 15 (1967), 376-385
- [10] D. Hummel, G. Redeker: Experimentelle Bestimmung der gebundenen Wirbellinien sowie des Strömungsverlaufs in der Umgebung der Hinterkante eines schlanken Deltaflügels. *Abhandlg. d. Braunsch. Wiss. Ges.* 22 (1972), 273-290
- [11] D. Küchemann: Aircraft shapes and their aerodynamics for flight at supersonic speeds. In: *Proceedings of the Second Internat. Congr. in the Aeronaut. Sciences*, Zürich 1960. *Advances in Aeronautical Sciences*, Vol. 3, Pergamon Press Oxford/London/New York/Paris 1962, 221-252
- [12] D. Küchemann: Die aerodynamische Entwicklung von schlanken Flügeln für den Überschallflug. *Jb. 1962 d. WGLR*, 66-77
- [13] J.H.B. Smith: A review of separation in steady, three-dimensional flow. *AGARD-CP* 168 (1975), 31-1 to 31-17
- [14] D.J. Peake: Controlled and uncontrolled flow separation in three dimensions. *NAE Aeron. Rep.* LR-591 (1976)
- [15] W. Bollay: A non-linear wing theory and its application to rectangular wings of small aspect ratio. *ZAMM* 19 (1939), 21-35
- [16] K. Gersten: Nichtlineare Tragflächentheorie, insbesondere für Flügel mit kleinem Seitenverhältnis. *Ing. Archiv* 30 (1961), 431-452
- [17] E.C. Polhamus: A concept of the vortex lift of sharp-edged delta wings based on a leading-edge-suction analogy. *NASA TN-D* 3767 (1966)
- [18] J.E. Lamar: Prediction of vortex flow characteristics of wings at subsonic and supersonic speeds. *J. Aircraft* 13 (1976), 490-494
- [19] R. Legendre: Ecoulement au voisinage de la pointe avant d'une aile à forte flèche aux incidences moyennes. 8ème Congr. Int. Méc. App. Istanbul 1952, *Rech. Aéro.* 30 (1952) et 31 (1953)
- [20] C.E. Brown, W.H. Michael: Effect of leading-edge separation on the lift of a delta wing. *J. Aero. Sci.* 21 (1954), 690-694 and 706, *NACA TN* 3430 (1955)
- [21] K.W. Mangler, J.H.B. Smith: A theory of the flow past a slender delta wing with leading-edge separation. *Proc. Roy. Soc. Lond. A* 251 (1959), 200-217, *RAE Rep. Aero* 2593 (1957)
- [22] J.H.B. Smith: Improved calculations of leading-edge separation from slender delta wings. *Proc. Roy. Soc. Lond. A* 306 (1968), 67-90 *RAE Tech. Rep.* 66070 (1966)

- [23] D. Küchemann: Entwicklungen in der Tragflügeltheorie. 11. Ludwig-Prandtl-Gedächtnis-Vorlesung. Jb. 1967 der WGLR, 11-22
- [24] J.H.B. Smith: Inviscid fluid models, based on rolled-up vortex sheets, for three-dimensional separation at high Reynolds number. RAE Tech. Memo. Aero 1738 (1977)
- [25] R.K. Nangia, G.J. Hancock: A theoretical investigation for delta wings with leading-edge separation at low speeds. ARC CP 1086 (1968)
- [26] T.K. Matoi, E.E. Covert, S.E. Widnall: A three-dimensional lifting-surface theory with leading-edge vortices. ONR-CR-215-230-2 (1975)
- [27] C. Rehbach: Numerical investigation of leading-edge vortex for low aspect ratio thin wings. AIAA J. 14 (1976), 253-255
- [28] O.A. Kandil, D.T. Mook, A.H. Nayfeh: Nonlinear prediction of the aerodynamic loads on lifting surfaces. J. Aircraft 13 (1976), 22-28
- [29] J.A. Weber, G.W. Brune, F.T. Johnson, P. Lu, P.E. Rubbert: Three-dimensional solution of flows over wings with leading-edge vortex separation. AIAA J. 14 (1976), 519-525, NASA CR 132709 and 132710 (1975)
- [30] F.T. Johnson, P. Lu, G.W. Brune, J.A. Weber, P.E. Rubbert: An improved method for the prediction of completely three-dimensional aerodynamic load distributions on configurations with leading-edge separation. AIAA Paper 76-147 (1976)
- [31] F.T. Johnson, P. Lu, G.W. Brune, J.A. Weber, P.E. Rubbert: Application of a higher order subsonic panel method to configurations with free vortex flow. EUROMECH Colloqu. 75, Rhode (Braunschweig), 1976
- [32] D. Hummel: Untersuchungen über das Aufplatzen der Wirbel an schlanken Delta-Flügeln. Z. Flugwiss. 13 (1965), 158-168
- [33] D. Hummel, P.S. Srinivasan: Vortex breakdown effects on the low-speed aerodynamic characteristics of slender delta wings in symmetrical flow. J. Roy. Aeron. Soc. 71 (1967), 319-322
- [34] D. Hummel, G. Redeker: Ueber den Einfluß des Aufplatzens der Wirbel auf die aerodynamischen Beiwerte von Deltaflügeln mit kleinem Seitenverhältnis beim Schiebflug. Jb. 1967 der WGLR, 232-240
- [35] J.C. Cooke: Laminar boundary layer calculations compared with measurements by Hummel. RAE Tech. Rep. 67227 (1967), ARC CP 1096 (1967)
- [36] R.T. Jones: Properties of low-aspect-ratio pointed wings at speeds below and above the speed of sound. NACA Rep. 835 (1946)
- [37] B.J. Elle, J.P. Jones: A note on the vorticity distribution on the surface of slender delta wings with leading-edge separation. J. Roy. Aero. Soc. 65 (1961), 195-198

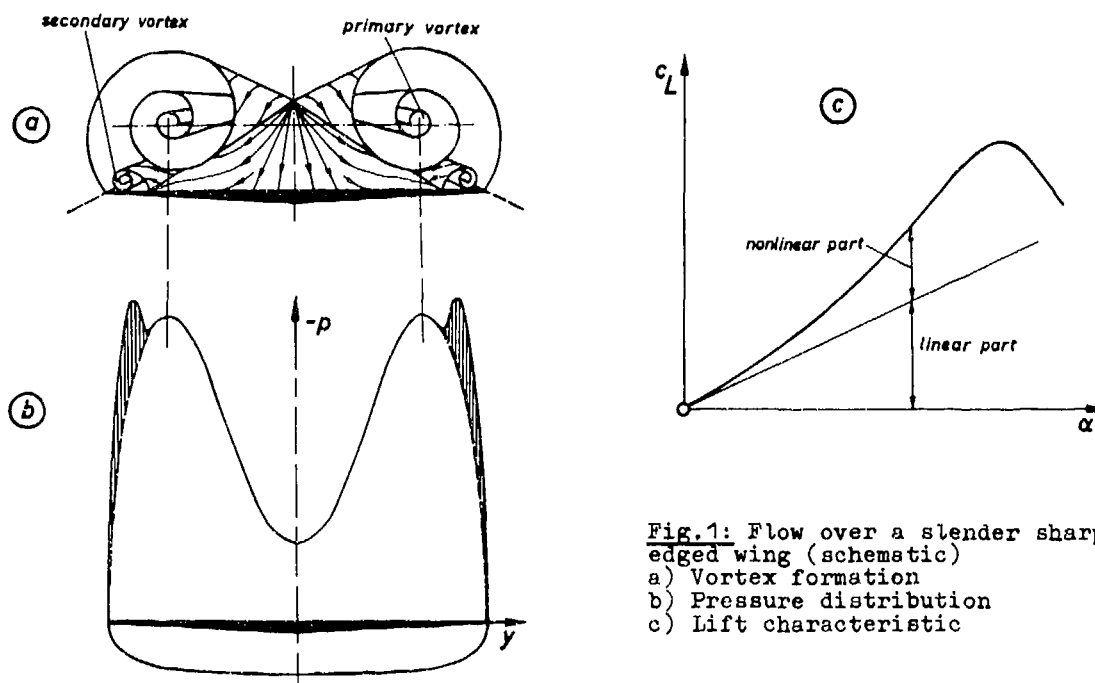


Fig.1: Flow over a slender sharp-edged wing (schematic)
a) Vortex formation
b) Pressure distribution
c) Lift characteristic

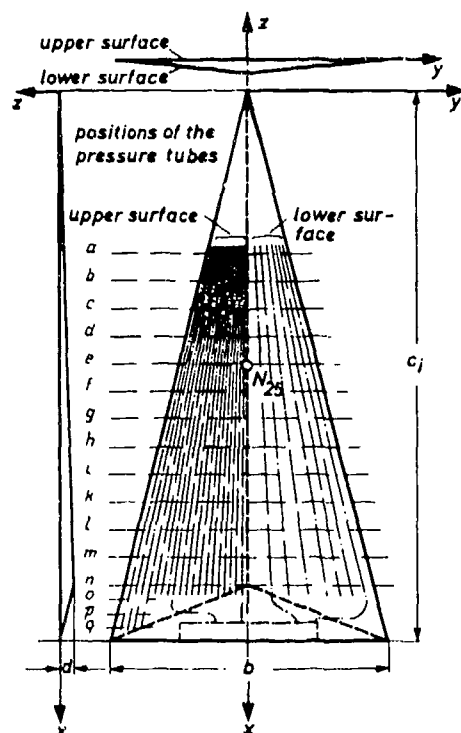


Fig. 2: Wind-tunnel model of delta wing $A = 1$

N_{25} : Quarter chord point of mean aerodynamic chord, situated at $x/c_1 = 0.5$

Dimensions: Length : $c_1 = 750$ mm
Span : $b = 375$ mm
Thickness: $d = 16$ mm

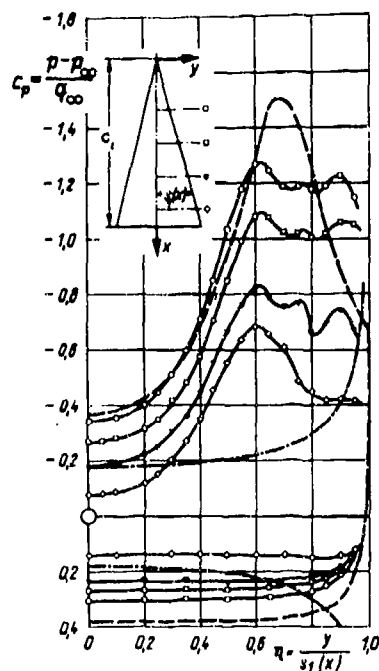


Fig. 4: Pressure distribution at the $A = 1$ delta wing at $\alpha = 20.5^\circ$ and $Re = 0.9 \times 10^6$, laminar boundary layers.

Experiments: Theories:
 $\circ x/c_1 = 0.3$ --- J.H.B. Smith [22]
 $\square x/c_1 = 0.5$ nonlinear, conical
 $\nabla x/c_1 = 0.7$ --- R.T. Jones [36]
 $\diamond x/c_1 = 0.9$ linear, conical

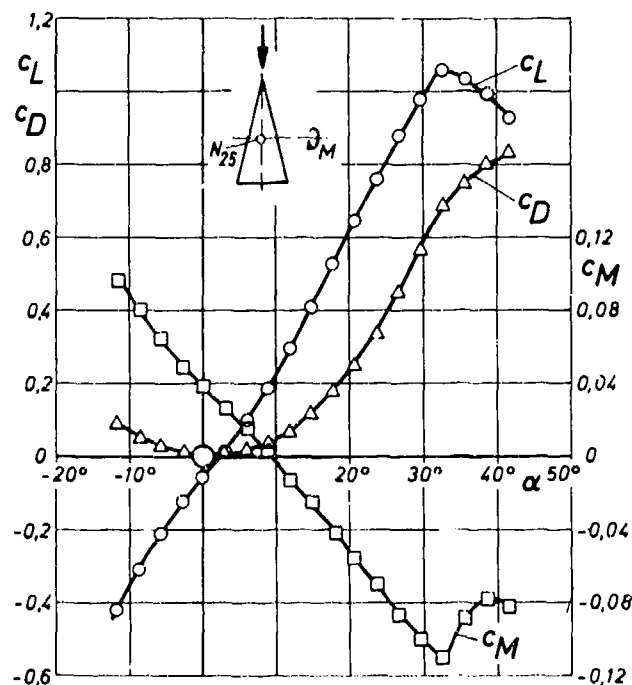


Fig. 3: Results of the three-component measurements on delta wing $A = 1$ at $Re = 2.10^6$.

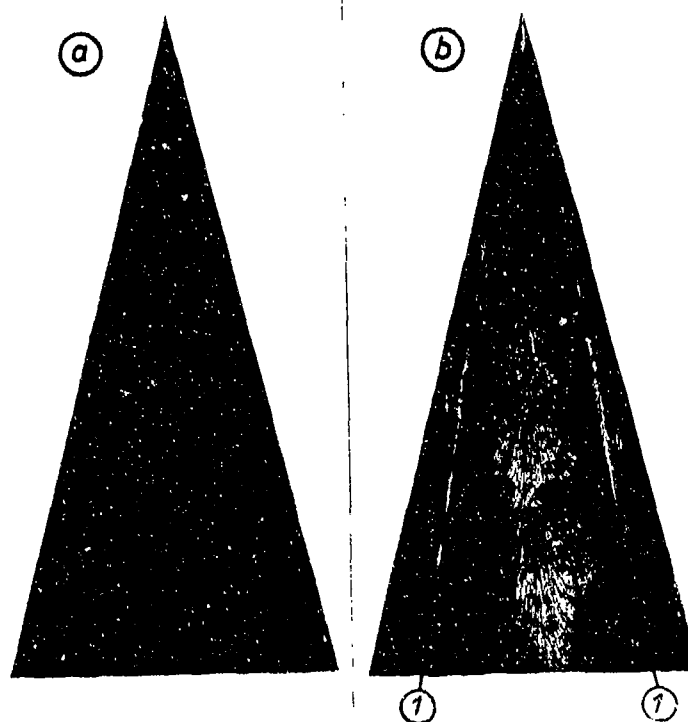


Fig. 5: Oilflow patterns at the $A = 1$ delta wing at $\alpha = 20.5^\circ$ and $Re = 0.9 \times 10^6$, boundary layers laminar.

a) lower surface
b) upper surface
① secondary separation line

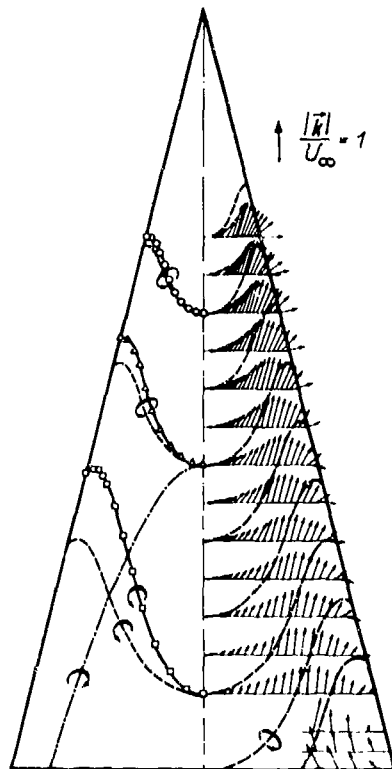


Fig. 6: Vorticity vectors (right-hand side) and bound vortex lines (left-hand side) at the $A = 1$ delta wing at $\alpha = 20.5^\circ$, boundary-layers laminar. Comparison of theory and experiment.

— Nonlinear theory, J.H.B. Smith [22]
 - - - Linear theory, R.T. Jones [36]

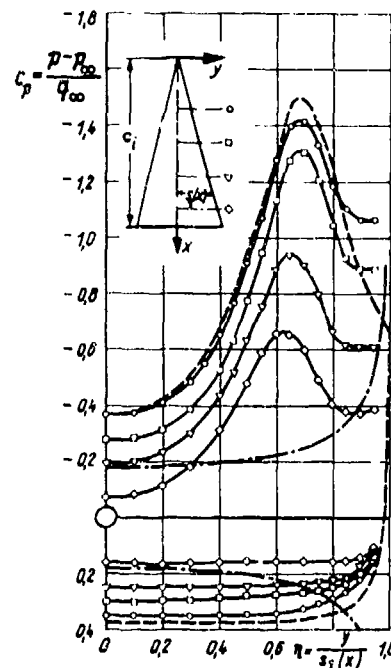


Fig. 7: Pressure distribution at the $A = 1$ delta wing at $\alpha = 20.5^\circ$ and turbulent boundary-layers.

Experiments:

○ $x/c_1 = 0.3$ ▽ $x/c_1 = 0.7$

□ $x/c_1 = 0.5$ ◇ $x/c_1 = 0.9$

Theories: — J.H.B. Smith [22],
 - - - R.T. Jones [36]



Fig. 8: Oilflow pattern at the upper surface of the $A = 1$ delta wing at $\alpha = 20.5^\circ$, artificially turbulent boundary-layers.

① secondary separation line
 ② turbulence generators

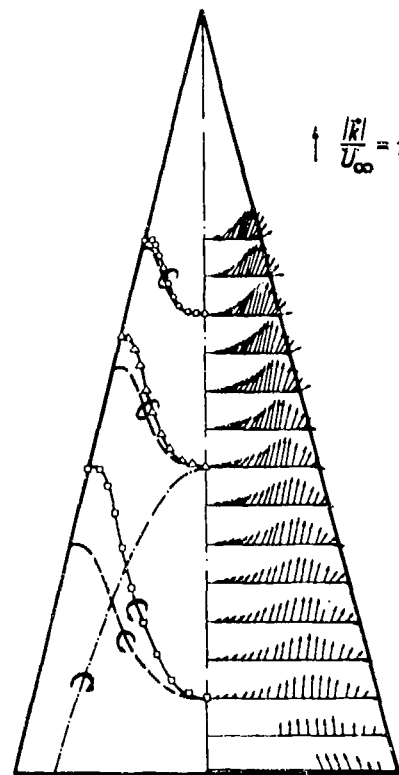


Fig. 9: Vorticity vectors (right-hand side) and bound vortex lines (left-hand side) at the $A = 1$ delta wing at $\alpha = 20.5^\circ$, boundary-layers turbulent. Comparison of theory and experiment.

— Nonlinear theory, J.H.B. Smith [22]
 - - - Linear theory, R.T. Jones [36]

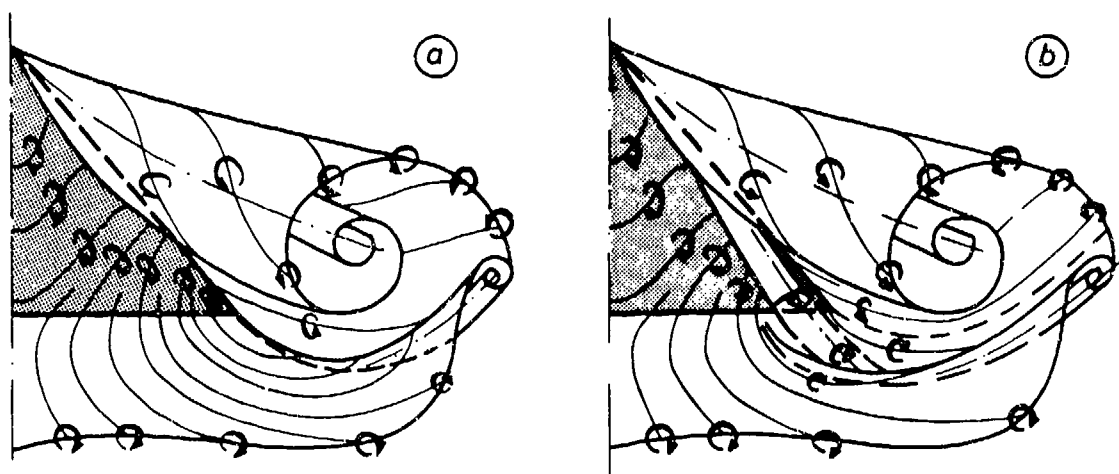


Fig.10: Vortex formation behind a slender delta wing (schematic)
 a) B.J. Elle, J.P. Jones [37], D. Hummel, G. Redeker [10]
 b) Present investigations

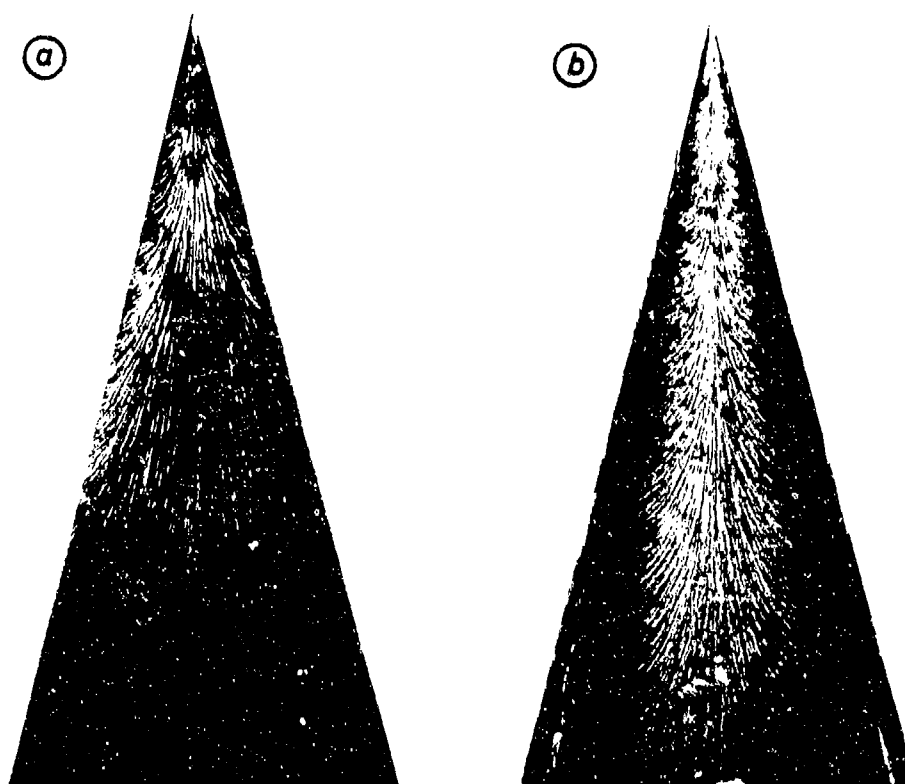
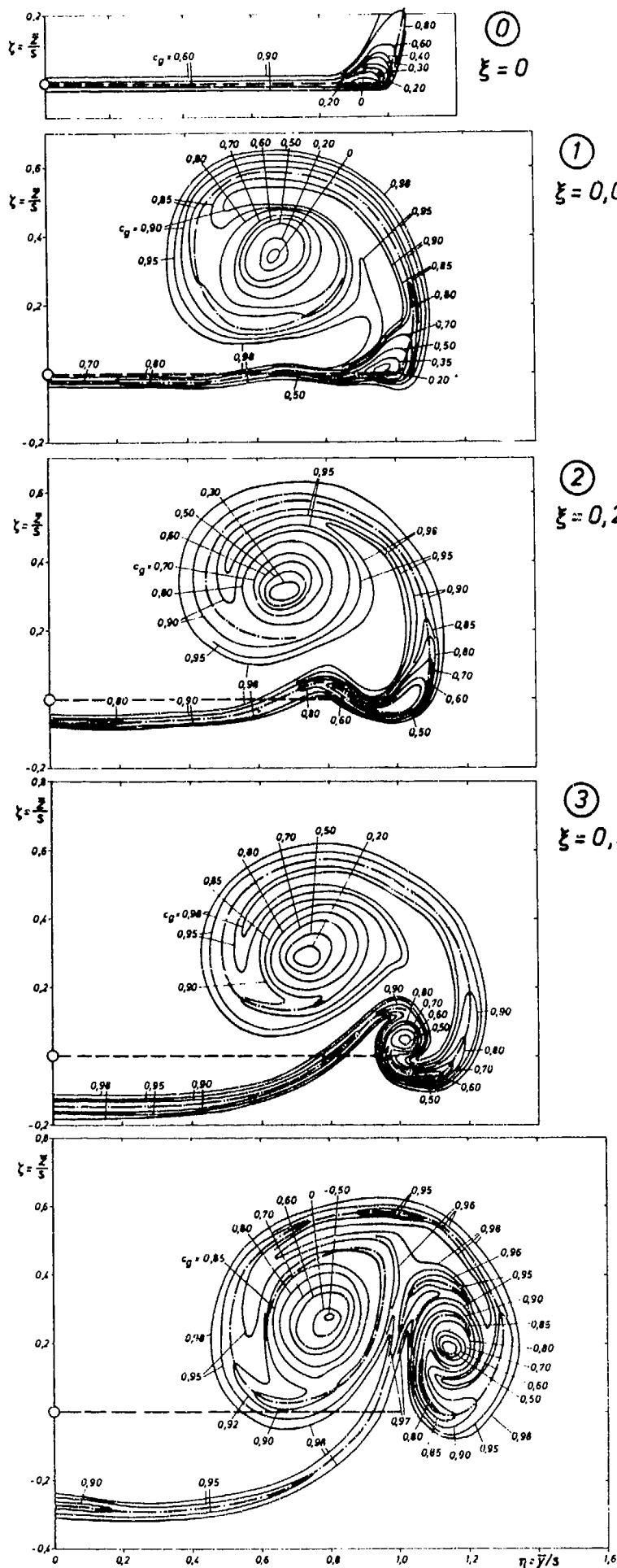
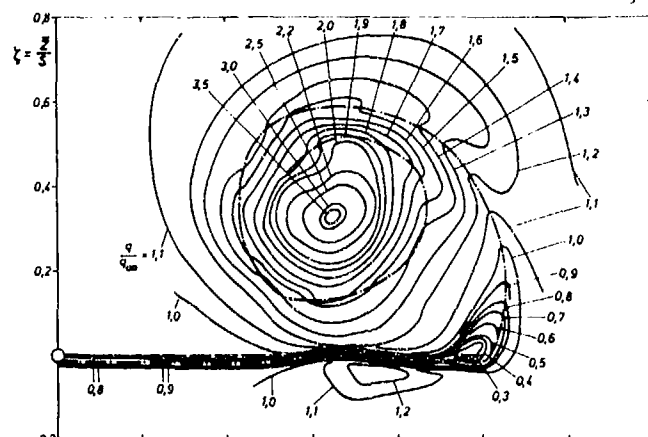


Fig.11: Oilflow patterns at the $A = 1$ delta wing at $\alpha = 20.5^\circ$ and $Re = 2.0 \times 10^6$.
 a) lower surface
 b) upper surface

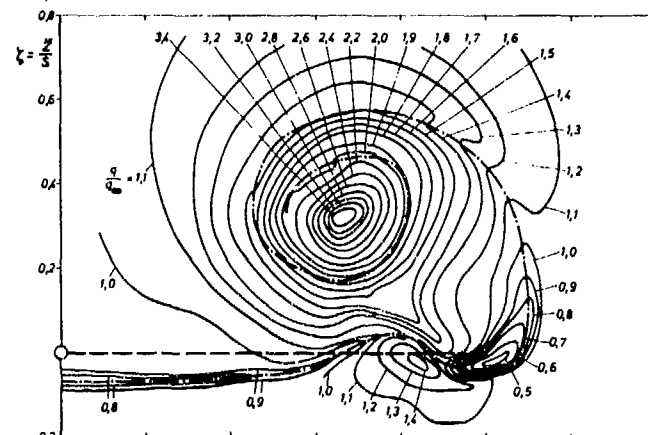


--- Projection of the wing
trailing-edge
--- Vortex sheet

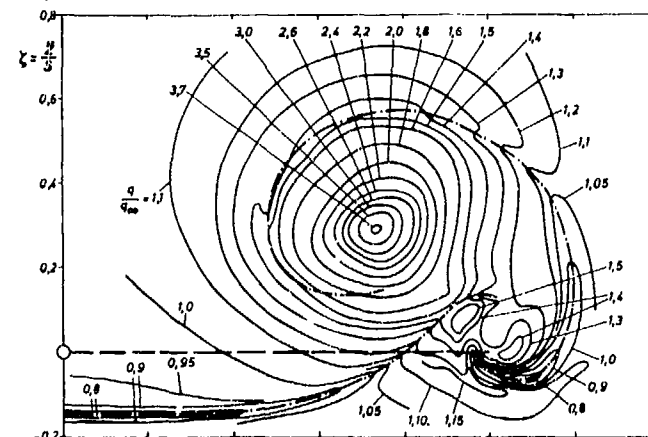
Fig.12: Distribution of total pressure in five planes behind the $A = 1$ delta wing at $\alpha = 20.5^\circ$ and $Re = 2.0 \times 10^6$. Lines $c_g = (p - p_\infty)/q_\infty = \text{const.}$



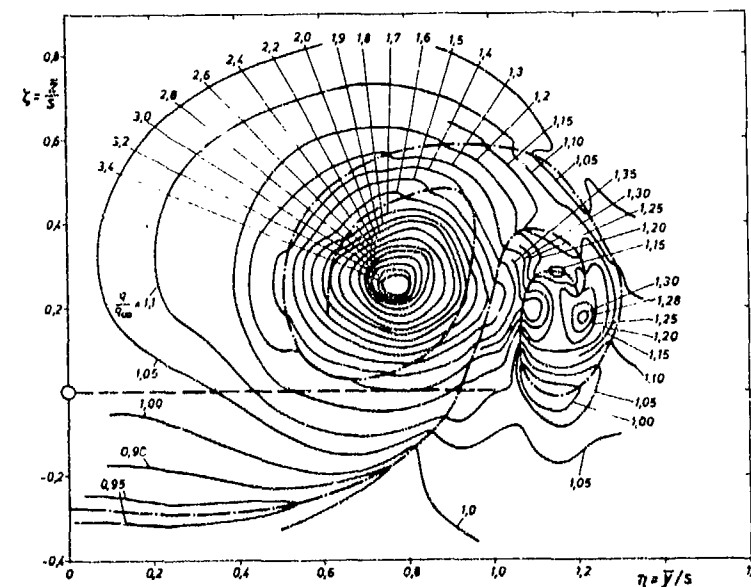
①
 $\xi = 0,08$



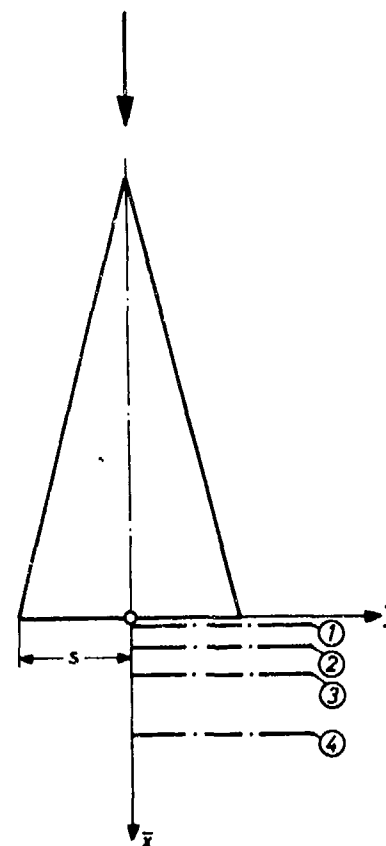
②
 $\xi = 0,267$



③
 $\xi = 0,533$

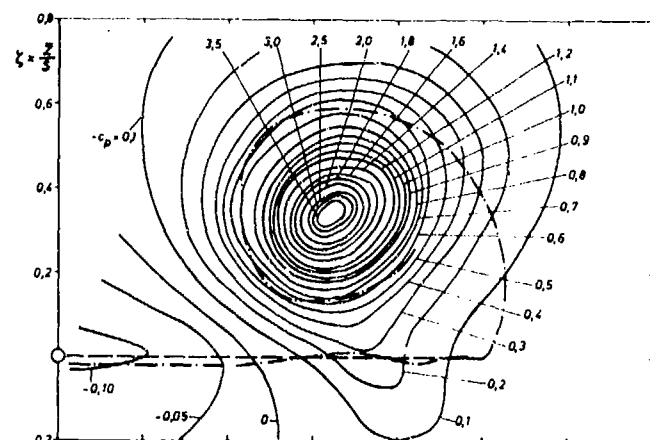


④
 $\xi = 1,066$

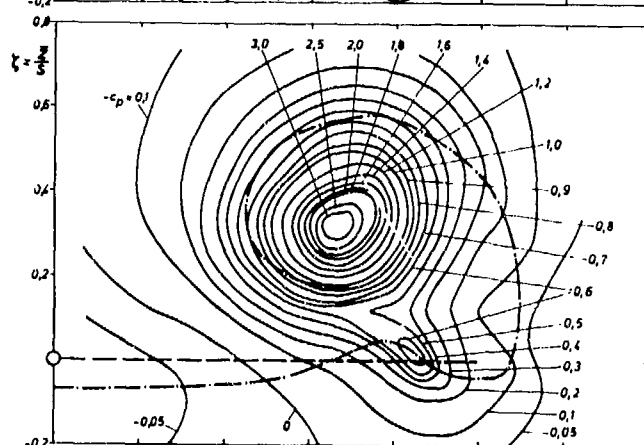


--- Projection of the wing
trailing-edge
-.- Vortex sheet

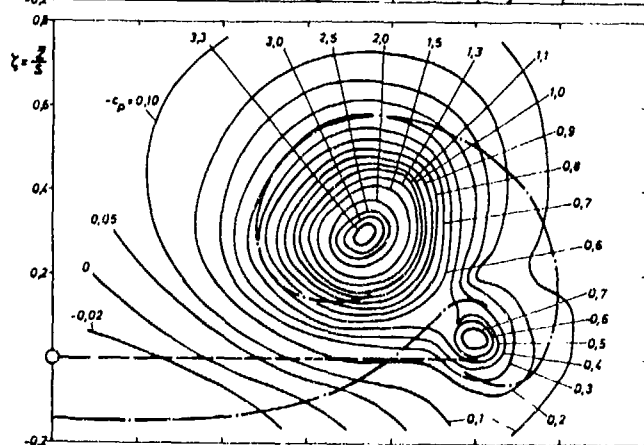
Fig.13: Distribution of dynamic pressure in four planes behind the $\Lambda = 1$ delta wing at $\alpha = 20.5^\circ$ and $Re = 2.0 \times 10^6$. Lines $c_q = q/q_\infty = \text{const.}$



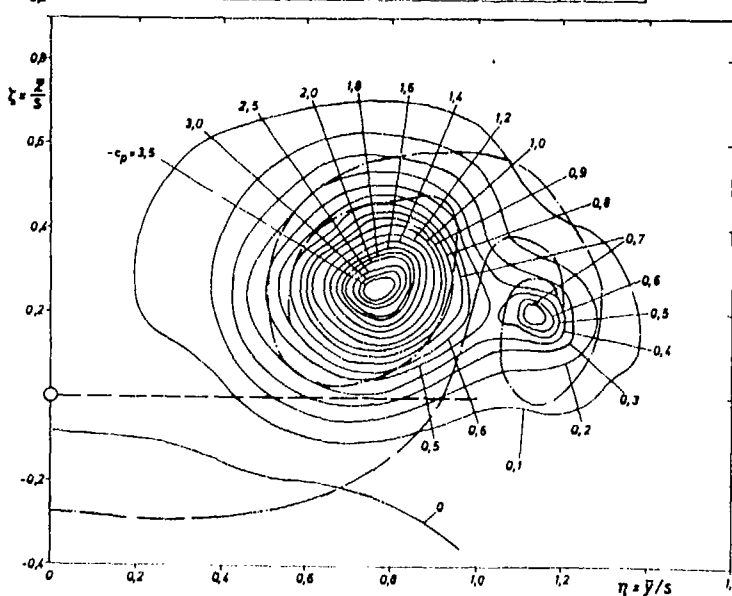
①
 $\xi = 0.08$



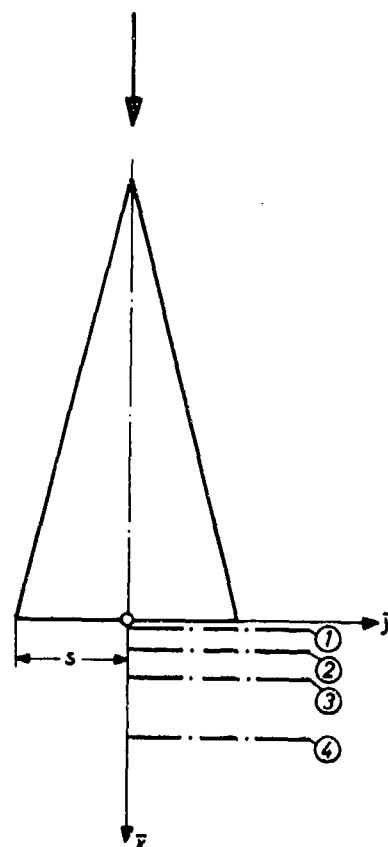
②
 $\xi = 0.267$



③
 $\xi = 0.533$



④
 $\xi = 1.066$



--- Projection of the wing
trailing-edge
--- Vortex sheet

Fig. 14: Distribution of static pressure in four planes behind the $\Delta = 1$ delta wing at $\alpha = 20.5^\circ$ and $Re = 2.0 \times 10^6$. Lines $-c_p = (p_\infty - p)/q_\infty = \text{const.}$

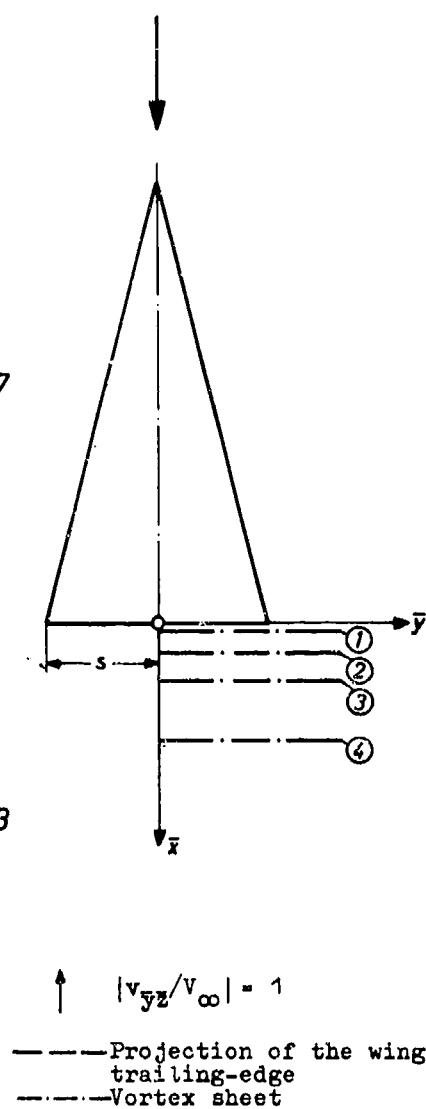
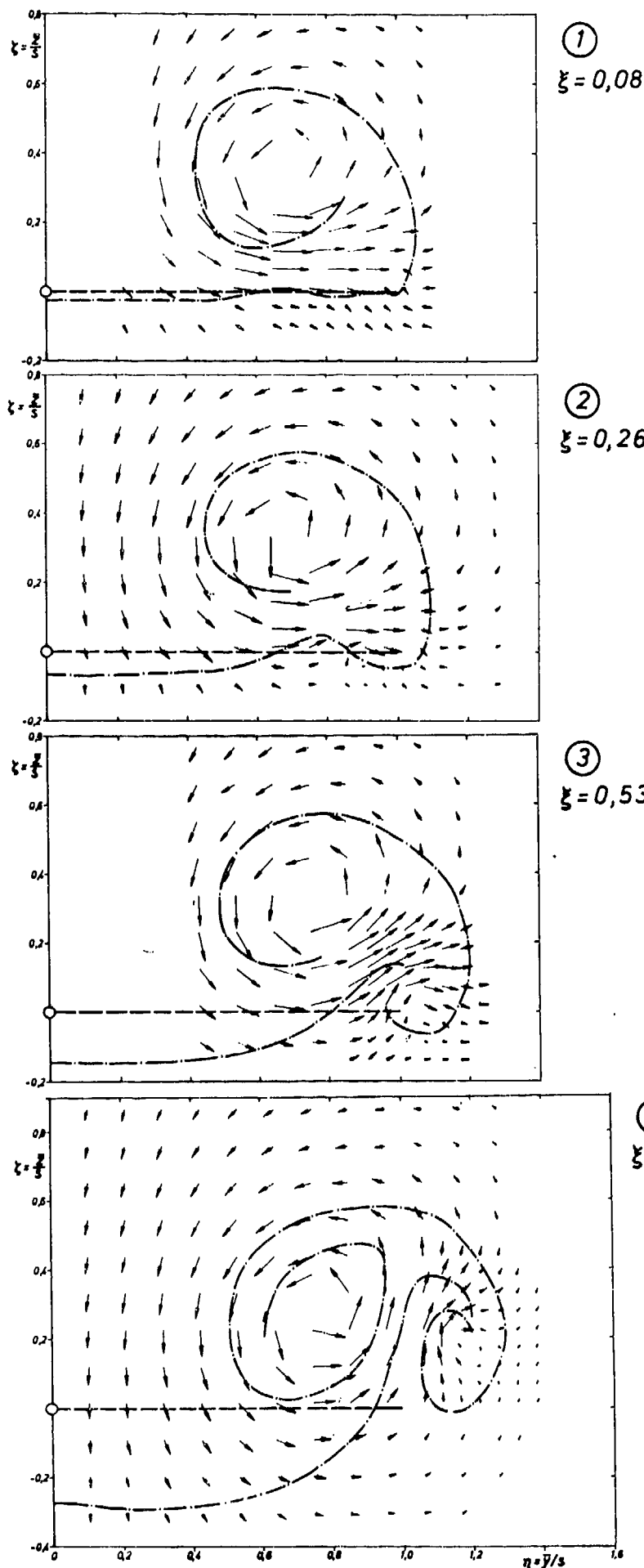


Fig. 15: Flow field in four planes behind the $A = 1$ delta wing at $\alpha = 20.5^\circ$ and $Re = 2.0 \times 10^6$. Component of the velocity vectors, v_{yz} , in the yz -plane

SYMMETRICAL AND ASYMMETRICAL SEPARATIONS ABOUT A YAWED CONE

David J. Peake
Senior NRC Research Associate
Ames Research Center, NASA
Moffett Field, California 94035, U.S.A.

F. Kevin Owen
Consultant, Owen International Inc.
Palo Alto, California 94302, U.S.A.

Hiroshi Higuchi
Research Scientist, Dynamics Technology Inc.
Torrance, California 90503, U.S.A.

SUMMARY

Three-dimensional flow separations about a 5° (semiapex angle, θ_c), 1.4-m (54-in.) long, circular cone up to moderately high relative incidences, $\alpha/\theta_c \sim 5$, have been investigated in the Mach number range $0.6 < M_\infty < 1.8$. The cone was tested in the Ames 1.8- by 1.8-m (6- by 6-ft) Wind Tunnel at Reynolds numbers, R_{L_∞} , based on the cone length, L , from 4.5×10^6 to 13.5×10^6 , under nominally zero heat transfer conditions. Overall forces and mean surface pressures were compared with earlier measurements made in the NAE Ottawa 1.5- by 1.5-m (5- by 5-ft) Blowdown Wind Tunnel, where $R_{L_\infty} \sim 35 \times 10^6$.

The lee-side separated flow develops from initially symmetrically disposed and near-conical separation lines at $\alpha/\theta_c \sim 1$, with the free shear layers eventually rolling up into tightly coiled vortices at all Mach numbers. At Mach 0.6, conditions in this symmetrical external separated flow at $\alpha/\theta_c = 2.5$, were probed with pitot pressure tubes and optically via laser/vapor screen flow visualization. Mean shear stresses and directions on the cone surface were inferred from a previously calibrated pair of yawed hot wires, while fluctuations at the surface were measured by the hot wires and pressure transducers, as the cone was rolled in small increments through separation.

The onset of asymmetry of the lee-side separated flow about the mean-pitch plane is sensitive to Mach number, Reynolds number, and the nose bluntness, varying between $2.5 < \alpha/\theta_c < 4.5$ in the Mach number range $0.6 < M_\infty < 1.8$. As the Mach number is increased beyond $M_\infty = 1.8$, the critical angle of incidence for the onset of asymmetry increases until at about $M_\infty = 2.75$ there is no longer any significant side force development.

Supportive three-dimensional laser velocimeter measurements of mean and fluctuating velocity in a slightly asymmetric vortex wake about a slender tangent ogive cylinder at incidence having respective nose and overall body fineness ratios of 3.5 and 12, are included. These measurements were obtained at $\alpha/\theta_c = 2.3$; at Mach 0.6; and at $R_{L_\infty} = 2 \times 10^6$, where $L = 0.3$ m (1 ft).

SYMBOLS

A	a constant, see Eq. (1)
B	a constant, see Eq. (1)
$C_f = \frac{\tau_w}{q_\infty}$	local resultant skin friction coefficient
C_N	normal force coefficient from balance, based on cone base area
$C_p = \frac{p - p_\infty}{q_\infty}$	local static pressure coefficient
$C_{pp} = \frac{p_p - p_\infty}{q_\infty}$	local pitot pressure coefficient
C_Y	side-force coefficient from balance, based on cone base area
D	base diameter of cone
d	diameter of tangent ogive/cylinder model
d_p	diameter of vent port to pressure transducer beneath cone surface
E	mean operating voltage of hot wire, flow on
E_0	mean operating voltage of hot wire, flow off
$e', e(t)$	instantaneous fluctuation voltage from hot wire
$\langle e' \rangle$	rms voltage from hot wire
h	height above cone surface, measured along extended radius of cone

$\bar{h} = \frac{h}{r}$	nondimensional height above cone surface
K	a constant. see Eq. (1)
L	axial length of cone
M	local Mach number
p	local static pressure
p'	instantaneous level of pressure fluctuation at cone surface
$\langle p' \rangle$	rms of pressure fluctuation at cone surface
p _p	local pitot pressure
q	local dynamic pressure
R	ohmic resistance
$\Delta R = (R_{op} - R_w)$	difference between resistances of a wire at, respectively, operating temperature and local wall temperature
R _{L_∞}	Reynolds number based on axial length of cone and tunnel free-stream conditions
r	local cone radius
S	electrical "power" term, defined in Eq. (2)
t	time
t _D	time delay
u	local velocity in direction of tunnel axis
\bar{u}	local velocity, parallel to model axis
$u_\tau = \sqrt{\frac{\tau_w}{\rho_w}}$	shear stress velocity
v	lateral velocity normal to tunnel or model axis
w	vertical velocity normal to tunnel axis
\bar{w}	vertical velocity normal to model axis
x	distance along tunnel axis
\bar{x}	distance along model axis
y	lateral distance from tunnel or model axis
z	vertical distance, normal to tunnel axis
\bar{z}	vertical distance, normal to model axis
α	angle of incidence
δ	boundary-layer displacement thickness
θ	angle between local shear stress vector and line bisecting internal angle between individual wires of buried wire skin — friction gage, see Fig. 4(a)
θ_c	cone semianale
μ	coefficient of viscosity
$\nu = \frac{\mu}{\rho}$	kinematic viscosity
ρ	local density
τ	mean shear stress
τ'	instantaneous level of shear stress fluctuation at cone surface
ϕ	circumferential angle around cone surface, measured from windward generator
ψ	angle between normal to buried wire and local surface shear stress direction, Fig. 5(a)

ω angle between tangent to limiting streamline (surface shear stress trajectory) and cone generator

Subscripts:

1,2 wires 1 and 2 of buried wire gage, see Fig. 4(d)
 A line of divergent surface shear stress trajectories ("attachment" or "reattachment" line)
 b cone base
 ∞ free-stream mean-flow conditions
 op operating temperature of hot wire
 S1 primary separation line
 S2 secondary separation line
 w cone surface (wall)

1. INTRODUCTION

1.1 Design Aims

To be successful throughout a wide range of flight conditions, the aerodynamic design of a lifting body must ensure that there is adequate control with no unpleasant changes in force and moment characteristics. In association with steady boundary conditions, the objective is to allow only steady three-dimensional swept separations to develop, to minimize buffet. A model for a desirable separated flow is provided by the sharp-edged slender delta wing or a body of revolution with fixed separation lines (Ref. 1). In aiming for this ideal goal, we find that flows should be dominated by coiled vortices — "the sinews and muscles of fluid motion" (Ref. 2) — rather than by large unsteady separation bubbles. This much wider than usual view of the aerodynamic design problem, attributable to Maskell and Küchemann (Ref. 3), should be contrasted with the restricted outlook of allowing separation only at a trailing-edge, as in the design of the classical airplane.

1.2. Asymmetric Separations

Our present-day missiles and military fighter aircraft must perform and be controllable at high angles of combined incidence and yaw, where three-dimensional flow separations from the forebodies may become asymmetric (Refs. 4-7). These separations, often in association with fixed-edge separations from strakes extending forward of the wing, may interfere with downstream control surfaces to provide nonlinearities and side forces that are not readily predictable. Here there is strong interaction between the coupled viscous and inviscid flow domains on the lee-side of the vehicle. The onset of asymmetry is responsive to small changes in geometry at the nose, Reynolds number and Mach number up to incidences where transonic crossflow conditions are formed. There the significant side forces disappear. The asymmetries occur in both laminar and turbulent flows, so that transition is presumably not the essential ingredient causing asymmetry. But local inflexional instability of the mean velocity profiles in the viscous flow may, perhaps, be mooted as a contributor (see Tobak's discussion, Ref. 8, of a linearized theory of two- and three-dimensional incompressible viscous flows resulting from locally unstable velocity profiles). It is conceivable that vorticity and acoustic disturbance levels in the wind tunnel will also affect the onset of asymmetry. As the development of the asymmetry is particularly sensitive to surface curvature and roughness at the nose, a potential means of controlling the forebody flow could be by deployment of a single small strake, small amounts of asymmetric blowing (or suction), or by spinning the nose. On the other hand, since we know that missiles having long cylindrical afterbodies will eventually develop asymmetrical flows regardless of nose conditions, we might be led to expect that such local treatment at the nose would probably not influence the downstream flow substantially. Notwithstanding, Rao (Ref. 9) has demonstrated that the utilization of helical (i.e., S-shaped) trip wires from the leeward to the windward meridian on the nose, disrupts the normal development of separation, and is very effective in alleviating high angle-of-attack side forces on short missile and fuselage shapes. It is considered that the helical trips upset the well-organized motion of the lee-side vortices and cause a relatively rapid diffusion.

The asymmetric vortex wake usually develops from asymmetric separation line positions on the body, but the latter does not appear to be a necessary condition for the former to occur. An appraisal (Ref. 10) of some earlier, low subsonic speed tests of Shanks (Ref. 11) where forces and moments were measured on very slender, flat plate, delta wings (sweep angles from 70° to 84°) at incidence, indicates that even though the separation lines were fixed at the sharp leading-edges, asymmetry in the leading-edge vortices, as determined by the onset of significant rolling moment, occurred when the angle of incidence was about 3 to 4 times the wing seminose angle. Nonetheless, the sharp edges have a beneficial effect in delaying the onset of asymmetry to higher relative incidences than those obtained with smooth pointed forebodies or forebody/cylinder configurations (Refs. 5-7).

1.3. Modeling of Asymmetries

The modeling of the lee-side flow asymmetries poses severe problems because the development of the turbulent flow structures in the three-dimensional swept separation zones and in the tightly coiled free shear layers is virtually unexplored. Recourse has typically been taken for rough predictions of the flows about missile shapes, to inviscid flow approximations of the lee-side region utilizing arrays of line-vortices (see Nielsen's review in Ref. 12 of nonlinearities in missile behavior at high angles of attack), or to the impulsively started flow analogy proposed many years ago by Allen and Perkins (Ref. 13). In this hypothesis, the development of the crossflow with distance along an inclined body of constant diameter is likened to the growth with time of the two-dimensional flow past the corresponding circular cylinder starting impulsively from rest. Useful engineering formulae have resulted, but given the complexities of the three-dimensional boundary-layer growth, separation, and vortex development on slender bodies, it seems unlikely that methods of this kind can adequately describe the flow. In general, we should note that the growth of the unsteady two-dimensional spiraling vortex differs essentially from that of the steady, three-dimensional vortex in space. Küchemann and Weber (Ref. 14) point out that in three dimensions, fluid entering the core of the vortex can be discharged axially, whereas in two dimensions no such escape is available. The core must expand continuously outward with time to accommodate all of the fluid entering the vortex. They show further (Ref. 14) that there is only one case in inviscid flow where the two kinds of vortex are formally identical: where the steady, three-dimensional flow is conical (so that slenderness assumptions can be invoked); and where the unsteady flow is permitted to grow linearly with time. Lamont and Hunt (Ref. 15) and Deffenbaugh and Koerner (Ref. 16) have probably extracted the limits of usefulness of the qualitative, two-dimensional, unsteady analogue to describe the nature of "out-of-plane" forces on a pointed body at high angles of incidence.

1.4. Cone at Incidence (or Yaw) - A Simple Model of Three-Dimensional Separation

Next to the slender delta wing, the simplest class of bodies on which three-dimensional separation can be studied is the cone. As well as being a typical forebody shape used in flight, the cone at incidence provides a very useful model to develop three-dimensional boundary layers, up to and beyond separation, to check against theory. On a conical surface, the condition for flow separation is simple; namely, that the limiting streamlines at the base of the skewed boundary layer (whose projections on to the surface are the directions of surface shear stress) coalesce from both sides to form an envelope (Refs. 17, 18) along, or are asymptotic (Refs. 19, 20) to, a cone generator. Even in incompressible flow about slender cones, the conical nature of the surface conditions with separation is preserved. This is because at relative incidences sufficient to cause separation, the circumferential pressure gradients are much larger than those in the axial sense (the latter due to thickness and base effects). For the incompressible case as well, then, the primary separation line lies essentially along a generator as illustrated by the limiting streamlines in laminar flow about a 1.5:1 elliptic cone with major axis vertical at 30° incidence (Ref. 21), shown in Fig. 1.

1.5. Computation of the Symmetrical Lee-side Flow about Cones

The computation of the symmetrical separated lee-side flow about cones is currently following two paths. One is the representation of the cone flow by parabolized approximations to the Navier-Stokes equations in supersonic flow (Refs. 22-24); the second is the inviscid modeling in incompressible flow of the free shear layers by spiral vortex sheets as for delta wings (Ref. 25).

McRae (Ref. 22) incorporated the conically symmetric flow approximation along with MacCormack's finite-difference time-dependent scheme (Ref. 26) to solve the laminar viscous flow field about a pointed circular cone. The calculation takes place on a spherical surface centered on the cone apex. The outer boundary condition for the integration is the free stream, so that the bow shock wave is captured and allowed for in the use of the conservative form of the governing equations. A comparison with the Mach-8 surface pressure and pitot measurements of Tracy (Ref. 27) showed good agreement with the calculations of the lee-side flow. McRae (Ref. 23) has now included a scalar eddy-viscosity model based on mixing-length hypotheses in his formulation. Provided certain constants are used to adjust the levels of eddy viscosity in each coordinate direction, coupled with relaxation beginning just prior to the primary separation, he finds very satisfactory agreement between his calculations of surface pressure and surface shear stress directions and the results of the high Reynolds number experiments of Rainbird (Refs. 28, 29). Both primary and secondary separation line positions were found to agree very closely with experimental results in a Mach 1.8 flow at $\alpha/\theta_c = 2.5$ and $R_{Lw} \sim 30 \times 10^6$.

Rakich and Lubard (Ref. 24) calculated the entire laminar separated flow field about a spherically blunted 15° circular cone in a Mach 10.6 flow to compare with the measurements of Cleary (Ref. 30) at $\alpha/\theta_c \sim 1$. The calculations are based on a single layer system of three-dimensional parabolic equations that are approximations to the full steady Navier-Stokes equations valid from the body surface to the bow shock wave. This system of equations includes the circumferential shear stress terms as well as the effects of viscous-inviscid interaction and entropy gradients due to both the curved bow shock and angle of attack. The calculated leeward surface pressures and heating distributions were in satisfactory agreement with experimental results and the calculation provided evidence of reversal in the boundary-layer crossflow; primary separation was placed at about 13° from the leeward meridian. The results from a variant of this program (Ref. 31), wherein an eddy viscosity model is inserted are also being compared against Rainbird's Mach 4.25 experiments (Ref. 29).

Pulliam and Steger (Ref. 32) have also made a notable contribution to the calculation of flows about missile-shaped bodies using a "thin layer" approximation of the Navier-Stokes equations.

The second avenue of modeling the lee-side vortex wake, in this case, by wholly inviscid means, is that due to J. H. B. Smith (Ref. 25). He proposes an inviscid vortex sheet model for incompressible (symmetrical, at this time) conical flow in which the vortex sheet must depart from the surface of the cone tangentially if vorticity is to be shed. The separation line position may be given from boundary-layer calculations (see Smith's review (Ref. 33) in AGARD CP-168) or from experiment (see Fig. 2). At the separation line in Smith's model, the inviscid flow on the downstream side is constrained to be parallel with the separation line, a condition to replace the Kutta condition at a sharp edge; whereas on the upstream side of the separation line, the surface streamlines of the inviscid model are inclined to the separation line (but are, of course, tangential to the wall). The coiled inviscid vortex sheet is then constructed as for the sharp-edged delta wing (Refs. 39, 40).

1.6 Cone for Experiment

The cone, then, is the basic nose of many flight vehicles. At incidences typically below $\alpha/\theta_c \sim 1$, it provides a useful configuration to develop a symmetrical three-dimensional attached boundary layer growing from the windward to the leeward meridian. Because of the near conicity of the separation lines and vortex development in both subsonic and supersonic flows (neglecting effects of transition), it also provides a convenient experimental model to explore three-dimensional separations from detailed measurements at only one axial station.

The essential objective of the present work is to achieve an understanding of the fluctuating quantities in three-dimensional separated flows, and how three-dimensional separations and their asymmetries may be controlled. The cone is a very convenient model on which to generate both three-dimensional attached and separated viscous flows. The present experiments then, extend the symmetric separation mean flow measurements of Rainbird (Refs. 28, 29) about circular cones (see also Ref. 41) to determine experimentally additional quantities at the cone surface (mean and fluctuating pressures, fluctuating heat transfer combined with mean shear stress magnitudes and direction) and to measure at the same time the mean and fluctuating flow field above the cone at moderately large relative incidence. Test results at Mach 0.6 are discussed herein. Force measurements in the range of Mach number $0.6 < M_\infty < 1.8$ have yielded the onsets of asymmetry of the lee-side flow for varying Reynolds numbers and for blunt and sharp nose shapes. These were supplemented herein by pictures of the crossflow facilitated by a laser-vapor screen flow visualization technique.

2. EXPERIMENTAL METHOD

Measurements have been made on a 1.4 m (54 in.) long, 5° semiangle circular cone, sting-mounted in the Ames 1.8- by 1.8-m (6- by 6-ft) closed circuit wind tunnel at Mach numbers in the range $0.6 < M_\infty < 1.8$ (Fig. 3). The cone model was fitted with a sharp nose (0.13-mm, i.e., 0.005-in. tip radius) and a blunted nose with a radius of 4% of the base radius. Stagnation pressures were subambient yielding Reynolds numbers based on the cone axial length and tunnel free-stream conditions of between 4.5×10^6 and 13.5×10^6 . No artificial tripping of the boundary layer was employed. At the relatively high acoustic disturbance levels pertaining in this tunnel, for example, $\langle p' \rangle / q_\infty \sim 3\%$ at $M_\infty = 0.6$, a Reynolds number based on wetted length to transition might be expected to be $3 \times 10^6 \pm 20\%$ (Ref. 42). At zero angle of attack, therefore, we anticipate transition to have been located, respectively, from about 0.7 to 0.2 of the cone length, corresponding with the aforementioned range of test Reynolds numbers with a tunnel stagnation temperature in the range of 20° - 40°C . The typical variation during a run of 20 min was less than 3° , however, so that with this immersion time, conditions of near zero heat transfer existed at the cone surface.

Because of the nominal conicity and symmetry of the flow (Refs. 4, 28, 29) up to angles of incidence at least 2.5 times the nose semiangle, θ_c , all detailed measurements were made at an axial station 0.85 of the cone length aft of the (pointed) apex and upon each half of the cone ($0^\circ < \phi < \pm 180^\circ$). Mean circumferential pressure distributions were obtained with 0.51-mm (0.020-in.) diameter static holes spaced 45° apart at the 0.85 station (see Fig. 4(a)). These orifices, as well as others along a cone generator at the 0.95 station and in the base region, were connected via a "Scanivalve" to an unbonded strain-gage pressure transducer. The static pressure from each point at the 0.85 station was also fed as a highly damped signal to the reference port of a 2.36-mm (0.093-in.) diameter "Kulite" pressure transducer situated on the same conical generator. The diaphragm was vented to the flow through a 1.00-mm (0.040-in.) diameter static hole but submerged beneath the surface in accordance with Hanly's recommendations about the effects of transducer flushness on fluctuating surface pressure measurements (Ref. 43) (see Fig. 4(b)). Preston tubes of diameter 0.42 mm (0.016 in.) were installed at the 0.85 station to determine the mean levels of skin friction at zero angle of attack and along the windward generator (Fig. 4(c)).

Two bidirectional, buried-wire, skin-friction gages (Ref. 44) were also situated in the cone surface at the 0.85 length station (see Fig. 4(a)), to measure the magnitude and direction of the resultant shear stress at the surface. The configuration of the gage is shown in Fig. 4(d), its fabrication following basically the same procedure as promoted for single wires by Murthy and Rose (Ref. 45) after the work of Rubesin et al. (Ref. 46). The following equations, the method of manufacturing the gages, and a full discussion of the calibrations are given in Ref. 44. In brief, temperature-resistance calibrations were obtained by placing the gages in an oven. Magnitude and directional sensitivities were found by flush-mounting the gages in a known subsonic channel flow and operating each wire with an overheat ratio of 1.1, utilizing "Disa" constant temperature anemometers. The wires were capable of operating with upper frequency responses close to 15 kHz. The sensitivities were checked again after installation in the cone surface and running at zero angle of attack. The shear stress at a station close by the gage was deduced from a Preston tube measurement in conjunction with the correlation due to Bradshaw and Unsworth (Ref. 47). Rotation of the probe about its axis to known angles of yaw permitted the directional sensitivity to be obtained at each Mach number and Reynolds number tested simultaneously with the shear stress magnitude according to the following equations. If the output of a single wire, yawed to the local shear stress direction at $(90 - \psi)^\circ$ (see Figs. 4(d) and 5(a)), is assumed to be of the form:

$$\frac{E^2}{RA^2} = A(\rho_w \mu_w \tau_w)^{1/3} (\cos^2 \psi + K^2 \sin^2 \psi)^{1/6} + B \quad (1)$$

where the symbols are defined at the beginning of the report, and

$$S = \frac{1}{A} \left(\frac{E^2}{R\Delta R} - B \right) \quad (2)$$

then for our pair of mutually perpendicular wires, respectively labeled 1 and 2, where $\psi_1 + \psi_2 = \frac{\pi}{2}$, we obtain

$$S_1 = (\rho_W \mu_W \tau_W)^{1/3} (\cos^2 \psi_1 + K_1^2 \sin^2 \psi_1)^{1/6} \quad (3)$$

and

$$S_2 = (\rho_W \mu_W \tau_W)^{1/3} (\sin^2 \psi_1 + K_2^2 \cos^2 \psi_1)^{1/6} \quad (4)$$

By eliminating ψ_1 , the wall shear stress is given by

$$(\rho_W \mu_W \tau_W) = \left[\frac{(1 - K_2^2) S_1^6 + (1 - K_1^2) S_2^6}{1 - K_1^2 K_2^2} \right]^{1/2} \quad (5)$$

We note that values of the coefficients of directional sensitivity K_1 and K_2 can be obtained from a plot of $S_1(\psi_1)$ or $S_2(\psi_2)$ when $\psi_1, \psi_2 = 0^\circ$. In general, $K_1 \neq K_2$, but the difference between the two sensors on each gage was found to be relatively small. If, for simplicity, we let $K_1 = K_2 = K$, then the absolute magnitude of the shear stress takes the form:

$$(\rho_W \mu_W \tau_W) = \frac{(S_1^6 + S_2^6)^{1/2}}{(1 + K^2)^{1/2}} \quad (6)$$

As for the direction of the skin friction vector, we see from Eqs. (3) and (4) that the quotient S_1/S_2 is a unique function of the direction ψ_1 and is independent of the magnitude of the skin friction. The assumption $K_1 = K_2$ is not a necessary one provided each wire of a pair is calibrated. McCroskey and Durbin (Ref. 48) discussed measurements of the direction of surface shear stress with a hot film gage and proposed that

$$\frac{S_1 - S_2}{S_1 + S_2} = f(\theta) \quad (7)$$

where θ is the direction of the flow relative to the probe centerline, and equals $(\psi_1 - \pi/4)$ in our present frame of reference.

The results of the directional calibration for one of the pairs of buried wires is shown in Fig. 5(a). We see that the direction of the skin friction vector can be determined to an accuracy within $\pm 5^\circ$ independently of its magnitude. The variation of the quantity $(S_1^6 + S_2^6)^{1/2}$ in a $\pm 40^\circ$ yaw angle range was demonstrated to be small. The magnitude of skin friction obtained with the Preston tube is plotted against the measured values of $(S_1^6 + S_2^6)^{1/2}$ in Fig. 5(b). From Eq. (6), the value of K is 0.35 for the particular gage shown. The surface shear stress directions obtained with the hot wire pair were compared against flow visualization traces taken with an oil-dot technique. Signals from the off-surface hot wires were also measured but await analysis.

Pitot pressures in the external flow above the cone surface were measured using an array of 77 pitot tubes mounted at the 0.85 station (Fig. 3).

Overall force and moment measurements were obtained with an internal strain-gage balance.

The cone was pitched to the desired angle of incidence, and for the measurements with symmetrical separation of the lee-side flow, the cone was rolled in increments from 0° to 180° and paused for typically 1 min while data were taken. Increments of 5° in roll were generally used. Neither fluctuating pressures nor hot wire data were collected at angles of incidence where asymmetric lee-side conditions prevailed.

Visualization of the vortex wake was obtained at the 0.85 station by saturating the tunnel flow with water vapor and illuminating a thin cross section of the flow with a 15-W laser beam passed through a cylindrical lens. Photographs of the scattered light were taken with a camera mounted to the sting/strut support, the camera axis being set nominally parallel with the cone surface. Prior to the runs, a grid placed at the test station was photographed against which the dimensions of the shear layer could be subsequently compared.

Some supportive three-component velocity measurements in the lee-side vortex wake just downstream of the junction between a 16° semiangle tangent ogive forebody joined to a cylinder aft-body were made by Owen and Johnson (Ref. 49) at a relative incidence of 2.3. These Mach 0.6 data are also presented here to provide an insight into possible orders of magnitude of fluctuation levels on the lee side of the cone.

3. RESULTS AND DISCUSSION

3.1 Symmetrical Separation of the Lee-Side Cone Flow

3.1.1 Forces

The physical characteristics of the mean flow field about the 5° circular cone in the Mach number range $0.6 < M_\infty < 1.8$ follow the descriptions by Rainbird (Refs. 28, 29) of the surface and external flow conditions that he measured at Mach 1.8 and 4.25.

The overall effects of boundary-layer growth and incidence on the development of normal forces on the 5° cone are illustrated in Fig. 6 up to relative incidences of almost 5. At relative incidences typically less than 0.7, the circumferential pressure gradient is favorable all the way from the windward to the leeward generator. The boundary layer grows in a regular manner developing very small crossflows. The normal force develops linearly in this range, and the slopes $dC_N/d\alpha$ near $\alpha = 0^\circ$, are affected only slightly by viscosity. In subsonic flow, the values are typically 6% larger than the slender body value of 2.0 (per radian). In supersonic flow, the discrepancies between experiment and those slopes given in Sims' tables (Ref. 50) are even less for both the blunt and sharp noses.

Figure 6 illustrates that, at Mach 1.8, there is substantial development of nonlinear lift* above a relative incidence of 1.5 (as found by Rainbird (Ref. 28), where the Reynolds number was more than double the existing test value) consistent with the formation of a well organized, symmetrical, coiled, free shear-layer flow on the lee side of the model. From pitching-moment data, a fixed center of pressure position at $0.667 L$ is in good agreement with the conical flow value of $(2/3)L \sec^2 \theta_C$. But below Mach 1.8, there is an apparent sensitivity of the onset of nonlinear normal force to both Reynolds number and nose shape, as we see on Fig. 7. At any given Mach number, we note that reduction in Reynolds number and introduction of bluntness delays the onset of nonlinear normal force. This dependency reduces rapidly as Mach number increases until at Mach 1.8, it has nominally disappeared.

The results in Fig. 7 for our cone model of fineness ratio, $L/D = 5.7$, are unexpected for the distinctive tardiness displayed in producing nonlinear normal force in the high subsonic and transonic speed ranges. Even though at Mach 0.6 and $\alpha/\theta_C \sim 2.5$, for example, where there was substantial vortex flow (see Figs. 8 and 9), the overall normal force lies just below the slope $(dC_N/d\alpha)_{\alpha=0}$.

The high negative values of base pressure coefficient (Fig. 10), are mooted as the key to the paradox, for at $M_\infty = 0.6$ near the base, they induce somewhat larger increments of suction pressure on the windward side of the cone near the base than on the leeward; see for example, the cone surface pressures along the windward and leeward generators on Fig. 11. Hence the development of nonlinear normal force appears suppressed by the base effect. This suppression reduces as Mach number increases until at $M_\infty \sim 1.8$, the upstream propagation from the base is negligible.

In Fig. 10, we also note that changes in Reynolds number and sting/base diameter at Mach 0.6 cause substantial changes of the base flow (see Ericsson (Ref. 53) for a discussion on aerodynamic support interference).

3.1.2 Mean Flow Measurements

The changes in three-dimensional boundary-layer development as the circumferential surface pressure distributions steepen with increasing angle of incidence are discussed in detail in Refs. 28 and 29. Herein, we shall concentrate on the flow at a relative incidence of 2.5, for the cone with nose radius equal to 4% of base radius. At this incidence (Figs. 12(a)-12(c)), display the surface pressure coefficients obtained at a constant length Reynolds number of $R_{L_\infty} = 13.5 \times 10^6$, for Mach numbers 1.8, 1.2, and 0.6. The pressures are plotted with respect to circumferential angle measured from the windward ($\phi = 0^\circ$) to the leeward generator ($\phi = 180^\circ$). Figure 12(a) shows good agreement at $M_\infty = 1.8$ between the measured circumferential pressures plotted at three axial stations along the cone. The present results at $R_{L_\infty} = 13.5 \times 10^6$ demonstrate a small but variable shift relative to the higher Reynolds number data of Refs. 28 and 29. The present results are uncorrected for errors due to static hole size (Refs. 54, 55) which, if included, would marginally increase the difference between the two sets of measurements. The calculation of surface pressures from McRae's Navier-Stokes code, corresponding with the Reynolds number $R_{L_\infty} = 32 \times 10^6$, are in close agreement with Rainbird's measurements (Refs. 28, 29). Figures 12(a)-12(c) illustrate corresponding qualitative trends in the circumferential pressure distributions at the 0.85 axial station for all Mach numbers tested.

As the three-dimensional boundary layer develops from the windward attachment line region ($\phi = 0^\circ$) toward the minimum pressure point at $\phi \sim 100^\circ$, the crossflow grows rapidly. At Mach 0.6, toward which the bulk of the remaining discussion in this paper will be devoted, Fig. 13 provides a comparison between some preliminary surface shear stress directions (relative to the cone generators), ω , obtained from oil dot streaks and those angles deduced from the bidirectional buried hot-wire gage. The maximum value of ω given from the gage is close to 40° in the vicinity of the minimum pressure point. The boundary layer, in proceeding around the lee side of the cone, now encounters a strong circumferential adverse pressure gradient and thickens rapidly (see Fig. 8). The crossflow angle, ω , reduces progressively to zero, Fig. 13, at which point the shear stress trajectories converge and run parallel to a generator, the primary

*We should be aware, however, that in solving the Euler equations of motion for the inviscid flow about a circular cone at incidence in supersonic flow (Refs. 51, 52), we find that nonlinear normal forces begin to develop also at a relative incidence close to 1.5 for this $M_\infty = 1.8$ case. These inviscid components of overall normal force are more than 50% of the total nonlinear force, as we see from the additional symbols plotted on Fig. 6. The effects of viscous growth on the windward circumferential pressure distribution are minor but, as expected, the inviscid lee-side pressures are changed substantially due to the vortices (see Fig. 12(a)).

separation line, ϕ_{S1} (see the schematic drawing in Fig. 4(a)). Discrepancies between the oil flow results and shear stress directions as deduced from the wire voltages await resolution in a forthcoming repeat experiment. The laser flow visualization in Fig. 8 and the contours of local pitot pressure deficit plotted in Fig. 9 illustrate the vortex core position and the close comparison between the boundaries of the free shear layers from these two measurements. The discrepancies in core position between the pitot and vapor screen measurements and the disagreement between ϕ_{S1} positions on Figs. 9 and 13 may be due to a displacement effect caused by the blockage of the pitot array. Beyond the circumferential angle ϕ_{S1} , Fig. 12 indicates there is a plateau of virtually constant pressure (particularly at Mach 1.8) followed by a second pronounced pressure minimum and finally a recovery toward the leeward generator. The second pressure minimum caused by the induced effect of the primary vortices drains fluid from the region of the leeward generator, appreciably thinning the flow there. This movement of fluid beneath the vortices itself separates from the cone surface at ϕ_{S2} on a scale substantially smaller than the primary flow. The lobular region of secondary flow is shown by the pitot contours of Fig. 9, although it is not evident on the vapor screen photograph shown in Fig. 8. Between ϕ_{S1} and ϕ_{S2} , there must be yet another divergent attachment line region where $\omega = 0$ (see Figs. 4(a) and 13) from which fluid diverges to feed both separation lines.

The magnitude of the resultant surface shear stress at the 0.85 axial station in subsonic flow obtained from the yawed buried hot wire pair is shown in Fig. 14. The maximum uncertainty in the absolute levels of shear stress deducible from the wires is about $\pm 15\%$. Again, the variation of the local skin friction coefficient with circumferential angle at Mach 0.6 follows the trends established in Rainbird's Mach 1.8 and 4.25 measurements (Refs. 28, 29). The skin friction reduces smoothly to a minimum, but finite, value at the primary separation line that is lower than the zero incidence attached flow value. The skin friction is again a minimum at the secondary separation with high values due to the divergent attachment line flows between the separation lines and along the leeward meridian. The boundary layer along the leeward generator, in fact, accelerates rapidly in the lateral sense due to the very favorable pressure gradient caused by the vortices (see Fig. 12(c)). The shear stress increases to a value well above that at the windward generator with a concomitant surface shear direction of -20° at $\phi \sim 170^\circ$.

3.1.3 Fluctuation Measurements

The fluctuating pressure field within a viscous flow is associated with the irregular motions of the turbulence; from the interaction of the turbulent fluctuations normal to the wall with the mean shear, and from the interaction of the turbulence with itself. In incompressible flow, the pressure fluctuations at one station in the flow are produced by momentum fluctuations at many other stations (Poisson's equation). Thus the pressure at one point will not correlate with velocity fluctuations at another point in close proximity (Ref. 56).

Now the pressure fluctuations have a wide range of sizes typically equal in scale to boundary-layer thickness on down to ν/u_τ . But according to Bradshaw (Ref. 57), the spectrum of pressure fluctuations at a wall beneath a two-dimensional turbulent boundary layer as it approaches separation is constituted of essentially high-frequency and low-frequency energy. The high-frequency components are generated in the small-scale inner region (the so-called law of the wall region) whereas the low-frequency pressure fluctuations emanate from the larger-scale outer region. In the latter, the fluctuations intensify as the wake region of the boundary layer increases in thickness. Under two-dimensional attached boundary layers, the level of pressure fluctuation also scales with the mean wall shear stress. In adverse pressure gradients, the pressure fluctuation scales with the outer variables as the law-of-the-wall region now becomes very small. Irrespective of the pressure gradient, however, the absolute level of the wall pressure fluctuations is small, and it is difficult to isolate the fluctuations from turbulence and sound generated by free-stream disturbances in a typical, large wind tunnel. At Mach 0.6, the disturbance level of the NASA 1.8- by 1.8-m tunnel stream is high, and probably consists of fluctuations in vorticity, temperature, and sound. It is thought that the signal at the cone surface is especially contaminated with the radiated sound from the tunnel wall boundary layers and slots in the tunnel ceiling and floor. Figure 15 shows the rms pressure fluctuation at the cone surface beneath the Mach 0.6 axisymmetric boundary layer to be $\langle p' \rangle / q_\infty \sim 0.03$, a value 10 times the level of mean shear stress (see Fig. 14). This is in contrast with a value of 3 times the mean shear stress quoted by Kistler and Chen (Ref. 58) for a two-dimensional, subsonic, attached flow, beneath a reasonably "quiet" free stream. The spectra at zero angle of attack (not shown) exhibited peaks at frequencies of 800 and 1600 Hz. Neither the levels of the peaks nor the areas beneath them appeared dependent on roll orientation or angle of incidence, however, and these peaks were not filtered out in the results to be presented. The interference of the tunnel noise field on the development of the attached boundary layers, may well have a different effect than on the free shear layers. Particular frequencies, if dominant, may excite instabilities in the latter flow. Under these circumstances then, Fig. 15 also shows the rms pressure fluctuations at the 0.85 station for the Mach 0.6 flow at a relative incidence of 2.5. These fluctuating pressures were measured simultaneously with the mean pressures already discussed on Fig. 12(c). We note from Fig. 15 that the absolute level of rms pressure fluctuation (actually plotted relative to the constant dynamic pressure of the free stream) increases in the favorable pressure gradient from the windward attachment line toward the minimum pressure point, then decreases smoothly in the adverse pressure gradient to a minimum value at the primary separation line. The signal increases rapidly again as the leeward attachment line region is approached. Between the positions of primary and secondary separation, ϕ_{S1} and ϕ_{S2} , there is slight evidence that the fluctuation level once more increases at the reattachment line, ϕ_A . These results bear comparison with those beneath two-dimensional separation bubbles (Ref. 59), although the two-dimensional separation is, of course, the special limiting case of the more general swept separation in three dimensions. Mabey (Ref. 59) showed that the pressure fluctuations caused by fluctuations in the two-dimensional separation line position were small, whereas at reattachment, the pressure fluctuations exceeded those at the separation point by 4 to 10 times.

In apparent contradistinction with these results, however, Schloemer (Ref. 60) and Burton (Ref. 61) have reported on pressure fluctuations beneath two-dimensional attached boundary layers in both adverse and favorable pressure gradient conditions, and found what appears to be the converse of the pressure fluctuation behavior on the cone surface. Relative to a zero pressure gradient flow, $\langle p' \rangle / q_\infty$ was greater in the adverse and less in the favorable pressure gradients. The differences were accentuated in the

two-dimensional flow if the normalizing parameter for the rms wall pressures was the wall shear stress. But, it should be noted that if the cone surface rms pressure data are plotted with respect to the resultant wall shear stress, a corresponding accentuation relative to the zero pressure gradient, $\alpha = 0^\circ$ case, is to be seen in Fig. 15.

On the basis of the dimensionless pressure measurement hole parameter, $(dp_w)/v$, which is upward of 300 in our Mach 0.6 experiment, we are probably missing the dramatic increase in intensity of the small-scale pressure fluctuations that Emmerling (Ref. 62) has noted, for example (see Ref. 56). This parameter should be less than 50 if the small-scale fluctuations are to be measured. But it will be shown that the pressure fluctuations are dominated by low-frequency components in the adverse pressure gradient regions so that loss of high-frequency response would not explain the substantial difference between the two-dimensional and the three-dimensional results. Neither would we expect, perhaps, that the grazing shear flow over a surface orifice would produce changes in acoustical impedance of the port (which are dependent on frequency) that were large enough to overturn the trends seen at the cone surface. Willmarth and Yang (Ref. 63) showed that the transverse curvature of the model surface alters the large eddies significantly; but their boundary-layer thickness was of order of model cross-section diameter, whereas on the cone, it is $1/100$ of the local cone diameter.

If the rms pressure results are not spurious because of the high background noise level, then the character difference may be attributable to the escape provided to the flow in a three-dimensional separation in contrast with the two-dimensional case.

The behavior of the rms values of output voltage signal (made nondimensional with respect to the flow-based signal strengths) for each of the buried hot-wire pair on the cone surface, peak at the separation lines. Figure 16, for example, presents the normalized fluctuations from one wire to illustrate that these peak levels are more than double those beneath the attached (and reattached) flow regions. The second wire provided essentially the same normalized output so that the normalization virtually removes the sensitivity to yaw.

If conduction losses are negligible from the wire to the substrate, and if the wire is normal to the local shear stress direction, we may see from Eq. (1) that the mean square of the voltage fluctuation at the wire is related to the pressure and shear stress fluctuations

$$\left(\frac{e'}{E}\right)^2 \sim \left[\left(\frac{p'}{p_w}\right)^2 + 2\left(\frac{p'\tau'}{p_w\tau_w}\right) + \left(\frac{\tau'}{\tau_w}\right)^2\right]$$

The order of the present results implies that at separation, if $\langle p' \rangle / p_w$ is a minimum (see Fig. 15) and $\langle e' \rangle / E$ is a maximum, then $\langle \tau' \rangle / \tau_w$ must be large for the equality to be valid, irrespective of the correlation between p' and τ' . Along a line of divergence of limiting streamlines, $\langle p' \rangle / p_w$ is large, $\langle e' \rangle / E$ is small, and hence $\langle \tau' \rangle / \tau_w$ must be equal to the order of the pressure fluctuation with a negative correlation. In other words, the shear stress fluctuations are large both at the separation lines and along the attachment line regions corresponding to large gradients of fluctuating velocity. Let us now look at the correlations between values of the fluctuating voltage at different instants of time for the same hot wire that was shown in Fig. 16; for how the correlation coefficient decreases with increasing time depends on the character of the turbulence. Seven such autocorrelations are presented in Fig. 17, corresponding to circumferential positions on the cone surface between $90^\circ < \phi < 180^\circ$. The correlation functions all decrease toward zero, more-or-less monotonically, falling faster initially from unity in the favorable pressure gradient three-dimensional boundary layer (e.g., at $\phi = 90^\circ$) than in the retarded flow ($\phi = 135^\circ, 140^\circ$). This corresponds with a preponderance of energy at higher frequencies in the attached flow and at lower frequencies in the retarded flow. At the separation lines, these large-scale motions give rise to the rms overshoots from the buried hot wire observed on Fig. 16, and the overshoots in pressure fluctuation normalized by the mean shear stress on Fig. 15. The correlation curves demonstrate the substantial changes in lee-side flow toward and subsequent to primary separation. A normalized time scale in terms of outer flow variables such as $(t p_w) / \delta^*$ is not used because the boundary-layer displacement thickness is unknown.

We may deduce some important notions concerning the eddy structure in the flow from the curvature of the correlation curves (Ref. 64). All component eddies are roughly of the same size when the curvature is not especially large anywhere. Such behavior is noted in the adverse pressure gradient flow ($\phi = 135^\circ, 140^\circ$, and up to $\phi = 145^\circ$) where large eddies dominate. (An approximate measure of the "longest connection in turbulent behavior" (Ref. 65) may be gained from the area beneath the correlation curve, and ϕ_{s1} provides the largest area.) The same characteristic is also shown in the very thin boundary layer along the leeward meridian where small eddies must be the overwhelming constituents. A wide range of eddy sizes, on the other hand, is indicated by local regions of high curvature in the correlation curves. This may occur near the origin, but cannot be ascertained categorically. Alternatively, when there are two distinct ranges of eddy size present, the correlation curve appears as a summation of two correlation functions of substantially different scales. We note this characteristic, in particular, for the boundary layer having reacted to the favorable pressure gradient ($\phi = 90^\circ$), then a diminution of this property through the primary separation region to begin again at the reattachment line, $\phi_A = 155^\circ$. The two ranges of eddy size would also appear to exist at the secondary separation line, $\phi_{s2} = 160^\circ$, from which a coiled vortex does not appear to have developed yet (see Fig. 9).

The autocorrelation is related approximately to the spectral density by a Fourier transform. Spectra are shown in Fig. 18 corresponding to most of the autocorrelations displayed in Fig. 17. The ordinates are in the ratio of the mean square values of voltage fluctuation at each circumferential station divided by the value at primary separation. In conjunction with previous observations, as the three-dimensional boundary layer thickens progressively toward ϕ_{s1} , the energy associated with the large eddies spreads to lower frequencies (as is the case at ϕ_{s2} also). The converse is noted along the leeward meridian. When two distinct ranges of eddy size exist, the spectrum functions should also take a noticeable two-component form similar to those of the correlation functions, as we see at $\phi_A = 155^\circ$ and $\phi_{s2} = 160^\circ$.

Having witnessed these substantial changes, it would appear that, in calculating complex, three-dimensional viscous flows leading to separation, the use of turbulence models that do not recognize the large changes in spectra in at least a qualitative way will not be representative of the physics of the flow.

3.2 Lee-Side Flow About a Tangent-Ogive/Cylinder

3.2.1 Mean Flow Field

As mentioned previously, some supportive three-dimensional laser velocimeter measurements of mean and fluctuating velocity about a slender tangent ogive/cylinder (Fig. 19) were obtained by Owen and Johnson (Ref. 49) at a relative incidence of 2.3. The measurements were made in the Ames 0.6- by 0.6-m (2- by 2-ft) Transonic Wind Tunnel at a Mach number of 0.6 and Reynolds number based on the 0.3-m (1-ft) total length of the body, equal to $Re = 2 \times 10^6$. The velocity field in the wake was measured with a two-color forward scatter frequency-offset laser velocimeter, allowing two velocity components perpendicular to the axis to be obtained simultaneously. Since we are seeking three velocity components, however, two sets of measurements must be taken. In the first set, the laser beams were normal to the tunnel axis so that the axial (u) and vertical (w) velocity components were found. From these two components could be obtained the vertical velocity in the crossflow plane perpendicular to the body axis (see Fig. 19). For the second set, the transmitting optics were rotated 30° about the z -axis and measurements taken again. Now, one velocity component measured was again the vertical velocity whereas the second was a combination of the axial velocity (u) and the lateral velocity (v) in wind-tunnel coordinates. Thus, since the axial velocity had already been measured, the lateral velocity could be calculated. In other words, the lateral velocity in the crossflow plane is obtained, since it is the same in both wind-tunnel and body coordinates.

Bragg cells, which produced zero-velocity frequency offsets in both color systems, were incorporated to remove directional ambiguity from the measurements. Without this capability, Owen and Johnson (Ref. 49) have cautioned against believing any measurements in flows that are unsteady or possess a high degree of turbulence. Since with increasing Mach number the helix angle of a streamtube becomes smaller with respect to the axis of the vortex, larger axial distances are required for particles to reach the core regions. Thus an artificial aerosol was introduced into the wind-tunnel flow to provide adequate intensity of the scattered light with a count mean diameter of 0.7 micron. Additional details of the instrumentation are given in Ref. 49.

Figure 20 shows the crossflow velocity vector field at 4 diameters from the nose, just aft of the ogive/cylinder junction where we detect that the vortex core positions are located along $\bar{z}/d \sim 0.9$ at $y/d \sim 0.3$. Note the slight asymmetry, but the resemblance to the cone lee-side flow. The vertical velocities, \bar{w} , in the crossflow plane are plotted in Fig. 21, the maximum down-flow values ($-\bar{w}_{\max}$) occurring in the pitch plane of symmetry as the leeward meridian is approached. This large down-flow is a relatively narrow region between the rotational pair and is highlighted as an intense line of maximum vapor concentration in the cone crossflow visualization displayed in Fig. 8 (and see later, Fig. 26). The velocity gradient through the core region at $\bar{z}/d \sim 0.9$ is virtually infinite on the scale of measurement resolution as it is on the axial velocity distributions displayed in Fig. 22. At the stations approaching the leeward meridian where the crossflow is largest, the axial velocity is lowest. The axial velocity then increases very rapidly across the vortex to a value overshooting the free-stream by about 20%.

Lateral crossflow velocities (\bar{v}) resolved from the measurements normal to and 30° to the tunnel axis are shown in Fig. 23. As expected, a pass through the core positions at $\bar{z}/d = 0.9$ shows virtually zero velocity. Moving to traverses above and below the vortex centers shows the lateral velocities to be at maximum levels at y/d values in line with the cores.

3.2.2 Fluctuating Velocities

Some insight into the turbulent and unsteady nature of the vortex flow field about the ogive-cylinder has also been obtained with the laser velocimeter. These data in Figs. 24 and 25, obtained at $\bar{z}/d = 0.9$ through the vortex cores, show peaks in the rms velocity, one on each side of the pitch-plane close to the regions of maximum mean velocity gradient (the core centers?). In addition, the rms fluctuation levels remain substantial in regions of small and zero mean velocity gradient, suggesting that large scale turbulence is present throughout the lee-side domain.

3.3 Asymmetrical Separation of the Lee-Side Cone Flow

Figure 26 is a laser-vapor screen crossflow picture of the Mach 0.6 lee-side separated flow about the cone once asymmetry has commenced at a relative incidence just less than 3. As the symmetry developed, the vortices began "bumping together" with increasing unsteadiness to cause large values of rms side force even when the mean side force was near zero. At this particular combination of Mach number, Reynolds number, and configuration of 4% nose bluntness, the starboard vortex moved away from the surface and the port vortex remained more-or-less stationary. As incidence increased to higher values, the unsteady interaction between the vortices increased in intensity and the starboard vortex moved even farther from the surface and rolled over the port side rotational flow. In so doing, the entire lee-side flow indicated diffusion of the well-organized helical vortex structures but there was no visual evidence of periodic shedding.

Along with this movement of the lee-side flow, we would expect the resultant force vector to move towards the side of the cone to which one vortex is closest. This is seen in Fig. 27, where in the subsonic/transonic Mach number range $0.6 < M_\infty < 0.95$ (at $Re = 13.5 \times 10^6$), the initial direction of side-force development remains the same. As Mach number increases to supersonic speeds, the start of the side force is less precise. Therefore, the critical angles of incidence for onset of side-force development are plotted in Fig. 28 as where the mean side force has reached 5% of the normal force. We detect that depending on the nose bluntness, free-stream Mach number, Reynolds number (and, no doubt, the unknown free-stream fluctuation level), the onset angle of incidence varies between 2.5 and 4.5 times the cone seminoise angle. This range is somewhat higher than the nominal values of 2 reported for sharp forebodies by Keener and

Chapman (Ref. 6) at Mach numbers less than 0.6. It is clear that operating with a sharp apex causes an earlier onset of side force as does the very high Reynolds number of 35×10^6 . Up to Mach 1, on the other hand, whereas the same observation can be made for the 13.5×10^6 relative to the 4.5×10^6 tests, the reverse is true in supersonic flow.

The effect of rolling the cone in 90° increments and then pitching through the α range is illustrated in Fig. 29 at a constant length Reynolds number of 13.5×10^6 . For roll angles 180° apart, the side-force development is in opposite directions as we might suppose if it were a small geometrical imperfection at the nose systematically perturbing the flow development. Figure 29 shows also that lowering the Reynolds number from 13.5×10^6 (essentially turbulent) to 4.5×10^6 (perhaps transitional) delays the onset of side force and shows that repeatability at a given test condition is good.

We await laser velocimeter measurements in the crossflow to report on the fluctuations in the lee-side flow as asymmetry develops.

4. CONCLUSIONS

Based on relatively high Reynolds number measurements of mean and fluctuating flow quantities on the surface of a yawed 5° semiangle circular cone at a Mach number of 0.6 in association with overall force, laser-vapor screen, and mean surface pressure measurements in the expanded Mach number range $0.6 < M_\infty < 1.8$, we conclude that:

1. The development of the viscous flow and separation about this cone at low Mach numbers follows closely the diagnosis of Rainbird (Refs. 28, 29) at higher Mach numbers. As the relative incidence increases, there is a progressive quasi-steady development of symmetrically disposed lobes of vortical fluid that eventually form tightly coiled vortices close to the leeward plane of symmetry. Secondary separations from the surface are found beneath the primary vortices with further increase of incidence. When the relative incidence exceeds about 2.5, the lee-side flow becomes increasingly unsteady and anti-symmetrical with respect to the pitching plane causing substantial side forces to develop of magnitude near the values of normal force.

2. In subsonic flow, the fluctuation voltage levels from buried wires in the cone surface, provided evidence of an increase in turbulent eddy size as the primary separation line was approached, and a decrease of eddy size in the thin boundary-layer leeward attachment line region. At the separation lines, these large-scale motions give rise to overshoots in rms fluctuating voltage levels from the buried wires in the surface, and overshoots in rms pressure fluctuations when normalized by the mean-shear stress. Notwithstanding, the absolute level of rms pressure fluctuation decreased in the circumferential adverse pressure gradient to a minimum at the positions of the conical separation lines, and increased to a maximum at the leeward attachment line. This behavior is contrary to that found beneath two-dimensional attached boundary layers in adverse and favorable pressure gradients by other experimenters.

3. The resultant mean-shear stress was always finite, being lower at the separation line positions and higher at the attachment lines.

REFERENCES

1. Peake, D. J.: Phenomenological Aspects of Quasi-Stationary Controlled and Uncontrolled Three-Dimensional Flow Separations. Three-Dimensional and Unsteady Separation at High Reynolds Numbers, AGARD-LS-94, Feb. 1978.
2. Küchemann, D.: Report on the IUTAM Symposium on Concentrated Vortex Motions in Fluids. Jour. Fluid Mechanics, part 1, vol. 21, 1965, pp. 1-20.
3. Maskell, E. C.; and Küchemann, D.: Controlled Separation in Aerodynamic Design. RAE TM 463, Mar. 1956.
4. Rainbird, W. J.; Crabbe, R. S.; Peake, D. J.; and Meyer, R. F.: Some Examples of Separation in Three-Dimensional Flows. CASI Journal, vol. 12, no. 10, Dec. 1966, pp. 409-423.
5. Peake, D. J.; Rainbird, W. J.; and Atraghji, E. G.: Three-Dimensional Flow Separations on Aircraft and Missiles. AIAA Journal, vol. 10, no. 5, May 1972, pp. 567-580.
6. Keener, E. R. and Chapman, G. T.: Onset of Aerodynamic Side Forces at Zero Sideslip on Symmetric Forebodies at High Angles of Attack. AIAA Paper 74-770, Aug. 1974.
7. Keener, E. R.; Chapman, G. T.; Kruse, R. L.: Effects of Mach Number and Afterbody Length on Onset of Asymmetric Forces on Bodies at Zero Sideslip and High Angles of Attack. AIAA Paper 76-66, Jan. 1976.
8. Tobak, M.: On Local Inflexional Instability in Boundary-Layer Flows. Journal of Applied Mathematics and Physics (ZAMP), vol. 24, 1973, pp. 330-354.
9. Rao, D. M.: Side-Force Alleviation on Slender, Pointed Forebodies at High Angles of Attack. AIAA 78-1339, Aug. 1978.
10. Keener, E. R.; and Chapman, G. T.: Similarity in Vortex Asymmetries over Slender Bodies and Wings. AIAA Journal, vol. 15, no. 9, September 1977, pp. 1370-1372.
11. Shanks, R. E.: Low-Subsonic Measurements of Static and Dynamic Stability Derivatives of Six Flat-Plate Wings having Leading-Edge Sweep Angles of 70° to 84° . NASA TN D-1822, 1963.

12. Nielsen, J. N.: Non-Linearities in Missile Aerodynamics. AIAA Paper 78-20, Jan. 1978.
13. Allen, H. J.; and Perkins, E. W.: Characteristics of Flow over Inclined Bodies of Revolution. NACA RM A50L07, Mar. 1951.
14. Küchemann, D.; and Weber, J.: Vortex Motions. Zamm 45, 1965, pp. 457-474.
15. Lamont, P. J.; and Hunt, B. L.: Prediction of Aerodynamic Out-of-Plane Forces on Ogive-Nosed Circular Cylinders. Journal Spacecraft and Rockets, vol. 14, no. 1, Jan. 1977, pp. 38-44.
16. Deffenbaugh, F. D.; and Koerner, W. G.: Asymmetric Vortex Wake Development on Missiles at High Angles of Attack. Journal Spacecraft and Rockets, vol. 14, no. 3, Mar. 1977, pp. 155-162.
17. Maskell, E. C.: Flow Separation in Three Dimensions. RAE Aero. Report 2565, Nov. 1955.
18. Brown, S.: Singularities Associated with Separating Boundary Layers. Royal Society of London Phil. Trans., Series A, vol. 257, 1965, pp. 409-444.
19. Legendre, R.: "Séparation de L'Écoulement Laminaire Tridimensionnel," La Recherche Aéronautique, No. 54, pp. 3-8, Nov.-Dec. 1956.
20. Lighthill, M. J.: Attachment and Separation in Three-Dimensional Flow. Laminar Boundary Layers, Sect. II.2.6, L. Rosenhead, ed., Oxford University Press, 1963, pp. 72-82.
21. Crabbe, R. S.: Flow Separation about Elliptic Cones at Incidence. NAE Aero. Report LR-436, National Research Council of Canada, Aug. 1965.
22. McRae, D. S.: The Conically Symmetric Navier-Stokes Equations: Numerical Solution for Hypersonic Cone Flow at High Angle of Attack. AFFDL-TR-76-139, Mar. 1977.
23. McRae, D. S.; and Hussaini, M. Y.: Supersonic Viscous Flow over Cones at Incidence. Sixth International Conference on Numerical Methods in Fluid Dynamics, Tbilisi, USSR, June 1978.
24. Rakich, J. V.; and Lubard, S. C.: Numerical Computation of Viscous Flows on the Lee Side of Blunt Shapes Flying at Supersonic Speeds. NASA SP-347, Mar. 1975, pp. 531-542.
25. Smith, J. H. B.: Inviscid Fluid Models, Based on Rolled-up Vortex Sheets, for Three-Dimensional Separation at High Reynolds number. Three-Dimensional and Unsteady Separation at High Reynolds Numbers, AGARD-LS-94, Feb. 1978.
26. McCormack, R. W.: The Effect of Viscosity in Hypervelocity Impact Cratering. AIAA Paper 69-354, 1969.
27. Tracy, R. R.: Hypersonic Flow over a Yawed Circular Cone. GALCIT Memo No. 69, Grad. Aero. Labs., California Institute of Technology, Pasadena, California, 1963.
28. Rainbird, W. J.: The External Flow Field about Yawed Circular Cones. AGARD CP-30, May 1968.
29. Rainbird, W. J.: Turbulent Boundary-Layer Growth and Separation on a Yawed Cone. AIAA Journal, vol. 6, no. 12, Dec. 1968.
30. Cleary, J. W.: Effects of Angle of Attack and Bluntness on Laminar Heating Rate Distribution on a 15° Cone at Mach Number of 10.6. NASA TN D-5450, Oct. 1969.
31. Agarwal, R.: Private communication, July 1978.
32. Pulliam, T. H.; and Steger, J. L.: On Implicit Finite-Difference Simulations of Three-Dimensional Flow. AIAA Paper 78-10, Jan. 1978.
33. Smith, J. H. B.: A Review of Separation in Steady, Three-Dimensional Flow. In Flow Separation, AGARD CP-168, May 1975.
34. Rainbird, W. J.; Crabbe, R. S.; and Jurewicz, L. S.: A Water Tunnel Investigation of the Flow Separation about Circular Cones at Incidence. National Research Council of Canada, Aero. Rept. LR-385, Sept. 1963.
35. Guffroy, D.; Roux, B.; Marcillot, J.; Brun, R.; and Valensi, J.: Étude Théorique et Expérimentale de la Couche Limite Autour d'un Cône Circulaire Placé en Incidence dans un Courant Hypersonique. AGARD CP 30, May 1968.
36. Stetson, K. F.: Experimental Results of Laminar Boundary-Layer Separation on a Slender Cone at Angle of Attack at $M_\infty = 14.2$. ARL 71-0127, Aug. 1971.
37. Nebbeling, C.; and Bannink, W. J.: Experimental Investigation of the Supersonic Flow Field about a Slender Cone at High Incidences. Delft University of Technology, Dept. of Aerospace Eng. Rept. LR-233, Nov. 1976.
38. McEliderry, E. D.: An Experimental Study of Sharp and Blunt 6-Degree Cones at Large Incidence with a Turbulent Boundary Layer at Mach 6. AFFDL-TM-74-170, Sept. 1974.
39. Mangler, K. W.; and Smith, J. H. B.: A Theory of the Flow Past a Slender Delta Wing with Leading-Edge Separation. Proc. Roy. Soc., Series A, No. 1265, May 1959, pp. 200-217.

40. Smith, J. H. B.: Improved Calculations of Leading-Edge Separation from Slender Delta Wings. *Proc. Roy. Soc., Series A*, vol. 306, 1968, pp. 67-90.
41. Nebbeling, C.; and Bannink, W. J.: Experimental Investigation of Supersonic Flow Past a Slender Cone at High Incidence. *Journal of Fluid Mechanics*, vol. 87, part 3, Aug. 1978, pp. 475-496.
42. Whitfield, J. D.; and Dougherty, N. S.: A Survey of Transition Research at AEDC. In *Laminar-Turbulent Transition*, AGARD CP-224, May 1977.
43. Haniy, R. D.: Effects of Transducer Flushness on Fluctuating Surface Pressure Measurements. *Progress in Astronautics and Aeronautics*, vol. 46, 1976, pp. 291-302.
44. Higuchi, H.; and Peake, D. J.: A Bi-Directional, Buried-Wire Skin Friction Gage. NASA TM-78531, 1978.
45. Murthy, V. S.; and Rose, W. C.: Wall Shear Stress Measurements in a Shock-Wave Boundary-Layer Interaction. *AIAA Journal*, vol. 16, no. 7, July 1978, pp. 667-672.
46. Rubesin, M. W.; Okuno, A. F.; Mateer, G. G.; and Brosh, A.: A Hot Wire Surface Gage for Skin Friction and Separation Detection Measurements. NASA TM X-62,465, July 1975.
47. Bradshaw, P.; and Unsworth, K.: A Note on Preston Tube Calibrations in Compressible Flow. Imperial College Aero. Report 73-07, Sept. 1973.
48. McCroskey, W. J.; and Durbin, E. J.: Flow Angle and Shear Stress Measurements Using Heated Films and Wires. *ASME Journal Basic Engineering*, 94D, pp. 46-52, Mar. 1972.
49. Owen, F. K.; and Johnson, D. A.: Wake Vortex Measurements of Bodies at High Angle of Attack. *AIAA Paper 78-23*, Jan. 1978.
50. Sims, J. L.: Tables for Supersonic Flow Around Right Circular Cones at Small Angle of Attack. NASA SP-3007, 1964.
51. Schiff, L. B.: A Study of the Nonlinear Aerodynamics of Bodies in Nonplanar Motion. NASA TR R-421, Jan. 1974.
52. Chaussee, D. S.; Kutler, P.; and Holtz, T.: Inviscid Supersonic/Hypersonic Body Flowfield and Aerodynamics from Shock-Capturing Technique Calculations. *Journal Spacecraft and Rockets*, vol. 13, no. 6, June 1976, pp. 325-331.
53. Ericsson, L. E.: Dynamic Support Interference. *Journal Spacecraft and Rockets*, vol. 9, no. 7, July 1972, pp. 547-553.
54. Rainbird, W. J.: Errors in Measurement of Mean Static Pressure of a Moving Fluid Due to Pressure Holes. *DME/NAE Quarterly Bulletin*, No. 1967(3), National Research Council of Canada, Oct. 1967.
55. Franklin, R. E.; and Wallace, J. M.: Absolute Measurements of Static-Hole Error Using Flush Transducers. *Journal of Fluid Mechanics*, vol. 42, part 1, 1970, pp. 33-48.
56. Willmarth, W. W.: Pressure Fluctuations Beneath Turbulent Boundary Layers. *Annual Review of Fluid Mechanics*, vol. 7, 1975, pp. 13-38.
57. Bradshaw, P.: Inactive Motion and Pressure Fluctuations in Turbulent Boundary Layers. NPL Aero. Report 1172, Oct. 1965.
58. Kistler, A. C.; and Chen, W. S.: The Fluctuating Pressure Field in a Supersonic Turbulent Boundary Layer. *Journal of Fluid Mechanics*, vol. 16, part 1, 1963, pp. 41-64.
59. Mabey, D. G.: Analysis and Correlation of Data on Pressure Fluctuations in Separated Flow. *Journal of Aircraft*, vol. 9, no. 9, Sept. 1972, pp. 642-645.
60. Schloemer, H. H.: Effects of Pressure Gradients on Turbulent Boundary-Layer Wall Pressure Fluctuations. U.S. Navy Underwater Sound Lab. Report No. 747, 1966.
61. Burton, T. E.: Wall Pressure Fluctuations at Smooth and Rough Surfaces under Turbulent Boundary Layers with Favorable and Adverse Pressure Gradients. *Acoustics and Vibration Lab. MIT Report No. 70208-9*, 1973.
62. Emmerling, R.: The Instantaneous Structure of the Wall Pressure Under a Turbulent Boundary Layer Flow. *Max-Planck-Institut für Strömungsforschung Rep. No. 9/1973*.
63. Willmarth, W. W.; and Yang, C. S.: Wall Pressure Fluctuations Beneath Turbulent Boundary Layers on a Flat Plate and a Cylinder. *Journal of Fluid Mechanics*, vol. 41, 1970, p. 47.
64. Townsend, A. A.: *The Structure of Turbulent Shear Flow*. Cambridge University Press, 1976.
65. Hinze, J. O.: *Turbulence*. McGraw Hill, 1959, pp. 34-42.

ACKNOWLEDGMENTS

The authors express their gratitude to L. H. Ohman, of NAE Ottawa, for kindly making available to NASA the basic 5° cone model and pitot rake. They also wish to acknowledge the substantial efforts of F. Lemos of Ames Research Center, who fabricated the hot-wire gages and who, along with S. J. Lockyear from NAE (on NASA support) assembled and fitted the intricate instrumentation in the model.

Special thanks are also due to: D. Peña of ARO Inc. for his fine services as project engineer in charge of the tunnel test; to W. J. Rainbird, for conveying previously unpublished side-force results obtained on the same model in the NAE 1.5- by 1.5-m (5- by 5-ft) blowdown wind tunnel; and to D. Chaussee of Nielsen Engineering and Research, for running the inviscid flow code of Ref. 52.

One of us, F. Kevin Owen, would also like to acknowledge the support of the Air Force Armament Laboratory, Eglin, AFB, Florida, and Ames Research Center, Moffett Field, California, under Contract No. NAS2-9663.

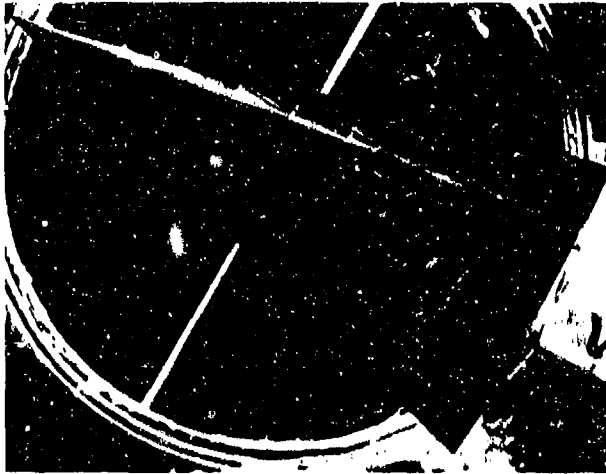
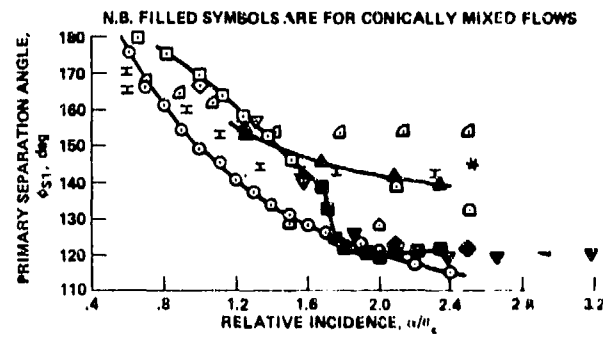


Fig.1 Limiting streamlines on 1-1/2:1 elliptic cone at 30° incidence in a water tunnel; laminar; $R_{L_\infty} = 2.7 \times 10^4$ (Crabbe (Ref.21))



AUTHOR	SYMBOL	M_∞	θ_c deg	R_{L_∞}	TYPE
RAINBIRD et al., 1963	○	~ 0	12.5	2.7×10^4	LAMINAR
GUFFROY et al., 1968	⊖	7.0	9.0	$\sim 5.0 \times 10^5$	
STETSON 1971	△	14.2	5.6	8.0×10^5	
RAINBIRD 1968a, b	□, △, ◇	1.80, 4.25, 1.80, 4.25	12.5, 12.5, 5.0, 5.0	$2.5 \times 10^7, 5.1 \times 10^7, 3.4 \times 10^7, 6.8 \times 10^7$	
PEAKE et al., 1978	*	0.60	5.0	1.4×10^7	TURBULENT
NEBBELING AND BANNINK 1976	▽	2.94	7.5	7.0×10^6	
McELDERRY 1974	△	6.06	6.0	16.0×10^6	

Fig.2 Circumferential primary separation angles on circular cones at incidence (or yaw)

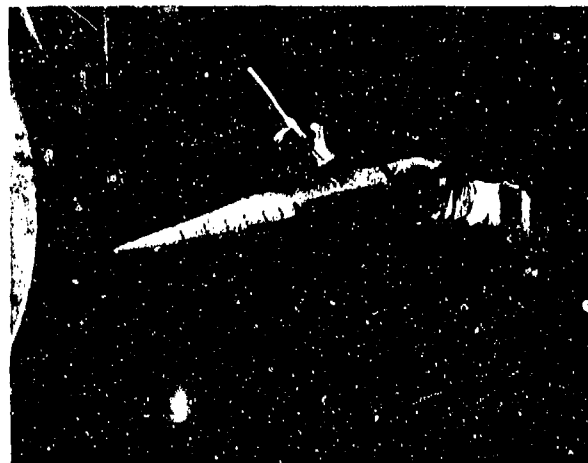


Fig.3 5° cone in NASA Ames 1.8- by 1.8-m (6- by 6-ft) wind tunnel

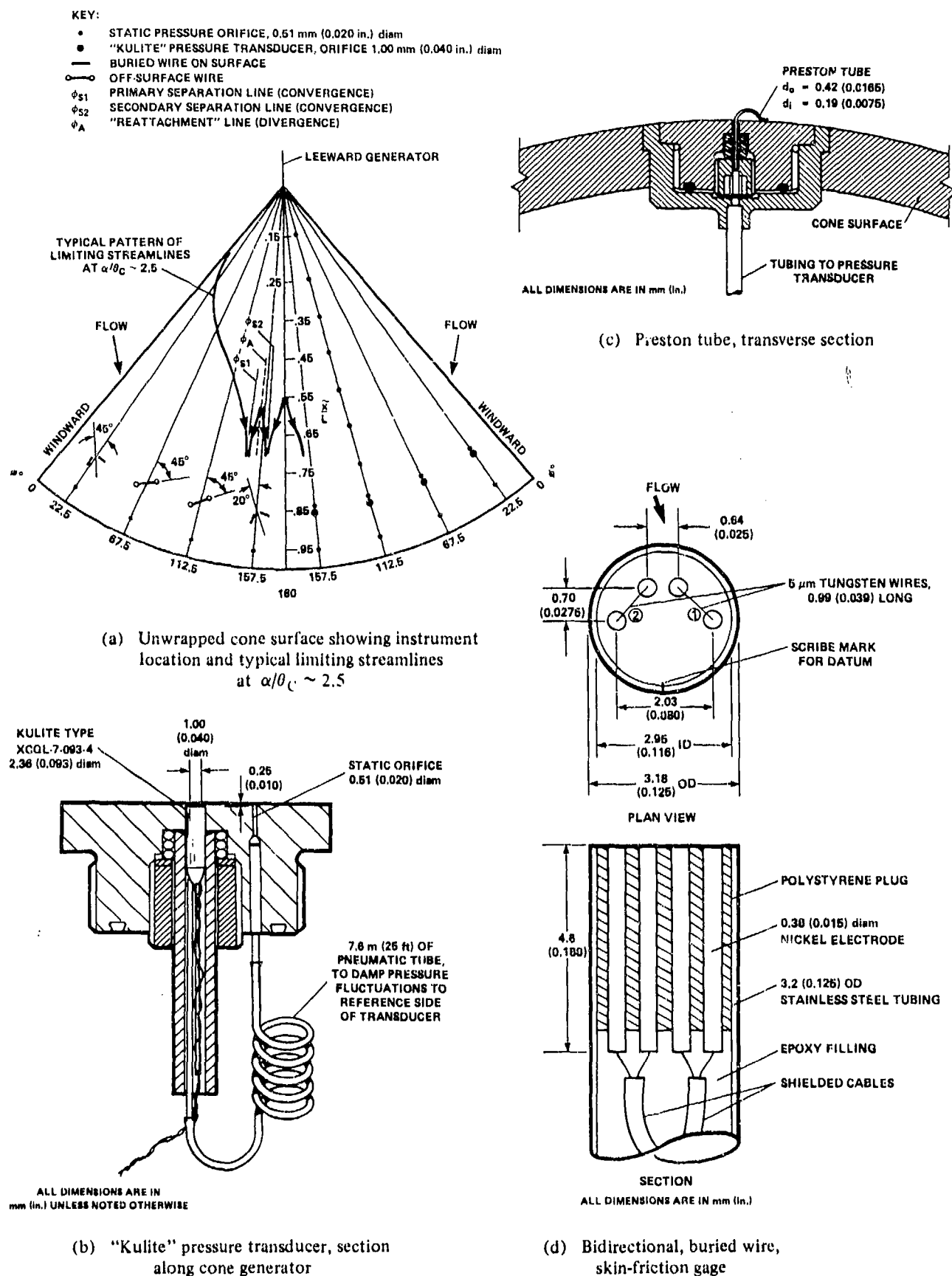
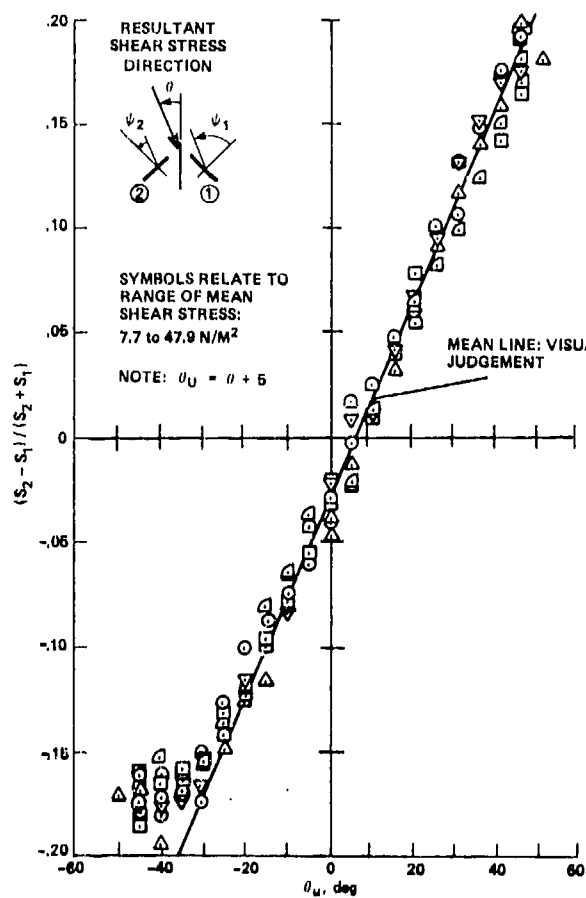
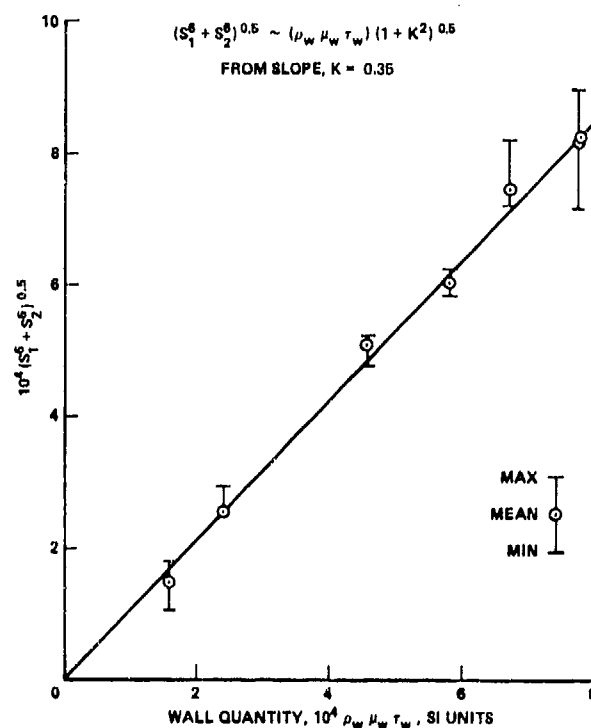


Fig.4 Instrumentation on cone surface

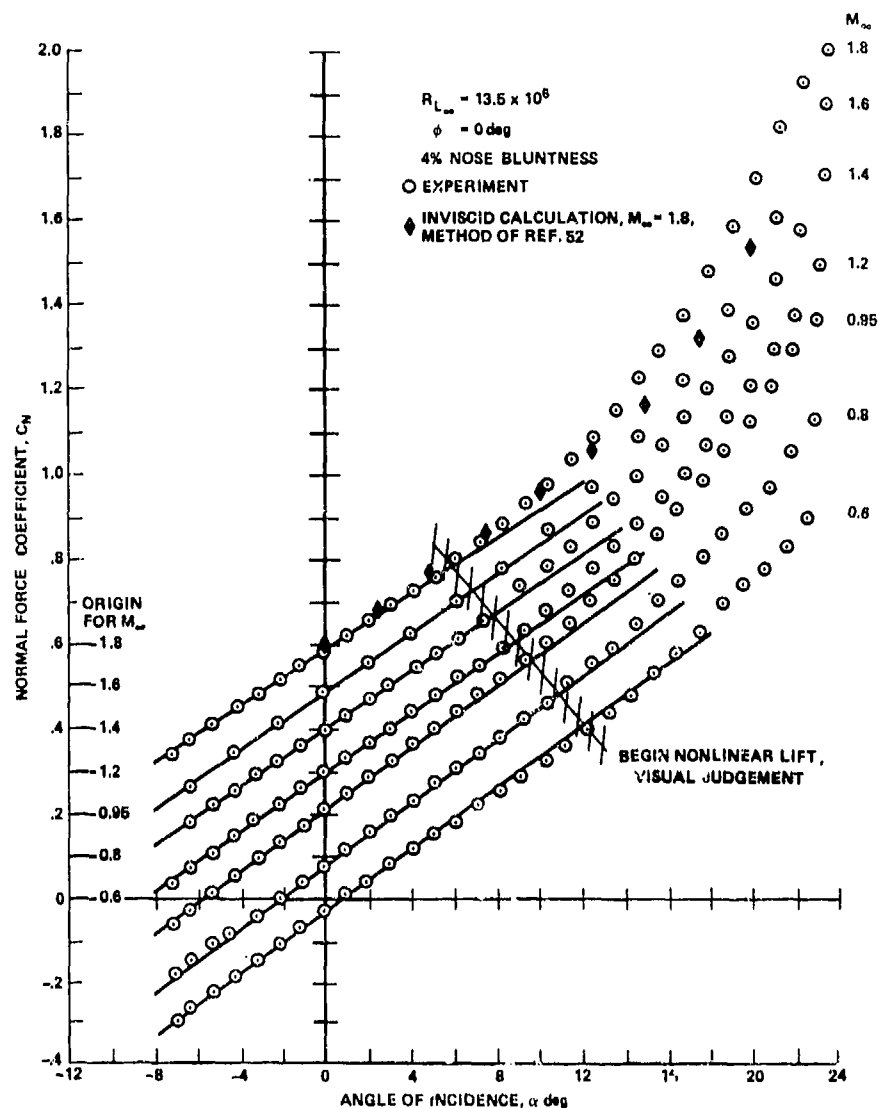
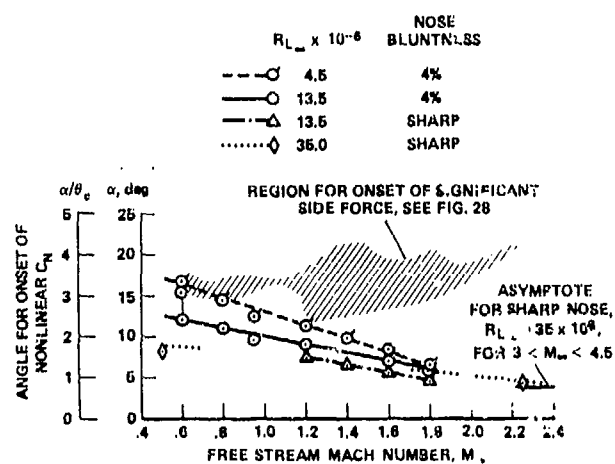


(a) Directional



(b) Magnitude of skin friction

Fig.5 Calibrations of bidirectional, buried wire skin-friction gage

Fig.6 Normal forces on 5° cone for $0.5 < M_\infty < 1.8$ Fig.7 Onset boundaries of nonlinear normal force for 5° cone

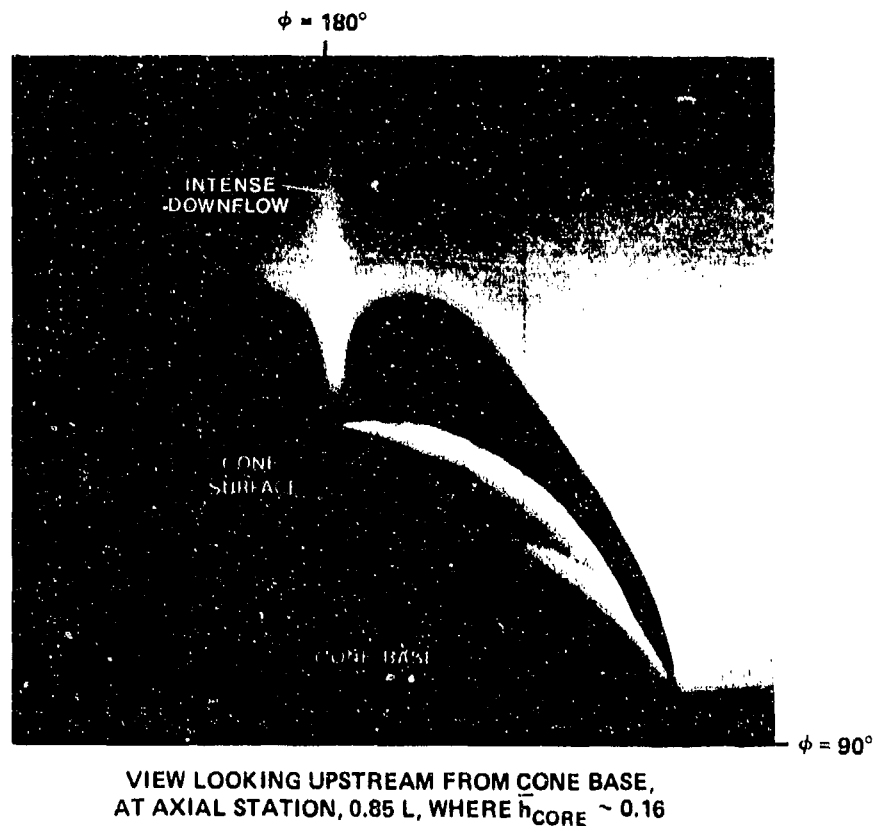


Fig.8 Laser vapor screen of symmetrical lee-side flow separation on 5° cone at $\alpha/\theta_C \sim 2.5$, $M_\infty = 0.6$, $R_{L_\infty} = 13.5 \times 10^6$

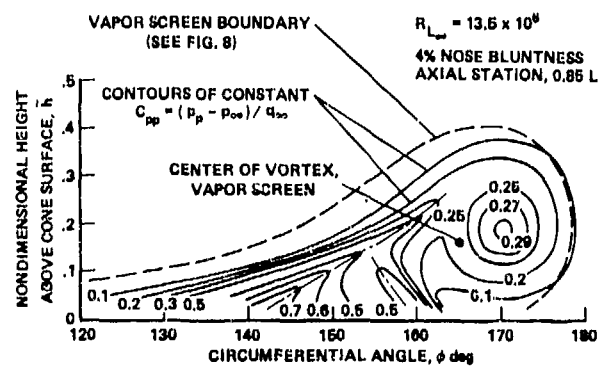


Fig.9 Contours of pitot pressure deficit in symmetrical lee-side flow separation at $\alpha/\theta_C \sim 2.5$, $M_\infty = 0.6$

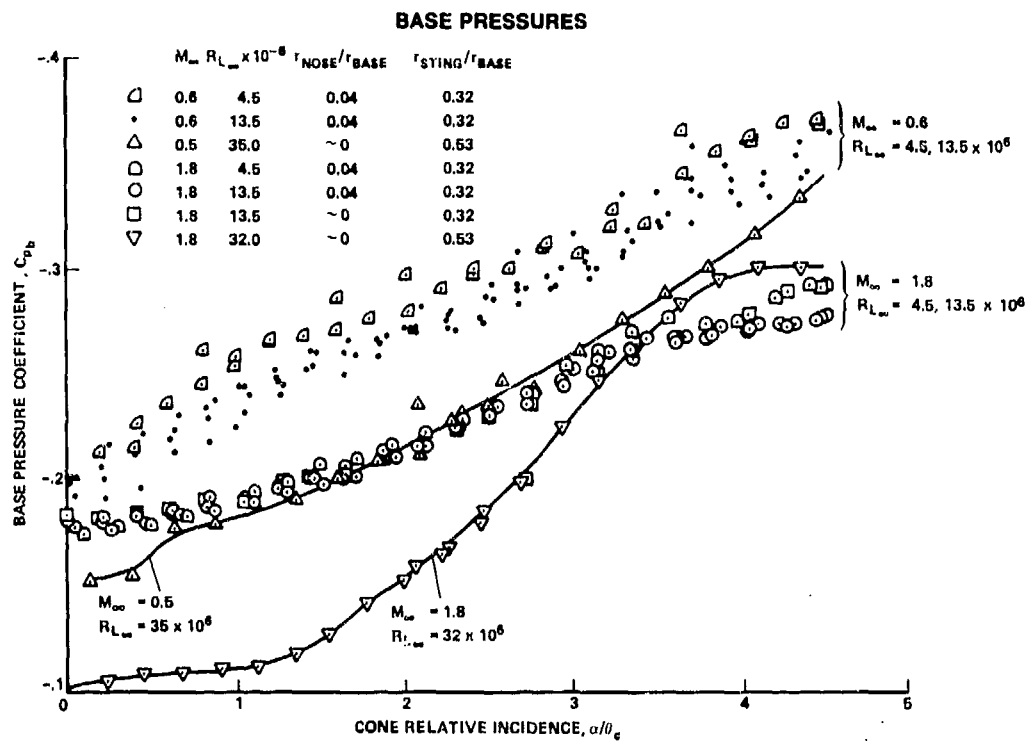
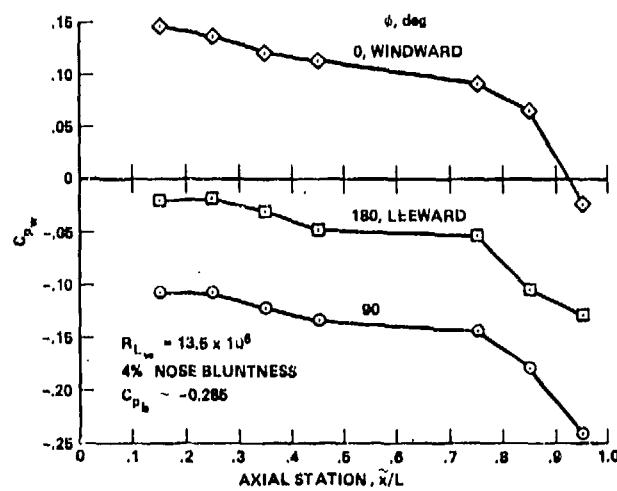
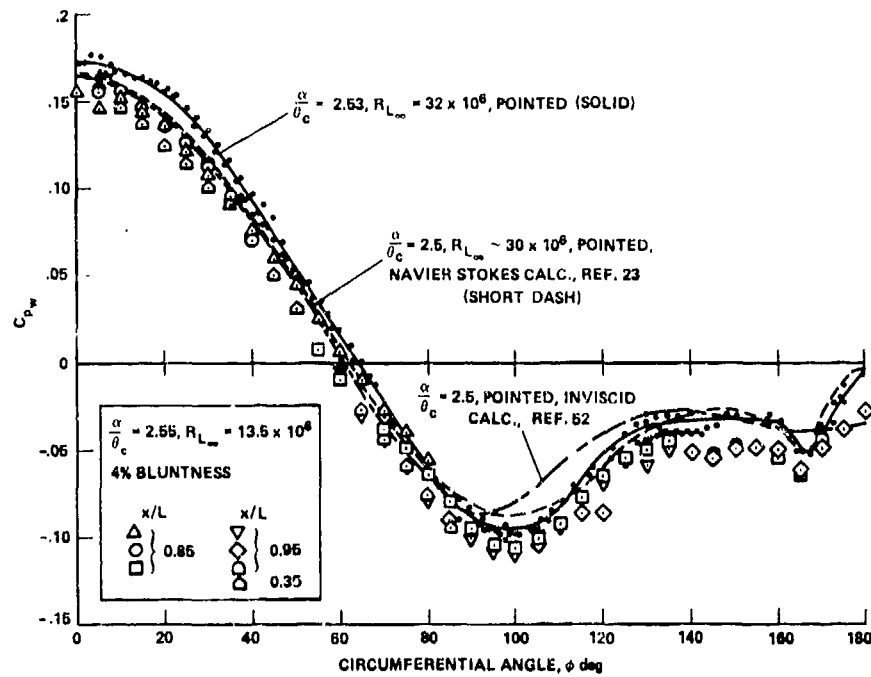
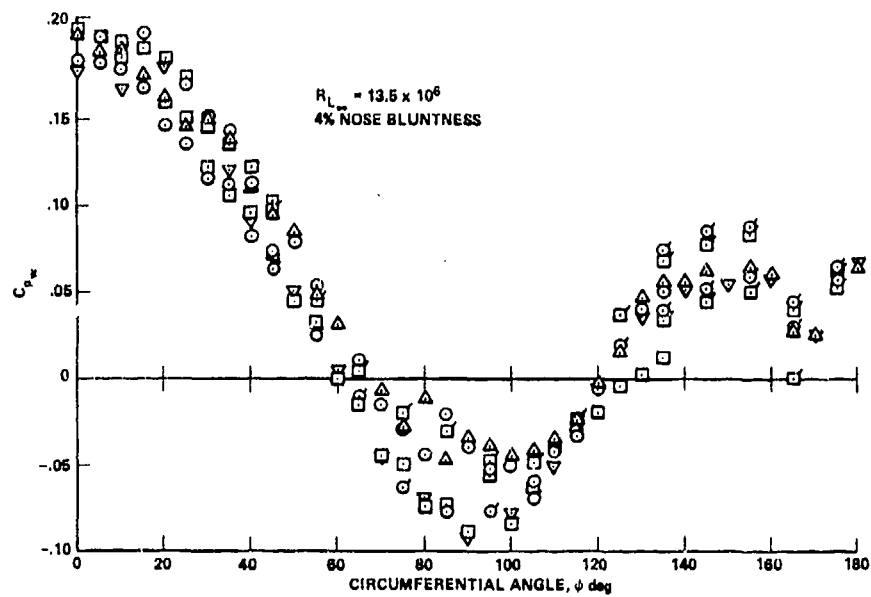


Fig.10 Base pressures on 5° cone

Fig.11 Base effect on pressure along cone generators
at $\alpha/\theta_c \sim 2.5$, $M_\infty = 0.6$

(a) $M_\infty = 1.8$ (b) $M_\infty = 1.2$ Fig.12 Circumferential distributions of mean static pressure on 5° cone at $\alpha/\theta_c \sim 2.5$

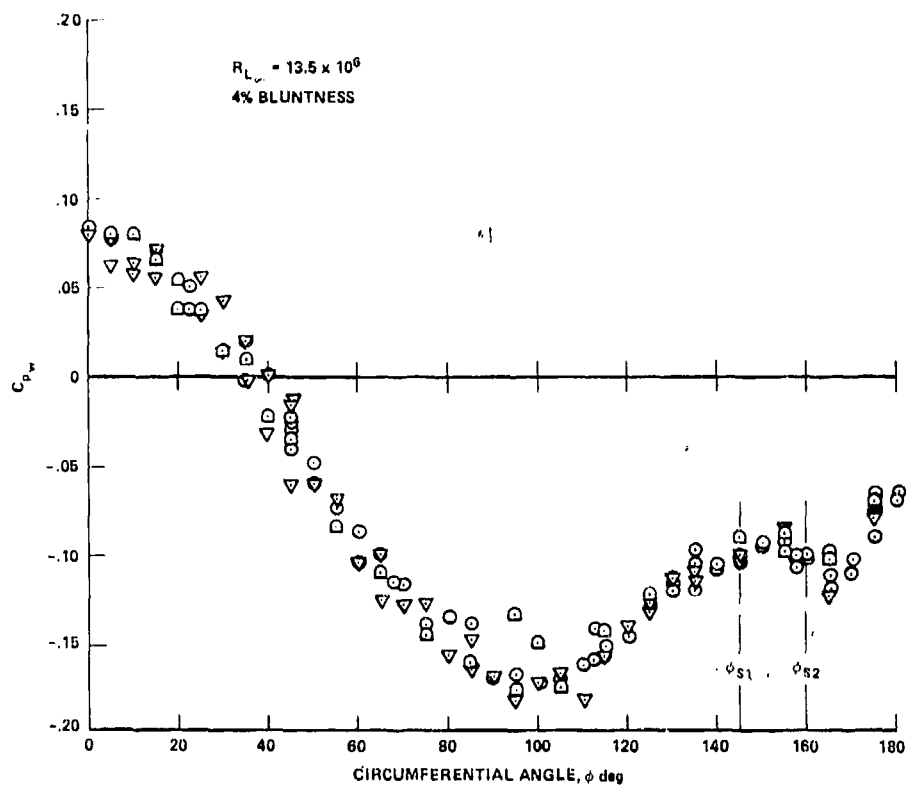


Fig.12 Concluded

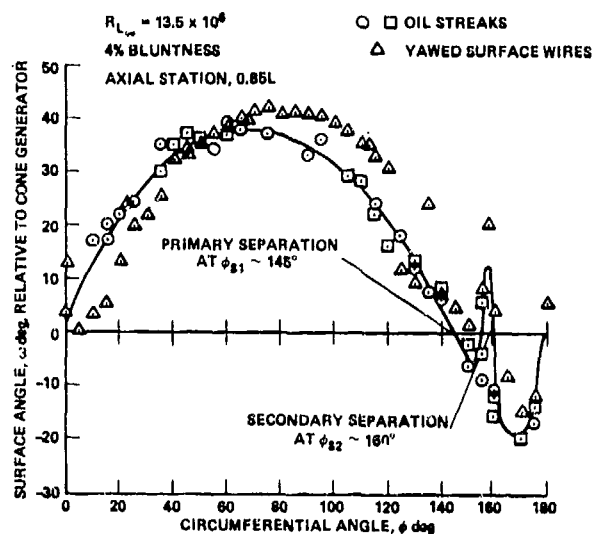


Fig.13 Surface shear stress directions
around 5° cone at $\alpha/\theta_c \sim 2.5$,
 $M_\infty = 0.6$

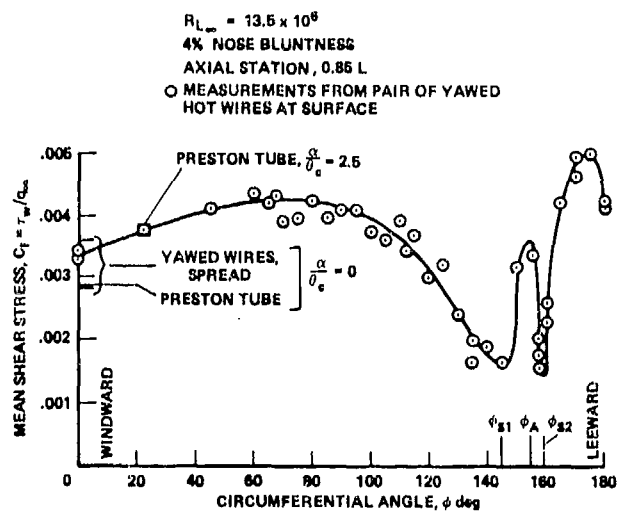


Fig.14 Skin-friction around 5° cone
at $\alpha/\theta_c \sim 2.5$, $M_\infty = 0.6$

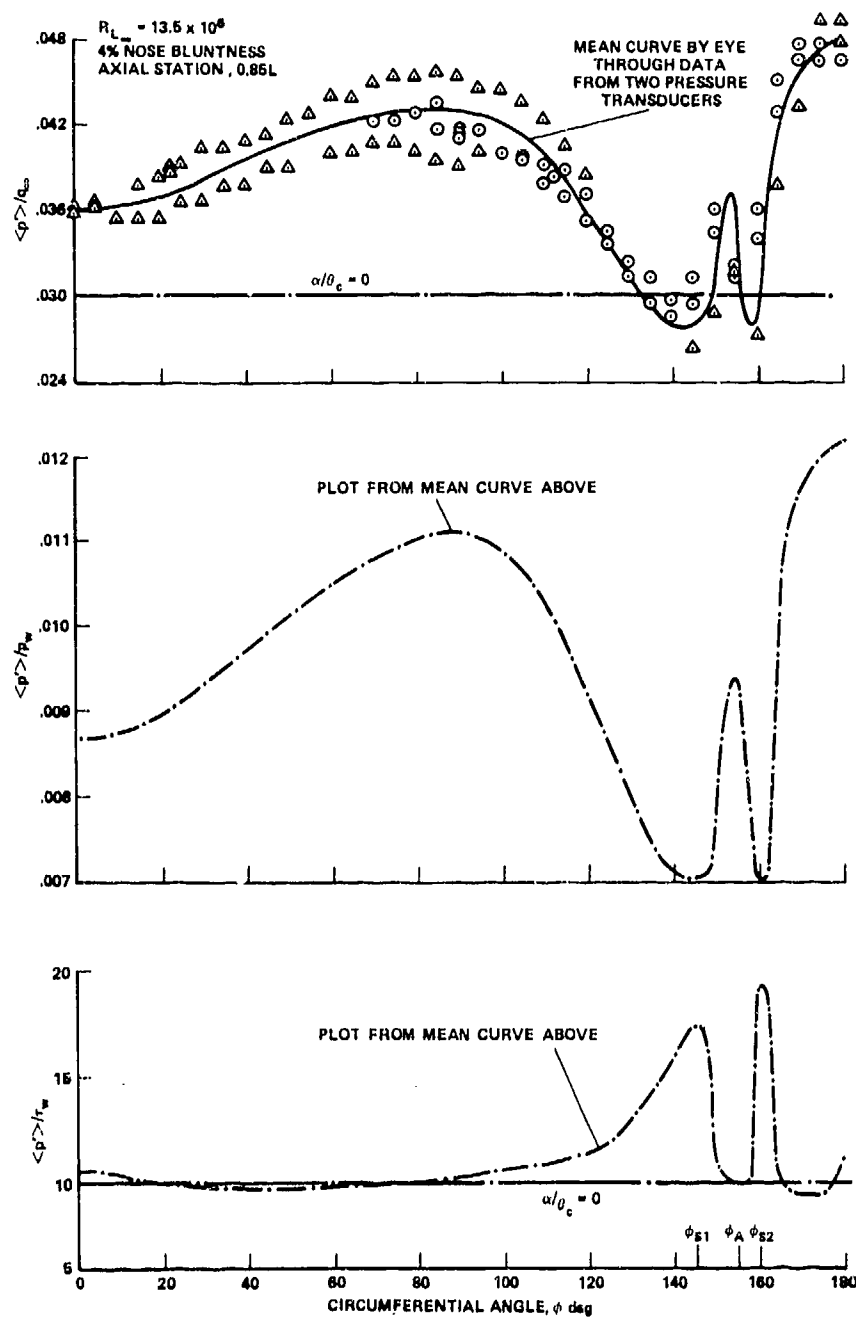


Fig.15 RMS pressures around 5° cone at $\alpha / \theta_c \sim 2.5$, $M_\infty = 0.6$

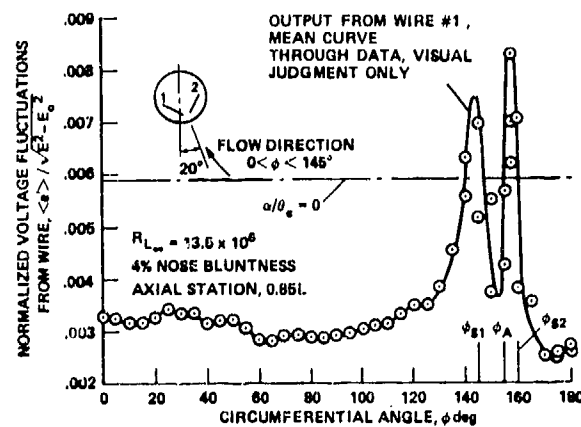


Fig.16 RMS voltages from buried wire on 5° cone at $\alpha / \theta_c \sim 2.5$, $M_\infty = 0.6$

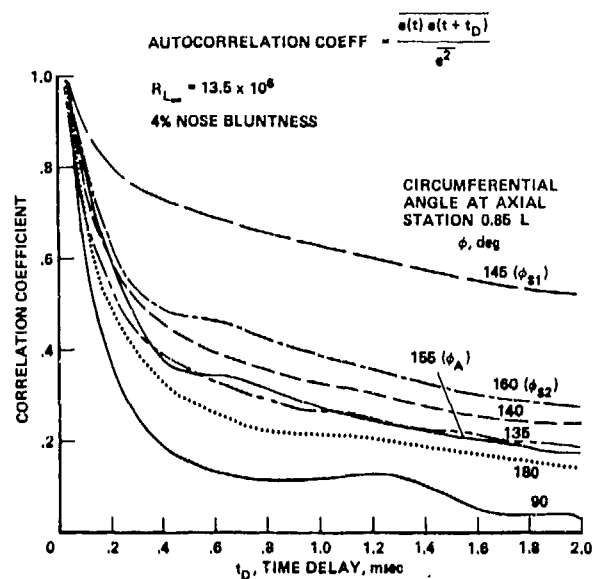


Fig.17 Autocorrelations from buried wire at $\alpha/\theta_C \sim 2.5$, $M_\infty = 0.6$

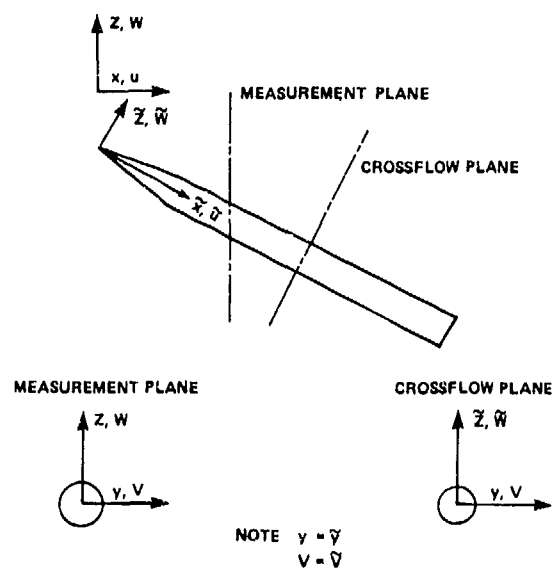


Fig.19 Coordinate system about 16° semiangle tangent ogive cylinder

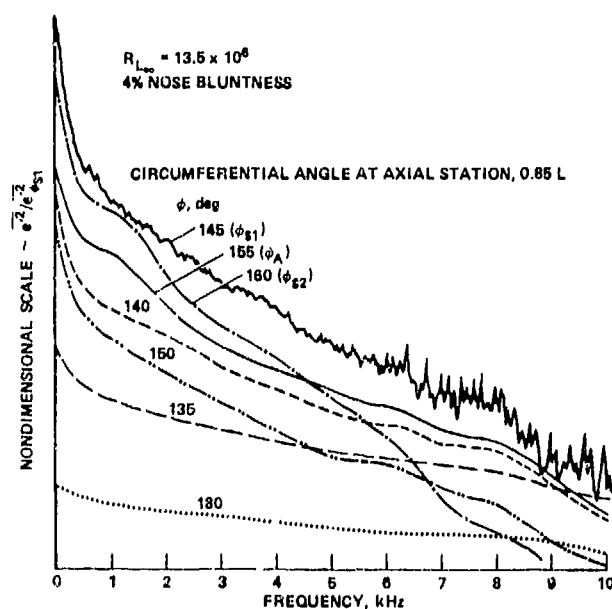


Fig.18 Spectra from buried wire at $\alpha/\theta_C \sim 2.5$, $M_\infty = 0.6$

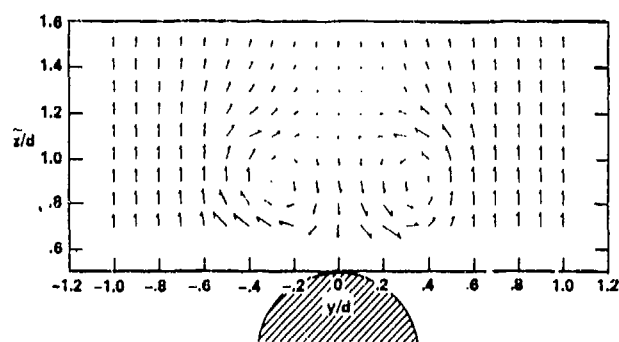


Fig.20 Crossflow velocity vectors on lee-side of 16° tangent ogive cylinder, $M_\infty = 0.6$, $\tilde{x}/d = 4$

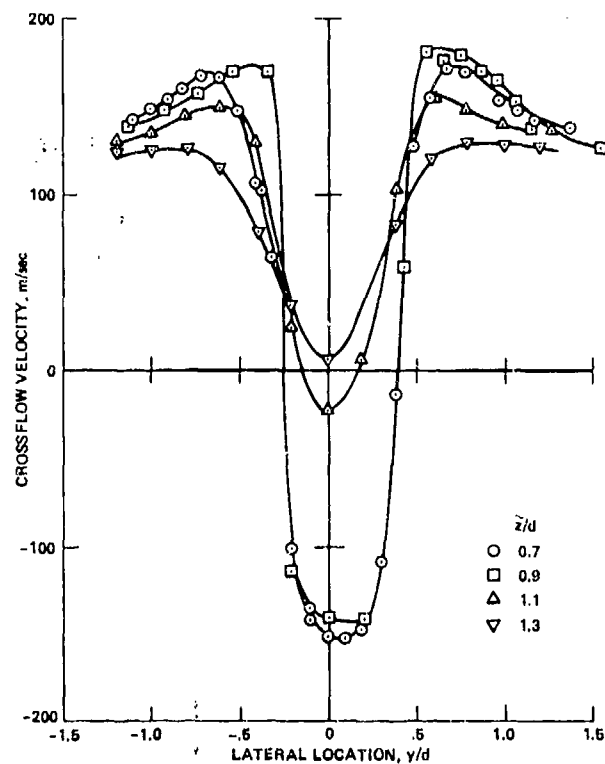


Fig. 21 Mean vertical velocity in crossflow plane of 16° tangent ogive cylinder, $M_\infty = 0.6$, $\bar{x}/d = 4$

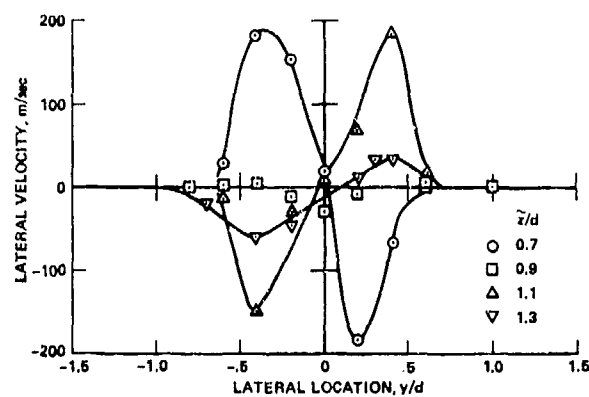


Fig. 23 Mean lateral velocity in crossflow plane about 16° tangent ogive cylinder, $M_\infty = 0.6$, $\bar{x}/d = 4$

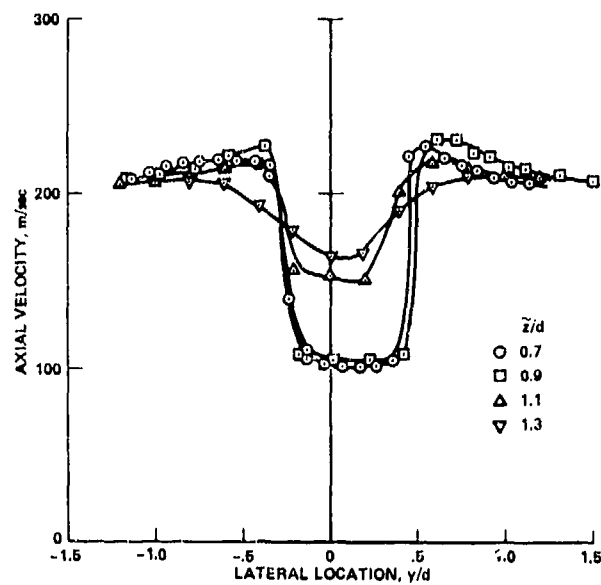


Fig. 22 Mean axial velocity in wind-tunnel coordinates about 16° tangent ogive cylinder, $M_\infty = 0.6$, $\bar{x}/d = 4$

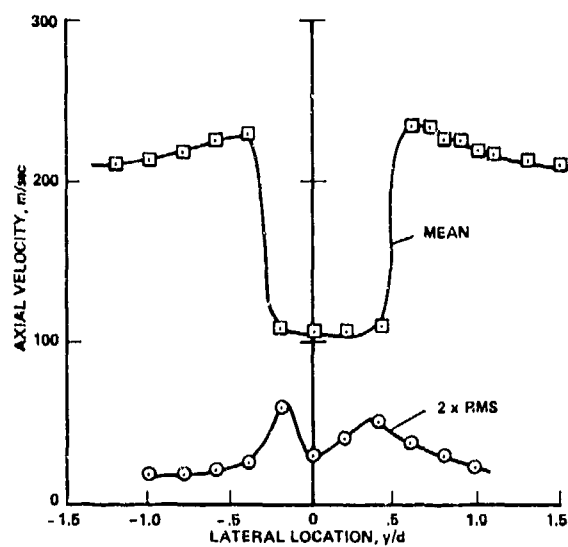


Fig. 24 Mean and RMS axial velocity about 16° tangent ogive cylinder, $M_\infty = 0.6$, $\bar{x}/d = 4$, $\bar{z}/d = 0.9$

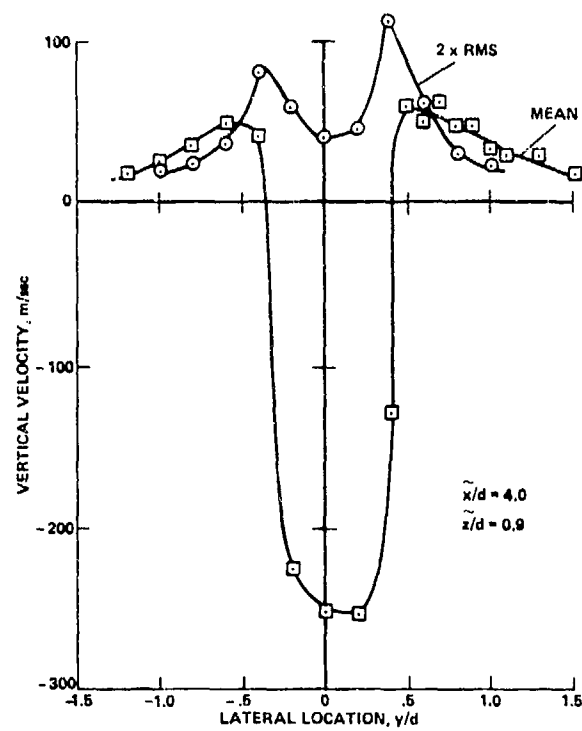


Fig.25 Mean and RMS vertical velocity about 16° tangent ogive cylinder,
 $M_\infty = 0.6$, $\bar{x}/d = 4$, $\bar{z}/d = 0.9$

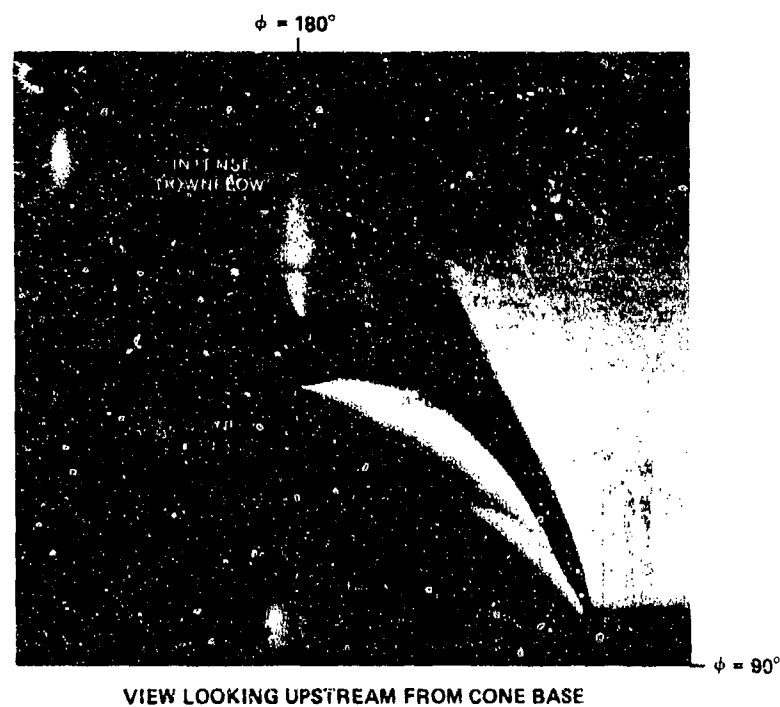
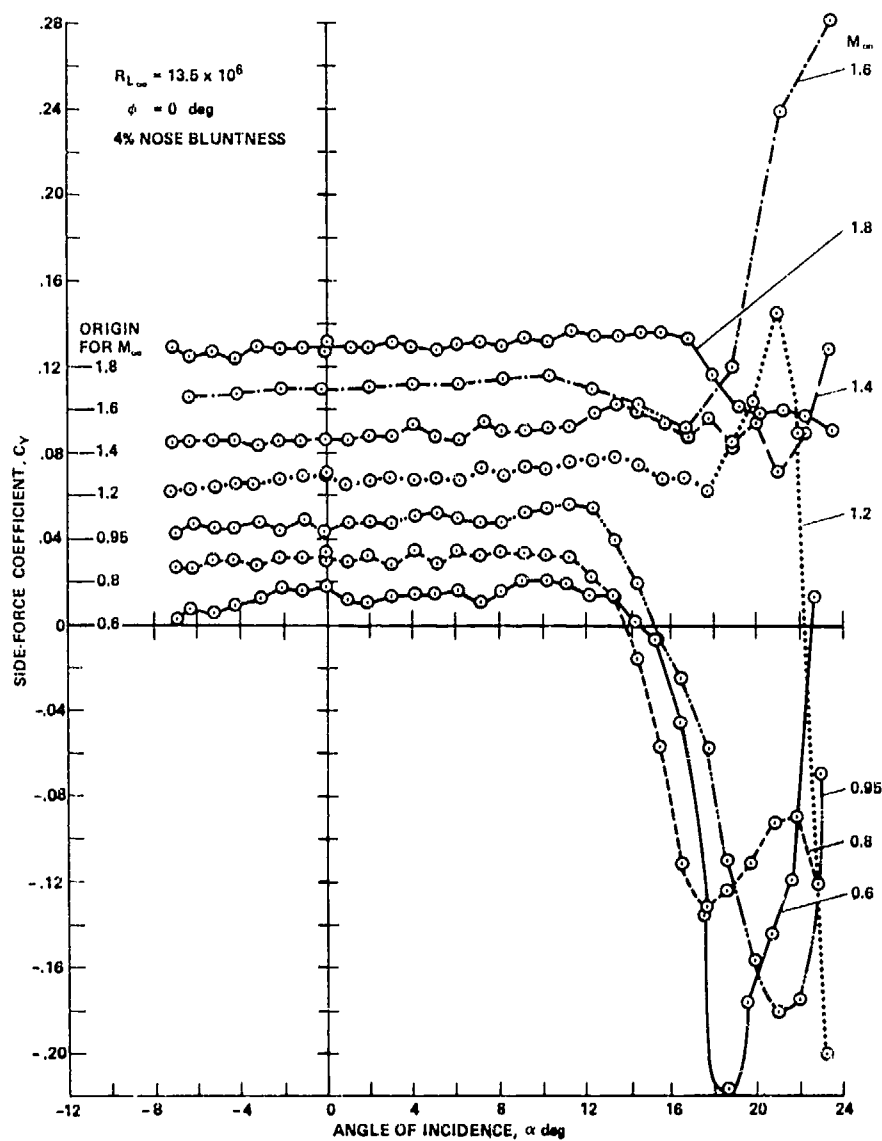
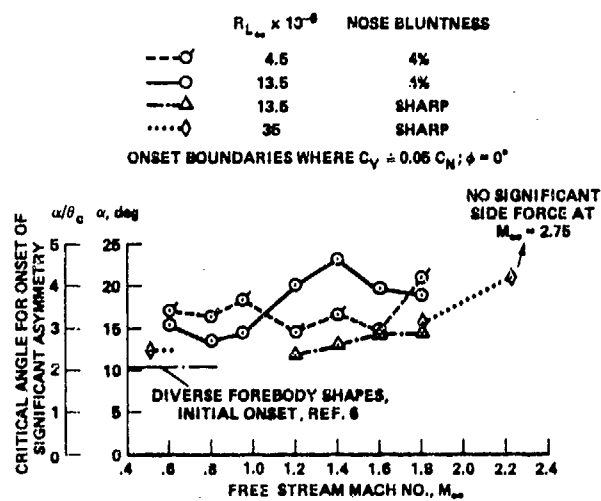


Fig.26 Laser vapor screen of nonsymmetrical lee-side flow separation on 5° cone
 at $\alpha/\theta_C \sim 2.9$, $M_\infty = 0.6$

Fig.27 Side forces on 5° cone for $0.6 < M_\infty < 1.8$ Fig.28 Onset of significant side-force asymmetry for 5° cone

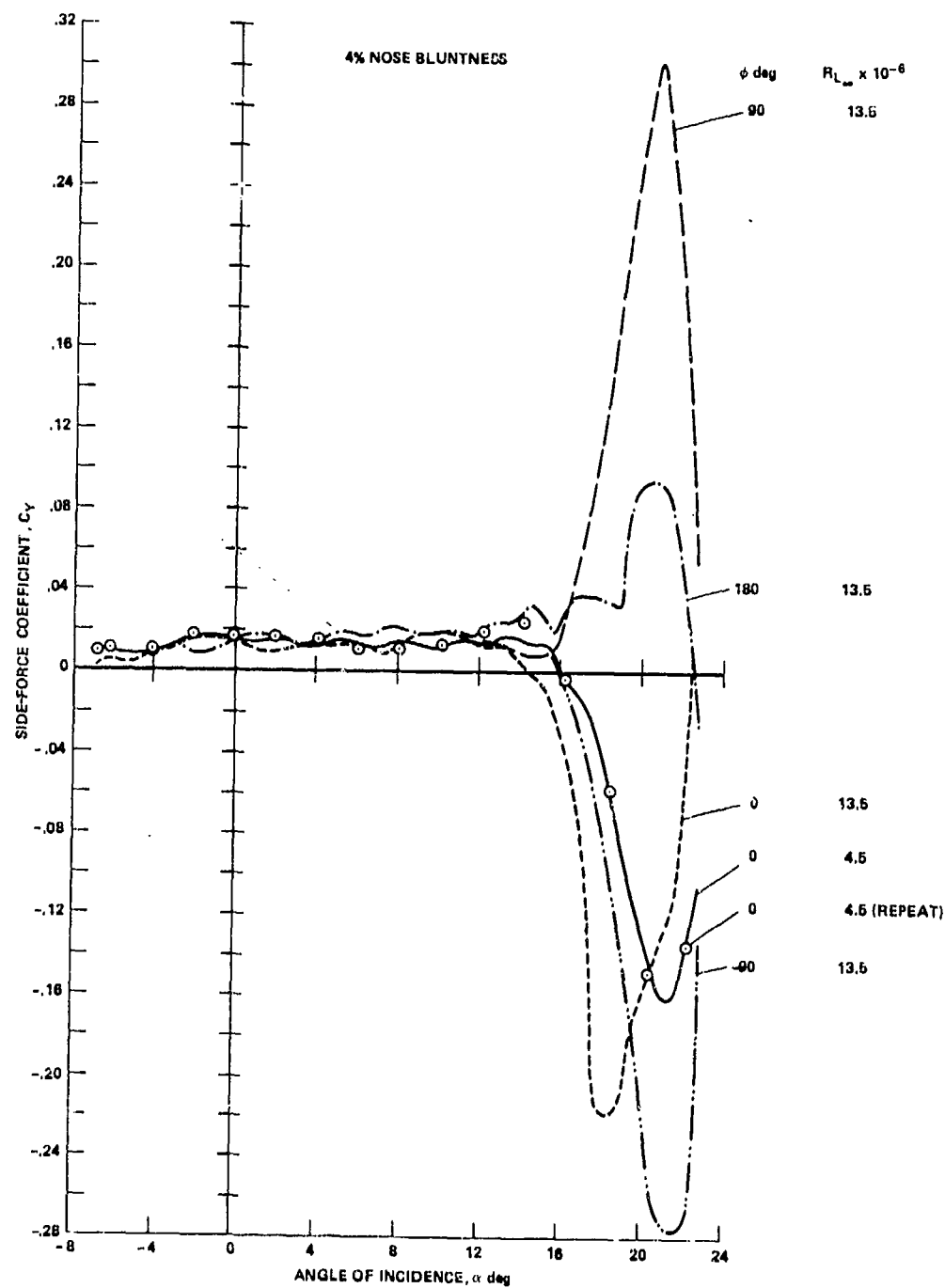


Fig.29 Effect of roll angle and Reynolds number on side force at $M_\infty = 0.6$

PRESSURES ON A SLENDER BODY AT HIGH ANGLE OF ATTACK
IN A VERY LOW TURBULENCE LEVEL AIR STREAM

by

B. L. Hunt and P. C. Dexter

Department of Aeronautical Engineering, University of Bristol,
Queen's Building, University Walk, Bristol, BS8 1TR

SUMMARY

This paper reports experimentally measured transient pressures at low speeds on a model consisting of a circular cylinder with a tangent ogive nose in the angle of attack range from 30° to 90° . Great care was taken to eliminate extraneous disturbances: a wind tunnel with an extremely low level of free stream turbulence (approx. 0.01%) was used, the model was rigidly mounted and efforts were made to ensure laminar separation without turbulent re-attachment. By comparing the results with those obtained previously on the same model in similar tests at a higher level of free stream turbulence (approx. 0.7%) it is shown that there is a dramatic reduction in unsteadiness in the low turbulence level air stream and switching of the flow pattern is virtually eliminated. However, it is also found that the mean unswitched level is dependent on the roll angle of the model and hence that strict control of the free stream conditions is not sufficient to guarantee results which are independent of the experimental equipment. Some details of the inherent unsteadiness present in the flow pattern are presented.

NOTATION

a	speed of sound
d	diameter of cylinder
k_{crit}	minimum height of roughness to promote transition
Re	Reynolds number, $Ud \cos \alpha / \nu$
p'	fluctuating pressure
U	free stream velocity
u'	fluctuating velocity
U_τ	friction velocity, $(\tau_w / \rho)^{1/2}$
x	axial distance measured from tip of nose
α	angle of attack
AC_p	coefficient of pressure difference based on cross flow dynamic head, $\Delta p / \frac{1}{2} \rho U^2 \sin^2 \alpha$
AC'_p	amplitude of fluctuations of pressure difference coefficient
$\overline{AC_p}$	mean value of pressure difference coefficient
Δp	difference between surface pressures at points $\pm 75^\circ$ from leading generator
ρ	density
ϕ	roll angle
τ_w	wall shear stress

1. INTRODUCTION

The existence of aerodynamic side forces on slender bodies of revolution at high angles of attack was first reported twenty five years ago^{1,2} but little further work was done during the subsequent fifteen years. Since the late 1960s, however, the desire to enlarge the flight envelopes of both missiles and military aircraft has promoted a large number of investigations of the phenomenon. References to many of these may be found in a paper by Nielsen,³ very recent work has mostly been reported in two AIAA conferences.^{4,5}

Despite the intensive research effort of the last ten years, very little understanding of the mechanisms by which the side force is determined has been achieved. One feature which has been established in numerous studies is that the side force is associated with an asymmetric vortex pattern in the lee of the body; an idealised sketch of the vortices is shown in Figure 1. However, few reliable details of the vortex pattern are known and its relationship to the sectional side force distribution is not understood.

Probably the major barrier to progress has been the difficulty of obtaining meaningful experimental results. If the published data is studied, certain trends emerge but it is usually not difficult to find unexplained exceptions. Furthermore, large discrepancies exist between the results obtained by different workers and the data often do not vary smoothly with the independent parameters. The extent of the difficulty is illustrated by the study conducted by Wardlaw and Morrison.⁶ They attempted to correlate all the measured values of overall side force against conventional flow and geometric parameters. However, they found the scatter to be so great that they were forced to adopt the view that these flows are non-deterministic and hence that the data

must be treated by linear regression techniques.

Previous experimental studies have given some clues to the origins of these difficulties. One of the most striking peculiarities observed by most (but not quite all) of the experimenters who have looked for it is the variation (in both direction and magnitude) of the side force with roll angle. Work by Keener et al.^{7,8} has provided strong evidence that this effect is somehow related to the detailed geometry or surface roughness of the tip of the nose. It is also a common experience that the force can be substantially altered by a change in surface conditions, such as is produced by a coat of paint. Again, the work of Keener et al.⁸ provides evidence of this behaviour. It thus seems that one of the sources of experimental problems is an extreme sensitivity to details of the model, particularly to the condition of the nose.

Another cause of experimental difficulties is unsteadiness. Lamont and Hunt⁹ recorded the transient behaviour of the difference between two surface pressure tappings at equal angles from the leading generator of the body. Two examples of the traces obtained are shown in Figure 2. It is clear that in Figure 2(a) a complete switch of the flow pattern has occurred from one state to its mirror image state. The trace in Figure 2(b) is less clear but again temporary changes in sign are present. After studying a large number of traces, Lamont and Hunt came to the conclusion that the major fluctuations are caused by a switching of the flow pattern towards and sometimes into the mirror image state. Since there appears to be a degree of stability in at least one of the two states, the switching must be caused by external disturbances. Lamont and Hunt suggested that the disturbances in their tests came from free stream turbulence. They showed by simple estimates that the observed behaviour was consistent with the scale and intensity of turbulence in the wind tunnel. They have pointed out^{10,11} that model vibration is another source of external disturbances which is likely to cause switching. It is clear that if Lamont and Hunt are correct, then time averaged measurements which are taken in the presence of unsteadiness will depend on the free stream turbulence level and on the dynamic behaviour of the model support. Clark¹² has observed the wake flow using a water tunnel and he supports the notion that unsteadiness is due to free stream turbulence and to model vibration. However, he suggests that the transient behaviour is more complex than that proposed by Lamont and Hunt. According to Clark, a number of different vortex patterns can exist and the flow jumps from one pattern to another under the influence of external disturbances.

Lamont and Hunt's transient records showed differences in switching pattern with roll angle while the inferred unswitched levels seemed to be unaffected. This lead Lamont and Hunt to suggest^{10,11} that the observed influence of roll angle on the time averaged readings would be eliminated if the unsteadiness were eliminated. Some support for this possibility is given by the fact that results which are independent of roll angle have, occasionally, been obtained.^{13,14}

The work reported here sets out to check Lamont and Hunt's notion of the importance of free stream turbulence. Great care has been taken to avoid switching. Lamont and Hunt's simple estimate⁹ of the effect of free stream turbulence indicates that switching should virtually cease when the turbulence level is reduced to 0.1%. However, this value is unlikely to be very accurate and a wind tunnel has been chosen with the lowest turbulence level that is likely to be achievable in practice, approximately 0.01%. The other features of the experiment are that the model is extremely rigidly clamped and an attempt has been made to avoid turbulent reattachment of the flow. The model used is the same as that used by Lamont and Hunt and hence a comparison of the present results with those obtained earlier by Lamont and Hunt shows the direct effect of a change to a wind tunnel of much lower free stream turbulence.

2. APPARATUS

Results will be presented from both the Bristol University 2.1 m x 1.5 m wind tunnel and the Royal Aircraft Establishment 1.2 m x 0.9 m wind tunnel. Both are low speed tunnels. The R.A.E. tunnel has a contraction ratio of 31:1 which gives a streamwise turbulence level of approximately 0.01% over roughly the central 1 m x 0.8 m of the tunnel. Full details of the tunnel characteristics are given in References 15-17. No direct measurements of turbulence level have been carried out as part of the current series of tests but the level of pressure fluctuations on the model at zero incidence has been obtained and will be discussed later. The Bristol tunnel has a much smaller contraction ratio (5:1). This and other factors contribute to producing a streamwise turbulence level of approximately 0.7%.¹⁸ This is quite high for a low speed tunnel but low compared to the level which might be expected in transonic or supersonic facilities, where many overall force measurements have been made.

The same model was used in both tunnels. It is the transient model of Lamont and Hunt's tests,⁹ a sketch can be seen in Figure 3. The constant diameter section is 51 mm in diameter and contains four pressure tapped stations spaced 51 mm apart, each with four pairs of pressure tappings, as shown in Figure 3. The nose of the model can either be fitted directly on to the measuring section or on to an untapped section of length four diameters which is then attached to the measuring section; it is thus possible to obtain measurements at one diameter spacing extending from one diameter to eight diameters from the nose junction. Several nose pieces were used: the results shown here were all obtained with a sharp tangent ogive having a length to maximum diameter ratio of 3. A constant diameter rear support section completes the model: this was clamped rigidly to the floor and roof of the tunnel by means of a 51 mm diameter vertical pylon. The clamps were located some six diameters aft of the most rearward measuring station. Any

angle of attack in the range 0 to 90° could be achieved. No vibration of the nose tip was visible when running except a slight motion at angles of attack around 70°. In the R.A.E. tunnel, the nose could be observed through a telescope which would have revealed a movement of ± 0.02 mm.

The surface pressures were recorded as the difference between two points symmetrically disposed about the plane of incidence; the tests reported here all used the tappings at $\pm 75^\circ$ from the leading generator. The measured values are therefore directly related to the magnitude of the sectional side force. In the Bristol tunnel and in early tests in the R.A.E. tunnel, the pressure difference was obtained by connecting the pressure tappings across a ± 0.1 p.s.i.d. Scanco variable reluctance transducer mounted inside the model. However, some concern was felt at feeding a fluctuating pressure to the back of the transducer and a new system was adopted. This used two transducers, each connected to one of the ports and with a common steady backing pressure (the tunnel free stream static pressure, appropriately damped); the difference of the outputs was then taken electrically. In this arrangement, the two transducers were Setra ± 0.1 p.s.i.d. variable capacitance type. A comparison of identical tests in the R.A.E. tunnel using the two different systems shows good agreement and the results with the single transducer are believed to be perfectly reliable. Nonetheless, the second arrangement is preferable in principle and was retained. In all cases, the pressure tubing was kept as short as possible. The system was estimated to be able to respond to a signal of 400 Hz without significant attenuation. The output was passed via a drive amplifier to an ultra-violet recorder.

3. TESTING

Tests were conducted at values of Reynolds number in the range 0.4×10^5 to 1.4×10^5 where the Reynolds number is defined as $Ud/\nu \sin \alpha$ and U is the free stream velocity, d is the diameter of the cylindrical section, ν is the kinematic viscosity and α is the angle of attack. A justification for the use of this definition is given by Lamont and Hunt.⁹ However, the question of the most appropriate definition is by no means settled and alternative views may be found in References 12, 19 and 20. In any event, it was hoped that sufficient margin was left so that the results would not be influenced by random effects from turbulent reattachment (but see the discussion in Section 4.3).

The other major parameters which were varied were angle of attack, α , axial location of the measuring station, x/d , and roll angle, ϕ . Up to six roll angles could be obtained for equivalent circumferential locations of the pressure tappings. Very great care was taken in setting up the roll angles so as to achieve symmetry of the pressure tappings.

In addition, a few ad hoc tests were carried out to examine the effect of adding imperfections to the nose in the form of plastic tape of thickness 0.15 mm. The dimensions and location of the tape are shown on Figure 4.

4. PRESENTATION AND DISCUSSION OF RESULTS

The pressures were recorded on the ultraviolet recorder for easy visual examination and most of the results presented here were traced directly from these records. Although this method is convenient for examining the qualitative behaviour, it is not so satisfactory when a quantitative analysis is required. In particular, there is bound to be a degree of subjectivity about the mean values and predominant frequencies which have been obtained, by hand, from the traces and this should be borne in mind when studying the results.

4.1 Zero angle of attack

Figure 5 shows traces obtained simultaneously from two ports in the same station on the model in the R.A.E. tunnel. Also shown is the difference in pressures. It can be seen that the disturbances present on the individual tappings are in phase and that the pressure difference is barely detectable. This situation is consistent with the disturbances being produced by plane sound waves. Now, the magnitudes of pressure, p' , and velocity, u' , fluctuations produced by plane sound waves are related by the expression

$$u' = \frac{p'}{\rho a} \quad (1)$$

where a is the speed of sound. Taking the maximum amplitudes of the traces for the individual ports from Figure 5, using Eq.(1) and assuming a simple sine wave form for the fluctuations, one obtains an estimate of 0.01% for the r.m.s. streamwise component of the turbulence. This is slightly higher than earlier measurements of the sound-induced turbulence level in this tunnel¹⁶ (which were approximately 0.005% at the tunnel speed of Figure 5) but considering the approximations necessary to obtain the current estimate, the two sets of values are acceptably close. These measurements provide a measure of the pressure fluctuations in the clean tunnel against which the values obtained at angle of attack can be compared.

4.2 Unsteadiness at angle of attack

One of the most important objectives of this work was to study the effect of conducting tests in the low turbulence flow on the fluctuating component of the surface pressures. It was found that, except for values of α near to 90°, the pressures in the

R.A.E. tunnel were dramatically more steady than those in the Bristol tunnel. A good example is provided by Figure 6 which is for a Reynolds number of 1.1×10^5 and $\alpha = 50^\circ$. The measuring station has been chosen close to the first peak of the sectional side force distribution, as determined from the time-averaged measurements of Lamont and Hunt.⁹ The approximate location on this distribution is indicated on sketches on Figure 6 and on subsequent Figures. It should be noted that it cannot be taken as certain that the same distribution will apply in the R.A.E. tunnel.

It can be seen that the trace from the Bristol tunnel, Figure 6(a), attains and holds roughly the level of Figure 6(b) for brief intervals, but is subject to massive departures from this level and reverses sign from time to time. This behaviour is entirely consistent with the turbulence-induced switching suggested by Lamont and Hunt. Figure 6(b) shows that the non-switching flow does have a small inherent unsteadiness but that this is unbiased in direction and a meaningful time average of such a trace should be obtainable. Of course, the existence of reduced unsteadiness in the R.A.E. tunnel does not allow us to distinguish between the suggestion of a flow which switches between mirror image states and Clark's description of randomly occurring multiple states.¹² This question is therefore unresolved at present; on the one hand, there are the transient records, such as Figure 6(a), which are more consistent with mirror image states and, on the other, there are Clark's observations and photographs.¹²

As far as the frequency of the unsteadiness present in Fig. 6(b) is concerned, it is difficult to make any deductions from the trace except that the form bears little resemblance to classical Karman vortex shedding for which the frequency would be 77 Hz, based on the cross-flow velocity and a Strouhal number of 0.2.

When the angle of attack is reduced to 30° , the situation seen in Figure 7 is produced. Again, the most important feature is the vastly reduced unsteadiness in the R.A.E. tunnel. On this occasion, however, the Bristol trace shows much greater instantaneous magnitudes than the R.A.E. record and it appears that the detailed action of the turbulent eddies is more complex than originally thought. The non-dimensional level of residual unsteadiness in the R.A.E. trace is approximately the same as that at $\alpha = 50^\circ$ (note the different scales on Figures 6(b) and 7(b)) and is, of course, very much higher than the amplitudes measured when $\alpha = 0^\circ$. The mean pressure difference has, however, fallen considerably. Again, Figure 7(b) does not have any obvious content at the cross-flow Strouhal frequency which is 32 Hz.

Figure 8 presents traces obtained at $\alpha = 60^\circ$. In this case, the measurements were taken close to the second peak of the sectional side force distribution because the first peak occurs on the nose at this angle. Once again, the influence of the higher level of turbulence is strikingly illustrated. The non-dimensional amplitude of fluctuation in the R.A.E. tunnel is slightly higher in this case than at the lower angles although this may be due to the measurements being on the second peak (see later comments). The nature of the fluctuations is now much more regular and the frequency obtained by counting what were considered significant peaks produced a value of 104 Hz, which is very close to the cross-flow Strouhal frequency of 99 Hz.

Further aft along the body at the last measuring station which is located at $x/d=11$, the behaviour is even more close to Karman vortex shedding. The trace is presented in Figure 9 (note the slightly lower value of Reynolds number). In this case, the mean value is almost zero and the fluctuations are relatively regular with an estimated frequency of 88 Hz which is virtually identical with the cross-flow Strouhal frequency of 90 Hz. This is not surprising since, at large distances from the nose, the body must behave like an infinite yawed cylinder, which is known to exhibit Karman vortex shedding. As the angle of attack increases, the region of Karman vortex shedding moves nearer to the nose and at $\alpha=75^\circ$, the trace shown in Figure 10 is obtained at $x/d=5$. The relatively regular nature of the fluctuations can again be seen; the estimated frequency is again virtually identical with the Strouhal frequency. Observations of this kind were made previously by Lamont and Hunt⁹ but it was thought to be worthwhile to confirm them under low turbulence conditions. It seems quite likely that the unsteadiness in the flow pattern near the nose is either some form of incipient vortex shedding or is induced by the forward transmission of information along the body from the rear portions where Karman vortex shedding exists.

The nature of the traces allow only approximate values of ΔC_p , the amplitude of the fluctuations, to be obtained. These have been plotted against α for a Reynolds number of 10^5 in Figure 11. It can be seen that the amplitude is roughly constant in the range $30^\circ < \alpha < 50^\circ$ and then rises rapidly as Karman vortex shedding develops.

4.3 Effect of roll angle

The results presented in the above section appear to throw a good deal of light on the problem of unsteadiness and hold out considerable promise that meaningful time-averaged readings can be taken if a wind tunnel of suitable quality is available. The other source of difficulty is that of sensitivity to minute details in the experimental model; this problem normally shows up as a dependence on roll angle. A series of tests at different roll angles was therefore undertaken. Great care was taken to ensure that the model was correctly lined up.

Figure 12 shows three traces at different roll angles for $\alpha=50^\circ$. It can be seen that the nature of the traces is similar but the mean levels vary by up to a factor of seven. This and similar results at other angles of attack show that the commonly

observed dependence of overall force on roll angle is not due to different patterns of switching, as had been suggested by Lamont and Hunt,¹¹ but is due to a genuine difference in the mean sectional side force. The variation in levels of disturbance with roll angle which were observed by Lamont and Hunt is most probably due to the fact that changing the mean level of side force in a stream of given turbulence results in a changing frequency of switching.

Figure 13 shows the traces obtained at the reduced value of Reynolds number of 0.5×10^5 ; it can be seen that there has been a small change in the mean level at $\phi=0^\circ$ but, in general, the traces are very similar to the corresponding traces in Figure 12.

Figure 14 shows the variation of the mean level of ΔC_p with α for the two roll angles 0 and 180° ; unfortunately, measurements for $\phi=150^\circ$ (which shows the strongest effect) were only taken at $\alpha=30^\circ$ and $\alpha=50^\circ$ and are not shown on this Figure. The absolute magnitudes of these curves have only limited significance since the measuring station is not always precisely at the peak of the side force distribution (indeed above 55° the first peak occurs on the nose and the values plotted correspond to the second peak). However, the relative magnitudes for the two roll angles are significant. It can be seen that the 0° roll angle gives consistently higher values than the 180° roll angle. This raises the hope that the difference may be due to identifiable asymmetries on the model. In view of the results obtained by Keener et al.,⁷ any such imperfections seem likely to be located near the tip of the nose. The nose of the model was therefore checked for eccentricity and surface roughness by means of "Talyrond" and "Talysurf" machines respectively. The nose cross-section was found to depart from a circle by less than 0.025 mm at all points along its length. It is difficult to imagine a mechanism by which this small amount of eccentricity can produce the observed effects, although the possibility cannot be ruled out altogether. The surface roughness of a tip region of axial length 20 mm was found to be uniform and the roughness height to be less than 0.002 mm. Nearer the base, larger, isolated grooves were found, the maximum depth being 0.004 mm. The join between the nose and the constant diameter section gave rise to a rather large step whose height was 0.165 mm at its maximum. For a two-dimensional laminar boundary layer, it is generally believed that there is a critical value of roughness height below which the roughness has no effect;^{21,22,23} above the critical value, transition occurs. The critical height, k_{crit} , for a single two-dimensional roughness element (such as a wire on the surface) is given by²¹

$$\frac{U_\tau k_{crit}}{\nu} = 7$$

where $U_\tau = (\tau_w/\rho)^{1/2}$ and τ_w is the laminar shear stress at the location of the roughness element. For isolated and distributed point roughness elements, the same parameter appears to apply but the constant is much larger, being in the range 24 to 30 .^{22,23} Consider the case of a 50 mm diameter cylinder at 90° to the free stream. The maximum laminar shear stress is given by the expression

$$\frac{\tau_w}{\rho U^2} Re^{1/2} = 6.36$$

This can be combined with the critical roughness height criteria to give

$$k_{crit} = d \frac{3.93}{Re^{3/4}} \text{ for two-dimensional roughness}$$

and

$$k_{crit} = d \frac{13.5}{Re^{3/4}} \text{ for point roughness.}$$

At a Reynolds number of 10^5 , these two expressions respectively give values of 0.035 mm and 0.12 mm for the critical roughness height. On this basis, only the junction between the nose and the body appears large enough to have any effect. However, while this comparison is helpful as a start in considering the significance of roughness magnitudes, its real relevance is very dubious for two reasons. Firstly, most of the measured roughness is in the form of circumferential grooves produced during the turning of the nose and hence the application of a criterion based on wires orientated perpendicular to the flow is likely to give a considerable over-estimate of the value of k_{crit} . Secondly, and more important, the boundary layer is in reality highly three-dimensional. Unfortunately, there does not appear to be any information on the effect of surface roughness on transition in a three-dimensional boundary layer. A further point is that the action of the surface roughness (if any) may not be to promote transition; indeed, the large range of Reynolds numbers over which roll angle effects have been observed makes it seem quite likely that transition is not the cause of the roll angle effect. On the other hand, it is difficult to think of another mechanism.

4.4 Effect of other asymmetries

Certain other limited studies were carried out in the hope of shedding light on the action of asymmetries. In the event, the results deepen the mystery but, since the tests were carefully conducted, the studies are summarised here.

In the first set of these tests, the nose normally used was replaced by an alternative manufactured to the same specifications. In the second set of tests, tape of thickness 0.15 mm was added to the tip of the nose, as shown on Figure 4. In both cases, measurements of ΔC_p were taken over a range of angles of attack at the station nearest to the first peak of sectional side force for $\alpha < 60^\circ$ and at the second peak for $\alpha \geq 60^\circ$. The Reynolds number was 1×10^5 and the roll angle was set at the datum value.

The mean values of ΔC_p are presented in Figure 15. It can be seen that both forms of modification to the model have profound effects. However, it is startling that there

appears to be no consistency about the nature of the effects: for example, at $\alpha=60^\circ$, tape in location "A" produces an increase in the force but at $\alpha=40^\circ$, it reduces the force to almost zero. There is little significant variation in the levels of unsteadiness between these various cases.

Further tests were conducted at $\alpha=50^\circ$ in which the tape was located on the shoulder of the nose (again see Fig. 4). In all cases, the sense of ΔC_p was unchanged from that with the plain nose; tape in location "C" increased $|\Delta C_p|$ from 2.23 to 2.27 while in location "D" and simultaneously in locations "C" and "D" the tape caused an increase to 2.52. It thus seems that the pressures are much more sensitive to imperfections near the tip of the nose than they are to imperfections elsewhere, as previously discovered by Keener et al.⁷

5. CONCLUSIONS

The two most important findings in this work are as follows:

- (1) The surface pressures on a rigidly clamped model are vastly more steady in a stream of turbulence level equal to 0.01% than they are in a stream of turbulence level 0.7%. Meaningful time-averaged data for the side force are therefore unlikely to be obtained in test conditions where the turbulence level is moderate or high.
- (2) The surface pressures are dependent on roll angle even in the low turbulence level stream. The mechanism for this is unknown at present but the implication is clear: even strict control of the free stream conditions is not sufficient to guarantee results which are independent of the experimental equipment.

The following conclusions can also be drawn:

- (3) Some inherent unsteadiness exists in the flow pattern but is unlikely to prevent the acquisition of reliable time-averaged measurements. The unsteadiness has the form of classical Karman vortex shedding at very high angles of attack and far from the nose at lower angles of attack.
- (4) No correlation could be found between isolated blemishes or surface roughness on the nose of the model and the measured variation with roll angle.
- (5) Fitting an alternative nose or adding tape to the nose tip produced large changes in the surface pressures but in a manner which varied with angle of attack.
- (6) The addition of tape to the shoulder produced relatively little effect, thus confirming the observations of Keener et al.⁷

REFERENCES

1. LETKO, W., "A low-speed experimental study of the directional characteristics of a sharp-nosed fuselage through a large angle of attack range at zero angle of side slip", NACA, 1953, TN2911.
2. DUNN, E. L., "A low-speed experimental study of yaw forces on bodies of revolution at large angles of pitch and zero angle of side slip", U.S. Naval Ordnance Test Station, China Lake, Calif., 1954, TM1588.
3. NIELSEN, J. N., "Non-linearities in missile aerodynamics", AIAA Paper 78-20, 1978.
4. AIAA, 4th Atmospheric Flight Mechanics Conference, Hollywood, Florida, August 8-10, 1977.
5. AIAA, 16th Aerospace Sciences Meeting, Huntsville, Alabama, January 16-18, 1978.
6. WARDLAW, A. B. and MORRISON, A. M., "Induced side forces at high angles of attack", J. Spacecraft, Vol. 13, No. 10, 1976, 589-593.
7. KEENER, E. R., CHAPMAN, G. T., COHEN, L. and TALEGHANI, J., "Side forces on a tangent ogive forebody with a fineness ratio of 3.5 at high angles of attack and Mach Numbers from 0.1 to 0.7", NASA, 1977, TM X-3437.
8. KEENER, E. R., CHAPMAN, G. T., COHEN, L. and TALEGHANI, J., "Side forces on forebodies at high angles of attack and Mach Numbers from 0.1 to 0.7: two tangent ogives, paraboloid and cone", NASA, 1977, TM X-3438.
9. LAMONT, P. J. and HUNT, B. L., "Pressure and force distributions on a sharp-nosed circular cylinder at large angles of inclination to a uniform, subsonic stream", J. Fluid Mechanics, Vol. 76, Part 3, 1976, 519-559.
10. LAMONT, P. J. and HUNT, B. L., "Prediction of aerodynamic out-of-plane forces on ogive-nosed circular cylinders", J. Spacecraft, Vol. 14, No. 1, 1977, 38-44.
11. LAMONT, P. J. and HUNT, B. L., "Comment on induced side forces at high angle of attack", J. Spacecraft, Vol. 14, No. 5, 1977, 319.

12. CLARK, W., "Body vortex formation on missiles in incompressible flows", AIAA Paper 77-1154, 1977.
13. COE, P. L., CHAMBERS, J. R. and LETKO, W., "Asymmetric lateral-direction characteristics of pointed bodies of revolution at high angles of attack", NASA, 1972, TND-7095.
14. BOSTOCK, B. R., "Slender bodies of revolution at incidence", University of Cambridge, 1972, Ph.D. Thesis.
15. SQUIRE, H. B. and WINTER, K. G., "The R.A.E. 4 ft x 3 ft experimental low turbulence wind tunnel", Part I, A.R.C., 1948, R & M 2690.
16. SCHUH, H. and WINTER, K. G., "The P.A.E. 4 ft x 3 ft experimental low turbulence wind tunnel", Part II, A.R.C., 1957, R & M 2905.
17. SCHUH, H. and WINTER, K. G., "The R.A.E. 4 ft x 3 ft experimental low turbulence wind tunnel", Part IV, A.R.C., 1962, R & M 3261.
18. LAMONT, P. J., "The out-of-plane force on an ogive nosed cylinder at large angles of inclination to a uniform stream", University of Bristol, 1973, Ph.D. Thesis.
19. REDING, J. P. and ERICSSON, L. E., "Maximum vortex-induced side forces on slender bodies, AIAA Paper 77-1155, 1977.
20. CLARKSON, M. H., MALCOLM, G. N. and CHAPMAN, G. T., "A subsonic, high angle-of-attack flow investigation at several Reynolds Numbers", AIAA, Vol. 16, No. 1, 1978, 53-60.
21. SCHLICHTING, H., Boundary Layer Theory, 4th Edition, New York, McGraw-Hill, 1960, 445-451.
22. TANI, I., "Effect of two-dimensional and isolated roughness on laminar flow", G. V. Lachmann (Ed.), Boundary Layer and Flow Control, Vol. 2, Pergamon, 1961, 637-656.
23. VON DOENHOFF, A. E. and BRASLOW, A. L., "The effect of distributed surface roughness on laminar flow", G. V. Lachmann (Ed.), Boundary Layer and Flow Control, Vol. 2, Pergamon, 1961, 657-681.

ACKNOWLEDGMENTS

The authors would like to acknowledge the earlier work of Dr. P. J. Lamont who obtained the results in the Bristol tunnel which are presented here. Very helpful discussions with Mr. E. C. Maskell and Dr. B. Earnshaw and the technical assistance of Mr. R. Hill are gratefully acknowledged. The interest and encouragement of Dr. D. C. Daniel and Dr. D. J. Spring are also gratefully acknowledged.

This work was supported by the European Research Office of the U.S. Army under Grant DAERO-77-G-073. Additional support was given by the Ministry of Defence (Procurement Executive).

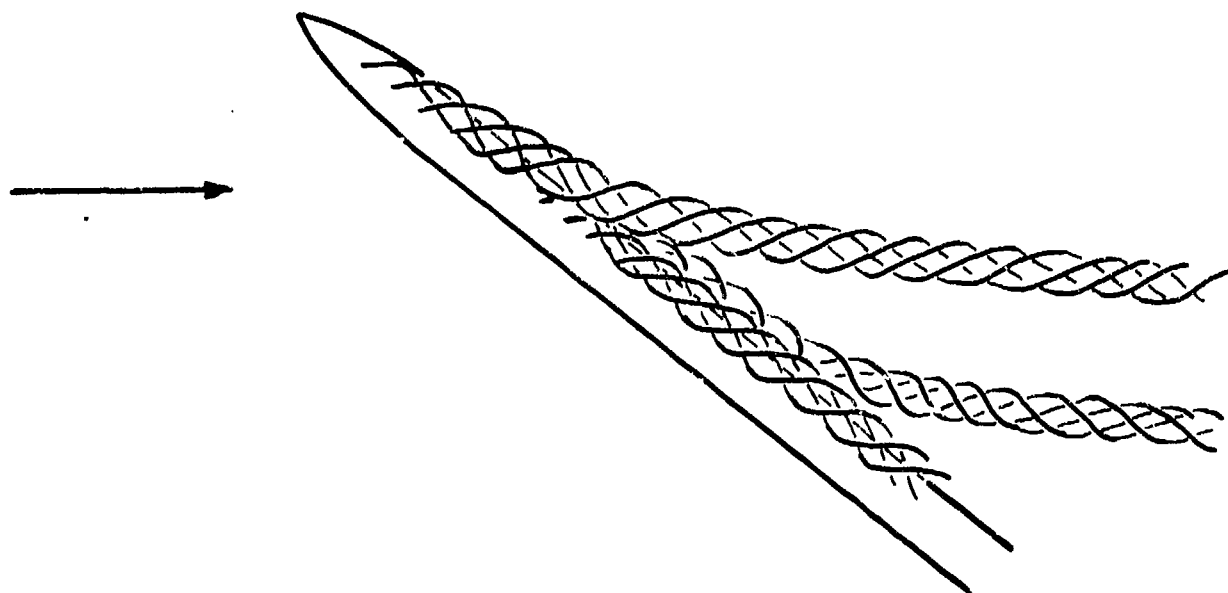


FIGURE 1 Sketch of idealised wake vortex pattern.

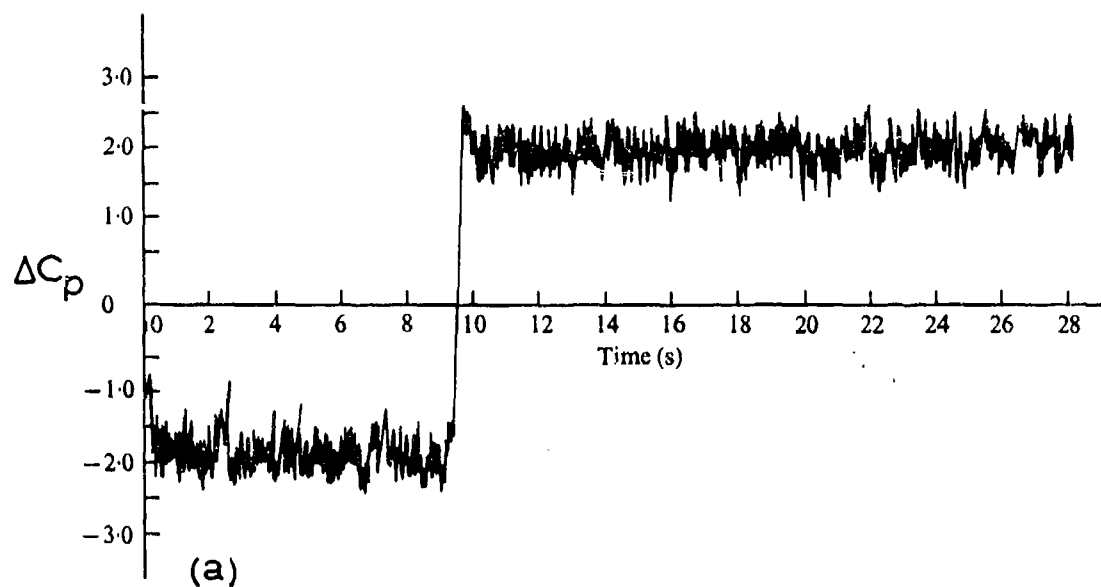


FIGURE 2a $\alpha=60^\circ$, $Re=6 \times 10^4$, $x/d=3$, 2 calibre nose.

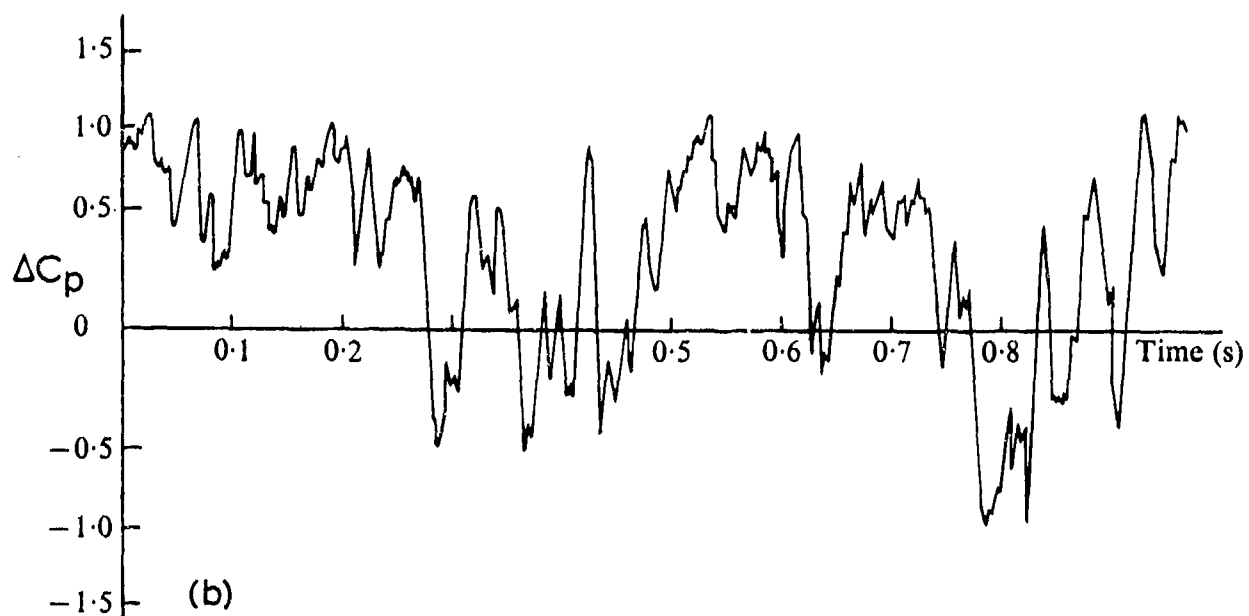


FIGURE 2b $\alpha=30^\circ$, $Re=1.1 \times 10^5$, $x/d=7$, 2 calibre nose.

FIGURE 2 Time dependent pressure differences recorded by Lamont and Hunt.⁹

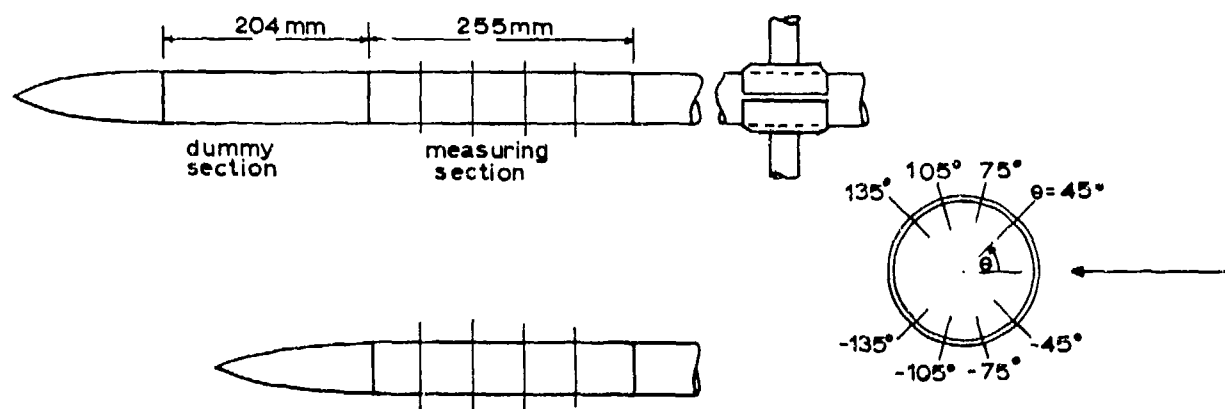


FIGURE 3 Sketch of wind tunnel model.

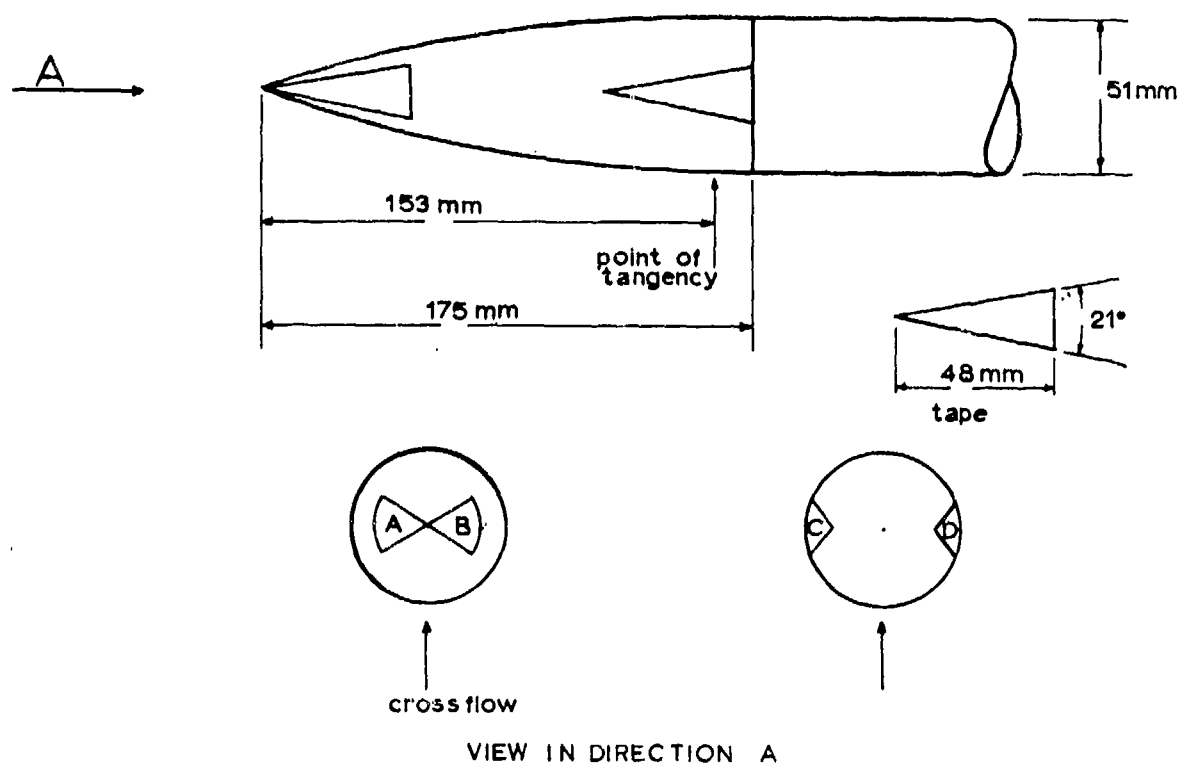


FIGURE 4 Location on nose of plastic tape of thickness 0.15 mm.

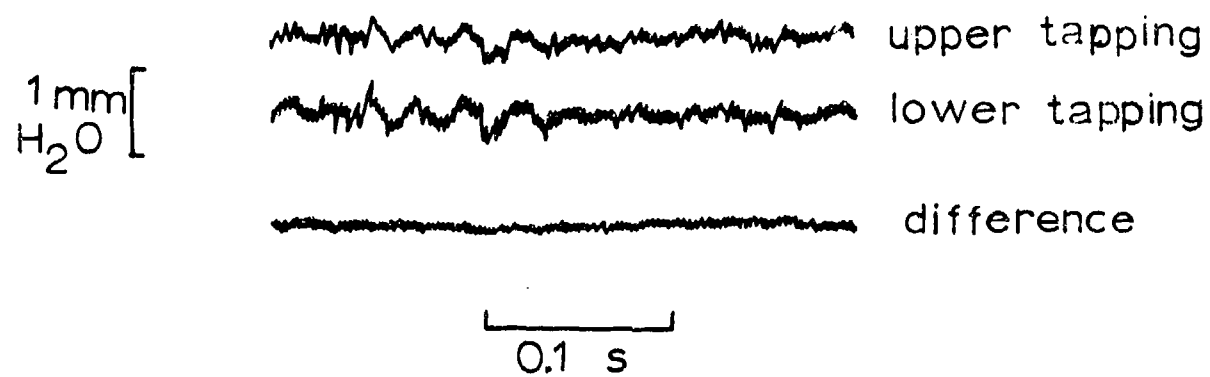


FIGURE 5 Transient pressures for $\alpha=0^\circ$, $x/d=5$, $U=30$ m/s.

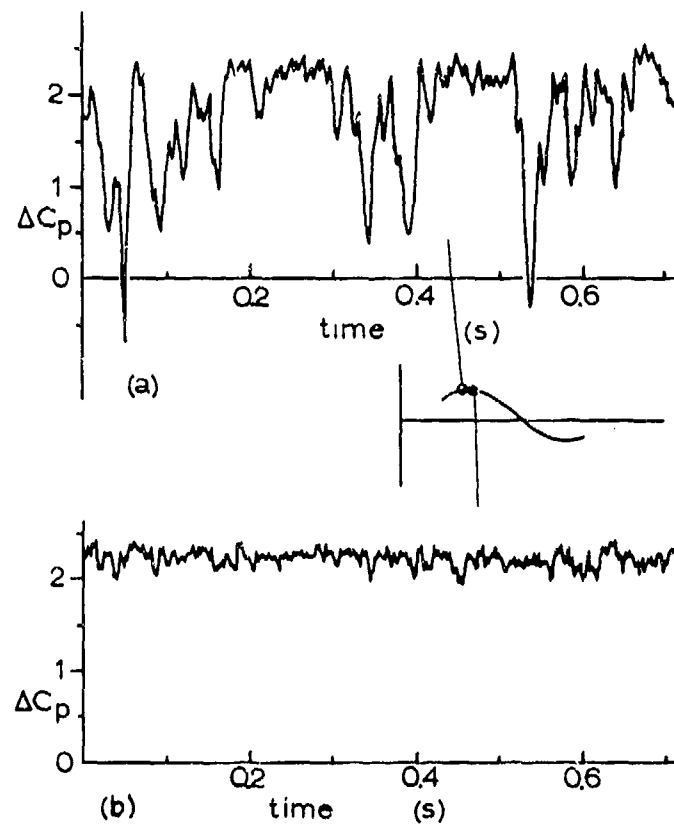


FIGURE 6 Transient pressure differences for $\alpha=50^\circ$, $Re=1.1 \times 10^5$;
(a) Bristol tunnel, $x/d=4$; (b) R.A.E. tunnel, $x/d=5$.

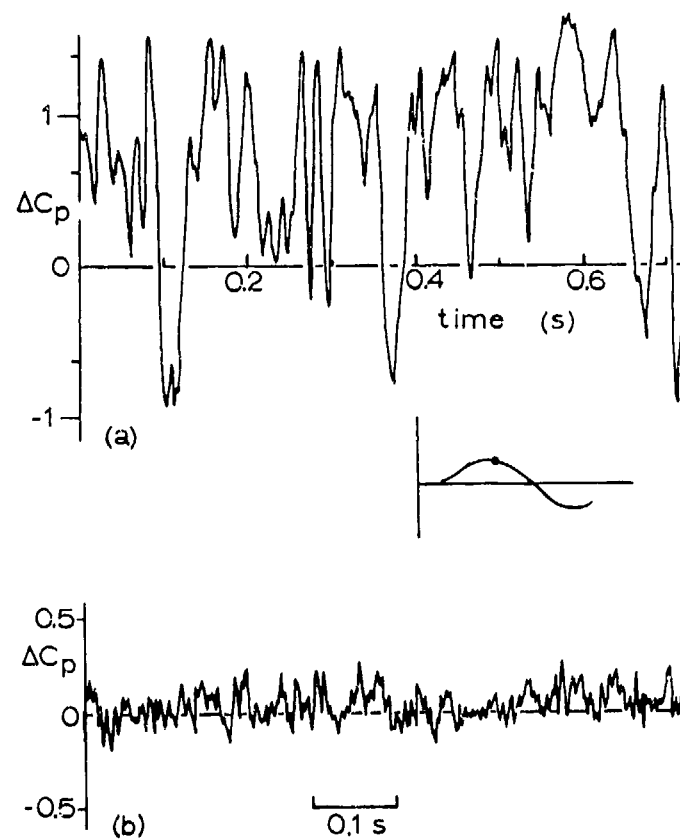


FIGURE 7 Transient pressure differences for $\alpha=30^\circ$, $Re=1.1 \times 10^5$, $x/d=8$; (a) Bristol tunnel; (b) R.A.E. tunnel.

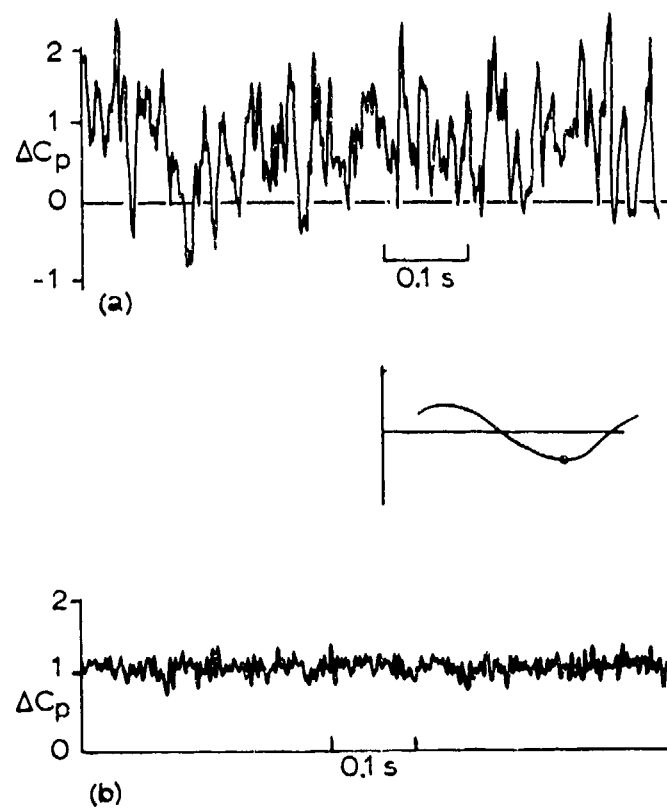


FIGURE 8 Transient pressure differences for $\alpha=60^\circ$, $Re=1.1 \times 10^5$, $x/d=5$; (a) Bristol tunnel; (b) R.A.E. tunnel.

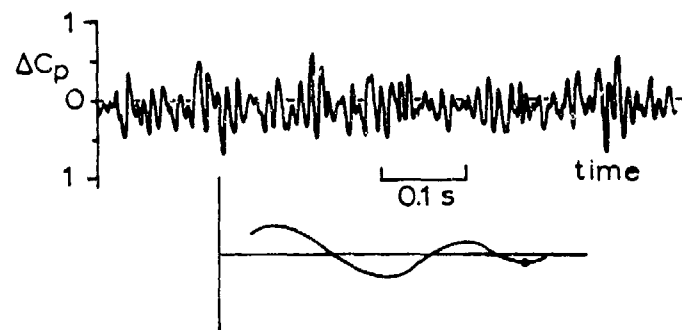


FIGURE 9 Transient pressure differences for $\alpha=60^\circ$, $Re=10^5$, $x/d=11$.



FIGURE 10 Transient pressure differences for $\alpha=75^\circ$, $Re=10^5$, $x/d=5$.

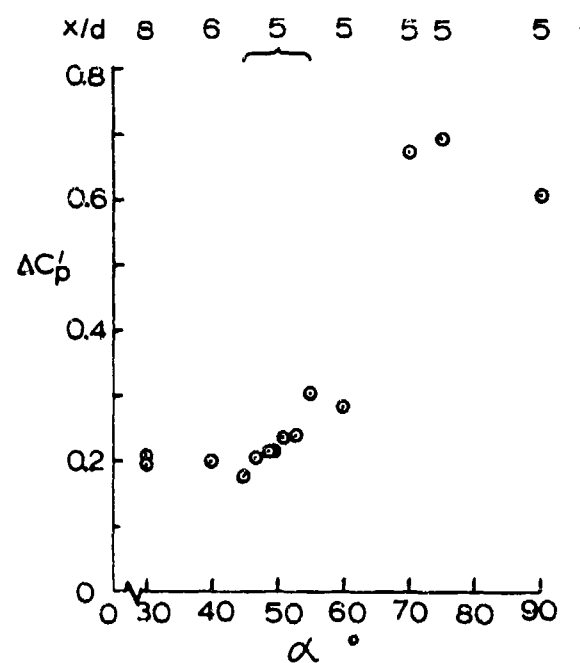


FIGURE 11 Variation of amplitude of fluctuating pressure differences with angle of attack at $Re=10^5$.

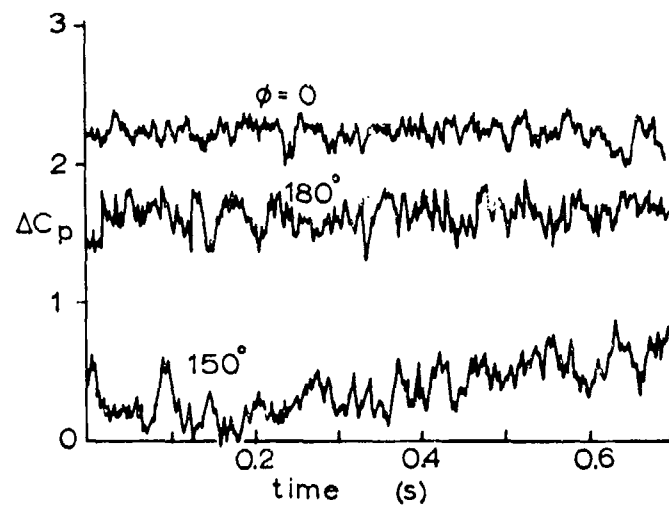


FIGURE 12 The effect of roll angle on transient pressure differences for $\alpha=50^\circ$, $Re=10^5$, $x/d=4$.

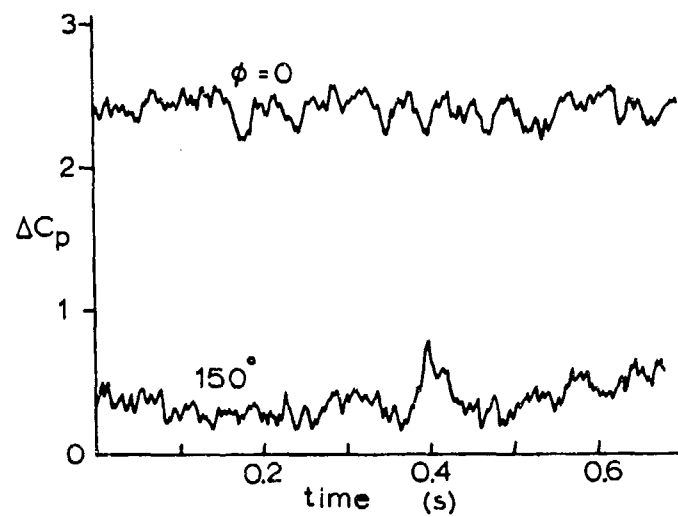


FIGURE 13 The effect of roll angle on transient pressure differences for $\alpha=50^\circ$, $Re=0.5 \times 10^5$, $x/d=4$.

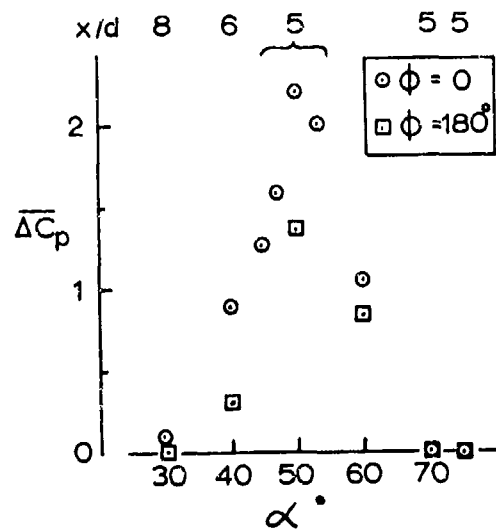


FIGURE 14 Variation of mean pressure difference with angle of attack for two roll angles at $Re=10^5$, $x/d=4$.

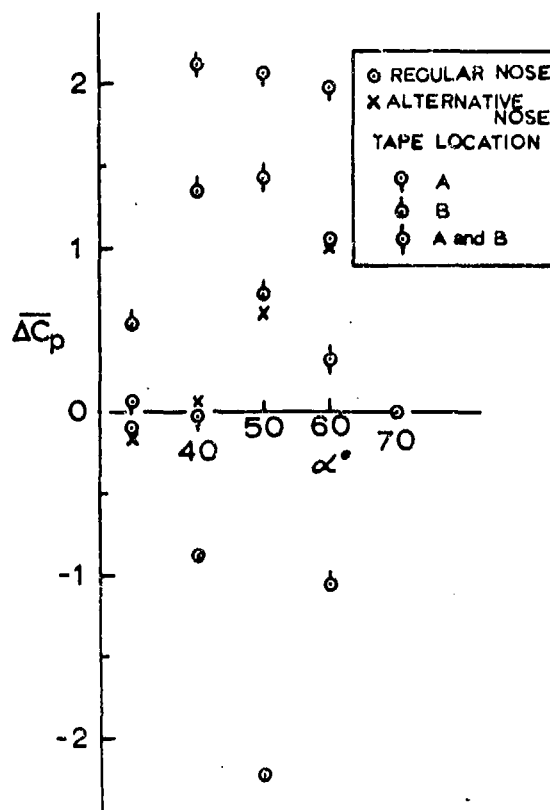


FIGURE 15 Effect on mean pressure difference of minor alterations to the nose at $Re=10^5$, $\phi=0$.

WIND AND WATER TUNNEL INVESTIGATIONS OF THE
INTERACTION OF BODY VORTICES AND THE WING
PANELS OF A MISSILE CONFIGURATION

by

J.R. Deane, Aerodynamics Research Group, Research Department (821),
British Aerospace - Dynamics Group, Filton, Bristol. BS99 7AR.

SUMMARY

Two experimental investigations have been carried out to study the interaction with wing panels of vortices formed by flow separation on the leeside of the forebody of an inclined, cruciform, wing-body combination.

A low-speed flow visualisation experiment, using the dye line technique in a water tunnel, has illustrated the generation of the symmetric body vortex pair in the incidence angle range 15° to 35° . The phenomenon of breakdown of the ordered vortex structure has been observed when the vortices pass in the vicinity of wing panels mounted downstream on the body.

Complementary tests have been carried out using a supersonic wind tunnel in which pressure plotting on a wing panel of a geometrically similar wing-body combination has been performed. Incidence angles in the range 15° to 25° have been considered at a Mach number of 2 with the pressure tapped wing panel rolled into the leeside flow field. Integration of the pressure distributions has yielded information on panel loads which has been compared with estimates available from semi-empirical prediction methods. It has been shown that prediction accuracy is low for the loads on panels when they are rolled into the vicinity of the vortices.

NOTATION

a	Local body radius	
C_{N_G}	Normal force curve slope of wing	
C_{N_p}	Panel normal force coefficient	$= \frac{N_p}{\frac{1}{2} \gamma p_\infty M^2 S_p}$
C_p	Pressure coefficient	$= \frac{p - p_\infty}{\frac{1}{2} \gamma p_\infty M^2}$
c_r	Root chord of wing panel	
i	Vortex interference factor	
k, m	Vortex identifiers	
K_{WB}	Wing-body interference factor	
M	Mach number	
N_p	Normal force on a wing panel	
p	Static pressure at a wing tapping	
p_∞	Tunnel working section static pressure	
Re_d	Reynolds number based on diameter of body	
r_N	Body radius at the base of the nose	
s	Gross semi-span of the wing-body combination	
S_p	Plan area of one wing panel	
s_w	Nett semi-span of wing panel	
V	Flow free stream velocity	
x	Longitudinal body co-ordinate measured along centre line of body from the tip of the nose	
x_s	Longitudinal body co-ordinate at which the first boundary layer separation occurs	
x_w	Longitudinal wing co-ordinate measured along root of wing panel from the wing-body junction at the panel leading edge	
y_w	Lateral co-ordinate measured outboard from the wing panel root	
y_B	Lateral co-ordinate of body vortex position	

z_B	Vertical co-ordinate of body vortex position; measured perpendicular to body longitudinal axis
γ	Ratio of specific heats for air = 1.4
Γ	Vortex strength
ΔC_p	Difference in pressure coefficients between upper and lower surfaces of wing panel = $C_{p_L} - C_{p_U}$
σ	Body incidence angle
ϕ	Roll angle of wing panel; measured positive anti-clockwise from upward vertical when viewed from the rear of the model

1. INTRODUCTION

It is of prime concern in the aerodynamic development of any missile project that reliable estimates should be available of the forces and moments which would be experienced in flight by the configuration under study.

Whereas overall estimates of normal force and pitching moment might be sufficient in the early stages, the later requirements would probably also include assessments of loads on the various external components of the total missile, e.g. wing and tail panels or those parts of the missile between the panels. A particular case for which this information would be required is that of the derivation of loading distributions for stressing purposes.

Depending on the actual project application, it might be necessary for such predictions to be made over a wide range of flow conditions covering low subsonic to high supersonic Mach numbers, an incidence angle range from 0° to 25° typically, although this can now be often extended to 90° and beyond for particular designs, and arbitrary roll orientations anywhere in the complete 0° to 360° coverage.

Development of prediction methods within the Research Department of British Aerospace (Dynamics Group) to cope with these wide ranging requirements has been in progress for some years. Analysis has mainly been from the empirical or semi-empirical standpoint by which predicted results from existing methods for normal force and pitching moment are compared with as wide a range of experimental data as can be found. If appropriate, modifications are then made to the methods to improve the estimation accuracy. These modifications mostly take the form of factors to be applied directly to the original estimates of force or moment coefficient. This process has, in the past, been found to be more effective than an effort to model the details of the flow field and, thence, to calculate the loads.

It is now thought, however, that further significant improvement of prediction methods can only be made by undertaking research into flow field phenomena. Such a statement assumes special relevance in the context of the estimation of the interference effects which occur between the components of the missile, since current prediction methods have been developed on the basis of an initial estimation of isolated body, wing or tail loads followed by their superposition with appropriate interference factors being applied. One aspect of particular importance here is the effect of vortices on the aerodynamics of a missile. Vortex formation can occur in many places and, indeed, may be a dominant feature of the flow field. Primary causes are flow separation on the forebody ahead of the wings and leading edge separation on the wing or tail panels themselves.

The phenomenon of body vortex formation is associated with moderate and high body incidence angles. Initially, the pattern will be of symmetrical form but, at higher incidence angles, it will be of an asymmetric nature leading to the development of side forces and yawing moments at zero sideslip. For a missile application, an important consideration and one which emphasises the need to fully understand the generation of body vortices and their subsequent behaviour is the arbitrary roll orientation which the missile may adopt. This could result in the wing and tail panels rolling through the body vortex cores so that the close interaction of the one with the other would become of primary interest.

As a first stage in a study of vortex dominated flow fields, which, it is hoped, will lead to improved prediction techniques, two experimental studies have been undertaken.

Firstly, a water tunnel flow visualisation experiment has been performed to illustrate the generation of a symmetric body vortex pair and to show their interaction with wing panels mounted downstream on the body.

Secondly, some measurements have been made in a supersonic wind tunnel to obtain pressure coefficient data and, hence, loading information on one wing panel of a cruciform wing-body model which is rolled such that the panel can interact closely with one of the body vortex pair.

The present paper describes results from these experiments which have concentrated on the incidence angle regime from 15° to 35° ; a range where symmetrical body vortex formation is encountered. Due to increased manoeuvrability requirements the angle of incidence range for missile operation has now become significantly more extensive. Much of the research on weapon aerodynamics, both experimental and theoretical, has therefore concentrated on increasing the aerodynamicist's understanding of the high angle of attack regime where asymmetric flows are of primary importance. However, it must be remembered that, although some designs are now intended to operate at various stages of their flight in this regime, the majority will still be confined to operation at lower incidence angles. For these cases, say for incidence angles of around 20° to 30° , the effects of symmetric body vortices are of crucial importance in the calculation of interference loads. Because it was considered that this particular aspect of vortex flow fields is still not fully understood and, consequently, the effects could not yet be adequately predicted, it was decided to concentrate the present research on the "conventional" angle of attack regime.

2. WATER TUNNEL TESTS

In any aerodynamic study it is often very helpful to be able to visualise the flow patterns around the configuration under study as an aid to understanding the flow mechanisms involved. It is thought that this is particularly true for the case of vortex dominated flow fields which occur around missile configurations and which can be extremely complex.

Although flow visualisation experiments can, however, be difficult to implement and their results hard to interpret, it would seem that the water tunnel with dye line injection is one facility for which results are immediately available and relatively easily interpreted.

To help in the understanding of body vortex interaction with wing panels an experimental study has been performed using the dye line technique for the missile type wing-body combination shown in Figure 1. The model is not representative of any particular current design but is of a suitable type for use in this research work. The shape chosen was such that its long forebody would ensure that, at all but low incidences, a well developed body vortex system would be evident ahead of the wing leading edge.

Flow visualisation could be carried out by ejecting a dye or water-based paint through an array of small holes along each side of the model, although for the sake of simplicity of interpretation only one side was generally in use at any one time. The facility was able to give simultaneous ejection of dye from fifteen holes down one side and eight disposed diametrically opposite on the other side of the body. The standard practice during any test was to operate the dye lines as three groups of five. Dye was fed to the model from header tanks above the level of the tunnel and the flow rates from each hole could be individually controlled by small valves.

A turntable in the rear of the water tunnel working section provided the means by which the incidence angle could be manually changed in the range $-35^\circ \leq \alpha \leq 35^\circ$ with the top and bottom limits being determined by the model or support system approaching too close to the tunnel walls. Incidence angle could be changed with the tunnel operating but roll angle of the model could only be adjusted by stopping the tunnel, draining it, and resetting the model orientation manually with the working section open. The part of the body on which the wings were mounted could be rotated around an inner cylindrical section and secured in position by the use of locking pins which were located in holes previously drilled in the inner section.

Cameras and lighting equipment were arranged to enable the model to be viewed and photographed from the side and the top of the tunnel simultaneously. This was considered most important so that features of the flow field visible in one view could be easily correlated with features shown in another. Electronic flash lighting was employed from two directions. Shadows on the model were not a problem since it was painted matt black which also meant that the various dye colours could be easily seen against its surface.

The tunnel itself is a facility operated by British Aerospace (Aircraft Group) at its Warton Division. It is a continuously operating recirculating facility driven by an axial impeller in the return section. The working section is 457 x 457 mm in size. As an alternative to the dye line technique, hydrogen bubbles or polystyrene flow tracers may be used for flow visualisation. These methods were not, however, employed in the present experiments.

A particular characteristic of conditions in the tunnel is that, after starting the drive motor and establishing a flow, there is a short period of only a few minutes duration when the flow quality is extremely good and virtually free from all disturbances and turbulence. Thereafter, the quality rapidly deteriorates, as disturbances from the impeller (which starts up stalled) are felt in the working section, but then gradually recovers towards the initial high quality smooth flow as the disturbances damp themselves out.

For effective flow visualisation using the dye line technique it is essential to have a smooth onset flow. Hence, the initial phase of tunnel running time has been used in each case although this has meant that many short runs are needed to achieve a particular set of photographs.

The tunnel speed itself was also of great importance in ensuring good flow visualisation results. If it was operated at too high a speed the dye lines would very soon break up and simply form a diffuse cloud of colour from which no really useful information could be gained. It was found that a reasonable compromise between minimum controllable speed and maximum speed for dye line quality was to run the tunnel at speeds of 90 mm/s which was equivalent to a Reynolds number of approximately 2000 based on body diameter.

This value of Reynolds number was obviously far lower than anything likely to be experienced in a wind tunnel or in flight conditions. This should therefore be borne in mind when assessing results on a quantitative basis and due allowance should be made for the lower Reynolds number when reading across results to higher speeds. However, on a qualitative level the results are very useful for providing an insight into the complex nature of vortex flow fields and it is considered that qualitative changes in flow patterns will be reliably modelled in the water tunnel.

Water tunnel tests have, of course, been used previously in work on high angle of attack aerodynamics. The work of Fiechter¹ on bodies alone is one example wherein dye line flow visualisation was employed to show asymmetric vortex behaviour at higher incidence angles than those dealt with in the present paper. Werle,² Rainbird et al³ and Poisson-Quinton and Werle⁴ have also performed experiments using water tunnels. However, these reports have not, to the author's knowledge, considered the particular problems associated with the interaction of body vortices with wing panels for a missile configuration.

The results shown herein represent a small selection of those available from a test programme which included the following flow conditions.

Body incidence angles α	15°, 20°, 25°	Wing-body models.
	(with some extra coverage for zero roll cases)	
	5° (5°) 35°	Body Alone models.
	(with some extra coverage at negative incidence angles)	
Roll angles ϕ	0° (10°) 40°, 45°	
Reynolds number	$Re_d \sim 2000$	

In addition, geometrical changes were made in the model shape. It was possible to mount the wings in both forward and aft positions and to remove them altogether. Body alone shapes with sharp (tangent ogive) and blunt noses were tested. In the latter case the nose profile was that of the tangent ogive but with 0.1 calibre spherical blunting applied at the apex.

Roll angle was simulated by rotating only that section of the body on which the wings were mounted. The dye ejection holes were thus maintained in their fixed model positions irrespective of wing roll angle, i.e. on a horizontal axis for the case of $\sigma = 0^\circ$.

2.1 Water Tunnel Test Results

2.1.1 Body Alone

Two body shapes were tested. These were, firstly, a combination of a 3-calibre tangent ogive nose and a 10-calibre afterbody and, secondly, the same basic shape except the nose was slightly shorter after a 0.1 calibre spherical blunting had been applied to the tip.

Figures 2, 3 show results for the sharp body at $\sigma = 30^\circ$. It can be seen how the dye lines (a) enclose the vortex core and (b) provide a clear indication of its position, both the vertical distance from the body centre line and the lateral distance.

Dye ejection for the three sets of 5 holes has been used to visualise the complete vortex development and to show that one set of data is comparable with the next. Figure 4 has been prepared. This shows for the $\sigma = 30^\circ$ case how the dye lines from the upstream set of holes lie in the centre of those from the second set of holes, which in turn lie in the centre of those from the third set of holes. The expanding area of the flow into which the dye lines pass is a measure of two effects. Firstly, the strength of the vortex grows as it passes back along the body and thus a greater area of the flow field will be affected by the induced velocities of the vortex. Secondly, the dye from the holes towards the aft end of the body feeds into the periphery of the area affected by the vortex and not into the core, whereas the dye from the upstream end of the body does feed into the vortex core.

The top views of the vortex system indicate a much smaller area of flow affected than the side views. In the top views it is apparent that the dye lines for one side of the body are not carried across to the other side but that there is a very definite limit to the field of influence of one vortex along the centre line of the model.

Here only illustrations showing dye injection from one side of the body are shown. Visual checks were made during the study with dye ejection from both sides and these indicated that the flow patterns for incidence angles up to 30° were symmetrical relative to the body centre line both in the vertical and lateral senses.

Some general features visible from the illustrations are worthy of comment. For the body alone the dye lines were both steady in space and maintained their well defined structure without diffusing as far aft as was possible to see in the field of view.

At a given axial location the core of the vortex moved upwards relative to the body centre line as increased, but changes in lateral co-ordinate were much less. This was simply observed by assessing the position of the mid-point of the dye line helix relative to the centre line of the body.

The strength of the body vortex at a given axial location increases with incidence and this was made apparent by an increase in pitch of the dye line traces. Thus an indication was given that the rotational velocities had become larger relative to the axial velocity.

2.1.1.1 Comparison of vortex core locations with previous data

As noted previously, the vortex core positions have been derived from the photographs by assessing the mid-point positions of the dye line traces. These data have been superimposed on the previous experimental information collated by Mendenhall and Nielsen⁵ as shown in Figures 5 and 6. It should be noted that it has been necessary to assume a position of first separation (x_s) in order to calculate the non-dimensional parameter $x - x_s \sin \sigma$. In the absence of an independent method of measuring x_s , and with the realisation

that, for the values of σ considered here (25° , 30° , 35°), the point at which separation first occurred was forward of the most upstream dye ejection hole, it was decided to use the predicted value of x_s from Mendenhall and Nielsen's empirical method. This gave a value of $x_s = 0$.

It can be seen (Figure 5) how the agreement between the vortex vertical location and the previous experimental results and, hence, with the suggested empirical prediction method, is good, although the present data is generally at slightly higher values of $z_{B/a}$. The agreement for the lateral position (Figure 6) is, however, poor with the present values of $y_{B/a}$ being significantly outboard of those obtained previously. It should be noted that the suggested correlation for $z_{B/a}$ from Reference 5 had been derived by a consideration of both subsonic and supersonic data, whereas those for $y_{B/a}$ were found from separate consideration of the two sets of data.

The use of nose blunting has very little effect on the vortex trajectories and strengths for the incidence angles considered here. Figure 7 shows the dye line paths for the blunt body case and this may be compared with Figure 4. It is probable that the value of σ is sufficiently high for the first separation to occur well forward on the body, at or near the apex, and that the addition of nose blunting cannot move it any further forward as might be the case for lower incidence angles.

2.1.2 Wing-Body Combination

Discussion here will be limited to results for wing-body combinations made up of the cruciform wing set either mounted forward or aft on the body with a sharp nose.

2.1.2.1 Zero Roll Angle Results

Comparison of dye line traces from the upstream holes for the cases of a body alone and for the wing-body

combination at zero roll shows that there are no apparent effects on the core position ahead of the wing panel leading edges due to the presence of the panel in this set of experiments.

It has been observed that for $\sigma = 15^\circ$, 20° the dye ejected from the rearmost holes on the forebody of the model is not entrained into the vortex structure but, after a small upwards movement, is quickly swept back down onto the upper surface of the adjacent horizontal wing panel. Figure 8 shows an example of these effects. Whereas the behaviour is quite marked for the lower incidence angles, for higher values of σ , 25° and above, the dye from the rearmost holes does not deviate onto the panel but passes upwards into the vortex core (see Figure 9).

The lifting panel and its associated flow field is thus shown to have a significant upstream effect on feeding into the vortex at these low speeds. For such cases it would obviously be inappropriate to assume that the strength of any vortex at the leading edge of the wing would be adequately predicted by the value at the same axial location on an equivalent body alone. It is apparent that at some axial location upstream of the wing leading edge, dependent on the value of σ , the flow around the body ceases to feed into the vortex core and, hence, the growth in strength of the core must be terminated. Core position is evidently less affected.

The behaviour of the vortex system adjacent to the leading edge of the panel is not the only item of interest however. For body incidences of 25° , 30° and 35° very clear visualisation has been achieved of a well defined body vortex system ahead of the panel leading edge. Figure 10 is an example.

On passing aft of the wing mid-chord the structure of the body vortex breaks down at a point which moves forward with increasing incidence and the dye lines which hitherto have neatly delineated the vortex become entrained into the separated flow from the wing panel.

In addition to the breakdown in structure the vortex cores also undergo deviations in position downwards towards the adjacent horizontal wing panel and laterally away from the body centre line for $\sigma = 25^\circ$, 30° . Figure 11 shows a top view of the phenomenon for the latter body incidence. This behaviour can be correlated with a downwards and outwards velocity field induced by a leading edge vortex system set up on the panel itself.

For the body incidence angle considered here (30°), and for lower values, the dye lines appeared fixed in space up to the point of breakdown near the wing panel. Thereafter, of course, a time dependent eddying flow was evident. Another effect was, however, shown at the extreme incidence angle used in the experiment, i.e. 35° , when the set of dye lines as a whole was seen to oscillate aft of the wing panel leading edge before their neatly defined structure broke down.

The phenomenon of vortex breakdown adjacent to wing panels has been recently referred to in the literature by Jorgensen⁶ as a possible explanation for some effects seen by the use of vapour screen flow visualisation. This was done at high subsonic speeds, for a monoplane cropped-delta wing-body combination, but with a shorter forebody than considered here, at angles of incidence of 30° and 40° and at zero roll angle. Whereas discrete vortices were observed near the base of the models at supersonic speeds, for the lower Mach numbers diffuse vortex regions were evident.

The behaviour observed in the present series of water tunnel tests is quite contrary to what has been assumed before concerning the behaviour of vortex systems passing close to wing panels and tail surfaces. Through the lack of any evidence to the contrary, it was considered that it would be sufficiently accurate to compute vortex strength and position at an appropriate body alone station corresponding to the leading edge location of the wing panel. This could be done using the empirical method of Mendenhall and Nielsen. For predicting the interference effects which this vortex system might have on the wing, and any other lifting surfaces, it was then assumed that the same vortex strength and lateral and vertical locations relative to the body centre line were maintained as the vortex trajectory passed to the trailing edge of the wing panel.

Evidently these assumptions must be reassessed in the light of the water tunnel results.

2.1.2.2 Some Effects of Roll Angle

Tests were carried out at 10° intervals of roll angle in the range 0° to 40° with a final increment of 5° to 45° . Thus the panel which was initially vertical at the top of the model for zero roll angle was progressively rolled towards and through the location of one of the body vortex cores.

Results for 10° of roll angle show very little difference from those for zero roll angle. As roll angle increases to 20° and 30° , the panel which was originally horizontal on the same side as the dye ejection points is rolling away from those points and, hence, the effects on the dye line traces from these downstream holes becomes less and less. Feeding into the body vortex core is not interrupted as was the case at zero roll (Figure 12) for a body incidence angle of 15° .

A further increase in roll angle to 40° and 45° does, conversely, result in an interaction but, this time, it is between the core and the upper of the panels, which was originally vertical and is now much closer to the body vortex than is the one which was originally horizontal (Figure 13).

Dye ejection from the upstream sets of holes which enables the core position to be visualised shows that the tightly rolled structure evident upstream of the panel is not maintained aft of the leading edge but somewhere within the root chord either breaks down or is deviated very significantly from the vertical and lateral co-ordinates it had at the leading edge.

At the higher roll angles (40° , 45°) the core passes to the right side (when viewed from the rear) of the top panel and undergoes a very rapid change in position. This behaviour is repeated over the whole range of incidence angle studied for the latter roll angle. Towards the other end of the roll range (i.e. 10°) the core is evidently passing to the left side of the upper panel.

For 20° of roll the situation of very close interaction of the body vortex with the panel occurs and the dye which marks the core in fact passes to either side of the panel, although the majority does come to the left side. It was observed that this situation was basically steady and that the core was not in a phase of oscillation from one side of the panel to the other (Figure 14). The effects of roll angle combine with

incidence in a complex fashion since they both dictate the relative position the body vortex core will take up relative to the wing panel and hence this will affect the nature of the interaction.

2.1.2.3 Wings in a Forward Position

When it was observed on the model with the wings mounted in the aft position that the vortex structure apparently broke up adjacent to the wing panel trailing edge at zero roll angle, it was suggested that this might not be a true phenomenon due to the close proximity between the panel and the vortex but might be due to some instability in the dye lines themselves which happened to occur at an axial location corresponding to the panel position.

To test this hypothesis two sets of tests have been undertaken. Firstly the body alone tests discussed in an earlier section have shown that it is possible to observe well defined dye lines far aft on the model and, indeed, beyond the model base. Secondly, tests have been carried out with the wings mounted forward on the body. Similar results showing vortex breakdown have been encountered - see Figure 15. It is thus concluded that the phenomenon is a result of the proximity of the panels.

2.2 Conclusions and Recommendations drawn from the Water Tunnel Tests

At the start of the programme of water tunnel tests it had been expected that the main value of the experiment would be in the visualisation of body vortex core position changes as they approached close to downstream wing panels. It is now quite apparent that due to the phenomenon of vortex breakdown adjacent to the panels, new avenues of enquiry have been opened up which require exploration.

The detailed flow patterns between and immediately in front of the wing panels should be studied. This should be done using both flow field visualisation and measurement techniques. Surface flow studies should be included so that the upstream effect of the wing on the flow separation and hence on body vortex formation can be more accurately quantified.

Wind tunnel studies should be exploited to investigate any effects of Reynolds number on the flow patterns. Attention needs to be paid to the consequences on prediction method techniques of the breakdown in body vortex structure and on how best to model the flow field changes.

3. WIND TUNNEL TESTS

As another item of an overall research programme into vortex dominated flow fields, a series of experiments have been performed using a small supersonic wind tunnel. These tests are complementary to those performed in the water tunnel and had a similar aim, i.e. an investigation of the close interaction of body vortices and wing panels. The test conditions for the experiments were chosen to yield, on the basis of predictions, conditions of close proximity of one body vortex from the symmetric pair with one of the wing panels of the cruciform set. Roll angles of 10° (5°) 30° were therefore used with body incidence angles in the range 15° (2.5°) 22.5° . The nominal Mach number was 2.0 and the Reynolds number 0.9×10^6 based on body diameter. The latter parameter was dictated by restrictions on operating pressure in the wind tunnel but this was not considered to be too great a restriction since for all the test cases the cross flow Mach number ($M \sin \sigma$) was greater than 0.4. For these conditions separation characteristics are dominated by local shockwave systems at the body shoulder rather than by Reynolds number considerations.

The tunnel used in these experiments was the 229 mm x 229 mm (9 in. x 9 in.) continuously operating supersonic facility at the Aerodynamics Department, Cranfield Institute of Technology. This was equipped with automatic means for setting of incidence angle although roll angle had to be adjusted manually with the tunnel open. As well as the pressure measurement apparatus, facilities for flow visualisation by the schlieren and vapour screen methods were also available.

3.1 Model and Test Details

The model tested was geometrically similar to that of the water tunnel programme except that the section shape of the wing panels had to be modified from a plate with sharp leading and trailing edges to a wedge shape. This was to enable the provision of tubing within the wing so that pressure data could be acquired. Where the wing was still too thin for this to be done, i.e. near the leading edge, holes were drilled directly through the panel into tubes attached to the surface of the wing opposite to that on which pressure data were being measured. Thus only one surface was pressure tapped and to obtain upper and lower surface pressure distributions the model was positioned in mirror image orientations relative to the incidence plane. Figure 16 illustrates the pressure hole distribution and the sectional shape of the wing. The whole wing-body combination could be rolled around the body axis. The pressures were measured using an automatic scanner and transducer system. Comprehensive pressure coefficient data were obtained for a variety of combinations of incidence and roll angles.

3.2 Results from the Wind Tunnel Tests

3.2.1 Flow Visualisation

The use of the schlieren and vapour screen methods was employed to visualise the flow around the wing-body combination and also around body alone models some of which were fitted with small forward surfaces. Particular interest was shown in the positions of the vortex system which started on the forebody of the model and whose core position could be identified by the light/dark boundary shown in the schlieren photographs or by the dark area in an otherwise light grey vapour screen photograph.

By direct measurement from these photographs it was possible to derive values for the vertical and lateral core positions relative to the body centre line for the wing-body combination, and these values are presented in Figures 17 and 18. Also included are some previous results given by Mendenhall and Nielsen⁵, together with their empirical curves. For the case of vertical core position it should be remembered that the latter curve was a result of a correlation employing data from both supersonic and subsonic tests. For lateral position separate correlations were suggested in Reference 5 for the two speed ranges. It can be

clearly seen that the vertical positions are much further upward and the lateral positions much further outboard than the previously accepted data. Since the schlieren photographs from which the present measurements were taken were small and thus measurement errors were probable, estimates of the error band have been made both in terms of lateral and vertical location and also the point at which separation first occurs (obtained by extrapolating the vortex trajectory into the body centre line). Even allowing for these error bands the points still occur at significantly higher values of vertical and lateral co-ordinate than would be expected. Clearly this trend leads to some doubt concerning the validity of the results and gives rise to the possibility of there being some forward interference from the wing panels which could affect the upstream body vortex development and hence the vortex trajectories.

A body alone model was therefore tested and similar data on body vortex vertical position (since only schlieren pictures were taken) derived. The results are shown in Figure 17 and illustrate that, accounting for the bands of experimental error, the data for the body alone case and for the wing-body combination do overlap. However, the data for the body alone case is generally at a lower value of $z_{B/a}$ than for the wing-body combination at the same value of $\frac{x - x_s}{r_N} \sin \sigma$. Both sets are at higher values than given by the

suggested correlation curve although this had been produced taking into account both supersonic and subsonic data. It may be seen in Figure 17 how, if attention is paid primarily to the previous results for an ogive cylinder at $M=2.0$, the agreement between present and past data is quite reasonable. The measurement of further sets of data at these supersonic speeds which give higher $z_{B/a}$ co-ordinates than previously found suggests that improvements to the data correlations might be found by using a curve which predicted a greater $z_{B/a}$ at high $\frac{x - x_s}{r_N} \sin \sigma$.

The effect of wing panels on body vortex trajectories upstream of the panel leading edges at these speeds is a topic which could most usefully be explored in more detail in further experiments. The tests detailed in this paper have given a preliminary indication that such effects might be apparent but more systematic and sophisticated experiments are necessary before the effects can be precisely quantified.

As the main purpose of these tests was to investigate the interaction of body vortices with wing panels, the actual generation of these vortices was in some ways a side issue. However, if predictions of their trajectory and strength could not be made with sufficient accuracy then analysis of the later results would prove difficult. It was thought that a more satisfactory approach to the experiment might be to try to force some pattern onto the vortex development by the use of small forward surfaces mounted on the body nose. Thus, instead of relying on natural body vortex generation, a trailing vortex system generated by the forward surfaces might be formed which would then interact with the downstream wing surfaces. The forward surfaces were positioned ahead of the predicted point for body vortex separation and consequently it was considered that suppression of the body vortices as such would occur.

The desired effect was therefore a trailing vortex pair symmetrically disposed with respect to the body centre line and which would be more accurately quantified in strength and position than would be the case with the body vortices.

In practice, however, the vortex system proved to be much more complex. Although the small forward panels did generate a system of vortices, it was evident that the body vortices were not suppressed, and between the trailing edges of the forward surfaces and the leading edges of the wing panels it was possible to observe four vortices in the flow. Figure 19 presents illustrations of (a) the arrangement of the monoplane forward surfaces and (b) the vortex pattern produced for a body incidence of 20° and which was obtained using the vapour screen method.

The generation of vortices aft of these forward surfaces was an unexpected feature although subsequently Hemsch et al⁷ have discussed the generation of "afterbody vortices".

From the vapour screen pictures it was possible to observe the coalescence of the two vortex systems, one from the panel and one from the forebody, as incidence angle was increased.

Because of this multi-vortex flow it was thought that any analysis of the resultant pressure distributions and, hence, loads on the downstream panels when interaction was taking place would be extremely difficult. The use of small forward surfaces to stabilise the vortex pattern was therefore abandoned and reliance placed on the use of a simple forebody, with natural body vortex formation.

3.2.2 Pressure Coefficient and Panel Load Results

In this section attention will be biased towards consideration of results for the particular condition of close panel/vortex interaction. From the use of Mendenhall and Nielsen's prediction method it was assumed that this situation would occur at a panel roll angle of 20° coupled with a body incidence angle of 20° . It should be noted that where roll angles (ϕ) are quoted these refer to the panel which was initially positioned vertically on the leeward side of the body.

A plot is presented in Figure 20 which sets out results for four longitudinal stations $x_w/c_r = 0.36, 0.46, 0.65, 0.87$ at which the pressure coefficient difference $\Delta C_p = C_{p_L} - C_{p_U}$ is given across the span. This represents the lifting contribution of the pressure distributions and the symmetrical effects of thickness of the panel are also removed by plotting the difference in pressure coefficients.

Features to note are the low and sometimes negative pressure coefficient differences near the root of the panel. These contribute to a negative local spanwise loading near the root (Figure 21) which in turn yields a net reduction in load and can sometimes lead to load reversal as the panel approaches the vertical. This phenomenon of very low panel load, even perhaps negative values, has been noted before for various sets of experimental results and has recently been referred to by Nielsen⁸ in his survey of non-linearities in missile aerodynamics.

The actual value of panel load coefficient which results from the integration of the pressure coefficient data over the whole of the panel is, in this case, small but positive (see Figure 22).

The variation of panel load with roll angle can be assessed also from Figure 22 for the case of a body

incidence angle of 20° . Here, as ϕ varies from 10° to 30° , the panel is initially above the vortex core and then below it.

The low values of panel load can be clearly seen as can the load reversal when at the extreme roll orientation of 10° . The equivalent value of panel load coefficient for $\phi = 90^\circ$ roll is approximately 0.3.

3.2.3 Comparisons of Experimental Panel Load Data with Predictions

It would be highly desirable to be able to predict accurately the individual panel loads for a cruciform configuration for all incidence and roll angles. This would be equally necessary for those orientations where the panel was at roll angles near to the vertical in the leeward quadrant as it would be for panels near the horizontal. Although the contribution to in-plane normal force would be very small owing to the small magnitude of load on the panel and the large angle through which it needs to be resolved, all the panels contribute in equal importance to rolling moment which can arise from small differences in relatively large panel loads.

A semi-empirical method has been developed which attempts to predict the panel loads. It relies on the usual assumption that they may be calculated by first making an estimate of the load on a wing in isolation and then applying interference factors to allow for the flow field induced on the wing by the presence of the body. This would give a panel load for $\phi = 90^\circ$. Suitable methods for the wing alone term and for the body-to-wing interference factor are contained in references by Collingbourne⁹ and Pitts, Nielsen and Kaattari,¹⁰ respectively. The effect of roll angle can then be incorporated in a manner similar to that developed by Spahr.¹¹ The result is to predict a variation of panel load with roll angle which is of a skewed cosine form, such that panels rolled into the windward quadrant experience an increase in load and those in the leeward quadrant a decrease relative to the $\phi = 90^\circ$ value.

These methods give values of panel loads at non-zero roll angle with the body at non-zero incidence angle, but the effects of any body vortices have not been considered. These can simply be taken into account by the use of the vortex interference factors presented by Spahr or by Pitts, Nielsen and Kaattari. An example plot of the factors is presented in Figure 23 and it can be seen that the result would be large changes in load if a vortex approached close to a panel.

The actual load change is found from the relationship:

$$\Delta C_{Np} = \frac{K_{WB}}{2\pi V(s-a)} \cdot C_{N0} \cdot \sum_{k=1}^n \Gamma_k i_k$$

The methods described above have been combined to yield the predicted values of panel normal force coefficient shown in Figure 22. It can be seen that the general level of prediction accuracy is low.

The derivation of the interference term 'i' has assumed a trapezoidal spanwise load distribution which has a root value twice that at the tip. In practice, this assumption would be adequate for the case of $\phi = 90^\circ$ but clearly has to be greatly modified for the panel rolled into the leeward quadrant.

3.3 Conclusions and Recommendations Drawn from the Wind Tunnel Tests

The experiments have shown that vortex trajectory data can be measured which is significantly displaced from that previously collated by Mendenhall and Nielsen although flow conditions for the experiments are not different.

It is apparent that the simple scheme of prediction detailed in the previous section can only provide an approximate solution to the problem of estimating loads on panels when they are rolled into the vicinity of body vortices.

To try to isolate the particular effects of body vortices it would be highly desirable to undertake a series of tests in which the effects were removed. This could be done in an experiment using a model with a much shorter nose length hence minimising body vortex formation ahead of the wing leading edge. Comparison of results with those from the present tests would yield the effect of the body vortices.

4. GENERAL CONCLUDING REMARKS

Much research is currently being undertaken to understand the complexities of high angle of attack aerodynamics where the phenomenon of asymmetric body vortex development gives rise to side forces and yawing moments.

The results detailed in this paper, however, show that attention still needs to be paid to the lower incidence angle regime where vortex patterns are still symmetric and where a complete understanding of the flow field development has by no means been achieved.

The need still exists for systematic series of experiments including both flow survey measurement and visualisation to try to pinpoint the important parameters in body vortex generation and to remove some of the uncertainty from strength and trajectory predictions.

For the purposes of accurately estimating the complete load distribution on a missile this will be just as necessary as the better understanding of vortex/panel interference which must start from an estimate of the characteristics of the body vortex itself.

The use of the two very different experimental techniques detailed in this paper has yielded information on flow fields at the extreme ends of a wide speed range. It is hoped that further testing will be possible in a low speed wind tunnel, thus closing the gap in the data coverage.

With the two sets of results currently available it is, of course, of little merit to attempt to read across detailed flow field information from one to the other owing to the undoubtedly important effects of compressibility. However, the flow visualisation results from the water tunnel are most useful in

stimulating investigations of flow phenomena at other speeds. As well as low speed wind tunnel experiments, further testing is also planned by the author which will incorporate supersonic Mach numbers and thus, prompted by the latest water tunnel results, particular attention will be given to careful observations of, for example, any vortex breakdown effects adjacent to the wing panels.

It is to be hoped that this work will form only one part of a wider effort to investigate and further understand the phenomena of symmetric body vortex generation and the subsequent interaction with wing panels. Preliminary work is in progress in the United Kingdom which will lead to extensive flow survey experiments in the lee side of bodies of revolution at incidence and a further assessment of body vortex interaction effects with panels. In the U.S.A., Oberkampf et al¹² have already recently published details of flow survey work aimed at producing a more detailed understanding of the flow field properties adjacent to a body vortex pair.

The continuation of such work in the future should yield significant advances in the understanding of the complex problems inherent in this topic of vortex dominated flow fields.

5. REFERENCES

1. Flechter, M.; "Ober wirbelsysteme an schlanken rotationskorpern und ihren einfluss auf die aerodynamischen beiwerte. (On the vortex systems of slender bodies of revolution and their influence on the aerodynamic coefficients)", (1966), Deutsch-Franzosisches Forschungsinstitut Saint-Louis, Report 10/66.
2. Werle, H.; "Investigations of blowing in a water tunnel by flow visualisation", (1960), NASA TT-F-13742. (Translation from ONERA NT-61).
3. Rainbird, W.J., Crabbe, R.S., Jurewicz, L.S.; "A water tunnel investigation of the flow separation about circular cones at incidences", (1963), National Research Council of Canada, Aeronautical Report LR-385.
4. Poisson-Quinton, P., Werle, H.; "Water tunnel visualisation of vortex flow", (1967), Astronautics and Aeronautics, Vol. 5, pp. 64-66.
5. Mendenhall, M.R., Nielsen, J.N.; "Effect of symmetrical vortex shedding on the longitudinal aerodynamic characteristics of wing-body-tail combinations", (1975), NASA CR 2473.
6. Jorgensen, L.H.; "Prediction of static aerodynamic characteristics for slender bodies alone and with lifting surfaces to very high angles of attack", (1977), NASA TR R-474.
7. Hensch, M.J., Smith, C.A., Nielsen, J.N., Perkins, S.C.; "Calculation of component forces and moments of arbitrarily banked cruciform missiles with control deflections", (1976), ONR CR 215-226-3.
8. Nielsen, J.N.; "Non-linearities in missile aerodynamics", (1978), AIAA Paper 78-20.
9. Collingbourne, J.R.; "An empirical prediction method for non-linear normal force on thin wings at supersonic speeds", (1963), ARC CP 662.
10. Pitts, W.C., Nielsen, J.N., Kaattari, G.E.; "Lift and centre of pressure of wing-body-tail combinations at subsonic, transonic and supersonic speeds", (1957), NACA Report 1307.
11. Spahr, J.R.; "Theoretical prediction of the effects of vortex flows on the loading, forces and moments of slender aircraft", (1961), NASA TR R-101.
12. Oberkampf, W.L., Bartel, T.J., Martindale, W.R.; "Supersonic flow measurements in the body vortex wake of an ogive nose cylinder", (1978), AIAA Paper 78-787.

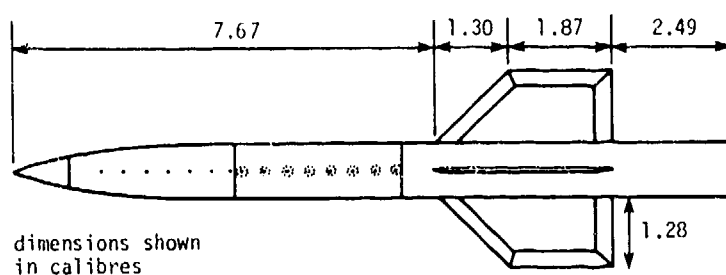
6. ACKNOWLEDGEMENTS

The author acknowledges the assistance and support of the following:

British Aerospace, Dynamics Group, Bristol for permission to publish this paper, and the particular assistance of members of the Aerodynamics Research Group.

Science Research Council for financial support during an M.Sc. programme at Cranfield Institute of Technology, during which the supersonic wind tunnel tests outlined here were undertaken.

Various staff at British Aerospace, Bristol and Warton, Cranfield Institute of Technology, Bristol University and the Royal Aircraft Establishments at Farnborough and Bedford for their help in the wind and water tunnel tests and for helpful discussions of results. In particular the assistance of the Warton Division, British Aerospace, in the provision of the water tunnel facility is acknowledged, as is the help in running the water tunnel tests by members of the staff of the Guided Weapons Wind Tunnel at Warton.



Nose Shape: Fineness ratio = 3 tangent ogive
 Holes Ringed: \odot are duplicated on opposite side of model

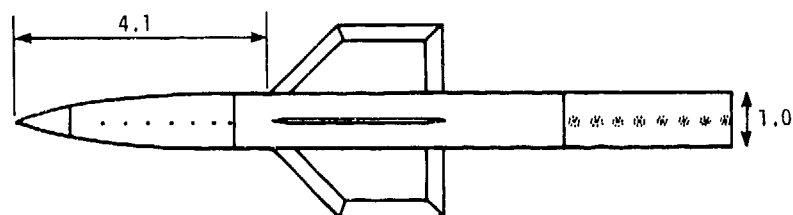


Fig.1: WATER TUNNEL MODEL: Alternative Wing Locations

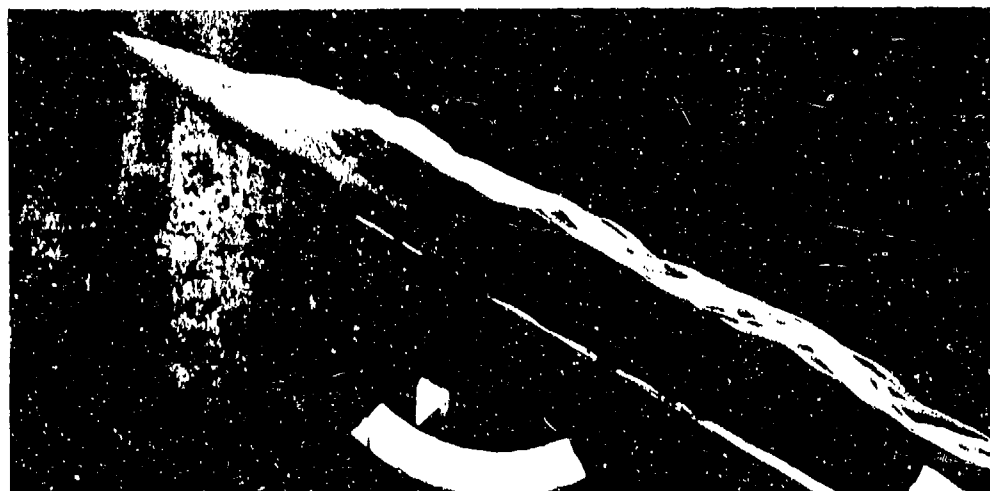


Fig.2: SHARP BODY: FORWARD DYELINES: $\sigma = 30^\circ$; SIDE VIEW

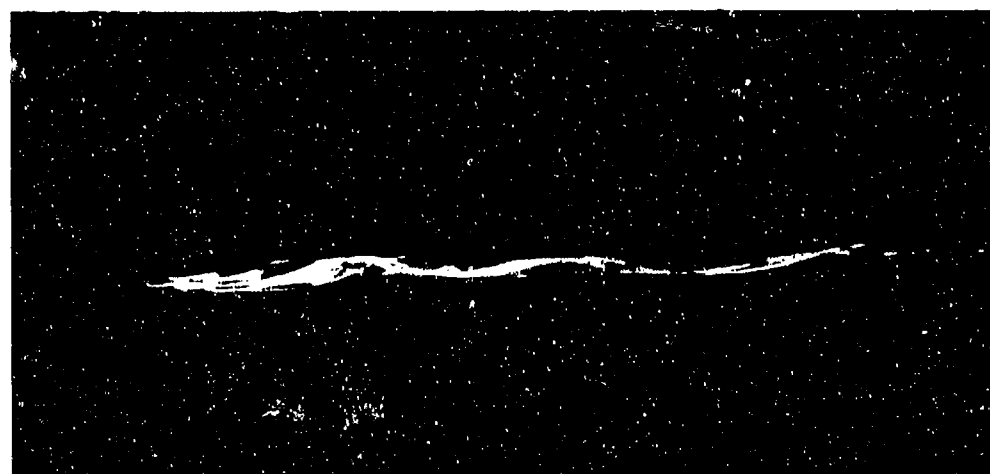


Fig.3: SHARP BODY: FORWARD DYELINES: $\sigma = 30^\circ$; TOP VIEW

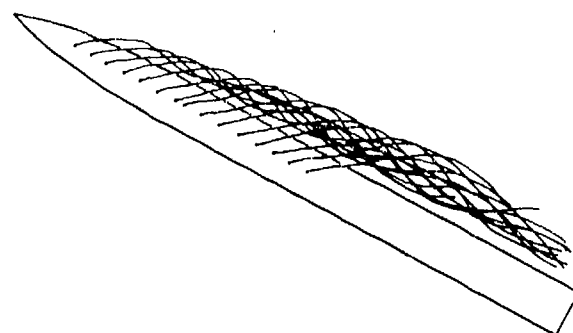


Fig.4: SUPER-POSITION OF DYELINE TRACES: Sharp
Body: $\sigma = 30^\circ$

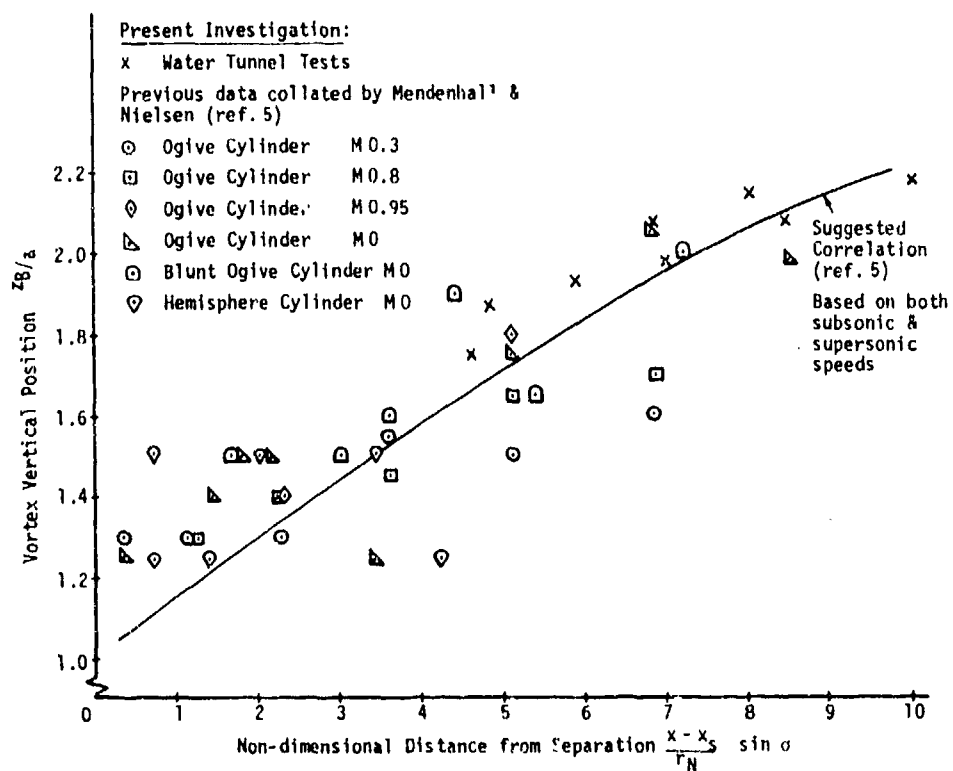


Fig.5: VORTEX VERTICAL POSITIONS:
Subsonic Speeds: Data from Water Tunnel Tests

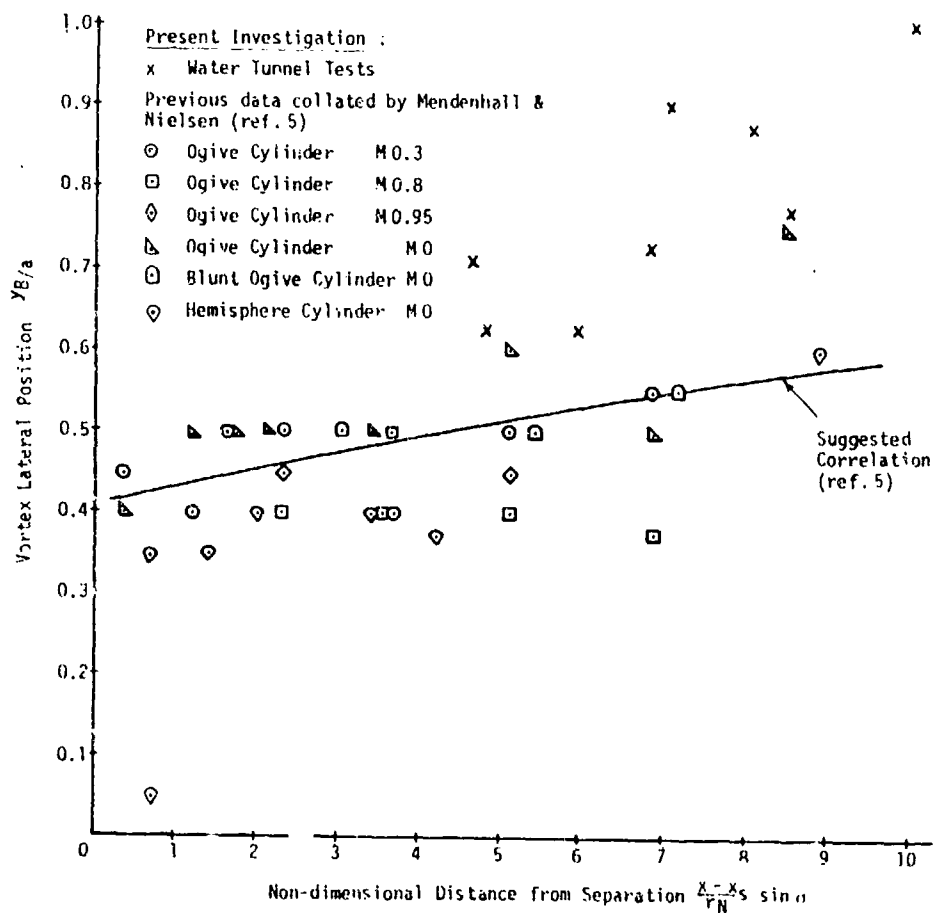


Fig.6: VORTEX LATERAL POSITIONS:
Subsonic Speeds: Data from Water Tunnel Tests

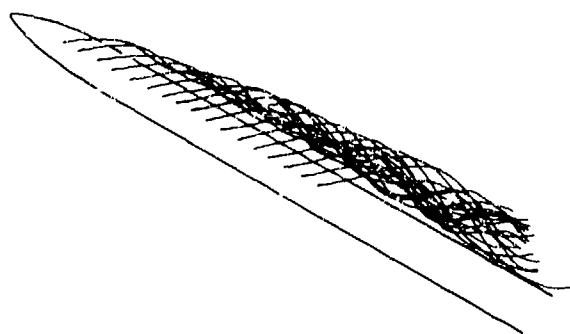


Fig.7: SUPER-POSITION OF DYELINE TRACES: Blunt
Body: $\alpha = 30^\circ$



Fig.8: AFT DYELINES: $\alpha = 15^\circ$; $\phi = 0^\circ$

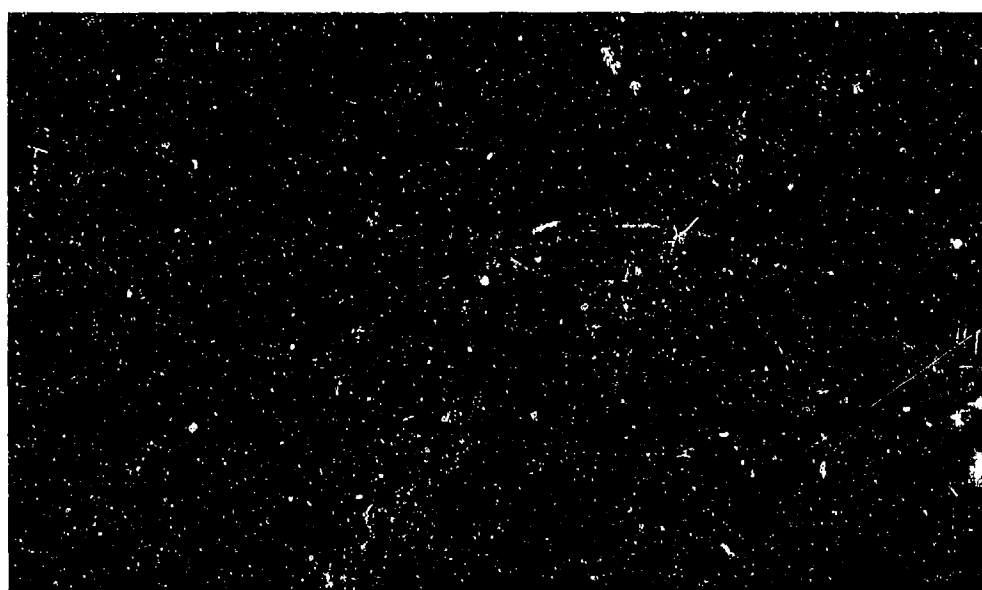


Fig.9: AFT DYELINES: $\alpha = 25^\circ$; $\phi = 0^\circ$

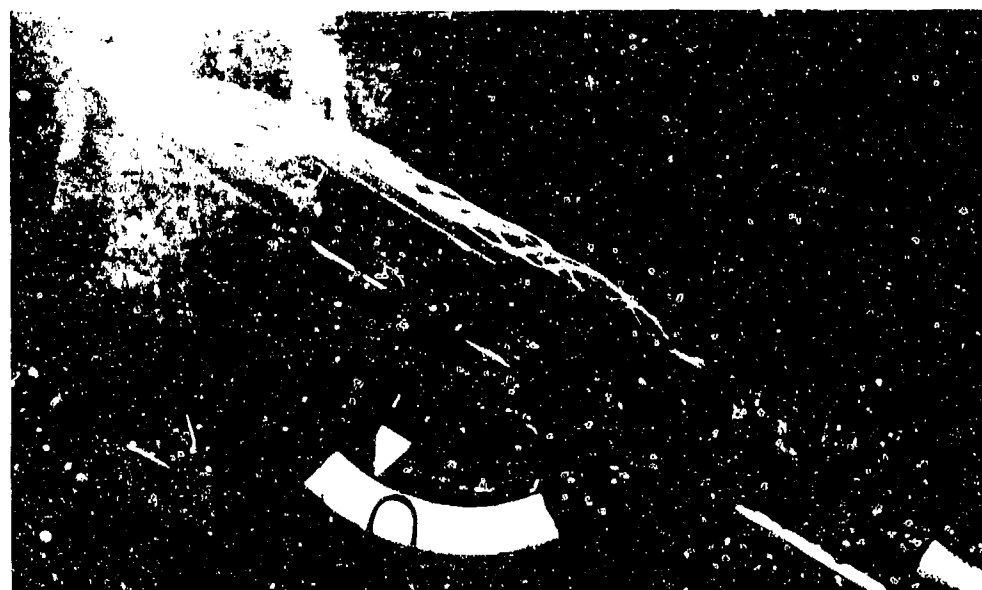


Fig.10: FORWARD DYELINES: $\alpha = 30^\circ$, $\phi = 0^\circ$; SIDE VIEW OF VORTEX BREAKDOWN

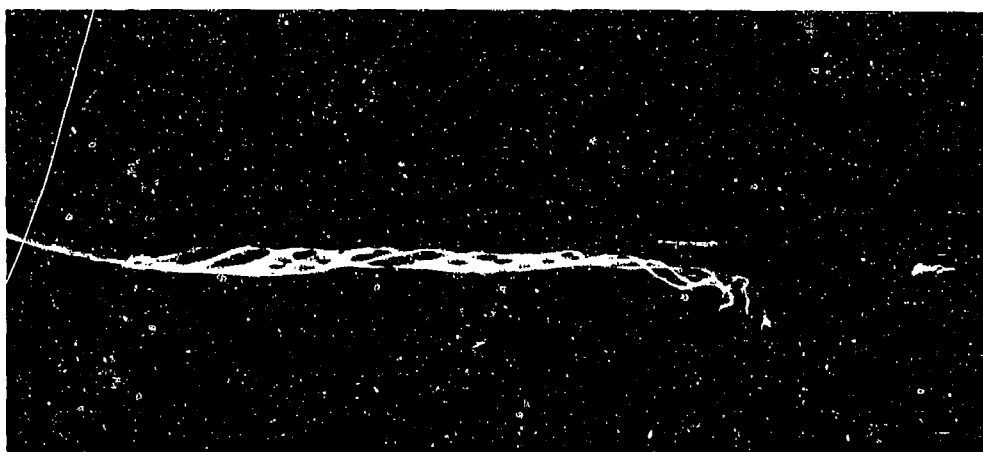


Fig.11: FORWARD DYELINES: $\sigma = 30^\circ$, $\phi = 0^\circ$, TOP VIEW OF VORTEX BREAKDOWN

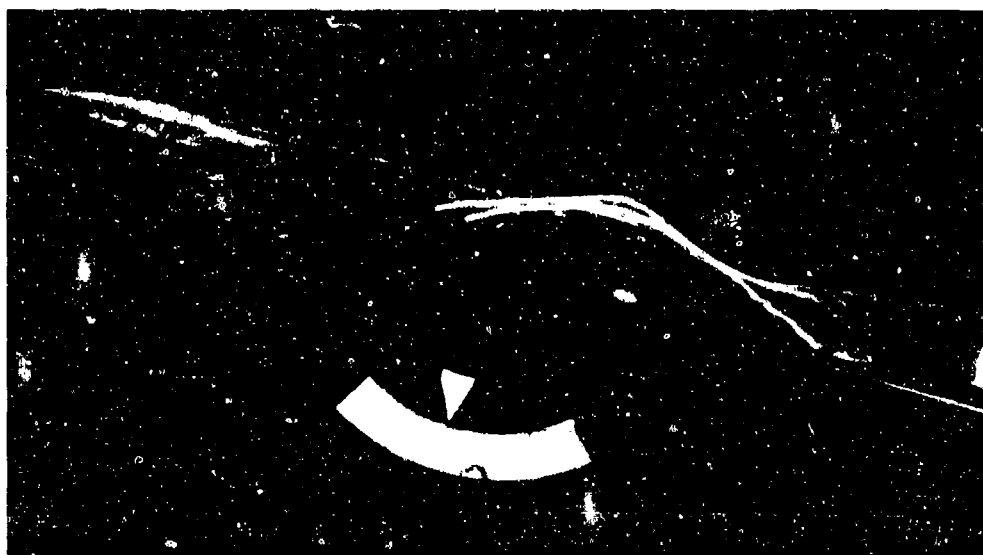


Fig.12: AFT DYELINES: $\sigma = 15^\circ$, $\phi = 30^\circ$



Fig.13: FORWARD DYELINES: $\sigma = 25^\circ$, $\phi = 45^\circ$

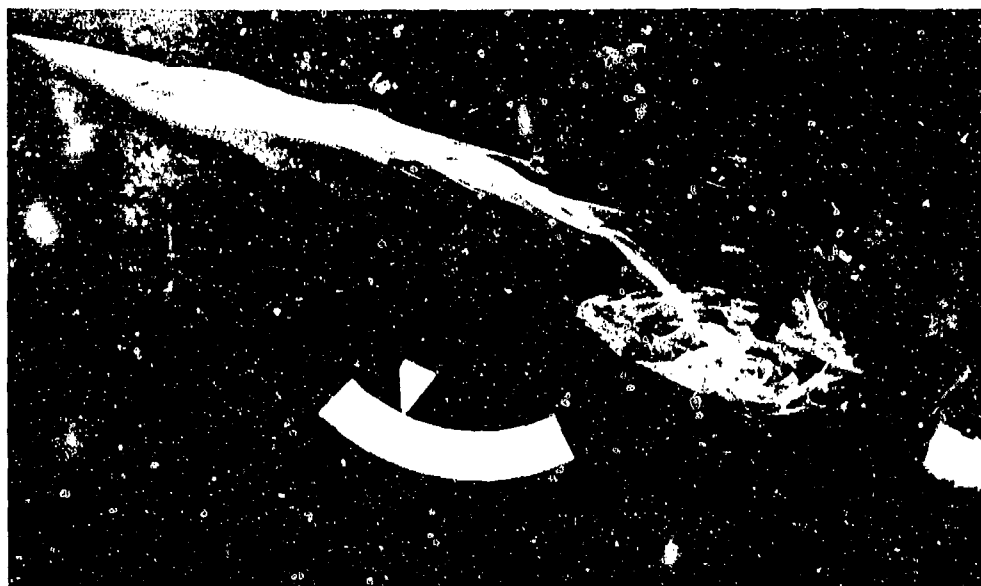


Fig.14: FORWARD DYELINES: $\alpha = 25^\circ$, $\phi = 20^\circ$

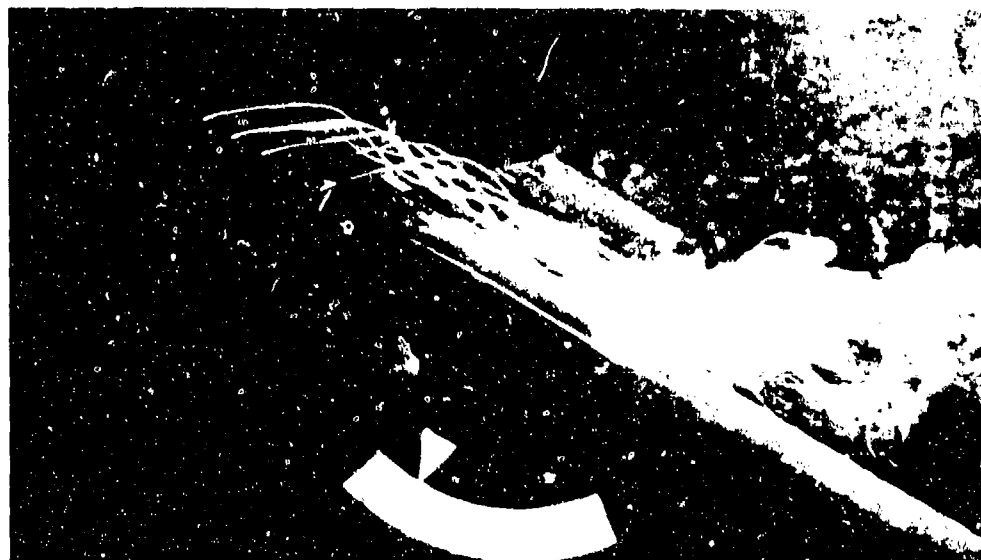


Fig.15: FORWARD WING POSITION: $\alpha = 30^\circ$, $\phi = 0^\circ$

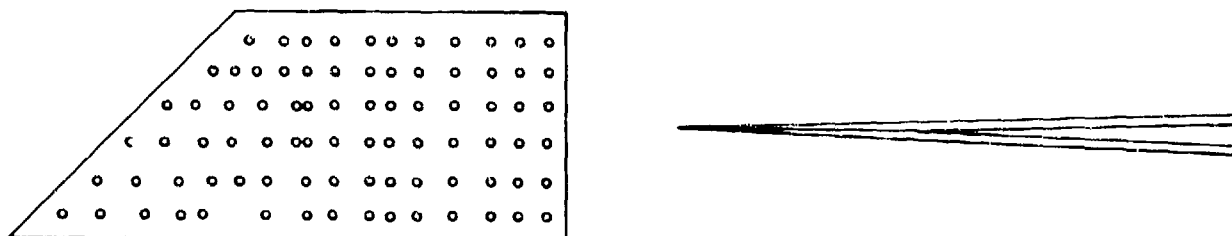


Fig.16: PRESSURE HOLE DISTRIBUTION AND SECTION
SHAPE OF WING PANELS USED IN SUPERSONIC
WIND TUNNEL TESTS

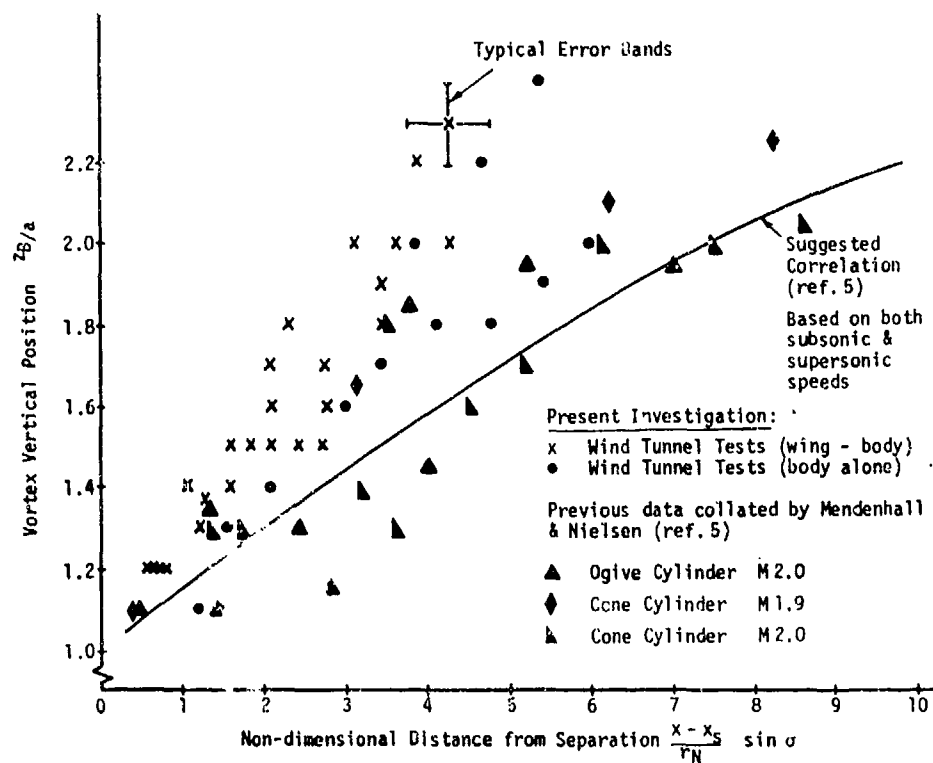


Fig.17: VORTEX VERTICAL POSITIONS:
Supersonic Speeds: Data from Wind Tunnel Tests

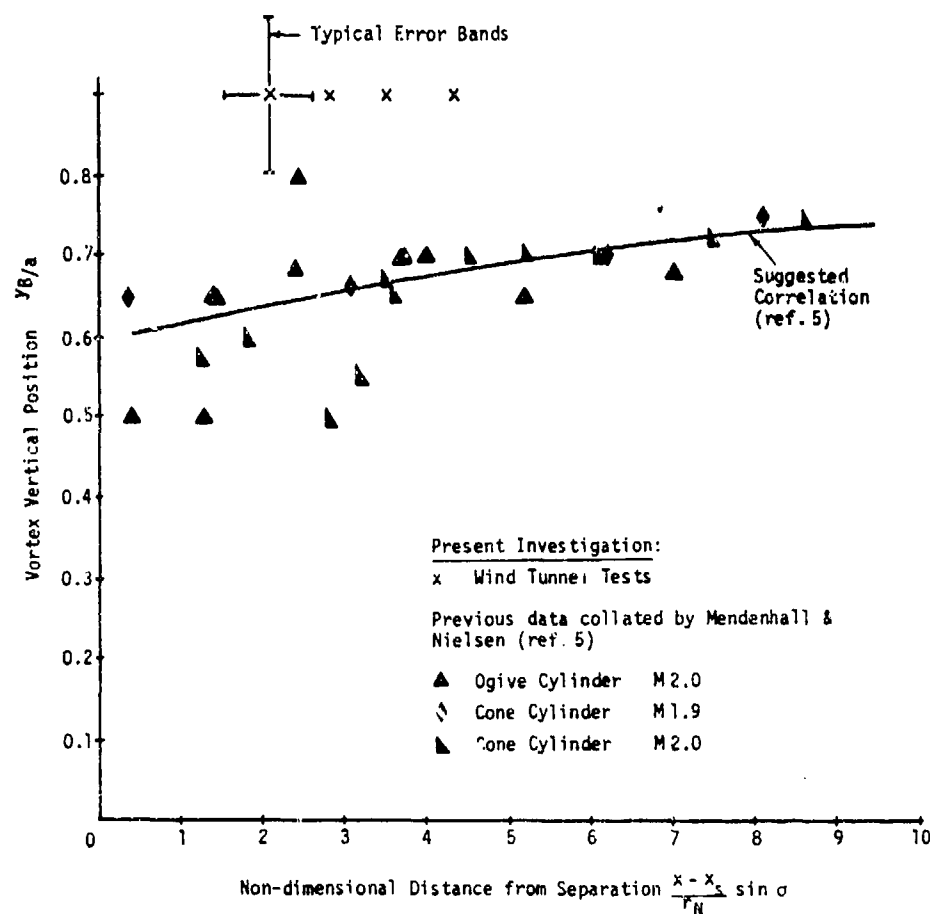


Fig.18: VORTEX LATERAL POSITIONS:
Supersonic Speeds: Data from Wind Tunnel Tests

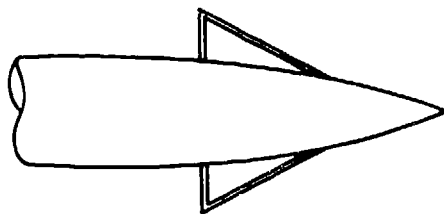


Fig. 19a: SMALL MONOPLANE FORWARD SURFACES USED ON FOREBODY FOR SOME SUPERSONIC WIND TUNNEL TESTS

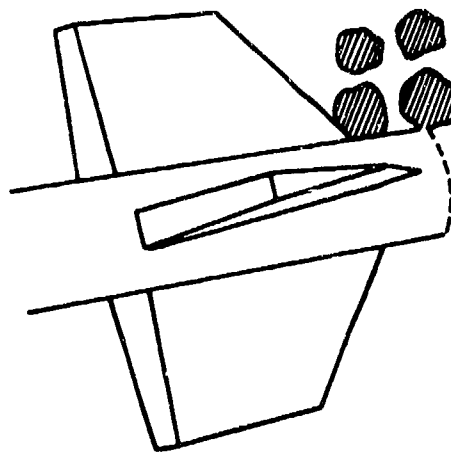


Fig. 19b: DUAL VORTEX SYSTEM TRAILING FROM FORWARD SURFACES AND FROM FOREBODY

$$M=2, \sigma=20^\circ, \phi=0^\circ$$

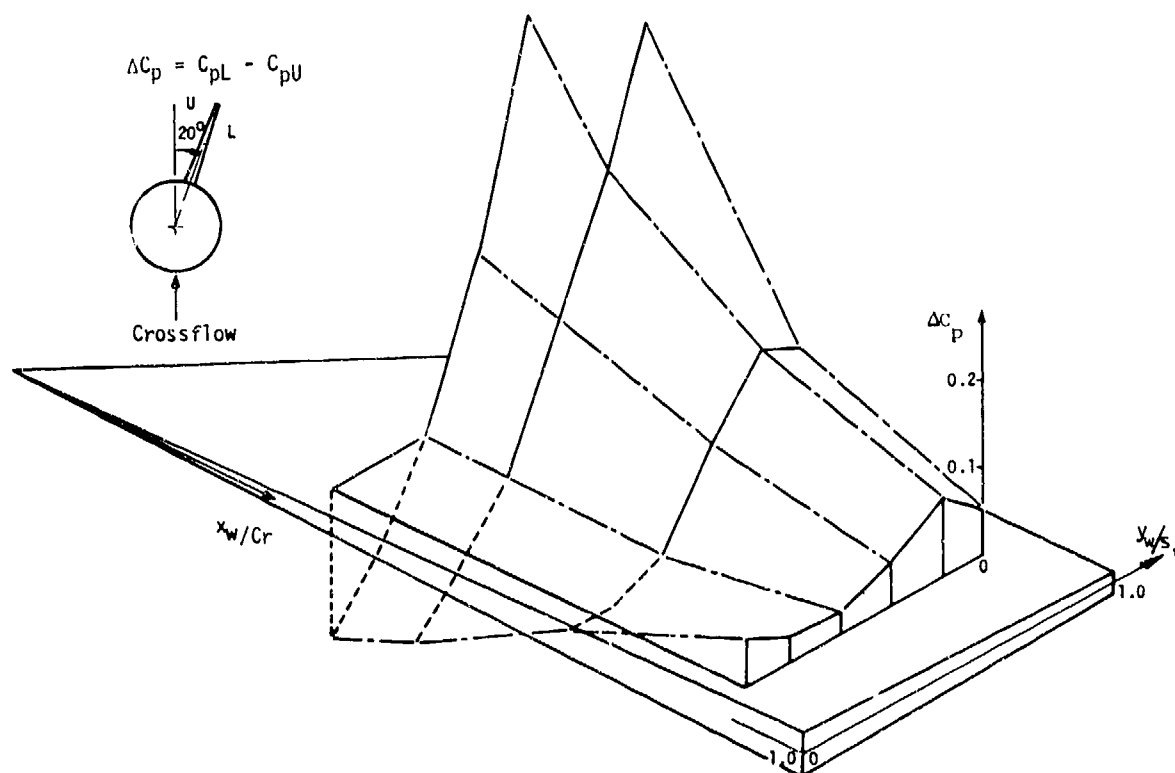


Fig. 20: PRESSURE COEFFICIENT DIFFERENCES ACROSS PANEL SURFACE

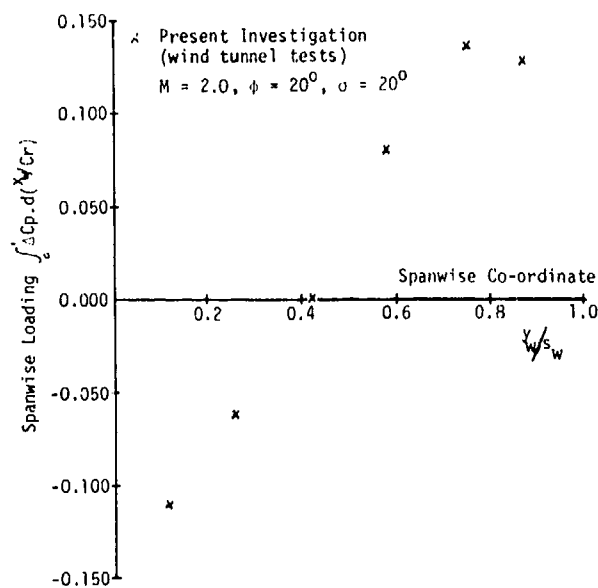


Fig. 21: SPANWISE LOADING DISTRIBUTION ON PANEL ROLLED INTO VICINITY OF BODY VORTEX

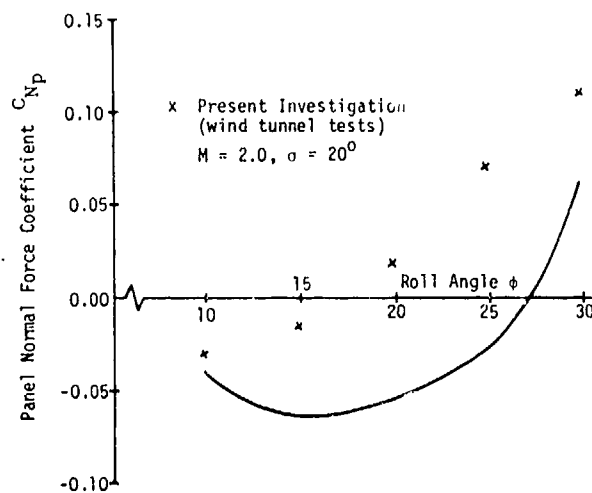
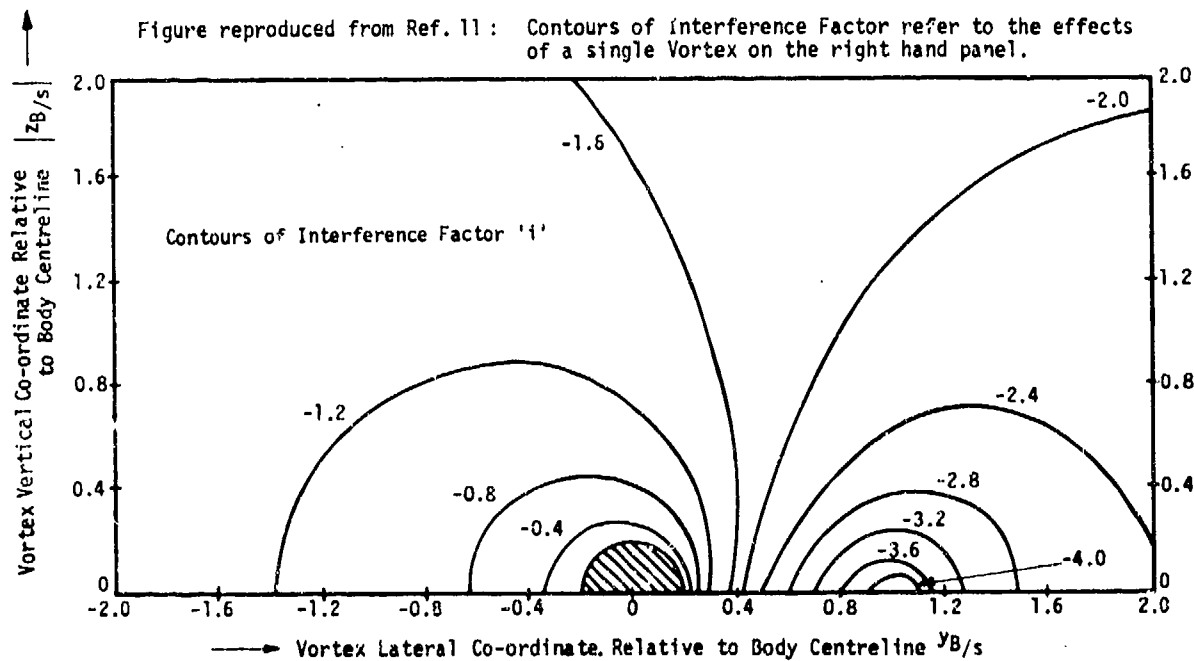


Fig. 22: NORMAL FORCE COEFFICIENTS FOR PANEL ROLLED INTO LEESIDE QUADRANT

Fig. 23: VORTEX INTERFERENCE FACTORS; ($a/s = 0.2$, TRAPEZOIDAL LOADING)

Caractéristiques Aérodynamiques des corps de révolution
munis d'ailes d'allongements divers

par L. MIFSUD

S.A. MATRA, BP 1, 78140 Vélizy (France)

Résumé

La communication présente les résultats d'essais faits au bassin hydrodynamique et en soufflerie sur des corps de révolution seuls d'une part, et munis d'ailes de très faibles allongements, d'autre part ($0,1 < \lambda < 0,3$). On donne les résultats de mesures des efforts verticaux et latéraux, ainsi que des mesures de pression pariétale sur des ailes, en fonction de l'incidence entre 0 et 45° ou 70°. Les paramètres sont le nombre de Mach, la longueur et l'envergure des ailes E/D.

$$M = 0,44 - 0,90 - 1,32 - \text{et } 1,4 < E/D < 2,5.$$

Les résultats permettent de voir dans quelle mesure la présence d'ailes et la variation de leurs paramètres peuvent influencer sur les phénomènes inhérents aux hautes incidences, et plus particulièrement sur les efforts latéraux.

Summary

The paper presents the results of experiments made in a water tank and wind tunnels on bodies of revolution and finned bodies of small wing aspect ratio. Results of lift and side force, pitching and yawing moments and wall pressure distributions are presented for angles of attack between 0 and 45 or 70°. The parameters are the Mach number, the wing length and the wing span E/D.

$$M = 0,44 - 0,90 - 1,32 - \text{and } 1,4 < E/D < 2,5.$$

The results show the effects of wing parameters on high incidence phenomena and specially on lateral forces and moments.

Notations

Cz	Coefficient de portance	Lc	Longueur du modèle
Cy	" de force latérale	Lo	Longueur de l'ogive
CL	" de moment de roulis	r	Rayon de l'émoussement
Cm	" de moment de tangage	S	Surface de référence : maître - couple
Cn	" de moment de lacet	θ	Angle de roulis
D	Longueur de référence : diamètre du corps	λ	Allongement de l'aile basé sur l'envergure et la surface nettes
E	Envergure totale des ailes	σ	Ecart - type moyen
i	Incidence	σ_0	Ecart - type moyen pour $i = 0^\circ$
La	Longueur de la corde à l'emplanture		

1 - INTRODUCTION.

Les performances dont doivent faire preuve les avions de combat futurs et a fortiori les missiles dont ils seront dotés sont caractérisées par une grande manoeuvrabilité, plus spécialement dans le domaine des grands angles d'incidence.

Dans l'optique de l'aérodynamique des missiles qui nous intéressent ici, le domaine des grandes incidences est abordé par un missile air - air pendant la phase de départ de l'engin de son avion porteur, puis le long d'une trajectoire à très fort facteur de charge.

De même, certains missiles sol - air prennent une incidence élevée pendant le vol de transition qui suit le tir à partir d'un silo.

Les incidences ainsi atteintes sont au moins doubles de celles où évoluent les missiles actuels.

Les ailes trapézoïdales classiques d'allongement d'environ 1,5 à 2 munissant la plupart des missiles actuels ont montré leur saturation et leur décrochage en subsonique pour des incidences de 20° environ comme le montrent les répartitions de pression (fig. 1 - 2) mesurées sur l'extrados d'une aile trapézoïdale d'allongement 1,71. De plus, cette perte d'efficacité est fonction de l'allongement (fig. 3). Pour éviter cette saturation à des incidences plus élevées, on a donc eu recours à des ailes de plus faibles allongements.

Il était donc opportun de faire une étude expérimentale pour mettre en évidence, par la mesure des efforts suivant les trois axes, les caractéristiques de corps de révolution munis d'ailes de faibles allongements $0,1 < \lambda < 0,3$ - Le domaine choisi fut celui des hautes incidences pour des régimes subsoniques et supersoniques d'écoulements.

2 - MOYENS D'ESSAIS.

2.1. - Bassin hydrodynamique.

Pour des raisons de facilité d'emploi et d'économie les études de base sur l'effet de l'allongement

des ailes ont été réalisées dans le bassin hydrodynamique de la Société MATRA.

Dans ce bassin (fig. 4), la maquette mobile suivant les trois axes est disposée au bout d'un bras pouvant lui donner des incidences comprises entre 0° et 90° . Les valeurs des angles d'incidence et de roulis sont repérées électroniquement.

Le chariot, support de bras, est animé d'un mouvement de translation horizontal par un moteur asservi qui lui donne une vitesse constante de 1,25 m/s correspondant à un nombre de Reynolds dans l'eau de $1,25 \times 10^6$ dans les conditions normales de température.

La maquette est portée par une balance à jauges de contraintes permettant de mesurer les forces et les moments suivant les trois axes. Les valeurs lues sont des moyennes effectuées sur 35 mesures obtenues pendant un parcours du bassin. Les signaux, après passage dans une baie électronique de mesure, sont traités numériquement par un ordinateur.

Les résultats obtenus (fig. 5, 6) sont particulièrement représentatifs des écoulements incompressibles.

2.2. - Soufflerie.

Pour mettre en évidence l'effet de Mach, des essais ont été effectués dans la soufflerie $\Sigma 4$ de l'Institut Aérotechnique de St. Cyr, à des incidences variant de façon continue de 0 à 70° environ et pour des nombres de Mach de 0,44 - 0,90 - et 1,32.

La pression génératrice étant la pression atmosphérique, cela correspondait à des nombres de Reynolds compris entre 0,8 et $1,9 \times 10^7$.

3 - RESULTATS DES MESURES.

Les résultats sont donnés dans le trièdre de référence et avec les notations précisées sur la figure 7. Les dimensions de référence sont le diamètre du corps et la surface du maître - couple. Dans tout ce qui suit, l'angle de dérapage des maquettes est resté nul.

3.1. - Corps de révolution.

A l'occasion de la détermination des efforts verticaux sur des corps de révolution à ogives tangentes, on a constaté l'établissement, à certaines incidences, d'efforts latéraux déjà mis en évidence par d'autres auteurs (1. 2. 3).

Ces efforts ont été mesurés en faisant varier les paramètres d'allongement L/D et d'émoussement r/D de l'ogive, la longueur du corps restant constante (17 diamètres).

Les mesures faites au bassin (fig. 8 - 9) confirment le résultat bien connu maintenant selon lequel les efforts latéraux croissent avec la longueur de l'ogive. Un autre phénomène est à remarquer au vu de ces courbes, la dispersion des points de mesure à partir d'une incidence que l'on peut situer aux alentours de 30° . Ceci laisse supposer l'existence de nappes tourbillonnaires instables autour du corps.

Des essais ont été effectués avec des ogives de différents émoussements. Par rapport aux mesures faites sur l'ogive pointue de même allongement, aucune influence nette de l'émoussement n'a pu être mise en évidence. Il semble donc que le phénomène de décollement des nappes tourbillonnaires soit plus sensible à l'allongement de l'ogive qu'à son émoussement.

La valeur de chaque point de mesure étant la moyenne entre 35 points, il nous a paru intéressant de tracer l'écart - type moyen en fonction de l'incidence, rapporté à l'écart - type à l'incidence nulle. On constate (fig. 10) une croissance continue de l'écart - type du moment de lacet. La dispersion des mesures des efforts latéraux se fait donc de façon continue depuis le domaine des faibles incidences. Bien que moindre, cette dispersion se fait sentir sur la mesure du moment de tangage. Enfin, les résultats des mesures sont plus dispersés lorsque l'ogive est plus élancée (fig. 11). L'allure de palier que prend la courbe de l'écart - type correspondant à l'ogive de plus faible allongement laisse présumer une structure plus organisée des tourbillons.

3.2. - Corps munis de surfaces portantes.

3.2.1. - Définition des modèles.

Les considérations de saturation de l'écoulement exposées dans l'introduction, alliées à des raisons plus pratiques d'encombrement d'ailes pour d'éventuelles réalisations, nous ont conduits à porter notre attention aux ailes de très faibles allongements.

Cependant, pour suppléer à la perte de portance linéaire qui en résulterait, et donc conserver des performances valables, on a été amené à augmenter la portance tourbillonnaire des ailes. Ceci a conduit, par un allongement appréciable de la corde, à équiper les corps étudiés de quatre ailes très élancées de type rectangulaire (fig. 12 configuration 1).

L'expérience a ensuite montré que ce type d'ailes était bien adapté aux hautes incidences. Dans tous les essais, la longueur de l'avant-corps du modèle et les caractéristiques de l'ogive sont restées constantes. Seules ont varié l'envergure et la longueur des ailes.

Seules des positions du missile à angle de roulis nul ont été considérées ($\theta = 0^\circ$) : les deux plans d'ailes étant confondus, d'une part avec le plan formé par le vent et l'axe du missile, et, d'autre part, avec le plan normal.

Sur ces configurations, on a de nouveau détecté des efforts latéraux aussi bien au bassin qu'en soufflerie.

3.2.2. - Portance.

Les courbes de portance correspondant à des configurations à envergure constante pour différentes longueurs d'aile (fig. 13, 14, 15) montrent que la pente des courbes à l'origine est la même pour toutes les ailes.

Par contre, les courbes (fig. 16) tracées en faisant varier l'envergure des ailes, la longueur restant constante, montrent que ces pentes sont nettement différenciées.

Si l'on admet de décomposer la portance des ailes en deux parties, l'une linéaire, l'autre d'origine tourbillonnaire, on peut dire que la portance linéaire est uniquement fonction de l'envergure des ailes. Cependant, la portance tourbillonnaire croît avec la longueur des ailes. Ce résultat, connu aux faibles incidences, est donc toujours valable jusqu'à 45° .

D'autre part, on peut constater que les courbes de portance sont très régulières et ne présentent pas de dispersion.

3.2.3. - Centre de poussée.

Au cours des mêmes essais, on a mesuré les moments de tangage par rapport à un point situé à une distance de $0,55 L_c$ de la pointe du modèle.

Les figures 17 à 19 présentent la position du centre de poussée C_m/C_z pour différentes configurations à envergure d'aile constante.

On constate dans tous les cas, un recul du centre de poussée en fonction de l'incidence. On peut aussi vérifier qu'à un accroissement de longueur de l'aile correspond un recul du centre de poussée. De plus, les courbes mettent en évidence un palier à partir de 20° d'incidence environ.

Tout ceci peut être interprété comme la naissance d'une portance non-linéaire qui croît avec l'incidence et qui agit en arrière de la portance linéaire. Aux hautes incidences, le point d'application de cette force est très stable. Il est à remarquer (fig. 19), que le palier est atteint pour des incidences plus fortes dans le cas d'ailes de plus faible envergure.

Lorsque seule l'envergure des ailes varie (fig. 20, 21), l'allure des courbes est la même, mais on constate qu'aux hautes incidences, la position du centre de poussée est pratiquement indépendante de l'envergure.

3.2.4. - Force latérale.

Les courbes donnant la force latérale sur des corps munis d'ailes de différentes envergures (fig. 22) montrent d'abord une croissance de la force avec l'incidence. Dans le domaine d'incidence décrit ($0 < i < 45^\circ$) les courbes ne font pas apparaître de maximum. De plus, au-delà de 30° , une variation de l'envergure correspond à une variation dans le même sens de la force latérale. Par contre, lors des expériences faites, la longueur des ailes n'a pas montré d'influence décelable (fig. 23 - 24). Ceci tendrait à prouver que les efforts latéraux sont principalement dus à une dissymétrie des tourbillons d'apex de l'ogive ; une influence prépondérante des tourbillons d'ailes aurait été révélée par une dépendance de la longueur d'aile, ce qui n'est pas le cas ici.

La comparaison avec les forces latérales sur le corps seul montre que la présence d'ailes accroît les efforts latéraux. Toutefois, la cause du décollement de l'écoulement étant inconnue, la comparaison n'est valable qu'en valeur absolue. De plus, une grande dispersion des résultats apparaît aux grandes incidences.

3.2.5. - Moment de lacet.

Les mesures du moment de lacet font apparaître une dispersion telle qu'elle empêche toute conclusion quant à l'influence des ailes (fig. 25 à 27). On peut seulement en déduire que le centre de poussée des forces latérales n'a pas une position stable lorsque le modèle se trouve dans le domaine des grandes incidences.

4 - EFFETS DE MACH AUX HAUTES INCIDENCES.

4.1. - Modèle.

Pour illustrer l'effet du nombre de Mach sur les phénomènes qui prennent naissance aux hautes incidences, nous présentons ici les résultats des essais faits en soufflerie sur un modèle qui se différencie du précédent par l'adjonction de quatre gouvernes trapézoïdales en arrière des ailes et dans leurs plans. (fig. 12 conf. 2). D'autre part, le domaine de variation de l'incidence a été étendu à 70° environ. Bien que ces résultats n'aient pas été obtenus à l'aide d'une configuration semblable à la précédente, il a été jugé intéressant d'en faire état surtout en ce qui concerne les efforts latéraux.

4.2. - Portance et moment de tangage.

Ils représentent le but principal des essais effectués, nous ne nous attarderons cependant pas

sur la mesure de ces efforts. Nous noterons seulement la faible influence du nombre de Mach sur la portance dans le domaine d'incidence décrit (fig. 28). Pour ce qui est du moment de tangage, l'allure particulière des courbes s'explique par la présence de la gouverne et il n'est pas dans notre intention d'en traiter ici (fig. 29).

4.3. - Force latérale et moment de lacet.

Les efforts latéraux mesurés pour trois nombres de Mach 0,44 - 0,90 - 1,32 montrent (fig. 30 - 31) une croissance très importante à partir d'une incidence de 35° environ. Au-dessous de cette incidence, les efforts latéraux sont négligeables. Ce phénomène s'accompagne, surtout dans le domaine subsonique, d'une grande dispersion des mesures ; l'enregistrement des mesures montre un signal totalement fluctuant au-delà de 30°. Ces grandes variations des résultats et le brusque changement de signe des mesures montrent une grande instabilité des nappes tourbillonnaires.

Comme l'ont observé différents auteurs (4 - 5) cette instabilité passe par un maximum pour une incidence située ici autour de 45°. Les efforts s'amoindrissent fortement à partir de 65° environ. La mise en évidence de cette zone d'instabilité que l'on peut s'attacher à réduire, présente un intérêt pratique important.

Un autre phénomène marquant et connu (2) est la diminution des efforts latéraux lorsqu'on atteint le domaine transsonique et leur disparition en supersonique.

4.4. - Moment de roulis.

Les moments de roulis correspondants montrent aussi des accroissements très importants en subsonique (fig. 32) avec de brusques changements de signe. Cependant, la zone d'instabilité n'est pas aussi nette que pour les efforts latéraux. En particulier, en subsonique, le moment reste encore très important au-delà de 65° d'incidence. De plus, l'effet de Mach est un peu moins marqué que pour le moment de lacet ; le moment de roulis est encore non négligeable pour $M = 1,32$.

4.5. - Effets de l'angle de roulis.

La position des missiles en vol étant a priori quelconque autour de leur axe de symétrie, il a paru intéressant de voir comment variaient les différents efforts lorsque l'angle de roulis \emptyset variait.

Les courbes de force et de moment latéraux (fig. 33 - 34) montrent une forte dépendance de ces efforts avec \emptyset . En particulier, le passage de $\emptyset = 0^\circ$ à $\emptyset = 45^\circ$ correspond, dans le cas de nos essais, à une diminution du maximum de la force latérale et à une plus grande diminution encore du moment correspondant. De plus, il coïncide avec un changement de signe de ces efforts. Cependant, on n'assiste pas au même phénomène lors des mesures du moment de roulis.

5 - CONCLUSIONS.

De l'étude expérimentale qui vient d'être faite, on peut tirer un certain nombre d'enseignements relatifs aux modèles expérimentés et qui peuvent se résumer comme suit :

- Les mesures faites sur les corps seuls au bassin hydrodynamique mettent en évidence une prépondérance de l'influence de l'allongement de l'ogive sur son écoulement. Les efforts latéraux croissent avec cet allongement. Le relevé des écarts - type montre une évolution progressive de l'instabilité de ces efforts avec l'incidence.

- La portance linéaire des modèles munis d'ailes est fonction de l'envergure alors que la portance non-linéaire et la position du centre de poussée de la portance est fonction de la longueur de l'aile. Ce résultat, déjà valable aux faibles incidences, le reste au moins jusqu'à 45°.

- Pour les ailes étudiées, la position du centre de poussée de la portance se stabilise au-delà de 20° d'incidence. Elle ne dépend pas de l'envergure.

- Une dispersion des résultats de mesure au bassin comme en soufflerie au-delà de 35° d'incidence environ, apparaît nettement sur les efforts latéraux. Elle est inexistante sur la mesure des efforts verticaux.

- Aux hautes incidences, les forces latérales croissent nettement avec l'envergure des ailes dans le domaine des envergures considérées. Elles sont cependant peu sensibles à la variation de la longueur d'aile.

- Les expériences en soufflerie montrent l'existence d'une plage d'incidences comprise entre 30° et 60° où la force latérale et le moment de lacet deviennent importants. Ces expériences confirment que la magnitude de ces efforts s'amoindrit quand le nombre de Mach augmente et devient négligeable en supersonique.

- La rotation de 45° de la maquette autour de son axe de symétrie diminue fortement les efforts latéraux mais pas le moment de roulis.

N.B. - Cette étude a été financée par le Service Technique des Engins Tactiques (STET).

REFERENCES

- 1 CLARK, PEOPLE "Occurrence and inhibition of large yawing moments during high Incidence flight of slender missile configuration".
J. Spacecraft Vol 10 n° 8 Août 1973.
- 2 PICK "Investigation of side forces on ogive - cylinder Bodies at high angles of attack".
AIAA Paper n° 71 - 570.
- 3 FLEEMAN, NELSON "Aerodynamic Forces and moments on a slender Body with a Jet Plume for angles of attack up to 180 degrees".
AIAA - Paper n° 74 - 110.
- 4 HOWARD, BROOK "Missile aerodynamic prediction up to 180°"
J. of Spacecraft Vol 8 n° 5 Mai 1971.
- 5 JORGENSEN, NELSON "Experimental aerodynamic characteristics of a cylindrical Body of revolution at angles of attack from 0° to 58°".
NASA - TM X - 3128 1974.
- 6 OBERKAMPF, NICOLAIDES "Aerodynamics of finned Bodies at high angle of attack".
AIAA J. Vol 9 n° 12 Déc. 1971.
- 7 OBERKAMPF "Theoretical prediction of roll moments on finned Bodies in supersonic flow".
AIAA - Paper n° 74 - 111.
- 8 DERRICK, SPRINE "Aerodynamic characteristics of a series of Bodies with and without tails".
NTIS AD - AD 28324 1976.
- 9 AGNONE, ZAKKAY "Aerodynamic of slender finned Bodies at large angles of attack".
AIAA - Paper 77 - 666.
- 10 KUBIN "An analysis of steady asymmetric vortex shedding from a missile at high angles of attack".
NTIS - AD - 774390.
- 11 USELTON, JENKE "Experimental missile pitch-and roll - damping characteristics at large angles of attack".
J. of Spacecraft Vol 14 n° 4 Avril 1977.

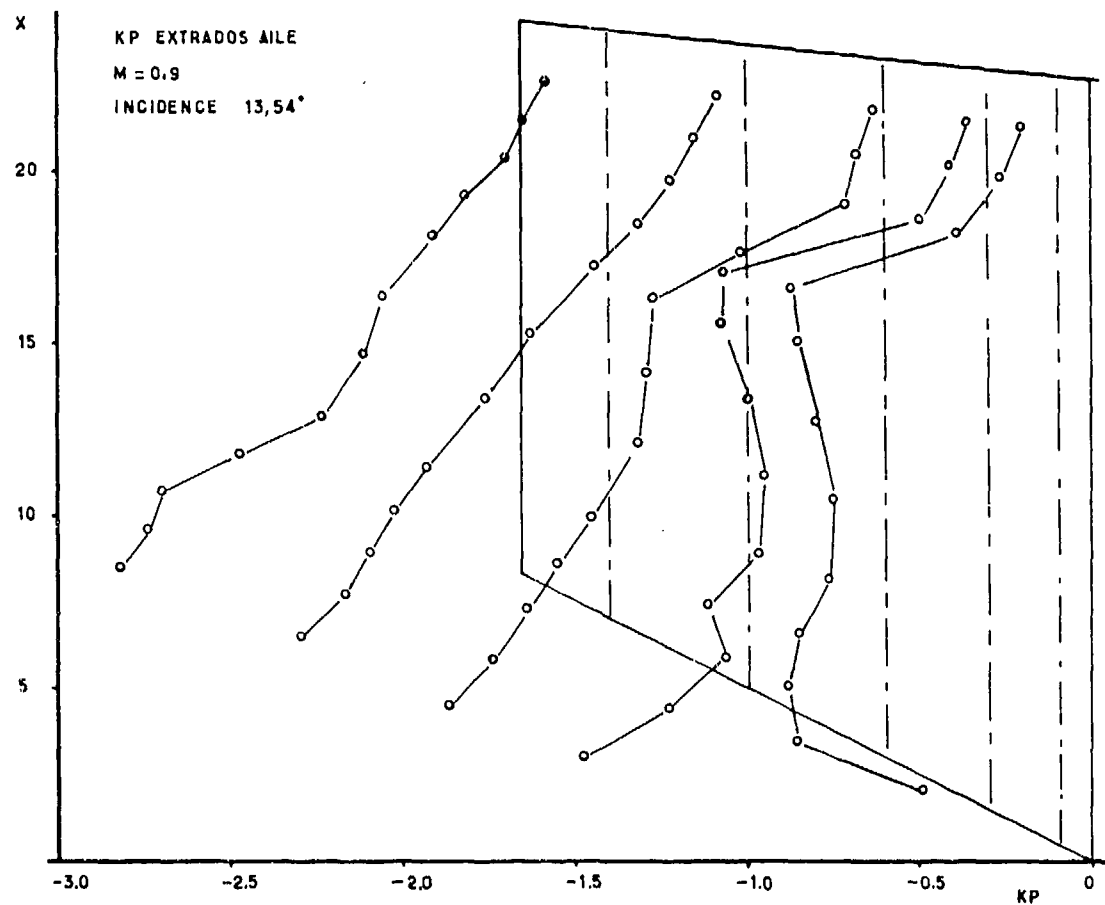


Fig.1 Répartition de pression sur une aile trapézoïdale $i = 13,54^\circ$

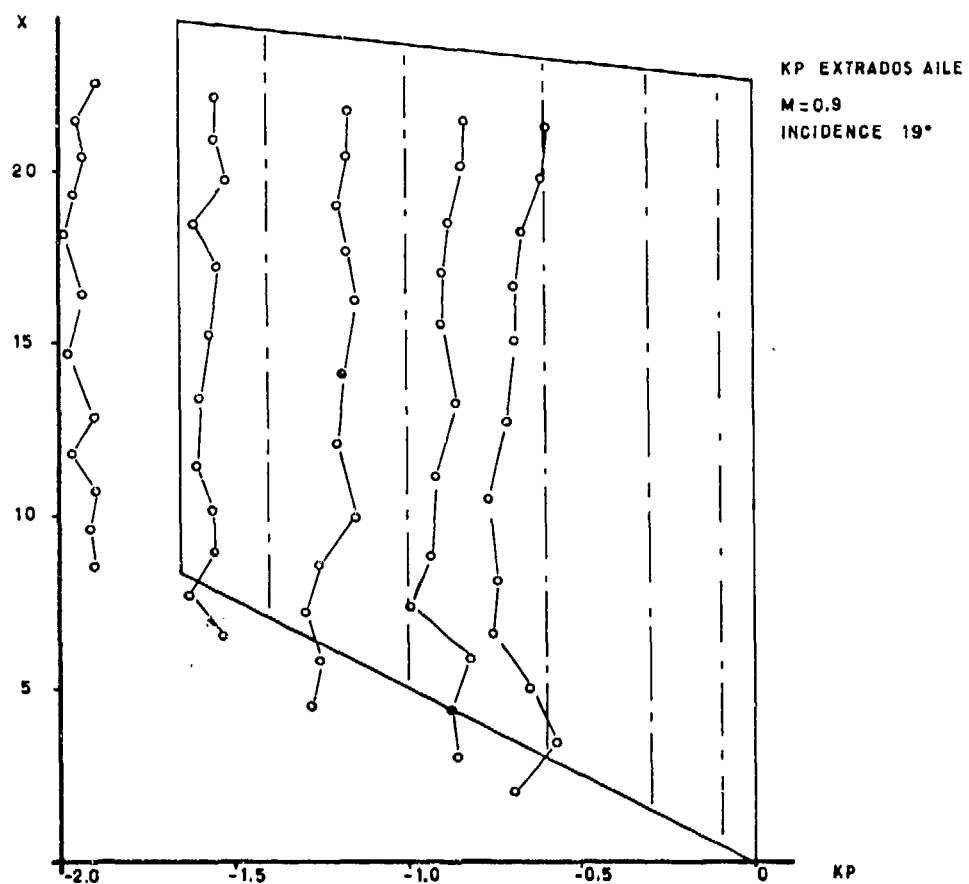


Fig.2 Idem 1 = 19°

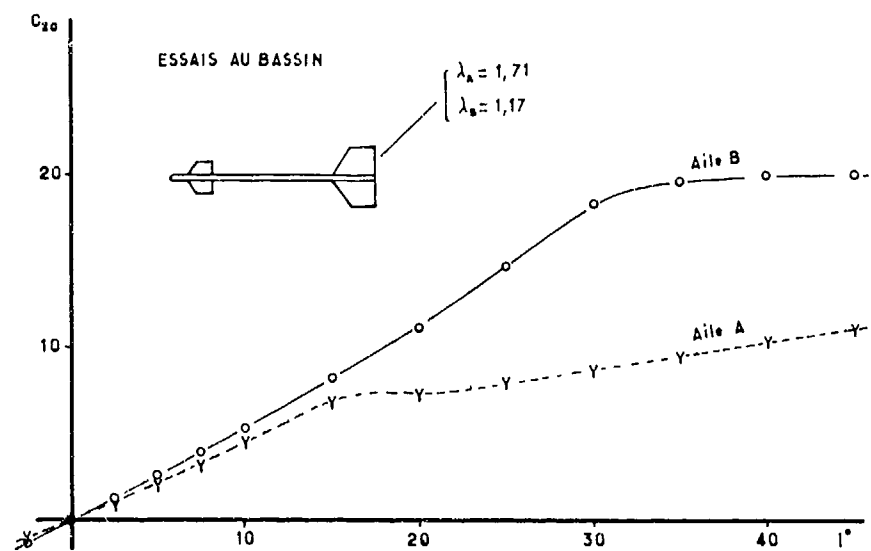


Fig.3 Ailes trapézoïdales: Influence de l'allongement

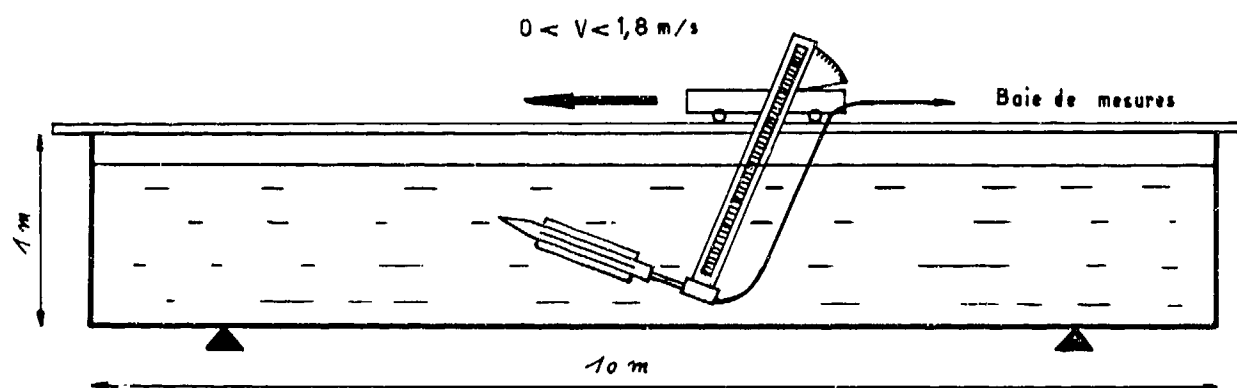


Fig.4 Schéma du bassin hydrodynamique

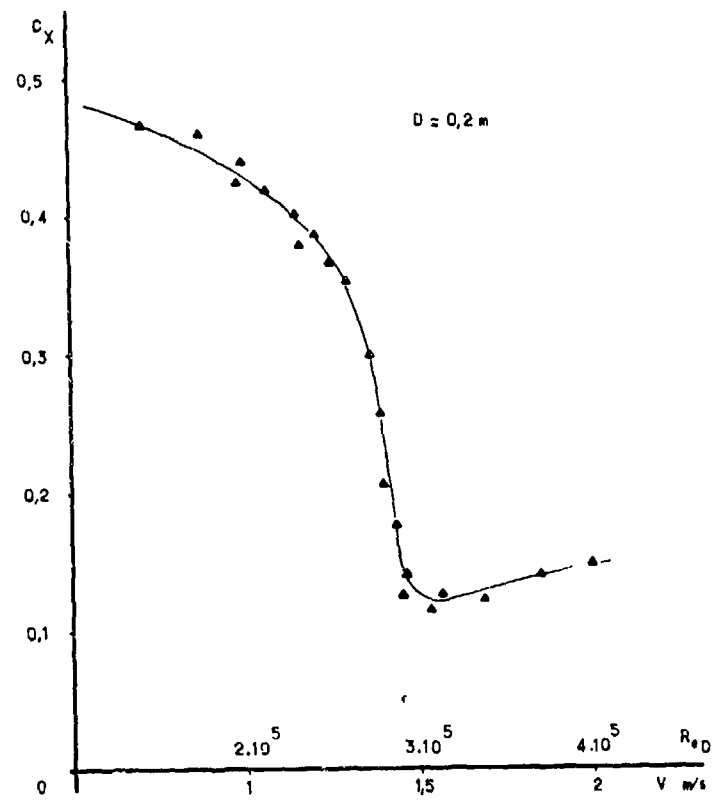


Fig.5 Trainée d'une sphère dans l'eau

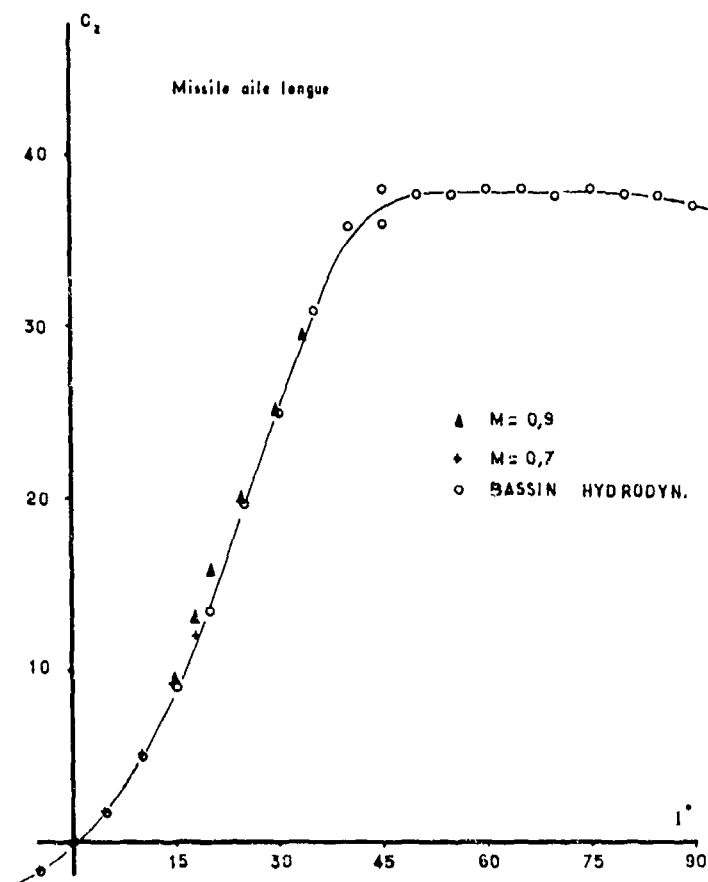


Fig.6 Comparaison bassin soufflerie

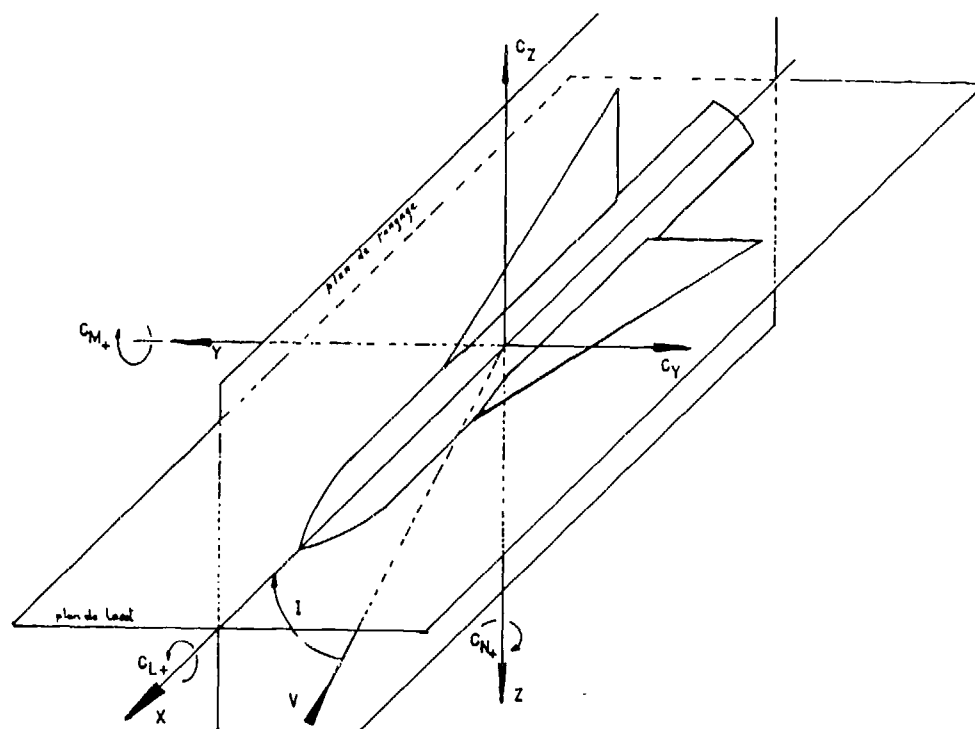


Fig.7 Conventions de signes et notations

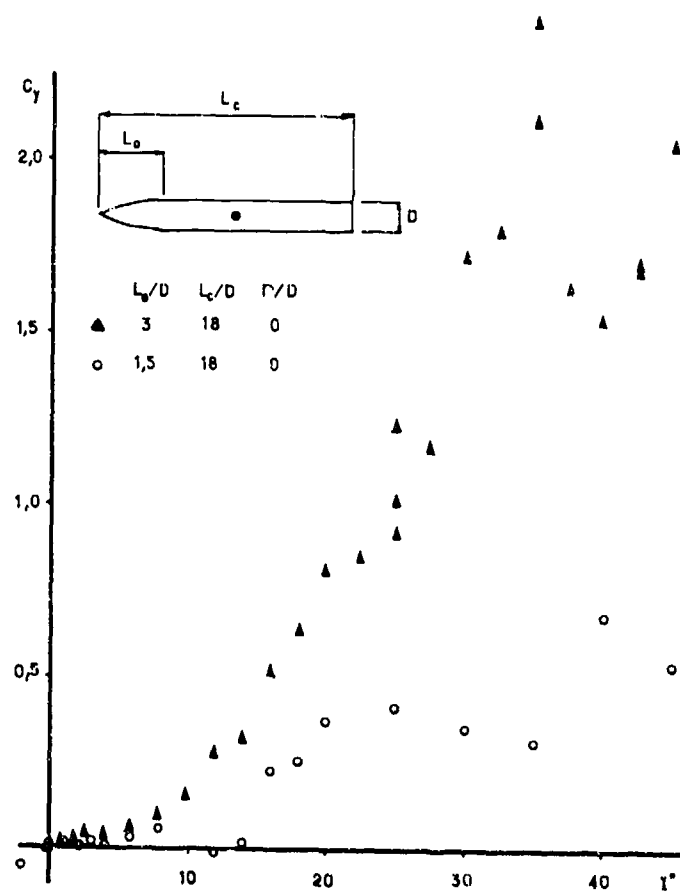


Fig.8 Force latérale: Corps de révolution

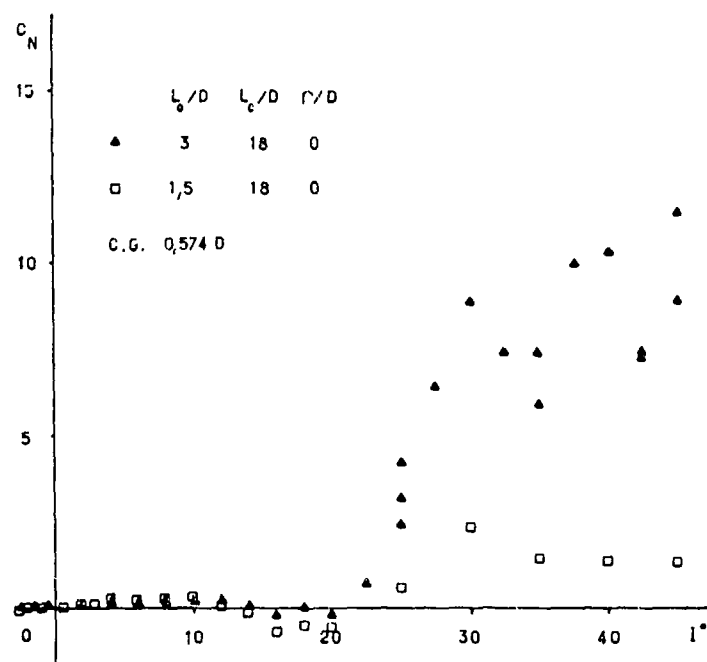


Fig.9 Corps de révolution: Moment de lacet

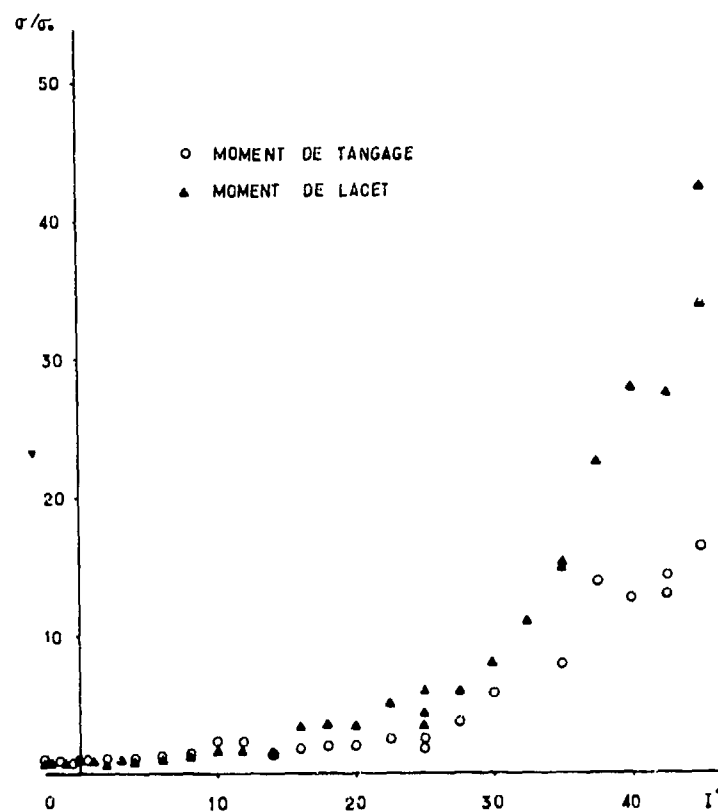


Fig.10 Corps de révolution: Ecart-type moyen

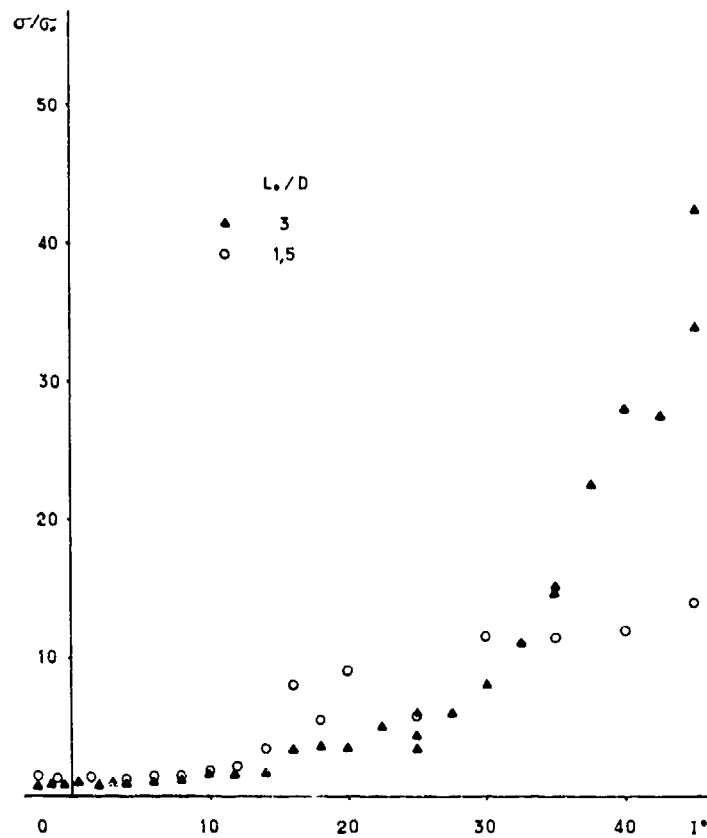


Fig.11 Effet de l'allongement de l'ogive sur l'écart-type

E/D	L_0/D	λ	E/D	L_0/D	λ	E/D	L_0/D	λ
2,43	7,32	0,20	2,15	7,32	0,15	1,48	4,83	0,10
	5,93	0,25		5,93	0,20		3,24	0,15
	4,93	0,30		4,76	0,25		2,44	0,20

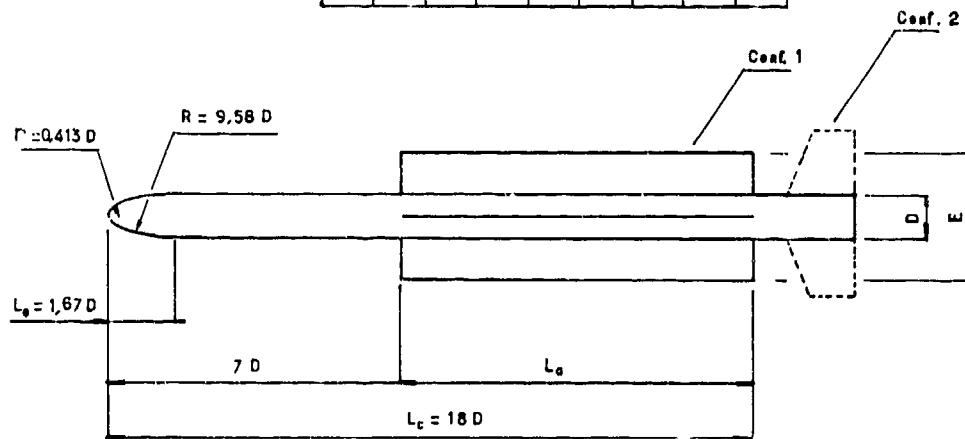


Fig.12 Définition des maquettes

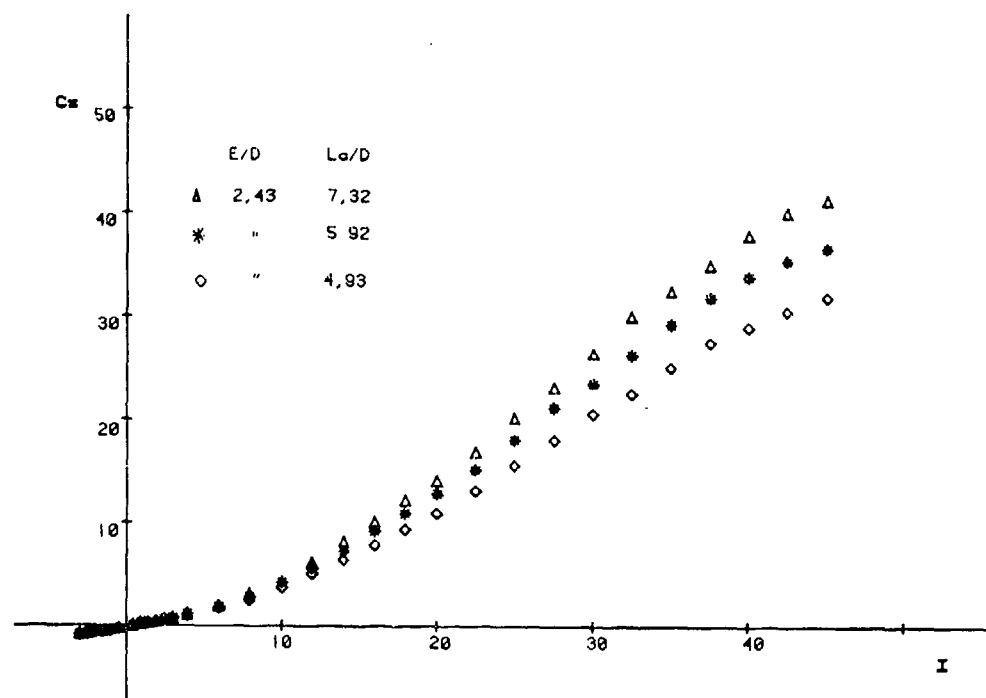


Fig.13 Effet de la longueur d'aile sur la portance

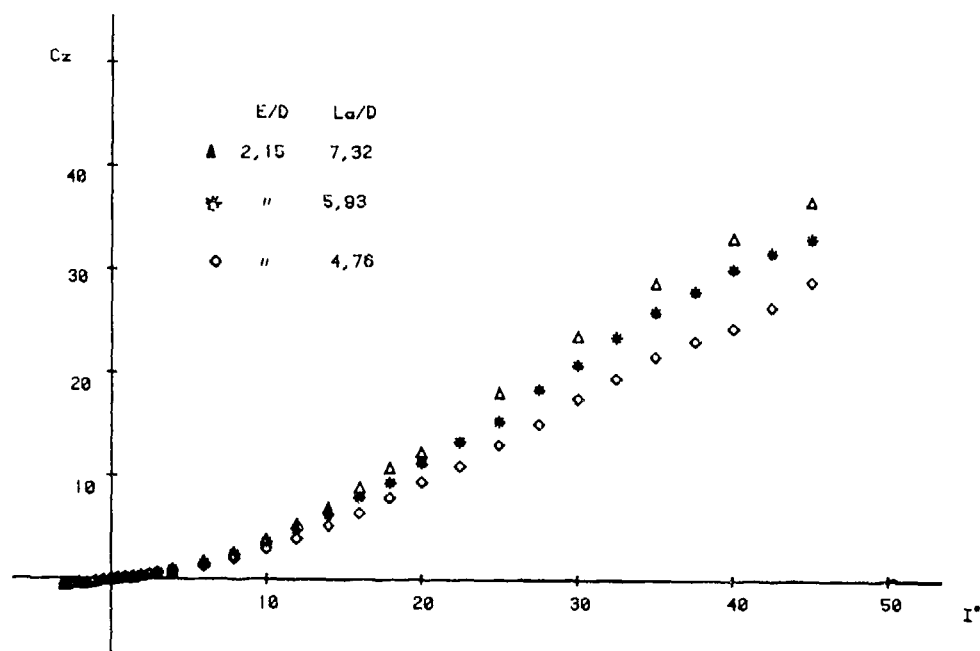


Fig.14 Effet de la longueur d'aile sur la portance

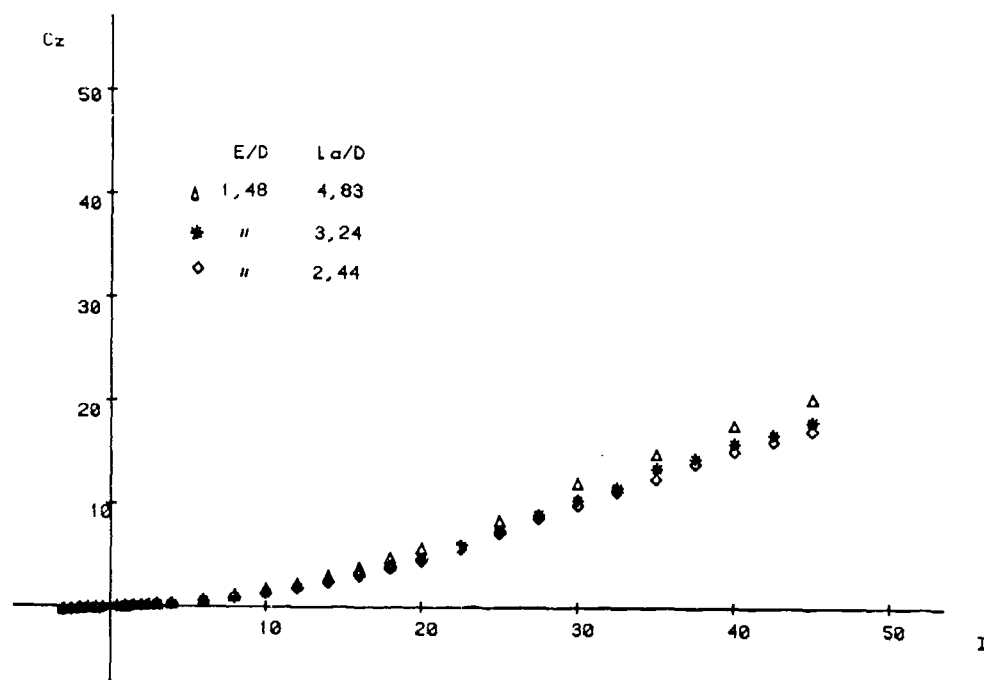


Fig.15 Effet de la longueur d'aile sur la portance

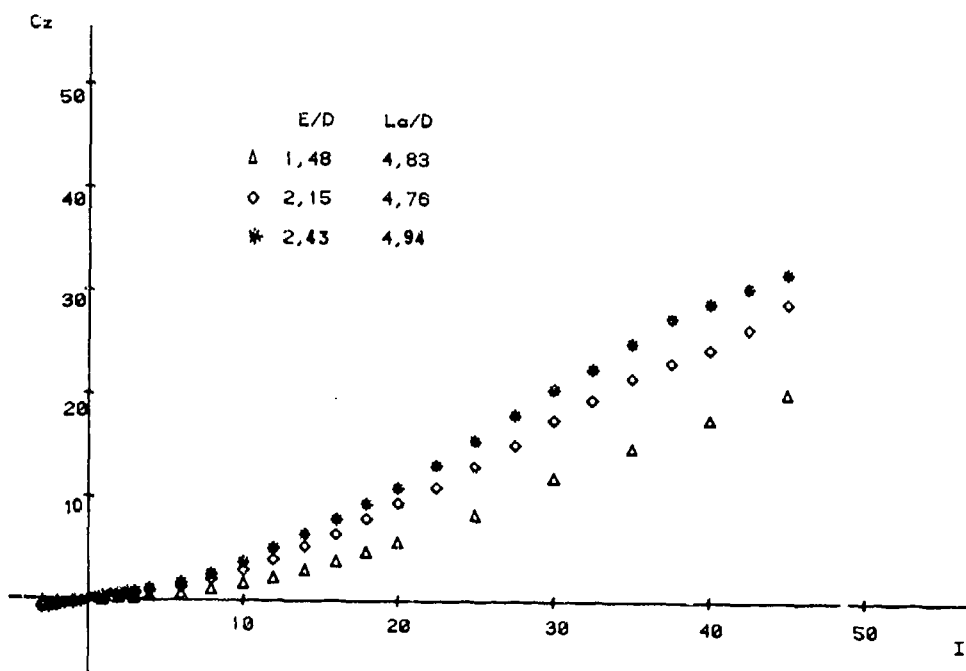


Fig.16 Effet de l'envergure sur la portance

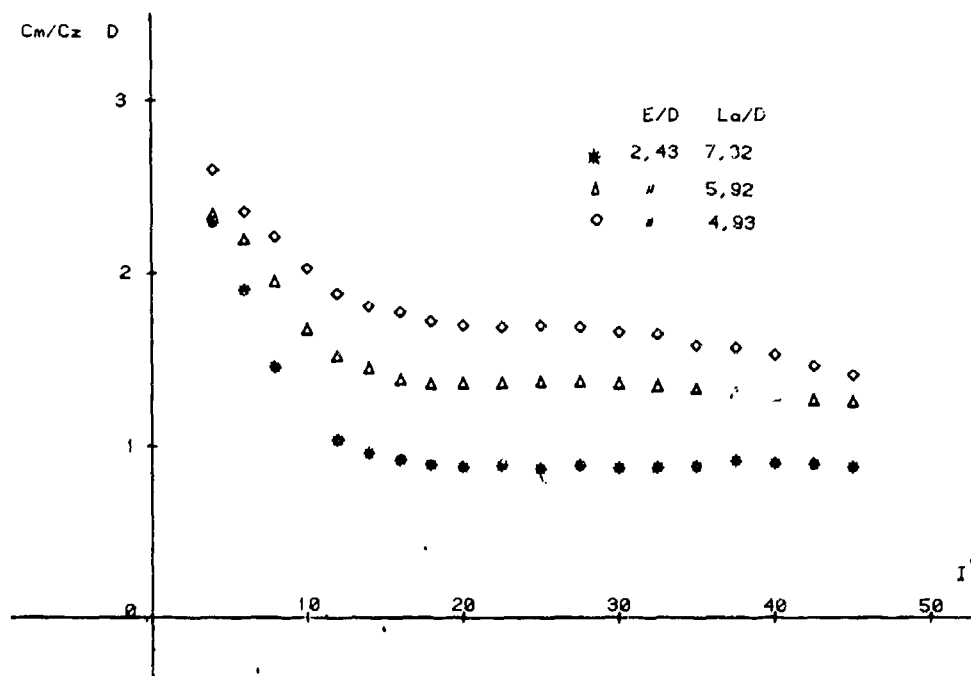


Fig.17 Effet de la longueur d'aile sur le centre de poussee

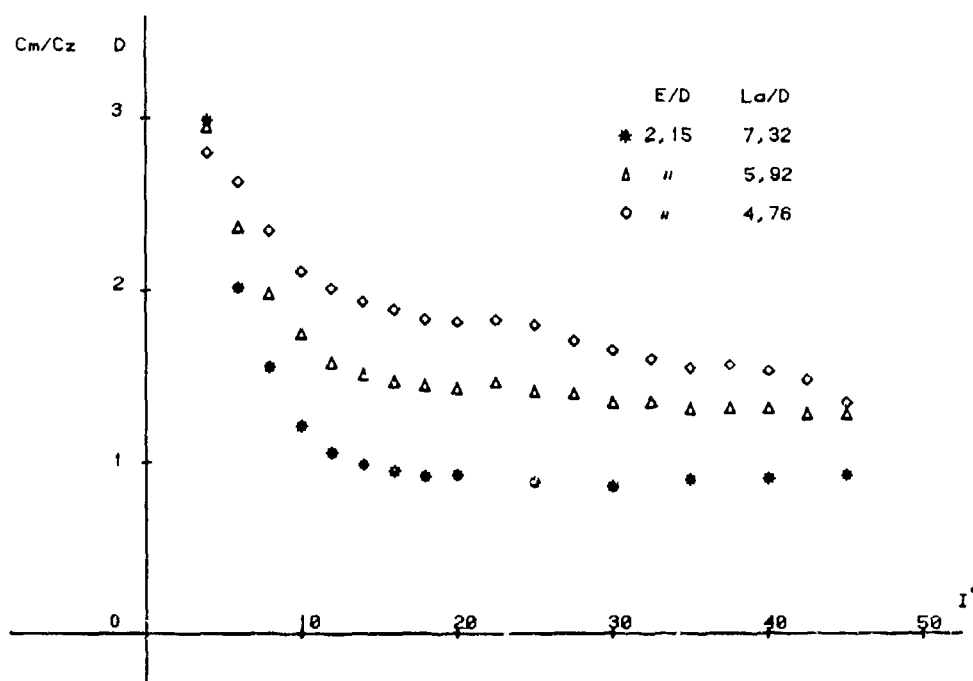


Fig.18 Idem

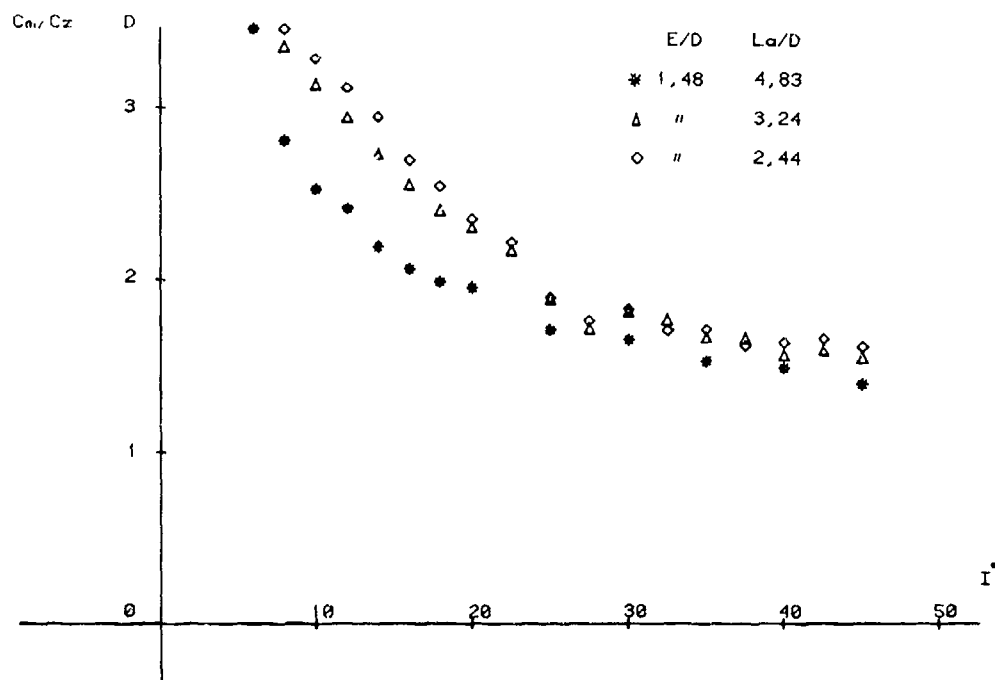


Fig.19 Idem

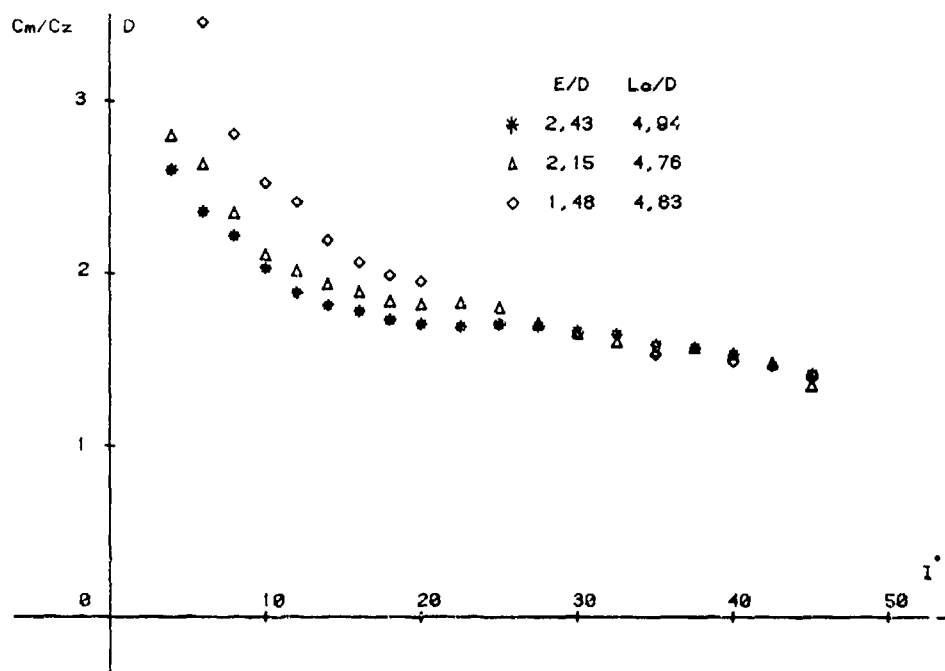


Fig.20 Effet de l'envergure sur le centre de pousse

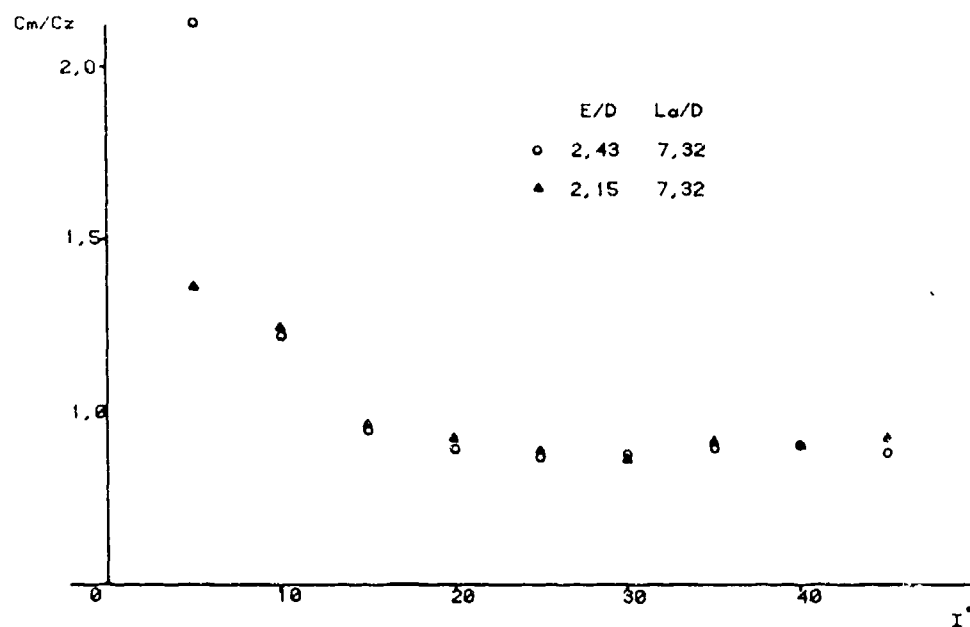


Fig.21 Effet de l'envergure sur le centre de pousse

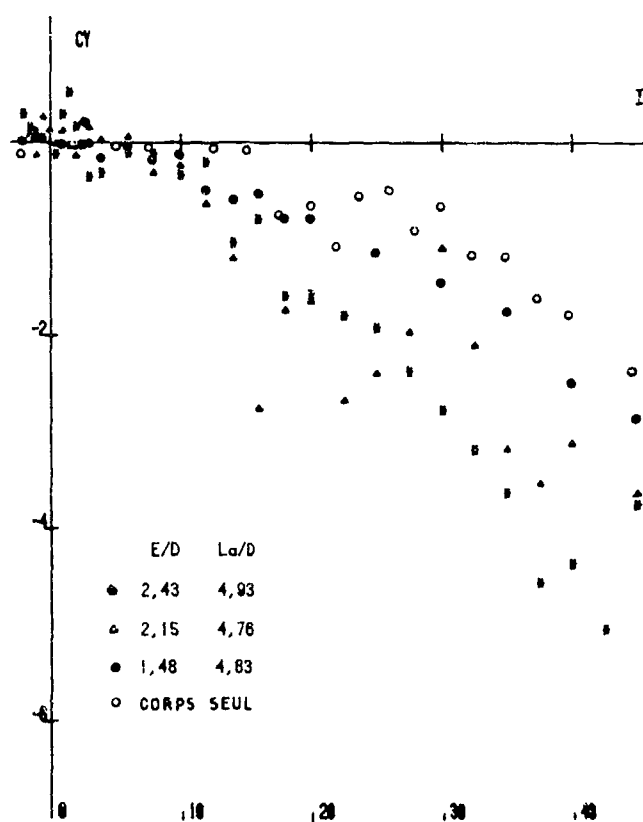


Figure 22

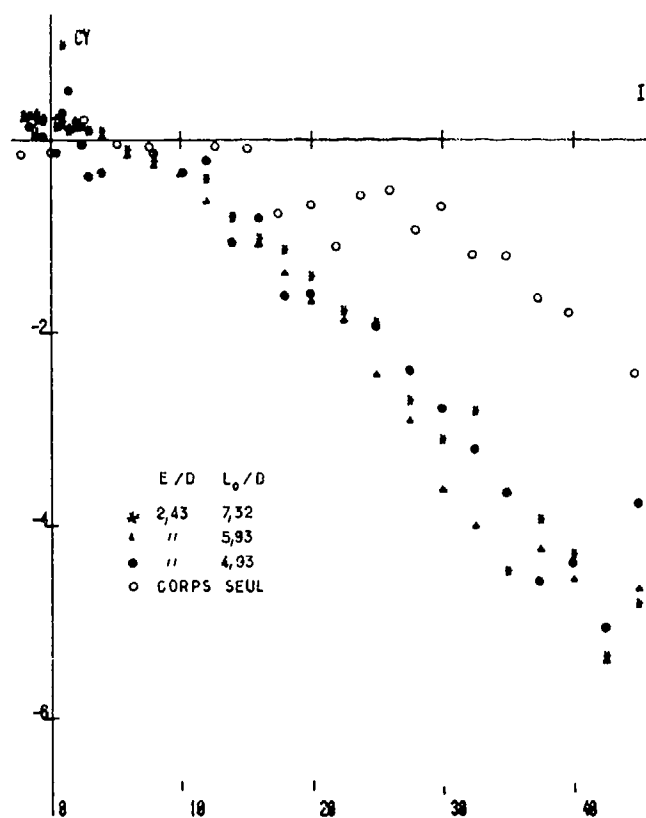


Figure 23

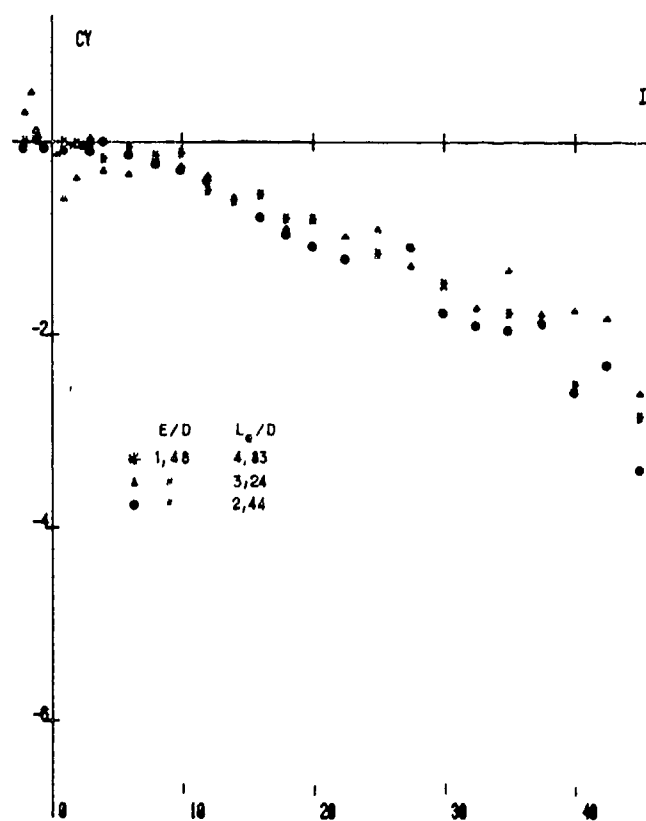


Figure 24

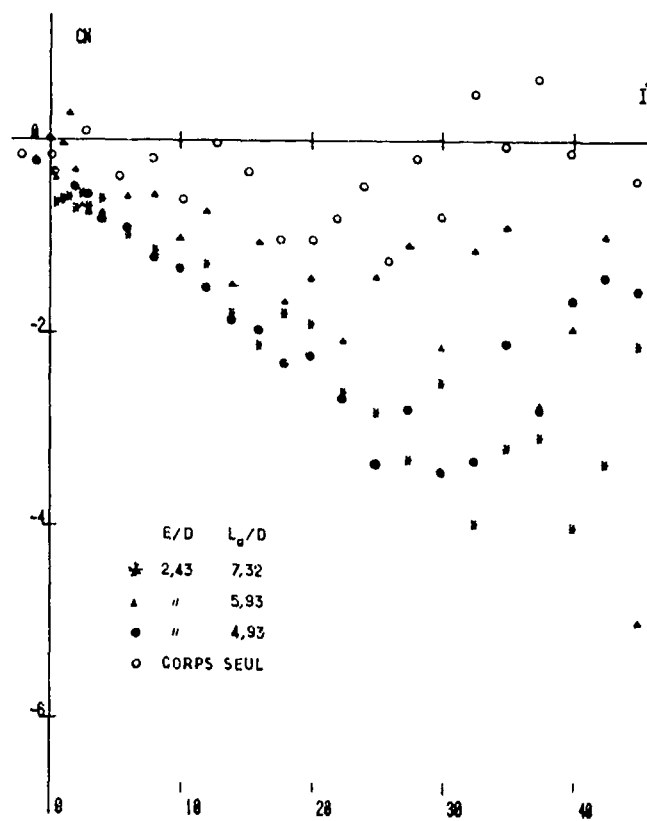


Figure 25

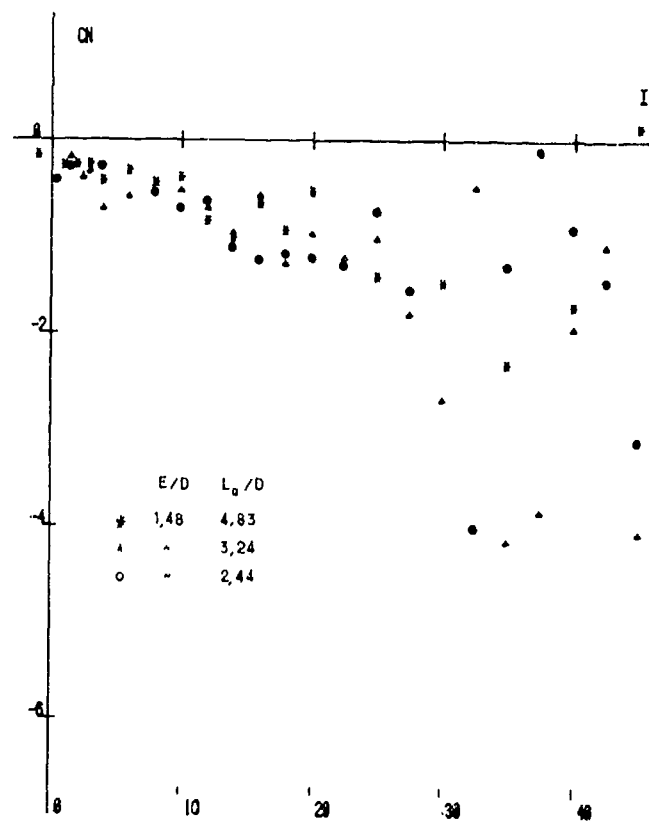


Figure 26

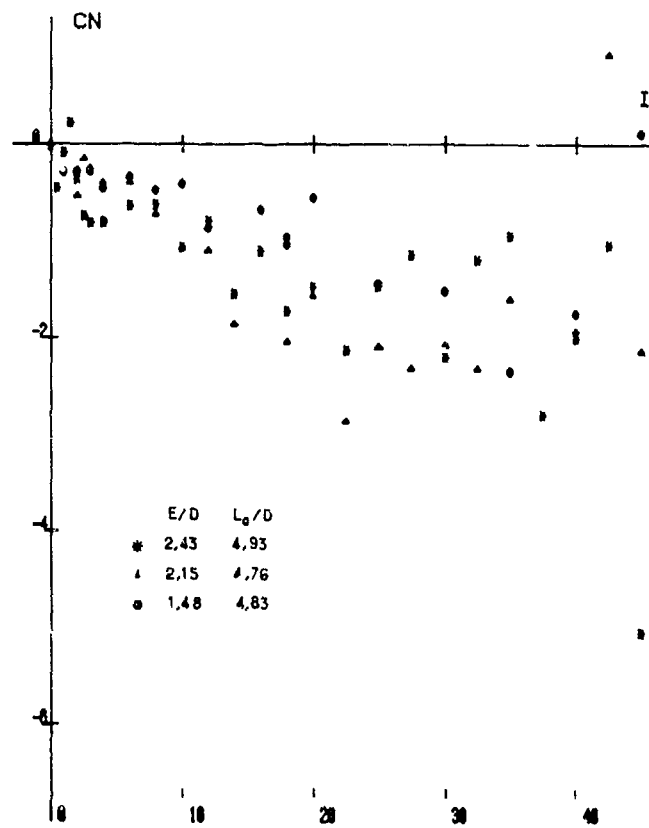


Figure 27

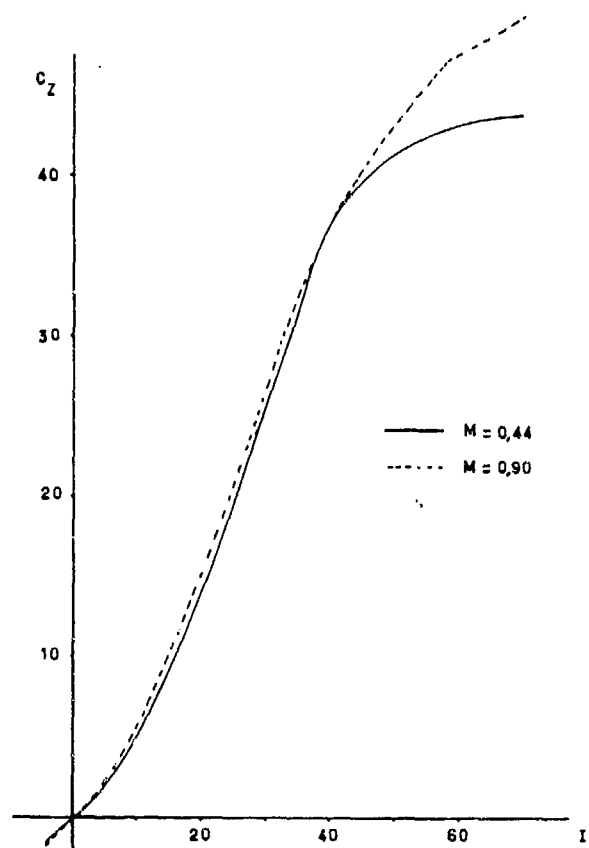


Figure 28 Effet du nb. de Mach sur la portance

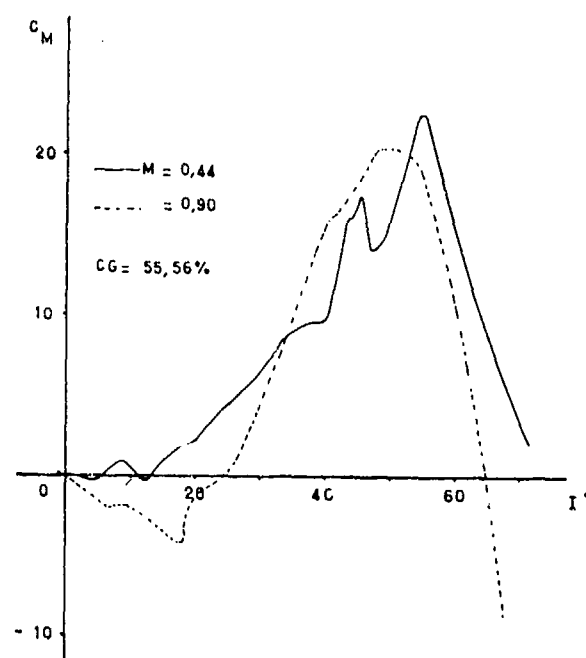


Fig.29 Effet du nb. de Mach sur le tangage

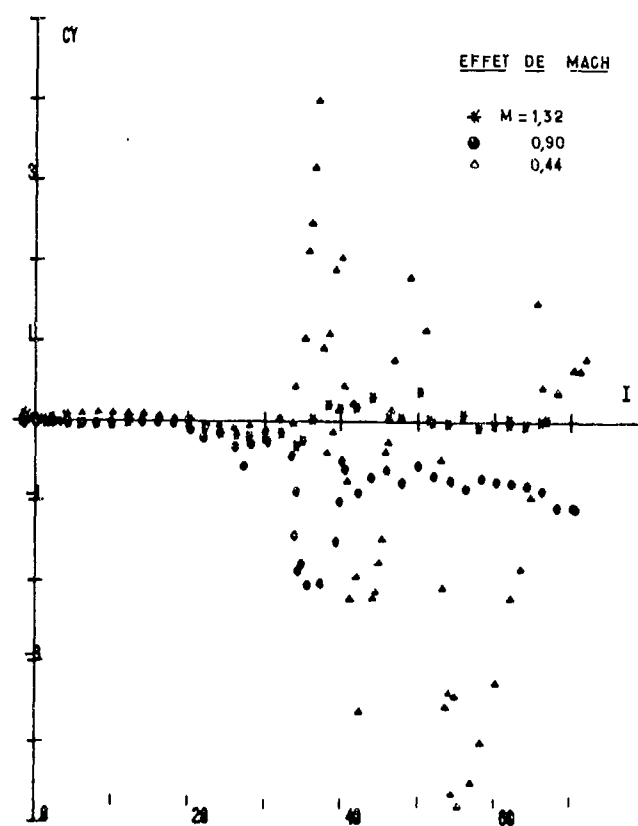


Figure 30

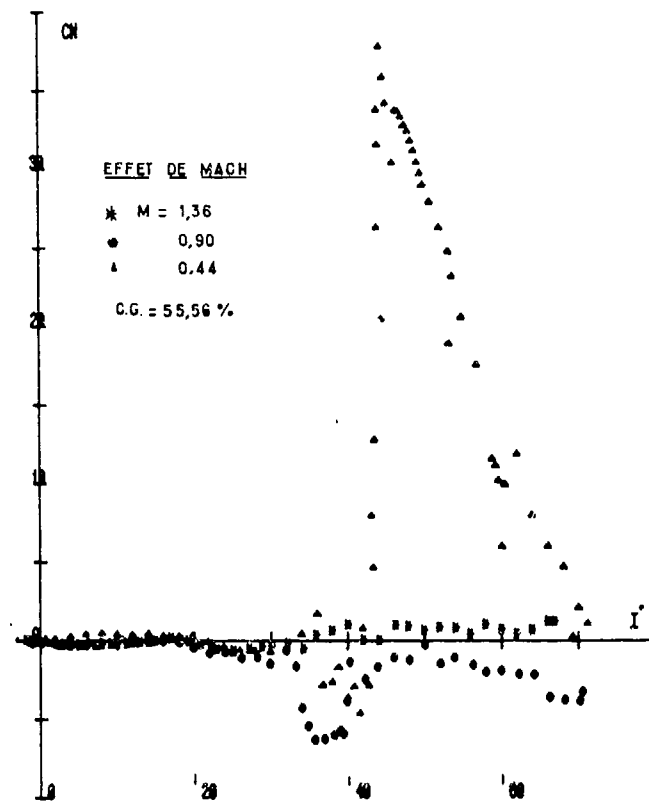


Figure 31

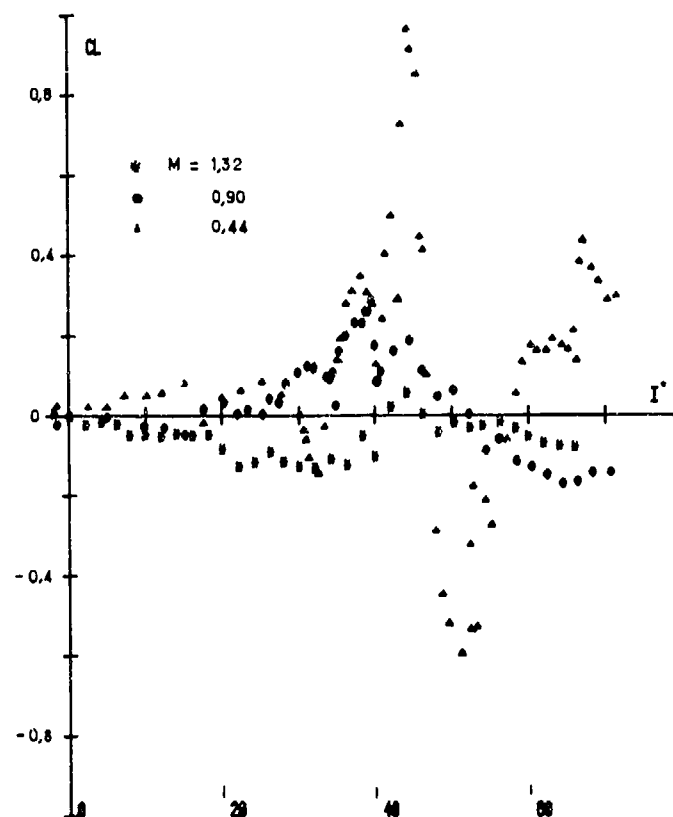


Figure 32

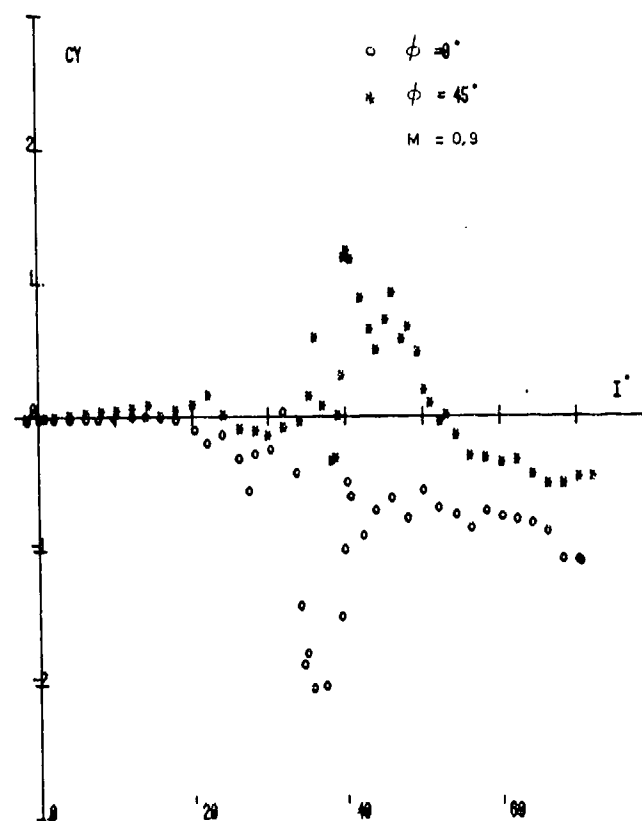


Figure 33

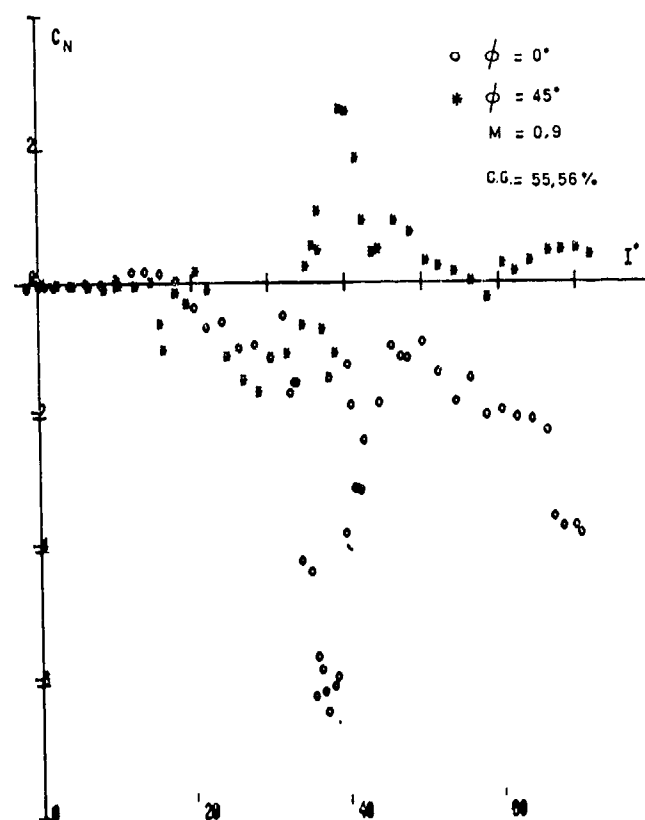


Figure 34

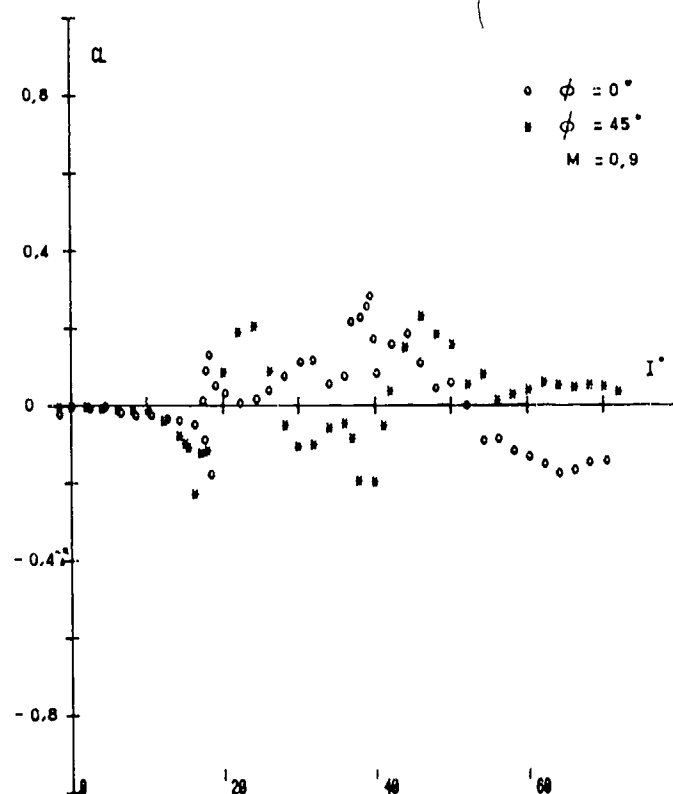


Figure 35

AERODYNAMIC CHARACTERISTICS OF A MISSILE FEATURING WING WITH STRAKES AT HIGH ANGLES OF ATTACK

M. Akcay, B.E. Richards, W. Stahl[†], A. Zarghami
von Karman Institute for Fluid Dynamics
Chaussée de Waterloo, 72
B - 1640 Rhode Saint Genèse, Belgium

Abstract

This note describes an experimental study of the forces and pressure distribution on a typical missile configuration with low aspect ratio trapezoidal wings fitted both with and without triangular strakes at angles of incidence up to 32° at a Mach number of 0.83 and a Reynolds number based on body diameter of 1.4×10^5 . Normal force and pitching moment measurements showed that different strakes extending forward from the inboard region of the trapezoidal wings straightened the normal force curve and increased the normal force coefficient considerably and improved the pitching moment variation at incidences above 12° . Subsequently, measurements of pressure over the suction side of the body, wings and one of the configuration of strakes and application of various flow visualization techniques at transonic speeds and water tunnel tests provided some insight into the mechanisms that cause the improvements in force characteristics. The vortices generated by the strakes are shown to interact favourably not only with the flow over the wing, to suppress the unfavourable effects of large separation, but also with the flow over the body. The distribution of the increment in normal force on the various parts of the configuration caused by the strakes was roughly analyzed.

1. INTRODUCTION

Strakes consisting of small slender delta wings attached ahead of the inner leading edge of the main wing have been demonstrated in a number of cases to improve the aerodynamic characteristics of aircraft at the high angles of attack often achieved in rapid manoeuvres and landing and take-off. They have been used in a variety of shapes on vehicles such as the SAAB-35 Draken with double delta wing planform, the Northrop F-5 'Tiger II', YF-16 and YF-17 with trapezoidal wings with strakes (Refs. 1, 2) and the Space Shuttle with double delta wings. These examples have in common the feature that the body cross sectional dimensional is relatively small in relation to the wing span. There have been reported no studies of the effect of strakes on missile type configurations which are characterized by small wings in relation to the body cross sectional dimension, such that wing body interference effects are important, and the wings themselves having simple un-optimized wing profiles. The experimental work carried out in this latter field at VKI during the past two years, following on from the preliminary work by Stahl and Movassaghie (Ref. 3) at this same establishment in 1976, will be described in the following chapters. Comparisons with results from tests on aircraft configurations reported in the literature are made. Such information is important to designers to evaluate whether strakes can contribute as favourably to the high speed manoeuvrability of a missile as has been found on aircraft.

2. DESCRIPTION OF MODELS AND TEST TECHNIQUES

The configurations chosen to be tested are illustrated in figure 1 with dimensions given as a proportion of body diameter, D. The body has an overall length of $10.8 D$ with an ogive nose of radius $6.5 D$ and length $2.5 D$. The trapezoidal wings have a semispan of $1.0 D$, a leading edge sweep angle of 27° and an aspect ratio of 1.99. The wings have flat upper wings whose surfaces are in the same plane as the body centerline. The lower surfaces are bevelled to 10° giving sharp leading and side edges. The wing trailing edges are $3.2 D$ upstream of the body base. Three different configurations of strake, designated 1, 2 and 3 were used in the force measurements study, only strake number 1 was used in the pressure and flow visualization studies. Strake 1 had a triangular shape with sharp 10° angle wedge leading edges which were swept at 77° and bisected the wing leading edge at $1/4$ span from the wing root. Its aspect ratio was 0.89, giving an overall wing with strake aspect ratio of 1.65. The addition of the strake increased the wing area by 11 per cent. Strake 2 had a larger chord and strake 3 had an additional curved fairing between itself and the wing leading edge as shown in Fig. 1. Both had larger areas than strake 1. The body diameter of the models was 35 mm.

The normal force and pitching moment were measured by means of a two component strain gauge balance designed and built at VKI as described in Ref. 4. The balance was mounted inside five hollow models specially built for these tests representing the configurations of body alone, body with wing alone, and three bodies with wings with the three different strake configurations. A model of the trapezoidal wings alone was also constructed which was attached ahead of the force balance while testing. The calibration process is described in detail in Refs. 4 and 5.

Three separate models representing the configurations body alone, body with wing and body with wing and strake 1 were instrumented with 30, 60 and 65 pressure taps respectively of 0.5 mm diameter. These were placed on body, wing and strake upper surfaces and distributed around five lengthwise stations designated E, F, G, H and I upstream of and in the

[†] DFVLR Visiting Professor, Institut für Strömungsmechanik, DFVLR/AVA, Bunsenstrasse 10, D - 3400 Göttingen, Germany.

regions of the wing as illustrated in Fig. 2. Scanivalves were used to connect the pressure taps sequentially to either 1 lb/in² or 2.5 lb/in² Statham PM6TC differential pressure transducers. The measurements were recorded on Sefram B-60 recorders. Measurements were referenced to one model pressure tap which itself was measured using a vacuum referenced mercury manometer. The transducers were calibrated against Betz and mercury manometers before each test.

Two additional but smaller models with base diameter of 20 mm representing configurations of body and wings and body and wings with strakes were built for flow visualization tests in the VKI Water Tunnel. These models were fitted with 7 and 9 passages respectively (four on the body, three on the wing and two on the strake) used to inject dyes to track the flow streamlines. Sublimation surface flow visualization was also used at $M = 0.83$ in the wind tunnels on the models used for force measurements.

The measurements at $M = 0.83$ were carried out in the VKI S-1 wind tunnel. It is a continuously operated closed circuit facility including longitudinal slotted top and bottom sections for subsonic and transonic operation (Ref. 4). The test section measures 36 cm x 40 cm. During the tests the total pressure was kept at 0.270 bars to provide a Reynolds number based on body diameter, Re_D , of 1.4×10^5 . Force measurements were made at angles of incidence from 0° to 18° on wings and bodies alone and from 0° to 32° on complete missile configurations while pressure measurements were made in the range of 11 to 30°. The test section was calibrated at $M = .83$ without the models and the flow Mach number was shown to be constant within 1% (Ref. 4).

The VKI Water Tunnel has a closed test section of 15 cm x 15 cm. The water is pumped continuously from a storage tank into the overhead reservoir and the velocity of the water is controlled by means of a valve and measured by a rotameter downstream of the test section. The tests were carried out at a flow speed of 0.21 m/sec giving a Reynolds number based on body diameter of 4200. To visualize the flow field, blue dye was ejected from the body and wings and red dye from the strake. The angle of incidence was changed from 0° to 25° in 5° steps. Both coloured photographs and ciné films of the resulting flow visualization were made.

The introduction of water tunnel tests into a transonic experiment with subsequent comparison of results may sound illogical, however, other experimenters have discovered that for flows over configurations in which extensive flow separation occurs surprisingly good agreement in flow behaviour is found. As shown later in this report, this similarity is demonstrated with a Reynolds number ratio of 33 indicating that such studies are relatively independent of flow speed and Reynolds number and can prove to be useful since such flow visualization is very difficult to accomplish in a transonic wind tunnel.

3. PRESENTATION OF BASIC RESULTS

The normal force coefficients in the trapezoidal wing alone, body alone and wing with body combination at $M = 0.83$ in the incidence range of 0° - 18° is shown in Fig. 3. Also plotted is a curve representing the sum of the wing alone and body alone results.

The normal force and pitching moments coefficients for complete missile configurations with trapezoidal wing alone and fitted with the three different strakes for $M = 0.83$ in the incidence range of 0° - 32° are presented in figures 4 and 5 respectively. The normal force coefficient is normalized with the body cross sectional area in all the curves.

The pressure measurements for body alone, body with trapezoidal wing and body and wing with strake number 1 for angles of incidence of 11°, 21° and 31° are presented in Figs. 6, 7, 8 respectively as a function of spanwise position at each longitudinal station. Not included in this report are presentations of the other angles tested, i.e., 15°, 18°, 24° and 27°. Details of these are given in Ref. 6.

The ensuing discussion is based on these figures in examining first the flow over the separate components, then over the body and wing and finally the effect of the strake on the configuration. Some use is made of the results not included, mentioned in the last paragraph.

4. DISCUSSION OF RESULTS

4.1 Effect of flow over trapezoidal wings and body alone

Figure 3 shows that the normal force coefficient induced over the wings alone increases non-linearly with increase of angle of attack at low angles of attack such that the rate of increase of force is positive. At 5°, however, the curve exhibits a point of inflection indicating the onset of flow separation over the wing. Above 12° the normal force coefficient is nearly constant with incidence indicating that the flow over the wing is fully separated.

The flow over the body alone also causes a non-linear change in normal force coefficient with angle of incidence as shown in Fig. 3 but in this case this behaviour occurs up to the maximum angle (18°) examined. The pressure measurements around the body taken from angles of 11° to 30° presented in Figs. 6, 7 and 8 demonstrate that this increase in lift with incidence is caused by increased suction created by the vortices shed from the body. At 11° the pressure distributions reflect little or no separation over the body, while at higher angles, the suction peak, whose location reflects the proximity of the vortex core moves away from the side of the body to an unchanging angle of 32° from the leeward surface generator. A test in which a sublimation flow visualization technique was carried out at $M = 0.83$ demonstrated this finding at 20° angle of attack.

4.2 Discussion of the interference between body and trapezoidal wing

An illustration of the overall result of interference between wing and body for this missile configuration is demonstrated in Fig. 3 in which the addition of the measured normal force coefficient on the wing and body alone are compared with the value of the overall coefficient for the combination. It can be seen that over the range of incidences from 0° to 18° , the interference effects contribute from between 25% to 40% of the overall force.

Comparison of the pressure measurements on the body alone and the wing-body configuration illustrated in Figs. 6, 7 and 8 demonstrate the origin of the interference. It appears from the very flat spanwise (and chordwise) distribution over the wings that the body has little influence on the wings (unfortunately pressure measurements over the wings alone were not taken to verify this). However, the pressure distribution around the body at the three stations in line with the wing (G, H and I) is influenced very strongly and favourably by the wing. The general effect is to bring the suction on the body to the level of that on the wings. This is expected to be caused by downwash over the body induced by the wings. The detrimental effect of the upwash before the wing is demonstrated by the loss in suction on the body just in front of the wing (position F), but this effect extends upstream from the wing leading edge no further than two chord lengths (position E).

The dye-line visualization on the body of the wing-body combination tested in the water tunnel at $\alpha = 20^\circ$ (Fig. 9a) demonstrates clearly the effect of the wing on the streamlines close to the body. The lines are shown to be swept to leeward strongly just before the wing but then sucked strongly towards the wing in line with the wing leading edge.

It appears that for configurations typical of missiles large benefits in force are achieved due to interference effects, and that these arise chiefly on the body due to the flow over the wing.

4.3 Addition of strakes to the wing-body configuration

4.3.1 The effect of the shape of the strake on forces and moments

The normal force coefficient, C_N , on the missile configurations with the three types of strake are compared to the values measured on the configuration without strakes from 0° to 32° in Fig. 4. It can be seen that the strakes have little effect on force for angles of incidence up to 8° , but that above this angle considerable benefit can be obtained. This is illustrated more clearly in Fig. 10 in which is plotted the increase in C_N on the configuration with strake 1 as a proportion of C_N on the wing-body configuration without strake. It can be seen that the strake provides most benefit at angles from 11° to 20° achieving 33% at 14° and this effect decreased to about 15% at 30° . Referring to Fig. 4, it is seen that the long strake (no 2) provides even higher forces, however, it should be indicated that its area is over 20% of that of the wing surface. For technical reasons, the tests on the curved strake (no 3) were discontinued above 18° and hence the characteristics of this configuration could not be evaluated.

The overall effect of the increase in force cause by the strakes is to straighten out the crooked variation with angle of attack cause by the separation over the wing without strake. This will help the controllability of the vehicle which will also be helped by the slightly more regular pitching moment variation with incidence (Fig. 5).

4.3.2 The effect of the strake on the flow over the wing

The spanwise pressure distribution on the strake at 68% of its chord shown in Figs. 6, 7 and 8 feature the high and localized suction peak at around 50% span from the root typical of the vortex shed from the leading edge of a highly swept delta wing. The level of the suction peak increases with angle of attack. The presence of the body becomes more pronounced with incidence by causing another localized peak suction near the inboard edge.

The most pronounced general effect of the strake vortex on the wing pressure distribution seen in Figs. 6, 7 and 8 is to cause a very important suction increase over the whole span near the leading edge (line G). This suction is decreased substantially, however, at the wing mid-chord position (line H) and falls below the wing-without-strake distribution near the trailing edge (line I). To be expected are localized peak suction along the path of the vortex and these can be identified easily at $\alpha = 11^\circ$ (Fig. 6) in which the peak moves out gradually from 18% span near the leading edge to 33% near the trailing edge. The less easily evident observations are not only that the suction peak is higher on the wing than on the strake but that the effect is felt so widely over the whole span outboard of the suction peak. Near the wing root, however, there exists in most cases a loss in suction due to the strake. At higher angles of attack there are signs of a second but much flatter suction peak occurring further towards the tip of the wing, and at the highest angles, this peak actually is larger than the inboard peak (if it exists at all). This is ascribed to the phenomena of vortex breakdown which would be expected to result in an attenuation and spreading of the suction. It is suggested that the double peaks may be caused by the fluctuating streamwise location of vortex breakdown.

Some clue as the reason for these favourable results may be gained from inspection of the dye-line visualization from the model with strakes tested in the water tunnel at $\alpha = 20^\circ$ (Fig. 9b). It can be seen that the streamlines on the body are sucked strongly by the strake vortex towards itself, pass below the vortex itself towards the wing tip. The resulting effect appears to be that the counter streamwise low energy and highly random flow on the wing characteristic of separated flow is discouraged thus forming a more orderly flow behaviour similar to that seen on highly swept wings at incidence. This

would explain not only the generally high suction on the outer forward panels of the wing, but also the loss in suction near the wing root.

4.3.3 The effect of the strake on the flow over the body

The most pronounced effect of the strake on the body pressure distribution is seen from examination of Figs. 6, 7 and 8 to occur on the sections level with the strake itself (section F) at which region the suction is strongly enhanced especially near the strake wing root. This strong suction in this region causes the biggest different in the dye-line visualization on the body of the missile configurations in the water tunnel at $\alpha = 20^\circ$ (Fig. 9) when it is seen that the body streamlines are sucked towards the wing leading edge on the strake configuration instead of being deflected away from this region. Upstream of this (section E), there is little or no effect as also is the case for the part of the body in line with the forward and mid parts of the wing (sections G and H). At angles of attack higher than 11° small increases in suction are sensed on the body at these same latter sections. At the downstream location (section I) which is near the trailing edge, the suction is decreased slightly.

4.3.4 Overall effect of strakes on the flow over the wing-body configuration

The pressure measurements presented in Figs. 6, 7 and 8 show that strakes cause increases in suction on both the wing and body at streamwise locations upstream of the wing mid-chord position but decreases aft of it. The effect is to cause the center of pressure on the configuration to move forward at high angles of attack explaining the improvement in variation of pitching moment coefficient variation with angle of incidence seen in figure 5.

An estimate of the change in normal force over the central regions of the configuration was made by integrating the normal components of the measured pressure distributions over the surface. The calculation was broken down into contributions to the wing, body and strake separately (Fig. 11). Figure 11 indicates that at low angle of attack, the increase in force is greater on the wing than on the body but above $\alpha = 24^\circ$ the effect is reversed. Then the distribution was 18% to the wing, 34% to the body and 48% to the strake and changed little with higher angles. At all angles of attack it is seen that the force on the strake itself is extremely important.

It is interesting to compare these results with those found on tests on an aircraft configuration in which the body size is less important than in missile configurations. Application of the "Sectional Loads Technique" to analyze the effect of flow over the strake on the VTOL fighter VAK 191B shows that the increase in lift due to the fitting of strakes is about 62% in comparison with the lift on the main wings and body at an angle of attack of 24° (Ref. 7). Approximately 8% of this increase is induced by the effect of strake on the fuselage, the main contribution of 54% induced on the wing and 38% of lift increase is directly created on the strake itself (Ref. 7, Fig. 16).

5. CONCLUSIONS

Experiments were carried out to determine the effect on normal force and pitching moment at high angles of attack of fitting small strakes to a vehicle configuration with flat plate trapezoidal wings of small dimensions in relation to a long ogive cylinder body typical of a missile. Force measurements carried out at $M = 0.83$ demonstrated: that increases in normal force of up to 33% could be obtained at angles of attack above 6° ; that the variation of normal force with incidence could be smoothed and the pitching moment characteristic improved by the addition of triangular strakes of 11% of the overall wing area. Surface pressure measurements also at $M = 0.83$ demonstrated that the strakes increased suction on both the wing and the body upstream of the wing mid chord, but reduced it downstream. At low incidences the largest contribution to the increase in force was to the wing, but with increased incidence this contribution became small in relation to the rapidly increasing favourable effect on the body. The contribution to the strake remained uniformly high. Flow visualization experiments in a water tunnel suggested a mechanism which involved the sucking of flow located near the body by the strake vortex out towards the tip of the wing causing re-energisation of the low energy reverse separated flow at high angles of attack. The measurements also provided some insight into the mechanisms creating favourable wing-body interference effects on missile shapes.

6. REFERENCES

1. STAHL, W.: Wings for missile configurations.
VKI LS 88 "Missile Aerodynamics", March 29-April 2, 1976.
2. WHITE, R.P.: Wing-vortex lift at high angles of attack.
AGARD CP 204, Paper 8, February 1977.
3. STAHL, W.; MOVASSAGHIE, B.; BROHEZ, G.: Aerodynamic characteristics of a missile configuration featuring a wing with strakes.
DLR FB 77-34, 1977.
4. MOVASSAGHIE, B.: Experimental study of a wing with strake for a missile configuration in high subsonic and transonic flows.
VKI PR 1976-5 (unpublished VKI note, June 1976).
5. ZARGHAMI, A.: Aerodynamic characteristics of a missile configuration featuring a wing with various strakes in subsonic and transonic flows up to high angles of incidence.
VKI PR 1977-8 (unpublished VKI note, June 1977).

6. AKCAY, M.: The flow field over a missile configuration fitted both with and without strake in transonic flow up to high angles of incidence.
VKI PR 1978-1 (unpublished VKI note, June 1978).
7. FRANZ, H.P. & EWALD, B.: Sectional loads technique.
AGARD CP 204, Paper 2, February 1977.

Acknowledgement

The experiments were carried out with the assistance of Roger Conniasselle and Robert Voets.

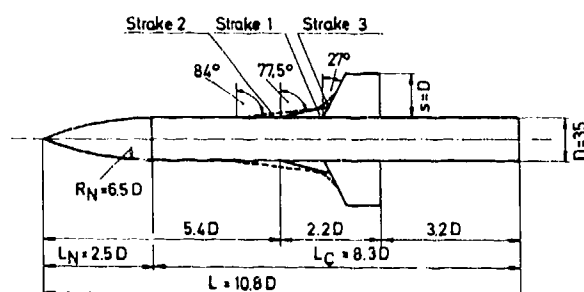


Fig. 1 Schematic of missile configuration with trapezoidal wing with various strakes

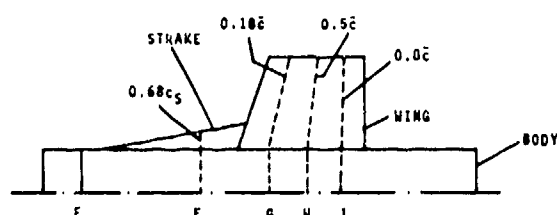


Fig. 2 Schematic of central part of the model illustrating the position of the rows of pressure holes

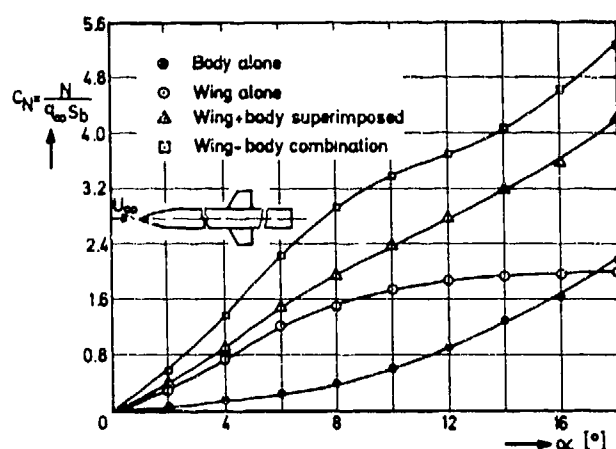


Fig. 3 Normal force coefficient vs incidence for body, wing and body with wing configuration : $M = 0.83, \text{Re} = 1.4 \times 10^5$

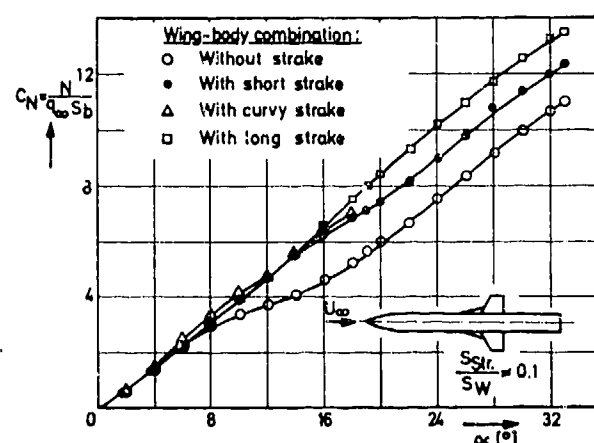


Fig. 4 Normal force coefficient vs incidence for configuration with various strake configurations : $M = 0.83, \text{Re} = 1.4 \times 10^5$

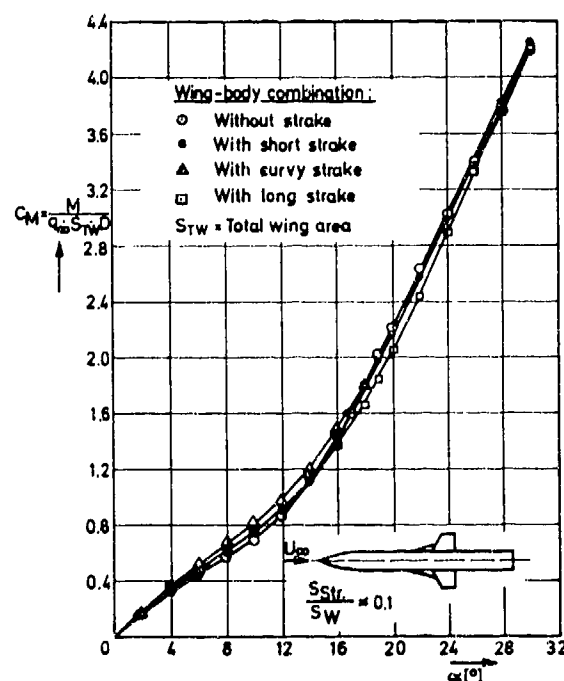


Fig. 5 Pitching moment coefficient vs incidence for configuration with various strake configurations : $M = 0.83, \text{Re} = 1.4 \times 10^5$

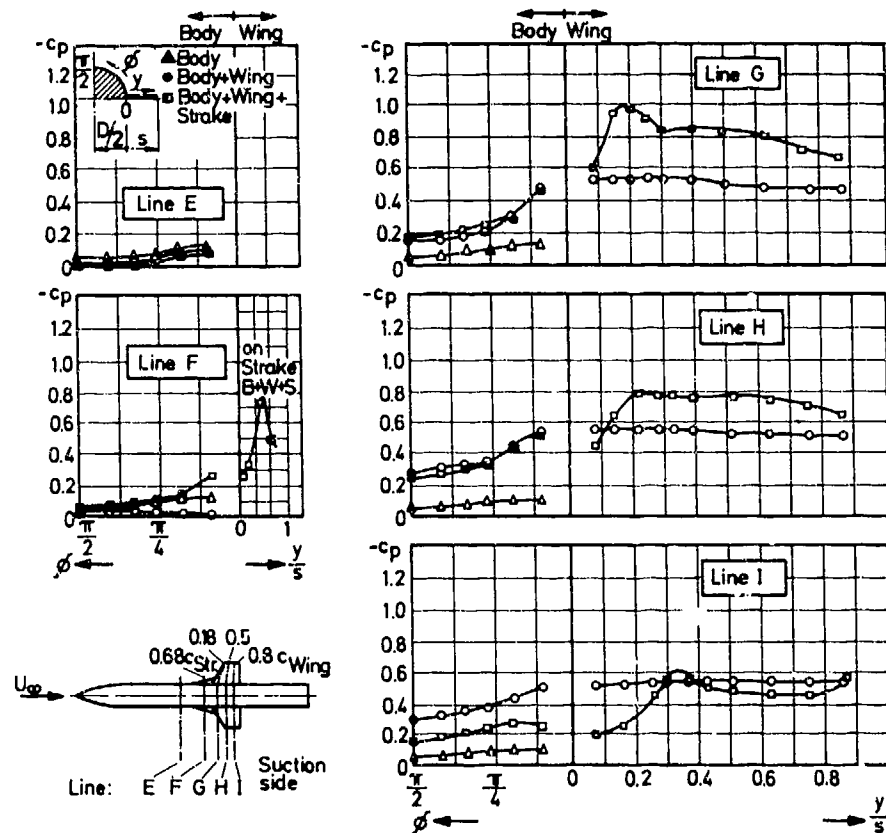


Fig. 6 Measured spanwise pressure distribution at $\alpha=11^\circ$, $M=0.83$, $Re_p=1.4 \times 10^5$

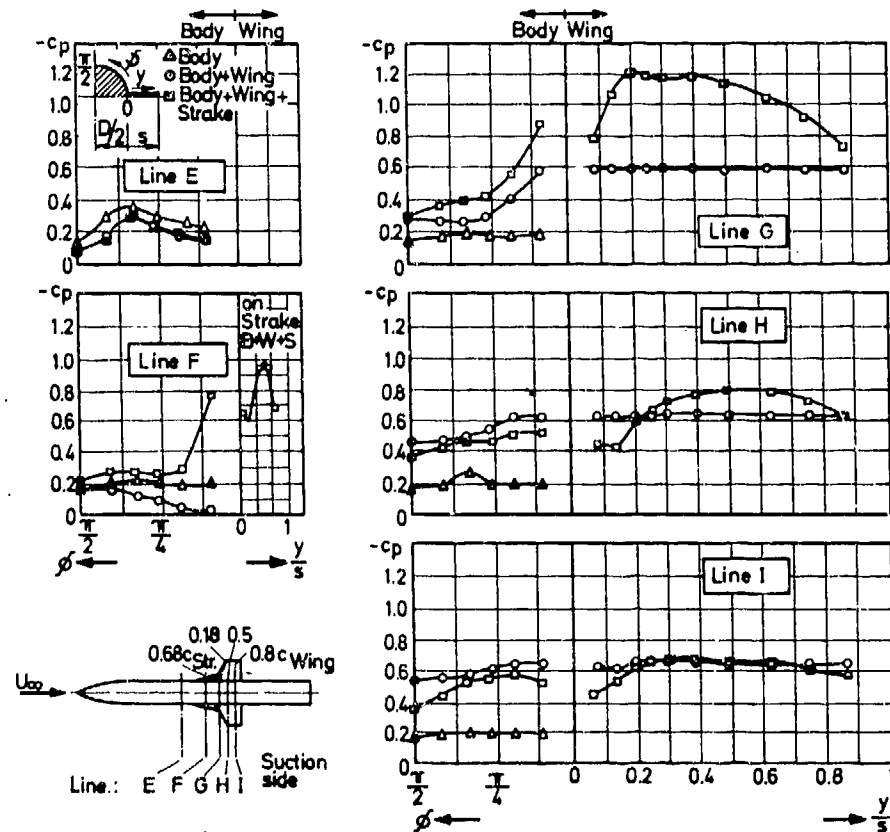


Fig. 7 Measured spanwise pressure distribution at $\alpha=21^\circ$, $M=0.83$, $Re_p=1.4 \times 10^5$

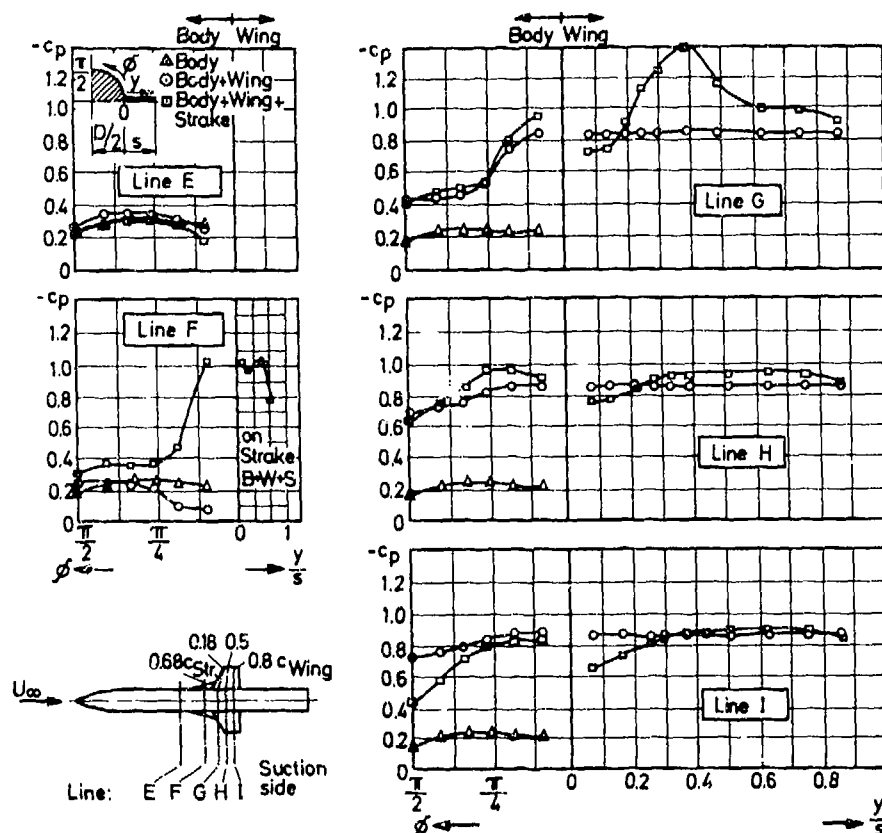


Fig. 8 Measured spanwise pressure distribution at $\alpha=30^\circ$, $M=0.83$, $Re_D=1.4 \times 10^5$

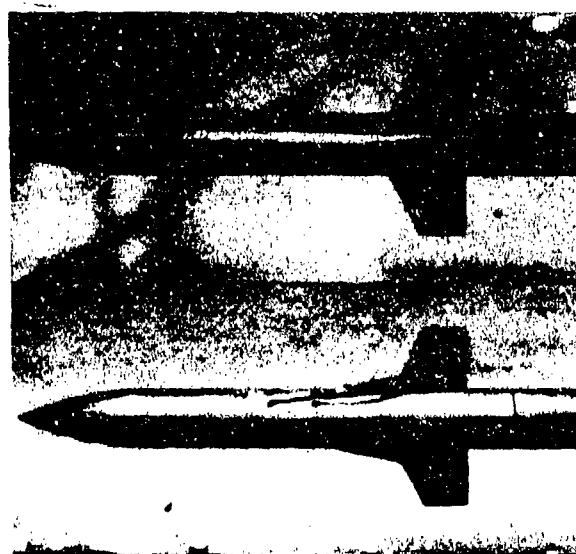


Fig. 9 Dyeline visualization in water tunnel of a) body with wing and b) body with wing and strake. $Re_D=4200$, $\alpha=20^\circ$

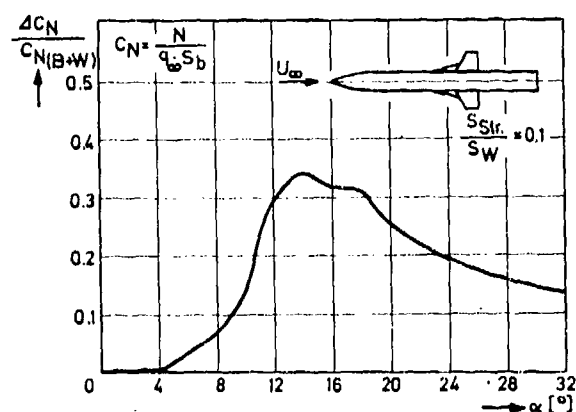


Fig. 10 Fractional increase in normal force coefficient, $\Delta C_N / C_{N_{ref}}$ due to addition of strake vs incidence from force measurements: $M=0.83$, $Re_D=1.4 \times 10^5$, $C_{N_{ref}}$ is value for body with wing only

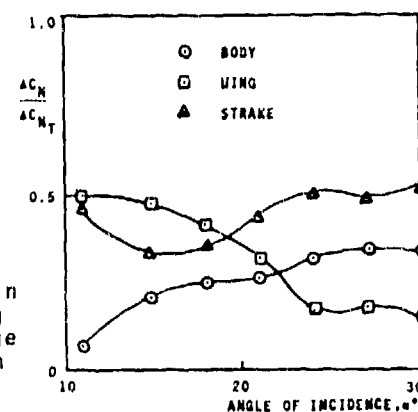


Fig. 11 Distribution of the increase in normal force coefficient to body, wing and strake on missile configuration due to the addition of strake derived from pressure measurements. $M=0.83$, $Re_D=1.4 \times 10^5$, $11^\circ \leq \alpha \leq 30^\circ$

ON THE LEE-SIDE FLOW OVER DELTA WINGS AT HIGH ANGLE OF ATTACK

by

Joachim Szodrach and

Uwe Ganzer

Technische Universität Berlin, Institut für Luft- und Raumfahrt

Marchstraße 14, Sekr. F 2

D-1000 Berlin 10

Germany

SUMMARY

A classification of various types of lee-side flow for slender delta wings is presented for a range of supersonic Mach number and angle of attack. Two particular types of flow which occur at high angle of attack are discussed in more detail. One type exists when the leading edges are subsonic or just sonic. It is distinguished by a shock wave between the strong counterrotating leading-edge-vortices. The other type of flow occurs for supersonic leading edges in which case a pair of separation bubbles occurs with embedded shock waves on top. In this case strong non-conical effects have been observed.

1. INTRODUCTION

The flow field of delta wings with sharp leading edges has been studied in connection with research work aimed at a hypersonic transport aircraft (HST) [1]. Such a hypothetical aircraft was thought of as being a waverider, i.e. a body producing lift by means of a shock wave. At supersonic speeds the pressures on the lee-side of a wing produce only a small part of the total lift. Therefore, as far as the aerodynamic forces are concerned, the lee-side flow is not of particular interest. On the other hand, aerodynamic heating at high cruising speed is strongly depending on the local flow conditions and it is mainly this problem which has generated the requirement for accurate predictions of the flow structure on the lee-side of delta wings at supersonic speeds.

2. A CLASSIFICATION OF VARIOUS TYPES OF LEE-SIDE FLOW

An experimental study was aimed at providing some fundamental information about the flow over delta wings for a range of supersonic freestream conditions and angles of attack. The majority of windtunnel tests were made using the model sketched in Figure 1. This model has a triangular cross-section and a flat upper surface. Leading edge sweep angle is $\Lambda = 73^\circ$ and thickness ratio (height to length) is $h/l = 0,25$. The flow field of such wing is expected to be conical so that similarity of flow conditions prevails at the various cross-sections $x = \text{const.}$. The components of freestream Mach number and angle of attack as they appear in the plane normal to the leading edge (M_N and α_N) are convenient for a general description of the flow field. These components have been used throughout earlier publications [2, 3, 4]. However, in this paper the resultant freestream values M_∞ and α will be used to facilitate appreciation of the experimental conditions.

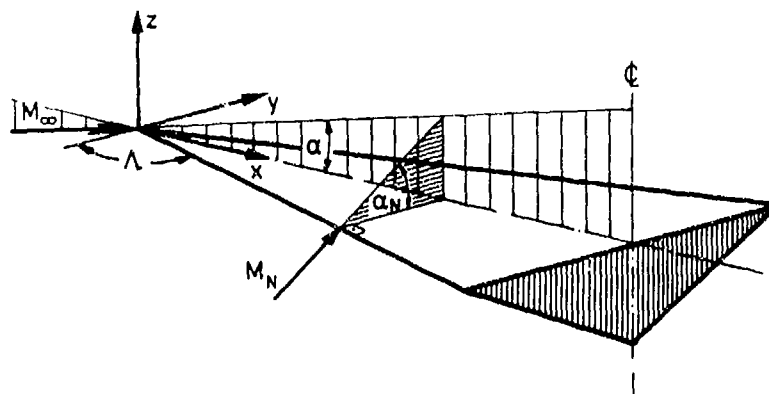


FIG. 1: DELTA WING MODEL

A summary of the results for the lee-side flow structure is presented in Figure 2, which provides a classification into various flow types. At low and moderate angles of attack the most extensively studied type of flow is that where leading edge separations roll up into spiral vortices. The vorticity is produced at the leading edge. A particular feature of this type of flow is the existence of small secondary vortices very near the leading edges. Such flow is found for subsonic leading edges, i.e. for Mach number components normal to the leading edges smaller than 1 ($M_N < 1$). Stanbrook and Squire have given a more specific limit for the occurrence of leading edge vortices as shown in the diagram. The Stanbrook-Squire boundary was however said to describe the change of flow type from leading edge separation to shock-induced separation. Our own experiments revealed that for the thick delta wing shock induced separation occurs only at much higher

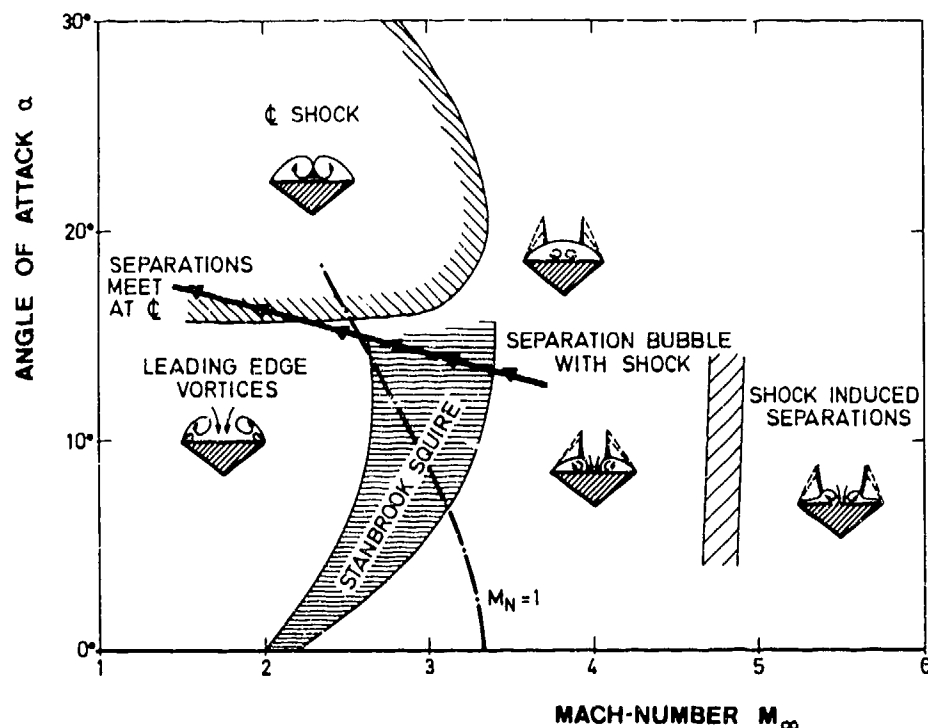


FIG. 2: LEE-SIDE FLOW TYPES FOR A DELTA WING

Mach numbers and that another type of flow exists just to the right of the Stanbrook-Squire boundary. This flow is characterised by a separation bubble starting at the leading edge and a shock on top of the bubble. The shock is not the cause of the separation but is a more or less independent part of the outer flow field terminating a local supersonic flow region. A vortex like flow movement exists within the bubble but secondary vortices have disappeared. Near the leading edge no flow movement has been observed and this appears to be truly a dead air region.

Both the leading edge vortices and the separation bubbles grow with increasing angle of attack at constant Mach number; consequently the separations from the two leading edges approach each other and eventually merge. The types of flow formed at higher angles of attack will be discussed below.

3. THE DEVELOPMENT OF LEADING EDGE VORTICES WITH ANGLE OF ATTACK

Oilflow pictures obtained for the flat upper surface of the wing provide the first information about the flow structure; see Figure 3. The flow conditions at $M_{\infty} = 2.5$ and $\alpha = 10^\circ$ are such that besides primary and secondary vortices traces of attached flow parallel to the plane of symmetry can be seen. This indicates that the two vortices are still separated. The disappearance of the parallel oilstreaks has been taken as an indication that the separations have met at the centreline.



FIG. 3: OILFLOW PICTURE OF THE LEE-SIDE FLOW AT
 $M_{\infty} = 2.5$ AND $\alpha = 10^\circ$

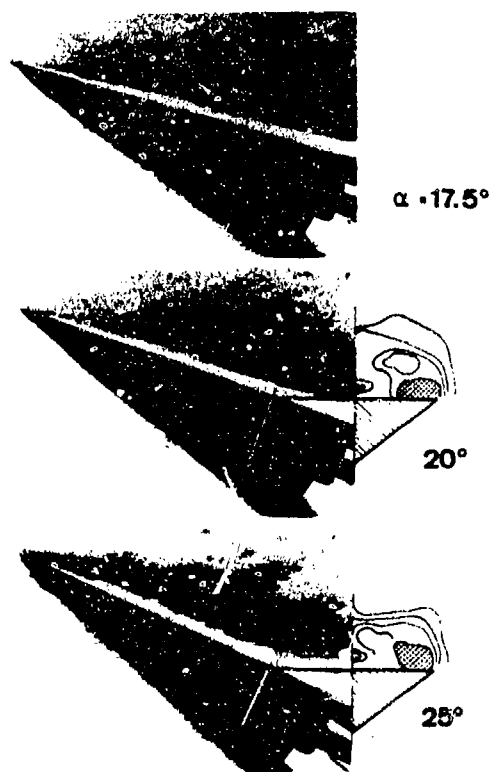


FIG. 4: SCHLIEREN PICTURES AND TOTAL HEAD MEASUREMENTS AT $M_{\infty} = 2.5$

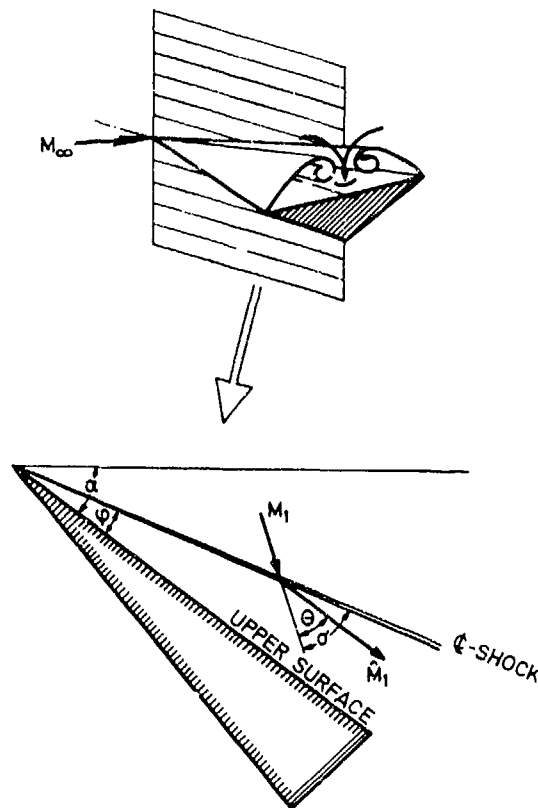


FIG. 5: FLOW CONDITIONS FOR THE CENTRELINE SHOCK

Additional information is provided by Schlieren pictures and total-head curves measured in a plane perpendicular to the upper surface of the wing, Figure 4. The Schlieren pictures show the lower part of the vortices as a dark region. In addition, a sharp light line is seen near the upper surface. The total head measurements confirm that this line is a shock located very close to the centreline. Such a centreline shock can be found for a fairly large range of Mach number and angle of attack, see Figure 2. Near the edge of that ζ -shock-margin the line in the Schlieren picture is blurred, but right in the centre of the margin it is clearly visible and sharp. Two facts are remarkable: The lower limit of the ζ -shock-margin is very close to, but clearly distinguished from the boundary for the meeting of the two separations at the centreline. At low supersonic Mach numbers the ζ -shock already exists before the vortices meet, and at higher Mach numbers just after they have met. The right hand limit of the ζ -shock-margin looks like a continuation of the Stanbrook-Squire boundary. Thus ζ -shocks obviously do not occur with separation bubbles but seem to be confined to leading edge vortex flow.

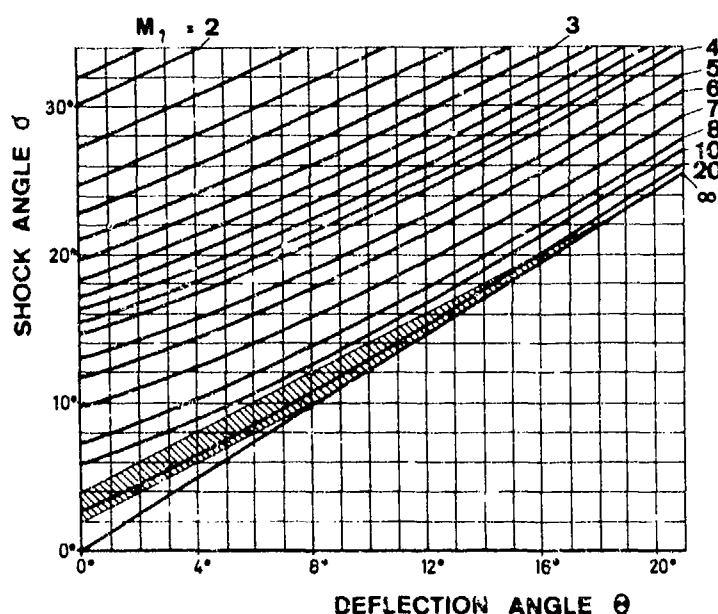


FIG. 6: OBLIQUE SHOCK RELATIONS-MARGIN CORRESPONDING TO THE CENTRELINE SHOCK

In order to explain the nature of the ϕ -shock the following argument can be made, (see Figure 5): Assuming the shock to be plane and oblique, the flow in the plane of symmetry would be deflected by the shock into a stream direction parallel to the upper surface. The angle between shock and upper surface can be measured from Schlieren pictures. It must be equal to the difference between shock angle ϕ and deflection angle θ , i.e. $\phi = \phi - \theta$. This value has been found to vary between $\phi = 2^\circ$ to 4° . If the ϕ -shock is a plane shock, as has been assumed, then the oblique shock relations will be applicable, (see Figure 6). It turns out that the Mach number in front of the shock then has to be between $M_1 = 10$ to 20 (and the deflection angle $\theta = 0$ to 16°). The measured pressure values are contradictory to such high Mach numbers. Thus it is concluded that the ϕ -shock is not a plane shock.

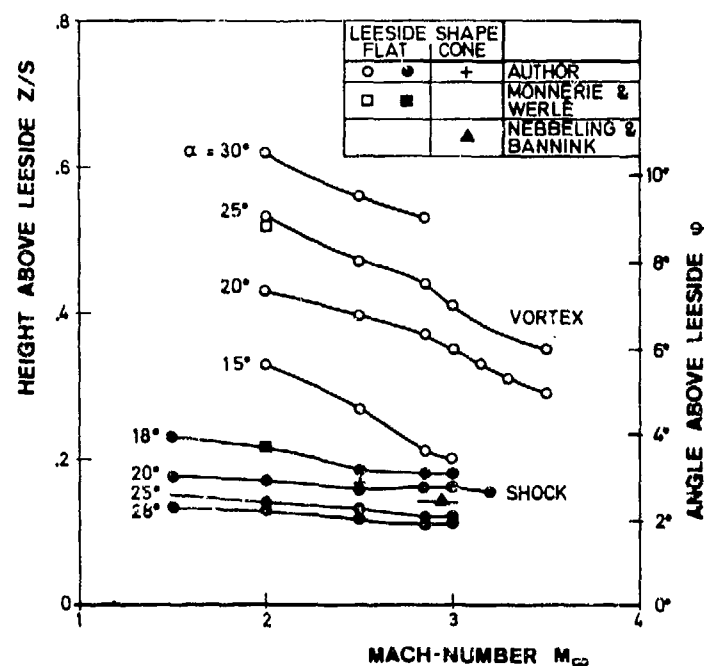


FIG. 7: CENTRE LINE SHOCK AND VORTEX POSITION ABOVE THE WING

In Figure 7 the measured shock angles are plotted. The shock position is nearly independent of Mach number but the shock moves toward the wing surface with increasing angle of attack, while the vortex core moves away at the same time. From comparison between the change of ϕ -shock inclination and vortex core position above the wing one might conclude that there is just one flow type which is developing gradually. It is then surprising to see in Figure 8 that the lateral movement of the vortex core is very different for two different Mach numbers: while for the lower Mach number the core position moves in a manner typical of leading edge vortices, the vortex core trace for $M_\infty = 2.5$ indicates a change of flow structure at high angles of attack. Looking again at Figure 2 one might conclude that an extension of the Stanbrook-Squire boundary into the region of high angle of attack could give an explanation of this behaviour, i.e. the experimental result at high incidence falls into the extended Stanbrook-Squire region for $M_\infty = 2.5$.

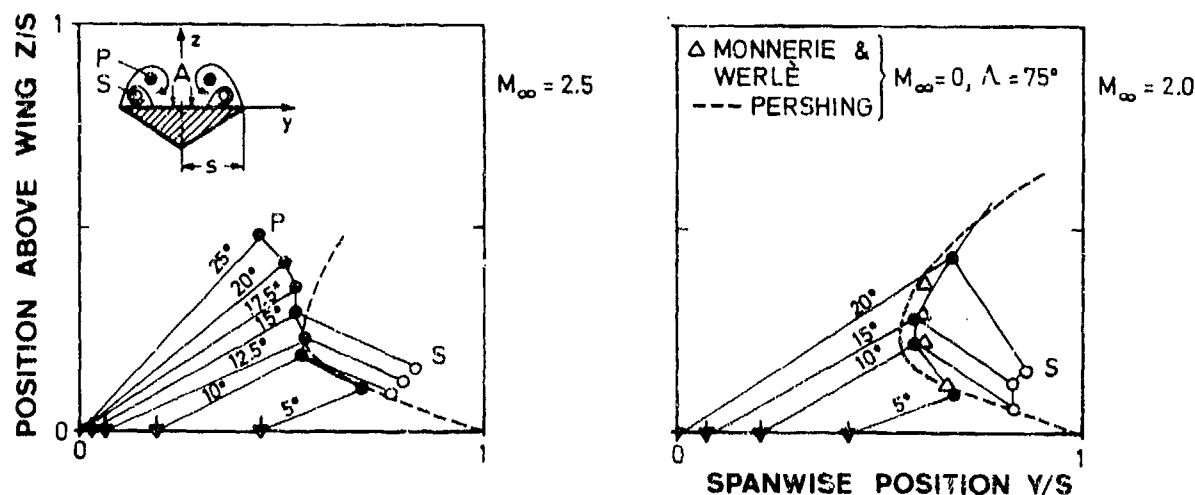


FIG. 8: POSITIONS OF PRIMARY & SECONDARY VORTICES AT $M_\infty = 2.0$ AND 2.5

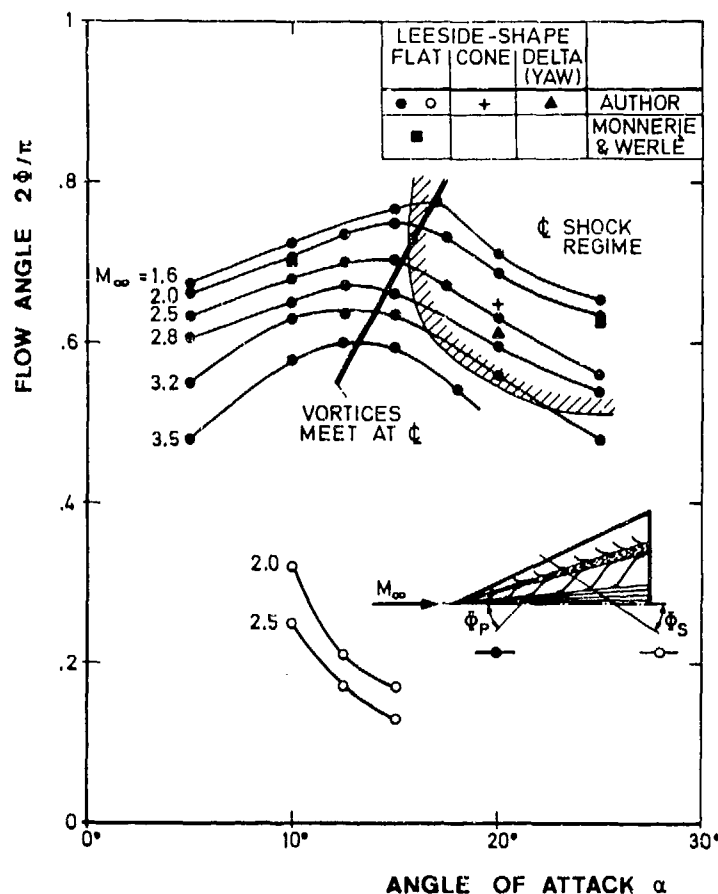
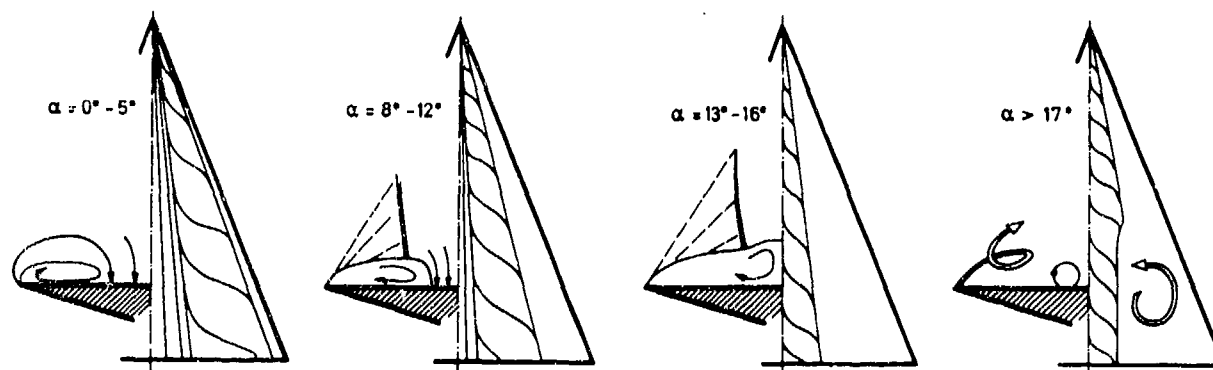


FIG. 9: INTENSITY OF PRIMARY AND SECONDARY VORTICES

Another approach is made in Figure 9 to explain the interdependence between the vortex flow and ζ -shock. Here the outflow angle of oil streaks has been measured from oilflow pictures and is plotted against the angle of attack with Mach number as a parameter. It is assumed that the angle can be taken as a measure of vortex intensity. The diagram shows that highest vortex intensity is reached just before the vortices meet at the centreline. The existence of a ζ -shock shows no clear dependence on the vortex intensity as one might perhaps expect.

4. DEVELOPMENT OF SEPARATION BUBBLES WITH ANGLE OF ATTACK

The experimental results presented here for separation bubbles with shocks are confined to a Mach number $M_\infty = 3.5$. Oilflow pictures reveal that at high angles of attack the flow develops into a non-conical manner; see Figure 10. At $\alpha = 17^\circ$ the vortex starts to detach from the wing surface near the trailing edge giving rise to an enlarged dead-air region. The oilflow pattern near the trailing edge suggests a slowly moving curl-like flow rising from the wing.

FIG. 10: DEVELOPMENT OF FLOW PATTERN AT $M_\infty = 3.5$

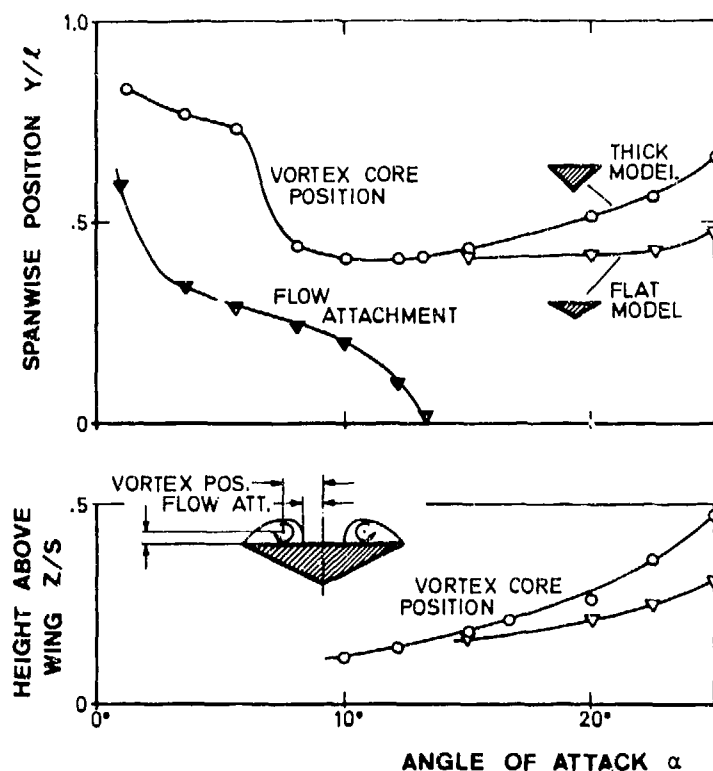


FIG. 11: VORTEX POSITION AND -EXTENSION AT $M_{\infty} = 3.5$

In Figure 11 the development of separation bubbles is shown as it has been observed for two different delta wing models, a thick and a flat one. At low angles of attack the flow does not differ for the two wings. With increasing angle of attack the attachment region decreases and finally disappears when the separations meet at the centreline. The core of the vortex-like flow within the separation bubble first remains in a position of roughly $3/4$ span while the separation grows extending further to the plane of symmetry. Then this growth almost stops and the core moves towards the plane of symmetry and then again the core stops its movement while the separation grows over the span covering finally the whole wing. Throughout the process the height of the vortex core increases rather gradually with angle of attack.

After the separations from the two leading edges have merged at the centreline the flow field develops in a different way for the two wings. For the flat wing there seems to be only insignificant change of flow structure; the spanwise position of the vortex remains nearly unchanged while the height of the separation grows slightly with increasing angle of attack. For the thick wing flow development is much more rapid.

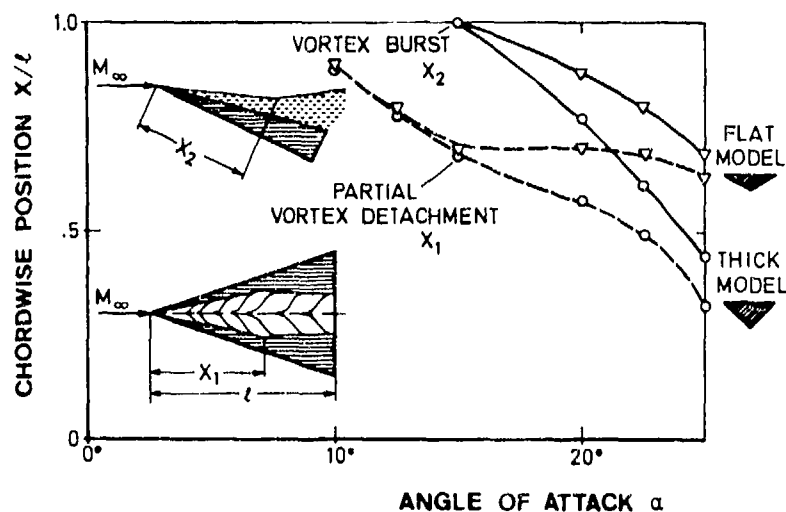


FIG. 12: NONCONICAL EFFECTS AT $M_{\infty} = 3.5$

Figure 12 reveals that the non-conical flow pattern develop more rapidly for the thick wing than for the flat wing, although qualitatively the flow development is the same: It starts at the trailing edge with an extension of the dead air region toward the plane of symmetry so that the oilflow pattern show a smaller part of the vortex-like flow attached to the wing surface. Increasing angle of attack causes the constriction of vortex pattern to extend further upstream. On the other hand the Schlieren pictures show something like a vortex burst - a sudden increase of vortex growth - first occurring at the trailing edge and moving upstream with increasing angle of attack. The experimental study was confined to an incidence range up to $\alpha = 25^\circ$. The flow development has not yet reached any final stage at that angle of attack.

5. CONCLUSION

Two different types of flow have been observed in supersonic freestream conditions at fairly high angle of attack: Leading edge vortices with centreline-shock and separation bubbles developing into a non-conical flow pattern. The first occurs at lower Mach numbers with subsonic and slightly supersonic leading edges. The second type has been found for higher Mach numbers. The main features of these flow patterns have been described and some boundaries have been given indicating the conditions under which these types of flow might be expected. However, the upper incidence limit, as well as the low and high Mach number boundaries of these flow regimes have not yet been discovered. Although the results are strictly valid only for the particular Reynolds-number and delta wing model used for the experiments, it is believed that the results provide some general information about the flow patterns that occur for delta wings with sharp leading edges at supersonic speeds.

7. REFERENCES

- [1] U. Ganzer On the aerodynamics of hypersonic cruise vehicles at off-design conditions.
H. Hoder ICAS Conf. Proceedings Vol. 1 Paper A2-03, 1978
J. Szodrich
- [2] J. Szodrich Leeseiten-Strömung bei schlanken Deltaflügeln endlicher Dicke.
ILR-Bericht 23, Techn. Univ. of Berlin, 1977
- [3] J. Szodrich Zur Systematik der Leeseiten-Strömung bei Deltaflügeln.
Submitted for publication in ZfW Journ. 1978
- [4] J. Szodrich Reynolds number influence on lee side flow fields.
Submitted for publication in AIAA Journ. 1978
- [5] A. Stanbrook Possible types of flow at swept leading edges.
L. C. Squire Aeron. Quarterly, vol. XV, Febr. 1964
- [6] B. Monerie Étude de l'écoulement supersonique et hypersonique au tour d'une aile élançée en
H. Werlé Incidence.
AGARD CP No. 30, 1978
- [7] C. Nebbelling Experimental investigation of the supersonic flow field about a slender cone at high
W.J. Bannink incidences.
Rep. LR-233, Delft Univ. of Techn., 1976

MEASUREMENTS OF THE SUPERSONIC FLOW FIELD PAST A
SLENDER CONE AT HIGH ANGLES OF ATTACK

W.J. Bannink and C. Nebbeling
Department of Aerospace Engineering, Delft University
of Technology, Kluyverweg 1, Delft, The Netherlands

SUMMARY

The flow field past a 7.5° semi-apex angle circular cone at angles of attack up to $\alpha = 34^\circ$ has been investigated experimentally at a free stream Mach number of 2.94. In a cross-sectional plane the conical flow direction, the conical Mach number and the static pressures were determined, using a conical-head directional probe. Surface pressure distributions and oil flow patterns revealed flow separation at an angle of attack of about the cone half-angle. The separation is coupled with the formation of a vortex system. At values of α exceeding 14° a double separation type of flow was observed: a primary and a secondary vortex at either side of the leeward symmetry plane. From $\alpha = 17^\circ$ onwards regions of embedded conical supersonic flow were detected, adjacent to the cone surface. Shock waves were measured inside the conical supersonic region, also the occurrence was verified of a shock wave close to the cone surface and extending slightly across the leeward symmetry plane. At 22° , the existence was confirmed of a separated vortical singularity in the leeward symmetry plane. Beyond $\alpha = 26^\circ$ the flow becomes asymmetric with respect to the leeward symmetry plane.

NOTATION

M	Mach number	x, y, z	cartesian coordinates
M_c	conical Mach number	α	angle of attack of the cone
p_1, p_2	surface pressures of the probe	γ	direction of conical streamlines, (Eq. 5)
p_3, p_4		θ, φ	coordinates on the unit sphere
p_5	pressure, measured by the central orifice of the probe	θ_p, φ_p	direction of local velocity vector with respect to probe axis
p_p	Pitot pressure	θ_f, φ_f	direction of local velocity vector with respect to coordinate system
p_{t_∞}	free stream stagnation pressure	θ_c	semi-apex angle of the cone
R	local radius of the cone		
U_∞	free stream velocity		
u, v, w	velocity components in spherical coordinate system		
q	$(v^2 + w^2)^{1/2}$		

1. INTRODUCTION

In the last decade the interest in the supersonic flow about cones at large angles of attack is considerably increased. This is not only due to the advent of the space shuttle concept, or to the requirements put by modern fast manoeuvrable missiles, but a large portion of the growing interest may also be attributed to the increasing capability to compute complex flow fields. However simple the geometry of a circular cone is, its inviscid flow field at high angles of attack is rather difficult to compute, not to speak about the viscous flow problems. It is worthwhile to review first in some detail the inviscid results available, numerical as well as analytical.

The first inviscid flow calculations were concerned with angles of attack α not or not noteworthy exceeding the cone half-angle θ_c , see for example Refs. 1 - 9. Nowadays it is possible to treat cases where $\alpha/\theta_c > 1$, of which Refs. 10 - 12 bear witness. At moderate angles of attack the conical cross flow (obtained by projecting the spatial flow on a unit sphere, having its centre in the apex of the cone) is subsonic everywhere in the flow field influenced by the cone. At high angles of attack (α/θ_c about 2) the conical cross flow around the cone will accelerate from the windward to the leeward side to such extent, that a conical supersonic pocket is formed on the cone surface. To satisfy the boundary conditions in the leeward symmetry plane the supersonic pocket may be terminated by a shock wave. In addition to the shock wave, other difficulties arise in the inviscid case, namely the so called vortical singularities, first mentioned by Ferri (Ref. 13). Such a singularity appears in the flow field where the conical velocity component vanishes; this means that the spatial streamline is coinciding with a ray emanating from the cone apex. This ray corresponds on the unit sphere with a conical stagnation point. According to the way in which the conical streamlines approach a conical stagnation point, one distinguishes nodal and saddle points. A nodal point is a singularity because here the velocity component along a ray through the cone apex, the entropy and the density are multivalued.

The nature of the singularities has been the subject of analytical studies in Refs. 14 - 16, and also one is able to determine numerically the flow in the vicinity of vortical singularities (Refs. 11, 12). The analytical investigations are restricted to local studies, and therefore no definite opinion can be given upon the overall character of the flow. It may be shown (Refs. 14, 17 - 19) that, since there is a close connection between the type of conical stagnation points and the pressure distribution in their immediate vicinity, it is possible to predict the local flow patterns. Using slender-body theory (Ref. 15), and linearized theory (Ref. 16), one has been successful to calculate analytically the flow about a circular cone at relative large angles of attack ($\alpha/\theta_c = 2$). These analyses led to a conical stagnation point in the leeward symmetry plane, away from the cone surface; this phenomenon was suggested in Refs. 13 and 14. Only recently (Refs. 11, 12) the presence of such a point was also revealed in numerical computations.

Up to now all local analytical investigations are concerned with "rectangular" stagnation points, i.e. points where the neighbourhood may be constructed into four quadrants, divided by conical streamlines normal to each other (separatrices). At the Delft Dept. of Aerospace Engineering a study is going on on conical stagnation points having non-orthogonal separatrices (Ref. 20).

The theoretical treatment of the viscous flow past a circular cone at high angles of attack is much more cumbersome, since it is concerned with the growth of the turbulent boundary layer, its separation and, eventually, the rolling up of the separated turbulent shear layer into a vortex system. The vortices interact with the inviscid outer flow, resulting in a different boundary value problem for the outer field. By altering the circular shape of the cone, to allow for the revised boundary conditions at the leeward side, an extension may be given to the range of computation possibilities at large angles of attack (Refs. 25, 26). The number of references on the numerical computation of viscous cone flow is rather restricted (Refs. 27 - 31). Only Ref. 30 covers angles of attack exceeding the cone half-angle for a not so slender

cone at hypersonic Mach numbers. The viscosity is included by adding stress terms to the inviscid flow equations, a procedure which is certainly insufficient to describe the complex vortex flow system. For large angles of attack one is dependent upon experimental results. Most experiments, however, are mainly concerned with surface flow in terms of the surface pressure distribution and oil flow pictures; in the outer flow field the results are restricted to Pitot pressures (Refs. 21, 22, 23, 25, 32 - 35). The Pitot pressure distribution shows the existence of vortices, it also reveals the presence of embedded shocks, as long as they are not too weak (Refs. 23, 25, 33, 34).

In Ref. 24 the authors of the present paper have reported of an experimental investigation, from which a first impression was obtained of the flow angularity about a 7.5° semi-apex angle circular cone at angles of attack up to 22.4° , and at a free stream Mach number of 2.94. In these experiments a relatively large probe was used (3.5 mm diam.), and the necessity was felt to repeat the measurements with a smaller probe, and also with an improved measuring technique and data reduction procedure. Therefore, the explorations reported in the present paper were made at approximately the same angles of attack as in Ref. 24, i.e. 12.4° , 17.2° and 22.6° , and a probe of 1.65 mm diam. was used. In addition, results are given at smaller angles of attack (9.2° and 11.1°), where some evidence of vortex formation could be detected. In order to complete the flow picture, surface pressure distributions were measured at angles of attack ranging from 6° to 28° and the already existing set of surface oil flow patterns of Ref. 24 was extended such as to make it compatible with the surface pressure data.

The results of the present investigation, together with those of Ref. 24, represent a rather detailed description of the flow field about a circular cone at large angles of attack, it may serve as a comparison to numerical computations.

2. DESCRIPTION OF EXPERIMENTS

2.1. Test arrangements and models

All experiments were performed at a Mach number of 2.94 and using a 7.5° semi-apex angle cone. They were carried out in two supersonic blow-down wind tunnels of the University of Technology Delft, Department of Aerospace Engineering, the TST 27, having a test section of 0.27 m x 0.27 m, and the ST 15, with a test section of 0.15 m x 0.15 m. In both wind tunnels the settling chamber pressure during the runs was kept constant at a value of 5.20 ± 0.03 bars, the corresponding Reynolds number of the free stream being 45.10^6 per meter. The surface oil flow patterns were made in the TST 27 wind tunnel, on a cone (with a length of 25 cm) covered with a thin adhesive plastic foil. The calibration of the probe was also made in the TST 27 wind tunnel, which is equipped with a variable nozzle.

The actual flow field exploration and the surface pressure measurements were obtained in the ST 15 wind tunnel with fixed nozzle blocks; two models with a length of 15 cm were available. One model was used for the flow direction measurements with the conical-head probe. The test arrangement and the traversing mechanism of the probe are schematically shown in Fig. 1. The diameter of the probe was 1.65 mm, and the conical head, with a semi-apex angle of 30° , was provided with four static pressure orifices equally divided, 90° apart; a central orifice served as a Pitot pressure tap. The orifices had a diameter of 0.2 mm, and the distance between two opposite orifices was 1.23 mm. The lateral displacement of the probe was measured by counting the number of steps of the stepping motor from a well defined reference position. The vertical position was determined optically during the runs.

The second model was provided with 32 pressure orifices. The test set up and the location and spacing of the pressure orifices are given in Fig. 2. The angle of attack of the model could be adjusted, a motordrive enabled intermittent rotation of the cone about its axis, with minimum increments of 0.125° .

2.2. Calibration of the probe

In the Appendix of Ref. 24 a detailed procedure of the probe calibration has been given. A complete computerized acquisition and reduction of data, in which the corrections to be mentioned in the next have been taken into account, provided a rapid and accurate flow field exploration. The calibration of the probe is based on the fact that the flow angularity with respect to the probe axis is related to the pressure differences measured across the two sets of opposite orifices. The local Mach number is to be determined from the calibrated ratio of the pressure measured at the central orifice of the probe, to the average of the four surface pressures on the conical head.

A number of factors affecting the measurements and for which corrections have been applied (Ref. 24), are:

1. at large flow angles with respect to the probe, the pressure measured at the central orifice differs from the Pitot pressure;
2. the average pressure obtained from the four surface orifices on the conical head is, at large flow angles, different from the surface pressure at zero flow inclination; the latter pressure is used for the determination of the Mach number;
3. since the ratio of the surface pressure (at zero flow inclination) to the Pitot pressure is dependent upon the semi-apex angle of the conical head, the derived local Mach number may deviate from the true value in local divergent or convergent flow;
4. pressure gradients in the flow field may contribute to the measured flow angularity.

The calibration was carried out at three Mach numbers, $M = 2.2$, 2.97 and 3.5, at eight different roll angles of the probe, the intervals between the roll angles being 45° . At a fixed Mach number and roll angle, the range in angle of pitch of the probe was from -2° to 16° . After applying all calibrated functions and taking into account the correction relations, eventually an expression is obtained, called a super-ellipse, which is written as

$$\left[\frac{p_2 - p_1}{p_5} - (A_o)_{\varphi=0} \right]^{n(\theta_p, M)} + \left[\frac{p_4 - p_3}{p_5} - (B_o)_{\varphi=90^\circ} \right]^{n(\theta_p, M)} = 1 \quad (1)$$

$$\left[\frac{F_1(\theta_p) - A_o}{F_1(\theta_p) - A_o} \right]_{\varphi=0} + \left[\frac{F_2(\theta_p) - B_o}{F_2(\theta_p) - B_o} \right]_{\varphi=90^\circ}$$

where p_1, \dots, p_5 are the pressures measured at the upper, lower, left, right and central orifice, respectively; $F_1(\theta_p)$, $F_2(\theta_p)$ are functions of the angle of pitch θ_p of the probe, derived from the calibration,

and A_0 , B_0 , are constants due to probe imperfections. The exponent n is a calibrated function of θ_p and M , n is close to the value 2. For each of the three Mach numbers, mentioned above, a set of super-ellipses was obtained.

2.3. Flow field explorations

The flow field about the cone was investigated at angles of attack ranging from $\alpha = 7.5^\circ$ to 22.6° . Special emphasis was given to the measurements at $\alpha = 12.4^\circ$, 17.2° and 22.6° , since additional information was desired to the results of Ref. 24. The probe was mounted approximately parallel to the wind tunnel axis; the exact position with respect to the model was incorporated in the data reduction. Because of the conicity of the flow field (Ref. 24), the measurements were made in only one plane, normal to the wind tunnel axis, at about 120 mm downstream of the cone apex. The probe was traversed laterally with intervals of 0.61 mm, at levels with a relative distance of about 0.6 mm, both values correspond approximately to half the distance between two opposite pressure orifices on the conical head. The accuracy of the probe position was 0.03 mm. During the runs the stagnation temperature in the settling chamber of the wind tunnel was measured, relative to the temperature of melting ice, by means of a thermocouple.

2.4. Surface pressure measurements

With the model shown in Fig. 2, surface pressure distributions were obtained at angles of attack between 7.5° and 28° . To check the conicity of the surface flow, the pressure orifices along the circumference of the stations A, B and C (Fig. 2), and those along a generatrix of the cone were connected to a scanning valve, after which the pressures were measured at $\alpha = 11^\circ$ and 20° . Although the conicity was somewhat less at the higher angle of attack, when comparing the results of the front station C to those of stations A and B, the results of the last two stations compared so well, that it was decided to make the pressure measurements at the rear station A only. The actual measurements were conducted utilizing orifice number 10 only. The cone was rotated about its axis from the initial position of orifice 10 over 380° , to have a fair overlap.

2.5. Data reduction

The measurements have been reduced in a spherical coordinate system with its origin in the apex of the cone, see Fig. 3. The coordinates are r , θ , ϕ , where r is measured along a ray, θ from the cone axis and ϕ in a plane normal to the cone axis, ϕ is zero in the windward symmetry plane of the cone. The components of the local velocity vector are u , v , w , in the directions of increasing r , θ , ϕ , respectively. The total conical velocity component q is normal to r , the conical Mach number M_c is defined as the ratio of $|q|$ to the local speed of sound. The flow angularity with respect to the probe is completely determined by θ_p , the angle between the local velocity vector and the probe axis, and by ϕ_p , the meridional angle. θ_p is obtained from Eq. (1), par. 2.2. and ϕ_p from the relation.

$$\phi_p = \tan^{-1} \left[\frac{P_2 - P_1}{P_4 - P_3} \right] \quad (2)$$

The local static pressure in the flow field is determined from the Mach number and the Pitot pressure. To compensate for inaccuracies due to the finite dimensions of the probe, an interpolation scheme is applied, such that the four cone surface pressures are adapted to the location of the central orifice of the probe. From the measured flow quantities and from the known position and inclination of the probe, the conical Mach number may be calculated using the equation

$$M_c = M \left[\sin^2 \theta_f \sin^2 (\phi - \phi_f) + \left\{ \sin \theta_f \cos (\phi - \phi_f) \cos \theta - \cos \theta_f \sin \theta \right\}^2 \right]^{1/2} \quad (3)$$

where θ , ϕ are the coordinates of a point on the unit sphere, and θ_f , ϕ_f denote the direction of the velocity vector with respect to the coordinate system. The reduced data are represented in a plane normal to the cone axis, by applying the conical property that flow quantities are constant on rays through the conical centre. A point in the plane is defined by the cartesian coordinates y and z , non-dimensionalized by the radius R of the local cross-section of the cone; θ , ϕ are related to y , z by the equations

$$\begin{aligned} y/R &= \frac{\tan \theta}{\tan \theta_c} \sin \phi \\ z/R &= -\frac{\tan \theta}{\tan \theta_c} \cos \phi \end{aligned} \quad (4)$$

and $R = x \tan \theta_c$, x being the coordinate of the cross-sectional plane, and θ_c is the semi-apex angle of the cone. The slope of the conical streamlines is given by

$$\tan \gamma = \frac{-\sin \theta_f \cos \phi_f + \tan \theta \cos \phi \cos \theta_f}{\sin \theta_f \sin \phi_f - \tan \theta \sin \phi \cos \theta_f} \quad (5)$$

γ , the angle with the positive y -axis, is measured counter clockwise.

3. RESULTS

The results of the present experiments, together with those already reported in Ref. 24, may serve to describe the supersonic flow field about a slender circular cone at high angles of attack.

3.1. Surface oil flow patterns and pressure distributions

The surface oil flow patterns are shown in Fig. 4, the straight edges represent the windward side of the cone. In Ref. 24 some of the photographs are used to derive the shear stress distribution in the circumferential direction. In the present paper the oil flow patterns will be compared to the surface pressure distributions. Although the angles of attack of the latter measurements do not fit completely with those of the oil flow pictures, a comparison is still possible, since the variation of the oil flow structure with α occurs only gradually, as may be seen in Fig. 5, which has been derived from the photographs. In Fig. 4 it is observed that, comparing $\alpha = 8^\circ$ to $\alpha = 6^\circ$ the oil flow structure reveals a change at the leeward side. The surface pressure distribution at $\alpha = 7.5^\circ$, however, is rather constant at the leeward side. At $\alpha = 10^\circ$ the first evidence of flow separation is visible in the oil flow structure. The pressure distribution corresponding to this angle of attack (Figs. 6 and 7) shows a slight hump around $\phi = 180^\circ$,

and a minimum at about $\phi = 115^\circ$. At values of α close to 10° , the flow directions given in Figs. 18 and 19, indicate initiation of a vortex formation, as will be seen later. From $\alpha = 10^\circ$ onwards, the flow pattern develops further into that of a double-separation type (Ref. 25), which, judging from the oil flow patterns, seems to be achieved at $\alpha = 14^\circ$, and which does not alter significantly until $\alpha = 26^\circ$. However, the pressure distribution does change, in that, at $\alpha = 16^\circ$ a pressure wiggle appears at $\phi = 150^\circ$, approximately, see Fig. 7. A general picture of the pressure distribution at the leeward side may now be described as follows: pressure minima occur at $\phi = 120^\circ$ and at $\phi = 165^\circ$, approximately; in between the minima the pressure shows a flat maximum, whereas in the plane of symmetry ($\phi = 180^\circ$) a much more pronounced maximum exists at a higher level. The wiggle in the pressure distribution, at $\phi = 150^\circ$, corresponds to the dark band in between the two separation lines of the oil flow pictures of 14° to 26° . It indicates the position of reattachment due to the secondary separation, see Fig. 8, where the surface oil flow structure at $\alpha = 18^\circ$ is compared to the measured pressure distribution. The separation lines in the surface flow correspond to locations in the pressure distribution which, looking in the local flow direction, lie beyond the pressure minima; this phenomenon was also observed in Ref. 33. The maximum in the pressure distribution normal to the cone surface at $\phi = 180^\circ$, shown in Fig. 9, together with the relative maximum in the surface pressure at $\phi = 180^\circ$, indicate a saddle point of the conical streamlines (Ref. 18).

At angles of attack above 26° the flow loses its symmetric character (Fig. 4 and Fig. 7, at $\alpha = 28^\circ$). The asymmetric flow field does not change with time, a behaviour also mentioned in Ref. 36, where Schlieren pictures of the stationary asymmetric flow are shown. The strong variation in the circumferential surface pressure distribution at $\alpha = 28^\circ$ (see Fig. 7) reproduced completely in several runs.

In the development of the surface pressure with increasing angle of attack, it may be observed that the pressure minimum corresponding to the second separation line decreases to a value, which reaches, at $\alpha = 26^\circ$, a level lower than that of the first separation. Increasing the angle of attack further, the symmetric flow breaks down.

The pressure distribution normal to the cone surface in the leeward symmetry plane reveals a minimum at some distance above the cone (Fig. 9, obtained from probe measurements), indicating the position where the conical cross-flow achieves its highest speed, as is shown in Fig. 17, to be discussed later. At $\alpha = 22.6^\circ$, evidently the boundary condition at the surface leeward meridian can only be met by the generation of a shock wave extending slightly across the symmetry plane; the associated pressure rise follows from Fig. 9. In Ref. 24 a Schlieren picture containing this shock wave, has been inserted.

The development of the surface pressure at the leeward meridian ($\phi = 180^\circ$) is given as a function of α in Fig. 10. For values of α between 0° and 6° the experimental results coincide with the numerical data of Ref. 7. For $\alpha = 12.4^\circ$ and 17.2° the pressures are computed using a shock capturing technique (SCT). In between $\alpha = 13^\circ$ and 17° the measured pressures remain constant. It appears that the SCT results are more or less confirmed by the experiments up to $\alpha = 17^\circ$. At larger angles of attack the pressure decreases again; unfortunately, no numerical data are available in this range.

3.2. Flow field experiments

The results of the present flow field measurements, made with a conical-head probe, are essentially in agreement with those of Ref. 24; they are more refined and yield a more complete overall picture of the flow field. For instance the lines of constant conical Mach number show, better than the lines of constant Pitot pressure in Ref. 24, the location of the shear layer in the shoulder region of the cone. From Fig. 11 it appears that across the shear layer and towards the cone surface, the pressure increases slightly to a maximum value and then decreases again. This behaviour suggests the occurrence of an inflection point in the paths of the conical streamlines, in such points the pressure gradient changes sign. At $\alpha = 17.2^\circ$ (Fig. 12) the elongated region of isobars, observed at $\alpha = 12.4^\circ$ along the shoulder of the cone, has disappeared and several isolated regions occur. Here, as well as for $\alpha = 22.6^\circ$, in Fig. 13, it is difficult to determine the shear layer from the lines of constant static pressure. The shear layer may rather be determined from cross plots of the Pitot pressure distribution or from the lines of constant conical Mach number (see also Figs. 14, 15, 16). The location of embedded shocks follows directly from the isobars, because locally the isobars have the tendency to bend along the shock wave. The core of the main vortex is revealed as an isolated region in Figs. 12 and 13. Since data could be obtained closer to the cone surface than in Ref. 24, the static pressures in the flow field could be matched adequately to the surface pressures.

In Figs. 14, 15 and 16 lines of constant conical Mach number M_c are presented. The shear layer manifests itself very well, because the lines of constant conical Mach number run parallel to it with a very narrow spacing in between them. A new aspect of the present results at $\alpha = 17.2^\circ$ is the bulge in the conical-sonic line at the separation point of the shear layer; in Ref. 24 only the onset of it could be observed. At $\alpha = 22.6^\circ$ the bulge is terminated by a weak shock wave (Fig. 16 and also Fig. 13). Although a faint evidence of it was detected in the results of Ref. 24, no attention was paid to it. The supersonic bulge probably corresponds to the supersonic tongue in the flow field that results from a normal shock wave-boundary layer interaction. In the shoulder region of the cone at $\alpha = 22.6^\circ$ a system of three shock waves exists, two of them join to form a lambda type of shock wave. The latter shock wave partly accomplishes a transition from conical supersonic to conical subsonic flow, and partly it maintains a conical supersonic flow.

The dashed lines in Figs. 15 and 16 represent the positions where the conical velocity components v or w are zero. These lines pass through the core of the main vortex, suggesting that the core is a conical stagnation point. If α is increased from 17.2° to 22.6° the line $v = 0$ extends towards the symmetry plane. One would expect that for larger angles of attack a lower and an upper intersection point with the symmetry plane exists, in other words two conical stagnation points, since $w = 0$ in the symmetry plane. In the lower conical stagnation point the dividing streamline, separating the outer inviscid flow from the flow absorbed by the vortex, terminates. The upper one represents the position of a vortical singularity.

In Fig. 17 the distribution of the conical Mach number in the leeward symmetry plane is given, the minus sign denotes a negative value of v . Since no datum points are available in the aerodynamic symmetry plane, the values of M_c have been obtained by extrapolation from both sides of the symmetry plane. For $\alpha = 22.6^\circ$, this procedure led to $M_c = 0 \pm 0.01$ for values of z/R in between 1.95 and 2.55. From this M_c distribution no conclusive judgement can be given about the existence of a vortical singularity at a z/R -value near 2.5.

In inviscid theory the velocity component u is discontinuous in a vortical singularity, therefore it is interesting to consider the measured u -distribution. A plot of u/U_∞ versus z/R in the neighbourhood of 2.5 has been inserted in Fig. 17, U_∞ is the free stream velocity. At either side of $z/R = 2.5$ the level of the u/U_∞ -distribution is different, which confirms the existence of the vortical singularity in the leeward symmetry plane. It is also in agreement with the flow direction measurements, given in Fig. 22, where a conical stagnation point is indicated at z/R of about 1.9 and one at about 2.5. The conical stagnation points in Ref. 24 were found at $z/R = 1.95$ and 2.75. Interpolating the results of Ref. 36, where a complete different measuring technique was used, the corresponding values are 1.95 and 2.65. It is not clear why, at $\alpha = 22.6^\circ$, in the present experiments the M_c -distribution in the symmetry plane shows such a flattened character, which is different from the results of Ref. 24. It may be assumed, however, that more values should be attached to the present measurements, because of the higher resolution of the measurements.

The flow directions have been plotted in Figs. 18 to 22. The length of the pointers is not completely related to the magnitude of the velocity, because the length is bounded by a minimum and a maximum value. Fig. 18 shows that already at $\alpha = 9.2^\circ$ vortex formation takes place, which is not in contradiction with the oil flow pattern at $\alpha = 10^\circ$ (Fig. 4). If α is increased, the vortex structure becomes more distinct, see Figs. 19 and 20. At $\alpha = 17.2^\circ$ a secondary vortex is observed in the flow field, since the probe is capable to reach the region where the secondary vortex is felt. Using the measured flow directions it has been possible to compute conical streamlines, see Figs. 21 and 22. The dividing streamline at $\alpha = 22.6^\circ$ (Fig. 22), separates the vortex flow from the outer inviscid flow. A phenomenon worth mentioning is the difference in the shape of the vortex at $\alpha = 17.2$ and the vortex at $\alpha = 22.6^\circ$. In the latter case a vortex is shown which is rather elongated in the vertical direction.

Finally, the most important results have been summarized in Fig. 23, where an overall picture of the flow pattern around the cone at high angle of attack has been constructed. Apart from minor retouches and with the exception of the conical streamlines towards the upper conical stagnation point (the vortical singularity), Fig. 23 represents to scale the results of the present experiments on the cone at $\alpha = 22.6^\circ$.

4. CONCLUDING REMARKS

An experimental investigation of the flow on the surface and in the external field of a 7.5° semi-apex angle cone has been performed at a free stream Mach number of 2.94 and a Reynolds number of $45 \cdot 10^6$ per meter. The explorations with a conical-head probe led to the determination of the conical Mach number, the conical flow direction and the static pressure in the leeward flow field of the cone at several angles of attack. The following conclusions may be drawn:

- By comparing detailed surface pressure measurements with surface oil flow patterns, it is possible to correlate the circumferential pressure distribution to the type of flow separation.
- At angles of attack (α) larger than approximately 1.5 times the cone half-angle (θ_c), the cross flow is found to separate from the cone surface. On either side of the cone a shear layer is generated, rolling up into a symmetrical vortex system.
- At α/θ_c of about 2.5 an embedded shock wave is observed, originating at the circumferential point where the shear layer separates from the cone surface.
- At $\alpha/\theta_c = 3$ ($\alpha = 22.6^\circ$ in the present explorations), a system of shock waves is found inside the region of conical supersonic flow. The core of the main vortex (only one half of the cone is considered) appears to be well away from the cone surface (0.25 R) and from the leeward symmetry plane (0.3 R).
- The vortex flow regime, at $\alpha/\theta_c = 3$, is separated from the external inviscid flow by a dividing streamline. In the external inviscid flow, evidence is found for the existence of a vortical singularity in the leeward symmetry plane.
- When α is increased beyond $\alpha/\theta_c = 3.5$ (26° in the present investigation), the flow loses its symmetry. The asymmetric surface oil flow pattern and circumferential surface pressure distribution suggest stationary flow.
- Based on the present measurements and on previous results, a model of the flow for $\alpha/\theta_c > 2.5$ has been constructed (Fig. 23).

REFERENCES

1. Radhakrishnan, R., The exact flow behind a yawed conical shock, College of Aeronautics, Cranfield, Rep. No. 116, 1958.
2. Stocker, P.M. and Mauger, F.E., Supersonic flow past cones of general cross-section, Journ. Fluid. Mech., Vol. 13, No. 3, July 1962, pp. 383-389.
3. Moretti, G., Inviscid flow field past a pointed cone at an angle of attack, Part I, Analysis, Techn. Rep. No. 577, General Applied Sciences Laboratories, Dec. 1965.
4. Babenko, K.I., Investigation of a three-dimensional supersonic gas flow around conic bodies, Proc. 11th Int. Congr. Appl. Mech., Munich, 1974, Springer-Verlag, 1966, pp 749-755.
5. Babenko, K.I., et al., Three-dimensional flow of ideal gas past smooth bodies, NASA TT F-380, April 1966.
6. Gonidou, R., Ecoulements supersoniques autour de cônes en incidences, La Recherche Aéronautique, No. 120, Sept.-Oct. 1967, pp 11-19.
7. Jones, D.J., Numerical solutions of the flow field for conical bodies in a supersonic stream, Nat. Res. Council Canada, Aeron. Rep. LR-507, July 1968.
8. Moretti, G., and Pandolfi, M., Analysis of the inviscid flow about a yawed cone, Preliminary Studies, Pibal Rep. No. 72-18, Polytechn. Inst. Brooklyn, May 1972.
9. Holt, M. and Adego, D.E., A numerical method for calculating steady unsymmetrical flow past cones, Journ. Comp. Phys., Vol. 5, 1970, pp 463-486.
10. Bachmanova, N.S., et al., Supersonic flow past circular cones at large angles of attack, Fluid Dynamics, Vol. 8, No. 6, May 1975, pp 915-919.
11. Fletcher, C.A.J., GTT method applied to cones at large angles of attack, Proc. 4th Int. Conf. Num. Meth. Fluid Dyn., Ed. R. Richtmyer, Lecture Notes in Physics, Vol. 35, Springer-Verlag, West Berlin, 1975.
12. Daywitt, J., et al., Supersonic flow about circular cones at large angles of attack; a floating discontinuity approach, AIAA 15th Aerospace Sci. Meeting, Los Angeles, Cal., Jan. 24-26, 1977, Paper No. 77-86.
13. Ferri, A., Supersonic flow around circular cones at angles of attack, NACA Techn. Note 2236, Nov. 1950.
14. Melnik, R.E., Vortical singularities in conical flow, AIAA Journ., Vol. 5, No. 4, April 1967, pp 631-637.
15. Smith, J.H.B., Remarks on the structure of conical flow, Progr. Aerospace Sci., Vol. 12, Pergamon Press, 1972, pp 241-272.

16. Bakker, P.G., and Bannink, W.J., Conical stagnation points in the supersonic flow around slender circular cones at incidence, Delft Univ. of Technology, Dept. Aeron. Eng., Rep. VTH-184, Delft, Nov. 1974.
17. Kurosaki, M., A study of supersonic conical flow, Inst. of Space and Aeron. Sci., Univ. of Tokyo, Rep. No. 498, July 1973, pp 263-313.
18. Bakker, P.G., Conical streamlines and pressure distribution in the vicinity of conical stagnation points in isentropic flow, Delft Univ. of Technology, Dept. Aerosp. Eng., Rep. LR-244, Delft, April 1977.
19. Salas, M., and Daywitt, J., Structure of the conical flow field about external corners, AIAA 16th Aerospace Sci. Meeting, Huntsville, Alabama, Jan. 16-18, 1978, Paper No. 78-59.
20. Bakker, P.G. et al., On the structure of the potential flow field near singularities in conical flow, Delft Univ. of Technology, Dept. Aerosp. Eng., to be published.
21. Feldhuhn, R.H., and Winkelmann, A.E., Separated flow phenomena on a slender cone at Mach 5, Naval Ordnance Lab, White Oak, Maryland, NOL-TR-69-36, March 1969.
22. Stetson, K.F., Boundary layer separation on slender cones at angle of attack, AIAA Journ., Vol. 10, No. 5, May 1972, pp 642-648.
23. Feldhuhn, R.H., et al., An experimental investigation of the flow field around a yawed cone, AIAA Journ., Vol. 9, No. 6, June 1971, pp 1074-1081.
24. Nebbeling, C., and Bannink, W.J., Experimental investigation of the supersonic flow past a slender cone at high incidence, Journ. Fluid Mech., Vol. 87, part 3, 1978, p 475.
25. Zakkay, V., et al., Leeward flow field description over cones at large incidence, Advanced Technology Laboratories Inc., Westbury, N.Y., Rep. AFFDL-TR-74-19, April 1974.
26. Miyazawa, M., A numerical analysis of conical flow fields, Proc. 10th Int. Symp. Space Technol. & Sci., Tokyo, 1973, pp 433-442.
27. Lubard, S.C., and Helliwell, W.S., Calculations of the flow on a cone at high angles of attack, AIAA 6th Fluid and Plasma Dyn. Conf., Palm Springs, Cal., July 16-18, 1973, Paper No. 73-636.
28. Bontoux, P., and Roux, B., Compressible turbulent boundary layer on a yawed cone, AIAA 8th Fluid and Plasma Dyn. Conf., Hartford, Connecticut, June 16-18, 1975, Paper No. 75-858.
29. Massot, P., Détermination de quelques caractéristiques de la couche limite tridimensionnelle turbulente autour d'un cône à $M_\infty = 5$, Thèse de Doctorat de Spécialité, Université d'Aix-Marseille, Avril 1976.
30. Fletcher, C.A.J., Supersonic viscous flow over cones at large angles of attack, Journ. Fluid Mech., Vol. 74, part 3, 1976, pp 561-591.
31. McRae, D.S., A numerical study of supersonic viscous cone flow at high angle of attack, AIAA 14th Aerospace Sci. Meeting, Washington D.C., Jan. 26-28, 1976, Paper No. 76-97.
32. Tracy, R.R., Hypersonic flow over a yawed cone, Graduate Aeron. Labs., Cal. Inst. Technol., Pasadena, Mem. No. 69, 1963.
33. Rainbird, W.J., The external flow field about yawed circular cones, Conf. Proc. Specialists Meeting Fluid Dyn. Panel AGARD on Hypersonic Bound. Layers & Flow Fields, London, May 1-3, 1968, CP No. 30, Paper No. 19.
34. Yahalom, R., An experimental investigation of supersonic flow past yawed cones, Aeron. Sci. Div., Univ. of California, Berkeley, 1970, AFOSR-TR-71-2183.
35. Guffroy, D, et al., Etude théorique et expérimentale de la couche limite autour d'un cône circulaire placé en incidence dans un courant hypersonique, Conf. Proc. Spec. Meeting Fluid Dyn. Panel AGARD on Hyp. Bound. Layers & Flow Fields, London, May 1-3, 1968, CP No. 30, Paper No. 20.
36. Houwink, R., and Nebbeling, C., Experimental investigation of the leeward flow field of a cone at high incidence in supersonic flow, Delft Progress Report, Series C, 1, 1975, pp 69-76.

ACKNOWLEDGEMENTS

The authors wish to express their appreciation to Messrs. P.G. Bakker and T.P.M. Hendriks for their valuable contribution to many discussions concerning the subject matter; also the expertness of Mr. Hendriks in preparing the computer program for the reduction of the data is greatly appreciated. The assistance of Messrs. E.W. de Keizer, N.J. Lam and G.A.F. Bekink is gratefully acknowledged for their efficient operation of the facilities and preparation of instrumentation.

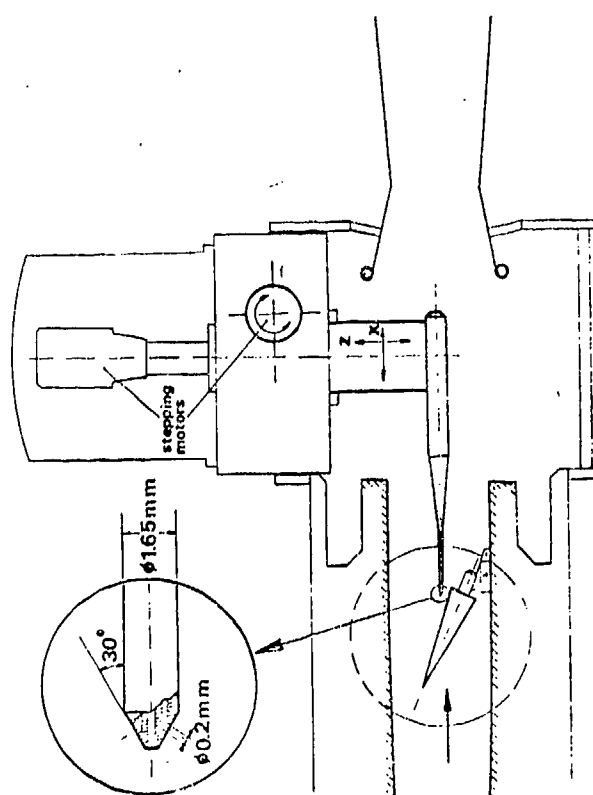


FIG.1 TEST ARRANGEMENT FOR FLOW FIELD EXPLORATION

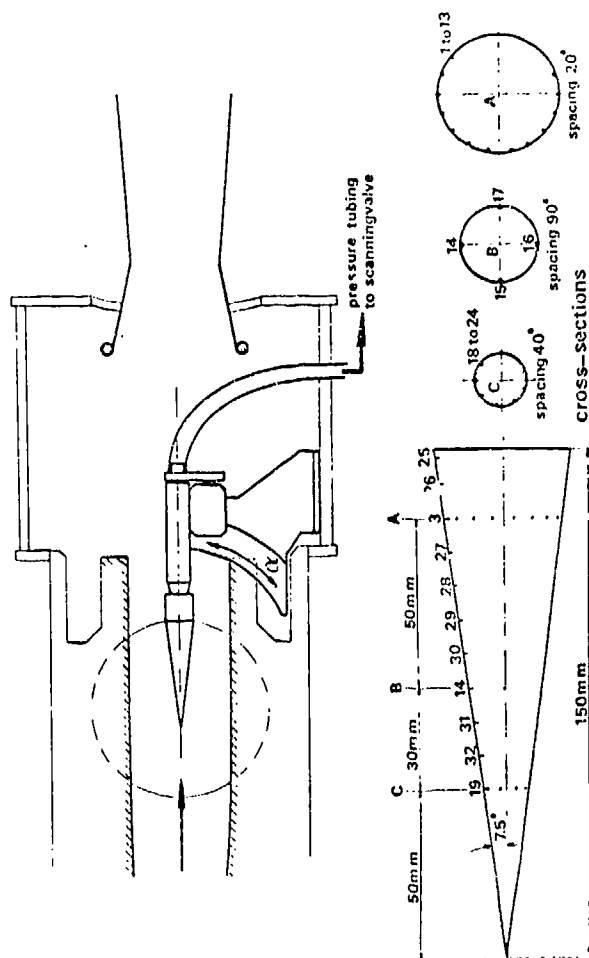


FIG.2 TEST ARRANGEMENT FOR SURFACE PRESSURE MEASUREMENTS

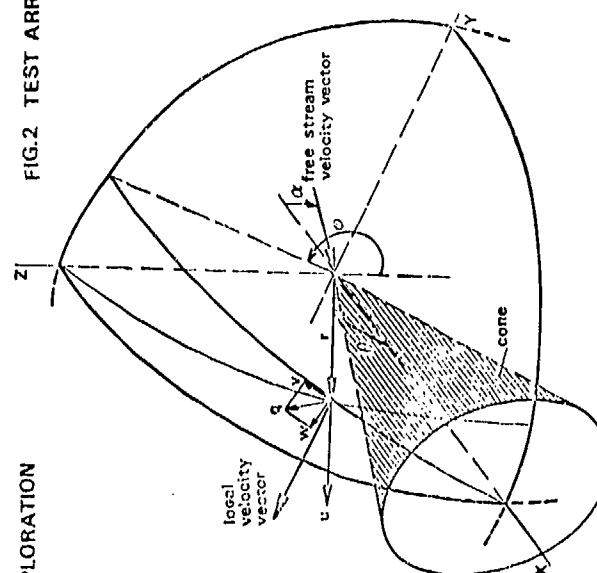


FIG.3 CONICAL COORDINATE SYSTEM AND VELOCITY COMPONENTS

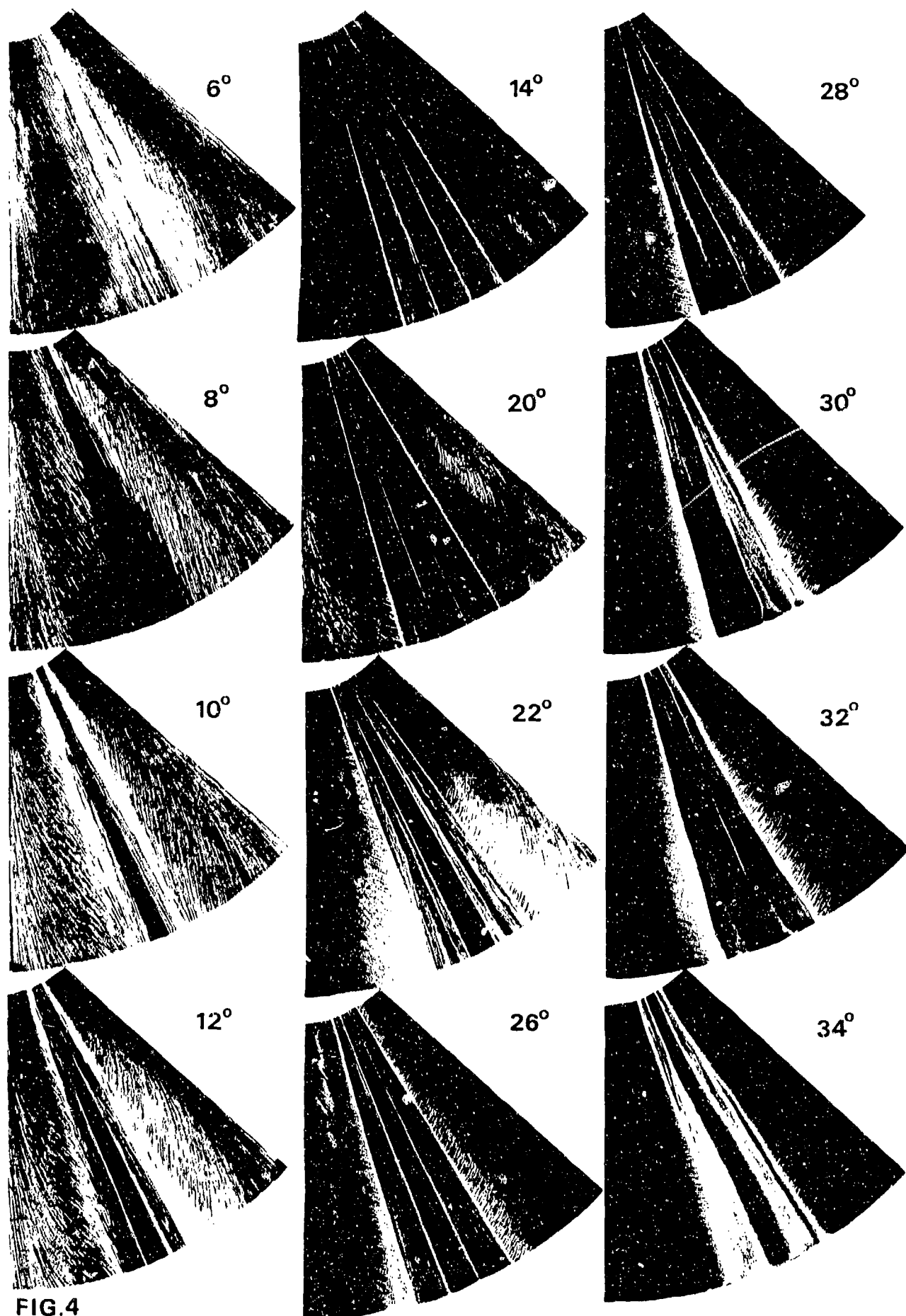


FIG.4

SURFACE OIL FLOW PATTERNS AT DIFFERENT ANGLES OF ATTACK

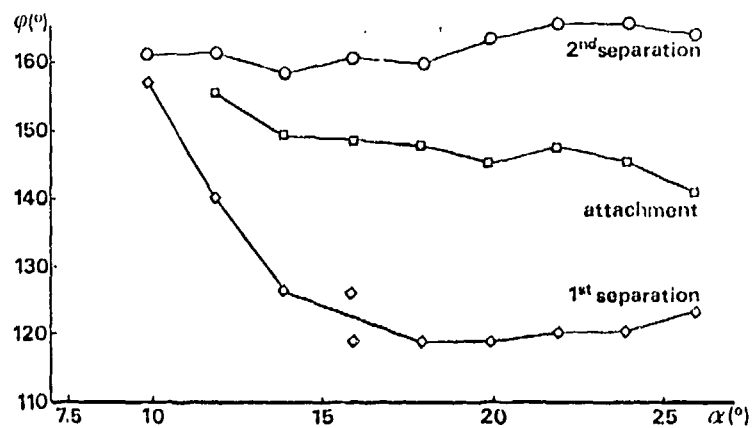


FIG. 5 CIRCUMFERENTIAL LOCATION OF SEPARATION AND ATTACHMENT LINES

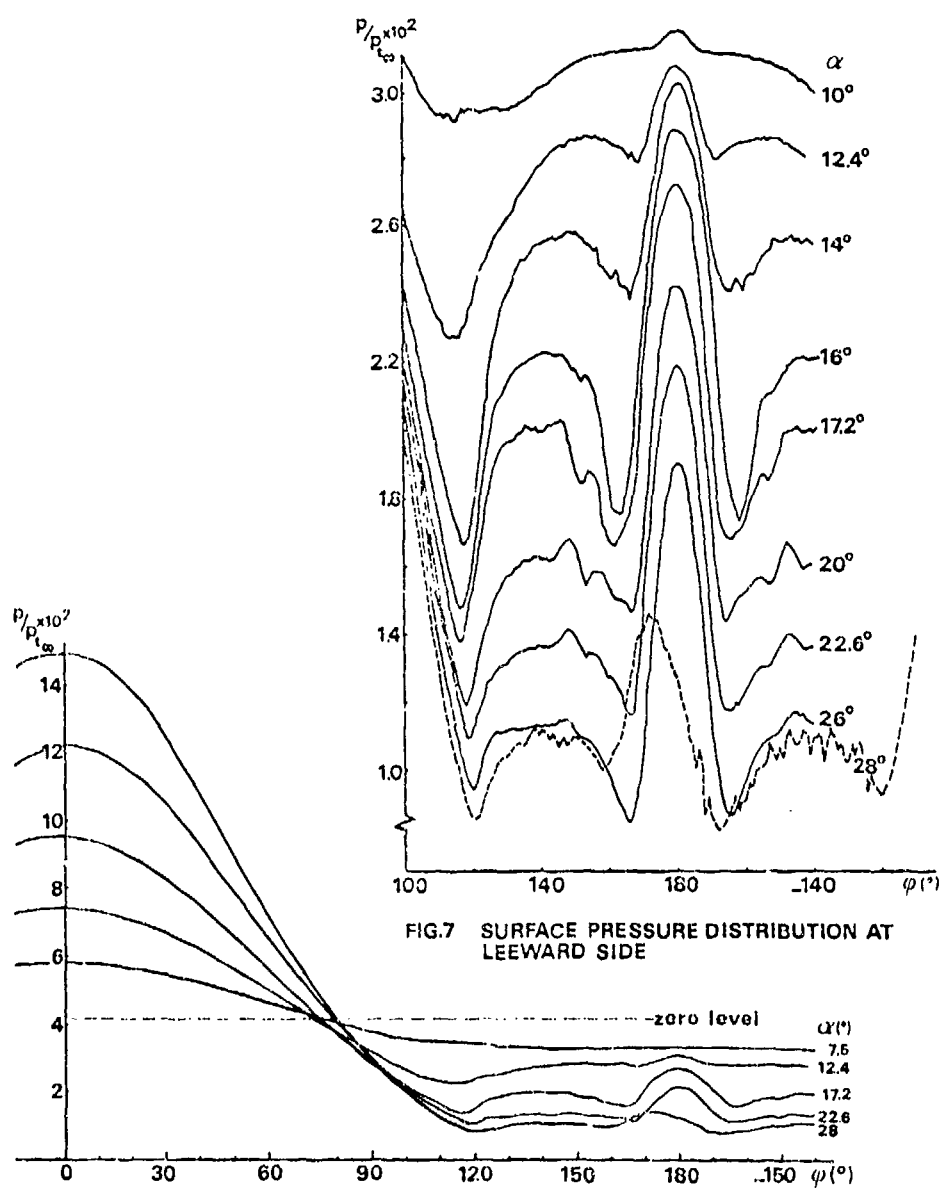


FIG. 6 SURFACE PRESSURE DISTRIBUTION

FIG. 7 SURFACE PRESSURE DISTRIBUTION AT LEEWARD SIDE

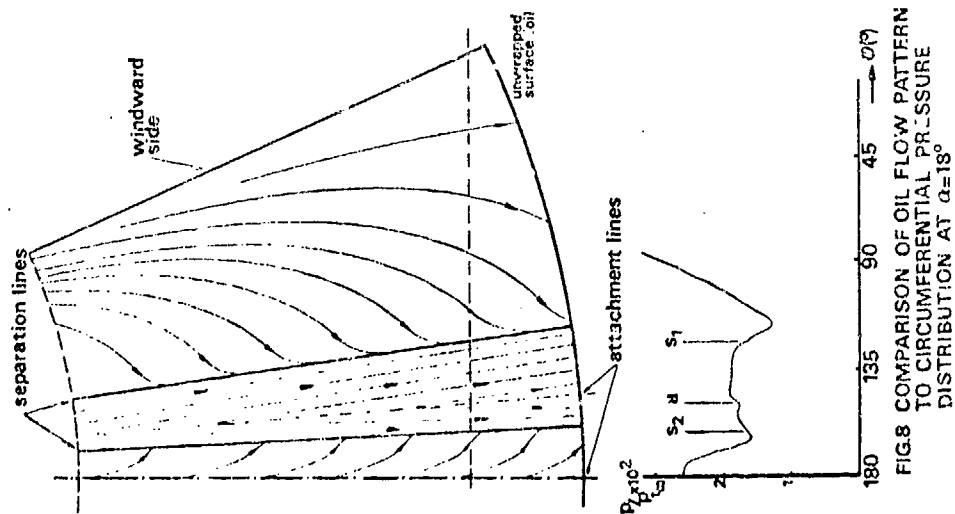


FIG. 8 COMPARISON OF OIL FLOW PATTERN TO CIRCUMFERENTIAL PRESSURE DISTRIBUTION AT $\alpha = 18^\circ$

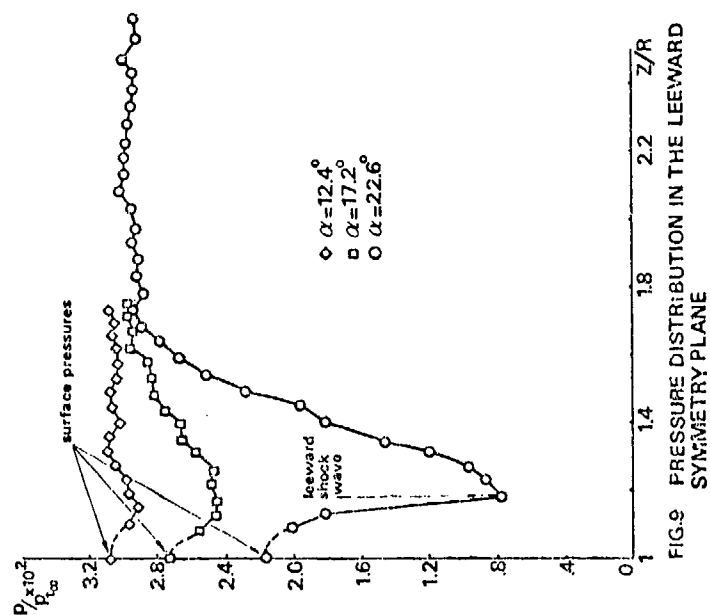


FIG. 9 PRESSURE DISTRIBUTION IN THE LEEWARD SYMMETRY PLANE

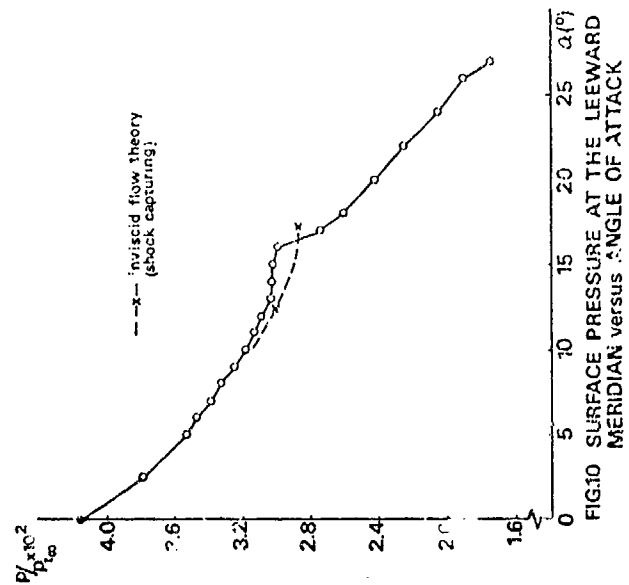
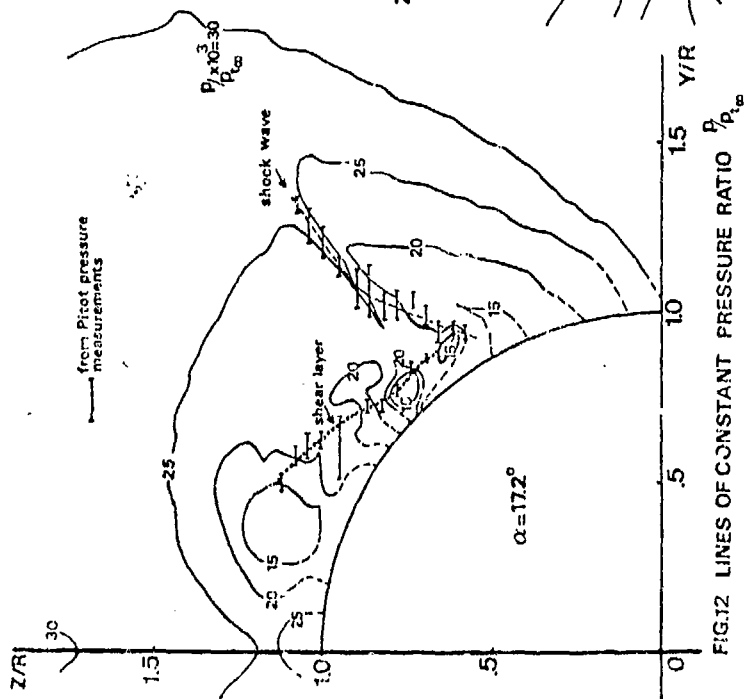
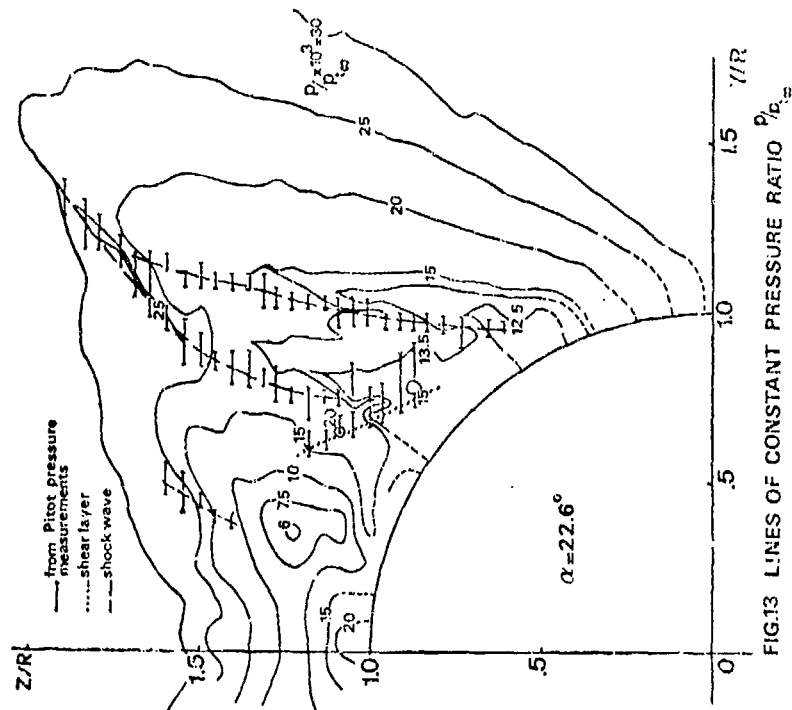
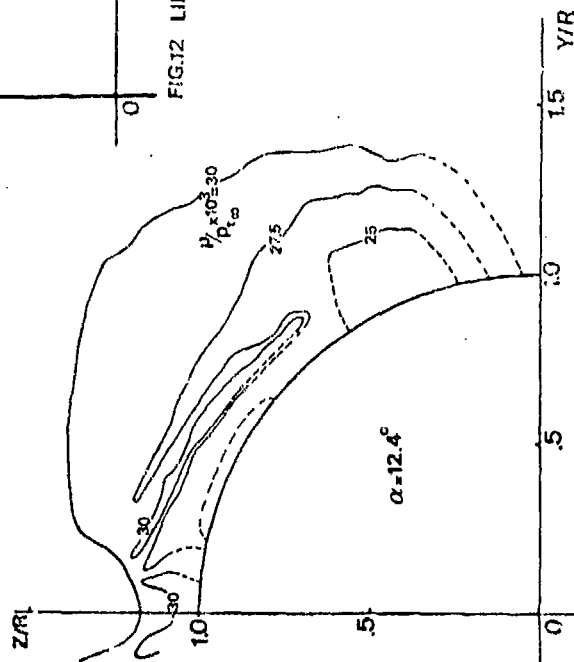


FIG. 10 SURFACE PRESSURE AT THE LEEWARD MERIDIAN VERSUS ANGLE OF ATTACK

FIG.11 LINES OF CONSTANT PRESSURE RATIO p/p_∞ FIG.12 LINES OF CONSTANT PRESSURE RATIO p/p_∞ FIG.13 LINES OF CONSTANT PRESSURE RATIO p/p_∞

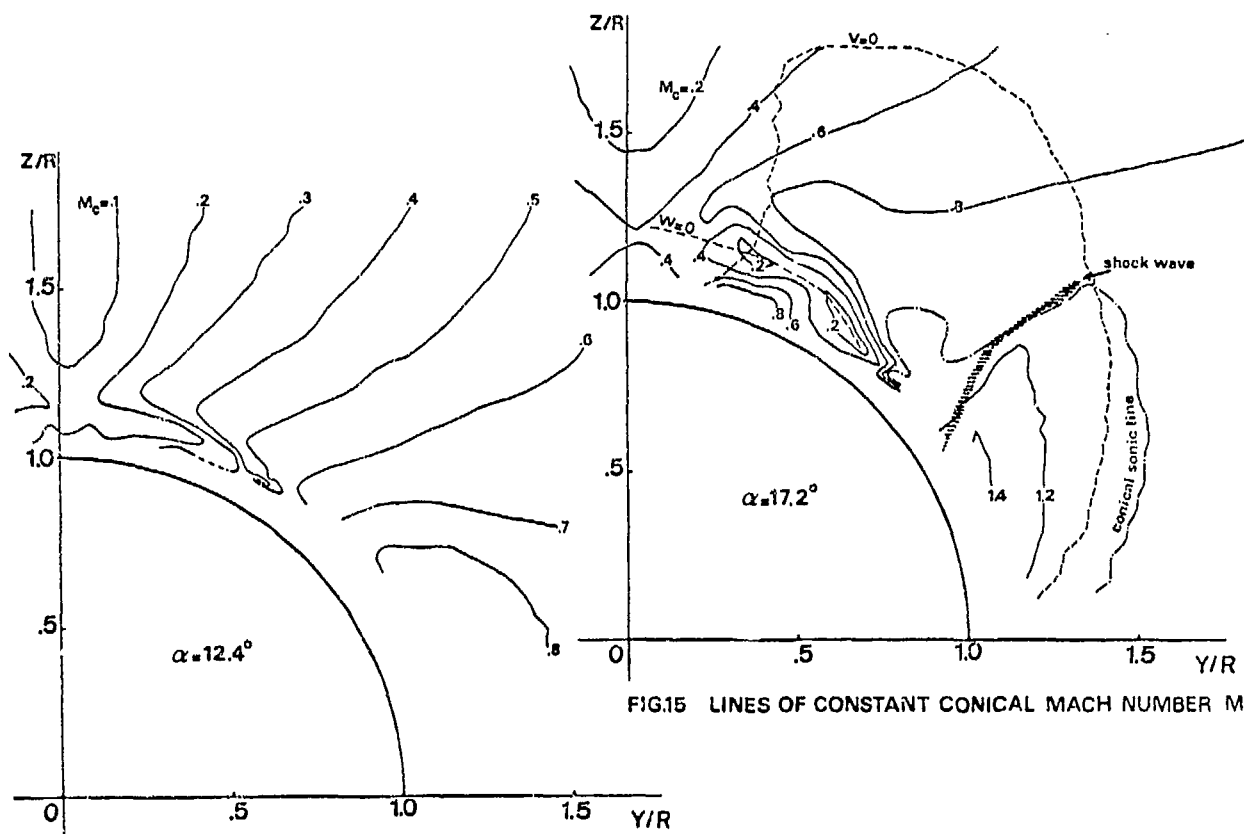


FIG.14 LINES OF CONSTANT CONICAL MACH NUMBER M_c

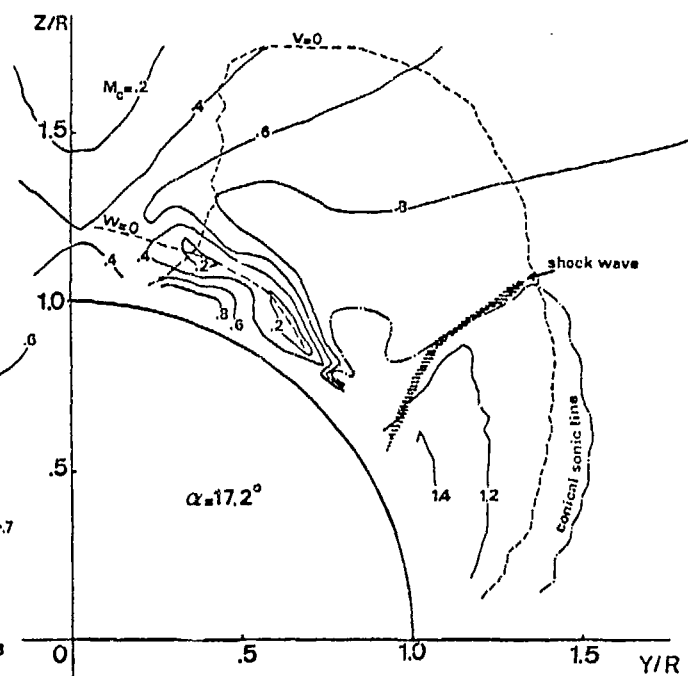


FIG.15 LINES OF CONSTANT CONICAL MACH NUMBER M_c

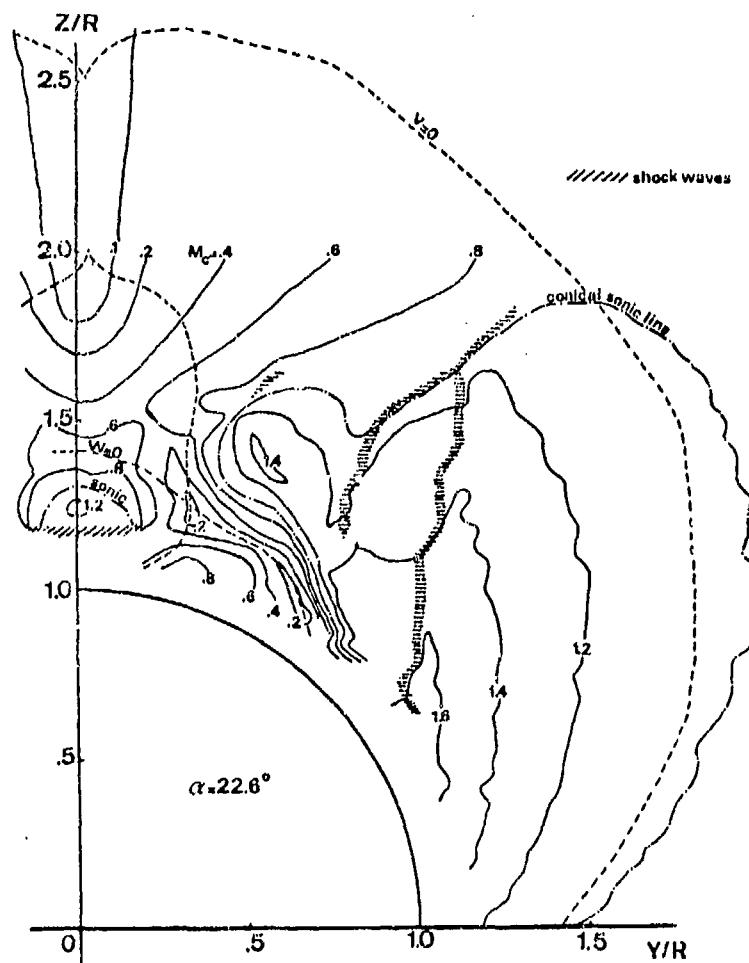
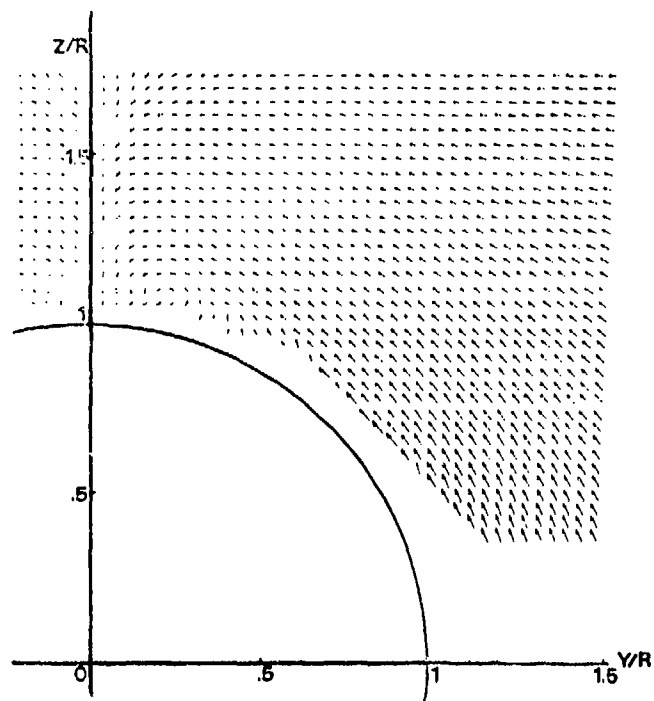
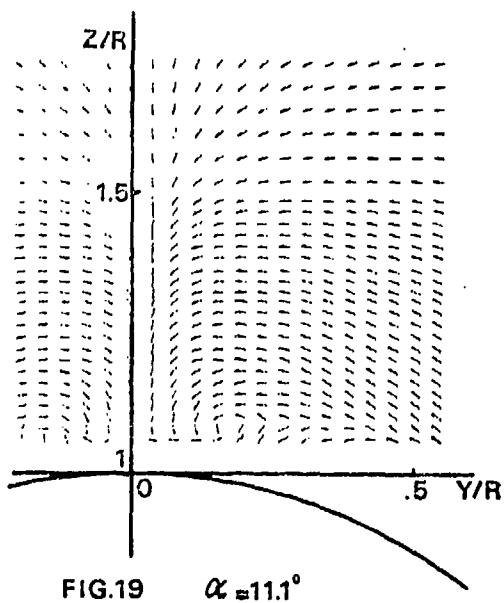
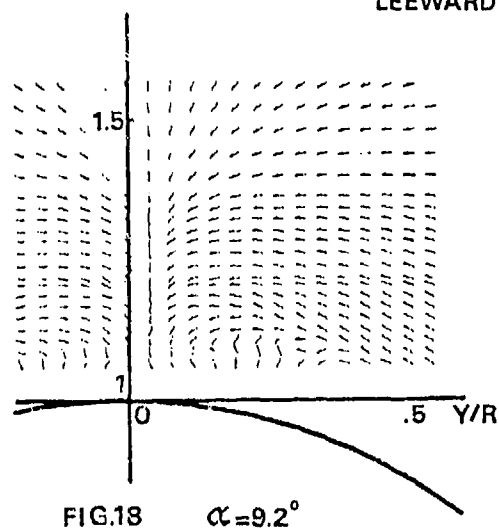
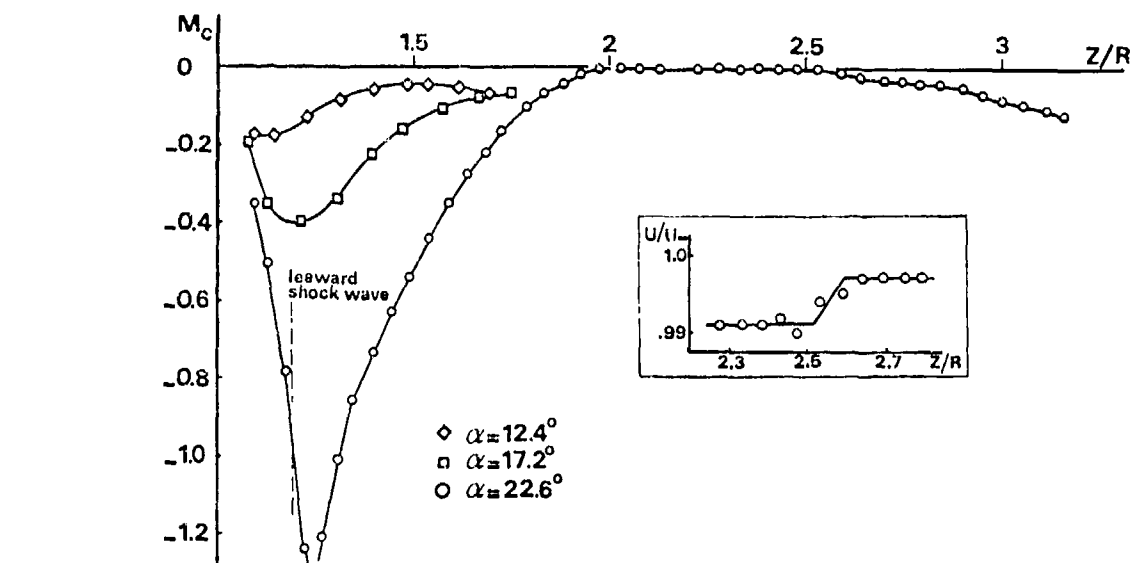
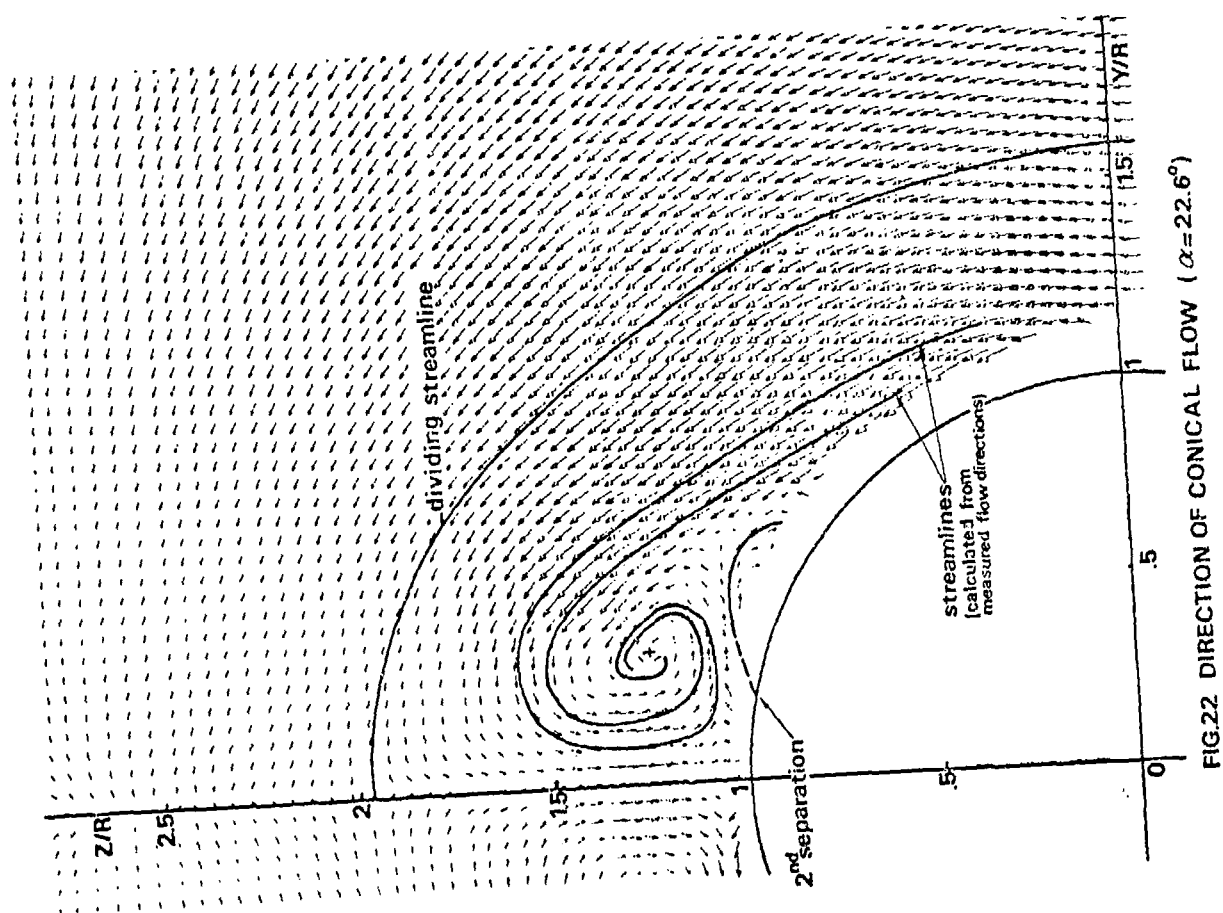
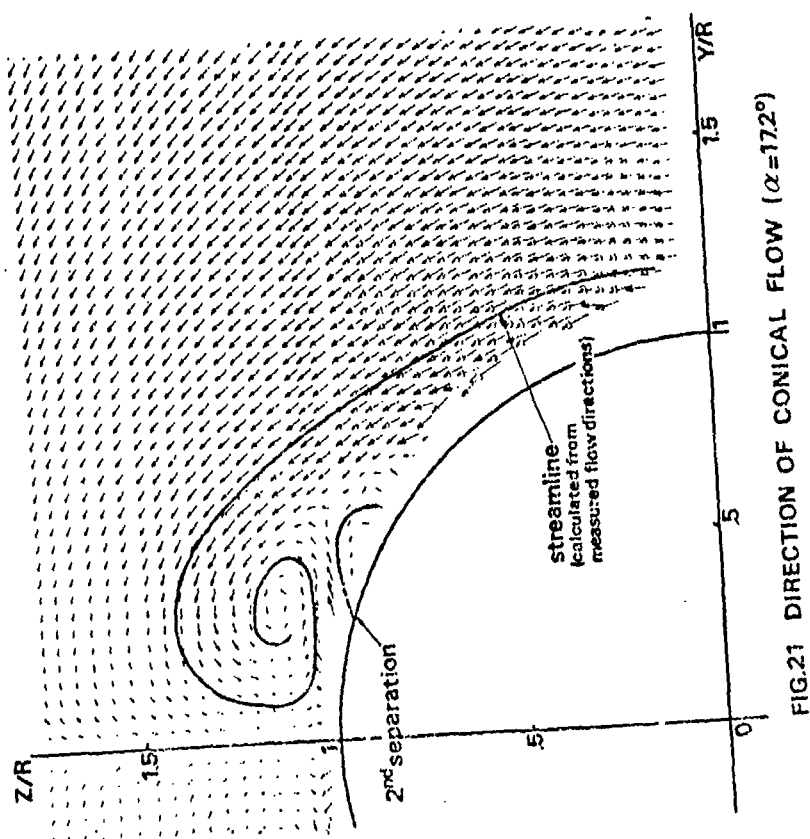


FIG.16 LINES OF CONSTANT CONICAL MACH NUMBER M_c



DIRECTION OF CONICAL FLOW

FIG.22 DIRECTION OF CONICAL FLOW ($\alpha = 22.6^\circ$)FIG.21 DIRECTION OF CONICAL FLOW ($\alpha = 172^\circ$)

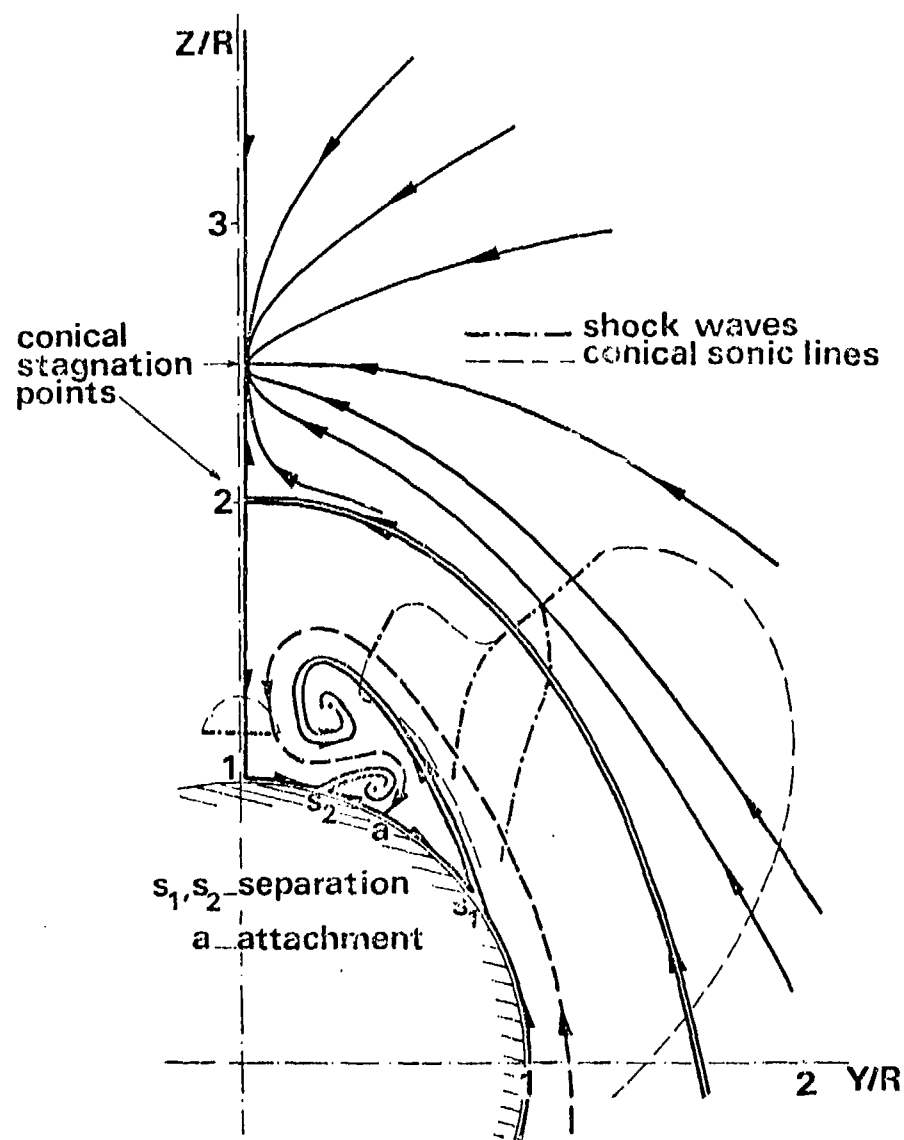


FIG.23 STRUCTURE OF CONICAL FLOW
($\alpha \sim 22^\circ$)

NUMERICAL SIMULATION OF SUPERSONIC CONE FLOW AT HIGH ANGLE OF ATTACK

Major David S. McRae
Air Force Flight Dynamics Laboratory
Ames Research Center, NASA
Mail Stop 206-3
Moffett Field, California 94035, U.S.A.

and

M. Y. Hussaini
ICASE, Langley Research Center, NASA
Langley AFB, Virginia 23665, U.S.A.

SUMMARY

A conical symmetry assumption is applied to the full Navier-Stokes equations resulting in an equation set containing time and two coordinate directions as independent variables. The set is integrated by use of MacCormack's finite difference technique for the particular case of sharp cones at incidence. Solutions are obtained and compared with experiment for auxiliary conditions corresponding to both laminar and turbulent flows. Closure for the turbulent flow case is provided by use of a scalar eddy viscosity model based on the mixing length hypothesis. The numerical results are compared with the experimental data of Tracy, McEldeery, and Rainbird. Excellent agreement is found between the numerical laminar flow results and the data of Tracy. Modifications to the eddy viscosity model were found which led to excellent surface pressure and surface flow direction agreement for turbulent flow at low supersonic Mach numbers. However, it is apparent that further work on the turbulence model is necessary for agreement at higher supersonic Mach numbers.

NOMENCLATURE

B	vector in governing equations	w	velocity in ϕ direction
C_p	specific heat at constant pressure	x	distance along cone surface, measured from vertex
C_v	specific heat at constant volume	Y	distance above cone surface
C_{pr}	local surface pressure coefficient, $(p_w - p_\infty)/0.7\rho_\infty M_\infty^2$	α	angle of attack
C_1, C_2	constants in turbulence model	γ	ratio of specific heats (C_p/C_v)
D	time vector in governing equations	θ	coordinate, conical angle
e	total internal energy ($C_v T + V^2/2$)	δ_e	boundary layer thickness
E	vector in governing equations (r coordinate)	λ	relaxation parameter
F	vector in governing equations (θ coordinate)	μ_∞	absolute viscosity
G	vector in governing equations (ϕ coordinate)	μ_t	eddy viscosity
H	vector in governing equations (constant terms)	ρ	density
\bar{h}	nondimensional height above cone surface, Y/R	σ_n	normal stress
J	vector resulting from application of conical symmetry assumption	τ	shear stress
K	thermal conductivity	ϕ	coordinate, circumferential angle
k	$(\gamma - 1)/2\gamma$	\bar{X}	hypersonic similarity parameter $(M_\infty^3/Re_x)^{1/2}$
λ	mixing length	SUBSCRIPTS	
Pr	Prandtl number	c	cone
p	pressure	e	edge value
\dot{q}	heat transfer rate	f	final location
R	radius of cone at distance r from apex	i	initial location
Re	Reynolds number ($V_{\max} \rho_\infty r / \mu$)	j, k	mesh point location
R_g	gas constant	ℓ	laminar quantity
r	radial coordinate (measured from cone vertex)	n	normal direction
S	shear stress tensor	P	Pitot quantity
T	temperature	s	stagnation quantity
t	time	t	turbulent quantity
\tilde{U}	predicted velocity	w	wall value
u	velocity in r direction	x	local quantity based on distance from cone vertex
V	total velocity $(u^2 + v^2 + w^2)^{1/2}$	∞	free-stream quantity
V_{\max}	maximum adiabatic velocity $(2\gamma/(\gamma - 1)R_g T_\infty)^{1/2}$	o	initial location
v	velocity in θ direction	1, 2, 3	pertaining to r, θ , ϕ , direction
		θ, ϕ	coordinate directions

SUPERSCRIPTS

T transpose

i time level

1. INTRODUCTION

Supersonic conical flow has been of interest to aerodynamicists for many years. The use of the slender cone as a basic shape for ballistic reentry vehicles has ensured a continued interest in the high-speed flow fields around these bodies. An additional reason for examining flow about cones is that it has (at angle of attack) the combination of a very simple geometry and a very complicated 3-dimensional separated flow field. Cone flows are therefore excellent models for experimental or computational studies of 3-dimensional separated flows.

The essential feature of inviscid conical flow is that no variation exists in any fluid quantity along rays passing through the conical vertex of the body. This feature, sometimes referred to as conical symmetry, allows steady-state solutions of the governing equations to be obtained in only two dimensions. Solutions for inviscid flow about conical bodies are available at a variety of conditions (Refs. 1-5). These steady-state solutions are normally obtained by two means: (1) the temporal derivative terms are retained and the solution is marched in time until a steady state is obtained; or (2) the spatial derivatives along the conical rays are retained and the solution is marched along the ray until a steady state is obtained. For the particular case of sharp cones, these inviscid solutions provide reasonable agreement with experiment up until relative incidences (α/α_c) at which significant nonlinear lift is generated (Ref. 6). This nonlinear lift apparently becomes significant at incidences where viscous influence on the lee side of the cone also becomes large. In addition to the obvious failure of the inviscid techniques to properly model the lee-side viscous effects as angle of attack increases, instabilities in these techniques are frequently encountered at higher values of relative incidence. Previous attempts to include the effects of viscosity without increased computational difficulty have resorted to fictitious alteration of the lee surface of the cone in order to obtain the proper pressure distribution (Refs. 7, 8). Unfortunately, these techniques require considerable knowledge about the pressure distribution to be matched before the computation can be successful. More suitable studies have been undertaken which include viscous effects through solution of the parabolized Navier-Stokes equations (Ref. 9) or of modified 3-dimensional boundary layer equations (Ref. 10). However, neither of these studies has taken full advantage of the inherent characteristics of conical flow. The remainder of this paper will present a means (Refs. 11, 12) of including viscous effects in the governing equations while retaining the simplification of conical symmetry. Solutions to the resulting equations are obtained for boundary conditions corresponding to both laminar and turbulent flow conditions.

2. GOVERNING EQUATIONS

The unsteady, compressible Navier-Stokes equations written in weak conservation form for a spherical polar coordinate system (as in Ref. 11):

$$\frac{\partial D}{\partial t} + \frac{\partial E}{\partial r} + \frac{\partial F}{\partial \theta} + \frac{\partial G}{\partial \phi} + H = 0 \quad (1)$$

The vectors D, E, F, G, and H denote

$$\begin{aligned} D^T &= r^2 \sin \theta (B), & E^T &= r^2 \sin \theta (uB - S_1), \\ F^T &= r \sin \theta (vB - S_2), & G^T &= r (wB - S_3) \end{aligned}$$

$$H = r \sin \theta \begin{bmatrix} 0 \\ -(\rho v^2 - \tau_{22}) - (\rho w^2 - \tau_{33}) \\ -\cot \theta (\rho w - \tau_{33}) + \rho uv - \tau_{12} \\ \cot \theta (\rho v - \tau_{23}) + \rho uw - \tau_{13} \\ 0 \end{bmatrix}$$

where

$$B = (\rho, \rho u, \rho v, \rho w, \rho e)$$

$$S_i = (0, \tau_{11}, \tau_{12}, \tau_{13}, -\dot{q}_1 + u\tau_{11} + v\tau_{12} + w\tau_{13}) ; \quad i = 1, 2, 3$$

$$k = \frac{\gamma - 1}{2\gamma} ; \quad \gamma = \text{ratio of specific heats}$$

and the superscript T denotes the transpose. The stress tensor terms will be defined in detail later. The velocity components are nondimensionalized with respect to the maximum adiabatic velocity V_{max} , the state variables with respect to their stagnation values, and the time with respect to r/V_{max} ; r is the spherical radius measured from the apex of the cone. The variables p, ρ, u, v, w , and e denote, respectively, the nondimensional pressure, the density, the velocity components in the (r, θ, ϕ) coordinate directions, and the total internal energy.

A conical flow, as noted in the previous section, can be described as an inviscid steady flow in which all flow quantities are constant along rays passing through the vertex of the conical body. If a body-fixed spherical coordinate system (Fig. 1) centered at the vertex of the conical body is used to describe the flow, then all spherical surfaces must have the same vector and scalar values of the flow quantities for a given (θ, ϕ) point on each surface. Therefore, all derivatives of flow quantities with respect to the spherical radius (r) of these spherical surfaces from the origin must be zero. This has the effect of reducing the number of independent variables in the problem by one.

Examination of experimental studies of supersonic flow over conical bodies (Refs. 13-15) reveals that these flows exhibit approximate conical behavior downstream from the nose region even though relatively

large viscous regions exist. Cross (Ref. 13) determined that the viscous layer growth on the lee side of a delta wing in supersonic flow was essentially conical. The oil flow separation traces for sharp cones in the experimental study of Stetson (Ref. 15) are approximately straight (but the conical vertex of these traces is displaced downstream by nose effects). Therefore, in concert with an idea first broached by D. A. Anderson of Iowa State University (private communication) for axial corner flow, the conically symmetric flow approximation ($\partial/\partial r \approx 0$) is applied to all terms in Eq. (1).

The resulting equation is:

$$\frac{\partial D}{\partial t} + \frac{\partial F}{\partial \theta} + \frac{\partial G}{\partial \phi} + H' = 0 \quad (2)$$

where:

(1) D, F, and G are unchanged except in the definition of the stress terms.

$$(2) \frac{\partial}{\partial r} \left[\frac{E}{r^2 \sin \theta} \right] = \frac{1}{r} (S_1) - \frac{1}{r} (0, 0, 0, 0, \dot{q}_1) = J$$

$$(3) H' = H + \frac{2E}{r} + Jr^2 \sin \theta$$

or

$$H' = r \sin \theta \begin{bmatrix} \rho u \\ -(\rho v^2 - \tau_{22}) - (\rho w^2 - \tau_{33}) + 2(\rho u^2 + kp) - (\tau_{11} + kp) \\ -\cot \theta (\rho w^2 - \tau_{33}) + 3\rho uv - 2\tau_{12} \\ \cot \theta (\rho vw - \tau_{23}) + 3\rho uw - 2\tau_{13} \\ -2u(\rho e + kp) - (\tau_{11} + kp)u - v\tau_{12} - w\tau_{13} \end{bmatrix}$$

It is significant that when time is nondimensionalized by the parameter r/V_{\max} , the r dependence in Eq. (2) is contained in the Reynolds number. The net effect is that the calculation is carried out at a single (θ, ϕ) spherical surface with the distance of this surface from the cone apex determined by the Reynolds number. Therefore, all spherical radius scaling is now contained in the Reynolds number alone.

The nondimensional stress and heat transfer terms for this equation set are defined as follows:

$$\begin{aligned} \tau_{12} = \tau_{21} &= \frac{1}{Re} \left(\frac{\partial u}{\partial \theta} - v \right) \\ \tau_{13} = \tau_{31} &= \frac{1}{Re \sin \theta} \left(\frac{\partial u}{\partial \phi} - w \sin \theta \right) \\ \tau_{23} = \tau_{32} &= \frac{1}{Re \sin \theta} \left[\frac{\partial}{\partial \theta} (w \sin \theta) - 2w \cos \theta + \frac{\partial v}{\partial \phi} \right] \\ \tau_{11} &= -kp + \sigma_n \\ \tau_{22} &= -kp + \frac{2}{Re} \left(\frac{\partial v}{\partial \theta} + u \right) + \sigma_n \\ \tau_{33} &= -kp + \frac{2}{Re \sin \theta} \left(\frac{\partial w}{\partial \phi} + u \sin \theta + v \cos \theta \right) + \sigma_n \end{aligned} \quad (3)$$

and

$$\dot{q}_1 = 0, \dot{q}_2 = -\frac{1}{2RePr} \frac{\partial T}{\partial \theta}, \dot{q}_3 = -\frac{1}{2RePr} \frac{\partial T}{\partial \phi}$$

where

$$\sigma_n = -\frac{2}{3Re \sin \theta} \left(2u \sin \theta + \frac{\partial}{\partial \theta} (v \sin \theta) + \frac{\partial w}{\partial \phi} \right)$$

$$Pr = \frac{\mu C_p}{K} = \text{Prandtl number}$$

At this point, it is prudent to examine further the physical implications of the approximations applied to the above equation set. It should first be noted that the only approximations now inherent to the equations are that a perfect gas is required and that conically symmetric flow is assumed at all points on the θ, ϕ calculation surface. The conical symmetry assumption seems to imply a linear growth of the viscous layer from the apex of the cone. However, this is not the case. The flow is in reality only locally linear with the viscous layer thickness properly scaled by the Reynolds number based on the spherical radius from the cone apex. Any differences noted between the calculated results and the experimentally measured results must be due to the neglect of the very small gradient in the r coordinate direction or to the neglect of upstream influence.

To further illustrate this point, computations were performed using the conically symmetric equation set for several stations along a cone at zero angle of attack and compared with the well-known hypersonic

weak interaction theory (Ref. 16). Results of the surface pressure comparison for Tracy's conditions (Ref. 17) are given in Fig. 2. The agreement is quite good and illustrates that the locus of viscous layer thicknesses is not linear when calculations are performed at several stations along a cone.

3. TURBULENCE MODEL

For the eddy viscosity of the turbulent flow, simple algebraic relations similar to those of Harris and Morris (Ref. 18) are assumed. The effective coefficient of viscosity μ and thermal conductivity K are then defined as follows:

$$\begin{aligned}\bar{\mu} &= \bar{\mu}_l + \bar{\mu}_t \\ K &= C_p \left(\frac{\bar{\mu}_l}{Pr_l} + \frac{\bar{\mu}_t}{Pr_t} \right)\end{aligned}\quad (4)$$

where μ_l is the molecular viscosity and Pr_l is the Prandtl number associated with the laminar flow (0.72). The turbulent Prandtl number Pr_t is assumed to be 0.9 in the present analysis; and

$$\begin{aligned}\bar{\mu}_t &= \bar{\rho} \frac{\bar{x}^2}{r} \left[\left(\frac{\tau_{12}}{\bar{\mu}} \right)^2 + \left(\frac{\tau_{32}}{\bar{\mu}} \right)^2 \right]^{1/2} \\ \bar{x} &= 0.09 r \theta_e \tanh \left[\frac{0.4}{0.09} \frac{\theta}{\theta_e} \right] Q \\ Q &= 1 - \exp \left(- \frac{r \theta}{A} \right), \quad A = 26.0 \frac{\bar{\mu}}{\bar{\rho}} \left(\frac{\bar{\rho}}{\bar{\tau}} \right)_w^{1/2} \\ \tau_w &= \left[(\tau_{12})_w^2 + (\tau_{23})_w^2 \right]^{1/2}\end{aligned}\quad (5)$$

A bar denotes a dimensional quantity and the subscript w indicates evaluation at the wall. The viscous layer edge (θ_e) is defined to be that mesh point nearest the wall where the modulus of vorticity is less than 0.0025 times the wall value.

During the course of this and previous calculations (Ref. 12) using this eddy viscosity turbulence model, it was found that modifications to the model were necessary to obtain adequate agreement with experiment. These modifications were aimed at obtaining a model for both the attached axial and the attached and separated circumferential flow structure on the lee side of the cone. This flow structure was modeled in the present study by separate descriptions of eddy viscosity for the (θ, ϕ) coordinate directions. The θ component of eddy viscosity was also used in the r momentum equation. However, since derivatives with respect to r are neglected when the conical symmetry assumption is applied, the θ component of eddy viscosity will in general multiply stress terms in which the leading derivative of the velocity components is with respect to θ . The ϕ component of eddy viscosity multiplies stress terms with respect to ϕ (exceptions to both statements are found in the H matrix). This implies, that the θ and ϕ components of eddy viscosity scale the axial and circumferential shear stress, respectively. It should be noted that Sturek et al. (Ref. 19) and Rotta (Ref. 20) have also found it beneficial to use different descriptions of eddy viscosity for different coordinate directions in 3-dimensional flow fields.

The specific modifications to Eq. (5) used in the present study were:

$$\begin{aligned}\bar{\mu}_{t\theta} &= C_1 \bar{\rho} \bar{x}^2 \left| \frac{\tau_{12}}{\bar{\mu}} \right| \\ \bar{\mu}_{t\phi} &= C_2 \bar{\rho} \bar{x}^2 \left| \frac{\tau_{32}}{\bar{\mu}} \right|\end{aligned}\quad \left. \vphantom{\begin{aligned}\bar{\mu}_{t\theta} &= C_1 \bar{\rho} \bar{x}^2 \left| \frac{\tau_{12}}{\bar{\mu}} \right| \\ \bar{\mu}_{t\phi} &= C_2 \bar{\rho} \bar{x}^2 \left| \frac{\tau_{32}}{\bar{\mu}} \right|} \right\} \text{Used for McElderry's data (Ref. 21)} \quad (6)$$

Although this model gave the best agreement attained with the $M = 6$ data of McElderry, it gave unrealistic behavior in the vicinity of the cross-flow separation point when applied at a lower Mach number.

A somewhat different approach, based on previous results (Ref. 12) was taken in the $M = 1.8$ case of Rainbird (Ref. 22). The eddy viscosity model [Eq. (5)] was used in unmodified form in the attached region up to the vicinity of the expected cross-flow separation line. The eddy viscosity in the cross-flow separated region was reduced by a constant factor, and a linear connection bracketing the expected separation line was used to connect the reduced value in the separated region to the unmodified eddy viscosity. Smoothing of the resulting θ component of the turbulent Reynolds number was used to insure no sharp discontinuities due to this procedure. In equation form, this procedure is:

$$\begin{aligned}\bar{\mu}_{t\theta} &= \bar{\mu}_{t\phi} = 1.0 \bar{\mu}_t \quad 0^\circ < \phi < \phi_i \\ \bar{\mu}_{t\theta} &= \bar{\mu}_{t\phi} = \left[1.0 - \frac{(1.0 - C_2)}{(\phi_f - \phi_i)} (\phi - \phi_i) \right] \bar{\mu}_t \quad \phi_i < \phi < \phi_f \\ \bar{\mu}_{t\theta} &= \bar{\mu}_{t\phi} = C_2 \bar{\mu}_t \quad \phi_f < \phi < 180^\circ\end{aligned}\quad (7)$$

where ϕ_i and ϕ_f indicate the beginning and end of the contour. In both McElderry's and Rainbird's cases, a relaxation procedure (Ref. 22) was used in the cross-flow direction ($\bar{\mu}_{t\phi}$) only:

$$\bar{\mu}'_{t\phi} = \bar{\mu}_{t\phi_0} + (\bar{\mu}_{\phi} - \bar{\mu}_{\phi_0}) \exp(-\Delta\phi/\lambda) \quad (8)$$

where

$$\lambda = 20\theta e_0$$

The initial point for the relaxation was the circumferential mesh point prior to cross-flow separation.

4. THE NUMERICAL INTEGRATION TECHNIQUE

The equation set resulting from the application of the conical symmetry assumption can be solved by time integration on a single spherical surface located at a distance r from the cone apex. A finite difference grid is defined on the spherical surface and MacCormack's (Ref. 24) well-known finite difference technique is applied.

If the solution $D_{j,k}^i$ is known at time $t = i\Delta t$ at each point of the computational mesh on the spherical surface (at a distance r from the cone apex), the solution at time $t = (i+1)\Delta t$ is calculated at each interior mesh point (θ, ϕ) as follows (Ref. 11):

$$\begin{aligned} \text{Predictor: } \bar{D}_{j,k}^{i+1} &= D_{j,k}^i - \frac{\Delta t}{\Delta\theta} (F_{j+1,k}^i - F_{j,k}^i) - \frac{\Delta t}{\Delta\phi} (G_{j,k+1}^i - G_{j,k}^i) - \Delta t H_{j,k}^i \\ \text{Corrector: } D_{j,k}^{i+1} &= \frac{1}{2} \left[D_{j,k}^i + \bar{D}_{j,k}^{i+1} - \frac{\Delta t}{\Delta\theta} (\bar{F}_{j,k}^{i+1} - \bar{F}_{j-1,k}^{i+1}) - \frac{\Delta t}{\Delta\phi} (\bar{G}_{j,k}^{i+1} - \bar{G}_{j,k-1}^{i+1}) - \Delta t \bar{H}_{j,k}^{i+1} \right] \end{aligned} \quad (9)$$

Auxiliary conditions imposed during the integration were as follows: (1) no slip conditions at the body surface with wall temperature maintained constant at the experimentally determined value; (2) free-stream conditions maintained at the outer edge of the mesh; (3) lateral symmetry of the flow quantities maintained along the $\phi = 0^\circ$ and $\phi = 180^\circ$ lines; and (4) initial values for all fluid quantities either free-stream or a previous solution at similar conditions.

The auxiliary conditions at the cone surface were implemented by analytically evaluating the θ momentum equation at the cone surface conditions. The resulting equation is solved for the θ derivative of pressure and is approximated by one-sided finite differences. The equation is applied to obtain the surface pressure after the above equations have been used to obtain updated values of all flow quantities at the interior mesh points. Surface density is then obtained from the equation of state.

The use of free-stream conditions at the outer mesh boundary required that the bow shock wave be captured during the integration. To overcome the oscillations that occurred in the vicinity of the shock wave for high Mach number conditions, a technique called normal stress damping was used (Ref. 11). This technique involved changing the sign on the normal stress term (σ_n) and increasing the magnitude of this term to provide the necessary damping.

5. NUMERICAL RESULTS

The validity of any heretofore untried assumption applied to the governing equations can only be determined through comparison of the results obtained by calculation with results of experiment. To test the validity of the present technique, published experimental data were chosen over a Mach number range of 1.8 to 14 for comparison. Brief comparisons of the calculated results with experimental data are presented here for Mach numbers through 8; further comparisons are available in Ref. 11.

For Reynolds numbers corresponding to laminar flow conditions, the well-documented experimental study of Tracy (Ref. 17) was chosen. These data were collected for a sharp 10° half-angle cone in air at a Mach number of 7.95. The free-stream Reynolds number was $4.1 \times 10^6/m$ with measurements taken 10.16cm from the cone apex. Other conditions were $P_\infty = 1.7878 \times 10^6 \text{ NT/m}^2$ and $T_\infty = 755 \text{ K}$. Calculated and experimental results were obtained at angles of attack from 0° to 24° . Shown in Fig. 3 is the comparison of the experimental and calculated surface pressure at $\alpha = 24^\circ$. The agreement is quite good except on the windward side of the cone, where experimental errors are suspected due to the use of pressure taps which were large in relation to boundary layer thickness.

Figure 4 shows the calculated cross-flow velocity vectors plotted for the $\alpha = 24^\circ$ case. This figure clearly shows the large lee-side vortices found in the experimental study. Also note that two stagnation points exist on the ice plane of symmetry; one associated with the dividing streamline around the vortex, and one "vortical singularity-like" stagnation point. The "vortical singularity-like" stagnation point is characterized by the convergence of the cross-flow velocity vectors to a single point. At the higher Mach numbers calculated, this stagnation point occurs near the edge of the viscous layer for laminar flow or on the cone surface for fully developed turbulent flow conditions. Since the stagnation point does occur at the edge of the viscous layer for the high Mach number cases, discontinuities or changes in gradients of entropy or density (as occurs in inviscid flow) which can be attributed separately to the singularity itself are not noted.

Figure 5 is a pictorial representation of all flow-field features compared with experiment. The calculated features, including the cross-flow separation point and imbedded shock wave position, agree quite well with experiment.

For Reynolds numbers at which boundary layer transition has occurred, two experimental cases were chosen for comparison. The first was the experimental study of McEllderry (Ref. 21), which was made using a 6° half-angle sharp cone at $M = 6.05$ in air. Data were collected at 1.106m along the cone at a free-stream Reynolds number of $1.64 \times 10^7/m$. Stagnation pressure and temperature of the flow were $1.931 \times 10^6 \text{ NT/m}^2$ and 472° K , respectively. Wall temperature was $0.61T_\infty$. Figure 6 gives the comparison of calculated and experimental surface pressure at an angle of attack of 12° . Two calculations are shown, one

for laminar flow at $Re_x = 1.5 \times 10^6$ and one for turbulent flow at $Re_x = 15.0 \times 10^6$. The surface pressure for the laminar case agrees well until the first experimental separation point is reached. The laminar numerical solution does not separate until $\phi = 163^\circ$ with the experimental primary separation occurring at $\phi = 130^\circ$ and a secondary separation at $\phi = 166^\circ$. The calculation using the turbulence model of the present study shows qualitatively a more accurate behavior of the pressure on the lee side (calculated primary separation point at $\phi = 130^\circ$), but too low a turbulent boundary layer displacement thickness from about $\phi = 45^\circ$ onward results in a lower surface pressure than that obtained in the experiment. The turbulence model was modified for this case by using $|\tau_{12}/\mu|$ in μ_t and $|\tau_{32}/\mu|$ in μ_t , rather than the vector sum of τ_{12}/μ and τ_{32}/μ with relaxation of μ_t occurring in accord with Eq. (8).

The second turbulent flow case chosen for comparison is that of Rainbird (Ref. 22). The data of interest were collected on a 5° sharp cone in air at a Mach number of 1.8. Measurements were taken 1.2m along the cone at a free-stream Reynolds number of $2.46 \times 10^7/m$. Stagnation pressure and temperature were $1.723 \times 10^5 \text{ NT/m}^2$ and 294°K , respectively, with wall temperature assumed to be T_{∞} . Figure 7 gives the comparison with experiment of the calculated surface pressure coefficient (Cpr) for three versions of the present turbulence model. The dashed line in Fig. 7 results when the original turbulence model is used at all locations in the flow field without modification or relaxation. As can be seen, the surface Cp resulting from use of the unmodified turbulence model does not match experimental surface Cp in the lee-side separated region. The primary separation line was too close to the leeward plane of symmetry and the secondary separation did not exist. The dotted line in the figure gives the results of freezing both components of the eddy viscosity at the minimum pressure location in the ϕ direction. No relaxation was used in this instance. The resulting surface Cpr distribution matches experiment more closely but the primary separation line was again too close to the leeward plane of symmetry. The secondary separation did exist but was smaller in extent than that of experiment. The solid line in Fig. 7 gives the results of the modified relaxation model [Eq. (7)]. Although little change was evident in surface Cp between the frozen model and the modified relaxation model, the primary and secondary separation lines were both located correctly for a value of $C_2 = 0.3$ in the modified relaxation model. A computation made at a value of $C_2 = 0.35$ (as used for C_1 in Ref. 12) gave results very nearly equal to those with $C_2 = 0.3$ with the exception that the extent of the secondary separated region for $C_2 = 0.35$ did not match experiment. The change in C_2 (0.35 to 0.3) required for agreement in the separated region is most likely due to elliptical effects caused by the change in the turbulence model in the attached region.

Figure 8 gives the comparison of the calculated limiting streamline angle with the experimental surface oil flow angle. Again, the dashed line gives the results using the unmodified turbulence model and the solid line the results of the modified relaxation model. The separation points for experiment and calculation are as follows:

	Primary	Secondary
Experiment	132°	157°
Turbulence model		
Unmodified [Eq. (5)]	139°	--
Frozen	138°	155°
Modified relaxation [Eqs. (7) and (8)]	131°	157°

The surface limiting streamline results using the modified relaxation model agree quite adequately with experiment. Detailed comparison with Rainbird's pitot probe surveys for the modified relaxation model are given in Figs. 9 through 12. The comparison is made normal to the cone centerline at four circumferential locations in the lee-side separated region. Agreement with experiment is quite good at $\phi = 168^\circ$ and $\phi = 160^\circ$, as shown in Figs. 9 and 10. These two pitot surveys bracket the center of the lee-side vortex which occurs at about $\phi = 165^\circ$ in the experiment. The comparison at $\phi = 152^\circ$, in the vicinity of the secondary reattachment, is given in Fig. 11. The agreement in this complex region of the flow is less adequate but still quite reasonable. The major differences seem to be a somewhat higher calculated pitot pressure in the outer part of the secondary separation bubble and a greater overall viscous layer thickness in the calculation at this circumferential station. The final comparison in Fig. 12 at $\phi = 140^\circ$, just after cross-flow separation at $\phi = 131^\circ$, shows again the somewhat greater viscous layer thickness at this location in the computed results.

6. CONCLUSIONS

The solution of the Navier-Stokes equations subject to a conical symmetry assumption is shown to result in entirely adequate agreement with experiment for laminar flow over cones at angle of attack. The present laminar solutions exhibit all of the features found in the experimental case without depending on experiment for input.

For calculations performed at conditions at which boundary layer transition has occurred, the following conclusions are evident:

- (1) Agreement with experiment in the lee-side separated region should not be expected when an unmodified eddy viscosity turbulence model is used.
- (2) The modified relaxation model developed during the present study gives excellent agreement with Rainbird's $M = 1.8$, $\alpha = 2.50^\circ$ experimental data.
- (3) Qualitative agreement with McElderry's data was obtained for the turbulence model proposed for this case. However, it is apparent that further work is required on the present turbulence model to obtain quantitative agreement for the higher Mach number conditions.

REFERENCES

1. Ferri, A.: Supersonic Flow Around Circular Cones at Angles of Attack. NACA Rep. 1045, 1951.
2. Babenko, K. I.; Noskresenskiy, G. P.; Lyubimov, A. N.; and Rusanov, V. V.: Three-Dimensional Flow of an Ideal Gas Past Smooth Bodies. NASA TT F-380, 1964.
3. Kutler, P.; and Lomax, H.: A Systematic Development of the Supersonic Flow Fields Over and Behind Wings and Wing-Body Configurations Using a Shock Capturing Finite Difference Approach. AIAA 9th Aerospace Sciences Meeting, New York, AIAA Paper 71-99, 1971.
4. Fletcher, C.A.J.: GIT Method Applied to Cones at Large Angles of Attack. Proceedings of the Fourth International Conference on Numerical Methods in Fluid Dynamics, Lecture Notes in Physics 35, Berlin, Springer Verlag, 1974, pp. 161-166.
5. Daywitt, J.; Anderson, D.; and Kutler, P.: Supersonic Flow About Circular Cones at Large Angles of Attack: A Floating Discontinuity Approach. AIAA 15th Aerospace Sciences Meeting, 1977, Paper 77-86.
6. Rainbird, W. J.: Turbulent Boundary Layer Growth and Separation on a Yawed Cone. AIAA Journal, vol. 6, no. 12, 1968, pp. 2410-2416.
7. Zakkay, V.; Economos, C.; and Alzner, E.: Leaside Flow Field Description Over Cones at Large Incidence. AFFDL-TR-74-19, Air Force Flight Dynamics Laboratory, Wright-Patterson AFB, Ohio, July 1974.
8. Miyazawa, M.: Numerical Analysis of Conical Flow Fields. Proceedings 10th International Symposium on Space Technology and Science, Tokyo, 1973, pp. 433-442.
9. Lubard, S. C.; and Helliwell, W. S.: Calculation of the Flow on a Cone at High Angle of Attack. AIAA 6th Fluid and Plasma Dynamics Conference, Palm Springs, Calif., AIAA Paper 73-636, 1973.
10. Lin, T. C.; and Rubin, S. G.: Viscous Flow Over a Cone at Moderate Incidence, Part 2, Supersonic Boundary Layer. J. Fluid Mech., vol. 69, pt. 3, 1973, pp. 593-620.
11. McRae, D. S.: The Conically Symmetric Navier Stokes Equations: Numerical Solution for Hypersonic Cone Flow at High Angle of Attack. AFFDL-TR-76-139, Air Force Flight Dynamics Laboratory, Wright-Patterson AFB, Ohio, Mar. 1977.
12. McRae, D. S.; and Hussaini, M. Y.: Supersonic Viscous Flow Over Cones at Incidence. Presented at Sixth International Conference on Numerical Methods in Fluid Dynamics, Tbilisi, USSR, 20 through 25 June, 1978.
13. Cross, Jr., E. J.: Experimental and Analytical Investigation of the Expansion Flow Field Over a Delta Wing at Hypersonic Speeds. ARL 68-0027, 1968, Aerospace Research Laboratories, Wright-Patterson AFB, Ohio, Feb. 1968.
14. Feldhun, R. F.; Winkelman, A. E.; and Pasiuk, L.: An Experimental Investigation of the Flowfield Around a Yawed Cone. AIAA J., vol. 9, 1971, pp. 1074-1081.
15. Stetson, K. F.: Experimental Results of Laminar Boundary Layer Separation on a Slender Cone at Angle of Attack at $M = 14.2$. ARL 71-0127, Aerospace Research Laboratories, Wright-Patterson AFB, Ohio, Aug. 1971.
16. Cox, R. N.; and Crabtree, L. F.: Elements of Hypersonic Aerodynamics. The English Universities Press Ltd. (London), 1965, pp. 195-200.
17. Tracy, R. R.: Hypersonic Flow Over a Yawed Circular Cone. California Institute of Technology, Aeronautical Laboratories Memorandum Number 69, 1963.
18. Harris, J. E.; and Morris, D. J.: Solution of the Three-Dimensional Compressible Boundary Layer Equations With Comparisons to Experimental Data. Proceedings 4th International Conference on Numerical Methods in Fluid Dynamics, 1974, Lecture Notes in Physics No. 35, pp. 204-211.
19. Sturek, W. B.; Dwyer, H. A.; Nietubicz, C. J.; and Kayser, L. D.: Effects of Nonisotropic Eddy Viscosity Models on the Turbulent Boundary Layer Development on a Yawed Spinning Body of Revolution. Presented at Viscous Interacting Flows, Data Exchange Agreement Meeting, Monterey, Calif., 25 through 27 April, 1978.
20. Rotta, J. C.: Turbulence Models for 3-D Thin Shear Layer. Data Exchange Agreement, Goettingen, West Germany, April 1977.
21. McElderry, Jr., E. D.: An Experimental Study of Sharp and Blunt 6 Degree Cones at Large Incidence with a Turbulent Boundary Layer at Mach 6. Air Force Flight Dynamics Laboratory, AFFDL TM-74-170, 1974.
22. Rainbird, W. J.: The External Flow Field About Yawed Circular Cones. AGARD Conference Proceedings No. 30, AGARD Specialists Meeting on Hypersonic Boundary Layers and Flow Fields, London, May 1-3, 1968, pp. 19-1 to 19-19.

23. Shang, J. W.; Hankey, W. L.; and Law, C. H.: Numerical Simulation of Shock Wave Turbulent Boundary Layer Interactions. AIAA J., vol. 14, 1976, pp. 1451-1457.
24. McCormack, R. W.: The Effect of Viscosity in Hypervelocity Impact Cratering. AIAA Paper 69-354, 1969.

ACKNOWLEDGMENT

The authors wish to thank W. L. Hankey, Jr., and J. L. Shang for their helpful suggestions during the present study. Computer resources for this study were supplied by Ames Research Center and the Air Force Flight Dynamics Laboratory. Research performed by the second author while in residence in Langley Research Center-NASA, was partially supported by NASA Contracts NAS1-14101 and NAS1-14472.

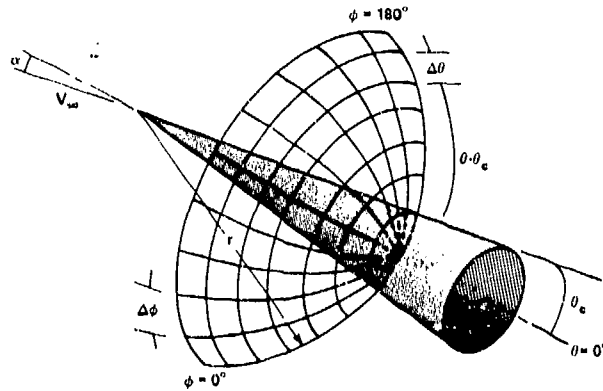


Fig. 1 Coordinate system and computational mesh.

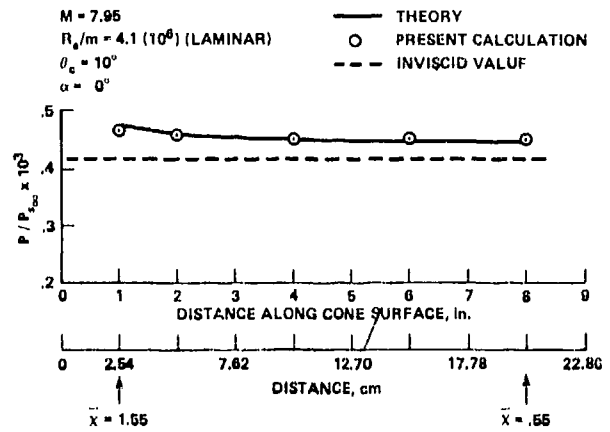
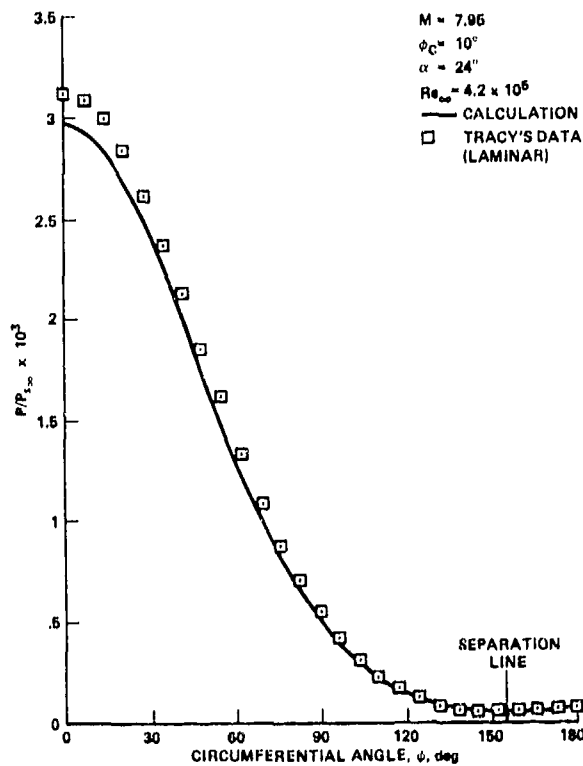
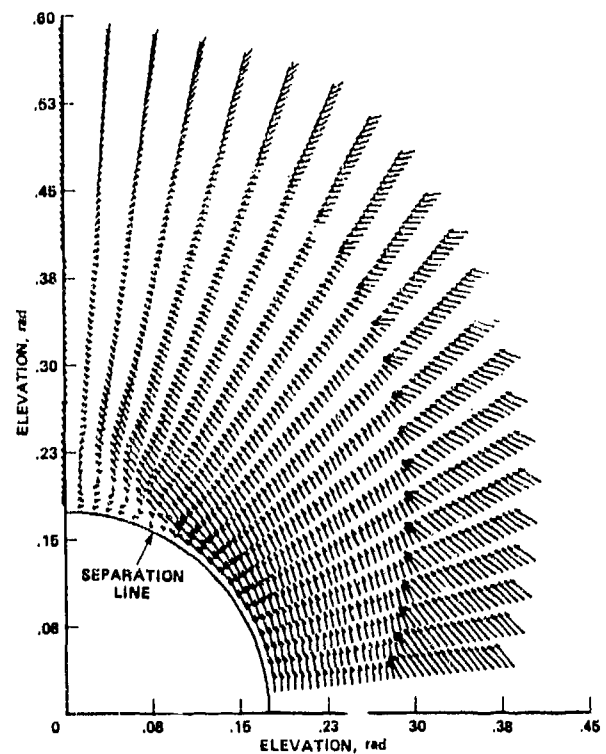


Fig. 2 Comparison with weak interaction theory.

Fig. 3 Comparison of calculated and experimental surface pressure at Tracy's conditions (Ref. 17), $\alpha = 24^\circ$.Fig. 4 Calculated cross-flow velocity vectors as seen on spherical surface at Tracy's conditions (Ref. 17), $\alpha = 24^\circ$.

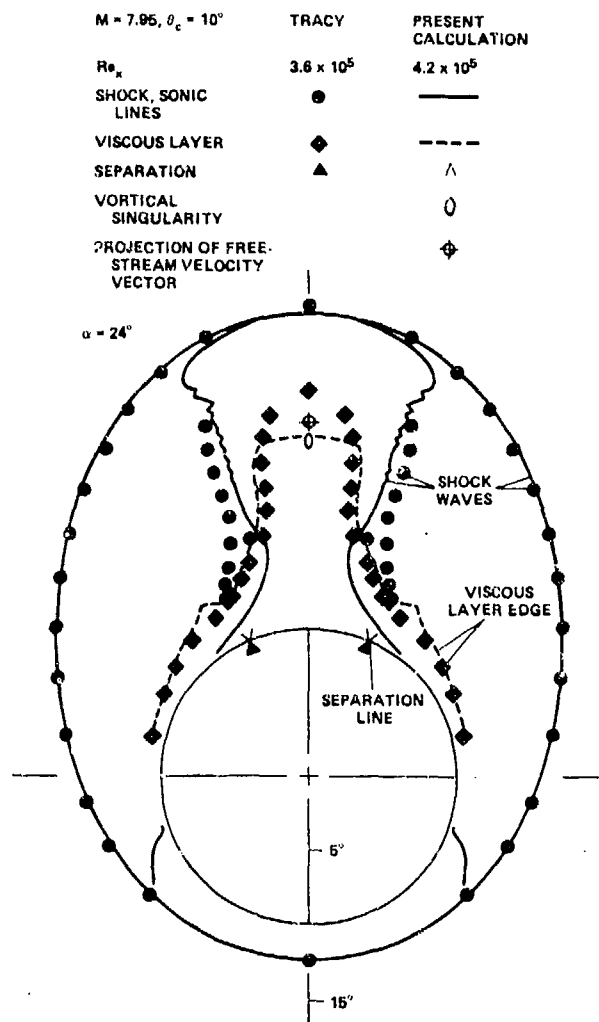


Fig. 5 Comparison of calculated and experimental flow-field features at Tracy's conditions (Ref. 17), $\alpha = 24^\circ$.

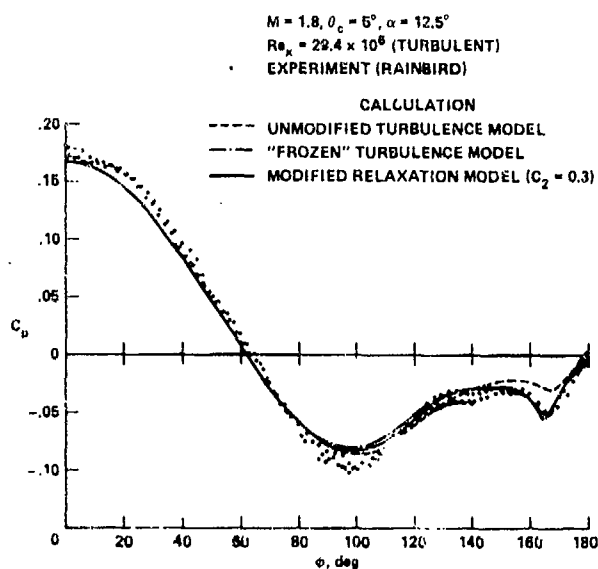


Fig. 7 Comparison of calculated and experimental surface pressure coefficient at Rainbird's conditions (Ref. 22), $\alpha = 12.5^\circ$.

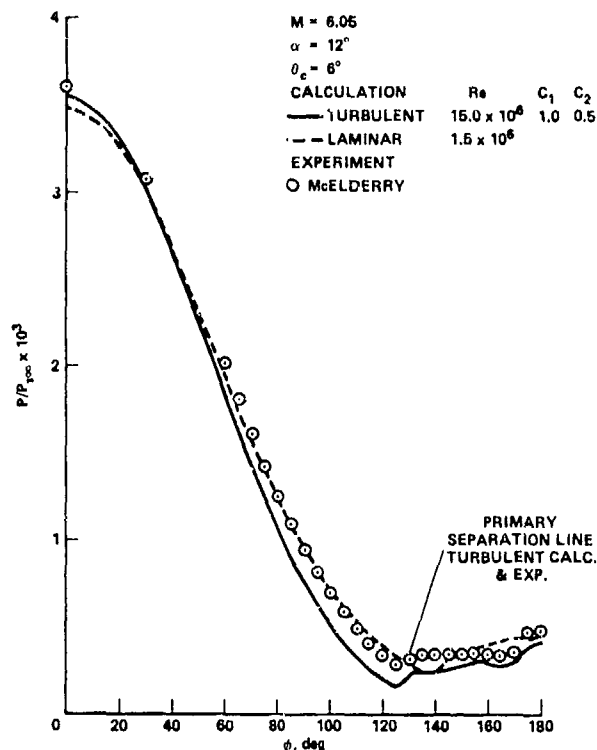


Fig. 6 Comparison of calculated and experimental surface pressure at McElderry's conditions (Ref. 21), $\alpha = 12^\circ$.

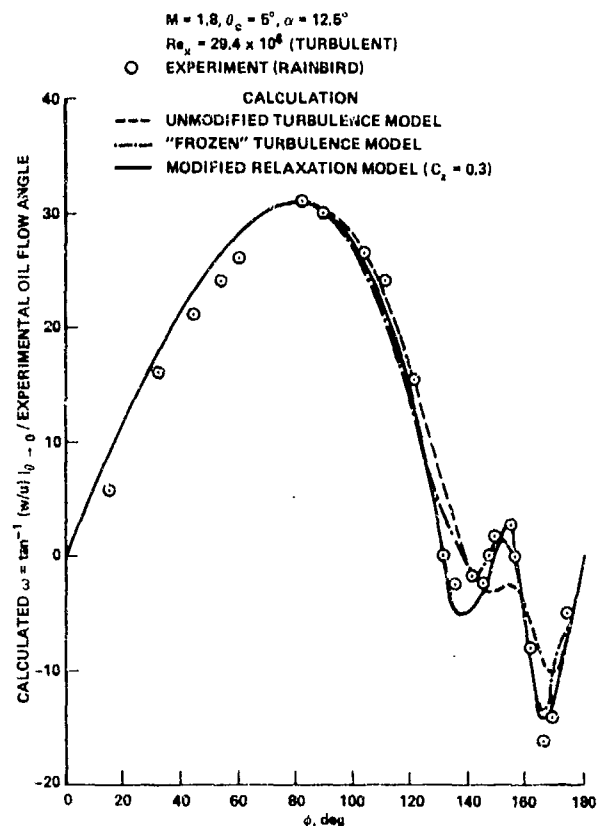


Fig. 8 Comparison of calculated surface streamline angle with experimental surface oil flow angle at Rainbird's conditions (Ref. 22), $\alpha = 12.5^\circ$.

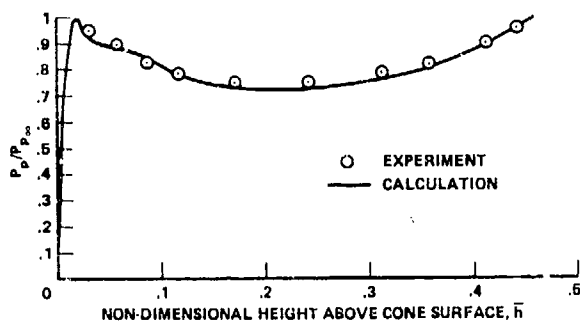


Fig. 9 Comparison of calculated and experimental pitot pressure survey at Rainbird's conditions (Ref. 22), $\phi = 168^\circ$.

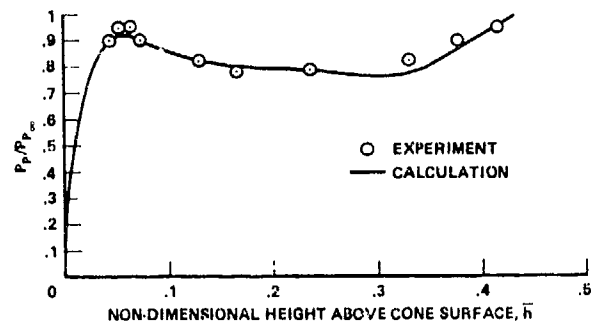


Fig. 10 Comparison of calculated and experimental pitot pressure survey at Rainbird's conditions (Ref. 22), $\phi = 168^\circ$.

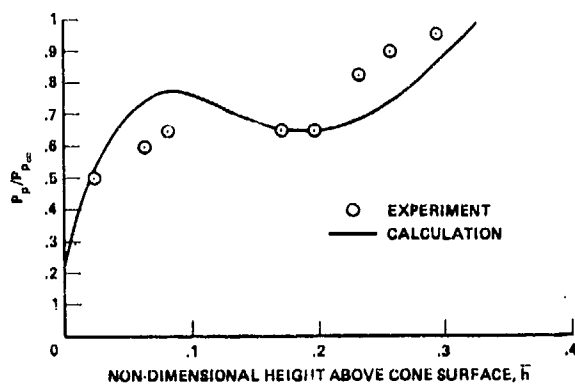


Fig. 11 Comparison of calculated and experimental pitot pressure survey at Rainbird's conditions (Ref. 22), $\phi = 152^\circ$.

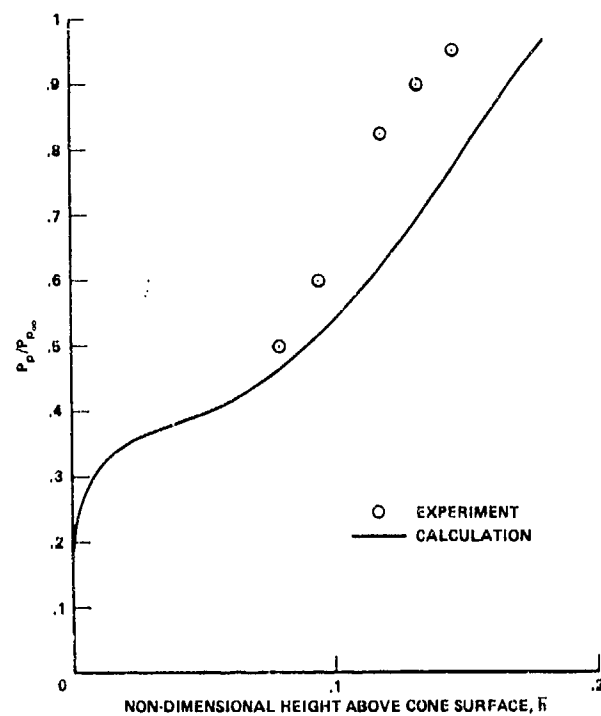


Fig. 12 Comparison of calculated and experimental pitot pressure surveys at Rainbird's conditions (Ref. 22), $\phi = 140^\circ$.

RECENT THEORETICAL DEVELOPMENTS AND EXPERIMENTAL STUDIES

PERTINENT TO VORTEX FLOW AERODYNAMICS -

WITH A VIEW TOWARDS DESIGN

John E. Lamar and James M. Luckring
 NASA Langley Research Center
 Hampton, Virginia 23665 U.S.A.

SUMMARY

This paper reviews recent progress in a research program directed toward an improved vortex flow technology base. In addition to analysis methods for conical flow, selected analysis and design methods for nonconical flows are presented. Applications are made for a variety of planar, nonplanar, and interfering lifting surfaces.

With regard to analysis, several methods are shown to provide reasonable estimates of over-all forces and moments for simple wing planforms with the suction analogy method currently offering the most versatility for arbitrary configuration applications. For the prediction of surface loadings the free vortex sheet method being developed by Boeing is shown to have considerable promise and further development of this type of method is encouraged.

In the design area, a data base for ogee strake-wing configurations is summarized with an emphasis on the requirements for maximizing the interference lift. A strake planform design procedure is discussed and a first solution (gothic in planview) is integrated with a wing body. The data show the strake to exhibit expected stable vortex characteristics.

Additional design activities center on reducing the drag-due-to-lift of highly swept delta wings having vortex flow. It was found that, apart from increasing sweep, conically cambered delta wings developed drag levels approaching that of attached flow with increasing either the lift or the wing camber height, lastly, an approximate vortex flow design method, based on the suction analogy, is outlined and an example is given. Further development of design capabilities based on more accurate flow modeling, such as possibly the free vortex sheet, is encouraged for the design of wings with efficient vortex lift characteristics.

SYMBOLS

A	aspect ratio
b	span
C_D	drag coefficient, $\frac{\text{Drag}}{q_\infty S_{\text{ref}}}$
$C_{D,0}$	experimental value of drag coefficient at $C_L = 0$
ΔC_D	drag-due-to-lift coefficient, Drag-due-to-Lift/ $q_\infty S_{\text{ref}}$
$\Delta C_D / C_L^2$	Drag-due-to-Lift parameter
C_L	lift coefficient, Lift/ $q_\infty S_{\text{ref}}$
$C_{L,\text{theory}}^*$	C_L due to vortex-lift-theory that uses a curve fitted $K_{v,\text{tot}}$ value
ΔC_L	increment in Lift-due-to-strake, C_L (strake on) - C_L (strake off)
C_l	rolling moment coefficient, $\frac{\text{Rolling Moment}}{q_\infty S_{\text{ref}} b}$
$C_{l\beta}$	rolling moment due to sideslip, $\frac{\partial C_l}{\partial \beta}$, per degree
C_m	pitching moment coefficient, Pitching Moment/ $q_\infty S_{\text{ref}} \bar{c}$: for planar wings about $\bar{c}/4$ unless otherwise stated, for strake-wing-body about 57.19 percent body length aft of body nose
C_N	normal-force coefficient, $\frac{\text{Normal Force}}{q_\infty S_{\text{ref}}}$
C_n	yawing moment coefficient, $\frac{\text{Yawing Moment}}{q_\infty S_{\text{ref}} b}$

$C_{n\beta}$	yawing moment due to sideslip, $\partial C_n / \partial \beta$, per degree
C_p	pressure coefficient, $\frac{P - P_{\text{free stream static}}}{q_\infty}$
ΔC_p	lifting pressure coefficient, $(P_l - P_u) / q_\infty$
C_s	leading-edge suction-force coefficient, $K_{v,le} \sin^2 \alpha$
C_T	leading-edge thrust-force coefficient, Leading-edge thrust / $q_\infty S_{\text{ref}}$
c	streamwise chord
\bar{c}	reference chord
\bar{c}	characteristic length used in determination of $K_{v,se}$
c_r	root chord
c_s	section suction-force coefficient, $\frac{\text{Section suction force}}{q_\infty \bar{c}}$
c_t	section thrust-force coefficient, Section thrust force / $q_\infty \bar{c}$, and tip chord
D	drag
D_1	payoff function, $D + (k/2)(L - L_D)^2$
dF_s	differential leading-edge suction force (fig. 3)
dl	differential leading-edge length
PLESAP	solution with full leading edge suction in attached flow
f	additional lifting surface efficiency factor (see fig. 28)
K_p	potential-lift factor, $\frac{\partial (C_{N,p})}{\partial (\sin \alpha \cos \alpha)}$
$K_{v,le}$	leading-edge-vortex-lift factor, $\frac{1}{q_\infty S_{\text{ref}}} \frac{\partial (S.F. _{le, \text{left}} + S.F. _{le, \text{right}})}{\partial \sin^2 \alpha}$
$K_{v,se}$	side-edge-vortex-lift factor, $\frac{1}{q_\infty S_{\text{ref}}} \frac{\partial (S.F. _{se, \text{left}} + S.F. _{se, \text{right}})}{\partial \sin^2 \alpha}$
$K_{v,se}$	augmented-vortex-lift factor
$K_{v,tot}$	$K_{v,le} + K_{v,se}$
K_3	$(\Delta C_D / C_L^2)_{\text{VORTEX}} / (\Delta C_D / C_L^2)_{\text{ATTACHED}}$
k	factor in payoff function
L	lift
l	length along which $K_{v,le}$ is assumed to develop
M	free-stream Mach number
\bar{N}_c	number of horseshoe vortices in a chordwise row in vortex-lattice method
\bar{N}_s	number of chordwise rows of horseshoe vortices in vortex-lattice method
P	pressure
p	nondimensional camber height for conically cambered wings in terms of local semispan
q_∞	free stream dynamic pressure
R_a	S_a / S_{ref}
RN	Reynolds Number
S	surface area
S_a	exposed area of strake or canard
$S.F.$	potential-flow suction force
s	local semispan

U	free-stream velocity
u	induced velocity in x-direction at point (x,y)
v	induced velocity in y-direction at point (x,y)
w_{net}	sum of induced downwash and $U\alpha$ at $\alpha = 1$ rad
\bar{w}_{net}	average value of w_{net}
x,y,z	distances from a coordinate origin located at leading-edge apex; x positive downstream, y positive toward right wing tip, z positive up
x/c	fractional streamwise distance along a chord
x/c_r	fraction distance along the root chord
Δx	distance along tip chord
y_b	spanwise location of leading-edge planform break
$2y/b(x)$	fractional distance along the local semispan
ZLESAP	solution with zero leading-edge suction in attached flow
z/c	local camber height in fraction of local chord
α	angle of attack
α_l	local geometric angle of attack along camber line
α_{l1}	new local geometric angle of attack along camber line
β	angle of sideslip, and $\sqrt{1 - M^2}$
Γ	local circulation
$\Gamma(1)$	equivalent circulation associated with leading-edge suction
$\bar{\Gamma}$	average value of Γ
γ	distributed bound vorticity at point (x,y)
δ	distributed trailing vorticity at point (x,y)
Λ	leading-edge sweep angle
λ	taper ratio, $\frac{c_t}{c_r}$
ρ	density of fluid
ϕ	dihedral angle, positive for wing tip up

Subscripts

ATTACHED	full leading edge suction attached flow
c	centroid
D	design
i	particular item of location
inb'd	inboard
l	lower
le	leading edge
max	maximum
outb'd	outboard
p	potential or attached flow
r	root
ref	reference

s	strake
se	side edge
<u>se</u>	augmented side edge
t	tip
te	trailing edge
tot	total
u	upper
VORTEX	total aerodynamic effect when vortex flow is present
v	vortex
vie	vortex effect at leading edge
vse	vortex effect at side edge
<u>vse</u>	augmented vortex effect
w	wing

NOTE: All coefficients refer to total loads unless stated otherwise. The subscript tot is selectively used for cases where confusion might occur.

INTRODUCTION

Separation induced vortex-flows from the leading and side edges play an important role in the high angle-of-attack aerodynamic characteristics of a wide range of modern aircraft. In the analysis and design of high-speed aircraft, a detailed knowledge of this type of separation is required, particularly with regard to critical wing loads and the stability and performance at various off-design conditions. Since attached-flow theories are inadequate for these conditions, the designer currently must rely on extensive and costly wind-tunnel tests which include detailed measurement of pressure distributions. In many cases, wind-tunnel tests occur too late in the cycle to impact the important aero/structural design trade-offs. In addition, for those aircraft which are required to provide high maneuver capability, a detailed knowledge of this type of flow is required if the vortex lift capabilities of slender wings or strake-wing configurations are to be fully utilized.

Although a considerable amount of research has been carried out relative to the vortex flow aerodynamics during the past twenty years important gaps in the technology still exist, particularly with regard to theoretical methods of predicting detailed wing pressure distributions, analytical methods for design optimization of vortex lift concepts and in certain areas an experimental data base for advanced design concepts utilizing interacting vortex flows.

This paper reviews recent progress in a research program at the Langley Research Center directed towards an improved vortex-flow technology base. Included is a review of selected analysis methods such as conical flow, (refs. 1 and 2) the suction analogy applied to both leading- (ref. 3) and side-edges (ref. 4) as well as an augmented term (ref. 5), the new quasi-vortex-lattice method with free trailing-vortex-filaments (ref. 6), and the Boeing free-vortex sheet method (refs. 7 and 8). To evaluate the accuracy of the methods comparisons are made with experimental results for a wide range of planar wings including slender planforms, a swept forward wing, oblique wings and multiple lifting surfaces such as close-coupled canard-wing configurations.

Details of an extensive parametric experimental study of close-coupled strake-wing configurations is also included (ref. 9). This data set includes variations in strake-to wing-span and wing sweep for angles of attack up to 50° , angles of sideslip from -5° to $+5^\circ$, and Mach numbers up to 0.8. The test utilized two balances so the strake-forebody loads could be separated from the total loads and compared directly with theory. Theoretical modeling of the flow is described followed by comparisons with experiment.

The vortex-flow design problem of strake planform shape is next addressed. A procedure for analytically developing strake perimeter lines is presented from reference 10 along with an example. The example shape was then integrated with a wing-body, the resulting configuration tested and results reported herein.

Following the planar wing studies the application of several of the theoretical methods to non-planar problems, such as the prediction of the effectiveness of conical camber height in reducing the drag in nonconical vortex flow (ref. 11) is described. Comparisons are made between the various methods and available data.

The final section of the paper deals with a vortex-flow problem related to the design of a slender wing having both efficient supersonic cruise and good transonic maneuver capability. For this class of wing the use of maneuver-flaps may not be practical and therefore the application of vortex lift appears attractive. However, if this vortex lift is to be generated efficiently, some means of shaping the wing to optimize the lift generated while minimizing the drag associated with the loss of leading-edge suction must be used. To accomplish this, it is necessary to apply an analysis code iteratively either under manual control or automatic control as in an optimization procedure. An example of the optimization procedure is determined by a recently developed vortex-lattice design code which includes the vortex flow aerodynamics by means of the suction analogy.

DESCRIPTION AND EVALUATION OF ANALYTICAL METHODS

DESCRIPTION OF ANALYTICAL METHODS

The theoretical methods employed herein are divided into two classes which are dependent upon the underlying aerodynamic assumptions. The classes are shown on figure 1 to be conical and nonconical flow for the vortex-flow aerodynamic problems. Though basically only one conical flow method is used in this paper, three different nonconical flow methods are described and employed. The order of their occurrence on figure 1 generally indicates the increasing order of accuracy in terms of surface load distribution, for the methods in their current state of development.

These two classes of methods are discussed in the following sections.

Conical Flow

The conical flow solutions come about from a simplification of the governing flow equation to not include any longitudinal flow dependence but only cross-flow plane velocities. The flow field is assumed to scale streamwise so that with a solution of vortex sheet shape and strength determined at one longitudinal location, solutions at other locations are readily calculable. This solution has no Mach number dependence because of the underlying assumption, i.e., $M = 1$, which is reasonable for very slender wings. This method does satisfy the leading-edge Kutta condition but not the trailing-edge one, thereby making its results less valid of course, as the trailing edge is approached.

Nonconical Flow

The three nonconical flow methods given on figure 1 are (1) the suction analogy-Polhamus, (2) the quasi-vortex-lattice-Mehrotra and (3) the free-vortex-sheet-Boeing. They are called nonconical because they each satisfy the trailing-edge Kutta condition. These methods differ in approach and to the degree to which they predict the surface load distributions. Some pertinent differences are highlighted as follows with individual descriptions given later:

1. The suction analogy is always coupled with a potential-flow solution and is useful for estimating the over-all forces and moments at small computer cost. However, it does not provide details of the surface load distribution.
2. The quasi-vortex-lattice potential flow method of Lan (ref. 12), QVLM, has been extended by Mehrotra (ref. 6) to include vortex-flow effects. This is done by modeling with discrete trailing-vortex filaments, in a manner similar to Mook and Maddox (ref. 13), the shape, position and influence of the shed vortex sheet for both complete or partial span leading-edge separation. Furthermore, the leading-edge boundary condition is exactly satisfied.
3. The free-vortex-sheet method of Boeing models the wing surface and free sheet with doublet panels that have biquadratic strength. Thickness effects may be modeled with source panels that have bilinear strength. The free sheet, whose shape and position must be determined by iteration, is kinematically coupled to a fixed (fed) sheet that approximately represents vortex core effects. The entire set of doublet strengths is also determined simultaneously during the iteration process.

Additional details of each method follow.

Suction Analogy

The suction analogy¹ method section is divided into three parts representative of its development and ongoing application. They are: (1) leading edge, (2) side edge (3) augmented term. A discussion of each part follows.

Leading Edge. - The concept embodied in the suction analogy of Polhamus is developed in reference 3 and originally applied to delta wings. Herein, the primary ideas are briefly reviewed.

Wings which have attached flows develop suction forces along their leading edges if the stagnation surface does not lie along that edge. This suction force can be determined by either of two processes: (1) the pressure near the leading edge acting over the edge thickness or (2) the product of the square of the induced tangential velocity and the distance to the edge. For a wing of infinitesimal thickness the induced tangential velocity, $u(x,y)$, approaches an infinite value as shown in figure 2 for the rectangular wing; however, its product (described previously) is still finite.

If the flow separates from the wing in going around the leading edge due to its sharpness or thinness, or due to a combination of thickness and angle of attack, the suction force in the chord plane is lost. However, if this separated flow forms into a shed vortex which causes the flow to reattach to the leeward surface of the wing then the fluid energy redistributes on the wing upper surface near the leading edge resulting in the development of vortex lift. The suction analogy states that for the separated flow situations, the potential-flow leading-edge suction force becomes reoriented from acting in the chord plane to acting normal to the chord plane (a rotation of 90°) by the local vortex action resulting in an additional normal force (see figure 2.) The reasoning is that the force required to maintain the reattached flow in a situation associated with the separation induced vortex flow is the same as that which had been required to maintain the potential flow around the leading edge. Therefore, the suction analogy concept provides a link between attached flow solutions and the effects of this particular type of separated flow.

According to the analogy, the reattachment line or details of the pressure field need not be known in advance in order to determine the reattached-flow force. However, if pitching-moment estimates are needed the distribution of the reattached force must be known and is determined in the near field. The centroid of the leading-edge suction has been used as the longitudinal location of this force. This assumption does not have provision for angle-of-attack effects on the location of the reattachment line or vortex core; hence the core is assumed to remain stationary near the wing leading edge.

In the application of the suction analogy one must add to a potential flow solution the contribution of this additional normal force, $C_{N,vie}$, acting at its centroid. The addition is of the form

$$C_L = C_{L,p} + C_{L,vie} = K_p \sin \alpha \cos^2 \alpha + K_{v,ie} |\sin \alpha| \sin \alpha \cos \alpha \quad (1)$$

where the trigonometric terms have been included for accuracy. This means that attached flow linear aerodynamic solutions can yield nonlinear potential flow C_L values as well as those from nonlinear vortex flow.

Side Edge. - The suction analogy is not limited to vortex flows around the leading edge but can be applied wherever singularities in the potential-flow induced velocities produce an edge force. Figure 2 shows that this can occur along the side edges because of the singularities in v . Hence, for vortex flows associated with separation around the side edges, the forces no longer act in the wing plane but in the normal-force direction as in the case of leading-edge separation.

A mathematical procedure for computing this side force has been developed initially, for wings at subsonic speeds, and is given in reference 4. The procedure employs the modified Multhopp method of reference 14 to provide the information needed to begin the side-force computation. In addition, three discrete-loading analyses of this procedure have been made employing the vortex-lattice method (refs. 15-17) and are discussed in reference 17. In reference 17, the vortex-lattice method (VLM) is shown to yield results in close agreement with those of reference 4, hence, the reference 17 method is utilized herein for some isolated planforms and all subsonic configurations for which the reference 4 method is not appropriate. An exception is for oblique wings or swept forward wings where the side-edge term is calculated using the Asymmetrical Vortex Lattice of Luckring (ref. 18). There a special procedure is used to account for the nature of the edge forces in the tip leading-edge region.

The following equations relate the potential- and vortex-lift factors to C_L , C_D , and C_m :

¹The method referred to as the "suction analogy" only calculates the vortex lift. However, for simplicity, the term "suction analogy" is generally used to identify those methods that rely on this concept of predicting the vortex lift in combination with the potential flow lift.

$$C_L = \overbrace{K_p \sin \alpha \cos^2 \alpha}^{C_{L,p}} + \overbrace{K_{v,ie} |\sin \alpha| \sin \alpha \cos \alpha}^{C_{L,vie}} + \overbrace{K_{v,se} |\sin \alpha| \sin \alpha \cos \alpha}^{C_{L,vse}} \quad (2)$$

or

$$C_L = K_p \sin \alpha \cos^2 \alpha + K_{v,tot} |\sin \alpha| \sin \alpha \cos \alpha \quad (3)$$

$$C_D = C_{D,o} + C_L \tan \alpha = C_{D,o} + K_p \sin^2 \alpha \cos \alpha + K_{v,tot} \sin^3 \alpha \quad (4)$$

and

$$C_m = \overbrace{K_p \sin \alpha \cos \alpha \frac{\bar{x}_p}{c}}^{C_{m,p}} + \overbrace{K_{v,ie} |\sin \alpha| \sin \alpha \frac{\bar{x}_{ie}}{c}}^{C_{m,vie}} + \overbrace{K_{v,se} |\sin \alpha| \sin \alpha \frac{\bar{x}_{se}}{c}}^{C_{m,vse}} \quad (5)$$

where the particular \bar{x} -terms equal $x_{ref} - x_{c,i}$ with i standing for p , ie , or se . Unless otherwise noted, x_{ref} is the quarter-chord location of the mean geometric chord.

Augmented Term. - The concept of an augmented vortex lift term arises from the well-established fact that for many delta wings the leading-edge vortex generated on the wing persists for a considerable distance downstream and therefore can act on other surfaces, such as the aft part of more generalized planforms or aircraft horizontal tails. This persistence is not accounted for in the suction analogy because the analogy deals only with the edge forces generated along a particular edge, such as leading-edge vortex lift resulting from the leading-edge suction force. Figure 3 shows examples of two systems employed that account for vortex lift on delta and cropped-delta wings. They are (1) a theoretical one developed from a planar potential theory and utilizing the suction analogy along the leading- and side-edges and (2) an extension that accounts for the action of the leading-edge shed vortex in the vicinity of the side edge of cropped-delta wings. The following important points are made from this figure: (1) the leading-edge suction distribution has a peak value somewhere along the leading edge away from the extremities and goes to zero at the tip because no edge forces are present beyond the point of maximum span; and (2) for the cropped-delta wing, the aft part of the wing can generate additional (augmented) vortex lift (above that associated with the direct side-edge effect) because of the presence of the leading-edge vortex (as discussed in reference 19).

In order to estimate the augmented vortex lift, it is first necessary to quantify the circulation of the shed vortex along the wing leading edge. This can be done as indicated by the lower sketch on figure 3. The Kutta-Joukowski Law has been employed to relate the differential suction force along the leading edge to an unknown circulation $\Gamma(i)$. By a coordinate transformation, it can also be related to the leading-edge suction distribution along the span as

$$\frac{c_s c(y)}{\alpha^2} = -2 \sec \Lambda \frac{\Gamma(i) w_{net,ie}(y)}{\alpha^2 U^2} \quad (6)$$

Figure 4 shows an idealized distribution of the product $\frac{-\Gamma(i) w_{net,ie}}{\alpha^2 U^2}$ along with a fairly reasonable $\frac{-w_{net,ie}}{U}$ (upwash) distribution for a cropped-delta wing. As a consequence, $\frac{\Gamma(i)}{\alpha^2 U}$ can be estimated as shown. Because the actual circulation does not go to zero (hence the vortex persists downstream), the distribution of circulation cannot be used. Instead, an average value is employed. With an average value used for $\frac{\Gamma(i)}{\alpha^2 U}$, it is consistent to utilize an average value for $\frac{-w_{net,ie}}{U}$ as well. This result can be expressed in terms of the leading-edge-vortex-lift factor by

$$\int_0^{b/2} \frac{c_s c dy}{\alpha^2} = \frac{K_{v,ie}}{2} S_{ref} = -2 \sec \Lambda \frac{\Gamma(i) \bar{w}_{net,ie}}{\alpha^2 U^2} \frac{b}{2} \quad (7)$$

Hence,

$$\frac{\Gamma(i)}{\alpha^2 U} = \frac{-K_{v,ie} S_{ref}}{2b \sec \Lambda \bar{w}_{net,ie}}$$

Employing this result in the Kutta-Joukowski Law, this time along the side edge, permits the estimation of the augmented vortex lift. The details are

$$\frac{\text{Augmented vortex lift along one edge}}{\alpha^2} = -\rho \bar{w}_{\text{net,se}} \frac{\Gamma(1)}{\alpha^2} \tilde{c} \quad (9)$$

where the $\frac{-w_{\text{net,se}}}{U}$ distribution and its average are again reasonably depicted at the bottom right of figure 4 and \tilde{c} is a characteristic streamwise length. By inspection of figure 4

$$\frac{\bar{w}_{\text{net,se}}}{U} \approx \frac{\bar{w}_{\text{net,le}}}{U} \quad (10)$$

Then defining the augmented vortex lift along one edge divided by α^2 as $\frac{K_{v,se}}{2} q_{\infty} S_{\text{ref}}$ leads to

$$\frac{K_{v,se}}{2} q_{\infty} S_{\text{ref}} = q_{\infty} \frac{K_{v,le}}{b \sec \Lambda} S_{\text{ref}} \tilde{c} \quad (11)$$

or

$$K_{v,se} = \left[\frac{K_{v,le}}{(b/2) \sec \Lambda} \right] \tilde{c} \quad (12)$$

The term in brackets results from the use of average values and amounts to assuming that the leading-edge-vortex-lift factor is developed at a constant rate along the leading edge length $(b/2) \sec \Lambda$. For cropped-delta wings the value of \tilde{c} is taken to be the length of the tip chord.

The contributions of the augmented term to vortex flow aerodynamics are

$$C_{L,vse} = K_{v,se} |\sin \alpha| \sin \alpha \cos \alpha \quad (13)$$

$$C_{D,vse} = K_{v,se} \sin^3 \alpha \quad (14)$$

and

$$C_{m,vse} = K_{v,se} |\sin \alpha| \sin \alpha \frac{\bar{x}_{se}}{\tilde{c}} \quad (15)$$

The distance \bar{x}_{se} is taken to be from the reference point to the centroid of the augmented vortex lift. This location is generally taken to occur at the centroid of the affected area.

QVLM - Mehrotra

Figure 5, taken from reference 6, is useful in explaining this method, which has been developed under the Langley sponsored effort. Shown on the left side of this figure is a typical planform with its potential flow bound and trailing vortex systems spaced in a cosine manner. Notice that the control points are also laid out in a cosine manner; in particular, such that one control point occurs along each chordwise row at the leading and trailing edges.

The leading-edge vortex system is superimposed on the regular quasi-vortex-lattice grid by using segmented vortex filaments, each group being called a vortex element. A typical vortex element is shown by points A through J on the right side of figure 5. These points are connected by the series of short straight segments shown. A typical set of initial locations for these segments is illustrated with dashed lines and the final or converged locations are given by solid lines.

The segments of the vortex element have the following characteristics:

- a. Initially, points A through E lie along a wing trailing vortex filament with point A being one root chord away from the trailing-edge (see point D) in the downstream direction, and the line segments between A and D are parallel to the axis of symmetry. The segments B-C and C-D are $0.1 c_r$ long. The length of each line segment between points A and B remains unchanged as the solution progresses. In the final converged position which is determined iteratively for each α , these segments are aligned in the direction of the local velocity at their mid-points to satisfy the force-free condition. Segment B-C is allowed to move only in the vertical direction whereas

segment C-D is fixed in the wing plane because the flow is parallel to the chord plane. Segment D-E is also fixed in the wing plane.

- b. Points E, F, G and H also lie in the wing plane. The location of segment E-F is ahead of the wing first bound element and is given in equation form in reference 6. The segments F-G and G-H are of the same length and point G lies on the leading-edge. These segments are fixed in the wing plane due to the leading-edge boundary condition.
- c. The initial location of point I, on the right side of figure 5, is also given in reference 6 and is seen there to be a function of α . Note in particular the initial z elevation of point I at a representative α . Initially point J is one root chord away from the trailing-edge. The line connecting I and J may be divided into segments of equal length which lie in a plane parallel to the x-z plane. The initial height of these segments is approximately $0.1 c_r$ above the wing plane. In the final converged position all the segments between points H and J are aligned in the direction of the local velocity vector at their mid-points to satisfy the force-free condition.
- d. The semi-infinite segments from points A to infinity and J to infinity are straight and are parallel to the undisturbed free-stream direction.

After the vortex segments have reached their converged location, representing a diffused vortex, then the circulations associated with the wing surface and the velocities there are used to calculate the lifting pressure distribution. From them the lift, drag and pitching moment are calculated. Additional computational details are found in reference 6.

Free Vortex Sheet - Boeing

As part of its vortex flow research program the NASA - Langley Research Center has also contracted with the Boeing Company for the development of a free vortex sheet method. Reference 20 gives a good overall review of the free vortex sheet method. Portions of that reference are discussed below.

Figure 6 shows a typical panel arrangement for a wing and its vortex sheets. The wing is paneled with biquadratically varying doublet panels and bilinearly varying source panels. Zero mass flux boundary conditions² are imposed on the wing surface. Also, the Kutta condition is satisfied at all edges if the wing is thin; however, the vortex sheet separation point can be moved aft of the leading edge to simulate the effect of a round edge on the separation line.

All the vortex sheets are paneled with biquadratically varying doublet panels. Zero mass flux boundary conditions are also imposed on the free-vortex sheet with the additional constraint that the vortex sheet be locally force free. The resultant system of equations is, therefore, nonlinear because both the strength and shape of the free vortex sheet (as had been the case for the trailing vortex filaments of QVLM) are unknown and an iterative solution procedure is necessitated.

The fed sheet is a simplified model of the physical vortex core region. For the results presented in this paper, the fed sheet is a kinematic extension of the free sheet. The assumption in this model is that the boundary conditions applied to the free sheet are adequate to position the fed sheet. Current work is on-going to improve the fed sheet model.

The trailing wake shape is frozen from the trailing edge of the wing and vortex sheets to a distance far downstream of the trailing edge. The boundary conditions for the wake are that it supports no pressure jump, i.e. $\Delta C_p = 0$ based on a first order pressure formulation. However, the wing loadings in the vicinity of swept trailing edges (such as for arrow wings) have been determined numerically to be unduly sensitive to the trailing edge sweep angle. As a temporary fix to this problem, the near wake boundary condition may be imposed utilizing a second order pressure formulation. Future work allowing the wake to be treated as a free sheet could resolve this difficulty.

Once the free sheet has been iterated to its converged location, along with the fed sheet, then the resulting doublet distributions provide local velocities which are then used to determine the pressures. Upon integration of the net pressures the over-all lift, drag and pitching moment are determined. Additional details of this method can be found in references 7 and 8. Detailed numerical and experimental evaluations of the theory are currently underway at the Langley Research Center and one phase of this study is presented in reference 21.

²Setting the mass flux vector equal to zero represents a generalization of the more common "no-flow" condition.

EVALUATION OF ANALYTICAL METHODS

This section offers comparisons between the previously described theoretical methods and available aerodynamic data. Not all methods will be employed for each set of data because (1) the method may not be applicable due to geometrical restriction, or (2) the code has yet to be exercised successfully for a particular geometry.

The types of configurations to be highlighted are (a) delta, (b) rectangular wing, (c) cropped delta, (d) cropped arrow, (e) arrow, (f) diamond, (g) oblique wing, (h) swept-forward wing, (i) wing-canard and (j) cropped double-delta.

Deltas

Subsonic Speed

The estimated and measured (ref. 22) lift and moment characteristics of an $A = 1.147$, $\Lambda = 74^\circ$, delta wing at $M \approx 0$ are given in figure 7, followed by two spanwise variations of lifting pressures in figure 8. Comparison of Smith's conical flow solution illustrates strong non-conical flow effects and emphasizes the importance of completely three-dimensional flow methods. The completely three-dimensional flow methods examined all provided large improvements over the conical flow and are in generally good agreement with the experimental lift measurements. With regard to the pitching moment the QVLM-Mehrotra provides the best prediction.

The spanwise ΔC_p also show the nonconical flow effects along with the effect of the leading-edge Kutta condition. The comparisons show the free vortex sheet method to better estimate the actual suction peak than the more diffuse representation associated with QVLM-Mehrotra.

Supersonic Speeds

Because vortex flow is most predominant on slender wings of interest for supersonic flight, methods of predicting the supersonic characteristics associated with vortex flow are highly desirable. At the present time, however, the suction analogy appears to be the only method available that accurately accounts for Mach number effects in the supersonic range. Polhamus in reference 23 gives the supersonic formulation of K_p and $K_{v,10}$ and applies them in the suction analogy for an $A = 1$ delta wing. The results for $M = 1.97$ and 3.30 are presented in figure 9 along with the incompressible results for comparison.

The experimental results substantiate, in general, the reduction in vortex lift with increasing Mach number predicted by the suction analogy and are in reasonably good quantitative agreement. An additional point of interest is the fact that for both supersonic Mach numbers the experimental lift slope is reasonably linear and at the highest Mach number the theory is reasonably linear. This linearity when observed alone could be interpreted as an indication of the absence of vortex lift. However, when compared with the potential flow lift, $C_{L,p}$, it is clear that the vortex lift is present and that its nonlinear characteristic is offset by the opposite nonlinear trend of the potential-flow lift with α . It should be mentioned that at high Mach numbers and angles of attack the upper surface vacuum limit will affect the lift. However, a knowledge of the surface loading is required before occurrence of the limit can be predicted.

Effect of Sideslip

During the maneuver portion of a flight envelope asymmetric load distributions can often arise due to sideslip effects and/or rotary motions. The asymmetric load distributions can considerably impact the design of maneuvering aircraft from the standpoint of stability and control as well as peak structural load considerations. However, the effects of asymmetry and, in particular, sideslip at high angle of attack on the vortex flow aerodynamics have not been addressed analytically to any great extent. As a consequence, the designer must currently rely on costly and time consuming wind tunnel tests to resolve lateral-directional design problems.

To this end applications of the Boeing free vortex sheet method (refs. 7 and 8) have recently been made for non zero values of sideslip. Sample calculations (fig. 10) for a 74° delta wing at twenty degrees angle of attack and ten degrees angle of sideslip demonstrate that this method provides reasonable estimates of the experimental surface load distributions obtained from ref. 27. Also apparent in figure 10 is the large effect of the nonconical nature of the flow and the ability of the theory to predict this effect. The complete inadequacy of the attached flow methods for lateral stability analysis and loads estimation is also apparent. Future studies are planned for applying this method to more general wing planforms and for estimating the vortex flow effects on rotary derivatives.

Rectangular Wing

As discussed in a previous section, prediction of the characteristics of wings with finite tip chords requires the consideration of the vortex lift associated with a separation induced tip vortex. Figure 11 presents a comparison of experimental and theoretical subsonic aerodynamic characteristics of an $A = 1$ rectangular wing. Also shown are the potential- and vortex-lift estimates determined in reference 4. The figure shows that the suction analogy estimates the C_L experimental data of reference 4 better than the other methods. (See reference 4 for a discussion of the methods in references 28-31.) This figure also shows that the C_m experimental data are better estimated by

the suction analogy up to $\alpha \sim 16^\circ$. For higher α 's, the data show a larger nosedown moment than the suction analogy estimate. This comparison indicates the magnitude of the error introduced by the suction analogy in assuming that the potential and vortex lifts, in particular the leading-edge one, do not move with increasing α .

With the vortex lift from the side edge identified, its magnitude estimated, and good agreement with experimental data shown, the vortex lifts on more generalized planforms will now be discussed.

Cropped Delta

The cropped wing shown in figure 12³ serves as a first application of the augmented vortex-lift concept in estimating longitudinal aerodynamic characteristics. The augmented lift can be seen for this wing to be about two-thirds of the other vortex lifts levels. Furthermore, the magnitude and centroid of the augmented vortex lift appears to be reasonably accurate in view of the improved agreement with both the C_L and C_m data. (For C_m estimates the augmented vortex lift is applied at the centroid of the side-edge suction distribution for cropped-delta wings.)

Cropped Arrow

Direct application of the suction analogy methodology to wings with notched trailing edges results in an overprediction of lift in the higher angle of attack range. This is illustrated in figure 13, where it will be noted that good agreement is only obtained up to 12° when the chord, \tilde{c} , used to define the augmentation term, is equal to the tip chord (reattachment line is near tip). At higher α 's the experimental lift is less than predicted apparently due to a reduction in the effective \tilde{c} as the reattachment line moves inboard. The combination of the helical path of the streamlines around the vortex and the reduced downstream area associated with the notch results in a reduced recovery of the edge forces as vortex lift similar to the effect discussed in reference 23 for arrow wings. To give an indication of the magnitude of the \tilde{c} effect, a value defined by the sketch as being "original" has been used to establish a lower curve. This "original" \tilde{c} was proposed in reference 5 as an approximation to the higher α effect.

The loss of the reattachment effect associated with the trailing edge notch requires improved theoretical approaches, and the free vortex sheet is one method which may eventually offer a solution.

Pointed Wings

The suction analogy has been applied to a wide range of pointed wings. Reference 33 presents data and theoretical comparisons for 75° swept delta, arrow, and diamond wings over a Mach range from 0.2 to 0.8. The delta wing data are well estimated with the combination of potential flow (0% leading-edge suction) and the direct application of the original leading-edge suction analogy vortex lift term, whereas those for the arrow and diamond wing are not. However, incorporating the augmented vortex lift produces improved agreement with the C_L and C_m data as seen in figures 14 and 15 for $M = 0.4$ and 0.8. Note especially the smaller sensitivity of the diamond wing C_m variation with Mach number. Also, note that due to the slenderness of these wings, the theoretical curves are almost identical for each wing over its entire subsonic speed regime.

The reasoning for an augmented lift is easier to understand when applied to a diamond wing or one with additional area aft of the leading-edge tip than when applied to arrow-type wings. However, the negative value of augmentation for these wings should be thought of as a lack of complete flow reattachment due to trailing-edge notching.

This notching effect is well documented by the transonic longitudinal load distribution of a highly swept and tapered cropped-arrow wing-body combination in reference 34. The distribution shows a sudden loss in lift just aft of the trailing-edge apex. This integrated loss is likened to the negative value of augmented vortex

³This figure points out the large side-edge vortex lift available in addition to the augmented vortex lift along the side edges. It was thought that if it were possible to turn off this lift on one side that a significant rolling moment could be generated especially at high α . This was tested experimentally on a higher swept cropped delta wing and as reported in reference 19 was determined to be true.

lift discussed previously. Reference 34 employed the augmented lift concept for this combination and reported improved agreement with the data.

Oblique Wings

The oblique wing concept is currently being studied as a possible approach to a transport aircraft designed for transonic or low supersonic cruise speeds (ref. 35). The concept may also become of interest for highly maneuverable aircraft as well, and a need for theoretical methods of predicting and obtaining the vortex flow of such wings may emerge.

Previous applications of the suction analogy, leading-edge side-edge and augmented term, have focused on symmetric flow calculations. However, these concepts are not limited to symmetric flow and should be applicable to asymmetric flow provided the appropriate potential flow solutions are employed.

The recently developed Asymmetric Vortex Lattice Method (ref. 18) has been coupled with the suction analogy to provide estimates for asymmetric flow situations and, in particular, for oblique wings. This method includes additional considerations for the effect of forward sweep on side edge suction and for the effect of a skewed planform on augmented vortex lift estimates. To demonstrate the large effect of vortex flow aerodynamics on the force-moment characteristics of skewed wings, theoretical solutions for sample configurations of reference 18 are compared with data in figures 16 and 17. This analytical method is seen to provide reasonable estimates of the over-all lift and pitching moment characteristics for both configurations because of the effective realization of the side-edge and augmented vortex lift terms. It is of interest to note the appreciable increments in lift and pitching moment due to vortex flow aerodynamics, the latter of which changes sign compared to attached flow theory. Other examples can be found in references 18 and 36. At the present time it appears that only the suction analogy has been applied to these types of wings. Utilization of the more advanced methods which predict surface load distributions would be helpful in optimizing the vortex flow aerodynamics of oblique wing designs for highly maneuverable aircraft or for providing analysis capability for off-design conditions of cruise vehicles.

Sweptforward Wings

Recent advances in the application of composite material concepts to wing design offer the possibility of greatly reducing the weight penalty previously associated with the divergence problem of sweptforward wings (ref. 37). This possibility has led to a renewed interest in this class of wings particularly for maneuvering aircraft. Although practical considerations may limit the leading-edge sweep angles to values somewhat less than those required for stable vortex flow without augmentation, an understanding of, and methods of predicting, the vortex lift characteristics of sweptforward wings would be desirable.

An example of the lift characteristics of a sweptforward wing over a wide angle-of-attack range and a comparison with a sweptback wing is presented in figure 18 for a configuration incorporating identical wings tested in the sweptback (ref. 9) and sweptforward (ref. 38) orientations. Utilizing the identical planform reversed provided for the same aerodynamic aspect ratio and the same half chord sweep angle thereby providing approximately the same structural aspect ratio. Both wings employed circular airfoils. Included are the theoretical estimates based on the suction analogy. Since the effects of the fuselage are small, the two configurations exhibit the same theoretical potential flow lift characteristics, as would be expected from flow reversibility considerations. Although both configurations developed comparable levels of theoretical leading-edge thrust, the sweptforward configuration developed less theoretical leading-edge suction due to the reduced leading-edge sweep angle and therefore less theoretical vortex lift. The correlation between theory and experiment is typical for these sweep angles; it becomes poor above approximately 12° for the sweptback configuration and at a very low angle of attack for the sweptforward configuration due to vortex breakdown effects. The net result for this wing is that less of the available vortex lift is realized in the sweptforward than in the sweptback orientation due primarily to the lower leading-edge sweep angle. If vortex lift were to be desired on a sweptforward wing it appears that some type of vortex augmentation will probably be required inasmuch as the leading-edge sweep angles will tend to be limited by structural and other practical problems. However, experimental studies with higher leading-edge sweep angles would be helpful in understanding the vortex development and stability and in evaluating analytical methods.

Wings in Multiple Vortex Flows

Turning now from basic wing alone and wing-body characteristics the next two sections review some of the characteristics of wings in multiple vortex flows. The configurations included in this category are canard-wing combinations and double-delta type wings. Characteristics of the strake-wing class of configurations are to be given in the design portion of this paper. Inasmuch as the theoretical approaches which actually model the edge separation induced vortex flows have not been developed to the stage that they can be directly applied to the various multiple surface configurations, the theory used for data comparison will be limited to the suction analogy.

Canard-Wing Configurations

Some of the studies related to canard-wing configurations are described in references 39-42. Figure 19 illustrates some of the favorable interference effects and the results of an application of the suction analogy prediction method. A double balance system was utilized in the experiment in order to separate the wing and canard loads. The configurations shown in figure 19 have a wing that would usually encounter vortex breakdown at an α of about 8° resulting in a large loss of vortex lift. However, in the presence of the canard, a favorable interference results, and the predicted amount of vortex lift is realized by the wing. A contributing factor to this favorable interference is probably that the spanwise flow induced by the canard augments and stabilizes the wing leading edge vortex similar to the effects of spanwise blowing. This is confirmed by data from reference 39 for both the high canard ($z/\bar{c} = 0.185$) with anhedral and the coplanar one.

In applying the suction analogy the potential flow interactions between the surfaces have been accounted for in the determination of the edge singularity strengths. However, for neither configuration has the augmented vortex lift due to the leading-edge vortex of the canard been utilized. This omission may be reasonable for the high canard but is, of course, questionable in the coplanar arrangement. This vortex lift was omitted because an appropriate method of determining \bar{c} has yet to be established.

In general it has been found that the suction analogy provides a reasonable "upper bound" for the lift generated on the wing in the presence of a canard. Extensions of the various advanced vortex flow modeling techniques to this class of configuration is needed as an important step towards the development of vortex lift analysis and design techniques.

Cropped Double-Delta

Another type of configuration that might be considered in the category of interferring lifting surfaces is the double-delta wing. Figure 20 shows a typical configuration and how one might theoretically model the various inner- and outer-panel vortex-flow contributions at both low and high α using the suction analogy. This modeling applies when the inner and outer panels have a relatively small leading-edge sweep angle difference.

The necessity for α dependent flow modeling is apparent from studies of surface oil flow patterns, examples of which are shown for two representative α 's. The oil flows consistently show for this wing, and for the other double-deltas of reference 10, evidence of two primary vortex systems at low α 's, followed by a merging into one system at high α 's.

At low α 's, the leading-edge vortex from the inboard wing panel passes over the root chord of the outboard wing panel and augmented vortex-lift estimates are made based on $K_{v,le(inb'd)}$ and $\bar{c}_{inb'd}$ or $K_{v,se(inb'd)}$. Additional augmented vortex-lift is available at the tip due to the action of the outboard leading-edge vortex, i.e., $K_{v,le(outb'd)}$ and $\bar{c}_{outb'd}$ or $K_{v,se(outb'd)}$. Therefore, the low- α vortex-lift theory combines the original vortex-lift theory with the other two contributors to vortex-flow aerodynamics.

At high α 's the assumption is that the single primary vortex system acts over the outer panel in a manner similar to that described previously for the cropped delta. Thus, the original \bar{c} definition is used as shown due to the increasing size of the vortex and the more inboard location of the reattachment line, as well as the loss in lift associated with the reduction of flow reattachment area through trailing edge notching. This \bar{c} in conjunction with the entire leading-edge contribution to $K_{v,le}$ provides $K_{v,se}$. Therefore, combining the original vortex-lift theory with contributions to vortex flow aerodynamics $K_{v,se}$ produces the high α vortex-lift theory.

These two new ways of modeling the vortex flow aerodynamics are compared in figure 21 along with the original method (no augmentation) and experimental data for a cropped double-delta. The low α theory does offer improvements in C_L estimation up to 8° over the original theory, and the high α theory predicts the C_L better above $\alpha = 16^\circ$. However, these improvements are not reflected in any better estimate of C_m vs C_L . The potential theory curves are presented as a reference to illustrate the large effects of vortex lift.

DESIGN RELATED RESEARCH

At the present time, the development of aircraft which utilize vortex flow as a fundamental aspect of their design concept must depend primarily on extensive and costly wind tunnel test programs with some guidance provided by a limited experimental data base.

The purpose of this part is to describe a recent parametric extension to the data base which is applicable to strake-wing configurations, present an analysis method to

handle this class of configurations, and to review some preliminary applications of the analysis methods directed towards the optimization of vortex flow aerodynamics.

DATA BASE

Model Description

A general drawing of the model used for the present investigation is presented in figure 22. The model was instrumented with two internally mounted strain gauge balances. One balance, referred to as the strake balance, measured loads on the strake and the forebody (see shaded portion of figure 22) and the other balance, referred to as the main balance, measured total loads. The difference between the main and strake balance measurements would, therefore, be the loads on the wing and afterbody. Noninterfering lap seals prevented air from bleeding through the gap between the forebody and afterbody segments of the model for all longitudinal studies.

The parameters varied for the present investigation were strake span and wing sweep. The wings had leading-edge sweep angles of 30° , 40° , 44° , 50° , and 59.45° , a reference aspect ratio of 2.5, and a reference taper ratio of 0.2. All wings had the same area, span, and mean geometric chord. They were untwisted and had biconvex airfoil sections which linearly varied in maximum thickness from 6 percent of the chord at the wing-fuselage juncture to 4 percent of the chord at the tip. The quarter-chord point of the wing chord at the fuselage was taken as the moment reference point and coincided for all wings.

The strakes had maximum exposed semispans of 10, 20, and 30 percent of the reference wing semispan. All strakes had the same root chord (at the strake-fuselage juncture) and had spanwise ordinates which were identical in percent maximum semispan (see references 43 and 44). The strakes were flat plates which, in accordance with the purposes of this study, had sharply beveled leading- and side-edges to assure the strong formation of separation induced vortex flows.

The vertical tail was swept 51.7° and its apex was situated roughly 28 percent of the fuselage length aft of the moment reference point. The tail area was approximately 14 percent of the wing reference area.

Experimental Results

Although measurements were obtained for the entire configuration matrix (including component configurations), this section will focus primarily on the characteristics of the configurations incorporating the 44° wing. The characteristics of the configurations incorporating the 44° wing are, in general, typical of the other configurations tested, but not discussed herein. Key aerodynamic quantities will be summarized as a function of strake span and/or wing sweep.

Aerodynamic Force Characteristics

The longitudinal aerodynamic characteristics of the configurations incorporating either the 44° or the 60° wing with the various strakes (as well as with no strake) are presented in figures 23 and 24. In figure 23, the parameters $C_{L,max}$ and $(\Delta C_L)_{max}$ are shown for the configuration incorporating the large strake with the 44° wing and will be used later to summarize planform effects. The addition of the various strakes to the 44° wing resulted in appreciable increases in lift coefficient at moderate to high α 's. Because the isolated 60° wing was sufficiently swept to develop appreciable vortex lift, the increments in lift realized by adding the various strakes to this wing tended to be smaller than they had been for the 44° configurations, although the overall levels of lift are comparable.

Even with the strakes providing appreciable lift increments at maneuver α 's, it is of interest to note that the strakes have very little influence on the lift characteristics at low α 's (fig. 23). The strake therefore provides a means to enhance the high- α maneuver aerodynamics without appreciably increasing the gust response during the low altitude dash portion of a mission.

The pitch characteristics of these same configurations (fig. 24) show that an increase in strake span extended the linearity of the pitch curves to increased lift coefficients. However, the straked configurations exhibited the well known pitch-up tendency near $C_{L,max}$, whereas the wing alone configurations exhibited stable characteristics. Surface flow visualization studies (ref. 9) indicated that the experimental trends discussed herein primarily arise from two sources; the vortex lift increments produced by the strake itself, and the effects of the strake vortex on the wing aerodynamics.

Figure 25 summarizes the effects of strake span and wing sweep on the maximum lift coefficient, $C_{L,max}$. The symbols refer to the variation of strake span on the left portion and the variation of wing sweep on the right portion of the figure. For the configuration incorporating the 50° wing with the medium strake, the data, though

repeatable, seem to be inconsistent with the other results and are shown as a dashed symbol. While the effects of wing sweep on $C_{L,max}$ were moderate for each strake, adding the strake to the wing caused the maximum lift coefficient to increase roughly three times as fast as the additional strake area. Hence, beneficial interference effects are occurring for the strake-wing configuration much as has been the case for canard-wing configuration. (refs. 39-42)

Interaction Effects

In addition to the maximum lift coefficient, $C_{L,max}$, the maximum increment in lift coefficient due to the addition of a strake to a configuration, $(\Delta C_L)_{max}$, can be a useful summary parameter. This parameter is illustrated in figure 24 for the configuration employing the 44° wing with the large strake and is summarized in figure 26 for the configurations of the present investigation. The higher curves shown in figure 26 represent the total value of $(\Delta C_L)_{max}$ which seems to reach a maximum level in the vicinity of 45° wing sweep for all three strakes. The wings having leading-edge sweep angles greater than 45° developed higher levels of vortex lift and, hence, the increment in lift realized by adding a strake to these wings was less. (This point was also shown in figure 23). The lower curves of figure 26 represent the increment in lift developed by the strake with the wing off at the angle of attack for which $(\Delta C_L)_{max}$ occurred. The increment between the lower and upper curves represents the interference lift which can be seen to be large when compared to the lift of the strake itself. It is interesting to note that the decrease in $(\Delta C_L)_{max}$ at the higher values of wing sweep angle seems to be due to a loss of interference lift.

These interference lift effects result in an aerodynamic synergism for strake-wing configurations much as has been observed for canard-wing configurations (ref. 39). A comparative example of the synergistic effects is presented in figure 27 between a high canard (ref. 39) and a coplanar strake (present investigation) of approximately the same area, each in the presence of the same wing ($\Lambda_w = 45^\circ$). The canard results are for the configuration which exhibited the maximum interference lift effects. The component loads for these same configurations illustrate that the wing developed more lift in the presence of the strake than it did in the presence of the high canard. In addition, the strake developed more lift in the presence of the wing and more interference lift referenced to the wing off case than did the canard. These combined effects demonstrated that, for the configurations of the present study, the strake-wing concept was preferable to the canard-wing concept insofar as lift is concerned due to increased favorable interference effects. Because of the vortex flow, the drag due to lift for these flat wing configurations can be approximated as

$$\Delta C_D = C_L \tan \alpha \quad (16)$$

The aforementioned interference lift effects result in the strake-wing configuration developing a given amount of lift at a lower α than the canard-wing configuration. Therefore, the strake-wing configuration exhibited lower levels of drag-due-to-lift than the canard-wing.

To help quantify the interference lift effects, a parameter, referred to as the additional lifting surface efficiency factor, is introduced. This parameter accounts for the additional lifting surface area of the strake or canard and is defined as

$$f = \frac{(C_{L,tot})_{ws}}{(C_{L,tot})_w} \left(\frac{S_{ref}}{S_{ref} + S_a} \right) \quad (17)$$

where $(C_{L,tot})_{ws}$ represents the experimental total lift coefficient of a configuration with a strake (or canard), $(C_{L,tot})_w$ represents the experimental total lift coefficient of the same configuration, but without the strake (or canard), S_a represents the additional exposed area of the strake or canard, and S_{ref} is the reference area. Using the strake-wing as an example, the parameter f will be unity if the increments in lift for the strake-on configurations divided by $(C_{L,tot})_w$ vary the same as the additional exposed area of the strake, S_a , divided by S_{ref} . Figure 28 shows the effect of strake area on f with α for the 44° wing and at $\alpha \approx 28^\circ$ for the range of wing sweeps tested. Limited canard-wing characteristics are also included. On the left side of figure 28, it can be seen for $\alpha > 16^\circ$ that adding area in the form of a strake to yield a strake-wing configuration is an appreciably more efficient concept ($f > 1$), due to favorable interference, than adding the same area by simply scaling the wing dimensions ($f = 1$). Similar calculations of f for the canard-wing configuration demonstrate that, for roughly the same amount of additional area, the strake-wing concept is far more efficient at producing lift than is the close coupled canard-wing concept. The general trends of f on sweep angle are shown on the right side of the figure for $\alpha \approx 28^\circ$ and are comparable

to the trends at other α 's; of course the level of the results will change with α . The decrease in f as the sweep angle exceeds 45° corresponds to the loss of interference lift such as was shown in figure 26 for $(\Delta C_L)_{\max}$. Even though the increments in lift for straked configurations incorporating the 60° wing might equally well be generated by appropriate increase in wing size ($f \approx 1$), the straked configurations may still be desirable since the strake represents a comparatively light structure compared to the higher aspect-ratio wing or canard. Therefore, even when the aforementioned benefits in lift due to interference effects are not realized, the strake-wing should result in a lighter lifting surface concept than could be realized by a wing alone or a canard-wing geometry.

It must be recognized that some of the flow improvement on the main wing induced by the strake interference could also be accomplished with variable geometry flow control devices on the wing but at the cost of some increased weight and complexity.

Mach Effects

Up to 0.8 Mach number the compressibility effects on total lift and drag coefficients were shown in reference 9 to be small for the configurations employing the 50° wing. However, as the Mach number was increased to 0.8, the strake loads decreased while the wing loads increased much as would be expected. This decrease in strake lift probably arose due to a decreased forward influence at the higher Mach numbers of the favorable induced effects of the wing on the strake.

Lateral-Directional Characteristics

The lateral-directional aerodynamic characteristics of the configurations incorporating the 44° wing are presented in figure 29. These body axis results include vertical tail and gap effects (ref. 44). Although the characteristics of the straked configurations were generally stable up to approximately 20° , they became highly nonlinear and adverse above this angle. The onset and nature of these nonlinearities involve induced effects on the wing as well as sidewash effects on the tail and afterbody and could be influenced by the bursting of the strake primary vortex ahead of the wing trailing edge on the windward side prior to the leeward side. These results as well as the extensive lateral-directional development involved during the recently successful light weight fighter programs demonstrate the configurational sensitivity of high- α lateral-directional aerodynamics and indicate the current need for detailed lateral-directional experimentation during the design of maneuvering aircraft. The development of analytical methods to predict these type of characteristics would be very useful in guiding future design programs.

THEORETICAL ANALYSIS

In the absence of an accurate method of actually modeling the flow on strake-wing combinations an attempt has been made to apply some of the suction analogy and augmentation concepts previously described.

The surface flow studies of reference 9 demonstrated that at low α 's the strake and wing leading edge vortices were individually distinguishable over the wing. However, at high α 's, the wing surface flow pattern evidenced one region of spanwise vortex flow. Although the high- α flow patterns might be interpreted as implication that the strake and wing vortices had coalesced, additional observations of the unburst wing leading-edge vortex core in addition to the strake core at these α 's suggest that the wing vortex had not coalesced with the strake vortex, but merely had been displaced away from the wing upper surface by the strake vortex, thus, allowing the strake vortex to dominate the surface flow patterns. Accordingly, the vortex lift effects due to the wing leading- and side-edge vortices may be decreased at high α 's due to vertical displacement.

The theoretical model of the vortex lift parameters for the strake-wing configurations is presented in figure 30. At low α 's, the augmented vortex lift for the strake itself will be zero due to the mild sweep differential between the leading and side edges (ref. 9). Augmented effects will occur on the wing due to both the wing and strake vortices and may be expressed as:

$$(K_{v,se})_w = \frac{(K_{v,le})_w}{\Gamma_w} \tilde{c}_{outb'd,w} + \frac{(K_{v,le})_s + (K_{v,se})_s}{\Gamma_s} \tilde{c}_{inb'd,w} \quad (18)$$

(see figure 30). At high α 's, vortex lift will be lost by the strake due to the trailing edge notch as would occur for an isolated strake. However, this vortex lift will not be

lost to the configuration; it will be recovered by the wing as part of the augmented vortex lift effect due to the strake vortex. To approximate the length which the strake vortex persists over the wing, the chord at the wing fuselage juncture was chosen. The augmented effects at high α 's may be expressed as

$$(K_{v,se})_s = \frac{(K_{v,le})_s + (K_{v,se})_s}{l_s} \tilde{c}_s \quad (19)$$

$$(K_{v,se})_w = \frac{(K_{v,le})_s + (K_{v,se})_s}{l_s} \tilde{c}_w \quad (20)$$

Because vortex lift associated with the wing leading- and side-edge vortices may be decreased due to the aforementioned vertical displacement effects, one may assume that

$$(K_{v,le})_w = (K_{v,se})_w = 0 \quad (21)$$

as a limiting case.

Correlations between this new theoretical approach and experimental lift coefficients for the configuration incorporating the 44° wing and the large strake are presented in figure 31. The high- α vortex flow theory can be seen to provide an accurate estimate of strake loads and a reasonable estimate of wing loads up to an α where vortex breakdown occurs. Correlations between theoretical and experimental pitching-moment characteristics (fig. 32) show that the low- and high- α vortex flow theories bracket the data and provide reasonable estimates of experimental trends.

Similar correlations were achieved for the other strake wing configurations (ref. 9).

VORTEX FLOW STRAKE DESIGN STUDY

General

In addition to the data base and theory development study discussed in the previous section an investigation has been conducted of a possible method for selecting vortex lift strake configurations which provide a delay in the adverse effects of vortex breakdown.

References 5 and 32 discuss the possibility that particular planforms may be superior in delaying vortex breakdown if the potential flow leading edge suction reaches high levels near the tip, implying (by the suction analogy) high levels of vortex lift near the tip. In order to apply this possibility in the design of vortex lift strakes reference 10 presents a method of designing an isolated planform for a specified potential flow suction distribution. From a study using this design procedure the gothic planform appeared desirable and the study was then extended to include the effect of the interaction between the wing and the strake on the suction distribution.

Strake Shape Effect

In order to obtain a near optimum gothic strake semispan for the integrated configuration, a study was done to size the strake semispan. Aerodynamic solutions for strake-to-wing semispan ratios ranging from 0.1 to 0.5 were studied using the VLM code. The resulting suction distributions indicated the configuration with a semispan ratio of 0.3 to be best over-all. Additional considerations must be made when the strake-wing is integrated with the body (see reference 10).

The resulting suction distribution is presented on the left of figure 33 and shows the large upwash influence that the wing has on the gothic strake. The influence is most apparent over the outermost 50 percent of strake semispan. This same curve appears on the right of figure 33 for comparison with suction distributions resulting from a delta strake of the same chord and span and the large ogee strake described in reference 9. It is interesting to note that, from this figure, the suction distribution peak for the gothic strake in the presence of the wing is the largest just as it was shown for the gothic wing of Earnshaw given in reference 10. This leads to the conclusion that the designed gothic strake may be a promising shape. All three strake-wing configurations were wind-tunnel tested. However, before these results are discussed, two water-tunnel photographs⁴ of a slightly smaller-scaled version of the designed gothic strake attached to a 50° cropped delta wing are presented at two different α 's at -5° sideslip (figs. 34 and 35). Additional water-tunnel photographs of a delta

⁴The photographs were taken by the Northrop Corporation in their water-tunnel and provided to NASA-Langley Research Center because of a mutual interest in improving the stability of the strake vortex on strake-wing configurations.

strake, having the same span and slenderness ratio as the gothic strake and mounted on the same wing, are shown for comparison. In the photographs, dark-colored water was introduced near the strake apex by means of a dye-probe to highlight the path of the vortex core. The comparative photographs show at these two α 's that the gothic strake promoted a vortex core which persisted farther into the wing pressure field before breaking down than did the core for the delta strake of the same slenderness. Similar results were obtained at intermediate and lower α 's and zero sideslip. These early water-tunnel results of the designed gothic strake tended to confirm the design approach.

With regard to the subsequent wind tunnel tests the over-all strake-wing-body C_L and C_m are presented in figure 36 for the designed gothic strake, a delta strake of the same slenderness ratio, 0.163, and the largest of the ogee strakes presented earlier. Both new strake-wing configurations were tested at subsonic speeds on a two-balance arrangement in the same manner as the ogee strake-wing configurations discussed previously. The ogee strake had a slenderness ratio of 0.237 and was chosen for comparison with the other two shapes because it performed best of all the ogees tested. Examining the C_L variations first, it can be seen that over the initial α range, the effect of the strake shape is not very important, but becomes so near $C_{L,max}$. For instance, the ogee strake configuration reaches its $C_{L,max}$ at the lowest α and after a drop-off retains a constant level; whereas, once the delta strake configuration reaches its $C_{L,max}$, the C_L continues to fall and reaches the level of the ogee strake configuration. The gothic strake configuration reaches comparable values of $C_{L,max}$ with that of the delta strake, after which the high value of C_L reached is better maintained.

All strake-wing curves show pitch-up occurring, but it is most severe on the gothic strake configuration because of the slow progression of vortex breakdown on the strake as shown by the water-tunnel photographs. This slow progression led to the relatively flat post $C_{L,max}$ behavior of its C_L vs α curve.

Component Loads

To get an idea of how well the C_L characteristics could be estimated for the gothic strake configuration, the component loads have been separated from the test data and are compared with various vortex-lift theories. The augmented lift concept described previously and advanced for the ogee-strake configuration is also employed here. Figure 37 shows that both the low- and high- α vortex-lift theories overpredict the strake C_L , whereas, the high- α vortex-lift theory estimates reasonably well the wing C_L . In order to determine the degree to which vortex breakdown effects reduced the lift on the strake, it was necessary to accurately extrapolate the pre-breakdown lift effectiveness to higher angles of attack. This was done by extracting the gothic strake $K_{v,tot}$ by a curve fitting technique and a value of 2.0 was determined. This procedure was also employed for the delta strake configuration. The ratio of the strake C_L data to the curve-fitted vortex-flow theory, $C_{L,theory}^*$ is presented in figure 38 for the previously mentioned strakes along with the largest ogee strake configuration, whose data were well estimated by the high- α vortex-flow theory. This figure shows the gothic strake to retain more of its vortex lift at higher α 's than either of the other strakes and, moreover, to lose that lift less suddenly than the others. That explains why the total C_L for the gothic strake-wing configuration is essentially constant for $\alpha > 38^\circ$ in figure 36, even though the wing lift rapidly falls off in that α range.

VORTEX FLOW DRAG STUDY

The previous portions of this paper have dealt primarily with the lift capability provided by vortex flow on slender lifting surfaces. However, while the high vortex lift capability can be provided with simple light-weight surfaces, it is generally accompanied by a drag-due-to-lift penalty associated with the loss of leading-edge thrust due to the leading-edge separation. Considerable improvement in the maneuver performance of slender wing aircraft could be provided if the wing could be shaped such that a sizeable portion of the leading-edge thrust could be recovered, possibly on a cambered leading edge, while still maintaining a large portion of the available vortex lift. This concept is not new, but the recent improvements in vortex flow analysis methods may provide at least design by analysis capabilities for an improved implementation of the concept. It is the purpose of this section to review some recent studies directed towards this goal, particularly as it might apply to maneuvering aircraft utilizing slender wings required for supersonic cruise.

The proposal to develop a wing with efficient vortex lift becomes a more realistic goal as the aspect ratio is reduced since studies (see reference 45, for example) have indicated that on very slender planar wings the lift dependent drag using vortex flow can be less than $1/\pi A$. Figure 39 is taken from reference 45 and shows an example for $M = 0.8$ and $C_L = 0.3$ indicating that for sweep angles larger than 83° measured drag-due-to-lift parameter values for wings with vortex flow are below that of $1/\pi A$. There are two ways of visualizing this occurrence: (1) in the "far field" sense, the leading-edge vortices act as fluid endplates and therefore deflect a larger mass of

air through a smaller angle to develop a given lift; and (2) in the "near field" sense, for slender wings, only a small component of the leading-edge suction is available for thrust in attached flow, so it is better to let the flow separate and form a vortex to reduce the α because of the additional flow entrainment occurring at a particular C_L . This also shows up in reduced ΔC_D because $\Delta C_D = C_L \tan \alpha$. The other two curves in figure 39, in addition to the $1/\pi A$ curve, are for zero percent leading-edge suction. The upper curve is based on attached-flow with zero leading edge suction (ZLESF), whereas, the one labeled suction analogy, which agrees with the data, assumes that leading-edge vortices are formed, promoting the upper surface flow reattachment and the development of vortex lift. The suction analogy confirms the reduced drag, but as is demonstrated, extremely large sweep angles are required in order to accomplish this task, resulting in aspect ratios of 0.5 or less. Wings in this aspect ratio range are, of course undesirable from an aircraft range-payload viewpoint; thus, improvements in the drag-due-to-lift parameter for wings with higher aspect ratio will be sought and the aforementioned concept of recovering an appreciable amount of leading-edge thrust on cambered, or nonplanar wings will be explored.

Theoretical Methods and Assessment

The theoretical methods used in the study are the Smith's (or Barsby's) conical flow and two nonconical ones, the vortex-lattice-method with suction analogy (VLM-SA) and the free-vortex-sheet (Boeing). These methods are depicted in idealized form for nonplanar wings in figure 40 and have been discussed previously. In the (VLM-SA) method it is assumed that the vortex lift is concentrated along the leading edge and therefore the drag calculations are expected to be somewhat optimistic particularly at high C_L 's. The methods have already been compared with data for a planar delta in figures 7 and 8. The nonconical methods are compared in figure 41 with over-all force and moment data for a nonplanar delta having conically cambered leading edges. Pressure distributions predicted by the free vortex sheet method are evaluated in figure 42.

The following conclusions are drawn from this study: (1) the two methods predict C_L vs α and C_L vs C_m equally well; (2) the free-vortex-sheet method predicts the C_D vs C_L results better; and (3) the free-vortex-sheet method predicts the experimental spanwise pressure distributions well though not to the extent that might be expected from the overall force results. This indicates that there is still room for improvement in the singularity representation and flow modeling.

Study of Drag-Due-to-Lift Parameter

Applying these three methods to 80° conically cambered delta wings, modeled first by Barsby using conical flow in reference 2, led to the $\Delta C_D/C_L^2$ results presented in figure 43. Barsby had noted that using conical flow the $\Delta C_D/C_L^2$ values decreased with increasing camber height (denoted p on this figure). Similar trends are noted for both nonconical methods developing vortex flow as presented in reference 11. It is interesting to note from figure 43 how well the two nonconical theories agree for camber values up to 0.4, although the levels are seen to be different than for conical flow theory due to the higher α 's required with the nonconical flow. The free-vortex-sheet method did not converge for $p = 0.6$ or $p = 1.0$ at any α and from reference 11 did not agree well with the VLM-SA drag polar which had been shown in that reference to agree well with data.

Figure 43 also presents the attached flow full suction solution (FLESF) from the VLM method for these wings. This curve will be different than that for the nonplanar optimum (see reference 46) because these conically cambered deltas are not optimum potential flow shapes.

Based on the general trends of the methods and the accuracy study of reference 11, it was decided to proceed with one nonconical flow method, that being the VLM-SA, and a camber range of $0 < p < 0.4$ for the remainder of this study. This method performs the computations with the same order of simplicity and cost as the conical-flow solution, but with comparable accuracy and two orders of magnitude lower cost than the free-vortex-sheet method.

Figure 44 presents the calculated $\Delta C_D/C_L^2$ data from the VLM-SA divided by the VLM (FLESF) solution (called K_3 from reference 11), crossplots at constant C_L , and the effect of sweep at constant p and C_L . Note on the left the steepness of the slope for all p values with increasing C_L . The C_L range for the entire figure is restricted because the FLESF solutions have a $C_{L,max} \approx 0.6$. Therefore, on the cross plot of K_3 with p , only $C_L = 0.3$ and 0.5 appear. The point is made though that increasing C_L or p does reduce K_3 . At the right for $p = 0.2$ the K_3 variation with Λ decreases with sweep and/or C_L increases. The results indicate that even for the arbitrary camber shapes used appreciable reductions in drag-due-to-lift can be achieved particularly at the high lift coefficient desired for maneuver conditions. Note that this is also true for the not-so-slender wings of more practical interest.

Figure 45 is a summary figure of the drag-due-to-lift parameter variation with C_L for an 80° delta wing with $p = 0.4$ and includes solutions due to two attached flow methods and one vortex flow method. This figure presents several interesting pieces of information: (1) for FLESAP the $(\Delta C_D/C_L^2)$ is almost the same as the nonplanar optimum at $C_L \approx 0.2$ even though the former is from a near-field solution; (2) for ZLESAP the $(\Delta C_D/C_L^2)$ reaches a minimum of about twice that of the nonplanar optimum and its curve exceeds a value of 1.4 for $\alpha > 30^\circ$; (3) if one thinks in terms of going from the FLESAP to the ZLESAP curve when the leading-edge force is lost, it is important to realize that for thin wings with high sweep the flow will form vortices so the change will be only from the FLESAP to the suction-analogy curve. Thus, the vortex formation provides a natural means of reducing $\Delta C_D/C_L^2$ and yields only a small fraction of the anticipated increase; (4) the $\Delta C_D/C_L^2$ associated with vortex flow, from the suction-analogy solution, continues to decrease over the α range, whereas, the FLESAP solution result increases after its minimum is reached; (5) due to the action of the vortex flow, much lower α 's are required to reach a given C_L and, in fact, it is not possible for this fixed geometry with FLESAP to reach C_L levels much larger than shown, since its $C_{L,max}$ is 0.597; and (6) the improvement in $\Delta C_D/C_L^2$ which may be gained by keeping the flow at the nonplanar optimum is difficult to maintain over the C_L range because of the tendency of the flow to separate. However, if variable geometry devices were added, primarily near the leading edge, the reduction available in $\Delta C_D/C_L^2$ would be the increment indicated from the suction-analogy curve. Thus, there is an α range for the vortex flow solution in which the increase in $\Delta C_D/C_L^2$ from the nonplanar optimum is small even though the C_L range is vastly extended from that of the FLESAP. Considering this fact and recognizing the extreme difficulty and weight penalty associated with attempting to keep the flow attached, it may be best to let the flow separate in the maneuver and utilize vortex lift. This approach appears particularly attractive for supersonic vehicles which require high maneuver capability at subsonic or transonic speeds.

VORTEX FLOW WING DESIGN USING SUCTION ANALOGY

In the absence of a design method based on the free vortex sheet type modeling of the flow, this section describes a procedure that uses the suction analogy in designing the mean-camber surface of a wing which is to have leading-edge vortex flow with minimized drag penalty. The resulting design represents an optimum shape for the assumptions employed just as the attached-smooth-onflow solution does and should, therefore, yield values of $\Delta C_D/C_L^2$ near the planar or nonplanar optimum depending on the wing geometry, just as the attached-flow solution does. The approach to be used is based on the assumption that the optimum vortex lift condition involves relatively small deviations from an attached-smooth-onflow solution, so that the vortex lift is concentrated on the cambered leading edge, an assumption which also allows the suction analogy to be employed. Therefore, the techniques used are: (1) the attached-smooth-onflow design-code of reference 47, based on the VLM, which is employed to obtain a starting solution and (2) the lift and drag equations from the VLM-SA which include nonlinear contributions from the circulation in addition to trigonometric terms involving α and the local angle of attack due to camber/twist, α_1 .

An expected limitation of this procedure is the same as for the VLM-SA, that is, the vortex generated is assumed to remain small and near the leading edge. Deviations from this size and location will cause a degradation in $\Delta C_D/C_L^2$, thereby making the computed results optimistic.

An outline or flow chart of the vortex-flow design-code is given on figure 46. It should be noted that this design method is an iterative one and not a direct solution as in the attached flow solution. The outlined solution steps are as follows: (1) determine $\{\alpha_1\}$ and $\{\Gamma\}$ from the linear theory (ref. 47); (2) enter the CONMIN optimizer (ref. 48) with $\{\alpha_1\}$ and $\{\Gamma\}$ and perturb each term in the $\{\Gamma\}$; (3) with the perturbed $\{\Gamma\}$ compute the pay-off function D_1 in terms of the lift and drag developed, L and D , respectively; (4) repeat for each perturbed $\{\Gamma\}$ set and then optimize so as to minimize D_1 ; (5) with the $\{\Gamma\}$ that minimizes D_1 determine if it satisfies the lift constraint to within a tolerance; (6) if not, change the scaling k by a factor of ten and begin repeating with step (2); (7) if so, determine from linear theory the $\{\alpha_1\}$ called $\{\alpha_1\}_1$, compatible with the $\{\Gamma\}$; (8) compare the $\{\alpha_1\}_1$ with the original $\{\alpha_1\}$ to determine if each term is within a tolerance; (9) if not, make $\{\alpha_1\} = \{\alpha_1\}_1$ and repeat from step (2); and (10) if so, then integrate using a spline routine the α_1 's associated with a particular spanwise position from the trailing edge forward to determine the local elevations along the chord, i.e., mean-camber lines. Repeat at each spanwise position then stop. This entire procedure for the example wing with 200 panels requires 9 iterations on $\{\Gamma\}$ and 6 iterations on $\{\alpha_1\}$ and is accomplished in about 400 central processing seconds on the CDC CYBER 175 digital computer.

Examples of the results of this procedure are given in figures 47 and 48 for a 75° planar delta wing at a $C_{L,D} = 0.3$ and $M = 0$. There are three sets of curves presented. Two are vortex-flow solutions with and without any constraint on the minimum levels of $\{\Gamma\}$, called side constraints, and the other is the attached-smooth-onflow solution, given for reference.

The detailed results for the three solutions on figures 47 and 48 will be discussed together. The only item to be discussed separately is found on figure 47 where the drag-due-to-lift parameters for the two vortex-flow solutions are seen to agree well with the planar optimum result of 0.2970. However, just as in reference 49 for low aspect ratio wings and small N_c values, the results from the attached flow solution are slightly low with respect to the planar optimum. Examining these two figures, it is obvious that both vortex-flow solutions lead to higher incidence angles inboard and less outboard; therefore, more washout is imposed. There appear to be two reasons for this occurrence. The first is to build up the loading (Γ/U) inboard and, consequently, the vortex lift in a region where the planar vortex lift is typically small. The second is that outboard where the planar vortex lift would be high, it is suppressed somewhat so that a ramp-like mean-camber-line can be generated. This camber line and the one near the midsemispan are so shaped as to allow the vortex flow that develops near the leading edge to generate a force component which can reduce the drag. The effect of imposing a constraint to keep the local lift positive, called side constraint and assured by keeping $(\Gamma/U) > 0$, is most noticed on the outermost 20 percent of the wing, especially near the wing tip, where, in order to keep $(\Gamma/U) > 0$ near the leading edge, the chord load and camber line are considerably altered.

There are two general observations which need to be made with regard to the presented results: (1) even though chord loadings (Γ/U) are graphed for the attached- and vortex-flow solutions, it should be understood that the suction pressures associated with the separated vortex are not modeled. They are only accounted for in an overall manner through the suction analogy, which leads to an estimate of the vortex-flow-aerodynamic results; and (2) vortex-flow mean-camber lines do differ by more than a small amount, except at midsemispan, from the attached-flow solutions. This possibility was not anticipated and could, therefore, impact on the effectiveness of the resulting wing. However, regardless of the final camber design, only by model construction and wind tunnel testing will an assessment be possible of this vortex-flow design-procedure.

Use of the suction analogy must be considered as only an intermediate approach and a concerted effort should be made to develop the actual flow modeling techniques to the stage that they can be utilized in the design process.

CONCLUDING REMARKS

This paper has reviewed some of the progress being made at the NASA Langley Research Center in the development of both analysis and design capabilities for high speed aircraft which involve vortex flow and its associated aerodynamic forces and moments.

With regard to analysis capabilities various nonconical flow methods have been described and evaluated by comparisons with experimental data for configurations ranging from simple delta wings to various strake-wing combinations. The extension of the suction analogy to arbitrary wing planforms and certain classes of multiple lifting surfaces was reviewed and comparisons with experimental results indicated it to be a reasonably accurate and economical method when only the over-all forces and moments are required. Where detailed surface pressure distributions are needed, in addition to forces and moments, the free vortex sheet method being developed under contract by Boeing was shown to offer considerable promise and should be further refined and extended to arbitrary configurations. Additional research is required to provide the criteria and flow modeling techniques needed to yield aerodynamic estimates at angles of attack where vortex breakdown has occurred ahead of the trailing edge. This would be particularly useful in establishing maximum lift and stability and control characteristics.

With regards to design related research the results of parametric wind tunnel and numerical studies were presented for a series of ogee strake-wing combinations and the favorable vortex interactions discussed. In addition an approach to a vortex strake design procedure was introduced and applied to a strake design. Wind tunnel tests of the design indicated that it provided good vortex stability characteristics.

As a step towards the development of a design procedure to provide optimum vortex flow aerodynamic performance through wing surface warp, the application of several analysis theories to the prediction of the drag due-to-lift for a series of conically cambered delta wings was described. These preliminary results, which accounted for trailing edge effects, were encouraging and indicated that the vortex flow drag could be reduced towards that associated with attached flow either by increasing conical camber or lift. Finally an application of the suction analogy in an approximate design mode was presented and the resulting surface warp shown to be much different than that for attached flow. However, the development of a more accurate flow modeling design method, possibly based on the free-vortex-sheet approach, is needed before wings with highly efficient vortex lift characteristics can be designed.

REFERENCES

1. Smith, J. H. B.: Improved Calculations of Leading-Edge Separation From Slender Delta Wings. R.A.E.-T.R. No. 66070, March 1966.
2. Barsby, J. E.: Flow Past Conically Cambered Slender Delta Wings with Leading-Edge Separation. A.R.C.-R.&M. No. 3748, 1974.
3. Polhamus, E. C.: A Concept of the Vortex Lift of Sharp-Edge Delta Wings Based on a Leading-Edge-Suction Analogy. NASA TN D-3767, 1966.
4. Lamar, J. E.: Extension of Leading-Edge-Suction Analogy to Wings With Separated Flow Around the Side Edges at Subsonic Speeds. NASA TR R-428, 1974.
5. Lamar, J. E.: Some Recent Applications of the Suction Analogy to Vortex-Lift Estimates. NASA SP-347, Part II, 1975, pp. 985-1011.
6. Mehrotra, S. C., and Lan, C. E.: A Theoretical Investigation of the Aerodynamics of Low Aspect-Ratio Wings With Partial Leading-Edge Separation. NASA CR-145304, 1978.
7. Brune, G. W.; Weber, J. A.; Johnson, F. T.; Lu, P.; and Rubbert, P. E.: A Three-Dimensional Solution of Flows Over Wings With Leading-Edge Vortex Separation. NASA CR-132709, 1975.
8. Johnson, F. T.; Lu, P.; Brune, G. W.; Weber, J. A.; and Rubbert, P. E.: An Improved Method for the Prediction of Completely Three-Dimensional Aerodynamic Load Distribution of Configurations with Leading Edge Vortex Separation. AIAA Paper No. 76-417, July 1976.
9. Luckring, J. M.: Theoretical and Experimental Aerodynamics of Strake-Wing Interactions Up to High Angles-of-Attack. AIAA Paper No. 78-1202, July 1978.
10. Lamar, J. E.: Strake Wing Analysis and Design. AIAA Paper No. 78-1201, July 1978.
11. Lamar, J. E.: Subsonic Vortex Flow Design Study for Slender Wings. AIAA Paper No. 78-154, January, 1978.
12. Lan, C. E.: A Quasi-Vortex-Lattice Method in Thin Wing Theory. J. Aircraft, vol. 11, no. 9, Sept. 1974, pp. 518-527.
13. Mook, D. T. and Maddox, S. A.: Extension of a Vortex-Lattice Method to Include the Effects of Leading-edge Separation. J. Aircraft, vol. 11, no. 2, Feb. 1974, pp. 127-128.
14. Lamar, J. E.: A Modified Multhopp Approach for Predicting Lifting Pressures and Camber Shape for Composite Planforms in Subsonic Flow. NASA TN D-4427, 1968.
15. Bradley, R. G.; Smith, C. W.; and Bhateley, I. C.: Vortex-Lift Prediction for Complex Wing Planforms. J. Aircraft, vol. 10, no. 6, June, 1973, pp. 379-381.
16. Mendenhall, M. R.; and Nielsen, J. N.: Effect of Symmetrical Vortex Shedding on the Longitudinal Aerodynamic Characteristics of Wing-Body-Tail Combinations. NASA CR-2473, 1975.
17. Lamar, J. E.; and Gloss, B. B.: Subsonic Aerodynamic Characteristics on Interacting Lifting Surfaces with Separated Flow Around Sharp Edges Predicted by Vortex-Lattice Method. NASA TN D-7921, 1975.
18. Luckring, J. M.: Some Recent Applications of the Suction Analogy to Asymmetric Flow Situations. Vortex-Lattice Utilization. NASA SP-405, 1976, pp. 219-236.
19. Lamar, J. E.: Prediction of Vortex Flow Characteristics of Wings at Subsonic and Supersonic Speeds. J. Aircraft vol. 13, no. 7, July 1976, pp. 490-494.
20. Gloss, B. B., and Johnson, F. T.: Development of an Aerodynamic Theory Capable of Predicting Surface Loads on Slender Wings With Vortex Flow. Proceedings of the SCAR Conference. NASA CP-001, 1976, pp. 55-67.
21. Kuhlman, J. M.: Analytical Studies of Separated Vortex Flow on Highly Swept Wings. NASA CR-3022, 1978.
22. Wentz, W. H., Jr.: Effects of Leading-Edge Camber on Low-Speed Characteristics of Slender Delta Wings. NASA CR-2002, 1972.
23. Polhamus, E. C.: Predictions of Vortex-Lift Characteristics by a Leading-Edge Suction Analogy. J. Aircraft, vol. 8, no. 4, April 1971, pp. 193-199.
24. Packham, D. H.: Low-Speed Wind-Tunnel Tests on a Series of Uncambered Slender Pointed Wings with Sharp Edges. British A.R.C.-R.&M. No. 3161, 1961.

25. Stahl, W.: Zum nichtlinearen Verhalten des Auftriebes schlanker, ebener Deltaflügel in Ueberschallströmung. Bericht 67 A 44, 1968.
26. Hill, W. A., Jr.: Experimental Lift of Low-Aspect-Ratio Triangular Wings at Large Angles of Attack and Supersonic Speeds. RM A57117, Nov. 1957.
27. Wentz, W. H., Jr.: Effects of Leading-Edge Camber on Low-Speed Characteristics of Slender Delta Wings - Techniques and Tabulated Data. NASA CR-112016, 1972.
28. Gersten, K.: Calculation of Non-Linear Aerodynamic Stability Derivative of Aeroplanes. AGARD Rep. 342, Apr. 1961.
29. Garner, H. C.; and Lehrian, Doris E.: Non-Linear Theory of Steady Forces on Wings With Leading-Edge Flow Separation. NPL Aero Rep. 1059, Brit. A.R.C., Feb. 15, 1963.
30. Belotserkovskii, S. M. (J. W. Palmer, transl.): Calculation of the Flow About Wings of Arbitrary Planform at a Wide Range of Angle of Attack. Libr. Transl. No. 1433, Brit. R.A.E., Feb. 1970.
31. Flax, A. H.; and Lawrence, H. R.: The Aerodynamics of Low-Aspect-Ratio Wings and Wing-Body Combination. Third Anglo-American Aeronautical Conference, Jean Bradbrooke and E. C. Pike, eds., Royal Aeronautical Soc., 1952, pp. 363-398.
32. Lamar, J. E.: Recent Studies of Subsonic Vortex Lift Including Parameters Affecting Stable Leading-Edge Vortex Flow. J. Aircraft, vol. 14, no. 12, December 1977, pp. 1205-1211.
33. Davenport, E. E. and Huffman, J. K.: Experimental and Analytical Investigation of Subsonic Longitudinal and Lateral Aerodynamic Characteristics of Slender Sharp-Edge 74° Swept Wings. NASA TN D-6344, 1971.
34. Manro, M. E., Manning, K. J. R., Hallstaff, T. H., and Rogers, J. T.: Transonic Pressure Measurements and Comparison of Theory to Experiment for an Arrow-Wing Configuration. NASA CR-2610, 1975.
35. Jones, R. T.: Reduction of Wave Drag by Antisymmetric Arrangement of Wings and Bodies. AIAA J., vol. 10, no. 2, Feb. 1972, pp. 171-176.
36. Luckring, J. M.: Theoretical and Experimental Analysis of the Longitudinal and Lateral Aerodynamic Characteristics of Skewed Wings at Subsonic Speeds to High Angles of Attack. NASA TN D-8512, 1977.
37. Krone, N. J.: Divergence Elimination With Advanced Composites. AIAA Paper No. 75-1009, 1975.
38. Huffman, J. K.; and Fox, C. H., Jr.: Subsonic Longitudinal and Lateral-Directional Static Aerodynamic Characteristics for a Model With Swept Back and Swept Forward Wings. NASA TM X-74093, 1978.
39. Gloss, B. B.: The Effect of Canard Leading-Edge Sweep and Dihedral Angle on the Longitudinal and Lateral Aerodynamic Characteristics of a Close-Coupled Canard-Wing Configuration. NASA TN D-7814, 1974.
40. Gloss, B. B., and McKinney, L. W.: Canard-Wing Lift Interference Related to Maneuvering Aircraft at Subsonic Speeds. NASA TM X-2897, 1973.
41. Gloss, B. B.: Effect of Canard Height and Size on Canard-Wing Interference and Aerodynamic Center Shift Related to Maneuvering Aircraft at Transonic Speeds. NASA TN D-7505, 1974.
42. Gloss, B. B.: Effect of Wing Planform and Canard Location and Geometry on the Longitudinal Aerodynamic Characteristics of a Close-Coupled Canard Wing Model at Subsonic Speeds. NASA TN D-7910, 1975.
43. Luckring, J. M.: Subsonic Longitudinal and Lateral Aerodynamic Characteristics for a Systematic Series of Strake Wing Configurations. NASA TM X-78642, 1978.
44. Fox, C. H., Jr.: Subsonic Longitudinal and Lateral Directional Static Stability Characteristics of a General Research Fighter Model Employing a Strake-Wing Concept. NASA TM X-74071, 1978.
45. Polhamus, E. C.: Subsonic and Transonic Aerodynamic Research. Vehicle Technology for Civil Aviation, NASA SP-292, 1971, pp. 27-44.
46. Cone, C. D., Jr.: The Aerodynamic Design of Wings with Cambered Span Having Minimum Induced Drag. NASA TR R-152, 1963.
47. Lamar, J. E.: A Vortex-Lattice Method for the Mean Camber Shapes of Trimmed Noncoplanar Planforms with Minimum Vortex Drag. NASA TN D-8090, 1976.
48. Vanderplaats, G. N.: CONMIN-A Fortran Program for Constrained Function Minimization - User's Manual. NASA TM X-62282, 1973.

49. Margason, R. J., Lamar, J. E.: Vortex-Lattice FORTRAN Program for Estimating Subsonic Aerodynamic Characteristics of Complex Planforms. NASA TN D-6142, 1971.

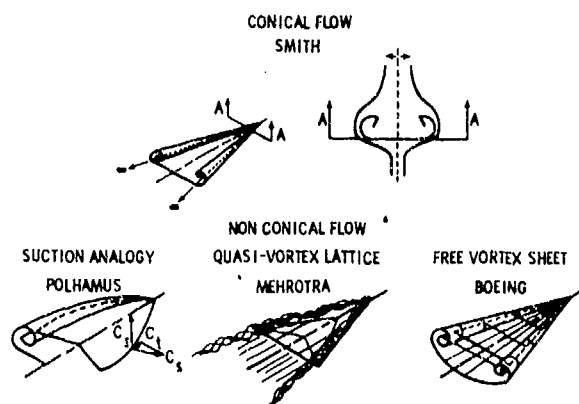


Figure 1.- Theoretical Methods.

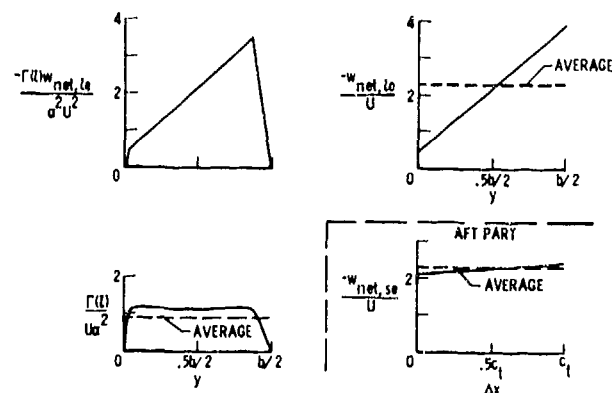


Figure 4.- Variables used in augmented vortex lift determination. Cropped delta wings, delta part idealized.

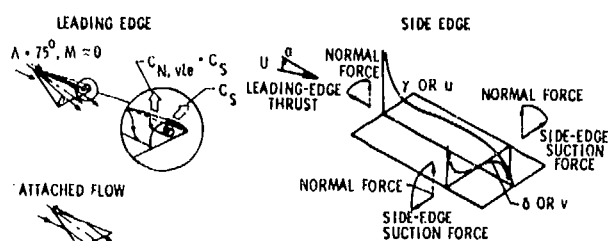


Figure 2.- Vortex-lift concept: Suction analogy applied to leading and side edge.

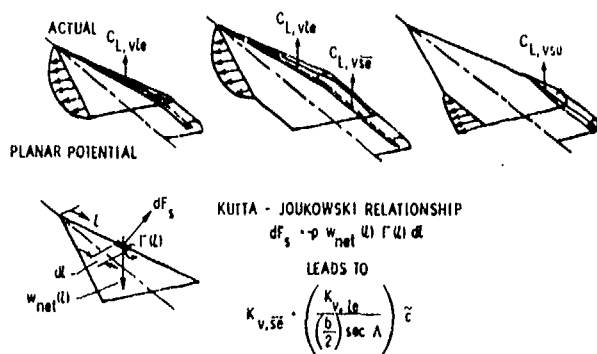


Figure 3.- Concept of augmented vortex lift.

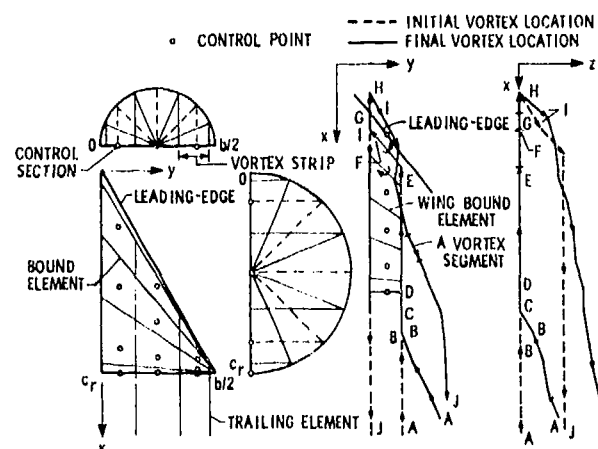


Figure 5.- Quasi-vortex lattice method - Mehrotra.

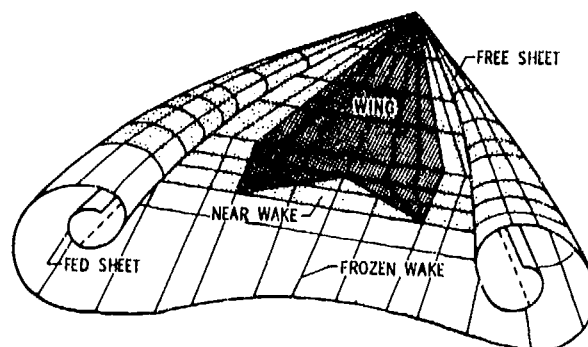


Figure 6.- Free vortex sheet method - Boeing.

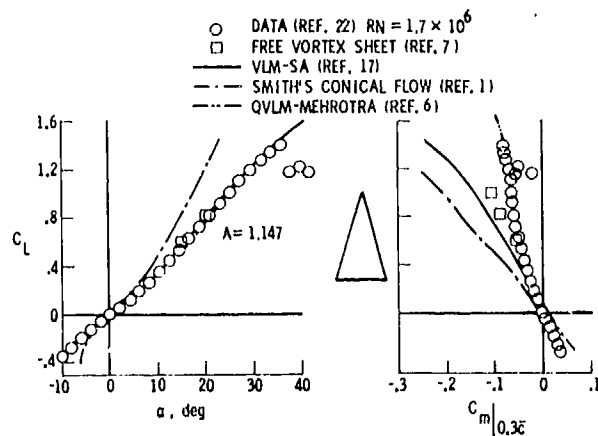


Figure 7.- Longitudinal aerodynamic estimates for a 74° flat delta wing.

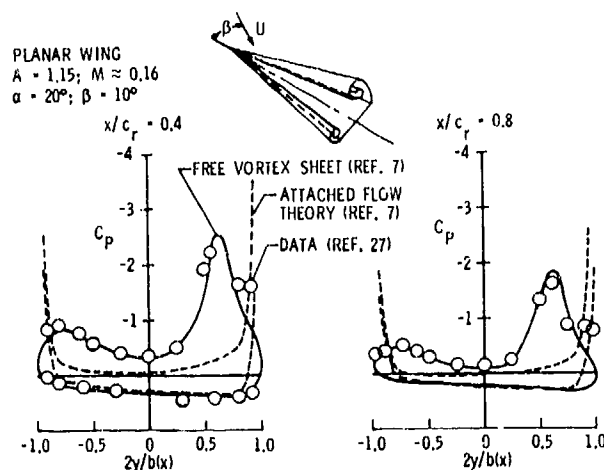


Figure 10.- Effect of sideslip on spanwise pressure distributions for a 74° flat delta wing.

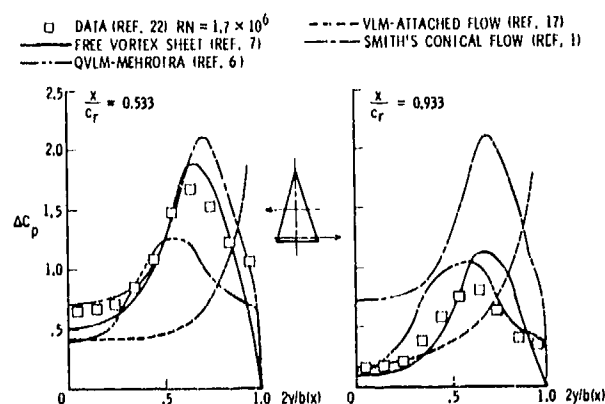


Figure 8.- Spanwise pressure distribution for a 74° flat delta wing. $\alpha = 20^\circ$, $M \approx 0$.

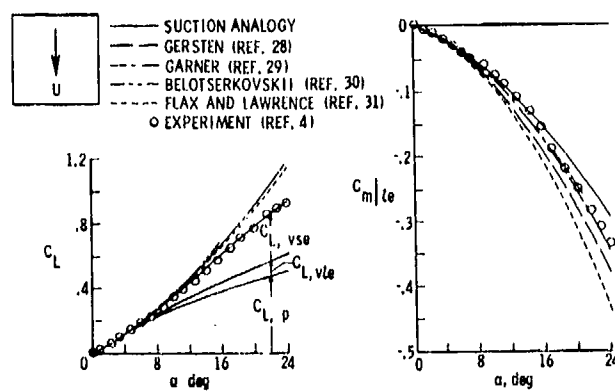


Figure 11.- Longitudinal aerodynamic estimates for a rectangular wing. $A = 1$, $M \approx 0$.

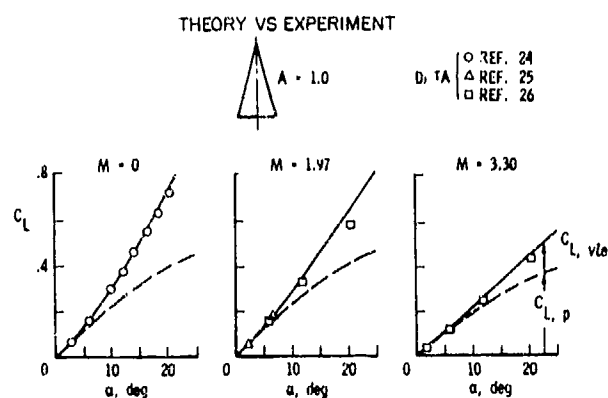


Figure 9.- Mach effects for supersonic vortex lift estimates.

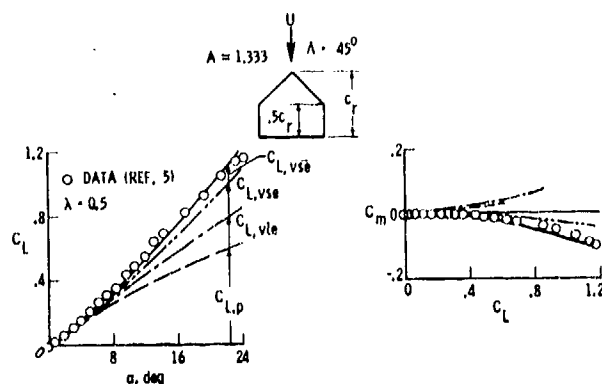


Figure 12.- Aerodynamic characteristics for a cropped delta wing. $M \approx 0$.

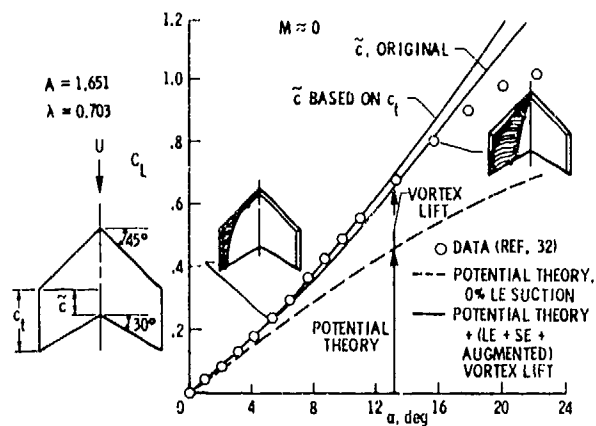


Figure 13.- Effect of \bar{c} definition on lift estimates. $M \approx 0$.

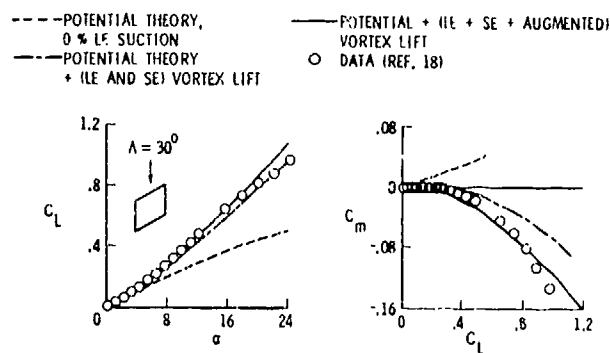


Figure 16.- Longitudinal aerodynamic characteristics of a skewed wing planform. $M \approx .10$.

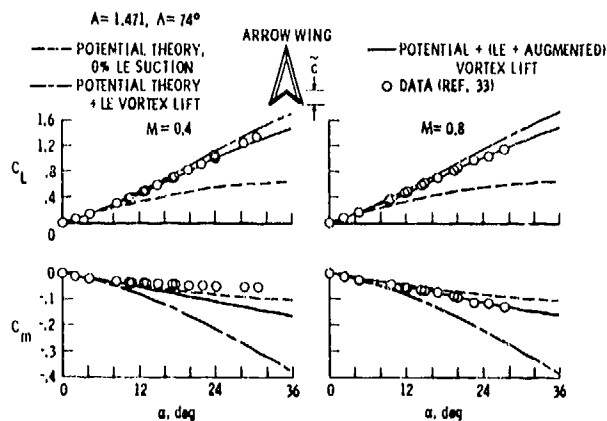


Figure 14.- Effect of Mach number on augmented vortex lift and pitch, arrow wing.

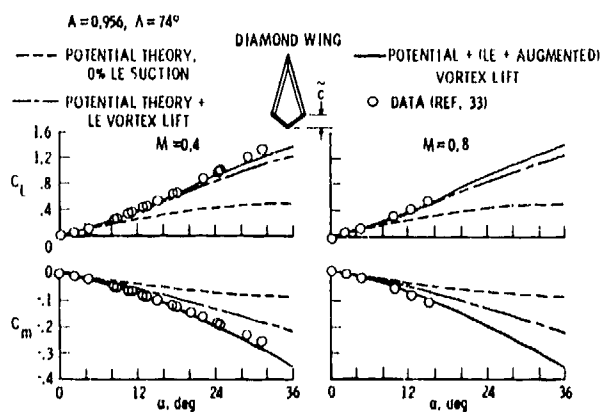


Figure 15.- Effect of Mach number on augmented vortex lift and pitch, diamond wing.

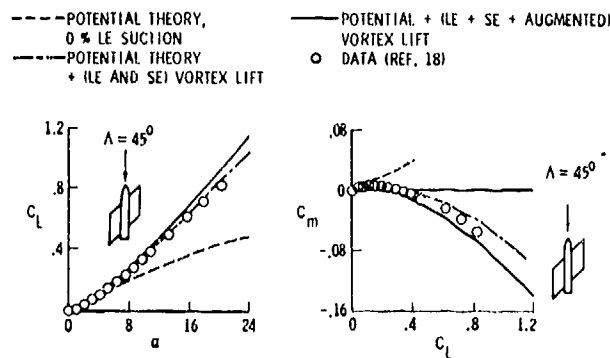


Figure 17.- Longitudinal aerodynamic characteristics of a skewed-wing body configuration. $M \approx .10$.

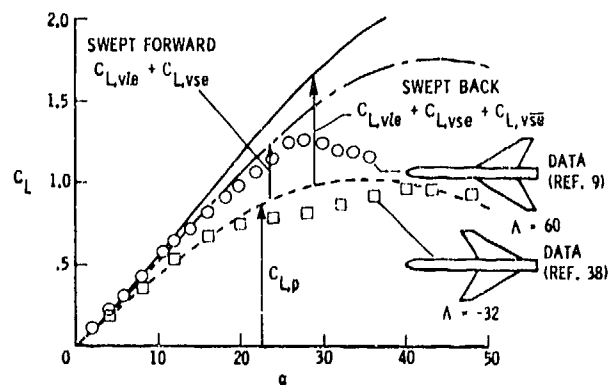


Figure 18.- Effect of forward sweep on vortex lift characteristics.

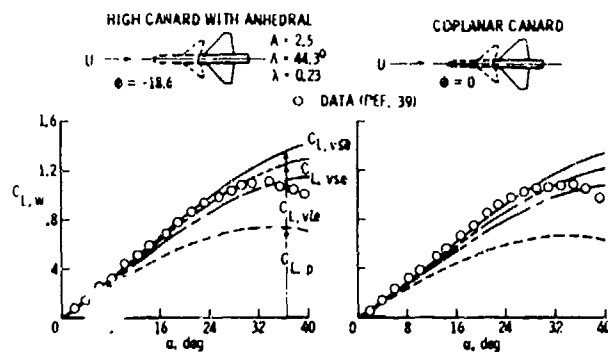


Figure 19.- Effect of canard position on wing lift characteristics for a canard-wing combination. $M = 0.3$.

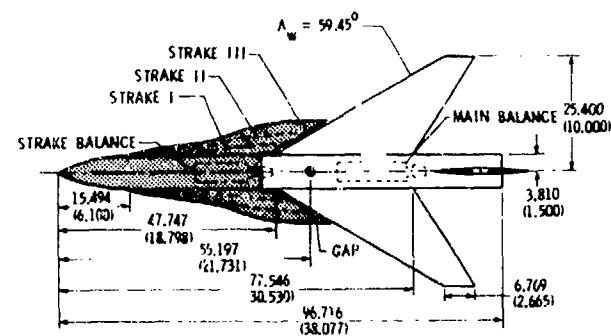


Figure 22.- Planform for parametric strake-wing study.

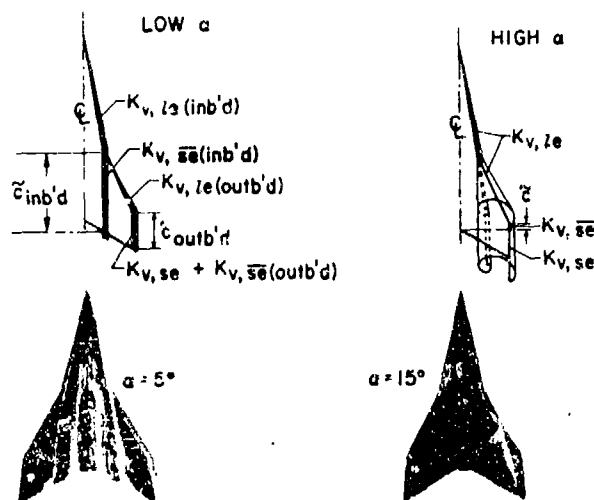


Figure 20.- Vortex flow modeling methods for double delta planforms. Suction analogy and augmented vortex lift.

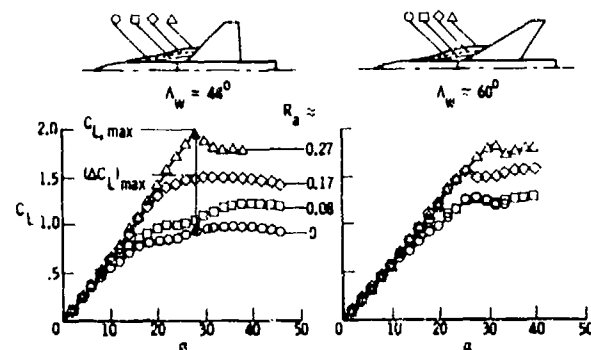


Figure 23.- Effect of strake span wing sweep on lift characteristics. $M = 0.3$, Ref. 9.

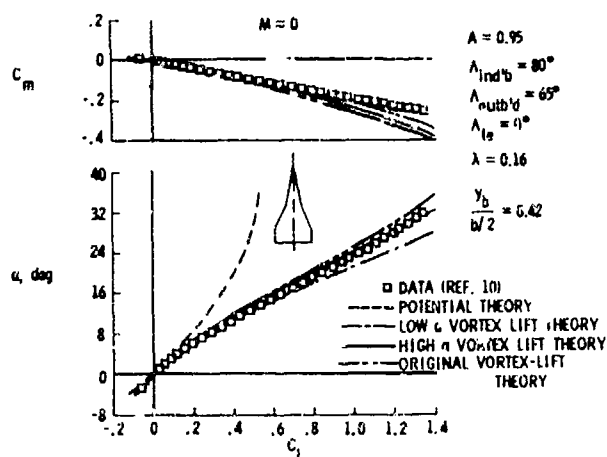


Figure 21.- Longitudinal aerodynamic characteristics for double delta planforms.

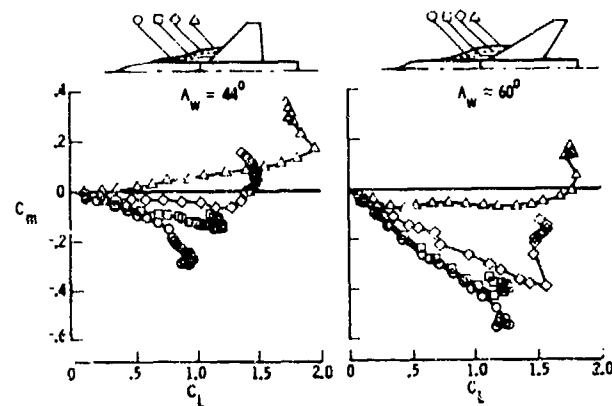


Figure 24.- Effect of strake span and wing sweep on pitch characteristics. $M = 0.3$, Ref. 9.

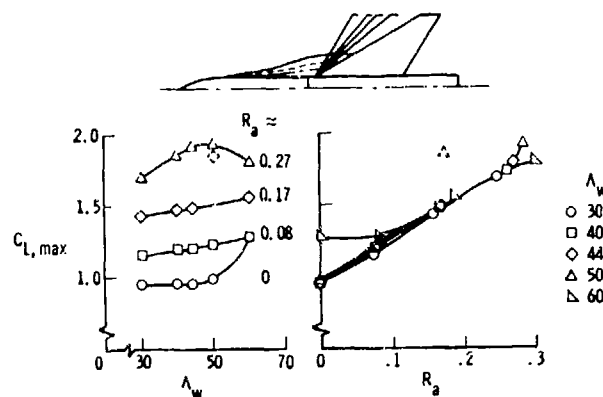


Figure 25.- Effect of strake span and wing sweep on $C_{L,max}$. $M = 0.3$.

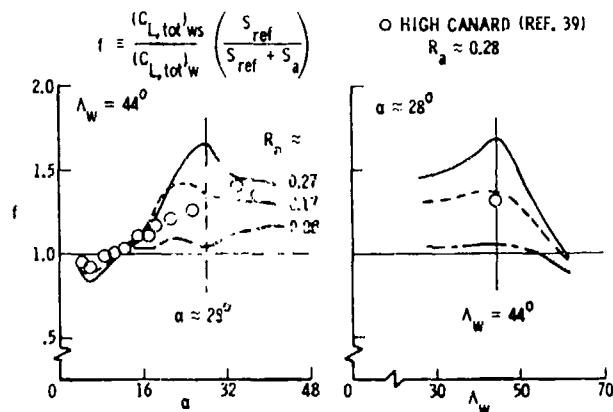


Figure 28.- Planform effect on additional lifting surface efficiency factor. $M = 0.3$.

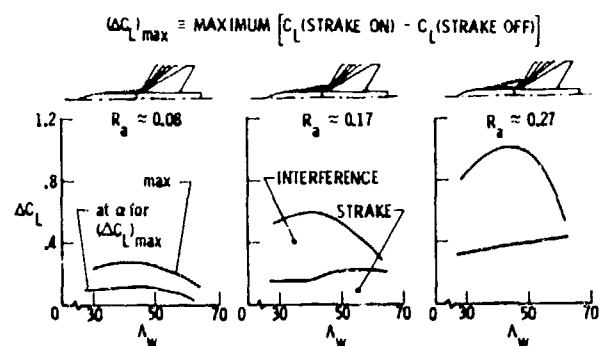


Figure 26.- Effect of strake span and wing sweep on $(\Delta C_L)_{max}$. $M = 0.3$.

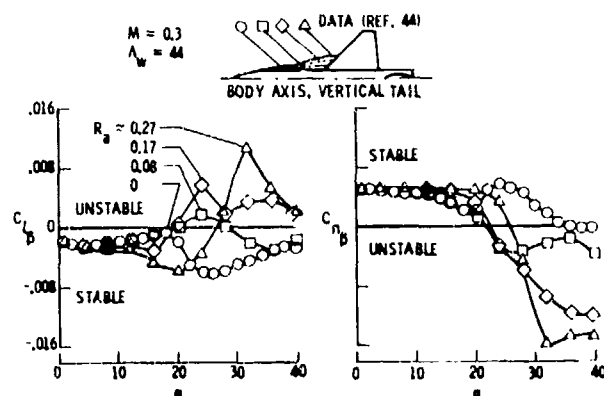


Figure 29.- Strake span effect on lateral-directional characteristics. $M = 0.3$.

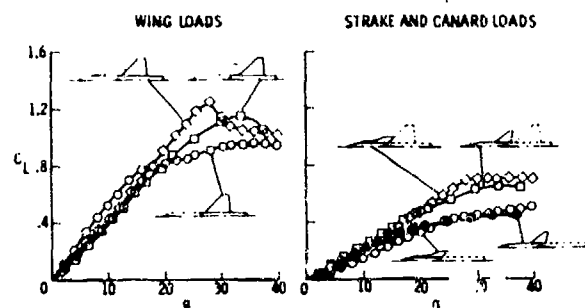


Figure 27.- Component loads for an aerodynamic synergism. High canard (ref. 39), coplanar strake (ref. 9). $\Lambda_w = 44^\circ$, $M = 0.3$.

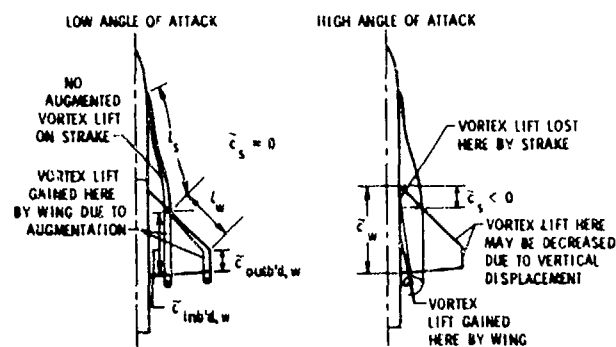


Figure 30.- Vortex flow modeling for strake-wing configurations.

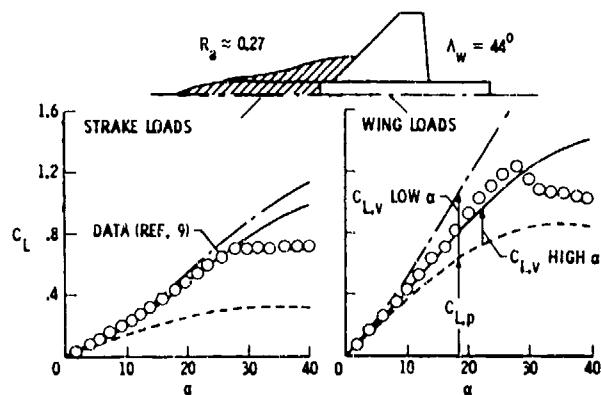


Figure 31.- Theoretical and experimental lift characteristics for a strake-wing configuration. $M = 0.3$.

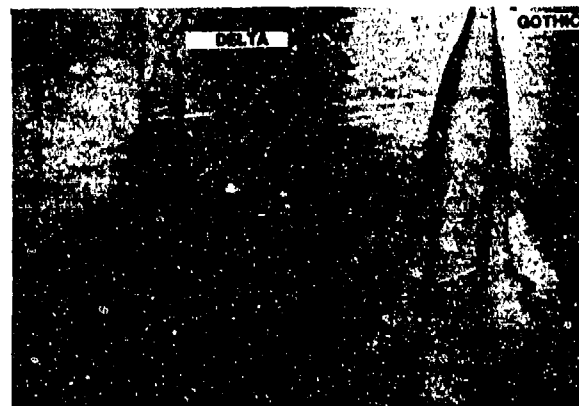


Figure 34.- Effect of strake shape on vortex breakdown - Northrop water tunnel results. $\alpha = 20^\circ$, $\beta = -5^\circ$.

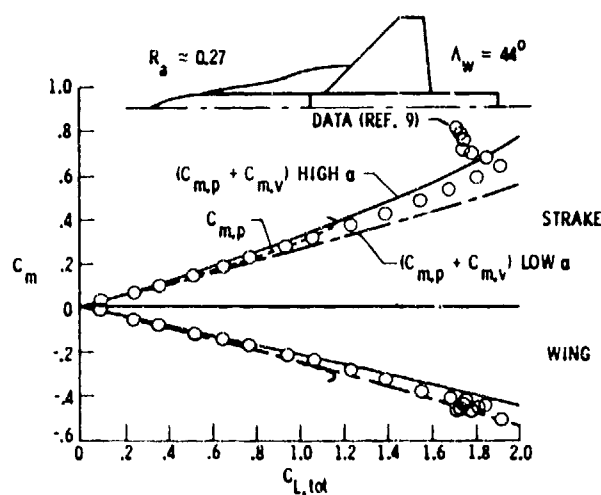


Figure 32.- Theoretical and experimental pitch characteristics for a strake-wing configuration. $M = 0.3$.



Figure 35.- Effect of strake shape on vortex breakdown - Northrop water tunnel results. $\alpha = 30^\circ$, $\beta = -5^\circ$.

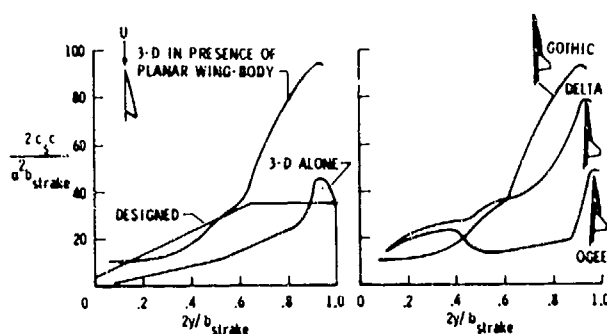


Figure 33.- Strake and strake-wing leading-edge suction distributions. $\Lambda = 44^\circ$, $M = 0.2, 0.3$.

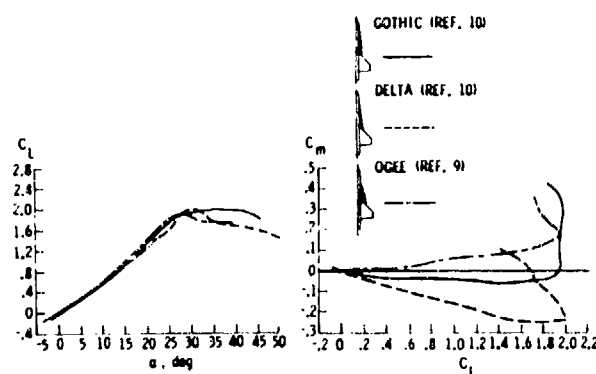


Figure 36.- Effect of strake shape on experimental lift and pitch characteristics. $\Lambda = 44^\circ$, $M = 0.2, 0.3$.

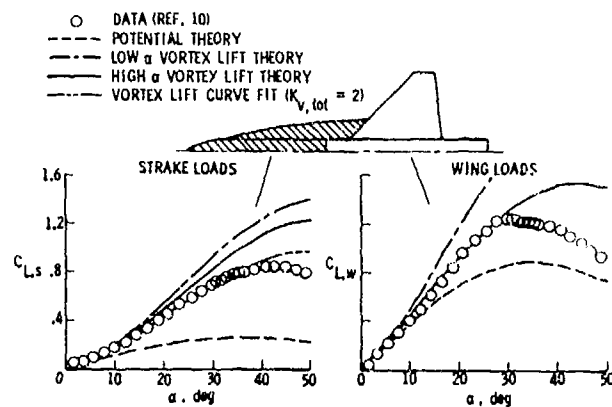


Figure 37.- Estimates of stroke and wing lift. $M = 0.2$.

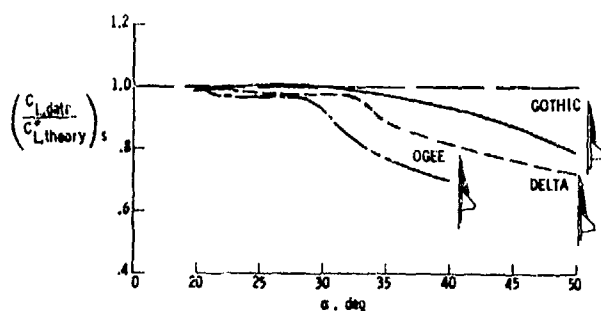


Figure 38.- Effect of stroke shape on $C_{L,s}$ characteristics at high α . $\Lambda = 44^\circ$, $M = 0.2, 0.3$.

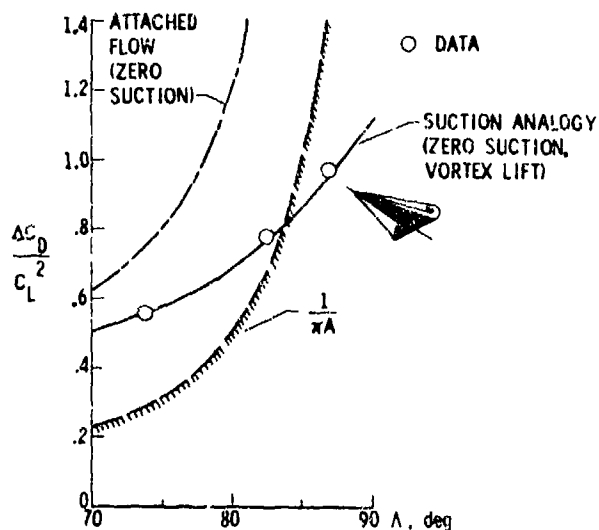


Figure 39.- Slender planar wings ($\Delta C_D / C_L^2$).
 $C_L = 0.3$, $M = 0.8$, Ref. 45.

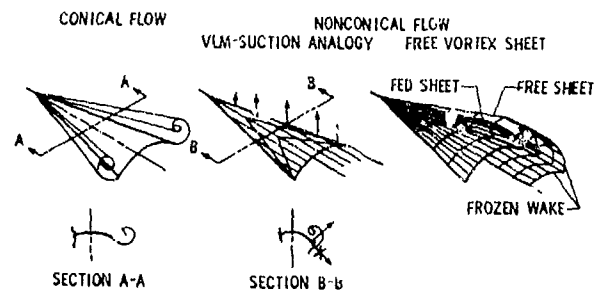


Figure 40.- Vortex flow aerodynamic representation for non-planar wings.

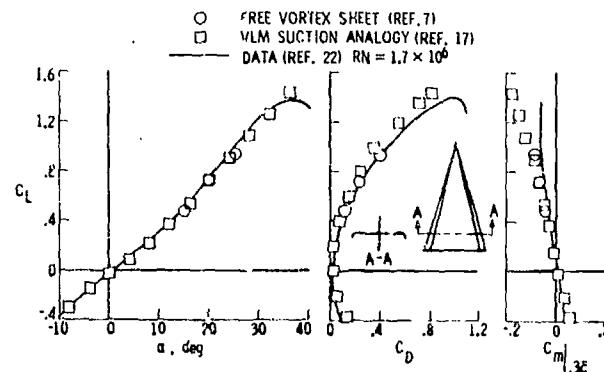


Figure 41.- Longitudinal aerodynamic characteristics for a 74° delta wing with conically cambered leading edges. $M \approx 0$.

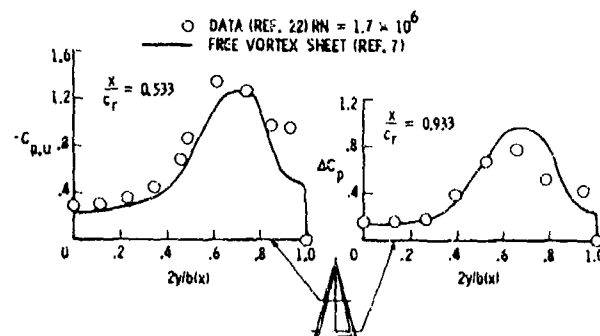


Figure 42.- Spanwise pressure distributions for a 74° delta wing with conically cambered leading edges. $\alpha = 20^\circ$, $M \approx 0$.

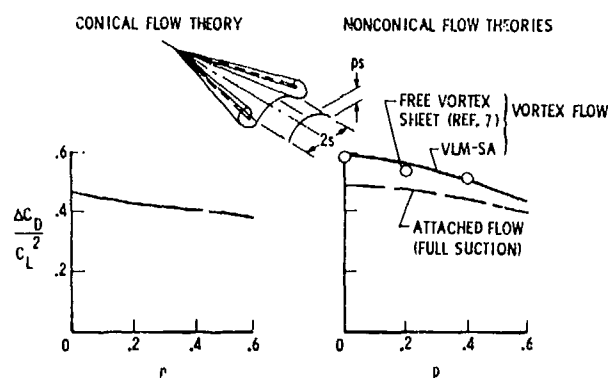


Figure 43.- Effect of camber height on $(\Delta C_D/C_L^2)$. $\Lambda = 80^\circ$, $M = 0$.

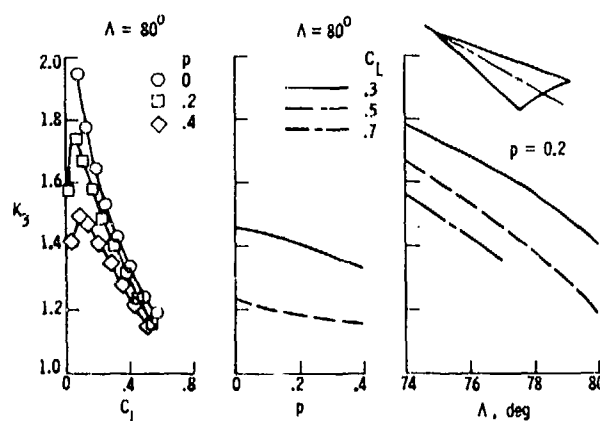


Figure 44.- Effect of delta wing geometry on K_3 . $M = 0$; VLM-SUCTION ANALOGY, $\bar{N}_C = 8$, $\bar{N}_B = 10$.

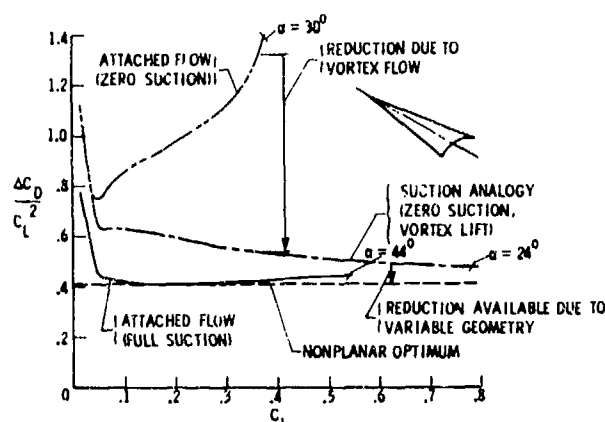


Figure 45.- Effect of flow type on $(\Delta C_D/C_L^2)$. $\Lambda = 80^\circ$, $p = 0.4$, $M = 0$; VLM, $\bar{N}_C = 8$, $\bar{N}_B = 10$.

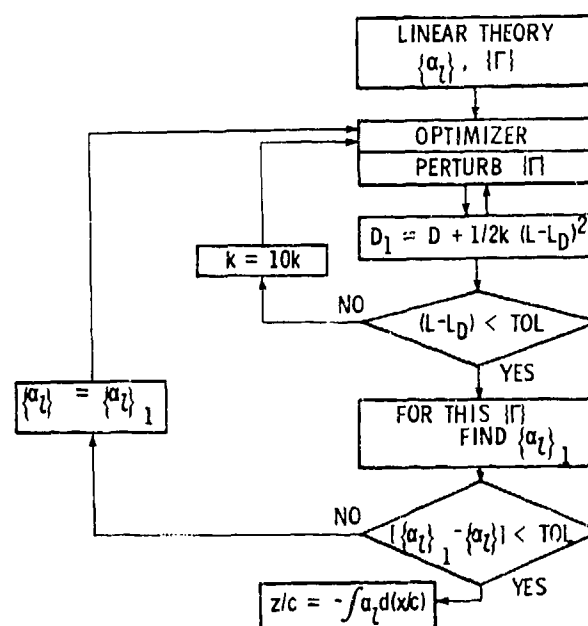


Fig. 46.- Flow chart of vortex flow design VLM for drag minimization with lift constraint.

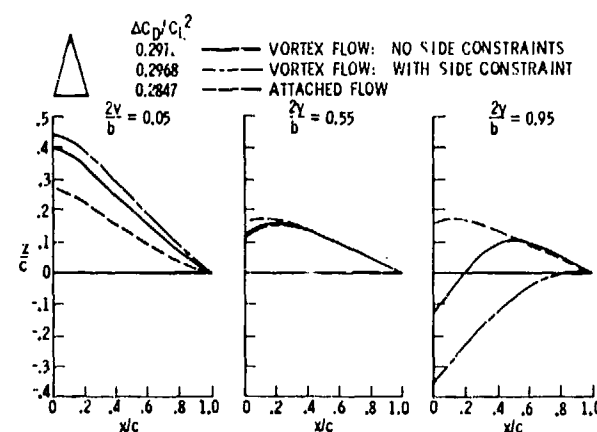


Figure 47.- Mean camber shapes designed from vortex flow (suction analogy). $\Lambda = 75^\circ$, $C_{L,D} = 0.3$, $1/\pi A = 0.2970$, $M = 0$; $\bar{N}_C = 20$, $\bar{N}_B = 10$.

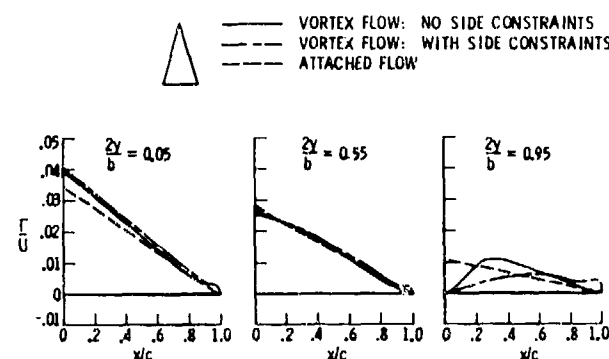


Figure 48.- Chord loadings from vortex flow (suction analogy) design. $\Lambda = 75^\circ$, $C_{L,D} = 0.3$, $M = 0$; $\bar{N}_C = 20$, $\bar{N}_B = 10$.

A COMPUTATIONAL MODEL FOR THE CALCULATION OF THE FLOW
ABOUT WINGS WITH LEADING-EDGE VORTICES *)

by

H.W.M. Hoesijmakers and B. Bennekers
National Aerospace Laboratory NLR
Anthony Fokkerweg 2
Amsterdam - 1017
The Netherlands

SUMMARY

A computational method is presented for the calculation of the incompressible flow about wings with leading-edge vortices. The mathematical model replaces the spiralling free shear layer springing from the leading edge by a free vortex sheet which is terminated by a combination of a feeding sheet plus a discrete line vortex/sink. The strenght of the sink is related to the entrainment of the rotational core and derived here from semi-empirical arguments. The resulting potential flow problem is solved employing a higher-order panel method which involves some recently developed ideas for obtaining a numerically efficient method with second-order accuracy. The method is applied to the calculation of the flow about a delta wing at incidence.

LIST OF SYMBOLS

\bar{a}_{mn}	aerodynamic influence coefficient
b	half span of configuration
$bl(s)$	arc length along curve $t = \text{constant}$ from $s = 0$ to $s = 1$
c	chord of configuration
C_p	pressure coefficient
L	characteristic length
M	number of panels in t -direction
MW	number of panels in t -direction on the wing
\bar{n}	unit vector normal to the surface
N	number of panels in s -direction
NW	number of panels in s -direction on the wing
NP	total number of panels ($N * M$)
NT	total number of unknowns
$N1$	number of unknowns on spanwise strip for which $s < 1$
$N2$	number of unknowns on spanwise strip for which $s > 1$
Q	entrainment of vortex core
Re	Reynolds number $U_\infty L / \nu$
S_f	value of s where far wake begins
S_v	vortex sheet surface
S_w	wing surface
(s, t)	parameters in the computational domain
T	value of t where feeding sheet begins
$\bar{u} = (u, v, w)^T$	total velocity in cartesian coordinate system
u_d	velocity induced by doublet distribution
U_∞	magnitude of velocity at infinity upstream
$\bar{x} = (x, y, z)^T$	position vector in a cartesian coordinate system
$X_L(s), Y_L(s), Z_L(s)$	parametric representation of leading edge
$X_T(t), Y_T(t), Z_T(t)$	parametric representation of trailing edge
$X_V(s), Y_V(s), Z_V(s)$	parametric representation of vortex/sink position
α	angle of attack
ϵ_Q	relative sink strength
Φ	velocity potential
$\mu(s, t)$	doublet distribution
ν	kinematic viscosity
Γ_v	circulation of vortex core
$[]$	matrix
$\{ \}$	column vector

1. INTRODUCTION

During the last few years there has been an increased interest in airplane configurations which to a certain extent derive their performance from flows with "controlled" separation. Such flows are characterized by the presence of a steady and stable separated-flow pattern, which is maintained within a wide range of incidence, yaw, etc. and is more or less independent of Reynolds number. Generally such flow patterns are achieved by the introduction of sharp edges, mostly at the leading edge of highly swept wings or wing like extensions.

At such edges, as well as at the trailing or the side edge of a wing a free shear layer is formed by

*) This investigation was carried out under contract for the Scientific Research Division Directorate of Materiel, Royal Netherlands Air Force.

the merging of the boundary layers flowing off the upper and lower surface of the wing. Under influence of the vorticity contained in it the free shear layer rolls up in a spiral fashion to form one or more cores of concentrated vorticity. In the trailing-edge case this mechanism is responsible for the formation of the wake and trailing vortex pair. In the side-edge case it is responsible for the formation of the side-edge vortex, which is of particular importance for rectangular and trapezoidal wings of small aspect ratio. In the leading-edge case it leads to the formation of the leading-edge vortex above slender delta-like wings and wing-strake combinations.

The interest in flows with vortex cores has been aroused by the observation that these cores affect the velocity distribution in the surrounding fluid dramatically. If the cores are close to the surface of the configuration the pressure distribution may be modified in such a way that the conventional type of boundary layer separation which often leads to the occurrence of unstable flow patterns is delayed to a higher angle of attack. Moreover it is observed that the resulting lift increases more rapidly with incidence than in absence of the vortex cores.

For sharp-edged slender delta wings a stable and steady flow pattern has been observed for angles of attack as high as 20 to 25 degrees, with the lift attaining values of 50 to 100 % above the theoretical value attainable for the same wing with rounded edges.

This paper reflects the first results of NLR efforts aimed at setting up a versatile computational method for the calculation of the airloads on a broad class of aircraft configurations with "controlled" separated-flow patterns.

In the literature there exist already a number of methods for the computation of the above described flow (Ref. 1). However, the method as put forward by Johnson et al (Ref. 2 and 3) appears to have the best prospects for being capable of handling sufficient general configurations efficiently. The method described here is more or less based on the same formulation as Johnson's. The most notable differences with the method of reference 2 and 3 are the inclusion of the entrainment effect of rotational cores, the numerical scheme for the calculation of the so-called influence coefficients and the iterative procedure for solving the system of non-linear equations.

As a first step towards a more general set-up, the flow is considered about thin pointed delta-like lifting surfaces with flow separation along leading (and trailing) edges. It is expected that this simplified problem will exhibit most of the essential features of the more general problem of the flow about airplane configurations with separation along fixed separation lines. In the following sections are discussed subsequently, the physics of the flow, the mathematical formulation of the problem, the description of the computational model and the numerical results obtained with the method for the case of a delta wing.

2. DESCRIPTION OF THE FLOW

In this section the physics of the flow are described in some more detail. As a result of numerous, primarily experimental, observations in the past by amongst others Earnshaw (Ref. 4) and Fink and Taylor (Ref. 5), the picture of the high-Reynolds-number flow about slender wings with regions of concentrated vorticity is well established.

The shear layer emanating from the leading-edge of a slender planform rolls up into the leading-edge vortex core (Fig. 1). This primary core is relatively close to the upper surface where it induces a high lateral velocity, resulting in a low pressure region just underneath the vortex core. The pressure distribution has a favourable gradient on the portion of the wing between the center-line and position of the vortex, which prevents the occurrence of boundary-layer separation in that region. Conversely, it has been observed experimentally that the adverse lateral pressure gradient in the region outboard of the position of the core causes a secondary separation and a secondary vortex core. A further point worthwhile noting is the behaviour of the leading-edge vortex layer downstream of the trailing edge of the wing. Because of the presence of vorticity of the opposite sign the layer tends to roll up in more than one vortex core.

The characteristic feature of the flow problem is the pre-dominant effect that position and strength of the vortex layer and vortex cores have on the surface pressure distribution. This is quite different from conventional attached flow problems where in most cases the shape and position of the wake (and trailing vortex pair) has been shown to have little effect on the surface pressure distribution. In the latter case there exists a more or less well-established asymptotic analysis of the flow for high Reynolds numbers, which leads to the potential flow + boundary layer type of computational model. Unfortunately a complete asymptotic analysis is not available for the present type of flow. This implies that the simplifications which inevitably have to be introduced in a computational model that is manageable on available computing facilities are necessarily based on heuristic arguments and experimental observations. It is generally understood (e.g. Hall, Ref. 6 and Maskell, Ref. 7) that in regions away from the surfaces of the configuration the shear layers and the cores of concentrated vorticity (see Fig. 2) the viscous forces are very much smaller than the inertia and pressure forces. Hence, in these regions the Navier-Stokes equations are simplified by dropping the viscous terms and so reduce to the steady Euler equations.

In those regions where the streamlines originating at infinity upstream did not pass through regions of rotational flow, the flow remains irrotational and is governed by Laplace's equation (potential flow). In regions adjacent to the surface of the configuration (boundary-layer) and in the free shear layers viscous forces become of the same order as the inertia and pressure forces.

In case of laminar flow the thickness of the boundary layers and shear layers is of order $(\nu t)^{1/2}$ where t is the time elapsed since the fluid was first subject to viscous forces. For the boundary layer t is proportional to L/U_∞ where L is a characteristic length of the configuration, hence the thickness of the boundary layer is of order $L/Re^{1/2}$. The Reynolds number is typically of order 10^6 to 10^7 or more, so that the boundary layer is very thin and in first approximation may be neglected, as is conventional for the attached flow problem.

For the free shear layer t is proportional to s/U_∞ where s is the path length along the streamline that emanates from the leading edge.

This means that the thickness is of order $L(s/L)^{1/2}/Re^{1/2}$. This leads to the following description of the rolling-up shear layers:

- (i) Near the edge of separation s is of the order of L . Here the thickness of the shear layer is neglected, and as a first approximation the shear layer is modelled as a sheet of infinitesimal thickness which contains the vorticity shed at the edge. Experimental evidence (Ref. 4, 5, 8) suggests that in the Reynolds number range of interest this simplification is appropriate for say, the first loop of the spiralling free shear layer.

- (ii) As s increases more and more (and becomes $\gg L$) as the fluid flows along the spiralling layer, the thickness becomes of the order of the distance between the subsequent loops, and no longer a distinct shear layer can be observed. In this way a region with a continuous distribution of vorticity is formed. This is what we call the leading-edge vortex core.

Experimental observations (Ref. 4, 5 and 8) and theoretical arguments put forward by Maskell (Ref. 7) and Moore (Ref. 9) suggest that the cross-sectional size of the rotational core is much larger than $L/Re^{1/2}$, and a weak function of Reynolds number. This is in agreement with the solution for infinite Reynolds number (Ref. 10) consisting of a tightly wound sheet of infinite length and a core of zero cross-sectional size. Based on arguments given in reference 9 for the trailing vortex case it is possible to arrive at a more precise estimate of the Reynolds number dependence of the size of the leading-edge core. According to reference 9 the distribution of the circulation inside the core may be written as

$$\Gamma(r) = 2\Gamma_0 \left(\frac{r}{L}\right)^{1-n}$$

where r is the distance from the center and Γ_0 is a measure for the wing loading. The power n , for the case of the trailing-edge vortex, is related to the shape of the spanwise load distribution. In a more general formulation which can be used also in the case of the leading-edge vortex, this means that n is related to the distribution of the shed vorticity along the shedding edge. It is argued in reference 9 that the magnitude of the radius of the (axisymmetric) core, denoted by R , is of the order of

$$R \propto \left[\Gamma_0^{n-1} \nu^{1/2} t^{1/2} \right]^{1/2+n}$$

In our case $t = s/U_\infty$, so that

$$\frac{R}{L} \propto \left(\frac{\Gamma_0}{U_\infty L} \right)^{1/2+n} \frac{1}{Re} - \frac{1}{2(2+n)} \left(\frac{s}{L} \right)^{1/2+n} \frac{1}{Re}$$

because s is of the order of L .

The circulation contained within the region, which is in fact the strength of the vortex, is now

$$\frac{\Gamma_V}{U_\infty L} \propto \left(\frac{\Gamma_0}{U_\infty L} \right)^{1/2+n} \frac{1}{Re} - \frac{1-n}{2(2+n)} \left(\frac{s}{L} \right)^{1/2+n} \frac{1}{Re}$$

Inside the core the flow is governed by the Euler equations, except for a small region around the center with a diameter of order $L/Re^{1/2}$, where the gradients are such that viscous forces are no longer negligible.

In order to get an impression about the influence of the presence of the core on the outer potential flow, we consider the solution for the case of inviscid flow inside a slender axisymmetric conical leading-edge core, which has been derived by Stewartson and Hall (Ref. 13). From this solution it can be derived that given the tangential velocity (i.e. the circulation) there is an inflow into the core, which in first approximation is proportional to Γ_V :

$$\frac{W}{U_\infty} = - \frac{1}{2\pi\sqrt{2}} \left| \frac{\Gamma_V}{U_\infty L} \right| \frac{1}{Re} - \frac{1-n}{2(2+n)}$$

For the outer potential flow a more meaningful quantity is the integral of the outflow over the surface of the core, which in first approximation is

$$\frac{Q}{U_\infty L} = 2\pi \frac{R}{L} \frac{W}{U_\infty} = - \frac{1}{\sqrt{2}} \frac{R}{L} \left| \frac{\Gamma_V}{U_\infty L} \right| \frac{1}{Re} - \frac{2-n}{2(2+n)}$$

In the case of the trailing-edge vortex sheet and an elliptic load distribution along the trailing edge n has the value $1/2$. For other types of spanwise load distribution it may be assumed that n has a value near $1/2$.

In the case of the leading-edge vortex the appropriate value of n is not so apparent. The circumferential velocity profile given in reference 13 as solution for the inviscid flow inside a conical core indicates that n has the value zero. On the other hand the empirical relations between the strength of the leading-edge vortex and the incidence given in reference 14, which presumably represent the case of turbulent flow, suggest that n has a value near $2/3$. Based on arguments used in reference 15, where the formation of the vortex is considered as the limit for large t of the impulsively started fluid round a sharp edge, one would arrive at a value near $1/2$.

In the table below the Reynolds number dependence of R , Γ_V and Q is given for three characteristic values of n .

n	R	Γ_V	Q
0	$Re^{-1/4}$	$Re^{-1/4}$	$Re^{-1/2}$
$1/2$	$Re^{-1/4}$	$Re^{-1/2}$	$Re^{-1/2}$
1	$Re^{-1/4}$	Re^0	$Re^{-1/4}$

The table shows for any n the size and strength of the leading-edge vortex are weak functions of Reynolds number, which is in agreement with experiments (Ref. 4, 5 and 8). The entrainment, which is the product of the two, becomes more Reynolds number dependent as n decreases to the limit n equal zero. In the latter case the entrainment effect is, for large Reynolds numbers, of the same order of magnitude as the displacement thickness of the boundary layer on the wing. Experimental investigation will be needed to determine the variation of the entrainment with Reynolds number.

Summarizing it is concluded that, for the range of Reynolds numbers of interest, an appropriate approximation is to consider the flow as inviscid and irrotational with embedded regions of inviscid rotational flow of infinitesimal extent (vortex sheets) that represent the shear layer near its generating edge and of small but finite extent (rotational cores, with inflow) that represent the rolled-up portions of the shear layer. Viscous dissipation is of importance only in a relatively small subcore and of course "far" downstream of the configuration.

3. MATHEMATICAL FORMULATION

The mathematical formulation as presented here is essentially the same as given in reference 2 and 3, which in turn is backed up by the studies of Brown and Michael (Ref. 11) and Smith (Ref. 12). The section falls into two parts. In the first part the (outer) potential flow is modelled and in the second part the representation of the core region is considered.

Potential flow

In the preceding section the flow outside the rotational cores has been reduced to a potential flow problem, i.e. there exists a velocity potential $\Phi(x, y, z)$ which satisfies Laplace's equation

$$\Phi_{xx} + \Phi_{yy} + \Phi_{zz} = 0 \quad (1)$$

where $\vec{u} = \vec{\nabla} \Phi$

This equation is subject to the following boundary conditions on the configuration and vortex sheets (Fig. 3)

- (i) Zero normal velocity on the configuration, i.e.

$$\vec{u} \cdot \vec{n} = 0 \quad \text{on } S_w \quad (2a)$$

- (ii) Vortex sheets are stream surfaces, i.e.

$$\vec{u} \cdot \vec{n} = 0 \quad \text{on } S_v \quad (2b)$$

- (iii) Zero pressure jump across vortex sheets, i.e.

$$\Delta C_p = C_p^+ - C_p^- = 0 \quad \text{on } S_v \quad (3)$$

- (iv) Kutta condition at the edges of separation

$$\vec{u} \neq \infty \quad \text{at } \partial S_w \quad (4)$$

The Kutta condition at the edges of flow separation will be satisfied implicitly by requiring the doublet strength to be continuous across the edges and requiring that the vortex sheets leave the leading and trailing edges smoothly.

- (v) At large distance upstream no disturbance, i.e.

$$\vec{u} = U_\infty \begin{Bmatrix} \cos \alpha \\ 0 \\ \sin \alpha \end{Bmatrix} \quad \text{for } x \rightarrow -\infty \quad (5)$$

Treatment of the core region

As argued in the preceding section the flow within the core region is governed by the Euler equations. The computation of the inner flow based on Euler's equations is beyond the scope of the present investigation and a simple representation of the core region has to be searched for. Since we are interested primarily in the effects of the core on the outer potential flow and not in the flowfield immediately near the core, a relatively simple representation of the core may suffice.

For the range of Reynolds numbers of interest the diameter of the core is still small as compared with the characteristic dimension of the wing. A suitable approximation is to let the vortex core shrink into a (curved) line which is assigned a vortex strength and a sink strength.

The vortex strength is related to the circulation of the core region and has to be determined as part of the solution. The sink strength represents the entrainment effect introduced in the preceding section. It was deduced that for conical flows its magnitude in first approximation is proportional to the vortex strength. The constant of proportionality between the circulation and the entrainment of the core has been determined from preliminary results of experiments carried out at the Delft University of Technology, at a Reynolds number of the order of 10^6 (Ref. 8) to be of the order of .03-.07. (See also the contribution to the Open Discussion of this Symposium, Ref. 21). Although the entrainment effect of rotational cores of finite extent seems to be of considerable magnitude it has been neglected in all existing computational methods. The model of the core region is made complete by linking the vortex/sink to the end of the vortex sheet by means of a so-called feeding sheet, which, going in downstream direction, feeds vorticity into the vortex (Fig. 3).

The conditions for matching the vortex/sink combination within the outer potential flow are analogous to those applied by Brown and Michael (Ref. 11) and Smith (Ref. 12), which is that the combination of vortex/sink and feeding sheet sustains no resultant force in the cross-flow plane (Fig. 4).

$$\vec{F}_{\text{vortex}} + \vec{F}_{\text{sink}} + \vec{F}_p = 0 \quad (6)$$

Since both the force on the vortex and the force on the sink are exactly perpendicular and the force on the feeding sheet is nearly perpendicular to the vortex/sink segment, eq. (6) results into two equations. Equation (6) determines therefore the vortex position in the cross-flow plane. In the method of reference 2 and 3 the feeding sheet is taken as a kinematic extension of the vortex sheet, while the length of the feeding sheet in the cross flow plane is taken from conical flow solutions of Smith (Ref. 12) or from empirical arguments.

4. DESCRIPTION OF THE COMPUTATIONAL MODEL

The computational method selected for the potential flow problem is the same as the one selected in reference 2, namely a so-called panel method. The panel method is chosen for because the alternative methods (Ref. 1) are either not applicable to more general configurations (the conical and quasi-conical methods, Ref. 12, 16) or lack such important capabilities as redistribution of vorticity (the multi-vortex methods, Ref. 17, 18).

In the panel method the wing and vortex sheets are divided into a large number of small elements, which carry a set of basic singularity distributions. The strength of the singularity distributions is determined through a collocation technique.

The numerical scheme resulting from the discretization to be described shortly has a truncation error which is second order in the panel width. Preliminary numerical investigations suggests that for the accuracy level in mind this leads to the most efficient computer program.

The description of the geometry

Rather than performing the computation in the physical (x, y, z) space, we have chosen for an approach in which the surface in space comprising the wing and the vortex sheet is transformed to a simple rectangular computational (s, t) domain (Fig. 5). The position vector $\bar{x} = (x, y, z)^T$ of a point on the surface is then given by the parameterical representation

$$\bar{x} = \begin{Bmatrix} x \\ y \\ z \end{Bmatrix} = \begin{Bmatrix} x(s, t) \\ y(s, t) \\ z(s, t) \end{Bmatrix} \quad (7)$$

The transformation is chosen such that there is the following correspondence between the physical and computational domains (only the starboard side of the symmetric configuration is considered):

- leading edge (L.E.) : $0 < s < 1, t = 1$
- trailing edge (T.E.) : $s = 1, 0 < t < 1$
- apex : $s = 0$
- wing surface S_w : $0 < s < 1, 0 < t < 1$
- leading edge vortex sheet S_v : $0 < s < 1, 1 < t < T$
- "near wake" : $1 < s < S_f$
- "far wake" : $s > S_f$
- feeding sheet : $t > T$

The curves $s = \text{constant}$ lie more or less in cross-flow planes (Fig. 5). The parameter t is chosen as the arclength along the curves $s = \text{constant}$ scaled with a quantity $bl(s)$ which is the arclength from $t = 0$ to $t = 1$ (from centerline to leading edge) along the same curve. This implies that T controls the out-off length of the vortex sheet, i.e. the length of the vortex sheet in the cross-flow plane is T times $bl(s)$.

The cross-sectional shape of the vortex sheet is determined as part of the solution and should correspond to the model explained earlier, i.e. continue for say one loop. Therefore it should be checked after that the solution for a particular choice of T has been obtained if the shape attained corresponds sufficiently to the physical model of the flow.

S_f is the out-off distance of the near wake. Its particular choice should be of little importance on the solution on the wing.

In appendix A the geometric description is dealt with in some more detail.

The singularity distribution

The singularity distribution chosen for here is the doublet distribution, which has the advantage over the vorticity distribution that it is a scalar function and that Helmholtz's vortex laws are automatically accounted for. The velocity induced at a point \bar{x}_0 by a continuous doublet distribution $\mu(s, t)$ on the surface S defined by equation (7) is (Fig. 6):

$$\bar{u}_d(\bar{x}_0) = - \iint_S \left[\frac{\partial \bar{x}}{\partial t} \frac{\partial \mu}{\partial s} - \frac{\partial \bar{x}}{\partial s} \frac{\partial \mu}{\partial t} \right] \otimes \frac{\bar{r}}{|\bar{r}|^3} ds dt + \int_{\partial S} \mu(s, t) d\bar{\ell} \otimes \frac{\bar{r}}{|\bar{r}|^3} \quad (8)$$

where $\bar{r} = \bar{x}_0 - \bar{x}(s, t)$

and the second integral has to be evaluated along the boundary ∂S of the surface S .

The doublet distribution $\mu(s, t)$ is assumed to be continuous across the leading and trailing edge of the wing, zero at the apex (the line $s = 0$), constant in s -direction on the far wake, constant in t -direction on the feeding sheet, and continuous across $s = S_f$ and $t = T$.

The unknowns of the problem are then:

- on the wing : $\mu(s, t)$
- on the vortex sheet and near wake : $\mu(s, t), y(s, t), z(s, t)$
- on the vortex : $y_v(s), z_v(s)$

The equations which apply are:

- on the wing : equ. (2a)
- on the vortex sheet and near wake : equ's (2b), (3), (A-4)
- on the vortex : equ. (6)

The discretization

The way in which the problem is discretized is the following.

The computational domain is divided into panels by lines

$$s = s_i, i = 1(1)N + 1$$

$$t = t_j, j = 1(1)M + 1$$

such that $s_1 = t_1 = 0$, $s_{N+1} = t_{M+1} = 1$ and $s_{N+1} = S_f, t_{M+1} = T$ (see Fig. 7)

The panels on the domain representing the wing, vortex sheet and near wake are rectangular, those on the domain representing the feeding sheet trapezoidal. The total number of rectangular panels is $NP = M \cdot N$

The midpoint of a panel on wing, vortex sheet and "near wake", say panel (i, j) is assigned an unknown doublet strength $\mu^{(n)}$, where $n = (i-1) \cdot M + j$ and in case of panels off the wing also the geometric unknowns $y^{(n)}$ and $z^{(n)}$. Finally, each midpoint of the vortex segment bounding the panels of the feeding sheet is assigned the vortex position unknowns $y_v^{(i)}$ and $z_v^{(i)}$. This implies that arranging the unknowns midpoint after midpoint in spanwise strips, that the first NW strips carry each a total of $N1 = MW + 3 \cdot (M-MW) + 2$ unknowns and the next (N-NW) strips of the "near wake" carry $N2 = 3 \cdot M + 2$ unknowns. Therefore the total number of unknowns amounts to $NT = NW \cdot N1 + (N-NW) \cdot N2$.

By applying at the same midpoints the afore-mentioned boundary conditions a system of NT (non-linear) equations is obtained for as many unknowns. In order to set up the equations the velocity induced at the collocation point m is written as (equ. 8)

$$\begin{aligned} \bar{u}_d(\bar{x}_m) = & - \sum_{n=1}^{NP} \left\{ \iint_{S_n} \left[\frac{\partial \bar{x}}{\partial t} \frac{\partial \mu}{\partial s} - \frac{\partial \bar{x}}{\partial s} \frac{\partial \mu}{\partial t} \right] \otimes \frac{\bar{r}}{|\bar{r}|^3} ds dt \right\}^{(n)} \\ & - \sum_{j=1}^N \left\{ \int_{s_j}^{s_{j+1}} \left[\mu(s, t_{M+1}) \frac{d\bar{x}_v}{ds} \otimes \frac{\bar{r}}{|\bar{r}|^3} + \right. \right. \\ & \left. \left. + \epsilon_Q \left| \mu(s, t_{M+1}) \right| \left| \frac{d\bar{x}_v}{ds} \right| \frac{\bar{r}}{|\bar{r}|^3} \right] ds \right\}^{(j)} \end{aligned} \quad (9a)$$

leading to

$$\bar{u}_d(\bar{x}_m) = \sum_{n=1}^{NP} \bar{a}_{mn} \mu^{(n)} \quad (9b)$$

In equ. (9a) the superscript n denotes that the integral over the panel surface S_n is considered. The double integral in equ. (9a) is the contribution of the continuous doublet distribution, the first of the single integrals is the contribution of the vortex and the second single integral is the contribution of the "entrainment" corresponding to a sink strength of ϵ_Q times the absolute value of the vortex strength. The aerodynamic influence coefficients \bar{a}_{mn} are calculated as follows:

- (i) If the point m lies on the panel n the integrand is approximated by a small curvature expansion and the resulting expression is integrated analytically.
- (ii) If the point m is near the influencing panel n the integral is approximated by a Gauss integration rule.
- (iii) In the remaining cases the integral is approximated by the midpoint rule.

The derivatives of the doublet distribution μ which appear in the expressions are approximated by finite differences involving μ -values in surrounding collocation points. This applies also to the derivatives of the y and z component of $\bar{x}(s, t)$ on the sheet and the y and z component of the vortex position $\bar{x}_v(s)$. Because the computational domain is divided into rectangular cells the finite difference formulas can be implemented quite straight forward.

The method described above results in an economic numerical scheme for the calculation of the influence coefficients, with a truncation error which is quadratic in the panel width. In equation (8) only the starboard side of the configuration is considered. The velocity $(u, v, w)^T$ induced at $(x, y, z)^T$ by a panel on the portside of the configuration is equivalent to the velocity $(u, -v, w)^T$ induced at $(x, -y, z)^T$ by the symmetrically situated panel on the starboard side of the configuration.

The system of non-linear algebraic equations

The system of NT non-linear algebraic equations is solved by a quasi-Newton method, that is, if the system is written as

$$\bar{F}(\bar{X}) = 0 \quad (10a)$$

where the components of the vector \bar{F} are the equations and those of \bar{X} the unknowns.

If $\bar{X}^{(k)}$ is a start vector (k=1) or the result of the previous iteration step, the increment $\Delta \bar{X} = \bar{X}^{(k+1)} - \bar{X}^{(k)}$ is found as the solution of

$$\left[\frac{\partial \bar{F}}{\partial \bar{X}} \right]^{(k)} \{ \Delta \bar{X} \} = - \{ \bar{F}(\bar{X}) \}^{(k)} \quad (10b)$$

or in matrix notation

$$[G]^{(k)} \{ \Delta \bar{X} \} = - \{ \bar{F} \}^{(k)} \quad (10c)$$

The components of \bar{X} are arranged spanwise (i.e. in t-direction), thus the first MW components are the unknown doublet strengths at the collocation points on the first MW panels of the first strip, followed by $\mu^{(n)}$, $y^{(n)}$, $z^{(n)}$ at the midpoints of the next collocation point in t-direction, etc. Following the 3 unknowns at the midpoint of the Mth panel of the first strip are the 2 unknown vortex positions $y_v^{(1)}$, $z_v^{(1)}$. The components of \bar{F} are arranged in the same fashion, that is, at the wing panels the normal velocity equation is applied, at the sheet panels the normal velocity equation, the pressure jump equation and the arclength equation are applied successively, and at the vortex the two force equations are applied. This special choice of \bar{X} and \bar{F} results in a gradient matrix G which exhibits a dominant tri-block diagonal structure. The tri-block diagonal structure may be thought of as representing the influence of a strip, say strip i, on itself (the block on the diagonal) and of the influence of the two neighbouring strips, say same strip, thus strip i-1 and i+1 on strip i (the two off-diagonal blocks).

In the present method the gradient matrix $G^{(k)}$ is simplified in the sense that only the elements in the dominant blocks are considered. The remainder of the matrix $G^{(k)}$ is assumed to be negligible, small and is put equal to zero. This has as important implication that the approximative of the matrix $G^{(k)}$ is quite rapidly computed, but also that the system (10c) of NT linear equations can be solved very rapidly.

For the computation of the elements of the stripped gradient matrix $G^{(k)}$ one needs in particular the derivative of the induced velocity with respect to the components of the vector X . The derivative with respect to the doublet unknowns is readily obtained from equation (9b). The derivative of the induced velocity with respect to the unknown geometric parameters is obtained by analytical differentiation of equation (9a) followed by panel wise integration in the fashion as indicated for the computation of the induced velocity itself.

5. NUMERICAL RESULTS

A computer program is being developed to verify the adequacy of the method. The program is coded for the NLR Cyber 72-14 computer under NOS/BE-1.2, has a field length of 16K 60 bits words of central memory in a segmented load structure, and uses magnetic disks for mass-storage. Since all arrays which contain the data related to the panel geometry, influence coefficients etc., have variable dimension, the maximum number of panels allowed is determined by the remainder of the available central memory. To give an impression of execution times involved, the computation of the matrix of influence coefficients for the 250 panel delta wing case takes 375 sec of central processor time and the computation of the gradient matrix about 550 sec central processor time.

At the present time the code is still under testing conditions and only a limited number of delta wing cases has been computed.

More numerical evaluation will be needed before the applicability to more general configurations such as gothic, ogee and arrow wings (with or without longitudinal and spanwise camber) can be evaluated.

The results obtained so far are for a planar delta wing of unit aspect ratio at 20 degrees incidence. This wing has been chosen as test case because of the ample availability of experimental data (Peckham, Ref. 19) and to allow future comparison with results of experiments carried out at the Delft University of Technology (Ref. 8 and 21).

The cut-off distance for the leading-edge vortex sheet, denoted by T , has been chosen as 1.9. This, according to experiments (Ref. 4, 5 and 8), corresponds to $1/2$ to $3/4$ turn of the spiralling shear layer. As a starting solution for the computation a conical flow solution of Smith (Ref. 12) has been used, which is extended on to the near wake in a smooth fashion.

Figure 8 shows the load distribution computed for 20 degrees incidence in comparison with experimental data from Peckham (Ref. 19) for 20.5 degrees incidence. The differences in the computed and experimental results are of the same nature and magnitude as found by Johnson (Ref. 2 and 3), and may partly be accounted for by secondary separation effects. The discrepancy in the region near the trailing edge is thought to be due to the fact that the solution for the wake was not quite converged. The solution in this region will require more attention in future computations. In figure 9 are shown the computed pressure distribution on the upper and lower wing surface at $x/c = .45$ and compared with the experimental values of Peckham (Ref. 19) and Hummel and Redeker (Ref. 20) and compared with the conical solution of Smith (Ref. 12). Furthermore is shown the position of the collocation points for the same cross-section.

The results given in figure 8 and 9 were obtained for a zero vortex entrainment strength factor ϵ_Q . Computations for a relative sink strength of .01 and .05 indicate that the load distribution depends quite strongly on the sink strength. This is illustrated in figure 10, where the load distribution is given for three different values of ϵ_Q . The inclusion of the "entrainment effect" results in a substantial increase in the normal force coefficient. For a relative sink strength of .0, .01 and .05 the computed normal force coefficient attains a value of .72, .76 and .95 respectively, which should be compared with a value of about .8 found in experiments. The inclusion of the entrainment effect results primarily into a stronger vortex, but to not a very significant change in the geometry of the vortex sheet.

6. CONCLUDING REMARKS

A computational panel-type method has been described for the flow about wings with leading-edge separation. The mathematical model differs from already existing ones in the sense that the concept of entrainment of the rotational leading-edge vortex core has been introduced. This presumably will result in a better simulation of the effects of the core on the outer potential flow field.

Results of preliminary computations for a delta wing of unit aspect ratio suggest that the inclusion of the entrainment results in a substantial increase in the computed normal force coefficient, caused primarily by the vortex which becomes stronger as the entrainment is increased.

Further numerical evaluation is needed to study in detail the convergence characteristics and more in general the computing capability of the method.

Appendix A Geometric description of wing and vortex sheet

In the present method the three-dimensional surface comprising the wing and vortex sheet is expressed as (equation (7)):

$$\bar{x} = \begin{Bmatrix} x \\ y \\ z \end{Bmatrix} = \begin{Bmatrix} x(s, t) \\ y(s, t) \\ z(s, t) \end{Bmatrix} \quad (A-1)$$

For the geometric representation of the wing it is assumed that the surface of the wing may be written as $z = z(x, y)$ where z is a single-valued function of x and y . This is equivalent to choosing both $x(s, t)$ and $y(s, t)$ which then determines $z(s, t)$ uniquely. On the wing equation (A-1) amounts to

$$\begin{cases} x = X_L(s)X_T(t)/c \\ y = Y_L(s)Y_T(t)/b \\ z = Z(s, t) \end{cases} \quad (A-2)$$

where X_L and Y_L are obtained from the parametric representation of the leading edge $\bar{x} = (X_L(s), Y_L(s), Z_L(s))^T$ and X_T, Y_T from the parametric representation of the trailing edge $\bar{x} = (X_T(t), Y_T(t), Z_T(t))^T$. In the parametric representation of the leading edge the parameter s is the arclength from $s = 0$ to $s = s$ divided by the total arclength. Equivalently the parameter t in the parametric representation of the trailing edge is the relative arclength along this edge.

For the geometric description of the vortex sheet only the function $x(s, t)$ can be chosen, which leads to

$$\begin{cases} x = X_L(s)X_T(t)/c \\ y = y(s, t) \\ z = z(s, t) \end{cases} \quad (A-3)$$

where now $x(s, t)$ and the two unknown functions $y(s, t)$ and $z(s, t)$ are related through the condition that the parameter t is the relative arclength along $s = \text{constant}$, namely

$$\left[\left(\frac{\partial x}{\partial t} \right)^2 + \left(\frac{\partial y}{\partial t} \right)^2 + \left(\frac{\partial z}{\partial t} \right)^2 \right]^{1/2} = bl(s) \quad (A-4)$$

In the computer program $X_L(s)$, $Y_L(s)$, $X_T(t)$ and $Y_T(t)$ are fitted by a cubic Hermite polynomial representation on the so-called geometric network in the (s, t) plane. In order to use the functions $X_L(s)$ and $X_T(t)$ for s greater than 1 and t greater than 1 respectively the functions are continued smoothly into the domain which represents the vortex sheet. Over one interval of the geometric network $X_L(s)$ joins smoothly with a linearly increasing function and $X_T(t)$ with a constant function.

In the computer program the wing surface is input as values of x and z for constant y . Therefore the surface is first determined as a bi-cubic Hermite representation of x divided through the local chord and y . Given z in this way and x and y as a function of s and t as in equation (A-2) the bi-cubic representation of $Z(s, t)$ on the geometric network is readily obtained.

The function $bl(s)$ which appears in equation (A-4) and which is easily obtained for $s < 1$ (on the wing) is extended onto the wake in some suitable chosen way. For the moment it is taken as constant one interval length of the geometric network beyond the trailing edge. If one would like to study the more complex wake roll-up behind the trailing edge, $bl(s)$ would have to increase more rapidly with s . The position of the vortex/sink combination is given by

$$\begin{cases} x = X_L(s)X_T(t)/c \\ y = y_v(s) \\ z = z_v(s) \end{cases} \quad (A-5)$$

where $y_v(s)$ and $z_v(s)$ are to be determined as part of the solution.

7. REFERENCES

- 1 Hoeijmakers, H.W.M. The flow about airplane configurations with separation along sharp edges. A survey of the literature. NLR TR 76007 U (1976).
- 2 Weber, J.A. et al. A three-dimensional solution of flows over wings with leading-edge vortex separation. AIAA Paper 75-866 (1975).
- 3 Johnson, F.T. et al. An improved method for the prediction of completely three-dimensional aerodynamic load distributions of configurations with leading-edge vortex separation AIAA paper 76-417 (1976).
- 4 Earnshaw, P.B. An experimental investigation of the structure of a leading-edge vortex. R and M 3281 (1962).
- 5 Fink, P.T.
Taylor, J. Some early experiments on vortex separation. R and M3489 (1967).
- 6 Hall, M.G. A theory for the core of a leading-edge vortex. JFM 11 (1961), pp 209-228.
- 7 Maskell, E.C. Some recent development in the study of edge vortices. Proc. 3rd Congress ICAS. Spartan books (1964).
- 8 Verhaagen, N.G. Department of Aerospace Engineering of the Delft University of Technology. Private Communication (1978).
- 9 Moore, D.W.
Saffman, P.G. Axial flow in laminar trailing vortices. Proc. R. Soc. Lond. A. 333 (1973) pp 491-508.
- 10 Kaden, H. Aufwicklung einer unstablen unstetigkeitsfläche. Ing. Arch. 2 (1931) p 140.
- 11 Brown, C.E.
Michael, W.H. On slender delta wings with leading-edge separation NACA TN 3430 (1955).
- 12 Smith, J.H.B. Improved calculations of leading-edge separation from slender delta wings. RAE TR 66070 (1966).
- 13 Stewartson, K.
Hall, M.G. The inner viscous solution for the core of a leading-edge vortex. JFM 15 (1963) pp 306-318.
- 14 Kirkpatrick, D.L.I. A study of the leading-edge vortices above slender wings. Thesis University of Southampton (1970).
- 15 Guiraud, J.P.
Zeytounian, R.Kh. Une théorie pour le noyau de nappes tourbillonnaires a enroulement serré. La Rech. Aéro. (1977) pp 205-212.
- 16 Clark, R.W. Non-conical flow past slender wings with leading-edge vortex sheets. RAE TR 76037 (1976).
- 17 Rehbach, C. Calcul d'écoulements au tour d'ailes sans épaisseur avec nappes tourbillonnaires évolutives. La Rech. Aéro. (1973) pp 53-61.
- 18 Kandil, O.A. et al. A numerical technique for computing subsonic flow past three-dimensional canard-wing configurations with edge separations. AIAA Paper 77-1 (1977).
- 19 Peckham, D.H. Low-speed wind-tunnel tests on a series of uncambered slender pointed wings with sharp edges. RAE Rep. Aero. 2613 (1958).
- 20 Hummel, D.
Redeker, G. Experimentelle Bestimmung der gebundenen Wirbellinien sowie des Strömungsverlaufs in der Umgebung der Hinterkante eines schlanken Delta-Flügels. Abh. Braunsch. Wiss. Ges. 22 (1972) pp 273-290.
- 21 Verhaagen, N.G.
Sneek, I. v.d. An experimental investigation of the entrainment effect of a leading-edge vortex. Open Discussion paper 7 of this symposium.

ACKNOWLEDGEMENTS

The authors are much indebted to Mr. J.W. Slooff for the many fruitful discussions concerning the method, and especially for bringing forward so persistently the idea about the importance of the entrainment effect.

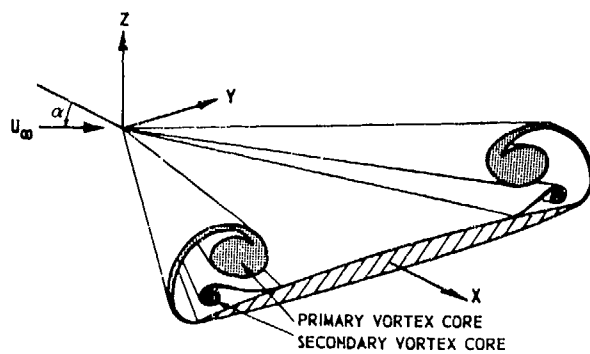


Fig. 1 Vortex system of delta wing

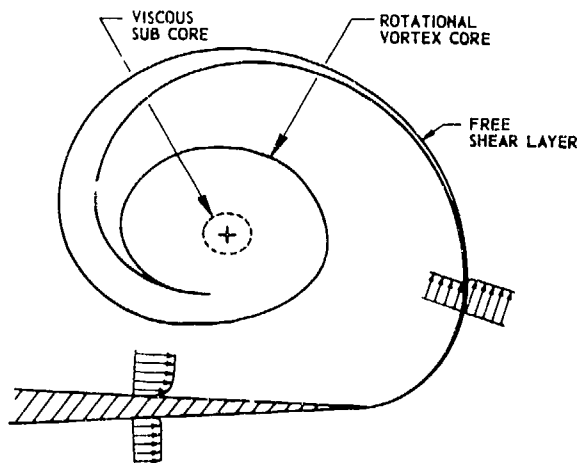


Fig. 2 Formation of edge vortex

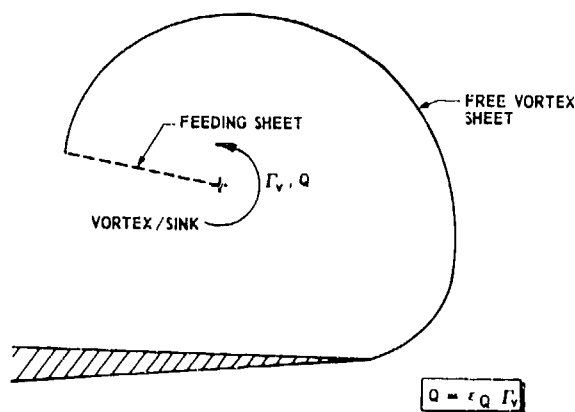


Fig. 3 Model of leading-edge shear layer

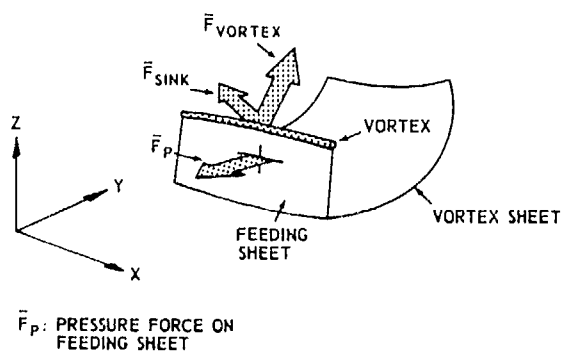


Fig. 4 Forces on model of vortex core

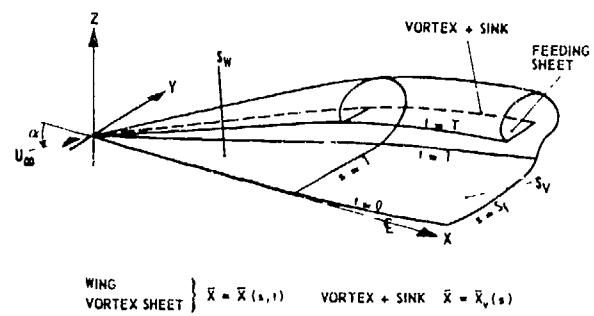


Fig. 5 Physical and computational domain

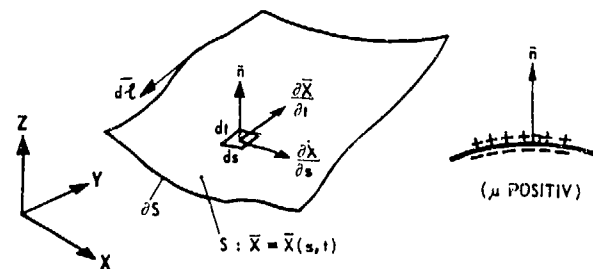


Fig. 6 Doublet distribution

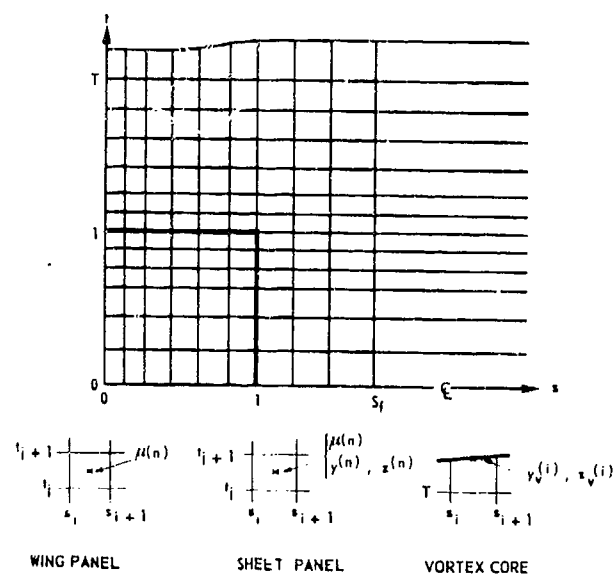


Fig. 7 Panel arrangement and position of unknowns

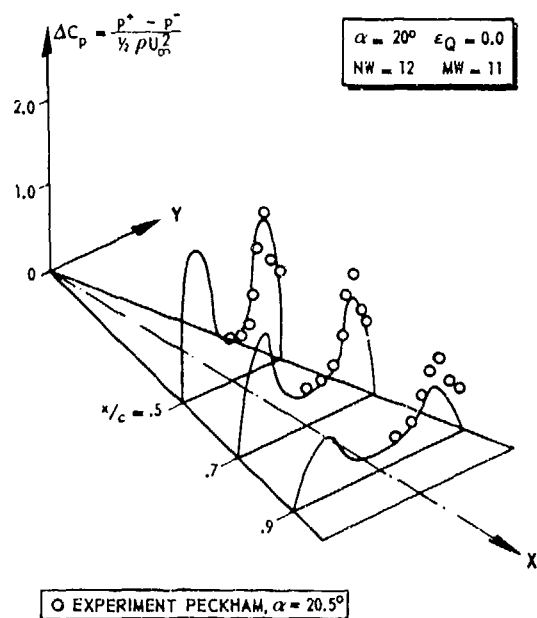


Fig. 8 Load distribution on delta wing of AR = 1

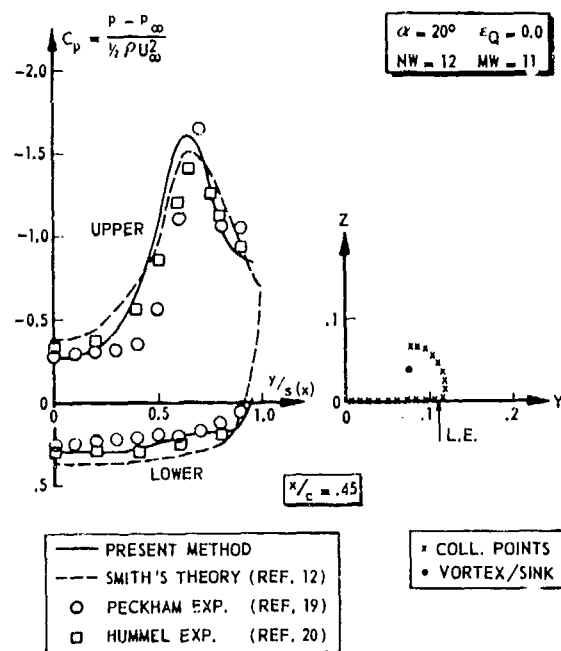
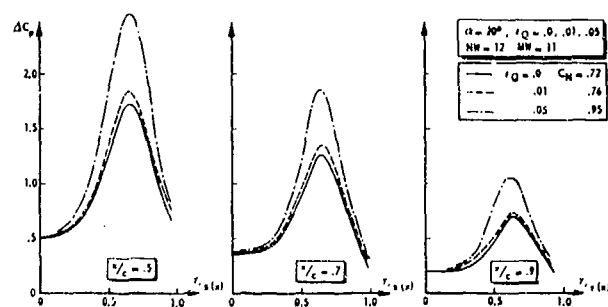


Fig. 9 Pressure distribution on wing

Fig. 10 Load distribution on delta wing at different ϵ_Q

Subcritical Drag Minimization for Highly Swept Wings with Leading Edge Vortices

by
E. N. Tinoco and H. Yoshihara
The Boeing Aerospace Company
P. O. Box 3999
Seattle, WA 98124

SUMMARY

A method is sought to improve the subsonic lift to drag ratio of supercruiser type wings at sufficiently large lifts for which flow separation cannot be avoided. In the presence of the resulting leading edge vortex, minimum drag due to lift is no longer dictated by spanwise load distribution alone but is also a function of the chordwise loading. For the resulting nonlinear problem a higher order panel method utilizing a vortex sheet model is used to search for an "optimal" design. A brief outline of the computational method is given followed by examples validating the procedures. Results of the search for an "optimal" camber are discussed.

1. INTRODUCTION

Our objective is the improvement of the subsonic lift to drag ratio of supercruiser type wings at sufficiently large lifts for which flow separation cannot be avoided. Since such wings are characterized by large leading edge sweep, low aspect ratio, and sharp leading edges, significant lift generation without large accompanying drags will be a difficult task. It is clear that sufficient deflection of a conformal leading edge flap can be provided to prevent leading edge separation, but for the large lifts of interest, the required deflection is so severe that separation downstream of the "hinge line" cannot be avoided. Since such separations are highly detrimental and usually ill behaved, it is preferable to waive leading edge attachment and permit the flow to form a stable leading edge vortex system. Preferability of such controlled separations was recognized early by Maskell and Küchemann, Ref. 1. With such leading edge vortices present, the dilemma is that the usual attached flow optimization procedures based upon the superposition of elemental flows can no longer be used. Though the flow equation is still linear, the problem is rendered non-linear by the contact conditions on the floating separation vortex sheet.

For a general non-planar lifting system, the minimum drag for a given lift, according to Jones (Ref. 2), is achieved when the trailing vortex system moves uniformly downward in the far downstream Trefftz plane where the streamwise variation of the flow becomes insignificant. This reduces in the simplified case of a planar trailing vortex system to the following consequences:

1. The minimum drag is known being equal to $C_{L,2}^2 / (\pi AR)$. (Nonplanar lifting systems can of course have lower drag due to lift).
2. This is achieved when the spanwise loading is elliptic, independent of the chordwise pressure distribution. (The optimal camber is therefore not unique).

In contrast, we have the following less fortunate situation for the leading edge vortex flow:

1. The minimum drag for a given lift is a priori unknown.
2. The optimal condition of the uniform downwash in the Trefftz plane still applies but is not explicitly translatable into the optimal loading or camber shape.

The causes for the above difficulties are clear. First, the minimum drag cannot be determined by a Trefftz plane analysis since the trace of the separation vortices is not known in advance being dependent upon the optimum camber which itself is being sought. Second, assuming that the trace of the separation vortices in the Trefftz plane can be approximated, one can determine the vorticity distribution along this trace to fulfill the uniform downwash condition, but there is no simple way to trace the trailing vorticity upstream from the Trefftz plane to the wing planform to construct the optimal pressure distribution.

In contrast to the attached flow case, the optimum pressure distribution is no longer defined only by its spanwise load distribution. Its chordwise variation is now significant, since the vorticity shed along the leading edge, as well as along the trailing edge, is a function of the overall flow including the positioning of the separation vortices. This then would suggest that the optimum camber may no longer be non-unique in contrast to the attached flow case.

In the above situation the optimization procedure at this stage must assume a relatively laborious searching process, wherein meaningful elemental camber patterns are parametrically combined to minimize the drag for a given lift. Such a search would be guided by monitoring the chordwise plots of the drag component of the pressure at several span stations and possibly by the Trefftz plane downwash.

Helpful in the search process are several earlier studies by Küchemann (Ref. 3), Lee (Ref. 4), Barsby (Ref. 5), and Poisson-Quinton (Ref. 6). More recently Lamar (Ref. 7) developed an optimization procedure using the Polhamus suction analogy to model the vortex flow. These contributions have suggested the use of nose-down leading edge camber to provide a forward-facing surface upon which the high suction generated by the leading edge vortices would act to reduce the drag. Such leading edge camber would of course also reduce the strength of the leading edge vortex, so that Lee and more recently Paulson and Middleton (Ref. 8) have suggested the addition of a small nose tab to control the leading edge vortex strength independent of the nose-down leading edge camber.

Lamar found additionally the importance of providing a wing washout, that is decreasing the local angle of attack in the tipward direction. Such a result is physically not surprising, since washout is simply a means of taking advantage of the large induced upwash in the outboard region of the wing. The Polhamus suction analogy used by Lamar has been shown to predict successfully the measured overall forces and moment over a wide range of cases. However it overly biases the nose suction to the leading edge, thereby tending to overweight the nose camber in the optimization process.

In any search process, it is essential to have on hand a reliable computing method that will reasonably predict the pressure distribution, since the optimization procedure is simply the proper mating of the local pressure with the local surface slope. Additionally it would be desirable to have a procedure requiring modest computer time since many cases usually must be computed.

Several theoretical approaches with varying degrees of sophistication and success have been investigated. The first attempts (Refs. 9, 10, and 11) were based on slender body and conical flow theory in which the trailing edge Kutta condition was ignored. These were followed by fully three dimensional solutions in which the vortex is represented by single or multiple line vortices, Refs. 12-16 or by a vortex sheet Refs. 17 and 18. The method presented in this paper is an improvement of the vortex sheet method of Weber and Johnson, et al., Ref. 17 and 18.

In the following, a brief description of this method and its improvements will be given followed by several test-theory comparisons validating the method. The results of the search for the "optimal" camber conclude the paper.

2. DESCRIPTION OF THE COMPUTER PROGRAM

The leading edge vortex program used is an improved version of the earlier Boeing/NASA Leading Edge Vortex Program described in detail in Refs. 17 and 18. A detailed account of the improved code will appear shortly, so only a condensed description is given here. Wing-fuselage configurations can be treated by this computer program, but the wing leading edge sweep must be sufficiently uniform that only a single vortex sheet is shed along each leading edge. That is, severe breaks in the leading edge, must therefore be excluded.

The modeling of the leading edge vortex sheet used is essentially that of Smith (Ref. 9). The essential elements (Figure 1) are the free sheet emerging from the leading edge, the core vortex, and the fed sheet connecting the two. The vortex sheet from the trailing edge is modeled in the planar fashion.

The flow is described by the subcritical small disturbance potential equation with the following boundary and interface conditions.

1. The flow must be parallel to the wing-body surface.
2. The free sheet and the trailing vortex sheet must be aligned with the streamlines with continuous pressures across the sheets.
3. Along the wing perimeter, the Kutta condition must be fulfilled.
4. On the traverse cut of the fed sheet and core vortex, the net pressure force must be zero. (Zero local loading on the fed sheet cut is not required).

When the flow tangency condition on the configuration is expressed as a zero normal mass flux condition and the pressure coefficient expressed to second order, the above boundary value problem transforms to the incompressible case when the G6thert rule is applied (Ref. 19).

To solve the resulting incompressible problem, a higher order panel method is used. A typical paneling scheme is shown in Figure 2. Here quadratic doublet distributions are used to represent the wing, the free and fed sheets and the wake. Linear source distributions are used to represent the body and the wing thickness.

In the earlier leading edge vortex code, flat panels and six degrees of freedom quadratic doublet splines were used. These would sometimes result in geometric mismatches between panels and discontinuities of the singularity strengths across the panel edges. These in turn led to the generation of infinite upwash at the panel edges which usually contaminated the velocities at the control points to produce unsatisfactory solutions. In the improved code, the flat panels have been replaced by hyperboloidal (hyperbolic-paraboloid) panels to ensure matching along the entire panel edges. The doublet distributions have been upgraded to nine degrees of freedom splines. This results in a continuous quadratic doublet distribution instead of the piece-wise continuous distribution previously used. These changes have resulted in a more reliable code for calculating leading edge vortex flows on twisted and cambered configurations.

With this abbreviated background, let us next proceed to the solution procedure. The basic difficulty is that the location of the separation vortex system is a priori unknown. The solution must therefore be carried out by an iterative procedure starting with an approximate location of the leading edge vortex. For this purpose the conical vortex configuration determined by Smith (Ref. 9) is used. In general the procedure is to determine first the doublet strengths to fulfill all of the boundary conditions except for the streamline alignment condition on the free sheet and the force condition on the fed sheet and core vortex. The latter conditions are then addressed by relocating the free and fed sheets while upgrading the doublet strengths by a linearized approximation. With the resulting upgraded leading edge vortex location and the upgraded doublet distribution, the iterative procedure is repeated until the required convergence is obtained.

More specifically the above successive approximation procedure can be described in terms of the functional equations symbolically representing the boundary conditions defined as follows:

$$\begin{aligned} F(\mu; \theta, \lambda, \nu) &= 0 & \begin{cases} \circ \text{ Flow tangency on configuration.} \\ \circ \text{ Kutta condition on wing.} \\ \circ \text{ Contact conditions on trailing vortex system.} \end{cases} \\ G(\mu; \theta, \lambda, \nu) &= 0 & \circ \text{ No load condition on free sheet.} \\ H(\mu; \theta, \lambda, \nu) &= 0 & \circ \text{ Flow tangency on free sheet.} \\ I(\mu; \theta, \lambda, \nu) &= 0 & \circ \text{ Force condition on fed sheet and core vortex.} \end{aligned}$$

Here μ is the panel doublet strength; and θ , λ , and ν are variables defining the free and fed sheets in a transverse cut where θ is the panel slope, λ scales the free and fed sheets as a whole, and ν scales the fed sheet separately (see Figure 3). The problem is now to determine μ , θ , λ , and ν such that the above boundary conditions are fulfilled.

As described earlier, the first step is to determine $\mu = \mu_0$ which fulfills $F = G = 0$, given the conical leading edge vortex calculated by Smith and defined by θ_0 , λ_0 , and ν_0 . To define the next approximation, perturbations $\Delta\mu$, $\Delta\theta$, $\Delta\lambda$, and $\Delta\nu$ about $(\mu_0; \theta_0, \lambda_0, \nu_0)$ are introduced in the above boundary conditions, and the resulting equations expanded to first order in the perturbation quantities. That is,

$$\begin{aligned} F_0 + F_\mu \Delta\mu + F_\theta \Delta\theta + F_\lambda \Delta\lambda + F_\nu \Delta\nu &= 0 \\ G_0 + G_\mu \Delta\mu + G_\theta \Delta\theta + G_\lambda \Delta\lambda + G_\nu \Delta\nu &= 0 \\ H_0 + H_\mu \Delta\mu + H_\theta \Delta\theta + H_\lambda \Delta\lambda + H_\nu \Delta\nu &= 0 \\ I_0 + I_\mu \Delta\mu + I_\theta \Delta\theta + I_\lambda \Delta\lambda + I_\nu \Delta\nu &= 0 \end{aligned}$$

where for example $F_0 = F(\mu_0; \theta_0, \lambda_0, \nu_0)$; and the subscripts denote known partial derivatives, which are expressed in terms of the aerodynamic influence coefficients or evaluated from a prior approximation. In vector notation the above set of linear equations can be rewritten as

$$C \vec{X} = -\vec{R}$$

where

$$C = \begin{bmatrix} F_\mu & F_\theta & F_\lambda & F_\nu \\ G_\mu & G_\theta & G_\lambda & G_\nu \\ H_\mu & H_\theta & H_\lambda & H_\nu \\ I_\mu & I_\theta & I_\lambda & I_\nu \end{bmatrix} \quad \vec{X} = \begin{bmatrix} \Delta\mu \\ \Delta\theta \\ \Delta\lambda \\ \Delta\nu \end{bmatrix} \quad \vec{R} = \begin{bmatrix} F_0 \\ G_0 \\ H_0 \\ I_0 \end{bmatrix}$$

The iteration procedure as defined above is repeated until the residual error in the fulfillment of the boundary conditions, denoted by the vector \vec{R} , is reduced to an acceptable value. Under-relaxation is employed between iterations.

3. VERIFICATION OF THE NUMERICAL RESULTS

We shall first validate the numerical procedure by comparison with experiments prior to the optimization search. In the comparisons, the possible appearance of secondary vortices in the experiments and the assumption of zero thickness in the calculations must be kept in mind.

A variety of test-theory comparison for flat delta and arrow wings, given earlier in Refs. 17 and 18, has shown that reasonable solutions can be achieved by the leading edge vortex code. In the present section further test-theory comparisons are given for more general cases.

The first comparisons are for the arrow wing with a leading edge sweep of 71° , aspect ratio of 1.65 and a taper ratio of 0.10 tested by Manro, Manning, Hallstaff, and Rodgers (Ref. 20). The comparisons are for the basic wing, Figure 4, and for an aft flap deployed, Figure 5. The change of the paneling in

the latter case is to accommodate the flap hinge line. In general there is good overall agreement between the experiments and the calculations, but the comparisons are distorted by the appearance of a secondary vortex in the experiments. The presence of the latter raises the suctions near the leading edge and lowers the suction peak due to the primary vortex. In addition the finite thickness of the wing and its attachment to a slender fuselage in the experiments will, to a lesser degree, also affect the comparison, though the consequences will be reduced by plotting the loading rather than the pressures as in the above figures. For comparison purposes, an attached flow solution for the flap case is also shown in Figure 5.

A different type of case is shown in Figure 6. Here we compare the loading for the case of a yawed delta wing tested by Harvey (Ref. 22). Again good agreement is seen with the exception of the effects of the secondary vortex. Additional comparisons were made for increasing yaw angles until one of the leading edges became parallel to the freestream. Agreement with test data comparable to that seen in Figure 6 was found in every case.

These examples and solutions obtained by other investigators (Refs. 7 and 23) using the early version of the Leading Vortex code have shown the method to give reasonable results for a range of delta and arrow wings. What is necessary for this drag minimization study is the ability of the code to reflect accurately the differences in pressure distributions and drag due to twist and camber changes. The aim of the recent improvements of the code was to improve its accuracy and reliability and to expand its range of validity to general camber shapes.

In order to validate the accuracy of the new code in reflecting aerodynamic differences due to camber changes, two wings first analyzed by Kuhlman (Ref. 23) were reanalyzed. These were delta wings of identical planform tested by Wentz (Ref. 21). The wing had an aspect ratio of 1.15 and 74° sweep. One wing was flat while the other had conical camber. These wings are illustrated in Figure 7. For the calculations, the wings were considered to have zero thickness. Calculated and measured pressure distributions are compared for both wings in Figure 8. While the difference in the measured pressure distributions due to the camber on the upper surface is small, the calculated results accurately portray these differences. On the lower surface near the leading edge, the greater differences in the experimental data between the flat and cambered wing are also reflected in the theoretical results.

The code must further accurately predict drag increments between different cambered wings. Drag polars are presented for the flat and cambered delta wings in Figure 9. Both calculated and measured results are shown. This comparison shows the drag differences to be predicted reasonably well by the improved code. At $C_L = 1.2$ the predicted drag reduction for the cambered wing is 5.7 percent compared to 7 percent given by Wentz for the measured data.

4. RESULTS OF THE PRELIMINARY OPTIMIZATION SEARCH

In the case of attached flow, one has a linear problem in that the solutions for two different camber distributions when added yield the solution for the wing with the combined camber. This then allows the determination of the optimum camber by ordinary calculus by suitably superpositioning meaningful elemental cambers. This superposition principle no longer holds in the case of leading edge vortex flows when the location of the separation vortices of the elemental cambers differs significantly. Here the superposition of the elemental flows clearly will not yield the correct vortex for the combined cambers.

The above nonlinearity has a severe consequence on the optimization procedure. A routine superposition exercise with a predetermined drag target in the case of attached flow worsens for the vortex flows to a laborious ad hoc search procedure with an unknown target. Such a search procedure for highly swept and low aspect ratio wings is impeded by the lack of detailed understanding of the resultant highly three-dimensional flows. Thus as a starting point we must generate a background data base by computing the flow for a range of meaningful camber shapes. For the present investigation we shall calculate the effect of nose-down leading edge camber and wing washout. Here the leading edge camber provides a more forward-facing inclination to the portion of the wing upon which the high vortex-induced suctions act to reduce the drag. Wing washout seeks to take advantage of the flow upwash usually generated upstream of the outboard portion of the wing that increases the local effective angle of attack.

Calculations were carried out at zero Mach number for a series of delta wings of identical planform to those tested by Wentz (Ref. 21). These included a flat and conical cambered wing previously shown in Figure 7 and two wings with 10° and 20° linear twist shown in Figure 10.

In Figure 11 we compare the spanwise pressure distributions at four streamwise stations for the flat and twisted wings at 25° angle of attack. On the upper surface, increase of washout has caused a narrowing of the vortex suction peak but no consistent effect on the suction peak height. A further result of the increased washout is the deepening of the inboard suction trough that significantly decreases the lift. Except for the tip region, there is little effect of the washout on the lower surface overpressures.

In Figure 12 we show comparable pressure distribution plots of the effect of the leading edge conical camber. (The case of the vortex control tab also shown here will be discussed below.) Quite clearly, the selected conical camber is far too small for the 25° angle of attack. The results however do suggest that leading edge camber has essentially the same effect as the washout on both the upper and lower surface pressures.

The resultant lift curves and drag polar curves for the above cases are shown in Figures 13 and 14. The expected lift loss at a given angle of attack due to washout or nose-down camber seen here is responsible for the modest improvement exhibited in the drag polars. To see in more detail now the

above changes affect the drag, we plot in Figure 15 the pressure coefficient along a chordwise trace versus the vertical coordinate of the airfoil for two span stations and for the constant lift coefficient of 1.1. Hence, the area within the drag loop is equal to the drag coefficient. Particularly noticeable here is the beneficial effect of the washout at the outboard span station.

The relative shapes of the resulting leading edge vortex are shown in Figure 16 where their trace in a transverse cut through the trailing edge is given.

The final example is that of the vortex controller tab shown in Figure 17. Here a conical tab is added to the leading edge of a wing with essentially the leading edge camber used above, but with the sweep of the latter increased to retain the same overall planform as the above examples. The rationale for the vortex controller tab configuration is to provide a forward facing surface segment to retain the benefits of the leading edge camber, but have the flexibility to control the strength of the leading edge vortex by varying the angle of the tab. In this way the forward facing segment can be placed directly under the suction peak.

The resulting pressure distributions for the vortex controller tab is given in Figure 12. Except for the higher suction peak, the effect of the tab is similar to the effects of the washout and leading edge camber. The resulting drag loop is shown in Figure 18 where the noticeable feature is the reduction of the outboard drag loop area by the decrease of the vertical height. The lift curve and the drag polar are shown in Figures 19 and 20. The resulting shape of the leading edge vortex is given in Figure 21.

Lack of significant improvement by the above vortex tab must be attributed to several causes. The first is quite clearly the insufficient downward forward cambering for the 25 angle of attack. Additionally the forward facing inclination of the flap is reduced by the greater sweep of the "hinge line" required to keep invariant the overall planform. The conical configuration of the vortex tab most probably had insufficient chord in the inboard region to generate the intended increased leading edge vortex strength. These configuration defects would be moderated by the configuration shown in Figure 22. Here a greater chord for the tab is provided inboard where most probably the strengthening of the leading edge vortex is largely determined. The apex of the conical leading edge flap is displaced rearward to increase its forward facing inclination by decreasing the camber sweep. Though not shown in Figure 22, a greater nose down camber than used above as well as washout could also be incorporated. Configurations of this type will be computed in the near future.

5. CONCLUDING REMARKS

The present experience with the improved leading edge vortex code suggests it to be reasonably reliable, yielding satisfactory solutions over a range of wing camber shapes. It is, however, restricted to cases with a single leading edge vortex precluding more complex configurations, for example resulting from secondary vortices which were evident in many of the experimental results.

The present preliminary computations suggest that significant reductions in the drag for a given lift will be difficult to achieve by use of nose down leading edge camber or wing washout alone due in large part to an accompanying loss of lift. When such lift loss is recovered by increased angle of attack, the net gain in the drag is significantly reduced. A more careful tailoring of the leading edge camber or the wing twist to the angle of attack at hand will improve this situation, but more promising gains most probably will require more elaborate cambering as the use of a device such as the vortex control tab.

In the present investigation we have confined our attention to those camber features that directly influence the leading edge vortex. We have deferred attention to other more familiar camber features such as aft flaps which would additionally improve the aerodynamic performance by filling in the upper surface suction trough downstream of the vortex suction peak as well as by increasing the overpressures over the lower surface. In particular an inboard part-span flap would be attractive through its favorable spanwise carryover effects.

The optimization search for leading edge vortex flows is made difficult by two factors. The first is due to the extreme three dimensionality of the flow wherein streamlines follow an extremely tortuous course. Thus, for example, streamlines passing over the outboard portion of the leading edge approach the wing at significantly further inboard paths. It is therefore difficult, to tailor the shaping of leading edge to shed a vortex of prescribed strength.

The second difficulty is that for vortex flows we do not know a priori the lower bound drag for a given lift as the classical "lift squared over π aspect ratio" for the case of attached flow over near-planar wings. Knowledge of the lower bound drag would be invaluable since it would permit the assessment of the optimization search as well as establishing its stopping point.

The Trefftz plane is a logical starting point for establishing the lower bound drag. For vortex flows the primary obstacle is that the Trefftz plane trace of the vortex sheet shed from the leading edge is a priori unknown. If this difficulty is surmounted by establishing an approximate trace, for example, from prior computations, it would then be a straightforward task to determine the optimal distribution of vortices along the trace yielding the required uniform downwash at the trace. The results would yield the lower drag bound for a given lift as well as the optimal partitioning between the vorticity shed from the leading and trailing edges, but in contrast to the attached flow case, it will not lead directly to the optimal cambering. Finally, the Trefftz plane concept should be validated by verifying the lift and drag for several computed examples obtained by a direct pressure integration.

In conclusion, the leading edge vortex code represents an important design tool. There remains only the ingenuity of the aerodynamicist to achieve the needed high lift performance for the difficult class of wings represented by the supercruiser planform.

6. REFERENCES

1. Maskell, E. C., and Küchemann, D., "Controlled Separation in Aerodynamic Design", RAE Tech. Memo. 453, (1956).
2. Jones, R. T., "Three-Dimensional Wings of Minimum Pressure Drag", Theory of Optimum Aerodynamic Shapes, Angelo Miele, Editor, New York, Academic Press, pp 125-134, (1965).
3. Küchemann, D., "The Aerodynamic Design of Aircraft - An Introduction," Part 5, RAE Tech. Memo., Aero 1627, (Feb. 1975).
4. Lee, G. H., "Reduction of Lift-Dependent Drag with Separated Flow," ARC C.P. No. 593, (Oct. 1959).
5. Barsby, J. E., "Flow Past Conically-Cambered Slender Delta Wings with Leading-Edge Separation," RAE Tech. Rep. 72179, ARC R&M 3748, (1972).
6. Poisson-Quinton, P., "Slender Wings for Civil and Military Aircraft," 8th Theodore Von Karman Memorial Lecture, Twelfth Israel Annual Conference on Aviation and Astronautics, (Feb. 1978).
7. Lamar, J. E., "Subsonic Vortex-Flow Design Study for Slender Wings," AIAA Paper No. 78-154, (Jan. 1978).
8. Paulson, J. A., and Middleton, W. D., Boeing Invention Disclosure 77-5, "A Leading Edge Flap Design for Swept Wings - A Vortex Flap," (1977).
9. Smith, J. H. B., "Improved Calculations of Leading-Edge Separation from Slender Delta Wings." Proc. R. Soc. Lond. A 306, pp 67-90, 1968, also RAE Technical Report 66070 (1966).
10. Mangler, K. W. and Smith, J. H. B., "A Theory of the Flow Past a Slender Delta Wing with Leading Edge Separation," Proc. R. Soc. Lond. A 251, pp 200-217, 1959, RAE Report Aero 2593 (1957).
11. Levinsky, E. S. and Wei, M. H. Y., "Nonlinear Lift and Pressure Distribution on Slender Conical Bodies with Strakes at Low Speeds," NASA CR 1202, (1968).
12. Nangia, R. K. and Hancock, G. J., "A Theoretical Investigation for Delta Wings with Leading-Edge Separation at Low Speeds," ARC CP 1086 (1968).
13. White, Jr. R. P., "Wing-Vortex Lift at High Angles of Attack," AGARD-CP-204. (Sept. 1976).
14. Kandil, O. A., Mook, D. T. and Nayfeh, A. H., "Nonlinear Prediction of the Aerodynamic Loads on Lifting Surfaces," J. of Aircraft 13, pp 22-28 (1976).
15. Rehbach, C., Etude, Numerique de Nappes Tourbillonnaires Issues D Une Ligne de Decollement Pres du Bord d Attaque," Rech. Aero. 1973-6, pp 325-330, (1973).
16. Kandil, O. A., Mook, D. T. and Nayfeh, A. H., "A Numerical Technique for Computing Subsonic Flow Past Three-dimensional Canard-wing Configurations with Edge Separations," AIAA Paper 71-1 (1977).
17. Weber, J. A., Brune, G. W., Johnson, F. T., Lu, P. and Rubbert, P. E., "Three-Dimensional Solution of Flows over Wings with Leading Edge Vortex Separation," AIAA Journal 14, pp 519-525, 1976, also NASA CR 132709 and 132710 (1975).
18. Johnson, F. T., Lu, P., Brune, G. W., Weber, J. A. and Rubbert, P. E., "An Improved Method for the Prediction of Completely Three-Dimensional Aerodynamic Load Distributions on Configurations with Leading-Edge Separation," AIAA Paper 76-417 (1976).
19. Brune, G. W. and Rubbert, P. E., "Boundary Value Problem of Configurations with Compressible Free Vortex Flow," AIAA Journal, Vol. 15, No. 10, pp 1521-1523, (Oct. 1977).
20. Manro, M. E., Manning, K. J. R., Hallstaff, T. H., and Rogers, J. T., "Transonic Pressure Measurements and Comparison of Theory to Experiment for an Arrow-Wing Configuration," NASA CR-132729, (Oct. 1975).
21. Wentz, W. H. "Effects of Leading-Edge Camber on Low-Speed Characteristics of Slender Delta Wings" NASA CR-2002 (1972).
22. Harvey, J. K., "Some Measurements on a Yawed Slender Delta Wing with Leading Edge Separation," British ARC Report 20451, (1958).
23. Kuhlman, J. M., "Analytical Studies of Separated Vortex Flow on Highly Swept Wings", NASA CR 3022, (1978).

7. ACKNOWLEDGEMENT

The authors wish to acknowledge the efforts of Dr. Forrester T. Johnson who directed the development of the improved leading edge vortex code and that of Mr. Paul Lu and Dr. Michael A. Epton who carried out the numerical analysis and computer programming. This study was carried out under joint sponsorship of the Boeing Company and the Subsonic-Transonic Aerodynamics Division of the Langley Research Center, National Aeronautics and Space Administration.

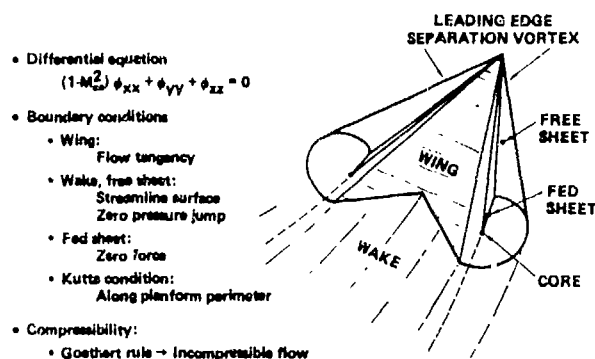


Figure 1. Flow Model

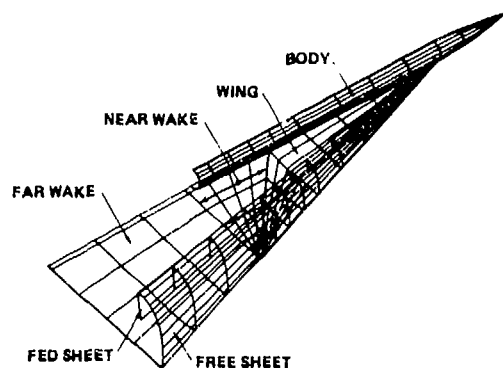


Figure 2. Panel Model

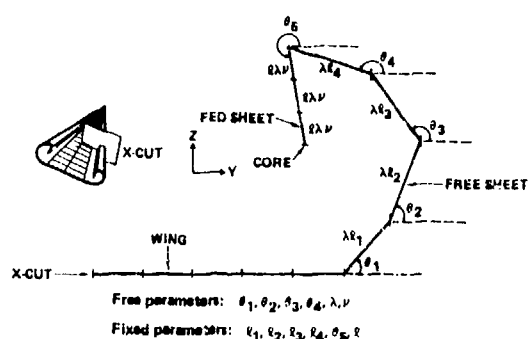


Figure 3. Free Sheet/Fed Sheet Kinematics

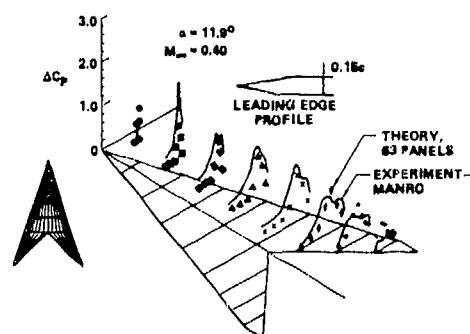


Figure 4. Lifting Pressure Distribution—Flat Arrow Wing

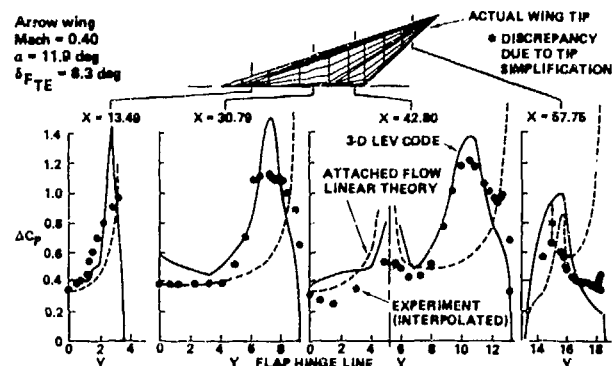


Figure 5. Lifting Pressure Distribution—Arrow Wing With Trailing Edge Flap

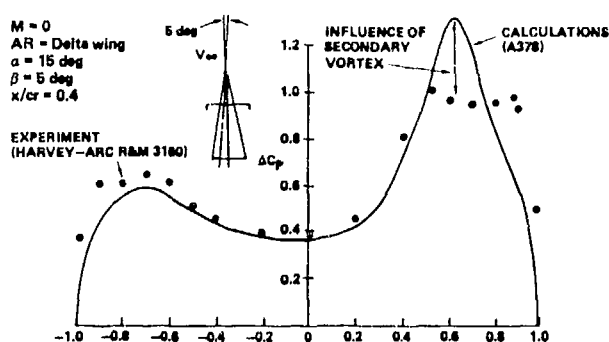


Figure 6. Lifting Pressure Distribution—Yawed Delta Wing

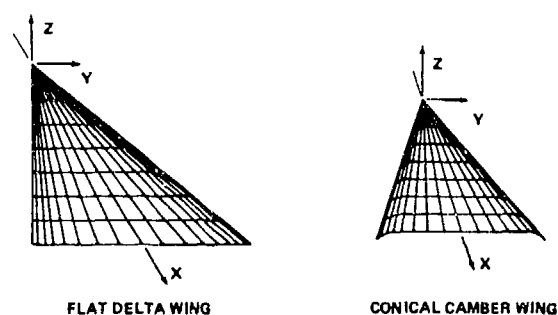


Figure 7. Flat and Conical Camber Delta Wing Paneling

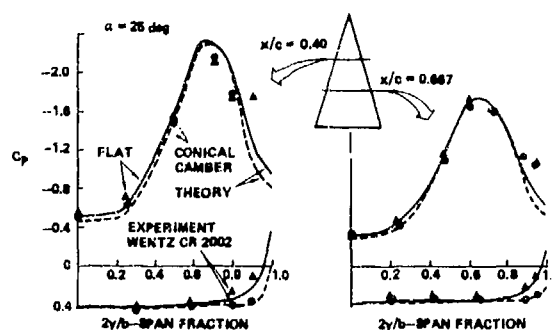


Figure 8. Surface Pressure Distribution—Flat and Conical Camber Delta Wing

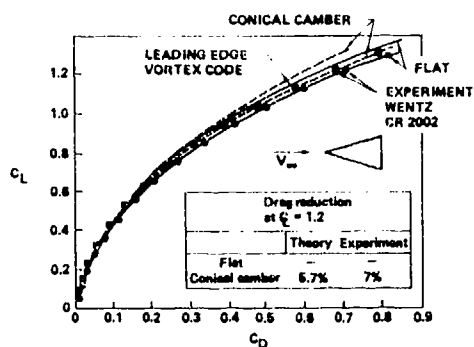


Figure 9. Drag Polar—Flat and Conical Camber Delta Wing

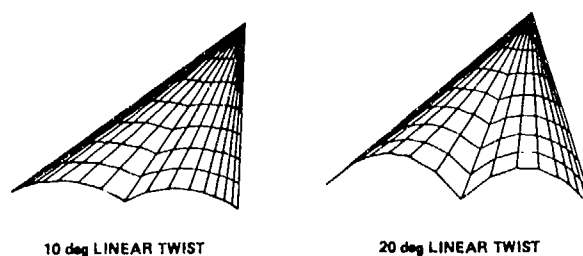


Figure 10. Twisted Delta Wing Paneling

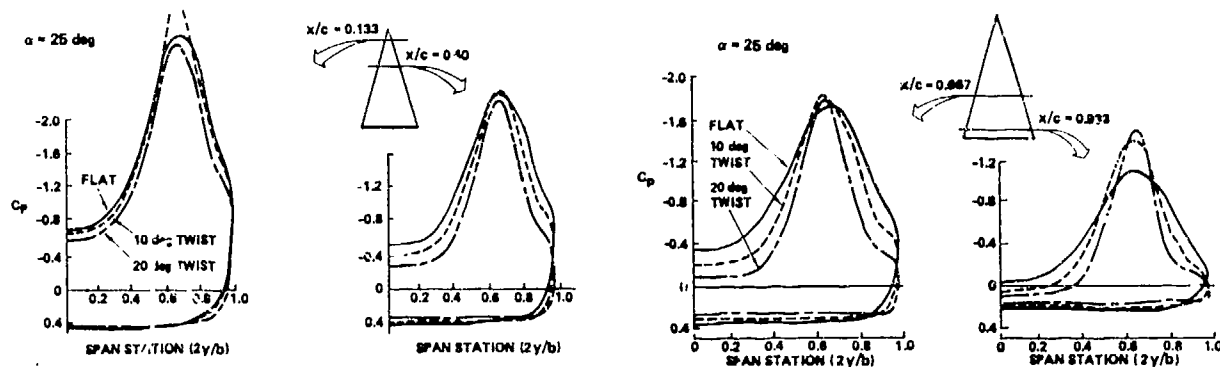


Figure 11. Surface Pressure Distribution—Effect of Twist

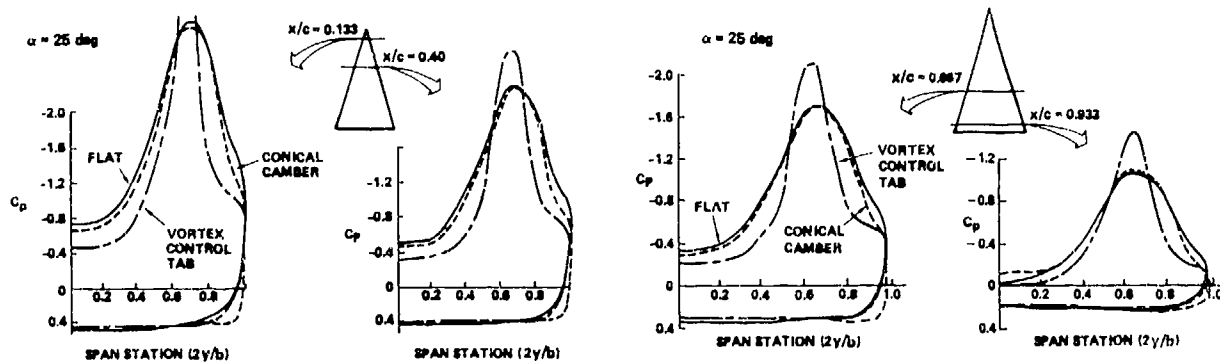


Figure 12. Surface Pressure Distribution—Effect of Camber

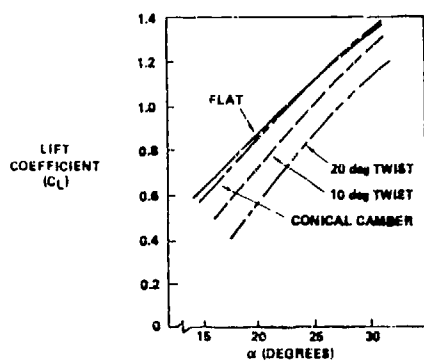


Figure 13. Lift Curve—Effects of Camber and Twist

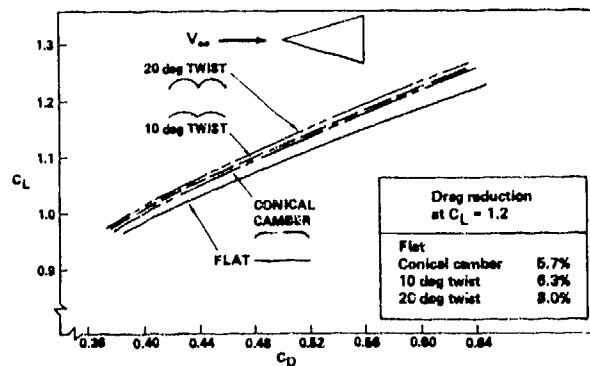


Figure 14. Drag Polar—Effects of Camber and Twist

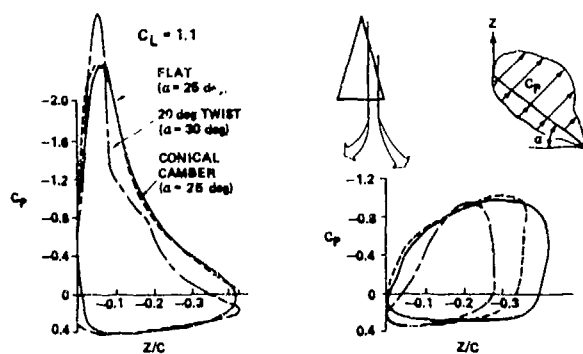


Figure 15. Drag Loop—Effects of Camber and Twist

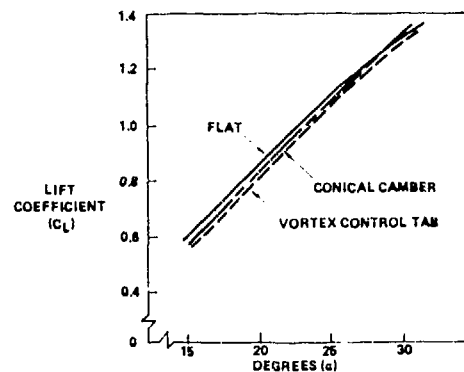


Figure 19. Lift Curve—Effects of Vortex Control Tab

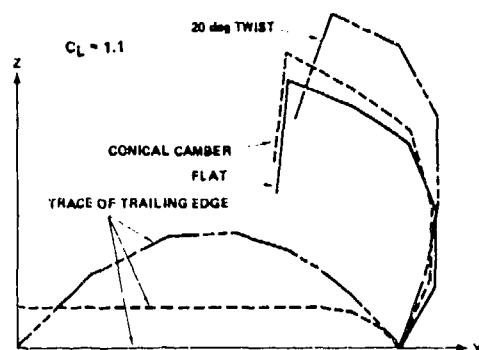


Figure 16. Leading Edge Vortex Shape

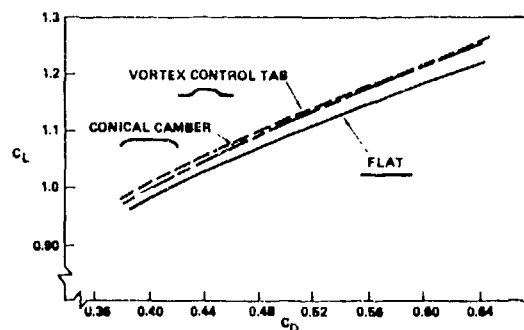


Figure 20. Drag Polar—Effects of Vortex Control Tab

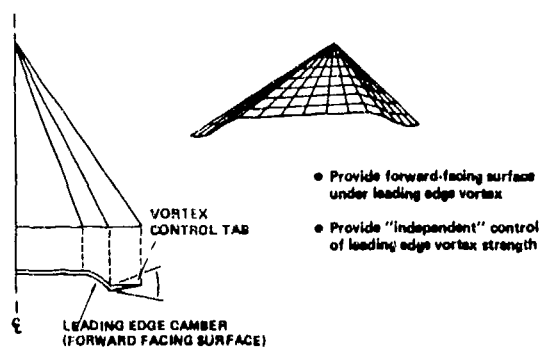


Figure 17. The Vortex Control Tab

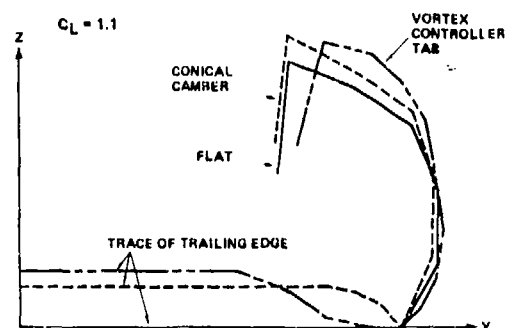


Figure 21. Leading Edge Vortex Shape

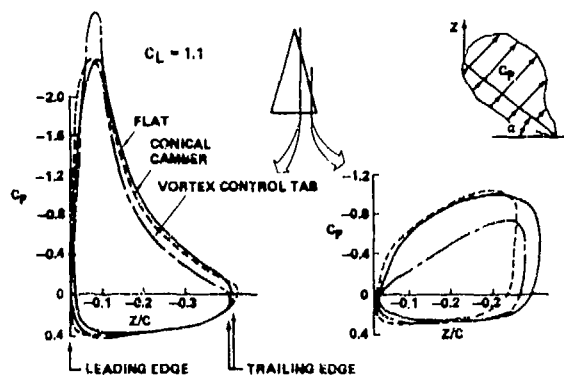


Figure 18. Drag Loop—Effects of Vortex Control Tab

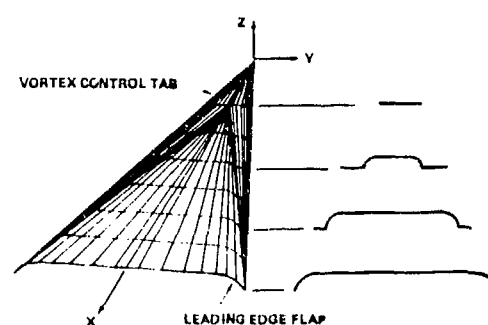


Figure 22. A Proposed Vortex Control Tab Configuration

NORMAL FORCE AND PITCHING MOMENT OF WING-BODY-
COMBINATIONS IN THE NON-LINEAR ANGLE-OF-ATTACK RANGE AT
SUBSONIC SPEEDS

by
C.P. Schneider and D. Nikolitsch
Messerschmitt-Bölkow-Blohm GmbH
Munich

SUMMARY

Two engineering methods predicting the angle-of-attack dependence of the interference factors of missile configurations at subsonic speeds and with quasisteady pitching motion are investigated of their accuracy. Both procedures are based on the non-linear lifting surface theory. One method for the determination of the factor $K_B(w)$ which represents the effect of the wing on the body-forces and -moments due to lift carry-over relies on the linear Lennertz theory. The latter is modified in order to provide for an inclusion of results of the non-linear lifting surface theory. This procedure will predict the normal force interference factors only. Also the other method determines $K_B(w)$. It uses the non-linear lifting surface theory twice, firstly for the calculation of normal force and moment of a slowly pitching wing alone, secondly to get the same quantities for a substitute wing which represents the original wing plus a rectangular flat middle section in place of the body between the wing root chords. The differences between the results of the two procedures call for an improved prediction method, as comparable quasisteady data from experiments, which may serve to confirm the results of one or the other method are not available at present. For the additional analysis, free vortex tracing of discrete vortices by conventional two-dimensional theory is proposed. Viscous vortices with core are assumed. Their initial strength and position are derived from three-dimensional non-linear lifting surface theory by conversion of the linear and non-linear circulation of the wing.

LIST OF SYMBOLS

c_o, \bar{c}	wing root chord, aerodynamic mean chord of wing
k, k'	reduced frequencies $k = ql/V$, $k' = kD/l$
l, l_c, l_w	body length, length of body cylindrical section with constant radius, distance from body nose tip to wing tip
q	pitching velocity
s	wing half span
w	velocity component in Z-direction
A	reference area
C	aerodynamic coefficient of forces and moments and their derivatives. The reference area and reference length are $A = \pi D^2/4$ and D , unless specified otherwise in the text
C_N	normal force coefficient

$$\begin{aligned}
 &= N/\frac{1}{2} \rho AV^2 = \alpha \frac{\partial C_N}{\partial \alpha} \bigg|_{\alpha=0} + \frac{\alpha^2}{2} \frac{\partial^2 C_N}{\partial \alpha^2} \bigg|_{\alpha=0} + \frac{kD}{1} \frac{\partial C_N}{\partial \frac{qD}{V}} \bigg|_{q=0} + \dots \\
 &= \alpha C_{N\alpha} \bigg|_{\alpha=0} + \alpha^2 C_1 + \frac{kD}{1} C_{Nq} \bigg|_{q=0} + \dots \\
 &= \alpha C_{Nn} + \frac{kD}{1} C_{Nq} \bigg|_{q=0} + \dots
 \end{aligned}$$

C_m	pitching moment coefficient
-------	-----------------------------

$$\begin{aligned}
 &= M/\frac{1}{2} \rho AV^2 D = \alpha \frac{\partial C_m}{\partial \alpha} \bigg|_{\alpha=0} + \frac{\alpha^2}{2} \frac{\partial^2 C_m}{\partial \alpha^2} \bigg|_{\alpha=0} + \frac{kD}{1} \frac{\partial C_m}{\partial \frac{qD}{V}} \bigg|_{q=0} + \dots \\
 &= \alpha C_{m\alpha} \bigg|_{\alpha=0} + \alpha^2 C_2 + \frac{kD}{1} C_{mq} \bigg|_{q=0} + \dots \\
 &= \alpha C_{mn} + \frac{kD}{1} C_{mq} \bigg|_{q=0} + \dots
 \end{aligned}$$

This investigation has been sponsored by the MOD of the FRG

D	body base diameter
K	interference factor
M	pitching moment
M_∞	Mach number
N	normal force
R	body radius
V	resultant velocity
V_c	cross-flow velocity
X, Y, Z	coordinates (fig. 12)
α	angle-of-attack
γ	strength of circulation
λ	wing taper ratio
η	dimensionless coordinate $\eta = Y/(R+s)$
η_R	location of wing root chord $\eta_R = R/(R+s)$
Λ	aspect ratio of exposed wing
ψ_{LE}, ψ_{TE}	wing leading and trailing edge sweep angle

1. INTRODUCTION

The interference of wing and body of missiles with high maneuverability in the non-linear angle-of-attack range causes a non-negligible contribution to the forces and moments governing the longitudinal stability. This is shown in a recent coefficient synthesis (ref. 1) of quasisteady derivatives of missile configurations in subsonic flow: Figs. 1 and 2 display as function of the angle-of-attack the pitch damping coefficient of wing-body-combinations at $M_\infty = 0.8$. The pitch axis is located at the center of gravity of the body with a homogeneous mass distribution. The fractions 1 and 2 represent the contribution of the body, the boundary layer of which is assumed to be laminar. The fraction 3 is the pitch damping of the wing alone, and parts 4 and 5 are caused by the interference between wing and body. With the wing position of fig. 1, the fraction due to wing-body-interference is small, with the wing position of fig. 2 however, this portion averages 17 % of the total pitch damping over the given angle-of-attack range. The half-empirical methods of ref. 1 used for the prediction of the forces and moments due to the wing-body-interference yielded differences of the results as shown in fig. 3, where the interference factors $K_{B(W)}$ of the normal force slope, pitch stiffness, normal force damping and pitch damping of the configuration of fig. 1 are plotted versus the incidence. These differences and the lack of comparable experimental data in the case of non-linear quasisteady factors called for additional theoretical methods in order to confirm the results of one or the other existing procedure.

2. WING-BODY INTERFERENCE FACTOR

The dimensionless interference factors K according to ref. 2 are formed with the lift or normal force of the wing in the presence of a body or viceversa in relation to the lift or normal force of the wing alone. The normal force of a missile configuration N_c may be defined as the sum

$$N_c = N_B + N_W + N_{W(B)} + N_{B(W)}$$

of the normal force of the body alone N_B , of the wing alone N_W , of the fraction gained or lost by the wing due to the presence of a body $N_{W(B)}$ and the part gained or lost by the body due to the interference of a wing. In the presence of a body the normal force of the wing is $N_W + N_{W(B)}$. This sum related to the normal force of an isolated wing N_W yields the factor

$$K_W = 1 + K_{W(B)}$$

where $K_{W(B)} = N_{W(B)}/N_W$. According to slender body theory (ref. 2), the factor K_W varies with the ratio η_R of the body radius R and the sum of wing half span and body radius (s+R) from 1 for a wing without body ($R=0$) up to 2 for a very wide body ($R \rightarrow \infty$) with a wing of a small half span. In the high angle-of-attack range, K_W may accept smaller values for a given η_R than slender body theory predicts. This can be caused by body vortices changing the downwash distribution and hence the loading over the wing surface. Linear slender body theory predicts a body normal force consisting of the nose or contoured aft body contribution N_N and the part due to the lift carry-over from the wing $N_{B(W)}$. For a cylindrical body of constant radius, i.e. without a contoured nose or aft body section we get $N_N = 0$. Then the body normal force in the presence of a wing is given by $N_B = N_W \cdot K_{B(W)}$, where $K_{B(W)} = N_{B(W)}/N_W$. In the high angle-of-attack range, the body normal force will be changed by a cross-flow term. Also, the $K_{B(W)}$ factor due to lift carry-over will change because of non-linear wing characteristics. The terminology of interference factors K as specified in ref. 2 for normal force N and moment M is extended here to account for the interference effects on pitch damping and normal force damping.

3. NON-LINEAR STEADY INTERFERENCE FACTOR K_W

The upwash distribution over the wing induced by symmetric body vortices and caused by the cross flow accelerating when passing around the body (ref. 3) can be fed into the relations of the non-linear lifting surface theory (ref. 4). This will provide the possibility of calculating non-linear steady and quasisteady interference factors K_W (ref. 1). In fig. 4 the steady non-linear normal force factor $K_W(N)$ obtained this way is compared to experimental results of ref. 5. The influence of different body lengths is noticeable with the experimental data: The normal force of the wing and hence the interference factor are lower with the longer fore body section. According to ref. 5, at low incidences this is due to change of the upwash velocity over the wing as consequence of the nose and body boundary influence. In the higher angle-of-attack range, the position and strength of the body vortices is changed which also may decrease the K_W -factor. Generally, the theory of ref. 1 determines higher K_W values than those obtained in the experiment. In particular a much weaker influence of the body vortices is predicted. As the present theory neglects the body boundary layer thickness which diminishes the effective wing area, the general differences between theory and experiment are understandable. A turbulent boundary layer can lower the interference factor by as much as 20 % (ref. 6). To some extent, the latter influence will also account for the lower K_W with the longer fore body section. The weak influence of body vortices on the wing normal force - predicted by theory - may be explained in fig. 5. Here, the free body vortices and their images, the vortex induced velocity and the cross flow velocity distribution over the wing span are displayed. The cross flow plane of this diagram lies at the wing trailing edge of the configuration of fig. 4. At subsonic speeds, the vortex positions are close to the body surface and near the vertical body axis. The induced upwash velocity w of an individual vortex is quite large, but the resultant induced by the two vortex pairs of the present model becomes small due to partial compensation. Also, arbitrary changes up to 20 % of either the vortex position or the vortex strength do not alter the induced upwash significantly as to reproduce the experimentally determined K_W for a wing with long forebody. Again in fig. 6, the present method overestimates K_W in comparison to the experimental data of ref. 7, but determines the correct slope of K_W with the incidence up to $\alpha \leq 20^\circ$, whereas the result of slender body theory matches the measured value of K_W at low incidences. If a correction for a body boundary layer were taken into account, a decrease of $\Delta K_W/K_W$ from - 10 % to - 20 % would render the slender body value too low, the data of the present method however would compare well with the experimental result. In conclusion of this paragraph, the body boundary layer growth must be taken into account with the present theory, if both the value and slope of K_W with α are to be simulated correctly.

4. MODIFIED LENNERTZ INTERFERENCE FACTOR $K_{B(W)}$

According to Lennertz' linear two-dimensional theory (ref. 8), the ratio of $N_{B(W)}/N_W$ of an wing-body combination is given by a factor $K_{B(W)} = \eta_R$. It changes from zero at $R = 0$, i.e. without the presence of a body to 1 for $R \rightarrow \infty$, as shown in fig. 7a. Here, $K_{B(W)}$ is plotted versus η_R for combinations of body and rectangular wings of various aspect ratios $0 < \Lambda < \infty$. The linear relation between $K_{B(W)}$ and η_R holds for a wing with $\Lambda \rightarrow \infty$. The corresponding normal force distribution over wing and body is shown in the diagram of fig. 7b. The wing normal force is proportional to the area $\Lambda \gamma_0 \cdot (1 - \eta_R)$, the portion carried over to the body amounts to $\Lambda \gamma_0 \cdot \eta_R (1 - \eta_R)$. In the modified version of Lennertz' theory, the normal force of a rectangular wing with finite aspect ratio is represented by the area $2\Lambda \gamma^*(\eta = \eta_R) \cdot \eta_W$ according to ref. 9. The length

$$\eta_W = (1 - \eta_R) \cdot C_{N_W} / (2\Lambda \gamma^*(\eta = \eta_R)) \quad (1)$$

shown in fig. 8 is folded about the wing root chord at $\eta = \eta_R$ on the body coordinate according to conformal mapping. Now a rectangular area $2\eta_W \cdot \eta_R \cdot \Lambda \gamma^*(\eta = \eta_R) / (\eta_W + \eta_R)$ will represent the portion of the normal force of the body due to the wing interference. The ratio $K_{B(W)} = N_{B(W)}/N_W$ combined with eq. 1 leads to the expression

$$K_{B(W)} = \frac{1}{1 + \frac{1 - \eta_R}{\eta_R} \frac{C_{N_W}}{2\Lambda \gamma^*(\eta = \eta_R)}} \quad (2)$$

The factor contains the ratio between the total normal force of the wing and the local normal force at the wing root. In the special case of $\Lambda \rightarrow \infty$, the ratio $C_{N_W} / 2\Lambda \gamma^*(\eta = \eta_R)$ approaches 1, which reduces $K_{B(W)}$ of eq. 2 to the one of Lennertz theory, shown in fig. 7a together with results of eq. 2 for rectangular wings of finite aspect ratio at zero incidence. Through the normal force ratio, a non-linear dependence on the incidence enters eq. 2 when a non-linear lifting surface theory is applied. For a family of wings characterized by straight trailing edges without sweep, of the normal force distribution over the span the local normal force at the wing root will be maximum. In this case, the product of two functions $C_{N_W} / 2\Lambda \gamma^*(\eta = \eta_R)$ for $\alpha = 0$ and $j(\alpha)$ match the result $C_{N_W} / 2\Lambda \gamma^*(\eta = \eta_R)$ of the non-linear lifting surface theory for $\alpha \neq 0$. They relate the normal force ratio to the wing form, i.e. the leading edge sweep and the taper ratio (fig. 9) and to the angle of attack (fig. 10). Within the subsonic range, the Mach number dependence was found negligibly small. As result, simple relations will provide an estimate of the dependence of the $K_{B(W)}$ factor on the incidence and wing form. As seen from fig. 10, delta wings reveal a stronger dependence on the incidence than rectangular or trapezoidal wings. The $K_{B(W)}(N)$ of trapezoidal wings are added to the diagrams of figs. 3 and 11. Only quanti-

ties of wing normal forces are used to obtain $K_{B(W)}$ by means of eq. 2. Therefore, no other information but $K_{B(W)}(N)$ can be given by the modification of the Lennertz theory.

5. $K_{B(W)}$ BY REPLACEMENT OF THE BODY WITH A RECTANGULAR FLAT MIDDLE SECTION

This procedure replaces the cylindrical body between the wing roots by a rectangular flat middle section. The non-linear lifting surface theory is applied twice in order to determine the normal forces and moments of the original wing and of the substitute wing consisting of the original one plus the rectangular middle section. The difference between forces (or moments) of the substitute and the original wing in relation to the corresponding force (or moment) of the original wing alone yields the interference factor $K_{B(W)}$. The normal force factor becomes

$$K_{B(W)}(N) = \frac{N_{SW} - N_W}{N_W} \quad (3)$$

where N_{SW} denotes the normal force of the substitute wing. Using dimensionless force or moment coefficients, the $K_{B(W)}$ of the pitch stiffness, normal force damping and pitch damping are given by

$$K_{B(W)}(M_n) = \frac{(C_{m_n})_{SW} - (C_{m_n})_W}{(C_{m_n})_W} = \frac{(C_{m_n})_{B(W)}}{(C_{m_n})_W}, \quad (4)$$

$$K_{B(W)}(N_q) = \frac{(C_{N_q})_{SW} - (C_{N_q})_W}{(C_{N_q})_W} = \frac{(C_{N_q})_{B(W)}}{(C_{N_q})_W}, \quad (5)$$

$$K_{B(W)}(M_q) = \frac{(C_{m_q})_{SW} - (C_{m_q})_W}{(C_{m_q})_W} = \frac{(C_{m_q})_{B(W)}}{(C_{m_q})_W}. \quad (6)$$

The coefficients of the derivatives in eqs. 4-6 have the wing root chord c_0 rather than the aerodynamic mean chord \bar{c} for reference length, as \bar{c} may vary with η_R . As reference area of the coefficients of the substitute wing $(C_N)_{SW}$ and $(C_m)_{SW}$, the planform of the original wing, i.e. the wetted wing area is chosen. Results of this procedure for the configurations of body and trapezoidal wings are displayed in figs. 3 and 11. The computer program which is used twice for the determination of $K_{B(W)}$ is designed for wings with straight leading edges or leading edges with one bend only. With exception of $\psi_{LE}=0$, the latter shape always applies for the substitute wing. Hence, the computer program cannot handle those original wings which already have a leading edge bend and angles $\psi_{LE} \neq 0$. In order to allow for this particular wing shape, eqs. 4-6 have been reformulated in terms of the normal force factor $K_{B(W)}(N)$, the ratio of the pressure point of original and substitute wing X_{NW}/X_{NSW} and the ratio of the locations of vanishing normal force damping X_{OW}/X_{OSW} :

$$K_{B(W)}(M_n) = (K_{B(W)}(\alpha)+1) \frac{X_{NW}}{X_{NSW}} - 1, \quad (7)$$

$$K_{B(W)}(N_q) = (K_{B(W)}(\alpha)+1) \frac{X_{OW}}{X_{OSW}} - 1 \quad (8)$$

and

$$K_{B(W)}(M_q) = (K_{B(W)}(\alpha)+1) \frac{(X_O^2 + X_N^2)_W}{(X_O^2 + X_N^2)_{SW}}. \quad (9)$$

Now, the normal force $K_{B(W)}$ of a wing (with leading edge bend for instance) may be taken from the modified Lennertz theory or from experiment. The ratios X_{NW}/X_{NSW} and X_{OW}/X_{OSW} still must be calculated for a wing the "substitute wing" method can handle and which approximates in shape the wing with leading edge bend. In ref. 1, empirical relations for X_{NW}/X_{NSW} and X_{OW}/X_{OSW} are fitted to the results of the non-linear lifting surface theory for a family of wings tabulated in fig. 9. The empirical relations were used in eqs. 7-9 obtain the $K_{B(W)}$ by the dashed curve in fig. 3. The differences of $K_{B(W)}$ calculated with various procedures relying on the non-linear lifting surface theory are noticeable in figs. 3 and 11.

6. INTERFERENCE FACTORS BY THE VORTEX TRACING METHOD

Without comparable experimental data, the results of one or the other preceding method can be confirmed only by a more refined analysis. The procedure proposed here for this purpose links the non-linear three-dimensional lifting surface theory with the two-dimensional theory of slender wing-body configurations. This way, forces and moments non-linear with the angle-of-attack ($\alpha \leq 25^\circ$) due to the interference of body and body vortices on the wing, and of the wing on the body can be determined step by step proceeding in the direction of the longitudinal (X) axis of the configuration (fig. 12).

Two different wing vortex models convert the wing circulation into discrete free vortices whose paths are traced along the X-axis (fig. 12). The wing-body section shown

in fig. 13 is supposed to oscillate harmonically about a specified incidence α with low frequency and amplitude, i.e. with a quasisteady lateral pitching motion. The linear and non-linear parts of the circulation obtained with the lifting surface theory are integrated over the wing chord. These parts are converted separately into discrete vortices. The lateral position (Y) on the wing surface and strength of the vortices are estimated with the methods of Rossow and Williams (refs. 10, 11). Vortices with a core will result. Only the X-coordinate of the vortex origin must be suitably selected. One of the vortex models locates the origins or separation points of the vortices representing the non-linear part of the circulation on the leading edge. The "linear" vortices separate from the trailing edge as shown in fig. 14. The other model provides for a sectioning of the non-linear part of the pressure distribution according to the arrangement of panel elements on the wing planform. A discrete vortex is assigned to each pressure section using the method in ref. 12. Again, the origins of linear vortices are located on the trailing edge (fig. 15). After shedding, each vortex is treated as a free viscous vortex (ref. 11). The subsequent positions will be computed step by step from the local induced velocity at the vortex. The induced velocity is obtained with conformal mapping of vortices in the cross flow plane. The relations for the vortex path tracing are available from refs. 13 or 14. The satisfaction of the Kutta condition at each step may require an additional vortex, the strength of which will be selected to yield zero induced normal velocity in the mean at the wing surface. The strength of the additional vortex relative to the strength of the vortices determined from the wing circulation, is a criterium for the qualification of the assumed vortex model in simulating the wing circulation.

Slender body theory will be applied to determine force and moment distribution induced by the free vortices along the X-axis of the wing-body combination. The steady derivatives and corresponding K-factors follow from the vortices which are derived from the real part of the wing circulation as determined by the non-linear lifting surface theory. The quasisteady derivatives and corresponding K-factors are calculated by tracing the vortices obtained with the imaginary part of the wing circulation. The steady interference factor $K_B(w)$ will be obtained when in the lifting surface theory, the linear upwash distribution over the wing is constant and proportional to the incidence α . When the upwash distribution varies over X corresponding to the pitching velocity $q \cdot X$, the quasisteady factor $K_B(w)$ will be determined. When in addition the velocities induced by the free body vortices and the cross flow velocity about the body are taken into account in the wing upwash distribution, the sum of the factors $K_W + K_B(w)$ will result.

Results of steady aerodynamic coefficients determined with the procedure using the vortex model of fig. 14 are shown in figs. 3 and 17. The diagram of fig. 17 displays the non-linear part of the normal force distribution along the wing-body longitudinal axis. The geometry and flight condition of the configuration is given in fig. 3. Although a non-linear circulation increasing quadratically with the incidence is converted to yield the initial values of the discrete vortices emanating from the wing leading edge, the vortex lift induced on the wing-body combination has a higher than quadratical exponential dependence. This is seen by the distribution of fig. 17 and also from fig. 3 where the steady $K_B(w)$ -factors of the vortex tracing procedure are added. In the low angle-of-attack range ($\alpha < 10^\circ$), the normal force factor follows the results obtained with the "substitute wing method", but deviates to larger values for $\alpha > 10^\circ$. The non-linear $K_B(w)$ of the normal force by the vortex method is derived from fig. 17 the following way: The total non-linear part of the vortex normal force is integrated from the distribution. The linear part of the wing-body configuration is determined with the linear wing normal force multiplied by the linear factor $1 + K_B(w)$ according to Lennertz. The sum of the non-linear and linear wing-body normal force is diminished by the non-linear normal force of the wing alone and then divided by the latter.

7. CONCLUSION

Critical examination of the interference factors K_W and $K_B(w)$ leads to the following proposal for the improvement of the analytical results. Including in the analysis of K_W the effect of boundary layer growth along the forebody section on the distribution of upwash velocity over the wing, will positively affect the K_W values in comparison to experimental results. This correction will be decisive on the improvement of the analytical results of K_W . The arbitrary change of body vortex strength and the vortex positions in the cross flow plane by as much as $\pm 20\%$ had no noticeable effect on K_W . The substitution of the applied symmetrical vortex model of Jorgensen and Perkins (ref. 3) by either of the asymmetric models of Wardlaw (ref. 15) or Deffenbaugh and Koerner (ref. 16) may not alter the present results appreciably in the range of incidence ($\alpha \leq 20^\circ$) considered here. Thus, the additional effort encountered with the use of these models may not be awarded. However, this will change at angles-of-attack $\alpha > 20^\circ$. Most critical in the analysis of $K_B(w)$ (figs 3 and 11) is the assumption that the replacement of the cylindrical body between wing root chords by a rectangular middle section will provide the correct locations in X-direction of the pressure point and of the point of zero normal force damping. The proposed procedure based on vortex tracing which determines the normal force distribution along the longitudinal (X) axis of the wing-body combination will certainly yield more accurate results. Considering in fig. 16 the dashed curves which represent the steady normal force and pitching moment of the wing-body combination treated throughout this report, one will anticipate, that at least the proposed corrections of K_W reflect favourably on the values of the normal force, as they will lower them to better agreement with experimental data.

REFERENCES

1. C.P. Schneider, "Instationäre Beiwerte von Flugkörpern: Derivative der Längsstabilität von Flügel-Rumpf-Anordnungen mit hohen Anstellwinkeln in Unterschallströmung", 1978, MBB UA-420-78.
2. W.C. Pitts, J.N. Nielsen, G.E. Kaattari, "Lift and center of pressure of wing-body-tail combinations at subsonic, transonic, and supersonic speeds", 1957, NACA Rep. 1307.
3. L.H. Jorgensen, E.W. Perkins, "Investigation of some wake vortex characteristics of an inclined ogive-cylinder body at Mach number 2", 1959, NACA Rep. 1371.
4. C.P. Schneider, D. Nikolitsch, "Längsmomentenderivative von Flügeln bei hohen Anstellwinkeln in Unterschallströmung", 1976, BMVg-FBWT 76-26.
5. H. Esch, "Windkanalmessungen zum Einfluß der Rollage auf die Normalkraft eines Flugkörperleitwerks", 1975, DFVLR-Bericht No. IB 351-75/7.
6. H. Mathauer, S. Schultz, "Die Berechnung aerodynamischer Daten von Artillerie-Konfigurationen mit Hilfe eines Digitalprogramms und Vergleich der Ergebnisse mit Windkanaluntersuchungen", 1972, BMVg-FBWT 72-28.
7. J.N. Nielsen, "Nonlinearities in missile aerodynamics", 1978, AIAA Paper 78-20
8. J. Lennertz, "Beitrag zur theoretischen Behandlung des gegenseitigen Einflusses von Tragfläche und Rumpf", ZAMM, Bd. 7, Heft 4, 1927, pp.249-276.
9. H. Schlichting, E. Truckenbrodt, "Aerodynamik des Flugzeuges", Bd. 2, Kap. 7.3, Springer-Verlag, Berlin, Heidelberg, New York 1969.
10. V.J. Rossow, "On the inviscid rolled-up structure of lift-generated vortices", J. Aircraft, Vol. 10, No. 11, 1973, pp. 647-650.
11. G.M. Williams, "Viscous modelling of wing-generated trailing vortices", Aeronautical Quarterly, May 1974, pp. 143-153.
12. R.R. Clements, D.J. Maul, "The rolling up of a trailing vortex sheet", Aeronautical J., January 1973, pp.46-51.
13. A.H. Sacks, R.E. Lundberg, C.W. Hanson, "A theoretical investigation of the aerodynamics of slender wing-body combinations exhibiting leading-edge separation", 1967, NASA CR-719.
14. M.R. Mendenhall, J.N. Nielsen, "Effect of symmetrical vortex shedding on the longitudinal aerodynamic characteristics of wing-body-tail combinations", 1975, NASA CR-2473.
15. A.G. Wardlaw, "Prediction of normal force, pitching moment, and yawing force on bodies of revolution on angles of attack up to 50 degrees using a concentrated vortex flow-field model", 1973, NOLTR 73-209.
16. F.D. Deffenbaugh, W.G. Koerner, "Asymmetric vortex wake development on missiles at high angles of attack", J. Spacecraft, Vol. 14, No. 3, March 1977, pp. 155-162.

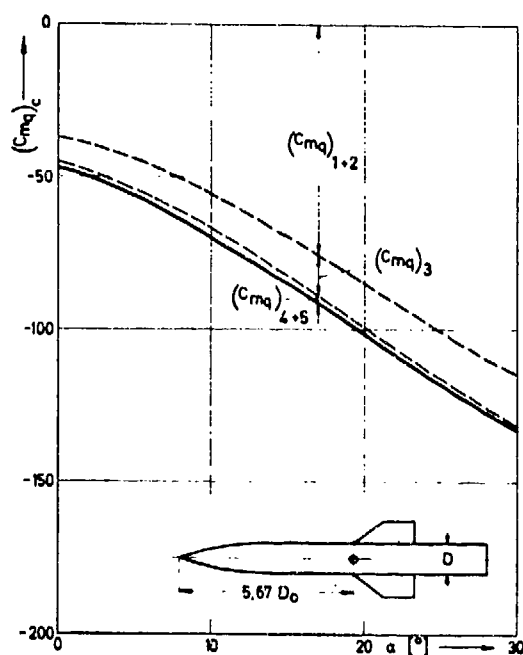


Fig. 1 Pitch damping of a wing-body configuration at $M=0.8$ as function of the angle-of-attack. Contributions of the body with laminar boundary layer $(Cmq)_{1+2}$, the wing $(Cmq)_3$ and the wing-body-interference $(Cmq)_{4+5}$

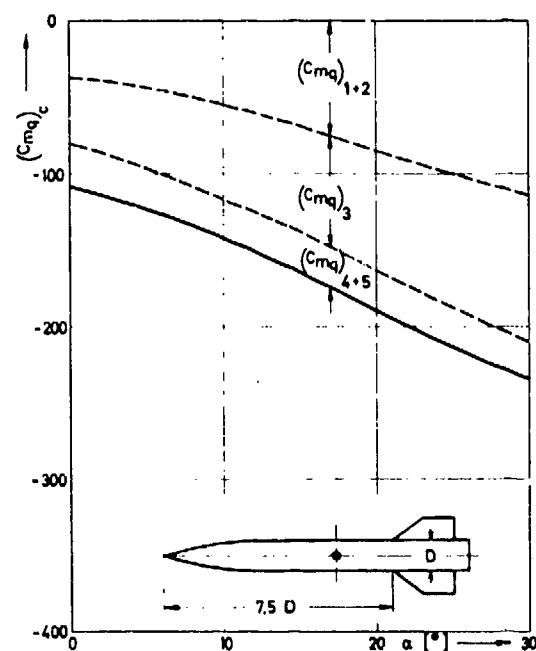


Fig. 2 Pitch damping of a wing-body configuration at $M=0.8$ as function of the angle-of-attack. Contributions of the body with laminar boundary layer $(Cmq)_{1+2}$, the wing $(Cmq)_3$ and the wing-body-interference $(Cmq)_{4+5}$

- ① ——— $K_{BW}(N_n)$, modified Lennertz theory
- ② ——— cylindrical body replaced by rectangular wing section
- ③ - - - - - empirical relations simulating ②
- ④ vortex separation, model fig. 14

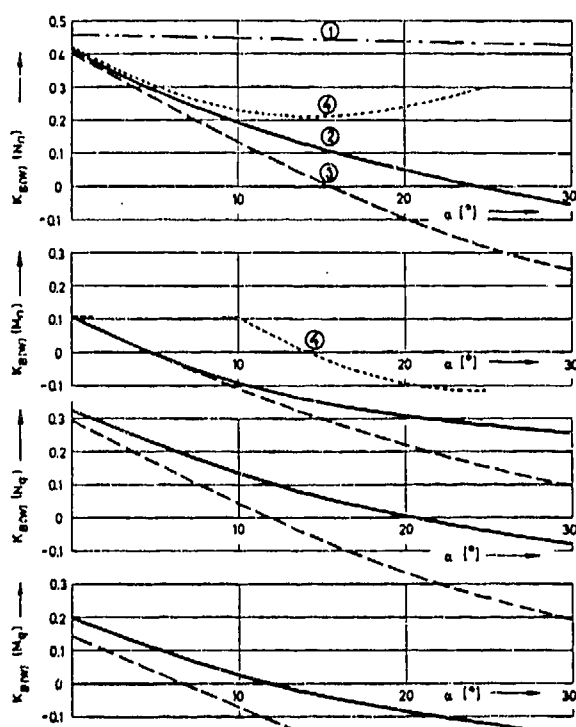


Fig. 3 Interference factors K_{BW} of the normal force slope N_n , pitch stiffness M_n , normal force damping N_q and pitch damping M_q of the wing-body config. of fig. 1: $M=0.8$, $\eta_R=0.4$, $\Lambda=1$, $\lambda=0.5$, $\psi_{LE}=53.13^\circ$

Experiment $M=0.5$, Esch

config.	l_c/D	l_w/D	ψ_{LE}	Λ	λ	η_R
A	4.8	6.63	63.4°	0.4	0.8575	0.5
B	9.8	11.63	63.4°	0.4	0.3575	0.5

Slender body theory; Pitts, Nielsen, Kaattari

—— $\eta_R = 0.5$

Non-linear lifting surface + symmetrical body vortices

—— configuration A

- - - - configuration B

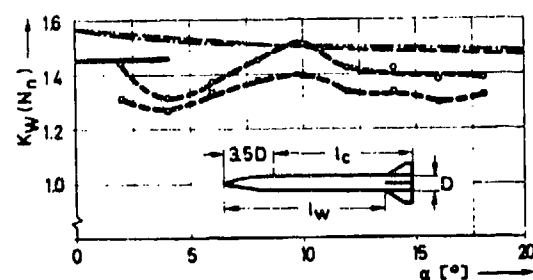


Fig. 4 Steady normal force interference factor $K_W(N_n)$ of a missile with cruciform fins in plus-position and with different body lengths. Comparison of theoretical and experimental results

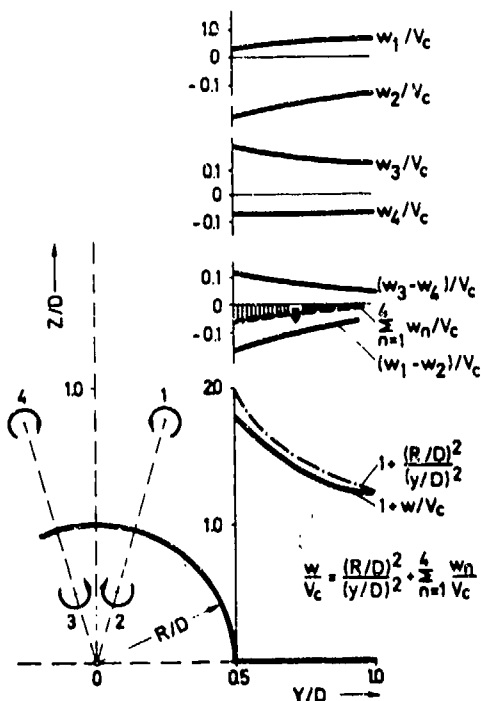


Fig. 5 Vortices and upwash velocity distribution in the cross-flow plane at the fin trailing edge of the config. of fig. 4 at $\alpha = 25^\circ$

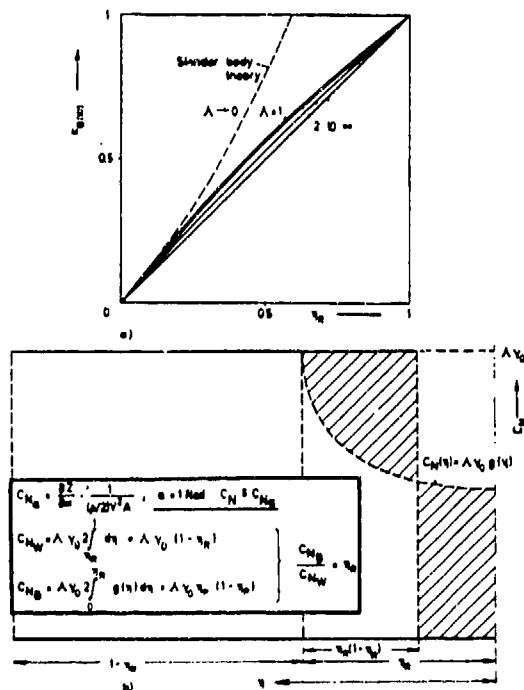


Fig. 7 Interference factor $K_B(W)$

- $K_B(W)$ for various wing aspect ratios as function of η_R (modified Lennertz theory)
- Normal force distribution of a rectangular wing-body configuration with $\Lambda = \infty$ and $\eta_R = 0.4$ (lin. Lennertz theory)

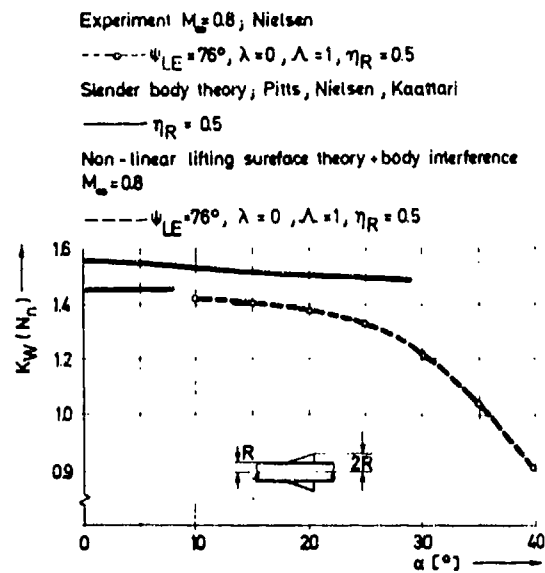


Fig. 6 Steady normal force interference factor $K_W(N_n)$ of a wing-body combination without nose. Comparison of theoretical and experimental results

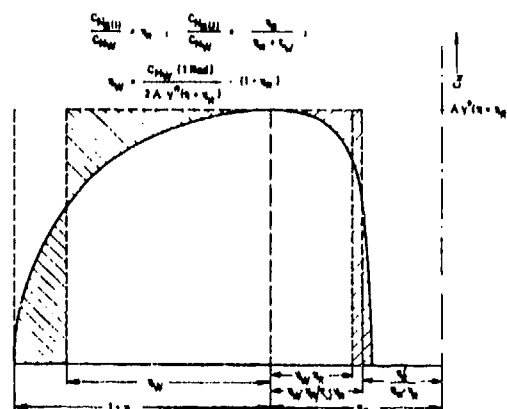


Fig. 8 Representation of the wing normal force $C_{Nw}/2$ by the area $\eta_w \cdot \eta_R \cdot \Lambda \cdot Y^H(\eta = \eta_R)$ and the body normal force $C_{N0}/2$ by the area $\eta_w \cdot \eta_R \cdot \Lambda \cdot Y^H(\eta = \eta_R)$ or $\eta_w \cdot \eta_R / (\eta_w + \eta_R) \cdot \Lambda \cdot Y^H(\eta = \eta_R)$. Rectangular wing-body config. $\eta_R = 0.4$, $\Lambda = 2$

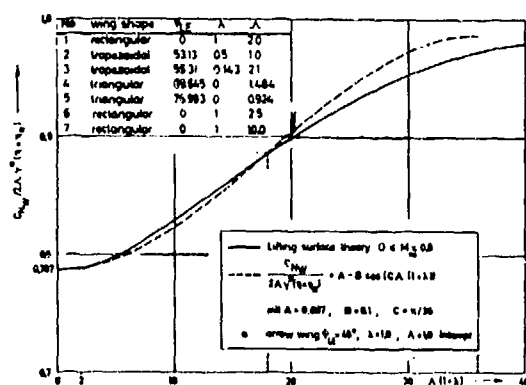


Fig. 9 Ratio of $C_{NW} / (2A^M(\eta = \eta_R))$ at $\alpha = 0^{\circ}$ for the tabulated wing shapes. Influence of taper ratio and leading edge sweep

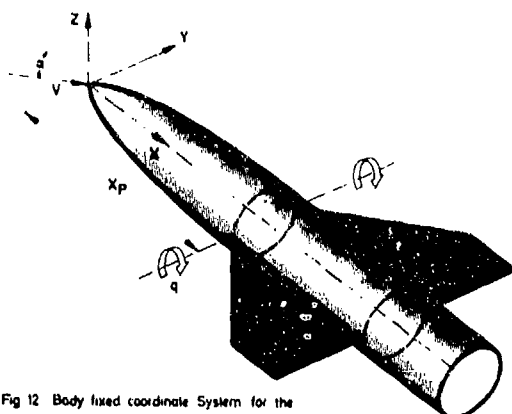


Fig. 12 Body fixed coordinate System for the determination of pitching derivatives

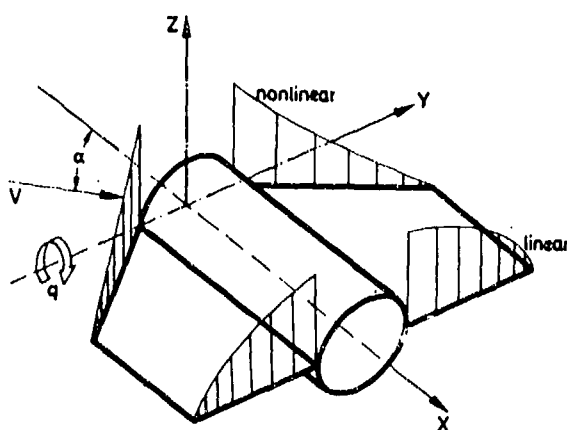


Fig. 13 Linear and non-linear circulation over the wing span

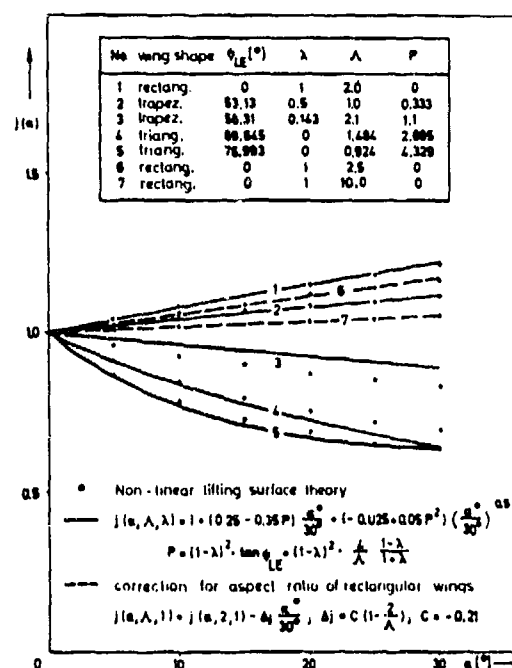


Fig. 10 Influence of the angle-of-attack on the ratio $C_{NW} / (2A^M(\eta = \eta_R))$ for the tabulated wing shapes

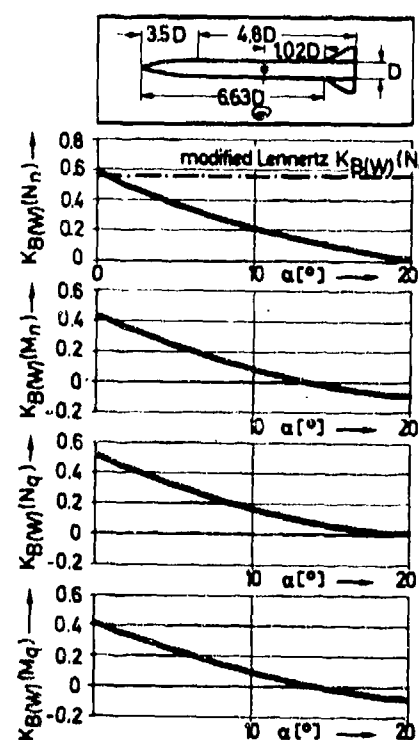


Fig. 11 Non-linear interference factor of a wing-body configuration at $M_{\infty} = 0.5$ with $\phi_{LE} = 83.4^{\circ}$, $\lambda = 0.4$, $\Lambda = 0.8575$ and $\eta_R = 0.5$

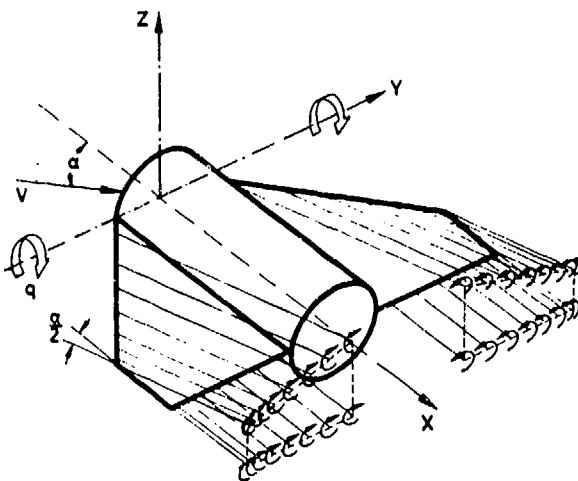


Fig. 14 Model of vortex separation from the wing leading and trailing edges

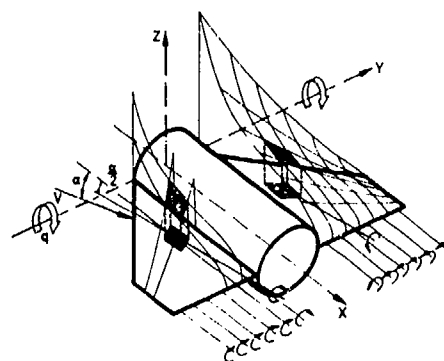


Fig. 15 Model of vortex separation from the wing surface and trailing edges

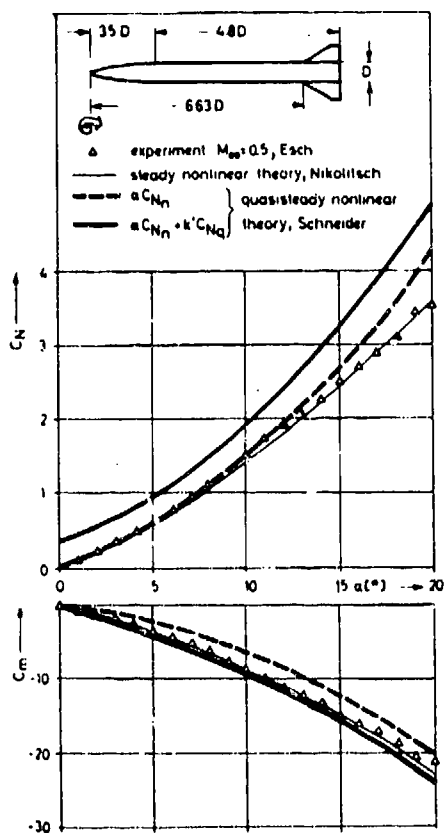


Fig. 16 Normal force and moment coefficients of a missile configuration with laminar body boundary layer, comparison of theoretical and experimental results, reduced frequency $k' = kD/l$ with $k = q/V = 0.05$

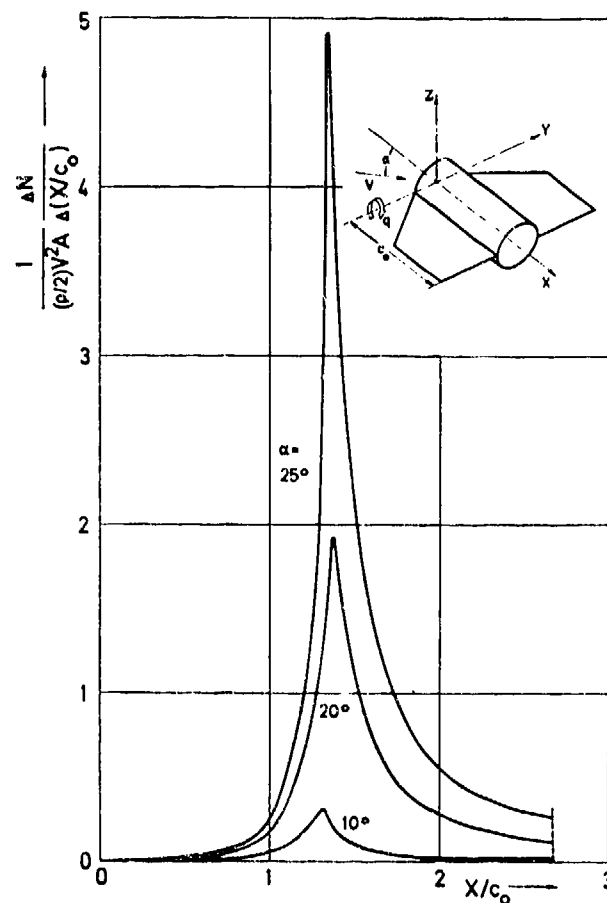


Fig. 17 Nonlinear part of the local lift along the wing-body longitudinal axis

PREDICTION OF AERODYNAMIC CHARACTERISTICS FOR SLENDER BODIES ALONE AND
WITH LIFTING SURFACES TO HIGH ANGLES OF ATTACK

Leland H. Jorgensen
Ames Research Center, NASA, Moffett Field, California 94035, U.S.A.

SUMMARY

An engineering-type method is presented for computing normal-force and pitching-moment coefficients for slender bodies of circular and noncircular cross section alone and with lifting surfaces. In this method, a semiempirical term representing viscous-separation crossflow is added to a term representing potential-theory crossflow.

For bodies of revolution, computed aerodynamic characteristics agree with measured results for investigated free-stream Mach numbers from 0.6 to 2.9 and for angles of attack (α) from 0° to 180°. For bodies of elliptic cross section, measured results are also predicted reasonably well over the investigated Mach number range from 0.6 to 2.0 and the α range from 0° to 60°. For all bodies the predictions are best at supersonic Mach numbers.

For body-wing and body-wing-tail configurations, measured normal-force coefficients and centers are predicted reasonably well at the upper test Mach number of 2.0. As the Mach number is decreased to 0.6, the agreement for the normal-force coefficients rapidly deteriorates.

When model flow-separation and vortex patterns are asymmetric, undesirable side forces are usually measured on the models at subsonic Mach numbers and zero sideslip angle. Generally, the side-force coefficients decrease or vanish with: increase in Mach number, decrease in nose fineness ratio, nose blunting, and flattening of body cross section (particularly the nose).

NOTATION

A	body cross-sectional area	x_A	body aftersection length
A_b	body base area (at $x = x_b$)	x_N	body nose length
A_p	planform area	M_n	Mach number component normal to body axis, $M_\infty \sin \alpha$
A_r	reference area (taken as A_b for the comparisons of computed with experimental results)	M_∞	free-stream Mach number
A_w	exposed wing planform area (two panels)	p	pressure
a, b	semimajor and semiminor axes of elliptic cross section	p_∞	free-stream static pressure
C_A	axial-force coefficient, $\frac{F_a}{q_\infty A_r}$	q_n	dynamic pressure component normal to body axis, $q_\infty \sin^2 \alpha$
C_{d_n}	crossflow drag coefficient of circular cylinder section, $\frac{F_n}{q_n (\Delta l_{cy}) d_{cy}}$	q_∞	free-stream dynamic pressure, $\frac{1}{2} \rho V_\infty^2$
C_m	pitching-moment coefficient about station at x_m from nose, $\frac{\text{pitching moment}}{q_\infty A_r x}$	r	body cross-section radius or corner radius
C_N	normal-force coefficient, $\frac{F_n}{q_\infty A_r}$	Re	free-stream Reynolds number, $\frac{\rho V_\infty x}{\mu}$
C_n	local normal-force coefficient per unit length	Re_n	Reynolds number component normal to body axis, $Re \frac{d}{x} \sin \alpha$
C_p	pressure coefficient, $\frac{p - p_\infty}{q_\infty}$	V	body volume
C_y	side-force coefficient, $\frac{F_y}{q_\infty A_r}$	V_n	velocity component normal to body axis, $V_\infty \sin \alpha$
d	body cross-section diameter	V_∞	free-stream velocity
F_a, F_n, F_y	axial, normal, and side force	w	body width
k	corner rounding for body cross section, $\frac{r}{w}$	x	reference length (generally taken as d for the comparisons of computed with experimental results)
	body length	x	axial distance from body nose
		x_{ac}	axial distance from body nose to normal-force aerodynamic center (center of pressure)
		x_c	axial distance from body nose to centroid of body planform area

x_m	axial distance from body nose to pitching-moment reference center	ρ	density of air
x_{sf}	axial distance from body nose to side-force aerodynamic center	ϕ	angle of roll about body longitudinal axis
α	angle of attack	Subscripts:	
β	angle of sideslip	b	body base
c	wing planform semiapex angle	cy	cylinder
n	crossflow drag proportionality factor (ratio of crossflow drag for a finite-length cylinder to that for an infinite-length cylinder)	Newt	Newtonian theory
μ	viscosity coefficient of air	nose	body nose
		o	equivalent circular body or cross section
		SB	slender-body theory
		stag	stagnation

1. INTRODUCTION

Over the last several years, high angle-of-attack aerodynamics has increased in importance because of the demand for greater maneuverability of space shuttle vehicles, missiles, and military aircraft (both manned and remotely piloted). Until recent years there has been a general lack of analytical methods and aerodynamic data suitable for use in the preliminary design of most advanced configurations for flight to high angles of attack over a wide range of Mach and Reynolds numbers. There has been, however, considerable research leading to the development of methods for predicting the static aerodynamic characteristics of simple shapes, primarily slender bodies of revolution.

Prior to the work of Allen in 1949 (Ref. 1), most analytical procedures for computing the aerodynamic characteristics of bodies were based on potential-flow theory, and their usefulness was limited to very low angles of attack. Allen proposed a method for predicting the static longitudinal forces and moments for bodies of revolution inclined to angles of attack considerably higher than those for which theories based only on potential-flow concepts are known to apply. In this method, a crossflow lift attributed to viscous-flow separation is added to the lift predicted by potential theory. This method has been used quite successfully to compute the aerodynamic coefficients of inclined bodies (e.g., Refs. 1-6), although most data available for study until 1961 were for bodies at angles of attack below about 20°, and the formulas were initially written to apply only over about this angle-of-attack range.

In 1961, Allen's concept was adapted by Jorgensen and Treon (Ref. 7) for computing the normal-force, axial-force, and pitching-moment coefficients for a rocket booster throughout the angle-of-attack range from 0° to 180°. Reasonable agreement of theory with experiment was obtained for a test model of the rocket booster over the Mach number range from 0.6 to 4. The Allen concept was further applied by Saffell, Howard, and Brooks (Ref. 8) in 1971 in a computer-programmed method for predicting the static longitudinal aerodynamic characteristics of low aspect-ratio missiles operating at angles up to 180°.

In 1958, a method for computing the aerodynamic characteristics for bodies of noncircular cross section was proposed by Jorgensen (Ref. 6). In this method, normal-force and pitching-moment coefficients (C_{N_0} and C_{m_0}) are computed by Allen's formulas for the equivalent body of revolution which has the same axial distribution of cross-sectional area as the noncircular body. Then the values of C_N and C_m for the noncircular body are computed from C_N/C_{N_0} and C_m/C_{m_0} ratios determined from apparent mass coefficients (i.e., from slender-body theory). Good agreement of theory with experiment (Ref. 6) was obtained by this procedure for bodies of elliptic cross section at the conditions investigated ($a/b = 1$ to 2, $\phi = 0^\circ$ and 90° , $M_\infty = 2$ to 4, and $\alpha = 0^\circ$ to 20°).

Early in 1973, the Allen concept was again applied by Jorgensen (Ref. 9) to further develop an engineering-type procedure for computing normal-force, axial-force, and pitching-moment coefficients for slender bodies of circular and noncircular cross sections at $\alpha = 0^\circ$ to 180° . The C_N and C_m formulas were written, however, for a body whose cross-sectional shape remains constant over the body length, but the cross-sectional area, of course, is allowed to vary.

In 1973, Jorgensen (Refs. 10 and 11) rewrote the C_N and C_m expressions to apply to the general case of a slender body alone or with lifting surfaces where the cross-sectional shape, as well as the cross-sectional area, is allowed to vary along the body length. For the special case of winged-elliptic cones, simplified expressions for C_N and C_m were also presented. Good agreement between predicted and experimental results was shown. However, experimental results available for comparison with the method were limited to simple elliptic bodies and winged-elliptic cones at angles of attack less than about 20° and at Mach numbers only from 2 to 4. Thus, it was concluded that additional comparisons for these and more diverse configurations were needed at higher angles of attack and at lower Mach numbers to determine validity limits for the method.

In 1972-73 there was a great need to enlarge the relatively small data base for bodies alone and in combination with wings and tails at subsonic, transonic, and supersonic Mach numbers. By 1976 this need was alleviated significantly by some introductory investigations into this high α field (e.g., Refs. 12-21). Most studies were initiated primarily for application to missile aerodynamics. Two recent studies, however, were more aircraft oriented in that they were directed toward the determination of

experimental aerodynamic characteristics for slender bodies with thin wings (Ref. 20) and with wings and a tail (Ref. 21).

In 1977, Jorgensen (Ref. 22) surveyed much of the recently obtained data in Refs. 12-21 and compared his predictive method with some experimental normal-force and normal-force center characteristics. Also included in the survey was a study of experimental side forces and yawing moments which have been shown to develop on models at high angle of attack even with zero sideslip ($\beta = 0^\circ$). These unwanted side forces and yawing moments, which probably lead to undesirable stall/spin characteristics, have been measured on noses alone, bodies alone, bodies with wings, and bodies with wings and a tail (e.g., Refs. 12-21).

In the present paper some of the most pertinent research findings of Ref. 22 are reviewed and updated. The prediction methodology of Jorgensen is first summarized. Then aerodynamic characteristics computed by the method are compared with measured characteristics for bodies of revolution, bodies of elliptic cross section, and bodies with thin wings alone and in combination with a tail. Following these comparisons, there is a discussion of recent data pertaining to the origin and alleviation of undesirable side forces and yawing moments associated with high α flight at $\beta = 0^\circ$. This discussion is based on measured side-force characteristics and some photographs, obtained with the oil-flow and vapor-screen techniques, that show the separation patterns and vortex flow fields over selected models.

2. PREDICTION METHODOLOGY

In this section the prediction methodology of Ref. 22 is summarized. Basic equations and empirical input values are presented.

2.1 Bodies of Revolution

In 1949, H. J. Allen (Ref. 1) proposed a heuristic concept for predicting the static longitudinal forces and moments for bodies of revolution inclined to angles of attack considerably higher than those for which theories based only on potential-flow concepts are known to apply. In this concept, a crossflow lift attributed to viscous crossflow separation is added to the crossflow lift predicted by potential-flow theory. For the potential-flow lift, Allen used the slender-body equation derived in 1923 by Max Munk for airship hulls (Ref. 23) and re-examined in 1949 by G. N. Ward (Ref. 24).

By using the Allen concept, Jorgensen (Ref. 22) wrote the following equations for normal-force and pitching-moment coefficients:

$$C_N = \frac{\sin 2\alpha \cos(\alpha/2)}{A_r} \int_0^l \frac{dA}{dx} dx + \frac{2nC_{d_n} \sin^2 \alpha}{A_r} \int_0^l r dx \quad (1)$$

and

$$C_m = \frac{\sin 2\alpha \cos(\alpha/2)}{A_r X} \int_0^l \frac{dA}{dx} (x_m - x) dx + \frac{2nC_{d_n} \sin^2 \alpha}{A_r X} \int_0^l r(x_m - x) dx \quad (2)$$

In each equation, the first term comes from slender-body theory, and the second term represents the viscous crossflow theory.

Integrated expressions for bodies of revolution at $\alpha = 0^\circ$ to 180° have been obtained from Eqs. (1) and (2). For the sign convention in sketch (a), page 4,

$$C_N = \frac{A_b}{A_r} \sin 2\alpha' \cos \frac{\alpha'}{2} + nC_{d_n} \frac{A_p}{A_r} \sin^2 \alpha'; \quad 0^\circ \leq \alpha \leq 180^\circ \quad (3)$$

$$C_m = \left[\frac{V - A_b(l - x_m)}{A_r X} \right] \sin 2\alpha' \cos \frac{\alpha'}{2} + nC_{d_n} \frac{A_p}{A_r} \left(\frac{x_m - x_c}{X} \right) \sin^2 \alpha'; \quad 0^\circ \leq \alpha \leq 90^\circ \quad (4)$$

and

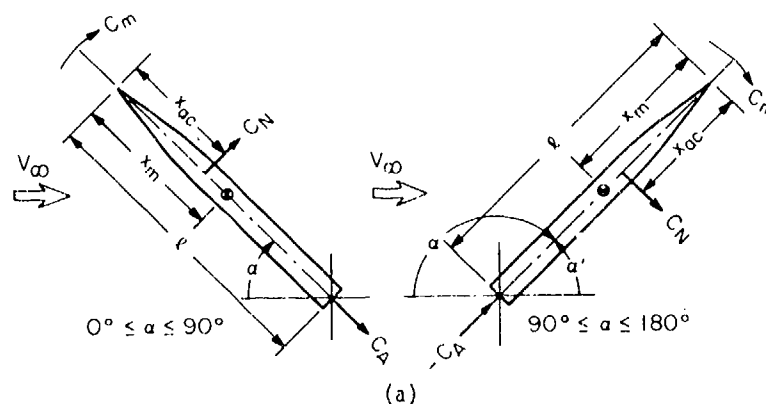
$$C_m = - \left(\frac{V - A_b x_m}{A_r X} \right) \sin 2\alpha' \cos \frac{\alpha'}{2} + nC_{d_n} \frac{A_p}{A_r} \left(\frac{x_m - x_c}{X} \right) \sin^2 \alpha'; \quad 90^\circ \leq \alpha \leq 180^\circ \quad (5)$$

where A_b is the body base area; A_p is the planform area; V is the body volume; x_c is the distance from the nose apex to the centroid of planform area; and $\alpha' = \alpha$ for $0^\circ \leq \alpha \leq 90^\circ$ and $\alpha' = 180^\circ - \alpha$ for $90^\circ \leq \alpha \leq 180^\circ$.

The axial distance from the nose apex to the normal-force aerodynamic center is then given by

$$x_{ac} = \left(\frac{x_m}{X} - \frac{C_m}{C_N} \right) X \quad (6)$$

In the viscous crossflow terms for C_N and C_m , C_{d_n} is the steady-state crossflow (or normal) drag coefficient for a two-dimensional circular cylinder. C_{d_n} is a function of both the Mach number and Reynolds number components normal to the body longitudinal axis.



Because of spillage flow around the ends of a finite length cylinder, the value of C_{d_n} is less than that for an infinitely long (truly two-dimensional) cylinder in the same free stream. Thus, C_{d_n} is multiplied by a proportionality factor η , which is the ratio of C_{d_n} for a finite length cylinder to that for an infinite length cylinder. This factor η , which approaches unity as the cylinder length to diameter approaches infinity, is given from experimental results (discussed later). In the practical use of η , it is assumed that the ℓ/d of the cylinder is the same as that for the body of revolution being considered. It is also assumed that the net-force effect of the front and rear end flows is approximately the same for both configurations.

2.2 Bodies of Circular and Noncircular Cross Section Alone and With Lifting Surfaces

For the general case of a body alone or with lifting surfaces where the cross-sectional shape can vary along the body length, both the potential and viscous separation crossflow terms for C_N and C_m have been written (Ref. 22) in integral form as follows:

$$C_N = \frac{\sin 2\alpha \cos(\alpha/2)}{A_r} \int_0^\ell \left(\frac{C_n}{C_{n_0}} \right)_{SB} \frac{dA}{dx} dx + \frac{2\eta C_{d_n} \sin^2 \alpha}{A_r} \int_0^\ell \left(\frac{C_n}{C_{n_0}} \right)_{Newt} r dx \quad (7)$$

and

$$C_m = \frac{\sin 2\alpha \cos(\alpha/2)}{A_r X} \int_0^\ell \left(\frac{C_n}{C_{n_0}} \right)_{SB} \frac{dA}{dx} (x_m - x) dx + \frac{2\eta C_{d_n} \sin^2 \alpha}{A_r X} \int_0^\ell \left(\frac{C_n}{C_{n_0}} \right)_{Newt} r (x_m - x) dx \quad (8)$$

In Eqs. (7) and (8), the first terms (from slender-body theory) are not applicable, as written, for winged-body sections where the dA/dx values are zero or negative, and procedures similar to those suggested in Ref. 25 probably should be used. Further adaptation of this method for use with body-wing and body-wing-tail configurations is considered in Sec. 5.

In each equation, the potential crossflow term is generalized by multiplying the value within the integral by the ratio $(C_n/C_{n_0})_{SB}$ — the ratio of the local normal-force coefficient per unit length C_n for the desired cross-sectional shape to the similar coefficient C_{n_0} for the equivalent circular shape having the same cross-sectional area. The necessary ratios can be determined from apparent mass coefficients (slender-body theory) for many cross-sectional shapes.

In each equation, the viscous crossflow term is generalized by multiplying the value within the integral by the ratio $(C_n/C_{n_0})_{Newt}$. Here the local ratio of C_n to C_{n_0} at each station is assumed to be given by Newtonian impact theory; C_{d_n} remains as the crossflow drag coefficient for the equivalent circular cylinder section.

In the second term of Eqs. (7) and (8), there is some experimental justification for formulating the ratio (C_n/C_{n_0}) from Newtonian theory and multiplying it by the available experimental or theoretical crossflow drag coefficient for the equivalent circular cross section C_{d_n} . For subcritical crossflow Mach and Reynolds numbers, Jorgensen (Ref. 11) has shown that C_n/C_{n_0} values from Newtonian theory agree reasonably well (but somewhat fortuitously) with those from two-dimensional tests (Refs. 26-30) of elliptic cross sections and square cross sections with rounded corners. Jorgensen's comparisons are shown in Table 1. Good agreement also can be expected at high supersonic and hypersonic crossflow Mach numbers where Newtonian theory by definition should be most applicable. The most doubtful regimes include the transonic crossflow Mach number regime and the supercritical crossflow Reynolds number regime. (These regimes are discussed further for circular cross sections in the following section.)

Where reliable experimental crossflow drag data exist for a desired noncircular cross section, these data, of course, can be used. Then the values of C_{d_n} for the particular cross sections can be substituted in Eqs. (7) and (8) in lieu of the product $C_{d_n}(C_n/C_{n_0})_{Newt}$, where C_{d_n} as now written is for a

circular cross section only. Of course, if the shape of the noncircular cross section varies along the body length, values of C_{d_n} must be substituted within the integral in the second term of Eqs. (7) and (8), and a great deal of empirical input data may be necessary for some configurations.

For the case of a body with the same cross-sectional shape along the body length, Eqs. (7) and (8) reduce to

$$C_N = \left(\frac{A_b}{A_r} \sin 2\alpha \cos \frac{\alpha}{2} \right) \left(\frac{C_N}{C_{N_0}} \right)_{SB} + \left(n C_{d_n} \frac{A_p}{A_r} \sin^2 \alpha \right) \left(\frac{C_N}{C_{N_0}} \right)_{Newt} \quad (9)$$

and

$$C_m = \left[\frac{V - A_b \left(\frac{x}{X} - x_m \right)}{A_r X} \right] \left(\sin 2\alpha \cos \frac{\alpha}{2} \right) \left(\frac{C_m}{C_{m_0}} \right)_{SB} + \left[n C_{d_n} \frac{A_p}{A_r} \left(\frac{x_m - x_c}{X} \right) \sin^2 \alpha \right] \left(\frac{C_m}{C_{m_0}} \right)_{Newt} \quad (10)$$

where

$$\left(\frac{C_N}{C_{N_0}} \right)_{SB} = \left(\frac{C_m}{C_{m_0}} \right)_{SB} = \left(\frac{C_n}{C_{n_0}} \right)_{SB}$$

$$\left(\frac{C_N}{C_{N_0}} \right)_{Newt} = \left(\frac{C_m}{C_{m_0}} \right)_{Newt} = \left(\frac{C_n}{C_{n_0}} \right)_{Newt}$$

These equations are applicable for values of α from 0° to 90° . For α from 90° to 180° , they can be rewritten in the form of Eqs. (3)-(5).

2.3 Empirical Input Values

2.3.1 Crossflow drag coefficient

To compute C_N and C_m from the equations presented in the previous sections, values of crossflow drag coefficient C_{d_n} are needed for an "infinite length" or truly two-dimensional circular cylinder placed normal to an airstream. As previously mentioned, C_{d_n} is a function of both the Mach number and Reynolds number components normal to the cylinder longitudinal axis, and hence for a configuration at angle of attack, it is a function of $M_n = M_\infty \sin \alpha$ and $Re_n = Re \sin \alpha$. M_n is commonly called the cross-flow Mach number and Re_n , the crossflow Reynolds number. For circular cylinders, necessary "state-of-the-knowledge" plots have been prepared for the variation of C_{d_n} with M_n and Re_n (Figs. 1-3).

In Fig. 1 is shown the variation of C_{d_n} with M_n over the M_n range from 0 to 8. Figure 1 was prepared from the data of Refs. 31 through 36 and from data for transonic Mach numbers obtained recently by Macha in the Ames 2- by 2-Foot Transonic Wind Tunnel (Ref. 37). Also shown for reference are the theoretical variations predicted from Newtonian and modified Newtonian theories. Because of the close agreement of the Newtonian values with experiment at the higher Mach numbers, it is not surprising that computer programs utilizing Newtonian theories have been used successfully to predict space-shuttle-booster results in wind tunnels at hypersonic Mach numbers (see, e.g., Ref. 38). Except for the transonic range, where data are questionable, the variation of C_{d_n} with M_n is well documented in Fig. 1.

In the transonic range, the black symbols in Fig. 1 represent values of C_{d_n} obtained recently (Ref. 37) from pressure-distribution tests of circular cylinders of various diameters (1.9 to 5.1 cm) at crossflow Reynolds numbers from about 1.3×10^5 to 4.9×10^5 . Many values of C_{d_n} were initially computed from the extensive pressure distributions measured by Macha on the cylinders in the Ames 2- by 2-Foot Transonic Wind Tunnel. Because there was a general increase in C_{d_n} with decrease in cylinder diameter d (but not Re_n) for M_n values from about 0.9 to 1.2, plots of C_{d_n} vs d were constructed, and values of C_{d_n} were obtained by extrapolating the curves to $d = 0$. The black symbols in Fig. 1 represent these extrapolated values of C_{d_n} , values that should come closest to representing data for no interference between the models and the wind tunnel. These data agree well with the rocket flight-test results obtained in 1953 by Welsh (Ref. 36), but these or similar-sized models should be tested further in a larger transonic wind tunnel.

As shown in Fig. 1, there is a critical crossflow Reynolds number effect that can drastically lower the values of C_{d_n} at M_n below about 0.5. For M_n less than about 0.5, if the crossflow Reynolds number Re_n exceeds the critical value of about 2×10^5 , the value of C_{d_n} decreases considerably. This variation is shown in greater detail in Figs. 2 and 3.

In Fig. 2 the variation of C_{d_n} with Re_n for M_n less than about 0.4 is presented. It has been well documented over the last 60 years (e.g., Refs. 26, 30, 32, 39) that $C_{d_n} \approx 1.2$ for laminar boundary-layer flow and separation just before the critical Reynolds number of about $Re_n = 2 \times 10^5$. At about $Re_n = 5 \times 10^5$ there is evidence (e.g., Refs. 40-42) of laminar boundary-layer flow around the front of the cylinder to an angular position of about 60° or 90° , where the flow separates, undergoes transition, and reattaches at an angular position of about 110° to form a laminar separation bubble. Then the

turbulent flow separates at some position downstream (an angular location of about 130°). With a further increase in Reynolds number into the supercritical regime, the bubble decreases in size until the transition to turbulent flow moves upstream of the location of laminar separation, and the bubble disappears (Ref. 42). From the low C_{d_n} value between about 0.15 and 0.30, C_{d_n} increases gradually, at least for an increase in Re_n up to about 5×10^6 . Over the supercritical Reynolds number regime there is still considerable uncertainty in the magnitude and trend of C_{d_n} with Re_n and M_n . The shading in Fig. 2 indicates the approximate spread or uncertainty in C_{d_n} based on known data.

Jones, Cincotta, and Walker (Ref. 42) probably have made the most detailed study of circular cylinders in supercritical flow. With the use of freon gas to obtain high Re_n , they have shown that there is an effect of M_n on the variation of C_{d_n} with Re_n . Figure 3 (taken from Ref. 42) summarizes their C_{d_n} results for $M_n = 0.25$ to 0.50 . The reader is referred to Ref. 42 for their interpretation of these C_{d_n} results based on pressure-distribution and visual-flow studies.

2.3.2 Crossflow drag proportionality factor

In the equations used to compute C_N and C_m , η is the crossflow drag proportionality factor, that is, the ratio of the crossflow drag coefficient for a finite-length cylinder to that for an infinite-length cylinder. Cylinder drag coefficients from which values of η can be determined have been measured (to the author's knowledge) only at very low subsonic Mach numbers (Refs. 43 and 44).

Values of η for circular cylinders at very low crossflow Mach numbers (from Ref. 43) are plotted as a function of length/diameter in Fig. 4. Values of η for flat plates are also plotted, but as a function of plate length/width. The values for the flat plates are only slightly less than those for the circular cylinders. Thus, it is likely that Fig. 4 can be used to estimate values of η for many cross sections varying from circular to flat. However, these values may be acceptable only for very low crossflow Mach numbers.

An indication of the variation of η with crossflow Mach number M_n can be obtained by computing values of η from high- α C_N data (Ref. 16) for slender bodies of revolution. From Eq. (3),

$$\eta C_{d_n} = \frac{C_N - \sin 2\alpha \cos(\alpha/2)(A_b/A_r)}{(A_p/A_r) \sin^2 \alpha} \quad (11)$$

For two bodies of fineness ratio 10 and 12 (sketched in Fig. 5), the variation of ηC_{d_n} with M_n (for $M_n = 0.4$ to 1.6) has been computed from Eq. (11) with the use of C_N data for values of α from about 45° to 60° . As shown in Fig. 5, the results for the two bodies agree closely. Now with the variation of C_{d_n} with M_n in Fig. 1 and the variation of ηC_{d_n} with M_n in Fig. 5, the variation of η with M_n has been computed and the results plotted in Fig. 6. (The circular symbols denote the computed values over the M_n range from 0.4 to 1.6 ; the square and diamond symbols represent values of η for very low crossflow Mach numbers obtained from Fig. 4.)

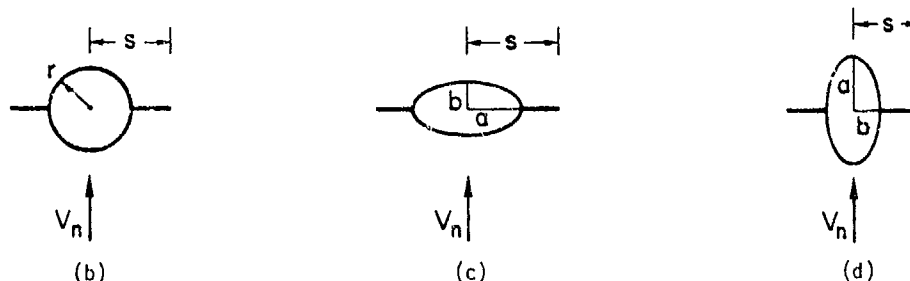
For most supersonic and hypersonic values of M_n , η probably can be assumed to be unity, an assumption indicated as being essentially correct from past investigations (e.g., Refs. 3, 6, 7, and 9). The greatest uncertainty appears to be within the transonic M_n range, and here further research is desirable. In this study, however, Figs. 5 and 6 are used in lieu of better information.

2.4 Formulas of $(C_n/C_{n_0})_{SB}$ and $(C_n/C_{n_0})_{Newt}$ for Winged-Circular and Winged-Elliptic Cross Sections

To use Eqs. (7)-(10) for computing C_N and C_m , ratios of the section normal-force coefficients (C_n) to those for the equivalent circular sections (C_{n_0}) must be determined. Formulas of $(C_n/C_{n_0})_{SB}$ and $(C_n/C_{n_0})_{Newt}$ are presented for winged-circular and winged-elliptic cross sections (with zero-thickness wings assumed). Similar results have been derived for winged-square cross sections with rounded corners (Ref. 22), but they are not presented in this paper.

2.4.1 Formulas of $(C_n/C_{n_0})_{SB}$

From slender-body theory (e.g., Refs. 45-48), $(C_n/C_{n_0})_{SB}$ expressions have been determined (Ref. 11) for winged-circular and winged-elliptic cross sections (see sketches (b), (c), and (d)).



For a winged-circular cross section with the wing planform perpendicular to the crossflow velocity V_n (sketch (b)),

$$\left(\frac{C_n}{C_{n0}}\right)_{SB} = \frac{s^2}{r^2} + \frac{r^2}{s^2} - 1 \quad (12)$$

For a winged-elliptic cross section with the semimajor axis a and wing planform perpendicular to the crossflow velocity V_n (sketch (c)),

$$\left(\frac{C_n}{C_{n0}}\right)_{SB} = \frac{1}{ab} (k_1^2 + a^2) \quad (13)$$

where

$$k_1 = \sigma_1 - \frac{(a+b)^2}{4\sigma_1}$$

$$\sigma_1 = \frac{1}{2} (s + \sqrt{s^2 + b^2 - a^2})$$

For a winged-elliptic cross section with the semiminor axis b and wing planform perpendicular to the crossflow velocity V_n (sketch (d)),

$$\left(\frac{C_n}{C_{n0}}\right)_{SB} = \frac{1}{ab} (k_2^2 + b^2) \quad (14)$$

where

$$k_2 = \sigma_2 - \frac{(a+b)^2}{4\sigma_2}$$

$$\sigma_2 = \frac{1}{2} (s + \sqrt{s^2 + a^2 - b^2})$$

For an elliptic cross section without a wing (e.g., Ref. 24),

$$\left(\frac{C_n}{C_{n0}}\right)_{SB} = \frac{a}{b} \cos^2 \phi + \frac{b}{a} \sin^2 \phi \quad (15)$$

where ϕ is the angle of roll about the body longitudinal axis, being 0° with the semimajor axis a perpendicular to the crossflow velocity and 90° with the semiminor axis b perpendicular to the crossflow velocity.

2.4.2 Formulas of $(C_n/C_{n0})_{\text{Newt}}$

From Newtonian impact theory, $(C_n/C_{n0})_{\text{Newt}}$ expressions also have been derived for winged-circular and winged-elliptic cross sections (Ref. 22).

For a winged-circular cross section with the wing planform perpendicular to the crossflow velocity V_n (sketch (b)),

$$\left(\frac{C_n}{C_{n0}}\right)_{\text{Newt}} = \frac{3}{2} \left(\frac{s}{r} - \frac{1}{3}\right) \quad (16)$$

For a winged-elliptic cross section with the semimajor axis a and wing planform perpendicular to the crossflow velocity V_n (sketch (c)),

$$\left(\frac{C_n}{C_{n0}}\right)_{\text{Newt}} = \frac{3}{2} \sqrt{\frac{a}{b}} \left\{ \frac{-b^2/a^2}{[1 - (b^2/a^2)]^{3/2}} \log \left[\frac{a}{b} \left(1 + \sqrt{1 - \frac{b^2}{a^2}} \right) \right] + \frac{1}{1 - (b^2/a^2)} + \frac{s}{a} - 1 \right\} \quad (17)$$

For a winged-elliptic cross section with the semiminor axis b and wing planform perpendicular to the crossflow velocity V_n (sketch (d)),

$$\left(\frac{C_n}{C_{n0}}\right)_{\text{Newt}} = \frac{3}{2} \sqrt{\frac{b}{a}} \left\{ \frac{a^2/b^2}{[(a^2/b^2) - 1]^{3/2}} \tan^{-1} \left(\sqrt{\frac{a^2}{b^2} - 1} \right) - \frac{1}{(a^2/b^2) - 1} + \frac{s}{b} - 1 \right\} \quad (18)$$

2.5 Relative Influence of Crossflow Terms

It is interesting to examine briefly the relative influence of the potential and viscous crossflow terms in the equations for C_N and C_M . For demonstration, Jorgensen (Ref. 9) compared the magnitudes of the terms for an ogive-cylinder body of fineness ratio 11 ($x_N/d = 5$) at $\alpha = 0^\circ$ to 180° and $M_\infty = 2.9$. The computed values (by Eqs. (3)-(5)) are presented in Fig. 7. For this body, the viscous crossflow term contributes most of the normal force at high values of α and, of course, all of the normal force at

$\alpha = 90^\circ$. Although the slender-body potential term contributes relatively little to C_N at high α , it has a significant influence on C_m .

The results in Fig. 7 are indicative of those computed for most slender bodies (Ref. 22). However, as shown in Sec. 5, the relative contributions of the crossflow terms can be modified considerably with the addition of thin lifting surfaces (wings and tails) to a body.

3. METHOD APPLIED TO BODIES OF REVOLUTION

In recent years, there has been increased interest in the basic aerodynamics of slender bodies of revolution because of emphasis on achieving more maneuverability from missiles. Some designs that use thrust-vector control systems have been considered for missile flight at angles of attack ranging from 0° to 180° (e.g., Refs. 13, 15, and 49).

The basic prediction method of Sec. 2 has been used recently to adequately predict the longitudinal aerodynamic characteristics of various bodies of revolution at Mach numbers from 0.6 to 3.0 and angles of attack from 0° to 180° (e.g., Refs. 9, 22, 49-51). In this section, some selected results from Ref. 22 are presented for cone-cylinder and ogive-cylinder bodies at $M_\infty = 2.9$ and for ogive-cylinder bodies at $M_\infty = 0.6$ to 2.0.

3.1 Cone-Cylinder and Ogive-Cylinder Bodies at $M_\infty = 2.9$

Longitudinal aerodynamic coefficients were measured by Jernell (Ref. 52) for a series of three cone-cylinder and four ogive-cylinder bodies, the dimensions of which are given in Fig. 8. All bodies were tested at α from -5° to 180° for $M_\infty = 2.9$ and $Re = 1.25 \times 10^5$ based on body diameter.

As shown in Figs. 9 to 12, computed values of C_N and C_m as a function of α agree rather closely with the experimental results for the seven bodies. Estimated values of C_A , however, do not agree as well. In this study, the values of C_A were merely estimated by

$$C_A \approx C_{A_{\alpha=0^\circ}} \cos^2 \alpha; \quad 0^\circ \leq \alpha \leq 90^\circ$$

and

$$C_A \approx C_{A_{\alpha=180^\circ}} \cos^2 \alpha; \quad 90^\circ \leq \alpha \leq 180^\circ$$

Here $\cos^2 \alpha$ is the ratio of the dynamic pressure in the axial direction to the dynamic pressure in the free-stream direction. Values of $C_{A_{\alpha=0^\circ}}$ and $C_{A_{\alpha=180^\circ}}$ were computed in Ref. 9 for the assumption of turbulent boundary-layer flow, and these values include the contributions of fore pressure, base pressure, and turbulent skin friction.

It is satisfying to find that effects of afterbody fineness ratio, nose fineness ratio, and nose shape on C_N and C_m are predicted so well. In Fig. 9 is shown the effect of afterbody fineness ratio for cone-cylinder bodies, all with fineness-ratio-3 conical noses. Likewise, in Fig. 10 is shown the effect of afterbody fineness ratio for ogive-cylinder bodies, all with fineness-ratio-5 ogival noses. In Fig. 11 the effect of nose fineness ratio for ogive-cylinder bodies is shown, and in Fig. 12 is shown the minor effect of change in nose shape from conical to ogival for a given nose fineness ratio of 3.

3.2 Ogive-Cylinder Bodies at $M_\infty = 0.6$ to 2.0

The four ogive-cylinder bodies sketched in Fig. 13 were tested in the NASA-Ames 6- by 6-Foot Wind Tunnel at α from 0° to 60° and $M_\infty = 0.6, 0.9, 1.2$, and 2.0 (Refs. 16 and 22). The bodies include nose fineness ratios of 2.5 and 3.5 (noses N_7 and N_2), aftersection fineness ratios of 7, 9, and 11 (aftersections C_1 , C_2 , and C_3), and overall fineness ratios of 9.5 (N_7C_1), 10.5 (N_2C_1), 12.5 ($N_2C_1C_2$), and 13.5 ($N_7C_1C_3$). In this paper, computed values of C_N and normal-force aerodynamic center (measured forward of each body base in terms of diameter) are compared with measured results for bodies N_2C_1 and $N_7C_1C_3$. All bodies, however, are considered in Ref. 22.

In Fig. 14, it is seen that the effect of Mach number on the variation of C_N with α is predicted closely for body N_2C_1 ($\ell/d = 10.5$). The normal-force centers, $(\ell - x_{ac})/d$, are predicted closely at $M_\infty = 2.0$, but with decrease in M_∞ the predicted values tend to lie somewhat rearward of the measured values.

Similar results are shown in Fig. 15 for the longest body, $N_7C_1C_3$ ($\ell/d = 13.5$), but the results for each Mach number are shown on separate plots to facilitate comparison of computed with measured characteristics. As for the shorter body N_2C_1 , the variation of C_N with α is predicted closely throughout the Mach number range. Again, however, the normal-force aerodynamic centers are predicted best at $M_\infty = 2.0$.

4. METHOD APPLIED TO BODIES OF ELLIPTIC CROSS SECTION

Although not as extensively confirmed as for bodies of revolution, the prediction method has been used to adequately predict the longitudinal aerodynamic characteristics for several bodies of elliptic cross section. In 1973, the method was used to predict the characteristics for elliptic bodies of $a/b = 2$ and fineness ratio 6 and 10, but the α range of available data extended only from 0° to 20° (Ref. 11). In 1975, aerodynamic data were obtained for several elliptic bodies of fineness ratio 10 tested at $M_\infty = 0.6$ to 2.0 and over the more extended α range from 0° to 60° (Ref. 18). Recently, computed characteristics have been compared with these data (Ref. 22); in this section some of these comparisons are reviewed.

In Figure 16 is shown the planform and end views of the two bodies considered here. The basic circular body B_1 consists of a circular-arc tangent-ogive nose of fineness ratio 3 followed by a cylindrical aftersection of fineness ratio 7. Body B_2 has the same length and axial distribution of cross-sectional area as B_1 , but the ratio of the semimajor to the semiminor cross-sectional axis is $a/b = 2$ at all positions along the body length. The fineness ratio of $\ell/d = 10$ for B_1 is also the equivalent fineness ratio for B_2 . As shown in Fig. 16, body B_2 was tested both at $\phi = 0^\circ$ (flattest side pitching against the flow) and $\phi = 90^\circ$ (thinnest side pitching against the flow).

The bodies were tested over the α range of 0° to 60° in the Ames 6- by 6-Foot Wind Tunnel. For the data used here, the Reynolds numbers, based on base diameter, are 6.5×10^5 at $M_\infty = 0.6$ and 0.9 and 3.8×10^5 at $M_\infty = 1.2, 1.5$, and 2.0 .

In Fig. 17, computed values of C_N and normal-force aerodynamic center $(\ell - x_{ac})/d$ vs α are compared with measured values. In general, there is reasonably good agreement. The agreement is, however, better at the higher supersonic Mach numbers ($M_\infty = 1.5$ and 2.0) than at the subsonic Mach numbers ($M_\infty = 0.6$ and 0.9). These comparisons, along with previous successful comparisons in Sec. 3, tend to validate the prediction method as a useful tool in body aerodynamic studies, at least for bodies with circular and elliptic cross sections of constant a/b .

5. METHOD APPLIED TO BODY-WING AND BODY-WING-TAIL CONFIGURATIONS

Obviously it is more difficult to predict the aerodynamic characteristics for body-wing and body-wing-tail configurations than for bodies alone. In this section, the prediction methodology of Sec. 2 is modified for use in computing estimates of C_N and C_m for these more complicated configurations. Then, predicted values of C_N and normal-force center $(\ell - x_{ac})/d$ are compared with measured values for some sample configurations selected from the many configurations in Refs. 20 and 21.

5.1 Methodology Used to Compute C_N and C_m

In Sec. 2, the first terms of Eqs. (7) and (8) represent the C_N and C_m values from slender-body potential-flow theory. The first terms are not applicable, as written, for body-wing shapes where the body dA/dx values are zero or negative. Also, for body-wing and body-wing-tail configurations, more comprehensive methods from potential theory are available.

For this study, the first-term (potential-flow) contributions to C_N and C_m were computed from the linear method presented in Ref. 25. This method, referred to as the N-K-P method (for Nielsen, Kaattari, and Pitts), is restricted to bodies of circular cross section with wings and tails that do not have swept-forward leading edges or swept-back trailing edges. It is further restricted to low angles of attack and low angles of wing and tail incidence in which the forces are linear with angle. To obtain the wing-body interference, certain factors are defined that are the ratios of the lift on the components in combination to the lift on the wing alone. These ratios are obtained primarily from slender-body theory, but the wing lift is obtained from linear potential theory. Wing-tail interference is treated by assuming one completely rolled-up vortex per wing panel and evaluating the tail load by strip theory.

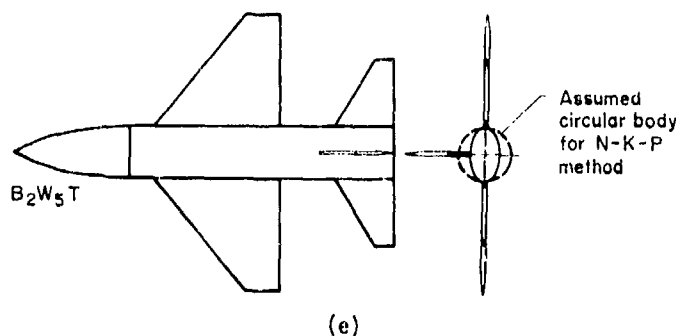
To combine the N-K-P method with the crossflow method, the N-K-P potential terms (for C_N and C_m) must be multiplied by a correction factor $(\sin 2\alpha)/2\alpha$ to produce a more correct type of nonlinear behavior to these terms and to eliminate the potential contribution as α approaches 90° . With this modification to Eqs. (7) and (8):

$$C_N = (C_N)_{N-K-P} \frac{\sin 2\alpha}{2\alpha} + \frac{2nC_{d_n} \sin^2 \alpha}{A_r} \int_0^\ell \left(\frac{C_n}{C_{n0}} \right)_{\text{Newt}} r dx \quad (19)$$

and

$$C_m = (C_m)_{N-K-P} \frac{\sin 2\alpha}{2\alpha} + \frac{2nC_{d_n} \sin^2 \alpha}{A_r X} \int_0^\ell \left(\frac{C_n}{C_{n0}} \right)_{\text{Newt}} r(x_m - x) dx \quad (20)$$

Since the N-K-P method is restricted to bodies of circular cross section with wings and tails, a further assumption must be made to estimate potential theory values of C_N and C_m for noncircular bodies with wings and tails. The local widths of the noncircular body in planform are replaced by the local diameters of a circular body, thus keeping the overall wing and tail spans constant (see sketch (e)). The crossflow method, of course, requires no such assumption for noncircular bodies.



For the way in which the crossflow method is formulated (Sec. 2), values of crossflow drag coefficient C_{d_n} for a circular cylinder are used. As shown in Fig. 1, there is considerable variation of C_{d_n} with crossflow Mach number M_n for values of M_n from about 0.4 to 3. Also, for M_n less than about 0.5, there is considerable change in C_{d_n} as the crossflow Reynolds number Re_n exceeds the critical value of about 2×10^5 (Figs. 2 and 3). These variations of C_{d_n} with M_n and Re_n may be expected for near-circular bodies, but surely not for very flat bodies or winged bodies. From the data available, values of C_{d_n} for flat bodies and plates do not appear to change nearly as appreciably with M_n and Re_n over the ranges shown in Figs. 1 and 2 (see, e.g., Refs. 28, 53, and 54). Thus, for the body-wing configurations, it is likely that a constant value of C_{d_n} will give closer agreement of theory with experiment, especially at α where M_n is near or in the transonic regime.

For flat-faced, two-dimensional configurations, reasonable values of crossflow drag coefficient can be computed from Newtonian or modified Newtonian theory (see, e.g., Table 1 and Ref. 53). For circular cylinders at low subsonic and hypersonic M_n , values of C_{d_n} computed from Newtonian or modified Newtonian theory also agree reasonably well with experiment (see Fig. 1). In this study, modified Newtonian theory is used to compute the circular-cylinder C_{d_n} value that is substituted into Eqs. (19) and (20).

From modified Newtonian theory,

$$C_{d_n} = \frac{2}{3} C_{p_{stag}} \\ = 1.2 \text{ for } C_{p_{stag}} = 1.8$$

For $M_n > \text{about } 4$, $C_{p_{stag}} \approx 1.8$ from perfect-gas relations (e.g., Ref. 55). In this study for wing-body and wing-body-tail configurations, it is assumed that $C_{d_n} = 1.2$ for all values of M_n (and hence, M_∞).

5.2 Configurations Tested at $M_\infty = 0.6$ to 2.0

Many body-wing and body-wing-tail model combinations have been tested, and the data are reported in Refs. 20 and 21. Planform views of the model components tested in the many model combinations are shown in Fig. 18. These components include a basic circular body B_1 , an elliptic body B_2 with $a/b = 2$, five flat-plate wings (W_1 to W_5), and a combination horizontal and vertical tail T . The bodies B_1 and B_2 are the same bodies considered in Sec. 4 (see Fig. 16)). All the wings were designed to have the same planform area ($16 d^2$) if the wings extended into the body B_1 to the axial centerline. Based on the phantom wing chord at the body centerline, the taper ratios for wings W_1 , W_2 , and W_3 were 0, 0.25, and 0.50, respectively (Fig. 18(a)). They were also 0.25 for W_4 and W_5 (Fig. 18(b)). Wings W_1 , W_2 , and W_3 (Fig. 18(a)) had an aspect ratio of about 4; wings W_4 , W_2 , and W_5 (Fig. 18(b)) had aspect ratios of about 5, 4, and 3, respectively. Pertinent planform dimensions of the exposed parts of the wings are given in the tables in Fig. 18. The tail dimensions are given in Fig. 18(a).

The tests (Refs. 20 and 21) were conducted in the Ames 6- by 6-Foot Wind Tunnel at $\alpha = 0^\circ$ to 60° and $M_\infty = 0.6$ to 2.0. The Reynolds number, based on body diameter d , was about 4×10^5 .

Results from these tests (Refs. 20 and 21) showed that changing wing taper ratio from 0 to 0.5 changed the aerodynamic characteristics very little. Also, changing wing aspect ratio from 3 to 5 changed the aerodynamic characteristics very little. Thus, to achieve more conciseness in the present summary, only two body-wing configurations (B_1W_5 and B_2W_5) and two body-wing-tail configurations (B_1W_5T and B_2W_5T) are considered in comparing computed with measured aerodynamic characteristics.

5.3 Comparison of Computed With Measured Normal-Force and Normal-Force-Center Characteristics

In Figs. 19 through 22, computed values of C_N and $(x - x_{ac})/d$ vs α are compared with measured values for configurations B_1W_5 , B_2W_5 , B_1W_5T , and B_2W_5T . As for the bodies alone, the C_N values are based on body cross-sectional area at the body base. Of course, they can be easily converted to the more often used exposed wing planform area by dividing by A_w/A_b , where $A_w/A_b = 15.92$ for the bodies with W_5 . For configuration B_1W_5 , the free-stream Mach numbers are 0.6, 0.9, 1.5, and 2.0 (Fig. 19). For the other configurations, the free-stream Mach numbers are 0.6 and 2.0 (Figs. 20-22).

For the circular body B_1 with the aspect-ratio-3 wing W_5 at $M_\infty = 0.6$ (Fig. 19(a)), the measured C_N values are predicted closely by the modified N-K-P potential method only for α up to about 15° . Then this method overestimates C_N over most of the higher α range considered. Thus, the addition of the crossflow method to this potential method greatly overestimates C_N . It is to be expected, however, that at α near 90° the combination method should predict C_N much closer, since C_N is given entirely by the crossflow method (modified Newtonian impact) at $\alpha = 90^\circ$. Despite the difficulty in predicting C_N over most of the high α range, the positions of the normal-force center are predicted closely by the combination method.

With increase in Mach number to $M_\infty = 0.9$, the comparisons of computed with measured results are not improved (Fig. 19(b)). However, with increase to $M_\infty = 1.5$ (Fig. 19(c)) and $M_\infty = 2.0$ (Fig. 19(d)); the comparisons are improved. At $M_\infty = 1.5$, the measured C_N values are only underestimated a small amount by the modified N-K-P method for α up to about 30° or 40° (Fig. 19(c)). At $M_\infty = 2.0$, the C_N results are estimated best by the combination method throughout the α range investigated, although the results are still somewhat overpredicted by this method (Fig. 19(d)). It appears that the combination method should improve in its prediction of C_N as M_∞ increases throughout the supersonic range.

When the body cross section is changed from circular to elliptical with the same aspect-ratio-3 wing (B_1W_5 to B_2W_5), the C_N results for $M_\infty = 0.6$ are predicted closely (possibly fortuitously) by the modified N-K-P method (Fig. 20(a)). As before, when the Mach number is increased to $M_\infty = 2.0$, the combination method still gives the best C_N prediction throughout the α range (Fig. 20(b)).

In Figs. 21 and 22 results are presented for the same body-wing combinations but with the tail attached. Generally, the comparisons of computed with measured results indicate similar trends as for the body-wing configurations.

For body-wing configurations, the initial break or significant deviation from linearity in the C_N (or C_L) curve with increasing angle of attack at the subsonic Mach numbers makes it extremely difficult to formulate a rational method for predicting C_N throughout the moderate to very high α range. This break is attributed to flow separation over the wing upper surface. For thin wings of generally lower aspect ratio and higher leading edge sweep than those studied here, the break has been attributed to vortex breakdown near the wing trailing edge of vortices shed from the leading edge. Vortex breakdown or bursting has been studied rather extensively by Wentz and Kohlman (Ref. 56) for thin delta and modified delta wings with sweep angles from 45° to 85° at low speed. They have observed that, as α increases, the position of vortex bursting of the trailing vortices moves upstream toward the trailing edge and crosses the trailing edge at a specific α . Above this α , a loss of lift occurs on the wing due to vortex bursting, and the effect becomes progressively larger as α increases. Mendenhall and Nielsen (Ref. 57) have more recently collected data from several investigators for the α value at which vortex bursting occurs at the trailing edge of delta wings tested at low speeds. They were unable to correlate the data and suggested that the factors which control vortex bursting were not reproduced or controlled between the various sets of test data. The wings used in the present investigation were generally swept less than those studied by Wentz and Kohlman (Ref. 56) and Mendenhall and Nielsen (Ref. 57). However, a 45° delta wing similar to that of W_1 (Fig. 18(a)) was investigated by Wentz and Kohlman (Ref. 56). For this wing they failed to observe vortices, but they, of course, measured a loss in C_L with increase in α over a particular value (near 20°). Despite the interesting research thus far, it seems that further research into the factors that control vortex bursting and flow separation is needed. The C_N versus α data presented here indicate that this is especially desirable for subsonic Mach numbers.

From the comparisons presented, it seems obvious that the methodology presented here represents only an initial step into the complex problem of predicting the aerodynamic characteristics of body-wing and body-wing-tail configurations to very high angles of attack. The reader interested in this field may wish to study several other initial approaches such as those of Mendenhall and Nielsen (Ref. 57), Axelsson (Ref. 58), and Thomson (Ref. 59). One should also include the Polhamus suction analogy for wings (Ref. 60) and some of its various adaptations and extensions (e.g., Refs. 57, 61, and 62). Much additional research is necessary in the high α field, and this research initially should include visual observations of the flow fields.

6. EXPERIMENTAL SIDE FORCES ON MODELS AT ZERO SIDESLIP

When models are pitched to high angles of attack, side forces can develop even at zero sideslip angle (e.g., Refs. 12-21, 63-65). These side forces generally occur at angles of attack between about 20° and 60° (but sometimes over a wider α range) and in the subsonic and transonic Mach number ranges. They result from asymmetric flow separation and vortex flow over the leeward side of the models, as shown, for example, in the many oil-flow and vapor-screen photographs in Ref. 22. Their signs can be randomly (\pm).

As noted in a recent paper by Keener, Chapman, and Kruse, (Ref. 63), some aircraft have been lost due to uncontrolled flight at high angles of attack, and some of the loss in controllability might have originated from the undesirable side forces and yawing moments attributed to asymmetric flow separation and vortex flow. Research on this phenomenon recently has increased considerably because the flight envelopes of modern aircraft and missiles are being extended into the higher angle-of-attack range.

Several interesting analytical and semiempirical modeling techniques for predicting these side forces have been explored recently (e.g., Refs. 59, 64-71). Most of these techniques are based on an impulsive flow analogy between the leeward flow field of a circular body at angle of attack and the developing wake behind an impulsively started cylinder in crossflow. Thus, only slender bodies of revolution have been considered to any degree. To date, some interesting but not always accurate results have been obtained, and one must still rely heavily on experiment.

The present study has been limited in scope to an experimental study of the side forces and vortex flow fields associated with bodies alone and bodies with thin wings and a tail. Most of the data discussed herein were obtained by Jorgensen and Nelson (Refs. 16, 18, 19, 21), Jorgensen and Howell (Ref. 20), and Jorgensen (Ref. 22) in the Ames 6- by 6-Foot Wind Tunnel and are presented in Ref. 22. Some additional data, obtained by Keener and Chapman (Ref. 17) and Keener et al. (Refs. 63, 72, 73) in both the Ames 6- by 6-Foot and 12-Foot Wind Tunnels, are also used. For simplicity, only the data that are not found in Ref. 22 are referenced herein.

The data taken from Ref. 22 refer to the configurations shown in Fig. 23. Relative dimensions for these configurations are given in Ref. 22 and in Figs. 13, 16, 18, and 24 of the present paper. Photographs from "oil-flow" and "vapor-screen" studies of the configurations in Fig. 23 are presented in Ref. 22.

6.1 Bodies Alone

6.1.1 Effect of Mach number

In 1971 Pick (Ref. 74) measured the side forces on ogive-cylinder bodies at high angles of attack in the $M_\infty = 0.5$ to 1.1 range, and he found that the maximum values of the side-force coefficients decrease with increasing Mach number. Most of the data obtained since then have supported Pick's finding, and the

development of these undesirable side forces appears to be a phenomenon that occurs primarily at subsonic Mach numbers (see, e.g., Refs. 16-21, 63, 65, 72, 73). With increase in Mach number into the supersonic range, the side forces tend to decrease to zero. However, Orlik-Rückermann et al. (Ref. 75) still measured a small side force on a 10° semivertex cone at $M_\infty = 2.0$, beginning at $\alpha \approx 26^\circ$ (maximum $\alpha = 29^\circ$ for the test). It appears that nose slenderness as well as Mach number is an essential variable, and the nose shape is important.

In Fig. 25, C_y data from Keener et al. (Ref. 72) for a tangent-ogive nose ($\ell_N/d = 3.5$) tested alone with no afterbody show that maximum values of C_y tend to decrease with increase in M_∞ throughout the α range from 0° to 90° . It is seen that there is considerable decrease in maximum C_y (from about -3 to -0.2) as Mach number increases just from $M_\infty = 0.25$ to 0.7 (the test range).

6.1.2 Effect of Reynolds number

To the author's knowledge, there have been almost no definitive tests in wind tunnels, or otherwise, concerning the effect of Reynolds number on the development of body side forces throughout the subsonic Mach number range. In 1975, Wardlaw and Morrison (Ref. 65) attempted to correlate available experimental data and found no conclusive effect of Reynolds number on either onset α for C_y or on maximum C_y .

More recently, in 1977, Keener et al. (Refs. 72 and 73) tested two tangent-ogive noses alone and with an afterbody at Reynolds numbers from about 0.3×10^6 to 3.8×10^6 at $M_\infty = 0.25$. From these rather limited data at low Mach number, there is indication of a significant Reynolds number effect.

This Reynolds number effect is illustrated by the C_y vs α data plotted in Fig. 26 for an ogive-cylinder body at $M_\infty = 0.25$ and $Re = 0.3 \times 10^6$ to 3.0×10^6 . As Re increases from 0.3×10^6 to 0.8×10^6 , the maximum level of C_y decreases. But then as Re increases above 0.8×10^6 , the maximum level of C_y increases with each successive increase in Re . This is almost a reminder of the drop and then increase in crossflow drag coefficient for a circular cylinder as the crossflow Reynolds number increases from subcritical to critical and then goes supercritical (see Fig. 2).

6.1.3 Effect of afterbody

Generally, it has been found that when a circular cylinder is attached to a tangent-ogive nose, the maximum values of C_y increase. Data to support this finding have been obtained from Refs. 63, 72, and 73. In Fig. 27, on plots of C_y vs α , it can be seen that the addition of a short ($\ell_A/d = 3.5$) aftersection to either a fineness-ratio 3.5 or 5 ogive nose tends to increase the maximum level of C_y as well as change the variation of C_y with α . However, in each case, the nose seems to initiate considerable asymmetric flow separation and contributes substantially to C_y .

There is indication in Ref. 63 that the addition of longer afterbodies (greater than $\ell_A/d = 3.5$) can reduce the maximum C_y . To resolve the question over effect of afterbody length on C_y , a test of a long pressure-distribution model with many orifices is recommended. Then the integrated forces from the nose tip to various length positions can be directly compared.

6.1.4 Effect of nose fineness ratio

In Fig. 28, the effect of nose fineness ratio ℓ_N/d on side-force coefficient C_y and center position $(\ell - x_{sf})/d$ for ogive-cylinder bodies of revolution is shown. Both C_y and $(\ell - x_{sf})/d$, measured from the body base, are plotted as a function of angle of attack α for α up to 60° . Plots are presented for $M_\infty = 0.6, 0.9$, and 1.2. The models were tested at Mach numbers up to $M_\infty = 2$, but there were no side forces above about $M_\infty = 1.2$. The magnitudes of C_y decrease with increasing M_∞ .

It is readily apparent from Fig. 28 that the largest side forces were obtained with the fineness-ratio-5 nose N_3 attached to the cylinder afterbody C_1 (of fineness ratio 7). With decrease in nose fineness ratio, the side forces decrease, and they almost disappear over most of the α range for the body with the fineness-ratio-3 nose (N_1C_1). For body N_3C_1 ($\ell_N/d = 5$) at $M_\infty = 0.6$, it has been shown that the maximum value of side force can become about 40% of the normal force (Ref. 16). Keener et al. (Ref. 63) have recently shown that the maximum value of C_y can increase even more (to the order of C_N or greater) as M_∞ is decreased from 0.6 to 0.25. There is no question that the side-force coefficients increase with decrease in Mach number and/or increase in nose fineness ratio. Wardlaw and Morrison (Ref. 65) also support these conclusions from their correlations of collected data.

Note that the side-force centers seem to start well back on the cylinder; then as α increases above about 25° , they move forward over a small α range onto the nose (see, e.g., Fig. 28(a)). At some much higher α (say about 45° to 55°), they then tend to move back onto the cylinder. Note also that for N_3C_1 , the body with the largest C_y , the maximum values of C_y are located well forward on the body.

The side forces can be studied in conjunction with the vapor-screen photographs shown in Ref. 22. In Fig. 29, the data for N_3C_1 at $M_\infty = 0.6$ and 0.9 are plotted along with the vapor-screen photographs taken at $\alpha = 10^\circ, 20^\circ, 30^\circ, 40^\circ$, and 50° . The vapor-screen photographs shown in Fig. 29 were taken at a crossplane station 3.5 diameters forward of the model base. It is obvious that when the vortices become asymmetric (between $\alpha = 20^\circ$ and 30°) the side forces develop. So long as the vortices remain steadily asymmetric, the side forces remain. Of course, as shown in Ref. 22, an asymmetric vortex system results from asymmetric flow separation from the body surface. There is obviously a need to analytically model the instability process that leads to asymmetric boundary-layer separation, asymmetric vortices, and undesirable side forces. Keener and Chapman (Ref. 76) suggest that the vortex flow may become asymmetric because of a hydrodynamic (inviscid) instability probably at or near the nose tip.

In lieu of a theoretical method for computing the angle of attack for onset of side force, experimental procedures must be used. Keener et al. (Ref. 63) have found that the onset α can be roughly correlated with nose fineness ratio (or semiapex angle) as families of curves of constant afterbody. They have found that onset α for a given body is essentially invariant with M_∞ , and, for a nose with no afterbody, onset α is given approximately by two times the semiapex angle. The general effect of increasing

When the body cross section is changed from circular to elliptical with the same aspect-ratio-3 wing (B_1W_5 to B_2W_5), the C_N results for $M_\infty = 0.6$ are predicted closely (possibly fortuitously) by the modified N-K-P method (Fig. 20(a)). As before, when the Mach number is increased to $M_\infty = 2.0$, the combination method still gives the best C_N prediction throughout the α range (Fig. 20(b)).

In Figs. 21 and 22 results are presented for the same body-wing combinations but with the tail attached. Generally, the comparisons of computed with measured results indicate similar trends as for the body-wing configurations.

For body-wing configurations, the initial break or significant deviation from linearity in the C_N (or C_L) curve with increasing angle of attack at the subsonic Mach numbers makes it extremely difficult to formulate a rational method for predicting C_N throughout the moderate to very high α range. This break is attributed to flow separation over the wing upper surface. For thin wings of generally lower aspect ratio and higher leading edge sweep than those studied here, the break has been attributed to vortex breakdown near the wing trailing edge of vortices shed from the leading edge. Vortex breakdown or bursting has been studied rather extensively by Wentz and Kohlman (Ref. 56) for thin delta and modified delta wings with sweep angles from 45° to 85° at low speed. They have observed that, as α increases, the position of vortex bursting of the trailing vortices moves upstream toward the trailing edge and crosses the trailing edge at a specific α . Above this α , a loss of lift occurs on the wing due to vortex bursting, and the effect becomes progressively larger as α increases. Mendenhall and Nielsen (Ref. 57) have more recently collected data from several investigators for the α value at which vortex bursting occurs at the trailing edge of delta wings tested at low speeds. They were unable to correlate the data and suggested that the factors which control vortex bursting were not reproduced or controlled between the various sets of test data. The wings used in the present investigation were generally swept less than those studied by Wentz and Kohlman (Ref. 56) and Mendenhall and Nielsen (Ref. 57). However, a 45° delta wing similar to that of W_1 (Fig. 18(a)) was investigated by Wentz and Kohlman (Ref. 56). For this wing they failed to observe vortices, but they, of course, measured a loss in C_L with increase in α over a particular value (near 20°). Despite the interesting research thus far, it seems that further research into the factors that control vortex bursting and flow separation is needed. The C_N versus α data presented here indicate that this is especially desirable for subsonic Mach numbers.

From the comparisons presented, it seems obvious that the methodology presented here represents only an initial step into the complex problem of predicting the aerodynamic characteristics of body-wing and body-wing-tail configurations to very high angles of attack. The reader interested in this field may wish to study several other initial approaches such as those of Mendenhall and Nielsen (Ref. 57), Axelsson (Ref. 58), and Thomson (Ref. 59). One should also include the Polhamus suction analogy for wings (Ref. 60) and some of its various adaptations and extensions (e.g., Refs. 57, 61, and 62). Much additional research is necessary in the high α field, and this research initially should include visual observations of the flow fields.

6. EXPERIMENTAL SIDE FORCES ON MODELS AT ZERO SIDESLIP

When models are pitched to high angles of attack, side forces can develop even at zero sideslip angle (e.g., Refs. 12-21, 63-65). These side forces generally occur at angles of attack between about 20° and 60° (but sometimes over a wider α range) and in the subsonic and transonic Mach number ranges. They result from asymmetric flow separation and vortex flow over the leeward side of the models, as shown, for example, in the many oil-flow and vapor-screen photographs in Ref. 22. Their signs can be randomly (\pm).

As noted in a recent paper by Keener, Chapman, and Kruse, (Ref. 63), some aircraft have been lost due to uncontrolled flight at high angles of attack, and some of the loss in controllability might have originated from the undesirable side forces and yawing moments attributed to asymmetric flow separation and vortex flow. Research on this phenomenon recently has increased considerably because the flight envelopes of modern aircraft and missiles are being extended into the higher angle-of-attack range.

Several interesting analytical and semiempirical modeling techniques for predicting these side forces have been explored recently (e.g., Refs. 59, 64-71). Most of these techniques are based on an impulsive flow analogy between the leeward flow field of a circular body at angle of attack and the developing wake behind an impulsively started cylinder in crossflow. Thus, only slender bodies of revolution have been considered to any degree. To date, some interesting but not always accurate results have been obtained, and one must still rely heavily on experiment.

The present study has been limited in scope to an experimental study of the side forces and vortex flow fields associated with bodies alone and bodies with thin wings and a tail. Most of the data discussed herein were obtained by Jorgensen and Nelson (Refs. 16, 18, 19, 21), Jorgensen and Howell (Ref. 20), and Jorgensen (Ref. 22) in the Ames 6- by 6-Foot Wind Tunnel and are presented in Ref. 22. Some additional data, obtained by Keener and Chapman (Ref. 17) and Keener et al. (Refs. 63, 72, 73) in both the Ames 6- by 6-Foot and 12-Foot Wind Tunnels, are also used. For simplicity, only the data that are not found in Ref. 22 are referenced herein.

The data taken from Ref. 22 refer to the configurations shown in Fig. 23. Relative dimensions for these configurations are given in Ref. 22 and in Figs. 13, 16, 18, and 24 of the present paper. Photographs from "oil-flow" and "vapor-screen" studies of the configurations in Fig. 23 are presented in Ref. 22.

6.1 Bodies Alone

6.1.1 Effect of Mach number

In 1971 Pick (Ref. 74) measured the side forces on ogive-cylinder bodies at high angles of attack in the $M_\infty = 0.5$ to 1.1 range, and he found that the maximum values of the side-force coefficients decrease with increasing Mach number. Most of the data obtained since then have supported Pick's finding, and the

development of these undesirable side forces appears to be a phenomenon that occurs primarily at subsonic Mach numbers (see, e.g., Refs. 16-21, 63, 65, 72, 73). With increase in Mach number into the supersonic range, the side forces tend to decrease to zero. However, Orlik-Rückermann et al. (Ref. 75) still measured a small side force on a 10° semivertex cone at $M_\infty = 2.0$, beginning at $\alpha \approx 26^\circ$ (maximum $\alpha = 29^\circ$ for the test). It appears that nose slenderness as well as Mach number is an essential variable, and the nose shape is important.

In Fig. 25, C_y data from Keener et al. (Ref. 72) for a tangent-ogive nose ($\ell_N/d = 3.5$) tested alone with no afterbody show that maximum values of C_y tend to decrease with increase in M_∞ throughout the α range from 0° to 90° . It is seen that there is considerable decrease in maximum C_y (from about -3 to -0.2) as Mach number increases just from $M_\infty = 0.25$ to 0.7 (the test range).

6.1.2 Effect of Reynolds number

To the author's knowledge, there have been almost no definitive tests in wind tunnels, or otherwise, concerning the effect of Reynolds number on the development of body side forces throughout the subsonic Mach number range. In 1975, Wardlaw and Morrison (Ref. 65) attempted to correlate available experimental data and found no conclusive effect of Reynolds number on either onset α for C_y or on maximum C_y .

More recently, in 1977, Keener et al. (Refs. 72 and 73) tested two tangent-ogive noses alone and with an afterbody at Reynolds numbers from about 0.3×10^6 to 3.8×10^6 at $M_\infty = 0.25$. From these rather limited data at low Mach number, there is indication of a significant Reynolds number effect.

This Reynolds number effect is illustrated by the C_y vs α data plotted in Fig. 26 for an ogive-cylinder body at $M_\infty = 0.25$ and $Re = 0.3 \times 10^6$ to 3.0×10^6 . As Re increases from 0.3×10^6 to 0.8×10^6 , the maximum level of C_y decreases. But then as Re increases above 0.8×10^6 , the maximum level of C_y increases with each successive increase in Re . This is almost a reminder of the drop and then increase in crossflow drag coefficient for a circular cylinder as the crossflow Reynolds number increases from subcritical to critical and then goes supercritical (see Fig. 2).

6.1.3 Effect of afterbody

Generally, it has been found that when a circular cylinder is attached to a tangent-ogive nose, the maximum values of C_y increase. Data to support this finding have been obtained from Refs. 63, 72, and 73. In Fig. 27, on plots of C_y vs α , it can be seen that the addition of a short ($\ell_A/d = 3.5$) aftersection to either a fineness-ratio 3.5 or 5 ogive nose tends to increase the maximum level of C_y as well as change the variation of C_y with α . However, in each case, the nose seems to initiate considerable asymmetric flow separation and contributes substantially to C_y .

There is indication in Ref. 63 that the addition of longer afterbodies (greater than $\ell_A/d = 3.5$) can reduce the maximum C_y . To resolve the question over effect of afterbody length on C_y , a test of a long pressure-distribution model with many orifices is recommended. Then the integrated forces from the nose tip to various length positions can be directly compared.

6.1.4 Effect of nose fineness ratio

In Fig. 28, the effect of nose fineness ratio ℓ_N/d on side-force coefficient C_y and center position $(\bar{x} - x_{cf})/d$ for ogive-cylinder bodies of revolution is shown. Both C_y and $(\bar{x} - x_{cf})/d$, measured from the body base, are plotted as a function of angle of attack α for α up to 60° . Plots are presented for $M_\infty = 0.6, 0.9$, and 1.2. The models were tested at Mach numbers up to $M_\infty = 2$, but there were no side forces above about $M_\infty = 1.2$. The magnitudes of C_y decrease with increasing M_∞ .

It is readily apparent from Fig. 28 that the largest side forces were obtained with the fineness-ratio-5 nose N_3 attached to the cylinder afterbody C_1 (of fineness ratio 7). With decrease in nose fineness ratio, the side forces decrease, and they almost disappear over most of the α range for the body with the fineness-ratio-3 nose (N_1C_1). For body N_3C_1 ($\ell_N/d = 5$) at $M_\infty = 0.6$, it has been shown that the maximum value of side force can become about 40% of the normal force (Ref. 16). Keener et al. (Ref. 63) have recently shown that the maximum value of C_y can increase even more (to the order of C_N or greater) as M_∞ is decreased from 0.6 to 0.25. There is no question that the side-force coefficients increase with decrease in Mach number and/or increase in nose fineness ratio. Wardlaw and Morrison (Ref. 65) also support these conclusions from their correlations of collected data.

Note that the side-force centers seem to start well back on the cylinder; then as α increases above about 25° , they move forward over a small α range onto the nose (see, e.g., Fig. 28(a)). At some much higher α (say about 45° to 55°), they then tend to move back onto the cylinder. Note also that for N_3C_1 , the body with the largest C_y , the maximum values of C_y are located well forward on the body.

The side forces can be studied in conjunction with the vapor-screen photographs shown in Ref. 22. In Fig. 29, the data for N_3C_1 at $M_\infty = 0.6$ and 0.9 are plotted along with the vapor-screen photographs taken at $\alpha = 10^\circ, 20^\circ, 30^\circ, 40^\circ$, and 50° . The vapor-screen photographs shown in Fig. 29 were taken at a crossplane station 3.5 diameters forward of the model base. It is obvious that when the vortices become asymmetric (between $\alpha = 20^\circ$ and 30°) the side forces develop. So long as the vortices remain steadily asymmetric, the side forces remain. Of course, as shown in Ref. 22, an asymmetric vortex system results from asymmetric flow separation from the body surface. There is obviously a need to analytically model the instability process that leads to asymmetric boundary-layer separation, asymmetric vortices, and undesirable side forces. Keener and Chapman (Ref. 76) suggest that the vortex flow may become asymmetric because of a hydrodynamic (inviscid) instability probably at or near the nose tip.

In lieu of a theoretical method for computing the angle of attack for onset of side force, experimental procedures must be used. Keener et al. (Ref. 63) have found that the onset α can be roughly correlated with nose fineness ratio (or semiapex angle) as families of curves of constant afterbody. They have found that onset α for a given body is essentially invariant with M_∞ , and, for a nose with no afterbody, onset α is given approximately by two times the semiapex angle. The general effect of increasing

afterbody length is to decrease onset α ; that is, the longer the afterbody the smaller the α at which a side force is first encountered. A somewhat similar finding is reported by Wardlaw and Morrison (Ref. 65). They also have produced (Ref. 65) a rough correlation of data for the α at which the maximum C_y is observed. It tends to decrease with increasing Mach number and body fineness ratio.

Keener et al. (Ref. 63) also have made a rough correlation of data for the "upper-limit" α at which the static C_y disappears and the wake flow becomes essentially oscillatory like a Karman vortex street from a two-dimensional cylinder. This upper-limit α also tends to decrease with increasing M_∞ , varying from about a maximum of 80° at $M_\infty = 0.25$ to a minimum of 50° at $M_\infty = 0.9$.

6.1.5 Effect of nose-tip rounding

When the sharp tip of a fineness-ratio-3.5 nose (N_2) was rounded to make a fineness-ratio-3 nose (N_4), the side forces at $M_\infty = 0.6$ and 0.9 almost disappeared. This is shown in Fig. 30 where C_y and its center position are plotted against α for bodies N_1C_1 , N_2C_1 , and N_4C_1 . Apparently this nose-tip rounding brought more symmetry to the flow field, as can be seen in the vapor-screen photographs for both N_2C_1 and N_4C_1 at $M_\infty = 0.6$ (see Fig. 31). For the blunt-nosed body, N_4C_1 , a strange vortex pattern developed at $\alpha \approx 40^\circ$ and 50° . This pattern (Fig. 31(b)) consists of two very symmetric vortices from the nose located above two separation regions stacked one on top of the other (at station 2). What appears to be the same or a similar phenomenon has been observed recently by Hsieh (Ref. 77) for a hemisphere-cylinder body at $M_\infty = 1.1$ to 1.5 . This so-called separation-bubble phenomenon diminishes with increasing M_∞ (Ref. 76). In fact, for N_4C_1 it was not observed at $M_\infty = 0.9$ and above.

In spite of the beneficial effect from blunting the fineness-ratio-3.5 nose (N_2) back to fineness-ratio 3 (N_4), it should be noted that the reduction in C_y was no better than that obtained with the sharp nose (N_1) of the same fineness ratio ($x_N/d = 3$).

6.1.6 Effect of nose-tip strakes

Even though nose-tip strakes appear to create severe problems for a radome, they have been considered for reducing unwanted side forces that develop on bodies at high α (e.g., Refs. 14, 16, 17, 19, and 72). The flow mechanism of the strakes is, of course, to force local flow separation to occur symmetrically on both sides of the body.

In Ref. 16 a study was made of the effect of nose strakes on a body consisting of a fineness-ratio-3 ogive nose attached to a fineness-ratio-7 cylinder. This configuration, designated as N_5C_1 in Fig. 24, was tested in the Ames 6- by 6-Foot Wind Tunnel at M_∞ from 0.6 to 2.0 .

As shown in the vapor-screen photographs in Fig. 32 for N_5C_1 at $M_\infty = 0.6$, the tip strakes apparently brought some separation and vortex-flow symmetry near the nose, but this symmetry did not persist back on the body at the higher angles of attack. As noted in Ref. 16, this nose-cylinder configuration also developed some undesirable, but not large, side forces at $M_\infty = 0.6$ and $\alpha > 20^\circ$. The C_y results for this configuration were generally not as good as those for the same configuration without the strakes.

For a nose alone of slightly higher fineness ratio ($x_N/d = 3.5$), Keener and Chapman (Ref. 17) and Keener et al. (Ref. 72) have found similar strakes to be very effective at $M_\infty = 0.25$, the only Mach number investigated. However, even these strakes produced mixed results when the nose was rolled and/or yawed, and multiple strakes around the nose might be required. Thus far, the indication is that nose-tip strakes may be very effective in decreasing C_y on noses alone but not so effective for noses attached to long aftersections.

6.1.7 Effect of afterbody side strakes

When strakes were attached to the sides of the cylinder C_1 of body N_3C_1 ($x_N/d = 5$), the side forces were not significantly changed. As shown in Fig. 33, the variation of C_y with α was changed somewhat, but the maximum values of C_y were about the same. Apparently the influence of this fineness-ratio-5 nose was so great that applying strakes to the afterbody was of no appreciable help.

6.1.8 Effect of elliptic cross section

The effect of elliptic cross section and roll angle on side-force coefficient and position is shown in Fig. 34. Results are compared for body B_1 (a circular body of $x/d = 10$) and body B_2 (the equivalent elliptic body of constant $a/b = 2$) at $M_\infty = 0.6$ and 0.9 . With the elliptic body B_2 oriented at $\phi = 0^\circ$ (flat side pitching against the free-stream flow), the side-force coefficients are very small and close to those for B_1 . However, when B_2 is rolled to $\phi = 90^\circ$, the side-force coefficients increase considerably. According to Ref. 18, C_y becomes more than twice C_N at $\alpha = 50^\circ$ for B_2 at $\phi = 90^\circ$ and $M_\infty = 0.6$. As shown in the oil-flow and vapor-screen photographs in Figs. 35 and 35, the separation and vortex patterns were very symmetric for B_2 at $\phi = 0^\circ$, but they became very asymmetric for B_2 at $\phi = 90^\circ$.

From tests of a body of elliptic cross section with variable a/b (body B_3), it was found that the wake flow-field asymmetry and side forces were influenced mostly by the nose. Body B_3 (Fig. 37) consists of the same nose as B_2 but has an afterbody section of variable a/b over four body diameters in length and a constant $a/b = 2$ over the rear three body diameters. Detailed dimensions are given in Refs. 18 and 22. As shown in Fig. 37, when B_3 was oriented at $\phi = 0^\circ$ (flattest side of nose pitching against the free-stream flow), the side-force coefficients were very small and close to those for B_1 (the equivalent body of revolution). However, when B_3 was rolled to $\phi = 90^\circ$ (thinnest side of nose pitching against the free-stream flow), undesirable side forces developed, and, as shown in Fig. 38, the vortex flow changed from symmetric to asymmetric.

Just as for the bodies of revolution, the maximum values of C_y decreased as M_∞ increased. At $M_\infty = 1.5$ there were essentially no side forces measured on any of the elliptic bodies, even for the worst roll orientation (Ref. 18).

6.2 Body-Wing and Body-Wing-Tail Configurations

6.2.1 Effects of adding a wing and a wing plus tail to a body

In Fig. 39, the effects on side-force coefficient and side-force position of adding a thin wing and wing plus tail to a body are shown. The body N_3C_1 , which has a fineness-ratio-5 nose, produced the largest side forces for the bodies of revolution tested. As shown in Fig. 39, these side forces and their positions remain about the same with the wing W_2 of aspect ratio 4 attached or even with the tail T added. (Dimensions for the wing and tail are given in Fig. 18 and for the body in Fig. 24.)

From these comparisons it can be concluded that the most important influence comes from the body nose. As seen in the vapor-screen photographs in Fig. 40, the vortex asymmetry that appeared from the fineness-ratio-5 nose, when tested with only the cylinder C_1 , still persisted when the wing and tail were attached.

6.2.2 Effects of wing aspect ratio and taper ratio

For thin wings of about equal planform area (Fig. 18) but with aspect ratios of 3, 4, and 5, there was essentially no effect of aspect ratio on the measured side forces for the body-wing models tested (Ref. 20). Likewise, a change in taper ratio from 0 to about 0.5 resulted in no appreciable side-force effect (Ref. 20). The results were also unchanged when the tail T (Fig. 18) was attached to the wing-body models (Ref. 21).

7. CONCLUDING REMARKS

An engineering-type method has been presented for computing normal-force and pitching-moment coefficients for slender bodies of circular and noncircular cross section alone and with lifting surfaces. In this method, a semiempirical term representing viscous-separation crossflow is added to a term representing potential-theory crossflow. In computing C_N and C_m for bodies alone, slender-body theory has been used for the term representing the potential crossflow. For bodies with thin wings and tails, the linearized potential method of Nielsen, Kaattari, and Pitts, modified for high angles of attack, has been used.

For bodies of revolution, computed aerodynamic characteristics were found to agree with measured results for the investigated free-stream Mach numbers from 0.6 to 2.9. The angles of attack extended from 0° to 180° for $M_\infty = 2.9$ and from 0° to 60° for $M_\infty = 0.6$ to 2.0.

For bodies of elliptic cross section, measured results were also predicted reasonably well over the investigated Mach-number range from 0.6 to 2.0 and the angle-of-attack range from 0° to 60° . Just as for the bodies of revolution, the predictions were best at supersonic Mach numbers.

For body-wing and body-wing-tail configurations, measured normal-force coefficients and centers were predicted reasonably well at the upper test Mach number of 2.0. However, with decrease in Mach number to 0.6, the agreement for C_N rapidly deteriorated, although the normal-force centers remained in close agreement.

When model-flow separation and vortex patterns became asymmetric, unwanted side forces were usually measured on the models at subsonic Mach numbers and zero sideslip angle. Generally, the unwanted side-force coefficients decreased or vanished with the following: (1) increase in Mach number, (2) decrease in nose fineness ratio, (3) change from sharp to somewhat rounded nose, and (4) flattening of body cross section (particularly the body nose). Additions of afterbody strakes, thin wings, or thin wings plus tail produced much smaller or no appreciable effects.

Perhaps the high- α flight characteristics of some aircraft could be improved with a fineness-ratio-3 or less nose that is slightly blunted and elliptically flattened.

REFERENCES



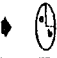

1. Allen, H. Julian: Estimation of the Forces and Moments Acting on Inclined Bodies of Revolution of High Fineness Ratio. NACA RM A9126, 1949.
2. Allen H. Julian and Perkins, Edward W.: A Study of Effects of Viscosity on Flow Over Slender Inclined Bodies of Revolution. NACA Rep. 1048, 1951.
3. Perkins, Edward M. and Kuehn, Donald M.: Comparison of the Experimental and Theoretical Distributions of Lift on a Slender Inclined Body of Revolution at $M = 2$. NACA TN 3715, 1956.
4. Perkins, Edward W. and Jorgensen, Leland H.: Comparison of Experimental and Theoretical Normal-Force Distributions (Including Reynolds Number Effects) on an Ogive-Cylinder Body at Mach Number 1.98. NACA TN 3716, 1956.
5. Jorgensen, Leland H. and Perkins, Edward W.: Investigation of Some Wake Vortex Characteristics of an Inclined Ogive-Cylinder Body at Mach Number 2. NACA Rep. 1371, 1958.
6. Jorgensen, Leland H.: Inclined Bodies of Various Cross Sections at Supersonic Speeds. NASA MEMO 10-3-58A, 1958.
7. Jorgensen, Leland H. and Treon, Stuart L.: Measured and Estimated Aerodynamic Characteristics for a Model of a Rocket Booster at Mach Numbers from 0.6 to 4 and at Angles of Attack from 0° to 180° . NASA TM X-580, 1961.

8. Saffell, Bernard F., Jr., Howard, Millard L., and Brooks, Eugene N., Jr.: Method for Predicting the Static Aerodynamic Characteristics of Typical Missile Configurations for Angles of Attack to 180 Degrees. Rep. 3645, Naval Ship Research and Development Center, March 1971.
9. Jorgensen, Leland H.: Prediction of Static Aerodynamic Characteristics for Space-Shuttle-Like and Other Bodies at Angles of Attack from 0° to 180°. NASA TN D-6996, 1973.
10. Jorgensen, Leland H.: Estimation of Aerodynamics for Slender Bodies Alone and With Lifting Surfaces at α 's From 0° to 90°. AIAA J., vol. 11, no. 3, March 1973, pp. 409-412.
11. Jorgensen, Leland H.: A Method for Estimating Static Aerodynamic Characteristics for Slender Bodies of Circular and Noncircular Cross Section Alone and With Lifting Surfaces at Angles of Attack from 0° to 90°. NASA TN D-7228, 1973.
12. Pick, George S.: Side Forces on Ogive-Cylinder Bodies at High Angles of Attack in Transonic Flow. J. Spacecraft & Rockets, vol. 9, no. 6, June 1972, pp. 389-390.
13. Clark, William H., Peoples, John R., and Briggs, M. Michael: Occurrence and Inhibition of Large Yawing Moments During High Incidence Flight of Slender Missile Configurations. AIAA Paper 72-968, 1972.
14. Coe, Paul L., Jr., Chambers, Joseph R., and Letko, William: Asymmetric Lateral-Directional Characteristics of Pointed Bodies of Revolution at High Angles of Attack. NASA TN D-7095, 1972.
15. Fleeman, E. L. and Nelson, R. C.: Aerodynamic Forces and Moments on a Slender Body With a Jet Plume for Angles of Attack Up to 180 Degrees. AIAA Paper 74-110, 1974.
16. Jorgensen, Leland H. and Nelson, Edgar R.: Experimental Aerodynamic Characteristics for a Cylindrical Body of Revolution With Various Noses at Angles of Attack from 0° to 58° and Mach Numbers from 0.6 to 2.0. NASA TM X-3128, 1974.
17. Keener, Earl R. and Chapman, Gary T.: Onset of Aerodynamic Side Forces at Zero Sideslip on Symmetric Forebodies at High Angles of Attack. AIAA Paper 74-770, 1974.
18. Jorgensen, Leland H. and Nelson, Edgar R.: Experimental Aerodynamic Characteristics for Bodies of Elliptic Cross Section at Angles of Attack from 0° to 58° and Mach Numbers from 0.6 to 2.0. NASA TM X-3129, 1975.
19. Jorgensen, Leland H. and Nelson, Edgar R.: Experimental Aerodynamic Characteristics for a Cylindrical Body of Revolution With Side Strakes and Various Noses at Angles of Attack from 0° to 58° and Mach Numbers from 0.6 to 2.0. NASA TM X-3130, 1975.
20. Jorgensen, Leland H. and Howell, Michael H.: Experimental Aerodynamic Characteristics for Slender Bodies With Thin Wings at Angles of Attack from 0° to 58° and Mach Numbers from 0.6 to 2.0. NASA TM X-3309, 1976.
21. Jorgensen, Leland H., and Nelson, Edgar R.: Experimental Aerodynamic Characteristics for Slender Bodies With Thin Wings and Tail at Angles of Attack from 0° to 58° and Mach Numbers from 0.6 to 2.0. NASA TM X-3310, 1976.
22. Jorgensen, Leland H.: Prediction of Static Aerodynamic Characteristics for Slender Bodies Alone and With Lifting Surfaces to Very High Angles of Attack. NASA TR R-474, 1977.
23. Munk, Max M.: The Aerodynamic Forces on Airship Hulls. NACA Rep. 184, 1923.
24. Ward, G. N.: Supersonic Flow Past Slender Pointed Bodies. Quar. J. Mech. & Appl. Math., vol. 2, pt. I, March 1949, pp. 75-97.
25. Pitts, William C., Nielsen, Jack N., and Kaattari, George E.: Lift and Center of Pressure of Wing-Body-Tail Combinations at Subsonic, Transonic, and Supersonic Speeds. NACA Rep. 1307, 1957.
26. Wieselberger, C.: New Data on the Laws of Fluid Resistance. NACA TN 84, 1922.
27. Lindsey, W. F.: Drag of Cylinders of Simple Shapes. NACA Rep. 619, 1938.
28. Delany, Noel K. and Sorensen, Norman E.: Low-Speed Drag of Cylinders of Various Shapes. NACA TN 3038, 1953.
29. Polhamus, Edward C., Geller, Edward W., and Grunwald, Kalman J.: Pressure and Force Characteristics of Noncircular Cylinders as Affected by Reynolds Number With a Method Included for Determining the Potential Flow about Arbitrary Shapes. NASA TR R-46, 1959.
30. Polhamus, Edward C.: Effect of Flow Incidence and Reynolds Number on Low-Speed Aerodynamic Characteristics of Several Noncircular Cylinders With Applications to Directional Stability and Spinning. NASA TR R-29, 1959.
31. Lindsey, W. F.: Drag of Cylinders of Simple Shapes. NACA Rep. 619, 1938.
32. Stack, John: Compressibility Effects in Aeronautical Engineering. NACA ACR, 1941.
33. Gowen, Forrest E. and Perkins, Edward W.: Drag of Circular Cylinders for a Wide Range of Reynolds Numbers and Mach Numbers. NACA TN 2960, 1953.

34. Walter, L. W. and Lange, A. H.: Surface Temperature and Pressure Distributions on a Circular Cylinder in Supersonic Cross-Flow. NAVJRD Rep. 2854 (Aerobalistic Res. Rep. 180), U.S. Naval Ord. Lab., White Oak, Md., June 5, 1953.
35. Penland, Jim A.: Aerodynamic Characteristics of a Circular Cylinder at Mach Number 6.86 and Angles of Attack up to 90°. NACA TN 3861, 1957.
36. Welsh, Clement J.: The Drag of Finite-Length Cylinders Determined from Flight Tests at High Reynolds Numbers for a Mach Number Range from 0.5 to 1.3. NACA TN 2941, 1953.
37. Macha, John M.: Drag of Circular Cylinders at Transonic Mach Numbers. J. Aircraft, vol. 14, no. 6, June 1977, pp. 605-607.
38. Hamilton, Richard K.: Correlation of Space Shuttle Applicable Experimental Hypersonic Aerodynamic Characteristics With Theory. NASA TM X-2272, 1971, pp. 455-492.
39. Relf, E. F.: Discussion of the Results of Measurements of the Resistance of Wires, With Some Additional Tests on the Resistance of Wires of Small Diameter. R&M 102, British A.C.A., 1914.
40. Roshko, Anatol: Experiments on the Flow Past a Circular Cylinder at Very High Reynolds Numbers. J. Fluid Mech., vol. 10, pt. 3, May 1961, pp. 345-356.
41. Schmidt, Louis V.: Fluctuating Force Measurements Upon a Circular Cylinder at Reynolds Numbers up to 5×10^6 . NASA TM X-57,779, 1966.
42. Jones, George W., Jr., Cincotta, Joseph J., and Walker, Robert W.: Aerodynamic Forces on a Stationary and Oscillating Circular Cylinder at High Reynolds Numbers. NASA TR R-300, 1969.
43. Goldstein, Sydney: Modern Developments in Fluid Dynamics. Oxford, The Clarendon Press, vol 2, sec. 195, 1938, pp. 439-440.
44. McKinney, Linwood W.: Effects of Fineness Ratio and Reynolds Number on the Low-Speed Crosswind Drag Characteristics of Circular and Modified-Square Cylinders. NASA TN D-540, 1960.
45. Bryson, Arthur E., Jr.: Stability Derivatives for a Slender Missile With Application to a Wing-Body-Vertical-Tail Configuration. J. Aeronaut. Sci., vol. 20, no. 5, May 1953, pp. 297-308.
46. Bryson, Arthur E., Jr.: Evaluation of the Inertia Coefficients of the Cross Section of a Slender Body. J. Aeronaut. Sci., vol. 21, no. 6, June 1954, pp. 424-427.
47. Bryson, Arthur E., Jr.: The Aerodynamic Forces on a Slender Low (or High) Wing, Circular Body, Vertical Tail Configuration. J. Aeronaut. Sci., vol. 21, no. 8, Aug. 1954, pp. 574-575.
48. Nielsen, Jack N.: Missile Aerodynamics. New York, McGraw-Hill Book Company, Inc., 1960.
49. Nelson, R. C. and Fleeman, E. L.: High Angle-of-Attack Aerodynamics on a Slender Body With a Jet Plume. J. Spacecraft & Rockets, vol. 12, no. 1, Jan. 1975, pp. 12-16.
50. Baker, William B., Jr.: An Aerodynamic Coefficient Prediction Technique for Slender Bodies With Low Aspect Ratio Fins at Mach Numbers from 0.6 to 3.0 and Angles of Attack from 0 to 180 Degrees. AEDC-TR-77-97, Air Force Flight Dynamics Laboratory, Wright-Patterson Air Force Base, Ohio, March 1978.
51. Altstatt, M. C., and Dietz, W. E., Jr.: Support Interference on an Ogive-Cylinder Model at High Angle of Attack in Transonic Flow. AEDC-TR-78-8, Arnold Engineering Development Center/DOTR, Arnold Air Force Station, Tennessee, March 1978.
52. Jernell, Lloyd S.: Aerodynamic Characteristics of Bodies of Revolution at Mach Numbers from 1.50 to 2.86 and Angles of Attack to 180°. NASA TM X-1658, 1968.
53. Jorgensen, Leland H. and Brownson, Jack J.: Effects of Reynolds Number and Body Corner Radius on Aerodynamic Characteristics of a Space Shuttle-Type Vehicle at Subsonic Mach Numbers. NASA TN D-6615, 1972.
54. Hoerner, Sighard F.: Fluid-Dynamic Drag. Published by the author, 2 King Lane, Greenbriar, Brick Town, New Jersey 08723, 1965.
55. Ames Research Staff: Equations, Tables, and Charts for Compressible Flow. NACA Rep. 1135, 1953.
56. Wentz, W. H., Jr. and Kohlman, D. L.: Wind Tunnel Investigations of Vortex Breakdown on Slender Sharp-Edged Wings. NASA CR-98737, 1968.
57. Mendenhall, Michael R. and Nielsen, Jack N.: Effect of Symmetrical Vortex Shedding on the Longitudinal Aerodynamic Characteristics of Wing-Body-Tail Combinations. NASA CR-2473, 1975.
58. Axelsson, John A.: Estimation of Transonic Aircraft Aerodynamics to High Angles of Attack. AIAA Paper 75-996, 1975.
59. Thomson, K. D.: Estimation at Subsonic Speeds of the Longitudinal and Lateral Aerodynamic Characteristics of Wing-Body Combinations at Angles of Attack up to 90°. Australian Weapons Research Est., WRE-Rep. 1672, 1976.

60. Polhamus, E. C.: Prediction of Vortex-Lift Characteristics by a Leading-Edge Suction Analogy. J. Aircraft, vol. 8, no. 4, April 1971, pp. 193-199.
61. Bradley, R. G., Smith, C. W. and Bateley, I. C.: Vortex-Lift Prediction for Complex Wing Planforms. J. Aircraft, vol. 10, no. 6, June 1973, pp. 379-381.
62. Lamar, J. E.: Extension of the Leading Edge Suction Analogy to Wings With Separated Flow Around the Side Edges at Subsonic Speeds. NASA TR R-428, 1974.
63. Keener, E. R., Chapman, G. T., and Kruse, R. L.: Effects of Mach Number and Afterbody Length on Onset of Asymmetric Forces on Bodies at Zero Sideslip and High Angles of Attack. AIAA Paper 76-66, 1976.
64. Thomson, K. D.: The Estimation of Viscous Normal Force, Pitching Moment, Side Force and Yawing Moment on Bodies of Revolution at Incidences up to 90°. Australian Weapons Research Est., WRE-Rep. 782, 1972.
65. Wardlaw, Andrew B., Jr. and Morrison, Alfred M.: Induced Side Forces on Bodies of Revolution at High Angle of Attack. Naval Surface Weapons Center, White Oak, Md., NSWC/WOL/TR 75-176, 1975.
66. Wardlaw, Andrew B., Jr.: Prediction of Yawing Force at High Angle of Attack. AIAA J., vol. 12, no. 8, Aug. 1974, pp. 1142-1144.
67. Wardlaw, Andrew B., Jr.: Multivortex Model of Asymmetric Shedding on Slender Bodies at High Angle of Attack. AIAA Paper 75-123, 1975.
68. Lamont, P. J. and Hunt, B. L.: Pressure and Force Distributions on a Sharp-Nosed Circular Cylinder at Large Angles of Inclination to a Uniform, Subsonic Stream. J. Fluid Mechanics, vol. 76, pt. 3, 1976, pp. 519-559.
69. Lamont, P. J. and Hunt, B. L.: Prediction of Aerodynamic Out-of-Plane Forces on Ogive-Nosed Circular Cylinders. J. Spacecraft, vol. 14, no. 1, Jan. 1977, pp. 38-44.
70. Deffenbaugh, F. D., and Marshall, F. J.: Time Development of the Flow About an Impulsively Started Cylinder. AIAA J., vol. 14, no. 7, July 1976, pp. 908-913.
71. Deffenbaugh, F. D. and Koerner, W. G.: Asymmetric Vortex Wake Development on Missiles at High Angles of Attack. J. Spacecraft & Rockets, vol. 14, no. 3, March 1977, pp. 155-162.
72. Keener, Earl R., Chapman, Gary T., Cohen, Lee, and Taleghani, Jamshid: Side Forces on a Tangent Ogive Forebody With a Fineness Ratio of 3.5 at High Angles of Attack and Mach Numbers from 0.1 to 0.7. NASA TM X-3437, 1977.
73. Keener, Earl R., Chapman, Gary T., Cohen, Lee, and Taleghani, Jamshid: Side Forces on Forebodies at High Angles of Attack and Mach Numbers From 0.1 to 0.7: Two Tangent Ogives, Paraboloid and Cone. NASA TM X-3438, 1977.
74. Pick, G. S.: Investigation of Side Forces on Ogive-Cylinder Bodies at High Angles of Attack in the $M = 0.5$ to 1.1 Range. AIAA Paper 71-570, 1971.
75. Orlik-Rückemann, K. J., LaBerge, J. G., and Iyengar, S.: Half- and Full-Model Experiments on Slender Cones at Angle of Attack. J. Spacecraft, vol. 10, no. 9, Sept. 1973, pp. 575-580.
76. Keener, Earl R. and Chapman, Gary T.: Similarity in Vortex Asymmetries Over Slender Bodies and Wings. AIAA J., vol. 15, no. 9, Sept. 1977, pp. 1370-1372.
77. Hsieh, Tsuying: Low Supersonic Flow Over Hemisphere-Cylinder at Incidence. J. Spacecraft, vol. 14, no. 11, Nov. 1977, pp. 662-668.

Table 1. C_{d_n} and C_n/C_{n_0} values for two-dimensional cylinders of various cross sections at $\alpha = 90^\circ$ as computed by Newtonian theories and measured at subcritical Mach and Reynolds numbers.

CROSS SECTION	NEWTONIAN THEORY		MOD. NEWT. THEORY FOR $C_{p_{stag}} = 1.8$		MEASURED		
	C_{d_n}	C_n/C_{n_0}	C_{d_n}	C_n/C_{n_0}	C_{d_n}	C_n/C_{n_0}	REF.
	1.33	1.00	1.20	1.00	1.20	1.00	26
	$a/b = 2$ 0.94	0.50	0.85	0.50	0.70	0.41	27, 28
	$a/b = 4$ 0.59	0.22	0.53	0.22	0.35	0.15	27
	$a/b = 2$ 1.65	1.75	1.48	1.75	1.60	1.89	28, 29
	$k = 0.0$ 2.00	1.33	1.80	1.33	2.05	1.51	27
	$k = 0.02$ 1.97	1.33	1.78	1.33	2.00	1.48	28
	$k = 0.08$ 1.89	1.26	1.70	1.26	1.85	1.22	30
	$k = 0.24$ 1.68	1.14	1.51	1.14	1.12	0.85	30
	$k = 0.50$ 1.33	1.00	1.20	1.00	1.20	1.00	26

NOTE: ALL C_{d_n} 's IN TABLE ARE BASED ON WIDTH OF CROSS SECTION, NOT EQUIVALENT d .

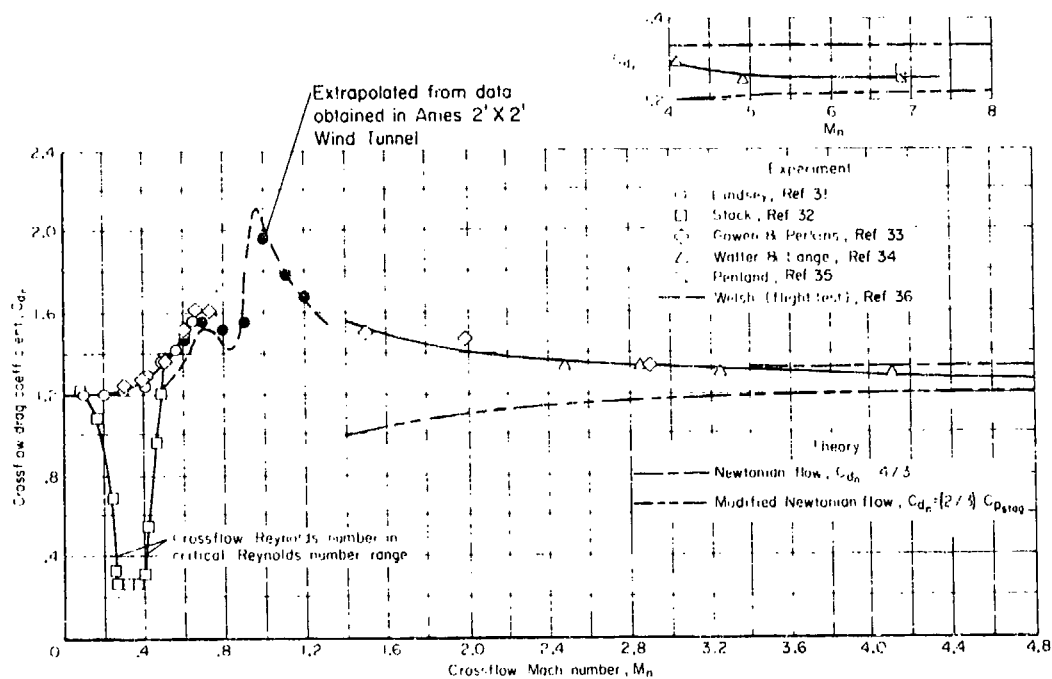


Fig. 1. Variation of crossflow drag coefficient with crossflow Mach number for circular cylinders.

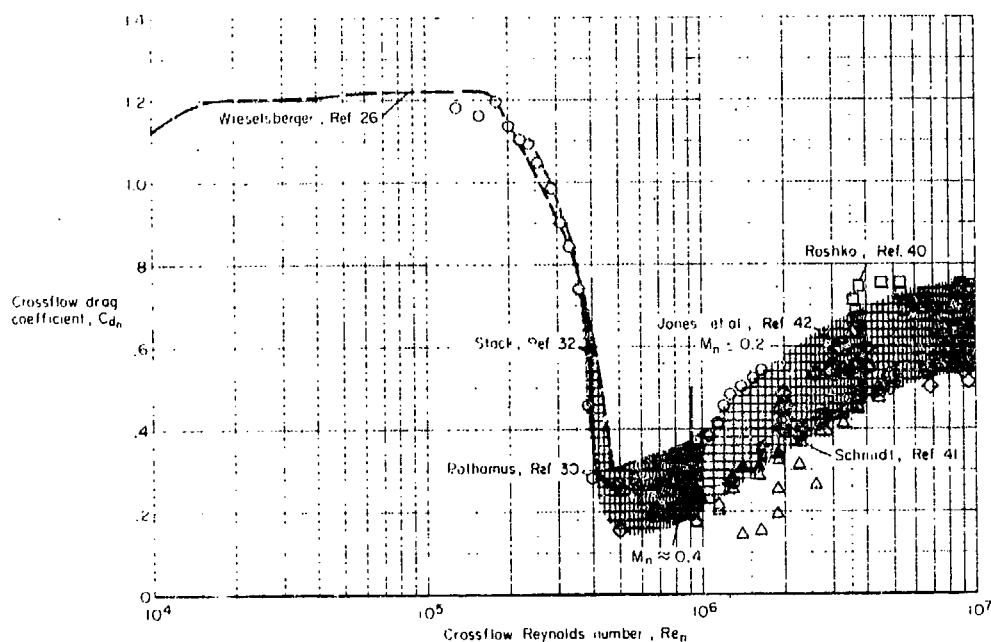


Fig. 2. Variation of crossflow drag coefficient with crossflow Reynolds number for circular cylinders at subcritical crossflow Mach numbers ($M_\infty \leq 0.4$).

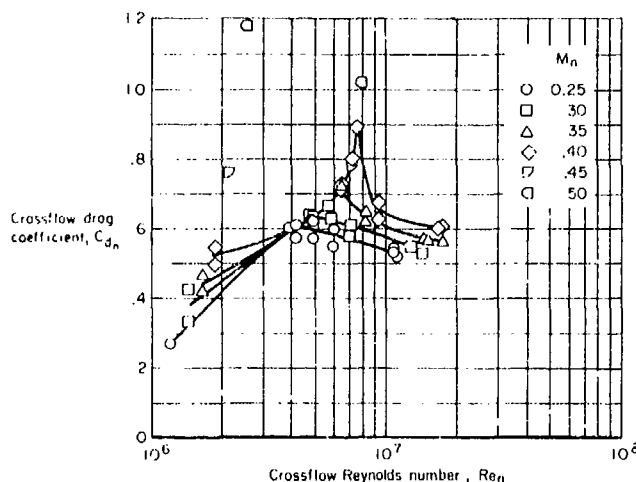


Fig. 3. Variation of crossflow drag coefficient with crossflow Reynolds number for circular cylinders at supercritical Reynolds numbers and at crossflow Mach numbers from 0.25 to 0.50 (from Ref. 42).

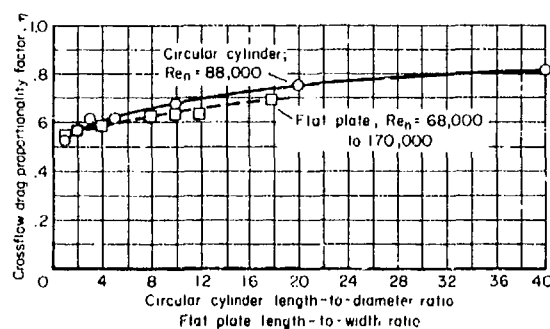


Fig. 4. Ratio of crossflow drag coefficient for a finite-length cylinder (or flat plate) to that for an infinite-length cylinder (or flat plate) (from Ref. 43).

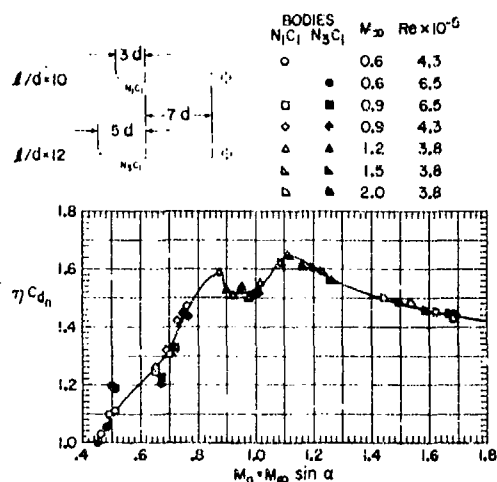


Fig. 5. Variation of ηC_{d_n} with M_n (crossflow Mach number) computed from experimental C_N data (Ref. 16) for bodies of revolution at high α ($45^\circ < \alpha < 60^\circ$).

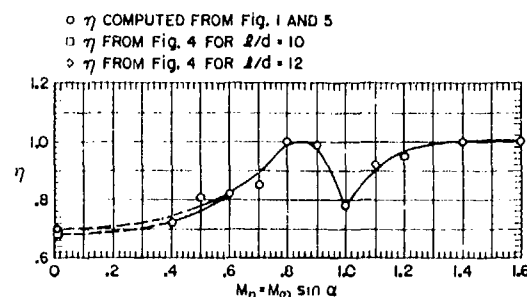


Fig. 6. Variation of η with M_n , obtained from experimental results in Figs. 1, 4, and 5.

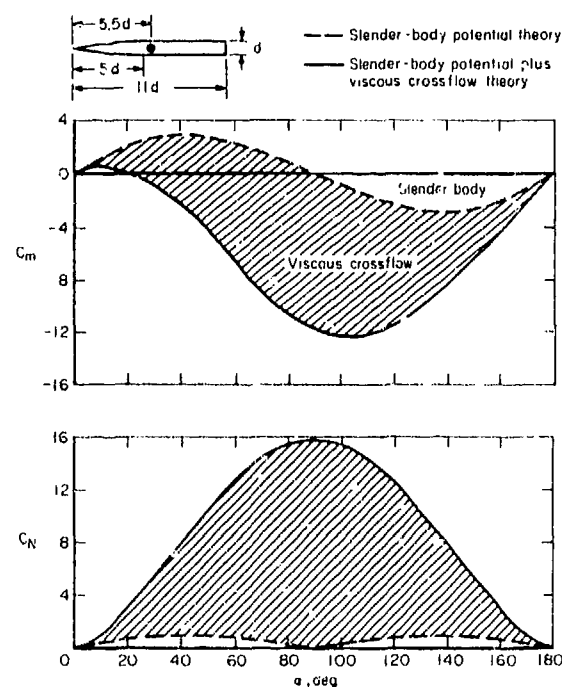


Fig. 7. Computed components of normal-force and pitching-moment coefficients for an ogive-cylinder body at $\alpha = 0^\circ$ to 180° and $M_\infty = 2.9$ (from Ref. 9).

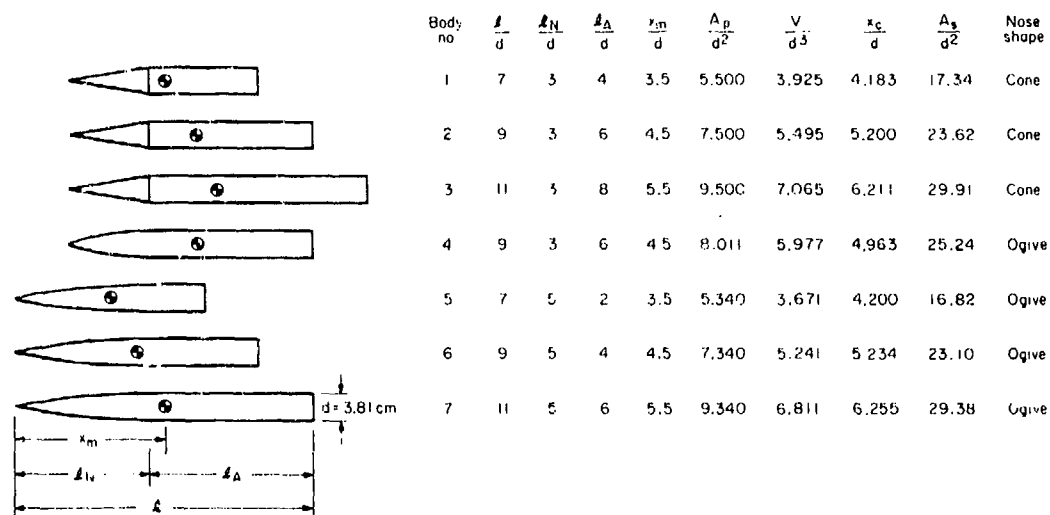


Fig. 8. Bodies for which the aerodynamic characteristics were measured in Ref. 52 and computed in Ref. 22 for $M_\infty = 2.9$.

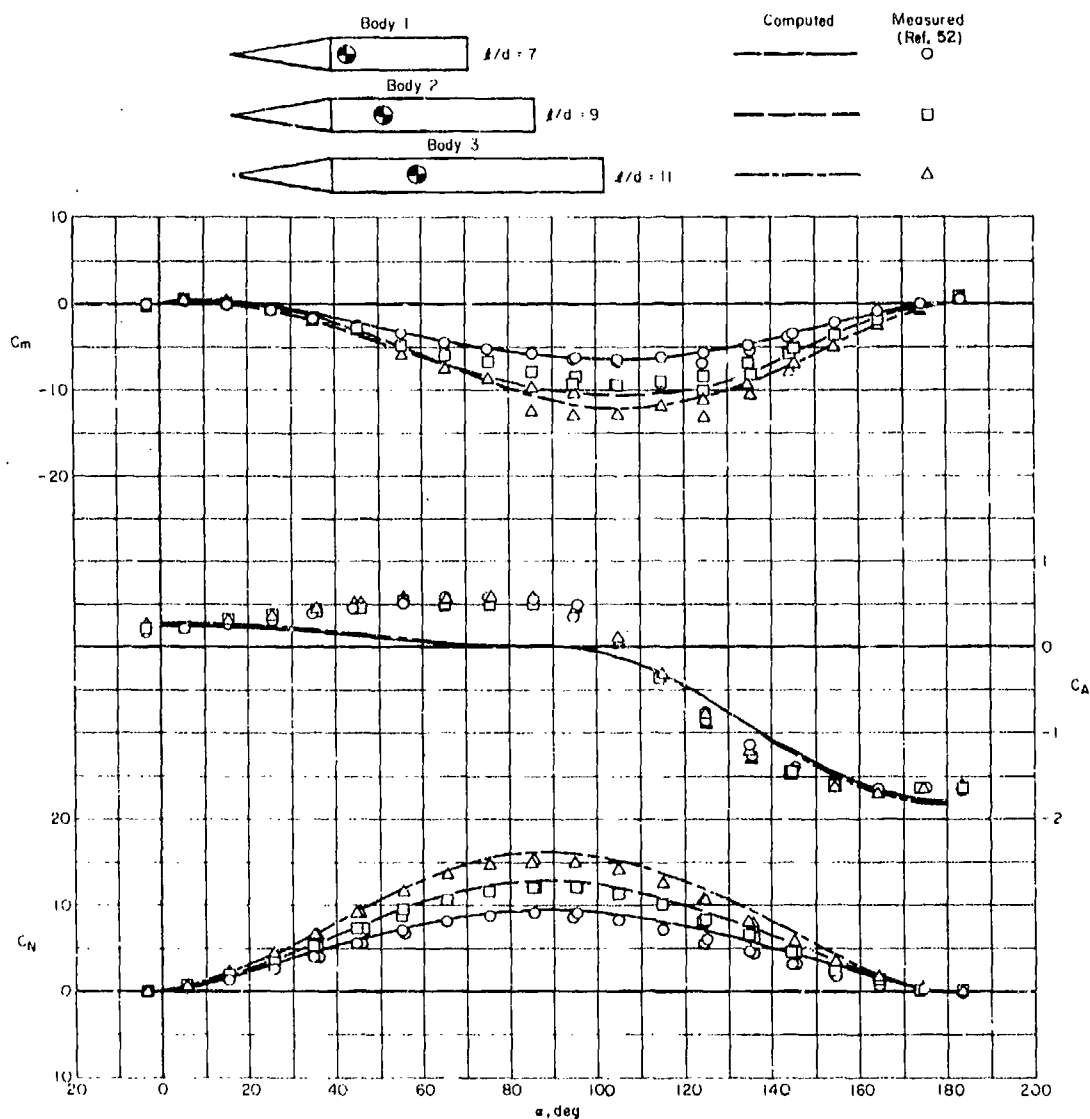


Fig. 9. Comparison of computed with measured aerodynamic characteristics for cylindrical bodies with conical noses of fineness ratio 3; $M_\infty = 2.9$.

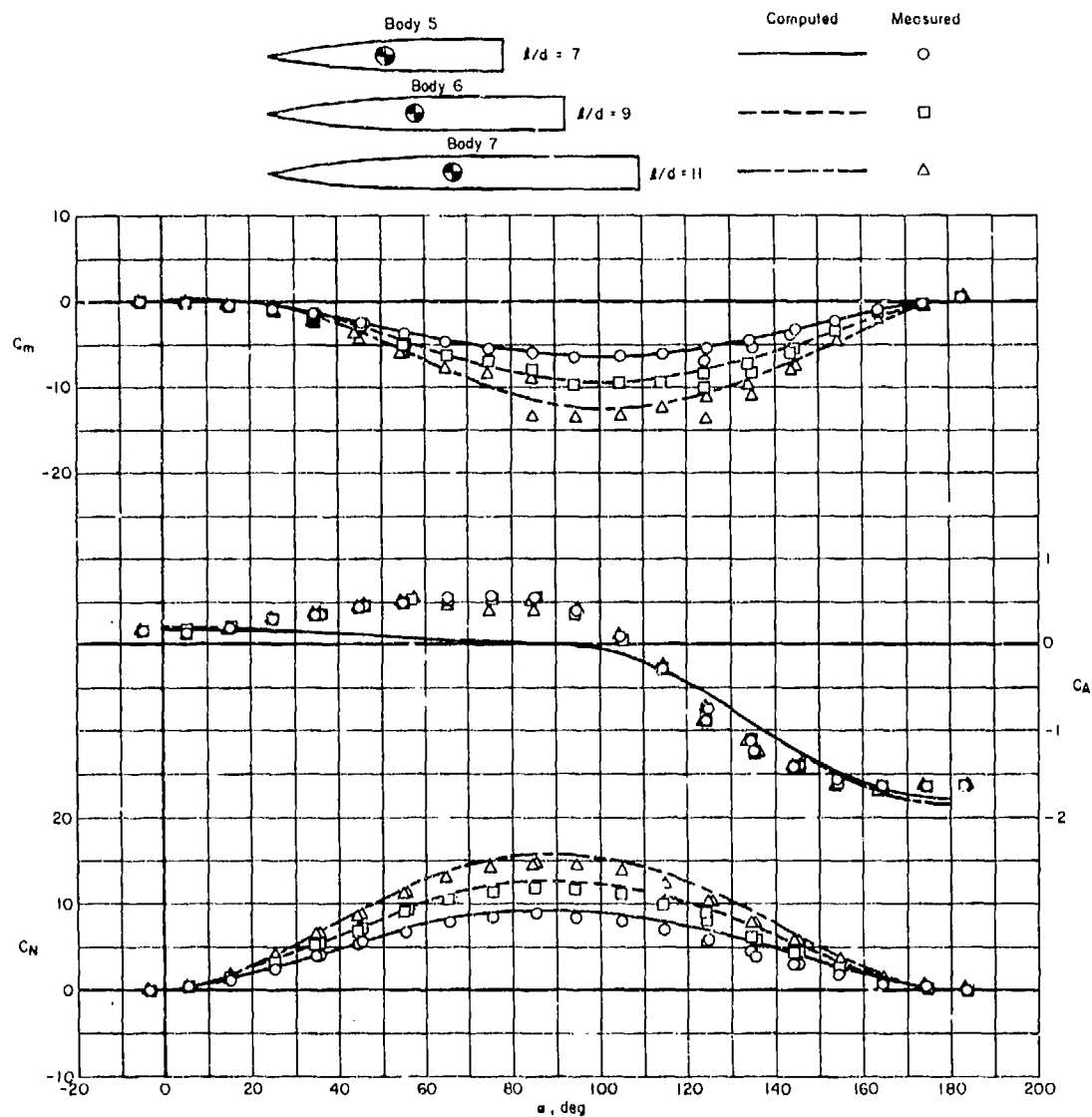


Fig. 10. Comparison of computed with measured aerodynamic characteristics for cylindrical bodies with ogival noses of fineness ratio 5; $M_\infty = 2.9$.

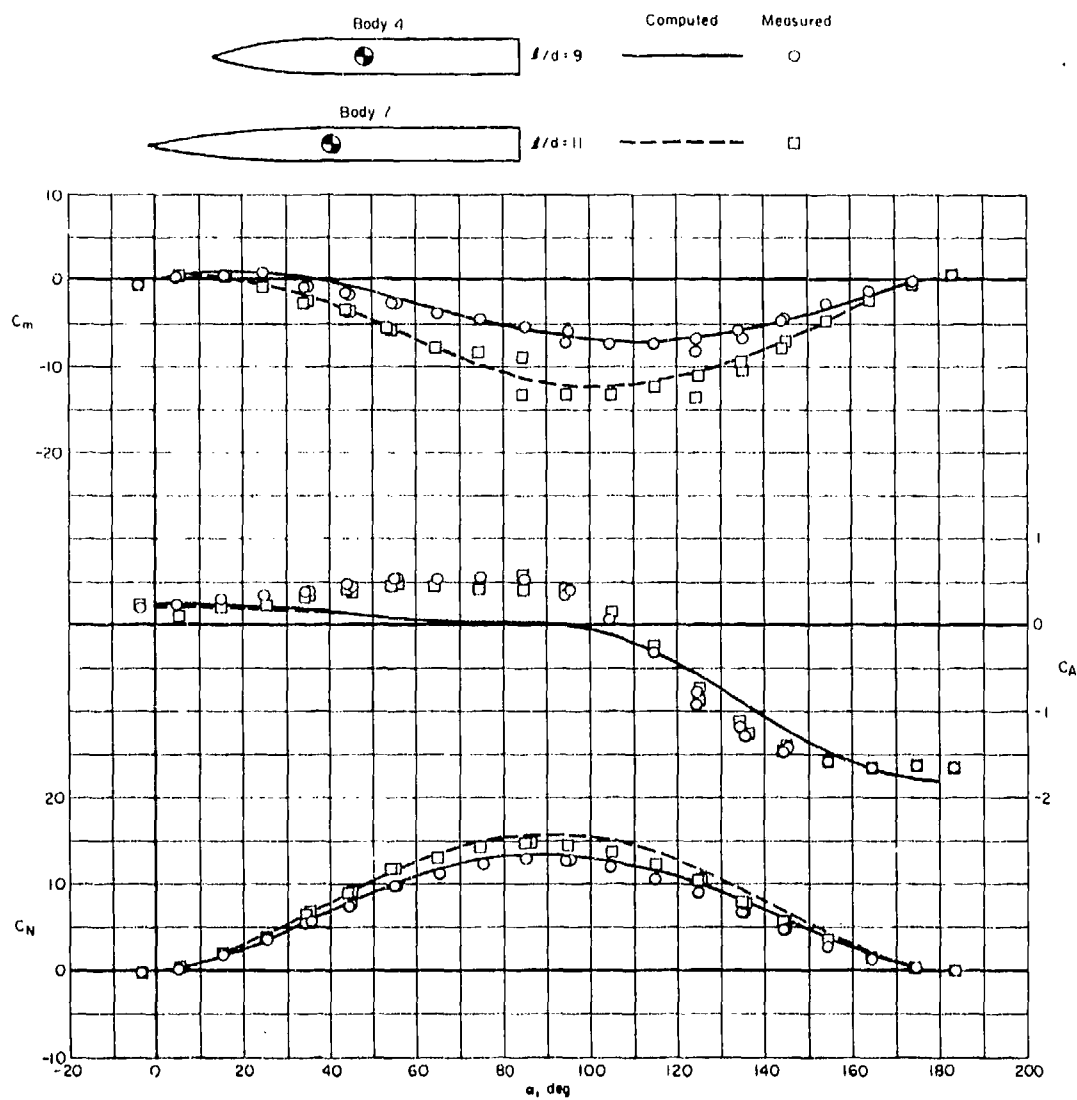


Fig. 11. Comparison of computed with measured aerodynamic characteristics for cylindrical bodies with ogival noses of fineness ratios 3 and 5; $M_\infty = 2.9$.

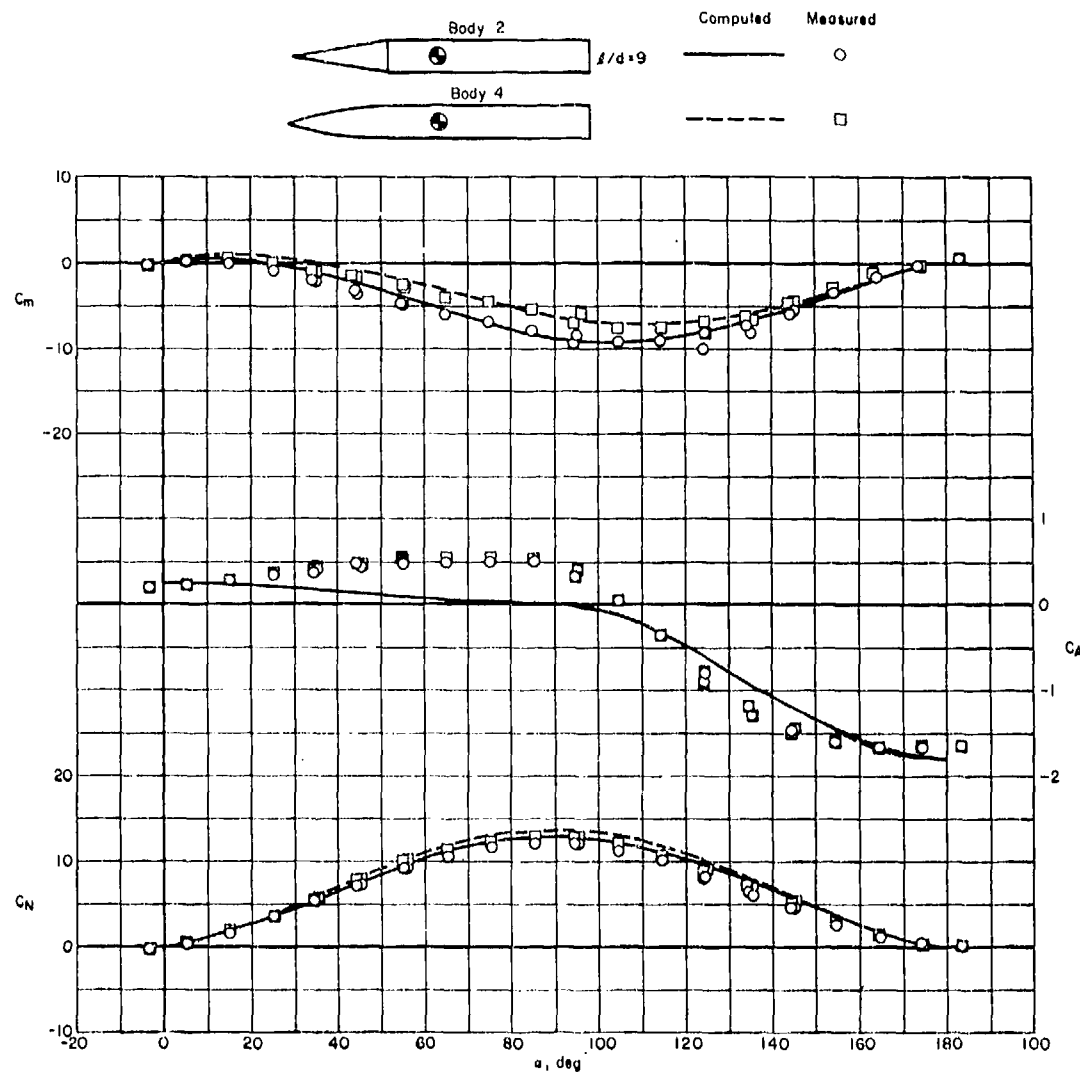


Fig. 12. Comparison of computed with measured aerodynamic characteristics for cylindrical bodies with conical and ogival noses of fineness ratio 3; $M_\infty = 2.9$.

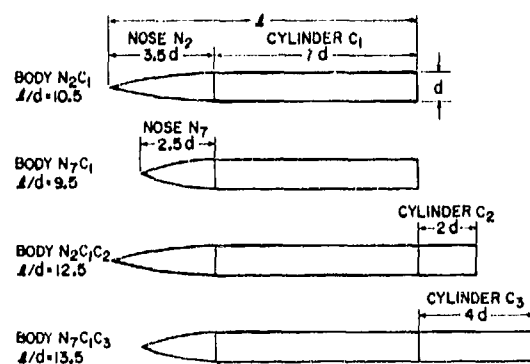


Fig. 13. Ogive-cylinder bodies for which the aerodynamic characteristics have been computed and measured for $0.6 \leq M_\infty \leq 2.0$.

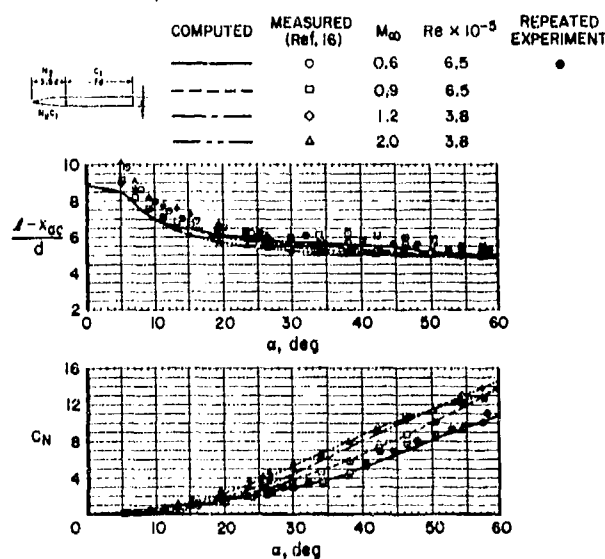


Fig. 14. Effect of Mach number on comparison of computed with measured aerodynamic characteristics for body N_2C_1 ; $0.6 \leq M_\infty \leq 2.0$.

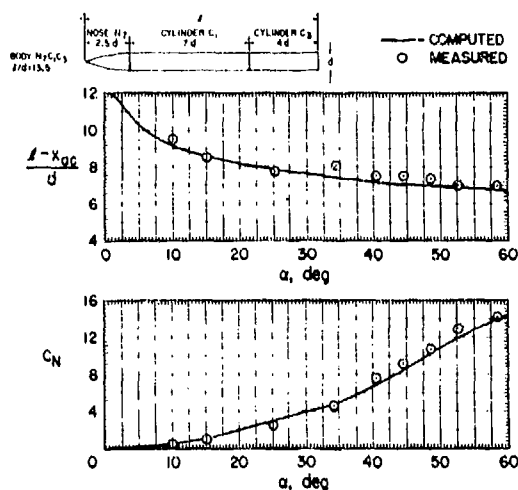
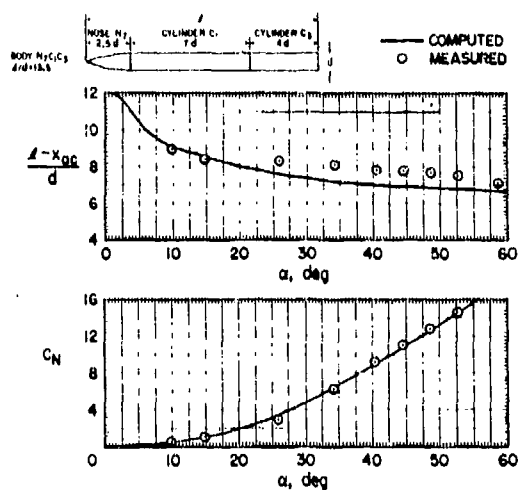
(a) $M_\infty = 0.6$.Fig. 15. Effect of Mach number on comparison of computed with measured aerodynamic characteristics for body $N_7C_1C_3$; $0.6 \leq M_\infty \leq 2.0$, $Re = 4.3 \times 10^5$.(b) $M_\infty = 0.9$.

Fig. 15. Continued.

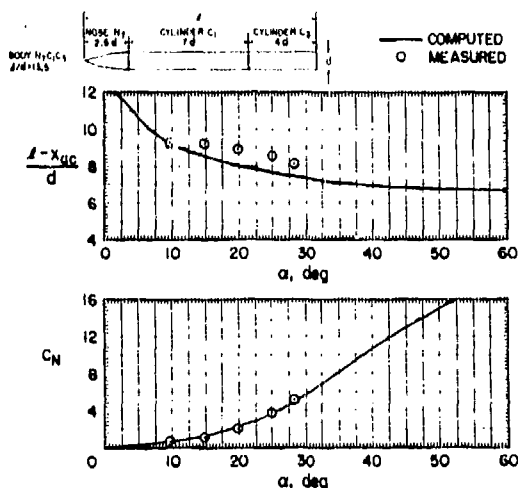
(c) $M_\infty = 1.2$.

Fig. 15. Continued.

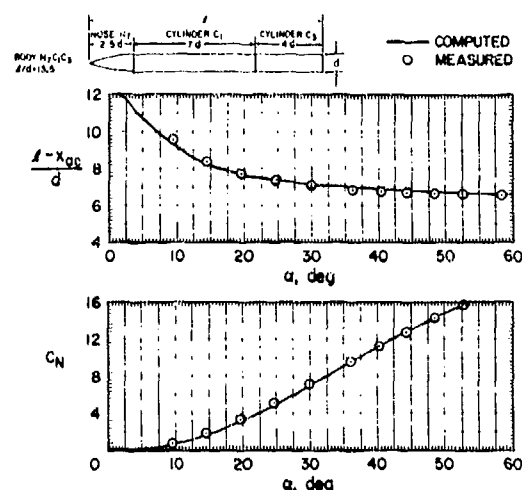
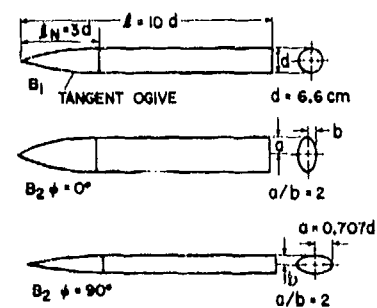
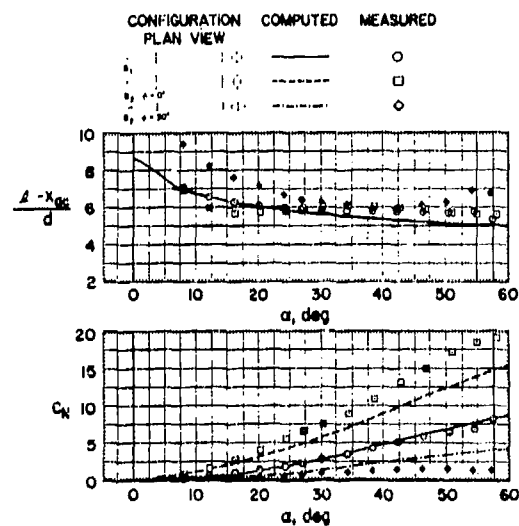
(d) $M_\infty = 2.0$.

Fig. 15. Concluded.

Fig. 16. Planform and end views of bodies of elliptic cross section for which the aerodynamic characteristics have been computed and measured for $0.6 \leq M_\infty \leq 2.0$.(a) $M_\infty = 0.6$, $Re = 6.5 \times 10^5$.Fig. 17. Comparison of computed with measured aerodynamic characteristics for bodies B_1 and B_2 ; $0.6 \leq M_\infty \leq 2.0$.

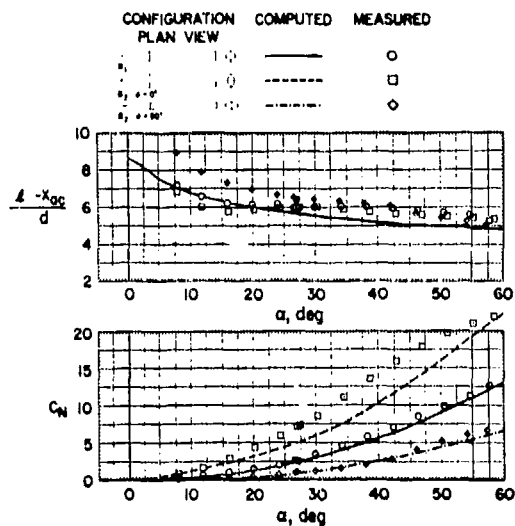
(b) $M_\infty = 0.9$, $Re = 6.5 \times 10^5$.

Fig. 17. Continued.

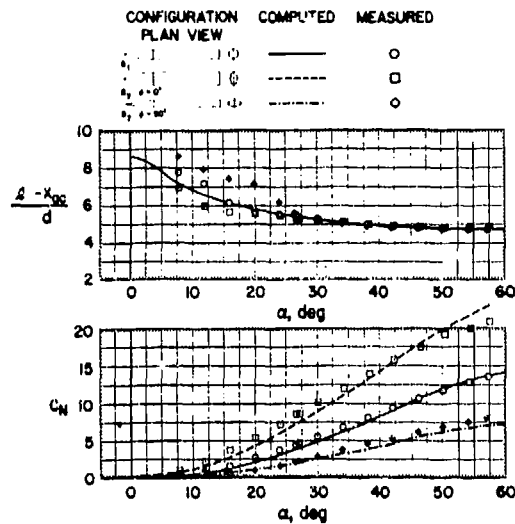
(d) $M_\infty = 1.5$, $Re = 3.8 \times 10^5$.

Fig. 17. Continued.

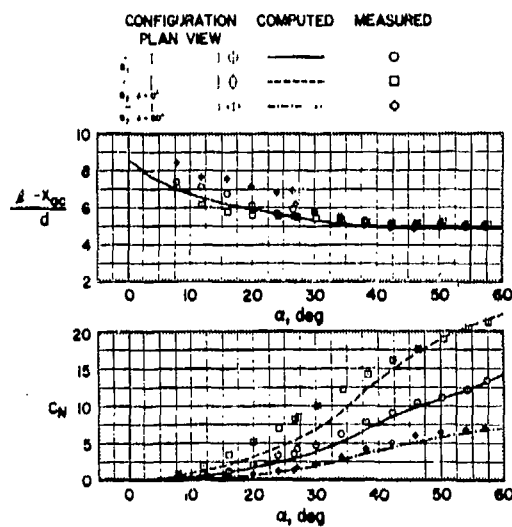
(c) $M_\infty = 1.2$, $Re = 3.8 \times 10^5$.

Fig. 17. Continued.

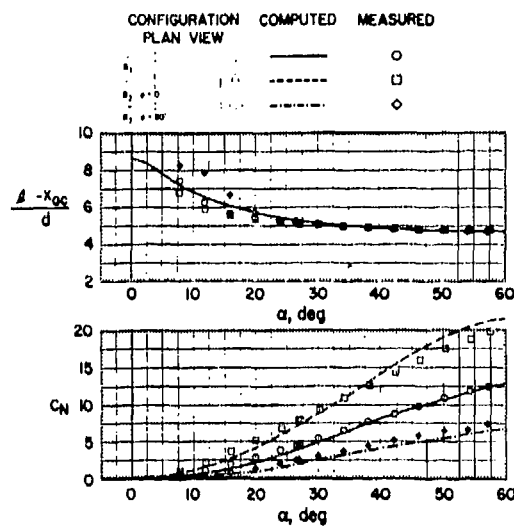
(e) $M_\infty = 2.0$, $Re = 3.8 \times 10^5$.

Fig. 17. Concluded.

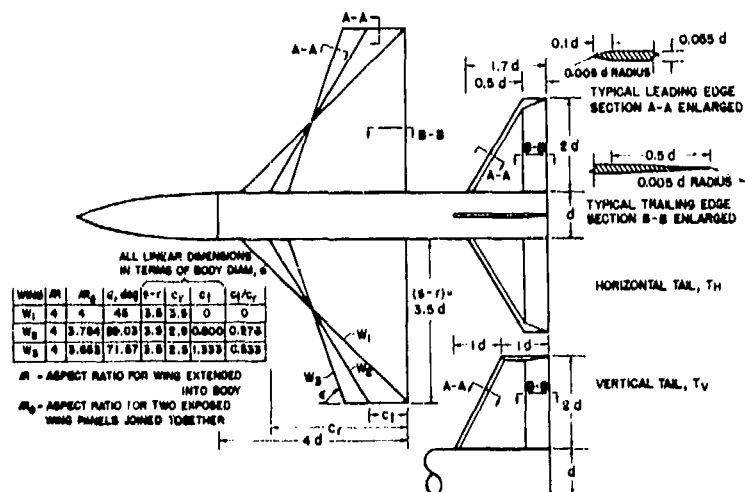
(a) Body B_1 with aspect-ratio 4 wings of various taper ratios and tail arrangement.

Fig. 18. Components for body-wing and body-wing-tail models tested in Refs. 20 and 21.

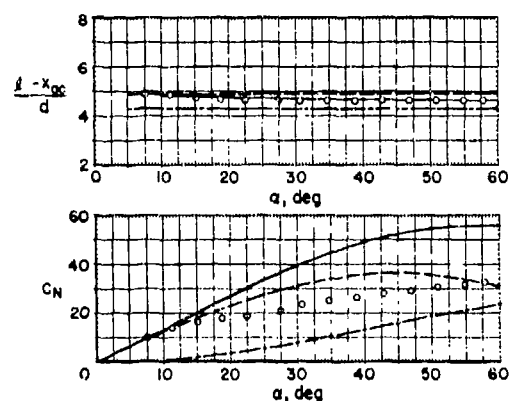
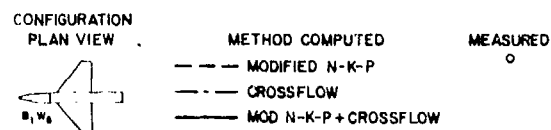
(a) $M_\infty = 0.6$, $Re = 4.3 \times 10^5$.

Fig. 19. Comparison of computed with measured aerodynamic characteristics for body-wing model B1W5.

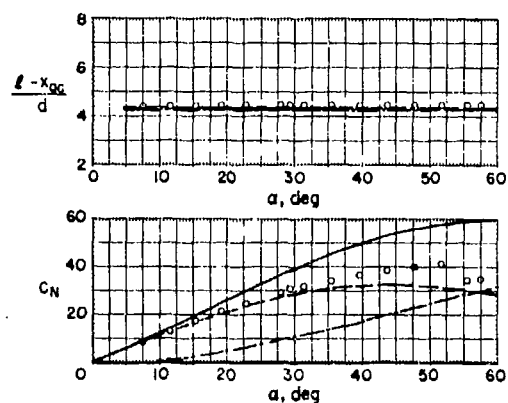
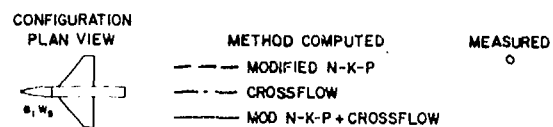
(c) $M_\infty = 1.5$, $Re = 3.8 \times 10^5$.

Fig. 19. Continued.

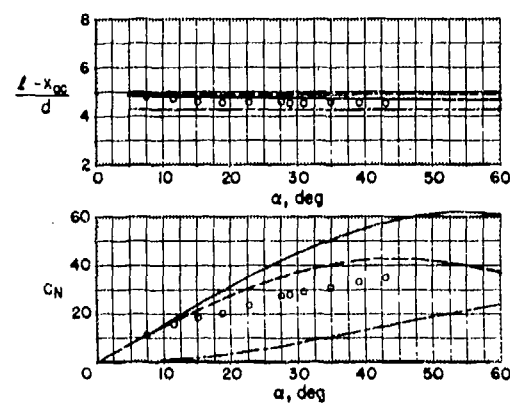
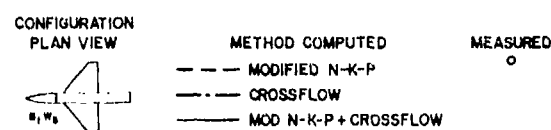
(b) $M_\infty = 0.9$, $Re = 4.3 \times 10^5$.

Fig. 19. Continued.

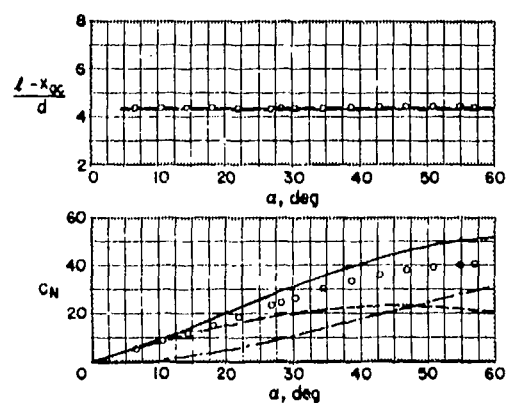
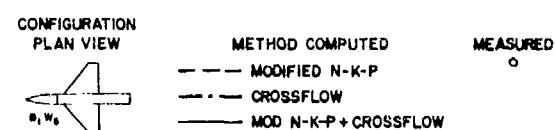
(d) $M_\infty = 2.0$, $Re = 3.8 \times 10^5$.

Fig. 19. Concluded.

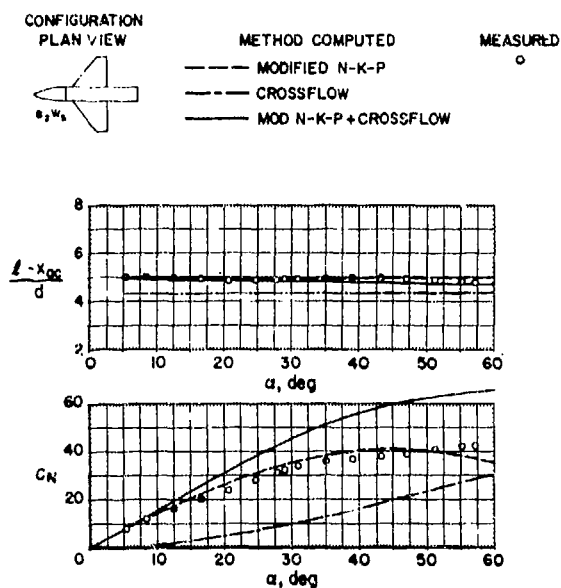
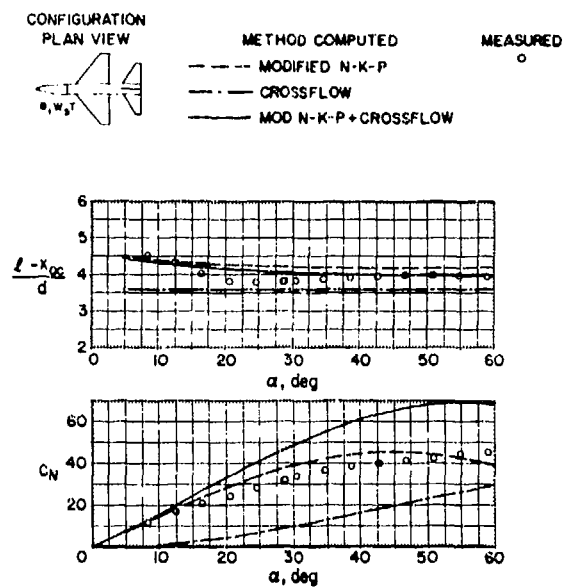
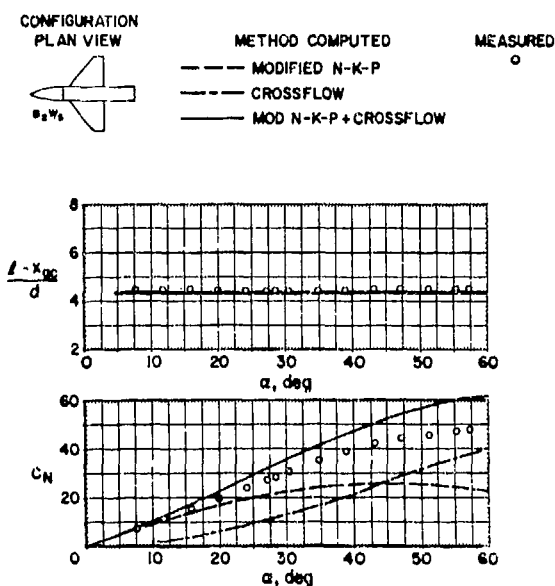
(a) $M_\infty = 0.6$, $Re = 4.3 \times 10^5$.Fig. 20. Comparison of computed with measured aerodynamic characteristics for body-wing model B_2W_5 .(a) $M_\infty = 0.6$, $Re = 4.3 \times 10^5$.Fig. 21. Comparison of computed with measured aerodynamic characteristics for body-wing-tail model B_1W_5T .(b) $M_\infty = 2.0$, $Re = 3.8 \times 10^5$.

Fig. 20. Concluded.

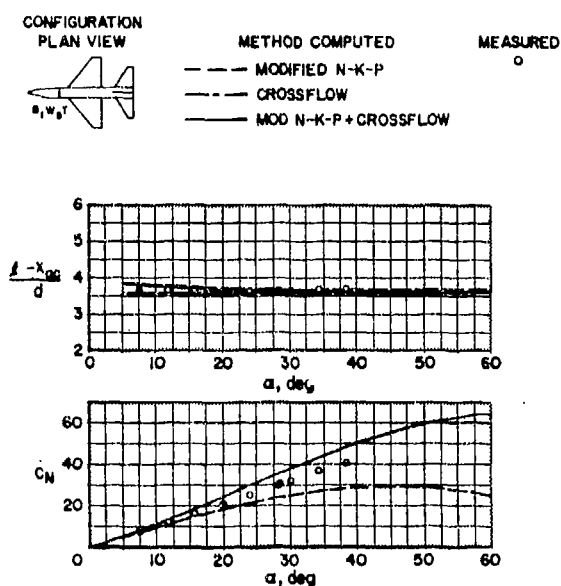
(b) $M_\infty = 2.0$, $Re = 3.8 \times 10^5$.

Fig. 21. Concluded.

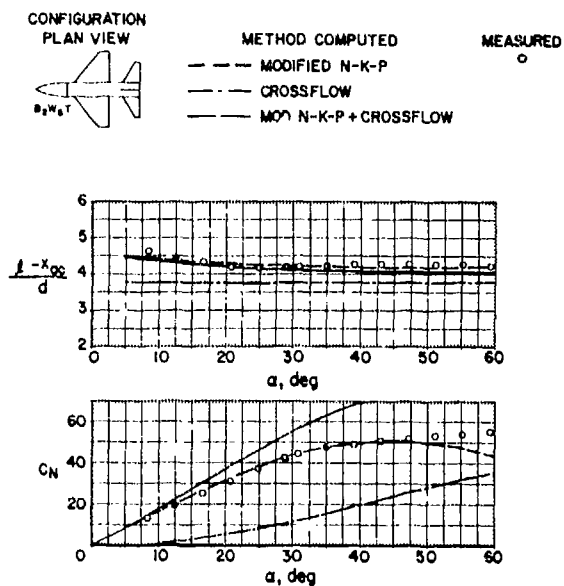
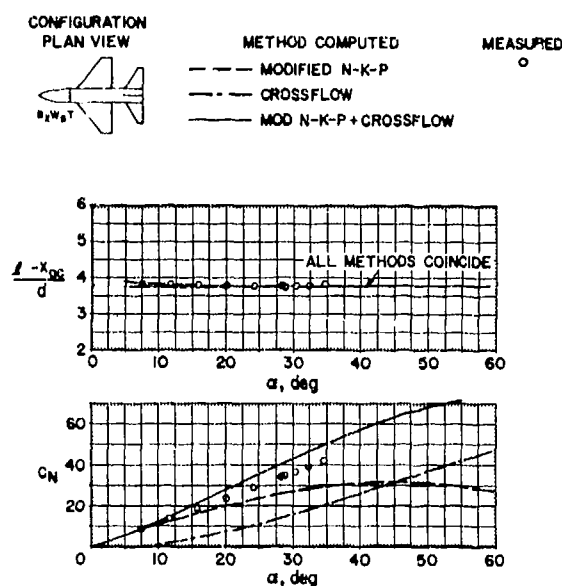
(a) $M_\infty = 0.6$, $Re = 4.3 \times 10^5$.Fig. 22. Comparison of computed with measured aerodynamic characteristics for body-wing-tail model B_2W_5T .(b) $M_\infty = 2.0$, $Re = 3.8 \times 10^5$.

Fig. 22. Concluded.

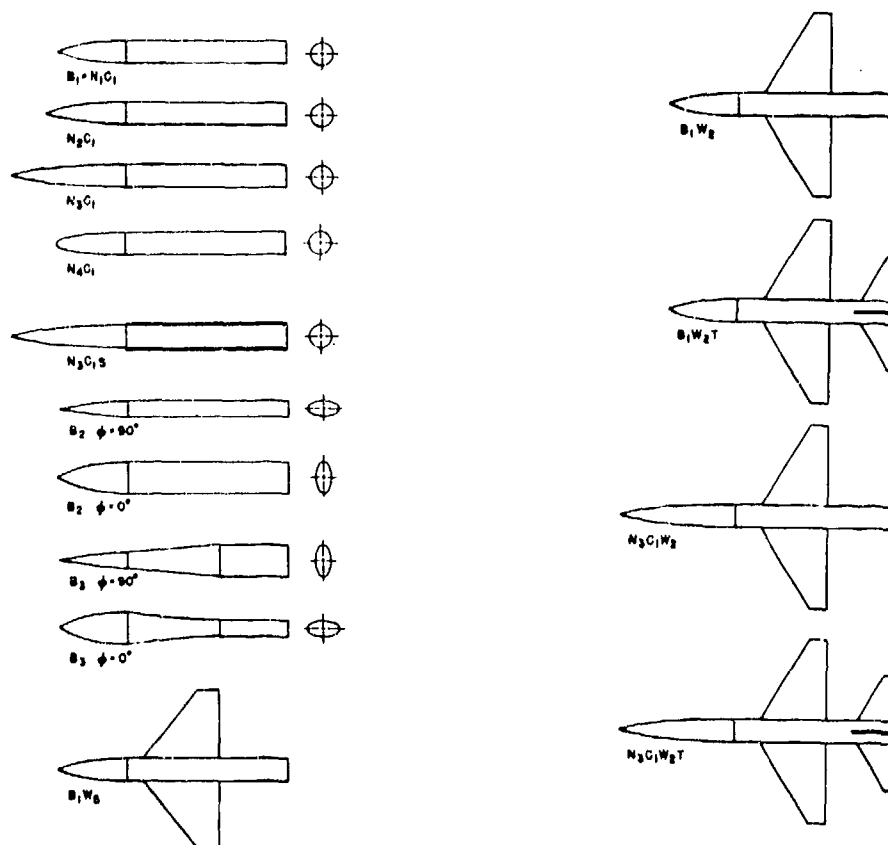


Fig. 23. Plan-view sketches of configurations used for vapor-screen and oil-flow studies in Ref. 22 and present side-force study.

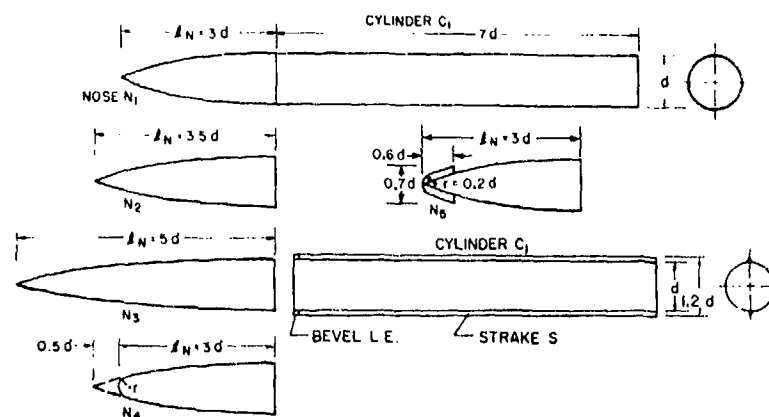


Fig. 24. Additional tangent ogive noses and strake for modification of body B_1 .

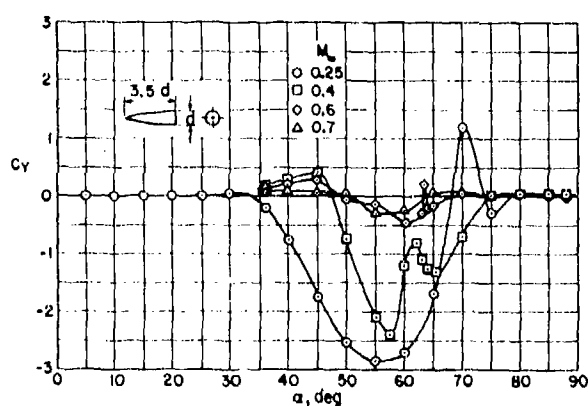
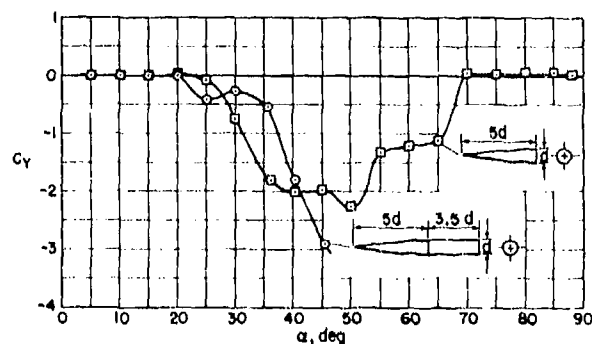


Fig. 25. Effect of Mach number on side-force coefficient for a tangent-ogive nose of $l_N/d = 3.5$ at $Re = 0.8 \times 10^6$; data from Ref. 72.



(a) $M_\infty = 0.25$, $Re = 0.8 \times 10^6$; data from Ref. 73.

Fig. 27. Effect of afterbody on side-force coefficient for ogive-cylinder bodies of revolution; data from Refs. 63, 72, and 73.

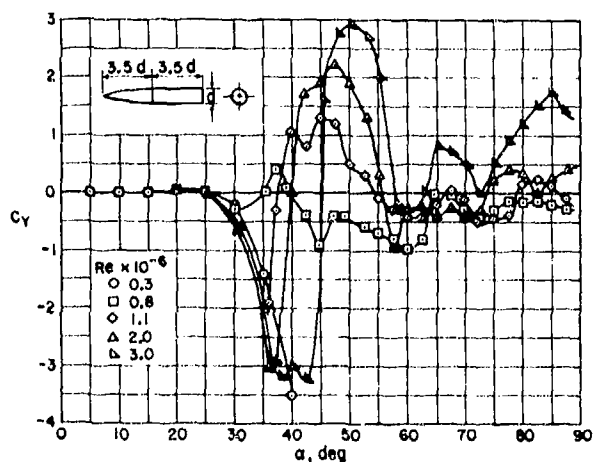
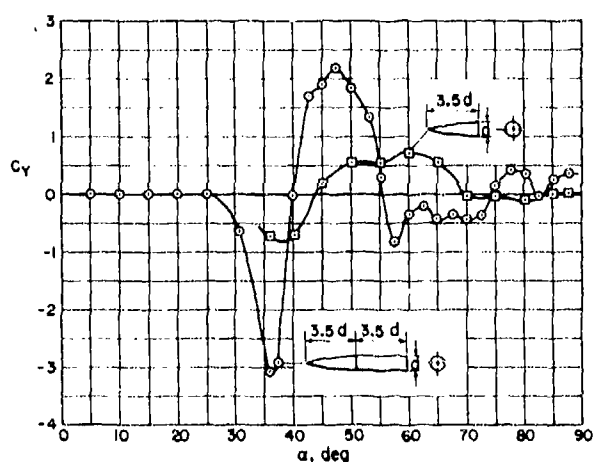


Fig. 26. Effect of Reynolds number on side-force coefficient for an ogive-cylinder body of revolution at $M_\infty = 0.25$; data from Ref. 72.



(b) $M_\infty = 0.25$, $Re = 2.0 \times 10^6$; data from Ref. 72.

Fig. 27. Continued.

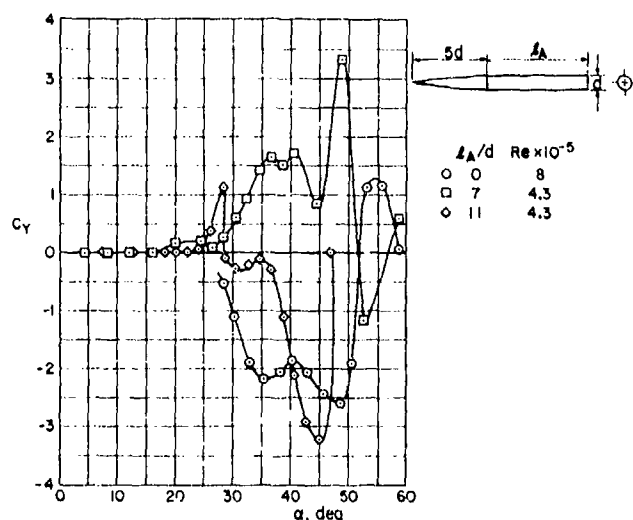
(c) $M_\infty = 0.6$; data from Ref. 63.

Fig. 27. Concluded.

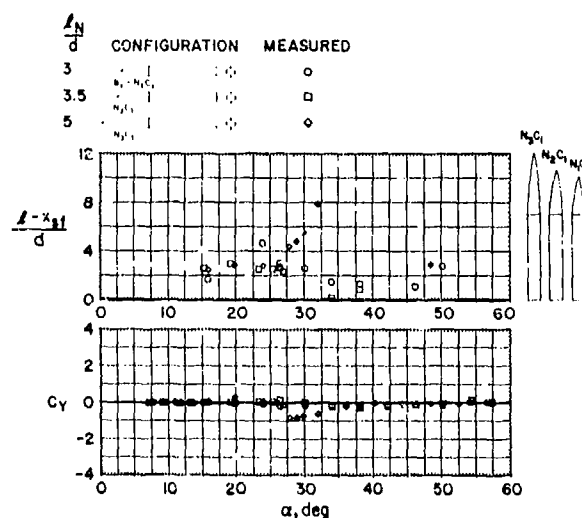
(c) $M_\infty = 1.2$, $Re = 3.8 \times 10^5$.

Fig. 28. Concluded.

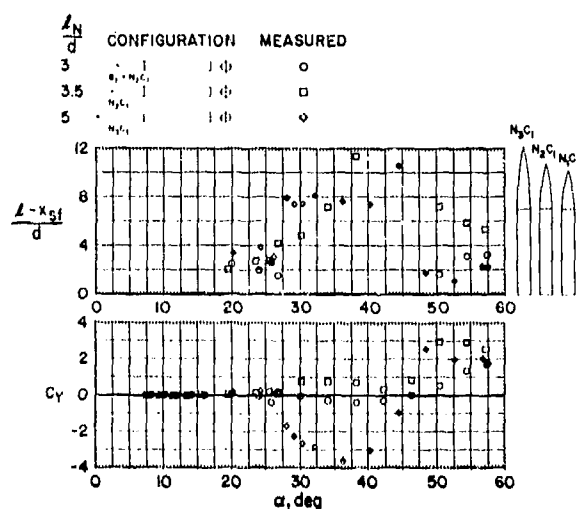
(a) $M_\infty = 0.6$, $Re = 4.3 \times 10^5$.

Fig. 28. Effect of nose fineness ratio on side-force coefficient and side-force position for ogive-cylinder bodies of revolution.

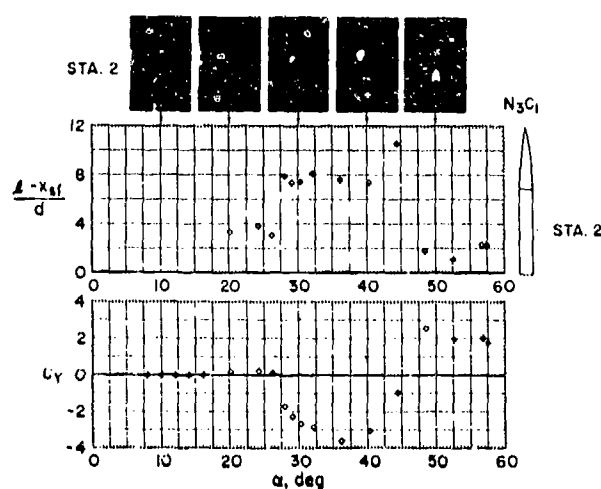
(a) $M_\infty = 0.6$, $Re = 4.3 \times 10^5$.

Fig. 29. Side-force coefficients, side-force positions, and vapor-screen photographs for ogive-cylinder body of revolution with fineness-ratio-5 nose.

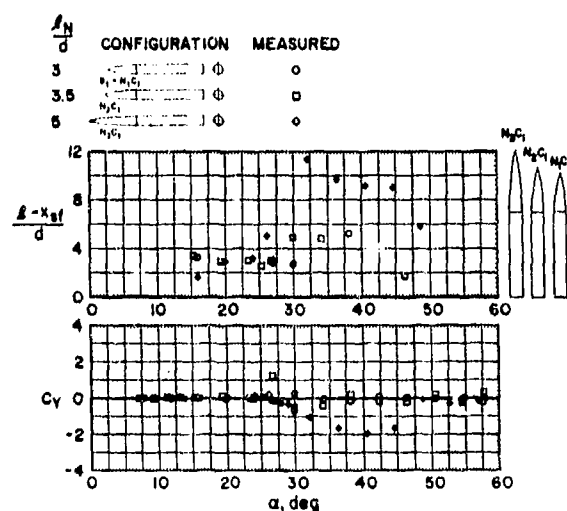
(b) $M_\infty = 0.9$, $Re = 6.5 \times 10^5$.

Fig. 28. Continued.

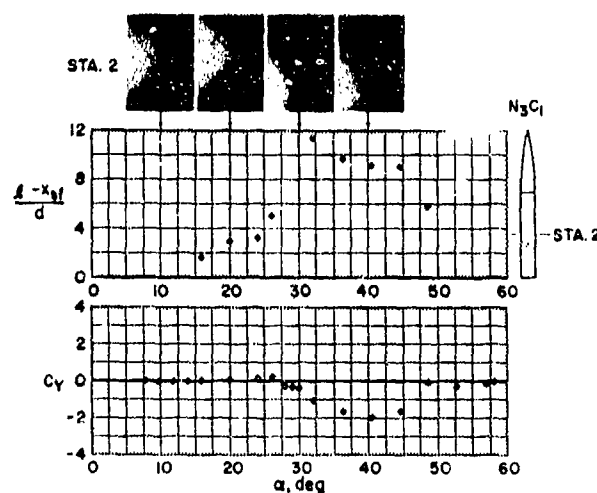
(b) $M_\infty = 0.9$, $Re = 6.5 \times 10^5$.

Fig. 29. Concluded.

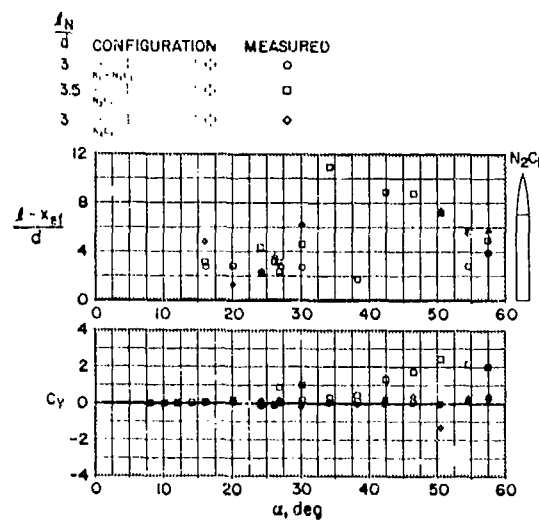
(a) $M_\infty = 0.6$, $Re = 6.5 \times 10^5$.

Fig. 30. Effect of nose-tip rounding on side-force coefficient and side-force position for an ogive-cylinder body of revolution.

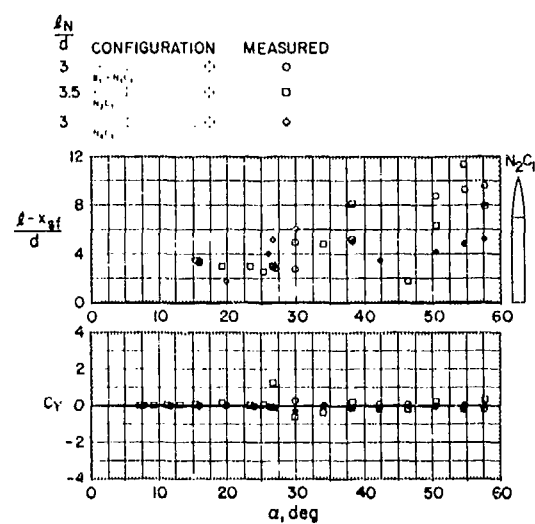
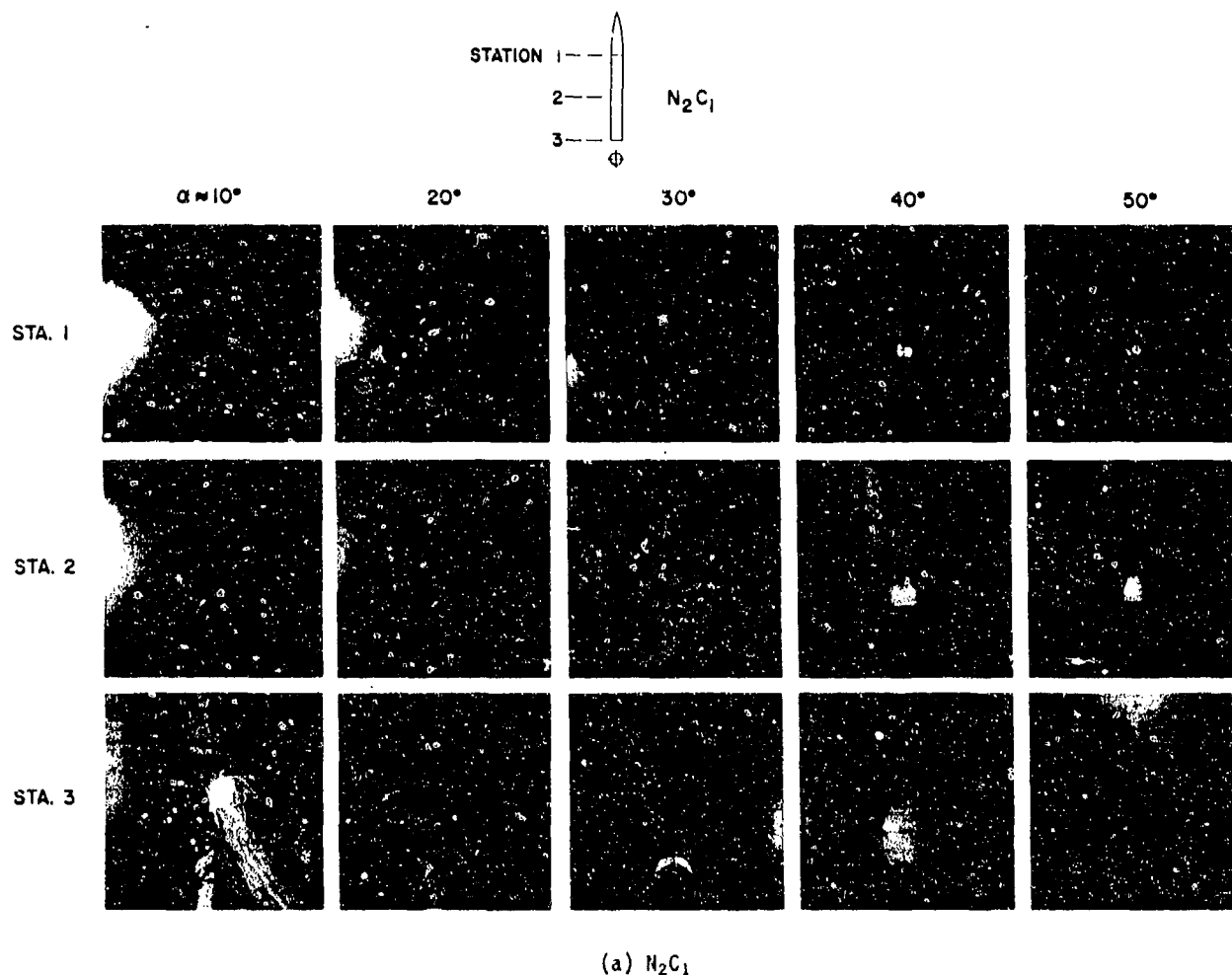
(b) $M_\infty = 0.9$, $Re = 6.5 \times 10^5$.

Fig. 30. Concluded.

(a) N_2C_1 Fig. 31. Vapor-screen photographs for N_2C_1 (body with fineness-ratio-3.5 nose) and N_4C_1 (body with blunt nose of fineness-ratio 3) at $M_\infty = 0.6$; $Re = 4.3 \times 10^5$.

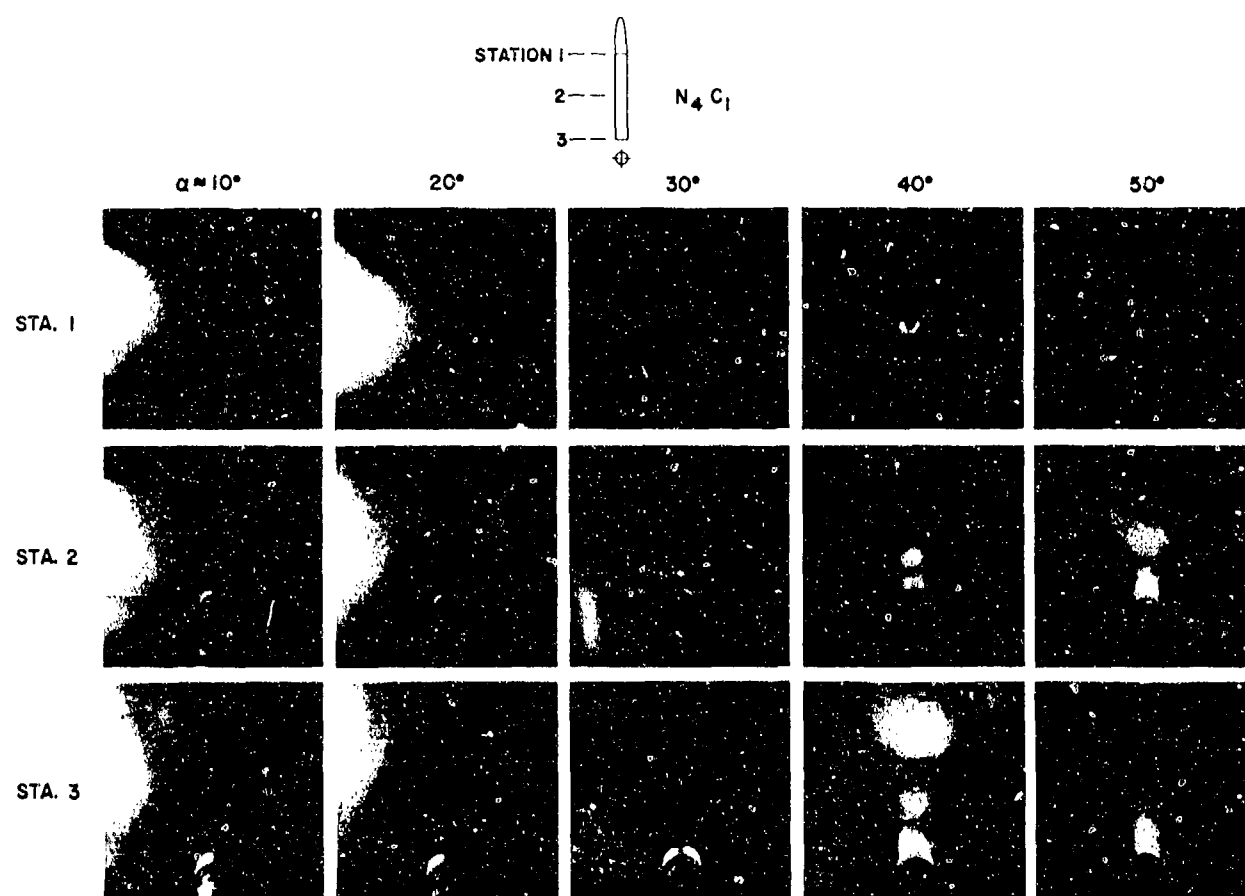
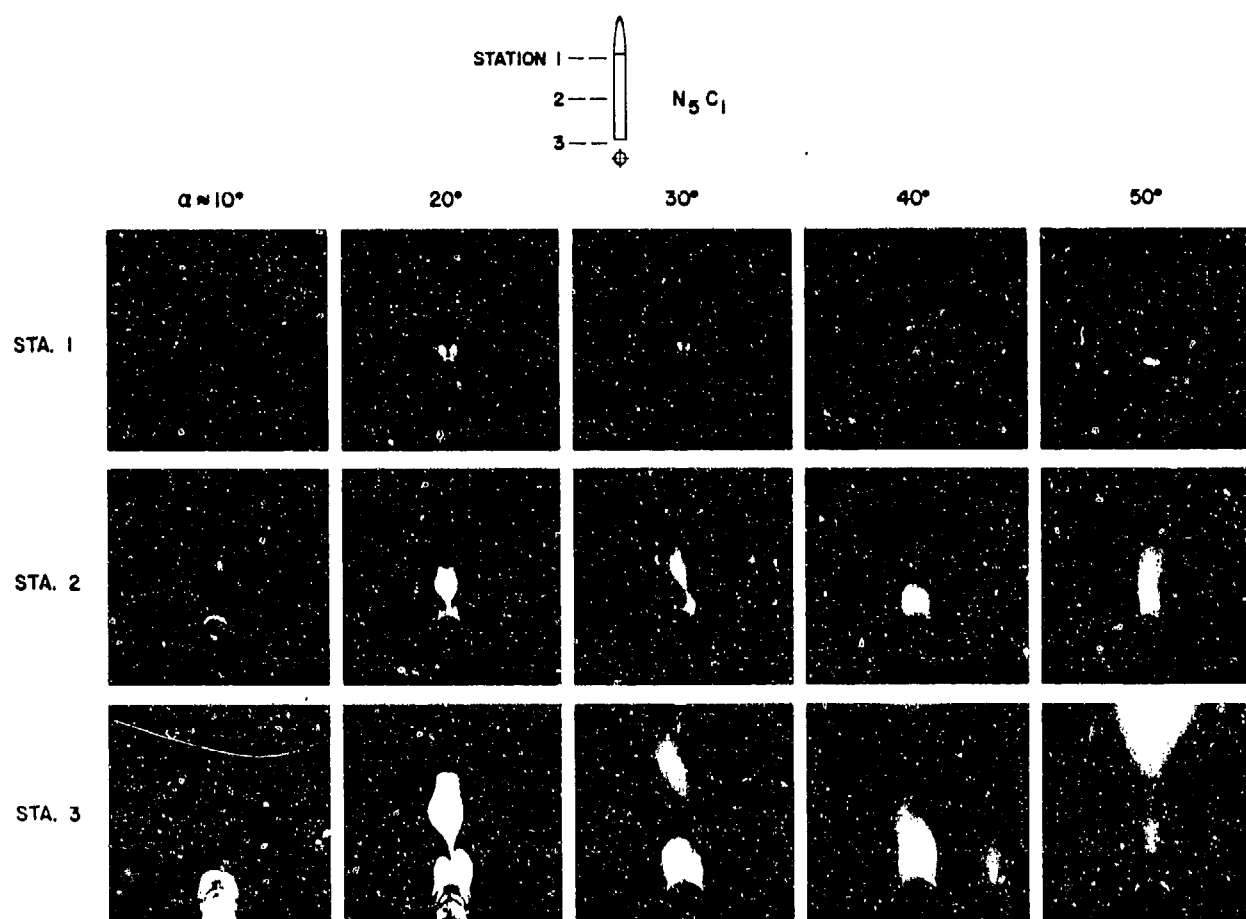
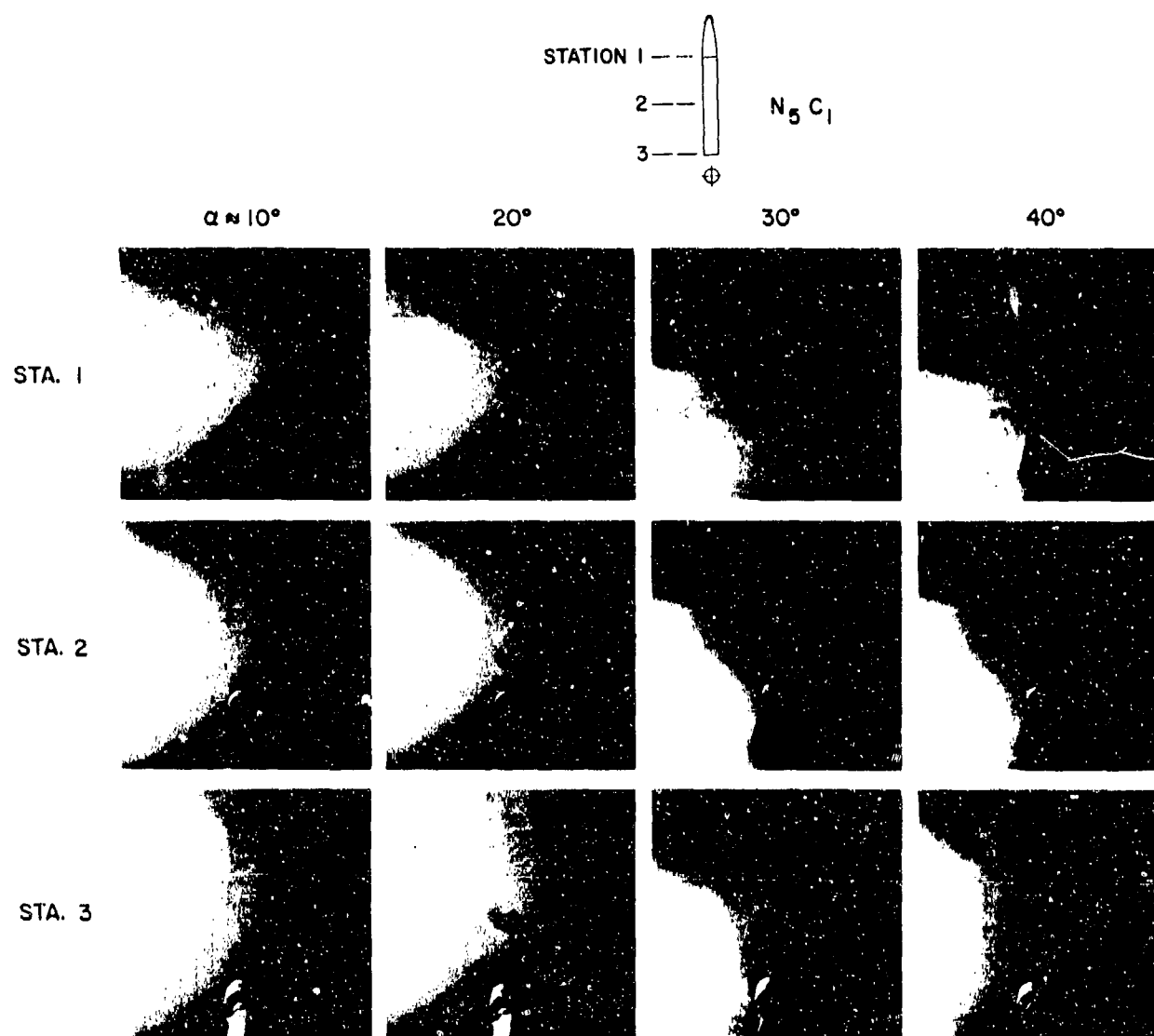
(b) $N_4 C_1$.

Fig. 31. Concluded.



(a) $M_\infty = 0.6$.

Fig. 32. Vapor-screen photographs for $N_5 C_1$ (body with fineness-ratio-3 nose with tip strakes); $Re = 4.3 \times 10^5$.



(b) $M_\infty = 0.9$.

Fig. 32. Concluded.

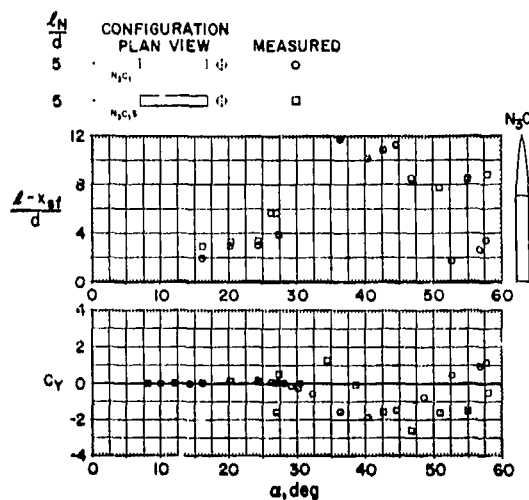
(a) $M_\infty = 0.6$, $Re = 6.5 \times 10^5$.

Fig. 33. Effect of afterbody side strakes on side-force coefficient and side-force position for an ogive-cylinder body of revolution with a fineness-ratio-5 nose.

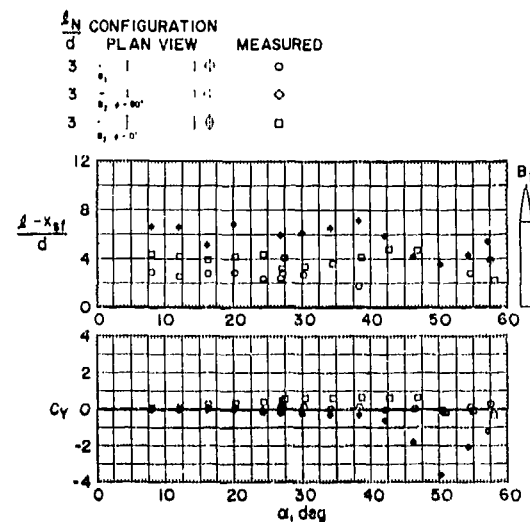
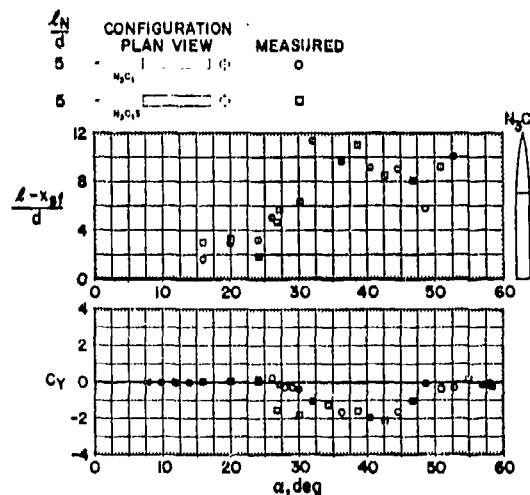
(a) $M_\infty = 0.6$, $Re = 6.5 \times 10^5$.Fig. 34. Effect of elliptic cross section and roll angle on side-force coefficient and side-force position (elliptic body of constant a/b).(b) $M_\infty = 0.9$, $Re = 6.5 \times 10^5$.

Fig. 33. Concluded.

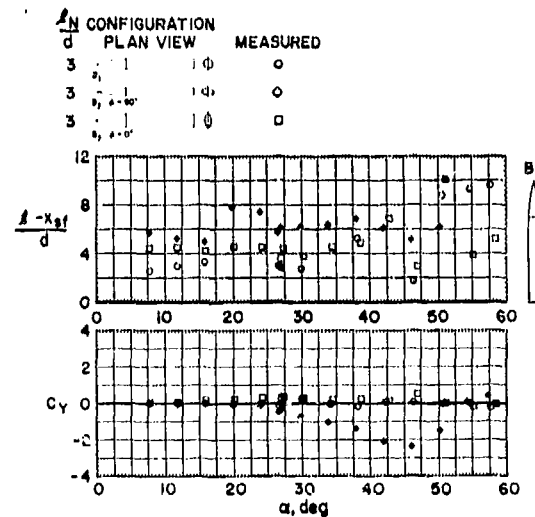
(b) $M_\infty = 0.9$, $Re = 6.5 \times 10^5$.

Fig. 34. Concluded.

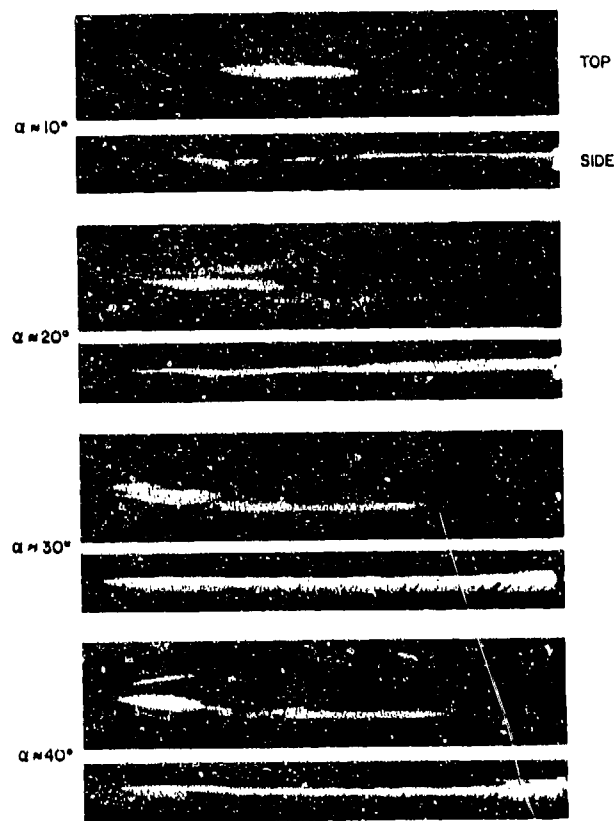
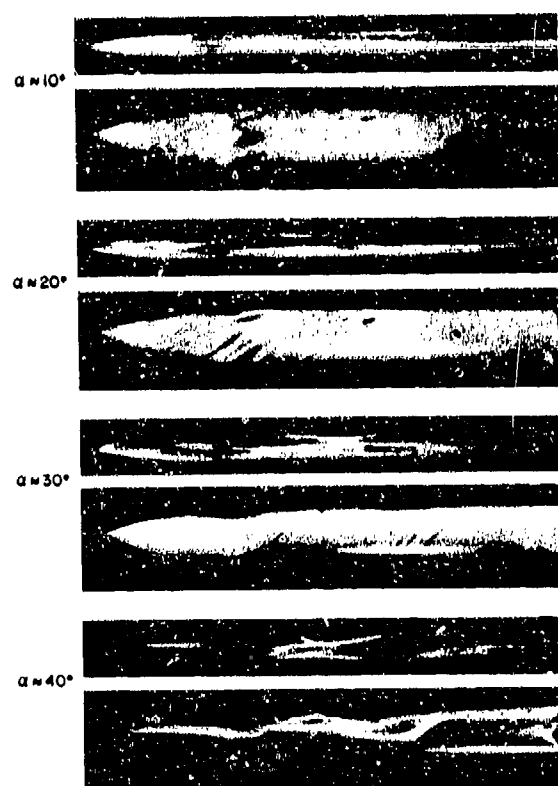
(a) $\phi = 0^\circ$.Fig. 35. Oil-flow photographs for B_2 (body with constant $a/b = 2$) at $M_\infty = 0.9$; $Re = 4.3 \times 10^5$.(b) $\phi = 90^\circ$.

Fig. 35. Concluded.

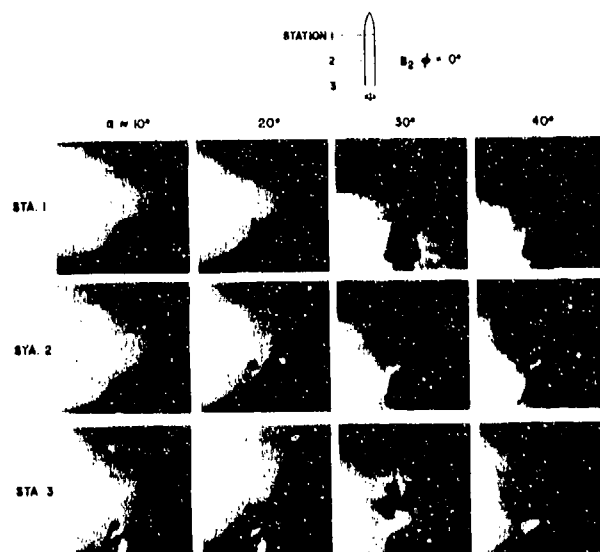
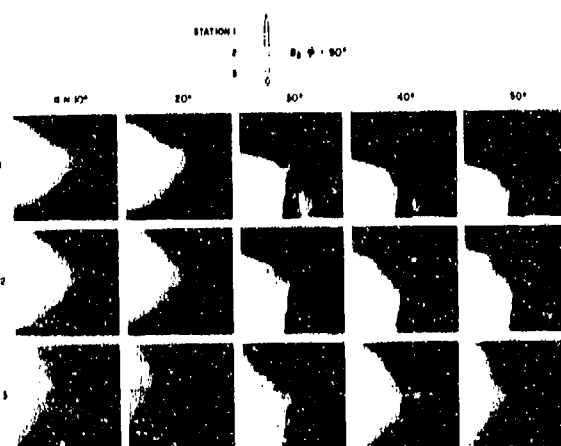
(a) $\phi = 0^\circ$.Fig. 36. Vapor-screen photographs for B_2 (body with constant $a/b = 2$) at $M_\infty = 0.9$; $Re = 4.3 \times 10^5$.(b) $\phi = 90^\circ$.

Fig. 36. Concluded.

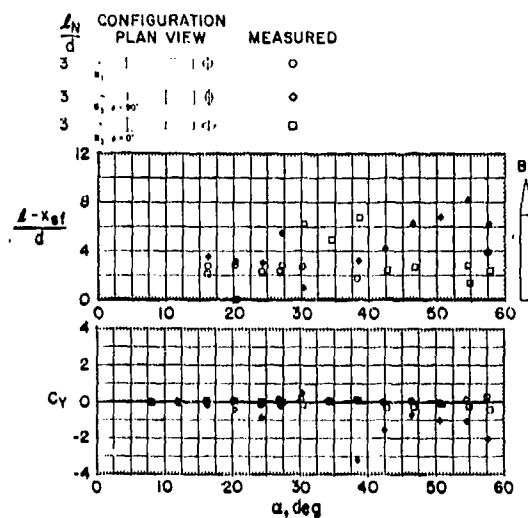
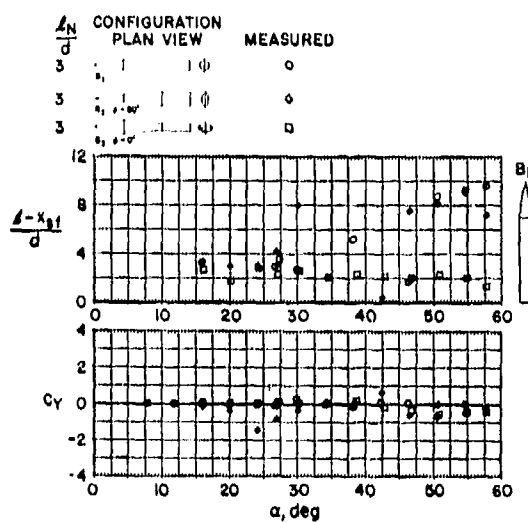
(a) $M_\infty = 0.6$, $Re = 6.5 \times 10^5$.Fig. 37. Effect of elliptic cross section and roll angle on side-force coefficient and side-force position (elliptic body of variable a/b).(b) $M_\infty = 0.9$, $Re = 6.5 \times 10^5$.

Fig. 37. Concluded.

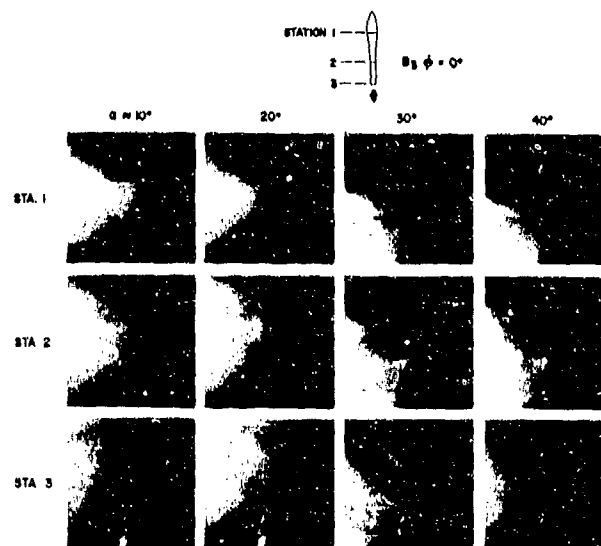
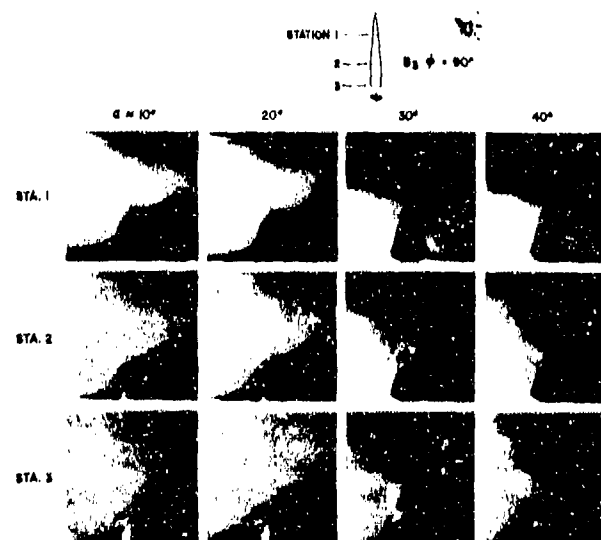
(a) $\phi = 0^\circ$.Fig. 38. Vapor-screen photographs for B_3 (body with variable a/b cross sections) at $M_\infty = 0.9$; $Re = 4.3 \times 10^5$.(b) $\phi = 90^\circ$.

Fig. 38. Concluded.

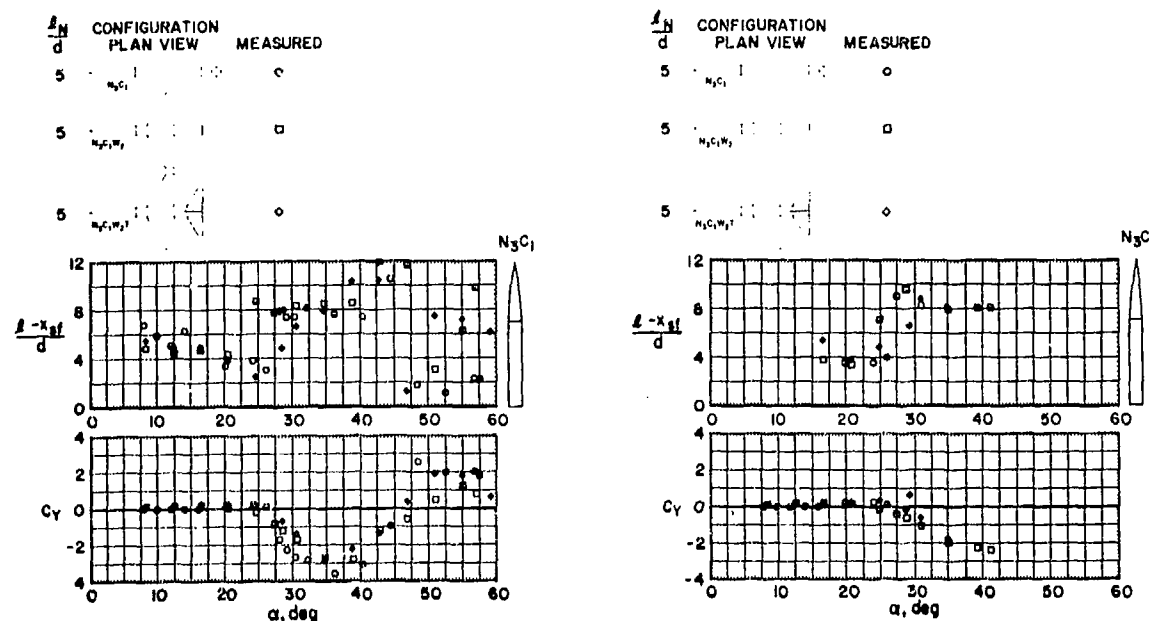


Fig. 39. Effects on side-force coefficient and side-force position of adding a wing and a wing plus tail to a body.

Fig. 39. Concluded.

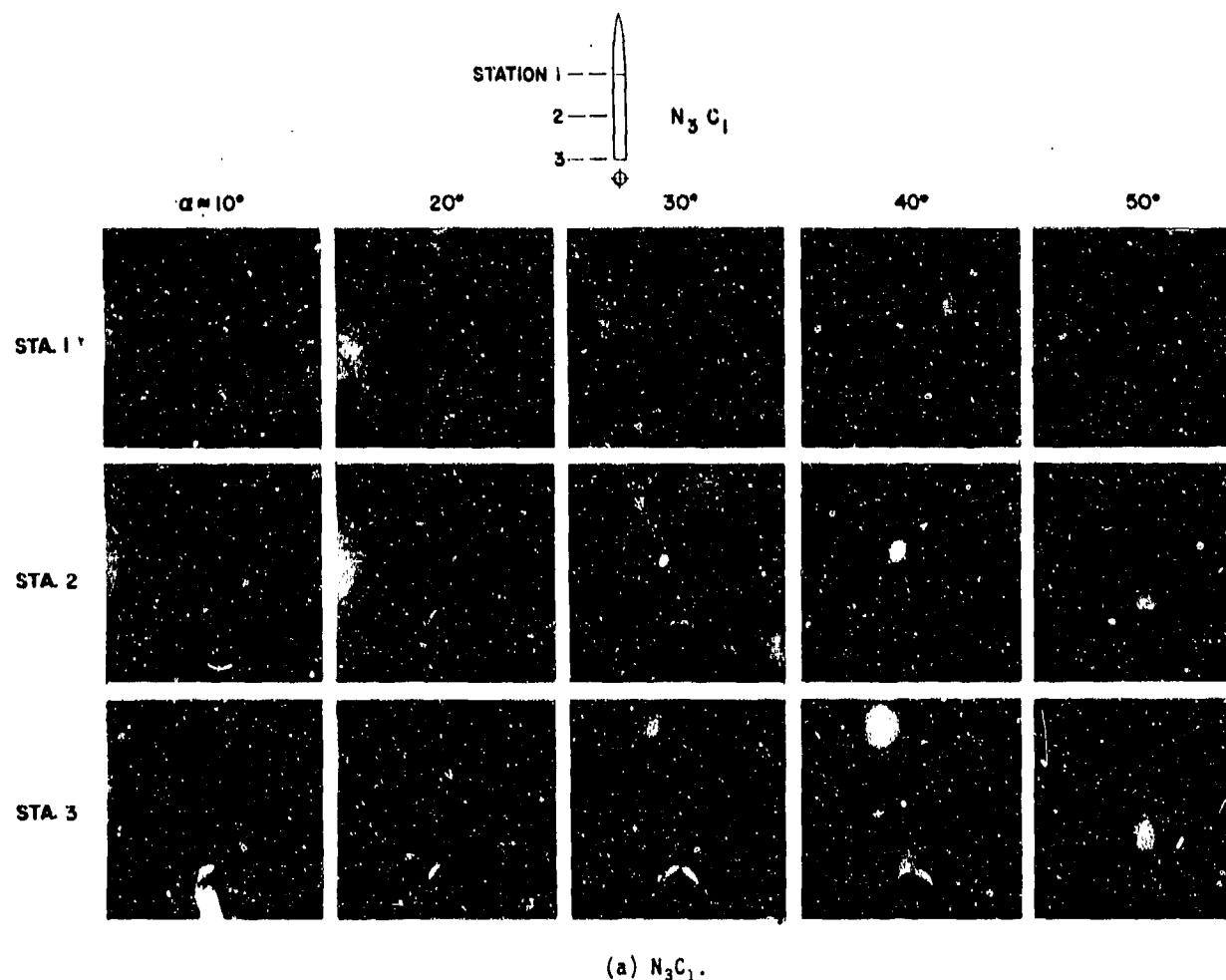


Fig. 40. Vapor-screen photographs for N_3C_1 (body with fineness-ratio-5 nose) and $N_3C_1W_2T$ (body with fineness-ratio-5 nose, aspect-ratio-4 wing, and tail) at $M_\infty = 0.6$; $Re = 4.3 \times 10^5$.

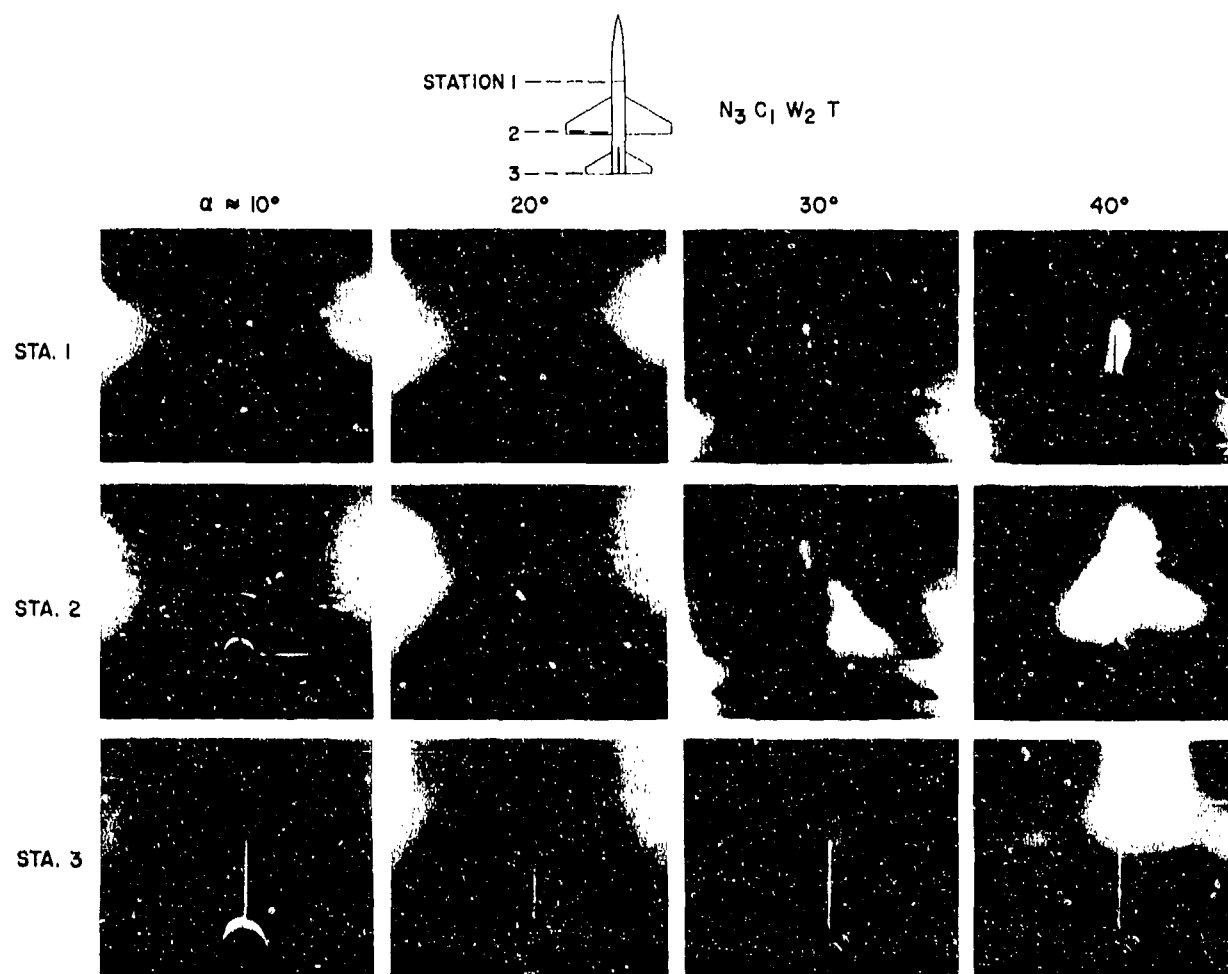
(b) $N_3 C_1 W_2 T$.

Fig. 40. Concluded.

PREDICTION OF LATERAL AERODYNAMIC LOADS ON AIRCRAFT AT HIGH ANGLES OF ATTACK

S. B. Spangler, S. C. Perkins, Jr., and M. R. Mendenhall
 Nielsen Engineering & Research, Inc.
 510 Clyde Avenue, Mountain View, CA 94043 USA

SUMMARY

Engineering methods have been developed to predict the lateral loads on high speed fighter-bomber configurations at high angles of attack and small angles of sideslip. The configurations of interest are characterized by slender pointed noses that generate asymmetric separation vortices at angles of attack in the 25 to 45 degree range. The methods consist of a nose vortex shedding flow model, a vortex lattice wing/body/strake flow model, and a tail interference model. All are potential flow methods and have been applied at incompressible speeds. The methods account for noncircular nose cross sections, prediction of separation location on the nose and interaction between nose and strake vortices. Calculations have been made to compare the predicted results with measurements of vorticity distribution, velocities in the separated region, and forces on noncircular noses and forces and moments on complete aircraft configurations. The predicted results generally agree with the data, show the proper trends, and demonstrate the proper physical characteristics of the flow. More data comparisons and some work on separation location are required to achieve a satisfactory predictive method.

1. NOMENCLATURE

C_n	yawing moment coefficient, based on wing planform area extended to model centerline and span
C_p	pressure coefficient, $(p-p_\infty)/\frac{1}{2}\rho V^2$
C_Y	side force coefficient, based on nose base area for noses or wing planform area extended to model centerline for complete configurations
d_{eq}	equivalent diameter, diameter of a circle having same cross section area as noncircular cross section
M	free stream Mach number
p	static pressure
p_∞	free stream static pressure
Re	Reynolds number, based on free stream velocity and density
Re_D	Reynolds number, based on body diameter
s	distance along the body surface from the stagnation point, in the crossflow plane
s'	virtual origin of boundary layer
t	time, in the unsteady two dimensional flow
u, v, w	velocity components along x, y, z directions, respectively
u'	boundary layer velocity
u'_δ	boundary layer edge velocity
V	free stream velocity
x, y, z	coordinates fixed in aircraft, with origin at nose, x positive aft, y positive to starboard and z positive up
α	angle of attack
α_c	angle between the free stream velocity vector and the body axis
β	angle of sideslip
Γ	vortex strength
ρ	free stream density

2. INTRODUCTION

Theoretical work, supplemented by critical experimental work, has been done to develop analytical methods for predicting the static lateral aerodynamic characteristics of high speed fighter-bomber type aircraft at high angles of attack and small sideslip angles. The flight condition of concern is one of incipient spin departure and includes angles of attack from 25 to 45 degrees and sideslip angles up to 10 degrees. This flight regime and aircraft configurations are characterized by asymmetric vortex shedding from the aircraft nose, even at zero sideslip. The steady asymmetric vortex system passes aft over the wing, body, and tail to induce a side force and yawing moment on the configuration, which are a major source of aerodynamic loads producing spin departure motion.

A considerable amount of work has been done on aspects of this problem. To a great extent, the work falls into three categories. The first constitutes experimental programs to measure overall loads on complete configurations which are used as input to dynamical simulation of the motion of the aircraft. Typically little or no division of loads, pressure distributions or flow field data are obtained in these tests which would provide insight into the nature of the flow or detailed loading distribution on or about the configurations. The second constitutes experimental and analytical work on vortex shedding from inclined bodies of revolution, which has been motivated largely by problems associated with missile aerodynamics. Although no completely theoretical method has been developed to predict vortex shedding, loads, and flow fields of circular cross section bodies, considerable information is available and useful engineering methods exist to describe the features of the problem. The third constitutes classical vortex interference methods which have been developed and proven by experiment over the last 20 years or so for predicting nonlinear force and moment characteristics associated with wing/body/tail interference in aircraft and missiles.

The principal characteristic that dominates the high angle fighter-bomber problem is the noncircular cross section nose. It was recognized a number of years ago (for example, ref. 1) that asymmetric vortex shedding from the nose at high angles of attack can produce large destabilizing yawing moments that promoted spin departure. More recently, it was recognized that proper tailoring of the nose shape can be used to achieve more desirable high angle handling qualities, and designs of recent fighter aircraft have evolved which make use of this feature. To date, however, little fundamental understanding nor predictive capability exists to describe the flow over non-circular nose shapes.

The objective of the present work is to develop through analysis and some critical experiments a better understanding and predictive engineering methods for the flow over arbitrary aircraft nose shapes and the resulting influence of the nose separation vortex system on the downstream components of the aircraft. This paper briefly describes the technical approach and presents some typical results obtained to date in the program. The work has been sponsored by the Vehicle Technology Branch of the Office of Naval Research.

3. OVERALL APPROACH

The problem of interest is the flow over a high speed fighter-bomber at angles of attack in the asymmetric steady vortex shedding range (perhaps 25 to 45 degrees) and small sideslip angles. The analysis and experiments have been limited to incompressible flow, although they can be extended to speeds up to the critical speed. The configurations of interest are nose/wing/body/strake/tail configurations typical of modern aircraft. The flow is dominated by separation on the nose and leading edges of the wing and strake. The aerodynamic loads of greatest interest are the side force and yawing moment which are strongly influenced by flow separation effects and in the case of zero sideslip are due entirely to these effects.

The configuration is divided into segments for purposes of analysis: the nose, the wing/strake/body, the afterbody (if present) and tail. Methods are developed to characterize the separated flow over the nose in terms of potential vortices. In order to model the important features of the flow, a large number, or "cloud", of vortices are used. The distribution of vortices in the cloud is calculated at the axial station of the strake leading edge intersection with the fuselage.

For purposes of calculating the influence of the nose shed vorticity on the aft surfaces of the aircraft, the cloud is modeled by a small number (two or four) of concentrated vortices. The paths of these vortices are computed over the axial extent of the wing, and the induced asymmetric flow field on the wing and body surfaces is calculated. A lifting surface method is then used to compute the load distribution on the wing/strake. Leading edge separation is treated using the "vortex lift" analogy of Polhamus (ref. 2). The leading, side, and trailing edge wing/strake vorticity is modeled by a number of concentrated potential vortex filaments.

The nose and wing/strake vortices are then considered to trail aft over the afterbody and tail, where they induce loads on these components. Combinations of slender body and strip methods are used to calculate the afterbody and tail loads.

4. NOSE ANALYSIS AND RESULTS

This section describes briefly the methods used to calculate the vortex shedding from the nose. Results of the calculations are then compared with measurements made on two noncircular shapes. The most extensive comparisons were made on a research configuration of a V/STOL fighter. An existing model of this configuration was tested in a cooperative program between the Office of Naval Research and the Langley Research Center, NASA. The second configuration is the F-5 fighter.

4.1 Theory

The theory is described in detail in reference 3. The major features are shown in figure 1. The analysis uses potential flow methods and slender body theory to model the steady three dimensional flow as an unsteady, two dimensional problem, where time in the unsteady problem is analogous to axial distance along the nose in the three dimensional case. The basic approach is the circular cross section model of Deffenbaugh (ref. 4), to which several features have been added.

Initially, a mapping function is developed to map the body cross section into a circle, using a numerical mapping scheme developed by Jameson (ref. 5) for airfoils. At a given axial station, the pressure distribution on the noncircular body is calculated in the presence of the uniform crossflow and any potential vortices that are in the flow field at that station. A windward stagnation point is located, and a two dimensional boundary layer is considered to exist on either side of the body starting at the stagnation point. One of the Stratford criteria (ref. 6), either laminar or turbulent as appropriate, is used to locate the two separation points on the flanks of the body. As can be seen in figure 1, the criteria depend upon C_p , the gradient of C_p along the surface, the distance along the surface, and for turbulent flow the Reynolds number. It was found in comparisons with three dimensional separation data on inclined bodies of revolution that separation occurred closer to the windward stagnation point than was predicted by the Stratford criterion shown in figure 1. Consequently, a correction factor $\sin \alpha$ was used with the numerical criteria 0.102 and 0.35 to represent the three dimensional effects in the boundary layers on inclined bodies, since this factor fit reasonably well the available data.

At each of the two separation points, a potential vortex is introduced a small distance off the body surface. The strength of each vortex is given by the vorticity flux in the boundary layer at separation, which depends only on the boundary layer edge velocity. With increasing distance downstream, these vortices remain constant in strength and move along streamlines in the flow. At successive increments in time, or distance along the body, the process of calculating boundary layer separation and introducing two vortices is repeated. Vortex positions are calculated in the circle plane and mapped into the noncircular plane.

The pressure distribution on the nose is calculated using the unsteady Bernoulli equation. In order to avoid a singularity in the velocity potential derivative term, which results in an unknown constant in calculation of the local pressure, a three dimensional source distribution is used to represent the nose area distribution in the presence of a crossflow. Pressures are integrated to obtain loads.

For the case of a nose with a vertical plane of symmetry in zero sideslip, some initial source of asymmetry must be introduced into the calculation to provide a disturbance to drive the vorticity shedding asymmetric. Typically, this is done by rotating the two separation points clockwise (or counterclockwise) through a small angle (the order of one-half a degree) over the first few increments in length in the calculation. Thereafter, the separation points used are those calculated using the pressure distribution. For nonzero sideslip, no initial disturbance is required.

4.2 Comparisons with Data

A comprehensive set of data was taken on a research configuration of a V/STOL fighter in the V/STOL wind tunnel at the Langley Research Center, NASA. The flow conditions were 35 degrees angle of attack and angles of sideslip of 0 and 10 degrees at a Mach number of 0.17 and $Re_p = 7.2 \times 10^5$. The configuration is shown in figure 2. The body cross section consists of circular arcs at the upper and lower surfaces, joined by flat sides. The data consist of six components of forces and moments with and without vertical tail and strakes, shown dashed in figure 2. In addition, flow field velocity measurements were taken with a rake consisting of seven tubes, each having 5 pressure holes on its hemispherical forward end calibrated so as to measure three orthogonal components of the local velocity vector. The rake was swept through arcs over the model at three axial stations shown in figure 2: body station 52, body station 69 (without the strakes present) and body station 98 (with and without strakes). The force and moment data and flow field data are reported in detail in reference 3.

A typical set of flow field velocity results is shown in figure 3 for body station 52 at $\alpha = 35^\circ$ and $\beta = 0^\circ$. The vector lengths represent the magnitudes of the velocity component in the crossflow plane and the vector direction represents the direction of the measured velocity component. The innermost row of measurements is approximately 2.5 cm above the body and the radial distance between rows is also 2.5 cm. In this

case, the vorticity is concentrated into two cores, near the body, unlike the case at more rearward stations, where it is distributed in the flow field above the body. It is possible to make contour integrations about various contours in the measured flow field to obtain the distribution of circulation in the flow above the body, and this was done.

These data permit for the first time a detailed evaluation of vortex shedding theory for a noncircular cross section nose shape. The comparisons that are possible are vorticity distribution in the flow field, velocity distributions, and forces and moments. Typical results are described below.

The method of section 4.1 was applied to the nose of the V/STOL configuration for $\alpha = 35^\circ$ and $\beta = 0^\circ$ assuming turbulent separation on the flanks of the nose. The resulting distribution of potential vortices in the flow field above the body is shown in figure 4. The crosses represent the right side (positive) vortex positions and the circles the left side (negative) vortex positions. The results are shown for body station 52, and indicate that at this station the separated right side vorticity has risen somewhat higher above the body than the left side vorticity.

A comparison of distribution of circulation for this case is shown in figure 5. The numbers with brackets represent the predicted values of circulation within the sectors shown and the values without brackets show the measured values. The predictions (figure 4) show some vortices closer to the body than the innermost sectors, and these are shown in figure 5. No data could be obtained this close to the body, so no measured values are shown. The total circulation for each side is shown in the lower part of the figure, with the predicted values including only that circulation within the sectors. The general distribution of circulation and the measured and predicted values are in reasonably good agreement, as are the total circulation values for each side.

Some typical comparisons for velocities in the flow field above the nose are shown in figure 6. The results shown are the variation of vertical (w) and lateral (v) velocities along rays. Figure 6a has results for the 90 degree ray, which is in the vertical plane of symmetry of the body. The predicted curves have the same form as the data, but show some differences in magnitude within a diameter of the body. The nonzero lateral velocity near the body is a measure of the asymmetry that has developed at this station, which is over-predicted by the theory.

Figure 6b shows similar results for a 99 degree ray, which passes near the center of the left vortex (see figure 3). Again the predicted and measured results have the same form, but the values do not agree well in the vicinity of the vortex core near the body.

These results are typical of those examined at other rays, body stations, and flow conditions, in that the form of the predicted and measured variations are similar, but there are regions in the flow in which the magnitudes do not agree well. The velocity comparisons are a very sensitive indicator for the method, and differences with measured results are due both to differences in vorticity distribution and unrealistic velocity contributions from adjacent vortices close to the point of interest. In the aircraft case, prediction of velocities at the body surface and on wings and tails removed somewhat from the nose wake region is important, whereas in the missile case, tail surfaces can be within the body wake region. Thus, for the aircraft case, the proper distribution of vorticity is probably more important than accurate velocities in the nose wake region, although the latter are very useful in evaluating the methods.

Calculations were also made for comparison with force and moment data on an F-5 nose configuration. The data sources are tests run in the Langley Research Center Full Scale Tunnel at $M < 0.1$ and $Re_p = 3 \times 10^5$ (ref. 7) and tests run in the Nielsen Engineering water tunnel at $Re_p = 1.4 \times 10^5$ and 3.6×10^5 (ref. 3). Some side force results for $\beta = 10^\circ$ are shown in figure 7. There is some influence of Reynolds number on the side force from the Nielsen data, and the Langley and Nielsen data agree reasonably well. The characteristic of particular interest is the change in sign of the side force at values of α between 30° and 35° from a destabilizing effect below this angle to a stabilizing effect above.

Several predicted values for $Re_p = 1.4 \times 10^5$ are shown for angles of attack of 30° and 40° . The lower values at each α are the side force in the absence of separation, which show a destabilizing effect. The upper values are the calculated results with separation using the modified turbulent Stratford criterion, $0.35 \sin \alpha$. The value at $\alpha = 40^\circ$ agrees well with the data where as the value at $\alpha = 30^\circ$ is high. Both calculations show a strong nose-vortex-induced stabilizing force.

There are no separation location data available on the F-5 experiments to assess the accuracy of that aspect of the calculations. The predicted vortex pattern for the $\alpha = 30^\circ$ case is shown in figure 8. The sidewash component is from left to right. Some vortices have been combined on the left side due to close proximity to each other. The location of the windward side vorticity agrees well with the observed water tunnel position of the vortex core in height and lateral position over the body, whereas the leeward side "center of vorticity" is somewhat higher and further outboard than the core observed in the water tunnel tests. Separation is predicted to the windward side about 30° degrees up from the horizontal axis near the upper end of the nearly flat surface; on the leeward side separation occurs at the lower end of the flat surface. These positions of the predicted "center of vorticity" relative to the measured ones

are consistent with the force data of figure 7 in that a larger differential in height between the right and left vortices than was observed experimentally produces a larger vortex-induced side force than was measured.

5. COMPLETE CONFIGURATIONS

This section describes briefly the methods used to calculate loads on a complete configuration subject to asymmetric vortex shedding from the nose. Results of the calculations are compared with data on the V/STOL fighter configuration discussed previously.

5.1 Theory

The methods are described in detail in references 8 and 9. The problem is divided into two parts. In the first, a vortex lattice model is used to calculate loads on the wing/strake/body at combined angles of attack and sideslip in the presence of an arbitrary asymmetric vortex system originating on the nose and passing over the configuration. For the body, an image system is used consisting of an image horseshoe vortex within the body for each horseshoe vortex on the wing/strake. The trailing legs of the image vortex lie at the inverse points within the body, which is assumed circular. The trailing legs of the wing horseshoe vortices are constrained to lie in the plane of the wing along lines parallel to the body longitudinal axis with sideslip.

A crossflow plane analysis is used to locate the nose vortices relative to the wing/body. For this purpose, the "cloud" of vortices at the aft end of the nose is approximated with from two to four concentrated vortices whose locations are the centers of gravity of the portion of the cloud each represents. At successive axial stations, the wing/body is mapped into a circle, and the nose vortices are permitted to move along streamlines in successive crossflow planes from the wing leading to trailing edge and along the afterbody, if present. Once the locations of the nose vortices are established, a crossflow plane method is used to compute the nose vortex-induced velocities at the vortex lattice control points. The vortex lattice is then calculated in the presence of the asymmetric nose-induced velocity field.

Leading edge separation on the wing and strake is treated using the Polhamus vortex lift concept (ref. 2). In an initial calculation in the presence of nose vortices, the leading edge suction is computed on the strake and wing. According to the vortex lift concept, a portion of the suction is rotated into the normal force direction when leading edge separation occurs. The fraction of suction rotated is a function of leading edge sweep angle and is obtained from reference 10, based on a correlation of data mostly from delta wings.

Most of the configurations of interest have wings with leading edges that are swept less than 45 degrees and leading edge extensions, or strakes, that are swept at least 60 degrees. Under these circumstances, the strake develops full vortex lift, a strake leading edge separation vortex is formed, the wing leading edge separates but does not develop vortex lift, and the strake vortex is "torn" from the leading edge at the strake-wing junction and passes aft over the wing. This condition is modeled in the following approximate way in the calculation method. After the first vortex lattice calculation is made and the vortex lift known, a strake vortex is considered to start above the wing-strake junction, and its position downstream of that point is calculated with the crossflow plane analysis, much like a nose vortex. Interaction between the strake and nose vortices occurs, which generally is significant because the strake vortices are stronger than the nose vortices. The strake vortex is assumed to originate laterally at the wing-strake junction, and the strake vortex strength is determined from the vortex span and vortex lift (normal force). The strake vortex height is chosen on the basis of observations of leading edge separation on delta wings.

Loads are calculated on the portion of the body within the wing root chord by locating a number of node points on the surface, calculating the velocity at these points, and using the full Bernoulli equation to calculate pressures. On the afterbody (if present), vortex impulse changes are used to calculate loads, based on the positions of the vortices at the wing trailing edge and the tail leading edge.

Tail vortex interference loads are calculated using the basic strip theory approach of reference 11. The method is generalized to a single panel, or arrangements of single panels, in the presence of single or multiple vortices in order to treat the most general empennage configuration in the presence of any number of vortices. Direct tail loads are calculated using tail-panel-alone lift-curve slopes from reference 12 and the "wing-body" interference factors of reference 11.

5.2 Comparisons with Data

Comparisons were made with data from the V/STOL research fighter tests. The data comparisons that are possible are overall forces and moments and strake vortex positions.

The table below shows the results for predicted side force and yawing moment for four configurations which differ in strake and vertical tail arrangement. The angle of

attack is 35 degrees and the angle of sideslip zero degrees. The Reynolds number is $Re_D = 7.2 \times 10^5$.

Comparison of Measured and Predicted Loads

Strake	Tail	Component	C_y		C_n	
			Meas.	Pred.	Meas.	Pred.
Off	Off	Nose		-.032		-.010
		Wing/Body		-.009		-.002
		Total	-.034	-.041	-.012	-.012
Off	On	Nose		-.032		-.010
		Wing/Body		-.010		-.002
		Tail		-.118		+.082
		Total	-.04	-.160	-.01	+.070
On	Off	Nose		-.012		-.006
		Wing/Body		-.030		+.011
		Total	-.03	-.042	+.001	+.005
On	On	Nose		-.012		-.006
		Wing/Body		-.011		-.001
		Tail		-.016		+.011
		Total	-.048	-.039	+.012	+.004

All of the loads represent nonlinear effects induced by the asymmetric nose vortex system and are relatively small. Generally the agreement is reasonably good except in the tail on/strakes off case, where it appears that the predicted tail load is too high. The flow field data at the wing trailing edge station indicate that most of the vertical tail is operating in a low axial velocity region for the no-strake case, due to the large separated flow region above the wing and body. When strakes are present, the strake vortex energizes the flow over the wing and provides a high axial velocity over the tail. Thus, the over prediction in forces without strakes is probably due to a low dynamic pressure acting on the tail.

Generally, predicted lateral loads on the portion of the body on which the wing is located and on the tail are of the same order as the nose loads. Thus, although nose flow separation is the basic source of lateral effects, important downstream interference effects induced by the nose vortices occur as well and need to be included in the total predicted loads.

The loci of vortex positions in the crossflow plane for the same flow condition with strakes is shown in figure 9. Values of the body station are noted at various positions on the vortex paths, and the vortex strengths are also shown for each vortex. The two nose vortices are a concentrated vortex representation of the distribution in figure 4 and show a small initial asymmetry in strength and position at the strake leading edge. They tend to rise slowly and move to the right under the influence of the free stream and self-induced velocities until the strake vortices are introduced. Because of the larger strengths of the strake vortices, these then dominate the motion of the nose vortices and force them down until at the base of the body they are close to the wing plane in height. The flow field data at the wing trailing edge do not show any indication of the presence of nose vortices, and it appears that these may have merged with the strake vortices, which are much stronger.

The strake vortices move upward under the influence of the free stream flow and remain laterally at about the position of the break in sweep between the strake and wing. Measured positions of the vortex core centers are shown at the wing trailing edge which agree reasonably well with the predicted positions. In the initial calculations made with this configuration, strake vortex heights at the wing/strake junction were selected based on observations of vortex formation on delta wings, which showed that the leading edge vortices trailed back over the wing at about half the angle of attack. These calculations resulted in strake vortex positions that were high compared to the measured positions. The strake vortex height shown in figure 9 are based on an initial height about half that deduced from the delta wing data, which indicate that there is a substantial influence of the wing presence on strake vortex height.

6. DISCUSSION

The real flow over a fighter-bomber at high angles of attack is obviously very complicated and impossible to model in detail. The engineering methods that are described in the preceding sections are an attempt to use vortex interference methods that have been applied successfully to computation of many nonlinear phenomena in aircraft and

missiles to model the high angle aircraft problem. This section discusses some of the results obtained in light of the real flow phenomena and insight gained in the data and calculations made.

Vortex bursting is known to occur on body/wing/strake combinations as the angle of attack increases. The flow field data on the V/STOL model nose indicates that the nose vortices have axial velocities in the core region that exceed those in the adjacent flow by about 50 percent. For the case of no strakes, the flow field data behind the wing show some indication of the presence of the nose vorticity about 3 equivalent body diameters above the body, but the vorticity is sufficiently diffuse that core regions are difficult to identify. This region has axial velocities that are about 20 percent less than the adjacent flow.

With strakes, the flow field velocity distribution behind the wing shows no indications of nose vorticity but does show a strong, well defined circulatory flow behind each wing panel characteristic of a vortex. The central regions of these vortices, however, have a very low velocity "core" whose diameter is the order of one-quarter of the wing semispan. Without additional measurements over the wing, it is difficult to judge the state of the vortices, but there remains a large amount of circulation in the flow behind the wing. These vortices were represented in the calculation by concentrated potential vortex filaments, and that may well be a reasonable approximation for purposes of calculating induced velocities away from the core region on the tail and afterbody. Additional work needs to be done to evaluate this matter.

The calculations on the F-5 nose, in particular, show that the asymmetric vortex pattern that develops is fairly sensitive to the location of separation. In some cases on both the F-5 and V/STOL noses which have regions of nearly flat sides with very low pressure gradients, the predicted separation location was found to oscillate across the flat faces from one body station to the next as the separation vortices changed the pressure distribution slightly, and this influences the shed vorticity pattern. The $\sin \alpha$ modification to the Stratford criterion as an approximate three dimensional correction was verified on some data on circular cross section bodies and appeared to work well in the few cases examined. It should be evaluated more thoroughly, on both circular and noncircular three dimensional bodies, and modified as necessary to give a more reliable indication of separation on typical noncircular aircraft nose shapes. No appropriate data exist on noncircular shapes, to our knowledge, and some such data would be essential in making such an evaluation.

Finally, the loads induced on the wing/body and tail are somewhat sensitive to the way in which the vorticity distribution at the aft end of the nose is modeled with a few concentrated vortices. Cases calculated with both 2 and 4 vortices modeling the cloud showed this effect. Additional work is indicated, perhaps using the entire cloud of vortices, to evaluate the detail with which the cloud vorticity distribution must be modeled to obtain proper downstream interference effects.

7. CONCLUDING REMARKS

Vortex interference methods were applied to the case of a high speed aircraft at high angles of attack to attempt to develop engineering prediction methods for nonlinear lateral effects induced by asymmetric vortex shedding on realistic noncircular nose shapes. The availability of detailed flow measurements made as a part of this study was a significant factor in evaluating the methods and insuring that the proper physical flow phenomena are contained in the flow models.

On the basis of the comparison that were made, the flow models appear to describe properly the flow phenomena and to give reasonable estimates of the nonlinear phenomena. The methods need some additional comparisons with data, particularly separation location information, in order to be considered reliable predictive methods useful in preliminary design and data analysis.

8. REFERENCES

1. Chambers, J. R., Anglin, E. L., and Bowman, J. S.: Effects of a Pointed Nose on Spin Characteristic of a Fighter Airplane Model Including Correlation with Theoretical Calculations. NASA TN D-5921, Sept. 1970.
2. Polhamus, E. C.: Predictions of Vortex Lift Characteristics by a Leading-Edge Suction Analogy. Jour. of Aircraft, Vol. 8, No. 4, April 1971.
3. Spangler, S. B. and Mendenhall, M. R.: Further Studies of Aerodynamic Loads at Spin Entry. Report ONR-CR-212-225-3, June 1977.
4. Deffenbaugh, F. D. and Koerner, W. G.: Asymmetric Wake Development and Associated Side Force on Missiles at High Angles of Attack. AIAA Paper No. 76-364, July 1976.
5. Jameson, A.: Iterative Solution of Transonic Flows Over Airfoils and Wings, Including Flows at Mach 1. Comm. Pure Appl. Math, Vol. 27, 1974, pp. 283-309.

6. Stratford, B. S.: The Prediction of Separation of the Turbulent Boundary Layer. Jour. Fluid Mech., Vol. 5, 1959, pp. 1-16.
7. Grafton, S. B., Chambers, J. R., and Coe, P. L.: Wind Tunnel Freeflight Investigation of a Model of a Spin Resistant Fighter Configuration. NASA TN D-7716, June 1974.
8. Spangler, S. B. and Dillenius, M. F. E.: Investigation of Aerodynamic Loads at Spin Entry. ONR Report No. CR-225-2, May 1976.
9. Spangler, S. B. and Nielsen, J. N.: Exploratory Study of Aerodynamic Loads on a Fighter-Bomber at Spin Entry. Nielsen Engineering & Research TR 87, May 1975.
10. Mendenhall, M. R. and Nielsen, J. N.: Effect of Symmetrical Vortex Shedding on the Longitudinal Aerodynamic Characteristics of Wing-Body Combinations. NASA CR-2473, Jan. 1975.
11. Pitts, W. C., Nielsen, J. N., and Kaattari, G. E.: Lift and Center of Pressure of Wing-Body-Tail Combinations at Subsonic, Transonic, and Supersonic Speeds. NACA Report 1307, 1959.
12. DeYoung, J. and Harper, C. W.: Theoretical Symmetric Span Loading at Subsonic Speeds for Wings Having Arbitrary Planform. NACA Report 921, 1948.

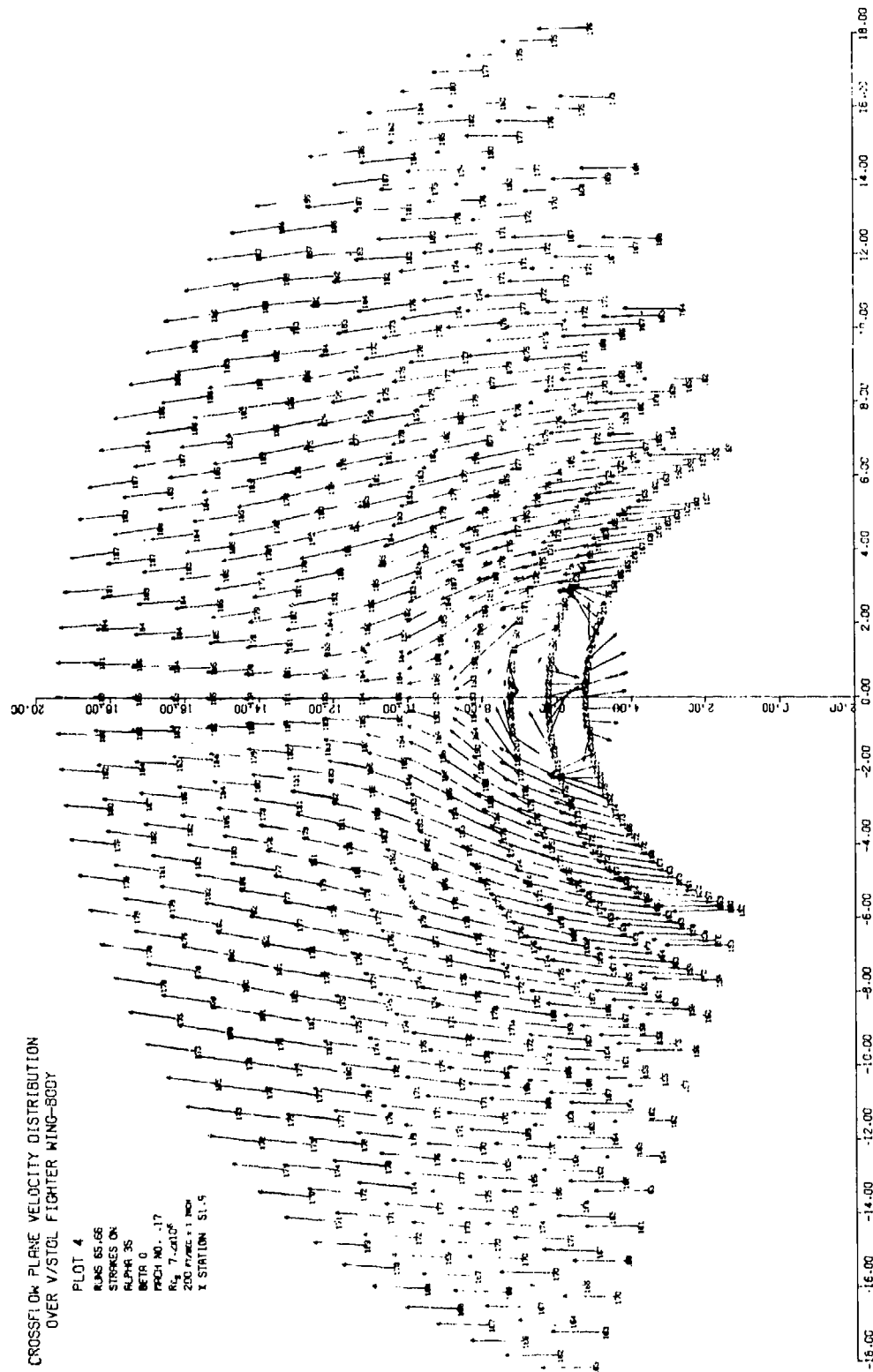


Figure 3.- Crossflow plane velocity vectors for V/STOL
model at $\alpha = 35^\circ$, $\beta = 0^\circ$, body station 52.

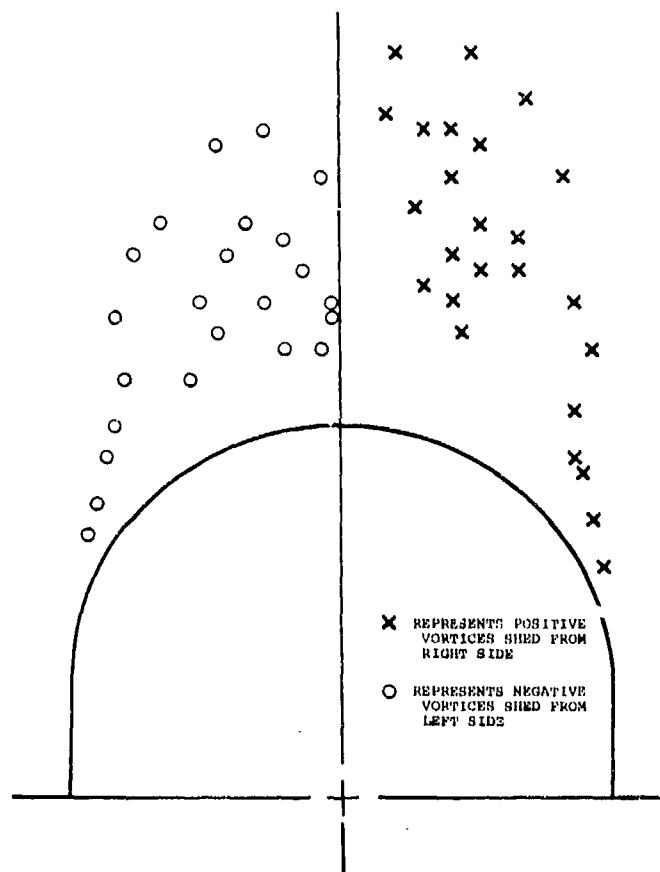


Figure 4.- Calculated distribution of shed vortices for V/STOL model at $\alpha = 35^\circ$, $\beta = 0^\circ$, body station 52.

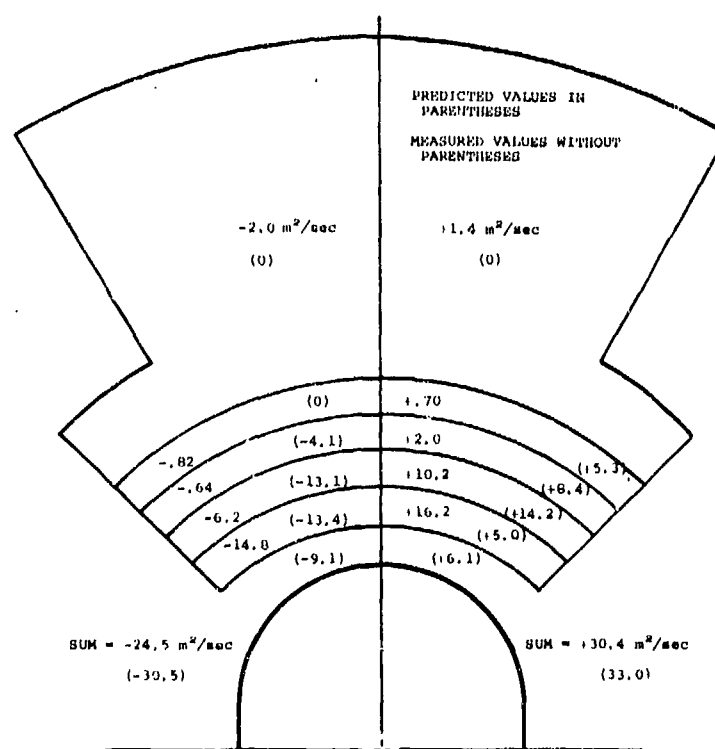


Figure 5.- Measured and predicted circulation distribution above the V/STOL model nose at $\alpha = 35^\circ$, $\alpha = 0^\circ$, body station 52.

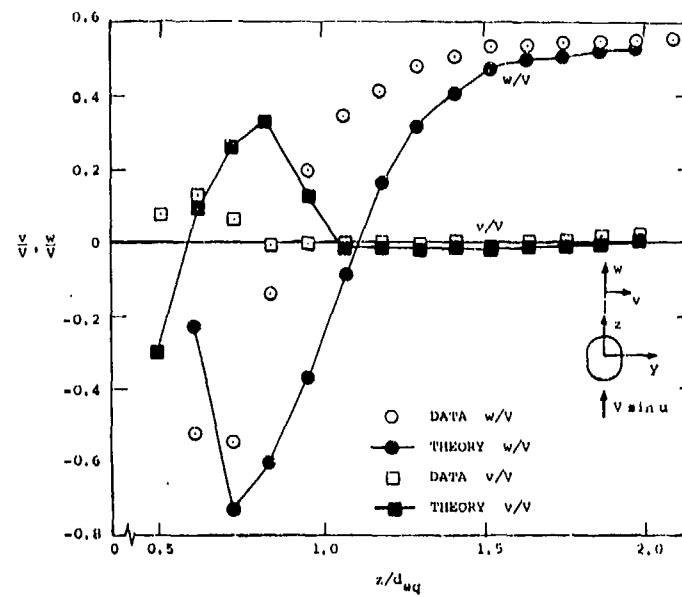


Figure 6.- Predicted and measured velocity distributions above V/STOL body at $\alpha = 35^\circ$, $\beta = 0^\circ$, body station 52.

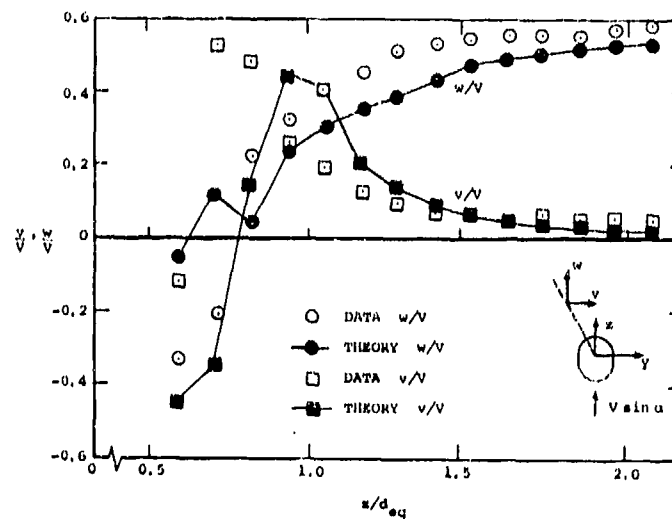


Figure 6.- Concluded.

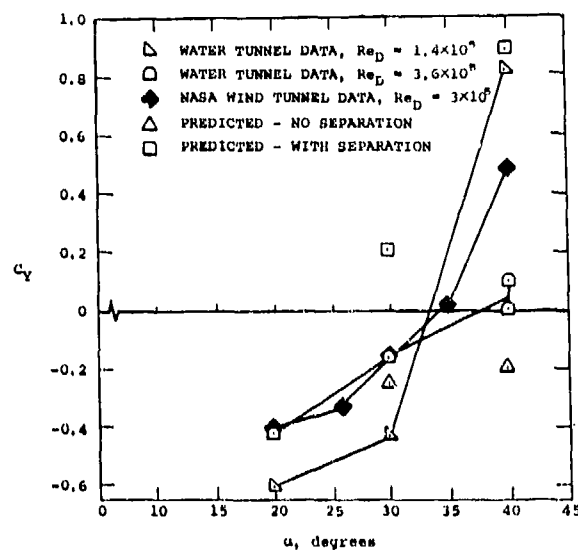


Figure 7.- Measured and predicted side-force coefficient variation with angle of attack for F-5 nose at 10° sideslip angle.

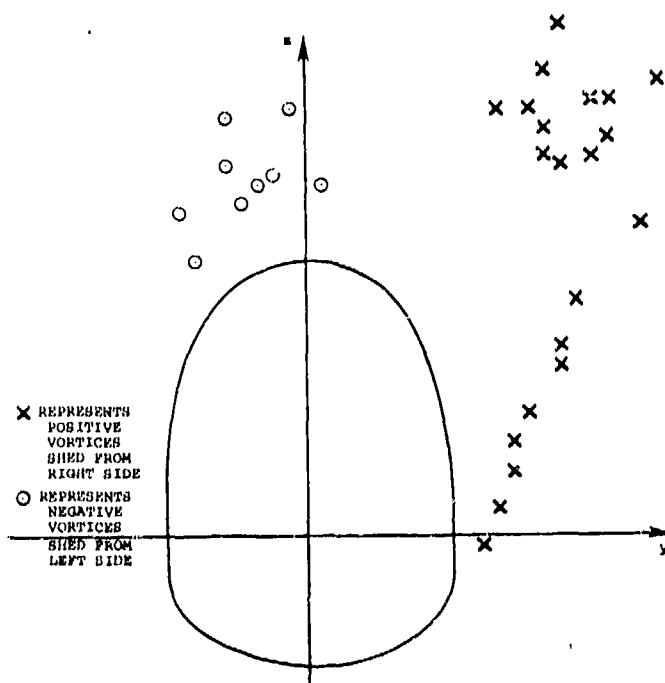


Figure 8.- Calculated distribution of shed vortices for F-5 nose at $\alpha = 30^\circ$, $\beta = -10^\circ$ and 41-percent length station for Stratford separation.

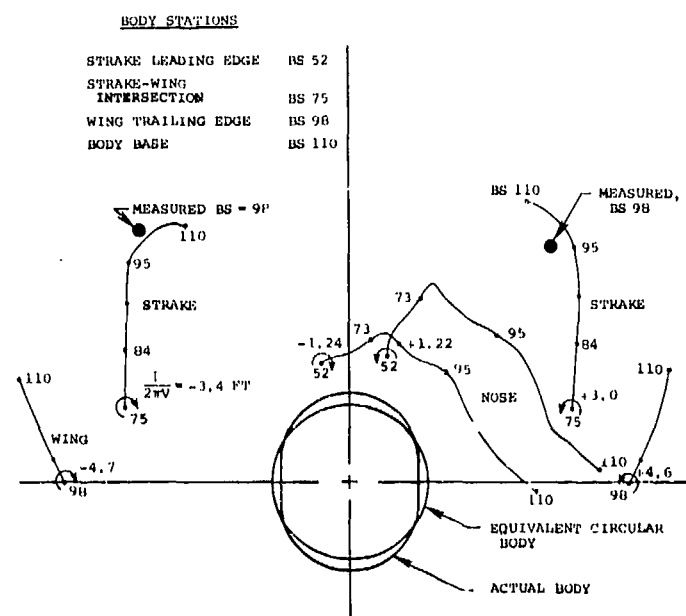


Figure 9.- Calculated variation of vortex positions with axial distance along body for V-STOL model at $\alpha = 35^\circ$, $\beta = 0^\circ$.

PREDICTION AND MEASUREMENT OF THE AERODYNAMIC
FORCES AND PRESSURE DISTRIBUTIONS OF WING-TAIL
CONFIGURATIONS AT VERY HIGH ANGLES OF ATTACK

Richard P. White, Jr.
Systems Research Laboratories, Inc.
1055 J. Clyde Morris Boulevard
Newport News, Virginia 23602

SUMMARY

The presentation starts with a brief review of the experimentally measured effects of vortex flows attached to the main lifting surface of a wing-tail configuration at high angles of attack. This review will be followed by a detailed presentation of the three-dimensional viscous lifting surface theory that has been developed to predict the distribution of aerodynamic loadings on arbitrary planforms having attached vortex flows at high angles of attack. The paper will conclude with comparisons between measured and predicted performance and pressure distribution data for a wing-strake configuration at a high angle of attack. Limitations of the prediction technique as well as the potential of utilizing "vortex lift" to amplify the performance characteristics of highly maneuverable aircraft will also be outlined.

LIST OF SYMBOLS

C_L	Lift coefficient of the wing
C_c	Chord length of tail surface
C_M	Pitching moment coefficient about the wing MAC
C_{pu}	Upper surface pressure coefficient
D	Doublet strength per unit area
H	Horizontal separation between the mean aerodynamic chords of the wing and the tail
L	Longitudinal separation between the mean aerodynamic centers of the wing and the tail
r_c	Radius of the viscous core of the leading edge vortex
U_i	Perturbation velocity component in the x direction at point i on the wing surface
U_0	Free stream velocity
V_i	Perturbation velocity component in the y direction at point i on the wing surface
W_i	Perturbation velocity component in the z direction at point i on the wing surface
x, y, z	Cartesian coordinate system fixed to the wing
α_0	Angle of attack of the wing
α_t	Angle of attack of tail with respect to wing mean chord
ν	Kinematic viscosity of the air
ν_t	Turbulent eddy viscosity of the vortex core
ϕ	Velocity potential
ϕ	Perturbation velocity potential
ϕ_0	Velocity potential of the undisturbed flow
ρ	Density of the air

1.0. INTRODUCTION

For the past several years, the RASA Division of Systems Research Laboratories, Inc., has been conducting an experimental and theoretical study of the vortex-flow interactions with low aspect ratio lifting surfaces. The general objective of this study has been to investigate the concept of vortex control for the improvement of the performance characteristics of lifting surfaces, especially low aspect ratio swept wings at high angles of attack. The initial experimental investigation conducted under this contract effort (Ref. 1) showed that significant improvement in the performance characteristics of low aspect ratio swept lifting surfaces could be achieved by the use of vortex generation and control techniques.

The experimental research conducted to date has been concerned primarily with a 1/4 scale model of an F4E wing planform and with retrofit leading edge vortex generating

devices attached to it. While the test results have shown that positive performance gains can be outlined by the interaction of the wing with the vortices generated by the leading edge surfaces, it was found that the pitching moment tended to become unstable (nose up) at the higher angles of attack. Because the possible interaction of the vortex flow generated by the wing with the tail plane might significantly reduce the effectiveness of the horizontal tail and not permit this unstable pitching moment to be neutralized, the effectiveness of the horizontal tail operating in the wake of the wing was recently investigated.

In addition to the experimental investigation of the effects of wing vortex flows on the effectiveness of the tail plane, the development of a theoretical prediction method was continued this past year and correlation of predicted and measured results was undertaken.

The prediction method, which will be briefly outlined herein, extended an original theoretical formulation of the problem (Ref. 2) so that the flow tangency boundary conditions can be satisfied on the total wetted surface of the wing instead of only the mean surface. This enables the computation of surface pressures on both the upper and lower airfoil surfaces. In addition, a more realistic mathematical model than the one utilized in Reference 2 was developed for the representation of the leading edge vortex system.

The following sections of this paper will first briefly summarize the experimental results obtained during the investigation of the effectiveness of the tail when operating in the wing wake and then the basic aspects of the theoretical prediction method will be presented. The paper will conclude with a comparison of predicted and measured pressure distribution over the surface of a wing-strake configuration at a high angle of attack.

2.0. BACKGROUND SUMMARY OF RESEARCH

The primary purpose of the research program that is being conducted with the support of the Office of Naval Research (ONR) is to understand and develop a means of predicting the effects of attached vortex flows on the aerodynamic characteristics of low aspect ratio wings of arbitrary planform operating at high angles of attack.

In order that the research to be reported on herein can be understood in the proper context, a brief review of the research effort conducted over the last few years will be presented first.

In the subject research effort a low aspect ratio swept-tapered lifting surface, with and without various appendages to develop vortex flows, has been tested and has been used as the model for the theoretical calculations. Figure 1 presents a photograph of the wing, with a root strake attached, mounted in a wind tunnel. In addition to measuring the six components of forces and moments about the quarter chord location of the MAC of the wing, pressure distributions over the surface were measured at 244 locations. A sample of the visualized attached vortex flows generated at high angles of attack by the wing-strake configurations shown in Figure 1, are presented in Figure 2 and Figure 3. Figure 2 shows the leading edge vortex which exists on the wing and Figure 3 shows the path of the strake vortex over the surface of the wing. As can be seen from the photographs, the leading edge vortex moves along and away from the leading edge as it travels out the span until it bursts, while the induced flows deform the strake vortex such that it is turned approximately 90 degrees to the free stream flow near the wing trailing edge. The surface flow over the wing induced by the strake and leading edge vortices are indicated by the tufts attached to the wing surface as shown in Figure 4. As indicated by the tufts in the photograph, the flow outboard of the burst leading edge vortex is completely separated and the induced velocity of the vortices has created a strong spanwise flow between the paths of the strake and leading edge vortices. The tufts also indicate that there are regions of potential flow inboard of the strake vortex aft of the 50% chord line and outboard of this vortex. As indicated by these pictures, the aerodynamic flows associated with a wing-strake configuration operating at high angles of attack are complicated and are typified by regions of separated flow, potential flow and regions where strong vortices interact with the wing surface. The effect of the interactive vortex flows on the total wing lift as a function of angle of attack are shown in Figure 5. As can be seen from the data presented in this figure, above an angle of attack of approximately 15 degrees the basic wing begins to show effects of stall while the wing with the leading edge vortex generating appendages continues to develop increasing lift with angle of attack in a linearized fashion up to an angle of attack of approximately 30 degrees at which angle abrupt stall occurs. While an abrupt stall occurs, the lift force generated by the vortex flows is only reduced by about 6% initially and then remains relatively constant as the angle of attack is increased to approximately 40 degrees.

The significant difference in the pressure distributions over the wing surface at an angle of attack of 27.7 degrees with the addition of the root strake is shown in Figure 6. At this angle of attack the pressure distributions indicate the basic wing is completely stalled over its entire surface except for a small region near the root when the remnants of the leading edge vortex are generating a small amount of increased lift. The pressure distributions measured on the wing strake configuration, on the other hand, indicate very strong pressure peaks from both the strake and leading edge vortex flows. By tracing the locations of the maximum pressures of the two pressure peaks, the paths of the two vortices over the wing surface can be determined. As can be seen, the paths of the stronger leading edge vortex and the strake vortex come together near the 80% chord line which corresponds to the flow pictures shown in Figures 2 and 3. It can also be noted from the pressure distributions, the leading edge vortex is probably changing from a line vortex to a fully turbulent burst vortex as it travels from the 5 to 20% chord position as indicated by the rapid decrease in the peak pressures. While the vortex flows were beneficial as they significantly increased the lifting capabilities of the wing surface at high

angles of attack, they also had a detrimental effect as they caused the pitching moment to become unstable about the quarter chord of the wing MAC. Figure 7 compares the pitching moment characteristic of the basic wing as a function of angle of attack with those measured with two configurations having leading edge vortex producing lifting devices. It can be noted from the data presented in this figure that when the leading edge vortex is formed at an angle of attack of approximately 13 degrees, the rate of increase in the negative pitching moment with angle of attack is temporarily decreased for the basic wing and the slope of the pitching moment with increasing angle of attack changes sign for the configurations with the strake attached. The reason for this significant change in the pitching moment characteristics of the wing is that the vortex flows that generate the lift at high angles of attack do so along the leading edge as indicated by the pressure distribution presented in Figure 6. Since the leading edge snag is located at the 68% span, the control it exerts on the wing lift is slightly aft of the quarter chord location of the MAC and thus, it tends to reduce the destabilizing pitching moment. While it was believed that a horizontal stabilizer could overcome this destabilizing pitching moment without difficulty, questions arose as to the effect of the wing vortex flows on the effectiveness of the horizontal stabilizer operating in the wing wake. It was concluded therefore, that a brief experimental investigation of the effect of the location of the horizontal stabilizer with respect to the wing on its effectiveness should be conducted.

3.0. DETERMINATION OF TAIL EFFECTIVENESS BY EXPERIMENTAL MEANS

The experimental test setup to evaluate the effectiveness of the horizontal tail in providing the pitching moment necessary to trim a wing-tail configuration is shown in Figure 8. The horizontal tail had an independent angle of attack control and could be located at various distances aft of the wing as well as at various locations along a line perpendicular to the wing chordplane. In order to study in detail the interaction of the wing wake with the tail surface, ninety eight (98) pressure taps were located over the surface of the horizontal tail along lines of constant percent chord. Figure 9 presents a sketch of the geometric orientation of the wing tail model as it was mounted in the wind tunnel. The angle of attack of the wing was varied by rotating the wind tunnel turntable which contained the balance system to which the wing and tail surfaces were mounted. At a given angle of attack of the wing, the angle of attack of the horizontal tail was altered until a zero pitching moment about the wing MAC was obtained. To determine the tail effectiveness of the tail surface at a given wing angle of attack, the variation of the pitching moment about the wing MAC due to angle of attack changes of the tail about its axis for system trim was determined. A sample of the results obtained for the basic wing tail configuration are presented in Figure 10. As can be seen from the data presented in Figure 10 the pitching moment generated by the tail surface as its angle of attack was altered about the trim angle was surprisingly linear regardless of the angle of attack of the main wing. The rate of change of the pitching moment with tail angle of attack $dC_M/d\alpha_T$, provides a measure of the effectiveness of the tail. The results presented in Figure 10 indicate that while there is some loss in tail effectiveness as the wing angle of attack is increased from 15 to 30 degrees, it is much less than might be expected.

The variation of the trim angle of attack of the tail relative to the wing chord shows that very large changes in the tail geometric angle of attack are required to maintain aircraft trim above a wing angle of attack of 20 degrees. In investigating the reasons for this apparent large change in angle of attack of the tail surface, the system forces and moments were inspected in detail as well as the tail pressure distributions. Figure 11 presents a sketch of the directions of the force and moments as well as the relative geometric orientations of the lifting surfaces at a moderate angle of attack. For the basic wing-tail configuration, the wing generates a nose down pitching moment about its MAC, and the drag force on the tail produces an opposing nose up pitching moment about the wing MAC. Since the moment due to tail drag is less than that developed by the wing, the tail must develop a lift force in the direction shown in order to provide moment trim about the wing MAC. Since the tail drag moment and the wing pitching moment tend to oppose each other, the lift developed by the tail tends to be relatively small in this angle of attack range. However, as the angle of attack of the wing is increased, the MAC of the tail surface will be located such that the drag force on the tail will create a nose down instead of a nose up pitching moment about the wing MAC. For the basic wing tail configuration, this shift occurs at a wing angle of attack of approximately 12 degrees. At wing angles of attack of between 12 and 20 degrees the rate of increase of the pitching moment is small due to the formation of the leading edge vortex (Fig. 7) and, therefore, the tail angle of attack required to maintain pitching moment trim in this angle of attack range does not have to change significantly. As the wing angle of attack is increased above 20 degrees however, the wing nose down pitching moment increases more rapidly and the pitching moment of the tail drag force adds to the nose down pitching moment about the wing MAC. Since the lift of the tail must now be increased to counter the nose down pitching moment, the additional induced drag of the tail also contributes to the nose down pitching moment about the MAC of the wing. Thus, the moments generated about the wing MAC by the tail lift and drag force tend to oppose each other. Since the lift force increases more rapidly than the drag force with increasing angle of attack, trim balance is obtained, but only with increasingly large angles of attack of the tail surface.

As previously discussed and as noted by the data presented in Figure 7, the addition of the strake to the leading edge of the wing changes significantly the pitching moment characteristics of the lifting surface with angle of attack. Comparison of the tail angle of attack for configuration trim and the tail effectiveness as a function of the wing angle of attack presented in Figure 12 indicate that there are some significant differences in these results when the strake was added to the leading edge of the wing. While the

average values of the tail effectiveness $dC_M/d\alpha_t$ as a function of wing angle of attack are approximately the same for the two configurations, there is a significant variation in the tail effectiveness of the wing-strake configuration in the angle of attack range of $10 \leq \alpha_t \leq 20$ degrees that is not present in the basic wing configuration. This variation in the tail effectiveness is noted to correlate with large variations in the tail geometric angle with respect to the wing chord for trim in the same range of wing angles of attack. Inspection of the tail pressure distributions in this angle of attack range indicates why there is a sufficient difference in the behavior of the variation of the tail trim angle between the two configurations. Figure 13 presents a comparison of the pressure distributions on the tail surface when the different wing-tail configurations are in trim at 13.1 degrees. As can be noted from a comparison of the pressure distributions, there is an obvious effect of vortex interaction with the tail surface outboard of the 50% span for the wing-strake tail configuration. It is believed that this reversal of the pressure distribution over the outboard span is caused by the induced effect of the strake vortex crossing the tail surface at approximately the 50% span. It is apparent that the induced effect of this vortex is sufficiently strong to reverse the angle of attack in the tip region and thus change the sign of the lift force. It is obvious that the reversal of the lift force developed by the tail in the tip region would tend to reduce the effectiveness at the tail.

At a wing angle of attack of 17.4 degrees, the pressure distributions over the tail surface at the trim angle of attack presented in Figure 14 are similar to those for a wing angle of attack of 13.1 degrees. The pressure distributions indicate, however, that the increased strength of the strake vortex causes a greater load reversal at approximately the 75% spanwise location which causes a greater loss of lift and thus a greater reduction in the tail effectiveness.

At a wing angle of attack of 21.7 degrees, no significant evidence of induced effects from a concentrated vortex could be found in the pressure distributions over the tail. Flow visualization pictures indicate that as the angle of attack of the wing is increased the strake vortex starts to curve outboard and at a wing angle of attack of approximately 20 degrees the strake vortex is outboard of the tail surface. As the wing angle of attack is increased above 21.7 degrees, a tail trim angle of attack trend similar to that obtained with the basic wing in the same angle of attack region is obtained. However, it is noted that the maximum change in trim angle of the tail is only 5 degrees instead of 16 degrees as it was for basic wing configuration. This much smaller tail trim angle variation is attributed to the fact that for the wing-strake configurations at high angles of attack, the pitching moment developed by the tail drag and lift are working together to counter the positive wing pitching moment instead of working against each other as they were to neutralize the negative pitching moment of the basic wing tail configuration.

It is interesting to note that at a wing-strake angle of attack of 30.3 degrees, the tail is at a geometric angle of attack of 27 degrees with respect to the airstream when trim is obtained. Since the lift force developed by the tail surface is relatively small as shown by the pressure distributions, it indicates that the flow angularity induced by the wing wake is of the order of 25 degrees which corresponds to a mean induced velocity from the wing wake of 47 feet per second. It is obvious, therefore, that this significant induced velocity of the wing wake cannot be ignored when considering the design of a tail operating in the wake of a lifting surface generating strong leading edge and strake vortex flows.

Similar results were obtained for the other wing and wing-strake tail configurations that were tested. Reference 3 discusses in detail the results that were obtained for the other configurations.

Additional basic conclusions that were reached from the experimental results are:

- a. While the effect of the induced velocities of the vortices shed from the wing were such as to cause large changes in the tail angle at which wing tail pitching moment was obtained, the tail effectiveness was not altered by more than 25% even when strong vortex interactions were present.
- b. For the wing-strake configuration, the lift force developed by the horizontal tail to reduce the total pitching moment to zero was in a direction as to noticeably increase the lift of the combined systems. This effect was more pronounced when the horizontal tail was closer to the wing trailing edge.

4.0. DESCRIPTION OF AERODYNAMIC PREDICTIVE ANALYSIS

The general representation of the aerodynamic flows that were considered in the theoretical analysis are shown in Figure 15. As indicated, the upper and lower surfaces of the wing are divided up into an arbitrary number of discrete boxes and the potential flow characteristics over the wing are predicted using a doublet representation. The leading edge vortex, or any other vortex attached to the lifting surface is represented as a viscous vortex flow whose position and strength are obtained as part of the solution. The theoretical technique includes, in varying degrees of sophistication, the potential flow and separated flow characteristics of the wing, the viscous characteristics of the vortices and the interaction effects between the attached vortex flows and the lifting surface. Based on some empirical data required as inputs, the program computes the strength and location of the vortex flows, the potential pressure distributions including the induced effects of the vortex flows, the pressure distributions in the predicted separated flow regimes, and the pressure distribution due to the low pressure regions associated with the vortex flows. A brief summary as to how the various flow characteristics are represented in the analysis will be presented below. More details of the theoretical formulation are presented in Reference 3.

4.1. Potential Flow Model

On the basis of the Cartesian coordinate system attached to the wing, shown in Figure 15, the x-y plane describes the mean angle of attack plane of the wing and the z-axis is directed away from the upper surface of the wing.

Potential flow implies that the flow is irrotational and thus, the velocity vector \vec{V} can be expressed by the gradient of a velocity potential ϕ ,

$$\vec{V} = \vec{\nabla} \phi. \quad (1)$$

Since the continuity equation is given by

$$\vec{\nabla} \cdot \vec{V} = 0 \quad (2)$$

for incompressible steady potential flows, the velocity potential ϕ of the flow around a wing surface satisfies the Laplace equation

$$\nabla^2 \phi = 0. \quad (3)$$

Therefore the problem of determining the steady, inviscid, irrotational, and incompressible flow around a wing surface described by a boundary surface S , involves the solution of the Laplace equation

$$\frac{\partial^2 \phi}{\partial x^2} + \frac{\partial^2 \phi}{\partial y^2} + \frac{\partial^2 \phi}{\partial z^2} = 0 \quad (4)$$

with appropriate boundary conditions.

For convenience ϕ is separated into two parts, i.e.,

$$\phi = \phi_0 + \phi \quad (5)$$

Here, ϕ is the perturbation velocity potential, which vanishes at infinity and ϕ_0 is that part of the potential associated with the free stream velocity, i.e.,

$$\vec{U}_0 = \vec{\nabla} \phi_0. \quad (6)$$

Since the Laplace equation is a second order differential equation, it requires two boundary conditions for its solution. In the regions very far from the wing, the perturbation potential is zero, and the total velocity at large upstream distances corresponds to the free stream velocity \vec{U}_0 . The second boundary condition, related to the requirement for flow tangency, states that over the wing surface S , the normal velocity \vec{V}_n must be zero, i.e.,

$$\vec{\nabla} \phi \cdot \hat{n} = 0 \quad (7)$$

where \hat{n} is the surface unit normal. The boundary condition as expressed in Equation (7) can be rewritten in terms of the perturbation potential and the free stream velocity after combining Equations (5) and (6) as follows:

$$\vec{\nabla} \phi \cdot \hat{n} = -\vec{U}_0 \cdot \hat{n} \quad (8)$$

For convenience $\vec{\nabla} \phi$ can be defined as the induced velocity vector \vec{V}_i , which allows the boundary condition, Equation (8), to be written as

$$\vec{V}_i \cdot \hat{n} = -\vec{U}_0 \cdot \hat{n} \quad (9)$$

The above boundary conditions and the Kutta condition are utilized for the determination of the perturbation potential ϕ . After the velocity potential ϕ is determined, the velocity can be obtained from Equation (1) and the pressure can be obtained from Bernoulli's equation.

It can be shown that the potential function induced by singularities such as a source, or doublet will identically satisfy the Laplace equation and will vanish at infinity. Therefore, the solution of the Laplace equation is one of finding a singularity distribution on the surface S that satisfies the normal boundary conditions in Equation (9). It can also be shown that since the source distribution does not produce any resultant lift, the doublet distribution must be utilized in the present formulation.

If "D" corresponds to a surface doublet distribution whose axis is everywhere along the outward normal to the local surface S , the potential induced at any point P is given by

$$\phi_P = - \iint_S \frac{D}{4\pi} \frac{\hat{n} \cdot \vec{r}}{r^3} ds \quad (10)$$

where \vec{r} is the distance vector from doublet source "D" on S to point P , and \hat{n} is the unit vector outward normal on the elemental local surface ds and S is the total surface on which doublets are distributed. In general, the surface S consists of the upper and lower surfaces of the lifting surface and the wake surfaces.

Substitution of Equation (10) into Equation (8) results in the following integral equation

$$\frac{1}{4\pi} \vec{\nabla} \iint_S D \frac{\hat{n} \cdot \vec{r}}{r^3} \cdot \hat{n} = -\vec{U}_0 \cdot \hat{n} \quad (11)$$

In the present analysis the integration of the above equation, for the determination of doublet distribution D , is carried out numerically. The details of the numerical method that is utilized is presented in Reference 3.

4.2. Summary of the Representation of the Viscous Vortex and the Suction Lift

The interaction of a concentrated free vortex with a lifting surface can be represented by two different mechanisms: (1) the influence of the vortex induced velocity field, and (2) the effect of the viscous core on the near field pressure distribution of the lifting surface. The first effect is easily accounted for as it can be included in determining the potential flow field. A discussion of the second mechanism, the non-linear suction lift, is presented in the following paragraphs.

Due to the complexity of the equations of motion, only simplified solutions of the wing-vortex interactions problem have been obtained to date. These simplified solutions are limited to predicting the pressure field generated in a uniform free stream due to a Rankine or to a decaying vortex, Batchelor's solution (Ref 4), and for the case of a line vortex adjacent to a slender body. A good review of these existing theoretical models is presented in Reference 5.

In general, the incremental suction peaks obtained, due to a wing-vortex interaction, are the results of the radial pressure gradient term which balances the centrifugal and/or Coriolis forces arising from the rotational flow as well as from the axial and radial velocities in the vortex. This type of flow was noted in the experimental results presented in Reference 6, where strong suction peaks are accompanied by high axial flows, core growth and vortex displacement. It is apparent therefore that an adequate accounting of the vortex axial and radial flow is essential for the correct prediction of the suction peaks associated with wing vortex interactions. The Rankine vortex completely neglects axial flow, while the Batchelor vortex is valid only for weak axial flows and neither of these representations include radial flow. Since for the leading edge vortex, both the axial flow and the radial flow effects are important, it was found necessary to define a theoretical model which can include these effects.

The vortex modeling that was undertaken for the present theory considered three different types of vortex flows in its life cycle. The first type considered was for the formation part of the vortex flow which was assumed to be represented by a line vortex. The second region was for the vortex when it became a free vortex. This region of the vortex flow was represented by a conical vortex for which the axial velocity is greater than the free stream velocity. When the axial velocity becomes less than the free stream velocity, the vortex representation was that due to Batchelor (Ref 4). The third vortex representation that was required was that for the burst vortex. This representation was basically the same as the Batchelor representation except the vortex core was assumed to rapidly increase in size as a function of downstream distance. The following discussion will present a discussion of the conical and Batchelor vortex representation utilized in the theory as the forming and burst vortex representations were variations of these vortex flows respectively.

It is observed that the leading edge vortex flow has some distinct characteristics, such as the presence of a turbulent core at the center, when the leading edge vortex sheet rolls up tightly to form a concentrated vortex. This turbulent core appears almost conical and there is a definite presence of a large axial flow in the core. These physical characteristics suggest that any mathematical representation of a leading edge vortex system should be such as to account for the large axial flow in the core compared to that outside or far away from the core of the vortex. T.R. Goodman (Ref 7) obtained a self-similar solution of the Navier-Stokes equations using boundary-layer approximations with some additional assumptions which represents the basic characteristics of leading edge vortex system immediately after its formation.

The leading edge vortex system modeled by Goodman contains a central core where viscous effects predominate. A characteristic feature of this core is the presence of a strong axial flow produced by an axial pressure gradient which is induced by the axial variations in the radial pressure gradient. The solution which was utilized for the prediction of suction pressure peak has been derived under the basic assumption that the axial flow in the core of the vortex is large in comparison with the axial velocity a great distance from the center of the vortex. In addition, radial flow effects are included in the representation of the vortex core flow. The equations which result are nonlinear and lead to a two-point boundary value problem. A brief description of the equations that have been utilized in the subject formulation to describe the conical leading edge vortex flow when it becomes a free vortex is presented in the following paragraphs.

The Navier-Stokes equations written in terms of the cylindrical coordinates x, r, θ with corresponding velocity components u, v, w and under the usual boundary layer approximations are:

$$u \frac{\partial u}{\partial x} + v \frac{\partial u}{\partial r} = -\frac{1}{\rho} \frac{\partial p}{\partial x} + \nu_t / r \frac{\partial^2}{\partial r^2} (r \frac{\partial u}{\partial r}) \quad (12)$$

$$-w^2/r = -\frac{1}{\rho} \frac{\partial p}{\partial r} \quad (13)$$

$$u \frac{\partial w}{\partial x} + v \frac{\partial w}{\partial r} + vw/r = \nu_t \frac{\partial}{\partial r} (1/r \frac{\partial}{\partial r} (rw)) \quad (14)$$

$$\frac{\partial}{\partial x} (ur) / \partial x + (vr) / \partial r = 0 \quad (15)$$

In the above equations ν_t corresponds to the kinematic turbulent eddy viscosity. Upon making the following substitutions:

$$k = rw, \quad h = rv, \quad y = \frac{r^2}{2}$$

in Equations (12) through (15) and upon defining a stream function ψ such that

$$\begin{aligned} h &= \partial\psi/\partial x, \quad u = \partial\psi/\partial y \\ \text{with } \psi &= v_t x F(\eta) \quad \text{where } \eta = \frac{K_\infty^2}{v_t^2} \frac{y}{x^2} \quad \text{and also letting } K = K_\infty G(\eta), \\ \frac{p}{\rho} &= \frac{K_\infty^4}{v_t^2 x^2} K(\eta) \end{aligned}$$

the partial differential equations are reduced to the following set of ordinary differential equations:

$$FF'' - F'^2 = 2(K + \eta K') + 2 \frac{d}{d\eta} (\eta F'') \quad (16)$$

$$\frac{G^2}{4\eta^2} = K' \quad (17)$$

$$-FG' = 2\eta G'' \quad (18)$$

In the above equations, K_∞ is the value of the circulation of the vortex divided by 2π . The corresponding set of boundary conditions are:

$$\begin{aligned} G &= 0, \quad F = 0 \quad \text{at } \eta = 0 \\ G &\rightarrow 1, \quad F' \rightarrow 0, \quad K\eta \rightarrow -1/4 \end{aligned}$$

Equations (16) through (18) indicate that a self-similar solution of Equations (12) through (15) can be obtained in terms of similarity variable η as defined above.

The details of the numerical solution of Equations (16) through (18) with the boundary conditions described above are given in Reference 7. In this representation of the vortex, the radial distribution of circumferential velocity is such that the vortex consists of a core near the center resembling a solid body rotation, but outside the core the circumferential velocity varies.

The maximum circumferential velocity is given by

$$w_{\max} = C_w \frac{K_\infty^2}{v_t x} \quad (19)$$

$$\text{and the core radius is defined as } r_c = C_r \frac{v_t x}{K_\infty} \quad (20)$$

Here C_w and C_r are constants depending on a parameter \bar{C} that can vary from 0 to $-1/2$.

The value of parameter \bar{C} can be related to the shape of the leading edge and how it affects the formation of the leading edge vortex. Physically, \bar{C} equal to -0.5 corresponds to a smooth formation of leading edge vortex with drag associated with it being a minimum. A vortex from a sharp leading edge should correspond to a value of \bar{C} which is greater than -0.5 such as -0.3 . A larger value of \bar{C} (e.g., -0.3) results in greater axial velocity at the center of the vortex and consequently corresponds to a vortex with higher drag associated with it. This vortex also has higher values of the maximum swirl velocity. For the present application the formation of the vortex has been assumed to be smooth and, therefore \bar{C} has been taken to be equal to -0.5 . For example, when $\bar{C} = -1/2$, $C_w = 0.16$ and $C_r = 4.2$. The radial flow behaves as a sink, entraining fluid which is transformed into axial flow in the vortex core. The maximum axial velocity for $\bar{C} = -1/2$ is defined by

$$U_{\max} = C_u \frac{K_\infty^2}{v_t x} \quad (21)$$

at the center of the core of the vortex. For $\bar{C} = -1/2$, C_u is equal 0.30. Reference 7 presents the procedure by which values of the constants C_w , C_r and C_u are computed for other values of \bar{C} .

It can be seen from Equation (21) that the axial velocity becomes smaller as the distance x along the vortex core increases. This indicates that after some downstream distance the axial velocity will no longer be large with respect to the free stream velocity and, therefore, at that stage the vortex should be represented by a different mathematical model such as that of Batchelor.

The self-similar solution of the conical vortex flow can be utilized for the prediction of the incremental suction in the vicinity of the vortex interacting with a lifting surface. Since it is assumed that the leading edge vortex immediately after its formation has radial, swirl, and axial flow characteristics, the solution of the similarity equation yields relations for the two velocity components as follows:

$$v_\phi = (w_{\max}) \frac{k}{d'} (1 - K_2 e^{-K_3 d'^2}) \quad \text{for } d' > 0 \quad (22)$$

$$v_a = (w_{\max}) K_4 e^{-K_5 d'} \quad \text{for } d' > 0 \quad (23)$$

$$\text{where } d' = \frac{d}{r_c}$$

Equations (22) and (23) describe the swirl velocity and axial velocity components of the vortex at any radial distance d from the center of the vortex when d is greater than r_c . Here, r_c is the core radius as described by Equation (20) and (W_{\max}) is the maximum swirl velocity given by Equation (19). K_1 , K_2 , K_3 , K_4 , and K_5 are constants obtained by curve fitting the numerical solution of Equations (16) through (18).

By placing two identical vortices, whose flow characteristics are represented by Equations (22) and (23), adjacent to a lifting surface, one above and its image below the wing at equal distances, the no flow boundary condition through the airfoil surface is identically satisfied. Since the distance d is greater than the viscous core radius r_c , the vortex flow characteristics outside of the core are assumed to be similar to that of a potential vortex. Due to the image vortex, the tangential velocity and axial velocity components in the image plane (wing surface) are doubled and the suction field is intensified by a factor of four compared to the isolated vortex. Thus, the incremental static pressure coefficient created by the wing vortex interaction on the surface for $d > r_c$ may be defined as

$$\Delta C_{pv} = \frac{4}{U_0^2} (v_\phi^2 + v_a^2) \quad (24)$$

Here the effects of the swirl flow and axial flow have been combined and Bernoulli's Law has been utilized. Also, the increment of suction pressure has been nondimensionalized with respect to $\frac{1}{2} \rho U_0^2$. Substitutions of Equations (22) and (23) into (24) results in the following relationship

$$\Delta C_{pv} = 4 \left(\frac{W_{\max}}{U_0} \right)^2 \left[K_4^2 e^{-2K_3 d} + \frac{K_1^2}{d^2} (1 - K_2 e^{-K_3 d^2})^2 \right] \quad (25)$$

Equation (25) in combination with Equations (20) and (21) describe, in general, the incremental suction peaks due to the vortices at any point on the wing surface, with d being the radial distance of the point on the wing surface from the axis of the vortex.

The prediction of the incremental suction peaks by application of Equation (25) is semi-empirical due to the fact that the turbulent kinematic viscosity ν_t and the parametric constant \bar{C} have to be established empirically at the present time. The other parameter, circulation K_∞ , is estimated initially by the application of the Helmholtz vorticity theorem and a simple roll up theory. The final strength of the vortex is determined by the program from the wing loading distribution that is predicted. The distance d is known once the force free position of the vortex is established.

The eddy viscosity in the core of the vortex, ν_t , has been shown to be a function of Reynolds number $2\pi K_\infty/\nu$ where ν is the kinematic viscosity of the air. Based upon experimentally obtained results from various sources, an empirical expression has been developed by various researchers for the eddy viscosity, ν_t (Ref. 8). If the Reynolds number R_N is defined as

$$R_N = \frac{2\pi K_\infty}{\nu}$$

and the kinematic eddy viscosity parameter α as

$$\alpha = \frac{\nu_t}{2\pi K_\infty}$$

then for Reynolds numbers R_N between 10^3 and 5×10^5 , the parameter α is given by

$$\alpha = 10^{-3} \left[\frac{197}{\sqrt{R_N}} + 0.6 \right]$$

For R_N outside the range mentioned above, α has to be obtained from some other source. For example, Reference (8) also gives a value of $\alpha = 0.2 \times 10^{-3}$ for very large Reynolds number ($> 10^7$). It is suggested that this value of α may be utilized for full scale wings with vortices of large magnitude.

The self-similar solution representing the conical upstream portion of the leading edge vortex indicates that the maximum axial velocity becomes smaller as the vortex moves downstream relative to the wing. It is obvious, therefore, that after some downstream distance, say at x equal to x_t , the conical flow representation of the vortex must evolve into a different vortex flow such as that described by Batchelor (Ref 4). Batchelor's solution is based on the assumption that the axial velocity in the core region is smaller than the free stream velocity. It is obvious that this assumption is clearly valid for downstream stations of the leading edge or strake vortices. One of the main differences between the two flows is in regards to the variation of the viscous core radius r_c with the downstream distance x . At upstream stations ($x < x_t$) where the conical flow representation of the vortex is utilized, r_c increase linearly with x while at downstream stations ($x > x_t$), for which the Batchelor vortex representation is utilized, r_c varies approximately as the square root of the distance, say $(x - x_t)^{1/2}$. At x_t , the velocity of the core is assumed to be approximately equal to the free stream

velocity and the vorticity, kinematic and potential energy volume flow, etc., are conserved as the representation of the vortex is changed from the conical representation developed from Goodman to that developed by Batchelor.

As the core velocity continues to decrease, keeping the flow of volume flux in the core approximately constant, the vortex will reach a set of flow conditions that will induce vortex bursting. The criterion for the determination of vortex breakdown that has been utilized in the present analysis is based on the theory of finite transition as given by Benjamin (Ref. 9). In this theory of finite transition, the breakdown is related to a process similar to the hydraulic jump or a shock wave. Using the hydraulic jump analog, the theory explains the vortex-breakdown phenomenon as a transition between two steady states of axisymmetric swirling flow. The state upstream from the breakdown is assumed to be super-critical and conservation equations for mass, axial momentum and angular momentum are applied to relate the flow conditions upstream and downstream of the transition. Barcilon (Ref. 10) has worked out the details of a simple case of a vortex having a core rotating as a solid body surrounded by potential flow and having uniform axial velocity in the core. The results indicate the existence of critical velocity u_c which is analogous to the velocity of sound in a compressible flow. Barcilon defines this critical velocity as

$$u_c = \frac{\pi K_\infty^2}{2Q}$$

with Q being the volume flux in the core and K_∞ is the strength of the vortex divided by 2π . It is noted that transition can occur only from a velocity higher than the critical (super-critical) velocity u_c to one that is lower.

4.3. Determination of Regions of Separated Flow

At moderate to high angles of attack, the flow over the surface of a low aspect ratio swept wing is very complex and may be described by a mixture of potential, vortex and separated flow regions. The separation and/or reattachment are highly influenced by the character of the boundary layer, such as a laminar or turbulent layer. Several methods have been developed for the calculation of three-dimensional boundary layers over swept wings. These methods are semi-empirical as regards the specification of shear stresses and the initial conditions. These methods are very successful in predicting separation at low angles of attack but the procedures seem to break down for wings at high angles of attack.

A simple criterion for the prediction of the separated flow regions was utilized in the earlier work of this investigation (Ref. 2) and reasonable results were obtained. Specifically, the procedure for determining whether at any point on the wing, separation had occurred or not, involved a comparison of the net aerodynamic angle of attack (the geometric angle of attack minus the induced angle) versus an empirically defined angle above which the section was assumed to be stalled. The evaluation as to whether or not separation had occurred or not, was conducted on an element-by-element basis so that at various geometric angles of attack, the lifting surface had different regions of separated flow.

Since in the present analysis, the slope of the surface of the airfoil is included, it is believed that an improvement in the determination of the fully separated flow regions based on the same criterion as used in Reference 2 is obtained. In the present analysis the aerodynamic angle corresponds to the local geometric angle of attack of the surface element with respect to flow minus the induced angle. It is noted that since the upper and lower surfaces of the wing are treated independently, the flow is always attached (potential) on the lower surface, while the upper surface has a mixture of potential and separated flow regions. It is recognized that it is difficult to predict the pressure coefficients in separated flow regions due to the highly complex nature of the flows. In fact, a rigorous flow analysis using Navier-Stokes equations is generally necessary to determine the pressure distribution in the separated flow region. In the present analysis, an approximate but simple expression based on Bernoulli's equation was used to determine the pressure distribution. In the separated flow region, the total pressure of the flow is reduced due to viscosity. Denoting this reduction by ΔH the pressure coefficient C_{pi} in the separated flow region can be expressed as

$$C_{pi} = 1 - \frac{V^2}{V_0^2} - \Delta H \quad \text{where } V \text{ is the total velocity and } V_0 \text{ is the free stream}$$

velocity. The discrete vortices in the flow (surface lattice in the attached flow and free vortices from the leading edge and trailing edges) are used to determine the induced velocities in the separated flow. Using these induced velocities, the pressure coefficient C_{pi} in the separated flow region was therefore assumed to be $C_{pi} = 1 - V_i^2/V_0^2$ where it is assumed that ΔH is small.

4.4. Manner of Conducting the Calculations

The theoretical formulation briefly outlined in the previous section has been programmed for use on high speed digital computers. While the computer program has been used on the CDC 7600, it is easily adaptable for use on the majority of commercially available computer systems.

Figure 16 presents a flow diagram that depicts the manner by which the calculations are carried out. On the basis of the various input data the influence coefficients of the surface lattice system are computed and with this information the potential flow solution of the wing at angle of attack without the influence of the vortex flows is obtained.

With this information, the initial estimate of the vortex strengths are determined. The influence coefficients for the relative wing-vortex positions are computed and using the initial value of the vortex strengths, the vortex induced velocity distribution over the surface of the wing is computed. Knowing the total induced velocity distribution over the surface of the wing, the areas of separated flow are first determined and then the strengths of the doublets over the potential flow regions are redetermined. With the areas of separated flow known and the new doublets strengths determined, the total velocity magnitude and direction at the vortex control points is determined and a new vortex position computed. If the new vortex position is not the same as the previous position (within specific limits) a new set of vortex strengths and wing vortex position influence coefficients are computed and the iteration procedure is continued as shown in Figure 16. Once convergence has been obtained, the pressure coefficients due to the vortex potential and separated flows are determined over the surface of the wing.

5.0. CORRELATION OF THEORETICAL AND EXPERIMENTAL RESULTS

Some predicted results as a sample of the effectiveness of the theory in predicting the measured aerodynamic characteristics of low aspect ratio wings at high angles of attack will be compared with experimental results obtained with the wing-strake configuration that was tested at an angle of attack of 21.6 degrees. Reference 3 presents additional correlation between experimental and theoretical results for the same wing-strake configuration at an angle of attack of 27.7 degrees as well as for the wing without the strake at angles of attack of 13.1 and 21.6 degrees. For the computation, the upper surface of the wing was represented by 104 quadrilateral elemental surfaces with thirteen control points along the chord at each of eight spanwise stations. The lower surface was divided into a total of 72 boxes with nine chordwise and eight spanwise control points. The free vortices such as the strake vortex, leading edge vortex, etc., were each represented by up to 30 segments. The effects of airfoil thickness and curvature were accounted for in the computations as the chordwise slopes of the surface (dz/dx) were obtained from the analytical expression describing the geometric characteristics of the NACA 006 airfoil. The effects of the spanwise slope (dy/dx) were not included in the present computations. For all computations the stall angle of the surface segments were assumed to occur at 20 degrees.

The predicted vortex geometries for the wing-strake configuration at an angle of attack of 21.6 degrees are shown in Figure 17. Comparison of these predicted vortex geometries with those determined by flow visualization during the tests indicated that the predicted geometries were close to those which existed on the wing at this angle of attack. Comparisons of the predicted and measured spanwise surface pressure distributions for the wing-strake configuration along several constant chord lines are shown in Figures 18a through 18d.

As can be seen from the data presented in these figures, the correlation between the measured and predicted pressure distribution is reasonably good. The greatest difference between the measured and predicted pressure distributions occurred along the 5% chord line as the predicted pressure spike due to the low pressure of the leading edge vortex is much narrower than that which was measured. This difference can be caused by two different effects. The first possibility is that the predicted vortex core size is too small, and the second and more likely reason is that the path of the leading edge vortex is predicted to cross the 5% chord line much more steeply than the real vortex. It is believed the latter reason is the cause of the relatively poor correlation as at more aft chord locations, where the vortex is crossing the lines of constant chord more rapidly, the correlation between the measured and predicted pressure distributions is much better.

Inspection of the pressure distributions for chord line positions greater than 20% shows that the prediction indicates that complete stall occurs over the outboard sections of the wing while the experimental data indicates that the wing was not fully stalled in this region. It is believed that this difference is due to the simplified stall criterion that is presently utilized in the theory. A more realistic stall criteria may evolve after the theory is more extensively utilized.

The total predicted lift for the wing and wing-strake configuration was within 5% of the measured lift for angles of attack up to 22 degrees. At 27.7 degrees angle of attack the predicted lift of the wing-strake configuration was 11% lower than the measured value. Considering the complexity of the flow over the wing surface, it is believed that the analysis has the capability of predicting the aerodynamic characteristics rather well.

CONCLUDING REMARKS

This paper has tried to summarize the highlights of an ONR sponsored research program that has been directed towards understanding and developing a predictive analysis for the aerodynamic flows developed by low aspect ratio swept wings operating at high angles of attack. The experimental data that was obtained illustrated the complexity of the aerodynamic flow developed by the attached vortices interacting with the wing surface. While the attached vortex flows were complex, the experimental data illustrated that they significantly increased the lift of the wing surface over that which could be developed by the wing surface without the vortex flows. The results of the tests demonstrated that the unstable pitching moment developed by a strong leading edge vortex could be counteracted by the horizontal tail surface even though it is operating in a highly concentrated vortex wake flow.

The research effort that has been conducted also demonstrated that a reasonably practical predictive analysis was developed that has the capability of predicting the surface pressure distributions generated by the complex mixed potential, separated and vortex flow fields developed by low aspect ratio swept wings operating at high angles of attack.

REFERENCES

1. White, Richard P. Jr. and Balcerak, John; An Experimental Investigation of Vortex Flow Control for High Lift Generation; ONR CR 212-223-2, December 1975.
2. White, Richard P. Jr., Gangwani, Santu T. and Balcerak, John; A Theoretical and Experimental Investigation of Vortex Flow Control for High Lift Generation; ONR CR 212-223-3, December 1976.
3. White, Richard P. Jr., Gangwani, Santu T., and JanakiRam, D. S.; A Theoretical and Experimental Investigation of Vortex Flow Control for High Lift Generation; ONR CR 212-223-4, December 1977.
4. Batchelor, G.K.; Axial Flow in Trailing Vortices, Journal of Fluid Mechanics, Vol. 20, Part 4, December 1964, pp. 645-658.
5. White, R. P. Jr. and Zalay, A. D.; High Lift Generation by Use of Vortices; ONR NR 212-223, RASA/SRL Report 74-12, July 1975.
6. Hale, R. W. and Ordway, D. E.; High Lift Capabilities from Favorable Flow Interaction with Close-Coupled Canards; Sage Action, Inc., SAI-RR 7501, December 1975.
7. Goodman, T. R.; The Vortex Core Jet Near the Point of Generation; AFOSR-TR-1158, Oceanics, Inc., Report No. 72-91, April 1972.
8. Owen, P. R.; The Decay of a Turbulent Trailing Vortex; The Aeronautical Quarterly, February 1970, pp. 69-78.
9. Benjamin, J. B.; Some Developments in the Theory of Vortex Breakdown; Journal 9 Fluid Mechanics, Vol. 28, Part 2, 1967, pp. 65-84.
10. Barcilon, A. I.; Vortex Decay Above a Stationary Boundary; Journal 9 Fluid Mechanics, Vol. 27, Part 1, 1967, pp. 155-175.

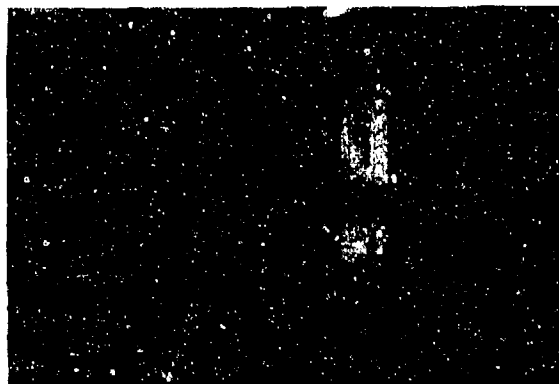


FIGURE 1: Wing-Strake Configuration Installed in the Wind Tunnel.

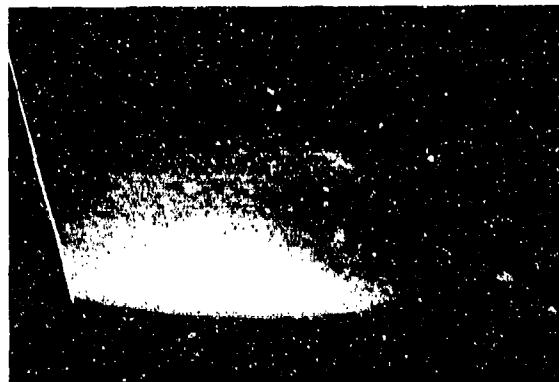


FIGURE 2: Leading Edge Vortex $\alpha_0 = 27.7$ Degrees.



FIGURE 3: Strake Vortex $\alpha_0 = 27.7$ Degrees

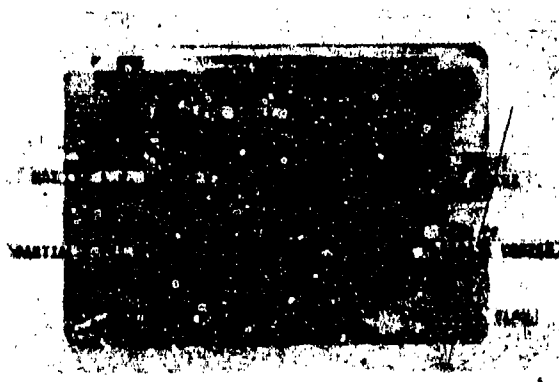


FIGURE 4: Surface Flow for Wing Strake Configuration $\alpha_0 = 27.7$ Degrees

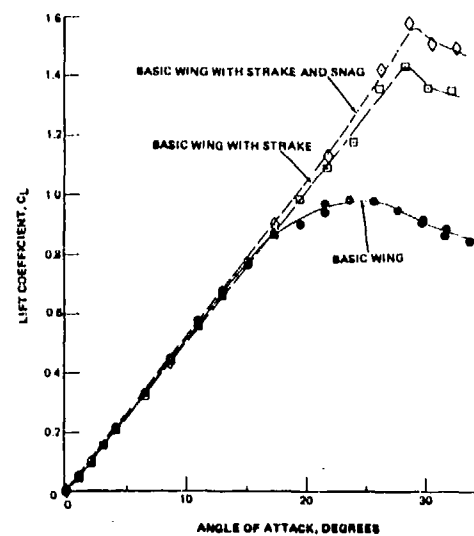


FIGURE 5: Lift Coefficient vs. Angle of Attack

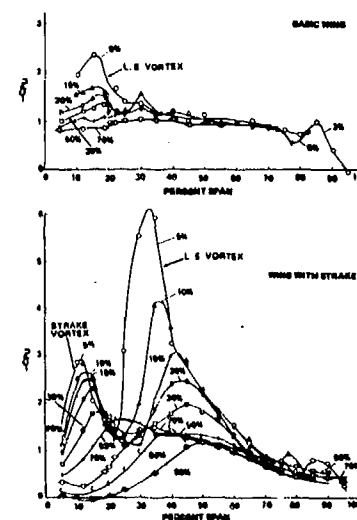


FIGURE 6: Effect of Strake on Wing Pressure Distribution at an Angle of Attack of 27.7 Degrees.

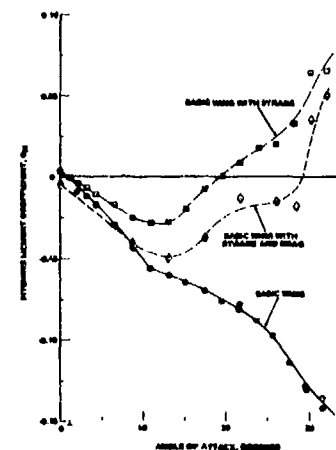


FIGURE 7: Pitching Moment Coefficient vs. Angle of Attack



FIGURE 8: Picture of Wing Tail Model in the Wind Tunnel.

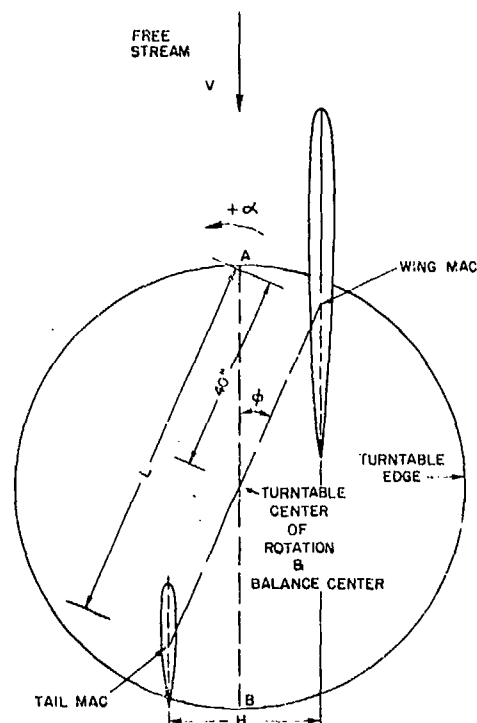


FIGURE 9: Model Arrangement on the Wind Tunnel Turntable.

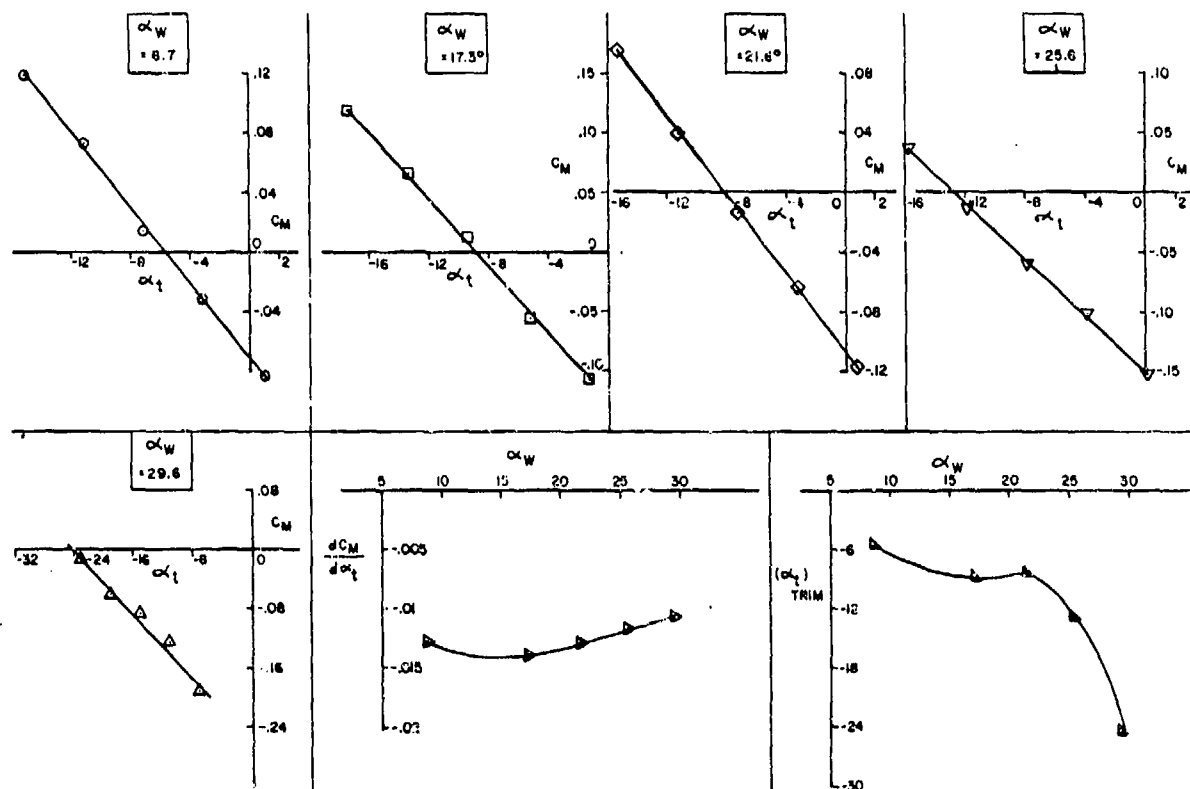


FIGURE 10: Tail Effectiveness of Basic Wing Tail Configuration ($L = 75$ inches, $H = 0.60 C_L$).

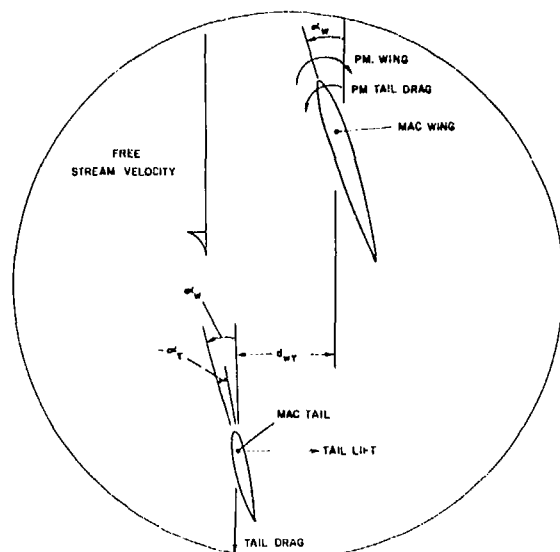
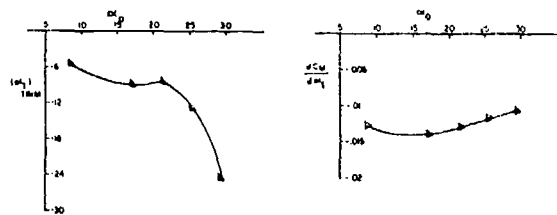
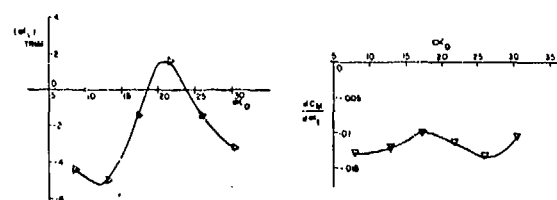


FIGURE 11: Wing-Tail Geometry, Forces and Moments at Angle of Attack.



(a) Basic Wing-Tail Configuration



(b) Wing-Strake-Tail Configuration.

FIGURE 12: Tail Effectiveness
[$L = 75''$; $H = 0.6 C_t$].

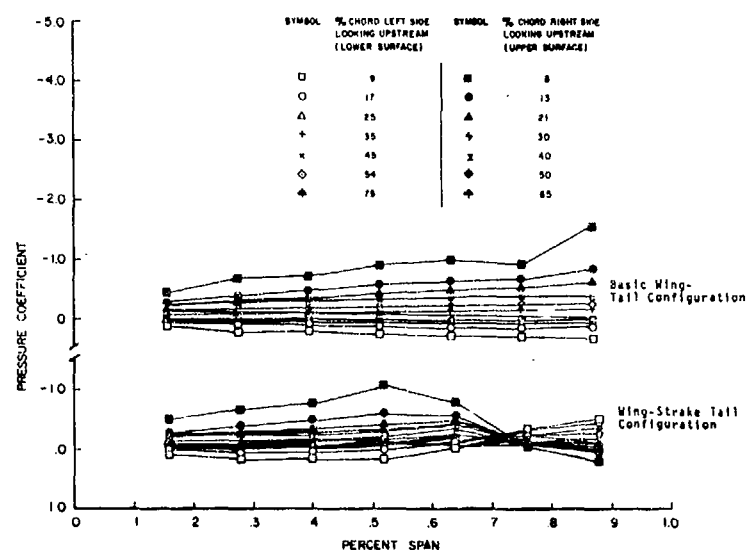


FIGURE 13: Tail Pressure Distributions at Trim
for $\alpha_0 = 13.1$ Degrees.

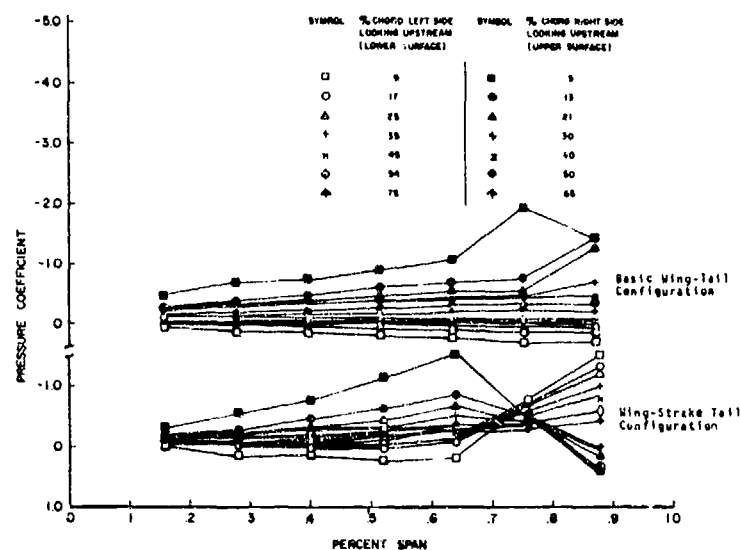


FIGURE 14: Tail Pressure Distributions at Trim
for $\alpha_0 = 17.4$ Degrees.

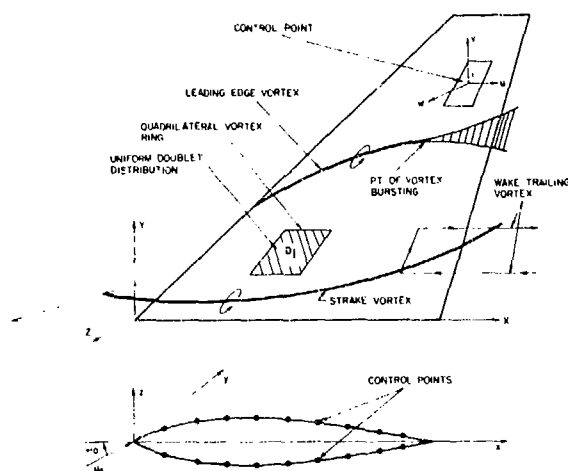


FIGURE 15: General Theoretical Representation of Aerodynamic Flows.

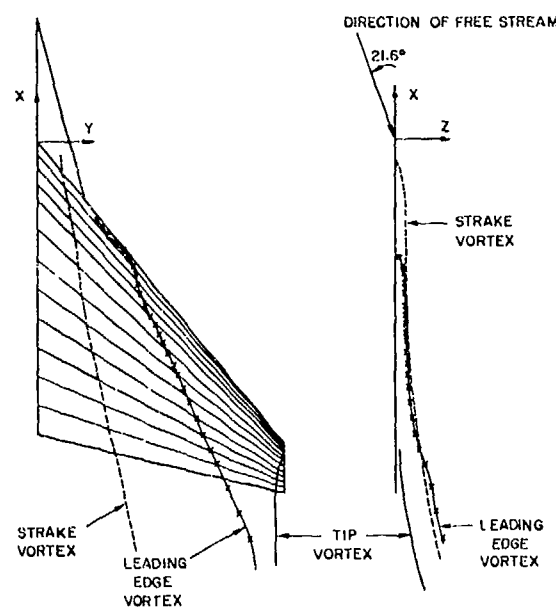


FIGURE 17: Predicted Vortex Geometry for the Wing-Strake Configuration at $\alpha_w = 21.6$ Degrees.

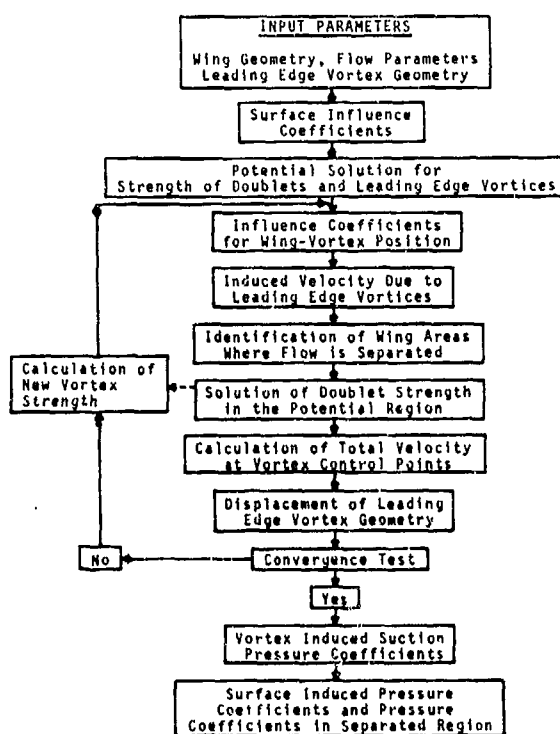


FIGURE 16. FLOW OF CALCULATION ITERATION PROCEDURE

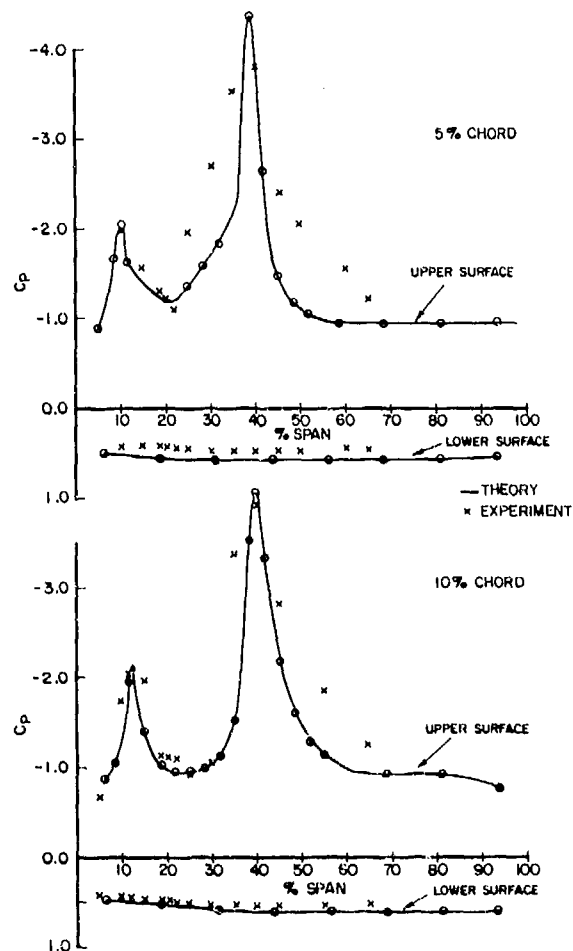


FIGURE 18a: Comparison of the Measured and Predicted Chordwise Pressure Distributions for Basic Wing $\alpha_0 = 21.6$ Degrees.

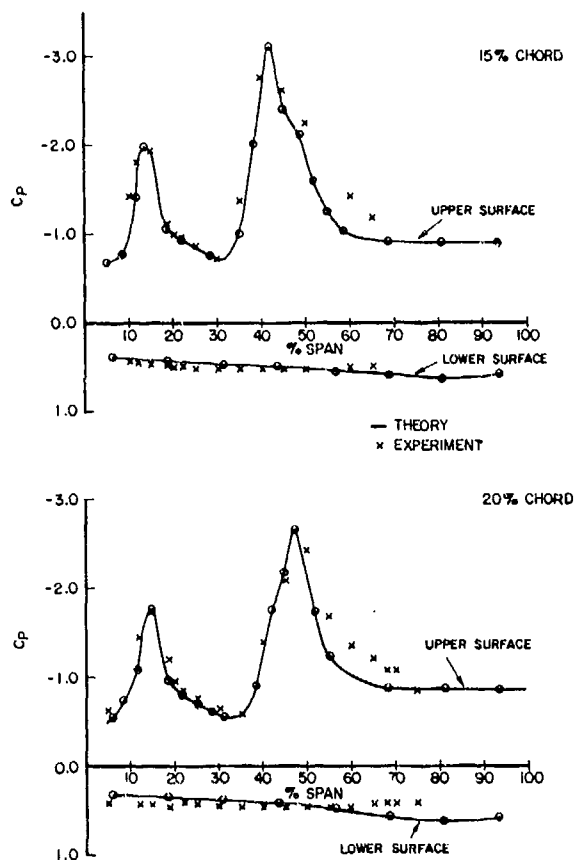


FIGURE 18b: Comparison of the Measured and Predicted Chordwise Pressure Distributions for Basic Wing $\alpha_0 = 21.6$ Degrees.

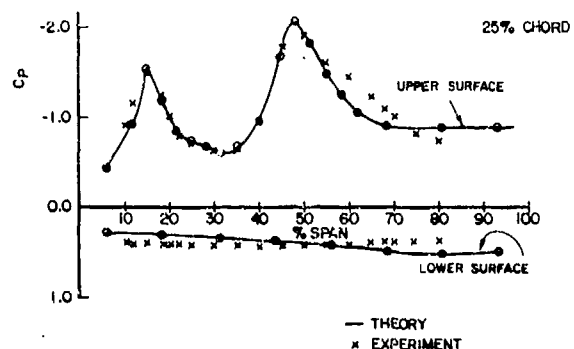


FIGURE 18c: Comparison of the Measured and Predicted Chordwise Pressure Distributions for Basic Wing $\alpha_0 = 21.6$ Degrees.

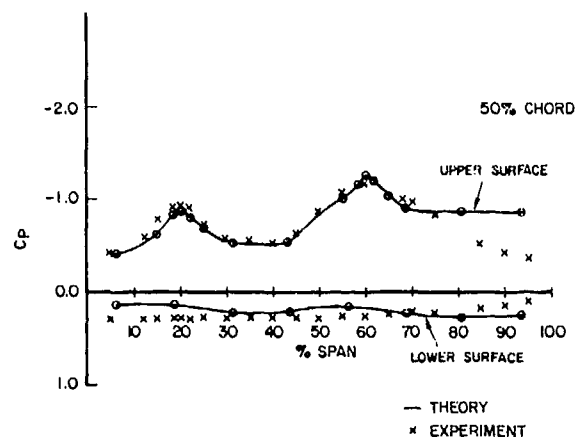


FIGURE 18d: Comparison of the Measured and Predicted Chordwise Pressure Distributions for Basic Wing $\alpha_0 = 21.6$ Degrees.

HIGH ANGLE OF INCIDENCE IMPLICATIONS UPON AIR INTAKE DESIGN AND LOCATION FOR SUPERSONIC CRUISE AIRCRAFT AND HIGHLY MANEUVERABLE TRANSONIC AIRCRAFT

Leroy L. Presley
Ames Research Center, Moffett Field, California 94035, U.S.A.

SUMMARY

Computational results which show the effects of angle of attack on supersonic mixed-compression inlet performance at four different locations about a hypothetical forebody have been obtained. These results demonstrate the power of the computational method to predict optimum inlet location, orientation, and centerbody control schedule for design and off-design performance.

The effects of inlet location and a forward canard on the angle-of-attack performance of a normal shock inlet at transonic speeds have been studied. The data show that proper integration of inlet location and a forward canard can enhance the angle-of-attack performance of a normal shock inlet.

Two lower lip treatments for improving the angle-of-attack performance of rectangular inlets at transonic speeds are discussed.

NOMENCLATURE

$k \frac{\gamma - 1}{2\gamma}$	α angle of attack
M Mach number	γ ratio of specific heats
n plane of known solution	ξ nondimensional coordinate-normalized by distance between inner and outer computational boundaries
p pressure	ρ density
q total velocity	ϕ azimuthal coordinate
r radius	ψ angle between total velocity vector and normal to cowl-lip plane
u Z component of velocity	Subscripts:
v r component of velocity	C cowl
w ϕ component of velocity	f forebody
x horizontal coordinate	i indices for ξ spacing of points
y vertical coordinate	j indices for ϕ spacing of points
Z longitudinal coordinate	T centerbody tip
\bar{Z} longitudinal coordinate normalized by r_c	t stagnation conditions
$\Delta \bar{Z}$ centerbody translation (positive forward)	∞ free-stream conditions
δ canard deflection angle	

1. INTRODUCTION

For most aircraft the propulsion system must be designed to maximize the net thrust when installed on the vehicle. This often requires that a compromise between drag, pressure recovery, and mass-flow capturing capability be made for the desired flight envelope of the aircraft. Changes in aircraft attitude and speed, as well as many other factors, must be considered for complete design of the propulsion system. This paper will address only the question of changes in angle of attack on inlet location and design. Two completely different types of aircraft will be considered: a supersonic cruise aircraft and a highly maneuverable, transonic aircraft.

Supersonic cruise aircraft are, for the most part, not designed to accommodate large excursions in angle of attack while at cruise conditions. The propulsion system is optimized for particular design conditions with some small margin allowed for excursions in airplane attitude. More often than not, the inlet is placed in a location to minimize upstream flow-field perturbations due to changes in airplane attitude. Precise location of the inlet is usually determined by empirical design rules or wind tunnel testing. However, recent developments in computational methods (see Refs. 1, 2) are, for the first time, providing the designer with the capability of determining the effects of angle of attack on inlet location and orientation and of determining the performance of a limited class of inlets (axisymmetric mixed-compression inlets) in three-dimensional flow fields. To demonstrate this capability, numerical solutions have been obtained for an ellipsoidal body at $M=2.65$ and at several angles of attack. Inlet solutions are then obtained at four different flow-field locations and compared with uniform flow-field solutions. The results show computational predictions of the effects of angle of attack on inlet location for this idealized geometry. This particular configuration demonstrates both the effects of fuselage shielding and the highly nonuniform flow around the sides of the aircraft.

2.2 Analytical Method

The analytical method used in this paper consists of three main components: (1) a technique for computing the supersonic flow about a fuselage of arbitrary cross section at angle of attack, the Kutler code; (2) a technique for computing the supersonic flow in a mixed compression, axisymmetric inlet with nonuniform upstream flow; and (3) a method to couple these two techniques so that a combined solution can be obtained.

The two flow computation techniques have a common basis, the finite-difference, shock-capturing technique described in Ref. 1. A brief description of the general features of the shock-capturing technique and details relevant to each technique are given below.

2.3 Shock-Capturing Technique

The finite-difference, shock-capturing technique described here consists of solving the equations of motion, written in conservative form, between the body and some outer computational boundary. The equations of motion are written in the following form:

$$E_z + F_r + G_\phi + H = 0$$

The terms E, F, G, and H are vector components defined as:

$$E = \begin{bmatrix} \rho u \\ k\rho + \rho u^2 \\ \rho uv \\ \rho uw \end{bmatrix} \quad F = \begin{bmatrix} \rho v \\ \rho uv \\ k\rho + \rho v^2 \\ \rho vw \end{bmatrix} \quad G = \frac{1}{r} \begin{bmatrix} \rho w \\ \rho uw \\ \rho vw \\ k\rho + \rho w^2 \end{bmatrix} \quad H = \frac{1}{r} \begin{bmatrix} \rho v \\ \rho uv \\ \rho(v^2 - w^2) \\ 2\rho vw \end{bmatrix}$$

A complete set of equations is obtained by employing the energy equation in the following form:

$$p = \rho(1 - q^2)$$

where

$$q = \sqrt{u^2 + v^2 + w^2}$$

The solution of these equations throughout a supersonic flow field proceeds from a plane wherein all the flow properties are known to a subsequent downstream plane. Spacing between the planes is controlled by the minimum domain of influence, that is, signal propagation along Mach lines, of all of the points in the known plane. Spacing between the planes or step size less than the above, Courant number less than one, can be used in some cases to improve accuracy.

In the shock-capturing solutions presented in this paper, MacCormack's second-order accurate finite-difference algorithm (Ref. 1) was used to obtain the conservative variables at each point in the downstream plane. This algorithm is a two-step process using first the following predictor equation

$$\bar{E}_{ij}^{n+1} = E_{ij}^n - \frac{\Delta z}{\Delta \xi} (F_{i+1,j}^n - F_{ij}^n) - \frac{\Delta z}{\Delta \phi} (G_{i,j+1}^n - G_{ij}^n) - \Delta Z H_{ij}^n$$

and subsequently, the following corrector equation:

$$E_{ij}^{n+1} = \frac{1}{2} \left[\bar{E}_{ij}^{n+1} + E_{ij}^n - \frac{\Delta z}{\Delta \xi} (\bar{F}_{ij}^{n+1} - \bar{F}_{i-1,j}^{n+1}) - \frac{\Delta z}{\Delta \phi} (\bar{G}_{ij}^{n+1} - \bar{G}_{i,j-1}^{n+1}) - \Delta Z H_{ij}^{n+1} \right]$$

After each step, the conservative variables must be decoded to find the physical variables at each point. Barred superscripts denote predicted values.

Further, both techniques use a common method for determining the flow along the body surface which is the inner computational boundary. After the flow is predicted at the body, the velocity vector will not necessarily satisfy the surface tangency condition. A small, local Prandtl-Meyer turning is imposed to satisfy the tangency condition, and the predicted flow variables are adjusted accordingly. A direct consequence of this approach is that the body surface becomes a constant entropy surface, even across discontinuities in surface curvature or shock wave reflections. The method does, however, give an accurate indication of surface pressures when compared to more accurate calculations, or experimental data (see Ref. 2).

The two techniques differ in their treatment of the outer boundary conditions. This difference is discussed in the following paragraphs.

2.3.1 Forebody Solutions

The outer computational boundary for the forebody code is the bow shock wave, which is maintained as a discrete shock wave in the solution. Conditions at the shock wave are found by solving the Rankine-Hugoniot equations at each computational point on the shock wave. All other shock waves that are generated within the solution are captured by the numerical technique and diffused over several streamwise mesh points. Presently, the forebody code is limited to flows at angle of attack, that is, yaw or sideslip cannot be considered. For detailed information of the forebody technique, the reader should refer to Ref. 1.

2.3.2 Inlet Solutions

The outer computational boundary for the inlet code is an arbitrary conical surface that is sized to contain the conical shock from the centerbody tip. Flow properties at this computational boundary must be known, either input as uniform flow or, as will be described later, obtained from another computational technique, such as a forebody flow-field solver. In this solution, the centerbody conical shock wave and all other shock waves are captured by the numerical technique and diffused over several streamwise mesh points.

Since several modifications to the inlet code described in Ref. 2 have been made to allow solution of flows wherein the initial flow is nonuniform, some discussion of these modifications is appropriate. As shown in Fig. 3(a), the computation of the inlet flow is divided into three domains: conical flow, external flow, and internal flow.

A small region of conical flow is computed at the centerbody tip in order to obtain a starting solution. This is, of course, an approximation since conical flow does not exist for flows with nonuniform upstream conditions. However, if this region is kept sufficiently small, then the effect of this approximation should also be small. For inlet solutions, in a nonuniform flow field, as described here, the flow properties from the forebody flow field at coordinates of the centerbody tip are used for the free-stream conditions. The three-dimensional velocity vector at that point is resolved into a simple "angle of attack" for the cone flow solution. Further details of the conical flow solution are presented in Ref. 2.

Computation of the flow in the external flow domain required the majority of the modifications from the uniform case. First, in nonuniform flow an axis of symmetry does not necessarily exist. This requires that the flow completely around the inlet be calculated using an indexing scheme as shown in Fig. 3(b). Secondly, the nonuniform flow on the outer computational boundary must be input from another solution, in this case the forebody solution. At every point on the outer computational boundary, the nonuniform upstream flow is required; the method for obtaining this flow will be described later.

No changes to the computation of the internal flow, other than the provision to compute completely around the inlet, were required.

2.4 Coupling Technique

Coupling of two supersonic solutions together is the easiest class of problem for two interacting flows. Since there are no upstream propagating disturbances, no iteration is needed, and coupling is reduced to determining the upstream boundary conditions for subsequent downstream solutions.

In this case, output from the forebody code is in the form of the flow properties, p , ρ , u , v , and w at each point in the forebody cylindrical coordinate system Z_f , r_f , and ϕ_f . The output data are for variable radii between the body and the shock wave at constant azimuthal angles, ϕ_f within a plane of constant Z . A portion of the total forebody solution that was adequate to bound the entire inlet solution was saved on a permanent file within the computer. Essentially, data are saved over a radius interval equal to twice the inlet diameter at azimuthal angles that bound twice the included angle of the inlet diameter and Z planes from the most forward position of the centerbody tip to just aft of the cowl-lip station, as shown in Fig. 4.

Two different kinds of information can be obtained from the computational data stored in the pie shaped volume shown in Fig. 4. First, data can be obtained in any plane within the volume for definition of the flow properties within that plane. (If experimental data are available in the plane, direct comparison with that data can be made.) Secondly, computational data are obtained along the outer computational boundary for the inlet solution. Droop and toe-in of the inlet axis relative to the fuselage axis, or similarly the orientation of any plane, can be accounted for by proper transformation. The first step in obtaining the desired information from the forebody data file is to transform the coordinates of a known point in the inlet geometry or some known plane to the forebody coordinate representation. Forebody flow properties at those points are obtained from the data file using a three-dimensional linear interpolation scheme. Flow velocities from the forebody solution are then transformed to the coordinates system of the known plane.

All inlet solutions are obtained in a cylindrical coordinate system whose origin is the centerbody tip and whose Z axis is coincident with the centerline of the inlet. Points on the outer computational boundary are transformed to the cylindrical coordinate system of the forebody solution and flow properties at those points are obtained by the interpolation scheme described above. The velocities of the forebody solution are then transformed to the inlet coordinate system and entered into the inlet solution as known properties along the outer computational boundary (see Fig. 3).

2.5 Results and Discussion

The results presented here have been chosen to demonstrate three points: (1) the nature of the flow in the inlet at $M=2.65$ and $\alpha=0$ when it is isolated from the forebody; (2) the effect of placing the same inlet at four different locations in the forebody flow field with the forebody at $M=2.65$ and $\alpha=0$, and (3) the effect of forebody angle of attack on the inlet flow at the four different locations.

The pressure distribution for the isolated inlet at $M=2.65$ and $\alpha=0$ is shown in Fig. 5. These inlet contours have been designed to produce a nearly isentropic internal flow with effectively no internal shock waves. The Z coordinate is measured from the centerbody tip and has been normalized by the radius of cowl. For these calculations, a complete solution, defined as one with supersonic flow throughout the inlet, was obtained with the cowl in the design position, $Z_a = 2.325$, which corresponds to a centerbody translation $\Delta Z = 0$.

Complex three-dimensional flows are not easily amenable to simple graphical description. Variation of the flow into an isolated axisymmetric inlet at angle of attack can be bounded by the flow along the

windward, $\phi = 0^\circ$, and leeward, $\phi = 180^\circ$, meridians. Once the inlet is immersed in a nonuniform upstream flow, no such convenient axis of symmetry exists. An a priori specification of the meridians where the maximum and minimum pressure distributions will exist is not possible and, for the most part, computational results must be interpreted with the aid of computer graphics. However, for ease of presentation and for reasons to be discussed later, pressure distributions will be shown on the two meridians that nearly bound the pressure distributions in the inlet.

The pressure distributions in the inlets for locations 1, 2, and 3 (see Fig. 1) are shown in Figs. 6 through 8, respectively, for a forebody angle of attack of zero. In addition to the pressure distributions, the local mach number, effective angle of attack, and meridional angle ϕ_r of the projection of the total velocity vector onto a plane normal to the fuselage Z axis at the centerbody tip are noted on the figures. A primary difference for all of these solutions from the isolated inlet solution (also included on the figures) is that the centerbody has been translated forward to maintain supersonic flow in the inlet at the slightly different Mach numbers and angles of attack. Results for location 1 are given at $\phi = 0^\circ$ and 180° while results for locations 2 and 3 are given for $\phi = 90^\circ$ and 270° . This is done to correspond to the windward and leeward meridians of the effective angle of attack. In all cases, it is noted that the internal pressures, and hence the peak attainable pressure recovery, are reduced due to translating the centerbody forward. Tilting the inlet axis by the effective angle of attack would reduce the required centerbody translation and hence result in higher pressure recovery. Results are not shown for location 4 because they are identical to those for location 1, except that they are all rotated through 180° . Note that location 1 appears to be the best position, as might be expected. Of the two side locations, the second appears to be the better at this angle of attack. However, as will be seen below when angle of attack effects are discussed, this will not be the case.

When the forebody angle of attack is increased to 8° , the forebody flow at the centerbody tip changes dramatically, as shown in Figs. 9-12. Optimum angle-of-attack shielding to produce a low effective angle of attack at the centerbody tip was obtained with the inlet in location 1, as also obtained experimentally in Ref. 3. However, the tip Mach number is low, requiring a large forward translation of the centerbody to maintain supersonic flow. This large centerbody translation could be reduced by changing the internal contours of the inlet to reflect a lower design Mach number.

At location 2, the basic forebody flow produces a large effective angle of attack of 11.3° at the centerbody tip. The rate of change of effective angle of attack with forebody angle of attack is greater than one in this location. This is due in part to the rapid expansion around the side of the body. Because mixed-compression axisymmetric inlets are not designed for such large angles of attack, some change in inlet orientation would be required for satisfactory inlet operation at this location. To obtain a complete solution, it was required to droop and toe-in the inlet axis relative to the fuselage by 8° and 4° , respectively. This reduced the effective angle of attack at the centerbody tip to 1.8° , as shown in parenthesis in Fig. 10. However, even then the large flow-property gradients upstream of the inlet required an extensive centerbody translation to obtain a complete solution. The variation in pressure distributions shown in Fig. 10 is, for this case, due to the large gradients in flow properties ahead of the inlet. Due to these large gradients, this location would probably be unsatisfactory for successful inlet operation at flight conditions wherein the forebody would be at angle of attack.

Both the effective angle of attack ($\alpha_T = 8.9^\circ$ for no droop or toe-in) and Mach number are reduced at location 3. Here a droop of 6° and a centerbody translation of $\Delta Z = 0.6$ allowed a complete supersonic solution to be obtained. More careful alignment of the inlet with the oncoming flow in this location could probably produce satisfactory inlet operation. Again, a slightly lower design Mach number might be helpful in producing better inlet performance.

The forebody flow at location 4 produced an inlet flow which was very close to the isolated inlet flow. Although the tip Mach number is above the design Mach number of 2.65, it reduces the required centerbody translation to account for angle-of-attack effects. Until significant flow separation effects occurred on the forebody, good inlet performance at angle of attack could probably be achieved in this location.

All of the forebody solutions were computed utilizing a mesh at 30 points in the azimuthal direction ($\phi = 0^\circ$ to 180°) and 11 in the r direction with a Courant number of 0.9. Complete forebody solutions required about 200 sec of CDC 7600 computing time. Inlet solutions were obtained utilizing 20 points in the azimuthal direction ($\phi = 0^\circ$ to 360°) and 21 points in the r direction and a Courant number of 1.0. Isolated inlet solutions required about 15 sec to compute and the nonuniform solutions required about 30 sec of CDC 7600 computing time.

The primary power of this analytical method, as demonstrated from results shown above, is its capability to determine required modifications to inlet design and location in order to achieve optimum performance when the inlet installed in a forebody flow field. Further, the effects of off-design airplane operation on inlet performance can be assessed and preliminary centerbody control schedules can be established. This should result in significantly improved designs as well as reduced design time and costs. Reductions in cost would result primarily from reductions in wind-tunnel testing to develop an optimum inlet configuration and location. Wind-tunnel testing could then focus on design refinements and on establishing final control schedules.

3. TRANSONIC AIRCRAFT

In contrast to the situation for supersonic flows, the capability to compute complex forebody and inlet flows at transonic speeds does not exist at present. However, a brief review of some current work to develop this methodology will be given here. Afterwards, a presentation will be given of some recent experimental results which will illustrate the difficulties of inlet location for operation of transonic aircraft at high angles of attack.

3.1 Transonic Computations

The computation of complex transonic flows is in a much more formative state than the computation of complex supersonic flows. Completely general methods, which can analyze the complex transonic flows discussed in this paper, must await the development of at least the next generation of computers (beyond the CDC STAR or the CRAY I, for example) as well as additional insight into the modeling of turbulent flows. However, some significant progress is being made toward computation of somewhat simpler transonic flows. Two efforts, currently under way on contract to Ames Research Center, are being developed to compute transonic flow about isolated forebodies of quite general cross section and into three-dimensional inlets, respectively. Coupling these two solution techniques together will provide the capability to solve airframe/inlet interaction problems of simple forebody-inlet configurations.

The forebody solution technique is a Navier-Stokes code being developed by Numerical Continuum Mechanics, Incorporated. An alternating-direction explicit algorithm is used to solve the full Navier-Stokes' equations. Computation of the flow proceeds in two different marching directions. Elliptic terms in either marching direction are evaluated from the previous calculation, or the initial approximation. Solution in any given marching direction reduces to solving for the flow in a plane which is either moving along the body or around the body at some uniform velocity. Typically, 8 to 10 points are included in the boundary layer with the viscous sublayer being resolved with the boundary-layer equations. Although a solution for a body of noncircular cross section has not been obtained to date, a solution of the flow about a tangent-ogive looks very encouraging in that vortex location has been accurately predicted. Completely converged solutions should be obtainable in three marching sweeps with satisfactory engineering solutions being obtainable in two sweeps. Ultimately, each sweep should take about 1 hr of CDC 7000 computer time.

The inlet solution technique is a time-dependent Euler code being developed by the General Dynamics Corporation. The goal of this effort is to generate a code that can analyze transonic flow into complex three-dimensional inlets. To date, most of the effort has focused on developing three-dimensional mesh generation techniques. A method, which is an extension of the Thompson 2-D mesh generation technique, Ref. 6, has been developed for generating three-dimensional meshes for any inlet configuration, and meshes have been generated for a circular transport type inlet with elliptical lips and for a horizontal ramp fighter type inlet with sharp lips. Future effort will concentrate on choosing the optimum computational algorithm (from a time and accuracy standpoint) and developing the computational code.

For engineering purposes, it is expected that these codes can be coupled in a noniterative mode for most problems at high subsonic ($M > 0.8$) and low supersonic flows ($M < 1.6$). Since both methods are finite difference techniques and will require a large number of mesh points to define the flow, large amounts of computer time will be required to obtain satisfactory solutions. Coupling the two solutions will require the development of special buffer programs in the interaction region to prevent the computational time from becoming totally unrealistic.

3.2 Experimental Results and Discussion

The limited data base for transonic aircraft design was discussed in the introduction. To extend the base of Ref. 3 for supersonic speeds to a different configuration, transonic speeds, and higher angles of attack, an effort was undertaken at Ames Research Center through a contract with Rockwell International (Ref. 4). This study investigated two different inlet shapes: (1) a kidney-shaped inlet in two fuselage locations with and without a forward canard, and (2) a rectangular inlet without a forward canard, but with several modifications to improve the high angle-of-attack performance (e.g., blunt lower lips, slats, and turning vanes).

3.2.1 Kidney-Shaped Inlets With and Without a Forward Canard

The forebody of the aircraft configuration, including the canard, is shown in Fig. 13. At the inlet face station, the inlet could be moved to two different locations: a high-shoulder location and a low-shoulder location, as shown in Fig. 14. The inlet was a kidney-shaped, normal-shock inlet having sharp lips for efficient supersonic flight. The width of the inlet face is about 1/7 of the half-span of the canard, whose deflection angle could be varied. Maximum chord of the canard was about 0.35 m.

All of the data discussed here were taken at a constant Mach number of 0.9 and a Reynolds number of $19 \times 10^6/\text{m}$. For subsonic inlet performance, it is usually customary to show pressure recovery versus mass-flow ratio at constant Mach number, model attitude, and geometry. Direct comparison of the effects of model attitude and geometry are often hard to make in this format. The data shown here will be for a mass flow ratio of 0.8 in order to remove one variable for ease of comparison. In some cases, showing inlet performance at a constant mass flow ratio will not show the total performance capability of a particular configuration, but the conclusions that will be drawn from this presentation will not be compromised by this restriction.

Total pressure recovery for the inlet in both positions, and without a forward canard, is shown in Fig. 15. As can be seen, nearly identical performance is obtained in both inlet locations up to an angle of attack of 20° . Additional tuft studies show little change in flow angularity at the two locations. Within the limitations of the geometric variations with this model, there seems to be little effect of angle of attack upon inlet location.

Pressure recovery, as a function of angle of attack for the lower and upper shoulder locations with a forward canard, is shown in Figs. 16 and 17, respectively. From Fig. 16 it is apparent that the performance at the inlet in the lower shoulder location is very sensitive to canard deflection angle. Although there seems to be some flow aligning or straightening effect of the canard, inlet performance seems to be more dependent on whether the canard wake is ingested into the inlet.

In contrast, the canard has a beneficial effect for the upper shoulder location where, as shown in Fig. 17, the pressure recovery is improved at all angles of attack for the canard deflection angles shown. Tuft studies show that straightening or aligning of the flow is effected by the canard at the upper shoulder location and there is no evidence that the canard wake is ingested into the inlet. Here, the canard is providing similar benefits to the fuselage and wing shielding obtained at supersonic speeds in Ref. 3 for the Tailor-Mate configurations. Proper integration of a forward canard and an inlet can be effective in improving the angle of attack performance of the inlet.

A limited investigation of the angle of yaw (or sideslip) effects upon inlet performance was conducted. Although no detailed data will be given here, the results will be discussed qualitatively. Data were obtained only for the inlet in the upper shoulder location with a forward canard at zero deflection. At an angle of attack of 4° , sideslip angles up to $\pm 10^\circ$ had little effect on inlet performance. At an angle of attack of 12° , some, but not drastic, loss in inlet performance was noted at a yaw angle of 10° for the windward inlet.

3.2.2 Rectangular Inlet

A rectangular inlet was mounted at the midshoulder location on the fuselage, as shown in Fig. 14, but without the forward canard shown in Fig. 13. Various lower-lip modifications were the primary geometric variables. Besides the two shown in Fig. 18, several others were tested: different slat positions, lip bluntness, and a turning vane.

Although detailed test results will not be presented, some qualitative discussion of the results is merited. The two-lip modifications shown in Fig. 18 provided the best performance, but were definitely not optimum. The internal slat configuration provided equal or better performance at high angles of attack than did the other configurations tested, including the kidney-shaped inlets. Very good high angle-of-attack performance was also provided by the thick, low-lip configuration, but this configuration was mass-flow limited at low angles of attack. Also, the blunt lip would incur a serious drag penalty at supersonic speeds. A thin lower lip with an inflatable boot might generate a blunt lip to obtain good high angle-of-attack performance and yet not have large supersonic drag.

4. CONCLUDING REMARKS

A computational method for coupling a three-dimensional supersonic forebody code and a three-dimensional supersonic inlet code together has been described. Computational results for a hypothetical supersonic configuration have been obtained. These results show the effects of angle of attack on inlet performance for four different inlet locations. The power of this computational method to indicate inlet location, orientation, and centerbody control schedule for optimum design and off-design performance is demonstrated by the computational results.

A brief description of some computational work under way to develop methods for airframe/inlet integration calculations for complex transonic flows has been given. Although much remains to be done, these techniques will ultimately provide the same capability as we now have for supersonic flows. Until then, systematic experimental studies of various configurations must be conducted to build a data base.

A recent series of experiments conducted for Ames Research Center by Rockwell International add the following results to the transonic data base:

(1) The effect of angle of attack, a forward canard, and inlet location on the performance of a kidney-shaped normal shock inlet for a hypothetical highly maneuverable transonic aircraft has been shown. Proper integration of a forward canard and an inlet has been shown to improve the angle-of-attack performance of a normal shock inlet at $M_\infty = 0.9$.

(2) The effects of lower-lip modifications and turning vanes on the performance of a rectangular normal shock inlet were investigated. Both a slat arrangement and a blunt lower lip provided very good high angle-of-attack performance at $M_\infty = 0.9$. The blunt lip produced a low mass-flow ratio at low angles of attack and would generate large supersonic drag.

REFERENCES

1. Kutler, P., Reinhardt, W. A., and Warming, R. F.: Multishocked, Three-Dimensional Supersonic Flow-fields with Real Gas Effects. AIAA J., vol. 11, 5, May 1973, pp. 657-664.
2. Presley, L. L.: Comparison of a Shock-Capturing Technique with Experimental Data for Three-Dimensional Internal Flows. NASA SP-347, pt. 1, 1975, pp. 623-642.
3. Serauer, Lewis E.: Effect of Forebody Shape and Shielding on 2-D Supersonic Inlet Performance. AIAA Paper 75-1183, AIAA/SDE 11th Propulsion Conf., October 1975, Anaheim, California.
4. Martin, Arnold W.: Investigation of Normal Shock Inlets for Highly Maneuverable Aircraft. NASA CR 137970.
5. Smetizer, D. B. and Sorensen, N. E.: Tests of a Mixed Compression Axisymmetric Inlet with Large Transonic Mass Flow at Mach Numbers 0.6 to 2.65. TN D-6971, 1972, NASA.
6. Thompson, J. F., Thames, F. C., and Martin, W. C.: Automatic Numerical Generation of Body-Fitted Curvilinear Coordinate System for Field Containing Any Number of Arbitrary Two-Dimensional Bodies. J. Computation Physics, vol. 15, no. 3, July 1974, pp. 299-319.

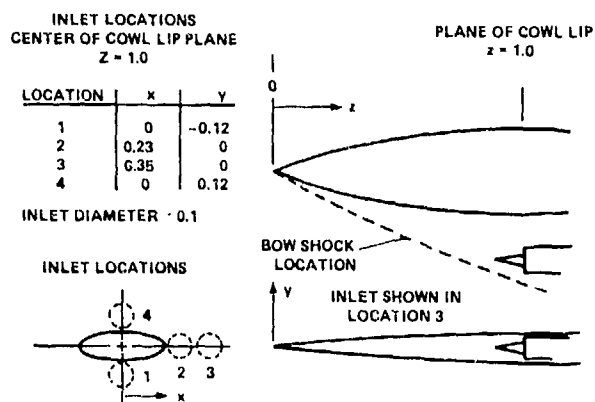
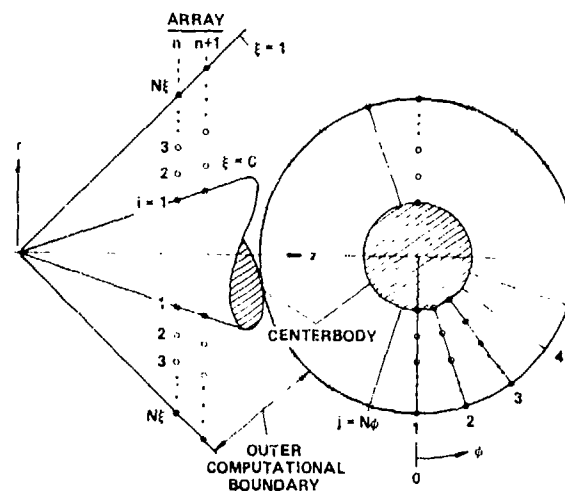


Fig. 1. Hypothetical supersonic cruise configuration.



(b) Indexing scheme for inlet solutions.

Fig. 3. Concluded.

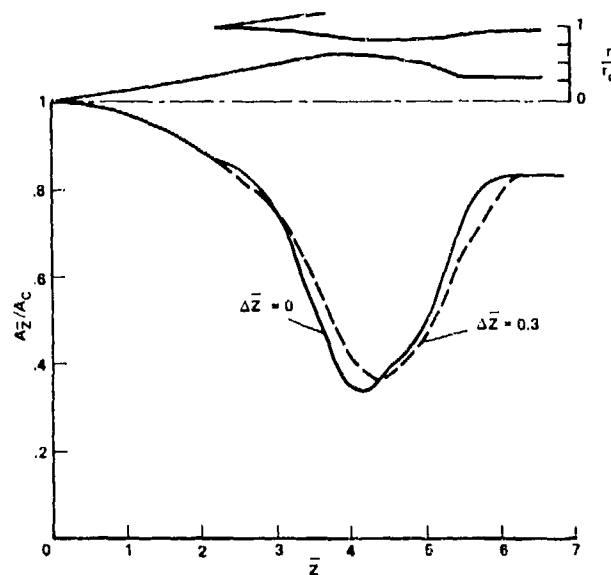


Fig. 2. Supersonic inlet contours and area distribution.

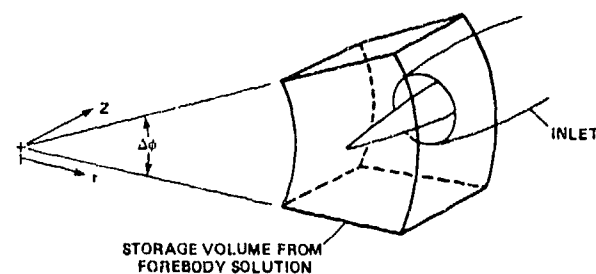
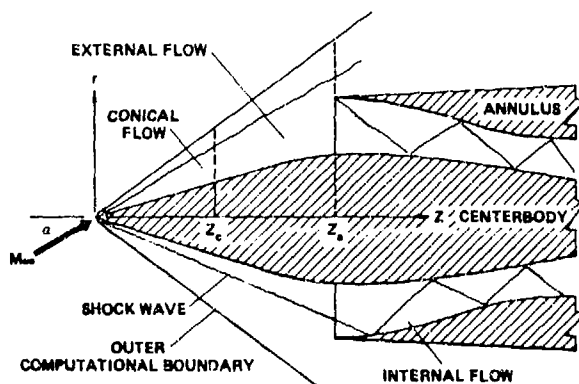


Fig. 4. Saved data volume from forebody solution.



(a) Domains of inlet solution.

Fig. 3. Conceptual details of inlet solution.

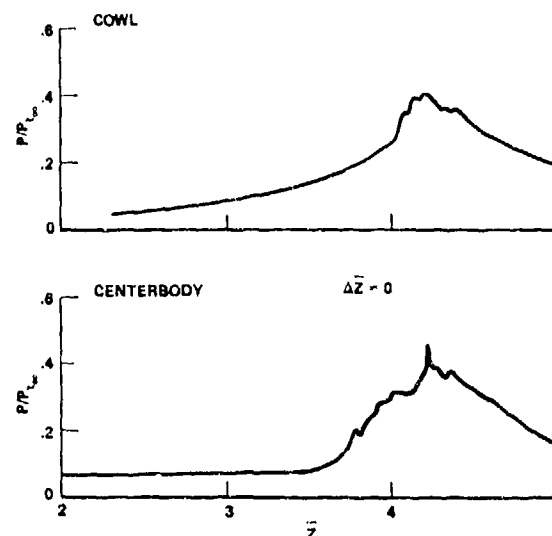
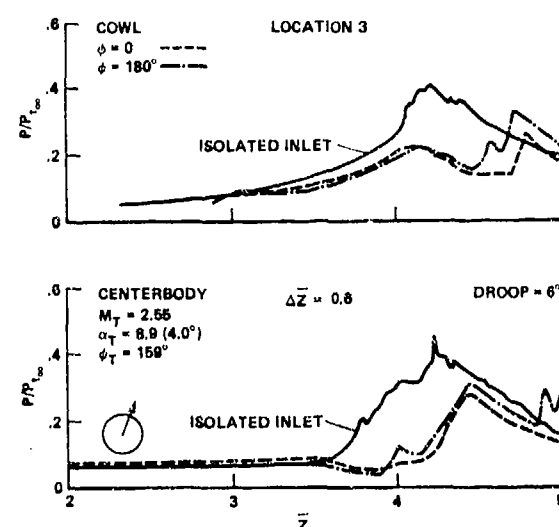
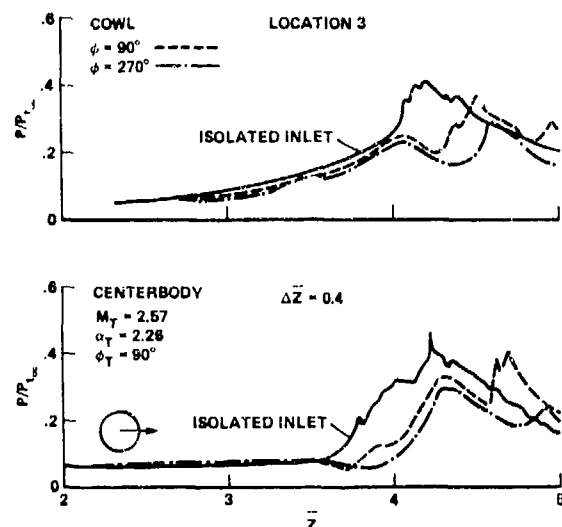
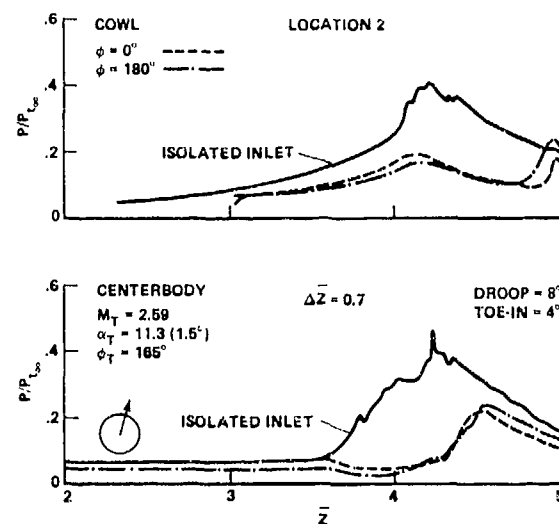
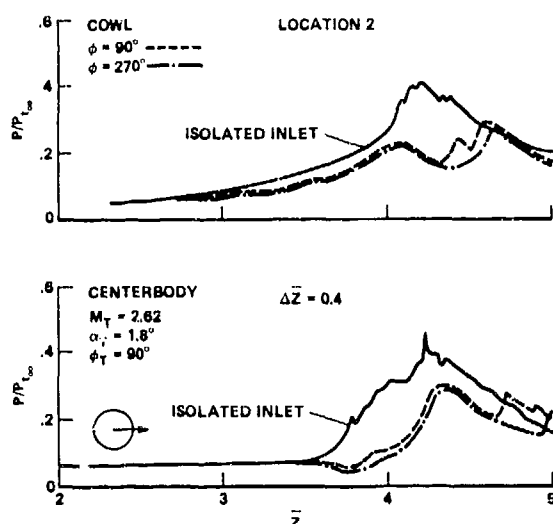
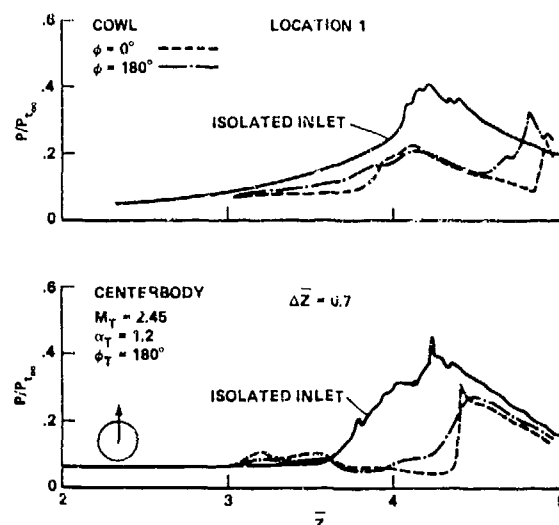
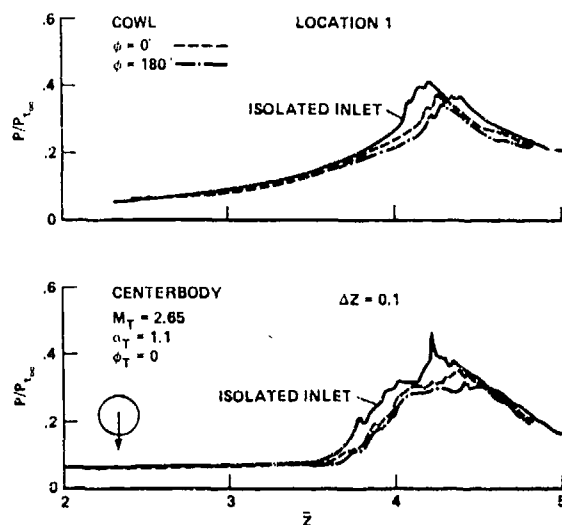


Fig. 5. Static pressure distribution, $M = 2.65$, $\alpha = 0$, $\Delta \bar{Z} = 0.0$.



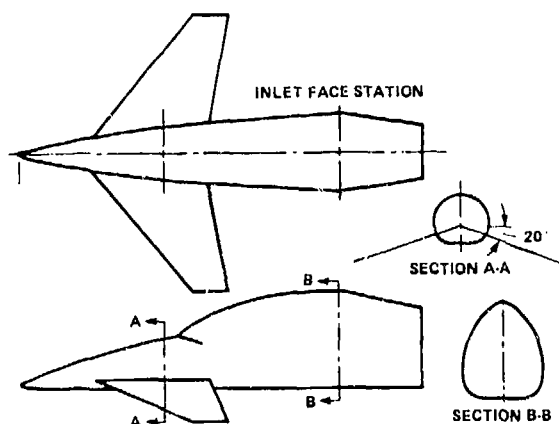
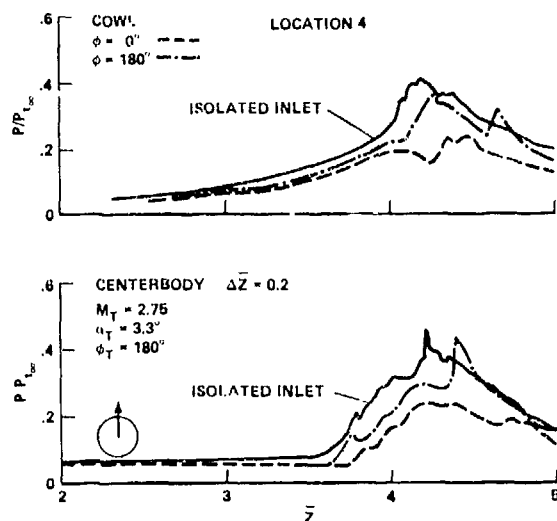


Fig. 13. Hypothetical highly-maneuverable transonic aircraft configuration.

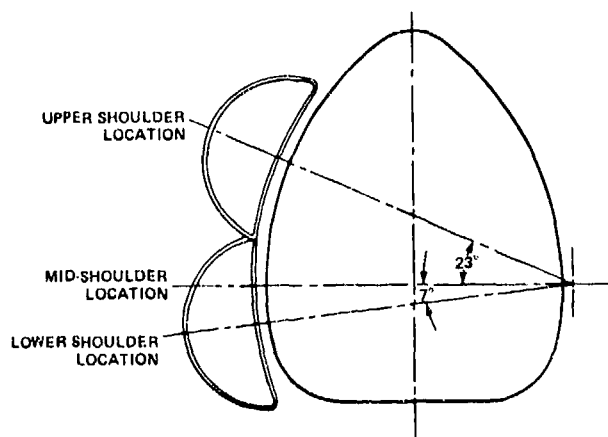


Fig. 14. Inlet shape and location.

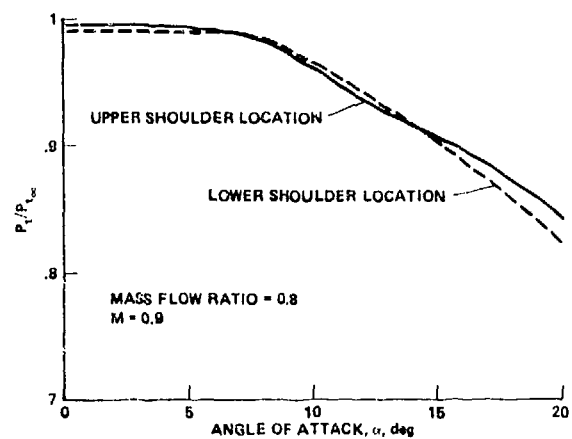


Fig. 15. Comparison of angle-of-attack performance for two inlet locations.

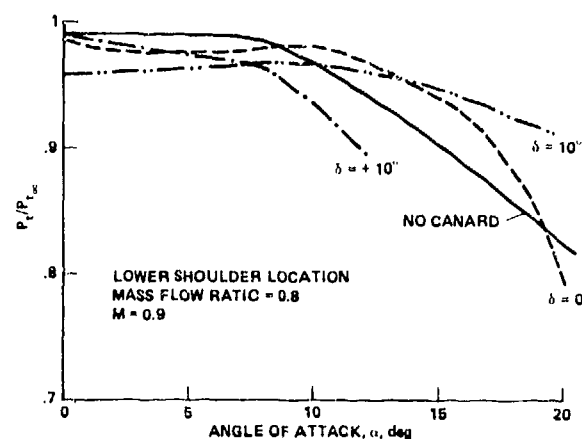


Fig. 16. Effect of canard deflection angle on low shoulder location inlet performance.

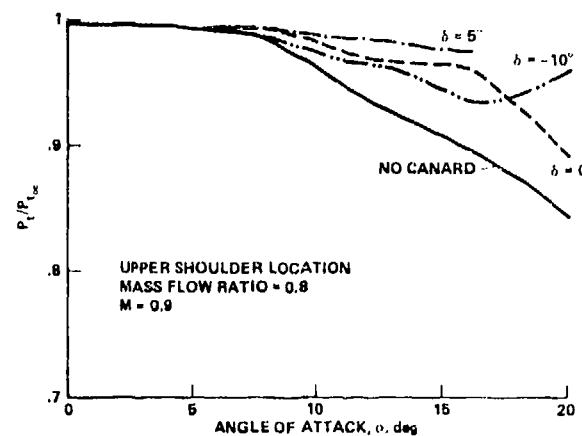


Fig. 17. Effect of canard deflection angle on upper shoulder location inlet performance.

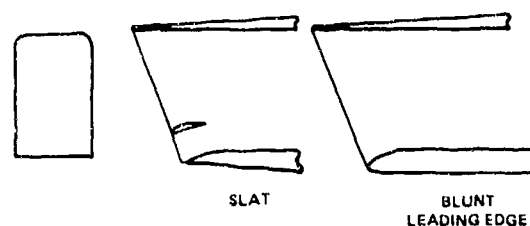


Fig. 18. Rectangular inlet lower lip modifications.

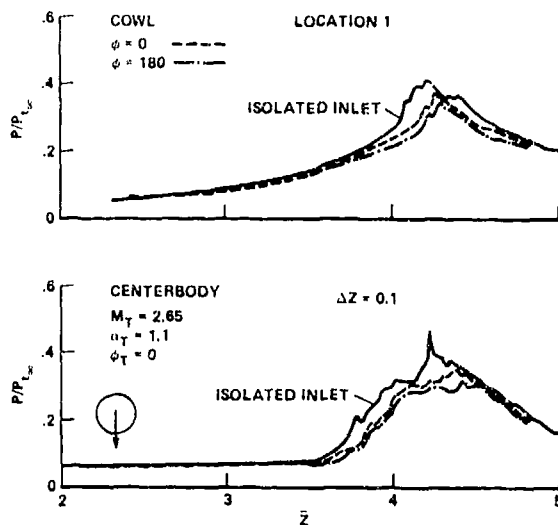


Fig. 6. Static pressure distribution, location 1 forebody: $M = 2.65$, $\alpha = 0$.

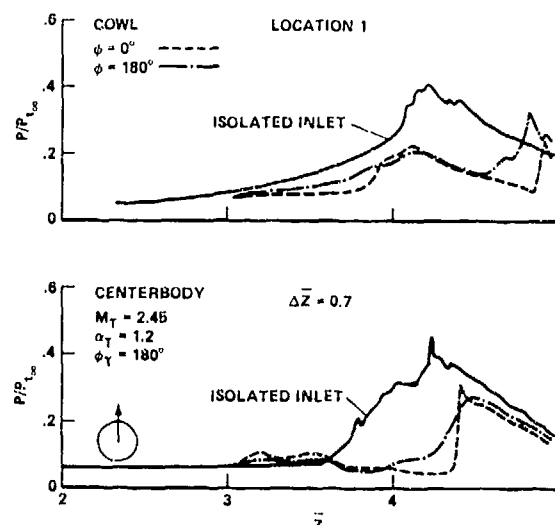


Fig. 9. Static pressure distribution, location 1 forebody: $M = 2.65$, $\alpha = 8^\circ$.

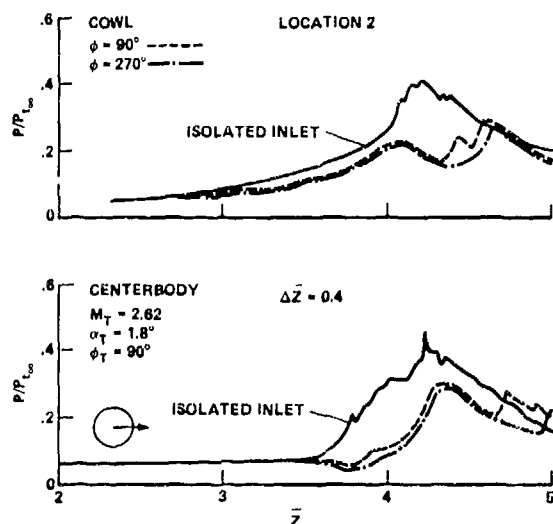


Fig. 7. Static pressure distribution, location 2 forebody: $M = 2.65$, $\alpha = 0$.

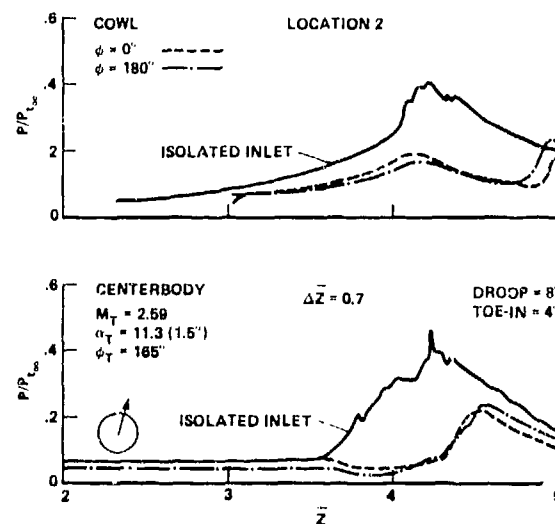


Fig. 10. Static pressure distribution, location 2 forebody: $M = 2.65$, $\alpha = 8^\circ$.

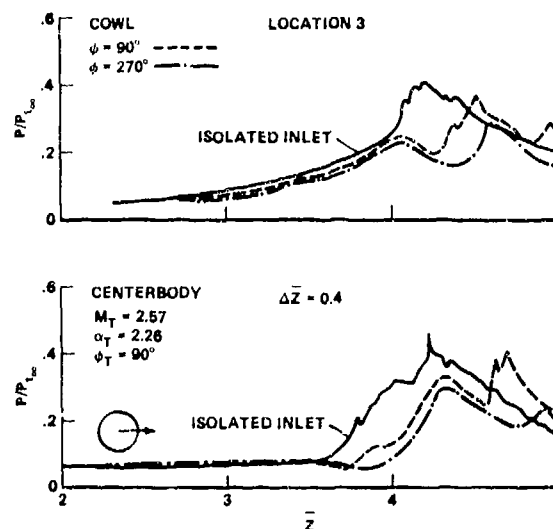


Fig. 8. Static pressure distribution, location 3 forebody: $M = 2.65$, $\alpha = 0$.

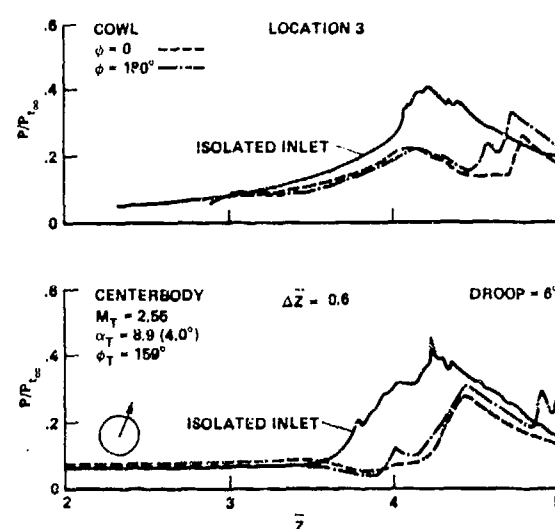


Fig. 11. Static pressure distribution, location 3 forebody: $M = 2.65$, $\alpha = 8^\circ$.

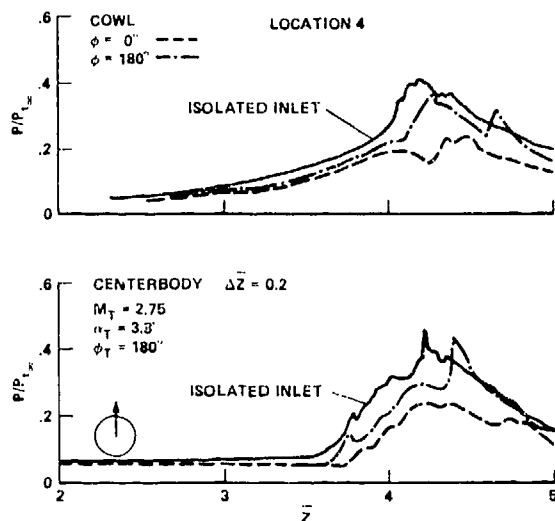


Fig. 12. Static pressure distribution, location 4 forebody: $M = 2.65$, $\alpha = 8^\circ$.

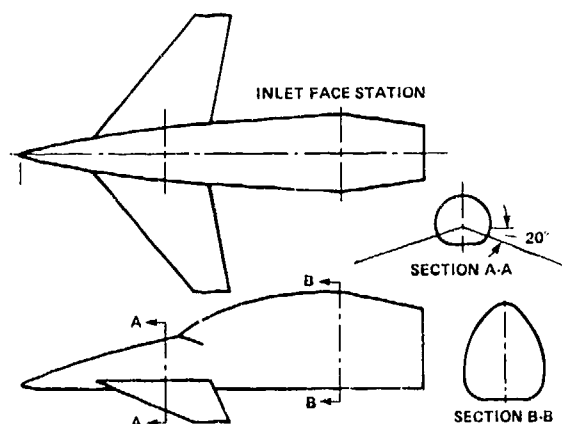


Fig. 13. Hypothetical highly-maneuverable transonic aircraft configuration.

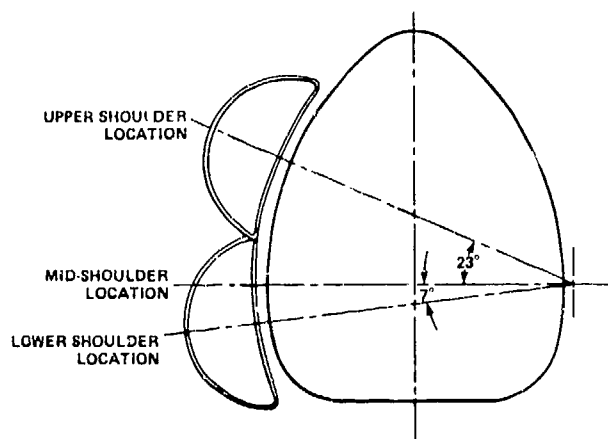


Fig. 14. Inlet shape and location.

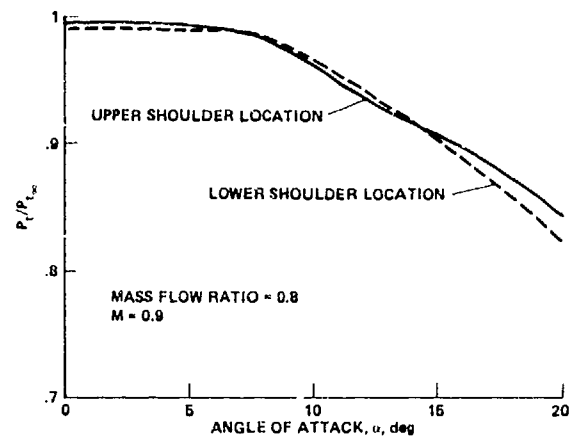


Fig. 15. Comparison of angle-of-attack performance for two inlet locations.

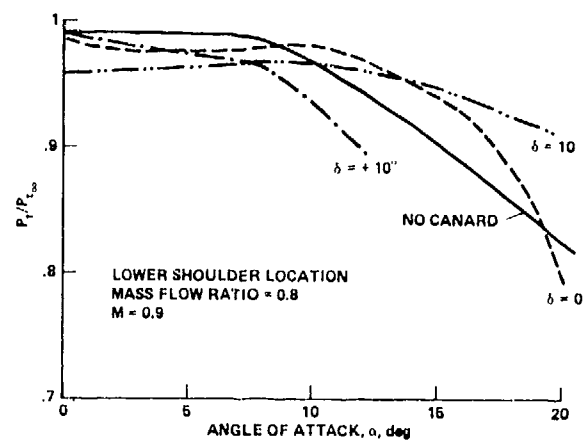


Fig. 16. Effect of canard deflection angle on low shoulder location inlet performance.

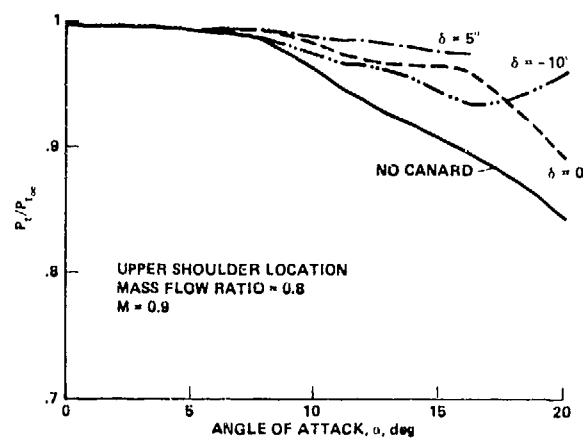


Fig. 17. Effect of canard deflection angle on upper shoulder location inlet performance.

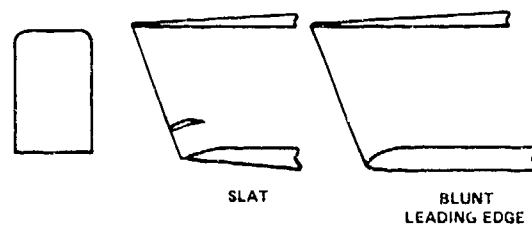


Fig. 18. Rectangular inlet lower lip modifications.

INTAKE DESIGN AND INTAKE/AIRFRAME INTEGRATION FOR A POST-STALL FIGHTER AIRCRAFT CONCEPT

by

K. W. Lotter and J. Malefakis

Messerschmitt-Bölkow-Blohm GmbH
Military Airplane Division
D 8000 München 80
Postfach 801160
Germany

SUMMARY

Due to advanced aerodynamic design and the use of thrust-vectoring systems the flight envelope of future tactical aircraft will be considerably expanded, especially at subsonic speeds. Aircraft angles of attack during manoeuvres in controlled separated flow conditions may reach 70° or even more. To attain these increased capabilities new intake design concepts and optimum integration of intake and airframe must be adopted to provide high pressure recovery and low instantaneous flow distortion for high thrust levels and satisfactory inlet/engine compatibility.

The paper discusses results from subsonic scale model tests carried out for intake geometries especially designed for high angle of attack capability. A unit-composed intake model representing a twin-engine fighter aircraft was tested with two basic intake positions in a shielded location, one under the fuselage and one under the wing strakes on both sides of the fuselage. In addition two different axial positions were tested. An external-compression, horizontal-ramp inlet design was chosen for the tests. Different auxiliary intakes, all fitted to the lower side of the intake were tested. Various rotatable forward cowl lip designs and a cowl slot were also included in the investigations.

The results show that a shielded intake location offers a high potential for improvement in inlet manoeuvre capability. Sufficient shielding is generally given for the under-fuselage position. For the side-intakes located under the strakes a position as far downstream as possible is desirable. For such shielded intakes only small performance losses occurred at incidences up to 35° . With auxiliary intakes properly integrated into the lower side of the intake duct and/or rotatable forward portions of the cowl lips incidences up to 70° are possible with only small performance degradations and low increase in turbulence.

Optimum performance of the intake over a wide range of incidences can be obtained when the auxiliary intake geometry and the cowl lip rotation is programmed as a function of aircraft angle of attack and flight Mach number.

It is further shown that variable cowl lip geometry introduced for subsonic manoeuvre improvement offers an attractive means for optimum intake/engine mass flow matching at supersonic speeds by varying the intake capture area.

LIST OF SYMBOLS

A_c	Intake capture area	$\bar{P}_{t_{60^\circ}}$	Mean engine face total pressure over 60° sector
DC60	Distortion parameter $\frac{\bar{P}_{t_{60^\circ, \min}} - \bar{P}_{t_2}}{q}$	\bar{q}	Mean engine face dynamic pressure
h_c	Intake capture height	v_o	Free stream velocity
H	Altitude	\bar{v}	Mean engine face velocity
M_o	Flight Mach number	α	Angle of attack
\bar{M}	Mean engine face Mach number	β	Yaw angle
P_{t_o}	Free stream total pressure	ϵ	Canard angle relative to fuselage datum
\bar{P}_{t_2}	Mean engine face total pressure	$\bar{\lambda}$	Mean engine face loss factor
		η	Engine face pressure recovery

1. INTRODUCTION

Conceptual studies for the next generation of fighter aircraft involve consideration of increased manoeuvrability and extended flight envelopes compared to the presently existing fighters. This leads to air vehicle designs capable of flying at extreme high angles of attack at conditions with completely separated flow. This will be accomplished by advanced control concepts and the use of thrust-vectoring systems. A major component requiring special attention during the development of such configurations is the engine air inlet system.

The purpose of the inlet is to supply, under all flight conditions, the air demanded by the engine at the maximum pressure and with the least drag and most favourable interference possible. Also, low flow angularity and sufficient uniform and steady flow at the engine entry plane is required to avoid compressor stall and engine surge. A large effort has been made over the past several years to meet these requirements for the conventional flight regime of supersonic fighter airplanes.

The envisaged penetration into the post-stall flight regime causes entirely new problems to the inlet flow and represents a challenge for the inlet designer. Flow separation at the forward intake must be avoided or sufficiently suppressed in order to keep the flow distortion within the limits defined by the engine manufacturer and to provide the highest possible pressure recovery at the compressor entrance. This may be achieved by special inlet design features and/or proper integration of the inlet system with the airframe.

This paper describes some inlet concepts especially designed to meet the above mentioned requirements during flight at extreme high angles of attack and presents results of low speed wind tunnel model tests carried out with a number of specially designed inlet configurations located at shielded positions.

2. AERODYNAMIC ASPECTS OF INLET/ENGINE/AIRFRAME INTEGRATION

The problems arising with inlet/engine/airframe integration during design of a new airplane are shown in fig. 1. Inlet performance is defined in terms of its effect on both the performance of the engine and the drag of the airframe. Parameters involved in the determination of inlet performance include spillage drag, total pressure recovery, flow distortion, bypass drag, boundary layer bleed system drag and the interference with external flow. For fighter type aircraft which operate at very different flight conditions the losses related to the inlet system can rise to high values at specific conditions since the engine is demanding a wide range of mass flow. Careful optimisation of the inlet geometry and the integration of the inlet with the airframe is required to achieve high overall performance.

Besides the performance aspects attention must also be paid to inlet/engine compatibility. Proper matching of inlet and engine mass flow by correct inlet sizing and control is required to guarantee stable operation under all flight conditions. Inlet flow distortion causes a reduction of engine surge margin and can cause engine malfunction at extreme manoeuvres. Therefore, steady state and time-variant distortion determination by model tests is required early during project development to identify areas of possible problems and to improve intake flow quality to meet the requirements of the engine.

The next generation of fighter airplanes is expected to penetrate into hitherto inaccessible flight regimes, embracing extreme high angles of attack at subsonic Mach numbers (fig. 2), where reliable engine system operation at steady state and transient engine conditions is required. Controlled separated flow at the wing is a basic feature for these new concepts but the inlet flow must be free of detrimental separations or disturbances must be sufficiently attenuated at the compressor entry plane.

3. INLET LOCATIONS AND CONCEPTS FOR HIGH ANGLE OF ATTACK

A basic approach to improve the inlet flow conditions at high angles of attack is shielding of the inlet either by the wing, wing strakes or fuselage. This has already been shown during the project "Tailor-Mate" [1], and was later applied in the F-16 and to some extent in the F-17 fighter designs [2, 3]. Fig. 3 qualitatively shows for shielded intake locations how the flow is turned ahead of the intake, thus considerably reducing the local flow angle at the inlet position. Very effective shielding is achieved with the underwing location but unfavourable fuselage effects at yaw are to be expected for high wing installations. Also, relatively high compressor face distortion and turbulence may be associated with the short inlet duct length for the underwing location. For configurations incorporating a wing strake, favourable overall inlet/airframe integration is possible with the inlet located under the strake. However, boundary layer removal from the fuselage side/strake-corner is difficult and the effectiveness of the strake may be influenced by the intake. At negative angles of attack there is also the possibility of the strake vortex being ingested into the inlet. Effective shielding and good yaw capability is achieved with the intake located under the fuselage and sufficient inlet duct length can be provided for that configuration to attenuate flow distortion.

In addition to shielding special devices are required for the inlet system at extreme high angles of attack. Fig. 4 depicts some possible design features to improve the inlet flow at very high angles of attack. The rotating forward intake offers an attractive means to avoid cowl lip separation provided that a sufficient large radius of the internal contour at the pivot axis can be achieved. Design, however, is

complex and difficult to realize. Cowl lip separation can also be avoided or delayed by features like cowl rotation, cowl slat or leading edge blowing [4].

Auxiliary intake doors arranged at the lower intake side are extremely effective at high incidences. Blow-in-doors or Venetian blinds are shown in fig. 4 as examples of a number of possibilities.

An inlet design incorporating the concept of the rotating cowl is depicted in fig. 5. This solution is attractive from an inlet aerodynamic point of view since it not only provides high angle of attack capabilities at low speed but also allows a variable capture area for nearly optimum inlet/engine airflow matching at supersonic speeds. The lower half of the figure shows the desired capture area variation over the supersonic flight envelope. For the special design shown, the minimum capture area has been limited in order to avoid excessive internal cowl angles.

4. LOW SPEED INLET MODEL TESTS

A series of low speed wind tunnel tests using a 1:7 scale model has been carried out to investigate different inlet configurations in shielded installations at angles of attack of up to 100° . The aim was to establish guidelines for inlet design and to select potential configurations for more detailed tests to be carried out later also at transonic and supersonic Mach numbers. Two test series were carried out and the configurations were judged on the basis of engine face pressure recovery and steady state distortion. During the second test phase the turbulence level ahead of the engine face was measured by 4 high response total pressure pick-ups (Kulites). Future tests will incorporate full time-variant distortion measurement.

4.1 Test Set-Up

The arrangement of the model is shown in fig. 6. It is supported at the wing tips and angle of attack variation is accomplished via the sting support, approaching the model from the upper rear side. Three exchangeable stings are provided for the different ranges of incidence. Yaw angle variation is made by rotation of the whole suspension system. Suction of the inlet air flow is provided by compressors for both intakes. The pipes for air flow suction approach the model from the rear. Easy modification of the inlet axial position over a range of 2.8 intake capture heights is possible by moving the inlet/duct system along the lower side of the fuselage.

4.2 Model Configurations

A unit-composed model design representing a twin-engine fighter was applied to allow easy and quick configuration changes. The various configurations tested within the two test phases are depicted in fig. 7. In the first test phase a trapezoidal wing with strakes was tested with two basically different inlet locations. These were an under fuselage and an under strake location. Both configurations were tested with two different axial intake positions with an axial movement of 2.8 intake capture heights. The intake considered is of the external compression type with a 7° overhead ramp and relatively blunt intake lips and sidewalls. The forward part of the intake cowl lip is exchangeable and can be replaced by different lip designs and auxiliary air intake types. In addition to the reference configuration (no auxiliary intake) three concepts (see fig. 7) of auxiliary intakes were tested during the first test phases, i.e. a fully open auxiliary intake, a Venetian blind type and variable cowl lip geometry.

For the second test phase the model was modified to represent a delta wing/canard configuration with under-fuselage inlets. Only the forward intake location was tested. A variety of variable geometry cowl schemes and auxiliary intakes was tested with that configuration. Pictures of the model installed in the tunnel and of the various intake configurations are shown in fig. 8.

4.3 Model Instrumentation and Data Acquisition

A mass flow measuring section was provided in each suction pipe. Instrumentation at the simulated compressor face consisted of a remotely controlled rotatable rake comprising 4 arms with 5 steady state total pressure probes on each arm (fig. 9). The probes were located on centroids of equal ring area. During the second test phase 4 high-response total pressure probes (Kulites) were installed in front of the engine face rake to measure time-variant pressures. During a test run the rotatable rake was stepped at increments of 15° . Pre-tests were made to adjust the rake starting position so that the wake from the Kulites did not affect the rake measurement at any rake arm position.

The data acquisition is depicted in fig. 10. The left hand side shows the dynamic data processing and the right hand side the steady state processing. The signals from the Kulites were amplified and then filtered by a low-pass and high-pass filter before storage on the magnetic tape was made. An oscilloscope and a voltmeter allowed observation of the signals during actual testing. The steady state data were recorded in the usual way using a scanivalve. Final data were made available on a plotter, line printer and punch tape.

4.4 Test Procedure

For the static tests ($M_0 = 0$), a range of intake mass flows was tested and suction could be provided up to a level corresponding to "combat" engine rating. The mean engine face loss factor is defined as

$$\bar{\lambda} = \frac{P_{t_0} - \bar{P}_{t_2}}{\bar{q}}$$

and is, for incompressible flow, considered to be independent of free stream or duct Mach number and then only a function of the velocity ratio v_0/V . Therefore, most of the tests were carried out at the maximum tunnel speed of $M_0 = 0.2$ and the velocity ratio was varied by control of suction mass flow. Predictions of the intake pressure recovery at other Mach numbers than that tested are possible on the basis of the established variation of the loss factor with velocity ratio using the expression:

$$\eta = \frac{1}{1 + \bar{\lambda} \left(\bar{q}/\bar{P}_{t_2} \right)}$$

After having set tunnel Mach number, angle of attack and yaw of the model the intake mass flow was varied from the maximum possible down to velocity ratios corresponding to "combat" mass flow at a flight Mach number of about $M_0 = 0.5$.

4.5 Results and Discussion

In the following the main results selected from a large number of test data will be presented and discussed. Fig. 11 shows the derived engine face pressure recovery as a function of angle of attack for the flight Mach numbers $M_0 = 0.1$ and 0.5 (upper and lower half of figure respectively) at two basically different intake locations, i.e. under the fuselage (left hand side of fig. 11) and under the strake on either side of the fuselage (right hand side of the figure). The diagrams essentially compare the reference intake which had no auxiliary air intake (AAI) with all the auxiliary air intake configurations tested during the first test phase. The results show that all auxiliary intakes tested fall within a relatively narrow band provided the variable auxiliary intake geometry is programmed to optimum position as a function of angle of attack. At low Mach numbers ($M_0 = 0.1$) the under fuselage inlet position shows worse results than the under strake position for the reference inlet (AAI closed). This is due to the unfavourable mutual interference of the narrow spaced intakes at the under fuselage position. However, with auxiliary intakes installed for the under fuselage position, extreme high pressure recovery is achieved at angles of attack of up to 70° even at a relatively high flight Mach number of $M_0 = 0.5$ because of effective fuselage shielding. A ten per cent improvement at $\alpha = 70^\circ$ compared to the reference inlet is possible resulting in about 15 per cent increase in installed net thrust. For the under strake position the shielding effect is less pronounced resulting in 2 to 3 per cent lower pressure recovery at $\alpha = 70^\circ$ and $M_0 = 0.5$.

The effect of yaw angle on pressure recovery is depicted in fig. 12 at angles of attack of 0° and 30° , again for both inlet positions. No noticeable effect with yaw was seen for the windward inlet. The leeward inlet showed nearly no pressure recovery degradation for yaw angles up to -10° for the under fuselage position and small losses at -20° . The right half of the figure shows the high sensitivity to negative yaw angles for the under strake position. This is clearly a result of the fuselage wake at negative yaw angles.

In fig. 13 the effect of axial inlet position on pressure recovery is shown at angles of attack of 30° and 70° . The axial distance between the two positions is 2.8 intake capture heights (see fig. 6). While little or no effect is found for the under fuselage position, the under strake position shows clear advantages for the rear position, especially at $\alpha = 70^\circ$, but the results are still worse than for both under fuselage positions. Because of the limited shielding effect of the strakes compared to the fuselage underside an inlet position as far downstream as possible for the under strake location is preferable.

The effect of a canard on pressure recovery, tested during the second test phase, is presented in fig. 14. For the static condition ($M_0 = 0$), neither the canard angle ϵ nor the removal of the canard showed any noticeable effect on the results for the range of engine face Mach numbers tested (typical "combat" engine setting corresponds to an engine face Mach number of about 0.6). At a flight Mach number of $M_0 = 0.5$ and maximum inlet air flow (combat) also little variation in pressure recovery was measured when the canard angle ϵ was changed. In fig. 14 results for a range of typical operating canard angles at $\alpha = 30^\circ$ and 70° are shown. Only at $\alpha = 70^\circ$ a variation of less than one per cent in pressure recovery was noticed.

In fig. 15 a comparison is made for the static condition ($M_0 = 0$) between the reference inlet, the rotatable cowl concept and two configurations with auxiliary air intakes. While the auxiliary intake configurations show some improvement in pressure recovery, the rotatable cowl yielded the best results. The steady state distortion, however, is worst for the rotatable cowl but well below a level which may deteriorate engine behaviour. The most encouraging result is the drastic reduction in engine face turbulence to about half the level of the reference inlet for the rotatable cowl.

Some more results of engine face turbulence at forward speed as a function of angle of attack are presented in fig. 16 for selected configurations. The three diagrams in fig. 16 correspond to different velocity ratios v_0/\bar{v} with the relevant engine face Mach numbers \bar{M} of 0.14, 0.23 and 0.45. The flight Mach number increases with v_0/\bar{v} from the right hand to the left hand diagram, but due to tunnel speed limitations the full engine mass flows (up to $\bar{M} = 0.6$) could not be simulated. Only the right hand diagram corresponds closely to typical engine mass flows. The diagram shows again the very high reduction in engine face turbulence for the rotatable cowl configuration. Only a very small increase in turbulence level can be seen when the angle of attack is varied from 30° to 70° . For the lower engine face Mach numbers of $\bar{M} = 0.23$ and 0.14 the turbulence levels are not representative but the same trend can be recognized. The limited dynamic data obtained so far are encouraging but it is essential that further testing incorporates full dynamic distortion measurements in order to allow assessment of inlet/engine compatibility to be made.

5. CONCLUSIONS

- o First low speed inlet model tests at angles of attack of up to 100° showed that most effective shielding is achieved with the under fuselage inlet position. For under strake positions the inlet shall be located as far downstream as possible. Extreme high internal intake performance for the under fuselage position can be achieved for angles of attack up to 70° when suitable cowl designs or auxiliary intakes are incorporated.
- o The under fuselage position is superior to the under strake position especially at yaw.
- o For the canard configuration the effect of the canard is negligible when the inlet is located under the fuselage.
- o The concept of a rotatable cowl is promising in terms of internal inlet performance and engine face turbulence. It is also attractive for inlet/engine mass flow matching at supersonic speeds because the feature of the rotatable cowl can be used to vary the intake capture area.

REFERENCES:

- | | | |
|-----|----------------------------|---|
| [1] | L.E. Surber and D.J. Stava | Supersonic Inlet Performance and Distortion during Maneuvering Flight
AGARD CP 91-71, No. 25, September 1971 |
| [2] | J.E. Hawkins | YF-16 Inlet Design and Performance
AIAA-Paper 74-1062, October 1974 |
| [3] | J. Patierno | YF-17 Design Concepts
AIAA-Paper 74-936, August 1974 |
| [4] | J.A. Cawthon | Design and preliminary evaluation of inlet concepts selected for maneuver improvement
AIAA-Paper 76-701, July 1976 |

ACKNOWLEDGEMENT

A part of the presented work was sponsored by the German Ministry of Defense, RÜ/IV/3 (contract T/R 420/60002/62006) and produced in cooperation with DFVLR Braunschweig and VFW-Fokker, Bremen.

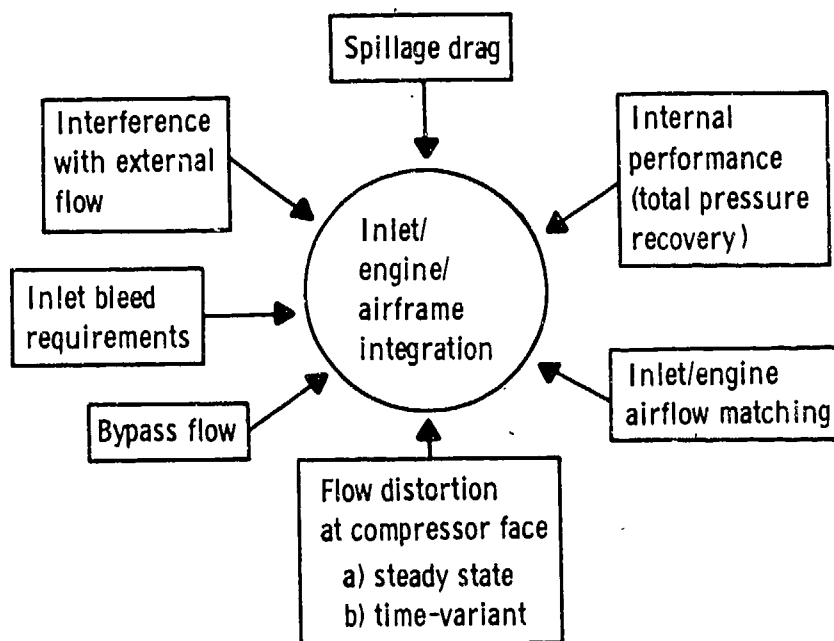


Fig. 1 Problems encountered with inlet/ engine integration

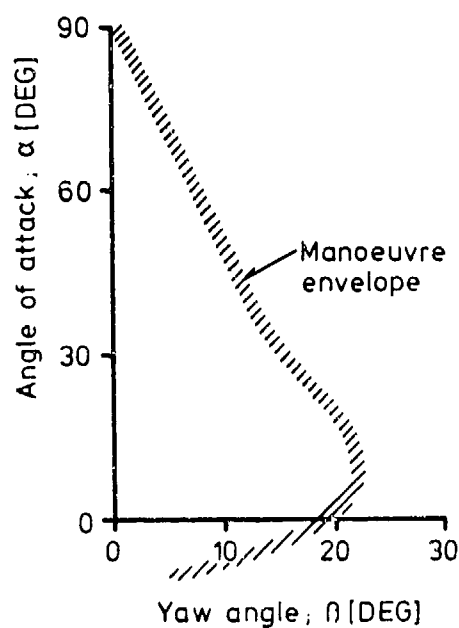


Fig. 2 Aircraft attitude envelope at low speed for future fighters

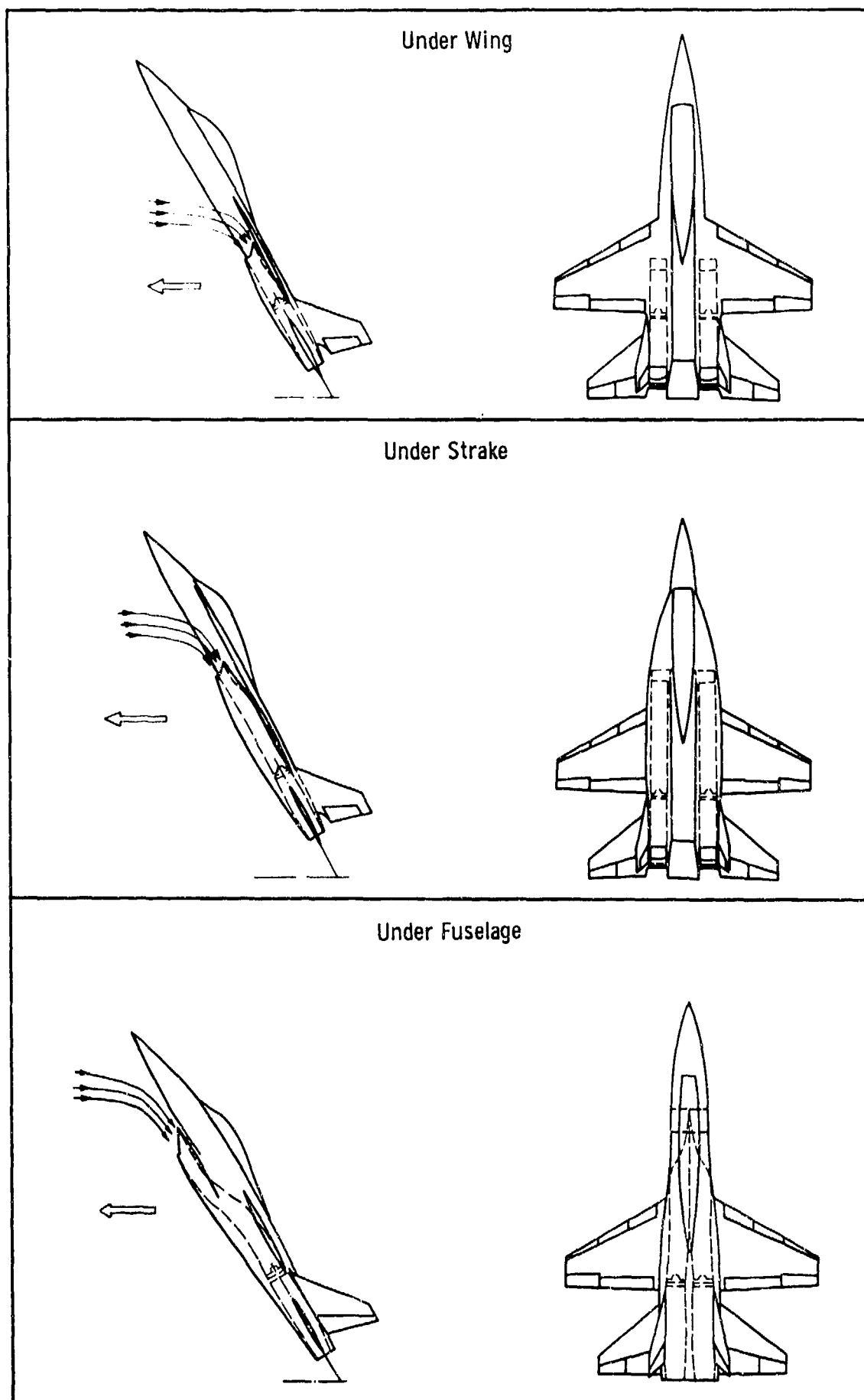


Fig. 3 Shielded intake location

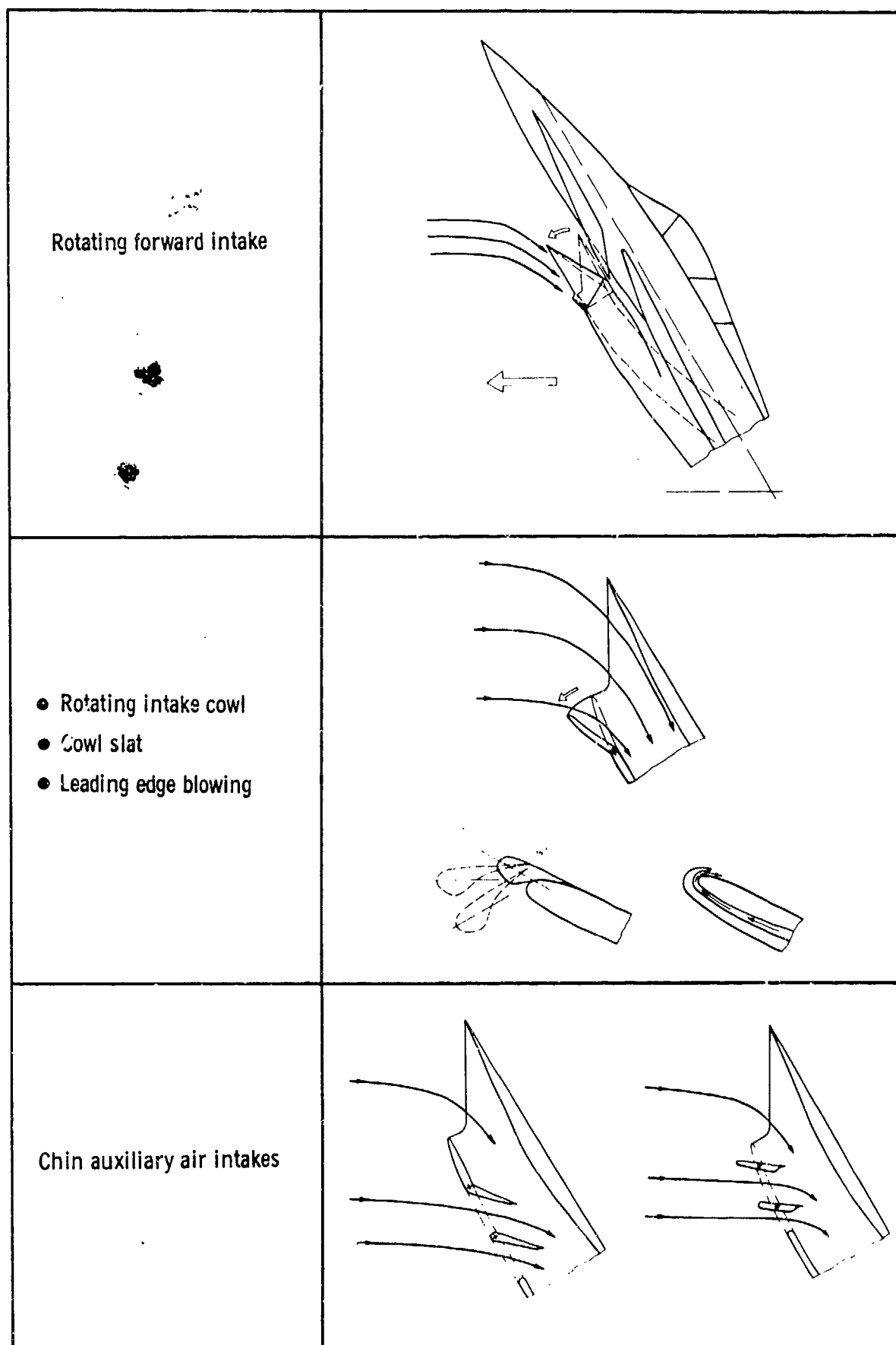


Fig. 4 Intake concepts for high angles of attack

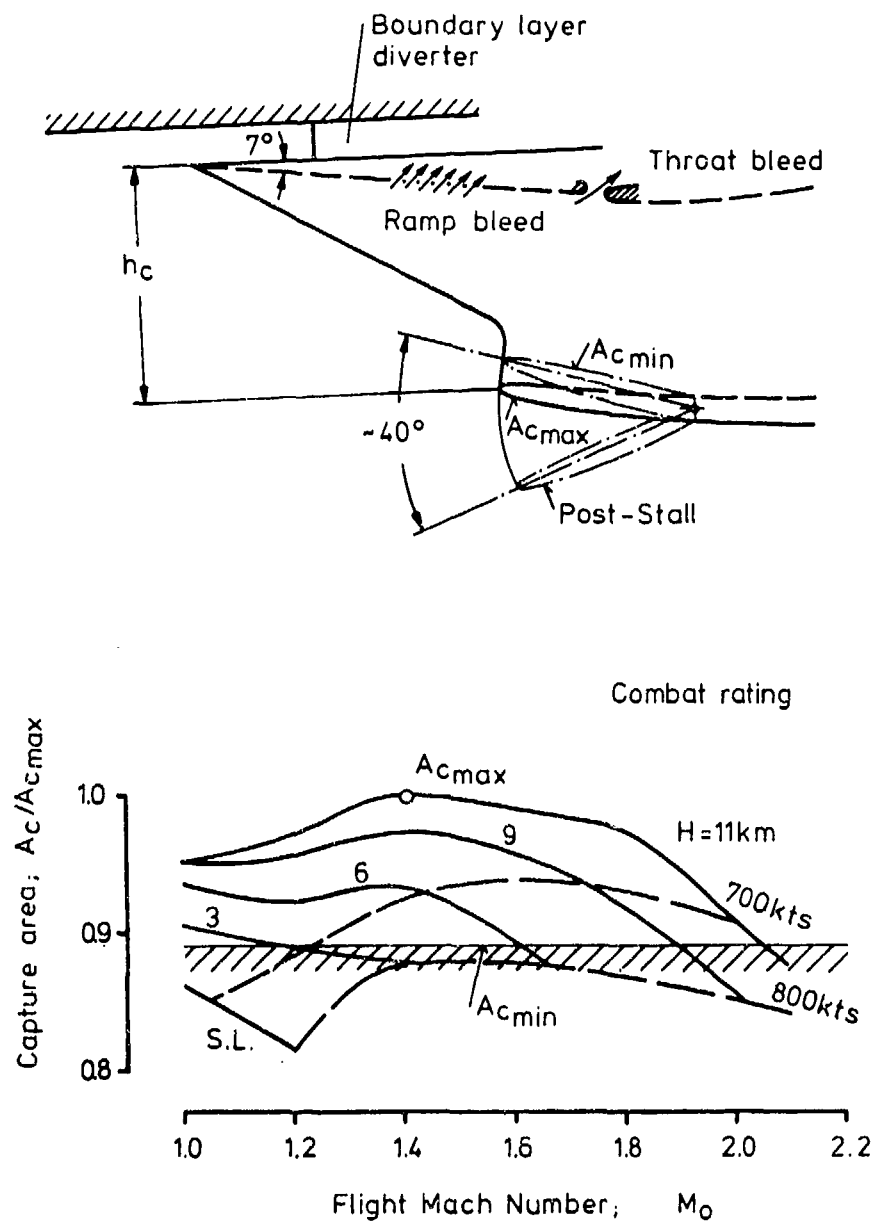


Fig. 5 Variable capture area intake with post-stall feature

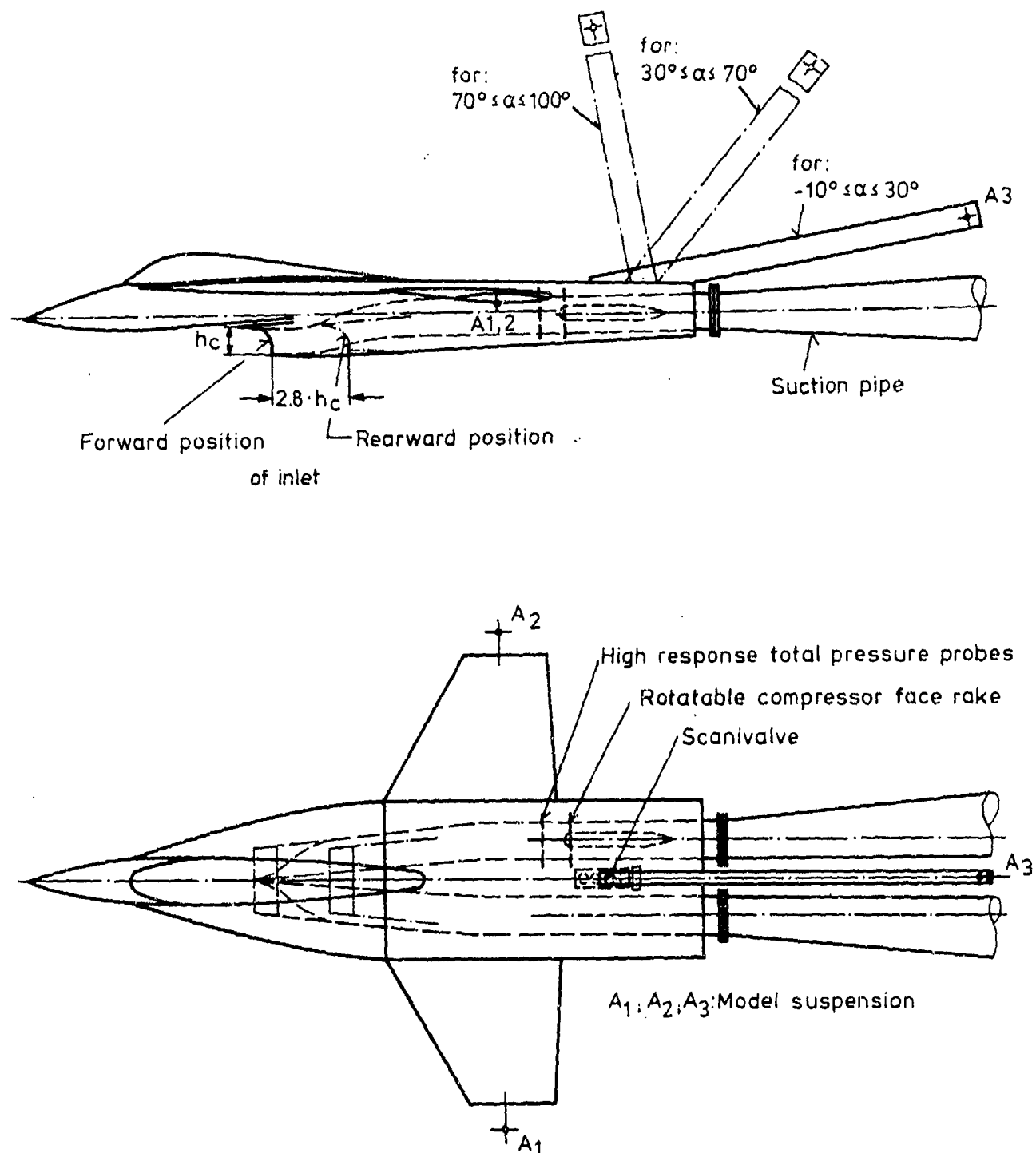


Fig. 6 Low speed intake windtunnel model

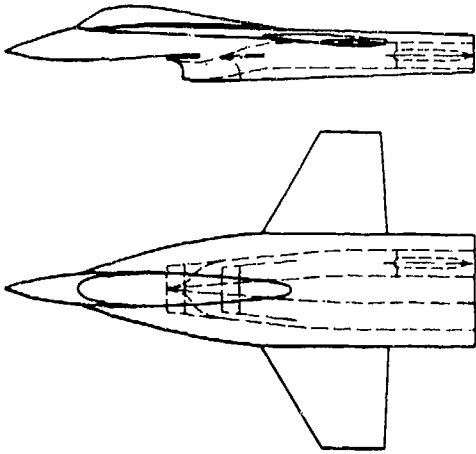
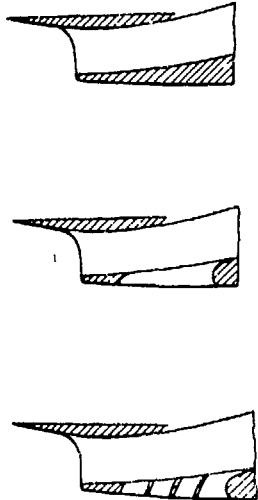
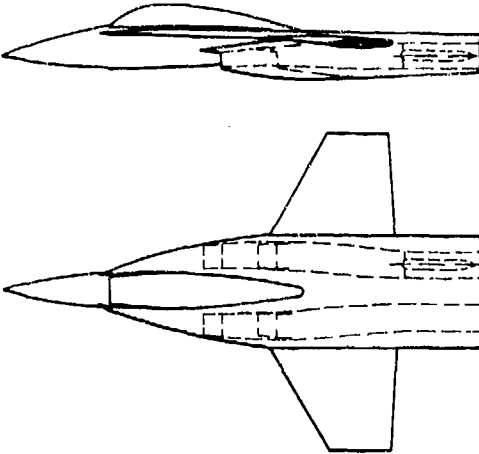
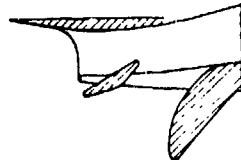
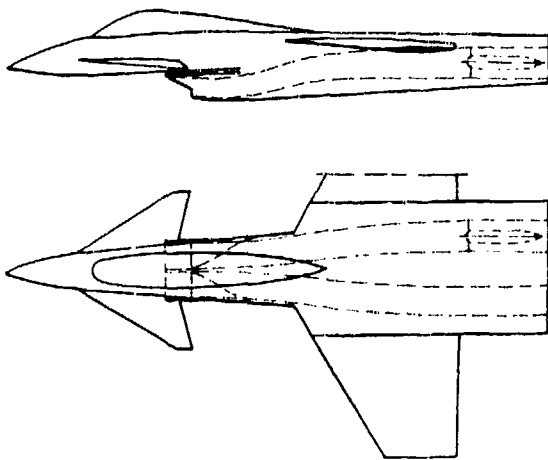
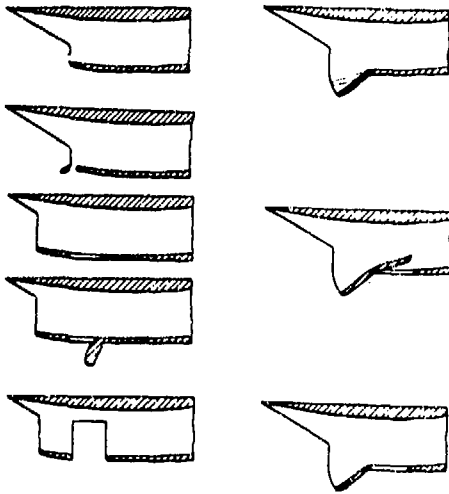
	Model Configuration	Auxiliary Intake Variation
1 st Test Phase (Strake Configuration)	Intake under Fuselage 	
	Intake under Strake 	
2 nd Test Phase (Delta-Canard Configuration)	Intake under Fuselage 	

Fig. 7 Model configurations

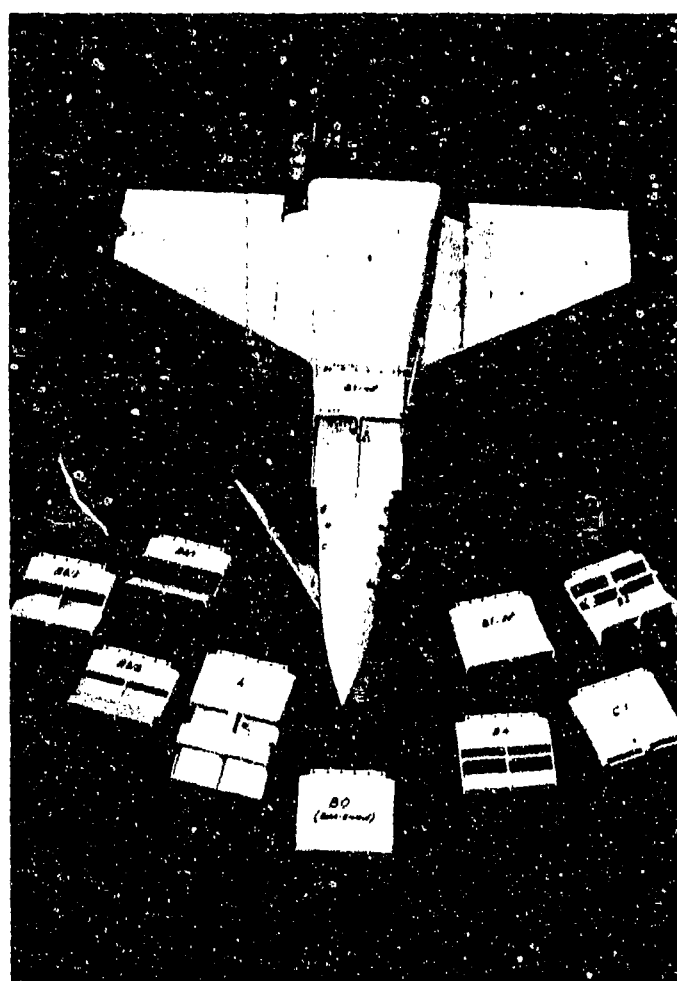
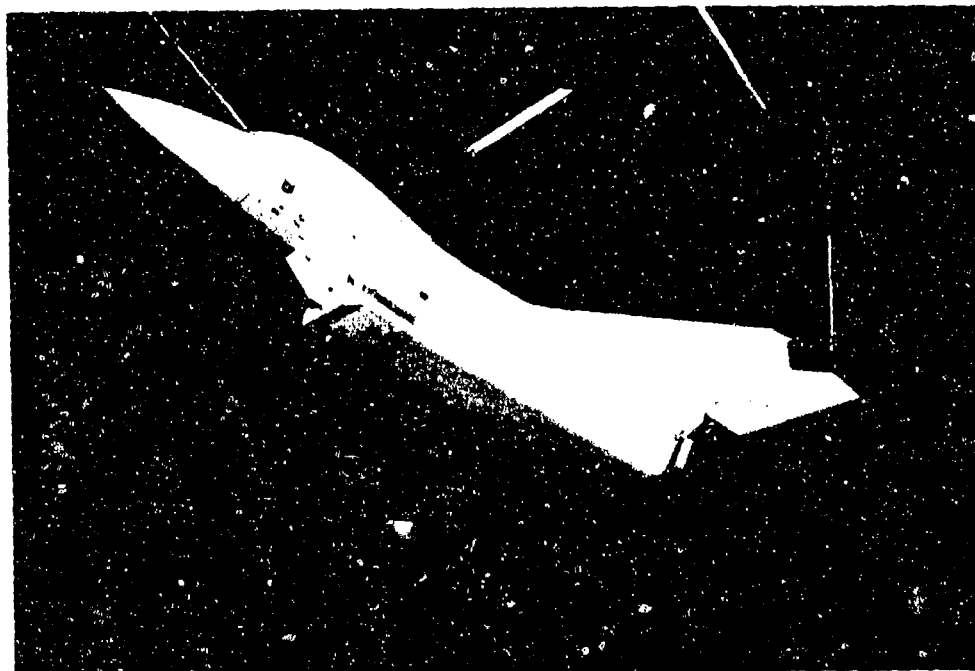


Fig. 8 Model installation and model configurations

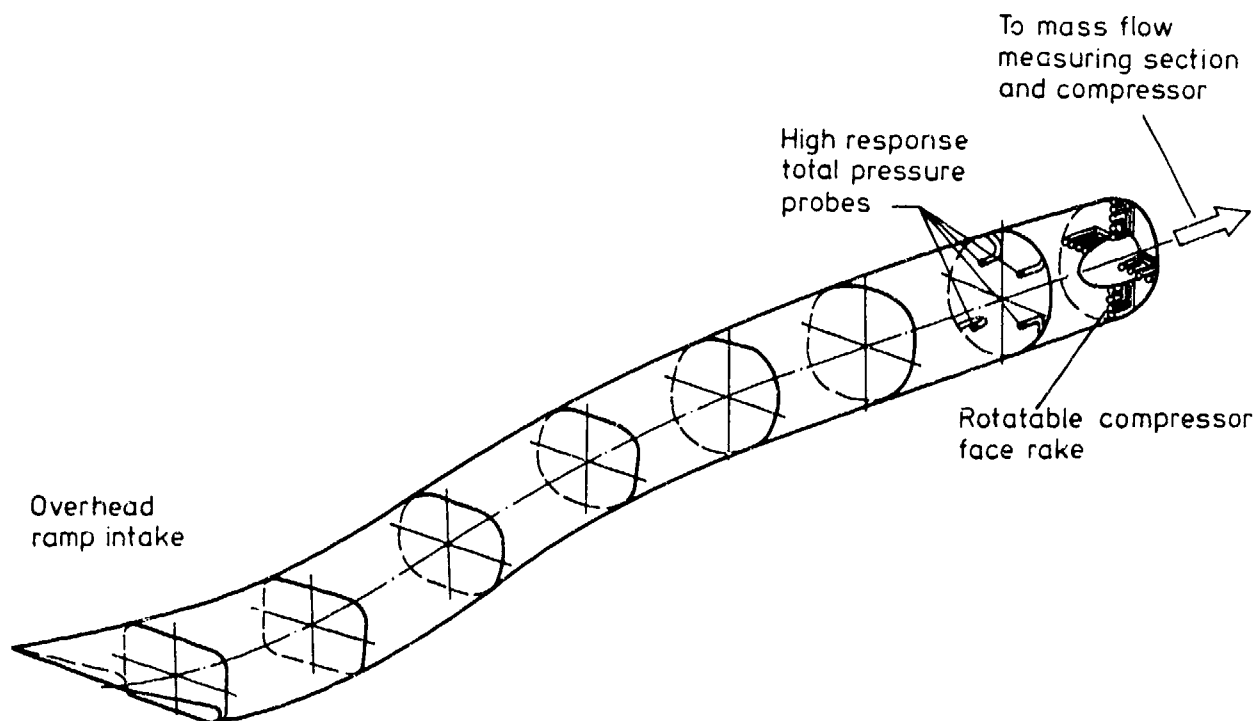


Fig. 9 Model instrumentation

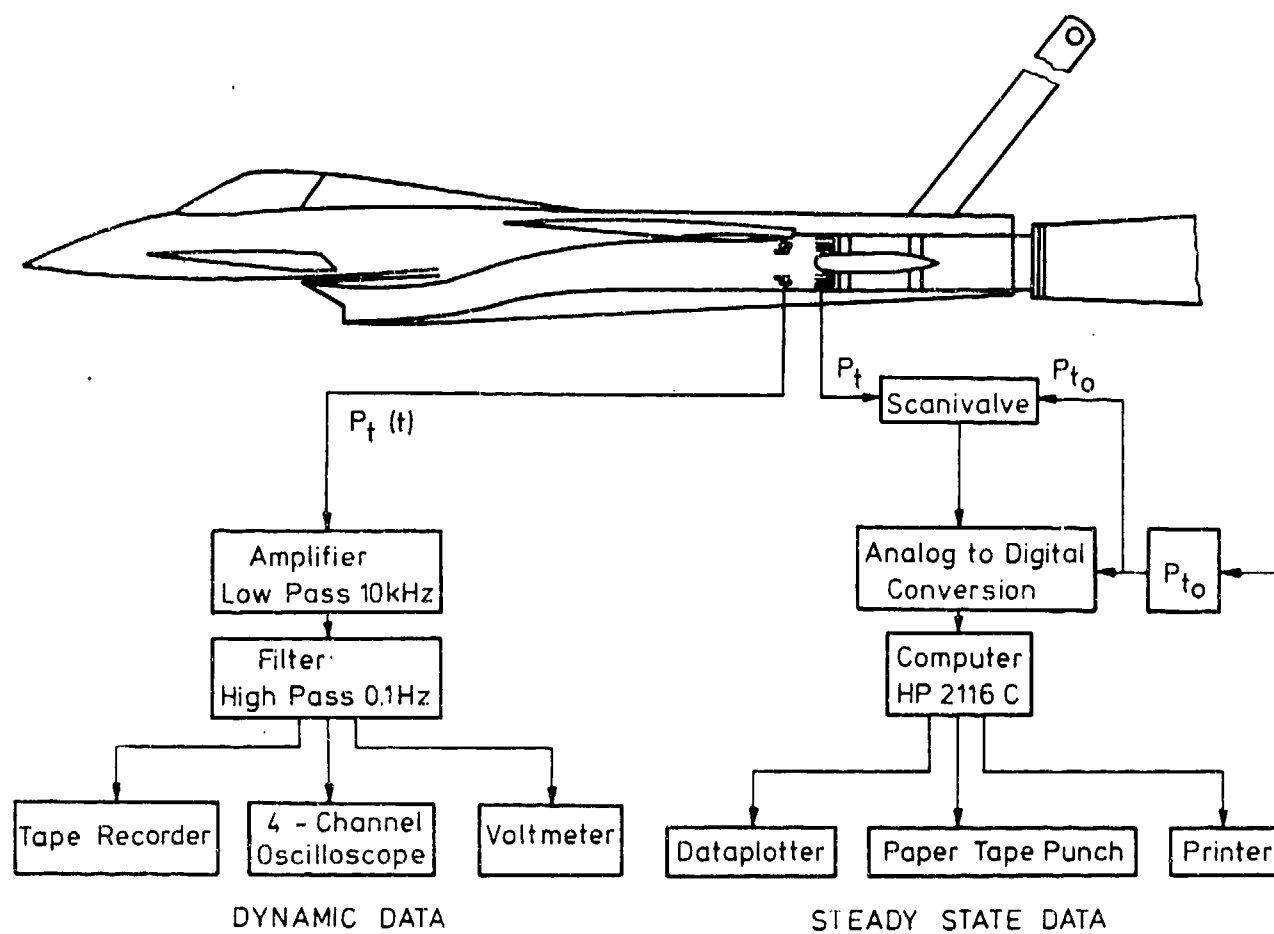


Fig. 10 Data acquisition

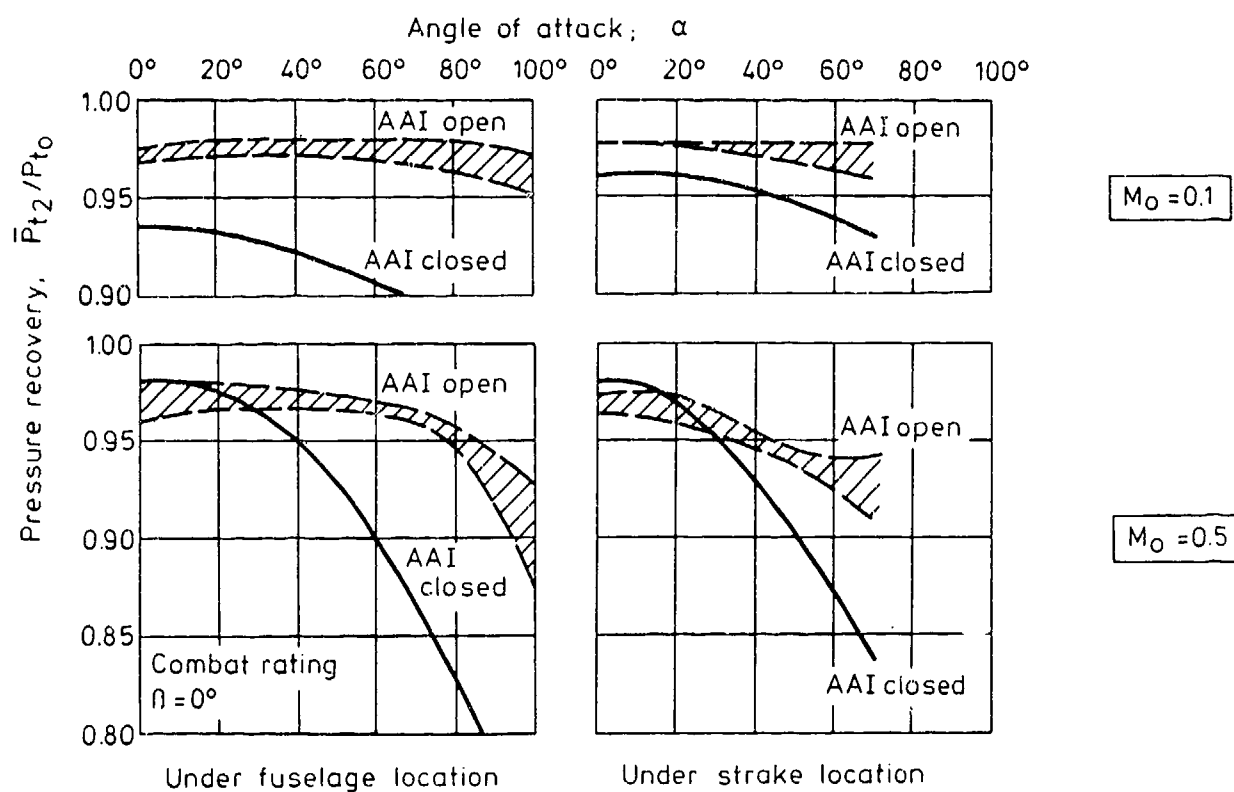


Fig. 11 Effect of angle of attack on pressure recovery

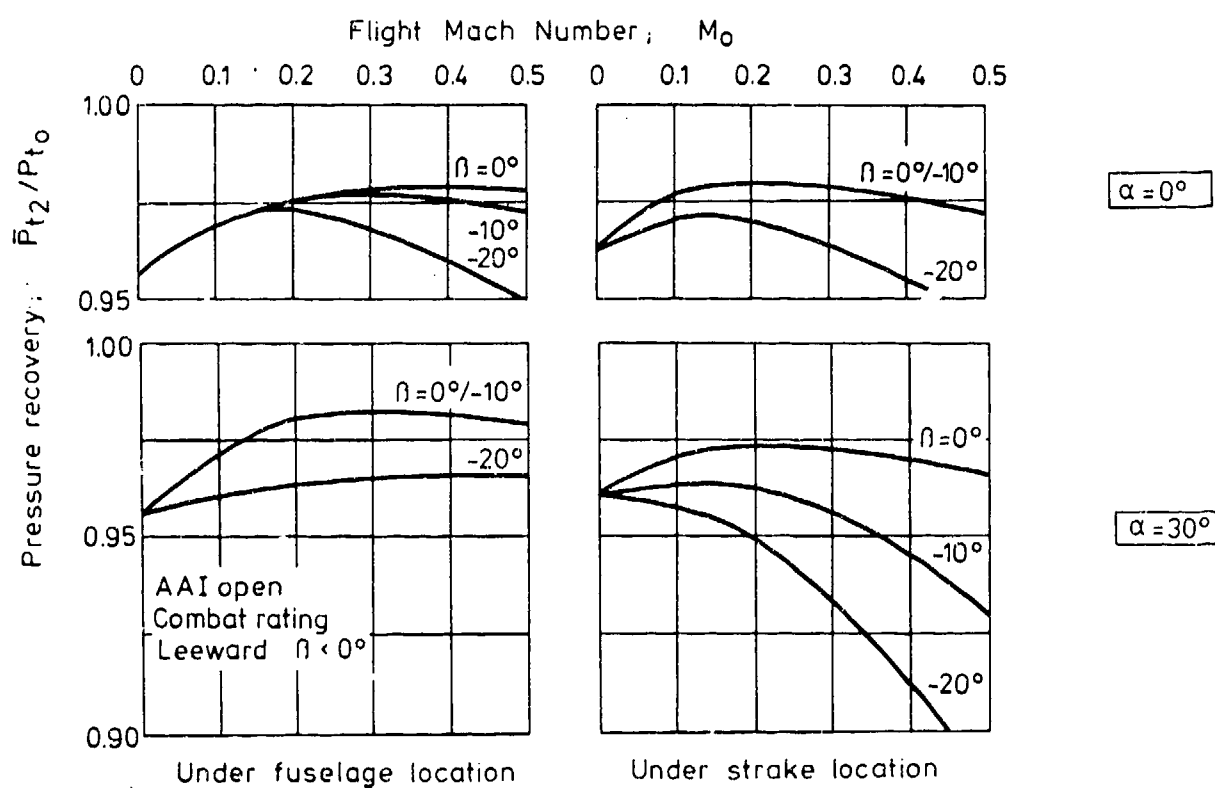


Fig. 12 Effect of yaw angle on pressure recovery

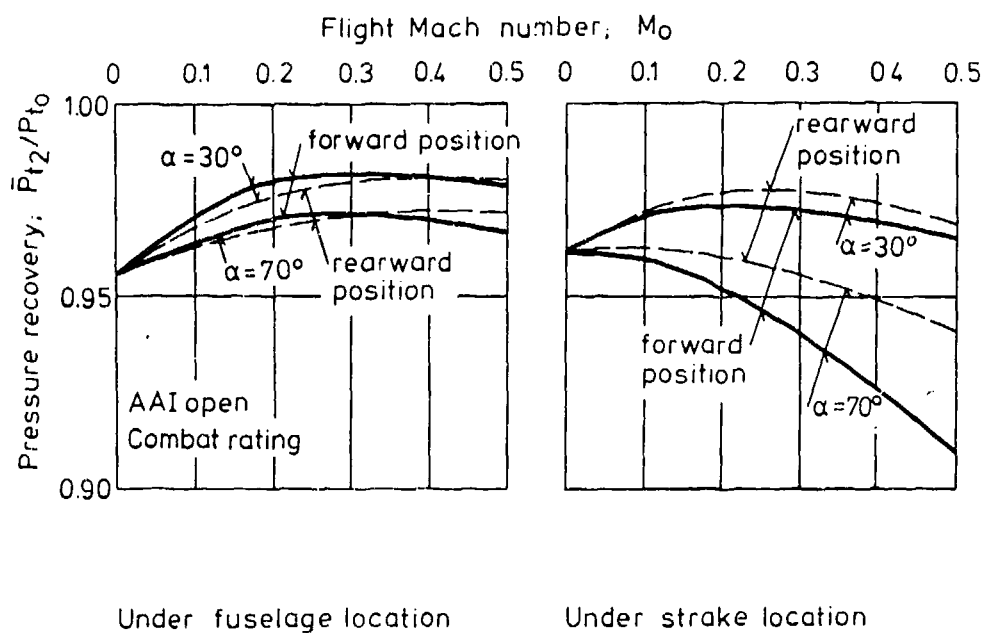


Fig. 13 Effect of axial inlet position on pressure recovery

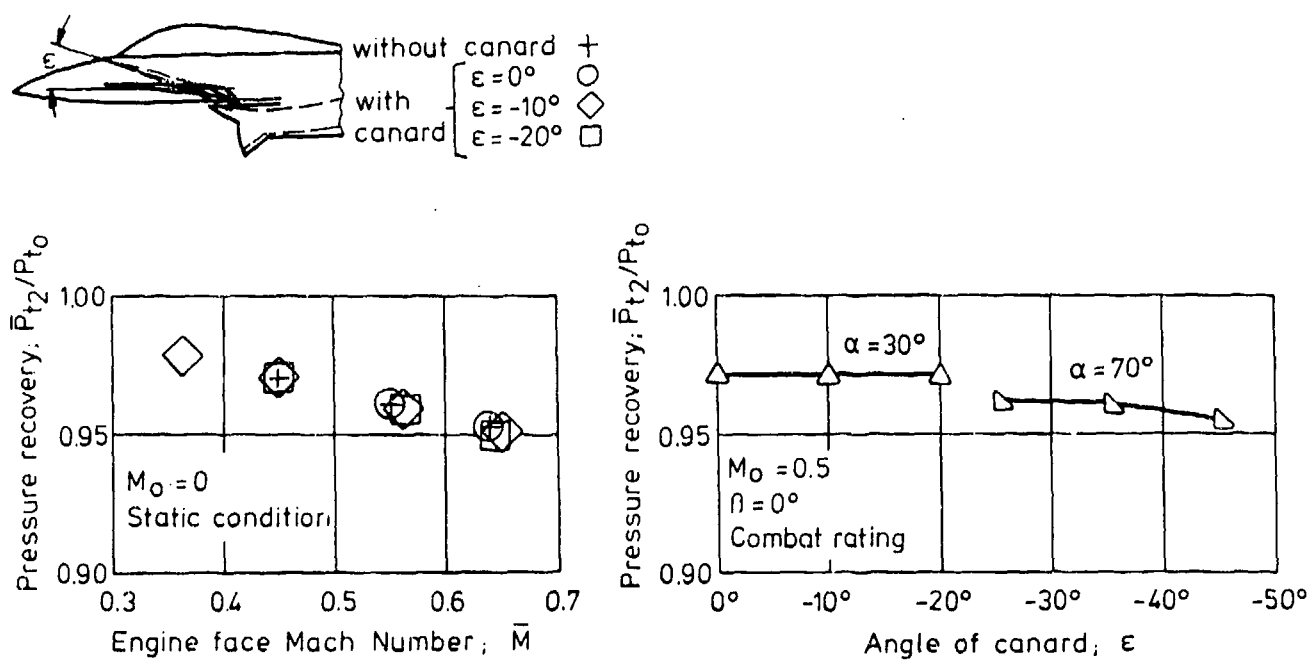


Fig. 14 Effect of canard on pressure recovery

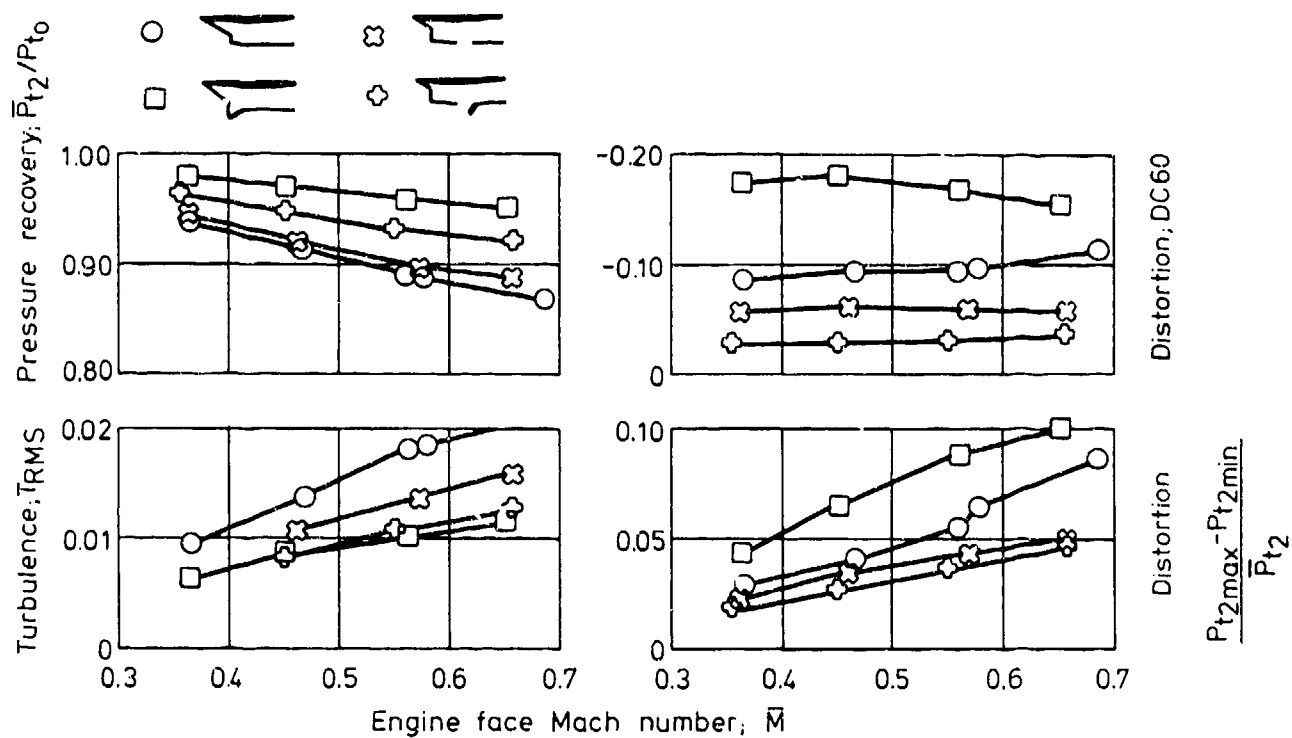


Fig. 15 Static intake performance

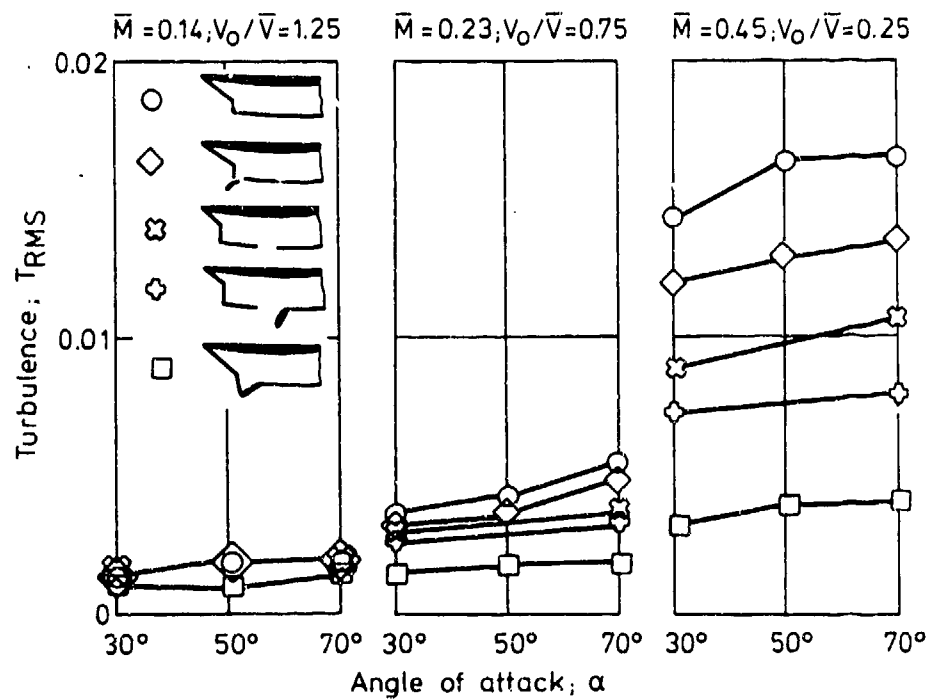


Fig. 16 Engine face turbulence

COMPRESSIBILITY EFFECTS ON THE SYMMETRIC BODY VORTEX WAKE OF AN OGIVE NOSE CYLINDER*

by
William L. Oberkampff** and Timothy J. Bartel†
Department of Mechanical Engineering
The University of Texas at Austin
Austin, Texas 78712
USA

SUMMARY

An extensive experimental investigation of the symmetric body vortex wake was conducted. Cone probe measurements were made on the leeside of an ogive nose circular cylinder for three different supersonic freestream conditions. Measurements of total pressure, Mach number, and three orthogonal velocity components were made at four angles of attack of the body at various axial stations. These data are processed to infer the position of the primary body vortex in the cross-flow plane, local circulation distribution in the cross-flow plane, vortex core size, and total circulation in the cross-flow plane. Although limited results are discussed in this paper, particular emphasis is placed on the effects of transonic cross-flow Mach numbers on the structure of the body vortex wake.

I. INTRODUCTION

High angle of attack aerodynamics has become an increasingly important topic in atmospheric flight mechanics. Nonlinear forces and moments which come into existence at high incidence angles have caused a number of flight stability and controllability problems on both missiles and aircraft. Many of the nonlinear forces and moments produced by a body or attached lifting surfaces are caused by the existence of the vortex wake on the leeside of the body. At angles of attack above about 10° symmetric vortices form on the leeside of the body and grow in strength along the body. If the angle of attack or body length is increased, the symmetric wake develops along the body into an asymmetric multiple vortex wake. The present investigation is concerned with the symmetric body vortex wake in supersonic flow.

This paper briefly describes the most comprehensive experimental investigation to date of the symmetric body vortex wake of a circular cylinder body in supersonic flow. Total pressure, Mach number, and three orthogonal velocity component measurements were made at various survey planes on the leeside of the body. Measurements were made at a nominal Mach number of 2 for two Reynolds numbers and at Mach number 3 for one Reynolds number. The high Reynolds number condition ($R_d = 1.75 \times 10^6$) represents a factor of four increase over previously published data (Refs. 1 and 2) for supersonic flow. The measurements were made using a conical pressure probe which was manipulated by computer in angular orientation and position in the wind tunnel. This paper summarizes results of the experiment which deal with the effects of transonic Mach number in the cross-flow plane. Additional analyses of these results are given in Refs. 3 and 4 and a complete reporting of the results are given in Ref. 5.

II. EXPERIMENTAL INVESTIGATION

The experimental program was conducted in Supersonic Tunnel A of the von Kármán Gas Dynamics Facility of the Arnold Engineering Development Center, Arnold Air Force Station, Tennessee. Tunnel A is a continuous flow, closed circuit, wind tunnel with a 1.02 m by 1.02 m (40 in. by 40 in.) test section. The model used in this experiment was a 76.2 mm (3 in.) diameter circular cylinder with a two caliber tangent ogive nose and a total length of 1.143 m (45 in.). It was supported by a 239 mm (9.4 in.) long sting and strut assembly. The wake flow measurements were made with a biconic shaped pressure probe with a diameter of 3.17 mm (.125 in.) at the union of the two cones and a 20° semi-apex angle of the tip cone. The probe was instrumented with four static pressure orifices on the cone surface and a total pressure orifice at the apex of the cone. The probe was supported by a double offset wedge-shaped strut mounted on the Captive Trajectory System (CTS) of the wind tunnel. A photograph of the model and probe installation is shown in Fig. 1.

The CTS is a computer controlled electro-mechanical drive system permitting variation of all six degrees of freedom. During the flow field probing phase, the CTS was programmed to position the probe at a series of grid points in the cross-flow plane; i.e., the y-z plane shown in Fig. 2. The pitch and yaw angles of the probe were varied for



Figure 1
Wind Tunnel Installation

*This work was supported by the Air Force Armament Laboratory, Eglin AFB, Florida, under USAF Contract F08635-77-C-0049.

**Associate Professor

†Presently, member of the Technical Staff, Sandia Laboratories, Albuquerque, New Mexico.

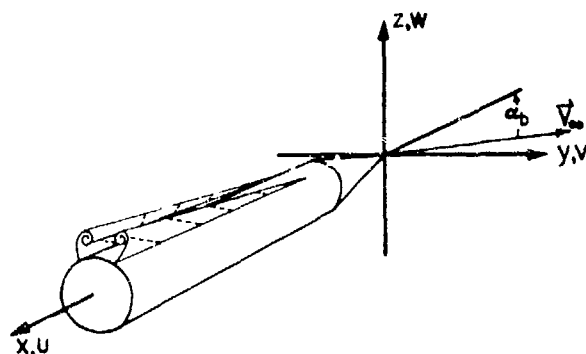


Figure 2
Coordinate System

grid points in the survey plane so that the angle between the probe axis and the local velocity vector was minimized. Data were taken in the right-half cross-flow plane as the axial locations of the survey grids were chosen such that the vortex wake would be symmetric at the survey locations. Two or three axially located grids were surveyed, depending on the angle of attack, with grid point spacing of 5.72 mm (0.225 in.). A summary of wind tunnel freestream conditions, model angles of attack, and axial grid locations is shown in Table 1. The final data set totaled 5342 survey points evenly distributed at the three freestream conditions. At each survey point the pressure data from the probe were reduced such that five flow parameters were obtained: total pressure, Mach number, and (u,v,w) velocity components.

III. RESULTS AND DISCUSSION

The cross-flow velocity field measured for $\alpha_b = 15^\circ$, $x/d = 13$, at both the Mach 2 and 3 conditions are shown in Fig. 3. All results presented in this paper are for $M_\infty = 2.00$, $R_d = 1.75 \times 10^6$ (based on body diameter), and $M_\infty = 3.01$, $R_d = 1.70 \times 10^6$. The base of the vector plotted is the location at which the measurement was made in the cross-flow plane. The characteristic rotational motion is clearly seen for the Mach 2 condition but only vaguely discerned for Mach 3. The highly elliptical nature of the vortex shown in Fig. 3b is due to the higher cross-flow Mach no., $M_{\infty c} = .78$, as compared to that of Fig. 3a, $M_{\infty c} = .52$. The center of the body vortex, which was determined from contour plots of local total pressure and magnitude of cross-flow velocity, $\sqrt{v^2 + w^2}$, is essentially identical for both the Mach 2 and Mach 3 conditions of Fig. 3.

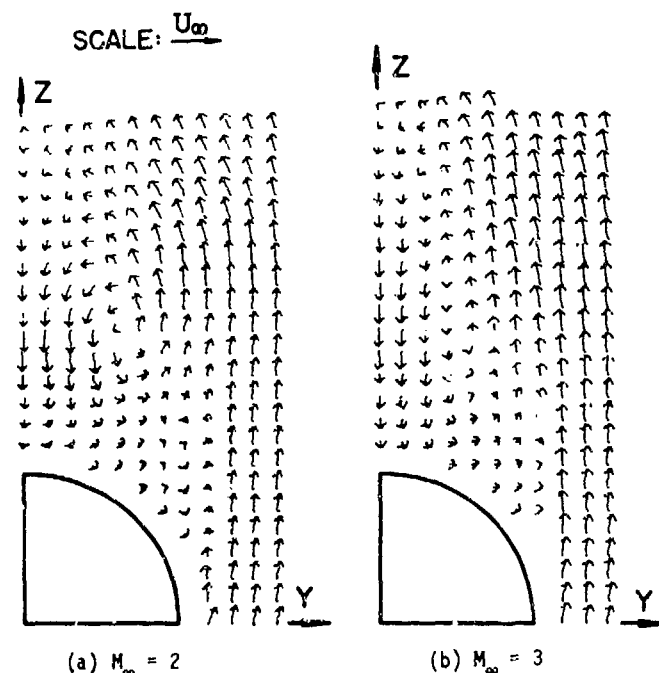


Figure 3
Cross-Flow Velocity Vectors
for $\alpha_b = 15^\circ$, $x/d = 13$

"blank" region in the upper right portion of the plot represents one quadrant of the body in the cross-flow plane and also the grid points near the body surface where data were not obtained. Lines hidden from the viewer are plotted as dashed lines. The surface of the perspective plot is numerically constructed by connecting the measured data points with the straight lines. Several very interesting features can be seen from Fig. 4. The general character of both surfaces shown in Fig. 4 displays the diffuse nature of circulation in the body vortex wake. Vorticity is not concentrated in a vortex core region but is spread over

TABLE I
Flow Field Survey Conditions

M_∞	$R_d \times 10^{-6}$	α_b (deg)	x/d
2.00	1.75	10	8,11,14
2.00	1.75	15	7,10,13
2.00	1.75	20	6,8,5,11
2.00	1.75	25	6,9
1.95	.48	10	8,11,14
1.95	.48	15	7,10,13
1.95	.48	20	6,8,5,11
1.95	.48	25	6,9
3.01	1.70	10	8,11,14
3.01	1.70	15	7,10,13
3.01	1.70	20	6,8,5,11
3.01	1.70	25	6,9

Using the measured cross-flow velocity field $\vec{V}_c = v\vec{j} + w\vec{k}$, the local circulation was calculated in each of the cross-flow survey planes. The distribution of local circulation $\Gamma(y,z)$ in the cross-flow plane provides significantly more insight to the fluid dynamics of the separated flow as compared to total circulation calculations of previous investigators. Local circulation was calculated on a square with side $h = .0375d$, i.e., one-half of the survey grid size. Using the definition of circulation, assuming two-dimensional flow in the cross-flow plane, one has

$$\Gamma \equiv \oint_R \vec{V} \cdot d\vec{s}$$

$$\Gamma = \int_{y,z}^{y+h,z} v \, dy - \int_{y,z+h}^{y+h,z+h} v \, dy + \int_{y+h,z}^{y,z+h} w \, dz - \int_{y,z}^{y,z+h} w \, dz,$$

where Γ is positive counterclockwise. A cubic spline approximation of the v and w velocity fields was used to carry out the numerical integration indicated above.

Figure 4 shows a perspective plot of the local circulation $\Gamma(y,z)$ in the cross-flow plane for $\alpha_b = 20^\circ$, $x/d = 8.5$, at both Mach 2 and Mach 3 conditions. The perspective view is from above the three dimensional surface $\Gamma(y,z)$ and looking in the positive y and negative z directions. The

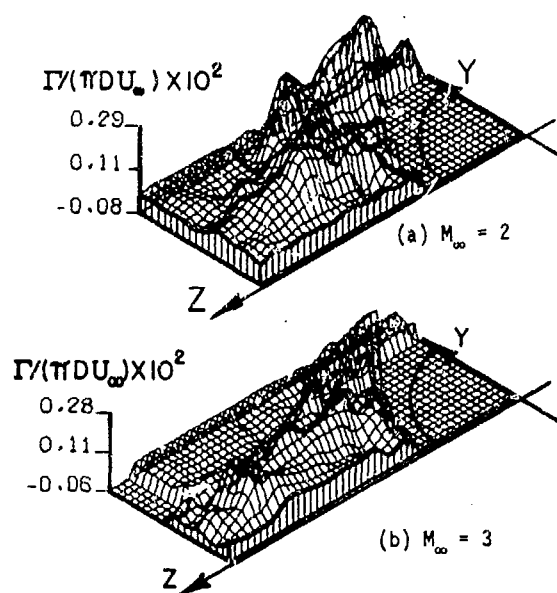


Figure 4
Local Circulation for $\alpha_b = 20^\circ$ and $x/d = 8.5$

the body (Fig. 5a). For the Mach 3 case, Fig. 5b, the sharp changes in local Mach number near the wake are striking. In the inviscid flow just outside the wake the Mach number is near 4.0 and in the wake the Mach number is near 2.0. These large changes in Mach number are brought about by the high cross-flow Mach number (compare Figs. 5a and 5b). The embedded shock in the angle of attack plane which occurred for Mach 2 also occurs for Mach 3, but for Mach 3 the flow rapidly accelerates again down the body. Another prominent feature of both Figs. 5a and 5b, particularly 5b, are the very low Mach number points at the top of the grid; i.e., the rows of points with large z . Analysis of the local total pressure, cross-flow velocities, local circulation, and Schlieren photographs in the neighborhood of these low Mach number points shows that this feature is a small secondary vortex. This secondary vortex originates near the nose-body juncture, is always above the primary body vortex, and rotates in the

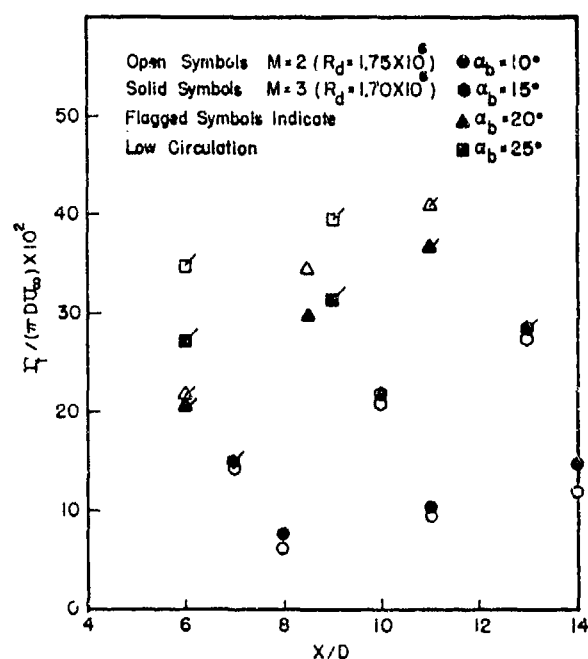


Figure 6
Total Circulation in the Cross-Flow Plane

most of the recirculating wake. For the most forward body stations the data show that the circulation is primarily confined to a core region, but for more aft body stations the circulation distributions are similar to Fig. 4. The vortex sheet in Fig. 4 can be identified as the high ridge extending downstream from near the separation point at the crest of the body. The strong effect of cross-flow compressibility can be seen by comparing Figs. 4a and 4b. For the lower cross-flow Mach number, Fig. 4a, the vortex sheet is roughly aligned with the z -axis similar to incompressible flow. For the higher cross-flow Mach number, Fig. 4b, the vortex sheet is convected toward the z -axis and the vorticity is more localized in a layer between the recirculating flow and the external flow. This characteristic becomes so dominant at $\alpha_b = 25^\circ$ for Mach 3 that the wake appears much more like a shear layer bounding a separated flow than a vortex wake.

A perspective plot of the local Mach number $M(y,z)$ in the cross-flow plane for $\alpha_b = 25^\circ$, $x/d = 6$, at both Mach 2 and Mach 3 is shown in Fig. 5. For Mach 2, Fig. 5a, the Mach number in the angle of attack plane, i.e., the z -axis, varies from about 1.9 far from the body to a peak of 3.16 near the body. Then a strong embedded shock wave passing normal through the angle of attack plane drops the Mach number to 2.2. The shock wave can be seen to extend in the y -direction for two grid spacings (11 mm) and then vanish into the low Mach number flow of the vortex core. A weak embedded shock wave emanating from the separation point can be seen near the crest of

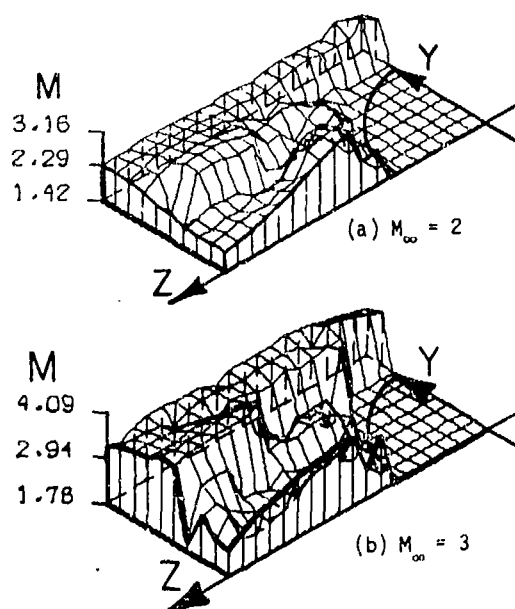


Figure 5
Mach Number in the Cross-Flow Plane
for $\alpha_b = 25^\circ$ and $x/d = 6$

opposite direction of the primary body vortex. Water tunnel photographs of Werle⁶ and the surface oil flow streaks of Hsieh⁷ suggest the existence of such a vortex on blunt missiles. The present experiment proves the existence of such a vortex, even on pointed bodies of revolution.

Figure 6 shows the measured relationship between the total circulation in the survey grid vs. body length for $\alpha_b = 10^\circ, 15^\circ, 20^\circ$, and 25° at Mach 2 and Mach 3. For $\alpha_b = 10^\circ$ and 15° a linear variation of total circulation vs. x is demonstrated. For $\alpha_b = 20^\circ$ and 25° , the variation is not as definite because many of the survey grids did not completely capture all of the circulation. That is, the flagged symbols in Fig. 6 denote that significant circulation passed through the top boundary of the grid.

Consequently, the flagged symbols are a lower bound on the total circulation in the cross-flow plane. For $\alpha_b = 10^\circ$ and 15° it is seen that the Mach number change from 2 to 3 has little effect on total circulation in the field. For $\alpha_b = 20^\circ$ and 25° the data indicate that the Mach 2 wake contains significantly more circulation than the Mach 3 wake. This characteristic could be related to the change in the wake from a vortex cloud for Mach 2 to a shear layer for Mach 3. To obtain an indication of the relationship of total circulation to angle of attack of the body, a least squares fit of the data was calculated. Using the total circulation data for $x/d = 8$ and 11 and $\alpha_b = 10^\circ, 15^\circ$ and 20° , a fit of Γ_t vs. $\sin^m \alpha_b$ was effected for the high Reynolds number conditions. The values of m were 2.33 and 1.90 for Mach 2 and Mach 3, respectively. The correlation coefficients for the power fits were approximately 0.99, indicating that the plot of $\log \Gamma_t$ vs. $\log \sin \alpha_b$ is very close to linear. The fit of the data demonstrates that the total circulation grows with angle of attack at a substantially lower rate as the Mach number increases.

IV. CONCLUSIONS

(1) The measured distribution of circulation in the cross-flow plane for Mach 2 shows that for $\alpha_b = 10^\circ$ and 15° and $x/d < 10$ the circulation is generally restricted to the vortex core and the vortex sheet. For $\alpha_b = 20^\circ$ and 25° the vorticity is generally diffused in the cross-flow plane to the extent that it could be described as a vortex cloud.

(2) The existence of a secondary nose vortex situated above the primary body vortex is confirmed. The secondary nose vortex rotates in the opposite direction as the body vortex. Although it is not believed significant with regard to missile flight dynamics, it is an interesting fluid dynamic phenomenon.

(3) The primary body vortex position in the cross-flow plane was measured for $M_\infty = 3$ at $\alpha_b = 10^\circ$ and 15° . For $\alpha_b = 20^\circ$ and 25° cross-flow compressibility distorts the body vortex to an extent that a body vortex cannot be defined. Local circulation in the cross-flow plane for $\alpha_b = 20^\circ$ and 25° shows that the vorticity is primarily located in a shear layer originating near the crest of the body and extending downstream.

(4) The total circulation in the wake for $\alpha_b < 15^\circ$ did not change between Mach 2 and Mach 3. For $\alpha_b > 20^\circ$ the measurements indicate that the Mach 2 wake contains significantly more circulation than the Mach 3 wake.

REFERENCES

1. Jorgensen, L. H., and E. W. Perkins, "Investigation of Some Wake Vortex Characteristics of an Inclined Ogive-Cylinder Body at Mach No. 2," NACA Report 1371, May, 1955.
2. Mello, J. F., "Investigation of Normal Force Distributions and Wake Vortex Characteristics of Bodies of Revolution at Supersonic Speeds," *J. Aero. Sci.*, Vol. 26, March, 1959, p. 155-168.
3. Oberkampf, W. L., T. J. Bartel and W. R. Martindale, "Supersonic Flow Measurements in the Body Vortex Wake of an Ogive Nose Cylinder," AIAA Paper No. 78-787, AIAA 10th Aerodynamics Testing Conference, San Diego, Calif., April, 1978.
4. Oberkampf, W. L. and T. J. Bartel, "Symmetric Body Vortex Wake Characteristics in Supersonic Flow," AIAA Paper No. 78-1337, AIAA Flight Dynamics Conference, Palo Alto, Calif., Aug., 1978.
5. Oberkampf, W. L., and T. J. Bartel, "Supersonic Flow Measurements in the Body Vortex Wake of an Ogive Nose Cylinder," prepared under AF Contract No. F08635-77-C-0049, Air Force Armament Lab. Report in preparation, Eglin AFB, Fla., Nov., 1978.
6. Werle, H., "Separation on Axisymmetrical Bodies at Low Speed," *La Recherche Aeronautique*, No. 90, Sept.-Oct., 1962.
7. Hsieh, T., "An Investigation of Separated Flows About a Hemisphere-Cylinder at Incidence in the Mach Number Range from 0.6 to 1.5," AIAA 15th Aerospace Sciences Meeting, AIAA Paper No. 77-179, Los Angeles, Calif., Jan., 1977.

ACKNOWLEDGEMENTS

The authors would like to thank Dr. Donald C. Daniel, Aerodynamics Research Manager, of the Air Force Armament Laboratory for his comments and suggestions during the investigation. We also thank the Project Engineers for our experiment, Mr. Bill Martindale and Mr. Terry Penny, ARO, Inc., AEDC, for their efforts.

WIND TUNNEL TEST AT LOW SPEEDS OF A DORSAL AIR INTAKE ON A FIGHTER CONFIGURATION

by

Sven-Olof Ridder
Department of Aeronautics
The Royal Institute of Technology
S-100 44 Stockholm, Sweden

SUMMARY

A wind tunnel model with a swept wing and a dorsal air intake mounted well aft on the fuselage has been investigated in a low speed wind tunnel with respect to the flow quality of the air intake flow.

It was found that the air intake flow was satisfactory at zero angle of yaw for angles of attack up to 20 degrees. Even a moderate angle of yaw, however, resulted in a rather high level of intake flow distortion as caused by the ingestion of forebody vortices. A large number of forebody mounted flow control devices were tested and among these only a canopy mounted device was found effective in reducing the intake flow distortion to an acceptable level.

1. DESCRIPTION OF THE WIND TUNNEL MODEL

The dorsal air intake position well aft on this aircraft configuration shown in Fig.1 should have several advantages compared with more conventional air intake positions. For example:

- Less problems with foreign object ingestion
- Minimum length engine installation
- Favorable axial area distribution
- etcetera

The main problem to be expected is to achieve satisfactory aerodynamic performance of the air intake at higher angles of attack in a complex flow field with many viscous effects. This problem is stressed by the fact that modern engines can tolerate only a moderate level of distortion of the flow entering the compressor due to compressor stall considerations.

The wind tunnel model has a 40° swept wing of aspect ratio 4 and a low set horizontal tailplane. The engine pod is blended with the rear part of the fuselage and tilted slightly in order to get the line of thrust close to the center of gravity. On top of the rear part of the canopy (in the plane of symmetry) is indicated the only flow control device so far found effective of a large number of forebody devices tested. The span of the model is 1 meter and the tests were carried out in an atmospheric low speed tunnel at about 60 m/s.

2. TEST RESULTS

The test program started with surveys of the total pressure losses at the intended position of the air intake, that is, without the engine pod mounted.

In Fig.2 are shown the results for the clean datum configuration. Vertical traverses with a total head probe starting from the upper side of the wing at five different span-wise stations are made and the recordings are arranged to present a perspective view with the air intake position indicated by the dashed circle.

At zero angle of yaw (left column) there appears to be very little pressure loss within the stream tube entering the intake, apart from a thin wake layer apparently shed from the canopy. The pronounced depression areas of the diffuse core of the forebody vortices pass outside the air intake. The situation at 20° of angle of attack (not shown) is also similar. Even a moderate angle of yaw, however, evidently upsets the symmetry of the forebody vortices and also creates a canopy vortex. The result is that large depression areas are fed into the air intake.

The corresponding total pressure surveys in the compressor section of the air intake mounted on the "clean" configuration are shown in Fig.3 ($\alpha = 10^\circ$, $\beta = 8^\circ$, $C_A = 1.0$). The recordings were obtained by means of a mechanism that could rotate the single probe and also perform radial traverses.

In the diagram are shown the pressure losses at a number of radial probe positions recorded during rotation of the probe with 180° corresponding to the 12 o'clock position. The horizontal part of each curve shows zero pressure loss. The magnitude of pressure losses and the distribution of the depression areas seem to correlate with the result of Fig.2 as could perhaps be expected considering the very short length intake duct.

In Fig.4 is shown the effect of the flow control device described in Fig.1. The situation on the lee side of the compressor section is very much improved at the expense of a slight degradation on the windward side.

The corresponding results of pressure surveys without engine pod of Fig.5 reveal that the major areas of depressions are made to pass outside the air intake. An astonishing fact is that this seems to be achieved at all tested combinations of α and β .

The data from the pressure surveys at the compressor section of the air intake has been evaluated to derive a distortion index. As a criterion has been chosen the DC60-index favoured by Rolls Royce. This distortion index relates the average pressure loss in the worst 60° sector to the average dynamic pressure of the flow at the compressor section.

With the type of pressure losses that are generated by the free stream flow around the forebody it is reasonable to assume that the distortion problem will be most severe at low inflow numbers, that is, when the dynamic pressure at the compressor section is low. Data from tests at inflow number 1.0 with a critical combination of α and β have been schematically recalculated to lower values of inflow numbers. It was found that the inflow number could be reduced to .46 before the critical value of distortion index was exceeded.

As a typical engine was chosen the RB 199 for which distortion criteria were available.

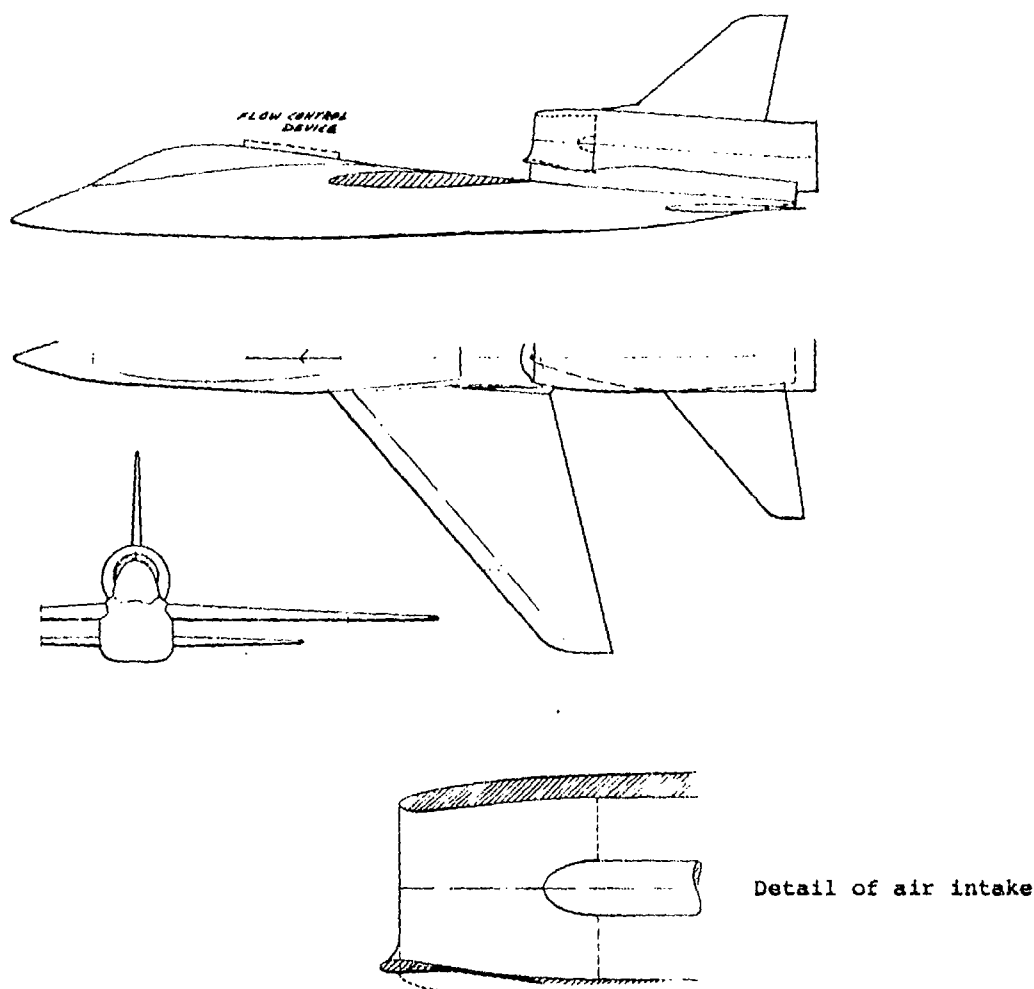


Fig.1 Sketch of wind tunnel model.

CLEAN CONFIG.

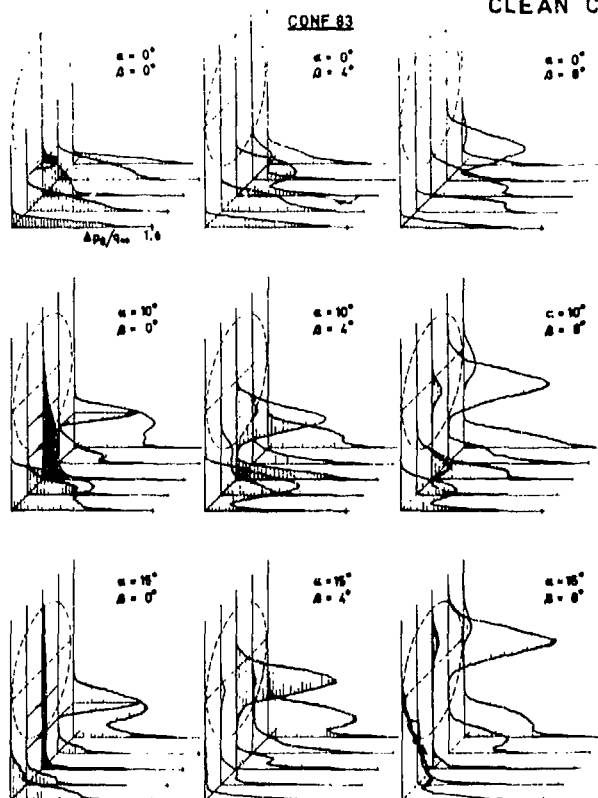


Fig. 2 Total pressure losses at the air intake position.

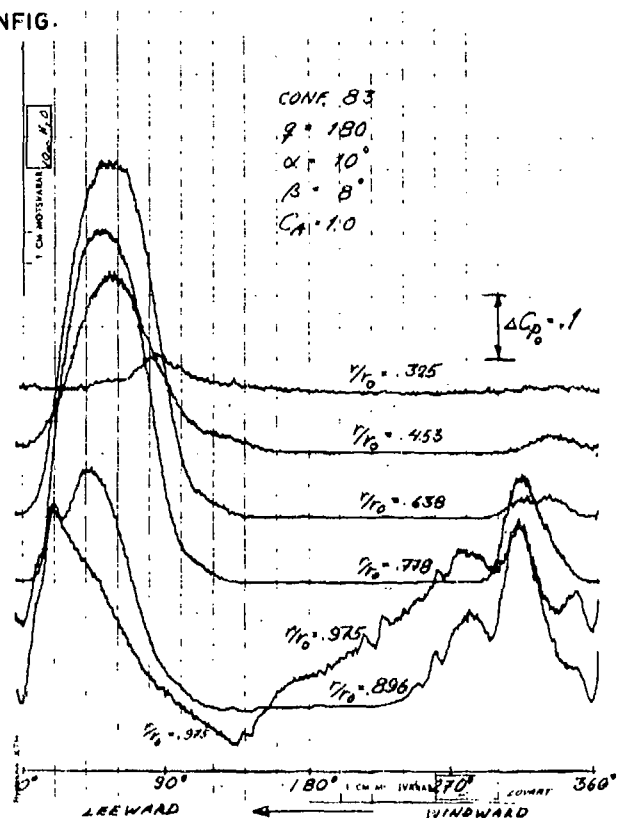


Fig. 3 Total pressure losses in the air intake at the compressor section.

CONFIG. WITH FLOW CONTROL DEVICE

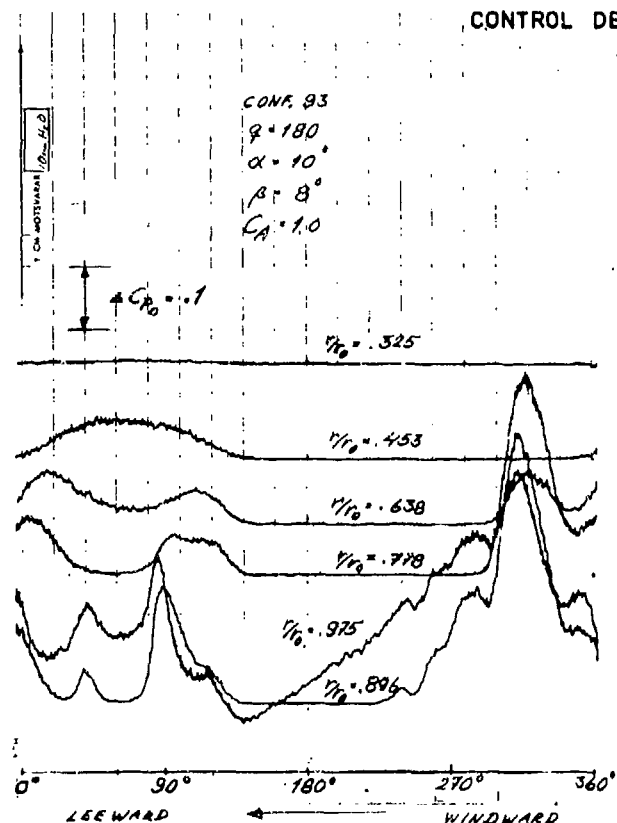


Fig. 4 Total pressure losses in the air intake at the compressor section.

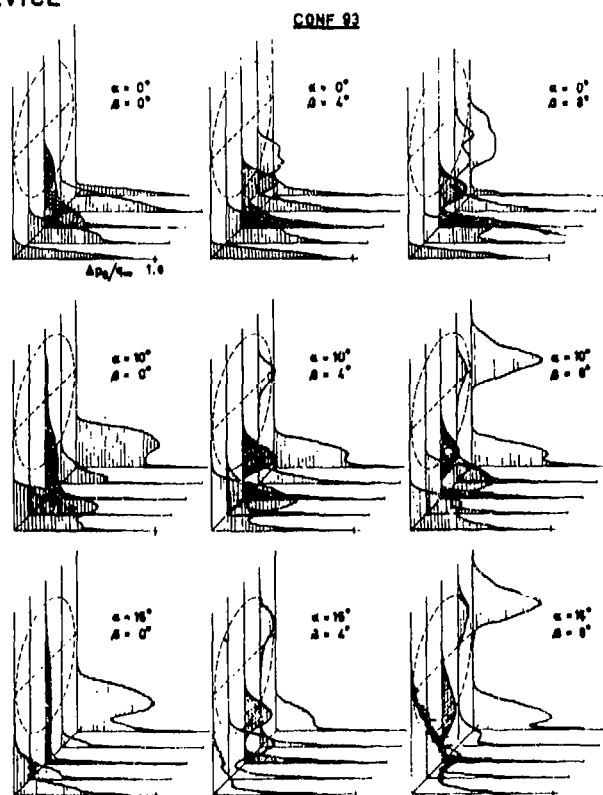


Fig. 5 Total pressure losses at the air intake position.

VISUALISATIONS AND CALCULATIONS OF AIR INTAKES
AT HIGH ANGLES OF ATTACK AND LOW REYNOLDS NUMBERS

by

P.C. PERRIER
J. PERIAUX

AVIONS MARCEL DASSAULT-BREGUET AVIATION
78, quai Carnot - 92214 ST CLOUD (France)

Le fonctionnement des compresseurs peut être fortement perturbé aux grandes incidences de vol par l'instationnarité de l'écoulement créé par les décollements aux lèvres de l'entrée d'air. On présente deux voies d'analyse des phénomènes qui sont complémentaires, l'une expérimentale de visualisations, l'autre par solution numérique directe des équations de Navier-Stokes.

Pour visualiser les phénomènes intervenant à l'intérieur de l'entrée d'air, on peut soit étudier l'écoulement à très faible vitesse, et donc à faible Reynolds, par injection de fluide coloré dans un écoulement bidimensionnel en tunnel hydrodynamique (réf.1) soit faire de la cinématographie ultra-rapide sur des strioscopies transsoniques (réf. 1 et 2). On met ainsi en évidence des grosses structures tourbillantes responsables de l'instationnarité de l'écoulement. On donne planche 1 un exemple de visualisation à la microseconde obtenue à l'Institut de Mécanique des Fluides de Lille.

En analysant en détail la turbulence dans l'entrée d'air (réf.3), on voit qu'on peut la considérer comme créée principalement par des grosses structures de la taille de la conduite et qui sont générées par le décollement issu des lèvres. Quoique ce décollement soit initialement calculable par des méthodes de singularité (réf.4, par exemple), c'est l'instabilité du décollement qui est en cause et qu'on ne peut calculer que par des méthodes plus complexes, solutions exactes ou approchées des équations de Navier-Stokes (cf. les papiers 22 et 29). Nous présentons ici des résultats de calcul obtenus par solution directe des équations de Navier-Stokes instationnaires par une méthode des éléments finis en moindres-carrés (réf.5). Cette méthode résout la non-linéarité des équations par itération sur l'équation linéaire de Stokes qui est elle-même résolue de façon originale (réf.6). On donne planche 2 une série de tracés des lignes iso-tourbillons calculés dans une entrée d'air à très grande incidence (40°) dans le cas où toute l'entrée d'air est entièrement occupée par les grosses structures et qui est directement comparable aux visualisations présentées dans le film de l'O.N.E.R.A.

A cause de l'augmentation prohibitive des temps de calcul avec le nombre de Reynolds, on a limité celui-ci à 250. Il est cependant suffisant pour capter les gros tourbillons. Il faudrait ajouter un modèle de turbulence de maille (cf. par exemple réf.7) ou un modèle de viscosité turbulente pour simuler l'écoulement à plus grand nombre de Reynolds.

REFERENCES :

- 1 H. WERLE (ONERA) - Film n° 848 Ecoulement autour d'une prise d'air à grande incidence
- 2 A. DYMENT - P. GRYSON - A. LAVOGIEZ - Modélisation des décollements dans une entrée d'air à grande incidence. Etude I.M.F.L. n° 1277/SR - Août 76.
- 3 J.F. ARNAUDON et L.F. TSEN - Etude exploratoire de la turbulence dans les prises d'air. 13e Colloque AAAF - Nov. 76.
- 4 P. CAUPENNE - Etudes expérimentales et Théoriques sur les décollements. 13e Colloque AAAF - Nov. 76.
- 5 R. GLOWINSKY - B. MANTEL - J. PERIAUX - O. PIRONNEAU - H^{-1} Least Squares Method for Navier-Stokes Equations. Numerical Methods in laminar and turbulent flows. SWANSEA July 78.
- 6 R. GLOWINSKY - O. PIRONNEAU - Approximation par éléments finis du problème de Stokes en formulation vitesse-pression. C.R.A.S. A181/A225 - Janv. 78.
- 7 P. PERRIER - O. PIRONNEAU - Couplage des grosses et petites structures par l'homogénéisation. C.R.A.S. E.286 A.635 - 1978.

PLANCHE 1

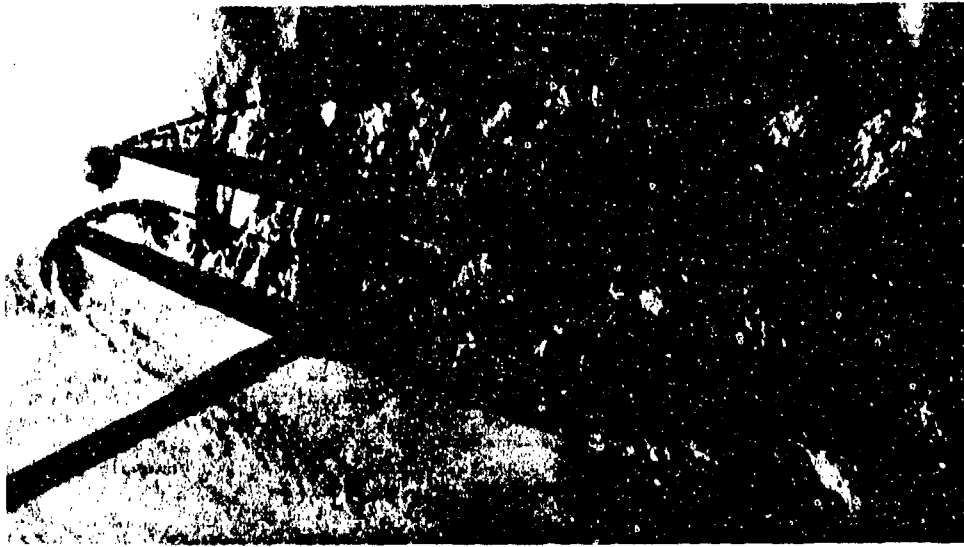
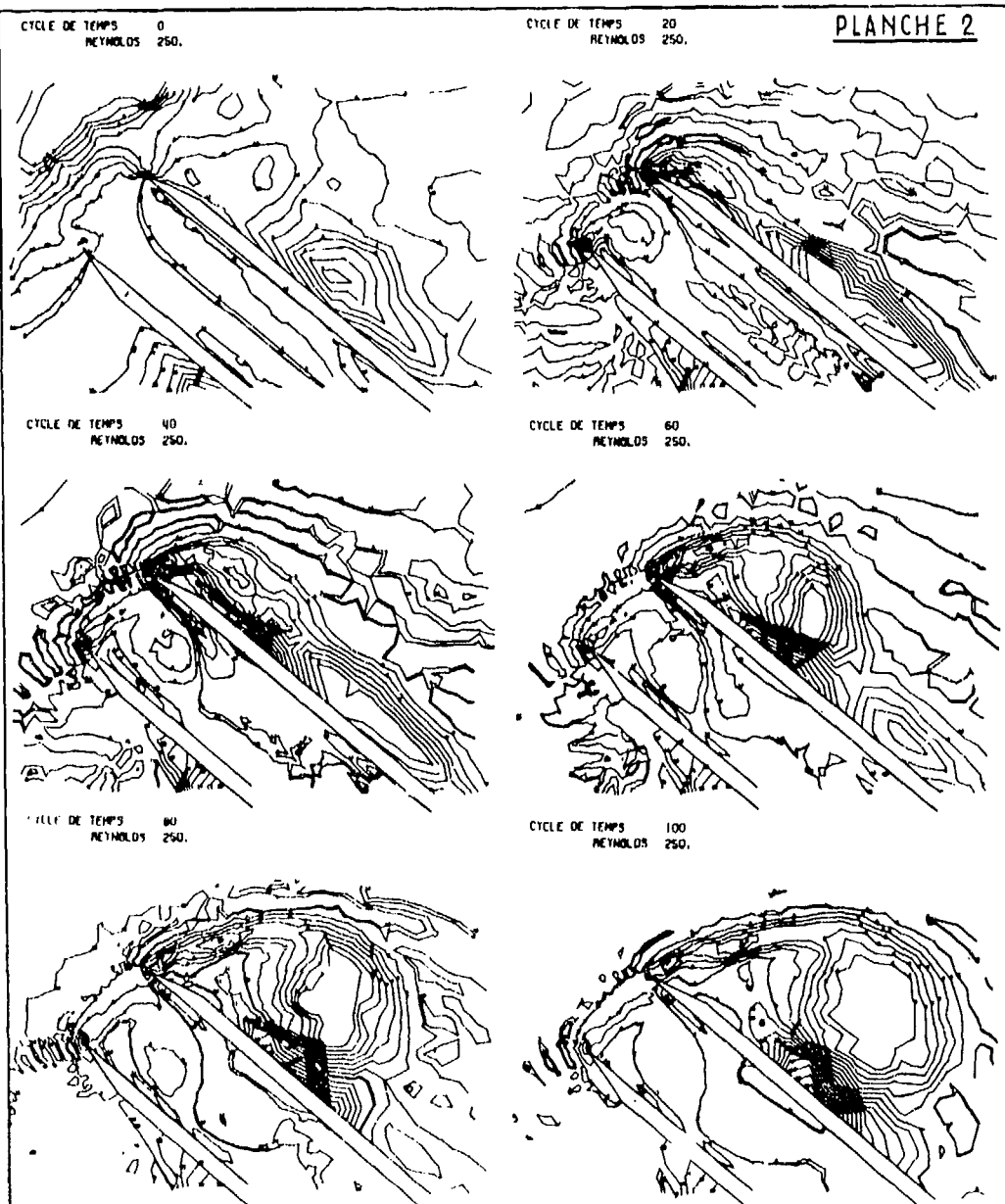


PLANCHE 2



STATE OF ART OF NONLINEAR, DISCRETE-VORTEX METHODS
FOR STEADY AND UNSTEADY HIGH ANGLE OF ATTACK AERODYNAMICS

Osama A. Kandil*
Department of Mechanical Engineering and Mechanics
Old Dominion University, Norfolk, Va. 23508

I. INTRODUCTION

In recent years, there has been a considerable interest in developing reliable methods for treating high angle of attack aerodynamics. With the advent of low-aspect-ratio and highly swept wings, large-fineness-ratio bodies and configurations of such aerodynamic components, three-dimensional flow analysis became of paramount necessity.

The fluid flow past these configurations is characterized with a strong cross flow which leads to flow separation in the vicinity of wing edges and lee sides of the bodies. The separated free-shear layer rolls-up spirally and forms a vortex core which is continuously fed with vorticity shed from the attached boundary layer on the wing surface through the free-shear layer. This type of flow separation is known as "primary separation".

For wings with sharp leading and side edges, the lines of primary separation are known a priori as they are fixed along these edges. Primary separation has the most dominant effect on the aerodynamic characteristics within the low-moderate range of angles of attack. In the case of highly swept wings (Delta and Delta-like wings), it increases the negative pressure under the primary vortex cores and produces suction peaks in this region.

The adverse pressure gradients created by the suction peaks affect the boundary layer flow in this region and another type of flow separation develops. This separation is known as "secondary separation". The secondary separated flow rolls-up spirally in an opposite sense to that of the primary separated flow and forms a vortex core opposite to that of the primary core¹⁻³.

For laminar flow over the wing surface, the effect of the secondary vortex on the pressure distribution is pronounced and another pressure peak can be seen in the span-wise pressure distribution. For turbulent flow over the wing surface, secondary pressure peaks are hardly noticed⁴⁻⁵ and its effect is negligible.

Secondary flow separation is seen to be a viscous phenomenon and cannot be modelled with an inviscid model only. Moreover, the secondary separation line is unknown a priori.

The stall phenomenon of low-aspect-ratio wings is attributed to breakdown (bursting) of the vortex core⁶⁻¹⁰. It is a complex viscous phenomenon and cannot be adequately treated before a satisfactory viscous-inviscid model of the vortex core is established.

Therefore, an inviscid model which neglects secondary separation is a reasonable model particularly for flows with large Reynolds number and without vortex breakdown in the vicinity of the wing.

II. DISCRETE-VORTEX METHOD

Development of inviscid models for predicting the aerodynamic characteristics of wings exhibiting leading-edge and/or wing-tip separations has recently received considerable efforts. The literature contains several models with various degrees of limitations and/or drawbacks. These include conical flow assumption (violates Kutta condition at the trailing edge), slender-body theory¹¹⁻¹⁶, and imposing the boundary conditions on frozen wake surfaces¹⁷.

In all the existing inviscid models, the lines of primary separation are assumed to be known a priori and, hence, these models can only treat wings with sharp edges. Moreover, the effects of secondary separation are completely neglected because secondary separation is a viscous phenomenon. The attached boundary layer on the wing surface is replaced by a bound sheet (a pressure jump exists across the sheet) of tangential velocity discontinuity. The free-shear layer of the separated flow is replaced by a free sheet (zero pressure jump across the sheet) of tangential velocity discontinuity. To present the subsequent steps of approximations and evaluate their effects, the model developed by the Principal Investigator¹⁸⁻²³ will be used. Similar models were used by other investigators^{24, 25}.

In this model, the continuous vortex sheets (bound and free) are approximated by a distribution of concentrated vortex lines. The bound sheet is modelled by a bound-vortex lattice and the free sheet is modelled by segmented free-vortex lines (steady-flow problem) or a growing free-vortex lattice (unsteady-flow problem). With this three-dimensional model the boundary conditions are satisfied at certain control points on the bound and free vortex system, the shape of the free-vortex lines is obtained, and the pressure distribution is calculated on the wing surface.

*Associate Professor

Excellent agreement was found between the calculated and experimental total-aerodynamic characteristics. On the otherhand, satisfactory or less than satisfactory agreement was found between the calculated and experimental distributed aerodynamic characteristics. The reason behind this less satisfactory agreement becomes apparent when we recall the discrete-vortex approximation.

The advantages of this method over other existing methods are the simplicity of the method and the relative short computation time. The method has been developed for the steady and unsteady wing problems. In the steady problem it is used to obtain solutions for isolated wings with rectangular, delta and delta-like planforms. It is also used for wing-wing configurations^{1,2,3}.

In the unsteady problem, there are two approaches. In the first approach, the problem is solved at discrete time steps. This approach is appropriate for transient solutions and large unsteady disturbances^{2,3}.

In the second approach, small-amplitude disturbances are assumed and the problem is linearized about nonlinear steady solutions^{2,3}. This approach is appropriate for the flutter analysis about large angles of attack.

III. NUMERICAL EXAMPLES

Figure 1 shows a typical solution of the roll-up shape of the leading edge vortex for a delta wing. The aspect ratio is 1.4, the angle of attack is 14° and the bound lattice is 12×12 . The upper figure is a three-dimensional view which shows the roll-up shape of the leading-edge vortices.

Figure 2 shows a typical solution of the roll-up shape of the leading-edge vortex for a steadily rolling wing at zero angle of attack. The rotation is clockwise as viewed from the rear. The aspect ratio is 0.7 and an 8×8 bound-vortex lattice is used. The antisymmetry of the leading-edge vortex is clearly seen in the upper figure.

Figure 3 shows a typical solution of the wake shape for a Canard-Wing configuration with high Canard which was considered for the SAAB-Viggen aircraft.

Figure 4 shows the spanwise position and the height of the vortex-core path on a delta wing of aspect ratio 1.4, $\alpha = 14^\circ$. It shows the convergence of the solution with increasing the number of elements of the bound lattice. Comparisons are shown with the experimental results of Marsden et al.^{2,6}

Figure 5 shows the upper and lower pressure distribution on the steady rolling wing which was shown before. The comparison is made with the experimental results of Harvey^{2,7} and with the slender body theory of Cohen & Nimri^{1,8} and Hanin & Mishne^{2,8}.

REFERENCES

1. Peckham, D.H., "Low-Speed Wing-Tunnel Tests on a Series of Uncambered Slender Pointed Wings with Sharp Edges," British ARC R&M No. 3186, December 1958.
2. Bergesen, A.H. and Porter, J.D., "An Investigation of the Flow Around Slender Delta Wings with Leading-Edge Separation," Princeton University, Department of Aeronautical Engineering, Report No. 510, May 1960.
3. Harvey, J.K., "Some Measurements on a Yawed Slender Delta Wing with Leading-Edge Separations," British ARC Report No. 20451, 1958.
4. Hummel, D., "Study of Flow Around Sharp-Edged Slender Delta Wings with Large Angles of Attack," NASA TT F-15, 107, September 1973.
5. Hummel, D., "On Vortex Formation over a Slender Wing at Large Angles of Incidence," AGARD-CCP-247, Paper No. 15, Sandefjord, Norway, October 4-6, 1978.
6. Peckham, D.H. and Atkinson, S.A., "Preliminary Results of Low Speed Wind Tunnel Tests on a Gothic Wing of Aspect Ratio 1," ARC, CP 508, 1957.
7. Lambourne, N.C. and Bryer, D.W. "The Bursting of Leading-Edge Vortices; Some Observations and Discussion of the Phenomenon," ARC, R&M 3282, 1962.
8. Lowson, M.V., "Some Experiments with Vortex Breakdown," Journal of the Royal Aeronautical Society, Vol. 68, 1964, pp. 343-346.
9. Hummel, D. and Srinivasan, P.S., "Vortex Breakdown Effects on the Low-Speed Aerodynamic Characteristics of Slender Delta Wings in Symmetrical Flow," Journal of the Royal Aeronautical Society, Vol. 71, April 1967, pp. 319-322.
10. Hummel, D. and Redeker, B., "Über den Einfluß des Aufplatzens der Wirbel auf die aerodynamischen Beiwerte von Deltaflügeln mit kleinem Seitenverhältnis beim Schiebflug," WGLR, 1967, pp. 232-240.
11. Brown, C.E. and Michael, W.H., "On Slender Delta Wings with Leading-Edge Separation," NACA Tech. Note 3430, April 1955.

12. Mangler, K.W. and Smith, J.H.B., "A Theory of the Flow Past a Slender Delta Wing with Leading-Edge Separation," Proc. Roy. Soc. of Lond. A, 251, 1959, pp. 200-217.
13. Smith, J.H.B., "Improved Calculations of Leading-Edge Separation from Slender Delta Wings," Proc. Roy. Soc., Lond. A, 305, 1968, pp. 67-90.
14. Pullin, D.I., "Calculations of the Steady Conical Flow Past a Yawed Slender Delta Wing with Leading-Edge Separation," Imperial College of Science and Technology, Lond., I.C. Aero Report 72-17, July 1972.
15. Jones, I.P., "Flow Separation from Yawed Delta Wings," Computer and Fluids, Vol. 3, 1975, pp. 155-177.
16. Cohen, M.J. and Nimri, D., "Aerodynamics of Slender Rolling Wings at Incidence in Separated Flow," AIAA Journal, Vol. 14, No. 7, July 1976, pp. 886-893.
17. Weber, J.A., Brune, G.T., Johnson, F.T., Lu, P., Rubbert, P.E.; "A Three-Dimensional Solution of Flows over Wings with Leading-Edge Vortex Separation," AIAA Paper No. 75-866, presented at 8th Fluid and Plasma Dynamics Conference, Hartford, Connecticut, June 16-18, 1975.
18. Kandil, O.A., "Prediction of the Steady Aerodynamic Loads on Lifting Surface Having Sharp-Edge Separation," Ph.D. Dissertation, Dept. of Engr. Sci. and Mechanics, Virginia Polytechnic Institute and State University, December 1974.
19. Kandil, O.A., Mook, D.T. and Nayfeh, A.H., "Nonlinear Prediction of the Aerodynamic Loads on Lifting Surfaces," Journal of Aircraft, Vol. 13, No. 1, January 1976, pp. 27-38.
20. Kandil, O.A., Mook, D.T. and Nayfeh, A.H., "New Convergence Criteria for the Vortex Lattice Models of the Leading-Edge Separation," NASA SP-405, No. 16, May 1976, pp. 285-300.
21. Kandil, O.A., Mook, D.T. and Nayfeh, A.H., "A Numerical Technique for Computing Subsonic Flow Past Three-Dimensional Canard-Wing Configurations with Edge Separation," AIAA Paper No. 77-1, January 1977.
22. Kandil, O.A., Atta, E.H., and Nayfeh, A.H., "Three-Dimensional Steady and Unsteady Asymmetric Flow Past Wings of Arbitrary Planforms," NASA CR 145 235, also Paper No. 2, AGARD Fluid Dynamic Symposium on Unsteady Aerodynamics, Ottawa, Canada, 26-28 September 1977.
23. Kandil, O.A., Page, M., "A Nonlinear, Discrete-Vortex-Perturbation Method for the Potential Unsteady, Lifting-Surface Problems with Edge Separation," the 11th Congress of ICAS, Lisbon, Portugal, September 14-16, 1978.
24. Belotserkovskii, S.M., "Calculation of the Flow Around Wings of Arbitrary Planforms over a Wide Range of Angle of Attacks," NASA TT F-12, 391, 1969.
25. Rehbach, C., "Calculation of Flow Around Zero-Thickness Wings with Evolute Vortex Sheets," NASA TT F-15, 183, 1973.
26. Marsden, D.J., Simpson, R.W., and Rainbird, B.E., "An Investigation into the Flow over Delta Wings at Low Speeds with Leading-Edge Separation," The College of Aeronautics, Cranfield, England, Report No. 114, February 1958.
27. Harvey, J.K., "A Study of Flow Field Associated with Steadily-Rolling Slender Delta Wings," Journal of the Royal Aeronautical Society, Vol. 58, Feb. 1964, pp. 106-110.
28. Hanin, M. and Mishne, D., "Flow About a Rolling Slender Wing with Leading-Edge Separation," Israel Journal of Technology, Vol. II, No. 3, 1973, pp. 131-136.

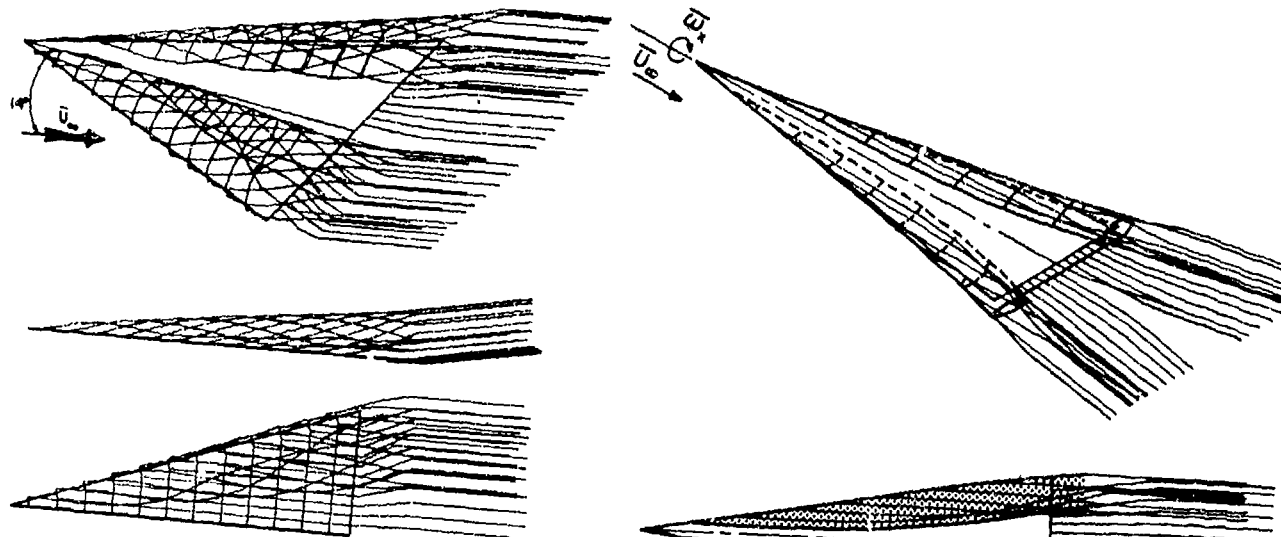


FIGURE 1. A TYPICAL SOLUTION OF THE WAKE SHAPE FOR A DELTA WING, 12 x 12 LATTICE, AR = 1.4, $\alpha = 14^\circ$

FIGURE 2. A TYPICAL SOLUTION OF A STEADILY ROLLING DELTA WING, $W_x = -0.2$, $\alpha = 0^\circ$, 8 x 8 LATTICE, AR = 0.7

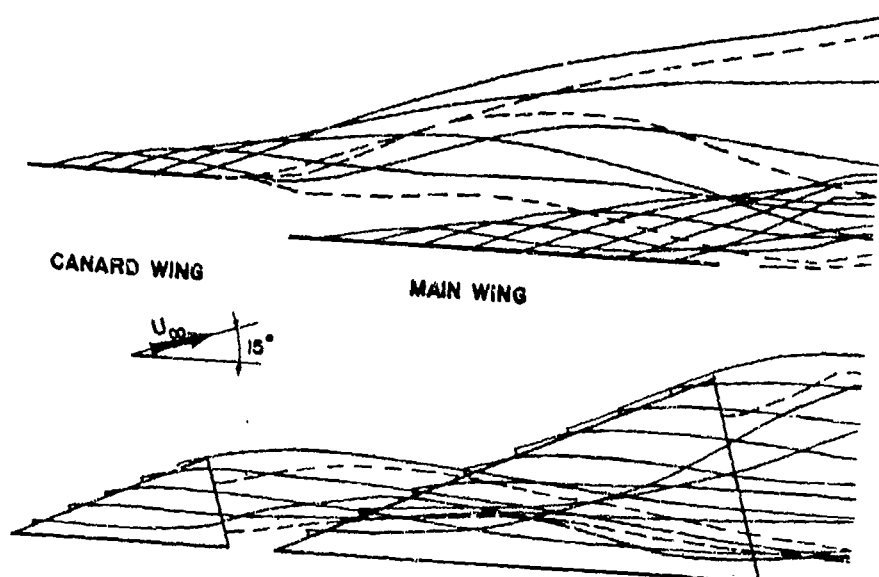


FIGURE 3. A TYPICAL SOLUTION OF THE WAKE SHAPE FOR A CANARD-WING CONFIGURATION, 5 x 5 LATTICE (CANARD), 8 x 8 LATTICE WING, $\alpha_C = \alpha_W = 15^\circ$

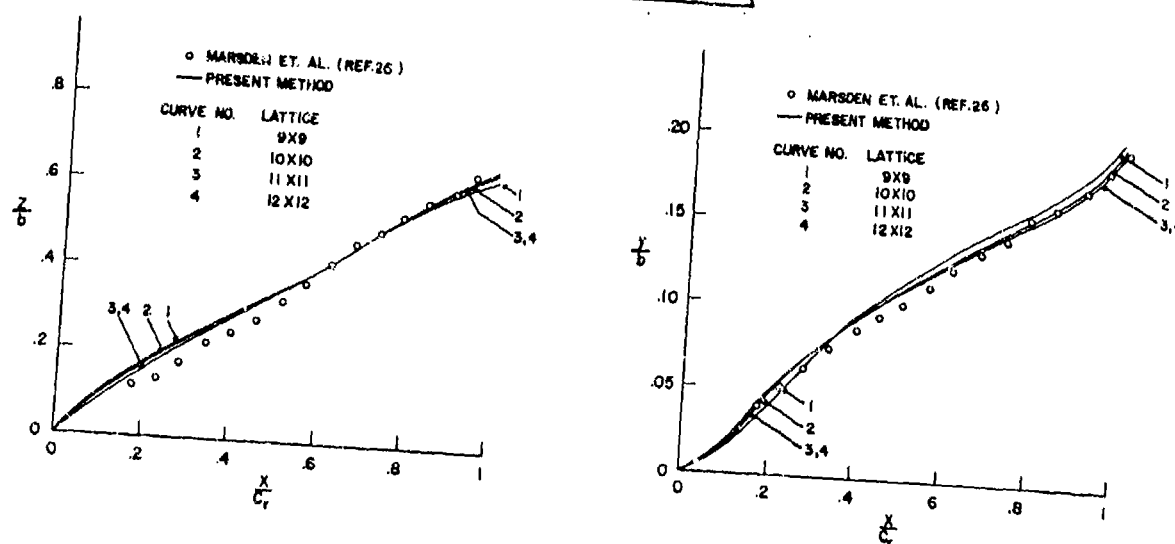


FIGURE 4. SPANWISE AND HEIGHT OF VORTEX-CORE PATH ON A DELTA WING, AR = 1.4, $\alpha = 14^\circ$

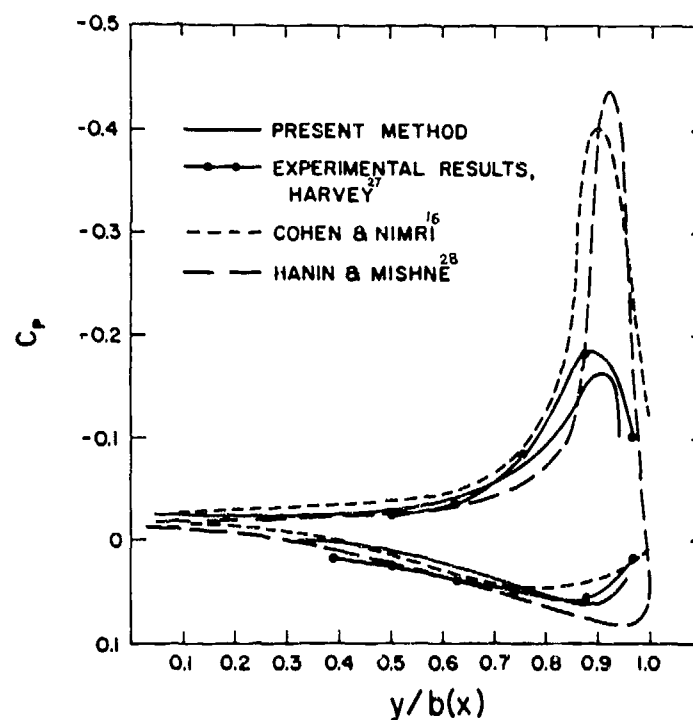


FIGURE 5. UPPER AND LOWER, SPANWISE PRESSURE DISTRIBUTION
ON A STEADILY ROLLING DELTA WING, $x = -0.2$,
 $\alpha = 0$, 8×8 LATTICE, $AR = 0.7$, $x/c_1 = 0.778$

ON SLENDER WINGS WITH LEADING EDGE CAMBER

by

R. K. Nangia

Department of Aeronautical Engineering,
University of Bristol, Queen's Building,
University Walk, Bristol, BS8 1TR, U.K.

SUMMARY

The presence of leading edge camber or wing or wing body configuration of low aspect ratio is known to improve their aerodynamic efficiency. A research programme to develop design methods on this subject has been sponsored by the USAF Office of Scientific Research at the University of Bristol. This short note is indicative of recent work.

1. INTRODUCTION

Under the framework of slender wing theory attempts have been made to model the flowfields on thin and thick wings and wing body configurations with realistic leading edge camber. Flow separation at the leading edges has been included.

2. THIN WINGS - CONICAL FLOW

Camber and droop have been developed in the cross-flow plane using the conformal transformations proposed by Maskell and Cooke (Ref. 1). The position of shoulder of camber and the amount of droop can be arbitrarily varied. Flow separations have been modelled as isolated vortex-cut arrangements. Two aspects of this work are:

(a) Lift induced drag factor $\pi A C_{Di}/C_L^2$ as a function of lift coefficient has been obtained for a series of camber parameters. Typical graph (Fig. 2) shows the effect of shoulder variation for fixed droop (0.1 semispan). Flat wing results are also compared. This type of graph aids in quantifying the reduction in lift induced drag due to camber parameter.

(b) For wings with shoulder position near the leading edge, a multiple-valued solution has been noted. This is exemplified by observing the vortex strength versus angle of attack relationship for a series of wings with fixed droop but varying shoulder position (Fig. 3(i)). For a particular unit aspect ratio wing with shoulder at 0.95 semi-span and droop .05 semi-span, we have for a small range of angle of attack (10° to 15°), the existence of up to 3 values of vortex strength. Taking the case of $\alpha = 11.7^\circ$ it can be shown that the flow patterns for attachment streamline are all of different type (Fig. 3(ii)). We note that a similar situation exists in the study by Levinsky and Wei (Ref. 2) on cones with strakes (Fig. 4).

Intuitively it may be argued that the multiple valued situation is not likely to exist in practice and this is a shortcoming of a model with simulation of one separation system. To render the result unique we need to use multiple vortex systems (Fig. 5) in the modelling. This conclusion applies equally to other methods using Panelling schemes for wing and separation sheets.

3. THIN WINGS - NON-CONICAL FLOW

An idea of the planform effects on a cambered wing, particularly for strake design, may be obtained by step by step approach as also used by Smith (Ref. 3) and Clarke (Ref. 4). Fig. 6 shows the effect of cambering the curved leading edge on the vortex paths. Two shapes of leading edges and corresponding vortex locations in projected yz-plane are depicted.

4. THICK SHARP-EDGED CONICAL WINGS

An example presented is that of Lift/Induced Drag (C_L/C_{Di}) variation against C_L for a series of four wings with same centre-line thickness and overall droop but of varying leading edge shape and angle. The wing with greatest leading edge angle appears to produce highest C_L/C_{Di} (Fig. 9).

5. WING-BODY OR STRAKE CONFIGURATIONS

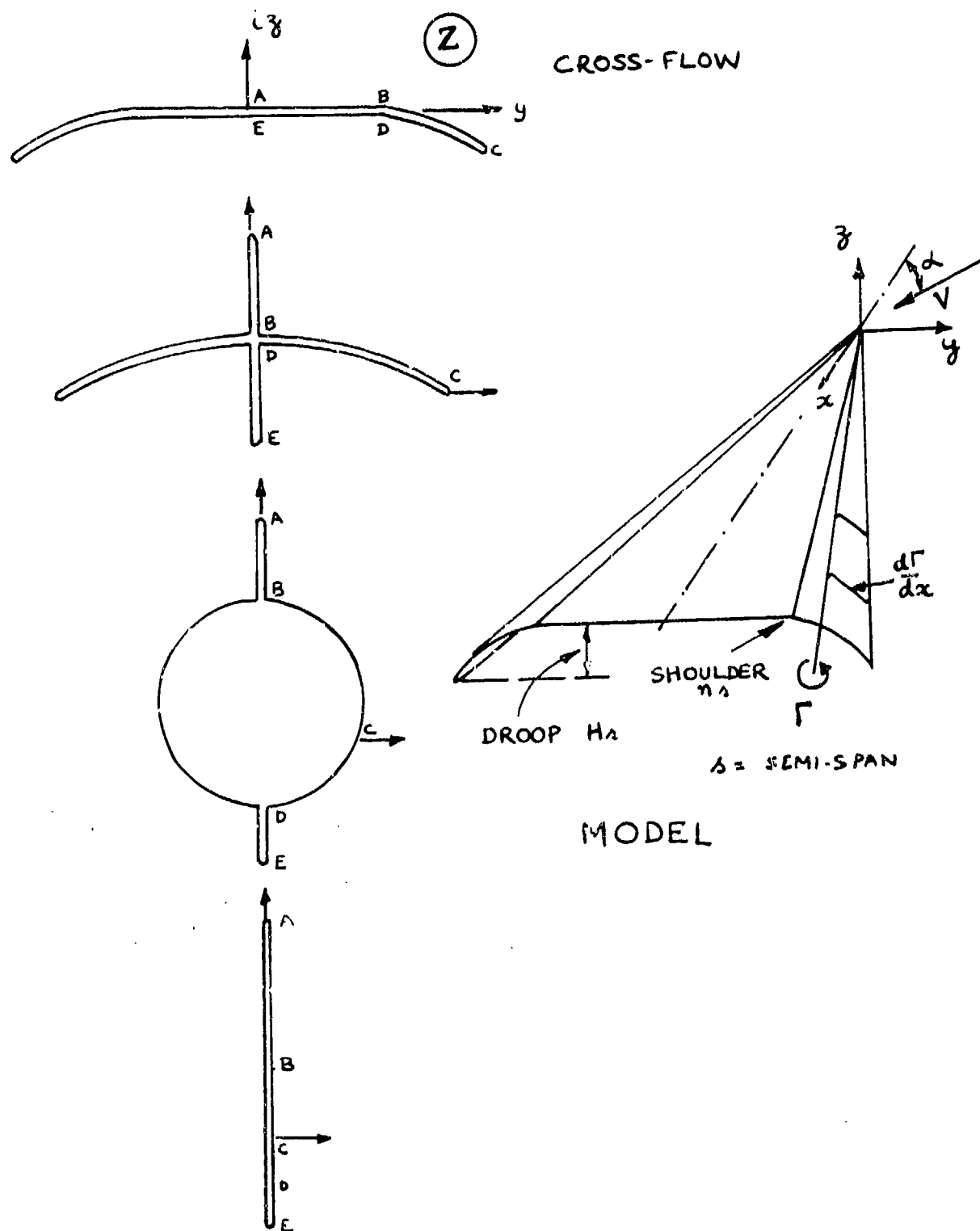
Wing body configurations with generalized strake shape and positions (Fig. 9) have also been considered by developing suitable conformal transformations. The capability of transformation is sketched in Fig. 10. It is hoped to publish a report on this work in the near future.

6. CONCLUDING REMARKS

Design methods developed under slender wing theory framework have proved useful in providing an improved understanding of leading edge flows. Further extensions of the methods and concepts are indicated.

7. REFERENCES

1. COOKE, J. C. "Properties of a Two-Parameter Family of Thin Conically Cambered Delta Wings by Slender Body Theory", RAE TN Aero 2698 (1960).
2. LEVINSKY, E. S. and WEI, M. H. Y. "Non-linear Lift and Pressure Distribution on Slender Conical Bodies with Strakes at Low Speeds", NASA CR-1202 (1968).
3. SMITH, J. H. B. "A Theory of the Separated Flow from the Curved Leading Edge of a Slender Wing", ARC R&M 3116 (1957).
4. CLARK, R. W. "Non-Conical Flow Past Slender Wings with Leading-edge Vortex Sheets", RAE TR 76037 (1976).



CONFORMAL TRANSFORMATIONS

FIGURE 1

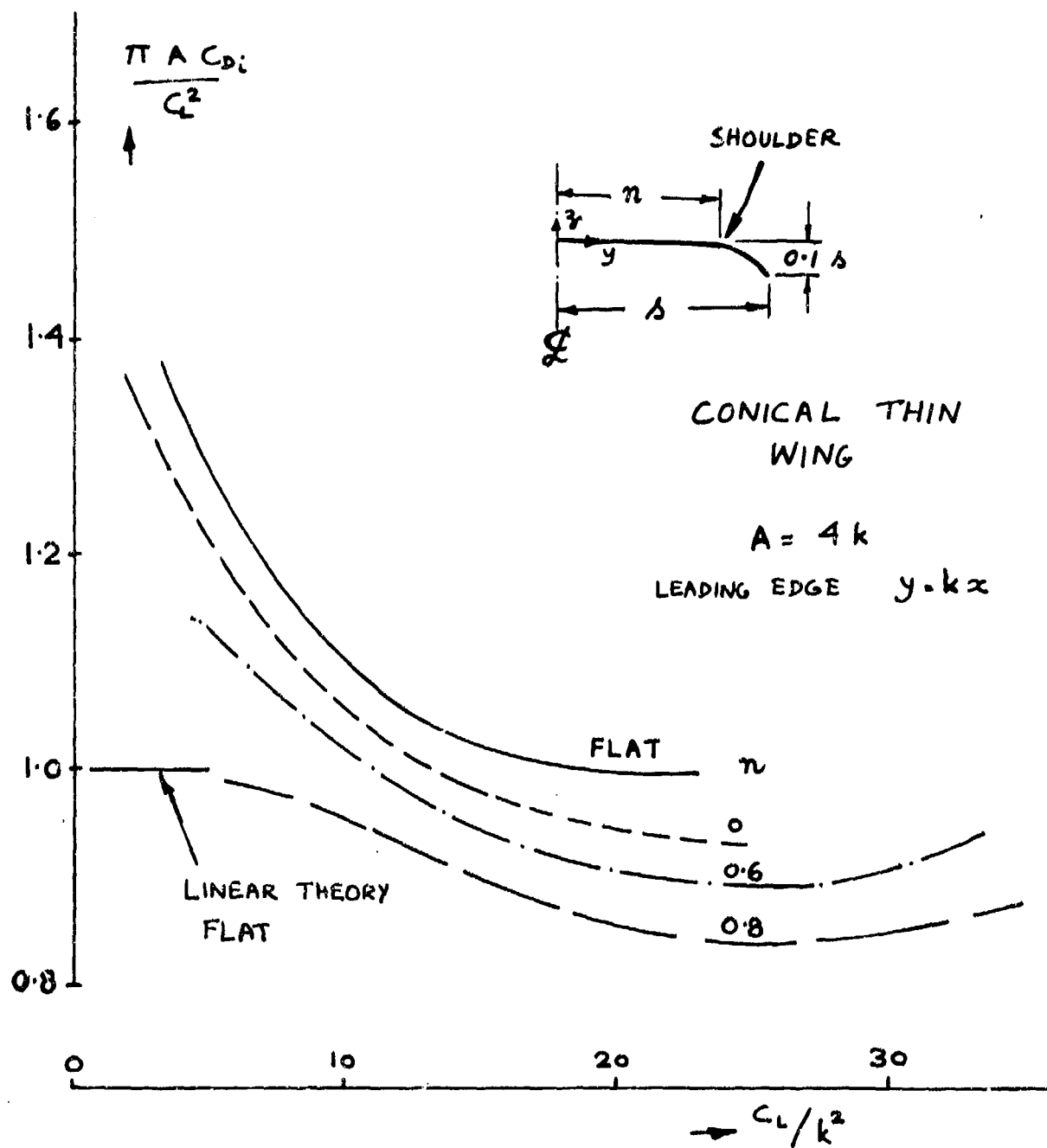


FIGURE 2 LIFT-INDUCED DRAG FACTOR VARIATION

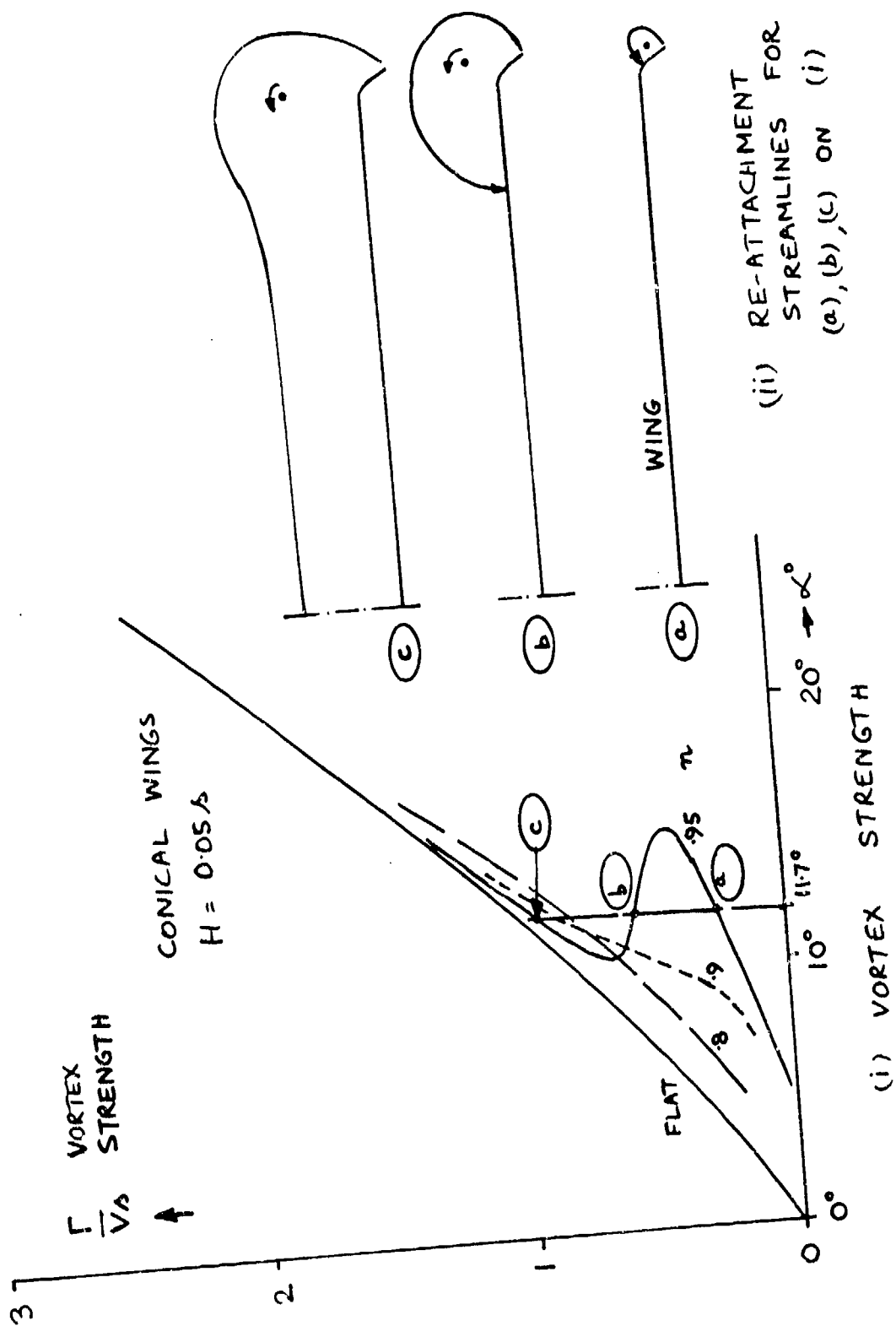


FIGURE 3

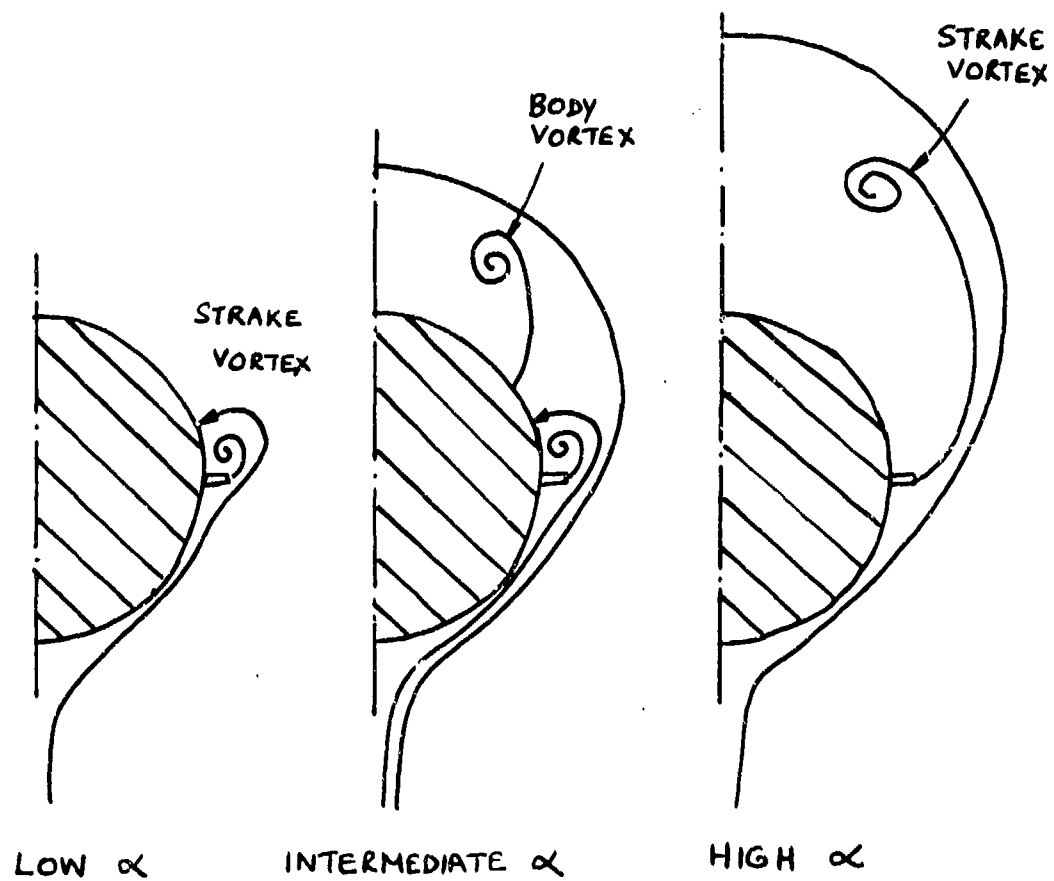


FIGURE 4 CONES WITH STRAKES ACCORDING TO LEVINSKY & WEI

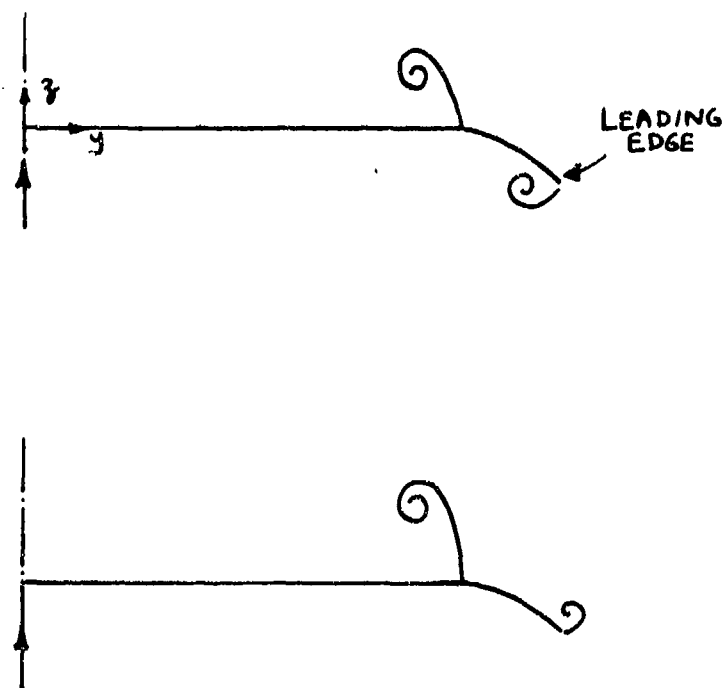


FIGURE 5 MULTIPLE VORTEX SYSTEMS

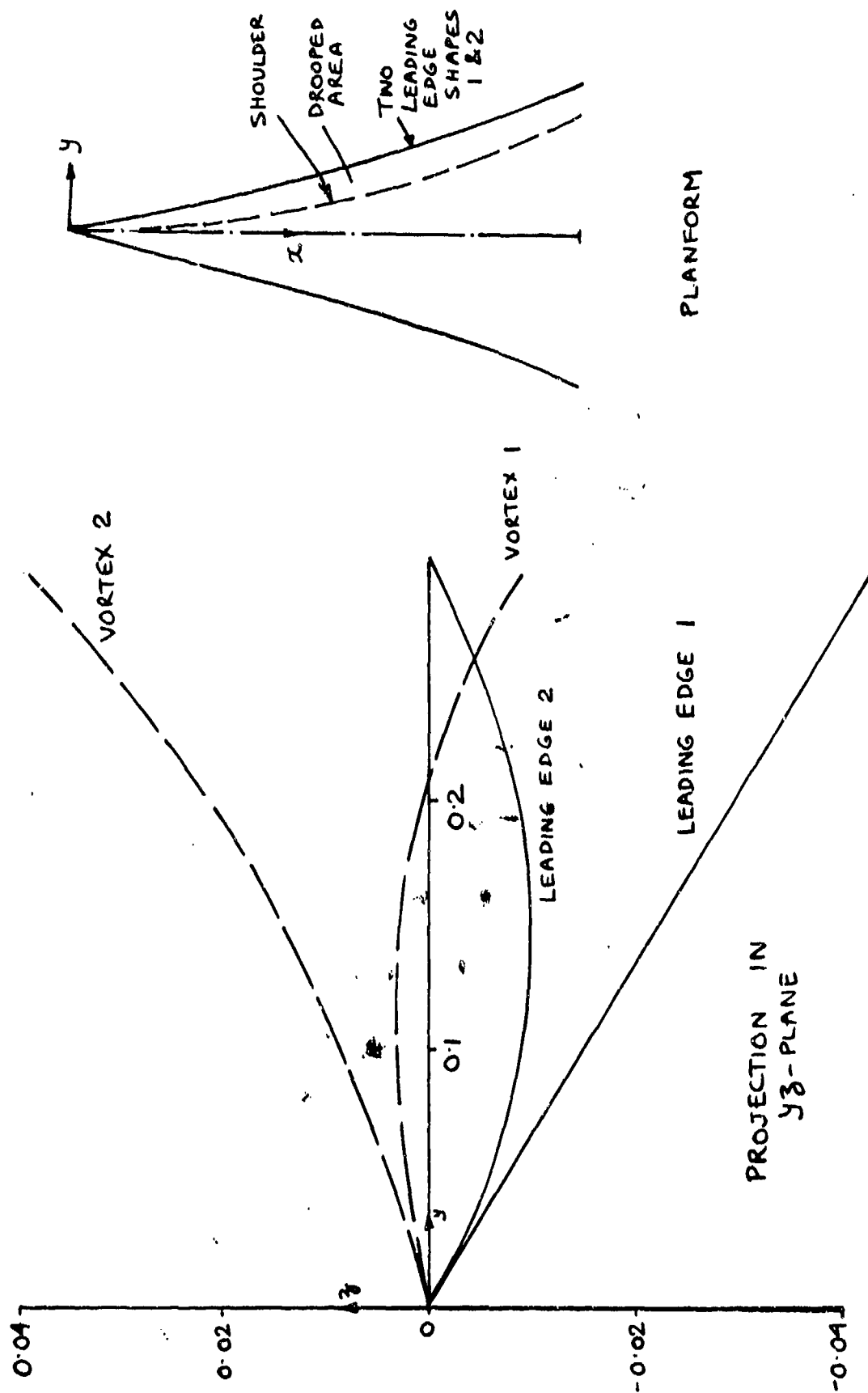


FIGURE 6 NON-CONICAL FLOW EFFECTS (STRAKE)

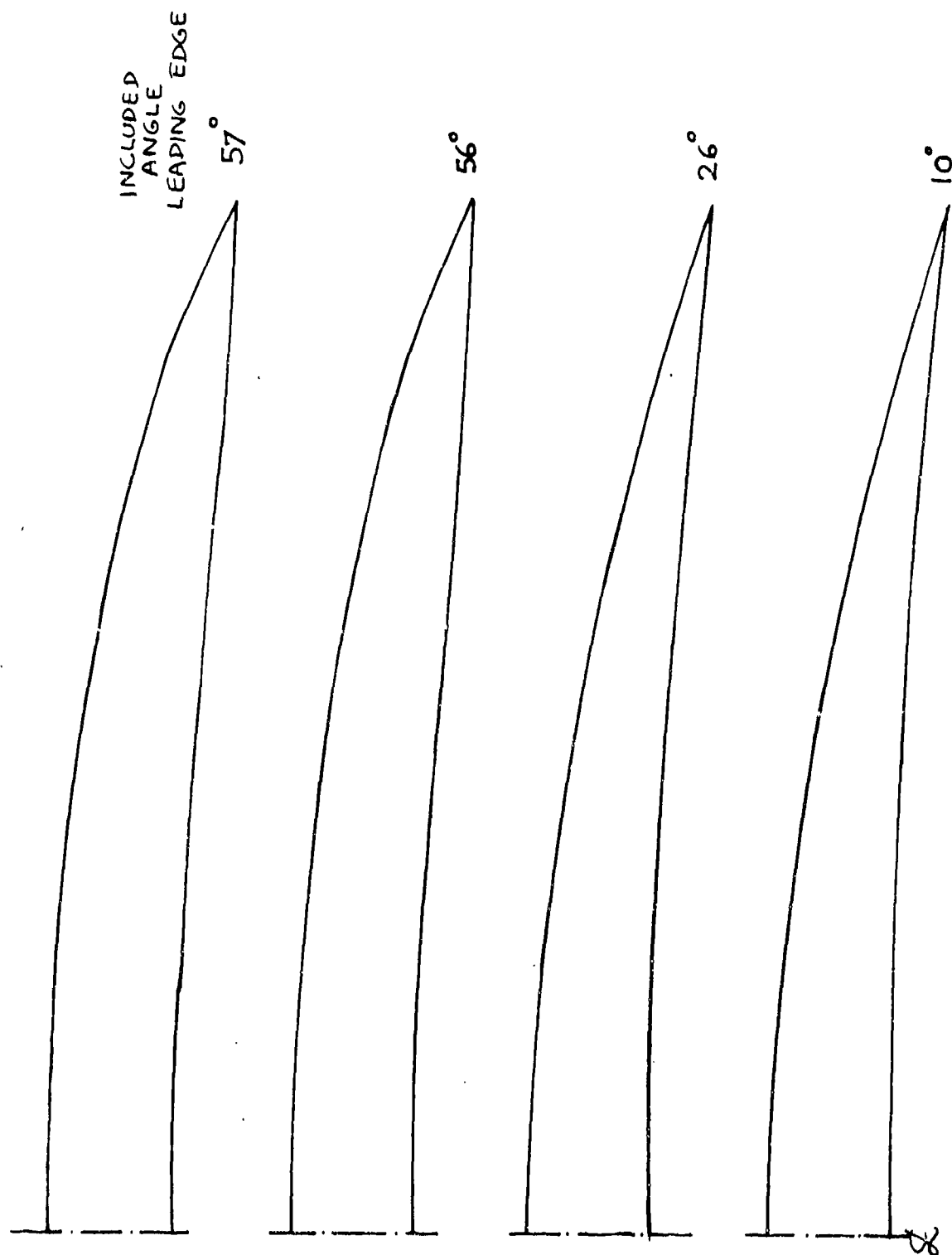


FIGURE 7 4 WINGS SERIES - SAME CENTRE-LINE THICKNESS
OVERALL DROOP - VARYING LEADING-EDGE ANGLE

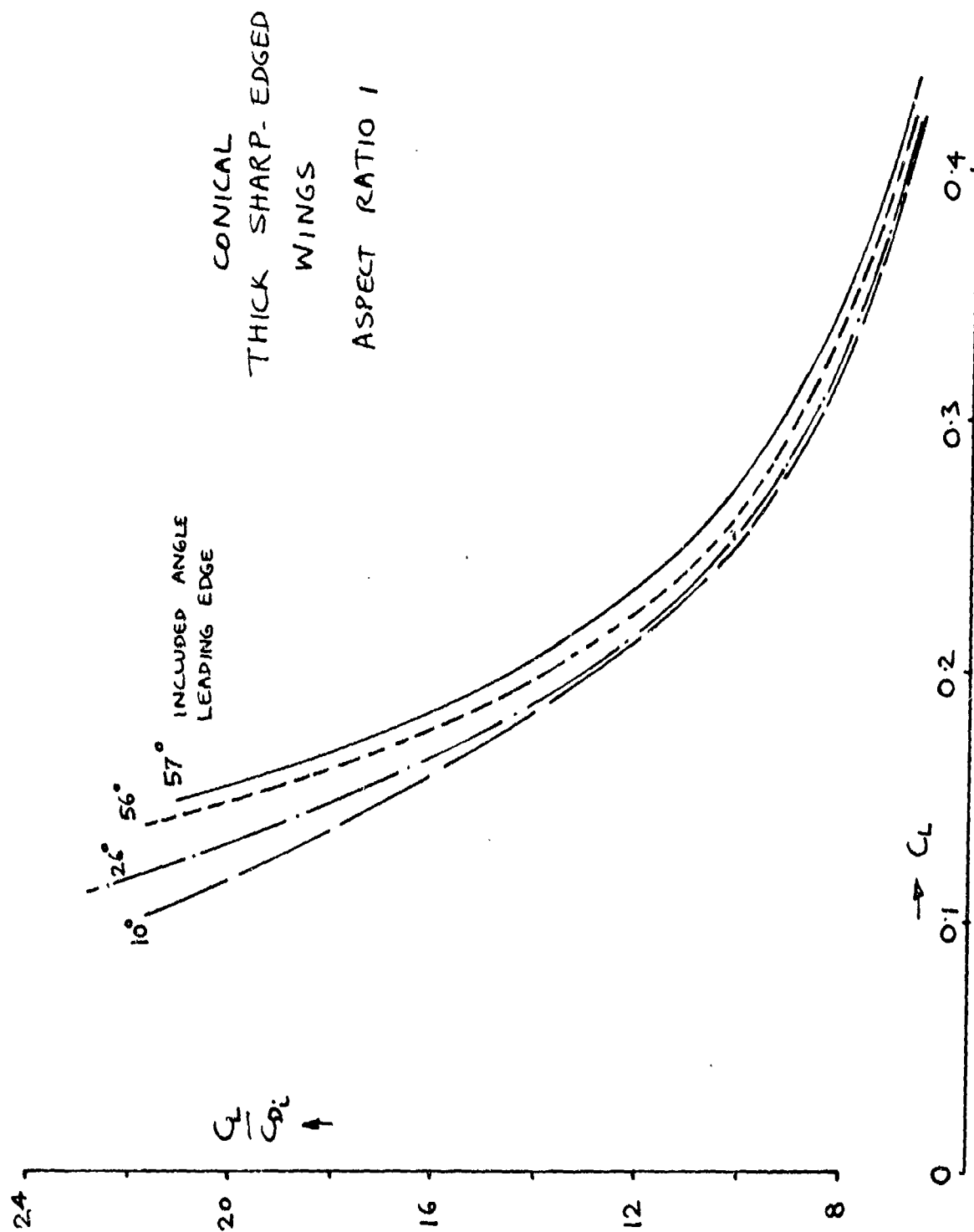


FIGURE 8 LIFT/INDUCED DRAG EFFICIENCY OF 4 WINGS OF FIGURE 7

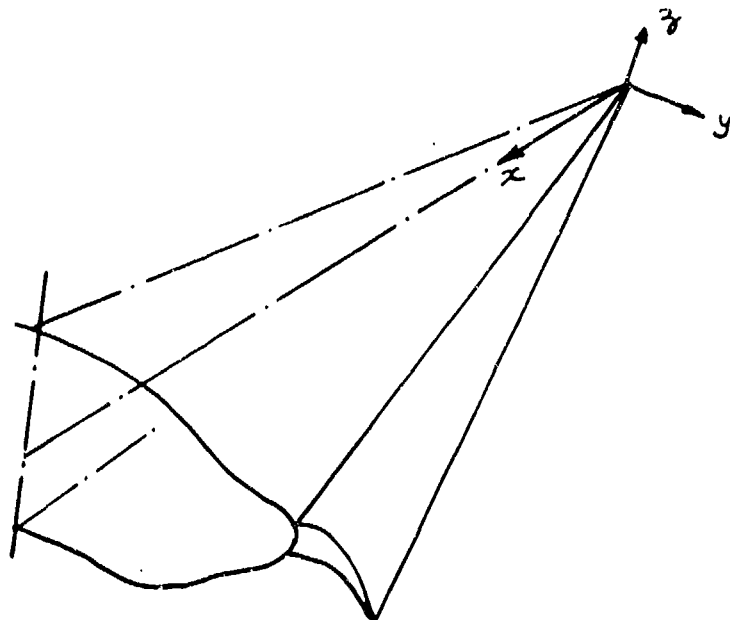


FIGURE 9 WING-BODY OR STRAKE CONFIGURATION

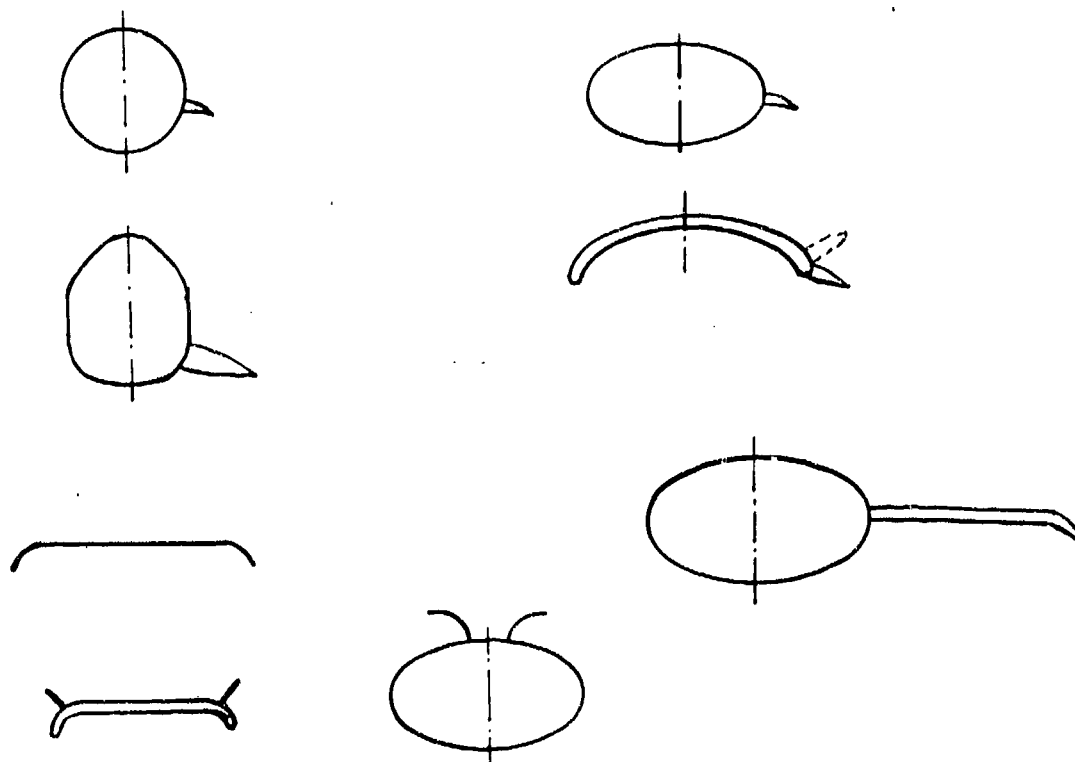


FIGURE 10 CAPABILITY OF TRANSFORMATIONS

AN EXPERIMENTAL INVESTIGATION OF THE ENTRAINMENT OF A LEADING-EDGE VORTEX.

by

N.G. Verhaagen and L. van der Snoek, Delft University of Technology, Department of Aerospace Engineering, Kluyverweg 1, 2629 HS Delft, the Netherlands.

Summary.

An experimental investigation of the flow field of a leading-edge vortex, produced by a sharp-edged unit-aspect ratio delta wing at an angle of attack of 20 deg, has been carried out at 45 m/sec. Velocity and total-pressure distributions were obtained by using a fixed-attitude five-hole probe. On the basis of the experimental results a number of control volumes of different cross-sectional dimensions enclosing the rotational vortex core were chosen. For each of the control volumes the entrainment was estimated; preliminary values for ϵ_Q range from .014 to .074.

1. List of symbols.

c_o	centerline chord	u, v, w	velocity components parallel, and perpendicular to vortex axis
M	axial massflow through vortex core	U_o	free-stream velocity
p_o	free-stream static pressure	x, y, z	coordinates along, and perpendicular to vortex axis
p_t	total pressure	ϵ_Q	relative sink strength
p_{t_o}	free-stream total pressure	Γ	circulation of vortex core
q_o	free-stream dynamic pressure	ρ	mass density of air
s	local half-span		
t	local thickness		
		<u>subscript</u>	
		x	vortex core at x/c_o

2. Introduction.

In ref. 1 a computational method is presented for the calculation of the flow about wings with leading-edge vortices. One of the differences between this and already existing methods is the inclusion of the entrainment effect of the rotational core. In the computational model for the separated flow ref. 1 approximates the vortex core by a line vortex/sink combination. The strength of the vortex is related to the circulation, the strength of the sink to the entrainment of the rotational core. Based on the solution of ref. 2 for the case of inviscid flow inside a slender axisymmetric conical core, it is assumed that the sink strength is ϵ_Q times the absolute value of the circulation. It is shown in ref. 1 that ϵ_Q , and so the entrainment, has a significant influence on the load distribution of a slender delta wing. The magnitude of the sink strength and of the circulation itself and hence the exact value of ϵ_Q are unknown. However, it is possible to determine these magnitudes experimentally. To provide the data for this determination an experimental investigation was carried out in a low-speed windtunnel on a sharp-edged delta wing model having an aspect ratio of one.

This paper presents some of the experimental results and gives preliminary values for ϵ_Q .

3. Apparatus and Tests.3.1. Wind tunnel.

The investigation was carried out in the low-speed wind tunnel of the Department of Aerospace Engineering at the Delft University of Technology (the Netherlands). The wind tunnel has an octagonal test section 1.25 m high x 1.80 m wide.

3.2. Model.

The delta wing model (fig. 1) is made for the most part of wood which was glued on a metal core inside the model. The sharp edges are made of aluminium. The model was suspended through a strut to the balance system of the wind tunnel.

3.3. Traversing mechanism and probe.

A traversing mechanism was used which is under development at the Department of Aerospace Engineering. It is installed in the diffuser of the wind tunnel and consists of a horizontal bar above which a small carriage is mounted (fig. 2). The ends of the bar are supported by jacks just outside the diffuser. These jacks are remotely operated and move the bar in a vertical direction, perpendicular to the tunnel axis. The carriage is also remotely operated and can be moved along the bar, that is horizontally in a direction perpendicular to the tunnel axis. A sting with a probe was mounted on the carriage. In order to measure the flow field on the suction side of the model a fixed-attitude five-hole probe was used which was calibrated extensively for angles up to ± 45 deg. (ref. 3). The model was given an angle of attack of 20 deg., this angle was taken positive downwards in order to avoid interference between strut and the flow on the suction side. To align the probe more or less with the axes of the leading-edge vortices, the forward part of the sting was bent in such a way that the axis of the probe made an angle of 15 deg. with the tunnel axis, or 5 deg. with the model. At the moment of the investigation the displacement of the sting plus probe parallel to the tunnel axis was not yet motorized and could only be carried out manually at zero free-stream velocity. This relatively complicated and time consuming operation was avoided as much as possible. For this reason, the measurements were performed in planes perpendicular to the tunnel axis.

3.4. Grid.

In total three planes perpendicular to the tunnel axis were explored, viz. at 50, 62.5 and 75% c_o . In order to check if the vortex flow could be assumed to be conical, the following data were obtained in the three planes:

- the positions of minimum p_t
- the contours of $p_t/p_{t_o} = .99$.

The results are shown in fig. 3. As can be seen, the differences are relatively small. This means that the assumption of a more or less conical vortex flow is justified. The measuring points in each plane form a rectangular grid. At 50% most of the grid consists of cells of 5 x 5 mm. The grids in the planes at 62.5% and at 75% c_0 arise by extending the grid of 50% c_0 along rays passing through the apex (fig. 4). Measuring points in the three planes that have similar y/s and z/s coordinates thus lay on one ray. For an exactly conical flow this would imply that the flow characteristics in such points are identical.

4. Experimental results.

4.1. General.

All measurements were carried out at a free-stream velocity of 45 m/sec which corresponds to a Reynolds number of 2.5×10^6 , based on c_0 . The fact that the points of the three measuring planes lay on rays passing through the apex made it possible to determine the pressures and velocities in points belonging to planes which are not perpendicular to the tunnel axis by means of interpolation or extrapolation. This way was used to obtain the pressure and velocity distributions in the planes at 50, 62.5 and 75% c_0 perpendicular to the leading-edge vortex axis. Below, the distributions at 62.5% c_0 are given, plotted versus the coordinates y/s and z/s . The distributions of the two other planes are not shown here because they are, especially at 50% c_0 , almost identical to those at 62.5% c_0 .

4.2. Velocity distributions in a plane at 62.5% c_0 perpendicular to the leading-edge vortex axis.

Fig. 5 shows the well-known distribution of the $(v+w/U_0)$ vectors, which belongs to the flow field of a leading-edge vortex. Near the leading-edge the influence of the secondary vortex is visible. Fig. 6 illustrates the distribution of the velocity component parallel to the vortex axis u/U_0 . As known, this axial velocity increases towards the vortex axis. A maximum was measured there of $u/U_0 = 2.2$.

4.3. Total pressure distribution in a plane at 62.5% c_0 perpendicular to the leading-edge vortex axis.

Fig. 7 shows the contours of $(p_t - p_0)/q_0$. The position of the vortex center corresponds with the position of the absolute total-pressure minimum ($(p_t - p_0)/q_0 = -0.6$), while the position of the free shear layer is determined by relative total-pressure minima. The shear layer could be traced over about 3/4 turn.

5. Determination of ϵ_Q .

The rotational core is defined as the region where no longer a distinct shear layer can be observed. The choice of its cross-sectional dimensions is still relatively free, conditions are that the cross-section must be kept at reasonable distance from the shear layer, the wing and the secondary vortex. In order to obtain some insight in the effect of the core dimensions on the entrainment, four control volumes of different cross-sections enclosing the core were chosen (fig. 8). The core cross-sections are composed of cells which belong to the grid of the plane perpendicular to the vortex axis. For each of the cells the vorticity and the axial massflow were calculated from the velocity distribution in the plane of 50% c_0 . As mentioned before, the vortex flow is conical there. Since the experimental results as presented in 4. came available only recently, the following simplification was used in order to have the calculations of ϵ_Q finished in time for this paper: the velocity components are assumed to vary linearly from grid point to grid point. The circulation and the axial massflow of the core cross-section are obtained by summing the contributions of the cells inside the cross-section. For the case of a slender axisymmetric conical vortex core ref. 2 derives that there exists a relation between the entrainment into the core and the circulation about it. In the computational model of ref. 1 the rotational core is approximated by a line vortex/sink combination. Based on ref. 2, ref. 1 derives for the ratio ϵ_Q of the sink strength to the absolute value of the circulation, that $\epsilon_Q = R/(\sqrt{2} L)$ (1). In this equation R is the radius of the core cross-section and L the distance to the apex. Since the core cross-sections considered here (fig. 8) do not have a circular cross-section, for R the radius is taken of an imaginary circular core having the same cross-sectional area. The values for ϵ_Q calculated with eq. (1) are presented in table I.

Another way to determine ϵ_Q is to put the sink strength proportional to the massflux dM_x/dx . This means that:

$$\epsilon_Q = (dM_x/dx)/(\rho \Gamma_x) \quad (2)$$

In the conical part of the vortex the velocity distribution at x/c_0 is identical to the one at 50% c_0 .

From this follows that

$$M_x = M_{50} (x/x_{50})^2 \quad (3)$$

and

$$\Gamma_x = \Gamma_{50} (x/x_{50}) \quad (4)$$

(3) and (4) substituted in (2) gives: $\epsilon_Q = 2 M_{50}/(\rho \Gamma_{50} x_{50})$ (5)

The calculated values of M_{50}/ρ , Γ_{50} and ϵ_Q are given also in table I.

6. Concluding remarks.

- The values of ϵ_Q determined by eq. (1) differ from those determined by eq. (2). It should be mentioned that eq. (1) is based on ref. 2 which assumes a vortex velocity distribution which, especially near the vortex center, deviates from the experimental distribution.
- The entrainment factor increases with increasing vortex-core cross-sectional dimensions.
- Inaccuracies in the determination of ϵ_Q performed here may be a consequence of the relative large cell dimensions (about 5 x 5 mm), and the fact that the velocity components were assumed to vary linearly from grid point to grid point. This investigation will however be proceeded by more exact calculations. Via interpolation, a non-linear variation of the velocity components will be introduced. Through this, it is possible that new values of ϵ_Q will be calculated which may differ by 10 to 20 per cent from the values presented in table I.

7. References.

1. H.W.M. Hoeijmakers and B. Bennekers
A computational method for the calculation of the flow about wings with leading-edge vortices. Paper 25 presented at the AGARD FDP symposium on high angle of attack aerodynamics, Sandefjord, Norway, 4-6 October, 1978. The inner viscous solution for the core of a leading-edge vortex. JFM 15 (1963) pp 306-318.
2. K. Stewartson and M.G. Hall
Determination of the velocity vector and the total pressure with a calibrated fixed-attitude five-hole probe, part A; calibration of the probe. Report LR-236, Dept. of Aerospace Engineering, Delft University of Technology, Delft, the Netherlands.
3. G.J. Voerman

Table I

Core cross-section (fig. 8)	M_{50}/ρ	Γ_{50}	ϵ_Q	
			Eq. (1)	Eq. (5)
A	.06752	4.22843	.031	.074
B	.05857	3.95762	.026	.068
C	.04530	3.44195	.020	.061
D	.03433	2.99807	.014	.053

At the centerline:

$$\frac{t}{c_0} = 0.056 \left(\frac{x_w}{c_0} - \left(\frac{x_w}{c_0} \right)^{5.9} \right)$$

x_w is the distance from the apex

The sections normal to the
centerline chord are of
circular biconvex shape.

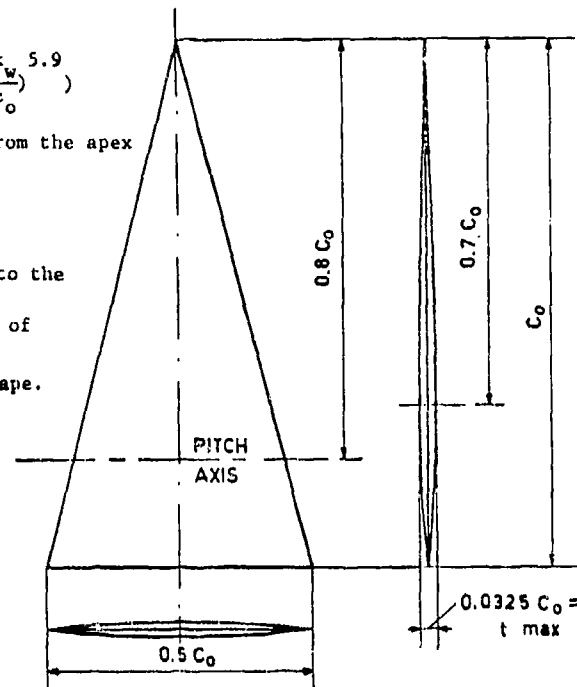


FIG.1. DELTA WING MODEL ($C_0 = 0.85 \text{ m}$)

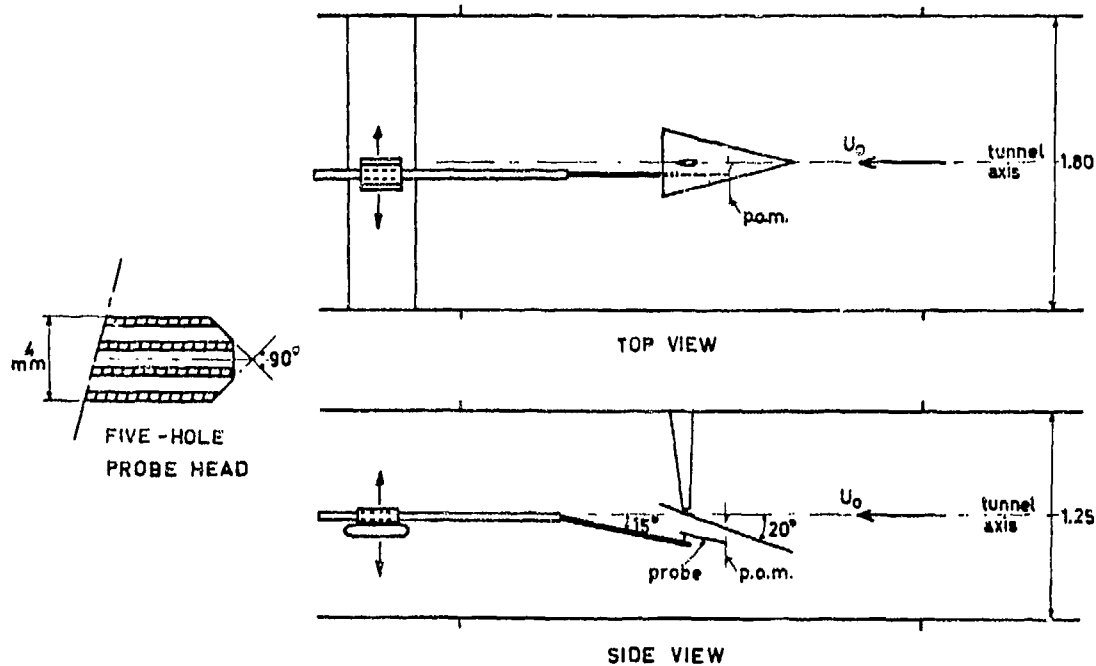


FIG.2. TEST SECTION (dimensions in m.)
p.o.m. = plane of measurement

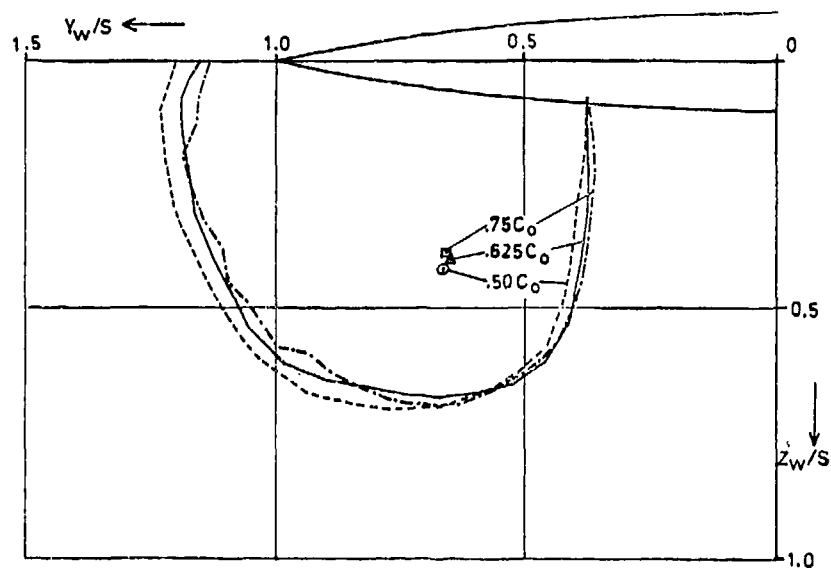


FIG.3. POSITIONS OF MIN. P_t , AND CONTOURS OF $P_t/P_{t0} = .99$
IN THE PLANES OF MEASUREMENT
(subscript w=wing axis system)

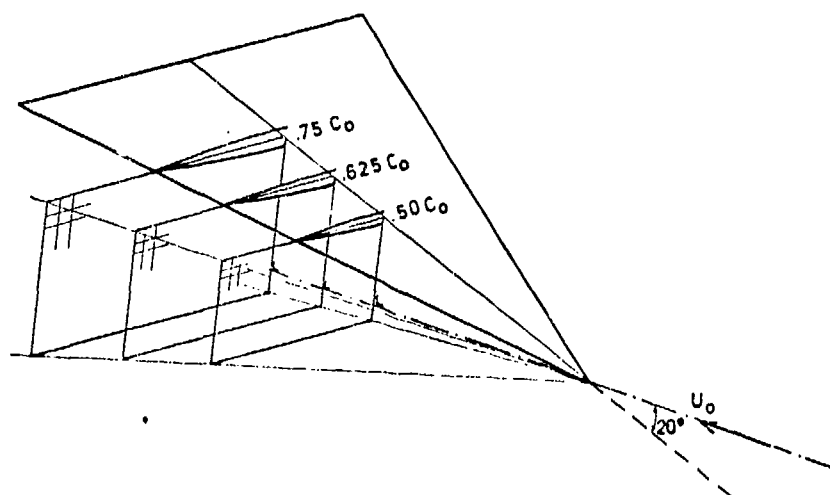


FIG.4. RELATIVE POSITION AND DIMENSION OF THE GRIDS
IN THE PLANES OF MEASUREMENT

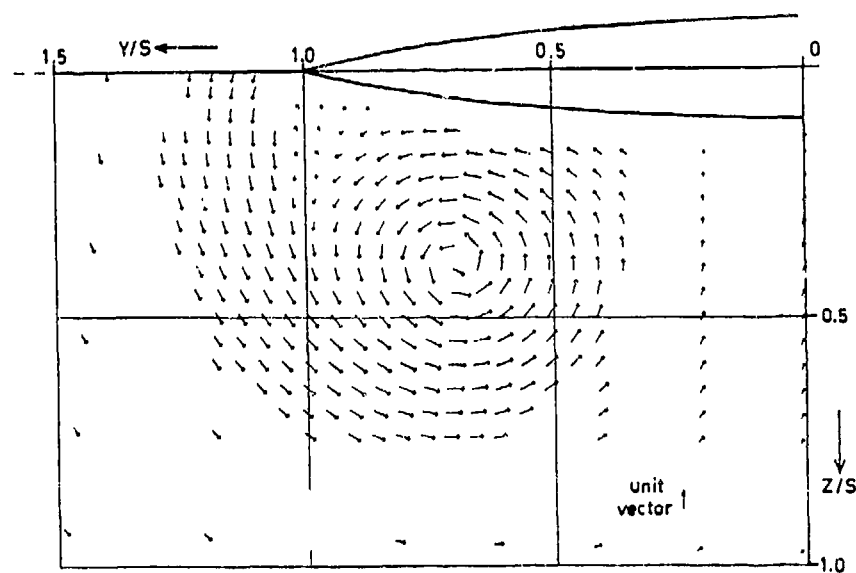


FIG.5. VELOCITY VECTORS $(v+w)/U_0$ IN PLANE NORMAL TO LEADING-
EDGE VORTEX AXIS ($.625 C_0$)

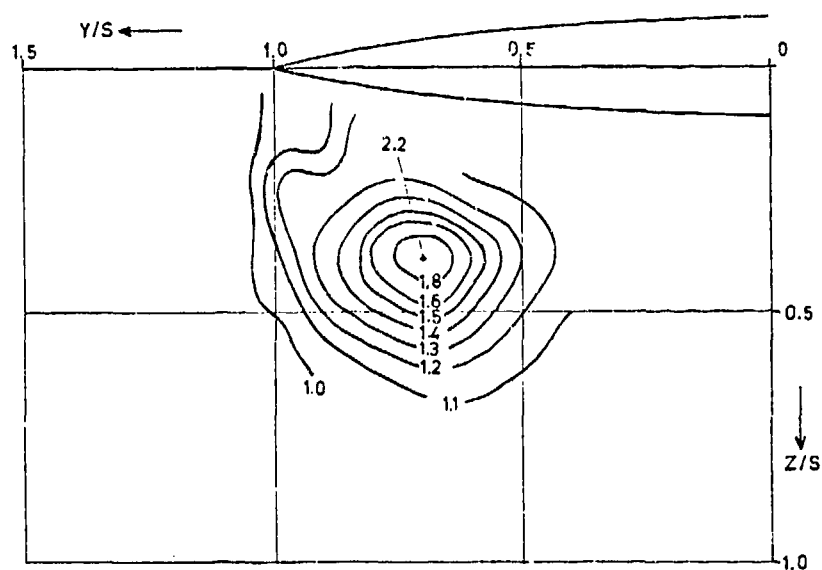


FIG.6. CONTOURS OF v/u_0 IN PLANE NORMAL TO LEADING-EDGE VORTEX AXIS ($.625 C_0$)

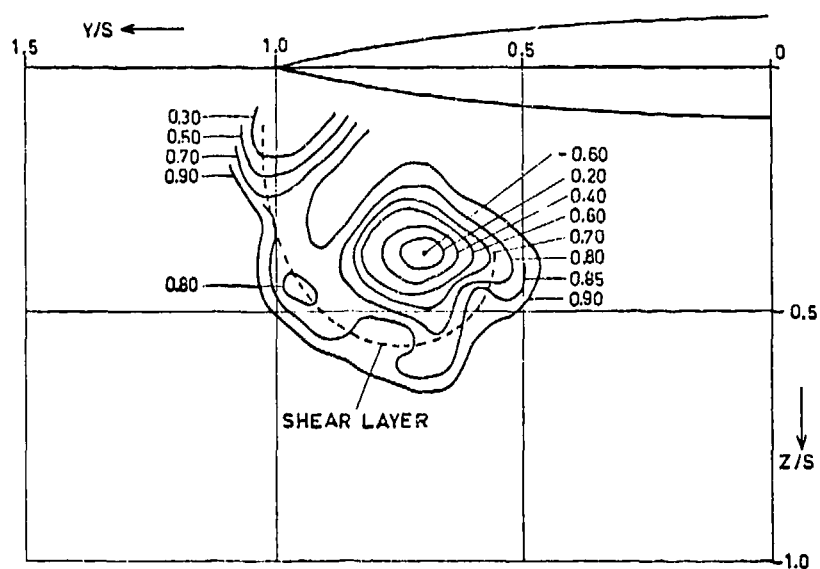


FIG.7. CONTOURS OF $(P_t - P_0)/q_0$ IN PLANE NORMAL TO LEADING-EDGE VORTEX AXIS ($.625 C_0$)

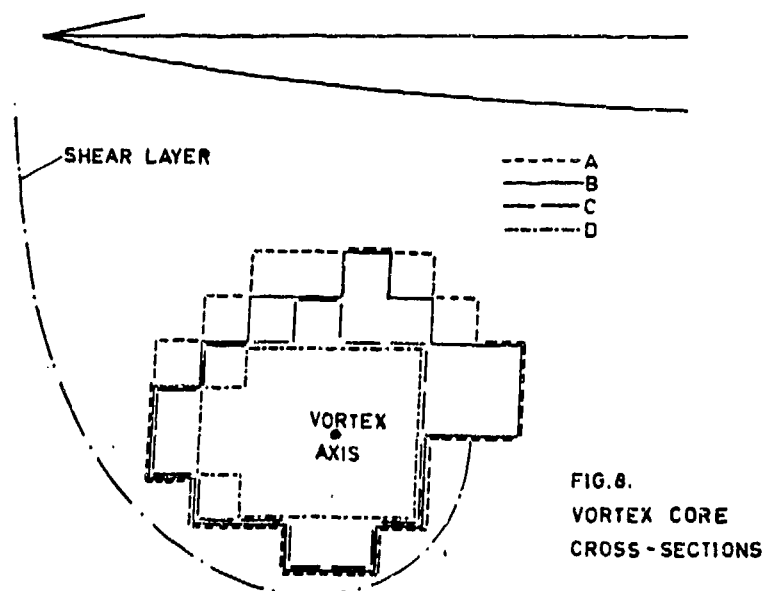


FIG.8.
VORTEX CORE
CROSS-SECTIONS

A SURVEY OF RECENT HIGH ANGLE OF ATTACK

WIND TUNNEL TESTING AT AERITALIA

by

G. Ducciantini, R. De Silvestro and L. Fornasier
AERITALIA, Combat Aircraft Division
Torino, ITALY

SUMMARY

This paper illustrates the present status of investigation at Aeritalia on wind tunnel testing techniques at high angles of attack and on stall/post stall characteristics of configurations typical of modern combat aircraft.

1. INTRODUCTION

The aerodynamic characteristics of a given aircraft configuration are currently obtained by wind tunnel tests, but at high angles of attack both the model mounting and the wall corrections require particular attention. For this reason, a model of a study development of the G91Y fighter has been tested, with the same support, up to high angles of attack in the Aeritalia 2.1m x 2.1m low speed wind tunnel and in that one 5m x 7m of the Eidgenossisches Flugzeugwerke (Emmen, Switzerland), for which the wall interference effect may be regarded as negligible. Besides, some selected test results on an advanced fighter model in the Aeritalia 2.1m x 2.1m wind tunnel are presented, which indicate the strong effect, on the high α aerodynamic characteristics, of some configuration variants like wing strakes, manoeuvre devices, vertical position of the horizontal tail and longitudinal position of the vertical tail.

2. TEST VALIDATION IN THE AIT WIND TUNNEL

The method of wall corrections so far used at AIT for the wake blockage effect was based on the standard formula (ref. 1)

$$\frac{\Delta \bar{q}}{q} = \frac{1}{2} C_{D_0} \frac{S}{C} \quad (1)$$

which however holds only for streamline flow and is no longer valid after the stall. To cover also the stalled wing conditions, the formula has been completed, following Maskell (ref. 2), into

$$\frac{\Delta \bar{q}}{q} = \frac{1}{2} C_{D_0} \frac{S}{C} + \underbrace{k \frac{5}{2} (C_D - C_{D_0} - k_1 C_L^2) \frac{S}{C}}_{\text{Maskell correction}} \quad (2)$$

where k is an empirical factor ($0 < k < 1$) to be determined experimentally, and $k_1 = \frac{d C_D}{d C_L^2}$ in the quadratic range of the drag polar. The other corrections are the classical ones (ref. 3). In order to check the validity of the test results in the AIT wind tunnel at high α , and to determine the k value, an 1/10th scale model of a former G91Y development study has been tested, with approximately the same mounting (purposely designed for low interference at high incidences), in the 5m x 7m low speed wind tunnel of the Eidgenossisches Flugzeugwerke (Emmen, Switzerland) where the wall corrections for that model can be considered negligible. Fig. 1 gives a view of the model in the AIT wind tunnel. The interference effects of the model suspension have been measured with the dummy sting technique and subtracted from the results. Typical examples of test result comparison in the AIT and EFW wind tunnels are shown in figs 2 + 4, where the following considerations can be made:

- The "fitting coefficient" k of the Maskell wake blockage term is approximately 0.5 (for the tested model-tunnel configuration, having $\frac{S}{C} \sim 0.05$, $\frac{b}{B} \sim 0.5$). This can be justified by the Maskell theory being valid for a bluff body or a completely stalled wing, whilst in the case of an aircraft configuration at the stall some components like wing root, fuselage, tailplane and, at high lift, slats and flaps are not completely stalled. Besides, the application of the Maskell theory to a developing separation according to equation (2) is an arbitrary assumption.
- In the clean configuration, the EFW results show a slightly higher (0.02) $C_{L_{max}}$, lower C_{D_0} and less pronounced pitch-up loop at the stall: these differences, which cannot be attributed neither to Reynolds effects (same model, same stream velocity) nor to wall corrections or model suspension interference, are probably caused by the different turbulence grain size of the streams in the two tunnels, smaller in the EFW one. This is confirmed by the effect of a net in front of the contraction cone (figs. 2-3), bringing the AIT results closer to the EFW ones. The lateral-directional characteristics agree closely in the two tunnels as shown in fig. 4 for the rolling moment coefficient.
- In the high lift configuration the comparison of the test results in the two tunnels shows that the lift curves have a larger $C_{L_{max}}$ difference (~ 0.05) than in clean, whilst the pitch-up loops at the stall, taking into account the different $C_{L_{max}}$, are practically the same. As in the clean configuration, the lateral-directional coefficients are in good agreement in the two tunnels.
- These results emphasize the validity for high α tests of the AIT wind tunnel, whose test section was designed square instead of rectangular having in mind such kind of tests (ref. 4).

3. TESTS AT HIGH ANGLES OF ATTACK ON AN ADVANCED FIGHTER CONFIGURATION (AIT 320)

Within researches at AIT for the evaluation of typical new combat aircraft configurations, a model has been finalised and wind-tunnel-tested for basic research and development up to high α and β values. Several basic variants have been tested, like manoeuvre and high lift devices at wing leading (droop nose) and trailing edge (flap), wing root strakes, vertical position and anhedral angle of the horizontal tail, longitudinal position of the vertical tail, etc. Some selected results of test analysis are presented in figs. 6 + 18. The following remarks can be done about the given results:

a) Longitudinal characteristics

The most innovative among the variants tested are two kinds of wing root uncambered, sharp leading-edge strakes differing in planform: strake 3 has triangular shape (straight leading-edge contour) whilst strake 5 is ogee-shaped with cusped leading-edge contour. The relevant geometry characteristics are sketched in fig. 5. The large lift gain obtained at high angle of attack through the stabilizing effect of the vortex flow developed by the strakes on the wing flow is evidenced by the comparison of the tail-off lift curves shown in fig. 6. The lift improvements appear to be much higher in the clean ($\delta_{fl} = 0^\circ$) configuration than at high lift ($\delta_{fl} = 40^\circ$) due to the detrimental effect of the vortex flow from the strakes on the potential lift increment developed by the flaps. The implications on the pitching moments (figs. 7 & 8) appear from the comparison of the strake-off and strake-on characteristics to cause large reduction of stability and sudden kinks at both flap settings for the basic configuration. The figures show that the stability problems associated with strakes in the high- α range can be cured by leading edge drooping ($\delta_{DN} = 30^\circ$) and by lowering the horizontal tail with respect to the wing. The forward shift of tail-off center-of-pressure position with strakes due to the steadily increasing importance of the forward-located vortex lift with the angle of incidence is evident from fig. 9.

b) Zero sideslip lateral-directional data

Presence of non-zero rolling and yawing moments in the wing stall incidence region is evident (fig. 10), the rolling moment being affected mainly by the wing, whilst the yawing moment is influenced also by the front fuselage (whose vortex system at high incidence may be asymmetric). A certain improvement in the zero sideslip characteristics at the stall may be obtained by the strakes which stabilize the wing flow.

c) Directional stability

The basic model configuration exhibits an acceptable level of directional stability up to and immediately beyond the wing stall region (fig. 11). At an incidence of 15° a progressive decrease in stability appears and at approximately 40° the configuration becomes directionally unstable; at higher angles of attack there is a region in which the stability is restored. From the breakdown of the directional stability, it is evident that the loss of stability in the post-stall range is due to the decrease of the vertical tail contribution associated with the low energy wake shedding from the wing and fuselage at high angles of attack (this phenomenon is evidenced also by the rudder effectiveness at zero sideslip, as shown in fig. 11). A clear picture of the progressive immersion of the vertical tail in the wing/fuselage wake when angle of attack is increased is given by the tuft visualizations shown in figs. 12 - 13. As the restoration of stability is exhibited by the fin-off contribution too, it is supposed that the component responsible for this unexpected characteristics is the fuselage forebody. A similar phenomenon but at lower incidence was discovered by NASA aerodynamicists during wind tunnel tests on an F-5 model (ref. 5).

Wing strakes influence on the directional stability (figs. 14-15) may be summarized as follows:

- Clean configuration

At angles approaching the stall incidence, the strakes improve appreciably the directional stability, for their vortex system delays the flow breakdown in the outer wing.

Beyond the wing stall, there is a sudden loss of stability for the straked configuration and the stability level is markedly influenced by the strake planform: their effect may be correlated with the burst of the vortex system on the strake. The strake 5 (gothic) shows a greater influence than strake 3 (triangular): for this strake, the loss of stability occurs at a higher incidence but the decrease is steeper so that the configuration becomes unstable at a lower angle of attack. This phenomenon is supposed to be caused by a more violent bursting of the strake vortex (e.g. see the analogous effect on the longitudinal characteristics, i.e. the centre of pressure movement reported in fig. 9). A comparison of the flow visualization between basic and basic + strake 3 configurations (fig. 16) substantiates the above interpretation. Focusing attention on rudder tufts, it may be seen that for the straked configuration the flow is more regular than for the basic one at the same angle of attack.

- High lift configuration

With flaps down, strakes have less effect on directional stability (fig. 15) for the same reason explained when dealing with longitudinal characteristics.

The effect of longitudinal position of the vertical tail is shown in the same figure where, apart from the obviously reduced basic level, the sudden drop of stability is eliminated due to the reduced interference of the fin with the wing and tail wakes.

To be noted that the results presented (especially the body contribution to the directional stability) are strongly influenced by the test conditions (Reynolds number referred to the mean aerodynamic chord $Re = 870,000$, and transition fixed on body nose and 5% c of wing and tailplanes).

d) Departure characteristics

A positive value of the directional departure parameter $C_{n\beta DYN} = C_{n\beta} \cos \alpha - \frac{I_z}{I_x} C_{l\beta} \sin \alpha$ is exhibited by the basic configuration (both clean and high lift) in the whole α range tested (fig.17). It increases with incidence up to the stall after which it drops but remains positive even where $C_{n\beta}$ becomes negative. It is worth noting the effect of moving forward the vertical tail, which delays appreciably the $C_{n\beta DYN}$ drop after the stall. Both strakes 3 and 5, whereas increase $C_{n\beta DYN}$ before the stall, anticipate the following drop.

No significant variations due to the strakes appear in the lateral control departure parameter $LCDP = C_{n\beta} - \frac{C_{l\beta}}{C_{l\alpha}} C_{l\beta}$ for both clean and high lift configurations. In the first case the LCPD parameter remains positive up to and beyond the stall, whilst at high lift it becomes negative at $\alpha = 18-20^\circ$, indicating a possible occurrence of mild lateral departure. This is mainly caused by the inverse yaw, in this configuration, of the lateral control device (ailerons) involved in the calculation of LCPD. An improvement (especially at high lift) is given by the additional use of the stabilizer as taileron which exhibits proverse yaw. It is worth noting that the above mentioned Reynolds effects on the directional stability and in general on the overall aerodynamic data affect directly the departure characteristics.

CONCLUDING REMARKS

Validation tests in the AERITALIA low speed wind tunnel have shown a good accuracy in testing at high incidences, with small adjustment of the wall interference correction and proper design of the model mounting. A preliminary investigation of an advanced combat aircraft configuration has shown the strong influence, on the high incidence characteristics, of configuration variants like wing strakes, wing leading edge and trailing edge devices, vertical position of the stabilizer and longitudinal position of the vertical tail.

REFERENCES

1. A. Thom: "Blockage Corrections in a Closed High-speed Tunnel" A.R.C. R.M. 2033, 1943
2. E.C. Maskell: "A Theory of Blockage effects on Bluff Bodies and Stalled Wings in a Closed Wind Tunnel" A.R.C. R.M. 3400, 1965
3. A. Pope: "Wind Tunnel Testing" John Wiley & Sons, Inc. 1954
4. R. Mautino: "Tecniche di prova in galleria del vento" Società Ingegneri e Architetti, Torino, 1968
5. J.R. Chambers, W.P. Bilbert, S.B. Grafton: "Results of Recent NASA Studies on Spin Resistance" AGARD CP199, 1975



Fig.1- Wind tunnel model of the G91Y development study

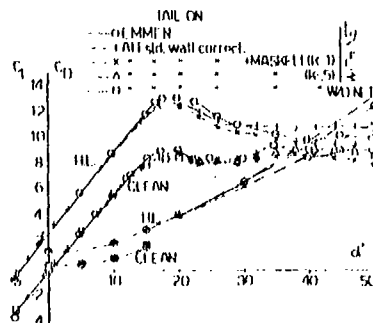


Fig.2- Lift and drag characteristics at AIT and Emmen wind tunnels

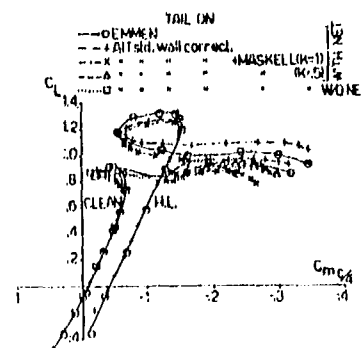


Fig.3- Pitching moment charact. at AIT and Emmen W.T.

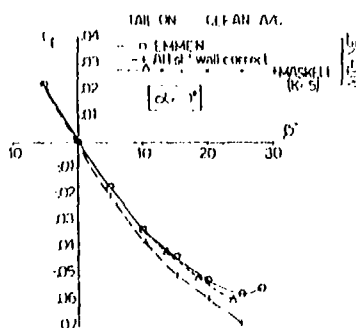


Fig.4- Rolling moment charact. at AIT and Emmen W.T.

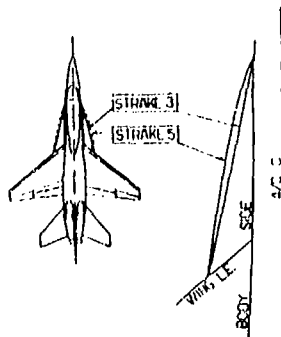


Fig.5- Model layout of AIT 320 configuration with strakes detail

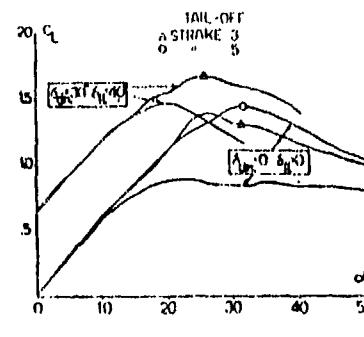


Fig.6- Lift characteristics

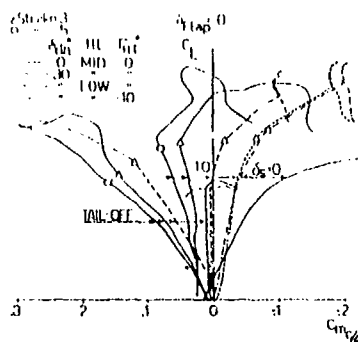


Fig. 7- Pitching moment charact. Flaps up

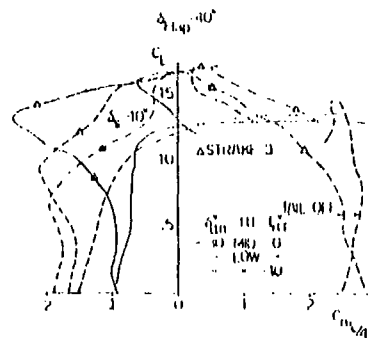


Fig. 8- Pitching moment charact. Flaps down

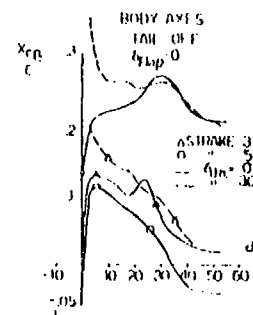


Fig. 9- Centre of pressure position

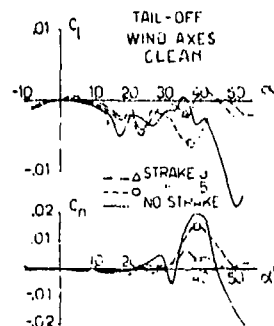
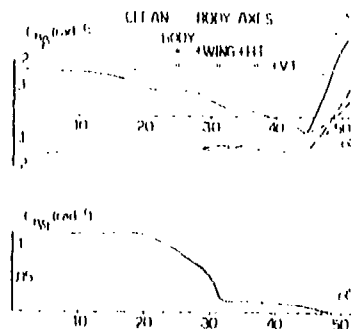
Fig. 10- Lateral-directional characteristics at $\beta = 0$ 

Fig. 11- Directional stability and control

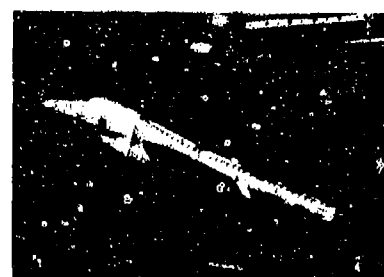
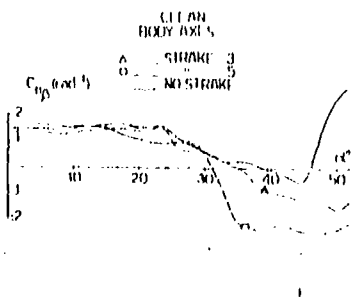
Fig. 12- Flow visualisation $\alpha = 20^\circ$. Flaps up. Strakes offFig. 13- Flow visualisation $\alpha = 32^\circ$. Flaps up.

Fig. 14- Wing strakes influence on directional stability. Flaps up.

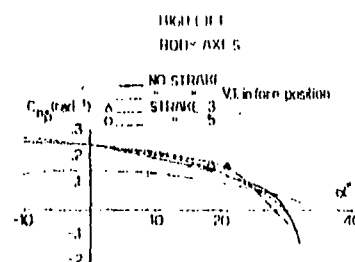


Fig. 15- Wing strakes influence on directional stability. Flaps down.

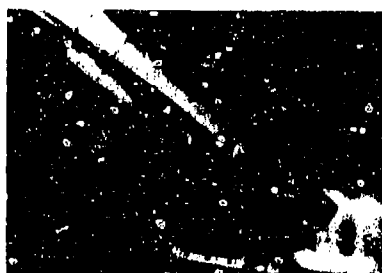
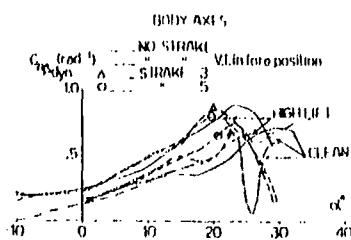
Fig. 16- Flow visualisation $\alpha = 32^\circ$. Flaps up. Strakes on

Fig. 17- Directional departure characteristics.

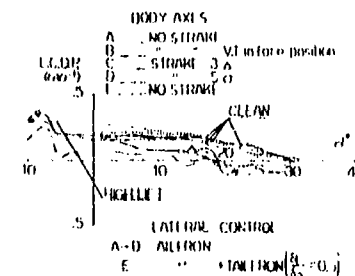


Fig. 18- Lateral Control Departure Parameter

ROUND TABLE DISCUSSION

Chairman, Dr. McCroskey

The purpose of this Round Table Discussion is, in my view, three-fold. One is to review and in some sense synthesize the new ideas and perhaps the new results that have come out during the course of the Symposium. Secondly, I think it is important to assess the subject matter and the results of the Symposium, to assess what benefits this new knowledge will provide to NATO. Thirdly, if at all possible, we should make some kinds of recommendations for future activities. Before we start, I want to remind you that the Round Table Discussion is being recorded, the first such session of this Symposium, and it will be transcribed into the proceedings. Therefore, when we do come to the point of discussion from the floor, it is very important that you identify yourself to the microphone. The principals for the RTD this afternoon are: Professor van Ingen, Professor of Aerodynamics, Department of Aerospace Engineering at Delft Technical University in the Netherlands; Dr. G. K. Richey, Chief of Internal Aerodynamics, U.S. Air Force Flight Dynamics Laboratory; Professor S. M. Bogdonoff, Chairman of the Department of Aerospace and Mechanical Sciences at Princeton University; Mr. G. F. Moss, Head of the Design Methods Division, Royal Aircraft Establishment, Farnborough; Mr. Andrew Skow, Manager of Aerodynamic Research of the Aircraft Division of Northrop Corporation; and Dr. H. H. John, Deputy Project Manager of the Technical Fighter Development Program at MBB. I have less to say than the gentlemen on my right, so I shall ask Prof. van Ingen to begin these remarks with his observations about the meeting.

Professor van Ingen

I think that I can start by saying that everyone of us has his bias, and I have, of course, mine. So I should mention that I was educated as an aeronautical engineer and have now the responsibility for the low speed lab at Delft. I am one of those old-fashioned people who thought that high angles of attack should be avoided, but I learned during this Symposium that they are becoming fashionable, and even that people want to fly in a controlled manner in that region. It is quite obvious that the aerodynamics needed for that is not yet in our books. I think that this was reflected to quite an extent in some papers in the first session because you found there key words like "design guidelines", "engineering judgement", "large data banks derived from extensive wind tunnel testing and previous flight tests". If you check the references in these papers you will not find many references to the speakers in the second session. I think that this is typical of the situation. I could advise everyone of you to read the letters and further notes by the Wright brothers. What is being done right now in the high angle of attack business has also been done by them: they provided themselves with an excellent data bank, doing wind tunnel experiments and flight experiments. Their letters and notes are very instructive.

My conclusion from Session 1 is that people apparently know how to design a flight vehicle that can perform a satisfactory flight, but that much basic understanding is missing. I think predicting these flows theoretically is still far off. Of course, the question is how can the fluid dynamicist help the designer. One of the possibilities is holding Symposia like this one. One of the problems that came up is the problem of asymmetric vortex shedding; it came up in Session 1 and again this morning, especially in the paper by Mr. Jorgensen. Apparently, asymmetric vortex shedding arises from small asymmetries maybe located in the nose region. Therefore, sticking out a boom in front of an aircraft may change things considerably.

This morning when I was taking my bath, I was thinking about this problem. (Of course, you remember from history that there have been scientists before who did their work while sitting in a bath.) If you assume a bathtub with a circular planform with the drain in the middle, and ask a fluid dynamicist, who never before saw a bath being drained, to calculate how the flow will leave that bath, of course, he will jump to the conclusion that since there is symmetry, he can strike out certain terms in his Navier-Stokes equations. Thus he will come up with a perfect solution for radial flow. Now, if you call in the man in the street and ask him how that bath is going to be drained, he will say it will go spiralling one way or the other depending on the hemisphere he is coming from. So, I think that this should warn us that we should not assume that given a symmetric geometry, the solution to the Navier-Stokes equations should be symmetric. It might even be that if you take a body of revolution at zero angle of attack, and you would do very careful measurements inside the boundary layer, it might quite well be that you would find non-symmetric flows. Then when you take these bodies up to high angles of attack, there is a symmetry plane in the geometry, but it doesn't necessarily mean that the flow will be symmetric as well. I think that there is a piece of homework for the experimental and theoretical aerodynamicists to study this problem in some more detail.

This brings me to Session 2. I think we had some fine examples of experimental investigations to support theoretical modelling. In my opinion, we cannot emphasize strongly enough the need for well-designed, well-executed and well-documented experiments. They will be most effective if designed in cooperation between theoreticians and experimentalists. Moreover, we should not be afraid to repeat each others' measurements using the same configuration, maybe even the same physical model, because we have seen that using the same model in two different wind tunnels can give widely different results. In doing this we will be prevented from accepting our own results to be the truth and nothing but the truth. Of course, the same applies to numerical simulations. I think it will be wise to select a few configurations on which people would concentrate their efforts much more than giving relatively small efforts to quite a number of different configurations.

Another point on my list was flow visualization in water tunnels at low Reynolds numbers. We should be very careful with these beautiful pictures, but Mr. Werlé himself has already elaborated upon this during the session, so I will skip that right now.

If I may make some remarks about today's session, I think that it has been shown that including the entrainment effect in vortex modelling is important. Session 3 this morning gave me some additional confidence that fundamentalists may be of some assistance to the designers. If this meeting gave some support to such a development, I think it was a success.

Dr. Richey

I would like to begin by commenting briefly on the application of high angle of attack for military aircraft and missiles. High angle of attack or high lift coefficient is generally used to provide a quick turn or rapidly change position in velocity and space. It is therefore a very dynamic and time-dependent phenomena. Some concepts were discussed in this symposium which even go beyond maximum lift coefficient into what is described as the post-stall regime. Therefore, in order to have a useful application of high

angle of attack aerodynamics, it will be required for the aircraft to be stable and controllable under those conditions. A high lift coefficient by itself will be useless unless it is accompanied by stable and controllable flight. In this symposium we saw progress in the definition of the longitudinal stability and control characteristics, but we need to also consider the lateral-directional characteristics and other stability parameters discussed on the first day by Dr. Orlik-Rückemann.

The vortex analysis methods described are making very good progress, but as was observed by several authors they do not predict the level of maximum C_L very accurately, nor do they accurately predict the angle of attack at which maximum C_L occurs. This appears to be primarily due to a modelling problem with respect to vortex bursting. The symposium papers indicated that wing-body interference design methods are emerging, but again, at subsonic flow, they appear to be limited by our understanding of vortex development, especially when the vortices become asymmetric near the body. This is an area where further research is needed.

The experimental data base that was described in several papers indicates that wing-forebody strakes improve lift, but they also give very sharp C_L breaks and rapid pitch-up near maximum C_L . This must be addressed further and understood to develop improved design methods and design criteria. A rapid C_L break could inhibit the useful application of high-lift devices. Again, there should be at least a preliminary understanding of some of the stability parameters along with the design methods which analyze the high alpha lift components. For example, a fundamental design choice is not very clear. That is, whether one should use a canard or a strake to generate high lift. Some of the data in the paper by Dr. Lamar, read by Mr. Pohlhamus, indicated that a canard can produce a somewhat less rapid C_L break and pitch-up at high C_L than a strake. A canard could be an active means to control the flight near C_L max, but a strake, if it was fixed in position, would be more locked-in with respect to high angle of attack.

With regard to the inlet or air intake, it is clear that useful applications of high angle of attack, again in a controllable manner, will require a compatibility between the inlet and the engine at extreme maneuvers, i.e., the engine has to remain free of compressor stall or surge under those conditions. High angle of attack/high lift maneuvers will not be useful if the engine flames out. This is particularly critical if thrust vectoring is used to augment stability and control at high angle of attack because, in that case, the lack of a powerful control power source from the exhaust nozzle could be catastrophic. Some very interesting concepts to help insure inlet-engine compatibility were shown at the meeting, and I reviewed some data from AIAA Paper 76-701 by Cawthon of the U.S.

Also, the exhaust nozzle flow can have an important influence on high angle of attack aerodynamics, particularly if the jet is placed near regions where the forebody or wing vortex flow is affected. As we get further into design criteria and design methods for high angle of attack which involve vortex lift, we need to examine the effects of propulsion both from the air intake and the exhaust nozzle of the engines on the aircraft or missile. We should not forget that air breathing missiles, although they were not addressed in this conference, could also be an application for some of the high angle of attack characteristics that we have seen.

In summary, the application of high angle of attack aerodynamics to enhance agility in controllable flight is the key issue to keep in mind. Design techniques are being developed and supported by fundamental descriptions of the phenomena. It appears that there is good progress for future useful applications of high angle of attack flight.

Professor Bodgonoff

I have been asked to make some comments from the point of view of the fundamental fluid mechanicist in a meeting which has been primarily aerodynamics. There are several observations which might be helpful in trying to make progress in this area. A primary one is the question of the use of terms. Two terms which are particularly important to clarify if we are going to make progress in the description of the physical flows are: what do we mean by a vortex, and what do we mean by separation. These terms were used rather loosely during these three days. Not only this group, but many groups, have had a tendency to use these terms, without defining them, as we have gone back and forth between two-dimensional and three-dimensional flows.

A vortex is pretty well-defined in most text books. To have a vortex, one must have at least several revolutions of a particle in a flow field and there is a specific pressure and rotational velocity field that goes with it. In many of the flows that were described in the last few days, vortices which were reasonably well-aligned with the flow, in many cases met the definition of a vortex. The strong vortices that were discussed were generally aligned with or were close to the flow direction. For the flow over wings, for example, the term vortex has been used to describe the flow generated by a nose strake (which is essentially in the direction of the free stream flow) and some flows on the wing, which are almost normal to the free stream flow. I think that these flows are not vortex flows in the same sense of the word, as has been discussed in some detail in this meeting.

Separation is the second term which we are using very loosely. Re-attachment is also not well-defined, but let me concentrate on separation. In two-dimensional flows, there is a reasonable understanding of the physics, and a relatively simple definition of separation: there is a reverse flow region; there is a strong component of velocity normal to the surface; there is a shear layer which separates, the skin friction goes to zero. The flow field which is associated with two-dimensional separation is also understood and well-defined. Three-dimensional flows are quite different, and three-dimensional separation is a very complex phenomena. We have used the description of "separated flow" in many of the papers during this conference which I don't think is correct. I believe that many of the flows are being misinterpreted because, in most cases, there is only surface data: pressure distributions, oil streaks, tufts. The oil streaks and tufts tell you something about a very thin layer close to the wall. The pressure distribution tells you about the integrated effect of the exterior flow field. Unless you have the flow field model and the surface information, some of the descriptions of the flow can be incorrect. I would like to point out that there are many cases where what looks like strong indications on the surface - oil flows and tufts - have little or nothing to do with the main flow-field which is generating the lift and drag of the bodies that we were examining. Many of these flows are complex three-dimensional flows. They have strong "secondary flows" (if you use the terminology of turbo-machinery) but they are not separated in the same sense as two dimensions of flows. A few three-dimensional flows may be separated, but many of them are not. If we are going to try to get some help from fundamental fluid mechanics, we must look closer at these complicated flows.

I got a great deal out of this meeting. It is very important that the fluid mechanicist and the aerodynamicist try to work a little bit more closely together because, while some of the phenomena may

be viscous dominated, many of the phenomena are clearly not viscous dominated. Perhaps we might make better progress if we could separate out many of the phenomena where computational techniques (inviscid rotational) may be able to give practical solutions. Some phenomena are triggered by small viscous effects. Separation, in particular, needs some viscous inputs (unless we are talking about separation from sharp leading edges). I believe a major contribution can be made in our understanding of such flows, if we can better describe the phenomena in language which is precise. The meeting has helped me a great deal.

Mr. Moss

At this fairly late stage in the lineup, one never knows what has been said before, but I think since I am in this position, speaking just before those from industry on my right, I think perhaps the thing for me to do is to look at the application to aircraft design methods. I will make one or two points that I hope will not steal anyone else's thunder. First, I would like to support strongly the more fundamental work we have heard about this week which can be seen either to be building a data bank for checking mathematical models or actually building the models themselves. Such models are the backbone of the engineering design methods which are so important to industry. We need to remember that the main task of industry is to make good airplanes and not to be clever in any other way; what matters is that an airplane flies and flies well. Powerful computers are now becoming increasingly available to us, and I think that the days of trial-and-error wind tunnelling are fast coming to an end. The effort, money, and above all, the time that has to be spent to design an aircraft this way (by cut-and-try in the wind tunnel) is simply prohibitive. In this respect I am going away from this symposium with one figure in my mind, that regarding the number of hours spent on the USA space shuttle wind-tunnel program, and it is going to give me nightmares. Surely, it is important to keep up the development of the new generation of design tools which will soon enable us to run rings around such expensive 'ad hoc' design procedures. This week we have taken that development process one step further and some of the presentations we have heard have been exceptionally welcome in this class. However, quite a few, if I may make a slightly provocative remark, have perhaps looked backwards too much. They have been referring to the state-of-the-art as it has been and not as it is or will be. Of course, in some ways this is not too bad a thing since at least it reminds us of what has gone on before, and, as I said earlier this week, there is always a danger of repeating ourselves in research work.

My second point is that high-incidence aerodynamic design is particularly concerned with the careful tailoring of non-linear aerodynamic effects by various means. The basic choice of configuration is of course a major one of these, but I am really referring to the use of added devices such as strakes, the use of variable geometry and the adoption of special control techniques. I think that we have to face up to the need for compromise in the design process of such features, that is, if the overall aircraft performance is to be satisfactory in all respects. If I have another misgiving about our discussions this week, it would be that this rather important fact hasn't been stressed enough. In the range of missions for any aircraft or missile, the time spent performing high incidence flight is probably a very small part of the whole. Unfortunately, we can pay a heavy price in performance all down the line somewhere for this, and in cost as well. So let's get this special requirement for high incidence flight into perspective.

My third point follows on from this and concerns the high angles of incidence which arise in operational requirements. Intriguing as the solutions to non-linear aerodynamic problems at high incidence are as topics for research, we need to be quite sure that we are solving the right ones. There is little or no effort to spare these days. The concept of an aircraft which, for instance, has what has been called a "carefree manoeuvring" capability is very attractive operationally, but we do need to have the likely limits firmly in mind that the aircraft will have to fit. The ways an aircraft of the future will actually need to be used, have to be taken very good note of at the research level as well as at the final development stage. In aerial combat, for example, it has been argued that to use the whole aircraft as a "brake" (as someone said this week) to reduce the speed drastically in order to turn quickly and attempt to gain a firing opportunity, could be a fairly suicidal thing to do in a modern battle arena. The loss of speed, the long delay before regaining energy and the increased infra-red signal emitted as speed is regained (with reheat) all increase vulnerability tremendously. It is very questionable to my mind therefore whether in fact these very high incidences at very low speeds are really going to happen. Again, it could be that the present balance between the agility of the aircraft and the homing-agility capability of the weapon could change. This alone would completely alter the requirements for high incidences. More simply, we need to keep reminding ourselves of those fundamental limitations which arise from pilot tolerance, high g, vibration and structural stress that have been mentioned this week, and from engine characteristics that have certainly been emphasized strongly this afternoon. But all the same, as I have been looking at this screen this week, I have seen incidences as much as 90° referred to more than once: I have even seen 180° incidence mentioned on one occasion! What on earth can such extreme conditions mean?

Fourthly, I think that we must carefully distinguish in our minds the high-incidence conditions which arise, as it were, by mistake. These are very important and many references to the spin and other departure phenomena have been made this week: I am sure we remember these. If I may be provocative just once more, please let us remember that the aircraft of the future is going to have a very good fly-by-wire system installed in it and thus it will be possible to protect, with complete reliability I believe, the pilot from inadvertently getting out of control at high incidence. What I get out of this particular line of thought, is the need for rather more attention than has been evident this week to control aerodynamics at high incidences. No incidence-limiter or spin-prevention system can work unless the aerodynamic motivators remain effective, however non-linear their characteristics. We can probably cope with any non-linearity short of reversal, but we have got to have the force there. This is something else that I think has had rather cursory treatment this week.

These four points are all I wanted to say. I hope they give a direct lead to the following speakers.

Mr. Skow

Following Dr. Moss' very provocative comments, I am tempted to digress into a discussion of air combat tactics and the usefulness of fighter aircraft operating at high angles of attack, although this was not my intention. Perhaps Dr. Moss and myself could enter into that discussion later on this evening over a couple of beers. I think that most people will admit however, that there will always be a need to operate fighter aircraft near the limits of their controllability, wherever those limits may be. Certainly 180° angle of attack is too high, but 90° may not be in the possibly upcoming era of V-STOL aircraft.

I also fully agree with Dr. Moss that you have to have effective aerodynamic control concepts at these angles of attack for any sophisticated control system to be able to prevent loss of control.

My overall impression from this meeting is that I came in with a fairly good appreciation of the sensitivity of certain parameters to the high-angle-of-attack characteristics of airplanes, but, unfortunately, because of this conference my level of confidence in our understanding of the mechanisms which are responsible for this sensitivity has not been elevated, and I had hoped that it would be. Dr. Hunt, for instance, in his excellent paper, did very little to make me stop worrying about our inability to measure, repeatably, forebody side forces at high angles of attack. But as has been said before, the designers have been able to come up with "engineering" methods to deal with these experimental difficulties that we run into. The extreme sensitivity of the stability of vortices to small geometry variations causes one to be concerned that the manufacturing tolerances that are required to prevent asymmetric vortex bursting from a strake or a wing leading-edge extension (LEX) may be unattainable. We have some personal experience, by the way, on the F-5 aircraft in which an indentation on one side of the aircraft near the apex of the leading-edge extension (LEX) with a depth of less than 0.10 inch could cause the aircraft to have very violent departure tendencies at high incidences whereas, when the left and right leading-edge extensions were made symmetric, thereby generating vortices which burst symmetrically, the airplane is quite resistant to loss of control. A tenth of an inch at airplane scale is rather minute at wind tunnel model scale, so it really makes you wonder whether we can produce reliable, repeatable wind tunnel data at high angles of attack at all.

The experimental difficulties in measuring forebody side forces are well known, and I wish we understood the effect of roll angle on the observed magnitude. In the past, aerodynamicists ignored the existence of asymmetries growing from an asymmetric vortex pattern on forebody, claiming that these were wind tunnel and water tunnel phenomena and not full-scale aircraft phenomena. We really could not be blamed for ignoring it because of the terrible repeatability which the wind tunnel data showed. Now we do know that the asymmetric forces and moments exist, and we have developed a correlation with a few flight-test extracted numbers. What we need is an experimental technique which is reliable and repeatable.

One thing that hasn't been talked about is the range of compromises that we aerodynamicists are asked to make by our engineering colleagues in other disciplines, such as the radar people. Unfortunately, even though we may think that we fluid mechanicians are in a very sad state of affairs as regards our ability to predict some of these high incidence aerodynamic effects, compared to the electromagnetic people we are in tremendous shape. They cannot predict, by analysis, radar performance effects due to radome geometry variations that are required. They can only do it by experiment and those experiments tend to be quite expensive. Some of the attenuation methods that Dr. Jorgensen presented are interesting, but some are perhaps not practical from the airplane standpoint. Take forebody blunting, as an example. We found that the amount of blunting that is required to attenuate the asymmetries on the F-5F represents too large a penalty in terms of drag, and also radar performance is adversely affected by a blunted tip. Perhaps blunting, when we view the planform of the forebody only, will produce the same net effect. For strakes on a forebody, we have seen answers that were both positive and negative as regards directional stability, but generally always positive as regards the asymmetries. But here again, if you want to see a radar guy got upset, start talking about putting strakes on a radome.

Several people mentioned concepts for controlling of the forebody vortices, and I get quite excited about this idea for departure recovery, because I believe that there is a tremendous amount of power in the forebody vortex system. If we can develop a method of controlling it reliably, we could prevent a lot of loss of equipment and life.

As regards the strake or the leading-edge-extension vortex system, I think it would be good to review the design requirements for a good LEX/wing configuration. At low angles of attack but large side-slip angles, designers require a knowledge of the path of the vortex to be able to calculate effects when vortices come near to aerodynamic surfaces such as twin vertical tails. The departure from controlled flight that can be generated when a vortex switches from one side to the other of a vertical tail can be quite violent. At higher angles of attack the bursting characteristics of the vortex are the things that designers are the most interested in. A LEX geometry with a slow progression of the vortex burst point forward with angle of attack is desirable. Trying to tailor geometries to produce the most symmetric vortex bursting that we can have requires analytical methods that can adequately predict the bursting phenomena. As another bit of experience that indicates how important a knowledge of burst characteristics is, moving the vertical tail forward during the development of the YF-17 into a region of more favorable vortex flow represented quite an increase in directional stability even though the tail volume coefficient, of course, went down.

As a final comment, as designers, we have developed engineering methods that allow us to design configurations that operate fairly well at high angles of attack, even though we are dealing with quite complex aerodynamic problems. But in many ways we are working with blindfolds on, unless we can develop a really good understanding of the fundamental fluid mechanics of these problems. People are always asking us to make this smaller or that smaller or do with less stability margin. In order to be able to design controllable airplanes in the future, we are going to have to have a better understanding of the fluid mechanics at work. I would, therefore, encourage the fundamental fluid mechanicians to continue their work in order to develop this understanding further.

Dr. John

I am in rather a difficult situation because I am the last speaker, and most of what is on my list has been said already. I would, therefore, try to be brief in my explanations. I find myself very much in line with Dr. Richey about what he has said of high angles of attack. Of course, I am not in the same line as Mr. Moss, because I have been presenting a paper about high angles of attack, but on the other side, I don't want to go into a big discussion about tactics with Mr. Moss. That is something I will leave to military people. I also have the same position as Dr. Skow about forebody shapes, forebody strakes, and it is indeed a question of compromise with radar people. I am very happy that I have seen such a lot of work in this area going on, that there are shapes which we think we can live with. I think that I have to mention something which hasn't been mentioned yet, that is something which we have seen here, i.e., the possibility to stabilize vortices by spanwise blowing that is the upcoming new technique. It is very interesting, but there has to be much more work done in that area, especially on the engine side to provide those amounts of mass flow which are necessary to stabilize vortices. More or less, it is all going in the same direction that the controllability of aircraft in an area where, on the wings there is a very difficult kind of flow situation. On one side you have still a properly ordered vortex

flow and on the other side you might have completely stalled flow. That is the biggest problem in that area, and we had no direct contribution to this other than the people who tried to explain the new techniques about spanwise blowing. I am not denying here the need for theoretical work, I am very much in favor of this, because it provides the designer the possibility to make trade studies and to optimize configuration, but I would like to express here on this podium, that we have to be careful that we are not deviating in the direction where we are doing too much academic work, since I would like to remind you all that for the industry there is a product. We often have to make compromises, and we have to come up with a relatively quick solution.

Dr. McCroskey

Well, we have drawn a number of points out from these panelists, I think you will agree. We now open the RTD to comments from the floor. I repeat that it is very important that you identify yourself into the microphone so that we know to whom to send the remarks for the editing. The recording system is a very democratic process: it doesn't care how important you are or how much you have been visible during the meeting, it still has to have some identification through the microphone, so that we know who made the comments.

Dr. Jorgensen

It seems to me that there must be a continual balance between experimental and theoretical research. I think that there are many advances that we could point to that have been discovered first from experimental research, and then analytical theories have been formulated in order to fit the experimental discoveries or observations. I am somewhat concerned that some researchers may be placing too much hope on future computers to aid them in the discovery of aerodynamic phenomena. Let's not forget our wind tunnels and flight-test techniques.

I agree with Prof. Bogdonoff that we should make an attempt to understand the fundamental fluid mechanics of some of these high angle-of-attack problems. We should continue to try to correlate our knowledge of two-dimensional crossflow with observations in three-dimensional flow. I also strongly agree with what Mr. Skow has said concerning the need for aircraft design methodology, and I might add, even if it is based initially on experimental empiricism.

I think there was a real need for this symposium on high angle-of-attack aerodynamics, and I think this symposium has been outstanding in presenting a balance between experimental and theoretical research.

Dr. D. J. Peake

I believe it was in the late 1940's that investigations into three-dimensional boundary-layer flows and three-dimensional separated viscous flows in general started to be published. I recommend that one renew one's acquaintance with the 'classical texts' of some years ago on the value of topology of the surface shear stress trajectories (the orthogonal of which are lines of constant vorticity) and the synthesis of the external flow fields from an examination of these topology patterns. Terminology is explained adequately in Maskell 1955, Cooke and Hall 1962 and Lighthill 1963^x. In fact a recent paper in the Journal of Fluid Mechanics by J.C.R. Hunt et al^x is very illustrative in this respect. Perhaps, I might also add that, to this end an AGARDograph is in publication on three-dimensional separations and vortical flows at both low and high speeds, that lists many other pertinent and helpful references.

Dr. Hunt

One reaction of mine to the comments of the Panel is that they have been phrased almost entirely in terms of aircraft design. I do wonder if there is anybody here who is able to give us a reaction to the Symposium on behalf of the missile designer.

Mr. Washington

I was just counting through the number of papers. Out of 32 papers, there were only 8 that I can see which were directly related to missile design. High angle of attack is something that we are getting more and more into with missiles, and I would like to have seen more papers on this subject. However, the ones that we did see were very useful to us, in particular the flow visualization studies and design papers. Probably, missiles will be seeing higher maneuvers and higher angles of attack than aircraft. I agree with you that the missiles may have been somewhat in the secondary in this conference. Maybe this is something that ought to be talked about in future conferences.

Dr. Richey

It might be of note to the audience that the Flight Mechanics Panel has a Symposium on Missile Aerodynamics coming up in the Spring.

Dr. McCroskey

Yes, and a lecture series on that subject, too. Perhaps Prof. Young can elaborate on the details of that lecture series.

Prof. Young

On this question of the lecture series, I can only confirm that there will be such a series on the Aerodynamics of Missiles. I believe that it is planned for early next year.

Dr. McCroskey

The Missile Aerodynamics course is to be given in Ankara, Turkey, 5-6 March; in Rome, Italy, 8-9 March; and at the von Karman Institute in Belgium, 12-16 March 1979.

- ^{x1}. Maskell, E.C., "Flow Separation in Three-Dimensions", RAE Aero. Rept. 2565, Nov. 1955.
- ^{x2}. Cooke, J. C., Hall, M. G., "Boundary Layers in Three Dimensions", Prog. in Aero. Sci., Vol. 2, 1962, pp. 222-282.
- ^{x3}. Lighthill, M. J., "Attachment and Separation in Three-Dimensional Flow", Section II 2-6 of 'Laminar Boundary Layers', Ed. by L. Rosenhead, Oxford Univ. Press, 1963, pp. 72-82.
- ^{x4}. Hunt, J. C. R. et al, "Kinematical Studies of the Flows Around Free or Surface-Mounted Obstacles; Applying Topology to Flow Visualization", Jour. Fluid Mech., Vol. 86, Part 1, 1978, pp. 179-200.

Prof. Young

I found the comments of the panel stimulated my reminiscences. I was particularly stimulated by what Prof. Bogdonoff had to say about the readiness with which one can misinterpret what the flows are doing in depth from looking solely at surface flows. I remember that when we first constructed a delta-shaped aircraft for research purposes, I think that was the AVRO 707, after it had been flying about a year some surface tufts were put on it and the pilot who flew it came down looking very ashen and white. He said, "My God, if I had known what the flow was doing on that wing, I would never have flown it!".

Turning to some of the other points that have been made, I find myself generally in agreement with most of them. I would particularly support the point that one can oversimplify some of the terms that we use. We talked about vortices and tended in the process to see them as the nice simple potential flow vortices described in text books, whereas in fact, they are regions of fairly complicated vorticity with marked axial flows. One has to bear that in mind. The question of separation, too, is often oversimplified, mainly because of our two-dimensional experience, but again if I may reminisce, I remember when we first studied the flow over slender delta wings and noticed the nicely-ordered separation that developed from the leading edges that Dr. Kuchemann said that we must now learn to live with separation. In a sense, what this meeting has been about is that process of cohabitation that we have experienced in the last few years. On the whole it seems that this process is moderately successful, but there are still a lot of problems left.

A number of the panelists have very briefly mentioned the question of controllability of the aircraft; this, in my mind needs a little more emphasis than it was given during the course of this Symposium. Perhaps controllability is more important than stability. If you haven't got the ability to control the aircraft, then there is very little you can do with it. If little has been said during the course of this Symposium about controllability, nevertheless, I can say that we plan that the next Symposium will deal with the aerodynamics of control and that should help to fill an important gap. At present, I have the impression that we are learning to live with separations, particularly in the form of vortical flows, in a rather interesting, exciting way. I think this process will improve as both the fluid mechanics and the flight dynamics people learn to understand each other more and more.

Monsieur Perrier

Just two remarks. The first is that in industry, we have many constraints to take into account, the shape of radar for example. When we speak of the problem of the effect of unsteady separation on Gy, we speak of an old problem; in the past we have coped with problems like that at the stall, and it was a long time in the design development of aircraft without slats to cope with unsymmetrical separation at the stall. I hope that we found solutions for that. The other comment that I wish to make is that it seems to me that a lot of work is to be done by fundamental fluid mechanics people. For example, we have not at all seen anything on what sort of Reynolds stress tensor we can put in order to make a modelization of turbulence inside the vortex. There is nothing at all, and it is surprising because we can do computations to verify them. There are a certain number of problems like that, so the question is: how long the people in industry can continue to make wind tunnel tests and wind tunnel tests without a guide by fundamental fluid mechanics people.

Prof. Bogdonoff

I would like to point out that AGARD is again one step ahead. Next fall, there is going to be a meeting at Den Hague, by this Panel, on turbulence, turbulent structures, and shear layers. It is our attempt to bring some of the new ideas in this area together. This is clearly needed if we are going to make rapid progress, for example, in using the full Navier-Stokes equations and some turbulence model in the solutions to real problems. Hopefully, the meeting will be of some help to the designers who are trying to put together computational techniques.

Dr. McCroskey

I must now exercise the unpleasant task of the panel moderator to close this off because of the late hour. I am hardly in any position to add to what has been said this afternoon. I would just like to note that, as you know, aircraft and missiles are flying at high angle of attack, and sometimes they fly there in a controlled manner. Furthermore, the designers of the vehicles on the drawing boards today, do in fact have better tools to work with than those who designed the aircraft that you saw the first day; but it is clear that we need to understand better the primary fluid dynamic phenomena. It is necessary to develop different and certainly more reliable design methods. The Program Committee sincerely hopes that what we have put together for this Symposium will make a contribution to the high alpha technology. We also hope that all of you as participants will share with your colleagues, and also with your management, what you have learned here. On the other hand, we would prefer that you direct your criticisms to the Panel. In fact, we want your criticisms so that we can plan future meetings to serve the aeronautical community better. The final announcement is that there will be a conference proceedings as I have said. The authors are requested to have their manuscripts to Mr. Rollins at AGARD headquarters by the first of November. Now Mr. Lloyd Jones, who is Chairman of the Fluid Dynamics Panel, will make his closing remarks.

Mr. Jones

Ladies and Gentlemen. We have come to the end of three rather long days of discussion in this room, and I promise to extend that time as little as possible. I said at the outset, three days ago, that it was reassuring to the Fluid Dynamics Panel to see so many people here for this meeting. It seems to me doubly reassuring, that at the end of the third day, we have nearly as many as when we began. I recognize that the location, with not too many external distractions, probably had an influence on that, but I do believe also because of the very high quality of the papers given here on this topic of extreme current interest, and because of the interesting summary activities that these factors have had an even larger influence on people staying to the very end. I would like to thank Dr. McCroskey and the Program Committee for the excellent job that they did in putting this meeting together. I would like to thank those contributing to the open discussion and the participants in this RTD, because I think it is extremely important that we examine the views that are presented.

The active participation by the attendees during the meeting is, of course, what makes these meetings most useful, and for that I thank you all. I would like also at this time to thank the Flight Mechanics Panel for their participation in this meeting, for their participation on the Planning Committee and for the attendance of M. Poisson-Quinton, representing that Panel. Once again, we owe thanks to our

hosts for their considerable efforts in the arrangements for this meeting; to the Norwegian Defense Research Establishment for providing that and particularly to Mr. Fred Kheuman, who acted as the coordinator for this meeting, and to members working with him at the Defense Research Establishment, Mr. Terje Kvisterdy and Mr. Bjørn Thorvaldsen, who have been exceedingly helpful with this meeting. I thank also Mrs. Liv Hovden from that organization and Melle Rivault from the AGARD staff, who so successfully managed the desk outside. I would like particularly to thank the interpreters, because I understand that trying to interpret and to keep up with enthusiastic experimenters and theoreticians when they are talking about their most recent work sometimes becomes quite a difficult task.

One other matter, I would like at this time to thank Mr. Chlassiou and Mr. Treff from SHAPE, who have been running the audio system here. I think we owe them double thanks for the extremely smooth and timely recovery when we exceeded the C_L max of their audio system.

Ladies and Gentlemen, I hope that you find that your attendance at this meeting will be useful to you in the future as you reflect back on the proceedings and as you receive the printed results. With that I declare the meeting adjourned.

REPORT DOCUMENTATION PAGE			
1. Recipient's Reference	2. Originator's Reference	3. Further Reference	4. Security Classification of Document
	AGARD-CP-247	ISBN 92-835-0230-2	UNCLASSIFIED
5. Originator	Advisory Group for Aerospace Research and Development North Atlantic Treaty Organization 7 rue Ancelle, 92200 Neuilly sur Seine, France		
6. Title	HIGH ANGLE OF ATTACK AERODYNAMICS		
7. Presented at	the Fluid Dynamics Panel Symposium held at the Park Hotel, Sandfjord, Norway, 4-6 October, 1978.		
8. Author(s)/Editor(s)	Various		9. Date January 1979
10. Author's/Editor's Address	Various		11. Pages 558
12. Distribution Statement	This document is distributed in accordance with AGARD policies and regulations, which are outlined on the Outside Back Covers of all AGARD publications.		
13. Keywords/Descriptors			
Aerodynamic characteristics Angle of attack Flight control		Design criteria Mathematical models Air intakes	
14. Abstract			
<p>↙ The Symposium was organized because of the continuing need for design data and principles relevant to the flight of aircraft and missiles at high angles of attack and the substantial efforts devoted to vehicles capable of controlled flight in that regime.</p> <p>Four sessions were held on (1) Studies of Configurations of Practical Application (10 Papers); (2) Mathematical Modelling and Supporting Investigations (12 Papers); (3) Design Methods (7 Papers), and (4) Air Intakes (2 Papers). Eight additional short presentations on these subjects are also documented.</p> <p>A Round Table Discussion on the state-of-art and recommendations for continuing effort in high-angle-of-attack aerodynamics is also documented in the report. ↗</p>			

<p>AGARD Conference Proceedings No.247 Advisory Group for Aerospace Research and Development, NATO HIGH ANGLE OF ATTACK AERODYNAMICS Published January 1979 558 pages</p> <p>The Symposium was organized because of the continuing need for design data and principles relevant to the flight of aircraft and missiles at high angles of attack and the substantial efforts devoted to vehicles capable of controlled flight in that regime.</p> <p>Four sessions were held on (1) Studies of Configurations of Practical Application (10 Papers); (2) Mathematical Modelling and Supporting Investigations</p> <p>P.T.O.</p>	<p>AGARD-CP-247</p> <p>Aerodynamic characteristics Angle of attack Flight control Design criteria Mathematical models Air intakes</p>	<p>AGARD Conference Proceedings No.247 Advisory Group for Aerospace Research and Development, NATO HIGH ANGLE OF ATTACK AERODYNAMICS Published January 1979 558 pages</p> <p>The Symposium was organized because of the continuing need for design data and principles relevant to the flight of aircraft and missiles at high angles of attack and the substantial efforts devoted to vehicles capable of controlled flight in that regime.</p> <p>Four sessions were held on (1) Studies of Configurations of Practical Application (10 Papers); (2) Mathematical Modelling and Supporting Investigations</p> <p>P.T.O.</p>	<p>AGARD-CP-247</p> <p>Aerodynamic characteristics Angle of Attack Flight control Design criteria Mathematical models Air intakes</p>
<p>AGARD Conference Proceedings No.247 Advisory Group for Aerospace Research and Development, NATO HIGH ANGLE OF ATTACK AERODYNAMICS Published January 1979 558 pages</p> <p>The Symposium was organized because of the continuing need for design data and principles relevant to the flight of aircraft and missiles at high angles of attack and the substantial efforts devoted to vehicles capable of controlled flight in that regime.</p> <p>Four sessions were held on (1) Studies of Configurations of Practical Application (10 Papers); (2) Mathematical Modelling and Supporting Investigations</p> <p>P.T.O.</p>	<p>AGARD-CP-247</p> <p>Aerodynamic characteristics Angle of attack Flight control Design criteria Mathematical models Air intakes</p>	<p>AGARD Conference Proceedings No.247 Advisory Group for Aerospace Research and Development, NATO HIGH ANGLE OF ATTACK AERODYNAMICS Published January 1979 558 pages</p> <p>The Symposium was organized because of the continuing need for design data and principles relevant to the flight of aircraft and missiles at high angles of attack and the substantial efforts devoted to vehicles capable of controlled flight in that regime.</p> <p>Four sessions were held on (1) Studies of Configurations of Practical Application (10 Papers); (2) Mathematical Modelling and Supporting Investigations</p> <p>P.T.O.</p>	<p>AGARD-CP-247</p> <p>Aerodynamic characteristics Angle of attack Flight control Design criteria Mathematical models Air intakes</p>

<p>(12 Papers); (3) Design Methods (7 Papers), and (4) Air Intakes (2 Papers). Eight additional short presentations on these subjects are also documented.</p> <p>A Round Table Discussion on the state-of-art and recommendations for continuing effort in high-angle-of-attack aerodynamics is also documented in the report.</p> <p>Papers presented and discussions from the Fluid Dynamics Panel Symposium held at the Park Hotel, Sandefjord, Norway, 4-6 October, 1978.</p> <p>ISBN 92-835-0230-2</p>	<p>(12 Papers); (3) Design Methods (7 Papers), and (4) Air Intakes (2 Papers). Eight additional short presentations on these subjects are also documented.</p> <p>A Round Table Discussion on the state-of-art and recommendations for continuing effort in high-angle-of-attack aerodynamics is also documented in the report.</p> <p>Papers presented and discussions from the Fluid Dynamics Panel Symposium held at the Park Hotel, Sandefjord, Norway, 4-6 October, 1978.</p> <p>ISBN 92-835-0230-2</p>
<p>(12 Papers); (3) Design Methods (7 Papers), and (4) Air Intakes (2 Papers). Eight additional short presentations on these subjects are also documented.</p> <p>A Round Table Discussion on the state-of-art and recommendations for continuing effort in high-angle-of-attack aerodynamics is also documented in the report.</p> <p>Papers presented and discussions from the Fluid Dynamics Panel Symposium held at the Park Hotel, Sandefjord, Norway, 4-6 October, 1978.</p> <p>ISBN 92-835-0230-2</p>	<p>(12 Papers); (3) Design Methods (7 Papers), and (4) Air Intakes (2 Papers). Eight additional short presentations on these subjects are also documented.</p> <p>A Round Table Discussion on the state-of-art and recommendations for continuing effort in high-angle-of-attack aerodynamics is also documented in the report.</p> <p>Papers presented and discussions from the Fluid Dynamics Panel Symposium held at the Park Hotel, Sandefjord, Norway, 4-6 October, 1978.</p> <p>ISBN 92-835-0230-2</p>

B3
4

AGARD

NATO OTAN

7 RUE ANCELLE · 92200 NEUILLY-SUR-SEINE
FRANCE

Telephone 745.08.10 · Telex 610176

DISTRIBUTION OF UNCLASSIFIED
AGARD PUBLICATIONS

AGARD does NOT hold stocks of AGARD publications at the above address for general distribution. Initial distribution of AGARD publications is made to AGARD Member Nations through the following National Distribution Centres. Further copies are sometimes available from these Centres, but if not may be purchased in Microfiche or Photocopy form from the Purchase Agencies listed below.

NATIONAL DISTRIBUTION CENTRES

BELGIUM

Coordonnateur AGARD VSL
Etat-Major de la Force Aérienne
Quartier Reine Elisabeth
Rue d'Evere, 1140 Bruxelles

CANADA

Defence Scientific Information Service
Department of National Defence
Ottawa, Ontario K1A 0Z2

DENMARK

Danish Defence Research Board
Østerbrogades Kaserne
Copenhagen Ø

FRANCE

O.N.E.R.A. (Direction)
29 Avenue de la Division Leclerc
92 Châtillon sous Bagneux

GERMANY

Zentralstelle für Luft- und Raumfahrt-
dokumentation und -information
c/o Fachinformationszentrum Energie,
Physik, Mathematik GmbH
Kernforschungszentrum
7514 Eggenstein-Leopoldshafen 2

GREECE

Hellenic Air Force General Staff
Research and Development Directorate
Holargos, Athens, Greece

ICELAND

Director of Aviation
c/o Flugrad
Reykjavik

ITALY

Aeronautica Militare
Ufficio del Delegato Nazionale all'AGARD
3, Piazzale Adenauer
Roma/EUR

LUXEMBOURG

See Belgium

NETHERLANDS

Netherlands Delegation to AGARD
National Aerospace Laboratory, NLR
P.O. Box 126
Delft

NORWAY

Norwegian Defence Research Establishment
Main Library
P.O. Box 25
N-2007 Kjeller

PORTUGAL

Direcção do Serviço de Material
da Força Aérea
Rua da Escola Politécnica 42
Lisboa
Attn: AGARD National Delegate

TURKEY

Department of Research and Development (ARGE)
Ministry of National Defence, Ankara

UNITED KINGDOM

Defence Research Information Centre
Station Square House
St. Mary Cray
Orpington, Kent BR5 3RE

UNITED STATES

National Aeronautics and Space Administration (NASA)
Langley Field, Virginia 23365
Attn: Report Distribution and Storage Unit

THE UNITED STATES NATIONAL DISTRIBUTION CENTRE (NASA) DOES NOT HOLD STOCKS OF AGARD PUBLICATIONS, AND APPLICATIONS FOR COPIES SHOULD BE MADE DIRECT TO THE NATIONAL TECHNICAL INFORMATION SERVICE (NTIS) AT THE ADDRESS BELOW.

PURCHASE AGENCIES

Microfiche or Photocopy

National Technical
Information Service (NTIS)
Port Royal Road
Springfield
Virginia 22161, USA

Microfiche

Space Documentation Service
European Space Agency
10, rue Mario Nikis
75015 Paris, France

Microfiche

Technology Reports
Centre (DTI)
Station Square House
St. Mary Cray
Orpington, Kent BR5 3RE
England

Requests for microfiche or photocopies of AGARD documents should include the AGARD serial number, title, author or editor, and publication date. Requests to NTIS should include the NASA accession report number. Full bibliographical references and abstracts of AGARD publications are given in the following journals:

Scientific and Technical Aerospace Reports (STAR)
published by NASA Scientific and Technical
Information Facility
Post Office Box 8757
Baltimore/Washington International Airport
Maryland 21240, USA

Government Reports Announcements (GRA)
published by the National Technical
Information Services, Springfield
Virginia 22161, USA



Printed by Technical Editing and Reproduction Ltd
Harford House, 7-9 Charlotte St., London W1P 1HD

ISBN 92-835-0230-2